The Dissertation Committee for Anand Subhash Nagoo Certifies that this is the approved version of the following dissertation:

Pipe Fractional Flow Theory: Principles and Applications

Committee:

Mukul M. Sharma, Supervisor

Roger T. Bonnecaze

Thomas F. Edgar

Gary T. Rochelle

Larry W. Lake

Pipe Fractional Flow Theory: Principles and Applications

by

Anand Subhash Nagoo, B.Sc., M.S., M.S.

Dissertation

Presented to the Faculty of the Graduate School of

The University of Texas at Austin

in Partial Fulfillment

of the Requirements

for the Degree of

Doctor of Philosophy

The University of Texas at Austin

December 2013

To Jacqueline, AJ and Jax

Acknowledgements

I would first like to sincerely thank my advisor, Professor Sharma. Without his unflinching support, scholastic guidance and belief in my abilities, this work would not have been possible. His first role in this research started in early 2008 when he planted the question in my mind of whether the averaged (1D) multiphase pipe flow problem could be approached in a similar way to how porous media investigators looked at their averaged multiphase flows. Since then, his constant questioning and challenging of some of the most basic ideas in this subject was instrumental in the development of the key insights of this work. At the same time, his leadership style afforded me the space and flexibility to independently pursue investigations and to initiate new lines of thinking. It is this kind of collaboration that led me to ultimately connect the core analytical principles of this work in a structured way.

Next, I am grateful for the insights and feedback on this research provided by my dissertation committee members: Professors R. T. Bonnecaze, T. F. Edgar, G. T. Rochelle and L. W. Lake. Indeed, there are outstanding (world-class) Professors in the chemical and petroleum engineering departments from whom I have learnt quite a lot. There are also many friends and colleagues in these departments (and in particular, Professor Sharma's research group) that have made my journey quite enjoyable.

Aside from the academic departments, the University of Texas's Interlibrary Loan (ILL) team members were quite important in helping me to track down and acquire large amounts of older classic literature in this subject. This would have been a very difficult task without their help. Additionally, I am thankful for Mr. T. J. Bowell's internship with me, which contributed significantly towards the benchmarking of the models developed

in this work with field data and current industry-standard software, respectively, in the oil, gas, chemical and geothermal industries.

Outside of the university, special acknowledgements are due to Emeritus Professor P. L. Spedding of the University of Belfast, Mr. M. Shippen of Schlumberger and Professor A. J. Ghajar of Oklahoma State University. These multiphase pipe flow investigators proved to be unique among the rest of the numerous investigators in this subject that I personally contacted over many years. They communicated in an open, unbiased, inclusive and uncompetitive manner on several topics with me – which I believe is important for encouraging new investigators (and thus advancing new approaches) in this field. I am also grateful to the university professors and industry professionals who were kind enough to respond to my clarification questions concerning their published experiments and models. Not forgetting the early years, I wish to kindly thank my past advisors at Penn State University (Professor M. A. Adewumi) and Stanford University (Professor K. Aziz) for introducing me to this subject.

Finally, the tremendous love and support of my wife Jacqueline, and two sons, AJ and Jax, are the driving forces that powered me. Throughout this time (and in the case of Jacqueline, much before), they have been sacrificing just as much as I have towards our shared dreams and goals. I would also like to thank my father, mother (deceased) and family for their love and unshakable support and for providing the environment and many opportunities that has eventually led to this accomplishment.

Pipe Fractional Flow Theory: Principles and Applications

Anand Subhash Nagoo, Ph.D.

The University of Texas at Austin, 2013

Supervisor: Mukul M. Sharma

The contribution of this research is a simple, analytical mathematical modeling framework that connects multiphase pipe flow phenomena and satisfactorily reproduces key multiphase pipe flow experimental findings and field observations, from older classic data to modern ones. The proposed unified formulation presents, for the first time, a reliably accurate analytical solution for averaged (1D) multiphase pipe flow over a wide range of applications.

The two new fundamental insights provided by this research are that: (a) macroscopic single-phase pipe flow fluid mechanics concepts can be generalized to multiphase pipe flow, and (b): viewing and analyzing multiphase pipe flow in general terms of averaged relative flow (or *fractional flow*) can lead to a unified understanding of its resultant (global) behavior.

The first insight stems from our finding that the universal relationship that exists between pressure and velocity in single-phase flow can also be found equivalently between pressure and relative velocity in multiphase flow. This eliminates the need for a-priori flow pattern determination in calculating multiphase flow pressure gradients.

The second insight signifies that, in general, averaged multiphase flow problems can be sufficiently modeled by knowing only the averaged volume fractions. This proves that flow patterns are merely the visual, spatial manifestations of the in-situ velocity and

volume fraction distributions (the quantities that govern the transport processes of the flow), which are neatly captured in the averaged sense as different fractional flow paths in our proposed fractional flow graphs.

Due to their simplicity, these new insights provide for a deeper understanding of flow phenomena and a broader capability to produce quantitative answers in response to what-if questions. Since these insights do not draw from any precedent in the prior literature, a science-oriented, comprehensive validation of our core analytical principles was performed. Model validation was performed against a diverse range of vapor-liquid, liquid-liquid, fluid-solid and vapor-liquid-liquid applications (over 74,000 experimental measurements from over 110 different labs and over 6,000 field measurements). Additionally, our analytical theory was benchmarked against other modeling methods and current industry codes with identical (unbiased), named published data.

The validation and benchmarking results affirm the central finding of this research – that simple, suitably-averaged analytical models can yield an improved understanding and significantly better accuracy than that obtained with extremely complex, tunable models. It is proven that the numerous, continuously interacting (local) flow microphysics effects in a multiphase flow can be (implicitly) accounted for by just a few properly validated (global) closure models that capture their net (resultant) behavior.

In essence, it is the claim of this research that there is an underlying simplicity and connectedness in this subject if looking at the resultant macroscopic (averaged) behaviors of the flow. The observed coherencies of the macroscopic, self-organizing physical structures that define the subject are equivalently present in the macroscopic mathematical descriptions of these systems, i.e., the flow-pattern-implicit, averaged-equations mixture models that describe the collective behavior of the flowing mixture.

Table of Contents

List of Tables

List of Figures

Chapter 1 – Problem Redefinition and Standardization

1.1 INTRODUCTION

1.1.1 Principal Insights of the Research

A mixture of two or more flowing phases in a stationary bounding medium occurs ubiquitously in various industries and is of considerable interest and importance. *Pipe flow* is a branch of fluid mechanics that represents one kind of multiphase flow in which one phase (the bounding medium at rest) completely encloses the adjoining phase or phases flowing through it. Bounded flows in which the adjoining flowing phases are not completely enclosed by a closed conduit represent another kind of multiphase flow (e.g. flow past a finite body, action of wind on ocean waves, etc.). Examples of closed conduits include pipes, channels, ducts, enclosed passages and tubes. The adjoining phases, flowing simultaneously in a multiphase mixture, can be any combination of vapor-like, liquid-like and solid-like substances.

In the general sense, pipe flow will include a set of scenarios in which one or more of the phases present do not flow. The phases that do not flow are the main source of the velocity gradients (and thus momentum transport, kinetic energy dissipation and flow regimes) in the adjoining phases that do flow. This is because the transport of quantities like momentum and energy occur in the direction from points in the flow field where velocity is large to those where it is small. We call this a *flow relative to no-flow* scenario. Indeed, a single-phase pipe flow is one special case of the general multiphase pipe flow problem – the fluid being a moving phase continually exchanging momentum and energy with a stationary phase, the pipe. In Bird et al., 2002 (or BSL), the multiphase language used to describe this scenario is *interphase* transport, meaning the macroscopic transport of mass, momentum, energy and entropy between a flowing phase

within a system and a bounding surface of that system (usually a stationary phase). Some investigators share this *generalist* view that, without further specification, multiphase pipe flow encompasses nearly all of fluid mechanics (e.g., Prosperetti and Trygvasson, 2007). In contrast, other investigators view multiphase pipe flow as a field that is distinct from applied fluid mechanics (e.g., Theophanous and Dinh, 2003). From the preceding discussion, specification is clearly necessary in multiphase pipe flow. In the sense in which this field of study is practically encountered at the industrial level in terms of averaged descriptions (as in this work), it is defined by a macroscopic *system* comprising two or more flowing phases which are completely enclosed by a stationary solid-phase (the boundary that is the pipe).

The invocation of BSL as the first reference of this work is rather purposeful, meant to highlight our first principal idea that BSL is an ideal starting point for an averaged description of multiphase flow. This is not an intuitive idea. As we will show, gaining a deeper insight into the well-validated, macroscopic single-phase fluid mechanics concepts as they are presented in BSL, will allow a generalization to the macroscopic multiphase fluid mechanics concepts that are presented in this work. Another principal idea overtly referenced above, is the concept of relative flow – which we will show, is a pathway to understanding multiphase flow behavior in terms of unifying (or generalized) principles. We will return to these ideas later in this work. For now, they serve only to introduce up front the <u>two new fundamental insights of this research</u>:

I. Macroscopic single-phase pipe flow fluid mechanics concepts can be generalized to multiphase pipe flow.

II. Viewing and analyzing multiphase pipe flow in general terms of averaged relative flow (or *fractional flow* in our language) can lead to a unified understanding of its resultant (global) behavior.

The first insight stems from our finding that there are no further immeasurable quantities that must be introduced to an averaged (1D) multiphase pipe flow problem than is already present in the corresponding single-phase pipe flow problem. This insight is summarized by stating that the universal relationship that exists between pressure and velocity in averaged single-phase flow (via the momentum balance equation for the flowing single phase), also exists in an equivalent way between pressure and relative velocity in averaged multiphase flow (via our momentum balance equation for the flowing multiphase mixture – Eqn. 5 of Section 2.2.2). This universal relationship eliminates the need for a-priori flow pattern determination for predicting multiphase flow pressure gradients.

The second insight signifies that averaged multiphase flow problems can be sufficiently modeled by knowing only averaged volume fractions (or equivalently, relative velocities) in the general case, or, by knowing only averaged volume and entrainment fractions in the special case of flows with multi-directional inter-phase entrainment. This insight is summarized by stating that a complete analytical solution to an averaged multiphase pipe flow is for the first time achieved whilst honoring the same limitations as the analytical solution to the corresponding single-phase pipe flow.

In this work, we demonstrate with overwhelming experimental evidence, that in averaged descriptions of multiphase pipe flow, flow patterns merely represent the different possible visual manifestations (spatial configurations) of in-situ velocities and volume fractions. This means that the impact of flow patterns both within and at the

boundaries of the flow field is *already captured* in these quantities. It is the velocity and volume fraction cross-sectional distributions as well as their associated space- and time-averaged values (which represent the net of competing microphysical flow interactions) that mathematically capture the prevailing state of agglomeration of the flow field bodies. These are the quantities that play determining roles in the transport processes of the flow. This is why flow patterns strongly affect the mass, momentum, energy and entropy transfer rates, and all other conceivable factors of interest in a multiphase flow problem – not because of what flow field morphology an investigator observes and *decides* to report – but because of the changes in the velocities and volume fractions associated with each physical flow pattern.

The combined insights described above do not draw from any precedent in the prior multiphase pipe flow literature. Together, they represent a much simpler description and logical re-structuring of the most basic ideas used to describe averaged multiphase flows. Additionally, due to their simplicity, these insights provide for a deeper understanding of multiphase pipe flow phenomena and a broader capability to produce quantitative answers in response to what-if questions. Indeed, the questions raised by this research are enormous – this is because our discovery of a universal, analytical mixture momentum balance equation signifies that prior calculations of multiphase flow pressure gradient may now be re-examined from the point of view of this universal relationship.

Lastly, in light of the potential high impact of this research and since there are no prior works directly relating to the combined insights above, it was decided to undertake a major, science-oriented, comprehensive validation of the core principles presented in this work in the main classes of problems already familiar to multiphase pipe flow investigators. This validation is discussed in Section 1.3.5.

1.1.2 Outline of Chapters

Chapters 2 and 3 represent the translation of our new ideas into simple physical arguments and mathematical (analytical) models – which we collectively refer to as the "Pipe Fractional Flow Theory". The core principles of the Pipe Fractional Flow Theory are identified as underlined sub-title headings in these two chapters. The validation and prediction performance of the Pipe Fractional Flow Theory in a wide range of vapor-liquid flow applications are presented in Chapter 4. The validation and prediction performance of the Pipe Fractional Flow Theory in liquid-liquid and fluid-solid applications constitute Chapter 5. Comparisons of the performance of the Pipe Fractional Flow Theory for complex flow applications (e.g., transient, non-Newtonian, three-phase, perforated pipes, etc.) are given in Chapter 6. Flow applications in specialized industries (namely, Petroleum and Geothermal) are highlighted in Chapter 7 to show the extensibility and ease-of-applicability of the Pipe Fractional Flow Theory both in partially-controlled field-scale tests as well as in actual, uncontrolled, in-operation field conditions.

Finally, a quite unique and important aspect of this research is the unbiased benchmarking comparisons of the results of the Pipe Fractional Flow Theory against other existing modeling methods and available ("best practice") industry codes in all of the Chapters. Not only do these comparisons highlight the performance of available modeling methods amongst themselves, but more pointedly in regards to this work, they also quantify the computational performance of the Pipe Fractional Flow Theory against the available modeling methods. In these comparisons, named (i.e., cross-referable), wide-ranging experimental data are chosen from the published (i.e., peer-reviewed and publicly-accessible) literature as unbiased, identical input into all of the models. This benchmarking feature, not only provides a long-overdue, independent assessment of

practical code capabilities in different industries, but also clearly demonstrates the significant increase in accuracy when using a hypothesis-based research approach (such as found in this work), proper model validation and conceptually simpler models.

1.1.3 Central Theme of the Research

The results from the benchmarking comparisons discussed above ratify the central theme of this work – that simple, properly validated (high fidelity) averaged-equations models can yield a deeper understanding and far better accuracy than obtained with extremely complex, tunable models.

In the latter case above, a major problem plaguing the very large, complex multi-physics models is that they often contain a multitude of closure relations none of which are derived from properly controlled experiments, i.e., properly isolated phenomena in which a particular influence is quantified without changing other properties. Therefore, there are no elementary tests designed to directly quantify their usage in a wide range of conditions. This problem is avoided by use of the simple, self-consistent models because careful model falsification and proper validation with experiments are requisites that underlay their development.

Furthermore, by comparing the results of different modeling methods over a wide range of conditions, the central argument proffered by the proponents of the very large, complex multi-physics models (i.e., that several effects need to be explicitly accounted for with new closure relations or more conservation equations) is directly countered by the simple, self-consistent models. The provable counter-argument (provided in this work) is that the numerous, competing, interacting, local flow microphysics effects can be (implicitly) accounted for by just a few simple and properly validated (global) closure models that capture their collective (resultant) behavior.

1.1.4 Research Objective

The purpose of this research is to show how one simple mathematical (averaged-equations) modeling framework, derived from the two basic insights in Section 1.1.1, can amalgamate and reliably reproduce key experimental findings and field observations of different kinds of averaged multiphase flow problems across time periods (from older classic data to modern ones) and across disciplines. As stated, this objective requires further qualification – our primary goal is to show *how* experimental averaged flow data can be reproduced using an analytical, averaged-equations modeling framework, i.e., the Pipe Fractional Flow Theory. As a consequence of answering the question of *how*, in many instances we further provide qualitative explanations of *why* the Pipe Fractional Flow Theory works so well in such a diverse set of seemingly different scenarios, and *when* it will fail. The question of *what* specific requirements are needed by the Pipe Fractional Flow Theory to provide solutions for given sets of conditions, is generally answered by the numerous practical applications of the theory for different types of problems in the subsequent chapters of this work.

1.2 SIGNIFICANCE OF MULTIPHASE PIPE FLOW

1.2.1 Engineering Practice

Examples of multiphase pipe flow are prevalent among many engineering disciplines and hold enormous economic significance. In chemical engineering (*process systems*), multiphase flow is found in process equipment such as pipelines, risers, tubular reactors, absorption towers, boilers, condensers, evaporators, fossil-fuel/solids-fuel processing devices and other unit operations. The design of these facilities require methods for predicting important integrative variables such as axial pressure gradient and in-situ phase volume fraction (alternatively called mean phase content, holdup, void

fraction, saturation, averaged volumetric concentration, etc.). The important role of improved modeling of the hydrodynamics of multiphase flow reactors in these facilities is well recognized, as noted for example by Sundaresan (2000): “Few things are more central to chemical engineering than multiphase flow chemical reactors; they are used in industry to produce a variety of chemicals, where economy of scale remains the driving factor”.

In petroleum and geo-systems engineering (*energy systems*), multiphase flow occurs during the transportation of crude oil, brine, natural gas, formation sand, liquid slurries, hydrates and coal granules. These multi-component, multiphase mixtures are produced through various types of closed conduits at all inclinations, at all scales and in many different scenarios, e.g., in pore networks, natural gas transmission and distribution pipelines, surface flow-lines, trunk-lines, production casing/tubing, risers, perforated wellbores, etc. Indeed, the justification for better knowledge and understanding in multiphase flow is due to both the qualitative and quantitative impacts that this area of technology holds in energy systems, as evidenced in the following quotes:

I. “The concept of multiphase flow is of significant importance in the search for more cost effective methods related to development and exploitation of offshore oil and gas fields. It is probably one of the most promising means for the oil and gas industry to meet the various challenges associated with low oil prices, deep water depths and iceberg-infested waters” – Hansen (1987).

II. “As manager of the BP Multiphase Flow Research and Development programme I confirm that a recent study conducted by ourselves estimated that improved understanding of slugging flows could save BP approximately $320 million over the next ten years. Slugging is one of the most significant

issues facing the design and operation of pipelines and risers carrying unprocessed multiphase fluids" – Fairhurst (2010).

III. "Understanding multiphase flow underlies the design of just about every piece of equipment in oil and gas industry, from transportation networks to subsea installations" – Biberg (2012).

In the nuclear and geothermal engineering (*power systems*), multiphase flow is important for plant reactor design, commissioning, incident analysis and safety, e.g. boiling single-component coolant flow and plant operating efficiency.

In aerospace engineering (*variable-gravity systems*), multiphase flow is important in refueling activities, advanced life support systems, transfer of cryogenic fluids, etc. A state-of-the-art review of averaged-equations modeling for two-phase flows in advanced life support systems (reduced and partial gravity systems) can be found in the NASA report of Balasubramaniam et al. (2006).

There are many other applications in which multiphase flow is relevant (pg. 1 of Ishii and Hibiki, 2006) – as examples – in heat transfer systems, transport systems, lubrication systems, micro-fluidics systems, environmental control, food processing, geo-meteorological systems and biological systems. Reviews of the significance of multiphase pipe flow in engineering systems are abundant in the literature (e.g. Loth, 2010, Hewitt, 2008, Brennen, 2005, Lareo et al., 1997, Heywood and Cheng, 1984, Hetsroni, 1982).

In view of the sundry multiphase pipe flow applications in practice and their major impacts, it is crucial that safe, reliably accurate and cost-effective *design methods* for these systems be advanced through a progressive understanding of the net (resultant)

aspects of multiphase flow behavior, that is, the inter-dependency of the known operating conditions and the desired (case-specific) space-/time-averaged dependent variables.

Indeed, inadequate multiphase flow *design methods* are usually at the root of pipe flow-related incidents and accidents. Facts and root causes pertaining to these increasingly frequent accidents are easily accessible via press releases and websites that monitor them (e.g., www.rigzone.com, ERCB investigation reports). In some cases, as documented on the monitoring websites, it is found that the hydrodynamics of the flow (e.g., pressures, velocities, wall shear stresses) plays a crucial part in the corrosion, erosion, vibration, wear or integrity issues leading to these incidents. Reviews and examples of multiphase flow-induced corrosion-erosion phenomena can be found in Tang et al. (2009), Zheng and Che (2007) and Wang et al. (2001). In the type of the accidents that result in the leak or release of a flammable/toxic product being transported by the pipeline, the consequences of the release can prove to be deadly to both humans and other living species.

Equivalently, the need for advances in multiphase pipe flow understanding is not only for better *design methods*, but also for:

I. Providing best-estimate codes for what-if and real-time *analysis*

II. Providing better *diagnostic* engineering tools for operations

III. *Detecting* hidden risks and profit opportunities

IV. *Screening* or *filtering* inaccurate measurements, noisy signals or sensor data

V. Efficiently *optimizing* piping components, equipment and integrated assets

VI. Flow *metering*, model *calibration* and data pattern *training*

VII. Providing simple and accurate models for *simulation* and *forecasting* (e.g., forecasting of in-situ flow rates of produced fluids and prediction of down-

hole pressures for production allocation/reserves management studies under given facility constraints in the oil and gas industry)

Local aspects of multiphase pipe flow, such as very complex, chaotic, continuously interacting and developing microphysical flow phenomena that are not under the control of any experimenter or designer are of little interest to the practicing engineer. This is because the dependent variables of interest in industrial multiphase flows are usually macroscopic, integrative quantities that represent the net effect of the competing, interacting physicochemical processes (the flow microphysics) across different length scales, such as axial pressure and temperature gradients, wall transfer coefficients and averaged phase volume and entrainment fractions. In fact, for most engineering purposes, it is quite unnecessary to resolve all details pertaining to turbulent fluctuations such as in DNS (direct numerical simulation) and LES (large eddy simulation) approaches.

1.2.2 Research Contribution

Due to the enormous complexities of the numerous moving deformable interfaces that define this subject, it is customary to apply a macroscopic formulation based on an averaging process. Even apart from the practical interest in averaged descriptions (as discussed in the previous section), the fact is that local microphysical flow interactions and effects are very difficult to experimentally isolate, let alone model. Therefore, from both practical and scholastic standpoints, fundamental knowledge of the *net of microscopic interactions* or the *resultant behaviors* of the multiphase flow is what matters ultimately. Moreover, it is well known among experienced multiphase flow investigators the high importance and impact of averaged descriptions, as examples:

I. In Prosperetti (2003): “There can be little doubt that, at the spatial and temporal scales of interest for most practical applications, the principal theoretical tool for the study of multiphase flow and design of multiphase flow equipment is – and for a long time to come will remain – computation based on some sort of averaged mathematical description of the system of interest.”

II. In Properetti and Tryggvason, 2007 (the last page in the Conclusions section, pg. 435): “The formulation of a satisfactory set of averaged-equations models emerges as the single highest priority in the modeling of complex multiphase flows”.

It is, therefore, clear the enormous significance that a satisfactory set of averaged-equations models hold in multiphase flow. It is the contribution of this thesis that averaged-equations mixture models are provided that are simple, analytical (i.e., flow-pattern-implicit and generalized) and reliably accurate over a wide range of multiphase flow applications. In particular, our discovery of the governing (unified) analytical relationships between the key hydrodynamic variables of pressure and volume fraction signifies that averaged multiphase pipe flow studies can shift towards science-oriented predictive research. Additionally, we demonstrate (quite overwhelmingly) that key prior observations of averaged multiphase flow data from classic experiments of the late 1940’s to modern ones, can be re-examined and re-understood from the point of view of our simple analytical models.

1.3 NEW PROBLEM APPROACH

1.3.1 Defining the Problem Differently

1.3.1.1 Existing Approaches

The most important task in multiphase pipe flow is to understand how the unknown dependent variables one is interested in solving are related to the known system operating conditions and parameters. It is not surprising then, that without understanding this general definition of the problem, there will be conceptual blocks to understanding specific applications. For instance, if a model (say model-U) requires a determination of the flow pattern *a priori* in order to provide a solution to the multiphase flow problem being considered, then understanding why the flowing phases self-organize in a certain way would represent a principal issue. If another model (say model-K) does not require a determination of the flow pattern *a priori* in order to provide a solution to the multiphase flow problem being considered, then understanding why the flowing phases self-organize in a certain way is an irrelevant issue. The validity of, or more specifically, the level of confidence in the differing modeling approaches will be determined by how well these models are tested for their ability to provide a satisfactory range of accuracy consistent with their intended application.

It is these two key questions of degree-of-testing and degree-of-accuracy that underlay the majority of the beliefs in this field. For example, U-modelers have historically found that a higher accuracy can be obtained by their approach. K-modelers, on the other hand, counter this historical trend. Indeed, with the view laid out above, it becomes easy for K-modelers to confront and clarify the often-repeated and sometimes dogmatic statements of U-modelers. There are many such statements dominating the

multiphase pipe flow literature and there seems to be a widespread consensus on the same basic theme:

I. One “must” start with predicting the flow pattern (e.g. Griffith and Wallis, 1959, Hubbard, 1965, Wallis, 1969, Dukler and Taitel, 1986, Antar and Nuotio-Antar, 1993, Shoham, 2006).

II. It is “impossible” to provide accurate solutions if approaching the problem in other ways (e.g. Hubbard, 1965, Delhaye, 1981, Ferguson and Spedding, 1995, Nilpueng and Wongwises, 2006).

With regard to the belief of the impossibility of achieving accurate solutions if approaching the problem differently, we note in particular, the opinions of:

I. Hanratty et al. (2003) on averaged conservation equations: “The development of universal equations which describe a large range of gas-liquid flow patterns could be an impossible task”.

II. Delhaye (1981) on accuracy of models: “It is obviously impossible to describe bubbly flows and annular flows with a good accuracy by means of the same model”.

III. Hubbard (1965) on the inescapable conclusion in the field of two-phase flow: “Recognition of flow regime differences leads to the inescapable conclusion that, to work in the field of two-phase flow, it is necessary to be able to predict the occurrence of the transitions to the various flow regimes”.

IV. Griffith and Wallis (1959) on two-phase flow regimes: “It is naive to expect that a single mathematical model would adequately encompass all possible two-phase flow regimes, even for a single geometric configuration”.

In contrast to the beliefs above, it is our view that a variety of different approaches should be pursued when solving averaged multiphase pipe flow problems. Such approaches can be new profound ideas or fundamental studies that reach beyond prior experience or understanding. We do not subscribe to the belief that it is an impossible task to provide a satisfactory set of practical equations that are applicable over broad ranges.

1.3.1.2 Redefining the Principal Scientific Issue

For the purposes of the remainder of this section as well as the next, we highlight an example statement that is archetypical of the consensus among U-modelers. Following a major international multiphase flow conference held just over a decade ago at Illinois, the post-conference *Workshop Findings* document (Hanratty et al., 2003) stated: "Since the behavior of these systems depends on the pattern, its prediction is the overriding scientific goal. Scientific understanding will be greatly enhanced if we recognized the task as being an issue of complexity that involves the definition of the organizing principles that govern these patterns". With a K-modeler's perspective, the first part of this statement can be clarified as: "Since the behavior of [the models that have been found to most accurately explain] these systems depends on the pattern …". This, in essence, is the U-modeler's view.

Our view, which we define henceforth as the K-modeler's view, is that the multiphase flowing mixture self-organizes in a particular spatio/temporal configuration in response to the imposed operating conditions of the system. For a given scenario, the imposed operating conditions create the interplay of inertial, buoyancy, surface tension and viscous forces (and other forces if present in the scenario) that then drives the peculiar behavior of all the competing microphysical processes. These continuously

interacting and developing microphysical processes in turn cause the morphological self-organization (or reaction) of the flow field bodies by way of macro-scale coherent flow structures and meso-scale flow clusters up until the point that the competition between the microphysical flow processes attains, on average, a net cancellation level (or maximal interaction level). It is at this point that investigators visually or statistically observe as a "developed" flow pattern. Each of these self-organized, developed flow patterns has a combination of time-averaged in-situ velocity and volume fraction cross-sectional distributions that characterize them. Therefore, by definition, the study of flow patterns (and thus time-averaged cross-sectional distributions) is one special case of the *inverse problem*. Solutions to inverse problems are prone to conjugate states and non-uniqueness, and consequently, this is *why* reliable predictability is notoriously difficult in the study of flow patterns.

Now, at any given axial position in a pipe in any multiphase flow scenario, a prevailing flow pattern will *only* affect the rates of mass, momentum, energy and entropy transfer (both phase-to-phase and phase-to-boundary) insofar as the time-averaged velocity and volume fraction cross-sectional distributions that characterize it. It is these cross-sectional distributions as well as their space-averaged values (which represent the net of microphysical interactions) that mathematically capture the prevailing state of agglomeration of the phases, i.e., the morphology of the flow field bodies and their interfacial structures. This is *why* flow patterns strongly affect the mass, momentum, energy and entropy transfer rates, and all other conceivable factors of interest in a multiphase pipe flow problem – not because of what flow field morphology an investigator observes and decides to report – but because of the changes in the velocities and volume fractions associated with each physical flow pattern. Velocities and volume fractions are always part of the set of dependent variables in the conservation equations

of multiphase pipe flow systems and therefore any and all flow pattern information are already captured in the way these variables are defined in the conservation equations.

So, in contrast to the flow pattern-explicit *inverse problem* discussed above, K-modelers focus on the flow-pattern-implicit *forward problem*. To K-modelers, the principal scientific issue is to understand how the self-organizing, continually-developing velocity and volume fraction profiles (or their averaged values) are related to the variables and parameters of the conservation (or balance) equations used to model the multiphase system. In this work, we present an integrative, theoretical analysis of this complex relationship when looking at averaged descriptions of multiphase flow (i.e., the time- and space-averaged balance equations which represent one type of asymptotic approximation analysis of the flow) with the ultimate aim of being able to draw simple, reasonable and unambiguous conclusions.

1.3.2 Advancing Towards Simplicity

1.3.2.1 Practical (Computational) Advantage

The second part of the Illinois conference statement in the previous section makes a case for the multiphase flow problem as being one of complexity, and suggests that scientific advances in the subject should give more attention to understanding this complexity with a goal of defining the organizing principles underlying it. We only agree with the latter part of this opinion. Whereas scientific advances in any subject must always lead in a general direction towards understanding the simplicity underlying observations (which is the same basic idea as aiming to define the organizing principles underlying the flow), we assert that this goal will only be achieved if the paths to understanding in the subject give more attention to discovering the simplest logical

explanations (i.e., the least primary concepts or hypotheses) for describing the greatest number of empirical facts governing the flow.

Nevertheless, viewing the multiphase flow problem as being one of complexity is a widely held opinion by investigators who share an affinity for explaining multiphase flow behaviors in overly-complex ways. Prominent features of their collective works show up as complex explanations (or several auxiliary hypotheses) for what can be simply explained (and simply tested). There can be found among many investigators an ever increasing complexity in their modeling, leading obviously towards unverifiable theory. In fact, there is fierce competition among many investigators to provide more complexity in their models. For example, Richard Lahey, Jr. noted: "Indeed, it is now almost a matter of national pride to have more conservation equations in your models than other laboratories have" (Lahey, Jr., 1981).

In stark contrast to the investigators who favor more complexity, there are multiphase flow modelers and experimenters who advance more simplicity as an important component of their investigations not only for its inherent practical (and thus computational) advantage but also as an intellectual ideal. Examples include:

I. The *basic philosophy* of Paul Maeder (quoted in DiPippo, 1980): "Keep things as simple as possible without losing the essence of the physics".

II. The *clarification comment* of Joseph Kestin (pg. 10 of Kestin and Podowski, 1985): "There is no limit to the degree of detail. The real art is determining how to get by with less detail, otherwise the conclusion one could reach is that we cannot solve any problems". Incidentally, Joseph Kestin's convictions in the philosophical credos of Josiah Willard Gibbs were highlighted in the form of several Gibbsian quotes in one of his classic contributions (Kestin, 1991).

III. *The principle of model selection* of Wulff (1992): “The principle of model selection is that one should choose the least complicated model which accommodates all available experimental information and the phenomena of interest”.

IV. The *summary opinion* by Levy, 1999 (pg. 156) on large-scale multiphase pipe flow codes: “System computer codes may be at the point of diminishing returns. In fact, there may be gains to be made by simplifying them and eliminating the prevailing inconsistencies rather than making their flow pattern maps and closure laws more precise or more complex”.

V. The *formulated conclusion* of Podowski, 2005 (pg. 19): “Multiphase flows are subject to a combination of deterministic and statistical phenomena, which are often difficult (if not impossible) to properly capture and quantify; thus, the appropriate (case-dependent) level of averaging is the key issue in the development of physically-sound models. In other words, more complex models are not always better than simpler but self-consistent and properly validated models”.

VI. The fluid dynamics *lessons learned* in the first Bachelor Prize Award lecture of Stone, 2010 (i.e., the Reciprocal Theorem, scaling arguments and characteristic lengths): “Over the years I have found several theoretical approaches have occurred so often in my work that I invariably think about these ideas first when exposed to a new problem. The ideas have in common that they yield quantitative estimates and tend to bypass many details of the actual flows”.

VII. The definition of *the best model* in Al-Sarkhi et al. (2012): "The best model would obviously be the one which is simple and explicit yet accurate and conforms to the physics of the flow".

VIII. The definition of *a good model* in Cocco and Hyrena (2006): "A good model is the one that makes the right assumptions of what NOT to include".

The last quote above is an outstanding example of the fundamentals of good engineering practice, i.e. to first test the extent of the simplest explanations – which necessarily require that the minimum approximations, primary concepts and relations be employed in the model. This is in contrast to the common practice of invoking more complex explanations right from the start without any test of the simplest ideas. In this latter case, modeling complexity is often constantly increased (mostly supported by "rigorous" formulations or simulation arguments) in response to the increased complexity of the actual applications, with no directly-measurable, publicly-scrutable experimental evidence to quantify the failure of simpler and therefore more reliable modeling solutions.

1.3.2.2 State of Affairs

Apart from the crucial role of simplicity in engineering practice as discussed in the previous section, the principle of simplicity has a long history in science-based subjects. In the widest sense, it can be thought of as an asymptote to which science-based fields of study must draw closer. Although this principle does not rest on the assumption that the laws governing the behavior of the studied system are simple, we choose the simplest among the hypotheses that explains the facts because to do otherwise will set us on a path which leads toward unverifiable theory (Feuer, 1957). As noted in

Keuzenkamp et al. (1997), one of the most important justifications for aiming at simplicity is that it supports the predictive power of models. A more modern justification is that "simplicity leads to depth" (Wilczek, 2012).

We put forward the view that there is an underlying simplicity to be found in multiphase pipe flow as indeed in any other subject. This view places multiphase pipe flow in a wider scientific context and signals that if the current status quo in this field is one that is engulfed in complexity, then this subject may actually be in its early infancy. The fact is that there is no way of telling. It is not uncommon, however, for experts in this field to frequently comment on the very immature state of the subject – as examples (in chronological order):

I. "Two-phase pressure drop has long been recognized as poorly correlated." (Hewitt and Boure, 1973).

II. "We know little of how to combine our single-phase methods of turbulence with the complexity of two-phase flow because of unresolved (and unmeasured) influences of length and time scales" (Stuhmiller and Ferguson, 1980).

III. "The criterion of objectivity (i.e., coordinate frame indifference) must be satisfied for the interfacial transfer laws. Current generation two-fluid models that account for virtual mass effects have generally ignored this important constraint. In addition, it can be easily shown that many two-fluid models violate the second law of thermodynamics, and are thus incorrect. Finally, virtually all two-fluid models utilize flow regime transition criteria and correlations that are inadequate. The old computer adage, 'garbage in, garbage out' (GIGO), seems to apply in the case of current generation two-fluid

models, since the ‘garbage’ is literally built into the models” (Lahey, Jr., 1981).

IV. “Two-phase flow is an insecure science” (Wallis, 1982).

V. “Two-phase flow conservation equations are not established for two principal reasons. The first reason is that no universal accord exists as to what constitutes a complete set of equations, and the second reason is that the constitutive equations which describe two-phase flow mixtures are still in the infancy of development” (Dobran, 1983).

VI. “The Achilles heel of this [two-fluid] approach is that no one has tested the closure laws, not even at an elementary level” (quote by Graham Wallis on pg. 3-162 of Lahey, Jr. and Wood, 1987).

VII. “Problems involving the motion of a mixture of two components, or phases as they are often called, are important in mechanical and chemical engineering, and a large body of data concerning two-phase flow systems has been compiled. Practical information and working guide-lines are available, but there is a shortage of physical understanding and a serious lack of a quantitative theory” (Batchelor, 1989b).

VIII. “Nobody really understands multiphase flow” (Hewitt, 1997).

IX. “For the chaotically deforming interfaces of two-phase flow patterns that occur in industrial systems, there is still no suitable instrumentation (microcalorimetry and micro-shear stress sensors), and, therefore, no experimental basis is available for supporting the development of transfer laws describing the split of total momentum and energy into phasic momentum and energy transfers at the wall” (Wulff, 1998).

X. "Reliable multiphase reactor models that can be used with confidence for improving existing processes and scale up of new processes are not yet available" (Sundaresan, 2000).

XI. "Pressure gradients vs. volume flux, holdup of phases and other process control data are not predictable from first principles or from empirical flow charting" (Joseph, 2003a).

XII. "Validated physically based models that describe the transition from one regime to another are not available. Here, validation implies the direct verification of the postulated physical mechanisms and the testing of the predictions over a wide range of conditions" (Hanratty et al., 2003).

XIII. "As a matter of fact, and broadly speaking, it is fair to say that averaged-equations models for multiphase flow are far less developed, and far less faithful to physical reality, than those of single-phase turbulence. There are considerable difficulties plaguing the modeling of many terms and the equations often appear to be somewhat deficient even at a purely mathematical level" (Prosperetti and Trygvasson, 2007).

Historically, the reasons *why* many multiphase pipe flow experts consider this very infant state as the most likely state-of-affairs can be traced back to the very little progress made towards understanding the processes involved in multiphase flow along a closed conduit. From an experimenter's perspective, this is mainly due to the large amount of experimental variables which are present in any given multiphase flow scenario and to the fact that early investigators in this area reported mainly effects on the pressure and heat transfer performance of a closed conduit resulting from independent

variables altered by the operator. It is not until the early 1960's have studies on the local or point conditions in closed conduits been published.

Additionally, the multitude of variables and a lack of understanding of their relative importance form part of the severe difficulty of setting up a multiphase flow experiment with the necessary degree of control. In fact, in terms of control, it is well known among experimenters the difficulty in avoiding the flow instabilities that may arise from the heterogeneity (the large-scale axial and lateral spatial distributions and motions) of one or more of the flowing phases imposed by the presence of the conduit walls. Apart from flow instabilities, extreme care must be taken to achieve the necessary degree of experimental control as exemplified in the Gill et al. (1962) investigation. Even though this example is restricted to a specific application (i.e., sampling probe studies of adiabatic annular vapor-liquid flow), the experimenters acknowledged that minor pipe bends and slight swirls had large effects on the velocity and mass flux profiles. They rightfully found it difficult to see how these seemingly minor effects could be eliminated in any practical application of multiphase flow, thereby highlighting the problem of control as worthy of further investigation in its own right.

A further complexity in the experiments is the large number of flow patterns which are observed when relative phase amounts are systematically changed – and an inability in the past to relate these complex flow patterns (which are unbounded, descriptive and subjectively decided) to other much simpler and therefore more reliable geometric quantities such as volume fractions (which are bounded, numeric and objectively measured). Also, there can be different interpretations of experimental (or field) observations with regard to the contribution of the various terms of the different total pressure gradient models.

From a modeler's view, one reason responsible for the very infant state of affairs is the incomplete understanding of the basic phenomena involved which prevents the right approach to the problem. This fact makes it quite difficult to evaluate (or interrogate) the influences of many variables – as examples – the effect of the entrance or exit conditions, or, the dependencies of the phenomenological transfer laws at the wall on the pipe system geometry. Indeed, according to Wulff (1998), the difficulties of predicting multiphase flow stems from the inability to "formulate the physics" of the multiphase flow in mathematical form (i.e., appealing to the physics), rather than from "finding solutions" to the mathematical statement of specific multiphase flow problems (i.e., appealing to the equations).

Lastly, for a balanced view, one must be aware of the relatively few investigators who subscribe to a very mature state of affairs of multiphase pipe flow. This group, almost exclusively, is comprised of investigators in the petroleum industry. In contrast to the previous comments noted above, their comments on the state of affairs of the subject are, as examples:

I. "The era from the early 1980s to the present experiences the emergence of the so-called 'mechanistic' models. These apply a modeling approach to the solution of the pressure drop calculation and are founded on a comprehensive description of the basic mechanisms occurring in multiphase flow" (Takacs, 2001). And again, in the same reference: "All the up-to-date mechanistic models employ theoretically sound solutions for flow pattern recognition".

II. "We can now identify flow patterns without seeing the fluids, and even agree in general about what we see (and don't see)" (Brill, 2003).

III. "The basic framework for modeling a wide variety of gas-liquid flow problems is now well-understood, much having been completed in recent years" (Golan, 2003).

IV. "Pressure drop is in general relatively easy to obtain with good accuracy" (Eidsmoen and Roberts, 2005).

Evidently, the combination of our own historical explanations in this section and the extreme contradictions among past and current investigators in this field (in their own words) substantiate the need for some type of unbiased and unified analysis. This work provides one type of unbiased, asymptotic approximation analysis (i.e., averaged analytical mixture models) by furnishing both quantitative solutions and qualitative explanations for a wide range of multiphase flow applications and phenomena.

1.3.2.3 Central Argument of the Research

This research amalgamates and reliably reproduces key experimental findings and field observations of different classes of averaged multiphase flow problems across time periods (from older classic data to modern ones) and across engineering disciplines in one simple, analytical and self-consistent mathematical modeling framework. That this is even possible is a very powerful argument in favor of the subject being in its early infancy. This, of course, bodes very well for researchers in this field.

The central argument of this research is that there is an underlying simplicity and connectedness in the subject if looking at the *net of microscopic interactions* or resultant macroscopic behaviors in the *forward* problem. The observed coherencies of the macroscopic (self-organizing) physical structures that define the subject are equivalently present in the macroscopic mathematical descriptions of these systems, i.e., the flow-

pattern-implicit, averaged-equations mixture models that describe the collective behavior of the flowing mixture.

If this approach finds favor among a critical mass of investigators, then the goal of future scientific research in averaged multiphase pipe flow will be to start asking fundamentally different questions that will aim to discover this macroscopic behavior – and specifically – to be able to predict the averaged volume and entrainment fractions, which represent the most important global variables of the flow. The task will then be, not to continue adding more modeling complexity in response to more complex flow problems, but to find the points of view from which a complex problem will appear in its greatest simplicity (i.e., to simplify rather than complicate). These points of view, if discovered, will not only permit a whole new learning of how to think about these problems in a simpler way, but also, how to generalize from a current problem to a related but presently unanticipated application. Elementary tests, designed to interrogate these points of view, must then be performed with the goal of achieving a deeper, predictive understanding.

Indeed, although it is easy (and therefore habitual) to think of averaged multiphase flow problems in overly-complex ways, this work comprehensively demonstrates that more insight and better predictive accuracy can be achieved if investigators perceive these problems in very simple ways.

1.3.3 Standardizing the Investigators and the Problems they Study

1.3.3.1 Existing Classifications

In any field of study, perhaps the first visible and publicly-known feature about the subject is the people who investigate it. In the Section 1.3.1, two groups of

multiphase flow modelers were introduced – U-modelers and K-modelers. This is one way to partition the investigators mostly involved in modeling.

Other ways of partitioning investigators can be found in the literature. In one instance, Prosperetti (2003) identifies purists, who "say that wrong equations are solved by inaccurate numerical methods to produce dubious solutions"; practically-oriented researchers, who "may be happy with computational results – however obtained – which mirror data with reasonable faithfulness"; and "a third group – which has grown in the last several years – [that] situates itself in the middle".

In another instance, Emmons (1970) also identifies three groups: "We will recognize the efforts of three groups, not always distinct: (a) those primarily interested in the numerical techniques; (b) those primarily interested in the fluid-mechanics phenomena; and (c) those primarily interested in getting the answer to some specific practical problem".

1.3.3.2 Modelers and Experimenters

Other than our classification of U-modelers and K-modelers, there are, of course, investigators who are mostly involved in experimentation. In many cases, there will be some degree of overlap where investigators engage in both modeling and experimentation with one activity being dominant. So in the broadest sense, in our view, there are modelers and experimenters in each of the disciplines where multiphase flow scenarios and problems are studied.

Within the modelers**,** there are different sub-classifications, ranging from:

I. *Purists*, whose works are typically heavy on theory, to

II. *Pragmatists*, whose works are typically heavy on engineering tools, to

III. *Computationalists*, who are somewhere in between the above extremes.

Some *purists* favor excessive amounts of auxiliary hypotheses and equations to provide a model with very scant (or no) validation with carefully-controlled data. In this instance, models are compared against analytical formulations, specially-chosen datasets or a few self-conducted datasets supporting the studied model. These purists claim that their models need only be verified and refined with limited experimental data. Fortunately, other purists recognize the critical role that comprehensive validation plays in regards to the scientific investigation itself, as exemplified in the quote by Thomas Hanratty in the previous section.

Some *pragmatists* favor large amounts of self-conducted, proprietary (i.e. secret, inaccessible and therefore irreproducible) data for their model validation to the extent that their models are made to fit these data for different purposes. In these instances, and quite surprisingly from a scientific standpoint, there may also be uncontrolled, unrepeatable field operating data that are utilized side by side with controlled, repeatable lab data in the closure relations tuning of the model – for example – as is performed in the OVIP (OLGA Verification and Improvement Program) multiphase flow database affiliated with the OLGA code. In this particular case, the uncontrolled, irreproducible (and oftentimes untraceable) field operating data originates from various industry and academic sources, as examples: (a) the thirteen months of the Gemini Gulf of Mexico field operating data, Kashou et al. (2002), (b) the inclusion of the Tulsa University Wells database, Nordsveen and Nossen (2007), and (c) the inclusion of North Sea and the Heidrun field data, Nordsveen and Nossen (2007). In a few extreme cases, the type of data used for model validation may be a few (sometimes even one) specially-chosen field operating data, in which very little information about the operating system (e.g., fluid properties) is actually measured or known. In these instances, pragmatists will

sometimes adjust parameters in their model to give the closest fit to the chosen field data (e.g. the field comparison to "Test 14" in Danielson, 2011).

Indeed, the type of field practice described above cannot (and must not) be relied upon for science-based predictions of multiphase flows – that is – forwarding uncontrolled, in-operation field data to a favored multiphase flow simulation vendor for the closure relations tuning of the model of the vendor. This is a particularly dangerous practice in high-pressure, high-temperature, high-risk field environments where it is vital to understand and thus predict the multiphase flow behaviors in scenarios that deviate from normal operating (model-tuned) conditions. It is obvious that such a tuned model will lock in the predictive behavior for the operating conditions it was tuned for. Therefore, no reliable knowledge is available for any deviation from the tuned operating conditions because the prediction path of the model is locked, and as such, the tuned model bears no relation to future operational scenarios (although this is incorrectly adopted as an operational "best practice" by some industry codes, e.g., the PROSPER code at http://www.petex.com/products/?ssi=3). This fact also applies to the practice of "regular calibration" (Corteville et al., 1991) in some industries for temporarily adjusting multiphase flow models to field measurements by use of tuning (regression) parameters.

Fortunately, there are other *pragmatists* who fully recognize the scientific importance of testing theories and models with wide-ranging, reproducible, publicly-accessible and cross-referable laboratory data before the models are adopted for application to field conditions.

Within the experimenters, we note that there are similar ranges of investigators, from:

I. *Model-less* experimenters, whose experiments focus on measurement methods, procedures and results that are farthest from theory (i.e., they aim to

capture the behavior of the studied phenomenon independent of preconceived expectations of results), to

II. *Model-driven* experimenters, whose experiments focus on measuring specific parameters of a theory for which the experiments were specially designed

Of course, the line between theory and observation is neither sharp nor fixed, and there are usually implicit theoretical assumptions in the measured data. This is why the general terms for the ranges of modelers and experimenters are kept as they are above.

1.3.3.3 Groups Based on Geographic Location

Apart from the groupings in the previous section, multiphase flow investigators can be differentiated by their:

I. Areas of specialization
II. Geographic location
III. Academic affiliations
IV. Disciplines

In the case of *geographical* groups, conferences and meetings target investigators belonging to nations from a particular geographical region (e.g., East Asia, Kakihana and Wakabayashi, 1986; North America, Brill and Gregory, 1998; Russia, Anisimov et al., 2010). Sometimes, there can be a danger with *geographical* groups who promote their contributions to the subject in various ways, for example – the groups of Italian (e.g., the TEASistemi group, www.tea-group.com) and Norwegian (e.g., the SPT Group, www.sptgroup.com) specialists who target multiphase pipe flow applications in the petroleum industry. To arrive at an objective view concerning such groups, one must

obtain independent access to the validation data of their publications, and, test their models in the simplest scenarios with identical input data (i.e., non-reacting, adiabatic flow with simple fluids and negligible mass exchange).

Unfortunately, with regard to the issue of public access to data and model interrogation, statements such as "The data is proprietary, and the exact information on the fluid composition and properties can therefore not be given" (Laux et al., 2008), are common. Among the users of country-based codes, it is well known the secretive nature of the underlying models as described, for example, in section 3.2.1 of Schietz (2009): "How exactly OLGA handles computations of three-phase flow is a treasured secret of SPT Group". Thus it is clear that some codes are double-blind engineering tools – meaning there are no access to their validation data and no detailed understanding of their underlying models – resulting in faith-based uses of such codes.

With regard to the issue of comparison to named, published data, we show the results of thirteen simple tests of two popular codes in the Petroleum industry, OLGA and LEDA, against named, readily-accessible, published (peer-reviewed) two-phase flow data. By naming the datasets, readers gain the ability to cross-reference the data with their source publications, learn about detailed descriptions of the experiments in these publications and better understand the associated uncertainties of the measurement instrumentation used for individual test runs. Also, the naming of datasets ensures that any user can independently input the identical data from the source publications into any preferred code, thus eliminating the problem of suspect problem set up.

The first four tests are gas (phase 2) and water (phase 1) flows at low gas densities – Figs. 1.3.1 to 1.3.4. The next five tests are gas (phase 2) and water (phase 1) flows in at high gas densities – Figs. 1.3.5 to 1.3.9. Figs. 1.3.10 and 1.3.11 are two examples of high-viscosity-ratio heavy oil (phase 2) and water (phase 1) flows. Figs. 1.3.12 and

1.3.13 are two examples of low-viscosity-ratio light oil (phase 2) and water (phase 1) flows. The data of the first test in Fig. 1.3.1 (and many similar experiments like it) can also be found in Table 12.1 of the classic multiphase flow text by Wallis (1969). As is evident, these tools can fail to predict the measured pressure or pressure gradient profiles by far more than 50% error. More importantly, they can provide solutions with the wrong trend compared to the data, as well as widely different trends compared to each other.

The results above, as surprising as they may first seem, are in alignment with prior, unbiased testing results (Theofanous and Amarasooriya, 1992, Pickering et al., 2001) that reveal the demonstrably poor prediction capability of "industry-standard" codes when they are independently tested with a wide range of reliable, verifiable experimental data from many different labs that are readily available from the published literature. In the references above, a small-diameter, vertical air-water flow dataset from Owen (1986) was selected for benchmarking comparisons with both commercial and research codes primarily in the chemical and nuclear engineering industries.

In fact, in the publications where country-based codes are compared against unverifiable data from private labs (e.g., OLGA's SINTEF-Tiller lab, LEDA's IFPEN-Total-Boussens lab), there is no science-based interpretation that can result from these comparisons because the data from these labs are irreproducible (unobtainable). It is little wonder then, why such publications will show very minimal differences between codes (e.g., Belt et al., 2011) – if there were significant differences, then the affected parties would demand the data be released to the public in order to eliminate the possibility of bad data. Aside from the fact that these data are not publicly-scrutable (a requisite for scientific data), no information is available on basic experimental procedures, repeatability tests, redundancy measures or instrumentation accuracy. The

issue of the level of competency of the trained professionals conducting the experiments in these for-profit labs is an irrelevant one compared to the lack of reproducibility or public access to the data. Obviously, non-profit public labs (e.g., academic or state labs) will equally attest to the level of competency of the trained professionals conducting their experiments.

Summarily, in view of the results and discussion above, the crucial question that the users of multiphase flow software tools must ask themselves is: If the behavior of a simple, verifiable laboratory test case with its restricted number of variables cannot be predicted, then is it reasonable to expect a reliable prediction for the real world prototype? We assert that this simple question must be used as a litmus test for distinguishing the degree of usefulness (or appropriateness) among the many available multiphase flow software tools in practice. As Ian Beck eloquently states with respect to engineering software technologies: "If the fundamental aspects of these technologies are not properly addressed, no amount of window-dressing is going to turn them into useful software products" (Beck, 1995).

1.3.3.4 Groups Based on Academic Affiliations

In addition to *geographical* groups, some investigators are identified by their affiliations to academic centers in various disciplines. Unlike *geographical* groups with niche commercial interests, however, research advances from *academic* groups are sometimes shared in the open literature (e.g., Peng et al., 2010). In some cases, *academic* groups may cooperate with each other and operate in broad multidisciplinary environments, e.g., the JMBC group (www.jmburgerscentrum.nl). In other cases, *academic* groups may operate in multidisciplinary partnerships but focus their efforts in

one problem with a specific approach, e.g., the MFDRC (Multiphase Fluid Dynamics Research Consortium) group focused on gas-solid flow using CMFD tools.

Unlike the cooperative partnerships among the example groups above, there may be academic groups that pursue investigations independent of other academic groups even though they operate in the same discipline environment (e.g., the groups focused on Petroleum applications). As examples, within the Petroleum groups, there are competing institutions such as the TMF (Transient Multiphase Flow) Joint Industry Program, the TUFFP (Tulsa University Fluid Flow Projects) group and the FACE (Flow Assurance Center) group, to name a few. The first group, for instance, is considered as: "the gold standard for similar programs in the world in an area that impacts directly on the oil and gas industry" (Rhyne, 2013).

In contrast to *geographical* groups, the models (and in a few cases, the data) from academic centers are usually available for public interrogation and testing. However, if we perform simple tests just as in previous section with academic research codes, similar poor prediction capabilities become evident (as was also evident in the Owen, 1986 benchmark comparisons with the research codes at that time). In fact, some flagship codes from academic groups may even produce worse results than the country-based codes in every category. We present three simple two-phase flow tests of one example *academic* group – the TUFFP model (TUFFP v.2011.1) – to showcase this fact. This model was chosen because of its ease of public access via the PIPESIM simulator. The first test in Fig. 1.3.14 is the same low gas density example test as shown in Fig. 1.3.4 with the TUFFP model predictions added. The second test in Fig. 1.3.15 is the same high gas density example test as shown in Fig. 1.3.8 with the TUFFP model predictions added. The third test in Fig. 1.3.16 is the same high viscosity ratio (heavy oil and water) example as shown in Fig. 1.3.11 with the TUFFP model predictions added.

Clearly, the rather enlightening results of the simple tests shown above (as well as in Section 1.3.3.3) bolster the argument for advancement towards major improvements in modeling, deeper fundamental insights and completely different approaches. This argument remains valid even in the scenarios where investigators with niche practical interests may be less concerned with the fundamental technologies behind multiphase flow theories. In this latter scenario, investigators may be solely be interested in tuning a model to a given set of field operating conditions without concern for a scientific understanding governing those observations, and may be happy if most (say 80%) of the commonly encountered field trends can be reproduced by the tuned model. Figs. 1.3.17 and 1.3.18 shows two commonly encountered circular and circular-annulus oil production examples that demonstrate why such practices in specialized industries (e.g., petroleum industry) can be very dangerous. These results can indeed be expected (and is in fact highlighted in prior unbiased studies, e.g., Ali and Yeung, 2010) since a lack of basic understanding propagates poor model predictions at the lab scale to poor predictions at the field scale.

1.3.3.5 Groups Based on Disciplines

Other than *generalist descriptors*, *geographical* or *academic* groups as described previously, by far, the most common way investigators identify themselves is according to *discipline*. Since some multiphase pipe flow problems may be similar among different disciplines, the investigators (i.e. academics, practitioners and consultants) of those "similar" disciplines frequently group together in conferences, meetings and workshops. Sometimes, investigators belonging to one group may have less than favorable views of other groups (pg. 88 in Kestin and Podowski, 1985, pg. 3-109 in Lahey, Jr. and Wood,

1987). In other cases, a group may identify specific reasons for the differences between what they study and what others study.

Aside from personal or group perceptions, in some cases, even the basic knowledge of whether a specific phenomenon has been studied or not in the past can be missed by an entire group of investigators who may be unaware of the vast amount of work already conducted in the studied area by other groups. A concrete example of this is the recent portrayal of film flow reversal as a "new perspective" (Veeken and Belfroid, 2011a,b) among petroleum investigators when in fact this phenomenon has been studied for well over 70 years (Moalem Maron and Dukler, 1981) with sundry reviews and well documented findings among nuclear, geothermal and chemical engineering investigators.

It would seem that these discipline groups would benefit from some kind of oversight, for example, by means of the presence of an external, independent observer (or observers) in their workshops or conferences. One role of the independent observer could be to act as an agent of knowledge review and technology transfer among different discipline or subject groups. Indeed, enormous amounts of information are already available and the literature should be consulted to take advantage of previous experience. In particular, the older (classic) literature contains quite a lot of good data that should be carefully examined before starting expensive physical experiments or time-consuming simulation exercises. This, of course, necessitates that the various subject bibliographic surveys be updated.

Another crucial role of the independent observer could be to act as an unbiased advisor in industry-focused multiphase flow investigations. This need is clear when one considers the clearly biased relationships that currently exist between some multiphase flow software vendors and the users of their codes. In extreme cases, for example, past employees of vendor companies later become the leading multiphase flow investigators

in the operator companies that utilize their simulators (their clients), and vice versa. A concrete example of this is shown in the published biographic sketches of a group of petroleum investigators at the recent 16th BHRG (British Hydromechanics Group) conference (www.bhrconferences.com/Portals/4/docs/MP2013meetthecommitteeV5.pdf).

Finally, some examples of frequent discipline-focused group gatherings include conferences and workshops held by investigators mostly in the:

I. Chemical, nuclear and geothermal engineering disciplines, e.g., Waterloo (Rhodes and Scott, 1968), Bosphorus (Kakac and Mayinger, 1976), Fort Lauderdale (Veziroglu and Kakac, 1976), Dubrovnik (Durst et al., 1979), Spitzingsee (Kakac and Ishii, 1982), Gaithersburg (Kestin and Podowski, 1985), Troy (Lahey, Jr. and Wood, 1987), London (Hewitt et al., 1994), Kyoto (Serizawa et al., 1995), Illinois (Hanratty et al., 2003).

II. Petrochemical, petroleum and geosystems engineering disciplines, e.g., SPE annual ATCE sessions and conferences, PSIG annual meetings, BHRG International and North America-focused Conferences on Multiphase Production (note that unlike the more inclusive, technology-focused SPE meetings, the BHRG meetings consist mostly of OLGA and LEDA software user groups, as evidenced in the most recent organizing committee members at http://www.bhrconferences.com/multiphasena2014committee.aspx).

III. Mechanical (CFD/CMFD), manufacturing, aerospace, industrial, oceanic, environmental, and other engineering disciplines, e.g., Morgantown (Shyamlal, 2006), Halle (Sommerfeld and Horender, 2010).

1.3.3.6 Standardizing the Problems

That there are different types of investigators, however separated, is not something peculiar to multiphase pipe flow. The question then arises whether there is any value to be gained from identification – either in identifying investigators, the problems they study, or even the discipline-specific terminology they use. Our view is that there is tremendous value in doing this, but rather than defining the types of investigators as shown above, it is more gainful to find an objective, standardized way of defining the classes of problems they are studying. We demonstrate this value of standardization by showing how the different problems and the investigators who study them are related, shown in Table 1.1. From this standardized view, when looking at this table row-wise, it is now clear to see that supposedly distinct problems in different disciplines are actually the same conceptual problem being studied, but by different people who use languages that are common to their heritage (the discipline they belong to). Therefore, methods found successful for solving a problem in one discipline may be applied to another discipline if the investigators across the disciplines realize they are solving the same general problem.

When looking at this table column-wise, one can now grasp the true multi-phenomena (and thus multi-variable) nature of multiphase flow problems even in the simplest cases – namely, that every problem is actually a collection of special cases within each group classification. The few specific examples shown in the table are merely to show how it is practical for several types of multiphase flow problems to be lumped within group classifications – certainly, this list is enormous within each group. Further example problems within each group can be found in the subsequent chapters of this work. Moreover, although it is ideal for one example problem to fit within one group, it is quite likely that a problem may fit within (or be defined by) two or more

groups. For example, a transient, compositional multiphase flow may be classified both within groups 6 and 16 in Table 1.1. This multi-group classification is especially helpful for complex problems because the same problem can now be seen in its true nature – as a simultaneous interaction of multiple topics – or, as "a family of topics" according to Batchelor (1989a). Table 1.1 empowers investigators with an organized and streamlined perspective of the inter-connectedness of multiphase flow problems.

Table 1.1 is different from prior attempts at identification and classification because it simplifies how multiphase pipe flow problems should be approached and presents an unbiased viewpoint of how the various problems can be brought into proper focus. This need had been identified over two decades ago (suggested by Theo Theophanous in pg. 3-166 of Lahey, Jr. and Wood, 1987) as a means to facilitate the transfer process between the multiphase flow problems in engineering science and practice. Other investigators in the past have:

I. Abandoned classifying problems due to the overwhelming possibilities.

II. Classified problems with a bias towards vapor-liquid flows (e.g. Wallis, 1969; Hewitt and Boure, 1973; Hewitt, Shires and Polezhaev, 1997).

III. Classified problems according to investigator-centric or discipline-centric contributions (e.g. Govier and Aziz, 1972; Hetsroni, 1982; Chereminisoff, 1986).

1.3.4 Standardizing the Terminology

Furthering our discussion on the value of standardization, we now turn to demonstrating this value in the terminology multiphase flow investigators use to describe their problems. Terminology is the generic term used in this work to include notation,

language, terms, semantics, industry jargon, and in some cases even mathematical concepts and equations when they are expressed in words.

One major problem associated with the multiphase pipe flow literature is the many different terms, variously defined, that have been used in the past for describing the same basic concepts. Since the experimental and modeling body of knowledge was built across different disciplines, the result is a great deal of variability in the definition of terms and notations that have only served in the past to compound the problems associated with terminology in this field. Even classic references in this subject can suffer from inconsistencies among basic variables, definitions and interpretations, such as pointed out by Peter Whalley (Whalley, 1983) in his book review of the time-honored text of Hetsroni (1982). There are, of course, cases where multiphase flow investigators in the past have championed the need for a more careful elucidation of terminology and semantics in their respective fields (e.g., Joseph Kestin's discussion on the use of the "principle of local state" instead of "local equilibrium", Kestin, 1992).

Another problematic issue found especially in multiphase pipe flow is the fact that in some applications, there have been only limited investigations. This naturally leads to the scenario of no commonly recognized definitions for the studied scenario (e.g., such as in three-phase vapor-liquid-liquid flow).

Now, if we look at a few concrete examples where there are wide differences in basic descriptions, terms, statements and notations among investigators, then it will become evident the value of standardizing the multiphase flow terminology.

We first note that there are various confusing (and sometimes incorrect) definitions, descriptions and statements that can be found in the literature. For example, the term "mass velocity" is commonly used among multiphase flow investigators to represent the mass flux of a phase. As other examples concerning definitions, one may

find that slip velocity is defined as an always-positive term between two phases (Time, 2011), or, that gas void fraction in a two-phase flow "is the ratio of the volumetric flow rate of the gas to the total volumetric flow rate" (pg. 7 in Addali, 2010) and that the liquid holdup is "the flow rate of the liquid phase divided by the total flowrate of both the gas and liquid flowrates" (pg. 68 in Addali, 2010). This confusion with respect to liquid holdup can also be found in Eqn. 4 of Zhou and Yuan (2009): "Liquid holdup can be used to represent the liquid droplet concentration in a gas well. Liquid holdup is defined as $H_l = v_l / \left(v_g + v_l \right)$, where H_l is liquid holdup, v_l and v_g are superficial liquid and gas velocities, respectively".

Concerning confusing/conflicting statements, the mechanistic models may be cast as somehow being almost devoid of empirical correlations, as in the opinion of Takacs (2001): "Any correlation, if used outside its original ranges, will produce increased calculation errors. Mechanistic models, on the contrary, may exhibit much wider ranges of applicability, partly because they almost completely eliminate the use of empirical correlations". As another example, the statement by Geoffrey Hewitt promoting the use of a three-fluid model for annular flow is clearly self-contradictory: "Apparent increases in sophistication may lead to worse prediction. For example, representing a dispersed annular flow in terms of a two-fluid (film and core) model may give worse predictions than using the empirical approach. However, using a three-fluid model (film, gas core and droplets) can give an improvement" (Hewitt, 1983).

Next, there can be found in the literature several investigator-specific meanings of various terms related to multiphase pipe flow. For example, "first principles" as used by some petroleum multiphase flow investigators (e.g., Danielson, 2011, 2012a; Nilsen, 2012, Adames and Young, 2013, LedaFlow Research Project, 2013) has a different meaning compared with investigators in other disciplines. Similarly, "unified" and

"comprehensive" (e.g., Ansari et al., 1994; Gomez et al., 1999) sometimes refers to models that can be used at any angle of pipe inclination and for commonly identified flow pattern descriptions at a given pipe inclination, respectively. In terms of accuracy, in one instance a transient flow computer model developed without any validation against published data (lab or field) is highlighted as one "which accurately describes transient heat transfer in buried multiphase pipelines" (Erickson and Mai, 1992). In another instance, a transient flow computer model which is claimed as "a more accurate simulation of multiphase flow is the wellbore and pipes" is validated against one run of one dataset from the literature (Shirdel and Sepehrnoori, 2012). In yet another instance, a transient flow computer model developed without any validation against published data (lab or field) is concluded as one which "represents an efficient tool in well design" (Khoriakov et al., 2012). Other examples of various investigator-chosen terms and descriptive (creative) language include:

I. The use of the term "analysis" when describing a flow-pattern-explicit model and "gross correlations" when describing a flow-pattern-implicit model (pg. 5 of Hubbard, 1965).

II. The use of the term "model" when describing the LEDA code and "empirical correlation" when describing the OLGA code in a comparison of these codes (Table 1 of Ellul, 2010).

III. The various manipulations of the term "3D", as in "Quasi-3D" (Laux et al., 2008), "3D flow description" (Biberg et al., 2009) and "3D plots" (Jackson et al., 2011).

Thus, from the various examples above, it is clear that there is a need for one simple, consistent and standardized frame of reference for multiphase pipe flow

terminology. This, by itself, can be an important tool to understand and compare data and models across disciplines. In this work, the approach with regard to terminology is to identify and appropriately use as few of them as possible. We will thus adhere to a consistent set of terms, definitions and notations as given in Appendix A. We will also avoid popular slangs and discipline-centric jargon/semantics associated with multiphase pipe flow, which (as shown above) can be vague, confusing and sometimes conflicting. In terms of mathematical notation, the terms and conventions of BSL are utilized as much as possible throughout this work. In cases where multiphase flow language is required, the BSL single-phase flow notation will be appropriately modified.

1.3.5 Standardizing the Data and the Model Validation Criteria

Apart from the various multiphase pipe flow *problems*, *people* and *language* (all of which represent both pathways and blockages to understanding), the next major issue is the *data* used to validate models and the *model validation* procedures. Here, there are a host of important related questions, as examples:

I. What types of data are available from lab experiments and field records?

II. What types of data are appropriate for different modeling purposes?

III. How can it be determined whether the data is good or bad?

IV. Is there a standardized way to view both developing and developed flow data?

While it is very challenging to provide simple, clear cut answers to the example questions above, it must be recognized that such questions inevitably form part of the overall validation plan of a multiphase pipe flow model. Indeed, most multiphase pipe flow computer codes (academic or otherwise) require many assumptions and a very large number of closure relations. These codes are thus empirically based tools with literally

hundreds of adjustable constants and correlations to fit their test data. It is therefore essential to test multiphase pipe flow models against a wide and diverse set of separate effects and global (integral) tests. In fact, some investigators consider that "a system computer code is only as good as the validation and verification to which it has been subjected" (pg. 153 in Levy, 1999).

However, as is evident in the multiphase pipe flow literature, there are various opinions on what constitutes validation of a mathematical model. This is a major problem. In many cases, investigators will compare one model result with other model results – e.g., comparisons with analytical models, with mechanistic models or with empirical models. These comparisons, of course, confirm nothing about any scientific fact but rather, are comparisons of one measure of ignorance with another. Nevertheless, some investigators may view these comparisons as representing "some notion of uncertainty" (Shippen and Bailey, 2012) or that "comparison with other models largely removes the validation problem" (Kabir and Hasan, 1990). As is evident in this work, the wide differences among current and prior multiphase flow model predictions under identical input data conditions demonstrably disproves such opinions. In fact, such wide differences among prior multiphase flow model predictions are well known among prior investigators, as found in:

I. The simple gas-water producing field well on pg. 68 of Lea et al. (2008).

II. The summary notes of Geoffrey Hewitt in Prosperetti et al. (2001): "Many examples can be made in which predictions of different codes differ substantially, and in which numerical results obtained after an experiment exhibit a marked difference with the pre-test ones".

III. The conclusion of Gregory and Aziz (1975a): “For a given two-phase pipeline design problem, the commonly accepted design methods and correlations can give widely varying predictions for the total pressure drop”.

In other cases where controlled experimental data is actually used, the terms validation, verification and qualification are sometimes loosely intermixed to describe model comparisons to the data. The classic operations research reference of Schlesinger (1979) clearly elucidates the differences among these terms in the context of scientific model validation. A more recent reference regarding validation in the context of scientific models can be found in the guest editorial of Lake and Bryant (2006).

In one instance, one may find a pipe flow code being compared to “published data”, when in fact the comparisons are against worked examples from a chosen textbook (http://www.pipeflow.com/public/documents/PipeFlowExpertResultsVerification.pdf).
In another instance, one may find in the summary section of a newly proposed wellbore model the explicit claim that: “The model is validated with published data and simplified analytical solutions for limiting flow conditions” (Mao and Harvey III, 2013), when in fact the published data referenced pertain only to the equilibrium flash calculations describing phase changes – with the fact remaining that no publicly-scrutable, verifiable, controlled data were present for comparison against the actual wellbore hydraulic (or thermal-hydraulic) predictions.

Sometimes, even unquantifiable “anecdotal” validation may be used as a quality assurance of a multiphase pipe flow code, such as described in the WELLFO 7 Technical Reference Manual, 2009, Maintenance and Quality Assurance Section: “Clients also give us many verbal reports regarding their successes in matching measured data from their pipeline and well systems with calculations carried out using our programs. Such reports,

combined with observations from our own studies, satisfy us that the accuracy of our programs is consistent with the most current technology that is commonly used throughout the oil and gas industry".

In relatively rare cases, one may also find back-calculations of existing models being presented as "synthetic data" for comparison against newly proposed models (e.g., Garg et al., 2004; Storkaas, 2005; Nilsen, 2012; Choi et al., 2012).

Clearly, the examples above highlight a need for some kind of standardization of data and model validation procedures. In section 1.3.5.1, a proposed, standardized set of operational and conceptual model validation criteria is provided for discerning the credibility of scientific multiphase pipe flow models. Then, section 1.3.5.2 describes the new data standards and classification put forward in this work (i.e., the publicly-accessible and searchable ANNA global pipe flow database) that accompanies the new validation criteria of section 1.3.5.1.

Lastly, a standardized model validation plan should eventually encompass a standardized way of viewing the data used in the validation process – which does not presently exist in the literature nor in this work. Indeed, data classification, graphing, statistics and how the data are viewed when comparing several disparate scenarios can prove a formidable challenge when the studied subject is cross-disciplinary. Even for a specific studied problem in one discipline, a statistical number (or several statistical numbers) arrived from a validation exercise can easily mask several problems either with the validation data or with the models used in the validation procedures. This is *why* direct comparisons of a model against one specific trend present in different datasets can yield a much better understanding of a model's true capabilities – with the best understanding afforded when properly-designed, well-instrumented experiments that capture the effect of a change in one variable (with all others being controlled) are used in

the comparisons. The approach used in this work when viewing and comparing averaged flow data is to use dimensionless variables as far as possible and SI units when dimensional charts are required. At the same time, in cases where direct comparisons to prior models/results are highlighted, the prior units are maintained for ease (and quickness) of visual interpretation. The central idea in this work in terms of viewing data is that the best representations of the data will serve as simple visual aids enabling readers to reach quick and unambiguous conclusions.

1.3.5.1 Operational and Conceptual Validation Criteria

As crucial as the model validation problem is for discerning model credibility, it must also be recognized that there is no totally objective and accepted approach to model validation (McCarl, 1984). Even if there was, the fact that validation testing results in accumulating evidence that the content of a model is correct, does not guarantee that the scientific basis of the model and its internal structure represent the actual processes or cause-effect relationships operating in the real system. A network of theories and observations are usually tested together (even though the theories may be implicit) and any particular hypothesis can be maintained by rejecting or adjusting other auxiliary hypotheses. Indeed, it is well known among many investigators that "completely different mechanistic models can predict the same physical phenomena" (attributed to S. G. Bankoff in pg. 875 of Kakac and Ishii, 1982). This is one reason why validation of a model cannot be easily accomplished with a small database.

Some investigators, however, are drawn into the belief that an agreement of a model to a small amount of selected data somehow vindicates the "soundness" of the model. For example, after putting forward a mechanistic slug flow model, Issa and Tang (1990) concluded: "The results are in remarkable agreement with all of the data which

vindicates the use of such a mechanistic approach that is little sensitive to flow conditions as opposed to purely empirical correlations". As another example, after describing a mechanistic vertical upward void fraction model, Hasan (1988) concluded: "The proposed method has been compared with data from several sources. The good agreement between the data and the predictions lend support to the soundness of the model presented".

It is therefore important to recognize that theoretical validity is never certain and always provisional. However, for practical purposes, we adopt the views of Rykiel, Jr. (1996) that operational and conceptual validation can serve as useful tools for discerning model credibility.

Therefore, one set of operational validation criteria that we will use to define an operational acceptance level for scientific multiphase pipe flow models are that they be tested against:

I. Wide-ranging, diverse conditions for generic models, and focused conditions at several different labs for models purposed for a particular scenario.

II. Well-designed, well-instrumented, carefully-controlled conditions.

III. Well-reported, archival data and traceable references.

IV. Independently-verifiable data (full accountability of data means that an independent confirmation of the facts must be afforded wherever required, i.e., the data must be both readily accessible and open to public scrutiny).

V. Repeatable data (preferably with redundant measurements).

VI. Reproducible data (preferably from different investigators in different labs).

Similarly, one set of conceptual validation criteria that we will use to define a conceptual acceptance level for scientific multiphase pipe flow models are that they:

I. Are not based on unreasonable arguments.

II. Are not based on appeal to private experience nor authority (in Carl Sagan's own words, "in science there are no authorities", Sagan, 1996)

III. Start with the simplest or obvious explanations and then test (and quantify) the extent of those explanations.

IV. Are (mathematically) self-consistent.

V. Are unbiased (validation datasets cannot include the closure datasets).

VI. Are falsifiable (theories must pass Karl Popper's Demarcation Criterion).

The emphasis on scientific model validation criteria, as outlined above, is a requisite for the advancement of science-oriented research in this subject. This opinion on the proposed future research direction of this field was also shared among the participants of the Illinois conference (Hanratty et al., 2003) mentioned earlier in Section 1.3.1.2 – in their own words: "A feeling, broadly shared by the Workshop participants, was that the best way to proceed is to promote an understanding of the basic physics of multiphase flows. In other words, the emphasis of research in this area should change from a strictly engineering viewpoint (which has had limited success in developing general approaches) to a science-oriented one".

Note that there are various prior operational model acceptance tests for engineering multiphase flow models – for example – the elimination of multiphase flow correlations according to the criteria of Gregory and Fogarasi (1985). However, the operational model acceptance criteria above are for use in testing and distinguishing scientific models from their engineering counterparts. The failure of any existing models to meet our acceptance standards will not (and should not) diminish their importance or

value. Rather, such failure only indicates that they cannot be classified as scientific models.

The scientific model validation criteria defined above will have far-reaching consequences if adopted. As examples of such consequences, this would mean that:

I. Any model or code whose underlying validation experiments cannot be independently (and therefore publicly) accessed and verified will fail the operational acceptance standard.

II. Any model or code whose validation experiments consists mostly of unrepeatable or untraceable data, i.e., unpublished/unknown sets of data (such as field data from various “companies”), will fail the operational acceptance standard.

III. Any model or code that is not validated with any type of data will fail the operational acceptance standard. This type of failure is indicative of the many purely theoretical or computational works which are unconcerned with the reproducibility of observations. Their merits reside in areas unrelated to a scientific understanding of those observations (e.g., for simplifying equations, for showcasing various model sensitivities or for comparing different numerical techniques).

IV. Any model or code will fail the conceptual acceptance standard if their underlying hypotheses cannot be falsified.

Now, although the stated operational validation criteria and most of the conceptual validation criteria are self-explanatory, the first conceptual model validation criterion is open for interpretation. This is deliberate. A key point in regards to the identification of unreasonable arguments is that in some disciplines, an unreasonable

argument may be a reasonable (and necessary) argument in other disciplines. A concrete example of this scenario is found in the complex fluid mixtures that are present in petroleum systems and their subsequent modeling with multiphase flow models. In most scenarios involving these systems, many of the properties (e.g., densities, viscosities, interfacial tensions, etc.) must be modeled with empirical property correlations for the granular, oleic, aqueous and vapor phases. Also, there may be empirical mass exchange correlations that are used to describe the inter-phase component mass exchange behavior between phases, usually as a function of the local pressure, local temperature and reference (surface) densities. In other disciplines, this rightfully constitutes a lack of proper control of important system variables (and thus high modeling uncertainty) in which adjustments to correlations or groups of parameters can mask several compensating inadequacies of the multiphase flow model itself. This is *why* multiphase flow models, particularly in such scenarios as described above, should be properly validated with suitable carefully-controlled experimental data before they are adapted to field conditions.

In all disciplines and scenarios, however, there are unreasonable arguments that will remain as obviously bad reasoning regardless of the scenario. There are numerous examples of such arguments (and practices) in the prior averaged multiphase flow literature, a few of which are provided in Appendix E.

1.3.5.2 Establishing a Global Pipe Flow Database, ANNA

In the previous section, a proposed standardized set of operational and conceptual model validation criteria was provided for discerning the credibility of scientific multiphase pipe flow models. In this work, the data that accompanies these model

validation criteria are also standardized. A small subset of these data is used throughout this work for validating the Pipe Fractional Flow Theory (in Chapters 3 to 7).

To accomplish this comprehensive validation, over 74,000 different time-averaged experimental measurements (at last check in April, 2012) of pressure gradients, wall and phase shear stresses, volume and entrainment fractions and accompanying system parameters/operating conditions from the publications of over 470 individual investigations in over 110 different laboratories from various countries are assimilated in the ANNA Global Pipe Flow Database. These experiments were conducted in the laboratories of state agencies, universities, private research institutes and corporations. This represents the world's largest and most diverse publicly-accessible and searchable database of averaged multiphase pipe flow experimental data. The database is accessible via a simple search interface on a website on the World Wide Web.

The publications from which the data in ANNA were sourced include dissertations, theses, university departmental reports, conference proceedings and peer-reviewed archival journal papers. The steady-state and transient flow data in ANNA are standardized in SI units regardless of what their units were in their original publications and, in most cases, retain their original flow pattern descriptions and experimental run numbers for cross-referencing purposes. Included in this database are data that were designed for understanding a specific phenomenon (separate effects tests) and data that were designed for investigating wide ranges of variables (integral tests). The data are cross-disciplinary and span over 60 years of history of averaged multiphase pipe flow investigations (inclusive of classic data from the late 1940's to present).

By retaining original dataset run numbers and names in ANNA, readers gain the unique ability to cross-reference data with their source publications, learn about detailed

descriptions of the experiments in these publications and better understand the associated uncertainties (and relevant statistics) of the measurements used for individual test runs.

In addition to the carefully-controlled, reproducible lab data in ANNA, more than 6,000 different field measurements (at last check in April, 2012) of pressure, volume fractions and accompanying system parameters/operating conditions from various petroleum and geothermal wells and pipelines are assimilated in ANNA. Included among these field datasets are both semi-controlled, field test data as well as uncontrolled, field operating data at field-scale conditions of large and very large-diameter conduits, complex compositional fluid mixtures (e.g., two-phase and three-phase flows of heavy oils, live oils, volatile oils and gas condensates), high pressures and high temperatures.

A unique feature of the ANNA database is that both developed and developing flow data are stored in the same format. This provides a standardized way to view developed and developing flow data. The in-house code used for this work, UTPipeFlow, stores cases as "utpf" files. Similarly, all of the data in ANNA are stored as "utpf" case files. This means that all of the data in ANNA can be opened and viewed within UTPipeFlow and is already prepped for subsequent simulation. These "utpf" case files can be downloaded from the ANNA database website and viewed in UTPipeFlow and, equivalently, new data (i.e., built "utpf" case files) can be uploaded from UTPipeFlow to the ANNA database website. This makes ANNA a "living" database with an unrestricted growth capability. A facility is also provided to convert Microsoft Excel files to "utpf" case files which can then be freely uploaded via UTPipeFlow to the ANNA database website. The ease of downloading from or uploading to the ANNA database website now provides investigators with a simple, standardized tool for sharing and using multiphase (or single-phase) pipe flow data. This, of course, creates a readily-

available means for investigators in any part of the world to access various types of data from different laboratories for use in their research studies.

Now, even though datasets from various publications/sources can contain bad or incorrectly measured data (e.g., typographical or systematic errors), the ability to cross-reference the individual run numbers of the datasets in ANNA allows investigators the opportunity to interrogate possible discrepancies or errors in the original experiments. Of course, the original investigators who conducted the experiments can be contacted for clarifications or questions regarding certain measurements (such as was done in many instances by this author). This is why all data of a given investigation are included in ANNA, regardless of the potential issue of whether there may be outliers/errors in the original datasets. In any event, the outlier data will show as outliers in relation to the other similar data (or in relation to other data in the overall dataset) in the better multiphase flow models, i.e., the models that correctly capture the observed trends.

In fact, ANNA makes it possible to objectively identify bad data. This is accomplished by comparing the measurements of several different labs of one set of similar operating conditions. If the phenomenon of interest is actually being measured by the various labs, then all the labs will provide very similar measurements for the studied operating condition. In other words, the reproducibility of the phenomenon would be demonstrated – a requisite for scientific data. In this way, outlier or erroneous data from one lab can be easily detected in comparison with the observations of other labs.

Fig. 1.3.19 highlights a simple scenario demonstrating the previous arguments. Fig. 1.3.19a shows two data-points from two different labs for a narrow range of operating conditions, namely, vertical two-phase flow of air and water in small-diameter (between 0.015 to 0.038 m) circular pipes at low air densities (between 1.2 to 3 kg/m^3) and at water superficial velocities from 0.2 to 0.25 m/s. These ranges were searched in

ANNA and the results of the search are shown in Fig. 1.3.19b. As Fig. 1.3.19b clearly shows, one of the data points is an outlier in comparison to the rest of the measurements from different labs (spanning about 50 years of investigations). Without this new capability provided by ANNA, it would be very difficult (if not impossible) to objectively determine which of the data points in Fig. 1.3.19a is a correct observation or an incorrect one. Such a basic question as to whether the data from a lab is good or bad must be satisfactorily answered before unambiguous conclusions can be drawn from the models that use such data in their testing and validation procedures.

Lastly, before leaving this section on model validation criteria, we briefly showcase in Table 1.2 the various degrees of expected accuracy for averaged (1D) multiphase pipe flow models. While different investigators may have their own opinions on the expected ranges of accuracy for a particular scenario, our emphasis is in relating the reported instrumentation uncertainty of the experiments in ANNA (e.g., in some cases, up to +/- 15% error for void fraction measurements) to what can therefore be considered as the best possible model accuracy (i.e., in the region of +/- 15 % error)

Standardized Problem Definitions for Multiphase Flow			Chemical, Process	Petroleum, Fossil Fuels	Nuclear, Geothermal	Mechanical Aerospace, all others
Problem Groups		Specific Examples	Discipline Groups			
PHASES	1. Effect of Combination	Vapor-liquid, vapor-solid, liquid-liquid, liquid-solid				
	2. Effect of Flow Rate	Low liquids loading, high-rate flow, ultra-high mass fluxes				
	3. Effect of Properties	Density, viscosity and interfacial tension, heavy oil, high density gases				
	4. Effect of Amount	Vapor-liquid-liquid, vapor-liquid-solid, liquid-liquid-solid				
	5. Effect of Flow Direction	Onset of flooding, onset of flow-reversal, stationary column flow				
	6. Effect of Mass Change	Single-component, compositional, black-oil, flow assurance, reactions				
	7. Effect of Rheology	Non-Newtonian liquids and mixtures, drag-reducing agents, foams				
CONDUIT	8. Effect of Size	Micro/mini-channel, small-tubing, large-bore, transmission/trunk lines				
	9. Effect of Inclination	Vertical up/down, inclined up/down, horizontal				
	10. Effect of Shape	Straight/curved, circular/non-circular pipe, constant/variable area				
	11. Effect of Network	Wells, pipelines, integrated assets, coupled porous-pipe media				
	12. Effect of Wall Change	Momentum transfer, heat transfer, mass transfer, elastic/non-elastic wall				
SYSTEM	13. Effect of Flow Pattern	Annular, bubbly, slug, stratified, wavy, churn, mist				
	14. Effect of Flow Development	Fully-developed/developing flow, porous pipe, sources/sinks				
	15. Effect of Extreme Condition	High pressure/temperature, rupture, blowout, reactor safety incident				
	16. Effect of Time Change	Slow/fast rate transient, blow-down, start-up, boundary changes				
	17. Effect of External Field	Micro-gravity, hyper-gravity, equal-density				
	18. Effect of Other Phenomena	Flow instabilities, porous media, mixing, magneto-hydrodynamics				
	19. Effect of Measurement Method	Direct/indirect measurements, simple/complex instrumentation				
	20. Effect of Modeling Method	Microscopic, mesoscopic, macroscopic				
	21. Effect of Computational Method	Continuum, integrated, multi-scale, multi-dimensional				

Table 1.1: Standardized problem definitions for multiphase flow.

Accuracy Error %	Suitability for Design	Degree of Model Accuracy
> +/- 50 %	Not suitable in most cases	Poor accuracy in most cases
+/- 35 - 50 %	Suitable in some cases	Reasonably accurate in some cases
+/- 25 - 35 %	Suitable and adequate in most cases	Accurate in most cases (present standard in averaged multiphase flow)
+/- 15 - 25 %	Excellent	Very accurate
< +/- 15 %	In general, this is the best achievable accuracy	Approaching the accuracy of measuring instrumentation

Table 1.2: Degrees of model accuracy in averaged (1D) multiphase pipe flow.

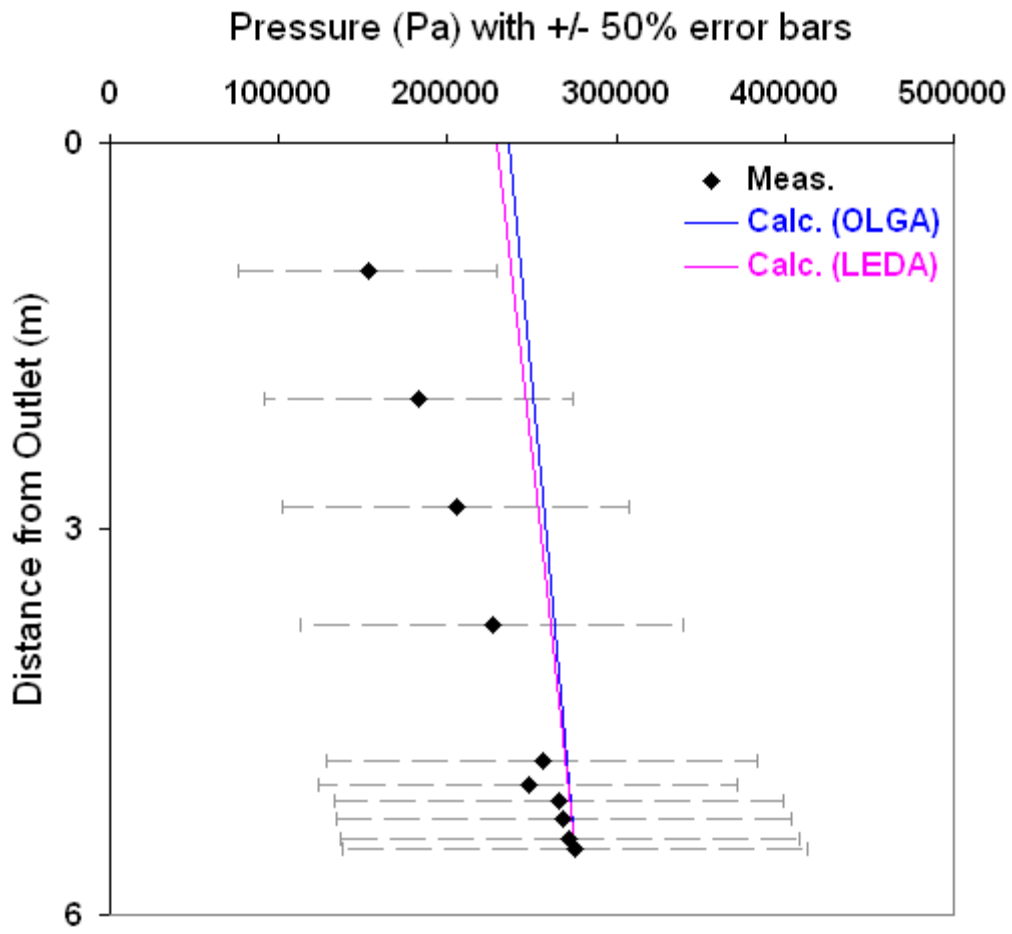

Figure 1.3.1: Comparison of one air (phase 2) and water (phase 1) dataset from Cousins et al. (1965) – run no. 49 in this reference – against the predictions of example industrial multiphase flow codes in practice. This run, and many others like it, can be found on pg. 395 in Table 12.1 of the classic multiphase flow textbook of Wallis, 1969 (denoted in this reference as M_{gas} = 70 lb/hr and M_{liquid} = 100 lb/hr).

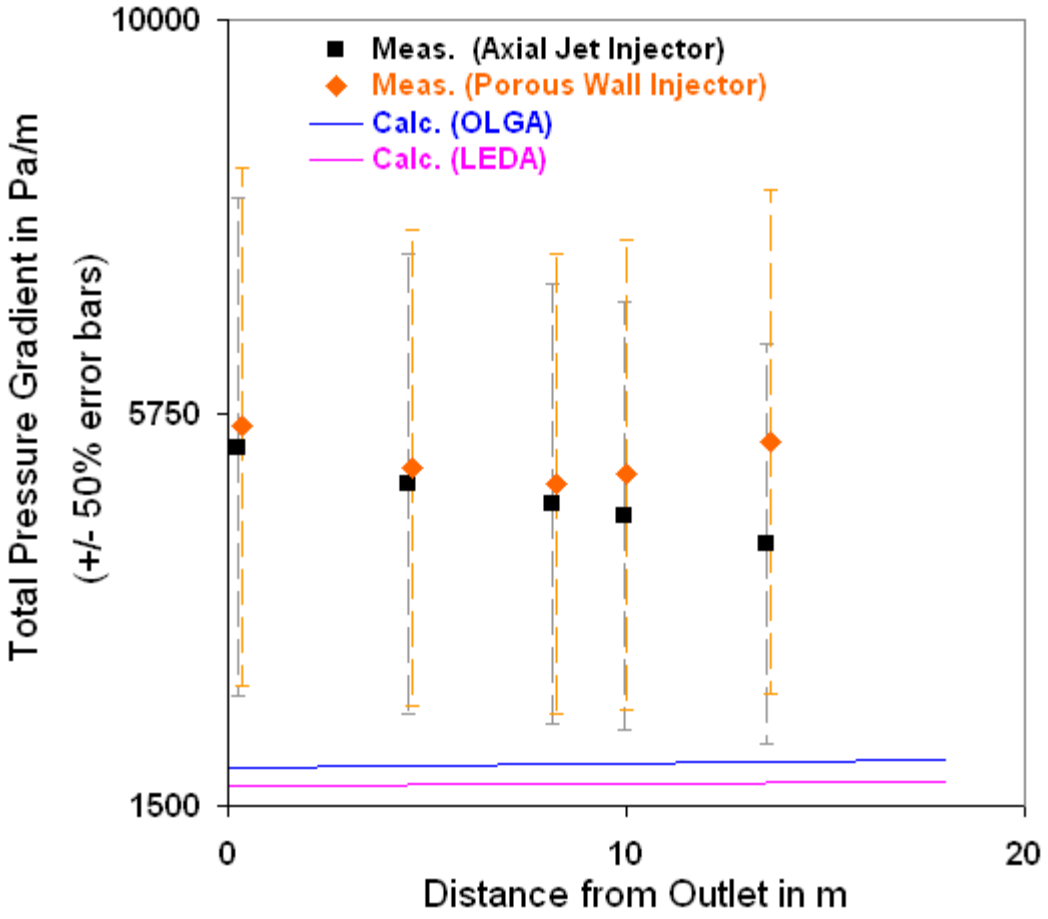

Figure 1.3.2: Comparison of one air (phase 2) and water (phase 1) dataset from Brown (1978) – run no. 2 in this reference – against the predictions of example industrial multiphase flow codes in practice.

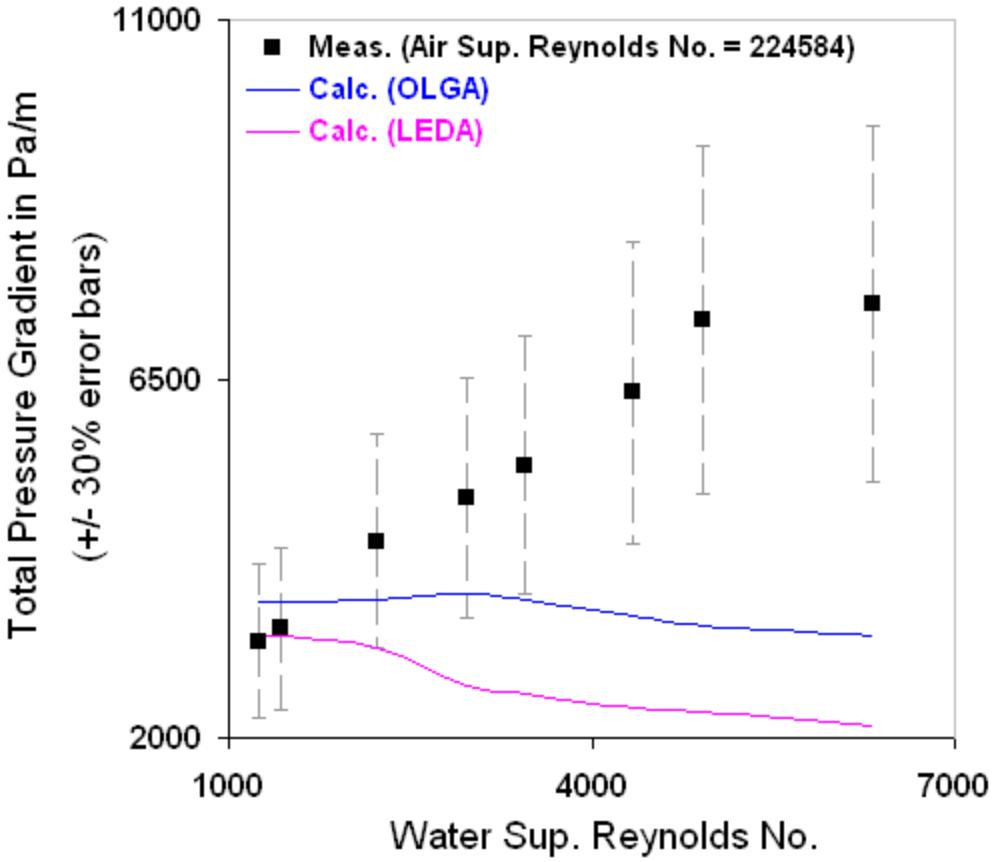

Figure 1.3.3: Comparison of one air (phase 2) and water (phase 1) dataset from Hewitt et al. (1961) – run nos. 7.02 to 7.09 in this reference – against the predictions of example industrial multiphase flow codes in practice.

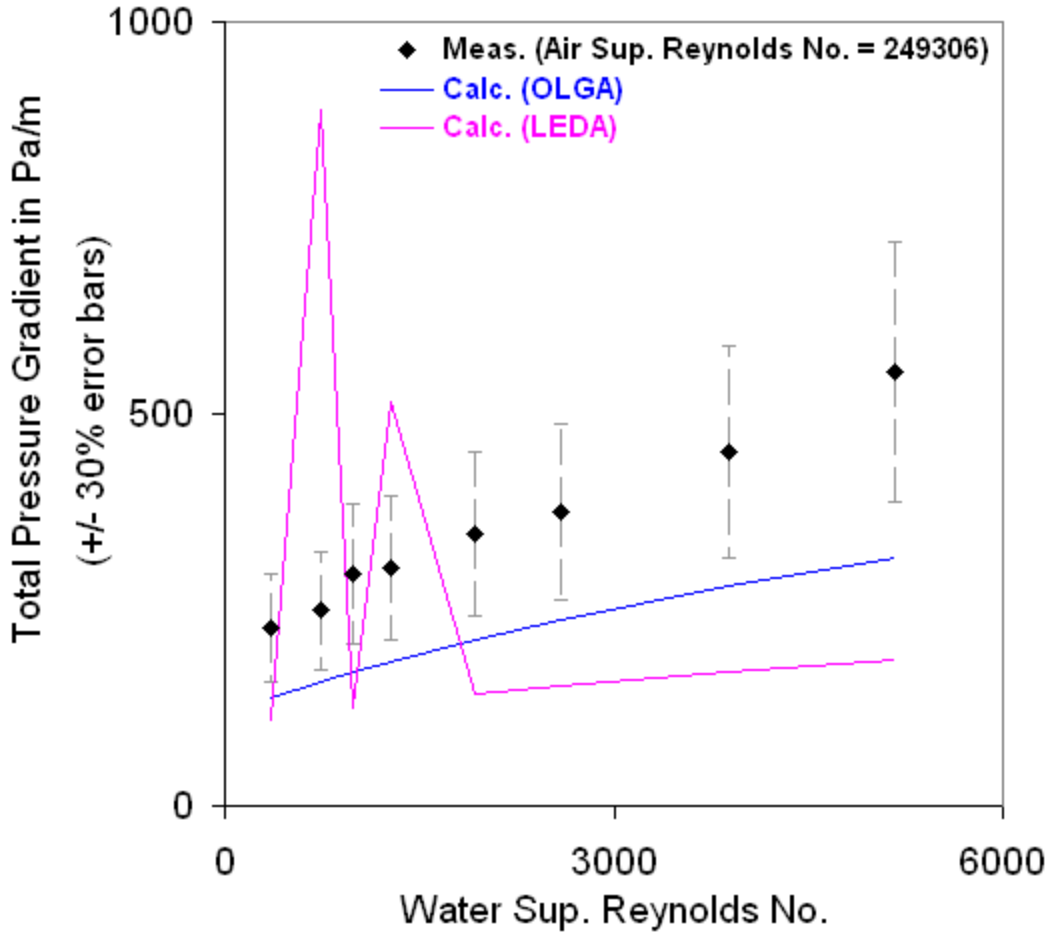

Figure 1.3.4: Comparison of a large-diameter air (phase 2) and water (phase 1) annular flow dataset from Azzopardi et al. (1983) against the predictions of example industrial multiphase flow codes in practice. This dataset can also be found in Oliemans et al. (1986).

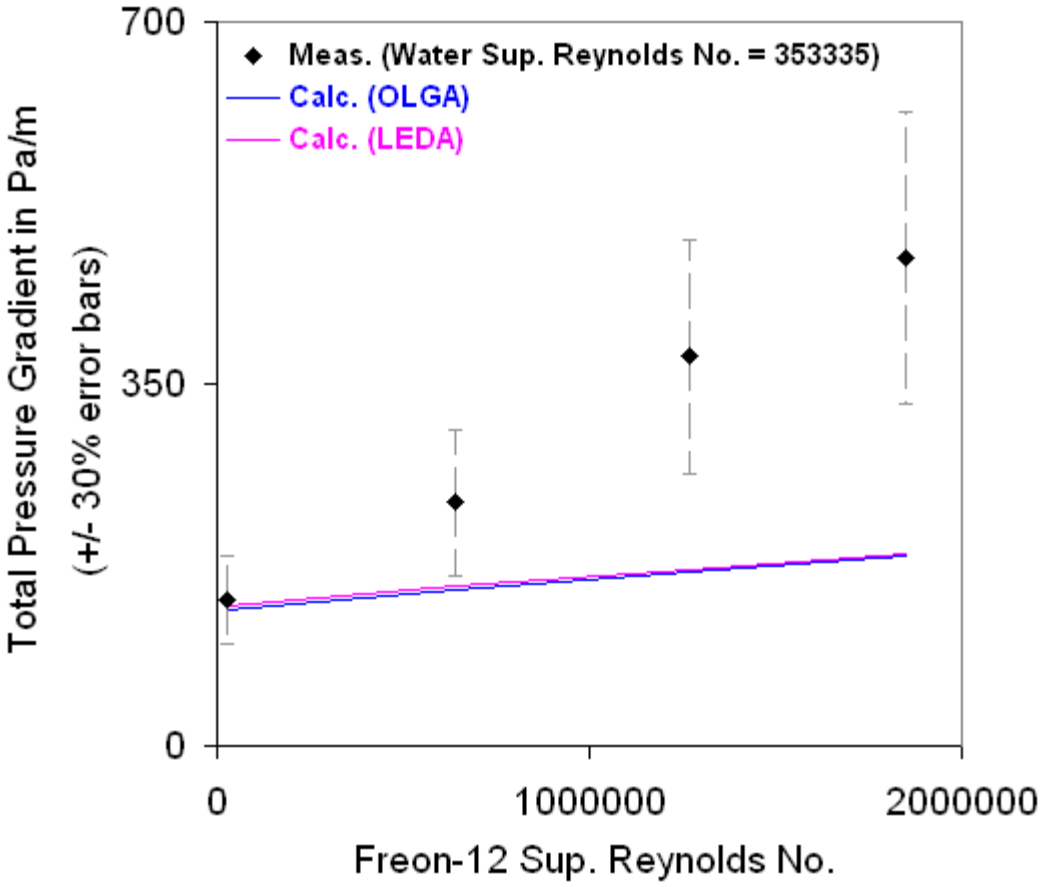

Figure 1.3.5: Comparison of one large-diameter, high gas density Freon-12 (phase 2) and water (phase 1) slug flow dataset from Crowley et al. (1986) – run nos. FHOPI-46 to FHOPI-49 in this reference – against the predictions of example industrial multiphase flow codes in practice.

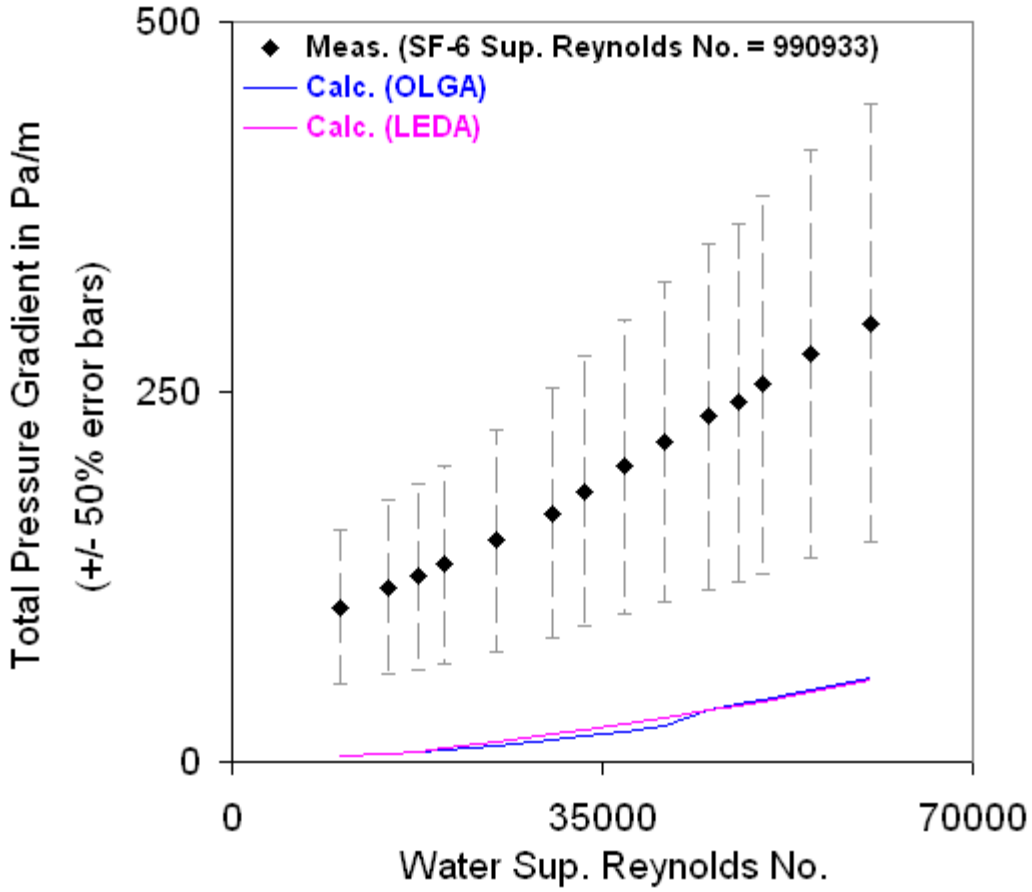

Figure 1.3.6: Comparison of one high gas density SF_6 (phase 2) and water (phase 1) stratified roll wave flow dataset from Johnson (2005) – test nos. 154 to 167 in this reference – against the predictions of example industrial multiphase flow codes in practice.

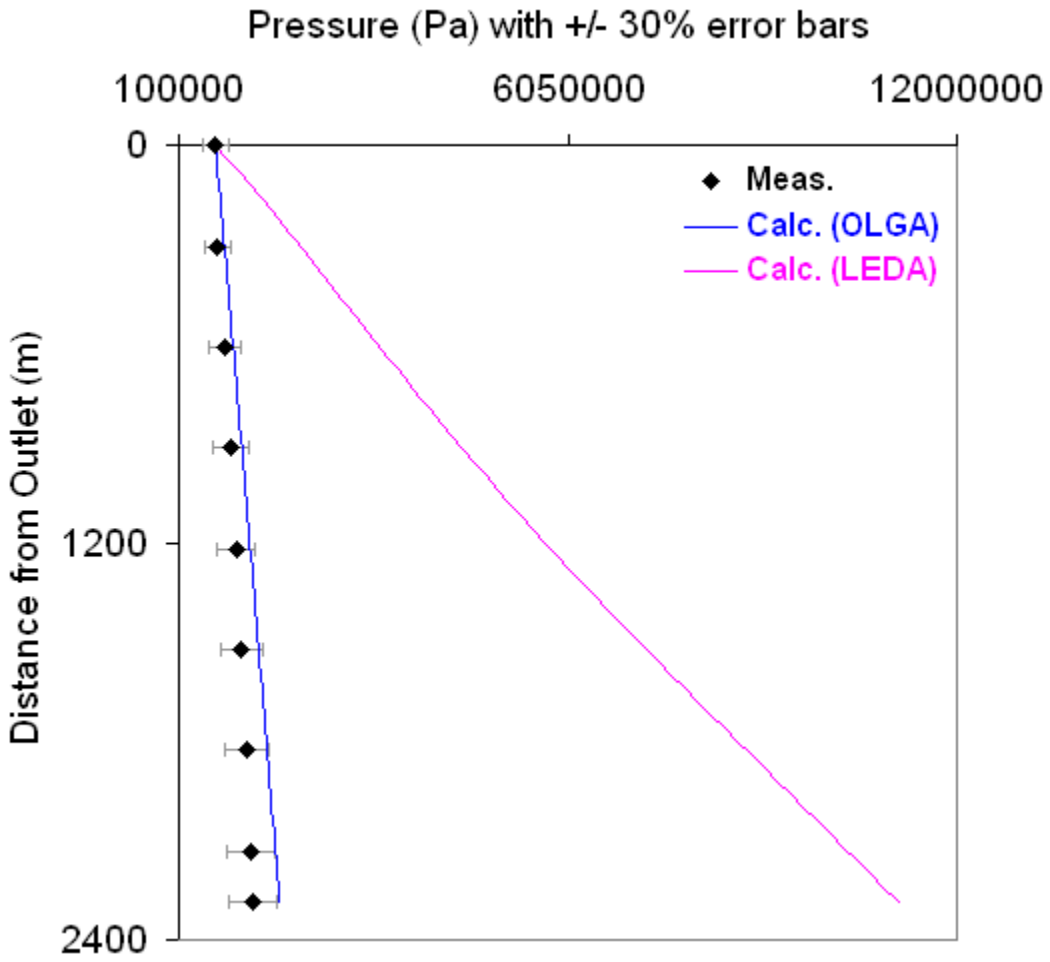

Figure 1.3.7: Comparison of one high gas density natural gas (phase 2) and water (phase 1) mist flow dataset from Kumar (2005) – Well J in this reference – against the predictions of example industrial multiphase flow codes in practice. The stated water production rate for this well is 2 BBL/d with a high GWR (Gas-to-Water Ratio) of 345,000 scf/BBL.

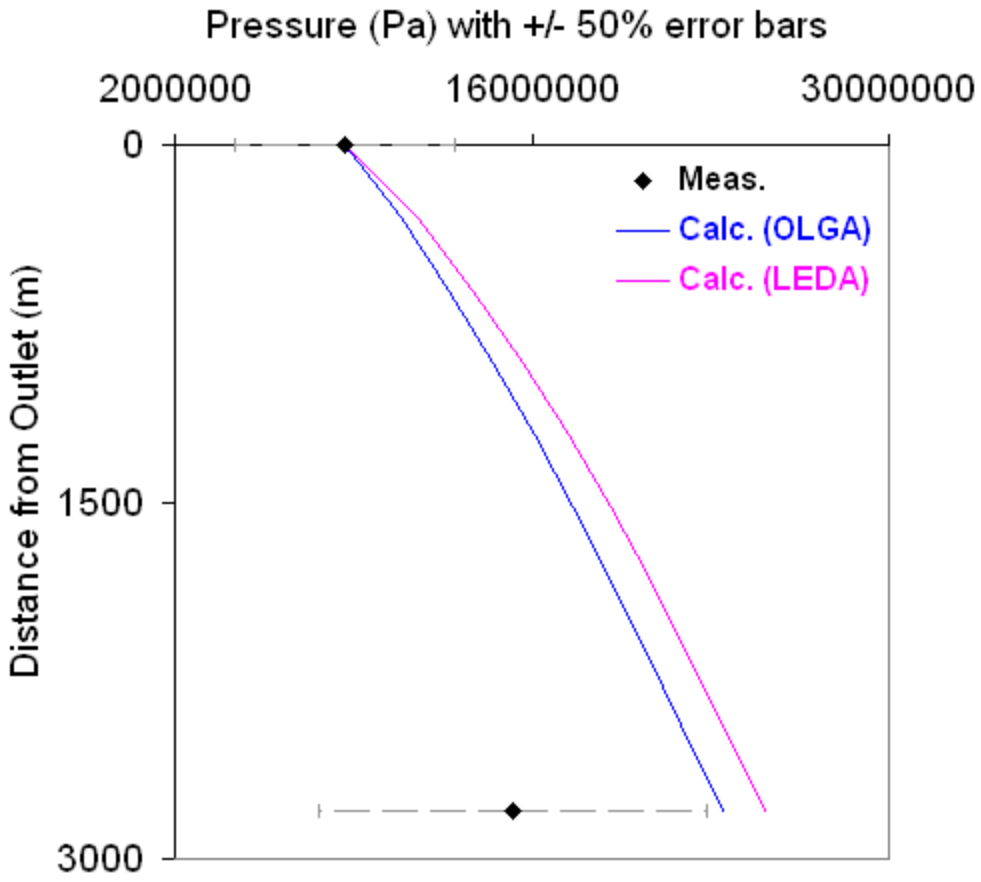

Figure 1.3.8: Comparison of one high gas density natural gas (phase 2) and water (phase 1) annular flow dataset from Chierici et al. (1974) – Well Case 6 in this reference – against the predictions of example industrial multiphase flow codes in practice. The stated water production rate for this well is 50 BBL/d with a high GWR (Gas-to-Water Ratio) of 311,630 scf/BBL.

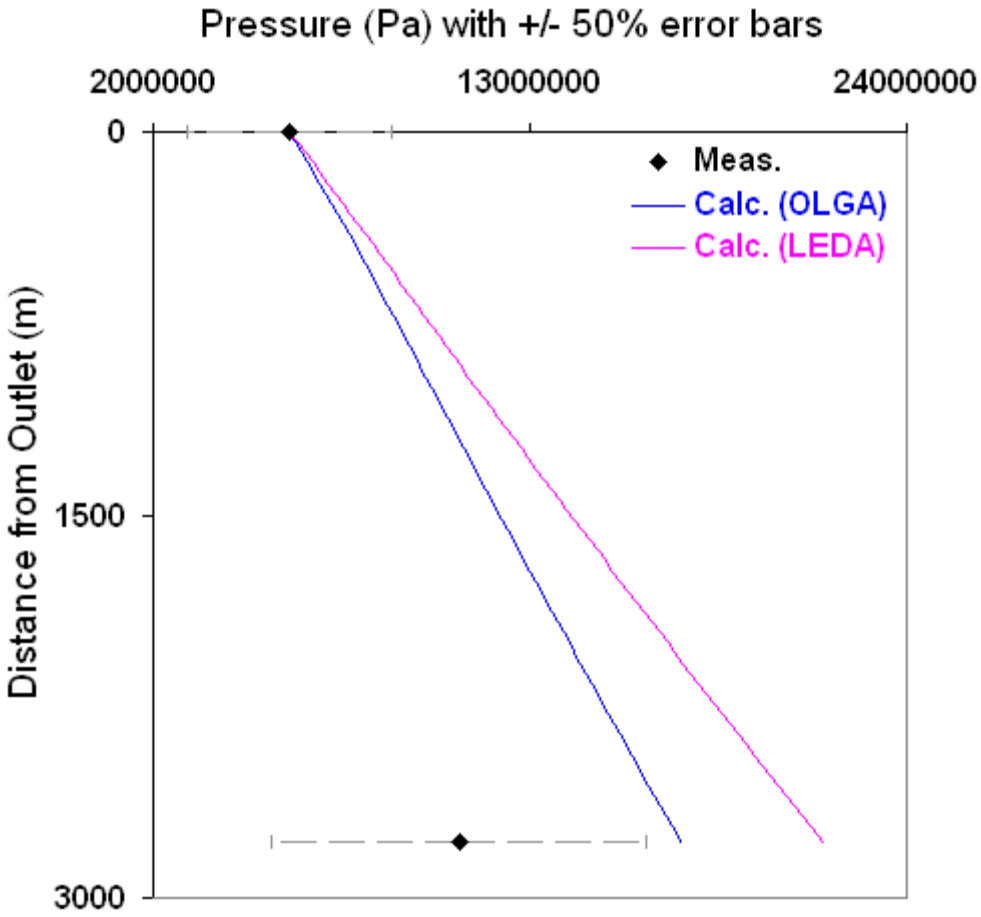

Figure 1.3.9: Comparison of one high gas density natural gas (phase 2) and water (phase 1) annular flow dataset from Peffer et al. (1988) – Well TRRC No. 49 in this reference – against the predictions of example industrial multiphase flow codes in practice. The stated water production rate for this well is 52 BBL/d with a low GWR (Gas-to-Water Ratio) of 8,846 scf/BBL.

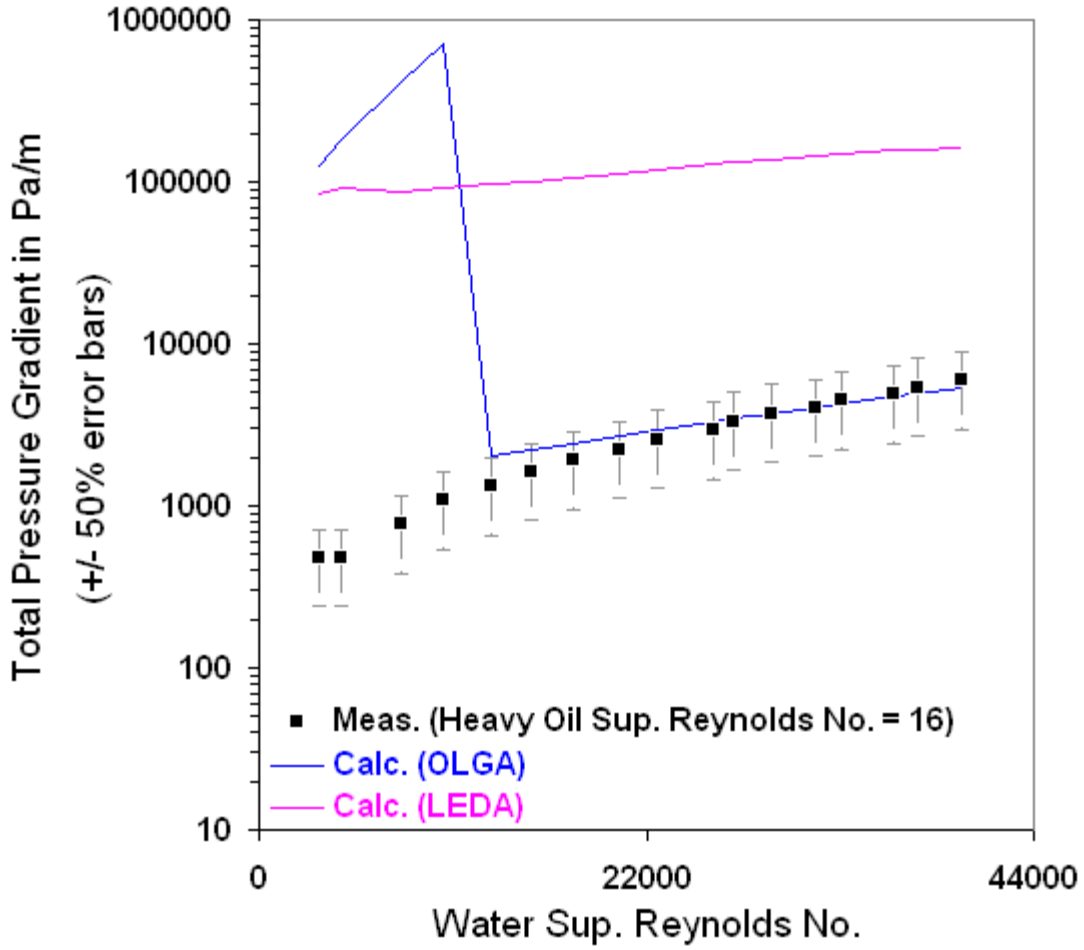

Figure 1.3.10: Comparison of one horizontal heavy paraffin oil (phase 2) and water (phase 1) dataset from Grassi et al. (2008) – runs at phase 2 superficial velocity = 0.695 m/s in this reference – against the predictions of example industrial multiphase flow codes in practice. The given heavy paraffin oil viscosity and density are 0.8 Pa-s and 886 kg/m^3, respectively.

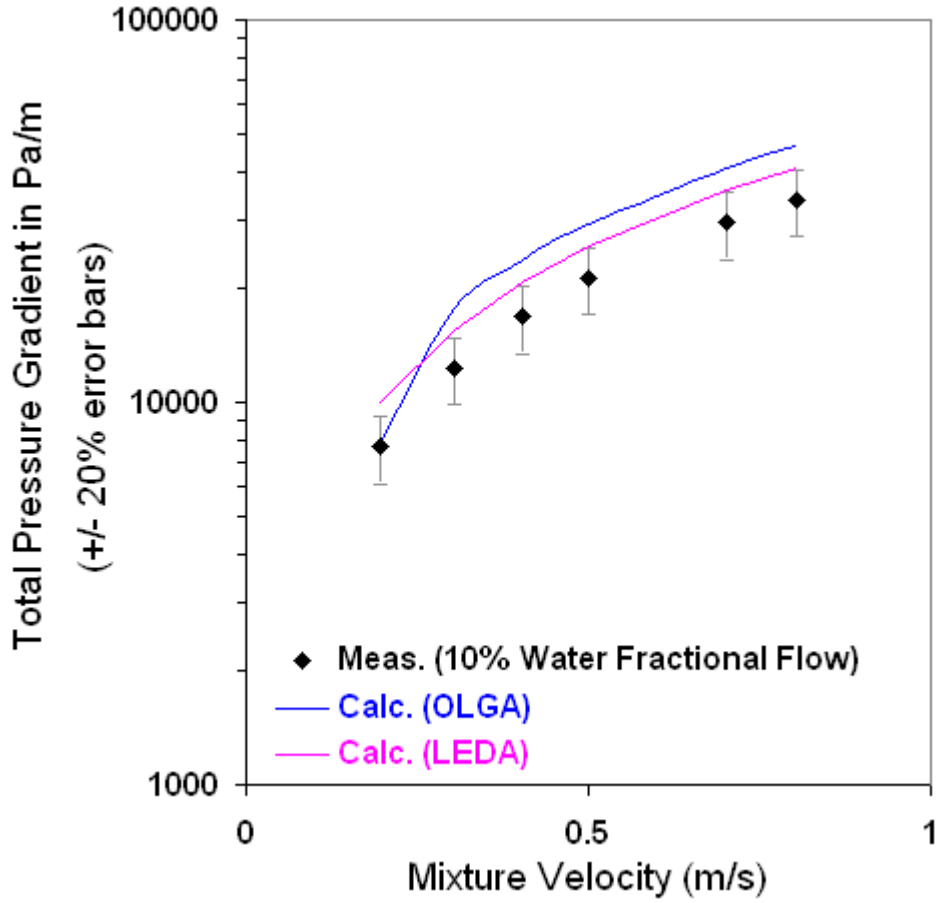

Figure 1.3.11: Comparison of one real heavy crude oil (phase 2) and water (phase 1) dataset from Wang et al. (2011) against the predictions of example industrial multiphase flow codes in practice. The given real heavy crude oil viscosity and density are 0.8 Pa-s and 953 kg/m^3, respectively.

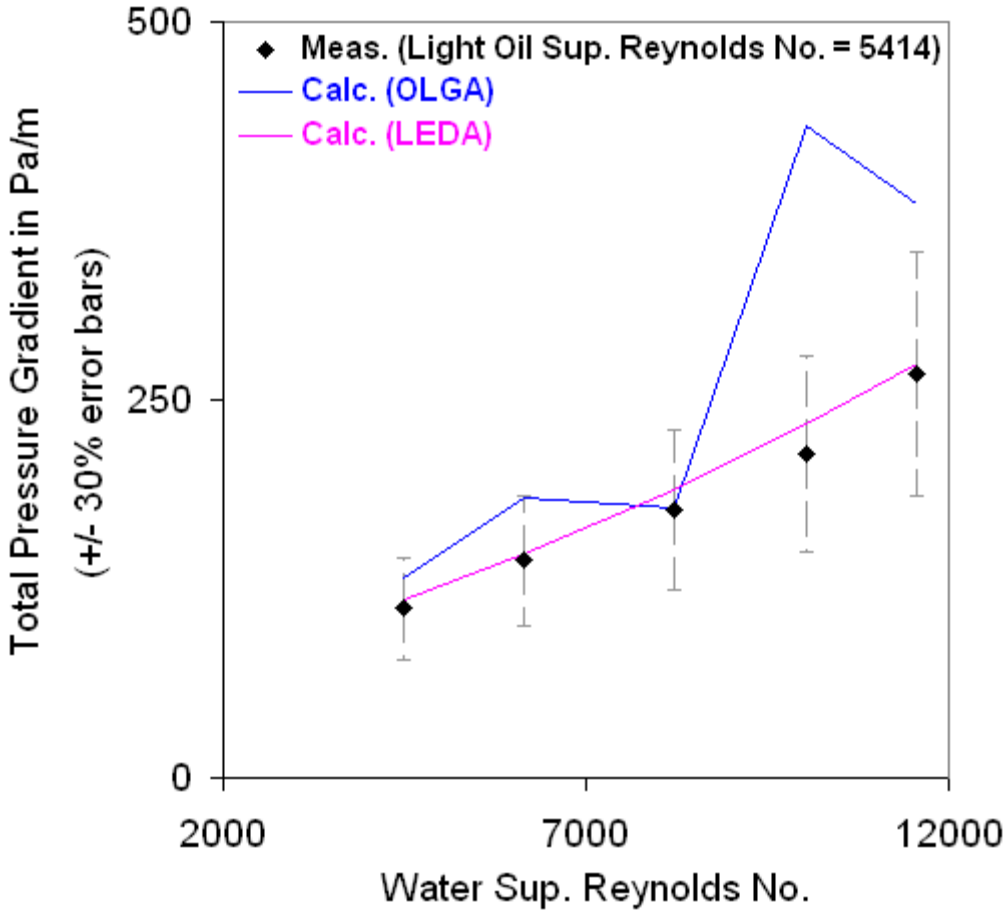

Figure 1.3.12: Comparison of one light refinery stream oil (phase 2) and water (phase 1) dataset from Plaxton (1995) – runs nos. 16 to 20 in this reference – against the predictions of example industrial multiphase flow codes in practice. The given light refinery stream oil viscosity ranged from 0.0011 to 0.0015 Pa-s for the conditions shown at a density of 845 kg/m^3.

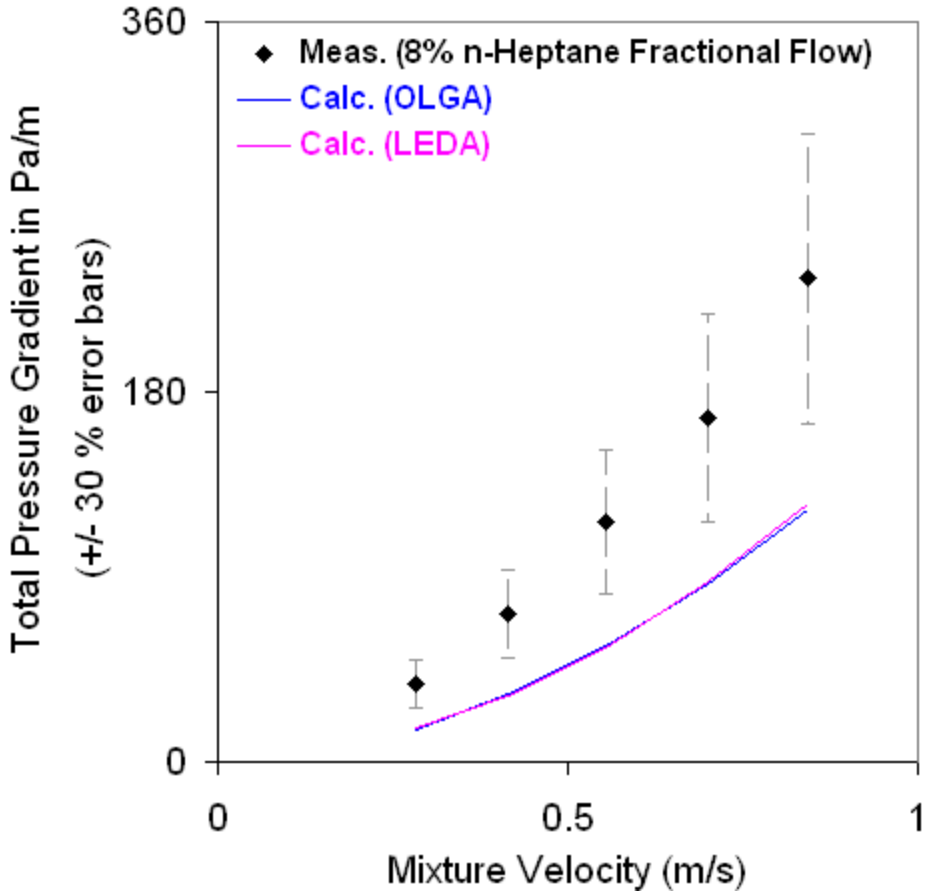

Figure 1.3.13: Comparison of one n-Heptane light oil (phase 2) and water-glycerine (phase 1) dataset from Pouplin et al. (2011) against the predictions of example industrial multiphase flow codes in practice. The given n-Heptane light oil viscosity and density are 0.0004 Pa-s and 684 kg/m^3, respectively.

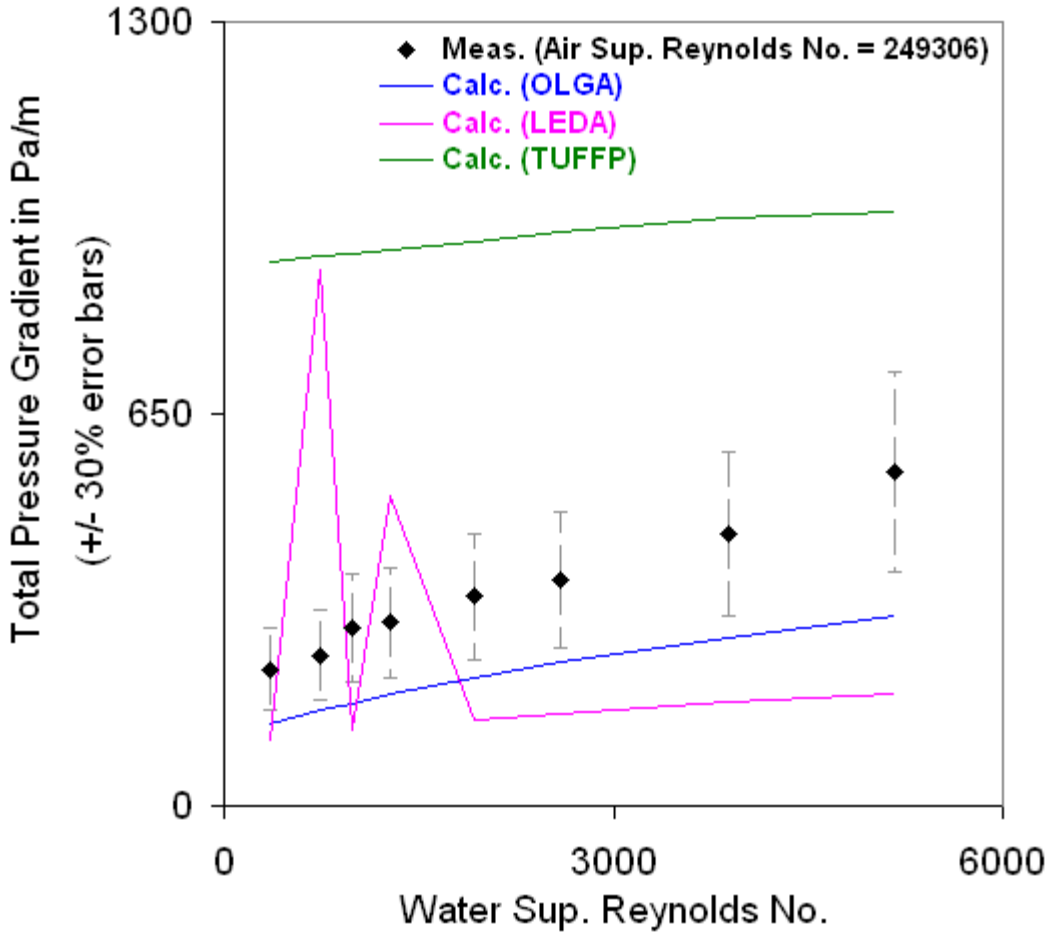

Figure 1.3.14: Comparison of a large-diameter air (phase 2) and water (phase 1) annular flow dataset from Azzopardi et al. (1983) against the predictions of example industrial and academic multiphase flow codes in practice. This dataset can also be found in Oliemans et al. (1986).

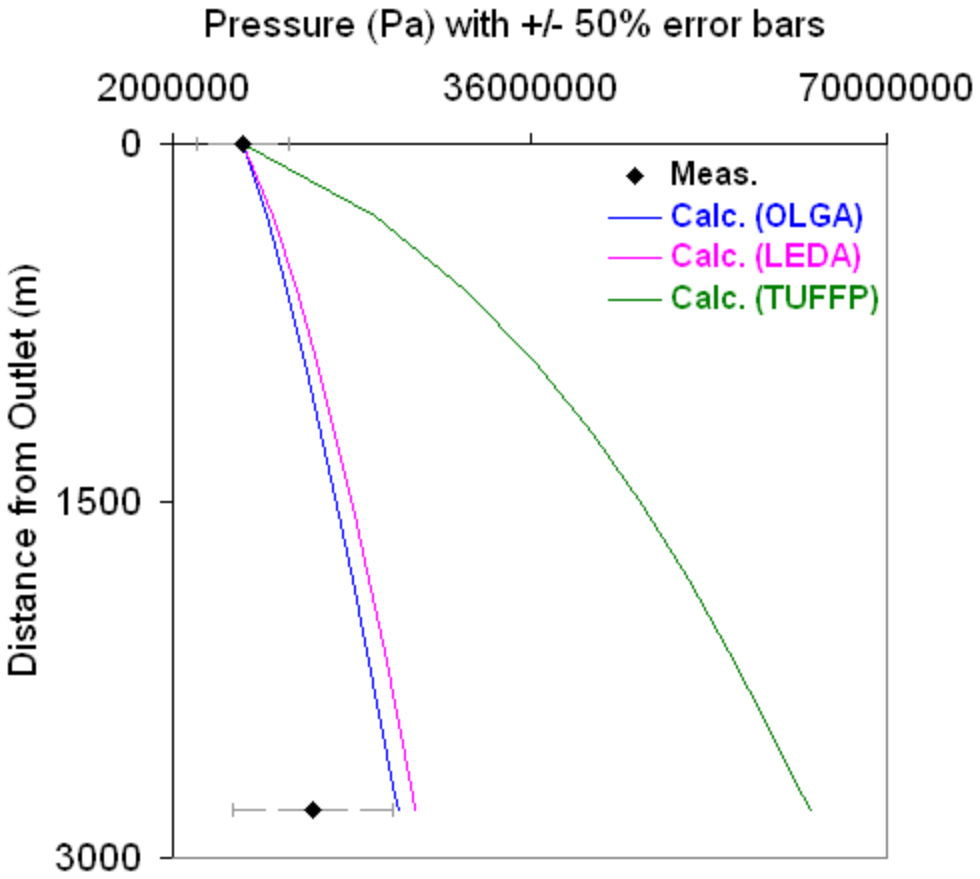

Figure 1.3.15: Comparison of one high gas density natural gas (phase 2) and water (phase 1) annular flow dataset from Chierici et al. (1974) – Well Case 6 in this reference – against the predictions of example industrial and academic multiphase flow codes in practice. The stated water production rate for this well is 50 BBL/d with a GWR (Gas-to-Water Ratio) of 311,630 scf/BBL.

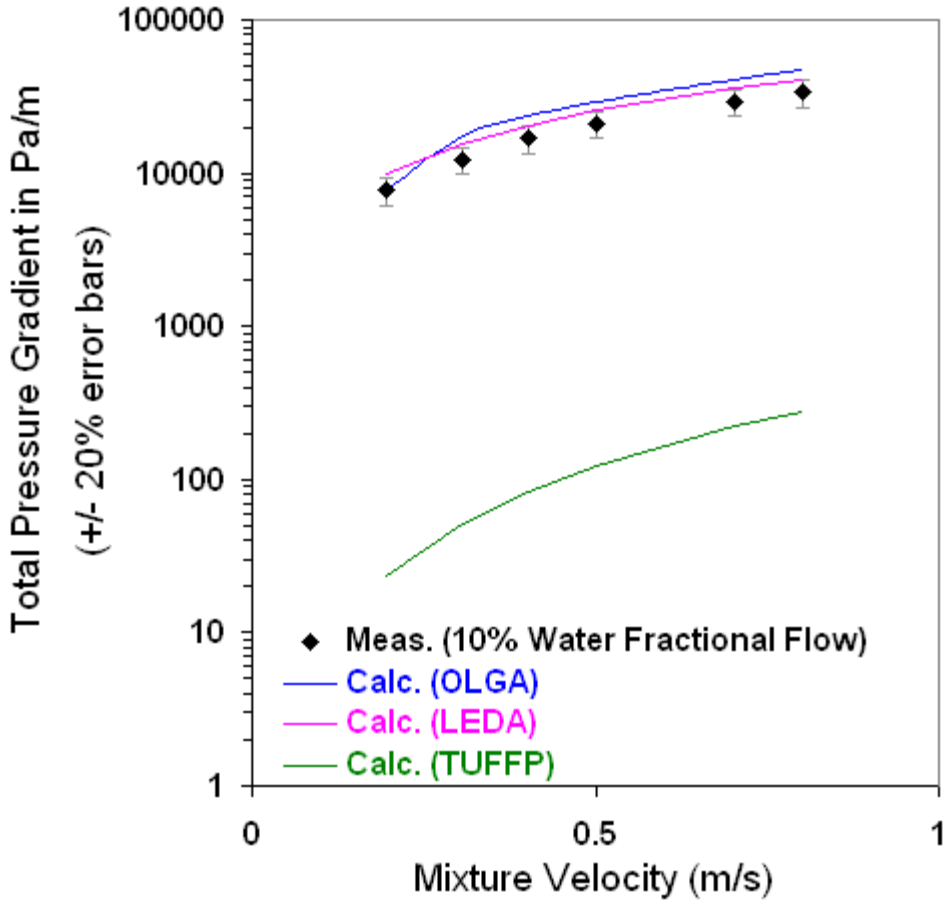

Figure 1.3.16: Comparison of one real heavy crude oil (phase 2) and water (phase 1) dataset from Wang et al. (2011) against the predictions of example industrial and academic multiphase flow codes in practice. The given real heavy crude oil viscosity and density are 0.8 Pa-s and 953 kg/m^3, respectively.

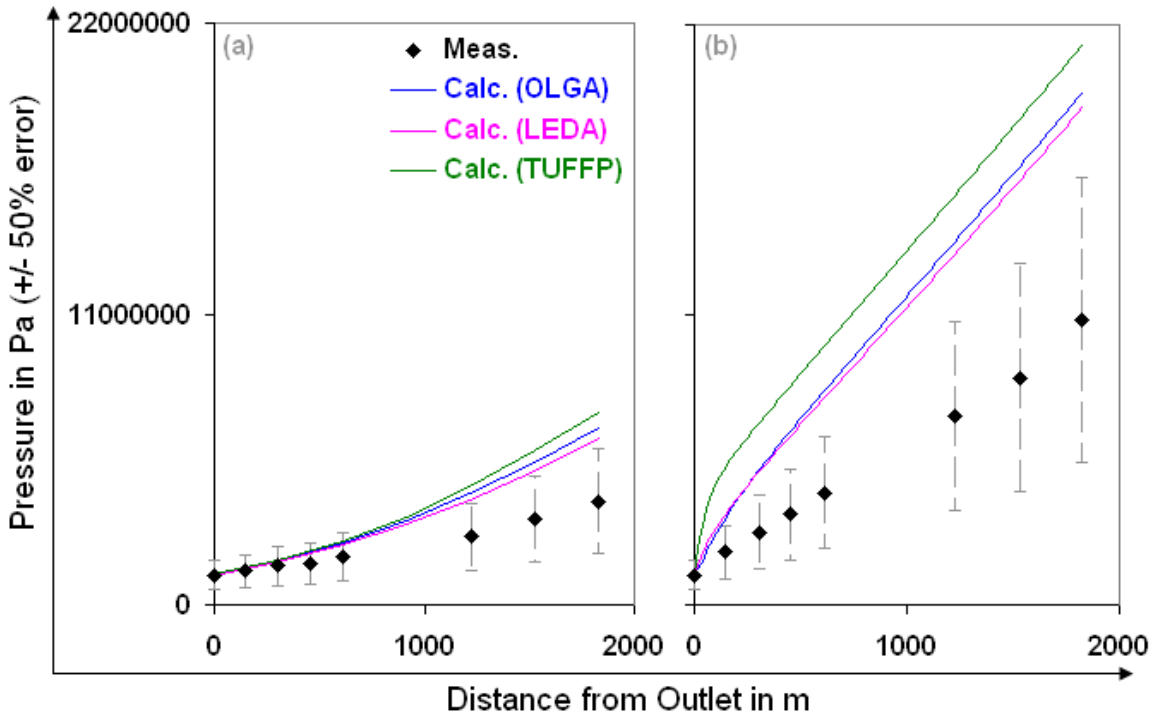

Figure 1.3.17: Comparison of two natural gas (phase 2) and real crude oil (phase 1) controlled field datasets from Baxendell and Thomas (1961) – test nos. 14 (Fig. 1.3.17-a) and 1 (Fig. 1.3.17-b) in Table 1 of this reference – against the predictions of example industrial and academic multiphase flow codes in practice. The stated crude oil production rates for these tests are 176 BBL/d with a GOR (Gas-to-Oil Ratio) of 758 scf/BBL for test no. 14, and 5,082 BBL/d with a GOR of 724 scf/BBL for test no. 1.

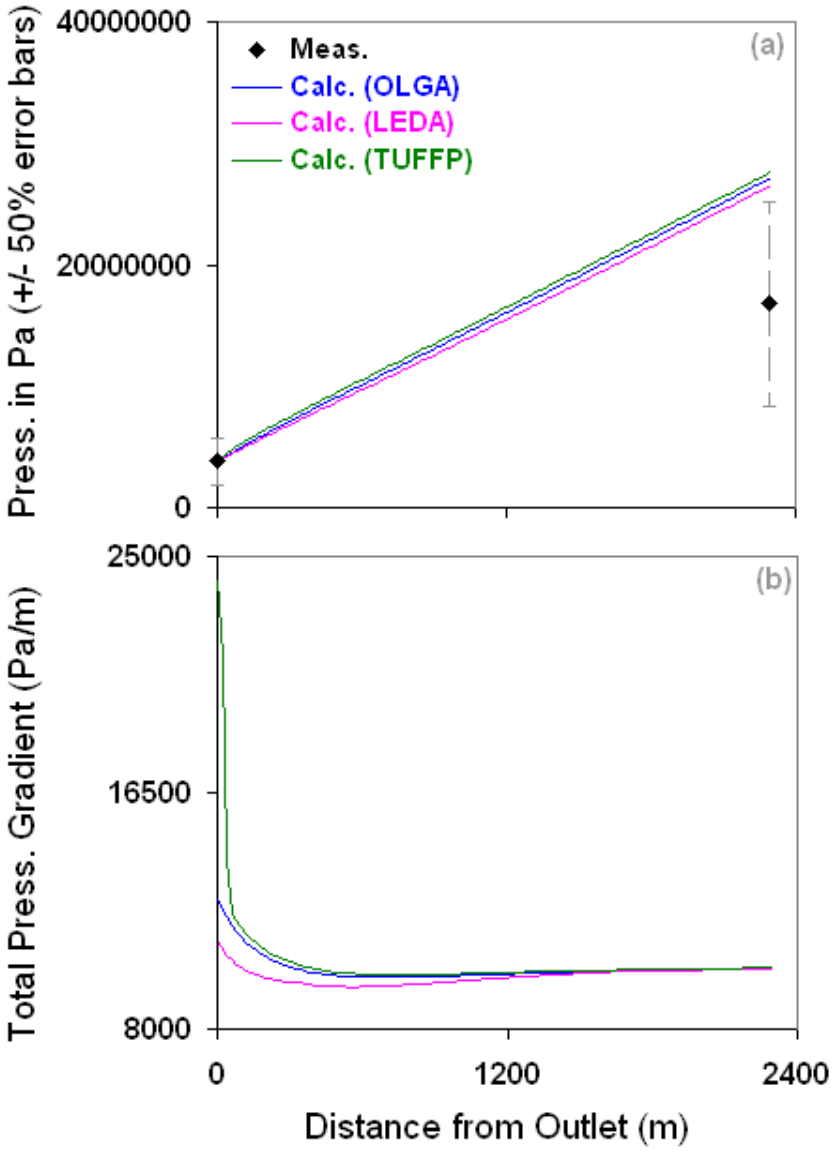

Figure 1.3.18: Comparison of one natural gas (phase 2) and real crude oil (phase 1) annulus-produced oil well dataset from Sanchez (1972) – well 77 in this reference – against the predictions of example industrial and academic multiphase flow codes in practice. The stated crude oil production rate for this well is 14,018 BBL/d with a GOR of 606 scf/BBL.

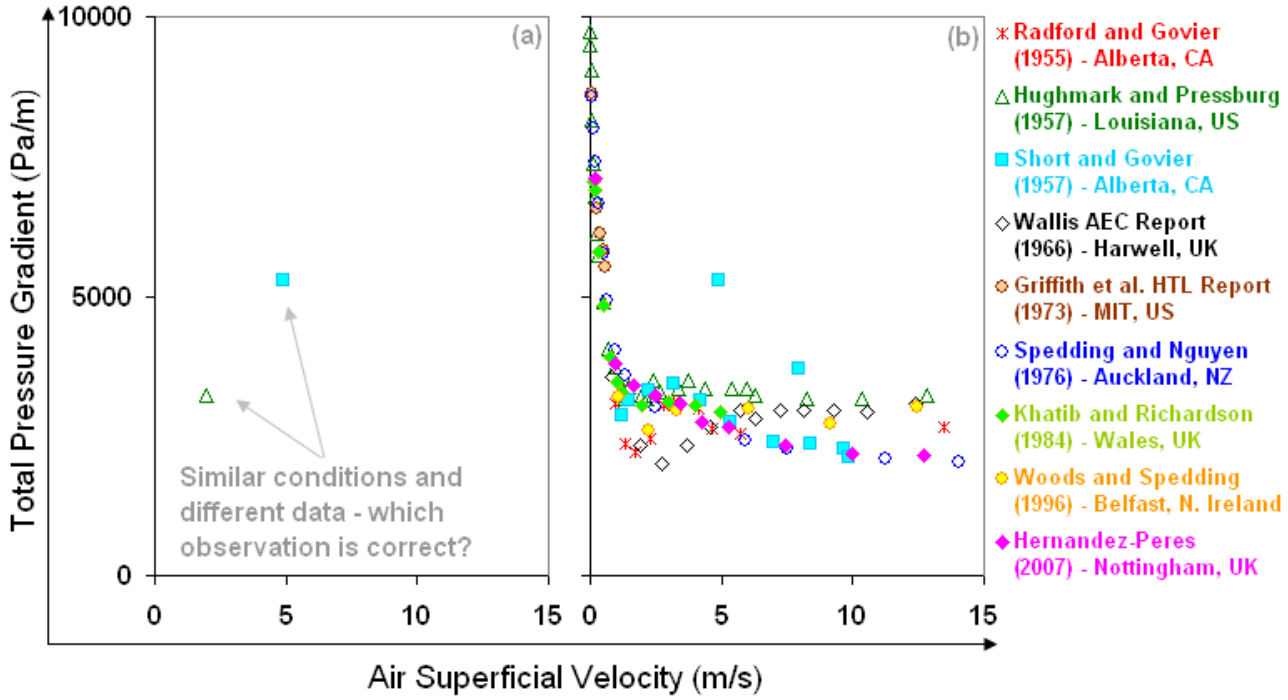

Figure 1.3.19: Comparison of various lab measurements over several decades for a narrow range of operating conditions, namely, vertical two-phase flow of air and water in small-diameter (between 0.015 to 0.038 m) circular pipes at low air densities (between 1.2 to 3 kg/m^3) and at water superficial velocities from 0.2 to 0.25 m/s.

Chapter 2 – The Nagoo-Sharma Equations

2.1 New Modeling Approach

In the previous chapter, we reviewed key aspects of past work in averaged multiphase pipe flow. With our perspective now in place (i.e., standardizing the people, problems, terminology and data), we next describe the development of the core principles and equations of this research. Moreover, since there are no precedents to the collective contributions of this research in the prior multiphase flow literature, only the major references to comprehensive review papers will be provided in the subsequent chapters in order to direct the reader to historical developments in specific averaged multiphase flow topics. Although review papers have an importance in their own right with regards to a particular studied phenomenon, the discovery of the interrelationships and connectivity among different phenomena (via the analytical averaged-equations models in this chapter as well as the next) is the main emphasis of this research.

2.1.1 Single-Phase Pipe Flow

In the balance equation for the rate of change of axial-momentum in single-phase pipe flow, there is one unmeasured system quantity – the wall friction (or viscous) loss factor. Understanding this loss factor is, therefore, where we must start. Note that it is far from obvious that the wall friction loss factor should be a starting point for the hydrodynamic modeling of multiphase pipe flow. We start here since it is an unreasonable approach, in our view, to attempt any multiphase flow problem (hydrodynamic or otherwise) without first understanding and carefully demarcating the ignorance-boundaries of the corresponding single-phase flow problem. If a multiphase problem is well understood, then the best indicator to infer this will be that the accuracy of its solutions will hopefully approach the corresponding single-phase flow accuracy. In

a general sense, however, the accuracy of any multiphase flow scenario will always be lower-bounded by the maximum of the corresponding single-phase flow accuracy and multiphase flow instrumentation error.

Now, the general form of the phase-to-boundary *phenomenological transfer laws* for any conservable or non-conservable quantity, Y, is expressed as:

$$\overbrace{\left(\begin{array}{c} wall\ \ flux \\ of\ Y \end{array}\right)}^{\substack{flux\ caused\ by\ macro\text{-}scale \\ phase\text{-}to\text{-}wall\ \ phenomena}} = \overbrace{+}^{\substack{\text{"high-to-low"} \\ \text{sign} \\ \text{convention}}} \overbrace{K_{phase\to wall}}^{\substack{Y-flux \\ transfer \\ coefficient}} \overbrace{\Delta\left(\begin{array}{c} conc. \\ of\ Y \end{array}\right)}^{\substack{relative \\ Y-concentration}} \tag{1}$$

A familiar example of Eqn. 1 is the transfer law for thermal energy (or heat), as:

$$\underbrace{\frac{Q_{wall\to phase}}{Z\Delta L}}_{\substack{surface\ over\ which \\ flux\ is\ transferred}} = \overbrace{q_{wall\to phase}}^{\substack{wall\text{-}to\text{-}phase \\ heat\ flux}} = \overbrace{+}^{\substack{\text{"high-to-low"} \\ \text{sign} \\ \text{convention}}} \overbrace{\left(\frac{h_{wall\to phase}}{\rho\hat{c}_p}\right)}^{\substack{heat\ flux \\ transfer\ coefficient}} \overbrace{\left(\overbrace{\rho\hat{c}_p T_{wall}}^{\substack{high\ conc.\ of \\ heat\ (wall)}} - \overbrace{\rho\hat{c}_p T}^{\substack{low\ conc.\ of \\ heat\ (phase)}}\right)}^{relative\ heat\ concentration} \tag{2}$$

As shown in the macroscopic single-phase flow formulations on the estimation of viscous loss on pg. 206 of BSL, the wall friction loss factor is the proportionality constant relating the rate of irreversible kinetic energy decrease due to the presence of the stationary pipe wall and the relative rate of change of kinetic energy, which, in the form of Eqn. 1, can be stated as:

$$\overbrace{E_{v,phase\to wall}}^{\substack{net\ rate\ of\ irreversible \\ mech.\ (kinetic)\ energy \\ decrease\ due\ to\ stationary \\ wall\ (viscous\ dissipation)}} = \overbrace{+}^{\substack{\text{"high-to-low"} \\ \text{sign} \\ \text{convention}}} \overbrace{e_{v,phase\to wall}}^{\substack{wall\ \ friction \\ loss\ \ factor}} \overbrace{\left(\frac{\left(\overbrace{\rho A\langle v\rangle|\langle v\rangle|}^{\dot{M}_{tot}}\right)\langle v\rangle}{2} - \frac{\left(\overbrace{\rho A\langle v\rangle|\langle v\rangle|}^{\dot{M}_{tot}}\right)\overbrace{v_{wall}}^{=0}}{2}\right)}^{\substack{relative\ rate\ of\ change\ of\ mech.\ (kinteic)\ energy \\ high\ rate\ of\ change\ of\ mech.\ energy\ (phase) \\ low\ rate\ of\ change\ of\ mech.\ energy\ (wall)}} \tag{3}$$

As seen in Eqn. 3, the wall friction loss factor is the *irreversible kinetic energy transfer coefficient* between the flowing phase and its stationary boundary. Note that the notation, terms and conventions of BSL are used as much as possible throughout this work. In cases where multiphase flow language is needed, the same notation, terms and conventions will be appropriately modified. This approach is deliberate and fits within the discussion in the Section 1.3.4 on the value of standardizing multiphase pipe flow language. For a straight pipe with uniform cross-sectional area open to flow, A, and length, ΔL, the wall friction loss factor is given in BSL in terms of a mean hydraulic diameter (D_H), defined as:

$$e_{v,\,phase\to wall} = \overbrace{f_{phase\to wall}}^{\substack{phase\ Fanning\\ friction\ factor}} \cdot \Delta L \cdot \overbrace{\left(\frac{\overbrace{Z}^{\substack{boundary\\ perimeter}}}{A} \right)}^{=\frac{4}{D_H}=\frac{1}{R_H}} = f_{phase\to wall} \left(\frac{\overbrace{Z\Delta L}^{\substack{momentum\ flux\ transfer\ area\\ (from\ phase\ to\ wall)}}}{\underbrace{A}_{\substack{area\ open\ to\ flow\\ (along\ pipe\ axis)}}} \right) \tag{4a}$$

Where:

$$f_{phase\to wall} = fn\left(\underbrace{\left(\frac{\rho \left| \langle v \rangle \right| D_H}{\mu} \right)}_{\substack{phase\ Reynolds\\ number,\ N_{Re}}}, \underbrace{\left(\frac{k_{wall}}{D_H} \right)}_{\substack{relative\ hydraulic\\ roughness}} \right) \tag{4b}$$

At first glance, it may appear that the stated relation in Eqn. 4a is a correlation, which may lead some investigators to consider the mean hydraulic diameter as a "vague concept" (Chin, 2009), or, in much stronger language, as "completely ad hoc in nature and cannot be extended to other situations" (pg. 3 in Chin, 2011). However, a deeper understanding reveals that the reason *why* the wall friction loss factor is defined in this way is that it allows us to re-express Eqn. 3 (i.e., combining Eqns. 4a and 3) in the general form of the phase-to-boundary *phenomenological transfer laws* (Eqn. 1), as:

$$\overbrace{\left(\frac{E_{v,\,phase\rightarrow wall}}{\underbrace{Z\Delta L}_{\substack{surface\ over\ which\\ flux\ is\ transferred}}}\right)}^{\substack{phase\text{-}to\text{-}wall\\ mechanical\ energy\ (or\ work)\ flux}} = \overbrace{+}^{\substack{"high\text{-}to\text{-}low"\\ sign\\ convention}} \overbrace{f_{phase\rightarrow wall}\left|\langle v\rangle\right|}^{\substack{mech.\ energy\ flux\\ transfer\ coefficient}} \overbrace{\left(\overbrace{\frac{\left(\rho\langle v\rangle\right)\langle v\rangle}{2}}^{\substack{high\ conc.\ of\\ mech.\ energy\\ (phase)}} - \overbrace{\frac{\left(\rho\langle v\rangle\right)\overbrace{v_{wall}}^{=0}}{2}}^{\substack{low\ conc.\ of\\ mech.\ energy\\ (wall)}}\right)}^{relative\ mech.\ energy\ concentration} \tag{5}$$

Note that the mean hydraulic diameter in Eqn. 4a above brings in the dependence of the phase-to-boundary mechanical (kinetic) energy flux on the laminar and turbulent flow regimes. This is an important step. In other balance equations, such as the continuity or momentum equations, it is of no consequence whether the flow regime is laminar or turbulent, but for the mechanical and thermal energy equations, these regimes are important. As Bobok (1993) points out, different formulations of the mechanical energy balance equation can be written for turbulent flow, based either on time-averaged velocities or on the actual velocity fluctuations. Also, note the rate at which the phase mechanical energy decreases (or viscously dissipates) due to the presence of the stationary pipe wall is related through Eqn. 5 to quantities that are subject to direct experimental observation.

Next, we highlight that it is the mean hydraulic diameter definition in Eqn. 4a that defines the surface area over which the flux of mass, momentum, energy or entropy is transferred, i.e. ZΔL. This has an importance all on its own aside from the wall friction factor. The key insight is that, at any given axial location in a pipe, the interface between the two phases (the flowing fluid phase and the stationary pipe phase) is localized with regard to cross-sectional position – it is always at the boundary of the flow field for closed-conduit flows. This interface defines the averaged momentum flux transfer surface between the flowing phase and its stationary boundary (the pipe wall).

Additionally, the Fanning friction factor can itself be interpreted as the quantity that directly relates the viscous loss factor with the ratio of the two most important surfaces bounding the flowing phase, $Z\Delta L$, and, A, as shown in Eqn. 4b.

Next, it is important to note that at any given axial location in a pipe, the area open to flow, A, in the mean hydraulic diameter definition in Eqn. 4a, is the area that cancels the area defining the mass flow rate of the phase in Eqn. 1. The result of this cancellation is that the right side of Eqn. 5 does not contain the term, A. In general, the area open to flow, A, is unrelated to the actual area occupied by the phase. The key insight is that in single-phase flow, it just so happens that these areas coincide, but in the multiphase flow scenario, they do not. In either scenario, the area open to flow, A, as defined in Eqn. 4a, is the area that defines the mass flow rate of the flowing phase and possesses no other meaning.

To close Eqn. 4a, the Fanning friction factor is found to be well-correlated in a wide range of single-phase fluid flow scenarios to the Reynolds number and relative hydraulic wall roughness (as shown in Eqn. 4b). Throughout this work, we have carefully defined the laminar, transitional and turbulent flow formulae for the Fanning friction factor (with Reynold's number ranges approximating those discussed in Mullin, 2011) as:

$$f_{phase\rightarrow wall} = \begin{cases} \overbrace{\left(\frac{16}{N_{Re}}\right)}^{Hagen-Poiseuille\ Eqn.} & \forall\ \overbrace{N_{Re} \le 2300}^{Laminar} \\ \overbrace{\left(\frac{7.05\times10^{-8}}{\left(N_{Re}\right)^{-1.5}}\right)}^{Manadilli\ (1997)} & \forall\ \overbrace{2300 < N_{Re} \le 2900}^{Transitional} \\ \overbrace{\left(-3.6\log_{10}\left(\frac{6.9}{N_{Re}} + \left(\frac{1}{3.7}\frac{k_{wall}}{D_H}\right)^{\frac{10}{9}}\right)\right)^{-2}}^{Haaland\ (1983)} & \forall\ \overbrace{N_{Re} > 2900}^{Turbulent} \end{cases} \tag{6}$$

Now, as shown in BSL, $E_{v,phase\rightarrow wall}$ can be related to the boundary force (i.e. the force the flowing phase exerts on the conduit wall), $F_{phase\rightarrow wall,}$ by equating the *axial force* and *mechanical energy gradient* balance equations, to yield:

$$F_{phase\rightarrow wall} = \frac{E_{v,\,phase\rightarrow wall}}{\langle v \rangle} \tag{7}$$

Note that there are specific assumptions for deriving Eqn. 7, as explained in BSL. Combining eqns. 5 and 7, we can re-state the *phenomenological transfer law* for the phase-to-boundary mechanical energy flux in Eqn. 5 in terms of the phase-to-boundary momentum flux, as:

$$\frac{F_{phase\rightarrow wall}}{\underbrace{Z\Delta L}_{\substack{surface\ over\ which \\ flux\ is\ transferred}}} = \overbrace{\tau_{phase\rightarrow wall}}^{\substack{phase\text{-}to\text{-}wall \\ momentum\ flux \\ (\text{"wall shear stress"})}} = \overset{\substack{\text{"high-to-low"} \\ \text{sign} \\ \text{convention}}}{+} \overbrace{\left(\frac{f_{phase\rightarrow wall}\left|\langle v \rangle\right|}{2}\right)}^{\substack{momentum\ flux \\ transfer\ coefficient}} \overbrace{\left(\overbrace{\left(\rho\langle v \rangle\right)}^{\substack{high\ conc.\ of \\ momentum \\ (phase)}} - \overbrace{\rho \underbrace{v_{wall}}_{=0}}^{\substack{low\ conc.\ of \\ momentum \\ (wall)}}\right)}^{relative\ momentum\ concentration} \tag{8a}$$

As a check of the consistency for the choice of the definition of momentum flux *transfer coefficient* as shown above, we note that the wall momentum flux to molecular (viscous) momentum flux ratio in the case of momentum transfer can be expressed in terms of a "Fanning-Reynolds Number" (defined in Appendix A), as:

$$N_{Fa-Re} = \left(\frac{\tau_{phase \to wall}}{\rho \left| \langle v \rangle \right| \langle v \rangle} \right) N_{\mathrm{Re}} \sim \frac{wall\ \ flux}{\cancel{convective\ \ flux}} \frac{\cancel{convective\ \ flux}}{molecular\ \ flux} = \left(\frac{f_{phase \to wall}}{2} \right) N_{\mathrm{Re}} \quad (9)$$

For laminar flow, $N_{Fa-Re} = 8$ since $f_{phase \to wall} = 16/N_{\mathrm{Re}}$ for laminar flow. Using the Reynolds momentum-heat analogy, the analogous dimensionless relationship to Eqn. 9 is the wall heat flux to molecular (conductive) heat flux ratio, or Nusselt number. Thus, simply from a consistent definition of momentum flux transfer coefficient, we can determine that the Nusselt number for laminar flow for a system with an averaged velocity (i.e. an unknown velocity profile but a constant cross-section averaged velocity value) will be equal to 8. In standard textbooks in convective heat transfer, this exact (analytical) result is derived using partial differential equations of change with constant wall heat flux boundary conditions.

As shown, Eqn. 8a is in the classic form of a phenomenological transfer law with flux transfer coefficients in front of relative quantity-concentrations. This is the form that makes it possible to see the generalization of transport phenomena as exemplified in BSL. Nonetheless, it is instructive to show this same equation in a form that may be familiar to the subset of investigators who prefer to interpret friction factor as a mechanical (kinetic) energy dissipation coefficient, as:

$$\tau_{phase \to wall} = \overbrace{f_{phase \to wall}}^{\text{phase Fanning friction factor}} \cdot \overbrace{\left(\frac{\rho \left| \langle v \rangle \right| \langle v \rangle}{2} \right)}^{\substack{\text{phase mechanical energy dissipated due to presence of stationary pipe wall per unit volume}}} \quad (8b)$$

Now that a consistent expression is in place (Eqn. 8a) for the boundary force, $F_{phase \to wall}$, the next basic question concerning the hydrodynamics of the flow, is to determine how this quantity contributes to the axial-momentum balance (and therefore,

pressure gradient) in pipe flow? The answer to this question is not trivial. In particular, two very important and related sub-questions arise:

I. How is $F_{phase \rightarrow wall}$, a macroscopic (global) quantity, related to the microscopic (local) equation of change for axial-momentum?

II. Is the equation of change for axial-momentum the only local conservation equation that should be used for defining this relationship?

As is evident from the averaged flow literature, there are several alternative approaches and answers to these very basic questions. In some cases, macroscopic and microscopic quantities are often mixed, in which case partial differential equations no longer describe microscopic (local) flow quantities, but rather, their time- and space-averaged descriptions. In contrast, this side-by-side mixing of microscopic and macroscopic quantities are absent in classical analyses of fluid mechanics (e.g. Whitaker, 1982, Landau and Lifshitz, 1987; BSL). In BSL, there is a clear separation of what constitutes microscopic *equations of change* within the flow system and what constitutes macroscopic *balance equations* when these equations of change are integrated over the entire volume of the flow system (Bird, 1957; Slattery and Gaggioli, 1962), represented as:

$$\int_{V(t)} \begin{pmatrix} eqns.\ of \\ change \end{pmatrix} dV = \begin{matrix} balance \\ eqns. \end{matrix} \tag{10}$$

Now, although this separation of microscopic and macroscopic quantities may seem to some investigators a matter of semantics, the separation of these quantities is very important, as shown in BSL. While the investigators who do not separate these quantities have clear reasons for doing so (e.g., they may want to enforce property spatial variations to be allowable only in the axial direction in their partial differential

equations), the key realization arising from this separation is that some terms will show up only at the macroscopic (or integral) level. This means that there will be some terms in the balance equations that are different from the terms in the equations of change. This is because the phase-to-wall (or *interphase*) flux terms in the balance equations describe the transfer processes at the boundary, whereas the flux terms in the equations of change describe the transport processes within the main stream (e.g. conduction, convection). This, of course, has dramatic mathematical modeling implications in either single-phase or multiphase pipe flow, namely, that the averaging method employed for the net accumulation, transport and source terms in the Eulerian formulation of the local equations of change does not apply to the separate (and usually empirical) net transfer terms at the boundary. Specifically in multiphase pipe flow, this means that:

I. Before averaging is performed, the *phase function*, as explained in Drew (1983), is multiplied by only the terms in the local equations of change.

II. After averaging the local equations of change, the multiphase wall flux transfer terms that appear in the macroscopic balance equations, have no fundamental basis for being *phase function*-weighted terms.

Additionally, we note that the general phenomenological forms of the *net transport* terms in the local equations of change are different from the general form of the *net transfer* terms in the integral balance equations, shown in Eqn. 3. For example, in most scenarios (though not all), conductive main stream fluxes can be generally expressed as:

$$\overbrace{\left(\overrightarrow{cond.\ flux\ of\ Y}\right)}^{\substack{flux\ caused\ by\ molecular\text{-}scale\\ conductive\ phenomena}} = \overbrace{\vec{\vec{K}}_{cond.}}^{\substack{Y-flux\\ transport\\ coefficient}} \bullet \overbrace{\left(-\vec{\nabla}\left(conc.\ of\ Y\right)\right)}^{\substack{Y-conc.\\ gradient}} \tag{11}$$

Fourier's law of heat conduction in a medium is one example of a *phenomenological transport law* in the form of Eqn. 11 where Y = phase thermal energy (or heat). As another example, convective main stream fluxes are generally expressed as:

$$\overbrace{\left(\begin{array}{c}\overrightarrow{conv.\ \ flux} \\ of\ Y\end{array}\right)}^{\substack{flux\ caused\ by\ micro\text{-}to\text{-}meso\ scale \\ convective\ phenomena}} = \left(\begin{array}{c}conc. \\ of\ Y\end{array}\right)\vec{v} \tag{12}$$

In light of the foregoing discussion, we are now in a position to relate $F_{phase \rightarrow wall}$ to the local equation of change for axial-momentum. We start from the *equation of motion*. As shown in BSL, it is the equation from which the Navier-Stokes equation can be derived. If we assume that the momentum transfer rates associated with the viscous stress are small compared to the fluid pressure forces across the entrance and exit planes of the considered system, we can arrive at a macroscopic balance equation for axial-momentum in an arbitrary x-direction, as:

$$\underbrace{\overbrace{\int_V \left(\frac{d\left(\rho\vec{v}\right)}{dt}\right) dV}^{\substack{resultant \\ force\ on\ phase}} = \overbrace{-\int_{A_x} \vec{n}\bullet P\, dA}^{\substack{net\ conductive\ (pressure) \\ force\ on\ phase}} \quad \overbrace{-\int_{A_x} \vec{n}\bullet\rho\vec{v}\vec{v}\, dA}^{\substack{net\ convective \\ force\ on\ phase}} \quad \overbrace{+\int_V \left(\rho\vec{g}\right) dV}^{\substack{net\ external\ (gravity) \\ force\ on\ phase}}}_{terms\ derived\ from\ the\ equation\ of\ motion} \quad \overbrace{+\vec{F}_{wall \rightarrow phase}}^{\substack{net\ boundary\ (wall) \\ force\ on\ phase}} \tag{13}$$

Eqn. 13 displays a deceivingly simple character. It shows the link between the macroscopic terms that are derived from basic principles and the one term that does not have a fundamental basis, the net wall flux transfer term (the last term in Eqn. 13). As we will show, the situation is not different for multiphase flow – there will be net accumulation, transport and source terms derived from basic principles and there will be net interfacial and wall flux transfer terms that are not. So, in general, it is not true to say that the single-phase or multiphase pipe flow balance equations lack a fundamental basis – this is only true for some of the terms. In Eqn. 13, when BSL notation is used, in the steady-state case, it becomes:

$$0 = -\Delta\left(PA\vec{e}\right) - \Delta\left(\rho\left\langle v\right\rangle \frac{\left\langle v^2\right\rangle}{\left\langle v\right\rangle} A\vec{e}\right) + M_{tot}\vec{g} + \vec{F}_{wall\to phase} \tag{14}$$

Eqn. 14 is the same as shown in pg. 200 of BSL. We refer the reader to the interpretations and assumptions found in BSL concerning the averaging procedure in arriving at Eqn. 14. We will now repeat the formulation above but with one change – we will combine the *equation of motion* with the viscous stress neglected (as above) and the *equation of continuity* to arrive at the familiar Euler's equation (as shown in pg. 3 of Landau and Lifshitz, 1987), namely:

$$\overbrace{\left(\frac{\partial\vec{v}}{\partial t}\right)}^{\substack{net\ temporal\ (or\ local)\\ acceleration/deceleration}} + \overbrace{\left(\vec{v}\bullet\vec{\nabla}\right)\vec{v}}^{\substack{net\ convective\\ acceleration/deceleration}} = \frac{D\vec{v}}{Dt} = -\frac{\vec{\nabla}P}{\rho} + \vec{g} \tag{15}$$

Note that the substantial time (or Lagrangian) derivative evaluated with the phase velocity in Eqn. 15 above denotes the rate of change of the velocity of a given fluid particle as it moves in space (i.e., its transportive velocity), whereas the partial time derivative denotes the rate of change of the fluid velocity at a fixed point in space, which is the local acceleration/deceleration. Similar to above, a macroscopic balance equation for axial-momentum in an arbitrary x-direction can be written from Eqn. 15, as:

$$\underbrace{\overbrace{\int_V\left(\rho\frac{D\vec{v}}{Dt}\right)dV}^{\substack{net\ accelerational/decelerational\\ forces\ on\ phase}} = -\int_{A_x}\vec{n}\bullet P\,dA + \int_V\left(\rho\vec{g}\right)dV}_{terms\ derived\ from\ combining\ equation\ of\ motion\ and\ equation\ of\ continuity} + \vec{F}_{wall\to phase} \tag{16}$$

When BSL notation is used for Eqn. 16, it can be written as:

$$M_{tot}\left(\frac{\Delta_t\left(\left\langle v\right\rangle\vec{e}\right)}{\Delta t}\right) = -\Delta\left(PA\vec{e}\right) - M_{tot}\left\langle v\right\rangle\left(\frac{\Delta\left(\left\langle v\right\rangle\vec{e}\right)}{\Delta L}\right) + M_{tot}\vec{g} + \vec{F}_{wall\to phase} \tag{17}$$

For a straight, constant cross-section pipe, with steady-state flow only in the arbitrary x-direction at an angle of θ degrees to vertical, Eqn. 17 becomes (using mass flux, G, in place of velocity, $\left\langle v\right\rangle$):

$$\frac{\Delta P}{\Delta L} = \frac{1}{A\Delta L}\left(F_{phase\rightarrow wall}\right) + \rho g \cos\theta - G\left(\frac{\Delta\left(\frac{G}{\rho}\right)}{\Delta L}\right) \tag{18}$$

Combining Eqns. 18 and 8a finally leads to:

$$\overbrace{\left(\frac{\Delta P}{\Delta L}\right)}^{\text{hydrodynamic}} = \overbrace{\left(\frac{Z}{A}\right)\tau_{phase\rightarrow wall}}^{\text{friction}} \overbrace{+\ \rho g \cos\theta}^{\text{hydrostatic}} \overbrace{-\ G\left(\frac{\Delta\left(\frac{G}{\rho}\right)}{\Delta L}\right)}^{\text{convective acceleration (+ve), or deceleration (−ve)}} \tag{19}$$

Eqn. 19 is the steady-state, single-phase, balance equation for the rate of change of axial-momentum in pipe flow re-expressed as an axial pressure gradient balance equation. For a very wide class of single-phase pipe flow problems in fluid dynamics, this equation has proven to work quite well. In the field of multiphase pipe flow, Eqn. 19 works so well that it is used by experimenters to test for proper operation and to calibrate multiphase measurements in experimental flow loops. Other than experimenters, many multiphase pipe flow modelers consider the single-phase rate of change of axial-momentum balance equation to be "well established" (Heywood and Cheng, 1984) or "firmly established" (Ishii and Hibiki, 2006).

Therefore, the questions that abound concerning Eqn. 19 for any particular single-phase flow scenario, by necessity, must also abound for the corresponding multiphase flow scenario. These are the reasons that Eqn. 19 is the most logical place to start an analysis of multiphase pipe flow – it defines our ignorance-boundary. As Geoffrey Hewitt and Joseph Kestin point out, "Even single-phase turbulent flows still defy prediction from a fundamental point of view" (Hewitt, 1983), and, "Even one-phase flows are not totally on a sound footing because turbulence is still untractable" (Kestin, quoted in DiPippo, 1980). Tom Mullin reminds us that even as basic a question as

transition to turbulence in single-phase pipe flow remains unsolved: “It is an enigma as all theoretical and numerical evidence suggests that the base state of fully developed flow, Hagen-Poiseuille flow, is linearly stable. The transition to turbulence is abrupt, mysterious, and largely dependent on the quality of the facility used in any experimental investigation. It is therefore not an example of transition via a sequence of instabilities or bifurcations” (Mullin, 2011).

2.1.1.1 Convective Acceleration or Deceleration

A caveat regarding Eqn. 19 is that in the majority of flow loop scenarios (e.g. unobstructed, constant cross-sectional area, low-to-moderate flow rates or steady-state flow), the convective acceleration/deceleration term was not tested in any serious way because its contribution was, by design, minimal. In some cases, investigators acknowledge this inherent design in their steady-state experiments. For example, in the “Analysis of the Two-Fluid Model” section of Danielson (2012b), it is noted: “The OLGA and LEDAFlow codes are largely based on data taken in the Tiller flow loop, an 8 in. line at -1°, -0.5°, 0°, +0.5°, +1° and +90° (vertical) incline, operated at pressures up to 90 bar, with three different liquids spanning 2 orders of magnitude in viscosity. Care is taken in the laboratory experiments to ensure that momentum terms are negligible”. These statements reveal that high rate flows are probably not conducted in this flow loop since the convective acceleration/deceleration term becomes quite important in high rate flows at these relatively low pressures.

In the cases where the convective acceleration/deceleration term is important (e.g., obstructed, varying cross-sectional area, high flow rates or transient flow), we will report evidence that shows that only the form of this term as derived in Eqn. 19 accurately reproduces a large variety of pipe flow data. As noted in prior investigations

(e.g., Majiros and Dukler, 1961, Silvestri, 1964), in both single-phase and multiphase flow scenarios, the contribution of this acceleration/deceleration term can be a substantial fraction of the total pressure gradient, especially in the case where vapor densities will vary considerably along the flow direction because of the relatively high variation of the line pressure (e.g., as in lower pressure systems). This work also substantiates these prior findings, as will be clearly demonstrated in the numerous applications in Chapters 4 to 7.

Nevertheless, it is important to recognize that this term is erroneously considered unimportant by some investigators and is crudely modeled in both single-phase and multiphase flow scenarios as a result of this preconceived belief. In some cases, one may find unsupported opinions concerning this term for a given scenario, for example, in the mechanistic slug flow model of Andreussi et al. (1993): "The acceleration term is only related to gas expansion effects". In other cases, one may find both unsupported and incorrect statements concerning this term, for example, in the overview chapter of Awad (2012): "The acceleration pressure drop (ΔP_a) can be neglected in the adiabatic flow". In another case concerning pipeline design, Greogory and Fogarasi (1985) opine that: "Except in relatively rare cases, the kinetic energy term is negligible, and can be safely ignored".

In the most extreme cases, the convective acceleration/deceleration term is completely left out of the calculations of total pressure gradient – as examples:

I. In the steady-state calculations of the PROSPER code, described in the Flow Modeling Applications section of the PROSPER Training Course Notes, 2004: "PROSPER evaluates the acceleration term explicitly at each calculation step, thereby avoiding any potential inaccuracy".

II. In the very definition of the total pressure gradient used in the steady-state momentum balance of Gregory et al. (1975b), Ashiem (1986), Rey-Fabret et

al. (2003), as well as in the steady-state momentum balance equations for annular flow in Alves et al. (1988), Ansari et al. (1994), Gomez et al. (1999), Kaya et al. (2001) and Shirdel (2013).

III. In the neglect of the inertial pressure gradient terms in the development of a set of transient multiphase "point-model" equations for oil and gas production in Danielson (2012b): "In practice, inertial forces are rarely important in upstream production apart from a few specific instances (e.g., water hammer). Thus, when inertia is ignored and a quasi-steady state is invoked, a very effective and simplified model can be developed, which should be perfectly adequate for nearly all cases of practical interest".

2.1.1.2 Wall Friction Factor

The most important thing to note about Eqn. 19 is that the dependent variables are related to each other as well as to known system parameters in this one equation through one unknown – the wall friction factor – which is the only quantity that cannot be directly measured. Also, note that the wall friction factor is not the only thing that is unknown because there was a series of assumptions invoked in the going from the local to the integral level. However, unlike the wall friction factor, all of the other quantities in Eqn. 19 can be carefully (though not easily) measured and therefore it is possible to falsify or validate any of the individual assumptions or hypotheses that led to it for a given friction factor. This is why the better pipe flow experiments (and models) enforce that the friction factor not be changed from its best tractable value for the scenario under consideration. For example, in flow loops, hydraulically smooth pipes are often used to force the behavior of friction factor to its best predictable state unless, of course, the departure from hydraulic smoothness is itself under investigation, e.g., the study by

Chisolm and Laird (1958) for multiphase flow or the Superpipe experiments for single-phase flow.

2.1.1.3 Existence of Different Formulations

It is instructive (and insightful) to carefully observe the familiar path taken to arrive at Eqn. 19 as discussed in BSL – that is – starting from the local (microscopic) conservation equations to eventually arrive at a global (macroscopic) momentum balance equation. Classical fluid dynamics treatments like Landau and Lifshitz (1987) and BSL clearly informs us of how other balance equations (e.g., the mechanical energy equation and its approximated form, the engineering Bernoulli equation) can be obtained from the equation of motion and what specific sets of assumptions are needed to arrive at them.

Nevertheless, there are some pipe flow investigators that do not follow this classical (correct) path and, instead, create their own interpretation of the mechanical energy balance equation as though it is derived from "extending" or "converting" the total energy balance equation. In this latter interpretation, closed-system, homogeneous (pure component), equilibrium thermodynamics relations are combined in an ad hoc way with the flux relations across the boundaries of a control volume described by an open-system total energy balance equation. In rare cases, even multiphase pipe flow investigators will base their open-system, multiphase, multi-component analyses on this interpretation. In these exceptional cases, investigators will claim a "general mechanical energy balance" for their multiphase flow by introducing various artificial definitions and mixing rules for different variables in their derived mechanical energy balance equation (e.g., mixture viscosity, mixture friction factor, and so on). One may even find among these exceptional cases "multiplier factors" that appear with their kinetic energy terms that take on different adjustable values for different scenarios, both in the single-phase

and multiphase mechanical energy balance equations (sometimes referred to as a "velocity profile correction term").

For obvious reasons, we do not identify the investigators belonging to the exceptional cases described above. What is of importance though is that it must be recognized that there is nothing "general" or fundamental about introducing artificial variables, i.e., variables that can only be inferred and not measured. These rather peculiar developments are in fact different total pressure gradient correlations depending on the choice of mixing rules and definitions for the different variables. We emphasize the following BSL quotes as being crucial to the correct understanding of the basic equations in single-phase flow: "The macroscopic mechanical energy balance is derived from the equation of motion (that is, from the law of conservation of momentum)" – pg. 204, and again on pg. 458: "The mechanical energy balance is not 'an alternative form' of the energy balance".

A concrete example of the different conceptual understanding of fundamental equations is clear when one considers the vast contrast in how one group of nuclear/chemical engineering multiphase flow investigators stated their basic equations ("Overview and Taxonomy of Models and Methods" by Drew and Wood, 1985) versus how one group of petroleum engineering multiphase investigators stated their basic equations ("Two-Phase Flow in Pipes" by Brill and Beggs, 1975).

2.1.1.4 Existence of Different Interpretations

Other than the core equations, even fundamental concepts such as what is irreversible energy conversion in multiphase flow can have different interpretations. A concrete (and historically traceable) example depicts this unfortunate fact and gives a glimpse into the widely differing levels of understanding of basic concepts: "For a single-

phase system, the pressure change due to elevation changes is in fact the pressure change due to potential energy changes and is a completely reversible term. In multiphase flow, this term still accounts for the effect of all elevation changes, but it is generally not the same for up-flow as for down-flow. That is because some of the irreversibility is transferred from the pressure change due to friction term. This distinction is important but it is also well established technology and need not concern us further here" – Simultaneous Temperature and Pressure Profile Calculations section of WELLFLO 7 Technical Reference Manual, 2009.

In fact, we can follow the same line of reasoning as above on this same issue of multiphase down-flow twenty years earlier in Baker et al. (1988a): "For downward-sloping pipe sections, it is assumed that only the continuous (gas) phase will contribute to the downhill pressure recovery and that any potential energy recovered from the liquid phase will be dissipated as frictional heat". Indeed, just a few years earlier in Gregory and Fogarasi (1985), we trace some of the earliest experience-based (not science-based) arguments concerning this issue: "Experience with two phase pipelines has shown that relatively little head is recovered in downhill flow, compared with the head loss in uphill flow. It has thus been common practice to ignore head recovery altogether. It must be noted however that it is also normal practice to use horizontal flow correlations to predict the liquid volume fraction in uphill flow without attempting to make any correction for inclination effects".

It must be recognized that experience-based arguments such as those above underlie the models produced by these investigators (i.e., WELLFLO, PIPEFLO and FORGAS). More significantly, these arguments continue to exist among some groups of investigators (particularly in the petroleum industry), as evidenced in the recent flow assurance review by Shippen and Bailey (2012): "In particular, steep downward flow, as

encountered in steam injection wells, mountainous terrain, and offshore down-comers, has received less attention in research studies and remains poorly understood. This is particularly important for calculating the elevation pressure gradient, which is not simply the inverse of that for upward flow. Depending on the overall pipe geometry and flow regime, slack or open-channel flow may occur and the head of the fluid may be dissipated as frictional heat rather than recovered by increasing pressure (Flanigan, 1958; Baker et al., 1988a; Nicholas, 1995)".

In another review by Danielson et al. (2000), it is noted the large discrepancies in predicted and measured pressure gradient for downward flow data compared with the OLGA code, and a rather strange reason suggested for these differences: "There are instances where OLGA underpredicts the pressure recovery in downward directed flow by several orders of magnitude. Figure 8 gives the performance of OLGA against the Beggs and Brill database. Note the collection of points along the zero pressure gradient axis. It is believed that this discrepancy is caused by OLGA selecting annular flow, when in fact the flow is bubble or slug".

2.1.1.5 Falsification, Traceability and Tractability

We next discuss some modeling concepts that will become quite important to explaining our new modeling approach and in discussing results in later sections of this work, namely – falsification, validation, traceability and tractability of models. With Eqn. 19 now in hand, it will serve as a representative model (the hypothesis) with the desired or unknown dependent variable being total pressure gradient (the LHS of Eqn. 19) and the wall friction factor being well-predicted to the point of being considered a known relation. In this case, if there are incorrect measurements of ***any*** of the quantities on the RHS of Eqn. 19 for a particular scenario, then the calculated pressure gradient will

be in false agreement with the measured pressure gradient – we say that the hypothesis that is Eqn. 19 will be falsified for the studied scenario.

If there are valid measurements available for *all* of the quantities on the RHS of Eqn. 19 in a diverse range of scenarios, then these datasets could be used to test if the calculated pressure gradient is in satisfactory agreement with the measured pressure gradient. The more this testing is performed, the more it will lead to accumulating evidence that infers Eqn. 19 is acceptable for its intended use – we say that the hypothesis that is Eqn. 19 will be validated.

Note that whereas model validation allows for global (integral) testing of the hypothesis when confronted with many data, it is model falsification that allows for the controlled, special effects testing necessary to interrogate specific assumptions in the hypothesis. Therefore, a thoroughly falsified hypothesis will greatly enhance the validation of the hypothesis. Extending the above concepts of validation and falsification to the multiphase flow scenario, we draw attention to readers that there is no existing multiphase flow commercial code that allows users to enforce that measured variables (e.g., averaged volume or entrainment fractions) participate in the pressure gradient computations. This means that, apart from the general nature of these commercial codes being "black boxes", it is furthermore very difficult to falsify (and therefore validate) any of their underlying sub-models because pressure gradients and all other dependent variables are always calculated by the codes. Some in-house or research codes, on the other hand, do allow the capability to falsify their underlying sub-models (e.g., the in-house code used for this work, UTPipeFlow).

If there are correct measurements of all of the quantities on the RHS of Eqn. 19 *except one*, say density, and it must be estimated say from a correlation, then failure of Eqn. 19 will be traceable only to density with the extent of its failure being directly

related to the how far the estimation of density is from the measurement of density. Traceability, by itself, is a very important and desirable characteristic of models because it focuses the uncertainty in the model's results.

If there are correct measurements for *some* of the quantities in Eqn. 19 but other quantities must be estimated by models, then changing the models for the estimated quantities to match the calculated pressure gradient to the measured pressure gradient will amount to either tractable or intractable (ad hoc) model tuning. In the former, the estimated quantities can eventually be measured and thus the effect of the various models for these quantities can be systematically interrogated and quantified. In the latter, the estimated quantities cannot be measured and thus any combination of these quantities can lead to a match between the calculated and measured pressure gradients. Therefore, ad hoc tuned models cannot be falsified. Examples of intractable model tuning in multiphase pipe flow applications in current practice can be found in Appendix C. As this Appendix highlights, if tuning of multiphase flow models for industrial problems is necessary (as it quite often is) then tractable tuning must be used for science-based predictions. As this work clearly demonstrates, tractable model tuning can be enforced in many practical scenarios and still result in very accurate solutions.

2.1.2 Multiphase Pipe Flow

Our approach to modeling the hydrodynamic multiphase pipe flow problem is to start with understanding and carefully demarcating the ignorance-boundaries of the corresponding single-phase pipe flow problem. In this way, what has been understood (and properly validated) in the single-phase flow problem can be leveraged and generalized to the multiphase problem. We provided a deeper insight into some important terms of the single-phase balance equations in the previous section. The next

basic question is: What changes when other flowing phases are introduced into the flow field?

Obviously, every multiphase flow investigator will have an opinion that answers this question. Their answers will most likely be tied to their individual experiences and specialist areas of expertise (e.g. pg. 291 in Govier and Aziz, 1972; Collier, 1976; Sec. 1 in Spalding, 1980; pg. 2 in Persen, 1986; pg. 86 in Levy, 1999). However, in the main, answers will mostly surround what is visually (or physically) observed to be different between single-phase and multiphase flow – the *large number of moving deformable interfaces* between the flowing phases, the flow patterns. If analyzing the flow field microscopically, these interfaces become very problematic to the modeler. The modeling difficulties in this approach will concern the physical transfer processes taking place across the interfaces such as mass, momentum, energy and entropy, as well as the resulting phase changes that may occur. The numerical simulation issues in this approach will arise because the interfaces are moving and some properties of the phases will be discontinuous across the interfaces, e.g. density, viscosity. The scale available for flow will bring additional complexities that will compound the mathematical modeling and computational issues above.

If analyzing the flow field in an averaged sense (as in this work), then the question above becomes much more focused because local flow field information, including flow pattern information, is basically lost in the averaging process – it is now: What changes in the balance equations when other flowing phases are introduced into the flow field? This is the principal question to be answered if looking at an averaged description of the flow. Our approach is to focus on the unknown (but directly measurable) variables that presently exist in the way we formulate the multiphase flow balance equations (as shown in Appendix B and Section 2.2.2) and to postulate a few key

hypotheses for arriving at closure laws for these unknowns (given in Sections 2.2.3 to 2.2.7).

2.1.2.1 Immeasurable Quantities (U-Variables)

Before we go on to answering the question above, it is important (and instructive) to clarify what are immeasurable versus measurable variables in the context of averaged multiphase pipe flow. Immeasurable variables are quantities that are introduced to the multiphase pipe flow balance equations by various investigators for different reasons (e.g., for easier tuning of models to data trends or by necessity according to the model formulation). They can only be inferred or back-calculated. We call these U-variables, the "U" signaling that these variables cannot be objectively measured and thus are unknown.

Sometimes, U-variables are explicitly referred to as "measurements" in literature publications when in fact they are back-calculations of models. For example, this is a common practice among *effective (*or *mixture) viscosity* modelers in liquid-liquid flows and *wall friction (or wall shear)* modelers in vapor-liquid flows. Surprisingly, some investigators will correlate back-calculations of models thereby treating the back-calculations just as data and then present their findings as new "correlations" of these calculations. Even as basic a quantity as total pressure gradient can suffer from this back-calculation practice. Of course, in this particular instance, if pressure is simultaneously measured along the conduit, then it becomes very easy to demonstrate that the measured pressure between two locations divided by the distance between them (i.e., $\Delta P/\Delta L$) will be inconsistent with the reported, back-calculated "measurements" of total pressure gradient. Unfortunately, when multiphase flow investigators are unaware of the

confusing trends above, a back-calculated "dataset" can be used to validate a newly proposed method.

If there are U-variables present in the multiphase balance equations, then this will lead to the inevitable state of the model being made to fit data in an intractable (ad hoc) way. This is aside from whether any of the introduced immeasurable quantities have their own closure relationships or not. This is one explanation why it is often found in the literature that several models with widely different assumptions will accurately fit the same data (e.g., the "salutary lesson" in Sec. 3 of Hewitt, 1987, or the "strangely flexible" nature of models discussed in Hewitt, 2000). This is also an explanation for *why* the majority of investigators believe that the "the price that is paid for a greater accuracy in prediction of results is an increase in complexity" (Wallis, 1969) – in this case, it is easy to see that the numerous introduced immeasurable quantities (that increases the complexity of models) will provide more capability and flexibility for tuning models because there are more quantities to change. When data are fitted with these more easily tunable (or flexibly tunable) models, this will then cause investigators to infer that the introduced quantities were necessary to capture the underlying physics of the data. However, such inferences can be demonstrably countered if other investigators accurately fit the same data without introducing these quantities.

The very reason *why* multiphase pipe flow investigators pursue a-priori calculations of flow patterns in their modeling efforts can be directly linked to the question of how to enable their models to be more easier tunable and hopefully better predictive – the central idea being that this will be more likely possible with models that are focused on distinctive flow behaviors (or more specifically, to restricted ranges of relative velocities). Geoffrey Hewitt drives this point in his response to Mao and Dukler (1993): "The whole purpose of designating a specific flow regime is to enable models to

be applied in that regime which are of a distinctive character; by dividing the full range of flows into specific regimes, the hope is that improved phenomenological prediction is possible" (Hewitt and Jayanti, 1993). Indeed, it can be reasonably argued that flow patterns are themselves U-variables. We present a justification of this contention in Appendix D.

2.1.2.2 Measurable Quantities (K-Variables)

Fortunately, the introduction of other flowing phases bring new quantities into the balance equations that can be measured, such as mean phase volume and entrainment fractions, structure (slug) velocities and frequencies, mean film thickness and film flow rates, mean liquid wave heights, mean solids bed heights and so on. These are the types of multiphase pipe flow variables that can be objectively measured and can thus be incorporated in the balance equations to provide a means of tractable model tuning. We call these K-variables, the "K" signaling that these can be known and therefore the balance equations that utilize them can be falsified. It will now become clear why we termed the multiphase flow modelers in Section 1.3.1 as K-modelers and U-modelers. K-modelers will admit only K-variables into their models to ensure that both tractable model tuning and falsifying hypotheses are possible. U-modelers will utilize U-variables in their models thus making it very difficult to properly falsify (and therefore validate) their hypotheses.

2.2 NEW MODEL FORMULATION: THE CORE PRINCIPLES

2.2.1 Basic Multiphase Pipe Flow Equations

Conceptual mathematical models for flow systems (multiphase pipe flow or not) ultimately require the solution of the local, instantaneous conservation field equations in some form. These equations are used directly in multiphase flow investigations, as in the study of bubble dynamics as an example, or indirectly, as in the study of averaged (1D) multiphase pipe flow as an example (i.e., this work). However, the basic understanding of how these equations are derived, the primary concepts they describe or how they are utilized in ultimately arriving at working equations can be very different among investigators. This is notwithstanding the fact that there are many (mostly application-specific) basic equations reviews that already exist in the literature. Additionally, the amount and type of terminology associated with these reviews can act as a mathematical barrier that prevents them from being simply understood. Some of the reviews can be comprehensive showing a depth of understanding (e.g. Drew, 1983; Drew and Wood, 1985).

Our goal is to demonstrate, in the simplest way, how multiphase pipe flow equations are conceptually related to their single-phase pipe flow counterparts. We will thus follow the development of single-phase flow principles as far as they will take us and then apply new postulates for multiphase flow that will allow us to generalize these principles to multiphase flow. The first two sub-sections of the first chapter in the classic multiphase flow handbook edited by Gad Hetsroni provide a similar type of analysis showing how single-phase, single-component flow continuum (microscopic) concepts are analogously represented in the multiphase flow equations (Whitaker, 1982, Boure and Delhaye, 1982). However, unlike this prior review, we will highlight the

macroscopic relationships and equations. This is in alignment with the first fundamental insight of this work – that single-phase macroscopic fluid mechanics concepts can be generalized to averaged multiphase flow. We will therefore adopt the terminology of the macroscopic chapters of BSL and adapt it to the appropriate multiphase scenario. This macroscopic-focused formulation of the basic multiphase pipe flow equations is given in Appendix B.

In the process of showing the generalization from single-phase to multiphase flow in Appendix B, several multiphase flow concepts will be shown in different light to how they were understood in the past (e.g., the compositional formulation of the component mass conservation equations). Furthermore, we will show how non-pipe media flow equations, specifically porous media flow equations, share an identical fundamental form to pipe flow equations in terms of conservation quantities. This, by itself, allows a different perspective and understanding of just how closely connected porous media flow quantities and equations are to pipe flow quantities and equations. Summarily, our main emphasis in Appendix B is to show how one can generalize BSL's Eulerian macroscopic developments for single-phase flow to Eulerian macroscopic multiphase flow developments.

2.2.2 Analytical Mixture Balance Equations

Following from Eqn. B.19 in Appendix B, and (as usual) neglecting the conductive (viscous) momentum flux in favor of more dominant conductive (pressure) and convective (inertial) momentum fluxes, we can re-state this time-averaged phase-j momentum conservation equation in a multiphase Euler form, as:

$$s_j\left(\frac{D\vec{v}_j}{Dt}\right) = -\frac{\vec{\nabla}\left(s_j P_j\right)}{\rho_j} + s_j\vec{g} + \frac{\sum_{f=1}^{N_f}\left(\vec{\Gamma}_{totf\to j}\right)}{\rho_j} \qquad (1)$$

In re-stating Eqn. B.19 in Appendix B in this way, one can now clearly see the key differences in the single-phase Euler equation (Eqn. 15 in Section 2.1.1) with respect to its multiphase flow counterpart. Note that unlike single-phase flow, there are now interfacial processes that contribute to the net sources of momentum in the flow field. Similar to the procedure for Eqn. 16 in Section 2.1.1, the Gauss-Ostrogradskii Divergence theorem can be applied to Eqn. 1 to arrive at a macroscopic balance equation for phase-j axial-momentum in an arbitrary x-direction as:

$$\overbrace{\int_V \left(\rho_j s_j \frac{D\vec{v}_j}{Dt} \right) dV}^{\substack{net\ accelerationa//decelerational \\ forces\ on\ phase-j}} = \overbrace{-\int_{A_x} \vec{n} \bullet \left(s_j P_j \right) dA}^{\substack{net\ conductive\ (pressure) \\ force\ on\ phase-j}} + \overbrace{\int_V \left(\rho_j s_j \vec{g} \right) dV}^{\substack{net\ external\ (gravity) \\ force\ on\ phase-j}} + \overbrace{\int_V \left(\sum_{f=1}^{N_f} \left(\vec{\Gamma}_{totf \to j} \right) \right) dV}^{\substack{net\ internal\ (interfacial) \\ forces\ on\ phase-j\ =\ \vec{F}_{totf \to j}}} + \overbrace{\vec{F}_{wall \to j}}^{\substack{net\ boundary\ (wall) \\ force\ on\ phase-j}} \tag{2}$$

As discussed in BSL (and Section B.3 of Appendix B), with regards to phase properties, the assumption of uniform phase properties across the flow field area is widely used and will also be adopted here. This assumption is valid since the transverse pressure gradient in pipe flow is relatively small as compared to the axial pressure gradient. A relaxation of this assumption can be found in Ishii (1971). When BSL notation is used for Eqn. 2, a similar expression (with similar assumptions) to Eqn. 17 in Section 2.1.1 can be written as:

$$\begin{aligned} M_j \left\langle s_j \right\rangle \left(\frac{\Delta_t \left(\left\langle \left\langle v_j \right\rangle \right\rangle \vec{e} \right)}{\Delta t} \right) &= -\Delta \left(\left\langle s_j P_j \right\rangle A\vec{e} \right) + M_j \left\langle s_j \right\rangle \vec{g} \\ &\quad - M_j \left\langle s_j v_j \right\rangle \left(\frac{\Delta \left(\left\langle \left\langle v_j \right\rangle \right\rangle \vec{e} \right)}{\Delta L} \right) + \vec{F}_{totf \to j} + \vec{F}_{wall \to j} \end{aligned} \tag{3}$$

In Eqn. 3, A is the cross-sectional area of the pipe in the arbitrary x-direction. Utilizing the definitions in eqns. A.6a and A.15 in Appendix A to Eqn. 3, and noting that the total

(or mixture) momentum rate is the sum of the phase-j momentum rates, we can write in the x-direction, that:

$$\sum_{j=1}^{N_p}\left(M_j\left\langle s_j\right\rangle\left(\frac{\Delta_t\left(\left\langle\left\langle v_j\right\rangle\right\rangle\right)}{\Delta t}\right)\right)=-\Delta\left(\underbrace{\sum_{j=1}^{N_p}\left(\left\langle s_j\right\rangle\left\langle\left\langle P_j\right\rangle\right\rangle\right)}_{=P_{mix}}A\right)+\left(\sum_{j=1}^{N_p}\left(M_j\left\langle s_j\right\rangle\right)\right)g_x$$
$$-\sum_{j=1}^{N_p}\left(M_j\left\langle s_j\right\rangle\left\langle\left\langle v_j\right\rangle\right\rangle\left(\frac{\Delta\left(\left\langle\left\langle v_j\right\rangle\right\rangle\right)}{\Delta L}\right)\right)-\sum_{j=1}^{N_p}\left(F_{wall\to j}\right) \tag{4}$$

Note that a mixture pressure emerges from this equation and the boundary forces act in an opposing direction to the flow. Also, as noted in Appendix B, net interfacial momentum sources are taken into account implicitly due to the volume-less phase interfaces criterion. For a straight, constant cross-section pipe with an arbitrary cross-sectional shape and area, A, we can rearrange Eqn. 4 (using the definition of phase-j mass flux, $G_j=\rho_j\left\langle\left\langle v_j\right\rangle\right\rangle\left\langle s_j\right\rangle$) to get:

$$\overbrace{\left(\frac{\Delta P_{mix}}{\Delta L}\right)}^{\text{hydrodynamic}}=\overbrace{\frac{1}{A\Delta L}\underbrace{\sum_{j=1}^{N_p}\left(F_{j\to wall}\right)}_{=F_{mix\to wall}}}^{\text{friction}}+\overbrace{\underbrace{\left(\sum_{j=1}^{N_p}\left(\rho_j\left\langle s_j\right\rangle\right)\right)}_{=\rho_{mix}}g\cos\theta}^{\text{hydrostatic}}$$
$$\overbrace{-\sum_{j=1}^{N_p}\left(\frac{G_j\Delta\left(\frac{G_j}{\rho_j\left\langle s_j\right\rangle}\right)}{\Delta L}\right)}^{\text{convective acceleration (+ve), or deceleration (-ve)}}\quad\overbrace{-\sum_{j=1}^{N_p}\left(\frac{\rho_j\left\langle s_j\right\rangle\Delta_t\left(\frac{G_j}{\rho_j\left\langle s_j\right\rangle}\right)}{\Delta t}\right)}^{\text{temporal (local) acceleration (+ve), or deceleration (-ve)}} \tag{5}$$

Eqn. 5 is a general total pressure gradient equation for any multiphase mixture flowing in any straight, constant cross-section pipe of any cross-sectional shape.

Of special significance, is the fact that up to this point, there has not been the need for any artificial variables or parameters (i.e. quantities that are not directly measurable)

in this equation. In this general form, the only unknown on the RHS of Eqn. B.5 beyond averaged phase volume fraction is the boundary force exerted on the wall by the mixture, $F_{mix \rightarrow wall}$. As discussed in the analogous single-phase scenario in Section 2.1.1, this boundary force that appears only at the integral (averaged flow) scale does not have a fundamental basis for its form, unlike the rest of the terms in Eqn. 5. Therefore, just as was done in the single-phase case, a hypothesis for the momentum transfer at the wall (i.e., a phase-to-wall phenomenological momentum transfer closure law) will have to be invoked for this term. It is only in the circumstance that analytical closure can be provided for this boundary force term (such as is demonstrated in later sections of this chapter) that Eqn. 5 will then be both general and analytical.

It must be noted that in formulating mixture balance equations in the way as shown above, finding analytical closure relations will now become a lot easier (since the closure problem is itself now simplified). This is because the mixture balance formulation implicitly accounts for the large amount of unknowns related to interfacial processes thus reducing (and therefore focusing) uncertainty in the mixture model. This significant narrowing of uncertainty leads to a substantive enhancement of predictive power and is perhaps the greatest attribute of the mixture model formulation, aside from its avoidance of the serious mathematical (ill-posedness) and thermodynamic (violation of second law) issues found in many multi-fluid models. Examples of these well-known issues can be found in numerous publications, such as Delhaye (1969), Ishii (1975), Hung (1979), Lahey, Jr., (1981), Stewart (1981), Stewart and Wendroff (1984), Arnold et al. (1990), Prosperetti (2003) and Dinh et al. (2003). As discussed in section 8.2 of Prosperetti and Trygvasson (2007), the troublesome issue of lack of hyperbolicity (found in many multi-fluid models) disappears since the mixture momentum formulation makes the characteristics of the system real. Moreover, if the uncertainty in the mixture model

consists only of terms that can be directly measured, then this would yield a model that is falsifiable, traceable and tractable.

Indeed, the mixture model formulation is itself merely one kind of asymptotic approximation method, the "asymptote" being the avoidance of many details of the flow. Asymptotic approximation methods, just as scaling arguments, transport analogies, non-dimensionalization, the Reciprocal theorem and characteristic lengths have well-established roles in the analysis and understanding of transport processes and fluid mechanics. The Reciprocal theorem, for example, is sometimes referred to as "getting something for nothing" (Stone, 2010) – a little known and seldom appreciated tool originally used in low-Reynolds-number hydrodynamcis in which one obtains answers for integrated quantities (such as forces, flow rates) without requiring the calculation of detailed velocity or stress fields (Youngren and Acrivos, 1975; Leal, 2007). The concepts of fugacity and entropy, and even the popular "black oil" formulation used in the petroleum industry, are all examples of asymptotic approximation methods re-phrased in terms of departures from a reference state (the reference state being the asymptote). These six powerful and generalized tools noted above, provide deeper insights about the nature of the transport processes.

In fact, some investigators consider that "asymptotic approximation methods are nothing more than a sophisticated version of dimensional analysis" (Leal, 2007). We subscribe to this suggestion and evidently, the results of this work demonstrate that the primary integrative variables of pressure and volume fraction are governed by a few key variables interrelated via the universal mixture momentum balance equations (Eqns. 6 and 7 of Section 2.2.4). This is the quintessence of dimensional analysis – the identification of the dominant physical balances and relationships governing a process.

Next, we note that all of the unknowns in Eqn. 5 (and from this point onwards until the end of this chapter) are colored in purple text. These are the unknowns that are present in a multiphase pipe flow experiment since mass fluxes, densities, θ, A and ΔL, are known system parameters in a carefully-controlled lab experiment. Also, note also just how strongly connected volume fraction (or alternatively, relative velocity) is related to total pressure gradient and how it is found in all of the various types of pressure gradients. Indeed, the boundary forces shown in Eqn. 5 are strong functions of volume fraction.

Now, restricting our attention to steady-state flows, Eqn. 5 becomes:

$$\overbrace{\frac{\Delta P_{mix}}{\Delta L}}^{\text{hydrodynamic}} = \overbrace{\frac{1}{A\Delta L}\underbrace{\sum_{j=1}^{N_p}\left(F_{j\to wall}\right)}_{=F_{mix\to wall}}}^{\text{friction}} + \overbrace{\underbrace{\left(\sum_{j=1}^{N_p}\left(\rho_j\left\langle s_j\right\rangle\right)\right)}_{=\rho_{mix}} g\cos\theta}^{\text{hydrostatic}} \overbrace{-\sum_{j=1}^{N_p}\left(\frac{G_j\Delta\left(\frac{G_j}{\rho_j\left\langle s_j\right\rangle}\right)}{\Delta L}\right)}^{\text{convective acceleration (+ve), or deceleration (-ve)}} \tag{6}$$

Note that a comparison of Eqn. 6 to its analogous single-phase, steady-state, total pressure gradient equation (Eqn. 18 in Section 2.1.1), shows a striking similarity between them. Eqn. 18 in Section 2.1.1 is restated below for visual comparison:

$$\overbrace{\frac{\Delta P}{\Delta L}}^{\text{hydrodynamic}} = \overbrace{\frac{1}{A\Delta L}\left(F_{phase\to wall}\right)}^{\text{friction}} \overbrace{+\rho g\cos\theta}^{\text{hydrostatic}} \overbrace{-G\left(\frac{\Delta\left(\frac{G}{\rho}\right)}{\Delta L}\right)}^{\text{convective acceleration (+ve), or deceleration (-ve)}} \tag{7}$$

Another striking similarity is found if we compare Eqn. 6 with its analogous macroscopic total (mixture) energy flux gradient equation (Eqn. B.39 of Appendix B) restated below as:

$$\overbrace{\frac{\Delta\left(\overbrace{\sum_{j=1}^{N_p}\left(G_j\hat{H}_j\right)}^{=\left(G\hat{H}\right)_{mix}}\right)}{\Delta L}}^{\text{thermal-dynamic}} = \overbrace{\frac{1}{A\Delta L}\underbrace{\sum_{j=1}^{N_p}\left(Q_{wall\to j}\right)}_{=Q_{wall\to mix}}}^{\text{wall heat transfer}} + \overbrace{\underbrace{\left(\sum_{j=1}^{N_p}\left(G_j\right)\right)}_{=G_{mix}} g\cos\theta}^{\text{gravitational}} \overbrace{-\frac{1}{2}\sum_{j=1}^{N_p}\left(\frac{\Delta\left(G_j\left(\frac{G_j}{\rho_j\left\langle s_j\right\rangle}\right)^2\right)}{\Delta L}\right)}^{\text{kinetic energy increase (+ve), or decrease (-ve)}} \quad (8a)$$

Note that, similar to Eqn. 6, Eqn. 8a is a generally valid balance equation for total (mixture) energy flux gradient calculation for any multiphase mixture flowing in any straight, constant cross-section pipe of any cross-sectional shape. Just as significant as Eqn. 6, is the fact that that there are no energy-related artificial multiphase pipe flow variables or parameters in Eqn. 8a. This is because in choosing the total (mixture) energy balance formulation over the thermal energy balance equation for energy flux gradient calculation, we avoided the need to provide empirical closure for the last two terms in Eqn. B.33 of Appendix B, i.e. the expansion/contraction term, E_c, and the viscous dissipation term, $E_{v,wall\to mix}$. Aside from having very subtle influences to the energy flux gradient relative to other dominant convective and wall energy transfer fluxes, these two terms are notoriously difficult to experimentally isolate (let alone model). Also, note that the subscripts "wall→j" and "j→wall" are interchangeable in Eqn. 8a depending on whether the multiphase mixture is being heated or cooled.

Lastly, Eqn. 8a can be tested for its general validity in much the same manner as is done in this work for Eqn. 6 (or Eqn. 5), with analogously defined analytical closure relations for the wall thermal energy fluxes. We simply plant the seed at this time for investigators to go forward and extend the simple, analytical hydrodynamic developments in this work to their analytical thermal-dynamic counterparts. For example, with the new knowledge provided in this work of how to analytically solve

$F_{j\to wall}$ in Eqn. 6 (or Eqn. 5), the phase-j wall heat transfer rate, $Q_{wall\to j}$, can be simply defined in terms of a phase-j wall heat transfer coefficient, as:

$$Q_{wall\to j} = \underbrace{Z_j^{net}\Delta L}_{\substack{\text{net surface area over}\\ \text{which } j \text{ heat flux}\\ \text{is transferred to } j}} \overbrace{q_{wall\to j}}^{\substack{\text{wall-to-}j\\ \text{heat flux}}} = Z_j^{net}\Delta L \; \overbrace{\gamma_j}^{j \text{ dominance}} \; \overbrace{h_{wall\to j}}^{\substack{j \text{ heat flux}\\ \text{transfer}\\ \text{coefficient}}} \left(T_{wall} - T_j\right) \qquad (8b)$$

In Eqn. 8b above, the phase-j net heat flux transfer surface can be obtained from Eqn. 10 below (discussed in the next section) and the phase-j dominance can be obtained from Eqn. 2 of Section 2.2.4 below. Also, note that the transient version of Eqn. 8a (which can be obtained from Eqn. B.36 of Appendix B) can be solved simultaneously with Eqn. 5 to yield an analytical, generalized (flow-pattern implicit), thermal-hydraulic, transient flow solution for the flowing mixture.

2.2.3 Coupled and Decoupled Flow

As seen previously, the only unknown on the RHS of Eqn. 5 in Section 2.2.2 beyond averaged phase volume fraction is the boundary force exerted on the wall by the multiphase mixture, $F_{mix\to wall}$. As discussed in Appendix B, this term does not have a form that can be derived from a basic flow principle. Therefore, we provide closure for this term by invoking a few key hypotheses. Additionally, we will also clearly state the rational bases underlying these hypotheses. We start by generalizing our understanding of how the analogous single-phase term in Section 2.1.1, $F_{phase\to wall}$, was closed. When describing phase-j-to-wall momentum flux in a generic multiphase flow, Eqn. 8a in Section 2.1.1 can be re-written as:

$$\frac{F_{j\to wall}}{\underbrace{Z_j^{net}\Delta L}_{\substack{\text{net surface area over which}\\ j \text{ momentum flux}\\ \text{is transferred to the wall}}}} = \overbrace{\tau_{j\to wall}}^{\substack{j\text{-to-wall momentum flux}\\ (\text{"}j\text{ shear stress"})}} \qquad (9)$$

In Eqn. 9, there are two unknowns – the net transfer surface over which phase-j momentum flux is transferred, $Z_j^{net}\Delta L$, and the phase-j-to-wall shear stress, $\tau_{j\rightarrow wall}$.

2.2.3.1 Net Momentum Flux Transfer Surface

In this section, we invoke a hypothesis for the net phase-j momentum flux transfer surface from the flow field to the wall. The net transfer surfaces are mathematical (not physical) averaged phase-j flow quantities that exist solely as a result of the definition of the averaged phase-j shear stress in Eqn. 9. This definition of the net transfer surface in Eqn. 9 above, shows that zero wall shear stress (or zero relative velocity between the velocity of the phase in the flow field and at the wall) only implies that there will be zero wall force, and bears no relation to the value of the net momentum flux transfer surface, shown in the denominator of Eqn. 9.

Now, we emphasize that this definition of a net transfer surface for phase-j momentum flux to the wall, $Z_j^{net}\Delta L$, must <u>not</u> be interpreted as the product of a "net wetted perimeter" and ΔL, since the macroscopic single-phase flow concept of "wetted perimeter" itself merely signifies the averaged momentum flux transfer surface between the flowing phase and the stationary wall. We recall that the single-phase wetted perimeter is simply an averaged flow quantity borne upon the need to mathematically define the viscous loss factor in Eqn. 4a of Section 2.1.1 in terms of other averaged flow quantities that are subject to direct experimental observation. Although the descriptive single-phase language of "wetting" can be misleading in a literal (superficial) sense, the macroscopic transport phenomena definition of wetted perimeter is that it defines <u>the averaged momentum flux transfer surface between a flowing phase and its stationary boundary (the pipe wall)</u>. Unfortunately, the rather literal interpretation of single-phase "wetted perimeter" is perhaps the root cause behind the various disparate multiphase

extensions of this term that currently exists in multiphase flow applications, and particularly, in stratified horizontal vapor-liquid flows (e.g., as reviewed in Pan, 1996, Shaha et al., 1999 and Omgba-Essama, 2004).

With the macroscopic transport phenomena definition of wetted perimeter now in place, it can thus be expected that just as there is a net momentum flux transfer surface for a flowing phase in the single-phase scenario, $Z\Delta L$ (as defined in Eqn. 4a of Section 2.1.1), there will be a net momentum flux transfer surface for a flowing phase-j in the multiphase scenario, $Z_j^{net}\Delta L$. Also, it is important to note that the unit net phase-j momentum flux transfer surface, Z_j^{net}, being an averaged flow quantity that is mathematically defined by Eqn. 9, cannot be used to ascertain characteristics of the flow patterns or flow field bodies within the main stream (e.g., the shape of a liquid interface in a stratified horizontal vapor-liquid flow). All prevailing flow patterns and orientations of flow field bodies are (and remain as) unknown variables during a multiphase flow.

Additionally, the definition of Z_j^{net}, cannot provide information as to which phase or parts of a phase (e.g., phase particles such as vapor bubbles or liquid droplets) are close to or far from the wall, since an averaged description of the flow field only allows for space- and time-averaged variables and parameters. We must constantly remind ourselves that all local information within the flow field is lost in the averaged-equations formulation, and can only be recovered through postulated closure hypotheses, phenomenological transfer relationships and/or constitutive equations.

We now postulate the following:

I. There are, in general, two different ways in which phase momentum fluxes are transported to the wall, corresponding to the scenarios where there will be either non-preferential (the first way) or preferential (the second way) directions for momentum transport from the flow field to the wall.

II. *If* there are no preferential directions, *then* only the momentum fluxes between flowing phases and the stationary wall, i.e. $Z_{j\rightarrow wall}$ (which is an unknown averaged flow variable), will contribute to the net momentum flux transfer surfaces from the phases to the wall.

III. *If* there are preferential directions, *then* both the momentum fluxes between flowing phases and the stationary wall, $Z_{j\rightarrow wall}$, and the momentum fluxes between adjacent flowing phases, $Z_{j,k\neq j}$ (which is another unknown averaged flow variable), will contribute to the net momentum flux transfer surface from the phases to the wall.

IV. In the first way, the general case (which we call "coupled flow"), *if* there are no preferential directions for momentum transfer from the flow field to the wall, *then* phase momentum fluxes will act upon the shared shear stress transfer surface for all of the phases, Z, which is equal to $\sum_{j=1}^{N_p}\left(Z_{j\rightarrow wall}\right)$. Therefore, coupled flow simply means that each phase's momentum flux to the wall is coupled to every other phase's momentum flux to the wall via the shared shear stress transfer surface at the wall, Z. We note that the single-phase flow scenario is one subset of this general "coupled flow" definition.

V. In the second way, a special case (which we call decoupled vapor-liquid flow or "decoupled flow"), *if* there are preferential directions for momentum transfer from the flow field to the wall, *then* the momentum transport from each phase to the wall must pass through the more efficient conductors of momentum, the more viscous phases, on its way to the wall. In this scenario, both the phase-to-wall ($Z_{j\rightarrow wall}$) and phase-to-phase ($Z_{j,k\neq j}$) momentum flux transfer surfaces will contribute to the net momentum flux transfer surface for

the considered phase, Z_j^{net}. Therefore, decoupled flow simply means that each phase's momentum flux to the wall is decoupled from every other phase's momentum flux to the wall via a different net shear stress transfer surface for each phase.

Throughout the numerous applications of the coupled flow hypothesis in this work, it will become evident that coupled flows are the general (or more common) case for multiphase pipe flows. This is found the vast majority of laboratory-scale (i.e., mostly low pressure and temperature, immiscible phases) flows and in all field-scale (i.e., mostly high pressure and temperature, miscible phases) flows. In fact, in this work, if not explicitly identified as a decoupled flow, coupled flow modeling is performed in each scenario.

On the other hand, it is found in this work that the decoupled flow hypothesis is only valid for immiscible vapor-liquid flows, and within this subgroup, in the special cases of laboratory-scale concurrent down-inclined flows and certain laboratory-scale horizontal low flow rate scenarios (e.g., low liquids loading). In these special (and relatively few) decoupled vapor-liquid flow scenarios, the net of the prevailing forces will tend to keep the bulk movements of phases within localized regions of the flow field during flow, thus furnishing the conditions for preferred directions for phase-to-wall momentum fluxes. We note that the preferred directions for momentum transport in this case will always be through the more efficient conductor of momentum (the more viscous liquid phase), which incidentally, is also the phase in which there are secondary flows, re-circulating motions and large-scale coherent structures such as different kinds of waves and/or vortices – all of which can significantly change the in-situ velocity and volume

fraction profiles, and subsequently, can greatly affect the net momentum transport to the wall.

We can convert our hypothesis of coupled and decoupled flow above into a simple mathematical form as shown below:

$$Z_j^{net} = \begin{cases} Z & \forall\ j \quad \overbrace{(Coupled\ Flows)}^{\text{There are no preferred directions for phase-to-wall momentum fluxes}} \\ Z_1^{net},\ Z_2^{net},\ ...,Z_{N_p}^{net} & \forall\ j=1,2,...,N_p \quad \overbrace{(Decoupled\ Flows)}^{\text{There are preferred directions for phase-to-wall momentum fluxes}} \end{cases} \tag{10}$$

Applying Eqns. 9 and 10 to Eqn. 5, we can write, for coupled flows (the general case):

$$\overbrace{\left(\frac{\Delta P_{mix}}{\Delta L}\right)}^{\text{hydrodynamic}} = \overbrace{\left(\frac{Z}{A}\right)}^{\text{friction}\ =\frac{4}{D_H}} \sum_{j=1}^{N_p}\left(\tau_{j\to wall}\right) + \overbrace{\left(\sum_{j=1}^{N_p}\left(\rho_j \left\langle s_j \right\rangle\right)\right) g\cos\theta}^{\text{hydrostatic}} \overbrace{-\sum_{j=1}^{N_p}\left(\frac{G_j \Delta\left(\frac{G_j}{\rho_j\left\langle s_j\right\rangle}\right)}{\Delta L}\right)}^{\text{convective acceleration (+ve), or deceleration (-ve)}} \overbrace{-\sum_{j=1}^{N_p}\left(\frac{\rho_j\left\langle s_j\right\rangle \Delta_t\left(\frac{G_j}{\rho_j\left\langle s_j\right\rangle}\right)}{\Delta t}\right)}^{\text{temporal (local) acceleration (+ve), or deceleration (-ve)}} \tag{11}$$

And for decoupled flows (a special case), Eqn. 5 now becomes:

$$\overbrace{\left(\frac{\Delta P_{mix}}{\Delta L}\right)}^{\text{hydrodynamic}} = \overbrace{\sum_{j=1}^{N_p}\left(\left(\frac{Z_j^{net}}{A}\right)\tau_{j\to wall}\right)}^{\text{friction}} + \overbrace{\left(\sum_{j=1}^{N_p}\left(\rho_j \left\langle s_j \right\rangle\right)\right) g\cos\theta}^{\text{hydrostatic}} \overbrace{-\sum_{j=1}^{N_p}\left(\frac{G_j \Delta\left(\frac{G_j}{\rho_j\left\langle s_j\right\rangle}\right)}{\Delta L}\right)}^{\text{convective acceleration (+ve), or deceleration (-ve)}} \overbrace{-\sum_{j=1}^{N_p}\left(\frac{\rho_j\left\langle s_j\right\rangle \Delta_t\left(\frac{G_j}{\rho_j\left\langle s_j\right\rangle}\right)}{\Delta t}\right)}^{\text{temporal (local) acceleration (+ve), or deceleration (-ve)}} \tag{12}$$

As before, we note the glaring similarity between eqns. 11, Eqn. 12 and Eqn. 19 of Section 2.1.1, which is restated below for visual comparison:

$$\overbrace{\left(\frac{\Delta P}{\Delta L}\right)}^{\text{hydrodynamic}} = \overbrace{\overbrace{\left(\frac{Z}{A}\right)}^{=\frac{4}{D_H}}\tau_{phase\to wall}}^{\text{friction}} \overbrace{+\ \rho g\cos\theta}^{\text{hydrostatic}} \overbrace{-\ G\left(\frac{\Delta\left(\frac{G}{\rho}\right)}{\Delta L}\right)}^{\text{convective acceleration (+ve), or deceleration (−ve)}} \qquad (13)$$

2.2.3.2 Decoupled Flow

Now, in order to arrive at analytical equations for the (unit) net phase momentum flux transfer surfaces defined in Eqn. 10, we must extend the rational basis behind the postulates in the previous section in terms of simple and explicit algebraic closure relations. The coupled flow hypothesis does not require any closure since Z is a known system parameter. However, the decoupled flow hypothesis indicates that there are (unit) net momentum flux surfaces for each phase, Z_j^{net}, that require specification. Fortunately, very simple physical arguments (assumptions) can be made about each phase's idealized flowing geometry in the pipe that will allow Z_j^{net} to be specified analytically in terms of D_H, A and $\langle s_j \rangle$. These physical arguments are transformed into the mathematical closure relations given in Appendix E.

2.2.4 Phase-to-Wall Shear Stress Dominance

As we saw in the previous section, Eqn. 9 showed that when describing phase-j-to-wall momentum flux, there were two unknowns – the net transfer surface over which phase-j momentum flux is transferred, Z_j^{net}, and the phase-j-to-wall shear stress, $\tau_{j\to wall}$. Analytical closure was provided for the momentum flux transfer surfaces in the previous section. In this section we provide analytical closure (a hypothesis) for the phase-j-to-

wall shear stress. We start by re-writing the single-phase phase-to-wall shear stress, Eqn. 8a in Section 2.1.1, as:

$$\overbrace{\tau_{phase\rightarrow wall}}^{\substack{\text{phase-to-wall}\\ \text{momentum flux}\\ \text{(“wall shear stress”)}}} = \overbrace{+}^{\substack{\text{“high-to-low”}\\ \text{sign}\\ \text{convention}}} \overbrace{\left(\frac{f_{phase\rightarrow wall}\left|\langle v\rangle\right|}{2}\right)}^{\substack{\text{momentum flux}\\ \text{transfer coefficient}}} \overbrace{\left(\overbrace{\left(\rho\langle v\rangle\right)}^{\substack{\text{high conc. of}\\ \text{momentum}\\ \text{(phase)}}} - \overbrace{\rho \underbrace{v_{wall}}_{=0}}^{\substack{\text{low conc. of}\\ \text{momentum}\\ \text{(wall)}}}\right)}^{\textit{relative momentum concentration}} \tag{1}$$

We now postulate the following:

I. In general, a directly equivalent definition to Eqn. 1 above can be written for phase-j-to-wall shear stress in multiphase flows, if it is recognized that the single-phase velocity, $\langle v\rangle$, must be replaced everywhere it is found in Eqn. 1 with its respective velocity for multiphase flows, $\langle\langle v_j\rangle\rangle$, i.e**.,** the actual in-situ mean phase-j velocity.

II. In certain vapor-liquid decoupled flow scenarios (e.g., Gazley, 1948), the combination of placement of local pressure instrumentation in the flow field and very low phase flow rates will allow the detection of phase-to-wall shear stress of only one phase in the flowing mixture. The detected phase will therefore be the only phase contributing to the mixture frictional pressure gradient. We call these scenarios as exhibiting “detected-phase shear stress dominance” or simply “detected-phase dominance”.

III. In liquid-liquid flow scenarios, there will be cases where a phase will remain the carrier or dominant phase (e.g., as found in core-annular flows such as Oliemans, 1986, Bai et al., 1992, Grassi et al., 2008), or, will physically invert from being a carrier phase to being a dispersed phase, such as is observed when transgressing the phase inversion point (e.g., as found in Wood, 1960, Arirachakaran, 1983, Trallero, 1995). In fluid-solid flows, since wall shear

stress-related variables such as friction factor or viscosity only has a physical significance (and experimental basis) for a fluid phase, the carrier fluid phase will always be the only phase that is responsible for shear stress from the flow field to the wall. In either scenario of liquid-liquid or fluid-solid flows above, the carrier or dominant phase will be the only phase contributing to the mixture frictional pressure gradient. We call these scenarios as exhibiting "carrier-phase shear stress dominance" or simply "carrier-phase dominance".

For a two-phase flow, we can represent the various possibilities of phase dominance discussed above, as:

$$\overbrace{\gamma_j}^{j\text{-dominance}} = \begin{cases} 1,1 & \forall\ j = dominant-vapor, dominant-liquid \\ 1,0 & \forall\ j = dominant-vapor, passive-liquid \\ 0,1 & \forall\ j = passive-vapor, dominant-liquid \\ 1,0 & \forall\ j = dominant-fluid, passive-solid \\ 1,0 & \forall\ j = dominant-liquid, passive-liquid \end{cases} \quad (2)$$

In Eqn. 2, the purple-colored text represent the very infrequent (though possible) cases that can exist in certain vapor-liquid decoupled flow scenarios, as will be shown in Chapter 4. The remaining black text on the RHS of Eqn. 2 represents the cases that are generally observed for these phase combinations. Eqn. 2 also acts as building blocks for more advanced phase combinations such as three-phase and four-phase flows, and so on. For example, in a three-phase vapor-liquid-liquid flow, only the vapor and one of the liquid phases will transport momentum fluxes from the flow field to the wall. The key insight with respect to the principle of phase-to-wall shear stress dominance is that, in general, both the vapor and liquid phases are equally dominant in vapor-liquid flows, only one of the liquid phases in a liquid-liquid flow is dominant and only the carrier fluid phase in a fluid-solid flow is dominant.

Representing the above hypotheses in an appropriate mathematical form, we thus postulate the following general phenomenological momentum flux transfer law for phase-j-to-wall shear stress in a multiphase flow, as:

$$\overbrace{\tau_{j\to wall}}^{\substack{j\text{-to-wall momentum flux} \\ (\text{"}j\text{ shear stress"})}} = \overbrace{+}^{\substack{\text{"high-to-low"} \\ \text{sign convention}}} \overbrace{\gamma_j}^{j\text{-dominance}} \overbrace{\left(\frac{f_{j\to wall} \left| \left\langle \left\langle v_j \right\rangle \right\rangle \right|}{2} \right)}^{\substack{j \text{ momentum flux} \\ \text{transfer coefficient}}} \overbrace{\left(\overbrace{\left(\rho_j \left\langle \left\langle v_j \right\rangle \right\rangle \right)}^{\substack{\text{high conc. of} \\ j \text{ momentum}}} - \overbrace{\left(\rho_j \underbrace{v_{wall}}_{=0} \right)}^{\substack{\text{low conc. of} \\ j \text{ momentum}}} \right)}^{relative\ j\ momentum\ concentration} \tag{3}$$

Where,

$$\overbrace{f_{j\to wall}}^{\substack{j\ Fanning \\ friction\ factor}} = \begin{cases} \overbrace{\left(\frac{16}{N_{\mathrm{Re},j}} \right)}^{Hagen-Poiseuille\ Eqn.} & \forall\ \overbrace{N_{\mathrm{Re},j} \le 2300}^{Laminar} \\ \overbrace{\left(\frac{7.05\times10^{-8}}{\left(N_{\mathrm{Re},j} \right)^{-1.5}} \right)}^{Manadilli\ (1997)} & \forall\ \overbrace{2300 < N_{\mathrm{Re},j} \le 2900}^{Transitional} \\ \overbrace{\left(-3.6\log_{10}\left(\frac{6.9}{N_{\mathrm{Re},j}} + \left(\frac{1}{3.7}\frac{k_{wall}}{D_H} \right)^{\frac{10}{9}} \right) \right)^{-2}}^{Haaland\ (1983)} & \forall\ \overbrace{N_{\mathrm{Re},j} > 2900}^{Turbulent} \end{cases} \tag{4}$$

And,

$$\overbrace{N_{\mathrm{Re},j}}^{\substack{In-situ \\ Reynolds\ Number}} = \frac{\rho_j \left| \left\langle \left\langle v_j \right\rangle \right\rangle \right| D_H}{\mu_j} = \frac{\left| G_j \right| D_H}{\mu_j \left\langle s_j \right\rangle} \tag{5}$$

In light of the obvious similarities between Eqns. 6 and 8a of Section 2.1.1 and Eqns. 3 to 5 above, we see that multiphase flow shear stress is a generalization of single-phase flow shear stress. Hence, one of the major insights gained from this research is that averaged multiphase pipe flow can be simply understood using applications of existing macroscopic fluid mechanics concepts. Substituting Eqns. 3 to 5 in Eqn. 11 of Section

2.2.3 will yield the universal mixture momentum balance equation for coupled flows (the general case), as:

$$\overbrace{\left(\frac{\Delta P_{mix}}{\Delta L}\right)}^{\text{hydrodynamic}} = \overbrace{\left(\frac{Z}{A}\right)}^{=\frac{4}{D_H}} \overbrace{\sum_{j=1}^{N_p} \left(\frac{\gamma_j f_{j\to wall}\left(\frac{|G_j| D_H}{\langle s_j \rangle \mu_j}, \frac{k_{wall}}{D_H}\right) |G_j| G_j}{2\rho_j \langle s_j \rangle^2} \right)}^{\text{friction}} \overbrace{\quad}^{=\tau_{j\to wall}}$$

$$+ \overbrace{\left(\sum_{j=1}^{N_p} \left(\rho_j \langle s_j \rangle \right) \right) g \cos\theta}^{\text{hydrostatic}} - \overbrace{\sum_{j=1}^{N_p} \left(\frac{G_j \Delta\left(\frac{G_j}{\rho_j \langle s_j \rangle}\right)}{\Delta L} \right)}^{\text{convective acceleration (+ve), or deceleration (-ve)}} - \overbrace{\sum_{j=1}^{N_p} \left(\frac{\rho_j \langle s_j \rangle \Delta_t\left(\frac{G_j}{\rho_j \langle s_j \rangle}\right)}{\Delta t} \right)}^{\text{temporal (local) acceleration (+ve), or deceleration (-ve)}} \tag{6}$$

Similarly, substituting Eqns. 3 to 5 in Eqn. 12 of Section 2.2.3 will yield the universal mixture momentum balance equation for decoupled flows (a special case), as:

$$\overbrace{\left(\frac{\Delta P_{mix}}{\Delta L}\right)}^{\text{hydrodynamic}} = \overbrace{\sum_{j=1}^{N_p} \left(\frac{Z_j^{net}\left(\langle s_j \rangle, D_H, A\right)}{A} \left(\frac{\gamma_j f_{j\to wall}\left(\frac{|G_j| D_H}{\langle s_j \rangle \mu_j}, \frac{k_{wall}}{D_H}\right) |G_j| G_j}{2\rho_j \langle s_j \rangle^2} \right) \right)}^{\text{friction}} \overbrace{\quad}^{=\tau_{j\to wall}}$$

$$+ \overbrace{\left(\sum_{j=1}^{N_p} \left(\rho_j \langle s_j \rangle \right) \right) g \cos\theta}^{\text{hydrostatic}} - \overbrace{\sum_{j=1}^{N_p} \left(\frac{G_j \Delta\left(\frac{G_j}{\rho_j \langle s_j \rangle}\right)}{\Delta L} \right)}^{\text{convective acceleration (+ve), or deceleration (-ve)}} - \overbrace{\sum_{j=1}^{N_p} \left(\frac{\rho_j \langle s_j \rangle \Delta_t\left(\frac{G_j}{\rho_j \langle s_j \rangle}\right)}{\Delta t} \right)}^{\text{temporal (local) acceleration (+ve), or deceleration (-ve)}} \tag{7}$$

2.2.5 Multiphase Non-Newtonian Flow

In single-phase pipe flow, the Metzner and Reed (1955) generalized definition of non-Newtonian Reynolds number for a power-law fluid phase j, or in general, any non-Newtonian fluid phase that can be described using power-law (or "PL") parameters, can be derived analytically (as shown on pg. 77 of Chhabra and Richardson, 1999) as:

$$N_{\mathrm{Re}}^{PL} = \frac{\rho \langle v \rangle^{2-n} \left(D_H\right)^n}{8^{n-1} \underbrace{\left(K \left(\frac{3n+1}{4n} \right)^n \right)}_{= K'}} \tag{1}$$

In Eqn. 1, K is the phase consistency coefficient and n is the phase flow behavior index. We can re-express Eqn. 1 in the conventional Reynolds number form as:

$$N_{\mathrm{Re}}^{PL} = \frac{\rho \langle v \rangle D_H}{\overbrace{\left(\frac{8\langle v \rangle}{D_H} \right)^{n-1} K'}^{\mu^{PL}}} \tag{2}$$

In Eqn. 2 above, a non-Newtonian power-law viscosity is shown in place of its Newtonian counterpart. For multiphase non-Newtonian flow, an equivalent multiphase definition of the single-phase non-Newtonian Reynolds number (i.e., a definition based on the in-situ phase-j velocity) can be obtained from the Metzner and Reed (1955) single-phase flow definition in Eqn. 1. To obtain this relationship, we start by rewriting Eqn. 1 in terms of phase-j volume flux, i.e., the superficial velocity of phase-j as if it were flowing in the pipe by itself, as:

$$N_{\mathrm{Re},sj}^{PL} = \frac{\rho_j \langle u_j \rangle^{2-n_j} \left(D_H\right)^{n_j}}{8^{n_j-1} K_j'} = \frac{\rho_j \langle u_j \rangle D_H}{\overbrace{\left(\frac{8\langle u_j \rangle}{D_H} \right)^{n_j-1} K_j'}^{=\mu_{sj}^{PL}}} = \left(\frac{\rho_j \langle\langle v_j \rangle\rangle D_H}{\left(\frac{8\langle\langle v_j \rangle\rangle}{D_H} \right)^{n_j-1} K_j'} \right) \overbrace{\left(\langle s_j \rangle^{2-n_j} \right)}^{\substack{j \text{ volume fraction} \\ \text{dependence}}} \tag{3}$$

From Eqn. 3, we see that a "j volume fraction dependence" factor comes out simply as a result of the mathematical relationship between phase-j volume flux and in-situ velocity (Eqn. A.6a in Appendix A). We thus postulate that this factor must also be present in the non-Newtonian viscosity definition of a phase-j Reynolds number based on the in-situ velocity – which the form of the Reynolds number that is applicable for multiphase flow. This new multiphase phase-j Reynolds number is therefore given as:

$$N_{\mathrm{Re},j}^{PL} = \frac{\rho_j \left\langle\left\langle v_j \right\rangle\right\rangle D_H}{\underbrace{\left(\frac{8\left\langle\left\langle v_j \right\rangle\right\rangle}{D_H}\right)^{n_j-1} K_j' \overbrace{\left\langle s_j \right\rangle^{2-n_j}}^{j \text{ volume fraction dependence}}}_{=\mu_j^{PL}}} \tag{4}$$

From eqns. 3 and 4, we find that:

$$\overbrace{\mu_{sj}^{PL} N_{\mathrm{Re},sj}^{PL}}^{=\rho_j \langle u_j \rangle D_H} = \overbrace{\left(\mu_j^{PL} N_{\mathrm{Re},j}^{PL}\right)\left\langle s_j \right\rangle}^{=\rho_j \left\langle\left\langle v_j \right\rangle\right\rangle D_H} \tag{5}$$

As clearly seen above, Eqn. 5 is simply the relationship between volume flux and in-situ velocity. If we now compare only the power-law viscosity terms in eqns. 3 and 4, we find that the relation between μ_{sj}^{PL} and μ_j^{PL} can be written as:

$$\mu_{sj}^{PL} = \mu_j^{PL} \left\langle s_j \right\rangle^{2n_j-3} \tag{6}$$

Substituting Eqn. 6 in Eqn. 5, we can arrive at a relation between $N_{\mathrm{Re},sj}^{PL}$ and $N_{\mathrm{Re},sj}^{PL}$ as:

$$N_{\mathrm{Re},sj}^{PL} = N_{\mathrm{Re},j}^{PL} \left\langle s_j \right\rangle^{4-2n_j} \tag{7}$$

Also, we can re-write μ_j^{PL} in Eqn. 4 in terms of mass flux as:

$$\mu_j^{PL} = \left(\frac{8G_j}{\rho_j \left\langle s_j \right\rangle D_H}\right)^{n_j-1} \underbrace{\left(K_j \left(\frac{3n_j+1}{4n_j}\right)^{n_j}\right)}_{=K_j'} \left(\left\langle s_j \right\rangle^{2-n_j}\right) \tag{8}$$

As is evident from the short analysis above, apart from Eqn. 4 being analytical, it also furnishes very simple relationships between superficial quantities (which are known

in experiments) and their in-situ counterparts. We will comprehensively validate Eqn. 4 for its ability to accurately represent a wide range (and amount) of published, carefully-controlled non-Newtonian multiphase pipe flow experiments in chapter 7 of this work.

Now, Eqn. 4 is more potent than it first appears. It allows us to account for non-Newtonian multiphase flows without modifying the form of the analytical momentum balance equations developed in the previous section (eqns. 6 and 7 in Section 2.2.4). The multiphase Newtonian viscosity, μ_j, is simply replaced with the multiphase non-Newtonian viscosity, μ_j^{PL}, in Eqn. 8 above. Thus, the applicable versions of eqns. 6 and 7 in Section 2.2.4 for non-Newtonian multiphase pipe flows are now shown below. Note that in a controlled experiment without entrainment, all of the terms on the RHS of the equations below are expressed in terms of known system quantities and, therefore, the averaged volume fraction is still the only unknown (and directly measurable) quantity. For coupled flows (the general case), we get:

$$\overbrace{\left(\frac{\Delta P_{mix}}{\Delta L}\right)}^{\text{hydrodynamic}} = \overbrace{\left(\frac{Z}{A}\right)}^{=\frac{4}{D_H}} \sum_{j=1}^{N_p} \overbrace{\left(\frac{\gamma_j f_{j\to wall}\left(\frac{\left|G_j\right| D_H}{\left\langle s_j \right\rangle \mu_j^{PL}\left(K_j, n_j, D_H, G_j, \rho_j, \left\langle s_j \right\rangle\right)}, \frac{k_{wall}}{D_H} \right) \left|G_j\right| G_j}{2\rho_j \left\langle s_j \right\rangle^2} \right)}^{\text{friction}} \quad (9)$$

$$\overbrace{+\sum_{j=1}^{N_p}\left(\rho_j \left\langle s_j \right\rangle g \cos\theta\right)}^{\text{hydrostatic}} \overbrace{-\sum_{j=1}^{N_p}\left(\frac{G_j \Delta\left(\frac{G_j}{\rho_j \left\langle s_j \right\rangle}\right)}{\Delta L} \right)}^{\text{convective acceleration (+ve), or deceleration (-ve)}} \overbrace{-\sum_{j=1}^{N_p}\left(\frac{\rho_j \left\langle s_j \right\rangle \Delta_t\left(\frac{G_j}{\rho_j \left\langle s_j \right\rangle}\right)}{\Delta t} \right)}^{\text{temporal (local) acceleration (+ve), or deceleration (-ve)}}$$

And, for decoupled flows (a special case), we get:

$$\overbrace{\left(\frac{\Delta P_{mix}}{\Delta L}\right)}^{\text{hydrodynamic}} = \overbrace{\sum_{j=1}^{N_p}\left(\frac{Z_j^{net}\left(\left\langle s_j\right\rangle, D_H, A\right)}{A}\overbrace{\left(\frac{\gamma_j f_{j\to wall}\left(\frac{\left|G_j\right| D_H}{\left\langle s_j\right\rangle \mu_j^{PL}\left(K_j, n_j, D_H, G_j, \rho_j, \left\langle s_j\right\rangle\right)}, \frac{k_{wall}}{D_H}\right)\left|G_j\right| G_j}{2\rho_j \left\langle s_j\right\rangle^2}\right)^{=\tau_{j\to wall}}\right)}^{\text{friction}}$$

$$\overbrace{+\sum_{j=1}^{N_p}\left(\rho_j \left\langle s_j\right\rangle g\cos\theta\right)}^{\text{hydrostatic}} \overbrace{-\sum_{j=1}^{N_p}\left(\frac{G_j \Delta\left(\frac{G_j}{\rho_j\left\langle s_j\right\rangle}\right)}{\Delta L}\right)}^{\text{convective acceleration (+ve), or deceleration (-ve)}} \overbrace{-\sum_{j=1}^{N_p}\left(\frac{\rho_j\left\langle s_j\right\rangle \Delta_t\left(\frac{G_j}{\rho_j\left\langle s_j\right\rangle}\right)}{\Delta t}\right)}^{\text{temporal (local) acceleration (+ve), or deceleration (-ve)}} \quad (10)$$

2.2.6 Analytical Multi-Directional Entrainment

The interaction and behavior of a particle field and its carrier medium (or media) has long since been the subject of investigation in academic and industrial communities. Bibliographic surveys are abundant in special cases of this general subject and are usually application-specific, e.g., the prediction of water droplets in a heated nuclear fuel channel for nuclear reactor safety investigations (Leung, 1977; Reyes, Jr., 1986).

Annular-dispersed vapor-liquid or vapor-liquid-liquid flows are special cases of this general problem in which a liquid film with large numbers of small bubbles flows adjacent to the conduit wall and surrounds a central vapor core laden with liquid droplets. This is alternatively referred to as annular vapor-liquid or vapor-liquid-liquid flow with multi-directional entrainment – with the direction of entrainment being either in one way,

from the liquid to the vapor core, or in multiple ways, between the vapor and the adjacent flowing liquid (or liquids).

Crucial parameters in the above scenario are the fraction of the total liquid flow entrained as droplets or other (wispy) structures in the vapor core and the fraction of total vapor flow entrained as large numbers of small bubbles in the liquid film (or films). These parameters represent the net or integral effects of liquid droplet deposition and formation (sometimes called entrainment or atomization), and vapor bubble entrainment. Several opinions as to the possible mechanisms responsible for these microphysical flow processes exist in the literature (e.g., Wallis, 1969, Andreussi, 1983; Hewitt, 1986; Oliemans et al., 1986; Azzopardi, 1997; Sawant et al., 2008). Reviews of various vapor-liquid inter-phase entrainment modeling approaches are also abundant (e.g., Hewitt and Hall-Taylor, 1970; Brown, 1978; Martin, 1983; Govan, 1990; Han, 2005; Schubring, 2009).

In Appendix F, we present new, simple analytical equations describing multi-directional inter-phase entrainment in the special case of annular-dispersed vapor-liquid (bi-directional, two-phase entrainment) and vapor-liquid-liquid flows (quad-directional, three-phase entrainment). In the detailed formulations shown in this Appendix, the key insight gained with regards to this special category of multiphase flow with inter-phase entrainment, is that only the mass fluxes and densities need to be corrected to accurately account for inter-phase entrainment in our universal mixture momentum balance equations (Eqns. 6 and 7 of Section 2.2.4). Therefore, rewriting our universal mixture momentum balance equations for vapor-liquid and vapor-liquid-liquid annular flows with multi-directional entrainment, we see for coupled flows (the general case), we get:

$$\overbrace{\left(\frac{\Delta P_{mix}}{\Delta L}\right)}^{\text{hydrodynamic}} = \overbrace{\left(\frac{Z}{A}\right)}^{=\frac{4}{D_H}} \overbrace{\sum_{j=1}^{N_p}\left(\frac{\overbrace{\gamma_j f_{j\to wall}\left(\frac{\left|G_j^{corr}\right| D_H}{\left\langle s_j\right\rangle \mu_j}, \frac{k_{wall}}{D_H}\right)\left|G_j^{corr}\right| G_j^{corr}}^{=\tau_{j\to wall}}}{2\rho_j^{corr}\left\langle s_j\right\rangle^2}\right)}^{\text{friction}}$$

$$+\overbrace{\sum_{j=1}^{N_p}\left(\rho_j^{corr}\left\langle s_j\right\rangle g\cos\theta\right)}^{\text{hydrostatic}} \qquad (1)$$

$$\overbrace{-\sum_{j=1}^{N_p}\left(\frac{G_j^{corr}\Delta\left(\frac{G_j^{corr}}{\rho_j^{corr}\left\langle s_j\right\rangle}\right)}{\Delta L}\right)}^{\text{convective acceleration (+ve) or deceleration (-ve)}} \quad \overbrace{-\sum_{j=1}^{N_p}\left(\frac{\rho_j^{corr}\left\langle s_j\right\rangle \Delta_t\left(\frac{G_j^{corr}}{\rho_j^{corr}\left\langle s_j\right\rangle}\right)}{\Delta t}\right)}^{\text{temporal (local) acceleration (+ve) or deceleration (-ve)}}$$

And for decoupled flows (a special case), we get:

$$\overbrace{\left(\frac{\Delta P_{mix}}{\Delta L}\right)}^{\text{hydrodynamic}} = \overbrace{\sum_{j=1}^{N_p}\left(\frac{Z_j^{net}\left(\left\langle s_j\right\rangle, D_H, A\right)}{A}\overbrace{\left(\frac{\overbrace{\gamma_j f_{j\to wall}\left(\frac{\left|G_j^{corr}\right| D_H}{\left\langle s_j\right\rangle \mu_j}, \frac{k_{wall}}{D_H}\right)\left|G_j^{corr}\right| G_j^{corr}}^{=\tau_{j\to wall}}}{2\rho_j^{corr}\left\langle s_j\right\rangle^2}\right)}^{\text{friction}}\right)}$$

$$+\overbrace{\sum_{j=1}^{N_p}\left(\rho_j^{corr}\left\langle s_j\right\rangle g\cos\theta\right)}^{\text{hydrostatic}} \qquad (2)$$

$$\overbrace{-\sum_{j=1}^{N_p}\left(\frac{G_j^{corr}\Delta\left(\frac{G_j^{corr}}{\rho_j^{corr}\left\langle s_j\right\rangle}\right)}{\Delta L}\right)}^{\text{convective acceleration (+ve) or deceleration (-ve)}} \quad \overbrace{-\sum_{j=1}^{N_p}\left(\frac{\rho_j^{corr}\left\langle s_j\right\rangle \Delta_t\left(\frac{G_j^{corr}}{\rho_j^{corr}\left\langle s_j\right\rangle}\right)}{\Delta t}\right)}^{\text{temporal (local) acceleration (+ve) or deceleration (-ve)}}$$

Also, for non-Newtonian annular vapor-liquid or vapor-liquid-liquid flows with multi-directional inter-phase entrainment, the non-Newtonian j-phase viscosity (from Eqn. 8 in Section 2.2.5) is corrected as:

$$\mu_j^{PL} = \left(\frac{8 G_j^{corr}}{\rho_j^{corr} \left\langle s_j \right\rangle D_H} \right)^{n_j - 1} \underbrace{\left(K_j \left(\frac{3n_j + 1}{4n_j} \right)^{n_j} \right)}_{= K_j'} \left(\left\langle s_j \right\rangle^{2 - n_j} \right) \tag{3}$$

In eqns. 1 to 3 above, it now becomes abundantly clear (via the purple-colored text) just how dominant the roles that averaged volume and entrainment fractions play in relation to pressure in multiphase pipe flows. Of significance, is the simple and unique way these equations describe the competing effects of volume fraction, entrainment fraction and the frictional, gravitational and acceleration/deceleration pressure gradients. Indeed, with this new understanding, it is now obvious *why* prior pressure gradient models performed so badly in the past in the special cases of annular vapor-liquid and vapor-liquid-liquid flows with inter-phase entrainment – as clearly shown, all of the pressure gradients are very strongly affected by the corrections to the mass fluxes and densities.

In a controlled lab experiment without entrainment, all of the terms on the RHS of the Eqns. 1 to 3 above are expressed in terms of known system quantities and therefore it is evident that averaged volume fraction is the only unknown quantity to be measured (or modeled). Therefore, in the general case of multiphase flows without entrainment, the most important scientific implication is that it is now possible to falsify these models since uncertainties are now focused in one directly measurable variable – the averaged volume fraction. In the special case of multiphase flows with entrainment, falsification is still obtainable because averaged entrainment fraction can also be objectively measured in addition to averaged volume fraction. Thus, with model falsification properly

conducted, either in cases with or without entrainment, the task of comprehensive model validation becomes a lot easier.

2.2.7 Local, Always-Developing Flow

2.2.7.1 Key Questions

A key insight in multiphase pipe flow is that there is no theoretical "fully-developed" state of flow in any type of flow pattern. This statement remains applicable to either hydrodynamic or thermal developing multiphase flows. As pointed out by Geoffrey Hewitt in responding to a specific adiabatic, vapor-liquid, vertical upward, constant cross-section-area question on the existence of a fully-developed state of flow on pg. 3-14 of Lahey, Jr. and Wood (1987): "There will always be a pressure gradient, and under its influence the gas velocity will be constantly increasing". Though Hewitt's comment above was intended to address one specific example of multiphase flow, it remains equally applicable to the key questions pertaining to flow development in many constant cross-section area closed conduit multiphase flows – which are – *if* pressure is always changing and therefore flow field body motions (and thus transport processes) are always evolving along the pipe axis, *then*:

I. Under what conditions will end effects in a multiphase flow loop (e.g. inlet or outlet conditions) become insignificant?

II. Can it be objectively determined when the maximal interaction (or net cancellation) level among the competing microphysical processes will occur?

III. Are local mass/volume fluxes at axial locations downstream of the injection manifold the same as the input mass/volume fluxes?

There are several opinions in the multiphase pipe flow literature regarding the first question above. As specific examples we note:

I. Peter Griffith and Graham Wallis's conclusion in regard to entrance effects in slug flow: "Entrance effects can persist for great lengths, L/D = 300, and long times, in developing two phase flows" (pg. 20 in Griffith and Wallis, 1959).

II. Martin Hubbard's summary in regard to adiabatic, horizontal slug flow development: "It was observed in this study, that the minimum entrance length required for fully developed stable slug flow ranged from 80 diameters at low gas rates and high liquid rates to 250 pipe diameters at high gas rates and moderate to low liquid rates. The slugs themselves ranged from 8 to 120 pipe diameters in length and the spacing between slugs ranged from 16 to 240 diameters" (pg. 32 in Hubbard, 1965).

III. The review of the influences of mixers, bends and exit sections in experimental studies of horizontal two-phase flows (Sekoguchi et al., 1968).

IV. The review of required thermal entry lengths in Shah (1981).

V. Leif Persen's comment in regard to entrance length: "Experimental evidence and theoretical investigations of single-phase situations indicate transition lengths of say 60-80 diameters. In two-phase flow, the flow may be under certain circumstances not be fully developed after 600-800 diameters" (pg. 3 of Persen, 1986).

VI. Geoffrey Hewitt's comment in regard to adiabatic vapor-liquid, vertical upward annular flow: "Data exist that demonstrates that at least 200-300 and maybe even more than 500 pipe diameters must be traveled before fully developed conditions are achieved" (pg. 3-14 in Lahey Jr. and Wood, 1987).

VII. The recommendation of Massey (1989) of an entrance length of 125 pipe diameters for fully-developed flow in horizontal pipes.

VIII. The discussion and detailed survey on hydrodynamic developing lengths in liquid-liquid experimental flows in Grassi et al. (2008): “To conclude, the problem of knowing where the two-phase flow is fully developed exists and, to our knowledge, no straightforward solutions are currently available in the literature”.

IX. The review of hydrodynamic vapor-liquid flow development (calming lengths) for horizontal and vertical pipes on pg. 13 in Ashwood (2010).

X. The review of the two-phase flow development length in Milan et al. (2013).

As evident from the above references, the flow development question is an important one. By itself, an insufficient flow development length can invalidate any or all of the results from an experimental campaign designed to provide fully-developed flow data. As a concrete example, the 6-inch circular-pipe multiphase flow experiments described in Oddie et al. (2003) were conducted on a rig that provided for a development length of about 50 diameters from the inlet valve before volume fraction measurements were recorded. The instrumented main pipe, inclusive of the test section itself, was merely 70 diameters in length. Thus, unless proven otherwise with verifiable evidence, it would be reasonable to expect that only the developing flow results from this multiphase pipe flow campaign to be useful for comparison against developing flow models. But even apart from the question of flow development for this dataset to which the prior evidence in the literature (as seen above) clearly points to a developing flow scenario, another important question in this case is whether the results and data from this campaign are publicly-scrutable (a requisite for scientific data).

The observation of a recognizable self-organized flow pattern in an experiment can itself represent one type of answer to the second question. Carefully instrumented experiments that simultaneously measure different local variables along the flow development path can help to answer the third question.

Regardless of how the above constant cross-section-area flow development questions are addressed, there are separate major issues related to variable cross-section-area flow development – such as in flow through nozzles, valves, chokes, and in general, obstructed flows. In the case of obstructed flows, the flow development is not only affected by pressure gradient, but in addition, by the type and shape of the physical boundaries that now traverse the flow path (rather than aligning the flow path).

2.2.7.2 Mutual Dependence

As can be seen from the discussion above, the flow development issue assumes central importance, even more so than (and before) the choice of the mathematical methods used to model the multiphase flow. Indeed, in any model that uses closure relations that relate dependent variables (e.g., volume fraction, entrainment fraction) to system variables (e.g., vapor density, liquid viscosity), the closure relations are more strongly coupled to pressure and temperature (and component composition in the general case) than first appears. This is because, in general, some system variables and parameters can be themselves dependent on pressure, temperature and composition. Of course, this results in a highly non-linear flow system. So even in an adiabatic system with negligible mass exchange, all of the variables and parameters that affect the total pressure gradient will also affect auxiliary and closure relations as well. It is therefore incorrect to claim that closure relations or correlations are "mutually independent" (Biberg et al., 2009) or that they will only account for a specific effect or phenomenon

and not account for other effects – and especially so for closure relations that contain fluid densities or viscosities in them.

The key insight into developing multiphase flow is that as long as a pressure gradient exists, the interactions among different phenomena will be coupled and there will be continuous (dynamic) competition among them that will cause the flow to continually evolve at the local level along the axial flow path. These interactions will be mathematically represented both explicitly as in the choices for the specific closure relations as well as implicitly as in the field conservation or balance equations themselves. In thermally developing flows and/or flows with mass exchange among the phases, the degree of coupling (and therefore non-linearity) is even higher than for strictly hydrodynamic developing flows.

2.2.7.3 Segmented Pipe

With the understanding above, it becomes clear that balance equations can only be expected to be accurate at the local level along the flow path, i.e., on an incremental or point-by-point basis. With this view, the length of pipe, its orientation, hydraulic diameter and other properties only affect the total pressure gradient (and other gradients if applicable) over the studied increment or pipe segment. Thus, differentiating between short distance and long distance transport of fluids (e.g., Eidsmoen and Roberts, 2005, Biberg et al., 2009) is quite superfluous – a short pipe, just as a long pipe, can be divided into any number of segments to any desired degree of "grid-resolution".

In single-phase flow, BSL uses the language of "d-forms" of the macroscopic balances (pg. 461 in this reference) describing the scenario where the transport flux terms of the balance equations are solved across the cross-sectional planes of a pipe segment which are separated by a differential distance ΔL apart.. In fact, any changes in flowing

area and inclination angle can be accounted for in this incremental manner as long as the total flow system is broken into segments and the balance equations are solved in each segment. This is the same procedure used to "discretize" a medium into *finite volumes* as is common in numerical simulation of either single-phase or multiphase flow ("grid blocks" in finite difference parlance). Just as in a numerical simulator, a system of non-linear equations will be formed that can be put in matrix form and solved simultaneously with given boundary conditions.

Summarily, by segmenting the total flow system as described above, we enforce that no new equations are required beyond our universal mixture momentum balance equations (Eqns. 6 and 7 of Section 2.2.4). All of the assumptions and limitations of these universal balance equations are maintained over the pipe segment being solved.

2.2.7.4 Segmented Pipe Approach in UTPipeFlow

In the in-house code for this work, UTPipeFlow, the segmented pipe approach discussed in the previous section is adopted by solving the analytical mixture momentum balance equations (Eqns. 6 or 7 in Section 2.2.4) in each segment. Note that if the inertial terms of these equations (i.e., the convective and temporal acceleration/deceleration terms) are not required to be solved, or, if analyzing a developed flow portion of an experimental test section, then the pressure gradients and averaged volume/entrainment fractions can be calculated by hand or using a spreadsheet tool and a numerical simulator is unnecessary.

In UTPipeFlow, the simplest fully-implicit finite difference methods are used. Time is discretized as a first-order backward finite difference, together with 100% upwind differencing of flux terms at segment faces in order to achieve unconditional stability and to avoid time step limitations. 100% upwinding allows us to numerically

simulate more properly the direction of information propagation in the flow field such that the calculation of very sharp discontinuities (spread over only a few segments) with no oscillations is afforded. This segmented pipe discretization (which allows for sources into or sinks from each pipe segment) results in a strongly-coupled system of non-linear algebraic equations, solved simultaneously by means of Newton-Raphson iteration. The linear equations arising at each iteration step are solved with LU-decomposition and back-substitution. Lastly, a given pressure and flow rates condition is specified either at the downstream or upstream boundary of the segmented (single branch, multiple inflow/outflow) pipe system.

Chapter 3 – The Fractional Flow Theory

3.1 FRACTIONAL FLOW FORMULATION: THE CORE PRINCIPLES

3.1.1 Fractional Flow Equations

In the previous chapter, it was shown (for the first time) just how strongly pressure gradients and averaged volume fractions are analytically connected. Therefore, the intimate connection between *velocity* and *pressure* in single-phase flows is represented analogously by the intimate connection between *relative velocity* and *pressure* in multiphase flows. This new finding now provides a reason why the existing "first step" of separating the flow patterns from the field equations (i.e., predicting the flow patterns *a-priori*) in most mechanistic models quite often leads to an incorrect pressure gradient prediction – in doing this, phase relative velocities are separated from their pressure gradients. This means that a-priori flow pattern determination will likely lock in investigators following this approach into an incorrect calculated pressure gradient right from the start. In terms of providing answers, a-priori determination of the flow pattern is equivalent to fixing the range of expected averaged relative velocities, which are themselves part the answer sought.

Since it is shown in the previous chapter that the relationship between pressure and averaged phase-j volume fraction, $\langle s_j \rangle$, is analytically known without the need for introducing application-specific (artificial) multiphase flow variables, then the next basic question is how can we determine $\langle s_j \rangle$? Fortunately, the literature on this important design parameter is quite large and there exist several empirical correlations for calculating (and in some cases predicting) it over a wide variety of applications. But questions about determining $\langle s_j \rangle$ do not subside beyond the availability of numerous empirical correlations. As example, we can ask:

I. Are there simple approximations that can be made to permit wholly-analytical (i.e., correlation-free and flow-pattern-implicit) closure models for $\langle s_j \rangle$?

II. Is there a functional (general) connection among the seemingly diverse and separately-applicable $\langle s_j \rangle$ correlations or observed data trends?

III. Can we infer which $\langle s_j \rangle$ correlations can be expected to work well, and which $\langle s_j \rangle$ correlations can be expected to perform poorly?

We propose that the types of fundamental questions posed above can be answered if we examine the relationship between the volume fraction and relative velocity. As discussed in Section 1.3.1.2 in Chapter 1, the averaged in-situ phase velocities and volume fractions mathematically represent the net of competing, interacting flow microphysics in any flow pattern and indeed in any multiphase pipe flow scenario. We define a dimensionless relative velocity, Omega, which captures all of the averaged in-situ phase velocities in its definition. Since relative velocity considers the relation between only two velocities at a time, Omega is subscripted by "j,k" to indicate a less-dense (or dispersed) phase-j, and a more-dense (or continuous) phase-k. So, in general, we define:

$$\underbrace{\Omega_{j,k\neq j}}_{\substack{\text{dimensionless} \\ \text{relative velocity}}} = \frac{\textit{relative velocity}}{\textit{mixture velocity}} = \frac{\langle\langle v_{j,k\neq j} \rangle\rangle}{\sum_{j=1}^{N_p} \left(\langle\langle v_j \rangle\rangle \langle s_j \rangle \right)} = \frac{\langle\langle v_j \rangle\rangle - \langle\langle v_{k\neq j} \rangle\rangle}{\langle u_{mix} \rangle} \tag{1}$$

Note that Omega can be defined by Eqn. 1 for more than two flowing phases. Limiting ourselves to a generic two-phase flow for the moment, Eqn. 1 can be expressed in terms of phase 1 and 2 volume fluxes and phase 2 volume fraction, as:

$$\Omega_{2,1} = \frac{\overbrace{\left(\frac{\langle u_2 \rangle}{\langle s_2 \rangle}\right)}^{\langle\langle v_2 \rangle\rangle} - \overbrace{\left(\frac{\langle u_1 \rangle}{1-\langle s_2 \rangle}\right)}^{\langle\langle v_1 \rangle\rangle}}{\overbrace{\langle u_2 \rangle + \langle u_1 \rangle}^{\langle u_{mix} \rangle}} = \frac{H_{2,1} - 1}{\langle s_2 \rangle \left(H_{2,1} - 1\right) + 1} \tag{2a}$$

We can then re-arrange Eqn. 2a above, to get:

$$\boxed{f_2 = \left(\frac{H_{2,1}}{1 + \left(H_{2,1} - 1\right)\langle s_2 \rangle}\right)\langle s_2 \rangle} \tag{2b}$$

Or,

$$\boxed{f_2 = \left(1 + \left(1 - \langle s_2 \rangle\right)\Omega_{2,1}\right)\langle s_2 \rangle} \tag{3}$$

We refer to Eqns. 2b or 3 as the general fractional flow equation for any two-phase flow. Note that the no-global-slip condition of $H_{2,1}$ = 1 or $\Omega_{2,1}$ = 0, correctly reduces Eqns. 2b or 3 to $f_2 = \langle s_2 \rangle$. Also, in either of these equations, at $\langle s_2 \rangle$ = 0 (i.e. no phase-2 present), f_2 = 0, and at $\langle s_2 \rangle$ = 1 (i.e. no phase-1 present), f_2 = 1. Note also, that depending on the representations of $H_{2,1}$ or $\Omega_{2,1}$, Eqns. 2b or 3 permits non-zero $\langle s_2 \rangle$ values that will satisfy the case of two-phase column flow (i.e. f_2 = 1, $\langle s_2 \rangle \neq 0$). In two-phase column flow, which represents a non-flowing phase-1 through which phase-2 flows, we see that Eqns. 2b or 3 honors the physical scenario of a non-zero $\langle s_2 \rangle$ even though phase-1 is stagnant.

Now, with regard to Eqn. 3, although it may initially appear that f_2 is quadratic in $\langle s_2 \rangle$, $\Omega_{2,1}$ can assume any definition (including being functions of f_2 and $\langle s_2 \rangle$) and thus the relationship between averaged fractional flow and averaged volume fraction will change depending on the definition of $\Omega_{2,1}$. It is only when $\Omega_{2,1}$ can be approximated as a constant value or as a function not containing $\langle s_2 \rangle$ over the range of conditions being investigated, will it be possible for f_2 in Eqn. 3 to be quadratic in $\langle s_2 \rangle$. We will show later in this chapter how past averaged two-phase volume fraction correlations can be

mathematically re-formulated simply as different expressions of $\Omega_{2,1}$, or more commonly, via approximations for $H_{2,1}$ in Eqn. 2b.

Indeed, the fractional flow framework proposed above is analogous to the fractional flow representation used in porous media (Buckley and Leverett, 1942). It now becomes clear how the volume fraction models in two-phase flow in porous media are related to their pipe flow counterpart. A famous example is shown in the "Koval factor" used in the prediction of unstable miscible displacement in heterogeneous porous media (Koval, 1962). In Eqn. 5 of this reference, which is the fractional flow equation for the miscible displacement of an oil (phase 2) by a solvent (phase 1), we clearly see that the Koval factor is exactly equal to the inverse of the averaged in-situ velocity ratio, $1/H_{2,1}$, signifying the effective relative mobility of the flowing phases considered. Larry Lake is to be credited with pointing out this analogy. In two-phase porous medium flow, $H_{2,1}$ is given as:

$$H_{2,1} = \frac{1}{Koval\ \ factor} = \left(\overbrace{H}^{\substack{Heterogeniety \\ factor}} \overbrace{\left(0.78 + 0.22 \left(\frac{\mu_2}{\mu_1} \right)^{0.25} \right)^4}^{Effective\ viscosity\ ratio} \right)^{-1} \tag{4a}$$

In two-phase pipe flow, $H_{2,1}$ can be given by a correlation which similarly scales with a viscosity ratio as in Eqn. 4a, for example, as in the Butterworth (1975) correlation (referred hereafter as the "BUTTERWORTH" model):

$$H_{2,1} = 0.28 \left(\overbrace{\left(\frac{1-f_2}{f_2} \right)^{0.9} \left(\frac{\rho_2}{\rho_1} \right)^{-0.4} \left(\frac{\mu_2}{\mu_1} \right)^{-0.1}}^{Lockhart\ and\ Martinelli\ (1949)\ parameter,\ X_{tt}} \right)^{0.71} \left(\frac{1-f_2}{f_2} \right)^{-1} \tag{4b}$$

Lastly, we can rearrange Eqn. 2b and 3 in terms of $\langle s_2 \rangle$, to arrive at the simple, explicit, analytical relations:

$$\langle s_2 \rangle = \frac{1}{H_{2,1}\left(\frac{1-f_2}{f_2}\right)+1} \tag{5a}$$

Or,

$$\langle s_2 \rangle = \frac{\left(\Omega_{2,1}+1\right) \pm \left(\left(\Omega_{2,1}+1\right)^2 - 4\Omega_{2,1} f_2\right)^{\frac{1}{2}}}{2\Omega_{2,1}} \tag{5b}$$

Note that there can be two possible solutions to $\langle s_2 \rangle$ in Eqn. 5b above only if $\Omega_{2,1}$ can be approximated as a constant value or as a function not containing $\langle s_2 \rangle$, for the conditions under study. As we will see later in this chapter, in this special case, the negative root will always be the applicable root in all concurrent flows, and the positive root will represent the applicable root for countercurrent pre-flooding or post-flow reversal scenarios. It must also be noted that, although not directly obvious, there are variations of Eqn. 5a that already exist in the literature. For example, Eqn. 5a can be reduced to the "fundamental void-quality relation" (pg. 201 in Lahey, Jr. and Moody, 1993) if mass fluxes are used instead of volume fluxes in defining the flow quality.

3.1.2 Fractional Flow Paths

Following from the basic fractional flow equations developed in the previous section, one may then ask:

I. What do these fractional flow equations (and the volume fraction data they represent) look like when viewed in graphical form?

II. In viewing fractional flow equations and volume fraction data in graphical form as fractional flow paths, can we gain a better understanding of the flow phenomena being represented?

III. Can fractional flow paths be used to discover connections between seemingly different flow phenomena that can be explained by similar mechanisms underlying their behavior?

In the remainder of this chapter, for simplicity, we will answer the questions above in a generic two-phase flow scenario. From Eqn. 5a, we see that every $\langle s_2 \rangle$ data point can be obtained from an appropriate model for $H_{2,1}$ (or equivalently, $\Omega_{2,1}$). Thus, a dataset (containing several data points at different $\langle s_2 \rangle$) can be represented by a series of transitionary $H_{2,1}$ values. The transition through different $H_{2,1}$ values (and thus a family of $H_{2,1}$ curves) will result in a unique fractional flow path for the dataset. This is the essence of the fractional flow representation of averaged volume fraction data, which characterizes in a general way, the averaged volume fraction behavior with respect to the prevailing system operating conditions and phase properties.

We next illustrate some key graphical representations that interrelate the major terms of the fractional flow framework, namely, f_2, $\langle s_2 \rangle$, $H_{2,1}$ and $\Omega_{2,1}$. Fig. 3.1.1 shows the relation of f_2 to the superficial phase 1 and phase 2 velocities. Note that although f_2 is well bounded in concurrent flows, it can take values of greater than 1 and less than 0 in countercurrent flows (shown as the dashed lines). Next, Fig. 3.1.2 shows how f_2 is related to $\Omega_{2,1}$ and $\langle s_2 \rangle$. Fig. 3.1.2 represents the family of $\Omega_{2,1}$ curves that all averaged volume fraction data must traverse in the general fractional flow equation for any two-phase flow, given in Eqn. 3 of Section 3.1.1.

An equivalent representation to the general fractional flow equation (Eqn. 3 of Section 3.1.1) is shown in Fig. 3.1.3 in terms of $H_{2,1}$, instead of $\Omega_{2,1}$. Fig. 3.1.3 is generated by Eqn. 5a in Section 3.1.1. In either Figs. 3.1.2 or 3.1.3, the averaged phase 2

volume fraction, $\langle s_2 \rangle$, is found from an appropriate definition of $H_{2,1}$ or $\Omega_{2,1}$ for the scenario under study and the given fractional flow of phase 2, f_2.

Throughout the remainder of this chapter, we will demonstrate how various averaged volume fraction data and models can be analyzed in the fractional flow versus volume fraction graphs (Figs. 3.1.1 to 3.1.3), referred hereafter as simply, the "fractional flow graphs".

Lastly, we note that there are variations of the fractional flow versus volume fraction graphs that have appeared in the prior literature (particularly with Russian investigators, e.g., Armand, 1946) as a means for displaying averaged two-phase volume fraction data. In some cases such as in experiments where the averaged slip velocity was low, such plots were also used to correlate and analyze averaged volume fraction data (e.g., Zuber, 1960, Bankoff, 1960). However, for low mass flow rates of the more dense phase (phase 1) where the averaged slip velocity was high, the fractional flow graph proved problematic to investigators who were seeking a straight line correlation of their averaged phase 2 volume fraction data. This is exactly the argument provided by Zuber and Findlay (1965) for selecting their "$\langle j_2 \rangle / \langle \alpha \rangle - \langle j \rangle$" plane. Zuber and Findlay (1965) recognized that their variant of the fractional flow graph, which they called the "$\langle \alpha \rangle - \langle \beta \rangle$" plane, would yield a family of curves for their Drift-flux theory. Since this was perceived as undesirable from a correlation standpoint, they therefore dismissed their $\langle \alpha \rangle - \langle \beta \rangle$ plane in favor of their "clearly superior" $\langle j_2 \rangle / \langle \alpha \rangle - \langle j \rangle$ plane.

In spite of this famous example of an early dismissal of displaying data in a fractional flow way because of a desire to correlate data on a straight line, the value of the fractional flow graphs transcends their usage as a data display or correlation tool. What is shown in this work is that the real power of the fractional flow graph lies in its ability to generate single-path or multiple-path traverses connecting different flow patterns (thus

capturing the connections between different flow phenomena), regardless of whether those paths correlates data on a straight line or not.

3.2 ANALYTICAL FRACTIONAL FLOW EQUATIONS

In light of the previous section, we see how simple it is to reformulate prior averaged volume fraction correlations in the fractional flow framework, i.e., in terms of dimensionless relative velocity ratio or slip ratio. Indeed, there are many tabular listings of averaged volume fraction correlations (and detailed descriptions of their experimental databases) in the literature that can be reformulated as fractional flow equations (e.g. Ghajar and Tang, 2010, Mathure, 2010, Godbole, 2009, Woldesmayat and Ghajar, 2007, Garcia et al. (2005), Manera et al. (2005), Coddington and Macian, 2002, IAEA, 2001, Vijayan et al., 2000, Diener and Friedel, 1998, Spedding and Spence, 1989, Papathanassiou et al., 1983). Nevertheless, a fundamental question that arises (listed as the first question at the start of section 3.1.1) is: Are there simple assumptions that can be made to permit wholly-analytical (i.e., correlation-free and flow-pattern-implicit) closure models for averaged volume fraction?

3.2.1 No Global Slip

The first, obvious answer in the affirmative to the above question is the condition of no global slip (referred hereafter as the "NOSLIP" model) between the considered phases, given as:

$$\Omega_{j,k(\neq j)} = 0 \tag{6a}$$

Or, equivalently as:

$$H_{j,k(\neq j)} = 1 \tag{6b}$$

When Eqn. 6a or 6b is used in conjunction with the analytical mixture momentum balance equations in the Chapter 2, this will yield a wholly-analytical multiphase flow

solution. We emphasize that the use of these equations with our analytical mixture momentum balance equations in Chapter 2 is devoid of any multiphase flow empirical correlation and therefore this solution attains the highest predictability possible (there are no multiphase flow variables/parameters that needs to be adjusted to data). Moreover, this solution is completely unrelated to any of the various "no-slip pressure gradient" correlations in the multiphase flow literature (found, for example, in the petroleum industry). These prior correlations are modifications of the single-phase momentum balance equation with different definitions of "no-slip mixture variables" used in place of corresponding single-phase flow variables, e.g., two-phase friction factor in place of single-phase friction factor, mixture viscosity in place of single-phase viscosity, mixture velocity in place of single-phase velocity, and so on.

An example of the use of the NOSLIP model in representing fractional flow data is shown in Fig. 3.2.1. In this figure, the vertical upward bubbly flow data from the air (phase 2) and water (phase 1) experiments of Rose (1964) is shown with the run numbers given for cross-referencing to the original dissertation. These data are selected as they show how a very simple (correlation-free) analytical model can be used to describe data. These runs were performed at a fairly constant water superficial velocity of 6 m/s with increasing air rates.

Similar to the results shown in Fig. 3.2.1, the NOSLIP model can also be used to represent liquid-liquid data in a wide range of conditions (as will be shown in much detail in Chapter 5). In Fig. 3.2.2, all 25 runs from Plaxton (1995) are shown to very accurately follow the NOSLIP model. In these experiments, various types of bubbly-to-stratified liquid-liquid flow patterns were observed in the horizontal flow of tap water (phase 1) and a light refinery stream oil (phase 2).

3.2.2 Constant Global Slip

A second analytical expression for Omega is based on the assumption of constant global slip. This is the generalization of Eqn. 6a or 6b – that is – the scenarios where the experimental averaged volume fractions for a studied scenario can be correlated by only a single-valued numerical constant, i.e.,:

$$\Omega_{j,k(\neq j)} = constant \tag{7a}$$

Or, as:

$$H_{j,k(\neq j)} = constant \tag{7b}$$

Note that, although Eqns. 6a and 6b are correlation-free, Eqns. 7a and 7b are not. This is because the constants in Eqns. 7a and 7b must be obtained from data. The reason why Eqns. 7a and 7b are analytical (but not general) expressions is due to the derived relationships that already exist among $\Omega_{j,k(\neq j)}$, $H_{j,k(\neq j)}$ and $\langle s_j \rangle$, as given for the two-phase case in Eqns. 2a and 2b above. No new relationships are required, and only one constant in Eqn. 7a or 7b will accurately describe the averaged volume fraction data trend. As will be seen in the later application chapters of this work, it is found that the extraordinarily simple analytical model of $H_{2,1} = constant$ (referred hereafter as the "SLIPRATIO" model), consistently describes an extensive range of stratified vapor-liquid flows, liquid-liquid flows with slip and dilute-phase fluid-solid flows.

In the general sense, Eqn. 7a or 7b can be used to match any volume fraction data-point (and in some cases, groups of data-points) in which model tractability is a desired feature in the scenario under investigation. This is because there is a single, traceable constant governing the volume fraction behavior in the model that can later be validated (or falsified) in comparison with measured volume fraction data.

An example of the use of the SLIPRATIO model in representing fractional flow data is shown in Fig. 3.2.3. We see from this example, that if the ratio of the relative

velocity to the mixture velocity for a system is fairly constant over the range of conditions under study, then the volume fraction data will be represented by constant values of $\Omega_{2,1}$ (or "iso-Omega" paths). Fig. 3.2.3 shows a vertical upward air (phase 2) and silicone oil (phase 1) dataset that is accurately represented by $\Omega_{2,1} = 1$. These runs were performed at a fairly constant silicone oil superficial velocity of 0.284 m/s with increasing air rates.

A more common scenario, found especially valid for stratified vapor-liquid, liquid-liquid flows with slip and dilute-phase fluid-solid flows, is when volume fraction data is represented by constant values of $H_{2,1}$. This very simple model can accurately describe a wide range of flow conditions, as will be shown in great detail in Chapters 4, 5 and 6. Fig. 3.2.4 shows one such example where the horizontal, stratified air (phase 2) and water (phase 1) flow data of Strand (1993) is shown to be represented quite accurately by $H_{2,1} = 16$. These runs were performed at a fairly constant air superficial velocity of 2.5 m/s with increasing water rates. Fig. 3.2.5 shows another example where all of the vertical air (phase 2) and glass beads (phase 1) data in Table A-20 of Luo (1987) are shown to be simply represented by $H_{2,1} = 1.8$. These runs were performed for phase 1 superficial velocities varying from of 0.005 to 0.019 m/s and phase 2 superficial velocities varying from 5 to 11 m/s.

3.2.3 Analytical Slip from Upper Limit Approximation

A third answer in the affirmative to the question of section 3.2 is found in an upper flow limit of Eqn. 2a. This is an asymptotic approximation analysis. For concurrent two-phase flow, we can postulate an upper limit for $\Omega_{2,1}$ in Eqn. 2a, as:

$$\Omega_{2,1} = \frac{\langle\langle v_2 \rangle\rangle - \langle\langle v_1 \rangle\rangle}{\langle u_{mix} \rangle} \overset{\text{in an upper flow limit}}{\rightarrow} \frac{\overbrace{\langle\langle v_2 \rangle\rangle}^{\text{approches } \langle u_2 \rangle \text{ in upper limit}} - \overbrace{\cancel{\langle\langle v_1 \rangle\rangle}}^{\text{relatively negligible in upper limit}}}{\langle u_{mix} \rangle} \tag{8}$$

The resulting model that describes the two-phase averaged volume fraction flow behavior in the upper limit of concurrent two-phase flow is:

$$\Omega_{2,1} = f_2 \tag{9a}$$

Or, equivalently,

$$H_{2,1} = \frac{1-\left(\langle s_2 \rangle - 1\right) f_2}{1-\langle s_2 \rangle f_2} \tag{9b}$$

Therefore, we can substitute Eqn. 9a (referred hereafter as the "ANSLIP" model) in Eqn. 3 to arrive at a wholly-analytical averaged volume fraction equation for phase-2 in a concurrent two-phase flow, as:

$$f_2 = \frac{\langle s_2 \rangle}{1-\langle s_2 \rangle\left(1-\langle s_2 \rangle\right)} \tag{10}$$

In Eqn. 10, if we are to examine the limit of $\langle s_2 \rangle$ = 0 (no phase-2 present), we see that this results in f_2 = 0 (no flow of phase-2). Also, the limit of $\langle s_2 \rangle$ = 1 (no phase-1 present) will result in f_2 = 1 (no flow of phase-1). As will be seen in the remaining validation chapters of this work, Eqn. 10 is found to be very accurate over an enormous range of different concurrent flow applications and flow patterns. It is <u>both analytical and general (i.e. flow-pattern-implicit)</u>. Furthermore, it is found in this work (and demonstrated in great detail in Chapter 4) that Eqn. 10 is the simplest and most consistently accurate, analytical annular flow model to date. In terms of $\langle s_2 \rangle$, Eqn. 10 can be re-arranged as:

$$\langle s_2 \rangle = \frac{f_2 + 1 \; - \left(\left(f_2 + 1 \right)^2 \; - 4 \left(f_2 \right)^2 \right)^{\frac{1}{2}}}{2 f_2} \tag{11}$$

Fig. 3.2.6 shows an example of how the ANSLIP model compares against an annular flow dataset. As seen in this figure, all of the annular air (phase 2) and water (phase 1) data in Table 1 of Andresussi and Zanelli (1978) condenses to the ANSLIP model. These runs were performed for phase 1 superficial velocities varying from of 0.01 to 0.29 m/s and phase 2 superficial velocities varying from 5 to 70 m/s.

As discussed above, the ANSLIP model is found to be very accurate over a wide range of scenarios and is especially so in annular vapor-liquid flow. Fig. 3.2.7 shows a recent vapor (phase 2) and liquid (phase 1) annular flow correlation (Cioncolini and Thome, 2012) over its stated range of applicability, i.e., $0.7 < \langle s_2 \rangle < 1$. Typical low-pressure experimental flow loop conditions of densities of air (1.2 kg/m^3) and water (1000 kg/m^3) were used in generating the fractional flow curve representing this correlation (given in Eqns. 51a and 51b in Section 3.3.2). As is evident, the very close match of the analytical ANSLIP model with this empirical correlation obtained through the traditional means of non-linear parametric regression, signifies that the time-consuming approach of gathering large amounts of data and regressing upon adjustable parameters of a favored model can be overcome by simple physical arguments (i.e., reasoning rather than "brute force"). More importantly, the data upon which regressed correlations are drawn are seldom accessible or verifiable by the public, are very rarely (if at all) cross-referenced to the test run numbers in the original publications and, in several cases (including the case of Cioncolini and Thome, 2012), excludes several test runs as a result of an investigator-decided (systematic) culling criteria.

Other than annular flow, the ANSLIP model can also accurately represent the averaged volume fraction data in other flow patterns. Fig. 3.2.8 shows one such example where all of the horizontal low-liquids loading stratified-wavy flow air (phase 2) and kerosene (phase 1) data in Figs. 6, 9 and 12 of the GRI-PSU-TUFFP report of Brill

(1996) condenses to the ANSLIP model. These runs were performed for phase 1 rates varying from of 0.004 to 0.046 m/s and phase 2 rates varying from 3.6 to 12 m/s.

Fig. 3.2.9 shows an example vertical air (phase 2) and water (phase 1) dataset covering the full range of flow patterns, with the ANSLIP model correctly traversing the fractional flow path of the observed data. The ANSLIP model was found to accurately represent the averaged volume fraction behavior of this entire dataset, which are the 99 air-water tests of Sujumnong (1997) spanning test numbers WR1.01 to WR7.13. Fig. 3.2.10 shows the specific flow patterns observed in the experiments for the conditions shown in Fig. 3.2.9. This example is important as it demonstrates in a very simple and unambiguous way how fractional flow paths can transition through various flow patterns, thus further substantiating one of the core principal insights of this research – that flow patterns are merely the visual manifestations (spatial configurations) of the in-situ velocity and volume fraction profiles, which are neatly captured in the averaged sense as different fractional flow paths in the fractional flow graph.

3.2.4 Analytical Slip from Equal Frictional Pressure Gradients

A fourth analytical fractional flow model is obtained if we consider another type of asymptotic approximation analysis – the "asymptote" being the equality of phase pressure changes due solely to friction. Note that this criterion (which is based on our definitions of the multiphase frictional pressure gradients in Chapter 2) is different from the Lockhart and Martinelli (1949) analysis of equating the ratio of the single-phase frictional pressure gradients of phase-1 and phase-2 to the square of their named parameter, X. Details of this latter analysis can be found in section 4.1 of Papathanassiou et al. (1983).

3.2.4.1 Coupled Flow

Now, for a *coupled* vapor-liquid flow, the asymptotic approximation analysis described above leads to the simple equality:

$$\underbrace{\left(\frac{Z}{A}\right)\overbrace{\left(\frac{f_{1\to wall}\rho_1\left\langle\left\langle v_1\right\rangle\right\rangle^2}{2}\right)}^{=\tau_{1\to wall}}}_{\text{Phase-1 Frictional Pressure Gradient}} = \underbrace{\left(\frac{Z}{A}\right)\overbrace{\left(\frac{f_{2\to wall}\rho_2\left\langle\left\langle v_2\right\rangle\right\rangle^2}{2}\right)}^{=\tau_{2\to wall}}}_{\text{Phase-2 Frictional Pressure Gradient}} \tag{12}$$

Re-arranging Eqn. 12 will yield:

$$H_{2,1} = \left(\left(\frac{f_{1\to wall}}{f_{2\to wall}}\right)\left(\frac{\rho_1}{\rho_2}\right)\right)^{0.5} \tag{13}$$

Eqn. 13 can then be closed with any combination of Fanning friction factor relations to arrive at various slip ratios. We next highlight two extents of Eqn. 13 that can lead to quite simple slip ratio solutions – the first case being laminar phase-1/laminar phase-2 flow and the second case being turbulent phase-1/turbulent phase-2 flow.

In the first *coupled flow* laminar-laminar case, Eqn. 13 simply reduces to:

$$H_{2,1} = \left(\frac{\mu_2}{\mu_1}\right)^{-1} \tag{14}$$

If Eqn. 14 is contrasted with Eqn. 4a, we see a physical underpinning of *why* the Koval factor is found to scale with the viscosity ratio in the laminar multiphase flows associated with porous media.

In the second *coupled flow* turbulent-turbulent case, Eqn. 13 reduces to:

$$H_{2,1} = \left(\frac{1-\langle s_2\rangle}{\langle s_2\rangle}\right)\left(\overbrace{\left(\frac{1-f_2}{f_2}\right)^{0.9}\left(\frac{\rho_2}{\rho_1}\right)^{-0.4}\left(\frac{\mu_2}{\mu_1}\right)^{-0.1}}^{\text{Lockhart and Martinelli (1949) parameter, } X_{tt}}\right)\left(\frac{1-f_2}{f_2}\right)^{-1} \tag{15}$$

Where the generalized form of the Blasius (1913) turbulent fanning friction factor relations is used for both phases, i.e., $f_{j\to wall}^{Blasius} = 0.046/\left(N_{\mathrm{Re},j}\right)^{0.2}$, and $N_{\mathrm{Re},j}$ is the same as

defined in Eqn. 5 of section 2.2.4. We note the striking similarity between Eqn. 15 and Eqn. 4b, repeated below for clarity:

$$H_{2,1} = 0.28\left(\overbrace{\left(\frac{1-f_2}{f_2}\right)^{0.9}\left(\frac{\rho_2}{\rho_1}\right)^{-0.4}\left(\frac{\mu_2}{\mu_1}\right)^{-0.1}}^{\textit{Lockhart and Martinelli (1949) parameter, } X_{tt}}\right)^{0.71}\left(\frac{1-f_2}{f_2}\right)^{-1} \tag{16}$$

Eqn. 15 now provides a physical basis (furnished by the asymptotic approximation criterion of Eqn. 12) for use of the Butterworth (1975) correlation in experimental and field scenarios. Indeed, with the insight above, rather than being classified as a "gross correlation", Eqn. 16 can be re-classified as an analytically derived relation in which two changes to its basic mathematical form (Eqn. 15) were made in order to tune one set of experimental data (i.e., Butterworth's coordinate transformation of the Lockhart and Martinelli, 1949, data). This re-classification places the Butterworth (1975) correlation in the same category as the drift-flux family of correlations – representing the set of correlations for averaged volume fraction that has an analytical unpinning. This is aside from the fact that both the Butterworth (1975) and drift-flux-type correlations are merely different slip ratio definitions (as shown in Eqns. 16 and 28). Also, note that more definitions of friction factors can be combined with Eqn. 13 to yield a slew of new *coupled flow* slip ratio solutions.

3.2.4.2 Decoupled Flow

We can repeat the analysis above for *decoupled* vapor-liquid flow. Similar to Eqn. 12, the asymptotic approximation analysis described above leads to the simple equality:

$$\underbrace{\left(\frac{Z_1^{net}}{\cancel{A}}\right)\overbrace{\left(\frac{f_{1\to wall}\rho_1\left\langle\left\langle v_1\right\rangle\right\rangle^2}{\cancel{2}}\right)}^{=\tau_{1\to wall}}}_{\text{Phase-1 Frictional Pressure Gradient}}=\underbrace{\left(\frac{Z_2^{net}}{\cancel{A}}\right)\overbrace{\left(\frac{f_{2\to wall}\rho_2\left\langle\left\langle v_2\right\rangle\right\rangle^2}{\cancel{2}}\right)}^{=\tau_{2\to wall}}}_{\text{Phase-2 Frictional Pressure Gradient}} \tag{17}$$

Re-arranging Eqn. 17 will yield:

$$H_{2,1}=\left(\left(\frac{f_{1\to wall}}{f_{2\to wall}}\right)\left(\frac{\rho_1}{\rho_2}\right)\left(\frac{Z_1^{net}}{Z_2^{net}}\right)\right)^{0.5} \tag{18}$$

Eqn. 18 can then be closed with any combination of Fanning friction factor relations to arrive various *decoupled flow* slip ratios. For illustrative purposes, we will now highlight one extent of Eqn. 18 that can lead to quite simple *decoupled flow* slip ratio solutions – the case of laminar phase-1/laminar phase-2 flow. If desired, the analysis for turbulent phase combinations as performed for the *coupled flow* scenario above can also be extended to the decoupled flow scenario. In the *decoupled flow* laminar-laminar case, we can utilize the relationships in Eqns. E.10 and E.11a in Appendix E for a rectangular pipe of width, w, and height, h, to reduce Eqn. 18 to:

$$H_{2,1}=\left(\frac{\mu_2}{\mu_1}\right)^{-1}\left(\frac{2h\left(1-\left\langle s_2\right\rangle\right)+\frac{3w}{2}}{2h\left(2-\left\langle s_2\right\rangle\right)+\frac{7w}{2}}\right) \tag{19}$$

If Eqn. 19 is now contrasted with Eqn. 14, we see a physical underpinning of *why* the conduit dimensions and shape can affect the averaged volume fraction (slip ratio) in a *decoupled flow* scenario. In fact, we can substitute Eqn. 19 into Eqn. 5a to arrive at the analytical volume fraction relation for *decoupled* laminar-laminar vapor-liquid flow in a rectangular conduit, as:

$$\left\langle s_2\right\rangle=\frac{1}{\left(\frac{\mu_2}{\mu_1}\right)^{-1}\left(\frac{2h\left(1-\left\langle s_2\right\rangle\right)+\frac{3w}{2}}{2h\left(2-\left\langle s_2\right\rangle\right)+\frac{7w}{2}}\right)\left(\frac{1-f_2}{f_2}\right)+1} \tag{20}$$

Note that Eqn. 20 also defines the rather simple fractional flow relationship for this scenario. We can also utilize the relationships in Eqns. E.10, E12a and E.12c in Appendix E for a circular pipe, to reduce Eqn. 18 to:

$$H_{2,1} = \left(\frac{\mu_2}{\mu_1}\right)^{-1} \left(\frac{\delta_1^{2P} + \sin\left(\frac{\delta_1^{2P}}{2}\right)}{2\pi + \delta_1^{2P} + \sin\left(\frac{\delta_1^{2P}}{2}\right)} \right) \tag{21}$$

Where, the circular-pipe center-angle subtending the phase-1 surface in a two-phase (or "2P") *decoupled* flow, δ_1^{2P}, is given (from the analytical Eqn. E.12b in Appendix E) as:

$$\delta_1^{2P} = 2\left(\pi\left(1-\langle s_2 \rangle\right) + \left(\frac{3\pi}{2}\right)^{\frac{1}{3}} \left(1 - 2\left(1-\langle s_2 \rangle\right) + \left(1-\langle s_2 \rangle\right)^{\frac{1}{3}} - \langle s_2 \rangle^{\frac{1}{3}} \right) \right) \tag{22}$$

As before, we can substitute Eqns. 21 and 22 into Eqn. 5a to arrive at the analytical volume fraction relation for *decoupled* laminar-laminar vapor-liquid flow in a circular conduit, as:

$$\langle s_2 \rangle = \frac{1}{\left(\frac{\mu_2}{\mu_1}\right)^{-1} \left(\frac{\delta_1^{2P} + \sin\left(\frac{\delta_1^{2P}}{2}\right)}{2\pi + \delta_1^{2P} + \sin\left(\frac{\delta_1^{2P}}{2}\right)} \right) \left(\frac{1-f_2}{f_2}\right) + 1} \tag{23}$$

Note that the above simple derivations for two phase flows can be extended to three phase flows for determining $H_{3,1}$ and $H_{2,1}$, in which phase-3 can be a vapor, phase-2 can be a liquid and phase-1 can be either a solid or a (more-dense) liquid.

It has been shown in this section that simple, reliably accurate, analytical averaged volume fraction models are possible and they should be pursued. We also plant the idea that it should be possible to create new analytical volume fraction models using simple assumptions (as shown in the examples above) for subsequent use in the universal balance equations of Chapter 2. Indeed, this is the direction of future averaged

multiphase flow research that is necessary for the wholly analytical prediction of multiphase flow pressure gradient with the universal balance equations of Chapter 2.

3.3 REFORMULATING PRIOR VOLUME FRACTION CORRELATIONS

The analytical relationships represented by Eqns. 2a, 2b, 3, 5a and 5b functionally connect the fractional flow of a phase to its averaged volume fraction. We now demonstrate a few examples of how prior averaged volume fraction correlations can be re-expressed in the fractional flow framework presented above.

3.3.1 Drift-flux Correlations as Slip Ratios

A large (and quite popular) class of averaged volume fraction correlations that can be represented as slip ratios are of the drift-flux (Zuber and Findlay, 1965) type. A historical perspective of the drift-flux model can be found in Appendix A of Chexal et al. (1992). The fundamental starting point of all two-phase drift-flux correlations is the local algebraic equation for the phase-2 (the less dense phase) velocity:

$$\vec{v}_2 = \vec{u}_{mix} + \overbrace{\left(\vec{v}_2 - \vec{u}_{mix}\right)}^{\text{"local drift velocity", } \vec{v}_{2,drift}} \tag{24}$$

In Eqn. 24, the local drift velocity can be defined in its alternative local relative velocity (or local slip velocity) form as:

$$\overbrace{\vec{v}_{2,drift}}^{\substack{local\\ drift\ velocity\\ of\ phase-2}} = \vec{v}_2 - \vec{u}_{mix} = \vec{v}_2 - \left(\vec{v}_2 s_2 + \vec{v}_1\left(1-s_2\right)\right) = \left(1-s_2\right)\left(\vec{v}_2 - \vec{v}_1\right) = \left(1-s_2\right)\overbrace{\vec{v}_{2,1}}^{\substack{local\\ slip\ velocity\\ of\ phase-2}} \tag{25}$$

Also, note that other than the customary practice of starting at the local algebraic equation for phase-2 (the less dense phase) as shown above, there can alternatively be a local algebraic equation for phase-1 (the more dense phase). In this latter case, the local drift velocity of phase-1 is:

$$\overbrace{\vec{v}_{1,drift}}^{\substack{local\\drift\ velocity\\of\ phase-1}} = \vec{v}_1 - \vec{u}_{mix} = \vec{v}_1 - \left(\vec{v}_2 s_2 + \vec{v}_1\left(1-s_2\right)\right) = s_2\left(\vec{v}_1 - \vec{v}_2\right) = s_2 \overbrace{\vec{v}_{1,2}}^{\substack{local\\slip\ velocity\\of\ phase-1}} = -s_2 \overbrace{\vec{v}_{2,1}}^{\substack{local\\slip\ velocity\\of\ phase-2}} \qquad (26)$$

Now, multiplying Eqn. 24 by the local phase-2 volume fraction, s_2, to convert from velocities to volume fluxes, considering only the axial components of these vectors and performing cross section area-averaging, we get:

$$\left\langle s_2 v_2 \right\rangle = \left\langle s_2 u_{mix} \right\rangle + \overbrace{\left\langle s_2 v_{2,drift} \right\rangle}^{\text{"global drift flux" parameter}} \qquad (27)$$

Eqn. 27 shows the reason *why* this class of correlations is referred to as "Drift-flux". Dividing all of the terms in Eqn. 27 by $\left\langle s_2 \right\rangle \left\langle u_{mix} \right\rangle$ and combining with Eqn. 5a, we can finally arrive at the form of the two-phase Drift-flux formulation that contains the Drift-flux parameters, as:

$$H_{2,1} = \left(\overbrace{\left(\frac{\left\langle s_2 u_{mix} \right\rangle}{\left\langle s_2 \right\rangle \left\langle u_{mix} \right\rangle} \right)}^{\text{"global distribution" parameter, } C_0} + \overbrace{\frac{\left(\left\langle s_2 v_{2,drift} \right\rangle \right)}{\left\langle s_2 \right\rangle \left\langle u_{mix} \right\rangle}}^{\text{"global drift flux" parameter}} \right) \left(\frac{1-\left\langle s_2 \right\rangle}{1-f_2} \right) = \left(C_0 + \overbrace{\frac{\left(\left\langle \left\langle v_{2,drift} \right\rangle \right\rangle \right)}{\left\langle u_{mix} \right\rangle}}^{\text{"global drift velocity" parameter}} \right) \left(\frac{1-\left\langle s_2 \right\rangle}{1-f_2} \right) \qquad (28)$$

As discussed in Zuber and Findlay (1965), the generalized global parameters in Eqn. 28 can be defined in various ways and then used to correlate the averaged volume fraction behavior over a wide range of two-phase flow patterns and conditions. There are some investigators, however, who incorrectly believe these parameters can only satisfactorily accommodate a restricted amount of system geometries, operational conditions or fluid properties. As a concrete example, in a specific situation, there can be a gross misunderstanding of the global drift velocity parameter in horizontal flow, leading some investigators to set this parameter to zero in this case. Franca and Lahey, Jr. (1992) puts this particular example into proper context in the discussion section of their paper: "It should be stressed that for horizontal flows the drift velocity, V_{Gj}, is not normally zero.

The fact that many previous authors have assumed it to be zero just highlights their misunderstanding of what the drift velocity represents".

From Eqn. 25, we see that the global drift-velocity parameter in Eqn. 28 can alternatively be expressed in terms of the actual local slip velocity, $v_{2,1}$, or the characteristic global slip velocity, as:

$$H_{2.1} = \left(C_0 + \overbrace{\left(\frac{\left\langle (1-s_2)\, s_2 v_{2,1} \right\rangle}{\left\langle s_2 \right\rangle} \right)}^{=\left\langle\left\langle v_{2,drift} \right\rangle\right\rangle} \left(\frac{1}{\left\langle u_{mix} \right\rangle} \right) \right) \left(\frac{1-\left\langle s_2 \right\rangle}{1-f_2} \right)$$

$$= \left(C_0 + \overbrace{\left(\overbrace{n\left(1-p\left\langle s_2 \right\rangle^q\right)^r}^{\substack{characteristic\ global \\ phase\text{-}2\ particle\ interaction}} \overbrace{\left(\frac{\left\langle s_2 v_{2,1} \right\rangle}{\left\langle s_2 \right\rangle} \right)}^{\substack{characteristic\ global \\ slip\ velocity}} \right)}^{=\left\langle\left\langle v_{2,drift} \right\rangle\right\rangle} \left(\frac{1}{\left\langle u_{mix} \right\rangle} \right) \right) \left(\frac{1-\left\langle s_2 \right\rangle}{1-f_2} \right) \tag{29}$$

In Eqn. 29, C_0, $\left\langle\left\langle v_{2,drift} \right\rangle\right\rangle$, "n", "p", "q", "r" or the characteristic global slip velocity can take different values (or functions of system parameters) for various scenarios resulting in a wide range of empirical correlations. Also, the characteristic global phase-2 particle interaction function is alternatively referred to as the "hindering" function in the literature (e.g. Guet and Ooms, 2006, Garnier et al., 2002). Eqn. 29 shows how the averaged (global) slip ratio combines the effect of individual particle slip and particle-to-particle interaction. It is thus clear how averaged slip velocities could be significantly different from individual particle slip velocity.

Two important examples of the various forms of Eqn. 29 are the Nicklin et al. (1962) vapor (phase 2) and liquid (phase-1) correlation valid for up-inclined bubbly,

bubbly-slug, slug, slug-churn, churn and column flows (referred hereafter as the "NICKLIN" model):

$$C_0 = 1.2\ ,$$
$$\left\langle\left\langle v_{2,drift}\right\rangle\right\rangle = 0.35\left(gD_H\right)^{0.5} \tag{30}$$

And, the Woldesmayat and Ghajar (2007) vapor (phase 2) and liquid (phase-1) correlation, valid for all inclinations and different flow patterns (referred hereafter as the "WOLGHA" model):

$$C_0 = f_2\left(1+\left(\frac{1-f_2}{f_2}\right)^{\left(\frac{\rho_2}{\rho_1}\right)^{0.1}}\right),$$
$$\left\langle\left\langle v_{2,drift}\right\rangle\right\rangle = 2.9\left(\frac{g\left|\left(\Delta\rho\right)\right|D_H\sigma_{2,1}\left(1+\cos\left(90-\theta\right)\right)}{\left(\rho_1\right)^2}\right)^{0.25}\left(1.22+1.22\sin\left(90-\theta\right)\right)^{\frac{P_{atm}}{P_{system}}} \tag{31}$$

Fig. 3.3.1 shows an example vertical air (phase 2) and water (phase 1) dataset covering the full range of flow patterns (Spedding and Nguyen, 1976) with the WOLGHA model in Eqn. 31 correctly traversing the multiple fractional flow paths of the observed data. Fig. 3.3.1a shows how the different observed flow patterns look like when put in the fractional flow format. The same data when viewed in terms of flow rates are shown in Fig. 3.3.1b. For this dataset, runs were performed at fairly constant phase 1 superficial velocities varying from of 0.005 to 1 m/s and increasing phase 2 superficial velocities varying from 0.1 to 58 m/s. Note that the general physical trend observed is that low liquid superficial velocities yield the highest averaged slip behavior, and that high liquid superficial velocities yield the lowest averaged slip behavior. Fig. 3.3.1c shows that the correlation used in this case, the WOLGHA model, captures both the qualitative data trend as well as the quantitative averaged slip behavior of the entire

dataset. This is another example that demonstrates in a very simple way how fractional flow paths transition through and connects different flow patterns.

Now, with the fractional flow definition of Eqn. 2a, we can now substitute Eqn. 29 in Eqn. 2a to relate the actual global slip velocity, $\overbrace{\left\langle\left\langle v_{2,1}\right\rangle\right\rangle}^{\substack{actual\ global \\ slip\ velocity}}$, to the actual local slip velocity, $v_{2,1}$, and the characteristic global slip velocity , as:

$$\overbrace{\left\langle\left\langle v_{2,1}\right\rangle\right\rangle}^{\substack{actual\ global \\ slip\ velocity}} = \Omega_{2,1}\left\langle u_{mix}\right\rangle = \left(\frac{C_0 - 1}{1-\left\langle s_2\right\rangle}\right)\left\langle u_{mix}\right\rangle + \frac{\overbrace{\left(\frac{\left\langle\left(1-s_2\right)s_2 v_{2,1}\right\rangle}{\left\langle s_2\right\rangle}\right)}^{=\left\langle\left\langle v_{2,drift}\right\rangle\right\rangle}}{1-\left\langle s_2\right\rangle}$$

$$= \left(\frac{C_0 - 1}{1-\left\langle s_2\right\rangle}\right)\left\langle u_{mix}\right\rangle + \frac{\overbrace{\left(\overbrace{n\left(1-p\left\langle s_2\right\rangle^q\right)^r}^{\substack{characteristic\ global \\ phase\text{-}2\ \ particle\ interaction}} \overbrace{\left(\frac{\left\langle s_2 v_{2,1}\right\rangle}{\left\langle s_2\right\rangle}\right)}^{\substack{characteristic\ global \\ slip\ velocity}}\right)}^{=\left\langle\left\langle v_{2,drift}\right\rangle\right\rangle}}{1-\left\langle s_2\right\rangle} \tag{32}$$

Eqn. 32 is a lot more important than first appears. It holds the key to explaining basic experimental observations with regards to the global-to-local interrelationships among C_0, $\left\langle\left\langle v_{2,drift}\right\rangle\right\rangle$, $\left\langle s_2\right\rangle$, s_2, $\left\langle\left\langle v_{2,1}\right\rangle\right\rangle$, $\Omega_{2,1}$ and $v_{2,1}$. For example, the characteristic global slip velocity is different from the actual global slip velocity, even though these variables can sometimes be incorrectly assumed as being equivalent (e.g., Mao and Harvey III, 2013). As another example, one can now clearly see from Eqn. 32 that it is incorrect to say that C_0 = 1, by itself, has a physical meaning associated with phase-2 being homogeneously distributed in phase-1, or, that this condition has a mathematical meaning of $\left\langle\left\langle v_{2,1}\right\rangle\right\rangle$ = 0. C_0, by itself, does not serve as "a correction factor to the homogenous flow theory" (Bhagwat and Ghajar, 2014). Similarly, $\left\langle\left\langle v_{2,drift}\right\rangle\right\rangle$ = 0, by itself, does not mean that $\left\langle\left\langle v_{2,1}\right\rangle\right\rangle$ = 0. In this latter case, non-uniform lateral distributions of phase-2 in

phase-1 in any pipe angle orientation, could result in $C_0 \neq 1$, and therefore ensure a non-zero $\left\langle\left\langle v_{2,1}\right\rangle\right\rangle$ – this is sometimes referred to as "integral slip" in the literature. It is only if <u>both</u> conditions of $C_0 = 1$ and $\left\langle\left\langle v_{2,drift}\right\rangle\right\rangle = 0$ are met, will $\left\langle\left\langle v_{2,1}\right\rangle\right\rangle = 0$ – this coupled criteria is sometimes referred to as the "critical pressure limit" in the single-component multiphase flow literature, or "homogeneous flow" in the multi-component multiphase flow literature. Indeed, Eqn. 32 infers that there cannot be a complete dissociation between C_0 and $\left\langle\left\langle v_{2,drift}\right\rangle\right\rangle$, because they are related to each other as well as to other global and local velocities (and volume fractions) via this equation. This is also analytically proven, as shown below.

Instead of a two-parameter form, Eqn. 28 can be re-stated in a three-parameter form in which the global distribution parameter is split into two terms (e.g., as described in Clark and Flemmer, 1985, Olekhnovich and Pokhvalov, 1989, Haoues et al., 2009):

$$H_{2,1} = \left(= \underbrace{\overbrace{\left(\frac{\langle s_2 u_1\rangle}{\langle s_2\rangle\langle u_1\rangle}\right)}^{\text{global phase-1 distribution parameter, } C_1}(1-f_2) + \overbrace{\left(\frac{\langle s_2 u_2\rangle}{\langle s_2\rangle\langle u_2\rangle}\right)}^{\text{global phase-2 distribution parameter, } C_2} f_2}_{C_0} + \frac{\overbrace{\left(\left\langle\left\langle v_{2,drift}\right\rangle\right\rangle\right)}^{\text{"global drift velcoity" parameter}}}{\langle u_{mix}\rangle} \right)\left(\frac{1-\langle s_2\rangle}{1-f_2}\right) \quad (33)$$

Note that the derivation of Eqn. 33 is simply from an analytical expansion of Eqn. 27 followed by a division of all terms by $\langle s_2\rangle\langle u_{mix}\rangle$ just as was done to arrive at Eqn. 28. The assumed advantage of Eqn. 33 over Eqn. 28 by some investigators is that the new global distribution parameters, C_1 and C_2, are now expressions of their individual (local) phase velocities, rather than only of the (local) mixture velocity, as in C_0. Additionally, from a correlation standpoint, there are now three (instead of two) fitting parameters available to match experimental $H_{2,1}$ data. These perceived benefits, however, are easily countered by the fact that C_0 is itself an analytical function of $\left\langle\left\langle v_{2,drift}\right\rangle\right\rangle$. To see this, we re-arrange Eqn. 33 as:

$$H_{2,1} = \left(\frac{C_1}{1-\langle s_2 \rangle (C_2 - C_1)} + \frac{\langle\langle v_{2,drift} \rangle\rangle}{\langle u_{mix} \rangle \left(1-\langle s_2 \rangle (C_2 - C_1)\right)} \right) \left(\frac{1-\langle s_2 \rangle}{1-f_2} \right) \tag{34}$$

Comparing Eqn. 34 with Eqn. 28 yields:

$$C_0 = \frac{C_1}{1-\langle s_2 \rangle (C_2 - C_1)} + \frac{\langle\langle v_{2,drift} \rangle\rangle}{\langle u_{mix} \rangle} \left(\frac{\langle s_2 \rangle (C_2 - C_1)}{1-\langle s_2 \rangle (C_2 - C_1)} \right) \tag{35}$$

Eqn. 35 now demonstrates, in a simple and mathematically self-consistent way, *why* there cannot be a complete dissociation between C_0 and $\langle\langle v_{2,drift} \rangle\rangle$. This fact also provides a rational explanation for the extreme difficulty in the past to resolve the influence of the global lateral distribution (multidimensional) effects of the dispersed phase in the flow (phase-2) on the overall flow characteristics such as averaged volume fraction, $\langle s_2 \rangle$, or equivalently, the averaged in-situ slip velocity, $\langle\langle v_{2,1} \rangle\rangle$.

Additionally, Eqn. 35 demonstrates that correlations for C_0 and $\langle\langle v_{2,drift} \rangle\rangle$ in which these terms are expressed explcitly from each other cannot claim a better understanding of the flow physics unless they capture this inherent analytical bi-directional dependency. All of the variables that affect $\langle\langle v_{2,drift} \rangle\rangle$ also affect C_0. Such explicit correlations can only claim a faithful representation of the specific data in their validation database, with the subsequent inference that similar data (or other extrapolated conditions) can also be represented. Indeed, it is unreasonable to suggest that such separately-defined correlations "adheres to the the two-phase flow physics" (Bhagwat and Ghajar, 2014), and especially so when these correlations are ad hoc constructed in mathematical form, contain layers of implictness that are not amenable to practical applications, contain numerous correction factors, are validated against poorly-controlled datasets and are verified for adequateness with ad hoc chosen statistical error bounds.

Even in a specific application of industrial relevance such as vertical upward bubbly flow, Eqn. 35 provides a mathematical justification of *why* a reduction in bubble

drift velocity (i.e., an increase in bubble residence time caused, for example, by a wall-peaking radial void fraction profile) will lead to a reduction in the global distribution parameter, as widely reported in the literature (e.g. Guet and Ooms, 2006, Guet et al., 2004, Hibiki and Ishii, 2002).

Apart from the fact that C_0 and $\left\langle\left\langle v_{2,drift}\right\rangle\right\rangle$ are functions of each other, they are specialized data-fitting parameters of the slip ratio, $H_{2,1}$, as shown in Eqn. 28, which is the basic one-parameter form of all Drift-flux correlations. Indeed, Eqn. 28 demonstrates, in a very simple way, *why* Drift-flux correlations are generally applicable to any flow scenario – the Drift-flux parameters themselves are merely specialized closure relationships for the slip ratio, $H_{2,1}$. This has an importance all on its own. It means that different averaged volume fraction correlations can be inter-related to each other via their reformulated slip ratio forms. Thus the data (phenomena) that these models represent can be inter-related and there are more models available for representing them. One example for the use of this capability is that practical two-phase codes with an inbuilt model dependent on, say the Lockhart and Martinelli (1946) parameter, X_{tt}, can now have their volume fraction model reformulated to be expressed in terms of, say Drift-flux parameters, thereby accessing the vast body of experimental knowledge on Drift-flux parameters for various scenarios.

Another example for the use of this capability is in inter-relating prior two-phase correlations to arrive at combined models. For example, the Butterworth (1975) correlation in Eqn. 4b can be equated with the Woldesmayat and Ghajar (2007) correlation (Eqns. 28 and 31) to arrive at a simple and explicit correlation for $\langle s_2 \rangle$ that is a function of densities, viscosities, interfacial tension, mass fluxes, hydraulic diameter, inclination, system pressure and gravity. This combined model can then be used either directly in testing against experimental data, or, as a starting point for the desired form of

a model for regression fitting against experimental data. Of course, any number correlations can be combined in any number of ways, thus leading to a slew of new solution possibilities. In these combined models, there may be explicit or implicit solutions for $\langle s_2 \rangle$, depending on the form of the correlations being combined.

Finally, Eqn. 28 can be reformulated in another one-parameter form following from the definitions in Eqn. 2a, as:

$$\Omega_{2,1} = \frac{C_0 - \overbrace{\left(1 - \frac{\langle\langle v_{2,drift} \rangle\rangle}{\langle u_{mix} \rangle}\right)}^{\text{"dimensionless global drift velocity" parameter}}}{1 - \langle s_2 \rangle} \tag{36}$$

Eqn. 36 now shows the exact conditions that will cause $\Omega_{2,1}$ to be negative for a given scenario, i.e., when C_0 is less than the dimensionless global drift velocity parameter defined in Eqn. 36.

3.3.2 Other Correlations as Slip Ratios

Apart from reformulating Drift-flux volume fraction correlations in the fractional flow framework as shown in the previous section, we can reformulate other literature correlations in terms of slip ratios. The transformed Lockhart and Martinelli (1949) correlation was already shown simply as an expression for $H_{2,1}$, in Eqn. 4b. Additionally, as shown in Butterworth (1975), other correlations such as Turner and Wallis (1965), Thom (1964) and Baroczy (1963) can be expressed as different $H_{2,1}$ models. The popular vapor (phase 2) and liquid (phase 1) correlation in Fauske (1961) can be cast as:

$$H_{2,1} = \left(\frac{\rho_2}{\rho_1}\right)^{-0.5} \tag{37}$$

The Zivi (1964) correlation which has proved quite successful in the heat transfer during condensation applications (e.g., Soliman et al., 1968) can be written as:

$$H_{2,1} = \left(\frac{\rho_2}{\rho_1} \right)^{-0.33} \tag{38}$$

The Nishino and Yamazaki (1963) correlation for steam (phase 2) and water (phase 1) is:

$$H_{2,1} = \frac{\left(\frac{G_2}{G_1} \right)^{-1} \left(\frac{\rho_2}{\rho_1} \right) + 2 - \langle s_2 \rangle}{\left(\frac{G_2}{G_1} \right)^{-1} \left(\frac{\rho_2}{\rho_1} \right) + 1 - \langle s_2 \rangle} \tag{39}$$

The Wallis (1969) correlation (referred hereafter as the "WALLIS" model) for vapor (phase 2) and liquid (phase 1) is:

$$H_{2,1} = \left(\left(1 + \left(\frac{1 - f_2}{f_2} \right)^{0.72} \left(\frac{\rho_2}{\rho_1} \right)^{-0.32} \left(\frac{\mu_2}{\mu_1} \right)^{-0.08} \right)^{0.378} - 1 \right) \left(\frac{1 - f_2}{f_2} \right)^{-1} \tag{40}$$

The annular flow vapor (phase 2) and liquid (phase 1) correlation of Ishii (1975) is:

$$H_{2,1} = \left(\frac{\rho_2}{\rho_1} \right)^{-0.5} \left(\frac{\langle s_2 \rangle^{0.5}}{1 + 75\left(1 - \langle s_2 \rangle\right)} \right)^{0.5} \tag{41}$$

The less-dense liquid (phase 2) and more-dense liquid (phase 1) correlation of Arney et al. (1993) is:

$$H_{2,1} = 1 + 0.35 \left(\frac{f_2}{\langle s_2 \rangle} \right) \tag{42}$$

Fig. 3.3.2 shows how this correlation describes averaged volume fraction data in the fractional flow graph as one fractional flow path.

An example of an averaged volume fraction correlation that describes multiple fractional flow paths is the horizontal flow vapor (phase 2) and liquid (phase 1) correlation of Garcia et al., 2005 (Eqn. 3 in the reference):

$$H_{2,1} = \frac{1}{C} \left(\frac{1 - f_2}{f_2} \right)^{a-1} = K^{-1} \left(\frac{1 - f_2}{f_2} \right)^{a-1} \left(\frac{\rho_2}{\rho_1} \right)^{-b} \left(\frac{\mu_2}{\mu_1} \right)^{-c} \tag{43}$$

Where, “C” and “a” in Eqn. 43 are given in Table 5 of Garcia et al. (2005), and which is repeated in Table 3.1 below. Additionally, “K”, “b” and “c” in Eqn. 43 above are given in Table 1 of Chen and Spedding (1983). The categories in the legend of Fig. 3.3.3 directly correspond to the categories in Table 3.1.

It is important to observe the identical mathematical form that exists between Eqns. 43 and 16. In viewing these seemingly different correlations in this unified way, it is now clear that the Garcia et al. (2005) correlation is simply a re-tuned Butterworth (1975) correlation with parameters that are fitted to more data. More data available for tuning, however, does not generally signify a better correlation. The sources and quality of the data matters a lot, apart from the ranges of the variables covered by the data. The Butterworth (1975) correlation in Eqn. 4b is a transformation of the Lockhart and Martinelli (1949) data, which is traceable and publicly-accessible (i.e., independently-verifiable) data. On the contrary, the majority of the data (about 60% of the entire database) used to create the Garcia et al. (2005) correlation are sourced from untraceable and publicly-inaccessible (unverifiable) data such as the 1,255 data-points of the “Companies” data in Table 2 of the reference, and the 64 data points from the PDVSA-Intevep internal company reports (Cabello et al., 2001, Ortega et al., 2000, 2001). Certainly, the use of unpublished, untraceable or secret data should be discouraged. The risk of their usage in closure relations could result in very poor performances of the tuned models.

A notable aspect of reformulating prior correlations in terms of slip ratio becomes clear in viewing the identical forms of Eqns. 43 and 16. With respect to Eqn. 43, the perceived benefits of seeking “a hidden property of self-similarity” leading to power law forms of equations (e.g., Joseph, 2001, 2003) to regress experimental data become inconsequential. As can be seen, Eqns. 43 and 16 share an analytical origin as shown in

Eqn. 15, which by itself, bears no connection to the question of whether or not there is a self-similarity underlying the experimental observations.

Next, the Premoli et. al (1970) vapor (phase 2) and liquid (phase 1) correlation of the Centro Information, Studied Esperienze group (referred hereafter as the "CISE" model) is:

$$H_{2,1} = 1 + E_1 \left(\frac{\left(\frac{f_2}{1-f_2} \right)}{1 + E_2 \left(\frac{f_2}{1-f_2} \right)} - E_3 \left(\frac{f_2}{1-f_2} \right) \right)^{0.5} \tag{44}$$

Where, "E_1", "E_2" and "E_3" in Eqn. 13 are given on pg. 2-83 of the classic Hetsroni (1982) handbook. Note that in viewing this correlation in this way, it is clear that it will fail in the circumstances where the terms in the square root yield a negative value. It is found in this work that this very frequently happens. A famous example of the failure of this correlation is found in the benchmark "fully-developed flow" problem of Theofanous and Amarasooriya (1987), presented as Table 1 of this reference. The vertical, small-diameter, air-water data shown in this table represent 40 out of the 42 runs performed at a system pressure of 240 kPa and water mass flux of 297 kg/m^2-s in the original Owen (1986) dissertation, corresponding to run numbers 1029701 to 1029742 in the dissertation. The last two data-points, run numbers 1029741 and 1029742, in addition to run numbers 1029737 to 1029740, result in a failure of the Premoli et. al (1970) correlation. Although these last two data-points were not given in Table 1 of Theofanous and Amarasooriya (1987), they were included in Figure 3 of Hewitt (1986).

Next, the famous Armand (1946) correlation (referred hereafter as the "ARMAND" model) for horizontal, vapor (phase 2) and liquid (phase 1) bubble/slug flow is:

$$H_{2,1} = C_0^{Armand}\left(\frac{1-\langle s_2\rangle}{1-f_2}\right) \tag{45}$$

Where, C_0^{Armand} in Eqn. 45 is an empirical parameter = 1.2. The Zhao et al. (2000) correlation for steam (phase 2) and water (phase 1) flow is:

$$H_{2,1} = \frac{1-\langle s_2\rangle}{\left(\langle s_2\rangle + \left(1-\langle s_2\rangle\right)^{\frac{8}{7}}\left(\frac{\mu_2}{\mu_1}\right)\right)\left(1-f_2\right)} \tag{46}$$

The Collier and Wallis (1966) annular flow air (phase 2) and water (phase 1) correlation, as given in Eqn. 8.222 of Govier and Aziz (1972), is:

$$H_{2,1} = \frac{\left(\frac{\rho_2}{\rho_1}\right)^{-0.5}\left(\frac{1-\lambda_{CW}\left(1-\langle s_2\rangle\right)}{\langle s_2\rangle}\right)\left(\frac{\lambda_{CW}\left(1-\langle s_2\rangle\right)}{N_{Fr,mix}^{axial}}+1\right)\left(\frac{1-\langle s_2\rangle}{1-f_2}\right)}{\left(\frac{\rho_2}{\rho_1}\right)^{-0.5}\left(1-\lambda_{CW}\left(1-\langle s_2\rangle\right)\right) + \lambda_{CW}\left(1-\langle s_2\rangle\right)} \tag{47a}$$

Where, $N_{Fr,mix}^{axial}$ is defined in Eqn. A.40 in Appendix A, in which θ = 0 for vertical flow and $D_H = D$ for circular pipe. Also, λ_{CW} in Eqn. 47a is an empirical data-fitting constant = 3.1 in the reference. In viewing Eqn. 47a in this way, it now becomes clear that this correlation will fail (i.e., the denominator will equate to zero) in the circumstances where $\langle s_2\rangle$ is defined as:

$$\langle s_2\rangle_{CW}^{Failure} = 1-\frac{\left(\frac{\rho_2}{\rho_1}\right)^{-0.5}}{\lambda_{CW}\left(\left(\frac{\rho_2}{\rho_1}\right)^{-0.5}-1\right)} \tag{47b}$$

From Eqn. 47b, for typical conditions of low pressure air and water flow with densities of 1.2 and 1000 kg/m^3, respectively, $\langle s_{air}\rangle_{CW}^{Failure}$ = 0.6658.

Next, the Guzhov et al. (1967) correlation developed for the transportation of natural gas (phase 2) and crude oil (phase 1) flow is:

$$H_{2,1} = C_0^{Armand}\left(\frac{1.0288}{1-\exp\left(-\frac{2.2\langle u_{mix}\rangle}{(gD)^{0.5}}\right)}\right)\left(\frac{1-\langle s_2\rangle}{1-f_2}\right) \tag{48}$$

Note that, in viewing Eqn. 48 in the slip ratio format, we can now clearly see that the Guzhov et al. (1967) correlation is simply a modified Armand (1946) correlation as shown in Eqn. 45. Indeed, the Greskovich and Cooper (1975) correlation can be seen, in a similar manner as above, as a modified Armand (1946) correlation. The reformulated Greskovich and Cooper (1975) correlation is:

$$H_{2,1} = C_0^{Armand}\left(0.833+\frac{(gD)^{0.5}\left(\sin(90-\theta)\right)^{0.263}}{1.788\langle u_{mix}\rangle}\right)\left(\frac{1-\langle s_2\rangle}{1-f_2}\right) \tag{49}$$

The Czop et al. (1994) correlation, in reformulated form, can also be shown as a modified Armand (1946) correlation:

$$H_{2,1} = C_0^{Armand}\left(0.7596+\frac{0.2165}{\langle s_2\rangle}\right)\left(\frac{1-\langle s_2\rangle}{1-f_2}\right) \tag{50}$$

The annular flow vapor (phase 2) and liquid (phase 1) correlation of Cioncolini and Thome (2012) is:

$$H_{2,1} = \frac{\left(\frac{\rho_2}{\rho_1}\right)^{-1}\left(\frac{\langle s_2\rangle^{1-n}}{h-\langle s_2\rangle(h-1)}\right)^{\frac{1}{n}}\left(\frac{1-\langle s_2\rangle}{1-f_2}\right)}{1+\left(1-\left(\frac{\rho_2}{\rho_1}\right)^{-1}\right)\left(\frac{\langle s_2\rangle}{h-\langle s_2\rangle(h-1)}\right)^{\frac{1}{n}}} \tag{51a}$$

Where, the designation “h” and “n” in Eqn. 51a is given as:

$$h = a+(1-a)\left(\frac{\rho_2}{\rho_2}\right)^{\alpha},\ n = b+(1-b)\left(\frac{\rho_2}{\rho_2}\right)^{\beta} \tag{51b}$$

In Eqn. 51b, “a”, “b”, “α” and “β” are empirical data-fitting constants derived from a non-linear regression technique described in the reference. In viewing Eqns. 51a and 51b

in this way, we see that the Cioncolini and Thome (2012) correlation will reduce to the no-global-slip condition of $f_2 = \langle s_2 \rangle$ very quickly as the vapor density approaches the liquid density (which is the stated upper limit of this correlation in Eqn. 15 of the reference). Annular flow in high-vapor-density conditions are commonplace in high-pressure systems (such as in petroleum systems), and thus it is obvious that this correlation cannot predict the annular flow condition in these cases. In general, this correlation (as well as that of Bhagwat and Ghajar, 2014) displays a systematic, physically incorrect behavior of approaching no-global-slip as the vapor density approaches the liquid density, independent of the prevailing void fraction or flow pattern (i.e., annular flow or not).

Indeed, an expected poor performance of an averaged volume fraction correlation can be pre-determined by reformulating in the manner done above. The Watterson et al. (2002) correlation for vapor (phase 2) and liquid (phase 1) stratified roll waves is:

$$H_{2,1} = 0.696 \left(\frac{\rho_2}{\rho_1} \right)^{-0.5} \left(\frac{1}{\langle u_1 \rangle} \right)^{0.28} \tag{52}$$

Clearly, Eqn. 52 is a dimensional correlation with tuning constants linked to a phase 1 superficial velocity in m/s. Another dimensional correlation that has been found to perform poorly is the Bankoff (1960) correlation, given as:

$$H_{2,1} = \left(0.71 \; + \; 1.45 \times 10^{-8} P_{sys} \right)^{-1} \left(\frac{1 - \langle s_2 \rangle}{1 - f_2} \right) \tag{53}$$

Where, the system pressure, P_{sys}, in Eqn. 53 is in Pa. The Flanigan (1958) correlation is:

$$H_{2,1} = 3.063 \left(\frac{1}{\langle u_1 \rangle} \right) \tag{54}$$

We see that Eqn. 54 is a dimensional correlation with a constant valid only for a phase 1 velocity in m/s. Also, we see that the Watterson et al. (2002) correlation in Eqn. 52, in reformulated form, can be shown as a modified Flanigan (1958) correlation. There are

many other correlations in the literature that will yield dimensional constants when re-formulated similar to above. One may even find dimensional correlations that are also implicit, such as the Hoogendorn (1959) correlation, shown as:

$$H_{2,1} = \left(\frac{f_2}{1 - f_2} \right) \left(0.6 \langle u_2 \rangle \left(\frac{H_{2,1} - 1}{H_{2,1}} \right) \right)^{-0.85} \tag{55}$$

3.4 UNDERSTANDING FRACTIONAL FLOW PATHS

The second and third questions raised at the beginning of section 3.1.2 concerned the use of the fractional flow graphs to better understand (and potentially connect) multiphase pipe flow phenomena. Specifically, the issues of interest are in understanding the inter-relationships among global (space- and time-averaged) variables such as volume fraction, relative velocity and total pressure gradient, and relating the global observations of different types of flow phenomena to what is happening at the local scale.

3.4.1 Total Pressure Gradient (Global-to-Global Relations)

In the next few examples in this section, we demonstrate that the total pressure gradient behavior of a flowing multiphase system is directly related to the changes in the fractional flow graph, i.e., looking at the inter-relationships among global variables. We recall that the fractional flow graph captures the relationships among the phase relative velocities, their volume fluxes and their volume fractions in an averaged sense. Indeed, the flow patterns are merely the visual manifestations (spatial configurations) of the velocity and volume fraction distributions, which are globally captured as different fractional flow paths in the fractional flow graph. Thus, we assert (and then test our assertion against observations) that: *if* the averaged variables mentioned above are related to each other, *then* there will be a direct relationship between the fractional flow graph and the total pressure gradient ratio (defined as the total pressure gradient of the

multiphase flow divided by the total pressure gradient of the least dense phase as if it were flowing in the pipe by itself).

3.4.1.1 Sharp-Transition Phenomena: Wavy-Ripply Flow

Fig. 3.4.1 shows an example vapor-liquid dataset (from the large-diameter study of Langsholt and Holm, 2007) demonstrating how sharp-transition phenomena in concurrent multiphase flow are represented as fractional flow paths. We recall that an example of sharp transition phenomena is already present in single-phase flow in the form of the laminar to turbulent transition, which is still an unsolved problem (Mullin, 2011). In Fig. 3.4.1 a-i, b-i, c-i and d-i, sharp changes in averaged volume fraction are observed in response to fairly small changes in gas superficial velocity in the slight up-inclined wavy-ripples flows of Exxol-D80 oil (phase 1) and SF_6 gas (phase 2) at 0.5°, 1°, 2.4° and 5° from horizontal, respectively. These runs were performed at a constant oil superficial velocity of 0.001 m/s (or oil superficial Reynolds number of 45) with increasing gas superficial velocity from 1 to 3.5 m/s. Note that both the shape and magnitude of the corresponding changes in the measured total pressure gradient (Fig. 3.4.1 a-ii, b-ii, c-ii and d-ii) scale directly with the measured averaged volume fraction.

3.4.1.2 Sharp-Transition Phenomena: Flooding

Fig. 3.4.2 shows two example vapor-liquid datasets (from the flooding study of Zabaras, 1985, Fig.3.4.2 b-i and b-ii, and the flow reversal study of Bharathan et al., 1979, Fig. 3.4.2 a-i and a-ii) demonstrating how sharp-transition phenomena in countercurrent multiphase flow are represented as fractional flow paths. In vapor-liquid flows, the vapor can flow upwards countercurrent to a downward liquid flow in the bubbly, slug, churn, churn-annular and annular flow patterns (point “1” in Fig. 3.4.2 b-ii). The *onset of flooding* (point “2” in Fig. 3.4.2 b-ii), known as the *flooding point* in the

literature, is the point that represents the upper limit of stable annular countercurrent flow in which the liquid falls as a film along the walls of the pipe and the vapor forms a rising central core. Just before the flooding point, the mean liquid (phase 1) film thickness remains constant and (approximately) equal to the Nusselt (1916) falling film thickness (Hewitt and Wallis, 1963), which is, in meters:

$$\overline{e}_{Nusselt} = \left(\frac{0.021 \mu_1 \langle u_1 \rangle D_H}{\rho_1 g} \right)^{\frac{1}{3}} \tag{56}$$

A review of falling liquid film thickness experiments and theories can be found in Karimi (1998). If the prevailing vapor rate rises above the *flooding* vapor rate, the falling film quickly becomes unstable (chaotic), waves of large amplitude appear and some liquid (probably as droplets torn off from the crests of the waves) is carried along the pipe by the upward moving vapor. Meanwhile, the total pressure gradient in the pipe increases drastically (point "3" in Fig. 3.4.2 b-ii) depending on the liquid rate as evidenced in the classic experiments depicted in "Figure IV-5" of Dukler and Smith (1977), which is perhaps the simplest unambiguous experimental evidence for the flooding phenomena in countercurrent flows. Note that the *flooding point* is not approached as the limit of a continuous process but is the result of a sudden and dramatic instability which increases the pressure gradient by orders of magnitude. Also, at the *flooding point*, the net liquid flow is still downward.

As the vapor rate is increased beyond flooding (points "4" to "9" in Fig. 3.4.2 b-ii), the downward liquid rate is decreased further until the net liquid downward rate becomes 0 (the intersection of the f_2 =1 line). At this intersection point, the wall friction is at its lowest value and the interfacial friction is at its highest value. After this intersection point, the phases flow concurrently upward as the vapor rate continues to increase along a concurrent fractional flow path of the fractional flow graph. In Fig.

3.4.2 b-i and b-ii, the different colored curves correspond to the two countercurrent annular flow datasets in Zabaras (1985) for a constant inlet liquid (phase 1) superficial Reynolds number of 3100 and probe-to-liquid feed distances of 0.15 and 1.7 m. Air (phase 2) superficial velocities varied from 5 to 12 m/s for both datasets. Note that the total pressure gradient ratio throughout the flooding process directly scales with the averaged volume fraction, e.g., a sudden increase in liquid film thickness yields a corresponding sudden increase in total pressure gradient (point "3" in Fig. 3.4.2 b-i and b-ii).

The flooding phenomenon is quite important in the energy, power and process industries. Detailed descriptions of the transition from the pre-flooding to post-flooding states can be found in Bharathan et al. (1979), Zabaras (1985), Zapke and Kroger (2000), among others. Although this phenomenon has been the subject of extensive research over a number of decades (over 50 years), controversy still exists as to the most likely mechanism of flooding. Some of the uncertainty is due to the experimental inlet and outlet pipe conditions which are known to have a strong effect on the flooding vapor velocities (Bankoff and Lee, 1983). Good discussions about the flooding point and the poorly understood mechanisms that are thought to control it can be found in Hewitt and Wallis (1963), Ragland and Ganic (1983), Bankoff and Lee (1983), among many others.

3.4.1.3 Sharp-Transition Phenomena: Flow Reversal

An important related sharp-transition countercurrent vapor-liquid flow phenomenon is the *onset of flow reversal* point, which describes the transition from concurrent to countercurrent flows. Some key literature references concerning this point can be found in Pushkina and Sorokin (1969), Wallis and Makkenchery (1974), Taitel *et al.* (1982), among many others.

Starting from a concurrent vapor-liquid upward churn-annular or annular flow, as the vapor rate is decreased, the liquid volume fraction increases and the total pressure gradient increases. If the vapor rate further decreases, a point is reached where the net liquid upward rate becomes 0 (the intersection of the f_2=1 line). Lowering the vapor rate beyond this point causes a countercurrent-annular "hanging film" of the liquid (points "1"and "2" in Fig. 3.4.2 a-ii). As the vapor rate continues to decrease, part of the liquid begins to creep downward resulting in a slight decrease in liquid volume fraction (points "3", "4" and "5" in Fig. 3.4.2 a-ii). These points represent the countercurrent-annular "pre-flow reversal" condition. A point is reached (the *onset of flow reversal* point – "6"in Fig. 3.4.2 a-ii) as the vapor rate continues to decrease where the "pre-flow reversal" liquid film becomes unstable (chaotic) and large amplitude waves appear on its surface. Further reduction in the vapor rate causes the net liquid flow to be downward and the total pressure gradient in the pipe to drastically decrease. This first post-flow reversal point ("7" in Fig. 3.4.2 a-ii) is sometimes called the "de-flooding" point in the literature (e.g., Clift et al., 1966) because it refers to the *flooding point* that would have been attained if the vapor rate was increasing rather than decreasing. In the post flow-reversal countercurrent flow state (points "8" and "9" in Fig. 3.4.2 a-ii), wall friction begins to increase and starts to regain dominance over the interfacial friction.

We note that similar to the *flooding point*, the *flow reversal point* is not approached as the limit of a continuous process but is the result of a sudden and dramatic instability which decreases the pressure gradient by orders of magnitude. More importantly, it must be recognized that flooding and flow reversal are different (though related) phenomena that are described by different theories, in which there are varying degrees of "hysteresis" reported in the literature (e.g., Becker and Letzter, 1978, Bankoff and Lee, 1983, Celata et al., 1991). Therefore, equating a flow-reversal limit with a

flooding curve (e.g., pg. 6-6 in the RELAP5-3D Code Manual, 2005, http://www.inl.gov/relap5/r5manuals/ver_2_3/rv4.pdf; the "Drift Flux Slip Model" section in Schlumberger's ECLIPSE Technical Description Manual, 2005; Shi et al., 2003), or, using a flooding theory if a flow reversal theory is desired (e.g., Cioncolini and Thome, 2012), may lead to resulting multiphase flow theories that are based on inconsistent representations of the underlying flow phenomena.

In Fig. 3.4.2 a-i and a-ii, the different colored curves correspond to two countercurrent air (phase 2) and water (phase 1) flow datasets originally from the Bharathan et al. (1979) EPRI (Electric Power Research Institute) report. The blue curves are for "Run 4" and the orange curves are for "Run 8" on pages 248 and 252, respectively, of Hewitt et al. (1987). As in the previous section, the total pressure gradient ratio throughout the flow reversal process directly scales with the averaged volume fraction, e.g., a sudden decrease in liquid film thickness yields a corresponding sudden decrease in total pressure gradient. Summarily, we see how these related phenomena (flooding and flow reversal) can be simply understood within the unifying framework of the fractional flow graph.

3.4.1.4 Complex Fractional Flow Paths: Mini-Channel

In the next few examples, we demonstrate how unusual or complex total pressure gradient behaviors observed in different scenarios are directly related to the complex changes in the fractional flow graph.

Fig. 3.4.3 shows an example horizontal vapor-liquid dataset (from the mini-channel study of Fujita et al., 1995) showing the inter-relationships among the observed flow patterns (Fig. 3.4.3 a), the fractional flow behaviors (Fig. 3.4.3 b, c) and the total pressure gradient ratio (Fig. 3.4.3 d) for the datasets obtained for a rectangular mini-

channel height of 1.2 mm. These runs were performed at a constant liquid (phase 1) superficial velocity of 0.2 m/s with increasing nitrogen (phase 2) superficial velocities from 0.1 to 14 m/s. Note the clear and direct relationship between the total pressure gradient (Fig. 3.4.3 d) and the fractional flow graph (Fig. 3.4.3 c).

Fig. 3.4.4 shows measurements obtained from the same Fujita et al. 1995 study but for the datasets at a rectangular mini-channel height of 2 mm. These runs were performed at a constant liquid (phase 1) superficial velocity of 0.8 m/s with increasing nitrogen (phase 2) superficial velocities from 0.1 to 14 m/s. The direct relationship between the total pressure gradient (Fig. 3.4.4 d) and the fractional flow graph (Fig. 3.4.4 c) is again demonstrated.

3.4.1.5 Complex Fractional Flow Paths: Large-Diameter

Complex fractional flow behaviors are present at all scales. Fig. 3.4.5 shows an example horizontal vapor-liquid dataset (from the 8.5 inches diameter pipe flow study of Simpson et al., 1976) showing both the observed flow patterns (Fig. 3.4.5 b) and the averaged volume fraction behaviors (Fig. 3.4.5 a) as fractional flow graphs. The 160 runs shown correspond to the “in-line injection” tests of the reference, performed at constant water (phase 1) superficial velocities from 0.081 to 1.66 m/s with increasing air (phase 2) superficial velocities from 0.04 to 8.6 m/s. Note that all of the flow pattern information (Fig. 3.4.5 b) are captured in the changes of the fractional flow paths in the fractional flow graph (Fig. 3.4.5 a).

If we select only one set of data from these runs (i.e., those runs performed at a water superficial velocity of 0.081 m/s shown in Fig. 3.4.6) and compare how existing codes in practice (e.g., OLGA and LEDA) predict the averaged volume fraction, we clearly see the need for major improvement in the current ability to model averaged

volume fraction in horizontal, large-diameter, stratified vapor-liquid flows. The identical test run numbers as found in the reference are shown in Fig. 3.4.6 for cross-referencing purposes.

3.4.1.6 Complex Fractional Flow Paths: Down-Inclined

Unusual or complex total pressure gradient behaviors are commonly observed in downward-inclined flows. Knowing that the total pressure gradient behavior directly scales with the fractional flow graph, we can now recognize the reason for this observation being due to the complex changes in the volume fraction behavior associated with downward multiphase flows. Fig. 3.4.7 shows an example vapor-liquid dataset (from Spedding and Nguyen, 1976) showing how downward flows can result in volume fractions that span various extents of the fractional flow graph in which the averaged in-situ liquid velocity can be much higher than the averaged in-situ vapor velocity.

It is not only at lab scale conditions that this complex behavior of strong negative global slip is clearly (and frequently) observed but also in field applications (e.g., Baldauff et al., 2004, Eriksen and Midttveit, 2010). The 113 concurrent downward flow runs shown were performed at a pipe inclination of -67.75° from horizontal at constant water (phase 1) superficial velocities from 0.005 to 1.4 m/s with increasing air (phase 2) superficial velocities from 0.1 to 54 m/s. It is found from this work, that similar to the results in Fig. 3.4.6, the prediction of downward vapor-liquid volume fraction using existing correlations is very poor. As will be demonstrated in Chapter 4, the BUTTERWORTH model is the best available general (i.e., flow-pattern-implicit) correlation for predicting averaged volume fraction in downward vapor-liquid flows.

3.4.2 Lateral Distribution Profiles (Local-to-Global Relations)

We next look at how the fractional flow graph captures the inter-relationships between local (lateral) distribution profiles and global variables. We will highlight a specific important practical application – vertical upward bubbly flow – to demonstrate the way in which changes at the local scale (such as the complex fluid mechanical, multidimensional flow phenomena causing wall-peaking to core-peaking bubble lateral distributions) are translated to changes at the global (area-averaged) 1D scale.

3.4.2.1 Example Application: Bubbly Flow

Vertical upward bubble lateral distribution is linked with many parameters and is one of the least understood (but very important) multidimensional phenomena. The lateral distribution of various physical quantities such as void fraction, velocities of phases, turbulence velocities/stresses of phases and interfacial area concentration are closely related to each other. For example, there are large amounts of experimental evidences that clearly indicate a strong lateral (non-drag) lift force on the dispersed (vapor) phase – this lift force being one of the main mechanisms leading to the observed phase distribution. The lift force, which is one of the lateral forces that is not related to buoyancy effects, is the net force acting laterally upon bubbles moving through a non-stagnant liquid velocity field (Drew and Lahey, Jr., 1987). A brief review of the lift force in relation to vapor-liquid and fluid-solid flows can be found in Lahey, Jr. (1990) and Joseph and Ocando (2002), respectively. In bubbly flow, this force will move bubbles either towards the center of the pipe or close to its wall depending on the direction of the net force acting on the bubbles. A simplified explanation for this behavior (in terms of a shear flow) can be found in Section 5 of Trygvasson et al. (2006).

There are numerous examples of vertical upward bubble lateral distributions in the literature. Pronounced wall-peaking of the local void fraction for turbulent upward

bubbly flow have been reported by several investigators (e.g., Serizawa et al., 1975, Wang et al., 1987). As far as the early 1960's, Staub and Zuber (1964) reported local void fraction distribution data obtained during boiling of refrigerant-22 at relatively low mass fluxes. These data indicated that the local void fraction peaked at the wall at low flow qualities and that this local peaking increased with increasing mass fluxes.

Malnes (1966) observed local void fraction peaking near the wall for upward flow of a bubbly air-water mixture in a pipe. An interesting result from this study was the occurrence of the peaking of air bubbles near the pipe wall at low values of averaged void fraction, and the increase in this tendency with increasing water velocity. A few example void fraction profiles from this reference was published in Rouhani (1974). Further void fraction distribution data demonstrating similar trends to the Malnes (1966) study were reported in Staub and Walmet (1969) and Shiralkar (1970).

In a crucial investigation, Serizawa et al. (1975) measured the lateral void fraction distribution and the turbulent liquid fluctuations for bubbly air-water upward flow in a vertical pipe. In this study, wall peaking can be seen for low flow quality bubbly flow, while core peaking evolves as the flow quality is increased and slug flow occurs. Some typical data from this study can be found in Figure 1 of Lahey, Jr. (1990).

In another key investigation of upward bubbly flow, systematic measurements (48 well-defined conditions) of liquid-phase local velocities and turbulent stresses were obtained covering a range of local void fractions from 0 to 50% (Liu and Bankoff, 1990a). Additionally, measurements of the radial profiles of void fraction, bubble velocity and bubbly size under the same conditions as Liu and Bankoff (1990a) were presented in Liu and Bankoff (1990b). In this latter work, the profiles of void fraction, bubble frequency and bubble size were found to show distinct peaks near the wall, becoming flat at the core, and with local mean bubble sizes varying from 2 – 4 mm. A

notable observation from this investigation was the substantial disagreement between the experimental data of Serizawa et al. (1975) and Wang et al. (1987) at similar reported conditions. It was suggested by the authors that performing the experiments under different bubble size conditions (presumably associated with the bubble generation methods) could be one of the major reasons causing the inconsistency of the published data. The results from Zun (1988) support this idea, especially since a carefully designed bubble injector was used to control the bubble size in this study.

In contrast to upward bubbly flows, Oshinowa and Charles (1974) observed core-peaking void fraction profiles for bubbly downward flows in a pipe. A review of the wide ranges of measurements (and explanations of those observations in terms of lift force, wall repulsion force and wall vortex effect) of local flow parameters in vertical downward bubbly flows can be found in Hibiki et al. (2004). According to this review, core-peaking, bell-typed and off-center-peaked phase distribution profiles are the more frequent profiles encountered in downward flows. Recently, peak structures in downward bubbly flows were studied by Das and Das (2012). Interestingly, this numerical investigation showed that by merely changing the direction of the flow, one gets a phenomenal shift in the transition boundary of bubbly flow.

In vertical upward bubbly flow, lateral distribution phenomena (and thus interfacial flow parameters) are significantly affected by the conduit hydraulic diameter (Shawkat et al., 2008). For example, in some cases (e.g., Shoukri et al., 2003), the wall-peaking void fraction distribution that are common in vertical upward bubbly flow in small diameter pipes can only be found under conditions of low area-averaged void fraction in large diameter pipes. In other cases (e.g., Mudde and Saito, 2001), at moderate to large area-averaged void fraction conditions, large diameter experimental (air-water) investigations show mostly core-peaking void fraction distributions. A

simplified explanation for this core-peaking observation in terms of a possible change of the lift force direction in the near wall region can be found in Guet et al. (2004).

Apart from circular conduits, phase distribution phenomena are also present in conduits of more complex geometries. A brief review of non-circular vertical upward bubbly flow can be found in Section 2 of Lahey, Jr. (1990). In these cases, just as for the circular conduit case, there are clear demonstrations of a strong lateral lift force on the dispersed (vapor) phase.

Reviews on various aspects of bubble lateral distribution in vertical upward bubbly flow are available in Spalding (1980), Serizawa and Kataoka (1987), Lahey, Jr. (1990), Mudde (2005), Nguyen et al. (2013), among many others.

3.4.2.2 Complex Effects: Beyond Buoyancy and Lift

Other than the lift force highlighted in the previous section, buoyancy has a significant effect on the lateral distribution of the dispersed (vapor) phase in bubbly flow. Figure 1 in Clarke and Rezkallh (2001) illustrates this effect quite clearly by comparing the observed differences in the void fraction profiles in an upward normal-gravity bubbly flow (a dataset from Serizawa et al., 1975), a downward normal-gravity bubbly flow (a dataset from Wang et al., 1987) and a microgravity bubbly flow (a dataset from Kamp et al., 1993). The key insight here is that forces such as buoyancy and lift, which may dominate in normal-gravity flows, can become insignificant in the near absence of gravity (Singhal, 2004). This naturally leads to a desire to better understand the complex effects beyond buoyancy and lift.

For example, the influence of average bubble size on the lateral phase distribution is not yet understood in vapor-liquid flows of practical interest in spite of the fact that many studies suggest that this effect is very important. An observation that seems

common in upward bubbly flow studies is that smaller bubbles tend to accumulate near the wall while bigger ones tend to concentrate at the center of the pipe (Politano et al., 2003). In relation to the lift force, a comparison of radial volume fraction profiles for bubbles of different sizes can be found in Krepper et al. (2005) showing a bubble size dependency of the lift force, apparently confirming the results from Tomiyama (1998). It is easy to see why knowledge of average bubble size (and bubble size distribution) is essential to complement the local void fraction distribution – the same void fraction may be due to either a small number of large bubbles or a large number of small bubbles.

As first noted in Serizawa and Kataoka (1987) and later in Liu (1997), even though most bubbly flow investigators in the past made efforts to control the average bubble size in their experiments, there was invariably a range of bubble sizes present. Relatively few experiments have been conducted in studying the effect of average bubble size by using different bubble generators. A major problem is that the use of different bubble generators inevitably results in a mixed (masked) effect of the inlet flow condition with the effect of average bubble size. Some investigators (e.g., Serizawa et al., 1988; Liu, 1997), however, modified the bubble generator to study the lateral phase distribution phenomena, with particular emphasis on the effects of the average bubble size and axial structure development under well-controlled inlet bubble size flow conditions.

One benefit of comparing experiments with the same average bubble size is that the role bubble size plays with respect to the lateral phase distribution is recast in proper perspective – as <u>not</u> the only relevant parameter governing the observed phase distribution. A result from a recent set of carefully controlled air (phase 2) and water (phase 1) experiments (Mendez Diaz, 2008; Chiva et al., 2010) highlights this fact. In these experiments, a careful variation of many physical parameters was conducted to analyze their individual effects on the void distribution. In Figure 3.4.8, the three

datasets in Figure 2 of Mendez Diaz et al. (2012) are shown on the fractional flow graph. The datasets shown in Figure 3.4.8 correspond to the water rates of $\langle u_1 \rangle$ = 1 m/s (wall-peaking squares), $\langle u_1 \rangle$ = 2 m/s (intermediate-peaking triangles) and $\langle u_1 \rangle$ = 3 m/s (core-peaking circles), and to the air rates of $\langle u_2 \rangle$ = 0.278 m/s, $\langle u_2 \rangle$ = 0.74 m/s and $\langle u_2 \rangle$ = 1.286 m/s, respectively. As noted in the reference, for these datasets, the Sauter mean diameter of the bubbles is about 3.4 mm and the area-averaged void fraction is about 20%. Clearly, varying only the phase flow rates can also cause a distribution to change its local peaking behavior for approximately the same average bubble size and area-averaged void fraction.

In spite of Figure 3.4.8, one must not ignore the strong (inherent) coupling that exists between phase flow rates, average bubble size and bubble size distribution. For example, it is reasonable to conceive that an increase in liquid flow rate at a given constant vapor rate could enhance the bubble breakup due to the liquid-induced turbulence, which in turn could decrease the bubble size. Indeed, it is also reasonable to conceive a net cancellation of different, local, competing bubble breakup and coalescence effects (a sort of equilibrium or continually-competing processes) that ultimately result in a given bubble size distribution and area-averaged void fraction for the studied scenario. For example, close to the wall, the higher void fraction due to the accumulation of smaller bubbles could tend to coalesce forming larger bubbles that would tend to travel to the center of the pipe provided that they can survive the breakup caused by the high shear stress and turbulence intensity (as noted in Liu, 1997). Simultaneously, close to the center of the pipe, larger bubbles could breakup thus resulting in smaller bubbles which would tend to migrate towards the wall.

Apart from the average bubble size, the shape of a bubble and its distortion are also known to have an influence on the lateral phase distribution (e.g., Kariyosaki, 1985;

Zun, 1988). Experimentally, the shape of the bubbles is determined by the balance between the hydrodynamic and surface tension forces. In order to clarify the mechanisms of bubble shape and distortion, the behavior of single bubbles in a shear flow have been studied by many investigators (e.g., Zun and Malahovsky, 1988; Tomiyama, 1998). The observation of single bubbles is, interestingly, also the experimental input for the study of the non-drag, non-lift forces, i.e., the turbulent dispersion force, the wall lubrication force and the various pressure forces. Beyond single bubble studies, investigating the effect of bubble shape and distortion with multiple bubbles at very low void fraction has also been pursued (e.g., Ervin and Tryggvason, 1997; Bunner and Tryggvason, 2003; Trygvasson et al., 2006).

Next, unlike upward dispersed bubbly flows at relatively high liquid flow rates and low void fractions with very little (or no) recirculation of phases and few bubble-bubble interactions, upward bubble-driven flows in pipes are characterized by prominent recirculating flows with generally high void fractions leading to intense interaction between bubbles and rapid bubble coalescence and breakup accompanied by large variations in average bubble size and shape. There are still open questions concerning these flows and detailed discussions of the various non-drag lateral forces involved can be found in the works of Zun (1980) and Jakobsen et al. (1997).

In summary, in light of the foregoing discussions in Sections 3.4.2.1 and 3.4.2.2, it is clear that the mechanisms which determine the phase distribution across the pipe are still only partially understood. Wish lists of future research and development needs for better understanding lateral phase distribution (multidimensional) phenomena can be found in Lahey, Jr. (1990) and Mudde (2005).

3.4.2.3 Complex Effects: Bubbly Flow Transition

As seen in the previous section, the complex effects associated with lateral phase distribution phenomena are only partially understood. We can look at one historically traceable example of lateral phase distribution phenomena – the bubbly-slug transition in vertical upward bubbly flow – to concretely demonstrate this fact. Recently, Prosperetti and Trygvasson (2007) summarized their opinions on this phenomenon (pg. 5 of the reference) as: "The transition from a bubbly to a slug flow regime is a typical phenomenon of gas-liquid flows, of great practical importance but still poorly understood. Here, in addition to understanding how the bubbles arrange themselves in space, it is necessary to model the forces which cause coalescence and the coalescence process itself".

Apart from bubble lateral distribution and the coalescence process, Guet et al. (2003) previously highlighted the wide differences in the bubble packing limit concerning this phenomenon, as: "Taitel et al. (1980) assumed that the transition from bubbly flow to slug flow occurs when the gas velocity is equal to the rise velocity of large bubbles moving with respect to the averaged liquid velocity and when the void fraction has a certain critical value. … By using some geometrical considerations Taitel et al. (1980) suggested $\varepsilon_c = 0.25$. Other studies proposed $\varepsilon_c = 0.30$ (for example, Mishima and Ishii, 1984), while the maximum gas fraction considering packed spherical shaped bubbles in a cubic lattice is $\varepsilon_c = 0.52$. In a body-centered cubic configuration, $\varepsilon_c = 0.68$. A generally accepted expression for the critical gas fraction is still lacking".

Additionally, Nguyen et al. (2013) drew attention to "Prof. Ishii's group" that considered the maximum bubble packing value that is actually occupied by identical spheres close-packed according to a face-centered cubic lattice as 0.741 – 0.8. Guet and Ooms (2006) cited a unique relation between bubble size, pipe diameter and the critical

bubbly flow void fraction (Song et al., 1995) as a result that "suggests that a constant critical void fraction model, such as $\varepsilon_c = 0.25$ (Taitel et al. 1980) or $\varepsilon_c = 0.3$ (Mishima and Ishii 1984), cannot be generally valid".

The issue of bubby flow transition is discussed in Section 3.1.2.1 of the RELAP5/MOD3 Code Manual at http://www.inl.gov/relap5/r5manuals/ver_2_3/rv4.pdf. In their detailed review of this transition, several issues are brought forward regarding the packing limit arguments of Taitel et al. (1980), in which the works of Griffith and Wallis (1961), Radovcich and Moissis (1962) and Griffith and Snyder (1964) were cited. This review also brings to attention the discussion by Hewitt (1977) in reference to some uncertainties and qualifications to the approach of Radovcich and Moissis (1962). Quoting from the RELAP5/MOD3 Code Manual: "Taitel et al. (1980) also cite Griffith and Snyder (1964), suggesting that the bubbly-to-slug transition takes place between 0.25 and 0.30. Actually, Griffith and Snyder were studying slug flow using a novel technique. They formed a plastic 'bubble' to simulate a Taylor bubble under which they injected air. Their setup allowed the bubble to remain stationary while the flow moved past it. While void fractions as low as 0.08 and no higher than 0.35 were obtained for 'slug flow', it seems inappropriate to use such information to set the bubbly-slug transition".

As obvious as demonstrated above, the bubbly-slug transition is poorly understood. Yet surprisingly, for some petroleum industry investigators, this phenomenon is considered well established. For example, Hasan and Kabir (1988b) opine: "In a vertical system, it appears well established that the transition from bubbly to slug flow occurs at a void fraction of about 0.25 (Hasan et al., 1988, Hasan and Kabir, 1988a, Radovcich and Moissis, 1962, Taitel et al., 1980). This criterion for the transition from bubbly to slug flow should also be applicable to deviated systems". In fact, in Hasan and Kabir (1988a) and Hasan (1988), this transition criterion is said to be

"confirmed" as being applicable for both circular and annular channels. Even without citing specific studies, Bratland (http://drbratland.com/PipeFlow2, pg. 179, 2010) summarizes: "For pipes with a large enough diameter for bubble flow to occur at relatively low superficial gas velocities, it is assumed that if we continue to increase the gas fraction, the bubble fraction will eventually become so high that neighboring bubbles start merging with each other. It turns out that the bubble fraction does not have to be so high that the bubbles actually touch each other before this starts to occur. Measurements have shown that Taylor-bubble growth takes place if $\alpha_G \geq 0.25$". Examples of this transition criterion can be found in most Petroleum industry mechanistic models (e.g., Ansari et al., 1994, Gomez et al., 1999, Kaya et al., 2001, Shirdel, 2013).

It is due to this observation of a very different understanding of bubbly flow among various investigators that provably incorrect statements concerning this basic flow pattern can be found in the published literature. For example, Danielson et al. (2000) opine: "Like annular flow, bubble flow is characterized by very little slip between the phases. However, unlike annular flow, the liquid hold-ups are very high – generally 95% or more. Bubble flows can be successfully modeled by assuming that the liquid holdup is equal to the no-slip holdup. Pressure drops can be calculated from a Moody chart, using a mixture density and liquid viscosity. All models do a reasonable job in describing bubble flow."

3.4.2.4 Complex Effects: Bubbly Flow in Averaged Models

Since the fractional flow theory is an averaged (1D) theory, we next look at how bubble lateral distribution phenomena are modeled in averaged flow models. In practical multiphase flow models, there are several ways to account for multidimensional phenomena. For example, appropriate closure relations are used in many averaged two-

fluid models in which there are postulates regarding interfacial and wall transfer processes which attempt to reintroduce some of the physics which was lost during the space/time/ensemble averaging process (e.g., such as those found in TRAC, PHOENICS and RELAP5 codes). Nevertheless, there remains considerable uncertainty concerning the proper formulation of the physical models (closure relations) describing these transfer processes.

In vertical upward bubbly flow, bubble coalescence and break-up rates, which form the source terms in these averaged two-fluid models, are determined by local events. These rates depend on local parameters of turbulence as well as on the local bubble size distribution. The interfacial area concentration is also an important quantity in some averaged two-fluid models in that it determines the intensity of inter-phase mass, momentum and energy transfer (Ishii, 1975; Ishii and Hibiki, 2006).

Another source of uncertainty regarding the closure relations in averaged two-fluid models that aim to account for the bubble lateral distribution, is that some of the models (e.g., the dispersion-type or bubble coalescence models) are ad hoc in nature and can apparently be made to work since they contain parameters that are not directly measured, but instead, are adjusted to produce agreement with the data. Examples of these ad hoc models are noted in Lahey, Jr. (1990) and Nguyen et al. (2013). Obviously, the question then arises (as discussed in Delhaye, 2001) – how does one adjust all these parameters as independently as possible in scenarios where a single phenomenon is of importance?

In addition, beyond the ad hoc nature of some averaged two-fluid models, there are serious limitations in terms of the choice of closure relations in these models and their inherent assumptions, as summarized in Politano et al. (2003).

From a (spatial) scale standpoint, the very definition of averaged-equations models indicates that it will not be possible to resolve any details at the scale of the bubble, i.e., flows around individual bubbles. Therefore, averaged flow models (two-fluid or not) will not be able explain phenomenon at the local bubble scale such as circulation around the bubble or bubble deformation.

Thus, in light of the vast complexity of the various lateral distribution phenomena, as discussed in Sections 3.4.2.1 – 3.4.2.3 as well as in this section, an important question arises – what is the simplest modeling possible that captures the global physics of this problem? Obviously, as the previous sections and the discussion above indicate, the answer to this question might not be found in the averaged multi-fluid models because of the ever increasing amount of details and their accompanying auxiliary hypotheses that are perceived as necessary among the investigators owning these models. We assert (and also demonstrate in the remaining sections of this chapter) that this question is already answered with the fractional flow theory described earlier in this Chapter.

As noted in Section 1.3.1.2 of Chapter 1, the averaged in-situ phase velocities and volume fractions mathematically represent the net of competing, interacting flow microphysics in any multiphase flow scenario (bubbly flow or not). These continuously interacting and locally developing physical processes compete against each other to give rise to various observed lateral phase distribution phenomena. This is *why* the lateral phase distribution strongly affects the transport processes both within the flow field and at its boundary – not because of whether the structural behavior is core-peaking or wall-peaking (which remains as continuously changing and unknown during the flow) – but because of the changes in the averaged in-situ velocities and volume fractions associated with the studied lateral distribution phenomenon. These changes are globally captured as different fractional flow paths in the fractional flow graph.

3.4.2.5 Developed Bubbly Flow

To see how the fractional flow graph captures the global (averaged) behavior in an upward bubbly flow displaying various lateral phase distributions, we consider a few of the developed air (phase 2) and water (phase 1) bubbly flow experiments highlighted in Nguyen et al. (2013). In this study, some of the experimental void fraction distribution results of Hibiki et al. (2001), referred to as the "PURDUE" data (run numbers "P1" – "P4" in the reference), are compared against data generated from the "KAERI-VAWL" facility (run numbers "KV1" – "KV6" in the reference). For cross-reference purposes, details of the flow and system conditions pertaining to each run can be found in Nguyen et al. (2013).

The KV1 and KV2 experiments in Figure 3.4.9 show two wall-peaking vertical upward bubbly flow void fraction profiles for increasing gas superficial velocity (from 0.054 to 0.232 m/s) at a constant liquid superficial velocity (1 m/s). As the void fraction lateral profiles in Figure 3.4.9 show, the effect of increasing the gas flow rate at a constant liquid flow increases the void fraction profile and bubble frequency (supposedly by promoting turbulent fluctuations of the bubbles) both in the core region as well as at the peak value near the wall. Also shown in Figure 3.4.9 is a comparison of the resulting averaged void fraction from these experiments against the BUTTERWORTH model. Note that this simple correlation captures the correct global trend (fairly accurately) of a change from a slight negative averaged slip velocity (KV1) to a slight positive averaged slip velocity (KV2) in the fractional flow graph.

Figure 3.4.10 shows three more datasets from Nguyen et al. (2013). At the low void fraction conditions shown, similar to before, an increase of the gas flow rate at a constant liquid flow augments the void fraction profile (P3 to P4), thus increasing the turbulence level. In contrast, an increase of the liquid flow rate at a constant gas flow

rate (P2 to P3) reduces the turbulence level, thus leading to a decrease in the averaged void fraction both in the core region as well as near the wall. This effect can be attributed to the (possibly) dominant effect of bubble-liquid interactions in producing liquid-phase turbulence. As before, a comparison of the resulting averaged void fraction from these experiments against the BUTTERWORTH model prediction shows excellent agreement. It is clear then, that the global (averaged) behavior indicative of the changes in the upward bubbly flow structures is simply captured as different paths in the fractional flow graph.

As seen in Figures 3.4.9 and 3.4.10, the resulting averaged void fraction from upward bubbly flow experiments can frequently yield a negative averaged slip velocity. Beyond the various lateral distribution phenomena discussed in Sections 3.4.2.1 – 3.4.2.4 leading to this averaged result (i.e., the net of the buoyancy, lift and non-lift lateral forces), it is important to recognize that the mathematical definition of the averaged slip velocity, $S_{2,1}$, depends only on the averaged superficial velocities and averaged void fraction, i.e., $S_{2,1} = \langle u_2 \rangle / \langle s_2 \rangle - \langle u_1 \rangle / \left(1 - \langle s_2 \rangle\right)$. This means that regardless of the local phenomena occurring, this definition dictates that for any combination of non-zero values of $\langle u_1 \rangle$ and $\langle u_2 \rangle$, as long as $1 + \left(\langle u_1 \rangle / \langle u_2 \rangle\right)$ exceeds $1/\langle s_2 \rangle$ then $S_{2,1}$ will become negative. This global (mathematical) flow definition must not be confused with the local (physical) flow scenario of different local slip velocities present at various lateral locations across the conduit cross-section. The key point is that the averaged void fraction, $\langle s_2 \rangle$, mathematically captures the net of the local interacting flow microphysics (inclusive of the peaking behavior of the bubbly structure and the effects of the various lateral non-drag forces) for a given combination of flow rates. Therefore, the complex lateral phase distribution phenomena at the local level are *already* captured in this global quantity.

One common example of this negative averaged slip behavior in upward bubbly flow is the case of a high liquid input condition (a high $\langle u_1 \rangle$) at a low gas flow rate (a low $\langle u_2 \rangle$), which typically results in a wall-peaking bubbly flow condition (a high $\langle s_2 \rangle$). In this case, the bubbles within the liquid mass near the wall region are subjected to an acceleration field caused by a wall-vortex effect resulting in a different bubble rise behavior near the wall compared to the core region of the flow (Rouhani, 1974). In fact, a different rise behavior (or slip velocity) across the conduit cross-section has been observed by several investigators (e.g., Zenit et al., 2001, Garnier et al., 2002; Bunner and Tryggvason, 2002; Guet et al., 2004), in which there is apparently a local decrease of the slip velocity at the void fraction peak location in a wall-peaking flow and a local increase of the slip velocity near the wall in a core-peaking flow.

Rouhani (1974) highlighted some of the many published experimental data which showed a negative averaged slip velocity in upward bubbly flow (e.g., Rose, 1964; Malnes, 1966; Staub and Walmet, 1969). Later, Stosic and Stevanovic (2001) noted this averaged result in the Bensler (1990) experiments as well as the experiments in Griffith (1987). Fig. 3.4.11, for example, shows all of the developed vertical upward bubbly flow data from the dissertation of Rose (1964). As is clear, there are large amounts of experimental evidences which show negative averaged slip velocities regardless of the type of inlet condition or the pipe diameter. In Fig. 3.4.11 (a) – 3.4.11 (c), the runs were performed with a 1-inch pipe and a “No. 3” mixing chamber, with a 1-inch pipe and a “No. 2” mixing chamber, with a 1-inch pipe and a “No. 1” mixing chamber, respectively, to observe the effect of the inlet condition. In Fig. 3.4.11 (d) – 3.4.11 (f), the runs were performed with a 1-inch pipe and a “No. 3” mixing chamber, with a 0.75-inch pipe and a “No. 3” mixing chamber, with a 0.5-inch pipe and a “No. 3” mixing chamber, respectively, to observe the effect of the pipe diameter.

Aside from upward bubbly flows, a negative averaged slip behavior is frequently observed in upward fluid-solid flows (e.g., Lareo et al., 1997, Lareo and Fryar, 1998) in which the more dense solid (phase 1) particles (analogous to the more-dense liquid phase in bubbly flow) can preferentially congregate in the high-velocity regions of the flow with a wall peaking of the less dense carrier (phase 2) fluid (analogous to the less-dense vapor phase in bubbly flows).

In spite of the fact that there is an enormous amount of studies available in the literature geared towards understanding the observations of lateral phase distribution phenomena (as discussed in Sections 3.4.2.1 – 3.4.2.4 and in this Section), it is important to recognize that there are groups of investigators who may be unaware of these studies, and specifically, may be unaware of the various lift and non-lift lateral (multidimensional) forces other than the buoyancy force present in upward bubbly flow. Even apart from upward bubbly flow, in a general sense, some investigators may incorrectly perceive basic quantities such as slip as a result of mainly a buoyancy effect from density differences, even in the presence of other forces or differing fluid properties. Of course, in this latter case, the observation of slip in horizontal, microgravity and neutrally-buoyant multiphase flows eradicates such perceptions.

A concrete (and historically traceable) example of this lack of awareness of the various lift and non-lift lateral forces discussed above is the case a group of petroleum investigators who perceive that a negative averaged slip velocity in upward vapor-liquid flow is “impossible” (Robinson, 1974), “physically unreasonable” (Rossland, 1981), “physically incorrect” (Corteville et al., 1991) or “clearly violating basic physical principles” (Hasan and Kabir, 2002). Note that unlike the previous group of petroleum investigators identified in Section 3.4.2.3 in which there was a wide difference in understanding, the group of Petroleum investigators above display an evident difference

in awareness. In fact, in some cases, some of the modelers belonging to this group will change a correct, factual experiment result to suit their incorrect perceptions, as seen in:

I. The manipulation of the Beggs and Brill (1973) experimental results in Gould and Ramsey (1977).

II. The manipulation of the original Hagedorn and Brown (1965) method (based on the experiments of Hagedorn, 1964) as a variation found in many petroleum industry multiphase flow codes.

III. The somewhat routine manipulation of the holdup calculations from multiphase flow models by petroleum investigators when a negative averaged slip velocity results from the model (e.g., Corteville et al., 1991).

In other cases, and quite surprising from a model testing standpoint, some of the modelers of this group of Petroleum investigators in their statistical model evaluation analyses, will exclude (or "screen") large amounts of experimental data generated by laboratories and field data that show a negative averaged slip result (e.g., Thompson, 1982, Ansari, 1988, Dhulesia and Lopez, 1996). Clearly, the result of being unaware of the large bodies of work conducted by investigators outside of one's immediate discipline, can lead to demonstrably incorrect assumptions. Unfortunately, these perceptions continue to exist at present, as evidenced in the various "no-slip" modifications for upward vapor-liquid flow models found in many petroleum industry multiphase pipe flow codes.

3.4.2.6 Developing Bubbly Flow: Gas-Lift Application

Apart from developed bubbly flow, there are large amounts of investigations concerning developing bubbly flow (e.g., Mendez-Diaz et al., 2012; Qi et al., 2012;

Morel et al., 2010; Krepper et al., 2005; Takamasa et al., 2003; Guet et al., 2003; Hibiki et al., 2001; Ilic and Senyolcu, 1989). These investigations offer valuable insight into the bubbly flow development along the conduit, which is most analogous to the continuous flow development occurring in field scale applications. As noted in Liu (1997), the bubble lateral distribution and migration effects are very sensitive to the variation in average bubble size and bubble coalescence/break up effects during the development of the flow. Mendez-Diaz et al. (2012) also demonstrated changes in both the peaking behavior as well as the average bubble size with axial position.

It must be noted that the same lateral distribution observations discussed in the previous section is similarly present at different axial locations along the development of the flow. For example, Fig. 3.4.12 shows three datasets from the air (phase 2) and water (phase 1) experiments of Takamasa et al. (2003) for which the void fraction profiles were obtained just three diameters from the test section entrance. Similar to the developed flow observations of Figs. 3.4.9 and 3.4.10, Fig. 3.4.12 shows that an increase in the gas flow rate (from 0.013 to 0.052 m/s) at constant liquid flow rate (0.58 m/s) tends to augment the void fraction albeit changing the peaking behavior in the process (Fig. 3.4.12-a to Fig. 3.4.12-b). Then, an increase in the liquid flow rate (from 0.58 to 1 m/s) at a constant gas flow rate (0.052 m/s) does not significantly change the void fraction or its peaking behavior (Fig. 3.4.12-b to Fig. 3.4.12-c).

Additionally, in Takamasa et al. (2003), careful measurements of the void fraction cross-sectional distributions along the conduit were performed, an example of which, is the controlled low averaged void fraction scenario of an increasing gas flow rate (from 0.013 m/s to 1 m/s) at a constant liquid flow rate (0.58 m/s). Fig. 3.4.13 shows these two upward bubbly flow cases in which it can be clearly seen that the accelerating gas along the conduit displays a higher slip behavior (i.e., further from the $\Omega_{2,1} = 0$ line) at higher

gas flow rates for the same liquid flow rate. As discussed in Takamasa et al. (2003), the reason for this behavior is explained in the void fraction cross-sectional profiles for these experiments in which it was observed that the wall-peaking was enhanced along the flow direction at the lower gas flow rate, resulting in less averaged slip (greater bubble residence times). Conversely, at the higher gas flow rate, less-pronounced wall peaking was observed and bubbles migrated toward the conduit core region far downstream of the flow, resulting in more slip (lower bubble residence times).

While the above results may seem benign, they are directly applicable to practical applications where an improved understanding of upward bubbly flow can prove beneficial to their optimization – such as the example of the gas-lift process in petroleum production systems. Guet and Ooms (2006) provide an overview of this process. The fluid mechanical phenomena already described in sections 3.4.2.1 – 3.4.2.5 and in this section can all be found in the upward bubbly flow aspect of the gas-lift process. Therefore, the observations and averaged flow modeling of these phenomena can be utilized in the optimization of this important practical application.

For example, in aiming to reduce the gravitational pressure gradient, the axial evolution of the area-averaged void fraction associated with given global flow conditions should ideally result in higher bubble residence times, i.e., lower bubble relative motion or lower slip and thus higher liquid production. This would mean an enhancement of a wall-peaking bubbly structure along the flow direction is desirable by ensuring more evenly distributed smaller bubbles (rather than core-peaking larger ones) and thus a higher area-averaged void fraction. A difficulty that exists in gas-lift scenarios, however, is the lack of operator control of the average bubble size due to:

I. The fairly long distances (and thus decreasing pressure and bubble size growth) the bubbles have to travel in a typical production wellbore, e.g., about 1 – 3 km.

II. The continuous release of dissolved gas coming out of solution for complex petroleum fluids as the pressure, temperature and composition changes.

The solution gas issue in II above is more problematic than first appears. It means that regardless of the upstream changes that may be made to the gas-lift process, for example, controlling the gas injection rate or the inlet valve chamber (bubble generator) configuration, the mass exchange behavior of the petroleum fluid would introduce an increasing amount of dissolved gas along the flow direction. It would therefore seem more prudent that the control of the average bubble size or its lateral distribution would stand a far better chance of success by making changes to the bubbly flow along the flow path. For example, optimum gas-lift valve placement along the flow path would result in improved control of the axially developing bubbly structure. As another example, optimum placement (and selection) of instruments along the flow path that would cause a reduced bubble size would result in improved control of the bubble size (e.g., Koide et al. 1968; Chiba and Takahashi, 1998; Fujikawa et al., 2003; Kawamura et al., 2004).

Next, Fig. 3.4.14 shows an important observation of bubbly flow development – that at higher liquid rates and low averaged void fraction (Fig.3.4.14-b), the flow tends to evolve towards a wall-peaking structure, whereas for lower liquid rates and higher averaged void fraction (Fig. 3.4.14-a), the flow tends to evolve towards a core-peaking structure. These datasets were taken from Mendez-Diaz et al. (2012). The reason they were selected beyond the clear observations regarding the axial position influence on the peaking behavior, is that their resulting area-averaged void fraction is mathematically

equivalent to a no-global-slip averaged flow result for both experiments. Clearly, these results indicate that it would be difficult to see how an averaged flow model (two-fluid or not) can provide definitive answers concerning the local physical inhomogeneity that can exist along the bubbly flow path (i.e., the non-flat void fraction profiles) in a no-global-slip scenario. As shown in these simple experiments, no-global-slip is an averaged-flow mathematical result and cannot provide information on whether the flow is locally homogenous (well-mixed) or not. No-global-slip in an averaged multiphase flow simply means that the in-situ (time- and area-averaged) velocities of the flowing phases are equal.

Finally, as discussed in Section 2.2.7, as long as a pressure gradient exists, the interactions among different phenomena will be coupled and there will be continuous competition among them that will cause the flow to continually evolve at the local level along the axial flow path. These interactions are *already* mathematically represented in the choices for the specific closure relations as well as in the conservation equations themselves. Therefore, the analytical averaged-equations models discussed in the previous chapter (without modification) will remain applicable at the local level along the flow path in the developing flow, i.e., on an incremental or point-by-point basis. The flow development (in any multiphase flow scenario including the bubbly flow applications previously discussed) is thus captured in the way the pipe system is segmented, as discussed in Sections 2.2.7.3 and 2.2.7.4.

3.4.2.7 Global (Area-Averaged) Bubbly Flow Prediction

We may next ask: how well do the analytical, averaged-equations mixture models developed in the previous chapter as well as the analytical fractional flow theory developed in this chapter, predict the averaged flow characteristics of bubbly flows? In

our methods, the way in which the phases distribute across the pipe have a fundamental influence on important averaged flow parameters such the wall shear stress or wall heat transfer coefficients via the area-averaged void fraction.

If we consider one bubbly flow characteristic, the wall shear stress for the flowing mixture, we can quantify the performance of the combination of the Nagoo-Sharma equations (Chapter 2) and the fractional flow theory (Chapter 3) against published bubbly flow wall shear stress data. Among the several experimental studies qualitatively relating the lateral phase distribution effect on the wall shear stress in bubbly flows (e.g., Davis, 1974; Herringe and Davis 1978; Nakoryakov et al., 1981; Avdeev 1984), we select the quantitative air (phase 2) and salts-in-distilled-water (phase 1) experimental results of Kashinsky and Randin (1999). In these carefully-controlled experiments, the mean cross-sectional wall shear stress was obtained by averaging the readings of eight wall-mounted circumferential probes in which local flow parameters were measured with an electrochemical method (Nakoryakov et al. 1981).

In Fig. 3.4.15, all of the averaged volume fraction and mixture wall shear stress measurements from Table 1 of Kashinsky and Randin (1999) are shown as the points in Fig. 3.4.15 (a-i) and Fig. 3.4.15 (a-ii). The lines in Fig. 3.4.15 (a-ii) are the calculations of $\tau_{1\rightarrow wall} + \tau_{2\rightarrow wall}$ $(= \tau_{mix\rightarrow wall})$ in Eqn. 6 of Section 2.2.4 with the measured values of $\langle s_2 \rangle$ given in the experiments, i.e., Fig. 3.4.15 (a-i). The lines in Fig. 3.4.15 (b-i) are the calculations of the NOSLIP model, and the lines in Fig. 3.4.15 (b-ii) are the calculations of $\tau_{mix\rightarrow wall}$ in Eqn. 6 of Section 2.2.4 with the NOSLIP model. As is evident, there is excellent agreement of all of the wall shear stress measurements with the analytical predictions of the Pipe Fractional Flow Theory.

We can even extend the predictions of bubbly flow characteristics to cases in which the longitudinal spatial arrangement of different sizes of bubbles are classified as

another flow pattern, such as the case of slug flow. In slug flow, there is a large bubble (the "Taylor bubble" or the "Gas Unit") followed by a collection of smaller-sized bubbles dispersed in the liquid slug. The study of Zheng and Che (2006) provides nitrogen (phase 2) and sodium-hydroxide-salt-electrolyte (phase 1) experimental results on several flow characteristics of upward vapor-liquid slug flow, in which there are measurements of time-averaged void fraction profiles both in the gas unit and liquid slug of an overall slug unit. Fig. 3.4.16 shows the measurements of these void fraction profiles and their resulting area-averaged void fraction (the light-blue and blue solid horizontal lines) for one of the global flow conditions in Table 3 of the reference (i.e., $\langle u_1 \rangle$ = 0.446 m/s, $\langle u_2 \rangle$ = 0.452 m/s). For this case, the area-averaged void fraction for the gas unit, liquid slug and overall slug unit are given in the reference as 0.475, 0.18 and 0.384, respectively.

Since the fractional flow theory only provides an area-averaged void fraction, $\langle s_2 \rangle$, for the flowing mixture (i.e., the mean value for the collection of differently-sized bubbles in the overall slug unit) at the axial location of interest, it cannot differentiate between the area-averaged void fraction contributions of the gas unit and the liquid slug separately. This is because there are no a-priori constitutive correlations or models for these quantities that are required by the fractional flow theory, i.e., these quantities remain as unknowns during the flow. Nevertheless, it is quite obvious from Fig. 3.4.16 that the area-averaged void fraction for the overall slug unit (the red solid line) is accurately predicted by any of the ANSLIP, WOLGHA or NICKLIN models shown (the dashed horizontal lines). This result is more useful than first appears because it means that this global prediction could be used to back-calculate any of the local flow parameters (e.g., the area-averaged void fraction in the gas unit) using existing correlations or models in the published literature. In this latter scenario, the net effect of the local, competing flow microphysics is known from the Pipe Fractional Flow Theory,

and this net result describing the collective behavior of the flowing mixture can then be used to restrain the existing correlations or models of the flow characteristics.

Finally, Fig. 3.4.17 shows the excellent agreement of the phase-2 fractional flow calculations (using the wholly-analytical ANSLIP model) against the slug unit phase-2 volume fraction measurements for all of the upward slug flow data in Zheng and Che (2006).

3.5 FINDING FRACTIONAL FLOW PATHS: RECOMMENDED EQUATIONS

Based on the fractional flow behavior of the sundry two-phase flow correlations discussed in this chapter in comparison with the numerous datasets in Chapters 4 to 7, it is found that only a few analytical models and existing correlations can be relied upon for satisfactory prediction of averaged volume fraction. Although there are several instances where no existing analytical model/correlation is capable of predicting the observed fractional flow behavior in some experiments (e.g., Fig. 3.4.6), it is still required from a design standpoint that the "overall best" among the available analytical models/correlations be identified. In this section, we simply summarize our recommended averaged two-phase flow analytical models and correlations, with the subsequent proof of their accuracy (and applicability) demonstrated in Chapters 4 to 7. Since two-phase flow models form the building blocks for three-phase flows, any of the analytical models and correlations in Table 3.2 can be extended in the scenarios of vapor-liquid-liquid and vapor-liquid-solid flows.

In Table 3.2, the analytical models and correlations are listed in their order of expected overall accuracy. The top-most listed analytical model/correlation (in bold, blue text) within each category represents the first choice to be tested (among the rest) in a new modeling or design scenario. This is not to say that other analytical

models/correlations excluded from this table, will fail to provide an adequate representation of volume fraction data in a particular application. Table 3.2 simply provides general guidance to investigators in terms of arriving at (hopefully) reliable estimates of averaged volume fraction in a new modeling or design scenario, based on the vast amounts of measured averaged volume fraction data analyzed in this work.

Lastly, the 100% liquid entrainment (e.g., in the case of a two-phase flow, $E_{1\rightarrow 2} = 1$) models discussed in Section 2.2.6 and in Appendix F, form another wholly-analytical model to be added to Table 3.2 for use in vapor-liquid and vapor-liquid-liquid applications. 100% liquid entrainment is hereafter referred to as the "MIST" flow model in this work. Therefore, it is the general finding of this work that only four analytical models (NOSLIP, ANSLIP, SLIPRATIO and MIST) and three existing correlations (WOLGHA, BUTTERWORTH and NICKLIN) are required to satisfactorily represent a wide range of averaged volume fraction behaviors. Additionally, for flows with inter-phase entrainment, it is found in this work (and also demonstrated) that the simple Ishii and Mishima (1982) entrainment correlation provides a satisfactory approximation for liquid entrainment fraction for a wide range of scenarios. These analytical models and correlations will be used in various applications throughout Chapters 4 to 7.

Category	Mixture Reynolds Number: $\frac{\rho_1 \langle u_{mix} \rangle D_H}{\mu_1}$		a	C
	Lower limit	Upper limit		
1	< 2000	2000	0.639	0.3372
2	2000	5000	0.4583	0.4379
3	5000	10000	0.5568	0.4424
4	10000	20000	0.5147	0.5693
5	20000	40000	0.5395	0.6215
6	40000	100000	0.5673	0.7095
7	100000	300000	0.6252	0.6735
8	300000	2670000	0.5407	1.1916

Table 3.1: Parameters "a" and "C" of Eqn. 43 in Section 3.3.2.

Phase Combination	Pipe Inclination	Analytical Models	Empirical Correlations
Vapor-Liquid	Up-Vertical, Up-Inclined, Horizontal and Down-Vertical	**ANSLIP** NOSLIP SLIPRATIO	**WOLGHA** BUTTERWORTH NICKLIN
	Down-Inclined	**SLIPRATIO** NOSLIP	**BUTTERWORTH** WOLGHA
	Liquid Column	**ANSLIP** SLIPRATIO	**NICKLIN** WOLGHA
Liquid-Liquid	Up-Vertical, Up-Inclined, Horizontal and Down-Vertical	**NOSLIP** ANSLIP SLIPRATIO	**WOLGHA** BUTTERWORTH
	Down-Inclined	**NOSLIP** SLIPRATIO	**BUTTERWORTH** WOLGHA
Fluid-Solid	All	**SLIPRATIO**	**BUTTERWORTH**

Table 3.2: Recommended averaged volume fraction models and correlations for two-phase flow modeling and design.

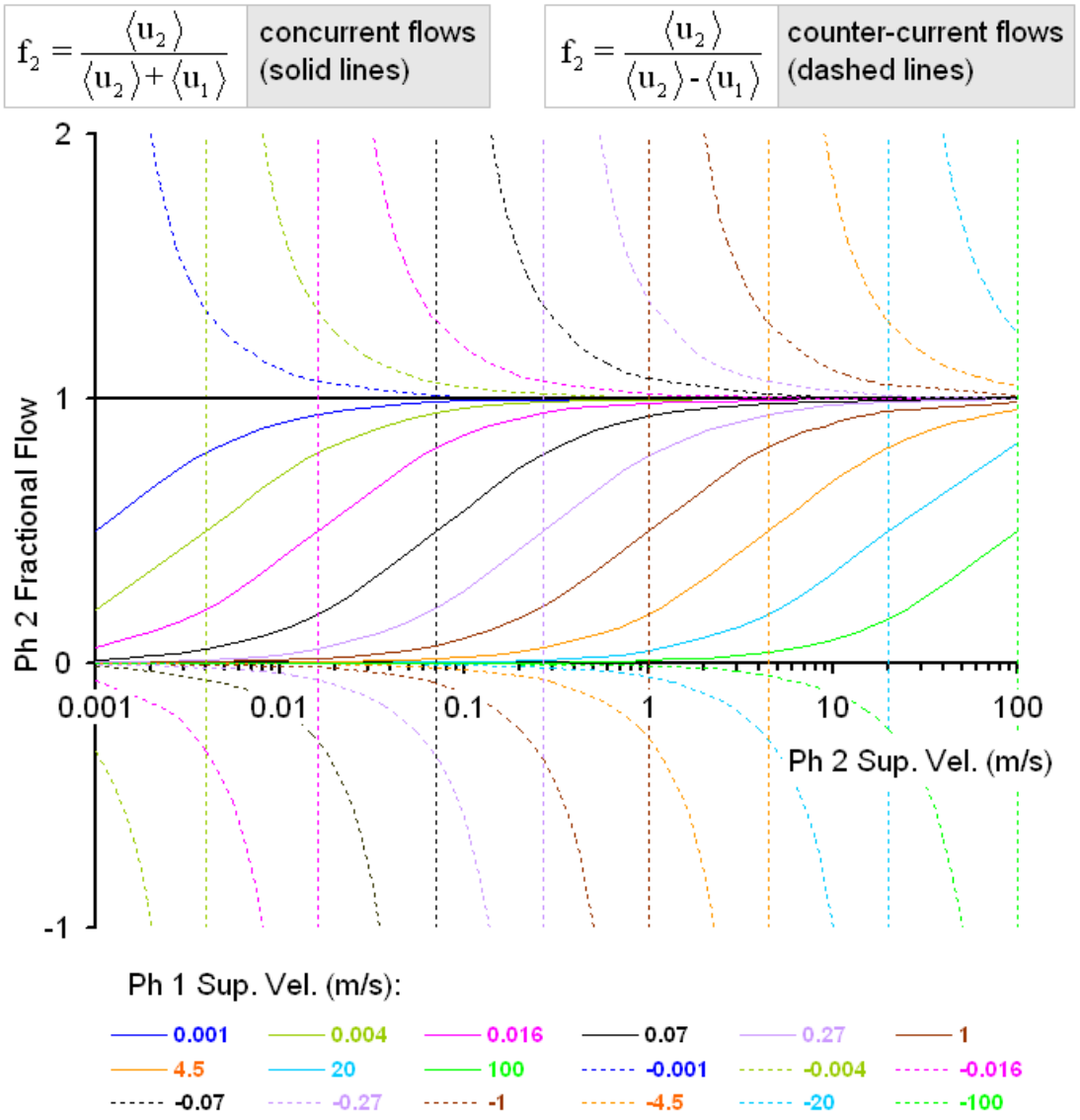

Figure 3.1.1: Phase 2 fractional flow as a function of phase 1 and phase 2 superficial velocities.

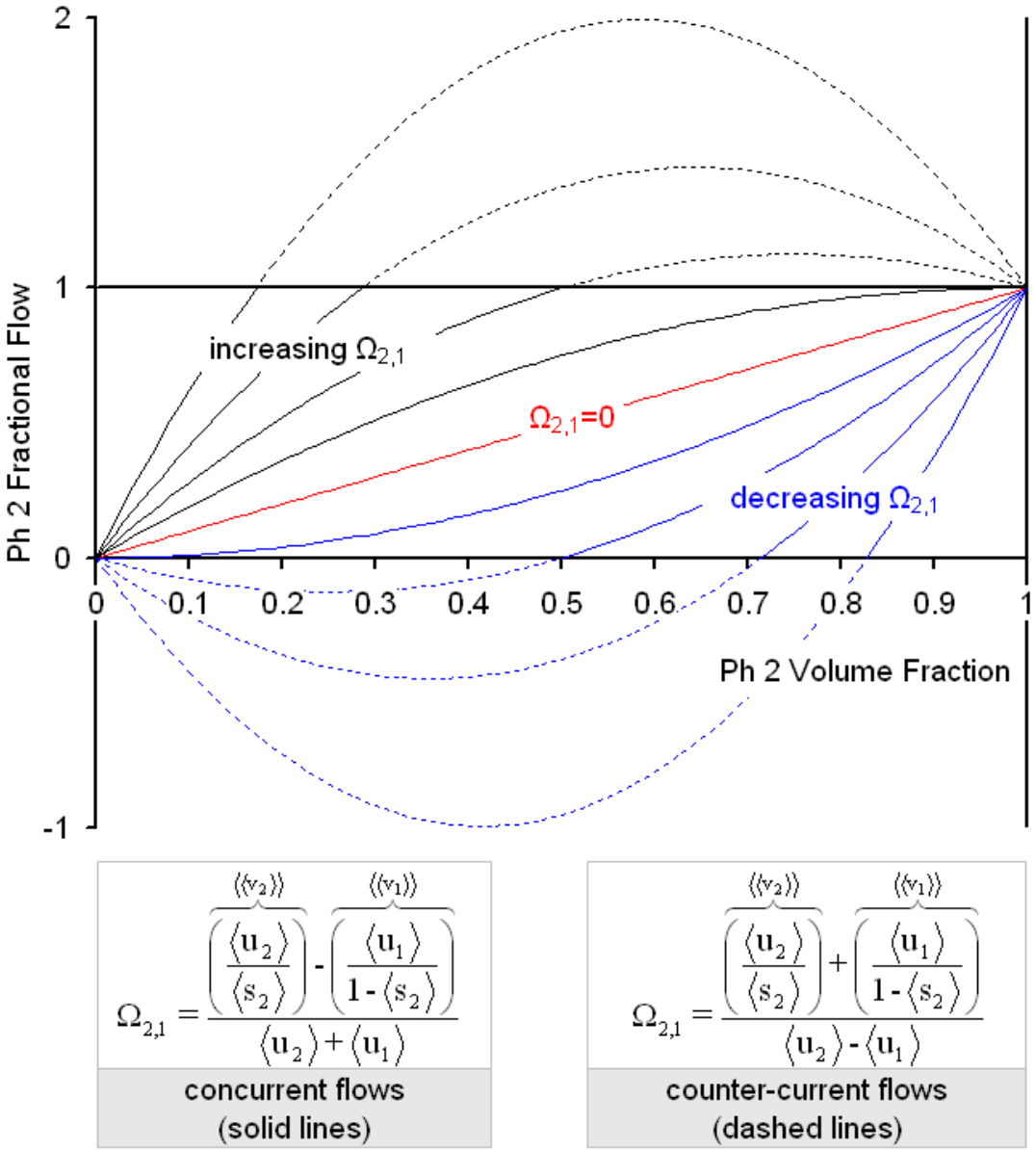

Figure 3.1.2: Phase 2 fractional flow as a function of dimensionless relative velocity and phase 2 volume fraction.

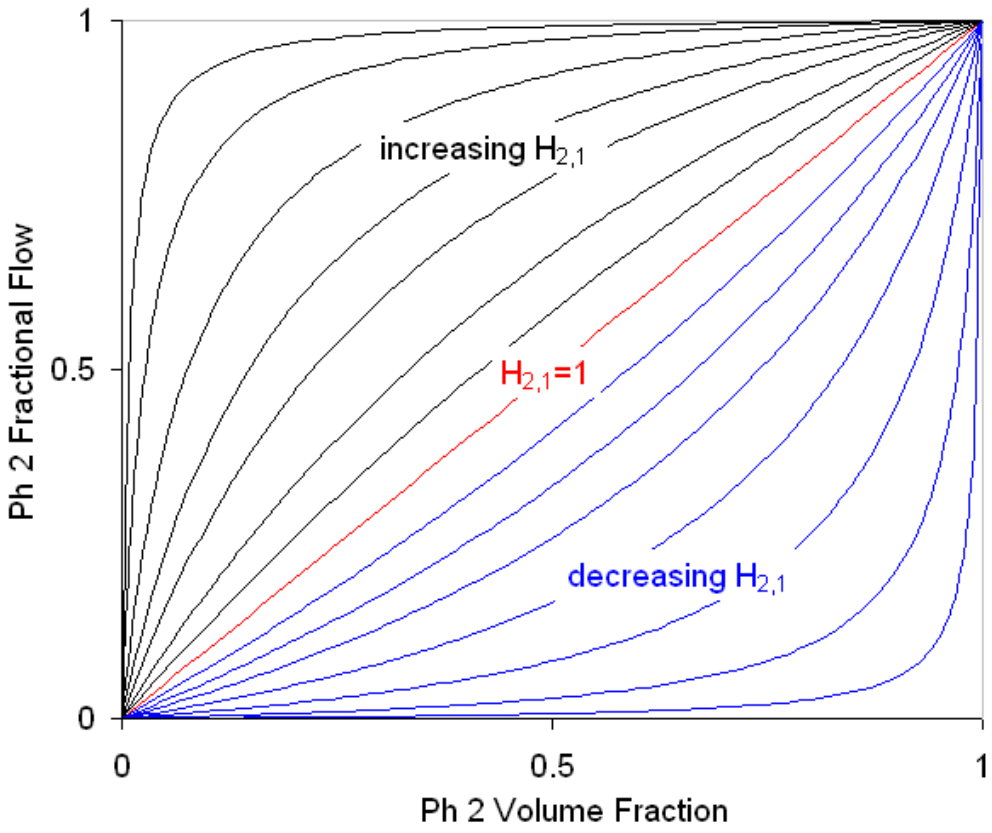

Figure 3.1.3: Phase 2 fractional flow as a function of dimensionless slip ratio and phase 2 volume fraction.

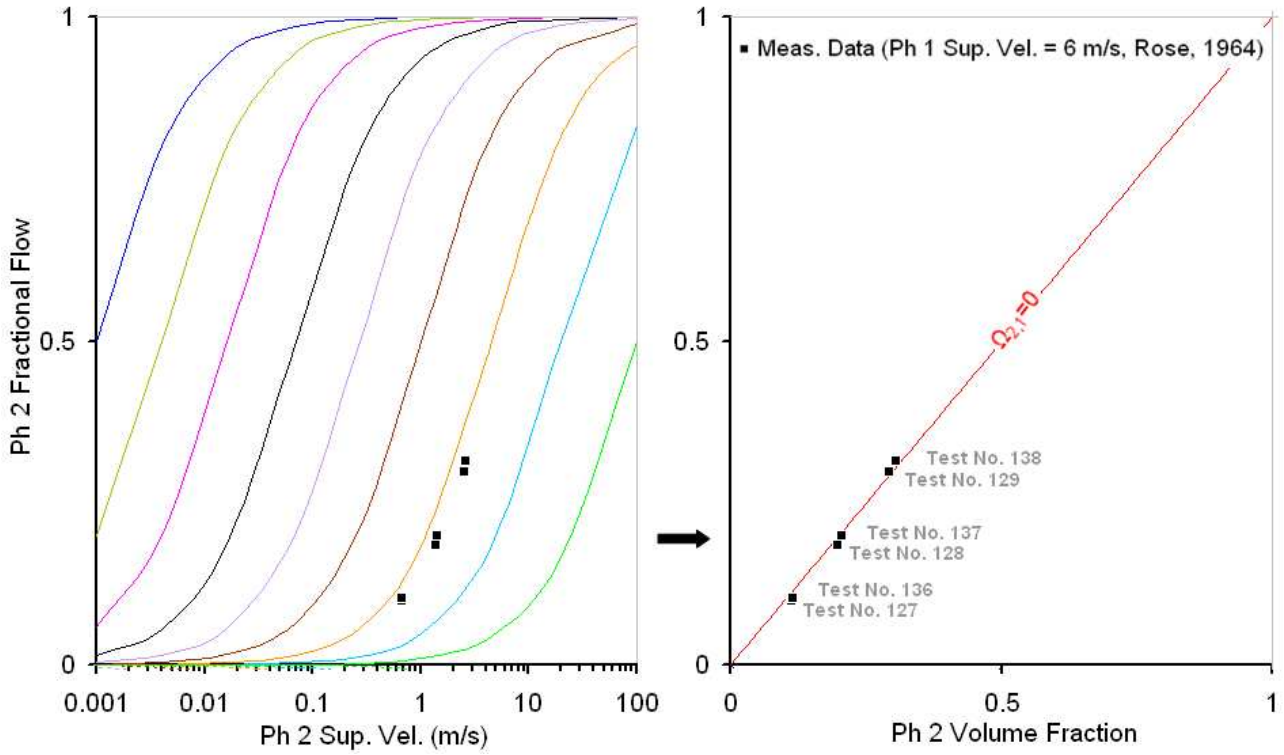

Figure 3.2.1: An example vapor-liquid fractional flow graph (right chart) of phase 2 (air) with the NOSLIP model. The legend for the left-most chart is the same as Figure 3.1.1.

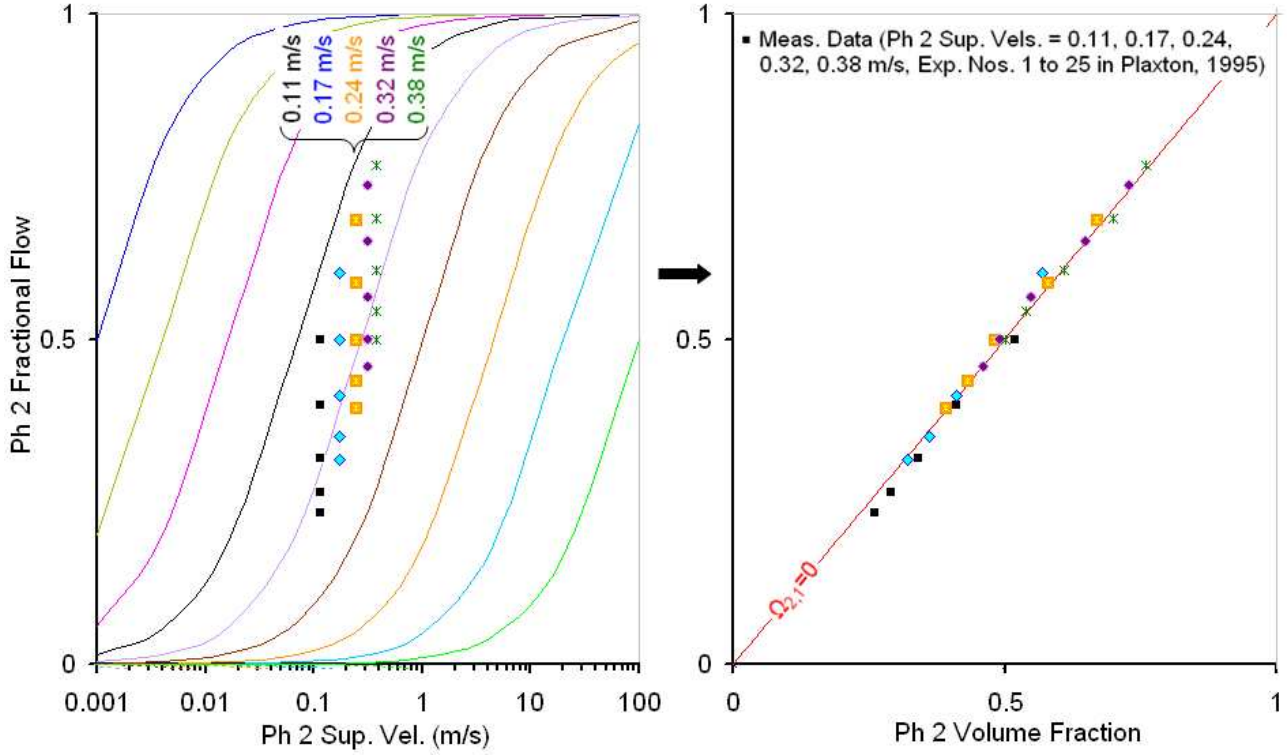

Figure 3.2.2: An example liquid-liquid fractional flow graph (right chart) of phase 2 (light refinery stream oil) with the NOSLIP model. The legend for the left-most chart is the same as Figure 3.1.1.

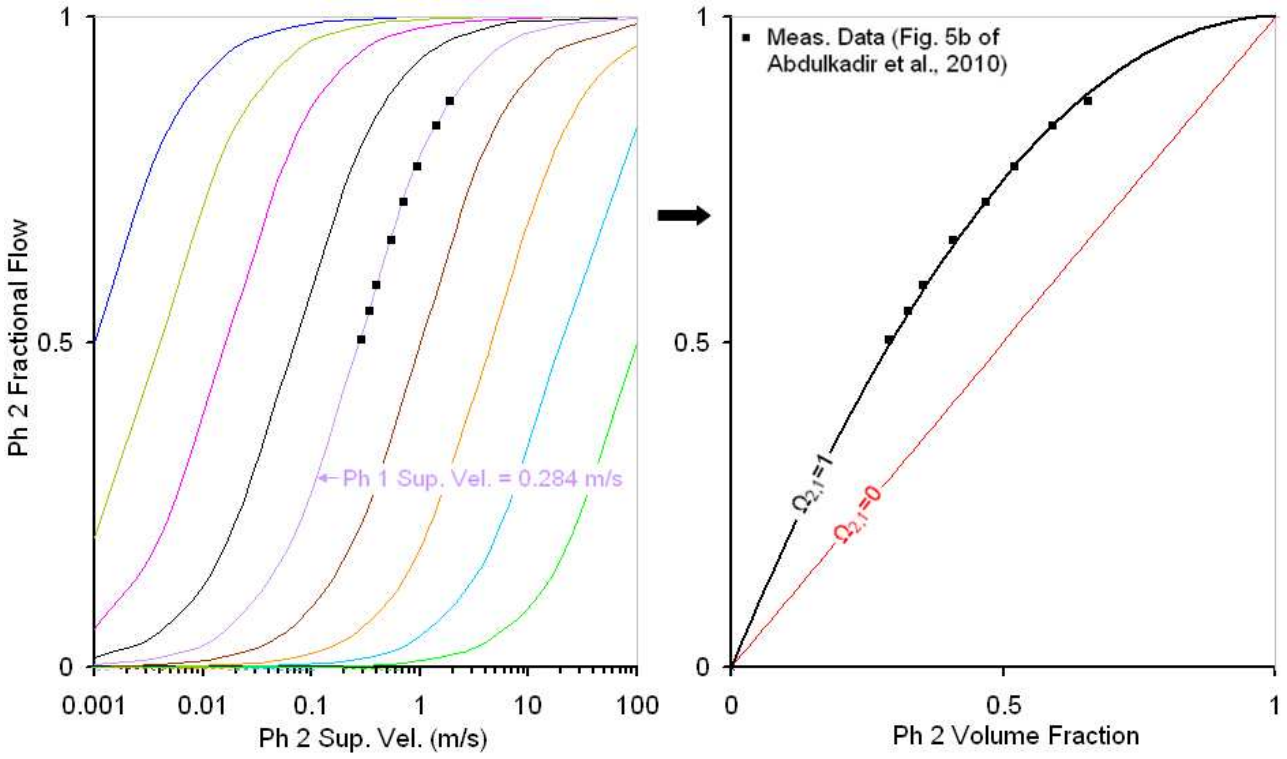

Figure 3.2.3: An example vapor-liquid fractional flow graph (right chart) of phase 2 (air) for a constant dimensionless relative velocity. The legend for the left-most chart is the same as Figure 3.1.1.

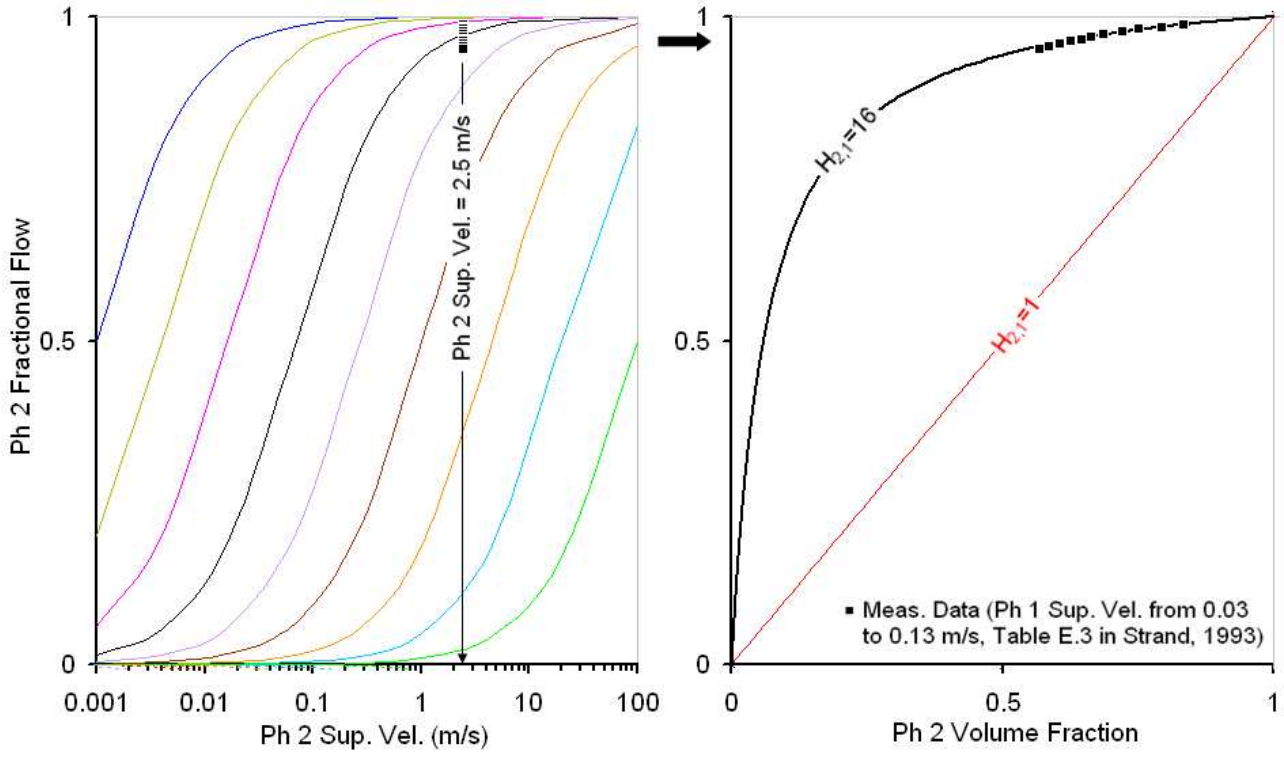

Figure 3.2.4: An example vapor-liquid fractional flow graph (right chart) of phase 2 (air) for a constant dimensionless slip ratio, i.e., the SLIPRATIO model. The legend for the left-most chart is the same as Figure 3.1.1.

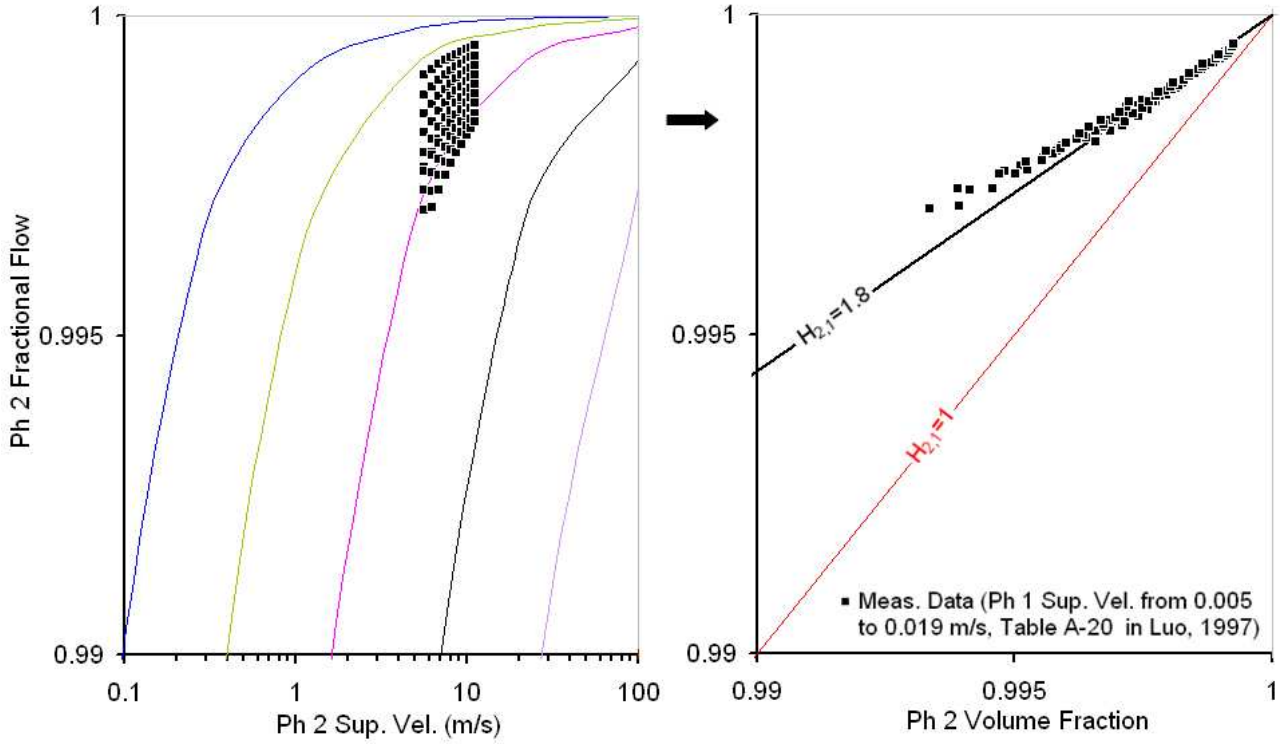

Figure 3.2.5: An example vapor-solid fractional flow graph (right chart) of phase 2 (air) for a constant dimensionless slip ratio, i.e., the SLIPRATIO model. The legend for the left-most chart is the same as Figure 3.1.1.

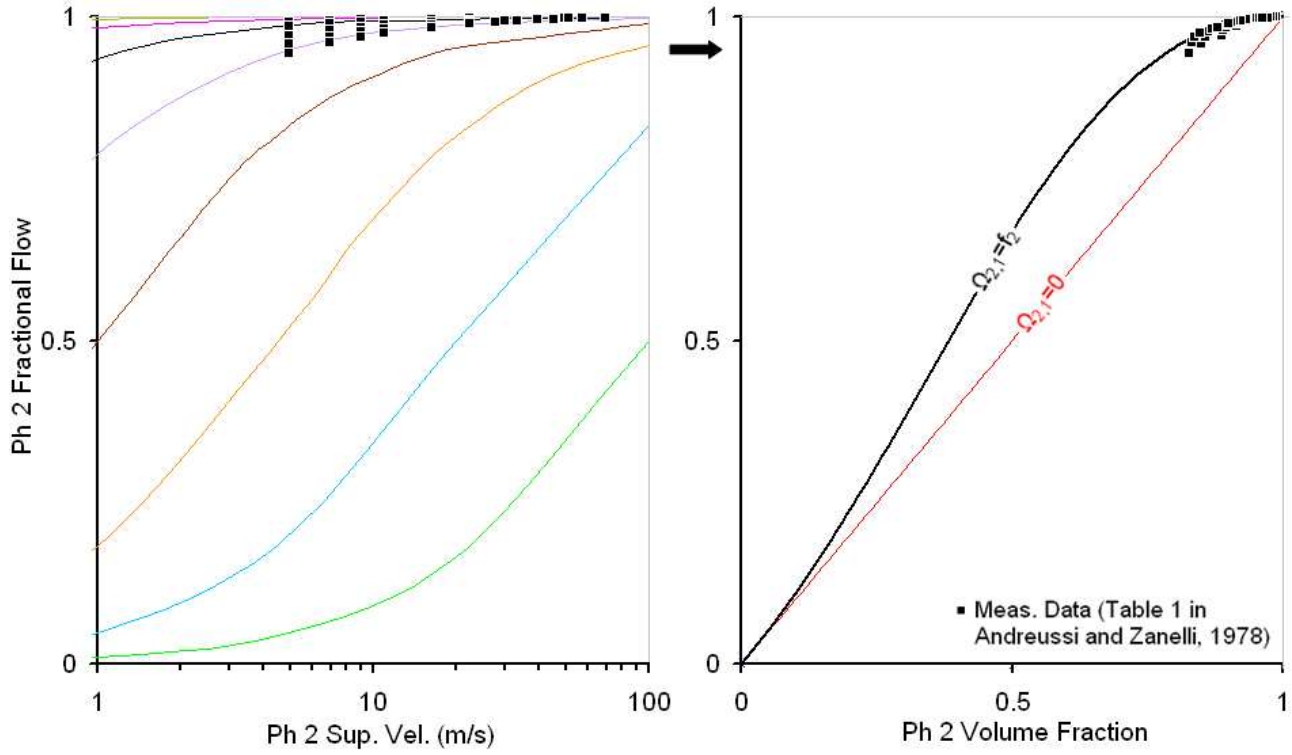

Figure 3.2.6: An example vapor-liquid fractional flow graph (right chart) of phase 2 (air) for the annular flow pattern with the ANSLIP model. The legend for the left-most chart is the same as Figure 3.1.1.

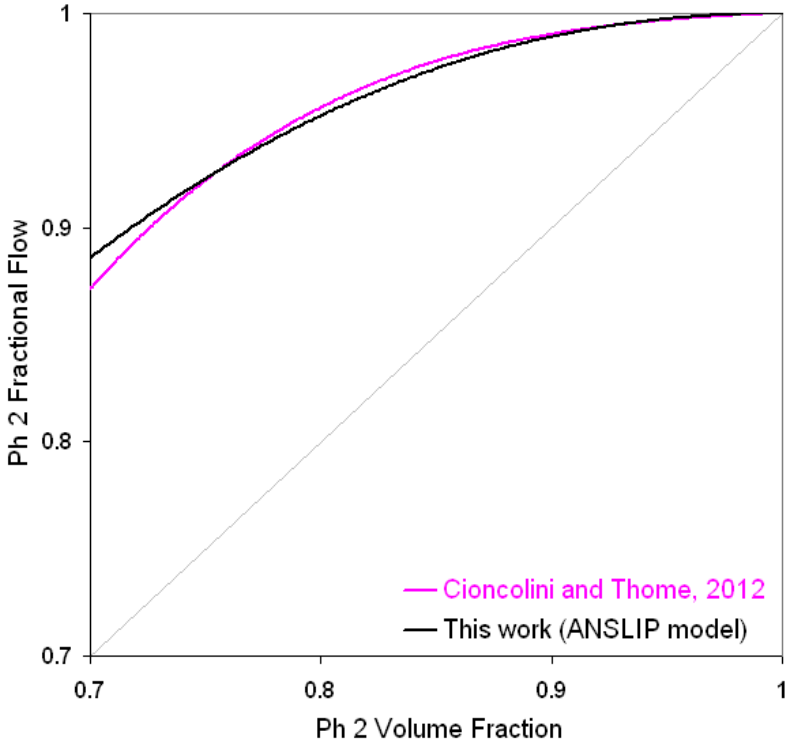

Figure 3.2.7: Comparison of the analytical ANSLIP model against a vapor (phase 2) and liquid (phase 1) annular flow empirical correlation (Cioncolini and Thome, 2012). The underlying experimental database for the correlation shown contains 2,633 datapoints for circular tubes covering macroscale to microscale flow conditions and 40 additional datapoints for non-circular channels.

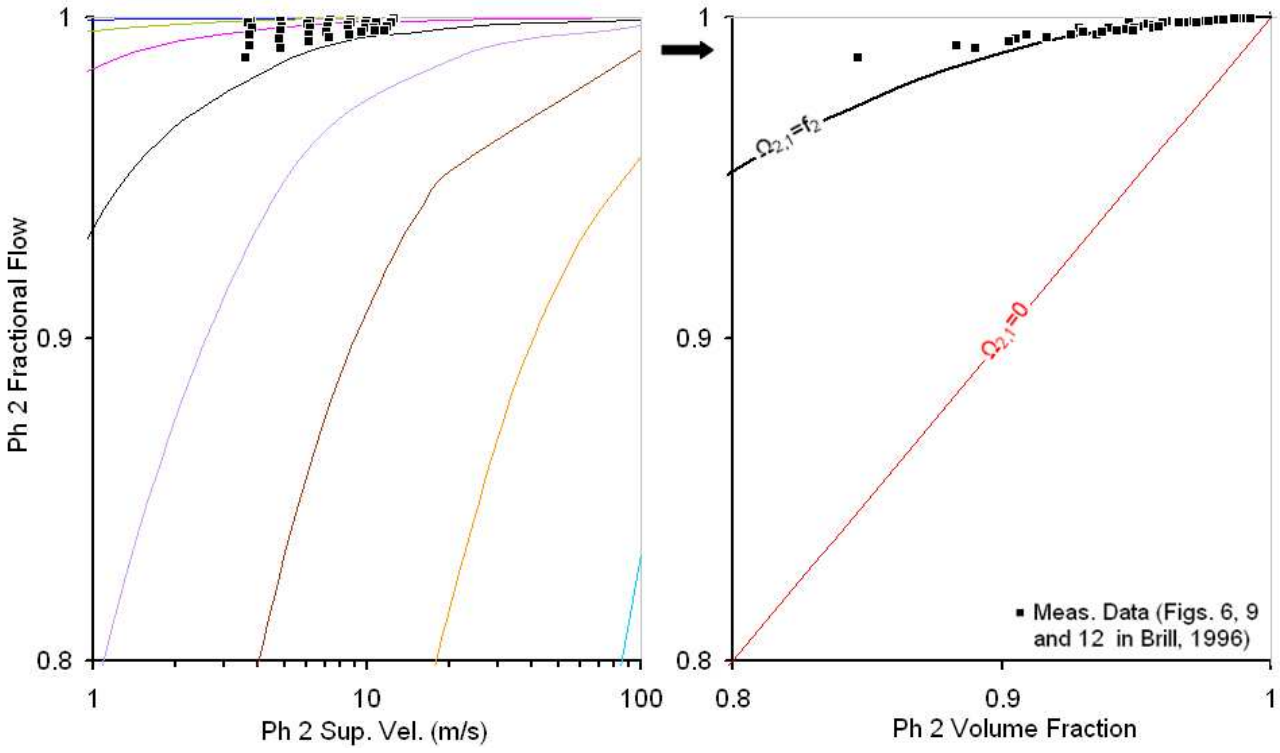

Figure 3.2.8: An example vapor-liquid fractional flow graph (right chart) of phase 2 (air) for the stratified-wavy flow pattern with the ANSLIP model. The legend for the left-most chart is the same as Figure 3.1.1.

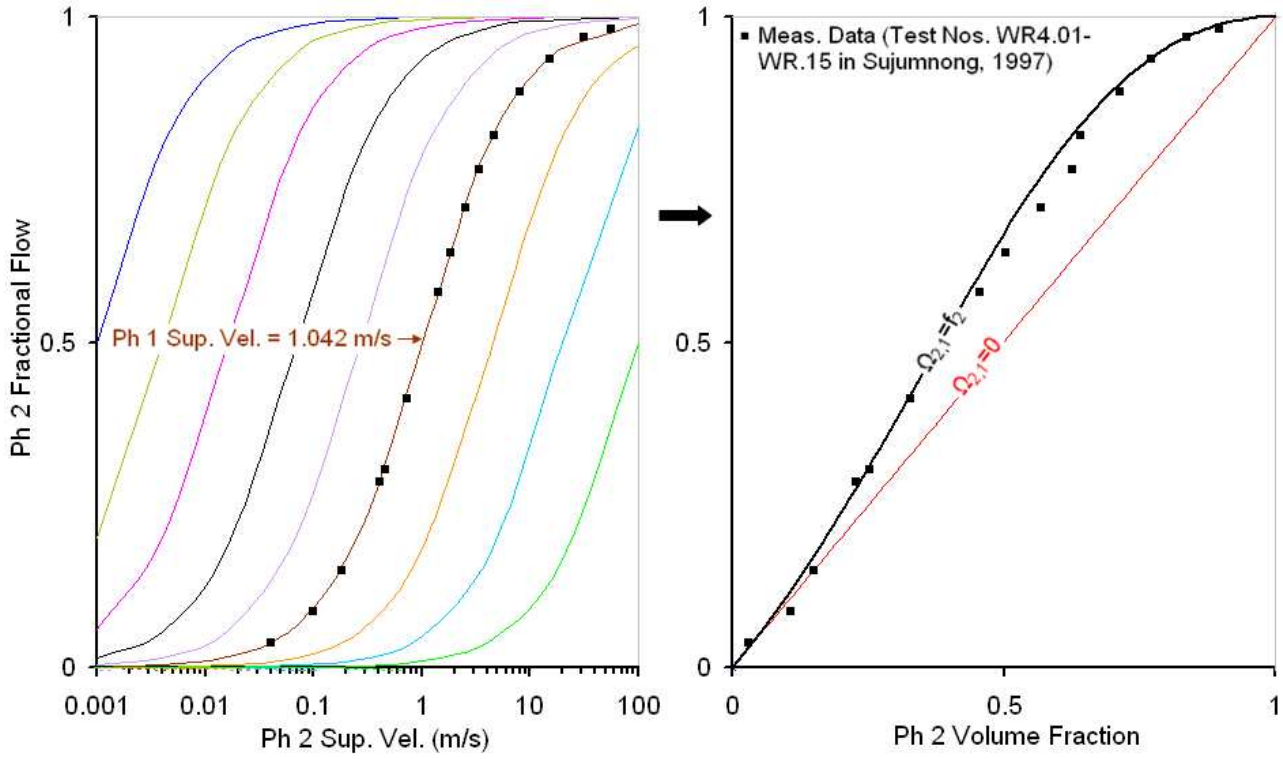

Figure 3.2.9: An example vapor-liquid fractional flow graph (right chart) of phase 2 (air) for the full range of flow patterns with the ANSLIP model. The legend for the left-most chart is the same as Figure 3.1.1.

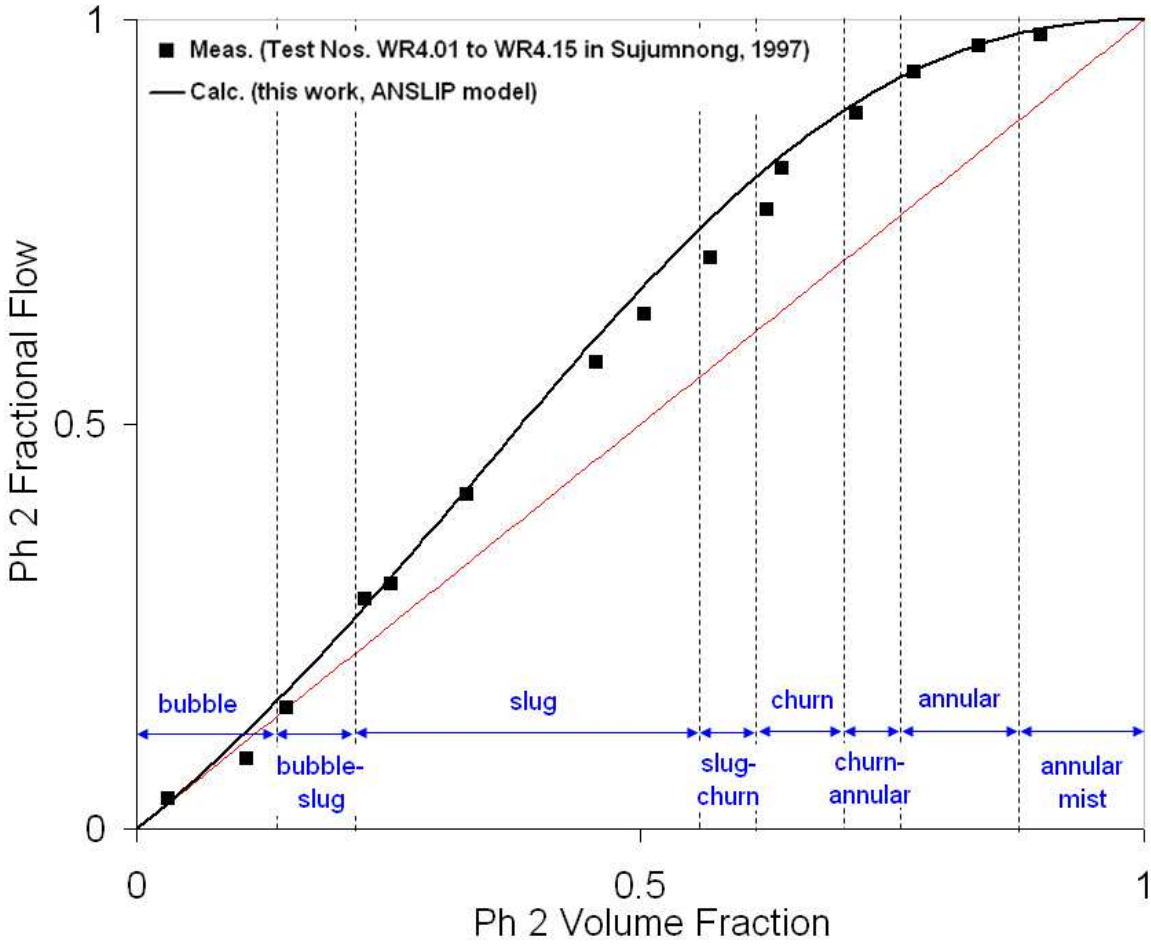

Figure 3.2.10: Demonstrating how a model (the ANSLIP model in this case) can form a fractional flow path which transitions through the full range of flow patterns.

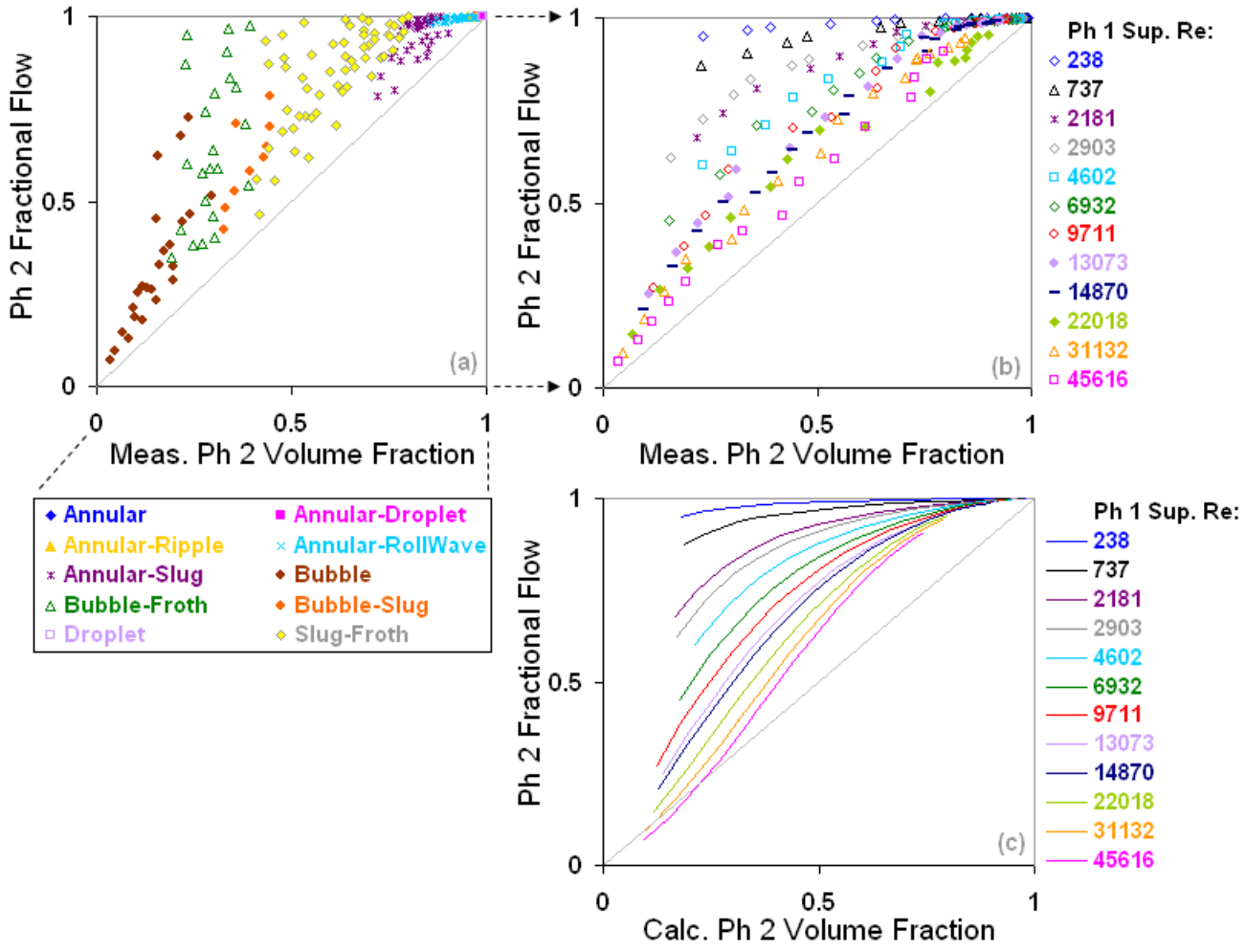

Figure 3.3.1: Demonstrating how a model (the WOLGHA model in this case) can form multiple fractional flow paths which transition through the full range of flow patterns. The 221 air (phase 2)-water (phase 1) tests shown are from Spedding and Nguyen (1976).

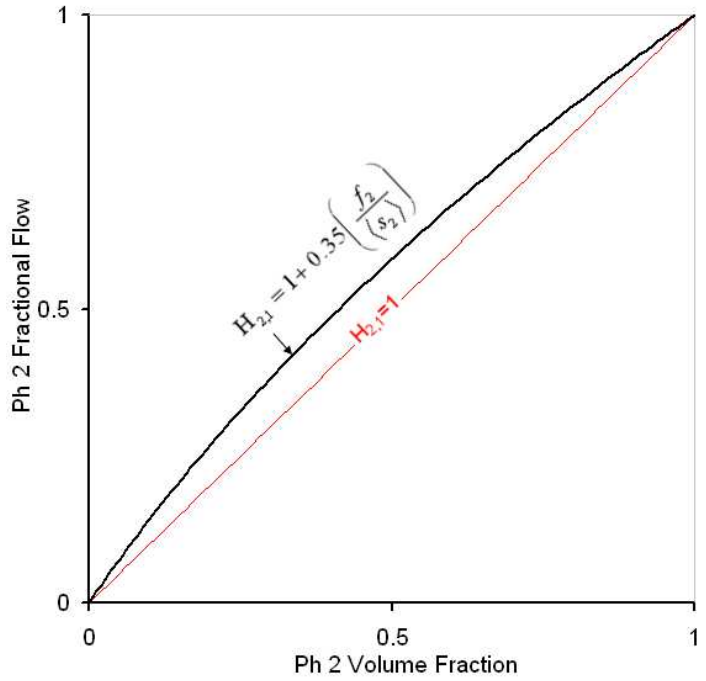

Figure 3.3.2: An example liquid-liquid fractional flow model: Eqn. 42 in Sec. 3.3.2

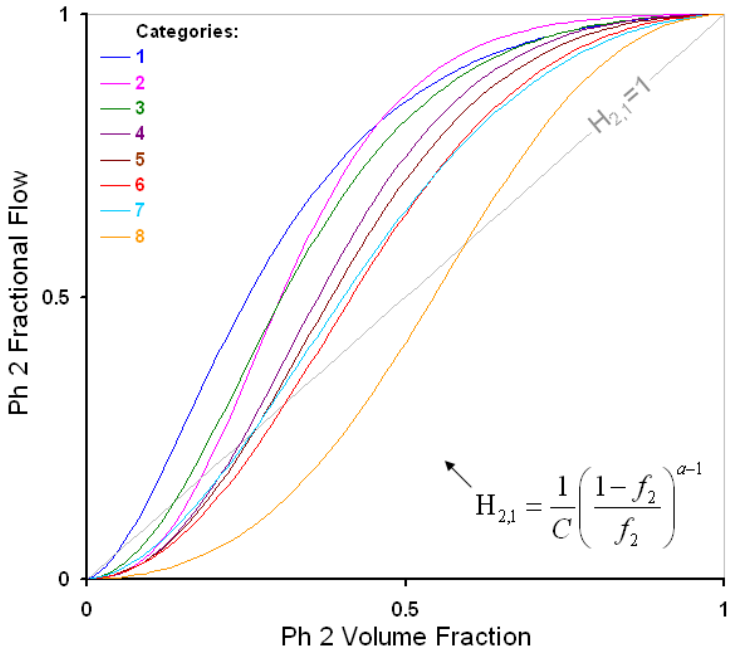

Figure 3.3.3: An example vapor-liquid fractional flow model: Eqn. 43 in Sec. 3.3.2

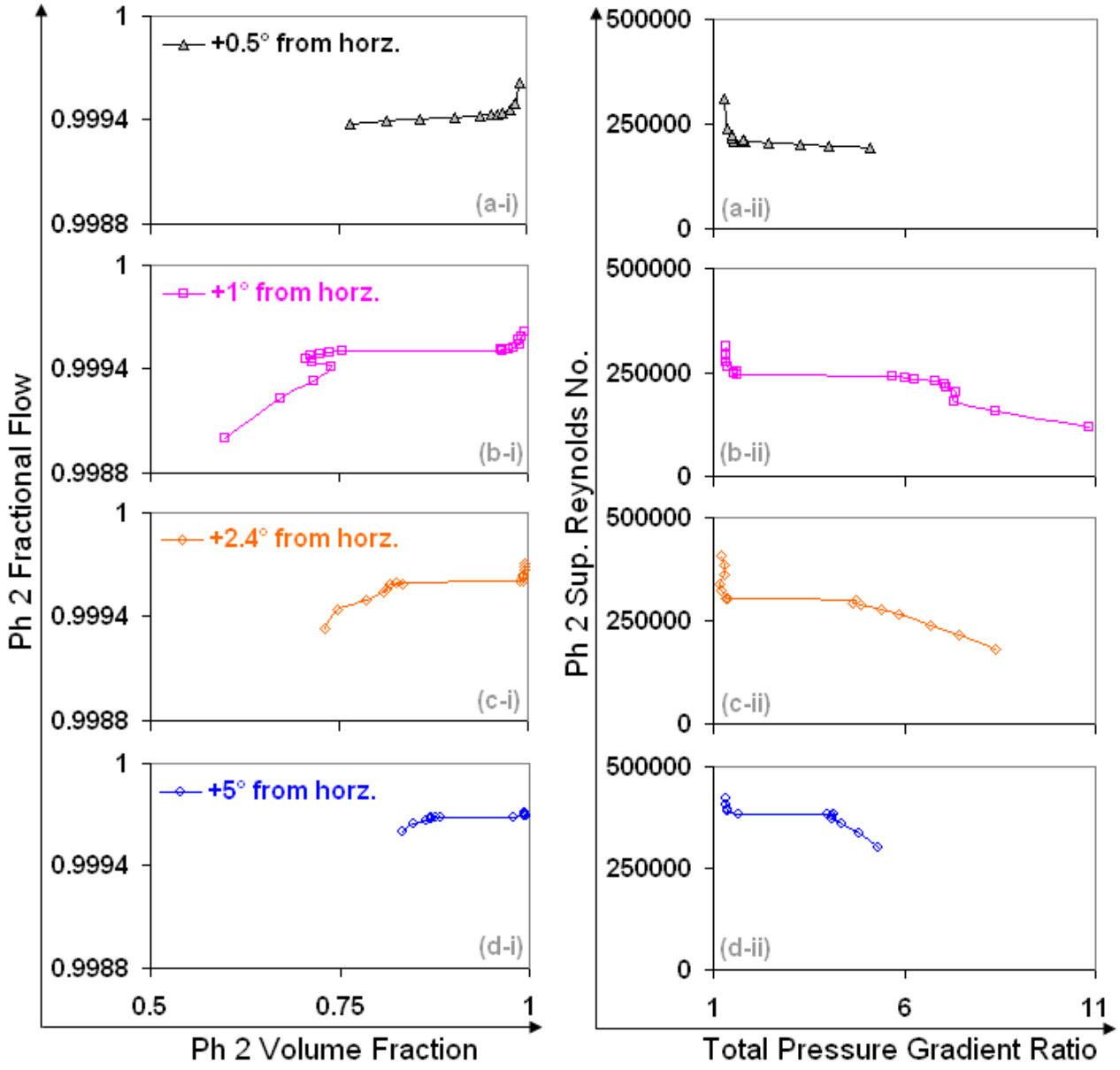

Figure 3.4.1: Demonstrating how sharp-transition phenomena (in this case, the sharp changes in volume fraction sometimes observed in slight up-inclined vapor-liquid wavy-ripply flows) are represented as fractional flow paths. Note that the both the shape and magnitude of the changes in total pressure gradient directly scale with volume fraction. The measured data are from the large-diameter study of Langsholt and Holm (2007).

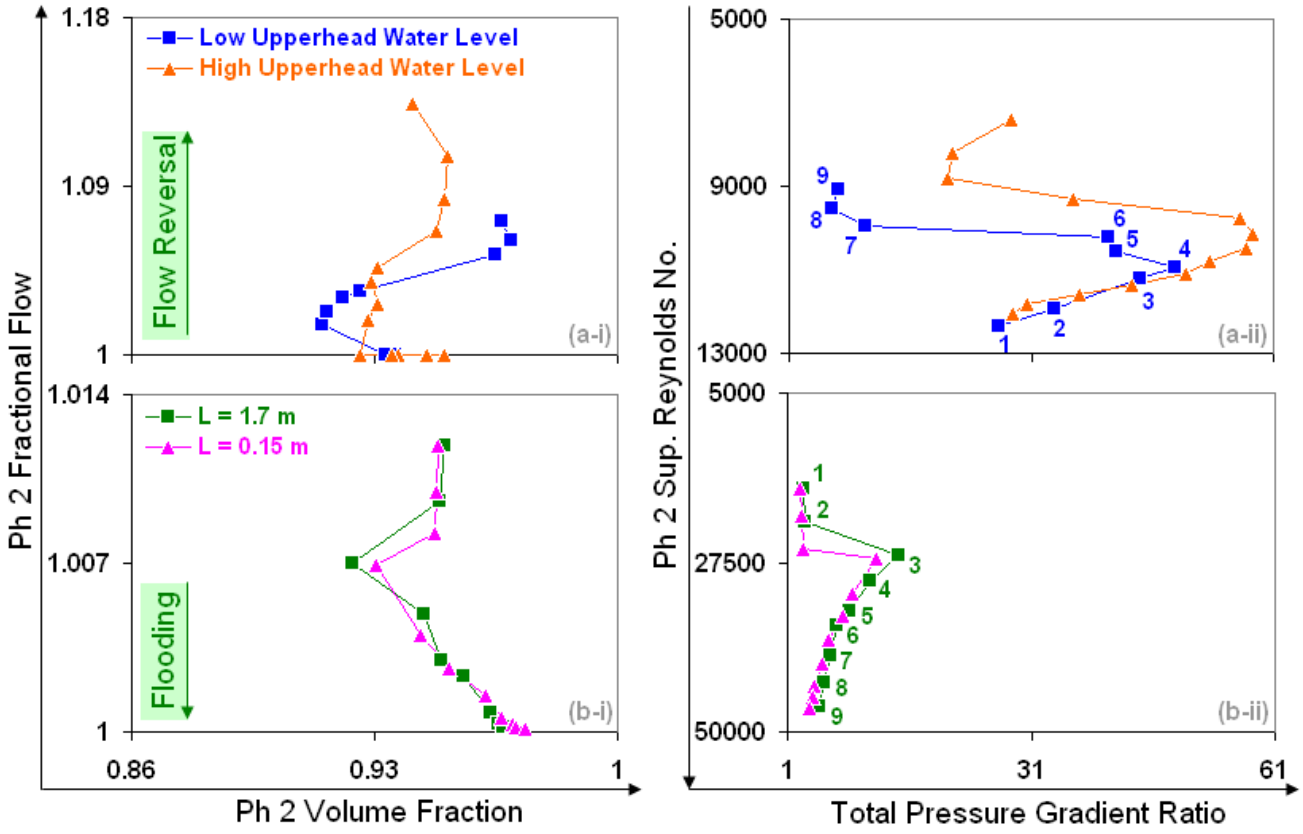

Figure 3.4.2: Demonstrating how sharp-transition phenomena (in this case, the characteristic sharp changes in volume fraction observed in countercurrent vapor-liquid flooding and flow reversal) are represented as fractional flow paths. Note that both the shape and magnitude of the changes in total pressure gradient directly scale with volume fraction. The measured data shown are from Zabaras, 1985 (b-i, ii) and Bharathan at al., 1979 (a-i, ii).

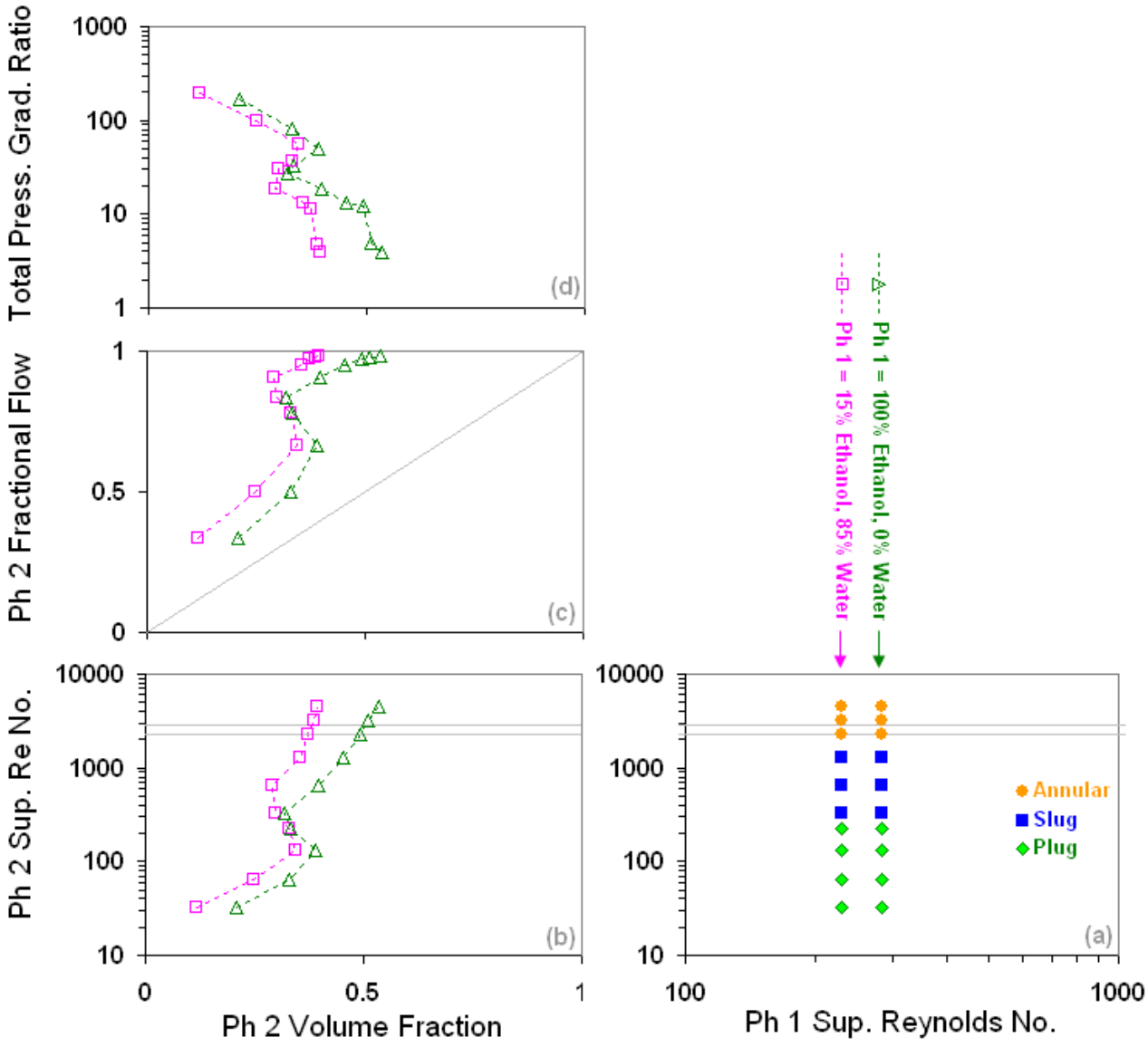

Figure 3.4.3: Demonstrating how unusual changes in total pressure gradient directly scale with the fractional flow graph and the comparisons of these charts with phase Reynolds number changes (i.e., the flow patterns). The horizontal rectangular mini-channel (height = 1.2 mm) nitrogen (phase 2) and ethanol solutions/water (phase 1) test measurements shown are from Fujita et al. (1995).

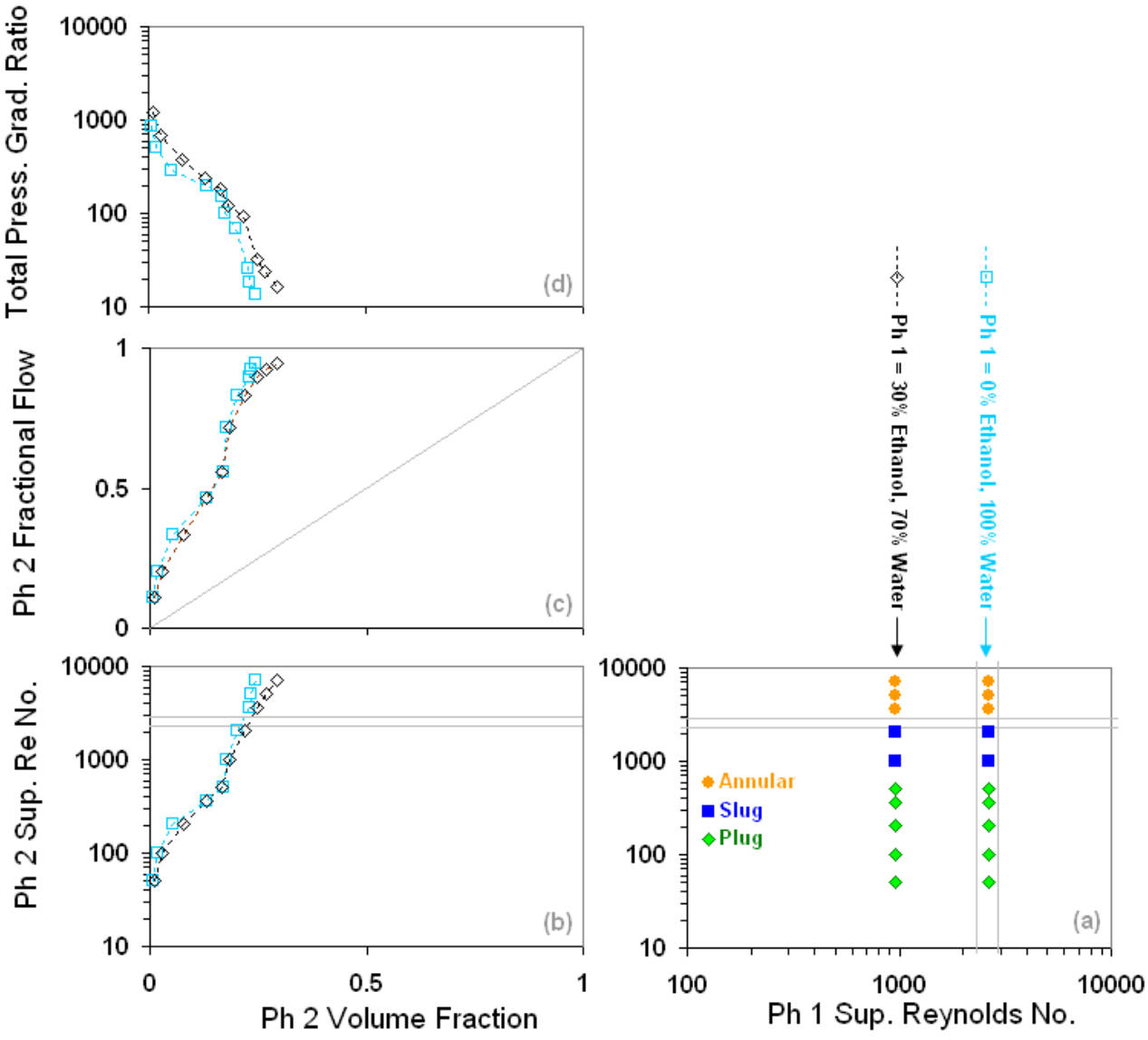

Figure 3.4.4: Demonstrating how unusual changes in total pressure gradient directly scale with the fractional flow graph and the comparisons of these charts with phase Reynolds number changes (i.e., the flow patterns). The horizontal rectangular mini-channel (height = 2 mm) nitrogen (phase 2) and ethanol solutions/water (phase 1) test measurements shown are from Fujita et al. (1995).

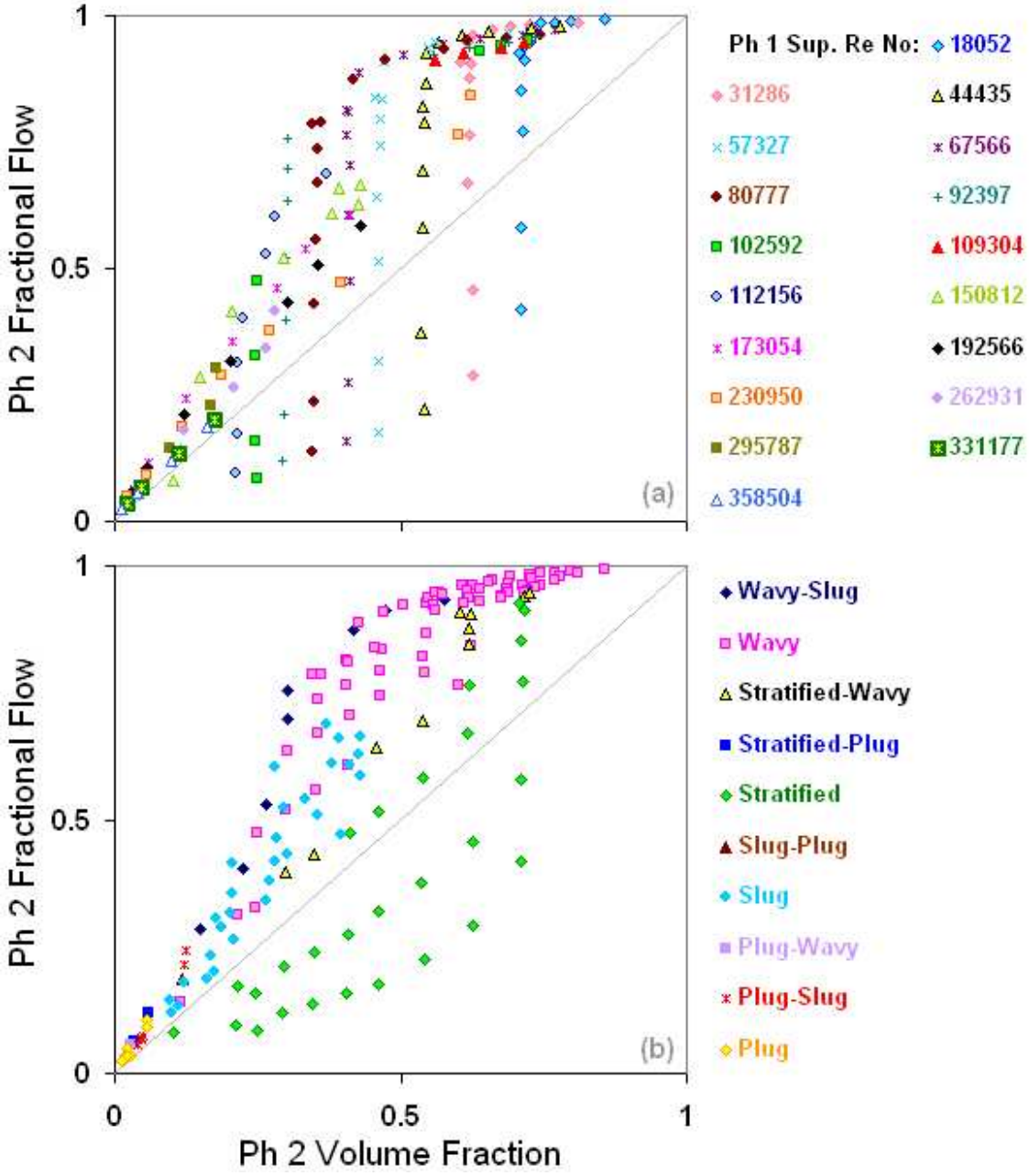

Figure 3.4.5: Demonstrating how complex changes in volume fraction data (and their respective flow patterns) are simply represented as fractional flow paths in the fractional flow graph. The horizontal large-diameter (8.5 inches) horizontal air (phase 2) and water (phase 1) test measurements shown are from Simpson et al. (1976).

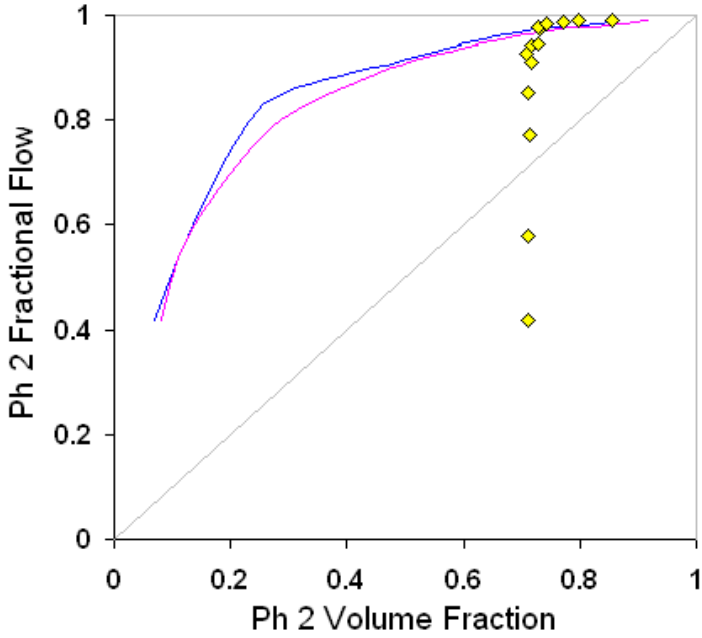

Test Nos.	Ph 2 Sup. Vel. (m/s)	Obs. Flow Pattern
0-905-07	0.060	Stratified
1-005-07	0.121	Stratified
1-105-07	0.287	Stratified
1-205-07	0.496	Stratified
1-305-07	0.848	Stratified
1-405-07	1.062	Stratified
1-505-07	1.360	Stratified-Wavy
0-112-07	1.357	Stratified-Wavy
0-212-07	2.559	Wavy
0-312-07	3.553	Wavy
0-412-07	5.245	Wavy
0-512-07	6.344	Wavy
0-612-07	7.417	Wavy
0-712-07	8.616	Wavy

Figure 3.4.6: Demonstrating how industrial codes compare with one example dataset (for phase 1 superficial Reynolds number = 18052) from the Simpson et al. (1976) data shown in Fig. 3.4.5. The need for major improvement in the ability to correctly predict the two-phase fractional flow behavior in horizontal large-diameter pipes is clear.

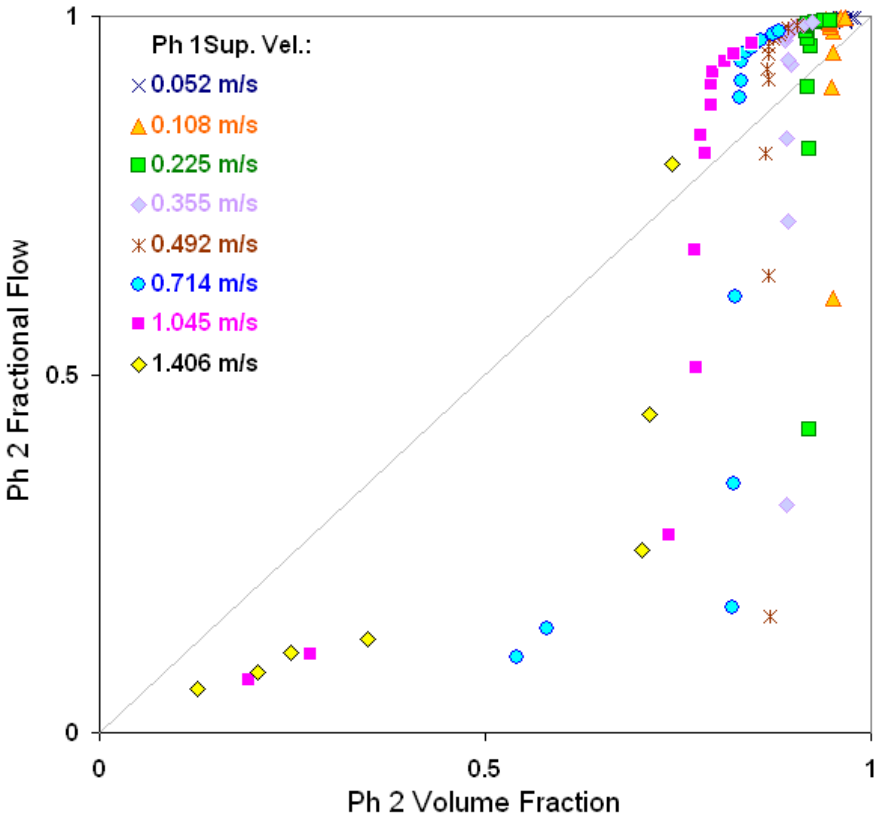

Figure 3.4.7: Demonstrating that complex changes in volume fraction data can occupy and span various extents of the fractional flow graph. The down-inclined (-67.75° from horizontal) air (phase 2) and water (phase 1) test measurements shown are from Spedding and Nguyen (1976).

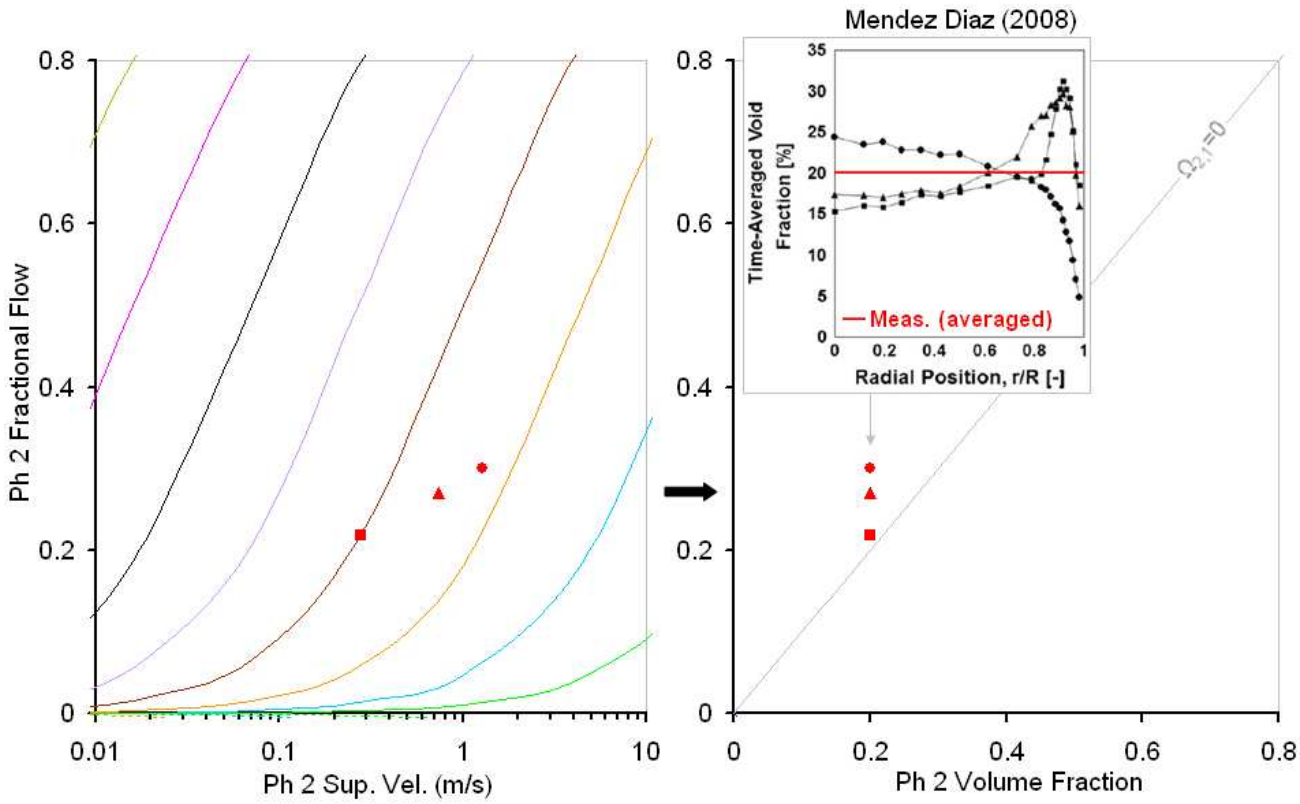

Figure 3.4.8: Demonstrating how complex fluid mechanical, multi-dimensional, multiphase flow phenomena (in this case, wall-peaking to core-peaking void fraction cross-sectional profiles) are simply represented in the fractional flow graph. The vertical upward bubbly air (phase 2) and water (phase 1) test measurements shown are from Figure 2 of Mendez Diaz et al. (2012). The legend for the left-most chart is the same as Figure 3.1.1.

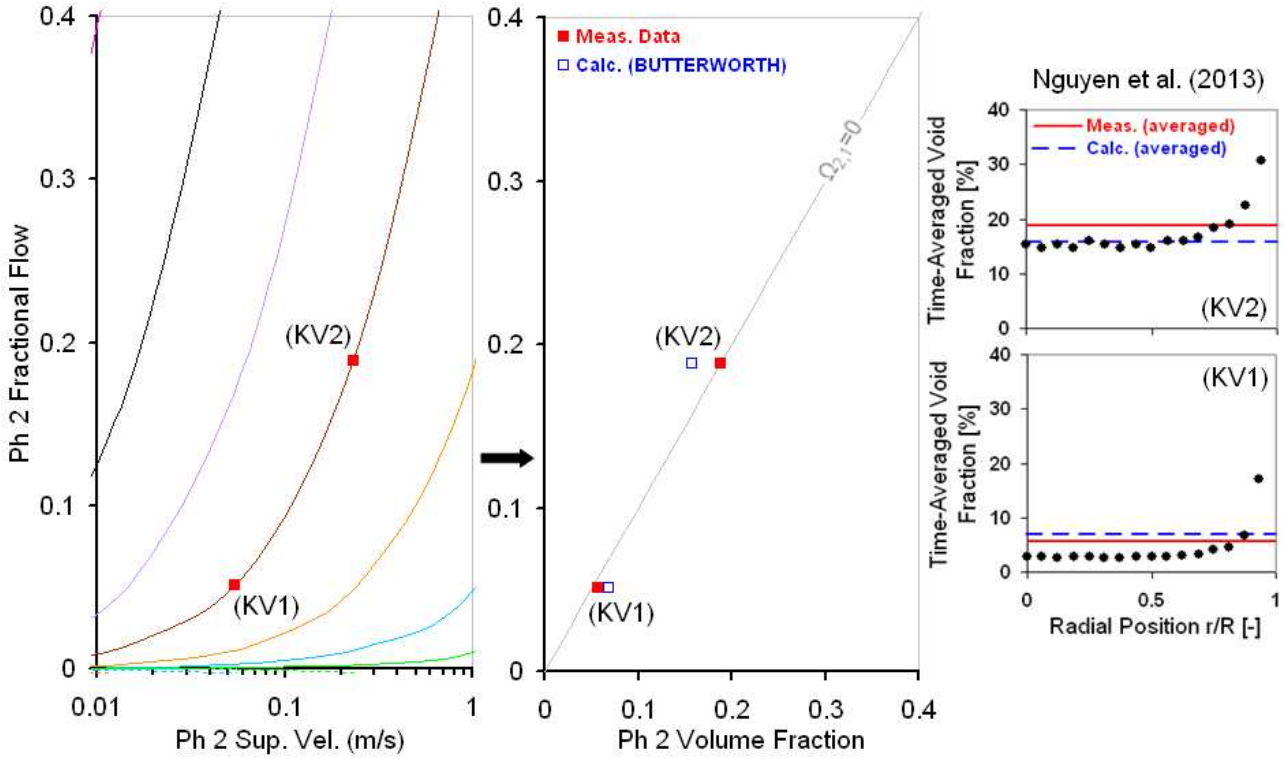

Figure 3.4.9: Demonstrating how complex fluid mechanical, multi-dimensional, multiphase flow phenomena are simply represented in the fractional flow graph and how their global (net) behavior can be predicted by existing global models (the BUTTERWORTH model in this case). The vertical upward bubbly air (phase 2) and water (phase 1) test measurements shown are from Nguyen et al. (2013). The legend for the left-most chart is the same as Figure 3.1.1.

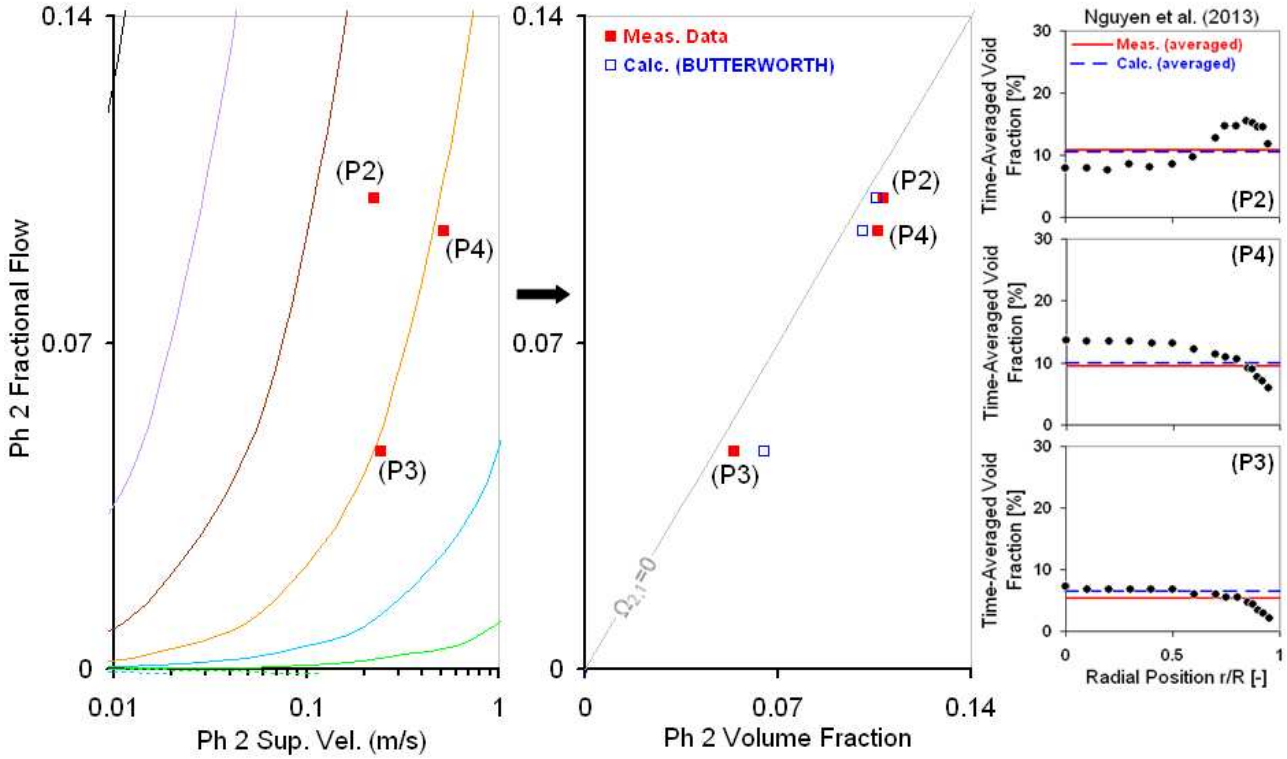

Figure 3.4.10: Demonstrating how complex changes in void fraction lateral distribution can result in negative averaged slip, and how this averaged result is simply represented in the fractional flow graph. The global (net) behavior of the lateral distribution changes can be predicted by existing global models (the BUTTERWORTH model in this case). The vertical upward bubbly air (phase 2) and water (phase 1) test measurements shown are from Nguyen et al. (2013). The legend for the left-most chart is the same as Figure 3.1.1.

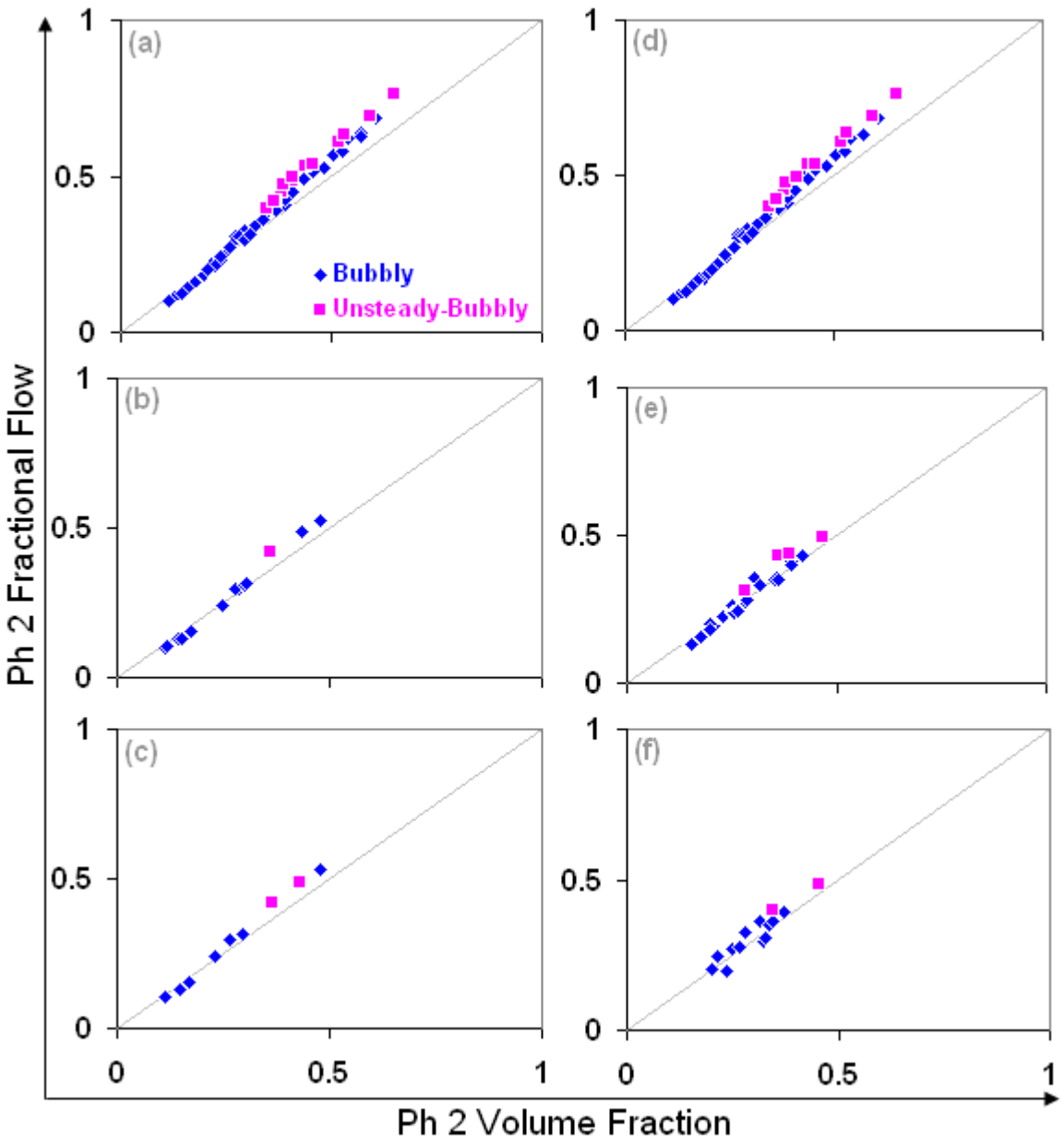

Figure 3.4.11: An example of the large amount of experimental evidences of upward bubbly flow in the literature that shows a negative to positive averaged slip velocity behavior. As seen above, these changes are represented as fractional flow paths in the fractional flow graph. The upward bubbly air (phase 2) and water (phase 1) test measurements shown are all of the experiments of Rose (1964).

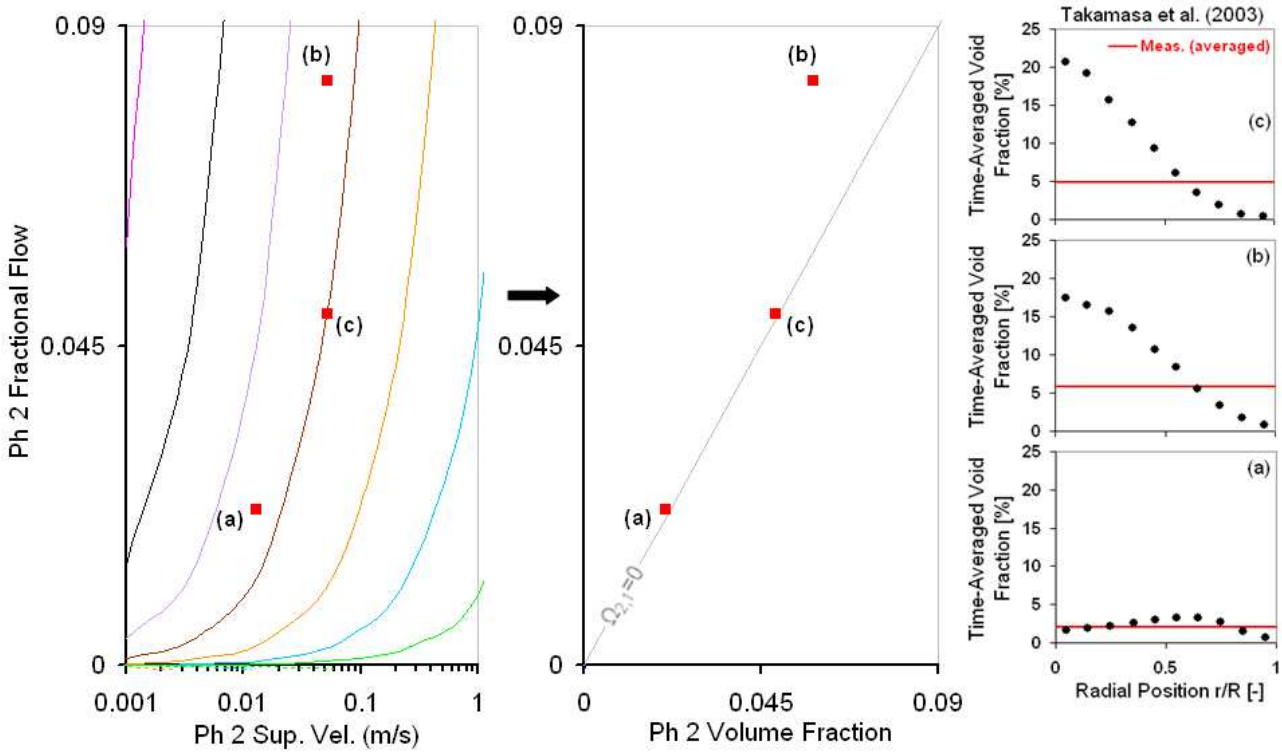

Figure 3.4.12: Demonstrating how complex changes in void fraction lateral distribution during bubbly flow development can be represented in the fractional flow graph. The vertical upward bubbly air (phase 2) and water (phase 1) test measurements shown are from Takamasa et al. (2003). The legend for the left-most chart is the same as Figure 3.1.1.

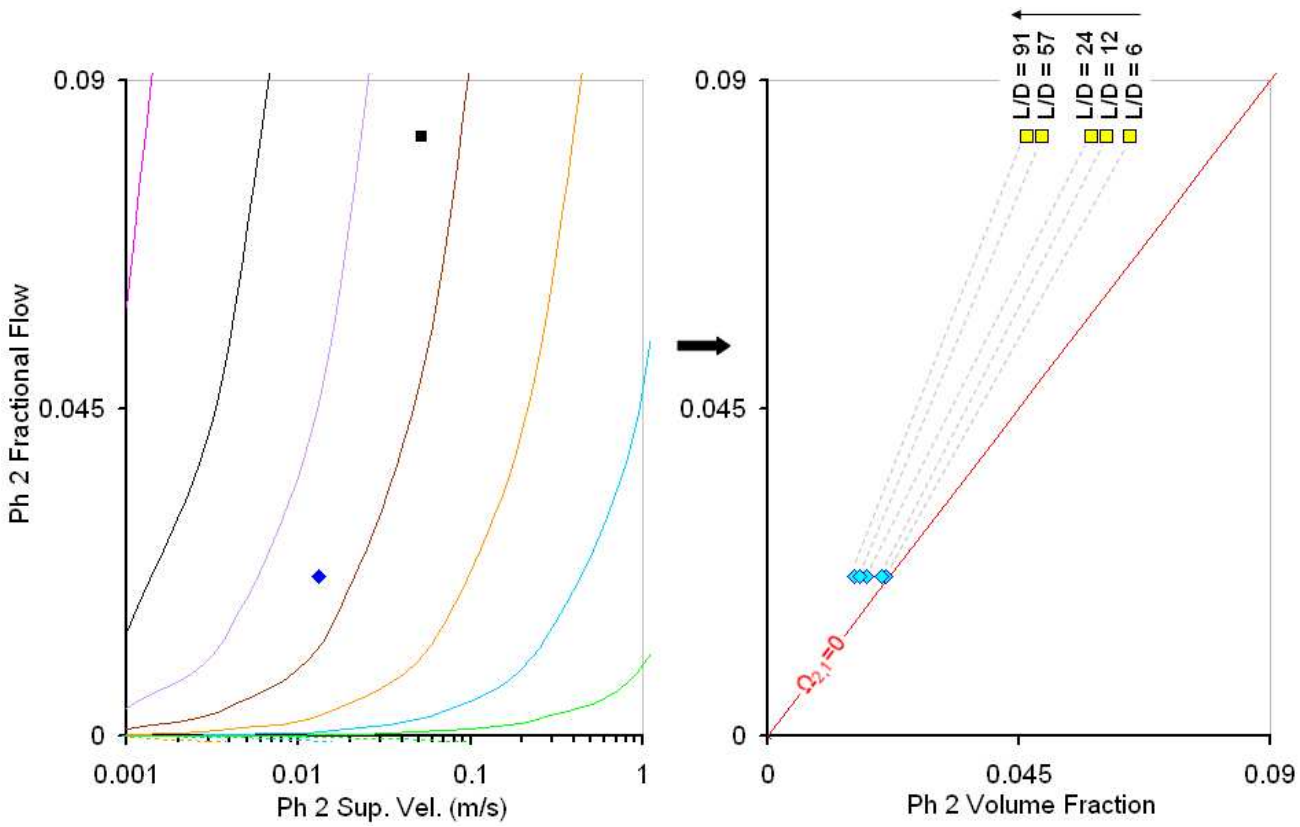

Figure 3.4.13: Demonstrating how the slip behavior during the bubbly flow development is enhanced at increasing vapor phase flow rates at a constant liquid phase flow rate. The vertical upward bubbly air (phase 2) and water (phase 1) test measurements shown are from Takamasa et al. (2003). The legend for the left-most chart is the same as Figure 3.1.1.

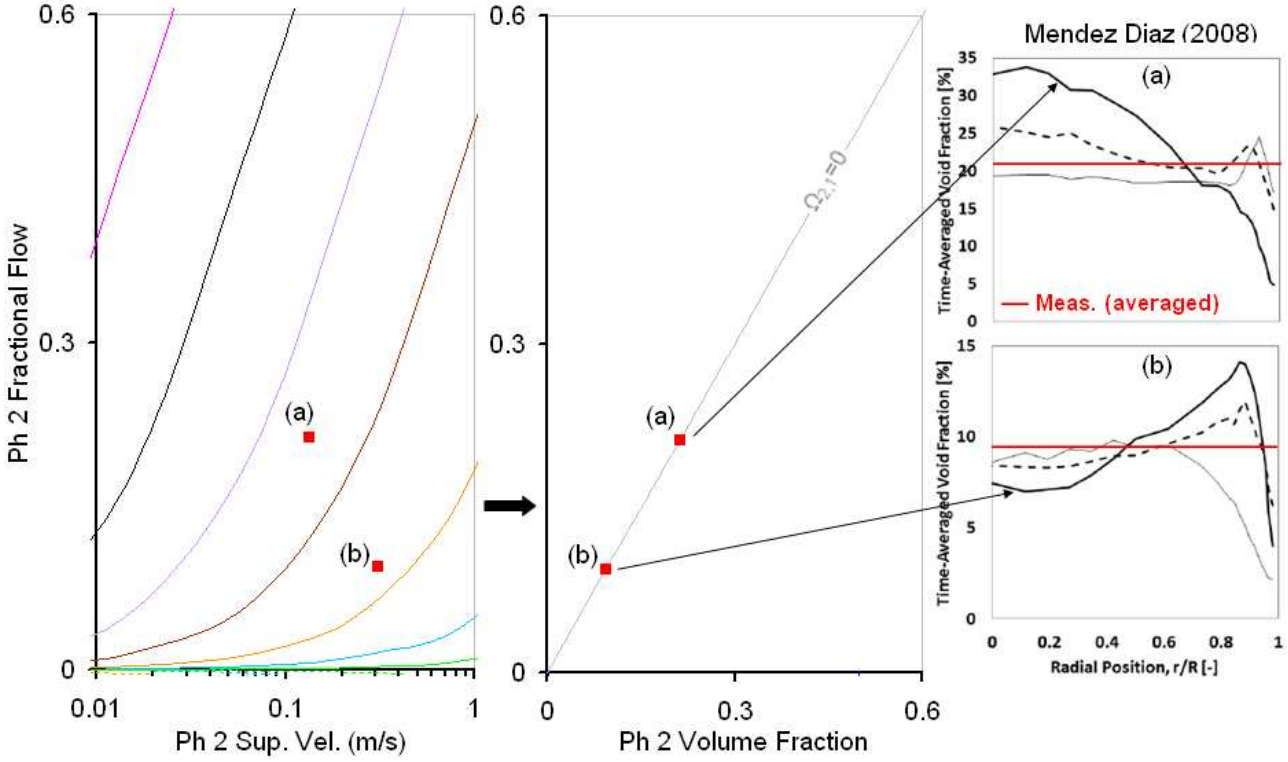

Figure 3.4.14: Two air (phase 2) and water (phase 1) datasets from Mendez-Diaz (2008) showing the axial position influence on the peaking behavior in upward bubbly flow. For both datasets, the axial position on the right-most charts are represented by a thin line (z/D = 2), a dashed line (z/D = 36) and a thick line (z/D = 52). The legend for the left-most chart is the same as Figure 3.1.1.

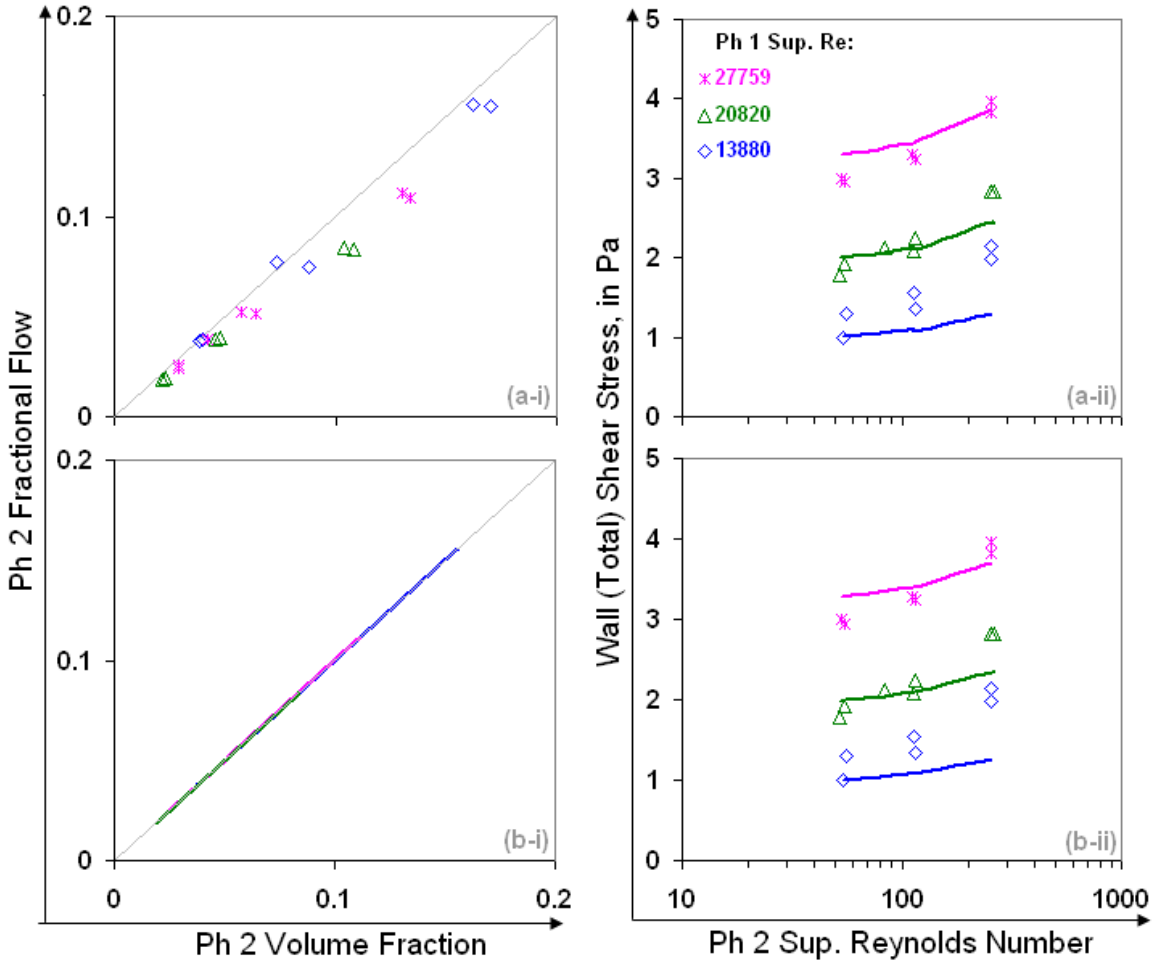

Figure 3.4.15: Comparison of averaged volume fraction and wall shear stress measurements with analytical Pipe Fractional Flow Theory predictions for the bubbly flow dataset of Kashinsky and Randin (1999).

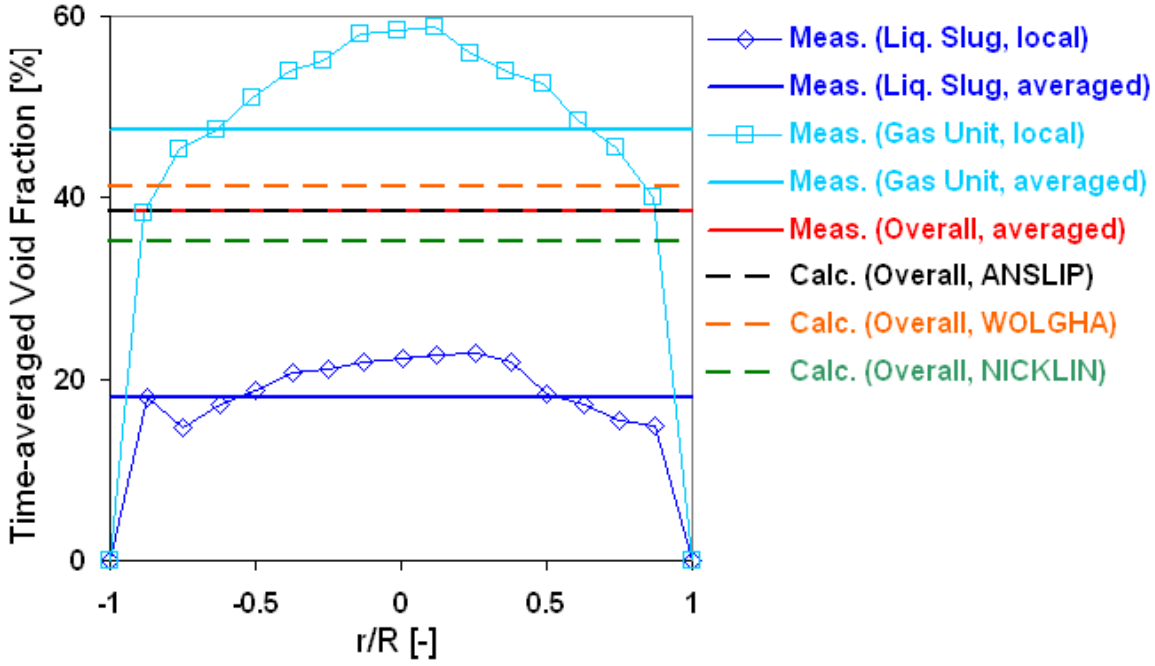

Figure 3.4.16: Comparison of the averaged volume fraction measurement for a slug unit with the Pipe Fractional Flow Theory predictions for one of the nitrogen (phase 2) and sodium-hydroxide-salt-electrolyte (phase 1) vertical upward slug flow datasets of Zheng and Che (2006).

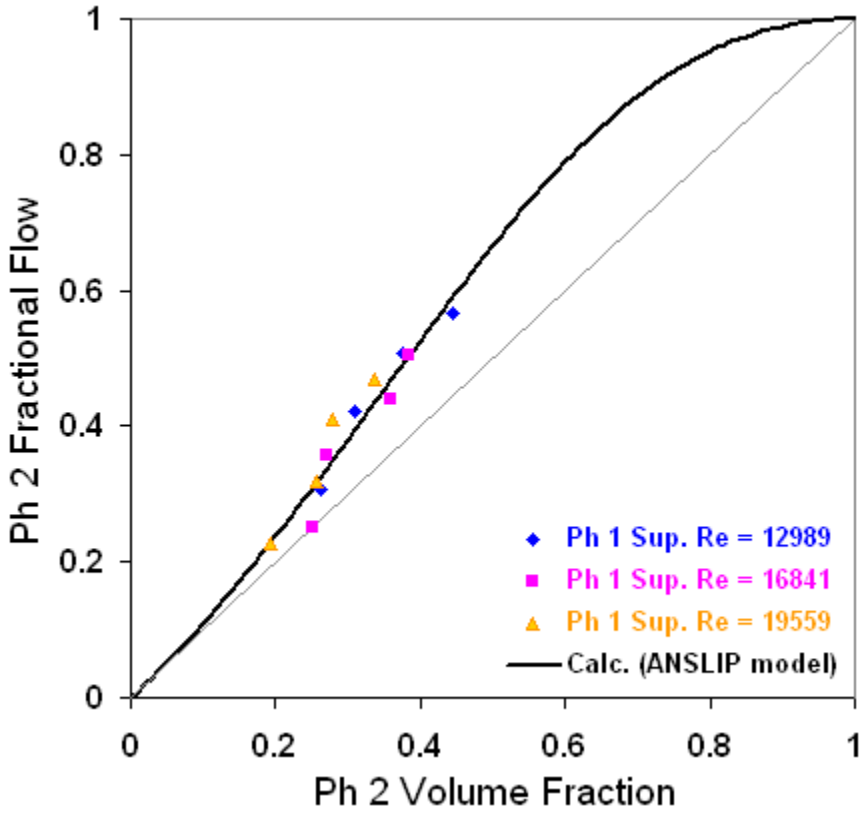

Figure 3.4.17: Comparison of all of the averaged volume fraction measurements for the vertical upward slug flow datasets of Zheng and Che (2006) with the ANSLIP model.

Chapter 4 – Vapor-Liquid Flow Applications

4.1 VALIDATION OF THE PIPE FRACTIONAL FLOW THEORY

In the previous section, it was shown that, in general, the only unknown dependent variable requiring closure in the universal mixture momentum balance equations (Eqns. 6 and 7 of Section 2.2.4) is the averaged phase volume fraction, $\langle s_j \rangle$. For example, for a two-phase vapor-liquid system, apart from system parameters/variables, we need only know the averaged vapor-phase volume fraction (or void fraction) or the averaged liquid-phase volume fraction (or liquid holdup), since the sum of these two is unity. It is therefore inferred that *if* there are carefully-controlled conditions in which only the flow hydrodynamics govern the flow mechanisms (i.e., immiscible, non-reacting, adiabatic flows), *then*:

I. Improved prediction of $\langle s_j \rangle$ will lead to the improved prediction of the various pressure gradients.

II. The uncertainty in the prediction of the pressure gradients will be, for the first time, tractable and traceable only to the directly measurable variable, $\langle s_j \rangle$.

Indeed, it is because averaged phase volume fraction (as well as averaged phase entrainment, in the case of flows with entrainment) is a K-variable, that any or all of the hypotheses in the previous section can be interrogated, falsified and validated. This, by itself, is a significant change from engineering-oriented approaches. Although model verification and validation can be a common to both engineering-oriented and science-oriented approaches, it is model falsification and the ability to interrogate that are requisites for a scientific model.

Specifically, in the context of this work, model falsification means that if there are both pressure gradient and $\langle s_j \rangle$ measurements in a carefully-controlled experiment, then

this will enable us to unambiguously falsify (and therefore validate) the universal mixture momentum balance equations (Eqns. 6 and 7 of Section 2.2.4) and determine the extent of their accuracy and thus ranges of applicability. This will be afforded via first inputting the $\langle s_j \rangle$ measurements into the proposed universal mixture momentum models, and comparing the calculated pressure gradients (or shear stresses) with their measured values. In this way, the pressure gradients are functions of all known quantities and, therefore, the proposed pressure gradient models can be falsified.

It must be noted, however, that if volume fractions and/or entrainment fractions are always calculated together with the pressure gradients, then it will not be possible to objectively determine which among these models can be shown to be false in comparison to an experiment. This is because each model can contain various compensating inadequacies when they are solved in concert with other models. This is one reason *why* different models may yield similar pressure gradients for a studied scenario but very different volume fractions results for the same scenario (or vice versa), as will be seen in several applications in the remaining chapters. It is only when one model (e.g., the total pressure gradient model) is expressed in terms of only measured/known quantities, can that model then be properly interrogated and its uncertainty be traced to specific quantities. This obviously will lead to a much better understanding of the model's sensitivities.

Thus, provided the experimental measurements of volume fractions, pressure gradients and all other measured system variables/parameters are themselves accurate (within instrumentation limits), *if* our proposed universal mixture momentum models are in fact representative of the observed data, *then* wrong $\langle s_j \rangle$ values inputted into the models will always lead to wrong calculations of pressure gradients compared to their measured values. Similarly, correct (i.e., measured) $\langle s_j \rangle$ values inputted into the models

will always lead to pressure gradient calculations in satisfactory agreement with their measured values, within the limits of applicability of the models. Additionally, the degree to which a satisfactory agreement is attained must be specified for the studied scenario. In this manner, we can properly validate our universal mixture momentum models provided there are verifiable, published datasets from various labs covering a wide and diverse range of scenarios.

In the remaining applications chapters of this work (Chapters 4 to 7), we will therefore first validate our universal mixture momentum models with measured volume fraction data whenever such measurements are available in a dataset (i.e., proving that it is relative velocity that governs multiphase flow pressure gradient – our first principal insight) and then, in many cases, we will further provide a volume fraction prediction from the fractional flow models of Chapter 3 to show how the universal mixture momentum models of Chapter 2 can be used for predictions. We refer to this process as a validation followed by a prediction. In some cases, particularly when measured volume fraction data are unavailable, only a prediction will be performed with the fractional flow models. In other cases, only a validation of our universal mixture momentum models will be performed. In the cases where an analytical fractional flow model is used in combination with our universal mixture momentum models, then this will yield a wholly-analytical prediction of multiphase flow pressure gradient (i.e., no multiphase flow correlation). Lastly, we will perform our analytical model validations for various flow scenarios categorized under the same standardized multiphase flow problem definitions proposed in Table 1.1 in chapter 1.

Before leaving this section, it is instructive to demonstrate some simple, unambiguous, representative calculation steps that provide the validation results of our analytical models. To do this, we select immiscible, non-reacting, adiabatic, carefully-

controlled, steady-state, fully-developed experimental multiphase flow loop measurements from different labs and then show how our analytical model calculations are performed, step-by-step, for the applicable versions of Eqns. 6 and 7 of Section 2.2.4 in the studied scenario. For the coupled flow worked-examples in Section 4.2 below, the applicable version is:

$$\overbrace{\left(\frac{\Delta P_{mix}}{\Delta L}\right)}^{\text{total (TPG)}} = \overbrace{\frac{Z}{A}\sum_{j=1}^{N_p}\left(\frac{\gamma_j f_{j\to wall}\left|G_j\right|G_j}{2\rho_j\left\langle s_j\right\rangle^2}\right)}^{\text{friction (FPG)}} + \overbrace{\left(\sum_{j=1}^{N_p}\left(\rho_j\left\langle s_j\right\rangle\right)\right)g\cos\theta}^{\text{hydrostatic (HPG)}} \quad (1)$$

Similarly, for the decoupled flow worked-examples in Section 4.2 below, the applicable version is:

$$\overbrace{\left(\frac{\Delta P_{mix}}{\Delta L}\right)}^{\text{total (TPG)}} = \overbrace{\sum_{j=1}^{N_p}\left(\frac{Z_j^{net}}{A}\left(\frac{\gamma_j f_{j\to wall}\left|G_j\right|G_j}{2\rho_j\left\langle s_j\right\rangle^2}\right)\right)}^{\text{friction (FPG)}} + \overbrace{\left(\sum_{j=1}^{N_p}\left(\rho_j\left\langle s_j\right\rangle\right)\right)g\cos\theta}^{\text{hydrostatic (HPG)}} \quad (2)$$

In Eqns. 1 or 2 above, $f_{j\to wall}$ is computed from Eqns. 4 and 5 of Section 2.2.4 in Chapter 2 and $\langle s_j \rangle$ is computed from the fractional flow models of Chapter 3. Additionally, for the two-phase vapor (phase 2) and liquid (phase 1) calculations of this chapter (j = 1, 2), only one volume fraction calculation is needed, $\langle s_2 \rangle$, since $\langle s_1 \rangle$ = 1 - $\langle s_2 \rangle$. Also, unless stated otherwise, for the vapor-liquid applications of this work, $\gamma_1 = \gamma_2 = 1$.

4.2 Immiscible Vapor-Liquid Flow: Simple Hand Calculations

4.2.1 Coupled Flow with Newtonian Liquids

For this first worked-example, we select vertical, small-diameter, low-pressure air (phase 2) and liquid (phase 1) data from Khatib and Richardson (1984). This dataset was selected because similar conditions were specified in the experimental flow loop for both Newtonian and Non-Newtonian liquids (as shown next in Section 4.2.2), thus properly

interrogating the effect of the rheology of the liquid phase. Also, the range of flow patterns observed for this dataset included bubble, slug, froth, churn and dispersed bubble. Air superficial velocities ranged from 0.1 to 7.5 m/s and liquid superficial velocities ranged from 0.244 to 3.05 m/s.

Since this is an upward-vertical flow dataset, we perform coupled flow calculations (i.e., Eqn. 1). The conditions of these experiments were for a system pressure and temperature of 200,000 Pa and 20 °C, respectively. This results in an ideal-gas air density, ρ_2, of 2.377 kg/m^3. The liquid is water in this case with a density, ρ_1, of 1,000 kg/m^3. The specified superficial velocity of the air, $\langle u_2 \rangle$, is 0.171 m/s. The specified superficial velocity of the water, $\langle u_1 \rangle$, is 0.305 m/s. Therefore the fractional flow of the air, f_2, is found from:

$$f_2 = \frac{\langle u_2 \rangle}{\langle u_2 \rangle + \langle u_1 \rangle} = 0.3595 \tag{3}$$

Using the ANSLIP analytical model for volume fraction prediction (Eqn. 11 of Section 3.2.3 of Chapter 3), we use the calculated air fractional flow in Eqn. 3 above, to arrive at:

$$\langle s_2 \rangle = \frac{f_2 + 1 \; - \left((f_2 + 1)^2 \; - 4 (f_2)^2 \right)^{\frac{1}{2}}}{2 f_2} = 0.2861 \tag{4}$$

Note that this prediction compares quite favorably with the measured air volume fraction given in the experiment as 0.31. At this point, the hydrostatic pressure gradient (HPG) for the multiphase mixture can be computed, as:

$$\begin{aligned} \left(\sum_{j=1}^{N_p} \left(\rho_j \langle s_j \rangle \right) \right) g \cos\theta &= \left(\rho_2 \langle s_2 \rangle + \rho_1 \left(1 - \langle s_2 \rangle \right) \right) g \cos\theta \\ &= \left((2.377)(0.2861) \; + \; (1000)(1 - 0.2861) \right)(9.81)(1) \\ &= 7010.4 \; \frac{Pa}{m} \end{aligned} \tag{5}$$

Next, we compute the frictional pressure gradient (FPG) for the multiphase mixture. The circular pipe diameter, D_H, is given as 0.0388 m. We also specify a hydraulic roughness, k_{wall}, of 0 m for the plastic pipe used in the experiment. For the conditions of the experiment, the viscosity of the air can be assumed as 0.000018 Pa-s. Similarly, the viscosity of the water can be assumed as 0.001 Pa-s. Therefore, the in-situ Reynolds number for the water (from Eqn. 5 of Section 2.2.4 of Chapter 2) is:

$$N_{\mathrm{Re},1} = \frac{|G_1| D_H}{\mu_1 \left(1 - \langle s_1 \rangle\right)} = \frac{\rho_1 \left|\langle u_1 \rangle\right| D_H}{\mu_1 \left(1 - \langle s_1 \rangle\right)} = \frac{(1000)(0.305)(0.0388)}{(0.001)(1 - 0.2861)} = 16575.7 \qquad (6)$$

And similarly, the in-situ Reynolds number for the air is:

$$N_{\mathrm{Re},2} = \frac{|G_2| D_H}{\mu_2 \langle s_2 \rangle} = \frac{\rho_2 \left|\langle u_2 \rangle\right| D_H}{\mu_2 \langle s_2 \rangle} = \frac{(2.377)(0.171)(0.0388)}{(0.000018)(0.2861)} = 3066.3 \qquad (7)$$

Since these Reynolds numbers classify as turbulent according to Eqn. 4 of Section 2.2.4 of Chapter 2, the applicable water friction factor is:

$$f_{1 \to wall} = \left(-3.6 \log_{10} \left(\frac{6.9}{N_{\mathrm{Re},1}} + 0 \right) \right)^{-2} = \left(-3.6 \log_{10} \left(\frac{6.9}{16575.7} + 0 \right) \right)^{-2} = 0.00675 \qquad (8)$$

And, the applicable air friction factor is:

$$f_{2 \to wall} = \left(-3.6 \log_{10} \left(\frac{6.9}{N_{\mathrm{Re},2}} + 0 \right) \right)^{-2} = \left(-3.6 \log_{10} \left(\frac{6.9}{3066.3} + 0 \right) \right)^{-2} = 0.011 \qquad (9)$$

Thus, we can now calculate the frictional pressure gradient (FPG) for the multiphase mixture as:

$$\frac{Z}{A}\sum_{j=1}^{N_p}\left(\frac{\gamma_j f_{j\to wall}\left|G_j\right|G_j}{2\rho_j\left\langle s_j\right\rangle^2}\right)$$
$$=\left(\frac{2}{D_H}\right)\left(\frac{f_{1\to wall}\rho_1\left|\left\langle u_1\right\rangle\right|\left\langle u_1\right\rangle}{\left(1-\left\langle s_2\right\rangle\right)^2}+\frac{f_{2\to wall}\rho_2\left|\left\langle u_2\right\rangle\right|\left\langle u_2\right\rangle}{\left\langle s_2\right\rangle^2}\right) \quad (10)$$
$$=\left(\frac{2}{0.0388}\right)\left(\frac{(0.00675)(1000)(0.305)^2}{(1-0.2861)^2}+\frac{(0.011)(2.377)(0.171)^2}{(0.2861)^2}\right)$$
$$=63.516+0.483=63.999\frac{Pa}{m}$$

The total pressure gradient (TPG) for the mixture is therefore 7014.4 + 64.0 = 7074.4 Pa/m. This analytical prediction compares very well with the measured total pressure gradient reported in the experiment as 6887 Pa/m. Also, note that the calculated percent contribution of the frictional pressure gradient towards the total pressure gradient is about 1% in this case.

4.2.2 Coupled Flow with Non-Newtonian Liquids

We next repeat the same calculation procedure above but for an air (phase 2) and shear-thinning slurry (phase 1) flow dataset in Khatib and Richardson (1984) at the slurry kaolin suspension concentration in water of 18.9% by volume. For this concentration, the slurry's reported values of the consistency coefficient, K_1, and its flow behavior index, n_1, were 11.2 Pa-s^n and 0.167, respectively. Also, the air-slurry dataset most closely approximating the rates in the air-water case above, were $\langle u_2\rangle$ = 0.220 m/s and $\langle u_1\rangle$ = 0.305 m/s. Therefore the fractional flow of the air, f_2, is:

$$f_2=\frac{\langle u_2\rangle}{\langle u_2\rangle+\langle u_1\rangle}=0.4186 \quad (11)$$

As before, using the ANSLIP analytical model for volume fraction prediction (Eqn. 11 of Section 3.2.3 of Chapter 3), we use the calculated air fractional flow in Eqn. 11 above, to arrive at:

$$\langle s_2 \rangle = \frac{f_2 + 1 \; - \; \left(\left(f_2 + 1 \right)^2 \; - 4 \left(f_2 \right)^2 \right)^{\frac{1}{2}}}{2 f_2} = 0.3265 \tag{12}$$

This prediction compares very favorably with the measured air volume fraction given in this experiment as 0.36. Since the system pressure and temperature conditions remain the same, the hydrostatic pressure gradient (HPG) for the multiphase mixture can then be computed, as:

$$\begin{aligned} \left(\sum_{j=1}^{N_p} \left(\rho_j \langle s_j \rangle \right) \right) g \cos\theta &= \left(\rho_2 \langle s_2 \rangle + \rho_1 \left(1 - \langle s_2 \rangle \right) \right) g \cos\theta \\ &= \left(\left(2.377 \right) \left(0.3265 \right) \; + \; \left(1000 \right) \left(1 - 0.3265 \right) \right) \left(9.81 \right) \left(1 \right) \\ &= 8728.5 \; \frac{Pa}{m} \end{aligned} \tag{13}$$

Next, we compute the frictional pressure gradient (FPG) for the multiphase mixture. As before, the viscosity of the air is 0.000018 Pa-s. The viscosity of the slurry is obtained from Eqn. 8 of Section 2.2.5 of Chapter 2, as:

$$\begin{aligned} \mu_1 &= \left(\frac{8 \langle u_1 \rangle}{\left(1 - \langle s_2 \rangle \right) D_H} \right)^{n_1 - 1} \left(K_1 \left(\frac{3 n_1 + 1}{4 n_1} \right)^{n_1} \right) \left(\left(1 - \langle s_2 \rangle \right)^{2 - n_1} \right) \\ &= \left(\frac{8 \left(0.305 \right)}{\left(1 - 0.3265 \right) \left(0.0388 \right)} \right)^{0.167 - 1} \left(11.2 \left(\frac{3 \left(0.167 \right) + 1}{4 \left(0.167 \right)} \right)^{0.167} \right) \left(\left(1 - 0.3265 \right)^{2 - 0.167} \right) \\ &= 0.142 \; Pa - s \end{aligned} \tag{14}$$

Therefore, the in-situ Reynolds number for the slurry is:

$$N_{\mathrm{Re},1} = \frac{\left| G_1 \right| D_H}{\mu_1 \left(1 - \langle s_1 \rangle \right)} = \frac{\rho_1 \left| \langle u_1 \rangle \right| D_H}{\mu_1 \left(1 - \langle s_1 \rangle \right)} = \frac{\left(1000 \right) \left(0.305 \right) \left(0.0388 \right)}{\left(0.142 \right) \left(1 - 0.3265 \right)} = 163.4 \tag{15}$$

And similarly, the in-situ Reynolds number for the air is:

$$N_{\mathrm{Re},2} = \frac{\left| G_2 \right| D_H}{\mu_2 \langle s_2 \rangle} = \frac{\rho_2 \left| \langle u_2 \rangle \right| D_H}{\mu_2 \langle s_2 \rangle} = \frac{\left(2.377 \right) \left(0.220 \right) \left(0.0388 \right)}{\left(0.000018 \right) \left(0.3265 \right)} = 3445.9 \tag{16}$$

The in-situ Reynolds number for the slurry (Eqn. 15) now classifies as laminar according to Eqn. 4 of Section 2.2.4 of Chapter 2, and thus the applicable slurry friction factor is:

$$f_{1\to wall} = \frac{16}{N_{\mathrm{Re},1}} = \frac{16}{163.4} = 0.0979 \tag{17}$$

The in-situ Reynolds number for air (Eqn. 16) classifies as turbulent and the applicable air friction factor is therefore:

$$f_{2\to wall} = \left(-3.6\log_{10}\left(\frac{6.9}{N_{\mathrm{Re},2}} + 0 \right) \right)^{-2} = \left(-3.6\log_{10}\left(\frac{6.9}{3445.9} + 0 \right) \right)^{-2} = 0.0106 \tag{18}$$

Thus, we can now calculate the frictional pressure gradient (FPG) for the multiphase air-slurry mixture as:

$$\begin{aligned} &\frac{Z}{A}\sum_{j=1}^{N_p}\left(\frac{\gamma_j f_{j\to wall} \left|G_j\right| G_j}{2\rho_j \left\langle s_j \right\rangle^2} \right) \\ &= \left(\frac{2}{D_H} \right)\left(\frac{f_{1\to wall}\rho_1 \left|\left\langle u_1 \right\rangle\right| \left\langle u_1 \right\rangle}{\left(1-\left\langle s_2 \right\rangle\right)^2} + \frac{f_{2\to wall}\rho_2 \left|\left\langle u_2 \right\rangle\right| \left\langle u_2 \right\rangle}{\left\langle s_2 \right\rangle^2} \right) \\ &= \left(\frac{2}{0.0388} \right)\left(\frac{(0.0979)(1000)(0.305)^2}{(1-0.3265)^2} + \frac{(0.0106)(2.377)(0.220)^2}{(0.3265)^2} \right) \\ &= 1366.146 + 0.587 = 1366.733 \frac{Pa}{m} \end{aligned} \tag{19}$$

The total pressure gradient (TPG) for the mixture is therefore 1366.7 + 8728.5 = 10095.2 Pa/m. This analytical prediction is very close to the measured total pressure gradient reported in the experiment as 9939 Pa/m. In this case, we note that the calculated percent contribution of the frictional pressure gradient towards the total pressure gradient is about 14%, which is much more than that for the air-water case at similar conditions – the changed variable being the liquid rheological parameters resulting in a different liquid viscosity.

4.2.3 Coupled Flow with Bi-Directional Entrainment

In this worked example, we showcase our bi-directional entrainment calculation procedures for an example annular two-phase air (phase 2) and water (phase 1) dataset from Hewitt et al. (1961) – run no. 4.08 in this reference. For this wide-ranging annular flow experimental investigation (which was also highlighted in Table 11.5 of Wallis, 1969), air superficial velocities ranged from 36 to 86 m/s and water superficial velocities ranged from 0 to 0.32 m/s.

Since this is an upward-vertical flow dataset, we perform coupled flow calculations. The circular pipe diameter, D_H, was given as 0.03175 m. We also specified a hydraulic roughness, k_{wall}, of 0.000015 m for the steel pipe used in the experiment. For the conditions of the experiment, the viscosity of the air was given as 0.000018 Pa-s. Similarly, the viscosity of the water was given as 0.001 Pa-s. The interfacial tension between the air and water, $\sigma_{2,1}$, was assumed as 0.0723 Pa-m.

In terms of the densities and superficial velocities, the specified air density, ρ_2, was 1.405 kg/m^3. The specified water density, ρ_1, was 998.43 kg/m^3. The specified superficial velocity of the air, $\langle u_2 \rangle$, was 46.48 m/s. The specified superficial velocity of the water, $\langle u_1 \rangle$, was 0.1565 m/s. These values of densities and superficial velocities are uncorrected values that must be corrected according to our bi-directional two-phase entrainment calculations in Eqn. G.14 of Appendix G. But in order to perform the corrections, either an estimate or measurement of the entrained liquid fraction in the vapor phase, $E_{1\rightarrow 2}$, must be obtained. Since only volume fraction and pressure gradient measurements were provided in this investigation, $E_{1\rightarrow 2}$ measurements are unavailable. We therefore estimate $E_{1\rightarrow 2}$ using the Ishii and Mishima (1982) entrainment correlation, as:

$$E_{1\to 2} = \tanh\left(7.25\times 10^{-7} \left(\overbrace{\left(\frac{\rho_2 \langle u_2 \rangle^2 D_H}{\sigma_{2,1}} \right)\left(\frac{|\Delta\rho|}{\rho_2} \right)^{\frac{1}{3}}}^{\textit{Effective Sup. phase-2 Weber No.}} \right)^{1.25} \times \left(\overbrace{\frac{\rho_1 \langle u_1 \rangle D_H}{\mu_1}}^{\textit{Sup. phase-1 Reynolds No.}} \right)^{0.25} \right)$$

$$= \tanh\left(7.25\times 10^{-7} \left(\left(\frac{(1.405)(46.48)^2 (0.03175)}{0.0723} \right)\left(\frac{998.43-1.405}{1.405} \right)^{\frac{1}{3}} \right)^{1.25} \times \left(\frac{(998.43)(0.1565)(0.03175)}{0.001} \right)^{0.25} \right) \tag{20}$$

$$= 0.631$$

From Eqn. G.18 of Appendix G, the entrained vapor fraction in the liquid phase, $E_{2'\to 1'}$ is:

$$E_{2'\to 1'} = E_{1\to 2}\left(\frac{\langle u_1 \rangle}{\langle u_2 \rangle} \right)^{2-E_{1\to 2}} = 0.631\left(\frac{0.1565}{46.48} \right)^{2-0.631} = 0.00026 \tag{21}$$

From the above calculated phase entrainment fractions, we can now calculate the corrected densities and superficial velocities to use in our coupled flow calculations. The corrected air density, $\rho_{2\leftarrow 1}^{corr}$, is:

$$\rho_{2\leftarrow 1}^{corr} = \frac{\rho_2 \langle u_2 \rangle + \rho_1 \langle u_1 \rangle E_{1\to 2}}{\langle u_2 \rangle + \langle u_1 \rangle E_{1\to 2}} = \frac{(1.405)(46.48) + (998.43)(0.1565)(0.631)}{46.48 + (0.1565)(0.631)} = 3.5187 \ \frac{kg}{m^3} \tag{22}$$

Next, the corrected water density, $\rho_{1'\leftarrow 2'}^{corr}$, is:

$$\rho_{1'\leftarrow 2'}^{corr} = \frac{\rho_1 \langle u_1 \rangle E_{1\to 2} + \rho_{2\leftarrow 1}^{corr} \langle u_2 \rangle E_{2'\to 1'}}{\langle u_1 \rangle (1-E_{1\to 2}) + \langle u_2 \rangle E_{2'\to 1'}} = \frac{(998.43)(0.1565)(0.631) + (3.5187)(46.48)(0.00026)}{(0.1565)(1-0.631) + (46.48)(0.00026)} = 826.13 \ \frac{kg}{m^3} \tag{23}$$

The corrected air superficial velocity, $\langle u_{2'}^{corr} \rangle$, is:

$$\langle u_{2'}^{corr} \rangle = \langle u_2 \rangle (1-E_{2'\leftarrow 1'}) = 46.48(1-0.00026) = 46.469 \ \frac{m}{s} \tag{24}$$

And, the corrected water superficial velocity, $\left\langle u_1^{corr} \right\rangle$, is:

$$\left\langle u_1^{corr} \right\rangle = \left\langle u_1 \right\rangle \left(1 - E_{1\to 2}\right) = 0.1565\left(1 - 0.631\right) = 0.0577 \ \frac{m}{s} \tag{25}$$

Therefore, the fractional flow of the air, f_2, is:

$$f_2 = \frac{\left\langle u_{2'}^{corr} \right\rangle}{\left\langle u_{2'}^{corr} \right\rangle + \left\langle u_1^{corr} \right\rangle} = 0.99876 \tag{26}$$

Using the ANSLIP analytical model for volume fraction prediction, we use the calculated air fractional flow in Eqn. 26 above, to arrive at:

$$\left\langle s_2 \right\rangle = \frac{f_2 + 1 \ - \left(\left(f_2 + 1 \right)^2 \ - 4\left(f_2 \right)^2 \right)^{\frac{1}{2}}}{2 f_2} = 0.965 \tag{27}$$

This prediction compares quite favorably with the measured air volume fraction given in this experiment as 0.955. The hydrostatic pressure gradient (HPG) for the multiphase mixture can now be computed (from Eqn. 1 of Section 2.2.6 of Chapter 2), as:

$$\begin{aligned} \left(\sum_{j=1}^{N_p} \left(\rho_j^{corr} \left\langle s_j \right\rangle \right) \right) g \cos\theta &= \left(\rho_{2\leftarrow 1}^{corr} \left\langle s_2 \right\rangle + \rho_{1'\leftarrow 2'}^{corr} \left(1 - \left\langle s_2 \right\rangle \right) \right) g \cos\theta \\ &= \left(\left(3.5187\right)\left(0.965\right) \ + \ \left(826.13\right)\left(1 - 0.965\right) \right)\left(9.81\right)\left(1\right) \\ &= 313.96 \ \frac{Pa}{m} \end{aligned} \tag{28}$$

Next, we compute the frictional pressure gradient (FPG) for the multiphase mixture. The in-situ Reynolds number for the water is:

$$N_{\mathrm{Re},1} = \frac{\left| G_1^{corr} \right| D_H}{\mu_1 \left(1 - \left\langle s_1 \right\rangle \right)} = \frac{\rho_{1'\leftarrow 2'}^{corr} \left| \left\langle u_1^{corr} \right\rangle \right| D_H}{\mu_1 \left(1 - \left\langle s_1 \right\rangle \right)} = \frac{\left(826.13\right)\left(0.0577\right)\left(0.03175\right)}{\left(0.001\right)\left(1 - 0.965\right)} = 40994 \tag{29}$$

Similarly, the in-situ Reynolds number for the air is:

$$N_{\mathrm{Re},2} = \frac{\left|G_{2'}^{corr}\right| D_H}{\mu_2 \left\langle s_2 \right\rangle} = \frac{\rho_{2\leftarrow 1}^{corr} \left|\left\langle u_{2'}^{corr} \right\rangle\right| D_H}{\mu_2 \left\langle s_2 \right\rangle} = \frac{(3.5187)(46.469)(0.03175)}{(0.000018)(0.965)} = 298763 \quad (30)$$

Since these Reynolds numbers classify as turbulent according to Eqn. 4 of Section 2.2.4 of Chapter 2, the applicable water friction factor is:

$$\begin{aligned} f_{1\rightarrow wall} &= \left(-3.6 \log_{10} \left(\frac{6.9}{N_{\mathrm{Re},1}} + \left(\frac{1}{3.7} \frac{k_{wall}}{D_H} \right)^{\frac{10}{9}} \right) \right)^{-2} \\ &= \left(-3.6 \log_{10} \left(\frac{6.9}{40994} + \left(\frac{1}{3.7} \frac{0.000015}{0.03175} \right)^{\frac{10}{9}} \right) \right)^{-2} = 0.00574 \end{aligned} \quad (31)$$

And, the applicable air friction factor is:

$$\begin{aligned} f_{2\rightarrow wall} &= \left(-3.6 \log_{10} \left(\frac{6.9}{N_{\mathrm{Re},2}} + \left(\frac{1}{3.7} \frac{k_{wall}}{D_H} \right)^{\frac{10}{9}} \right) \right)^{-2} \\ &= \left(-3.6 \log_{10} \left(\frac{6.9}{298763} + \left(\frac{1}{3.7} \frac{0.000015}{0.03175} \right)^{\frac{10}{9}} \right) \right)^{-2} = 0.00447 \end{aligned} \quad (32)$$

Thus, we can now calculate the frictional pressure gradient for the multiphase mixture, as:

$$\begin{aligned} &\frac{Z}{A} \sum_{j=1}^{N_p} \left(\frac{\gamma_j f_{j\rightarrow wall} \left|G_j^{corr}\right| G_j^{corr}}{2\rho_j^{corr} \left\langle s_j \right\rangle^2} \right) \\ &= \left(\frac{2}{D_H} \right) \left(\frac{f_{1\rightarrow wall} \rho_{1'\leftarrow 2'}^{corr} \left|\left\langle u_1^{corr} \right\rangle\right| \left\langle u_1^{corr} \right\rangle}{\left(1 - \left\langle s_2 \right\rangle\right)^2} + \frac{f_{2\rightarrow wall} \rho_{2\leftarrow 1}^{corr} \left|\left\langle u_{2'}^{corr} \right\rangle\right| \left\langle u_{2'}^{corr} \right\rangle}{\left\langle s_2 \right\rangle^2} \right) \\ &= \left(\frac{2}{0.03175} \right) \left(\frac{(0.00574)(826.13)(0.0577)^2}{(1-0.965)^2} + \frac{(0.00447)(3.5187)(46.469)^2}{(0.965)^2} \right) \\ &= 829.84 + 2297.25 = 3127.09 \frac{Pa}{m} \end{aligned} \quad (33)$$

The total pressure gradient (TPG) for the mixture is therefore 3127.09 + 313.96 = 3441.05 Pa/m. This analytical prediction is close to the measured total pressure gradient reported in the experiment as 3283 Pa/m. We note that this is a friction-dominated system for high-rate vertical vapor-liquid flow.

4.2.4 Coupled Flow in Non-Circular Conduits

For this worked example, we demonstrate the simple way in which the combination of hydraulic diameter, D_H, and area open to flow, A, allows for the capability to simulate any conduit cross-sectional shape with our universal analytical momentum balance equations. We select a dataset from the horizontal annulus air (phase 2) and water (phase 1) experiments of Ekberg (1998) – Run no. 630, Set A in this reference. The circular-annulus pipe hydraulic diameter, D_H, is 0.00203 m (0.03518 – 0.03315 m) and the area open to flow is 0.00010894 m^2. The hydraulic roughness, k_{wall}, was specified as 0.00002 m. For the conditions of this experimental run (system pressure = 223400 Pa, system temperature = 22 °C), the viscosity of the air was assumed as 0.000018 Pa-s. Similarly, the viscosity of the water was assumed as 0.001 Pa-s. The ideal-gas air density was calculated as 2.637 kg/m^3 and the water density was assumed as 1000 kg/m^3.

The specified superficial velocity of the air, $\langle u_2 \rangle$, is 16.49 m/s. The specified superficial velocity of the water, $\langle u_1 \rangle$, is 1.442 m/s. Therefore the fractional flow of the air, f_2, is:

$$f_2 = \frac{\langle u_2 \rangle}{\langle u_2 \rangle + \langle u_1 \rangle} = 0.9196 \tag{34}$$

Using the BUTTERWORTH model for volume fraction prediction (Eqns. 4b and 5a of Section 3.1.1 of Chapter 3), we find:

$$\langle s_2 \rangle = \left(0.28 \left(\left(\frac{1-f_2}{f_2} \right)^{0.9} \left(\frac{\rho_2}{\rho_1} \right)^{-0.4} \left(\frac{\mu_2}{\mu_1} \right)^{-0.1} \right)^{0.71} + 1 \right)^{-1}$$

$$= \left(0.28 \left(\left(\frac{1-0.9196}{0.9196} \right)^{0.9} \left(\frac{2.637}{1000} \right)^{-0.4} \left(\frac{0.000018}{0.001} \right)^{-0.1} \right)^{0.71} + 1 \right)^{-1}$$

$$= 0.7023 \tag{35}$$

Next, the in-situ Reynolds number for the water is:

$$N_{\mathrm{Re},1} = \frac{|G_1| D_H}{\mu_1 (1 - \langle s_1 \rangle)} = \frac{\rho_1 |\langle u_1 \rangle| D_H}{\mu_1 (1 - \langle s_1 \rangle)} = \frac{(1000)(1.442)(0.00203)}{(0.001)(1-0.7023)} = 9834 \tag{36}$$

Similarly, the in-situ Reynolds number for the air is:

$$N_{\mathrm{Re},2} = \frac{|G_2| D_H}{\mu_2 \langle s_2 \rangle} = \frac{\rho_2 |\langle u_2 \rangle| D_H}{\mu_2 \langle s_2 \rangle} = \frac{(2.637)(16.49)(0.00203)}{(0.000018)(0.7023)} = 6984 \tag{37}$$

Since these Reynolds numbers classify as turbulent according to Eqn. 4 of Section 2.2.4 of Chapter 2, the applicable water friction factor is:

$$f_{1 \to wall} = \left(-3.6 \log_{10} \left(\frac{6.9}{N_{\mathrm{Re},1}} + \left(\frac{1}{3.7} \frac{k_{wall}}{D_H} \right)^{\frac{10}{9}} \right) \right)^{-2}$$

$$= \left(-3.6 \log_{10} \left(\frac{6.9}{9834} + \left(\frac{1}{3.7} \frac{0.00002}{0.00203} \right)^{\frac{10}{9}} \right) \right)^{-2} = 0.0107 \tag{38}$$

And, the applicable air friction factor is:

$$f_{2 \to wall} = \left(-3.6 \log_{10} \left(\frac{6.9}{N_{\mathrm{Re},2}} + \left(\frac{1}{3.7} \frac{k_{wall}}{D_H} \right)^{\frac{10}{9}} \right) \right)^{-2}$$

$$= \left(-3.6 \log_{10} \left(\frac{6.9}{6984} + \left(\frac{1}{3.7} \frac{0.00002}{0.00203} \right)^{\frac{10}{9}} \right) \right)^{-2} = 0.0112 \tag{39}$$

We can now calculate the total (frictional) pressure gradient for the multiphase mixture, as:

$$\frac{Z}{A}\sum_{j=1}^{N_p}\left(\frac{\gamma_j f_{j\to wall}\left|G_j\right|G_j}{2\rho_j\left\langle s_j\right\rangle^2}\right)$$
$$=\left(\frac{2}{D_H}\right)\left(\frac{f_{1\to wall}\rho_1\left|\left\langle u_1\right\rangle\right|\left\langle u_1\right\rangle}{\left(1-\left\langle s_2\right\rangle\right)^2}+\frac{f_{2\to wall}\rho_2\left|\left\langle u_2\right\rangle\right|\left\langle u_2\right\rangle}{\left\langle s_2\right\rangle^2}\right) \tag{40}$$
$$=\left(\frac{2}{0.00203}\right)\left(\frac{(0.0107)(1000)(1.442)^2}{(1-0.7023)^2}+\frac{(0.0112)(2.637)(16.49)^2}{(0.7023)^2}\right)$$
$$=248011+16028=264039\frac{Pa}{m}$$

This total pressure gradient prediction above is in very close agreement with the measured total pressure gradient reported in the experiment as 265600 Pa/m.

4.2.5 Coupled Flow in Micro-Channels

We now repeat the horizontal, coupled flow calculations as in the previous worked example but with a very small diameter, such as found in a micro-channel. We select a dataset from the experiments of Saisorn and Wongwises (2009) – specifically from Fig. 17 of this reference. In these experiments, volume fraction and pressure gradient measurements were obtained from a 150 microns (D_H = 0.00015 m) fused silica circular tube. For the conditions of these experiments (system pressure = 101325 Pa, system temperature = 25 °C), the viscosity of the air was specified as 0.000012 Pa-s. The viscosity of the water was specified as 0.00065 Pa-s. The ideal-gas air density was calculated as 1.184 kg/m^3 and the water density was specified as 995 kg/m^3.

The specified superficial velocity of the air, $\left\langle u_2\right\rangle$, is 28.28 m/s. The specified superficial velocity of the water, $\left\langle u_1\right\rangle$, is 0.237 m/s. Therefore the fractional flow of the air, f_2, is:

$$f_2=\frac{\left\langle u_2\right\rangle}{\left\langle u_2\right\rangle+\left\langle u_1\right\rangle}=0.9917 \tag{41}$$

Using the BUTTERWORTH model for volume fraction prediction (Eqns. 4b and 5a of Section 3.1.1 of Chapter 3), we find:

$$\begin{aligned}\langle s_2 \rangle &= \left(0.28 \left(\left(\frac{1-f_2}{f_2} \right)^{0.9} \left(\frac{\rho_2}{\rho_1} \right)^{-0.4} \left(\frac{\mu_2}{\mu_1} \right)^{-0.1} \right)^{0.71} + 1 \right)^{-1} \\ &= \left(0.28 \left(\left(\frac{1-0.9917}{0.9917} \right)^{0.9} \left(\frac{1.184}{995} \right)^{-0.4} \left(\frac{0.000012}{0.00065} \right)^{-0.1} \right)^{0.71} + 1 \right)^{-1} \\ &= 0.894 \end{aligned} \tag{42}$$

Next, the in-situ Reynolds number for the water is:

$$N_{\mathrm{Re},1} = \frac{|G_1| D_H}{\mu_1 (1-\langle s_1 \rangle)} = \frac{\rho_1 |\langle u_1 \rangle| D_H}{\mu_1 (1-\langle s_1 \rangle)} = \frac{(995)(0.237)(0.00015)}{(0.00065)(1-0.894)} = 513 \tag{43}$$

And, the in-situ Reynolds number for the air is:

$$N_{\mathrm{Re},2} = \frac{|G_2| D_H}{\mu_2 \langle s_2 \rangle} = \frac{\rho_2 |\langle u_2 \rangle| D_H}{\mu_2 \langle s_2 \rangle} = \frac{(1.184)(28.28)(0.00015)}{(0.000012)(0.894)} = 468 \tag{44}$$

Since these Reynolds numbers classify as laminar according to Eqn. 4 of Section 2.2.4 of Chapter 2, the applicable water friction factor is:

$$f_{1 \to wall} = \frac{16}{N_{\mathrm{Re},1}} = \frac{16}{513} = 0.0312 \tag{45}$$

And, the applicable air friction factor is:

$$f_{2 \to wall} = \frac{16}{N_{\mathrm{Re},2}} = \frac{16}{468} = 0.0342 \tag{46}$$

Note that these laminar-laminar flows in micron-scale flows are most analogous to that found in the multiphase flows in pore-network models for porous media modeling. We can now calculate the total (frictional) pressure gradient for the multiphase mixture, as:

$$
\begin{aligned}
&\frac{Z}{A}\sum_{j=1}^{N_p}\left(\frac{\gamma_j f_{j\to wall}\left|G_j\right|G_j}{2\rho_j\left\langle s_j\right\rangle^2}\right)\\
&=\left(\frac{2}{D_H}\right)\left(\frac{f_{1\to wall}\rho_1\left|\left\langle u_1\right\rangle\right|\left\langle u_1\right\rangle}{\left(1-\left\langle s_2\right\rangle\right)^2}+\frac{f_{2\to wall}\rho_2\left|\left\langle u_2\right\rangle\right|\left\langle u_2\right\rangle}{\left\langle s_2\right\rangle^2}\right) \qquad (47)\\
&=\left(\frac{2}{0.00015}\right)\left(\frac{(0.0312)(995)(0.237)^2}{(1-0.894)^2}+\frac{(0.0342)(1.184)(28.28)^2}{(0.894)^2}\right)\\
&=2067151+539877=2607028\frac{Pa}{m}
\end{aligned}
$$

The total pressure gradient prediction above is in very close agreement with the measured total pressure gradient reported in the experiment as 2533088 Pa/m.

4.2.6 Decoupled Flow

In this last worked-example, we go to the other extent of scale from the previous example and look at subset of the down-inclined, low-liquids loading, large-diameter experiments of Fan (2005) – specifically, test no. 199 in this reference. We will use this dataset to showcase our decoupled flow calculations.

In these air (phase 2) and water (phase 1) experiments, volume fraction and pressure gradient measurements were obtained from a circular pipe of diameter, D_H, of 0.1496 m at a slightly downward inclination of 2 degrees from horizontal. The hydraulic roughness, k_{wall}, was specified as 0.00003 m. For the conditions of these experiments (system pressure = 101325 Pa, system temperature = 25 °C), the viscosity of the air was assumed as 0.000018 Pa-s. The viscosity of the water was assumed as 0.001 Pa-s. The air density was specified as 1.22 kg/m^3 and the water density was specified as 950 kg/m^3.

The specified superficial velocity of the air, $\langle u_2 \rangle$, is 16.2 m/s. The specified superficial velocity of the water, $\langle u_1 \rangle$, is 0.0102 m/s. Therefore the fractional flow of the air, f_2, is:

$$f_2 = \frac{\langle u_2 \rangle}{\langle u_2 \rangle + \langle u_1 \rangle} = 0.99937 \tag{48}$$

The ANSLIP analytical model for volume fraction could be used to predict this quantity, resulting in $\langle s_2 \rangle$ = 0.975. However, because we want to demonstrate the validity of our decoupled flow equations, we will use the measured air volume fraction of 0.988 in our analysis. Though this difference is fairly minor, by using the measured volume fraction, we eliminate the possibility that the difference in our calculated total pressure gradient with respect to its measured value can be due to an error in volume fraction calculation.

The hydrostatic pressure gradient (HPG) for the multiphase mixture can now be computed, as:

$$\begin{aligned} \left(\sum_{j=1}^{N_p} \left(\rho_j \langle s_j \rangle \right) \right) g \cos\theta &= \left(\rho_2 \langle s_2 \rangle + \rho_1 \left(1 - \langle s_2 \rangle \right) \right) g \cos\theta \\ &= \left((1.22)(0.988) \; + \; (950)(1-0.988) \right)(9.81)(-0.0349) \\ &= -4.283 \; \frac{Pa}{m} \end{aligned} \tag{49}$$

Next, the (unit) net momentum flux transfer surface, Z_j^{net}, for each phase must be computed. For a two-phase circular pipe, the applicable decoupled flow equations are F.10, F.12a and F.12c in Appendix F. From Eqn. F.12c of Appendix F, we find that the circular-pipe center angle subtending phase-1, δ_1^{2P}, is 0.7738 radians at $\langle s_2 \rangle$ = 0.988. Thus, from Eqn. F.12a, we thus arrive at:

$$Z_{1\to wall} = D_H\left(\frac{\delta_1^{2P}}{2}\right) = 0.1496\left(\frac{0.7738}{2}\right) = 0.0579\ m,$$
$$Z_{2\to wall} = D_H\left(\pi - \left(\frac{\delta_1^{2P}}{2}\right)\right) = 0.1496\left(\pi - \frac{0.7738}{2}\right) = 0.4121\ m, \tag{50}$$
$$Z_{2,1} = D_H \sin\left(\frac{\delta_1^{2P}}{2}\right) = 0.1496\sin\left(\frac{0.7738}{2}\right) = 0.0565\ m$$

And, from Eqn. F.10 of Appendix F, we get:

$$Z_1^{net} = Z_{1\to wall} + \frac{Z_{2,1}}{2} = 0.0579 + \frac{0.0565}{2} = 0.0861\ m,$$
$$Z_2^{net} = Z_{2\to wall} + 2Z_{1\to wall} + \frac{Z_{2,1}}{2} = 0.4121 + 2\left(0.0579\right) + \frac{0.0565}{2} = 0.5561\ m \tag{51}$$

Therefore, the decoupled flow hydraulic diameters can be calculated as:

$$D_{H,1}^{net} = \frac{4A}{Z_1^{net}} = \frac{4\left(0.017577\right)}{0.0861} = 0.8165\ m,$$
$$D_{H,2}^{net} = \frac{4A}{Z_2^{net}} = \frac{4\left(0.017577\right)}{0.5561} = 0.1264\ m \tag{52}$$

Next, the in-situ Reynolds number for the water is:

$$N_{\mathrm{Re},1} = \frac{\left|G_1\right| D_{H,1}^{net}}{\mu_1\left(1-\left\langle s_1\right\rangle\right)} = \frac{\rho_1\left|\left\langle u_1\right\rangle\right| D_{H,1}^{net}}{\mu_1\left(1-\left\langle s_1\right\rangle\right)} = \frac{\left(950\right)\left(0.0102\right)\left(0.8165\right)}{\left(0.001\right)\left(1-0.988\right)} = 664879 \tag{53}$$

And, the in-situ Reynolds number for the air is:

$$N_{\mathrm{Re},2} = \frac{\left|G_2\right| D_{H,2}^{net}}{\mu_2\left\langle s_2\right\rangle} = \frac{\rho_2\left|\left\langle u_2\right\rangle\right| D_{H,2}^{net}}{\mu_2\left\langle s_2\right\rangle} = \frac{\left(1.22\right)\left(16.2\right)\left(0.1264\right)}{\left(0.000018\right)\left(0.988\right)} = 140498 \tag{54}$$

Since these Reynolds numbers classify as turbulent according to Eqn. 4 of Section 2.2.4 of Chapter 2, the applicable water friction factor is:

$$f_{1\to wall} = \left(-3.6\log_{10}\left(\frac{6.9}{N_{\mathrm{Re},1}} + \left(\frac{1}{3.7}\frac{k_{wall}}{D_{H,1}^{net}}\right)^{\frac{10}{9}}\right)\right)^{-2}$$
$$= \left(-3.6\log_{10}\left(\frac{6.9}{664879} + \left(\frac{1}{3.7}\frac{0.00003}{0.8165}\right)^{\frac{10}{9}}\right)\right)^{-2} = 0.00324 \tag{55}$$

And, the applicable air friction factor is:

$$f_{2\to wall} = \left(-3.6\log_{10}\left(\frac{6.9}{N_{\mathrm{Re},2}} + \left(\frac{1}{3.7}\frac{k_{wall}}{D_{H,2}^{net}} \right)^{\frac{10}{9}} \right) \right)^{-2}$$
$$= \left(-3.6\log_{10}\left(\frac{6.9}{140498} + \left(\frac{1}{3.7}\frac{0.00003}{0.1264} \right)^{\frac{10}{9}} \right) \right)^{-2} = 0.00448 \quad (56)$$

We can now calculate the frictional pressure gradient for the multiphase mixture from Eqn. 2 of Section 4.1, as:

$$\sum_{j=1}^{N_p}\left(\frac{Z_j^{net}}{A}\left(\frac{\gamma_j f_{j\to wall}\left|G_j\right|G_j}{2\rho_j\left\langle s_j\right\rangle^2} \right) \right)$$
$$= \left(\frac{2}{D_{H,1}^{net}} \right)\left(\frac{f_{1\to wall}\rho_1\left|\left\langle u_1\right\rangle\right|\left\langle u_1\right\rangle}{\left(1-\left\langle s_2\right\rangle\right)^2} \right) + \left(\frac{2}{D_{H,2}^{net}} \right)\left(\frac{f_{2\to wall}\rho_2\left|\left\langle u_2\right\rangle\right|\left\langle u_2\right\rangle}{\left\langle s_2\right\rangle^2} \right) \quad (57)$$
$$= \left(\frac{2}{0.8165} \right)\left(\frac{(0.00324)(950)(0.0102)^2}{(1-0.988)^2} \right) + \left(\frac{2}{0.1264} \right)\left(\frac{(0.00448)(1.22)(16.2)^2}{(0.988)^2} \right)$$
$$= 5.536 + 23.258 = 28.794\frac{Pa}{m}$$

The total pressure gradient (TPG) for the mixture is therefore 28.794 – 4.283 = 24.51 Pa/m. This analytical prediction is very close to the measured total pressure gradient reported in the experiment as 23.8 Pa/m.

4.3 Effect of Flow Rate

Now that the calculations steps of our analytical equations are clear, we next provide validation and prediction for specific types of problems according to the standardized multiphase flow problem definitions proposed in Table 1.1 in Chapter 1. For the fully-developed flow datasets analyzed in Sections 4.3 to 4.13, the same simplified versions of Eqns. 6 and 7 of Section 2.2.4 that was used in Eqns. 1 and 2 of

Section 4.1 above, will also be used in our calculations. These are spreadsheet calculations of the appropriate frictional and hydrostatic pressure gradient terms. It is only for the developing flow datasets (which require computations along the pipe) will the convective and/or temporal acceleration/deceleration terms be solved together with the frictional and hydrostatic terms. In these latter cases, the UTPipeFlow code is run to furnish computations along the pipe.

In this section, we look at experiments that highlight the effect of flow rate. One popular class of flow rate problems that falls under this effect is the low liquids loading problem. It is found in this work, that pressure gradients in low liquids loading problems can be satisfactorily described with the decoupled flow hypothesis. Fig. 4.3.1 shows some of the experiments from Badie (2000). This work was concerned with horizontal stratifying/annular air (phase 2) and liquid (phase 1) flows at low liquid rates. To demonstrate the validity of our decoupled flow equations for this dataset, we isolate the decoupled flow pressure gradient calculations by inputting the measured air volume fractions into the equations. Fig. 4.3.1a shows the decoupled-flow total pressure gradient calculations against all of the air-water flows in this investigation. As is evident, there is an excellent agreement between the model and experiments. To investigate whether our model can correctly account for a change in fluid properties at these low flow rates, an air-oil experiment at the same air superficial velocity as for the air-water case, was tested. This is shown in Fig. 4.3.1b. The decoupled flow models can clearly reproduce this dataset.

Next, we validate our decoupled flow analytical models against the entire air (phase 2) and kerosene (phase 1) dataset of Brill (1996). This dataset was analyzed previously in Fig.3.2.8 of Chapter 3, where it was shown that the stratified-wavy volume fraction behavior in these low liquids loading experiments could be accurately modeled

analytically with the ANSLIP model. This is also shown in Fig. 4.3.2a and 4.3.2b. Using the ANSLIP model, the predictions of the decoupled flow equations are shown in Fig. 4.3.2c. As seen, the agreement of our models with the data is excellent. Note that in many cases, we will report the total pressure gradient ratio, which is the total pressure gradient of the multiphase flow divided by the total pressure gradient of the least dense phase (the vapor phase in this case) as if it were flowing in the pipe alone.

We next validate our decoupled flow analytical models with a subset of the large-diameter low liquids loading air (phase 2) and water (phase 1) experiments of Fan (2005). This experimental investigation was previously highlighted in Section 4.2.6 above. Fig. 4.3.3 shows all of the slightly downward flow stratified-wavy experiments (test nos. 198 – 231) at an angle of 2 degrees from horizontal. The measured air volume fractions were used in our calculations. It is clear that the pressure gradient calculations are accurate at this larger scale. Fig. 4.3.4 shows all of the horizontal flow stratified-wavy experiments (test nos. 232 – 287). As before, the decoupled flow equations are validated. Fig. 4.3.5 shows all of the slightly upward flow stratified-wavy experiments (test nos. 288 – 320) at an angle of 2 degrees from horizontal. Evidently, these results prove that once the volume fraction is correct, our decoupled flow equations are not only accurate but also correctly capture slight inclination changes at these low flow rates and large diameter.

4.4 EFFECT OF PROPERTIES

We next perform validation of our analytical models against experiments with changing fluid and system properties. We first select all of the experiments from the classic reference of Hughmark (1959). This choice of dataset is deliberate since the flow patterns were not reported for the experiments. Thus, the ability to accurately reproduce these experiments would validate the first insight of this research – that pressure gradient

is governed by relative velocity and that the flow patterns are merely the visual manifestations of relative velocity. In this wide-ranging investigation, several liquids (phase 1) were flowed with air (phase 2) with different viscosities, densities and interfacial tensions. To properly isolate (and therefore properly validate) whether our pressure gradient calculations can correctly describe these wide differences in liquid properties, we use the measured air volume fractions in our calculations.

Fig. 4.4.1b shows all of the air-water comparisons. In Fig. 4.4.1a, the conditions at which the experiments were conducted are shown in terms of a dimensionless Reynolds number plot. It is evident that once the volume fraction is known, our analytical models are accurate and captures the physical trends in the data. Fig. 4.4.2b shows all of the air-sodium carbonate comparisons. The sodium carbonate liquid had a viscosity of 0.00315 Pa-s, a density of 1185 kg/m^3 and an interfacial tension with air of 0.0759 Pa-m. Fig. 4.4.3b shows all of the air-varsol comparisons. The varsol liquid had a viscosity of 0.00107 Pa-s, a density of 777 kg/m^3 and an interfacial tension with air of 0.0249 Pa-m. Fig. 4.4.5b shows all of the air-oil blend 1 comparisons. The oil blend 1 liquid had a viscosity of 0.00583 Pa-s, a density of 825 kg/m^3 and an interfacial tension with air of 0.0274 Pa-m. Fig. 4.4.6b shows all of the air-oil blend 2 comparisons. The oil blend 2 liquid had a viscosity of 0.02859 Pa-s, a density of 868 kg/m^3 and an interfacial tension with air of 0.0299 Pa-m. Fig. 4.4.7b shows all of the air-trichloroethylene comparisons. The trichloroethylene liquid had a viscosity of 0.00055 Pa-s, a density of 1424 kg/m^3 and an interfacial tension with air of 0.0288 Pa-m. As seen from these results, our analytical calculations not only correctly capture the trends in the data but are consistently accurate.

Having validated that changes in fluid properties are accurately captured with our analytical models so long as the volume fraction is known (thus narrowing modeling

uncertainty to this tractable variable), we next showcase how analytical predictions can be provided for volume fractions in concert with our analytical pressure gradient models. Figs. 4.4.8 – 4.4.10 show all of the data from the wide-ranging vertical upward flow experimental campaign of Sujumnong (1997). As in the Hughmark (1959) work, different liquids (phase 1) were flowed with air (phase 2) having different viscosities, densities and interfacial tensions.

Fig. 4.4.8b shows all of the air-water comparisons (run nos. WR1.01 – WR7.13). In Fig. 4.4.8a, the conditions at which the experiments were conducted are displayed in terms of a dimensionless Reynolds number plot, but this time, parameterized by flow pattern to show the wide ranges in observed flow patterns for the different runs. The ANSLIP analytical model was used for the air volume fraction predictions. Thus, the excellent agreement shown in Fig. 4.4.8b represents a wholly-analytical prediction of multiphase flow total pressure gradient and volume fraction. Significantly, we observe that the data displays a marked transition from laminar to turbulent flow in Fig. 4.4.8b, which is correctly reproduced by our analytical models (the lines).

Fig. 4.4.9b shows all of the air-glycerine blend 1 comparisons (run nos. G1R1.01 – G1R5.14). The glycerine blend 1 liquid had a variable viscosity at around 0.009 Pa-s, a variable density at around 1148 kg/m^3 and a variable interfacial tension with air at around 0.067 Pa-m. Fig. 4.4.10b shows all of the air-glycerine bland 2 comparisons (run nos. G2R1.01 – G2R4.06). The glycerine blend 2 liquid had a variable viscosity at around 0.078 Pa-s, a variable density at around 1212 kg/m^3 and a variable interfacial tension with air at around 0.068 Pa-m. From these comparisons over a wide range of flow rates, liquid properties and flow patterns, it is evident that our analytical models can predict these vapor-liquid flows quite accurately and they capture the physical trends in the data.

Other than the ANSLIP model, other models can be used for volume fraction predictions in scenarios with changing fluid properties. Fig. 4.4.11a shows the total pressure gradient predictions of Eqn. 1 of Section 4.1 with the WOLGHA model, for all the air (phase 2) and kerosene (phase 1) vertical upward data of Mukherjee (1979). Similarly, Fig. 4.4.11b shows the predictions with the WOLGHA model for all of the air-lube oil vertical upward datasets in this reference. It is clearly demonstrated that our analytical models can satisfactorily reproduce these experiments. In this experimental study, several types of flow patterns were observed.

Even within a particular flow pattern, our analytical models can be used for reliable prediction capturing the effect of changing fluid properties. Fig. 4.4.12 shows all the vertical upward churn-annular experiments of Hewitt et al. (1985). The trichloroethylene liquid in this investigation had a viscosity 0.00061 Pa-s, a density of 1460 kg/m^3 and an interfacial tension with air of 0.016 Pa-m. The air density and viscosity were 4.25 kg/m^3 and 0.0000283 Pa-s, respectively.

With the ability of our analytical models to account for changing fluid properties demonstrated, we now show how scenarios found difficult to model in the past can be effectively (and simply) modeled. Fig. 4.4.13 shows our pressure gradient predictions for the conditions of Figs. 8 and 9 of Brito et al. (2012) with the CISE model. This experimental investigation was concerned with stratified downward high viscosity ratio flows. Air (phase 2) and a heavy oil (phase 1) were flowed at a downward angle of 2 degrees from horizontal. The mineral heavy oil used in this investigation had a viscosity 0.181 Pa-s, a density of 890 kg/m^3 and an interfacial tension with air of 0.03 Pa-m.

In Fig. 4.4.13a, which were for a fixed air superficial velocity of 4.5 m/s and increasing heavy oil superficial velocities, we see that our analytical models predict that as the heavy oil rate increases, the liquid level height increases which leads to an

increasingly negative mixture hydrostatic pressure gradient (harder to flow downhill). In contrast, in Fig. 4.4.13b, which were for a fixed heavy oil superficial velocity of 0.03 m/s and an increasing air rate, we see that our analytical models predict that as the air rate increases, the liquid level height decreases which leads to an decreasingly negative mixture hydrostatic pressure gradient (easier to flow downhill).

Fig. 4.4.14 shows our analytical model's predictions compared against the given time traces for these conditions. Fig. 4.4.14a-i represents the conditions at a fixed air superficial velocity of 4.5 m/s with the lowest heavy oil superficial velocity of 0.03 m/s, and Figs 4.4.14a-ii to a-iv represents heavy oil superficial velocities of 0.05, 0.07, and 0.09, respectively. Fig. 4.4.14b-i represents the conditions at a fixed heavy oil superficial velocity of 0.03 m/s with the lowest air superficial velocity of 4.5 m/s, and Figs 4.4.14b-ii and b-iii represents air superficial velocities of 5.5 and 6.5, respectively. Clearly, the changes in the liquid level heights are accurately predicted. Note that the dimensionless mean liquid level heights shown in Fig. 4.4.14 were calculated from the air volume fractions resulting from our models in combination with Eqn. F.12c of Appendix F, as:

$$\begin{aligned}\frac{h_1}{D} &= 1-\cos\left(\frac{\delta_1^{2P}}{2}\right) \\ &= 1-\cos\left(\pi\left(1-\langle s_2\rangle\right)+\left(\frac{3\pi}{2}\right)^{\frac{1}{3}}\left(1-2\left(1-\langle s_2\rangle\right)+\left(1-\langle s_2\rangle\right)^{\frac{1}{3}}-\langle s_2\rangle^{\frac{1}{3}}\right)\right)\end{aligned} \tag{58}$$

Next, we look at a dataset where only the interfacial tension was decreased for the same set of operating conditions. This allows us to investigate the effect of a change in this property. We select the air (phase 2) and water-foam (phase 1) vertical upward experiments presented in van Nimwegan et al. (2012). This experimental investigation was geared towards analyzing a specific practical application in the petroleum industry – gas well deliquification (an artificial lift concept) – in which purely hydrodynamically-

formed foam could be utilized to reduce the hydrostatic pressure gradient by adding surfactants (foamers) to the water phase.

Fig. 4.4.15a shows our analytical model's predictions with the WOLGHA model for the air-water and air-water-foam cases corresponding to a fixed water or water-foam superficial velocity of 0.01 m/s and increasing air rates from 5 to 40 m/s. Since the stable Newtonian water-foam viscosity was not reported in the reference, we varied this parameter to show how this variation affects the total pressure gradient predictions. Note that the WOLGHA model is the only of our "recommended" models of Section 3.5 in Chapter 3 that has interfacial tension dependence and it is for this reason this model was chosen. For the air-water flows, the interfacial tension was specified as 72 dynes/cm and for the air-water-foam flows the interfacial tension was reduced to 1 dynes/cm. As is evident, the correct trends in the data are predicted for both the pressure gradient (Fig. 4.4.15a) and volume fraction (Fig. 4.4.15b).

Lastly, we investigate whether a change in the wall roughness property can be satisfactorily captured by our analytical models. To do this, we select the carefully-controlled air (phase 2) and water (phase 1) horizontal flow wall roughness experiments of Chisolm and Laird (1958). In these experiments, similar operating conditions and rates were maintained with an increase in only the wall roughness. Because these are horizontal fully-developed flow experiments, this helps to isolate (and quantify) the ability of our models to correctly predict the frictional pressure gradient. Figs. 4.4.16a-i, b-i, c-i and d-i shows the validation of our total (frictional) pressure gradient calculations for relative wall roughness values of 0.000056 (smooth brass pipe), 0.0025 (commercial galvanize pipe), 0.037 (internally threaded pipe) and 0.068 (pipe with uniformly distributed sand layer), respectively.

Figs. 4.4.16a-ii, b-ii, c-ii and d-ii show the measured air volume fractions used in our pressure gradient calculations. The ANSLIP model (the solid red line) is superimposed in these figures for reference. It is clear from the right-most figures of Fig. 4.4.16, that a change in wall roughness causes a change in the volume fractions. This is a key insight. It means that it is reasonable to expect that other wall-related phenomena, such as wettability, will also affect the volume fraction behavior (the in-situ relative velocity behavior) of the flow. In experiments where there are measured volume fractions, it will thus be possible to unambiguously quantify (and relate) the effect of these wall changes to the volume fraction behavior and thus the resulting pressure gradient behavior. We will clearly demonstrate this in later sections of this chapter as well as in the liquid-liquid flows of the next chapter. As is evident in Fig. 4.4.16, our models accurately account for changes in wall roughness. Note also how the change in the pressure gradients with respect to the laminar to turbulent transition is sharper at higher wall roughness values.

Fig. 4.4.17 shows the same results as Fig. 4.4.16 but with the ANSLIP analytical model used for volume fraction prediction. As expected, the difference in the pressure gradients calculated in Fig. 4.4.16 and 4.4.17 can be directly traced to the difference in the volume fraction – particularly at the lower water rates and higher roughness values where there is more observed averaged slip than that provided by the ANSLIP model prediction. These figures are important because they unambiguously trace the root causes of the dominant errors in models, i.e., the determination of the averaged volume fraction.

4.5 EFFECT OF MASS CHANGE

We next interrogate our analytical models for their ability to account for inter-phase mass exchange such as that which occurs in annular flows with bi-directional entrainment. We will validate our entrainment models developed in Appendix G with carefully-controlled vapor-liquid annular flow experiments.

Fig. 4.5.1 shows three different air (phase 2) and water (phase 1) annular flow datasets in which both the measured air volume fraction, $\langle s_2 \rangle$, and the measured liquid entrainment fraction, $E_{1\to 2}$, are available. Therefore, the simplest, unambiguous way to demonstrate the need for including entrainment in total pressure gradient calculations is to input both the measured $\langle s_2 \rangle$ and $E_{1\to 2}$ into our universal analytical models (Fig. 4.5.1a) and then to only input the measured $\langle s_2 \rangle$ with $E_{1\to 2}$ set to 0 (no entrainment, Fig. 4.5.1b). Not only do these graphs clearly show the need for including entrainment, but they also show that our universal analytical models are very accurate if these quantities are known (yet again proving the first insight of this work). This is proper model falsification – in which our universal analytical models can be shown to be in false agreement with measured pressure gradients if the volume and entrainment fractions are wrong. The degree of error from the measured pressure gradients will directly depend on (and be traceable to) the degree to which the volume and entrainment fractions are wrong.

We repeat this model falsification but for large-diameter annular flows with entrainment such as provided in the Hossfield and Bharathan (1982) vertical upward air (phase 2) and water (phase 1) experimental investigation. In this experimental work, a circular pipe of diameter 0.152 m was carefully instrumented to acquire measurements of volume fraction, entrainment fraction and total pressure gradient. Similar to before, Fig. 4.5.2a shows the calculations of our universal analytical models when the measured $\langle s_2 \rangle$

and $E_{1\to 2}$ are input into them. Fig. 4.52b represent the case where the measured $\langle s_2 \rangle$ and $E_{1\to 2}$ = 0 are input into our universal analytical models.

Now that it is clear that bi-directional inter-phase entrainment is correctly captured by our models, we next show how either volume fraction or entrainment fraction (or both) can be predicted using either analytical models or correlations for use with our universal analytical models. Fig. 4.5.3 shows the classic air (phase 2) and water (phase 1) vertical upward annular flow dataset of Anderson and Mantzouranis (1960) in which the measured volume fraction is input into our universal analytical models and entrainment fractions are provided by the Ishii and Mishima (1982) entrainment correlation.

Fig. 4.5.4 shows another classic vertical upward annular flow dataset of Hewitt et al. (1961) in which the volume fractions and total pressure gradients were measured. Fig. 4.5.4a-i shows how far off the total pressure gradient can be when compared with measurements if entrainment is not accounted for. Figs. 4.52.a-ii shows the water densities that are used in calculations if not accounting for entrainment and Fig. 4.5.4a-iii shows the air densities that are used in calculations if not accounting for entrainment. If we account for entrainment by using the Ishii and Mishima (1982) predictions in concert with our entrainment models, then we see in Fig. 4.5.4b-i that our universal analytical models are very accurate. Indeed, Fig. 4.5.4b-ii shows how the water densities (and water superficial velocities) are reduced as a result of the entrainment process and Fig. 4.5.4b-iii shows how the air densities are increased due to entrainment. The higher the liquid entrainment, the lower the water density (and water superficial velocities) and the higher the air density. This represents a clear validation of our entrainment models as well as the need for properly accounting for entrainment.

To demonstrate the validity of our volume fraction calculations in annular flows with entrainment, we compare our analytical model predictions in cases where the measured $E_{1\to 2}$ is used in our calculations and $\langle s_2 \rangle$ is predicted. This represents the opposite scenario to the previous model validations. In Fig. 4.5.5, two different vertical upward annular flow datasets are accurately predicted in this way with the ANSLIP analytical model.

We can thus use the ANSLIP model for volume fraction prediction and the Ishii and Mishima (1982) model for liquid entrainment fraction prediction for annular flows with entrainment. Fig. 4.5.6 shows all of the data from another classic vertical upward annular flow dataset of Gill et al. (1963) predicted in this way. In this investigation, a porous sinter injection method was used. In contrast, an annular slot injection method was used for the vertical upward annular flows in Gill et al. (1965) – Fig. 4.5.7. In this latter case the ANSLIP model was again used for volume fraction predictions. As is evident, both datasets are accurately predicted with the ANSLIP model. In this work, it is found that most annular flows can be predicted with the ANSLIP model. However, in some higher liquid rate annular flows (approaching churn-annular) the BUTTERWORTH or WOLGHA models can provide a somewhat more accurate prediction.

Lastly, the previously mentioned datasets bring to light a problem of great prior concern with regards to annular flows with entrainment – that is – the question of the dependence of these flows on the injection method. A classic set of experiments clearly displaying this dependence are the annular flow sampling probe studies performed by Gill et al. 1962, 1963, 1967 in which the same operating conditions and rates were enforced with the only a change in injection method. We can carefully analyze these developing flow experiments to ascertain whether it is the injection method or the ensuing volume and entrainment fraction axial flow development (or axial volume and

entrainment fraction profiles) that cause the observed changes in the pressure and total pressure gradient along the flow. To do this, for each injection method, we will step-by-step enforce that the axial $\langle s_2 \rangle$ and $E_{1\to 2}$ measurements participate in our pressure gradient calculations.

Fig. 4.5.8 shows the porous sinter experimental results from this investigation, shown as the square points. We now first provide volume fraction predictions with the ANSLIP analytical model and enforce no liquid entrainment (the fine, solid green line). Clearly, only the latter part of the total pressure gradient axial profile is simulated with these models. We next include the effect of entrainment provided by a prediction with the Ishii and Mishima (1982) correlation (the fine, solid blue line). These combined models do not explain the observed trend in the axial total pressure gradient. If we keep the ANSLIP prediction for volume fractions but enforce that the measured axial entrainment fractions participate in our pressure gradient calculations (the fine, solid purple line), we still cannot explain the observed trends in the data. It is only if we enforce that both the measured volume and entrainment fractions participate in our pressure gradient calculations (the heavy, solid black line) that our models accurately capture both the pressure and total pressure gradient data trends. This procedure is repeated for the case where the experiments are performed with central jet injection (Fig. 4.5.9).

These results are a strong validation of our first insight – that it is the volume and entrainment fractions that govern pressure gradients. These are the principal (global) variables that must be correctly predicted to ensure an accurate prediction for averaged multiphase flow pressure gradients with our analytical models in either fully-developed or developing flow scenarios.

4.6 EFFECT OF SIZE

We next perform validation of our universal analytical models against experiments with widely differing pipe cross-sectional areas open to flow. We first select the laminar-flow air-water micro-channel experiments of Saisorn and Wongwises (2009) – specifically, Fig. 17 of this reference. In these experiments, volume fraction and pressure gradient measurements were obtained from a 150 microns (D = 0.00015 m) fused silica circular tube. Fig. 4.6.1 shows that the BUTTERWORTH model accurately predicts this dataset.

We next validate our analytical models with the classic air-water dataset of Short (1957). In Fig. 4.6.2a, the ANSLIP analytical model accurately predicts the total pressure gradients of all the data at this pipe diameter of 0.016 m. Figs. 4.6.2b and 4.6.2b shows the accurate predictions of the ANSLIP model for the other pipe sizes of 0.026 m and 0.038 m, respectively.

Fig. 4.6.3 shows a subset of the large diameter (D = 0.216 m) horizontal flow loop air-water datasets of Simpson et al. (1976). As seen in the fractional flow graph in Fig. 4.6.3a, there is a wide range of observed flow patterns. Fig. 4.6.3b shows our total pressure gradient calculations with the measured air volume fractions. Clearly, all of the trends in the total (frictional) pressure gradient are fully as a result of the changes in the fractional flow graph. This is another strong validation of the principal insights of this work.

Fig. 4.6.4 shows all of the data of another large diameter (D = 0.17145 m) gas-water dataset (Crowley et al. 1986), but this time at high gas (Freon-12) densities. Fig. 4.6.4a shows the horizontal runs of this dataset, Fig. 4.6.4b shows the runs at a slight upward inclination of 2 degrees from horizontal and Fig. 4.6.4c shows the runs at a slight downward inclination of 2 degrees from horizontal. The lines in these figures are our

total pressure gradient calculations with the measured gas volume fractions. Also, the calculations for the horizontal and downward flows were performed with the decoupled flow models, and the calculations for the upward flows were performed with the coupled flow models. This is a clear validation that our universal analytical models can satisfactorily account for large-diameter slightly inclined flows at high gas density.

We note that there is a minimum in the total pressure gradient for the +2 degrees from horizontal flows in Fig. 4.6.4b. This represents an optimum scenario for flowing these fluids, and thus a wide potential application in industry (e.g., the determination of the optimum multiphase flow scenario for slightly inclined/horizontal wells in the petroleum industry). We will see later in this chapter that there are large amounts of experimental evidences that also show a clear minimum in the multiphase total pressure gradient at slight inclinations. More significantly, our analytical models accurately capture this minimum total pressure gradient trend as observed in the experiments.

Fig. 4.6.5 shows the Crowley et al. (1986) dataset being analytically predicted with the ANSLIP model. Indeed, the ANSLIP model can be shown to predict other large-diameter coupled and decoupled multiphase flows. Fig. 4.6.6 shows the results from the SINTEF-IFE lab that was originally used to demonstrate the first set of experimental predictions of the OLGA code, as given in Table 3 of Bendikson et al. (1987). These are stratified nitrogen (phase 2) and diesel (phase 1) horizontal flow experiments in a large-diameter (D = 0.189 m) circular pipe. Evidently, the ANSLIP model accurately predicts these data.

Of course, other volume fraction models can be used to accurately account for changes in diameter. Fig. 4.6.7 shows that all of the total pressure gradient and wall (total) shear stress data of the classic vertical upward annular flow dataset of Martin (1983) are accurately predicted with the BUTTERWORTH model. Though not shown,

the ANSLIP model also provides a reliable prediction. These annular flow wall (total) shear stress predictions are quite important as they clearly demonstrate that the constituent parts of our frictional pressure gradient model in Eqn. 6 of Section 2.2.4 are correct. Fig. 4.6.7a-i and a-ii represent the results for runs 1 to 18 in the reference in a pipe of diameter = 0.058 m. Fig. 4.6.7b-i and b-ii represent the results for runs 19 to 36 in the reference in a pipe of diameter = 0.032 m. Fig. 4.6.7c-i and c-ii represent the results for runs 37 to 56 in the reference in a pipe of diameter = 0.01 m.

In addition to large-diameter stratified, wavy or annular flows, our analytical models can also accurately predict large-diameter vapor-liquid slug flows. Fig. 4.6.8 shows one such example from the natural gas (phase 2) and water (phase 1) large-diameter (D = 0.15 m) horizontal slug flow dataset given in Marruaz et al. (2001). Both the drift-flux model provided in this reference as well as a simple SLIPRATIO model of $H_{2,1}$ = 4 furnish a reliably accurate total (frictional) pressure gradient prediction for this dataset.

4.7 EFFECT OF INCLINATION

We next perform validation of our analytical models against experiments with changing pipe inclinations. We first select experiments from the classic reference of Nichols (1965). This choice of dataset is deliberate since the flow patterns were not reported for the experiments. Thus, the ability to accurately reproduce these experiments would very strongly validate the first insight of this research – that pressure gradient is governed by relative velocity and that the flow patterns are merely the visual, spatial manifestations of relative velocity. In this wide-ranging air (phase 2) and water (phase 1) investigation, similar operating conditions and flow rates were maintained with only a change in the pipe inclination from vertical upwards to vertical downwards multiphase

flow. To properly isolate (and therefore properly validate) whether our analytical equations can correctly describe these changes in pipe inclinations, we use the measured air volume fractions in our pressure gradient calculations.

Fig. 4.7.1a shows all of the comparisons of our total pressure gradient calculations for the vertical upwards flow runs – run nos. 1 – 61 in this reference. Fig. 4.7.1b shows all of the comparisons of our total pressure gradient calculations for the vertical downwards flow runs – run nos. 116 – 197. These results represent clear and unambiguous experimental evidence that once the volume fraction is known, the pressure gradient calculations from our universal analytical models are accurate and correctly capture the physical trends in the data. Also, we note the higher sensitivity to the laminar to turbulent flow transition at the lower water rates (and thus higher slip behavior) in comparison to the higher water rates for the vertical downwards flows (Fig. 4.7.1b).

We next look at a comprehensive experimental investigation aimed at understanding the effect of inclination – the Spedding and Nguyen (1976) study. Several hundred air (phase 2) and water (phase 1) experimental runs were performed in which there were wide ranges in phase flow rates at 0, 20, 45, 70, 87, 90, 96, 110, 135, 158 and 180 degrees from vertical. In these runs, the observed flow pattern, air volume fraction and total pressure gradient were reported. This allows us to validate our analytical pressure gradient models (Eqns. 1 and 2 of Section 4.1 for the runs at $0° \leq \theta \leq 90°$ and $90° < \theta < 180°$, respectively) with the measured volume fractions.

Fig. 4.7.2 shows all the data for the vertical upwards flows and a comparison with our total pressure gradient calculations. The measured air volume fractions were used in our pressure gradient calculations. Note that there is a wide range of flow patterns in this dataset. It is evident that this entire dataset is very accurately reproduced by our analytical equations once the volume fractions are known. However, due to the large

number of experiments, it is difficult to analyze comparisons of our theory with the data for individual datasets amongst the numerous runs. We therefore select the datasets for the various pipe inclinations at one low water rate, one medium water rate and one high water rate, and then compare with our analytical model calculations. Figs. 4.7.4 – 4.7.12 show these systematic model validations at the various pipe inclinations. We note, in particular, that the complex data trends observed in the total pressure gradient at downward flows are captured by our analytical models. These results once again prove, resoundingly, that *if* the volume fraction is known, *then* our analytical models are reliably accurate.

Fig. 4.7.13 shows the volume fractions of the same vertical upwards dataset presented previously in Fig. 4.7.2. As seen, these volume fractions are re-expressed in terms of the fractional flow graphs. Fig. 4.7.13a shows the flow patterns in terms of fractional flow. Fig. 4.7.13b shows the same fractional flow graph of Fig. 4.7.13a but this time parameterized by phase 1 superficial Reynolds number. Clearly, all of the flow pattern information (and thus their influences) are *already present* as various fractional flow paths in the fractional flow graph for the dataset. Fig. 4.7.13c show the volume fraction predictions of this dataset with the WOLGHA model and Fig. 4.7.14 show our pressure gradient predictions of this dataset with the WOLGHA model.

Fig. 4.7.15 shows another classic dataset that investigated the effect of pipe inclination – the air (phase 2) and water (phase 1) Beggs (1972) dataset for 1-inch and 1.5 inch pipes. In this experimental study, the operational conditions and rates were kept the same and only the pipe inclination was changed for each pipe. Fig 4.7.15 shows some representative data for the 1.5-inch pipe flows and a comparison with our total pressure gradient calculations. The measured air volume fractions were used in our pressure gradient calculations. Note that, as in the previous dataset, there is a wide range of flow

patterns in this dataset. It is evident that this dataset is very accurately reproduced by our analytical equations once the volume fractions are known.

If we look at one low water rate and one high water rate for this dataset (Fig. 4.7.16), we can trace where the uncertainty in the total pressure gradient calculations are coming from. To do this, we compare the predictions of the air volume fraction with the WOLGHA model (the solid lines in Fig. 4.7.16a) and its subsequent use in our analytical equations (the solid lines in Fig. 4.7.16b). Even though the total pressure gradient predictions are quite satisfactory, we can be more accurate if we now use the measurements of the air volume fractions (the symbols in Fig. 4.7.16a) in our analytical equations (the dashed lines in Fig. 4.7.16b). Yet again, it is proven that once the volume fraction is known, our analytical models are reliably accurate. Also, note that Fig. 4.7.16a clearly shows that multiphase flows resulting in lower liquid volume fractions will be more sensitive to inclination changes. This, of course, has important implications in practical applications such as gas lift in horizontal/slightly-inclined wells.

Fig. 4.7.17a-i and a-ii show the validation of our analytical models with the measured volume fractions for the 1.5-inch and 1-inch datasets of Beggs (1972), respectively. Fig. 4.7.17b-i and b-ii show the corresponding predictions of our analytical models with the WOLGHA model for the 1.5-inch and 1-inch datasets, respectively. Clearly, the WOLGHA model provides a quite satisfactory prediction for this dataset. It must be noted, however, that the biased reason for this capability of the WOLGHA model is because parts of both the Beggs (1972) and Spedding and Nguyen (1976) datasets were used in the validation tuning of the WOLGHA model – which is essentially a drift-flux model with tuned drift-flux parameters for various published datasets.

Indeed, there are other volume fraction models that can provide reliable prediction accuracy for datasets with changing pipe inclinations. Fig. 4.7.18 shows the NICKLIN

model used with our analytical models to accurately predict the entire Griffith et al. (1973) dataset. This investigation consisted of mostly air (phase 2) and water (phase 1) upward slug flows at inclinations of 0, 20, 30, 40 and 60 degrees from vertical. Fig. 4.7.19 shows the up-inclined air (phase 2) and kerosene (phase 1) slug flow experiments of Felizola and Shoham (1995) predicted by our analytical models with the ANSLIP model. Fig. 4.7.20b shows the slightly up-inclined air (phase 2) and oil (phase 1) slug flow experiments of Mattar (1973) predicted by our analytical models with the BUTTERWORTH model. Fig. 4.7.20a is the validation of our analytical models with the air volume fraction measurements.

Note that Fig. 4.7.20 once again shows a minimum in the total pressure gradient, as was previously shown in the Crowley et al. (1986) slightly up-inclined dataset. Our analytical models clearly (and accurately) reproduce this observation. In fact, another classic up-inclined dataset that perhaps first demonstrated this minimum in total pressure gradient is the air (phase 2) and water (phase 1) slug flow dataset of Singh and Griffith (1970). Fig. 4.7.21 shows this dataset being accurately predicted by our analytical models with the NICKLIN model. As seen in Fig. 4.7.21, the appearance of the minimum is determined by a combination of the pipe size, inclination angle and phase flow rates.

We next validate our analytical models with slightly down-inclined experiments. Fig. 4.7.22a, b and c show the slightly down-inclined air (phase 2) and water (phase 1) experiments of Espedal (1998) at pipe inclinations of -0.104, -0.5 and -3 degrees from horizontal, respectively. In this experimental investigation, the air shear stress was also measured with a Preston tube (shown in Fig. 4.7.22a-ii, b-ii and c-ii). Similar to the coupled-flow wall shear stress predictions of the Martin (1983) dataset in Section 4.6,

these results clearly validate that the constituent parts of our decoupled-flow frictional pressure gradient model in Eqn. 7 of Section 2.2.4 are correct.

Fig. 4.7.23 shows the stratified slightly down-inclined air (phase 2) and water (phase 1) dataset of Andreussi and Persen (1987) predicted by our analytical models with the WOLGHA model. In this case the downward inclination was -0.65 degrees from horizontal.

Lastly, in some cases, slightly up-inclined flows can display a sharp-transition behavior, as seen in the large diameter (D = 0.1 m) wavy-ripply SF_6 (phase 2) and Exxol-D80 oil (phase 1) flows in Langsholt and Holm (2007). The volume fraction behavior of these experiments was previously highlighted in Fig. 3.4.1 in Chapter 3 where it was shown that both the shape and magnitude of the changes in the total pressure gradients of these experiments directly scale with the measured gas volume fraction. This is shown in Fig. 4.7.24b in which the measured gas volume fractions are input into our analytical models yielding an accurate reproduction of the total pressure gradient data. Fig. 4.7.24a shows the scenario where an incorrect estimation of the gas volume fraction (provided in this case by the WOLGHA model), will lead to an incorrect prediction of the total pressure gradient. This, of course, is proper model falsification. Note also, that although the WOLGHA model does not furnish an accurate total pressure gradient prediction in this case, the trends in the data are still captured.

4.8 EFFECT OF FLOW PATTERN

We next perform validation of our analytical models against experiments focused on specific flow patterns. We first select the air (phase 2) and water (phase 1) annular flow experiments from the classic reference of Owen (1986). Fig. 4.8.1 shows a representative dataset from this reference (the experiments at 240 kPa) being accurately

predicted with the ANSLIP analytical model and the Ishii and Mishima (1982) entrainment correlation. Other datasets in this work at other pressures of 364 kPa, 377 kPa and 150 kPa are accurately predicted with these same models as shown in Fig. 4.8.2a, b and c, respectively.

This type of accurate prediction with the ANSLIP analytical model is also found with wall shear stress datasets in annular flows. Fig. 4.8.3 shows the air-water annular flow wall shear stress measurements of Pecherkin (1990) being very accurately predicted with the ANSLIP analytical model and the Ishii and Mishima (1982) entrainment correlation. These models, when combined, can explain and accurately predict large amounts of vapor-liquid annular flow data with entrainment. The hundreds of air-water annular flow datasets for the 1-inch pipe in Turner (1966) are shown to be accurately predicted with these models in Fig. 4.8.4. In fact, all of the several hundred datasets for both the 1-inch and 0.75-inch pipes can be predicted with these models as shown in Fig. 4.8.5.

Fig. 4.8.6 shows all of the annular flow datasets of Asali (1984). For the air-water cases, the ANSLIP model provided an accurate prediction of the total pressure gradient. For the air-oil cases, the CISE model furnished an accurate prediction of total pressure gradient.

Other than vertical upward annular flow, the ANSLIP analytical model can provide an accurate prediction for horizontal annular flows. Fig. 4.8.7 shows the horizontal air-water annular flow datasets from Schubring (2009) predicted quite accurately with the ANSLIP model. In fact, wall (total) shear stress measurements were provided in Fig. 4 of Schubring and Shedd (2009) based on this experimental investigation, a reproduction of which is provided in Fig. 4.8.8. We used the same axes and variables of Fig. 4 of Schubring and Shedd (2009) to enable a quick comparison. We

emphasize that this prediction of horizontal annular flow wall shear stress is devoid of any multiphase flow correlation when the ANSLIP model is used.

Fig. 4.8.9 shows the ANSLIP model accurately predicting the vertical downward air frictional pressure gradient measurements reported in Andreussi and Zanelli (1978). The Ishii and Mishia (1982) correlation was used for predicting the water entrainment fraction. The same combination of models can be used to accurately predict the reported air frictional pressure gradient measurements reported in Webb (1970), as seen in Fig. 4.8.10.

As mentioned previously, although it is found in this work that the majority of vapor-liquid annular flow scenarios can be accurately predicted with the ANSLIP model, in some cases the CISE, BUTTERWORTH or WOLGHA models can provide a somewhat better accuracy. Fig. 4.8.11 shows all of the vertical annular air-water (5.1 cm tube) experiments of Hossfield and Bharathan (1982) being accurately predicted with the CISE model.

Fig. 4.8.12a shows all of the low-liquid-flow-rate Unit-C-PVC vertical air-water annular flow measurements (in Fig. 4.8.12a-i) of Bennet and Thornton (1961) being accurately predicted with the BUTTERWORTH model (in Fig. 4.8.12a-ii). The same model also accurately predicts (in Fig. 4.8.12b-ii) all of the high-liquid-flow-rate Unit-C-PVC vertical annular flow measurements (in Fig. 4.8.12b-i) of this reference. In Fig. 4.8.13a, the low-liquid-flow-rate Unit-B-Glass vertical annular flow measurements (in Fig. 4.8.13a-i) of Bennet and Thornton (1961) are accurately predicted with this same model (in Fig. 4.8.13a-ii). In Fig. 4.8.13b, the Unit-A-Annulus vertical annular flow measurements (in Fig. 4.8.13b-i) of Bennet and Thornton (1961) are accurately predicted with this same model (in Fig. 4.8.13b-ii).

In Fig. 4.8.14, all of the round quartz tube (D = 0.0234 m) vertical air-water annular flow measurements of Ashwood (2010) are accurately predicted with the ANSLIP model. In Figs. 4.8.12 – 4.8.14, the predictions and measurements are separated to clearly demonstrate that our analytical models are correctly capturing the observed trends in these annular flow datasets.

Other than annular flow, the ANSLIP analytical model can be used for other flow patterns as previously demonstrated in Chapter 3. Fig. 4.8.15 shows the classic air-water churn-annular dataset of Wallis (1966) being satisfactorily predicted with the ANSLIP analytical model.

In some cases, in addition to liquid droplet entrainment in annular flow, there can be droplet entrainment in churn-annular flow, as discussed in van't Westende et al. (2007). Fig. 4.8.16 shows the churn-annular to annular flow measurements provided van't Westende et al. (2007) with a satisfactory total pressure gradient prediction furnished by the CISE model and the Ishii and Mishima (1982) entrainment correlation.

For horizontal slug flows, the BUTTERWORTH model can furnish a reliable prediction of the total pressure gradient. Fig. 4.8.17 shows the horizontal slug flow air-kerosene measurements of Yang (1996) being accurately predicted with the BUTTERWORTH model. The horizontal slug flow air-kerosene experiments of Marcano (1996) can also be accurately predicted with BUTTERWORTH model, as shown in Fig. 4.8.18. A model very similar to the BUTTERWORTH model, the WALLIS model, can be seen (in Fig. 4.8.19) to accurately predict the carbon dioxide-water horizontal slug flow experiments of Gregory and Scott (1968).

Next, we note that the BUTTERWORTH model can be used (just as the ANSLIP model) to accurately predict the volume fraction behaviors for many different flow patterns, i.e., it is a flow-pattern-implicit model just as the ANSLIP and WOLGHA

models. Fig. 4.8.20 shows the horizontal air-oil bubbly flow experiments of Aziz et al. (1974) accurately predicted with the BUTTERWORTH model. Fig. 4.8.21 shows another classic dataset – the Agrawal (1971) horizontal air-oil stratified flow experiments – being satisfactorily predicted with the BUTTERWORTH model. Note all of the trends in the data are captured by our analytical models.

For stratified vapor-liquid flows, we note that the SLIPRATIO and ANSLIP models can be used for reliable predictions. Fig. 4.8.22 shows all of the horizontal stratified roll wave experiments of Johnson (2005) being very accurately predicted with the ANSLIP model and our decoupled-flow analytical models. It should be noted that the total pressure gradient behavior of this entire experimental investigation, which included hundreds of stratified roll wave experiments at slight inclinations, could be accurately predicted with a simple SLIPRATIO model of $H_{2,1}$ = 3.5.

Other than total pressure gradient, we note that the SLIPRATIO model can be used to reliably predict the mean liquid film thickness in stratified decoupled flows. Fig. 4.8.23 shows the liquid film thickness time tracings for two stratified-wavy carbon dioxide-water flow experiments provided in Fig. 2 of Tzotzi and Andritsos (2013). The dashed lines in Fig. 4.8.23 represent the calculations provided by a simple SLIPRATIO model of $H_{2,1}$ = 7.5, in combination with Eqn. 58 in Section 4.4.

Lastly, flow-pattern-implicit models such as ANSLIP, BUTTERWORTH and WOLGHA can provide reliable predictions of total pressure gradients in scenarios with wide ranges of observed flow patterns. In Fig. 4.8.24, the 2-inch pipe horizontal air-oil flow total pressure gradient measurements of Kokal (1987) are accurately predicted with the WOLGHA model. The WOLGHA model also accurately predicts the total pressure gradients of the vertical multiple-flow-pattern datasets of Hlaing et al. (2007), as shown in Fig. 4.8.25. As seen in the classic horizontal air-water dataset of Govier and Omer

(1962) shown in Fig. 4.8.26a, the transition through different flow patterns (provided by the WOLGHA model in this case) are neatly captured in the averaged sense as different fractional flow paths in the fractional flow graph (Fig. 4.8.26b) thus accurately representing the different relative velocity behaviors of the experiments which is related, in a universal way (via our analytical models), to the multiphase flow pressure gradients (Fig. 4.8.26c and d)

4.9 Effect of Flow Development

In this section, we perform validation of the steady-state, developing flow version of our universal analytical models (i.e., Eqn. 6 of Section 2.2.4 without the temporal acceleration/deceleration term) against steady-state, developing flow experiments. As these are developing flows, the UTPipeFlow code must be run on a segmented pipe system with a given pressure and flow rates boundary condition either at the outlet (preferred) or at the inlet.

Fig. 4.9.1b shows all the axial air volume fraction developing flow measurements for the 3-inch pipe in the air-oil experiments of Kokal (1987) at a pipe inclination of +1 degrees from horizontal. These axial air volume fraction measurements were inputted into the UTPipeFlow code, thus forcing the code to honor them. The calculations (starting from the outlet) of the local pressures in the pipe with our universal analytical models using the measured air volume fractions are shown in Fig. 4.9.1a. As is evident, there is an excellent agreement with our pressure calculations and the local pressure measurements.

Fig. 4.9.2b now shows the calculated axial air volume fractions using the WOLGHA model. When these predictions are compared to Fig. 4.9.1b, it is thus clear that the correct trends in the volume fractions are captured with the WOLGHA model.

Fig. 4.9.2a shows the axial pressure predictions using the WOLHA air volume fraction predictions in Fig. 4.9.2b. As is evident, there is a negligible difference between Figs. 4.9.2a and 4.9.1a, thus validating that an accurate prediction of volume fraction will lead to an accurate prediction of pressure – the first insight of this work.

The same procedure as above is repeated in Figs. 4.9.3 and 4.9.4 but this time with the same 3-inch pipe at a steeper inclination of +9 degrees from horizontal. As seen in Fig. 4.9.3, there are now different flow patterns and different relative contributions of the frictional (FPG) and hydrostatic (HPG) pressure gradient contributions to the total pressure gradient (TPG). This is reflected in different axial air volume fraction behaviors as seen in Fig. 4.9.3b, and correctly predicted by the WOLGHA model in Fig. 4.9.4b. As before, a comparison of the pressure calculations in Figs. 4.9.3a and 4.9.4a show that an accurate prediction of pressure will be afforded by an accurate prediction of volume fraction.

We now focus our analytical model validation for developing flows of specific flow patterns. Fig. 4.9.5 shows two experimental datasets of a classic developing flow dataset (Moissis and Griffith, 1960) for developing slug flows being accurately predicted with the NICKLIN model. The NICKLIN model can also be used to accurately predict developing churn flows, as seen in Fig 4.9.6a. In Fig. 4.9.6, which represents a subset of the vertical air-water developing flows of Woods and Spedding (1996), the solid symbols represent a lower liquid rate and the open symbols represent a higher liquid rate, at the same fixed gas rate

Fig. 4.9.6b shows two developing annular-ripply experiments from Woods and Spedding (1996). As expected, the ANSLIP model accurately predicts these developing annular flows.

Figs. 4.9.7 – 4.9.10 show experiments from the vertical air-water disequilibrium annular flow experimental investigation of Brown (1978) being accurately predicted with the ANSLIP model. Fig. 4.9.7 shows the comparisons for run no. 9 in this reference (a low gas rate run) with an axial jet injector with and without the measured axial entrainment fraction participating in the pressure gradient calculations of UTPipeFlow. Fig. 4.9.8 shows the same comparisons for run no. 9 in Fig. 4.9.7 but with a porous wall injector. There are evidently only minor differences from including the measured axial entrainment fractions at this low gas rate.

Fig. 4.9.9 shows the comparisons for run no. 3 in this reference (a high gas rate run) with an axial jet injector with and without the measured axial entrainment fraction participating in the pressure gradient calculations of UTPipeFlow. Fig. 4.9.10 shows the same comparisons for run no. 3 in Fig. 4.9.9 but with a porous wall injector. There are slightly more differences from including the measured axial entrainment fractions at this high gas rate. As seen, the ANSLIP model is quite accurate for this vertical developing annular flow dataset.

In high-rate annular flows at fairly low pressures, the contributions of the convective acceleration//deceleration pressure gradient (CADPG) can be quite significant. To concretely demonstrate this, we select six experimental runs from the Cousins et al. (1965) air-water developing vertical annular flow dataset – run nos. 15, 17, 19 (low water rates runs shown in Fig. 4.9.11) and run nos. 21, 24, 26 (high water rate runs shown in Fig. 4.9.12). These six runs represent a systematic increase in the water mass flow rate (from 0.00126 to 0.02898 kg/s) at a constant air mass flow rate (0.0063 kg/s). The air volume fraction in both Figs. 4.9.11 and 4.9.12 are predicted with the ANSLIP analytical model. As shown in these figures, not only does the ANSLIP model furnish very accurate axial pressure predictions, but more importantly as seen in a-ii to f-

ii in these figures, the CADPG increases quite substantially (i.e., increasing acceleration at higher liquid rates) to the point that it becomes much greater than the hydrostatic pressure gradient (HPG).

Figs. 4.9.13 – 4.9.15 show the results from another air (phase 2) and water (phase 1) vertical developing annular flow dataset – that of Wolf (1995). In this experimental investigation, both the axial pressure and axial mean film thickness measurements are available for comparing against our analytical model predictions. Additionally the axial water film mass fluxes (and therefore entrainment fractions) were measured and reported. This combination of measurements affords us a unique opportunity to comprehensively validate our universal analytical models as implemented in the UTPipeFlow code. We can enforce the measured axial water entrainment fractions participate in the UTPipeFlow code's computations and then compare to results without entrainment to demonstrate (and quantify) the influence of entrainment on the pressure and mean film thickness results.

Fig. 4.9.13 shows our predictions using the ANSLIP model against the experimental measurements at an air mass flux of 154 kg/m^2-s and water mass flux of 80 kg/m^2-s. The solid lines in this figure represent the enforced condition that the axial entrainment measurements participate in the UTPipeFlow code's calculations and the thin lines represent no entrainment. As is evident in Fig. 4.9.13a, the effect of including entrainment has a minor influence on the pressure prediction but a significant influence on the film thickness prediction. Indeed, it is clear that the mean water film thickness axial trend is a direct result of the axial entrainment fraction. The mean film thickness, $m_{1,film}$, in Figs. 4.9.13 – 4.9.15, in meters, is calculated from the ANSLIP model predictions via the simple approximation:

$$m_{1,\,film} = \frac{D}{2}\left(1 - \sqrt{\langle s_2 \rangle}\right) \tag{59}$$

Fig. 4.9.14 shows decreasing air mass fluxes (from 154 kg/m2-s in Fig. 4.9.14a, to 124 kg/m2-s in Fig. 4.9.14b, to 97 kg/m2-s in Fig. 4.9.14c) at the same water mass flux (120 kg/m2-s). As seen the effect of entrainment becomes more prominent at higher air flow rates. As before, the solid lines in this figure represent the enforced condition that the axial entrainment measurements participate in the UTPipeFlow code's calculations and the thin lines represent no entrainment. The ANSLIP analytical model furnishes accurate calculations of pressure for these runs.

Figs. 4.9.15a-i to f-i show the pressure profile changes for decreasing water mass fluxes from 100, 80, 60, 40, 20 and 10 kg/m2-s at the same air mass flux of 154 kg/m2-s. In these figures, the axial entrainment measurements participate in the UTPipeFlow code's calculations. Figs. 4.9.15a-ii to f-ii show the mean film thickness profile changes calculated by the ANSLIP analytical model. As seen in these figures, once the entrainment fraction is correct, the ANSLIP model will provide a reliably accurate prediction for volume fractions (film thicknesses) and pressure gradients.

We next validate our analytical models with a subset of the horizontal developing flow datasets of Eaton (1966). In this experimental investigation, 500 m lengths of 2-inch and 4-inch pipes were carefully instrumented to obtain pressure and volume fraction measurements at different stations. Fig. 4.9.16a shows the comparisons of our predictions against some of the runs of this investigation. In the runs shown, the WOLGHA model was used for volume fraction calculations and the Ishii and Mishima (1982) correlation was used for entrainment fraction calculations. As is evident, these models accurately predict the local pressures along the pipe for these datasets. Moreover, in Fig. 4.9.16b, the WOLGHA model's volume fraction predictions are quite accurate in

comparison to the volume fraction measurements of run 2W06709. It is also instructive to observe the significant contribution of the convective acceleration/deceleration pressure gradient (CADPG) for this run.

We next analyze the vertical developing flows of the experiments of Hagedorn (1964). We will perform all of our predictions of this dataset with the NICKLIN model. In this investigation, three 430 m long circular pipes (with diameters of 1-inch, 1.25-inch and 1.5 inch) were instrumented at various axial positions to obtain a large number of pressure measurements with different liquids (having different densities and viscosities) and air. We will use the large number of experiments in this study to analyze a specific important issue – that is – the identification of the various scenarios that will cause a multiphase flow to transition from being a hydrostatic-dominant (HPG-dominant) system to a friction-dominant (FPG-dominant) one. The comparisons of our analytical models in each case will validate that our models can accurately account for these effects.

One scenario that will cause system to transition from a HPG-dominant to a FPG-dominant one is an increase in GLR (gas-to-liquid ratio) at a given liquid rate. Figs. 4.9.17a to d show an increasing air mass flow rate of 0.009, 0.022, 0.0421 and 0.0504 kg/s, respectively, at the same water rate of about 0.1155 kg/s. The outlet pipe pressure boundary condition for these runs was fixed at 240 kPa (or 20 psig). In terms of the petroleum industry language used in Hagedorn (1964), these correspond to the datasets with GWR's of 310, 755, 1983 and 2350, respectively, at the same water rate of about 63 BBL/d. As seen in Figs. 4.9.17a-i to d-i, the NICKLIN model provides an accurate prediction of the changes in pressure for this scenario. As seen in Figs. 4.9.17a-ii to d-ii, the increase in GWR at a constant water rate is a sufficient condition for a change from a HPG-dominant system to a FPG-dominant one.

Another scenario that will cause system to transition from a HPG-dominant to a FPG-dominant one is a change in the outlet pressure boundary condition (the "flowing well head" pressure) for about same flow rates and fluids. Figs. 4.9.18a and b show an increase in the outlet boundary pressure from 240 kPa (or 20 psig) to 791 kPa (or 100 psig), respectively, at the same water mass flow rate of about 0.1295 kg/s and the same air mass flow rate of about 0.0295 kg/s. These correspond to the datasets with GWR's of 1083 and 1000, respectively, at the same water rate of about 70 BBL/d. As seen in Figs. 4.9.18a-i and b-i, the NICKLIN model provides an accurate prediction of the changes in pressure for this scenario. As seen in Figs. 4.9.18a-ii and b-ii, the decrease in outlet pressure at constant water and air rates is a sufficient condition for a change from a HPG-dominant system to a FPG-dominant one.

A third scenario that will cause system to transition from a HPG-dominant to a FPG-dominant one is a change in liquid rate for the same GLR. Figs. 4.9.19a and b show a decrease in the water mass flow rate from 0.1863 kg/s to 0.1214 kg/s, respectively. These correspond to the datasets with GWR's of 1260 and 1420 and water rates of 101.3 and 66 BBL/d, respectively. The outlet pipe pressure boundary condition for these runs was fixed at 791 kPa (or 100 psig). As seen in Figs. 4.9.19a-i and b-i, the NICKLIN model provides an accurate prediction of the changes in pressure for this scenario. As seen in Figs. 4.9.19a-ii and b-ii, an increase in liquid rate at a fixed GLR is a sufficient condition for a change from a HPG-dominant system to a FPG-dominant one. This, of course, has important industry implications for high liquid rate systems. One real, practical example is the high liquid rate wells common in Saudi Arabia. The results of Fig. 4.9.19 clearly demonstrate, in a simple way, that multiphase flow models that are validated with mostly HPG-dominant wells will not be able to predict FPG-dominant wells.

A fourth scenario that will cause system to transition from a HPG-dominant to a FPG-dominant one is a change in pipe diameter for the same GLR and liquid rate. Figs. 4.9.20a and b show an increase in pipe diameter from 0.0243 m to 0.0325 m, respectively. These correspond to the datasets with GWR's of 1317 and 1338 and water rates of 59 and 61.8 BBL/d, respectively. The outlet pipe pressure boundary condition for these runs was fixed at 240 kPa (or 20 psig). As seen in Figs. 4.9.20a-i and b-i, the NICKLIN model provides an accurate prediction of the changes in pressure for this scenario. As seen in Figs. 4.9.20a-ii and b-ii, a decrease in pipe diameter at a fixed GLR and liquid rate is a sufficient condition for a change from a HPG-dominant system to a FPG-dominant one. The results in Fig. 4.9.20 have important industry implications in terms of the optimum sizing of pipes (e.g., wellbores) for various multiphase flow scenarios.

4.10 EFFECT OF SHAPE

We next perform validation of our analytical models against experiments with changing pipe cross-sectional shapes. Under this category, there are two subsets: (a) constant cross-sectional area pipes with different cross-sectional shapes, and (b) variable cross-sectional area pipes. Figs. 4.10.1 – 4.10.7 are applications regarding the first subset. Figs. 4.10.8 – 4.10.17 are applications regarding the second subset.

Fig. 4.10.1 shows the validation of our analytical model calculations with the annulus flow experiments of Caetano-Filho (1984). The lines in Fig. 4.10.1 are the calculations of our analytical models with the measured air volume fractions in the experiments. Evidently, once the volume fractions are known, our pressure gradient calculations are accurate.

Fig. 4.10.2 shows another validation of our analytical models for annulus flows. However, unlike the vertical annulus flows of the Caetano-Filho (1984) dataset above, these are the horizontal annulus experiments of Ekberg (1998). This is a unique investigation because two sets of annulus flow measurements were obtained – one for a thin annulus in a small pipe and one for the same-sized thin annulus in a larger pipe. Therefore, the hydraulic diameter is the same for both datasets (D_H = 0.00203 m) and the only system change between the datasets is therefore the area open to flow, A. Fig. 4.10.2a shows the calculations of our analytical models against the pressure gradient measurements for the smaller area datasets (A = 0.00002428 m^2), and Fig. 4.10.2b shows our calculations against the pressure gradient measurements for the larger area datasets (A = 0.00010894 m^2). As seen, our analytical models are quite accurate for this dataset.

Fig. 4.10.3 shows the validation of our analytical models with the experimental investigation of Holt (1996). The lines in Fig. 4.10.3 are the calculations of our analytical models with the measured vapor volume fractions. Fig. 4.10.3a shows the helium-water experiments in a circular 5 mm pipe and Fig. 4.10.3b shows the air-water experiments in the same circular 5 mm pipe. Thus, these two datasets represent a change in fluid properties at the same hydraulic diameter. Evidently, our analytical models accurately capture this change once the volume fraction is known. Fig. 4.10.3c shows the nitrogen-water experiments in a trapezoidal pipe (D_H = 0.004142 m). As seen, our analytical models will accurately predict the total pressure gradient as long as the volume fraction is correct.

Fig. 4.10.4 shows the validation of our analytical models with the rectangular mini-channel experiments of Fujita et al. (1995). This dataset was previously highlighted in Figs. 3.4.3 and 3.4.4 in Chapter 3. The lines in Fig. 4.10.4 are the calculations of our

total (frictional) pressure gradient model with the measured nitrogen volume fractions. It is evident that our analytical models satisfactorily reproduce these experiments.

Now that we have shown the validation of our analytical models with different cross-sectional shapes, we next show how the fractional flow models of Chapter 3 can be used with our models to enable predictions. Fig. 4.10.5 shows the flat, rectangular mini-channel experiments (width = 20 mm) in Lee and Lee (2001) being accurately predicted with the CISE model. Fig. 4.10.6 shows the horizontal annular flow datasets of Ashwood (2010) being accurately predicted with the ANSLIP model in both the circular 22.3 mm pipe and the 20.3 mm x 33 mm rectangular pipe. Fig. 4.10.8 shows the 2 x 3 rod bundle channel of Sadatomi et al. (2006) being accurately predicted with the NICKLIN model (Fig. 4.10.8b). Fig.4.10.8a is a validation of our analytical models with the measured air volume fractions. For these experiments, the rod bundle had a hydraulic diameter of 0.0143 m and an area open to flow of 0.000194 m^2.

We next validate our analytical models with experiments having variable pipe cross-sectional areas along the flow. These pipes represent developing flows and thus the UTPipeFlow code must be used on a segmented pipe system, just as was done in the previous section.

Fig. 4.10.8 shows careful model falsification against Run 16SC (a short, sharp insert dataset) of the Tapucu et al. (1988) square-pipe blockage experiments. In these well-instrumented experiments, axial air volume fractions and pressures were measured in a vertical square pipe with both small, sharp inserts as well as long, smooth ones. These axial measurements before and after the blockages allow us to quantify the influence of an error in the volume fraction prediction in regards to the pressure drop across the blockage.

In Fig. 4.10.8, it can be seen that an unblocked pipe with the air volume fraction in UTPipeFlow fixed at the value given at the outlet, will not enable an accurate calculation of the pressure profile. If the axial measured air volume fraction is enforced in the UTPipeFlow code's computations but the channel remains unblocked, then this will still not yield an accurate pressure profile. If the channel is blocked but the air volume fraction in UTPipeFlow is fixed at the value given at the outlet, then this will still not yield an accurate pressure profile. It is only in the condition of a blocked pipe with the correct (measured) axial air volume fractions participating in UTPipeFlow's computations, will an accurate calculation of the pressure profile be obtained. These results are a strong validation of the first insight of this work.

The same procedure as above can be repeated for a smooth, long insert, as shown in Fig. 4.10.9 (Run 21C in the reference). Evidently, once the correct volume fraction is known, our universal analytical models are accurate, regardless of the type of blockage or shape of the pipe.

Fig. 4.10.10 shows other datasets from this experimental investigation with systematic changes in the area reduction percent. The measured axial air volume fractions were used in the UTPipeFlow code's pressure calculations in this figure.

There are many experimental multiphase flow datasets in which there are variable cross-sectional areas along the flow. Nozzle, valve and choke flows belong to this category. Fig. 4.10.11 shows a validation of our analytical models with the air-water converging-diverging nozzle experiments of Vogrin (1963). This experimental investigation aimed to quantity the extent to which a liquid could be accelerated through a nozzle by the vapor phase. This question, of course, has important industry applications, such as in regards to the design of nozzle-type devices for gas lift applications in the petroleum industry.

In Fig. 4.10.11, the in-situ water velocity calculations of UTPipeFlow are compared with the axial in-situ water velocity measurements. Fig. 4.10.12 shows an example calculation for run no. 1 of Vogrin (1965). Clearly, the axial air volume fraction governs the calculated pressure and pressure gradient profiles. Figs. 4.10.13 and 4.10.14 present more calculations of the water in-situ velocity for low and high air volume fractions, respectively.

Fig. 4.10.15 shows representative sub-critical to critical flow datasets (at low void fractions) from the Pilehvari (1980) multiphase choke flow experiments being accurately predicted with the ANSLIP model. Fig. 4.10.16 shows further sub-critical to critical (at high void fractions) datasets from this reference being accurately predicted with the ANSLIP model.

Fig. 4.10.17 shows representative datasets at high and low liquid rates from the high gas mass quality critical nozzle flows of Camelo et al. (1995). The WOLGHA model was used to furnish satisfactory predictions of these datasets.

4.11 Effect of Network

Now that it has been demonstrated that developing flows are accurately modeled with our analytical models (as implemented in the UTPipeFlow code), we can discretize any pipe system into any number of segments and solve the entire pipe system with a fixed boundary condition specified at either the outlet (preferred) or inlet. In this way, any single-branch-type pipe network can be specified in UTPipeFlow and solved.

Fig. 4.11.1 shows representative runs from the Juprasert (1978) pipeline-riser network experiments. With a specified boundary condition at the outlet, the MIST flow analytical model provides quite accurate predictions for the pressure profile in both cases where the feed pipeline is -5 and +5 degrees from horizontal. In this experimental

investigation, the BUTTERWORTH model was also found to provide reliable predictions.

A much more complex pipeline network is described in Gregory et al. (1975b) in which there are about 188 elevation changes, as shown in Fig. 4.11.2. For this natural gas and oil network, there were systematic changes in the phase flow rates and outlet pressures. Also, local pressures were measured at different stations along the pipeline. Fig. 4.11.3a, b and c show a sample of those systematic changes in which the oil mass flow rate was kept at 8 kg/s and the natural gas mass flow rate was kept at 0.3 kg/s, with the outlet pressure (the boundary condition) increasing from 446 to 790 to 2170 kPa, respectively. The heavy solid lines in Fig. 4.11.3 represent the predictions of our analytical models with the NICKLIN model for all up-inclined pipe segments and the BUTTERWORTH model for all down-inclined pipe segments. There is an excellent agreement between our predictions and the measured pressures.

We next make the simple assumption of a horizontal pipe for all runs in Fig. 4.11.3, and perform predictions with the WOLGHA model. These predictions are the red lines in Fig. 4.11.3. This simplification results in a +/- 15% prediction of the local pressure measurements. As is evident, such simplifications must first be attempted as a matter of good engineering practice, up until their extent (or usefulness) can be proven to be exceeded.

4.12 Effect of Other Phenomena

We now perform validation of our universal analytical equations in scenarios involving other phenomena beyond that normally encountered in an averaged (1D) multiphase pipe flow.

Fig. 4.12.1a shows the validation of our analytical models with the helical coil (coiled tubing) air-water measurements of Boyce et al. (1968). In this experimental investigation, a 1.25-inch diameter pipe was coiled to the main coil diameter of 10 ft at an angle of +3 degrees from horizontal. The observed flow patterns included slug, wavy, wavy-spray, annular and annular-mist. In Fig. 4.12.1a, the measured air volume fraction was used in our analytical models with the Ito (1959) helical coil turbulent flow friction factor used in place of the Haaland (1983) circular pipe turbulent friction factor (Eqn. 4 of Section 2.2.4). Fig. 4.12.1b shows the prediction of this dataset with the WOLGHA model and the Ito (1959) helical coil turbulent flow friction factor. Evidently, our analytical models satisfactorily predict this dataset.

Fig. 4.12.2 shows the comparisons of the mean film thickness predicted with the WOLGHA model (the red lines) and the measured film thickness time traces for all of the runs given in Fig. 7 of Sawant et al. (2008). Clearly, the film thickness trends in this reference (a property of annular flow disturbance waves) are satisfactorily captured with this simple model. In fact, the simple ANSLIP and WOLGHA models can be used with our analytical models to satisfactorily predict both the developed and developing mean film thickness in annular flows with disturbance waves, such as shown in Figs. 4.12.3 and 4.12.4. Fig. 4.12.3 shows the predictions of our analytical models with the ANSLIP model and the Ishii and Mishima (1982) correlation against the dimensionless mean film thickness data of Zhao et al. (2013). Fig. 4.12.4 shows the predictions of our analytical models against the same data but now with the WOLGHA model instead of the ANSLIP model.

Lastly, Fig. 4.12.5a shows the predictions of our analytical models with the ANSLIP model for the vertical quartz tube annular flow datasets in Schubring (2009) and Fig. 4.12.5b shows our analytical model predictions with the ANSLIP model for the

vertical FEP tube annular flow datasets in this reference. Both of these datasets are accurately predicted with our analytical models without regard for the tube material.

4.13 Effect of Modeling Method

In this section, we compare (benchmark) the predictions of our universal analytical models against other models in the literature as well as against currently available industry codes over a wide range of scenarios.

Fig. 4.13.1 shows one of the datasets from the vertical churn-annular experiments of Hewitt et al. (1985) when compared with other models. This dataset was discussed in Section 4.4 (Fig. 4.4.12). It is evident that the models shown cannot accurately predict this dataset.

Fig. 4.13.2 compares the results of other models with one dataset from the annular flow experiments of Hewitt et al. (1961). These experiments were previously highlighted in Fig. 4.5.4. These comparisons demonstrate that these models do not properly account for the effect of mass change due to bi-directional entrainment. Moreover, they display the opposite trend as compared to the data.

Next, the same dataset from Azzopardi et al. (1983) that was discussed in Fig. 1.3.4 in Chapter 1 is accurately modeled with our analytical models, as shown in Fig. 4.13.3. This large diameter annular flow dataset can also be found in Oliemans et al. (1986).

Fig. 4.13.4 compares the results of other models for one of the large-diameter, high gas density, horizontal datasets from Crowley et al. (1986). This dataset was previously analyzed in Section 4.6 (Fig. 4.6.4) and discussed in Chapter 1 (Fig. 1.3.5). It is clear that the other models shown cannot accurately predict this dataset. The data shown correspond to run nos. FHOPI-46 to FHOPI-49 in the reference.

Fig. 4.13.5 shows the large-diameter (D = 0.2 m) horizontal slug flow experiments shown in Fig. 6 of Andreussi et al. (2008) and used to validate the MAST code. Even though this data is publicly-inaccessible data from a private, for-profit lab (and therefore will fail the operational acceptance standard of Section 1.3.5.1 of Chapter 1), we still show an accurate prediction of this dataset with our pressure gradient models and the BUTTERWORTH model – based solely on the information provided in the reference.

Fig. 4.14.5 shows the predictions of different horizontal mechanistic models against a simple 1-inch air-water dataset from Andritsos (1986). Our analytical ANSLIP model predictions demonstrate a correlation-free prediction of this dataset, as compared to the extremely complex mechanistic models that cannot model this dataset.

Following the discussion on the minimum total pressure gradient in slightly inclined flows in Sections 4.6 and 4.7, Fig. 4.13.7 shows a validation of our analytical models to reproduce the carefully-controlled (+1 degrees from horizontal) wavy flow dataset presented in Fig. 5 in Grollman and Fortuin (1995). The measured air volume fractions were used in our total pressure gradient calculations. As seen, once the volume fraction is known, then our analytical models are very accurate and will reproduce this observed minimum in total pressure gradient. The other models shown do not display this observed behavior.

Fig. 4.13.8 shows one of the dataset from the horizontal stratified roll wave flows of Johnson (2005). This experimental investigation was previously highlighted in Section 4.8 (Fig. 4.8.22) and discussed in Chapter 1 (Fig. 1.3.6). As is evident, the other models shown in Fig. 4.13.8 cannot predict this dataset, which corresponds to test nos. 154 to 167 in the reference.

Fig. 4.13.9 shows a famous annular flow dataset (from Owen, 1986) that was previously used to benchmark the models and codes primarily in the nuclear and chemical industries (given as “Data Set 1” in Hewitt et al., 1987). We add popular petroleum industry models and codes to this benchmarking to demonstrate that none of these models can satisfactorily predict this dataset. We note that this experimental investigation was previously analyzed in Section 4.8 (Figs. 4.8.1 and 4.8.2). As seen previously in Section 4.8, all of the datasets of this reference are accurately predicted with our analytical models using the ANSLIP model for volume fraction and the Ishii and Mishima (1982) correlation for entrainment.

Fig. 4.13.10 shows other datasets from Owen (1986) that displays the same characteristic hump as seen in Fig. 4.13.9. This trend is correctly predicted with the ANSLIP model in combination with the Ishii and Mishima (1982) correlation and is a direct result of the bi-directional entrainment of vapor (bubbles) into the liquid film and the liquid (droplets) into the vapor core. This hump is not present if entrainment is not included with the ANSLIP model.

In addition to the churn-annular datasets discussed in Section 4.8, Fig. 4.13.11a shows another churn-annular dataset provided in Barbosa Jr. et al. (2002). As seen, the other models shown cannot correctly predict the trends of this dataset. Fig. 4.13.11b shows that different volume fraction models will provide and accurate prediction of the total pressure gradient with our pressure gradient models. The reason for this is shown in Fig. 4.13.11c, in which it is shown that the volume fraction models of Fig. 4.13.11b all lead to similar fractional flow paths for this dataset and thus similar pressure gradient behaviors.

Fig. 4.13.12 shows the comparisons of other models and our pressure gradient models with the ANSLIP model. This is run no. 2 (with an axial jet injector) of the

disequilibrium annular flow experiments of Brown (1978). As seen, the pressure gradient profile is more sensitive to the inclusion of entrainment than the pressure profile.

Fig. 4.13.13a shows the comparisons of other models and our pressure gradient models with the ANSLIP model for run no. 49 of Cousins et al. (1965). This run was previously highlighted in Fig. 1.3.1 in Chapter 1. We note that the other models predict far off for this vertical annular flow dataset. Fig. 4.13.13b shows the axial development of the various pressure gradients for this dataset. We draw attention to the very significant contribution of the convective acceleration/deceleration pressure gradient (CADPG) for this adiabatic flow dataset. Indeed, the CADPG becomes much more dominant than the hydrostatic pressure gradient (HPG) for this high rate vertical flow at low gas density.

Fig. 4.13.14 shows the various pressure gradients and liquid holdup predicted by all the models of Fig. 4.13.13a. It now becomes clear that our analytical models provide very different predictions in comparison to the other models for each pressure gradient term and for the liquid holdup, whereas the other models offer very similar predictions in every category.

Fig. 4.13.15 shows the predictions of our universal analytical models using the WOLGHA model for one of the convergent-divergent-convergent multiphase nozzle flow runs provided in Pougatch et al. (2008). In this reference, an Eulerian-Eulerian 3D/two-fluid (CMFD) model was used with various interfacial closure equations and different sets of fine to course grids in order to simulate the experimental compressible air-water nozzle flow datasets. This represents a modeling approach that involves a large number of conservation and empirical closure equations – the opposite of the modeling approach of this work (i.e., the use of the simplest concepts and equations to explain the global physics of the flow).

Fig. 4.13.16 shows the direct comparison between the predictions of the 3D/two-fluid model and our analytical models for the in-situ bubbles and water velocities of run no. 1 of the reference. As is evident, our simple analytical models provide a very close prediction in comparison to the multi-physics 3D/two-fluid model thus validating that our analytical global models correctly capture the resultant collective behavior of the flow (the net of the flow microphysics). Fig. 4.13.17 shows the comparison of our analytical model predictions (from UTPipeFlow) against the nozzle pressure profile for various case runs provided in the reference. Evidently, our analytical models accurately predict this very complex set of compressible gas-liquid flows through a convergent-divergent-convergent nozzle.

Lastly, we show the comparisons of our analytical models against other models for another complex application – the pipeline-riser developing flow experiments of Zabaras et al. (2013). In this experimental investigation, a large diameter vertical riser (D = 0.2794 m) is connected to a same-sized pipeline at a downward inclination of 11.6 degrees from horizontal. Additionally, a long radius 90-degree elbow at the same size of the riser connects the top of the riser to a gas-liquid separator. Steady-state and transient flow air-water experiments were conducted, particularly to investigate riser-base gas lift injection and riser liquids removal capability. Fig. 4.13.18 shows some of the steady-state results. For this dataset, the BUTTERWORTH model was used for the down-inclined pipe and the NICKLIN model was used for the vertical riser. The outlet pressure boundary condition was set at 101325 Pa. Fig. 4.13.18 shows the total pressure gradient measurements at the riser top at a water mass flow rate of 6.3 kg/s (Fig.4.13.18a) and a water mass flow rate of 9.5 kg/s (Fig. 4.13.18b). As seen, our analytical model satisfactorily predicts these results. The results of the other models were taken from the reference.

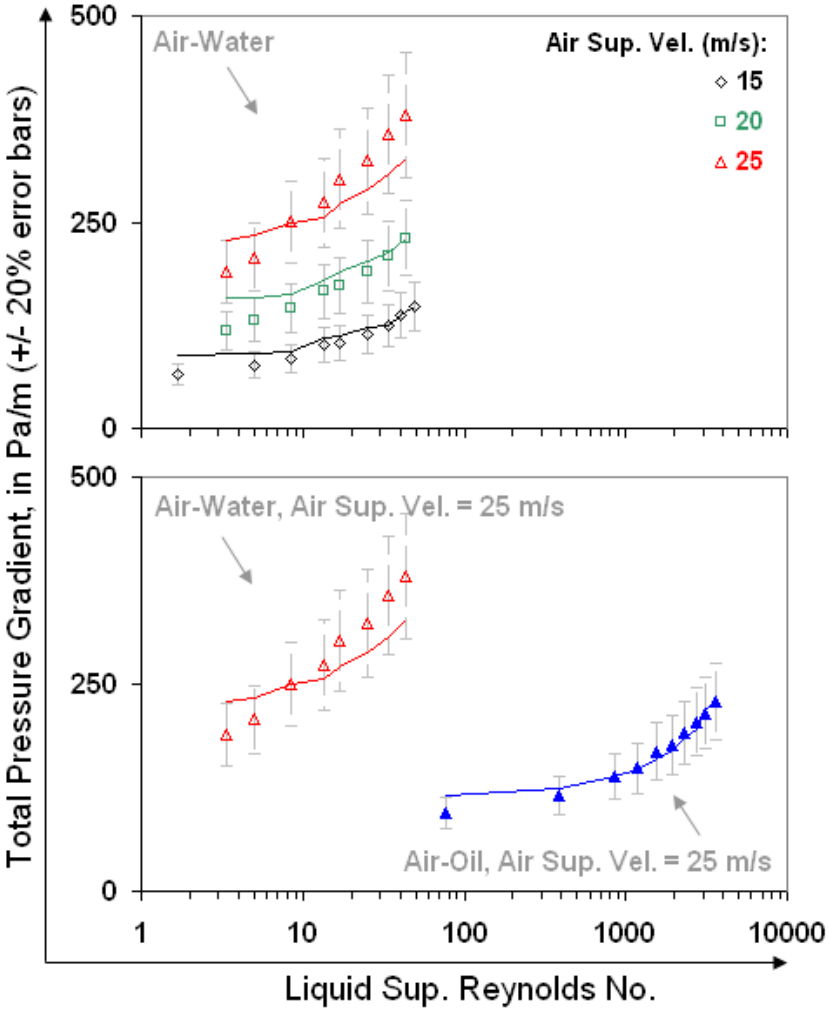

Figure 4.3.1: Low liquids loading horizontal stratifying/annular flow experiments of Badie (2007). Lines are our calculations and the points are measurements.

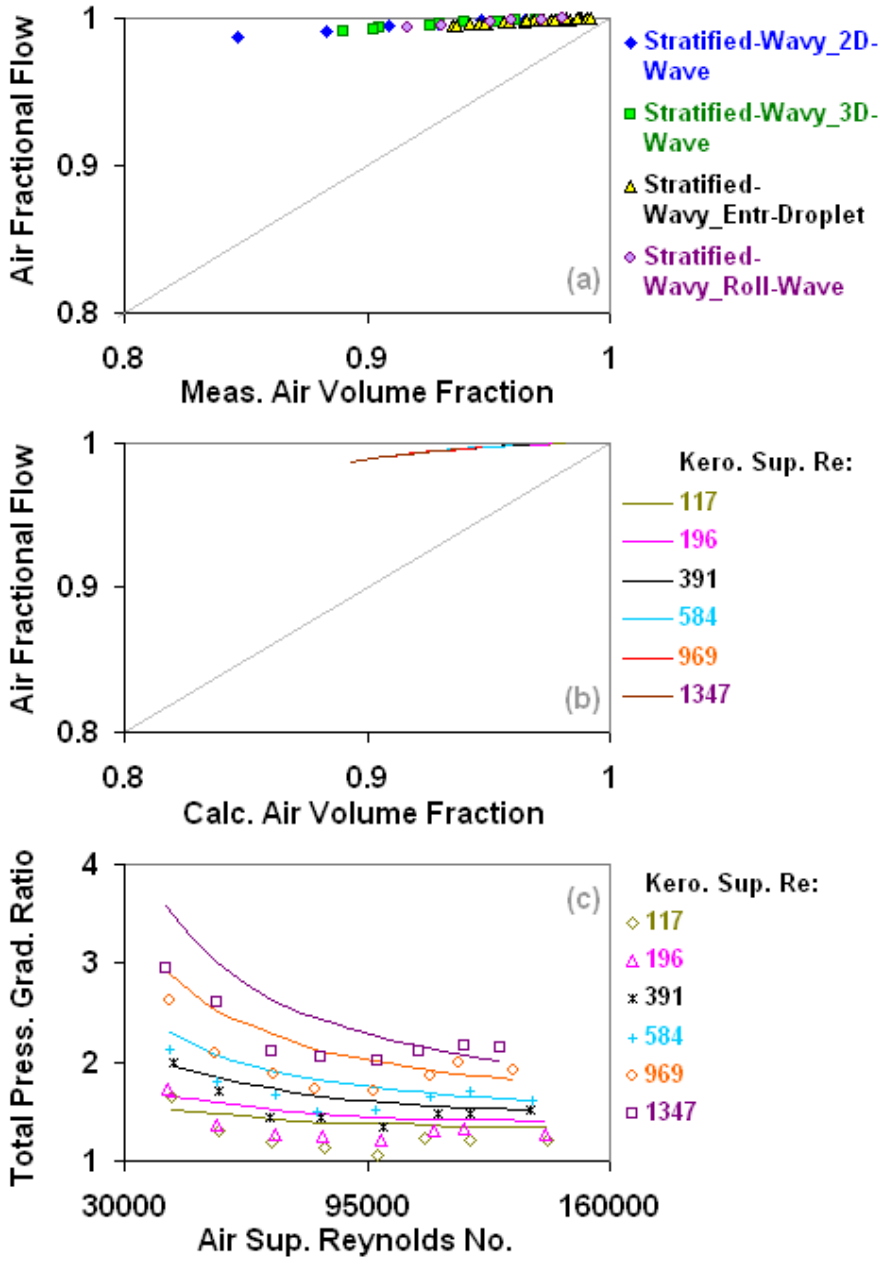

Figure 4.3.2: Low liquids loading horizontal stratified-wavy experiments of Brill (1996). Lines are our calculations and the points are measurements.

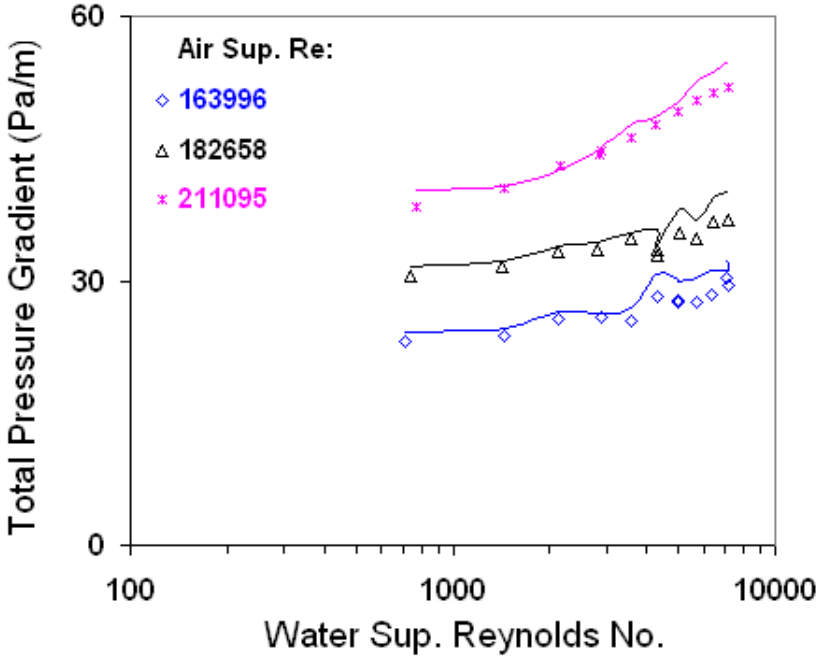

Figure 4.3.3: Low liquids loading slightly downward stratified-wavy experiments of Fan (2005) for runs at -2 degrees from horizontal. Lines are our calculations and the points are measurements.

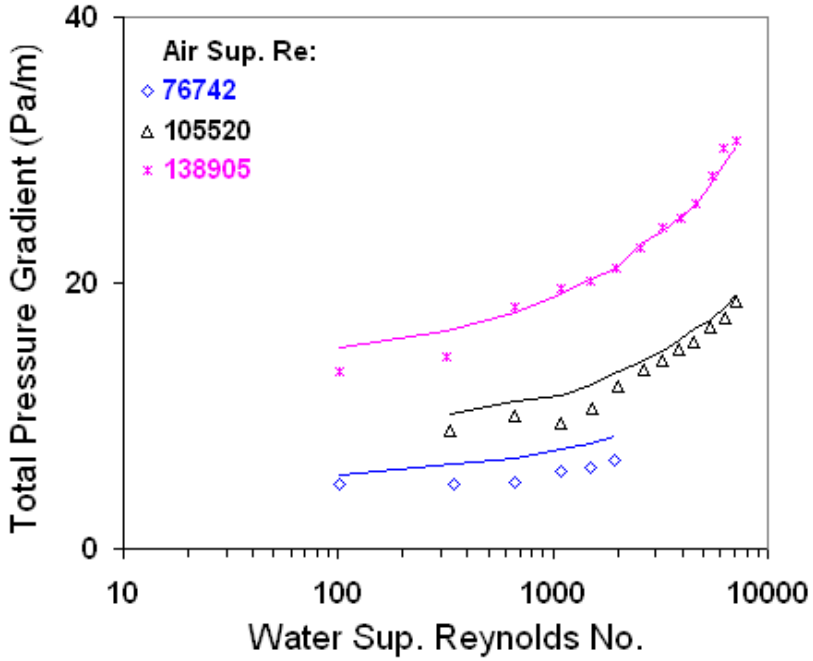

Figure 4.3.4: Low liquids loading horizontal stratified-wavy experiments of Fan (2005). Lines are our calculations and the points are measurements.

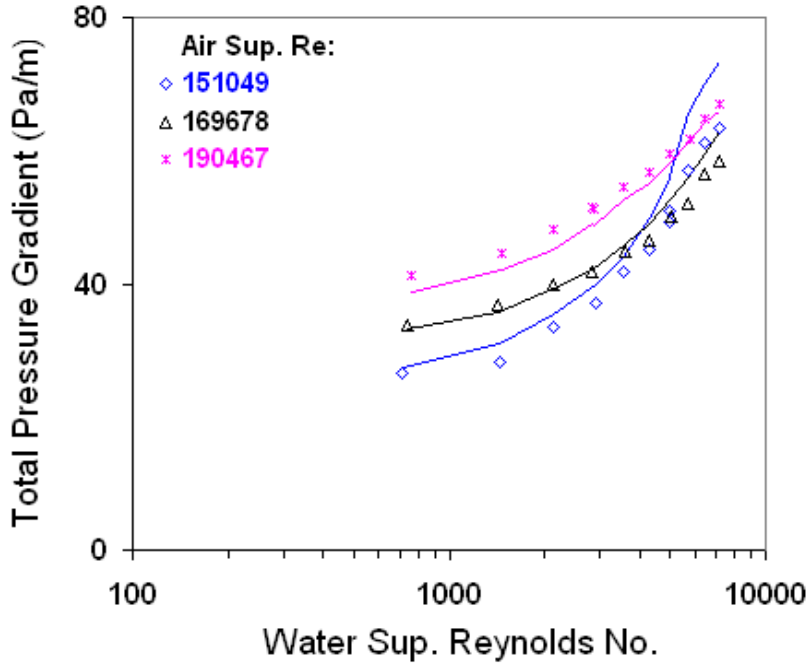

Figure 4.3.5: Low liquids loading slightly upward stratified-wavy experiments of Fan (2005) for runs at +2 degrees from horizontal. Lines are our calculations and the points are measurements.

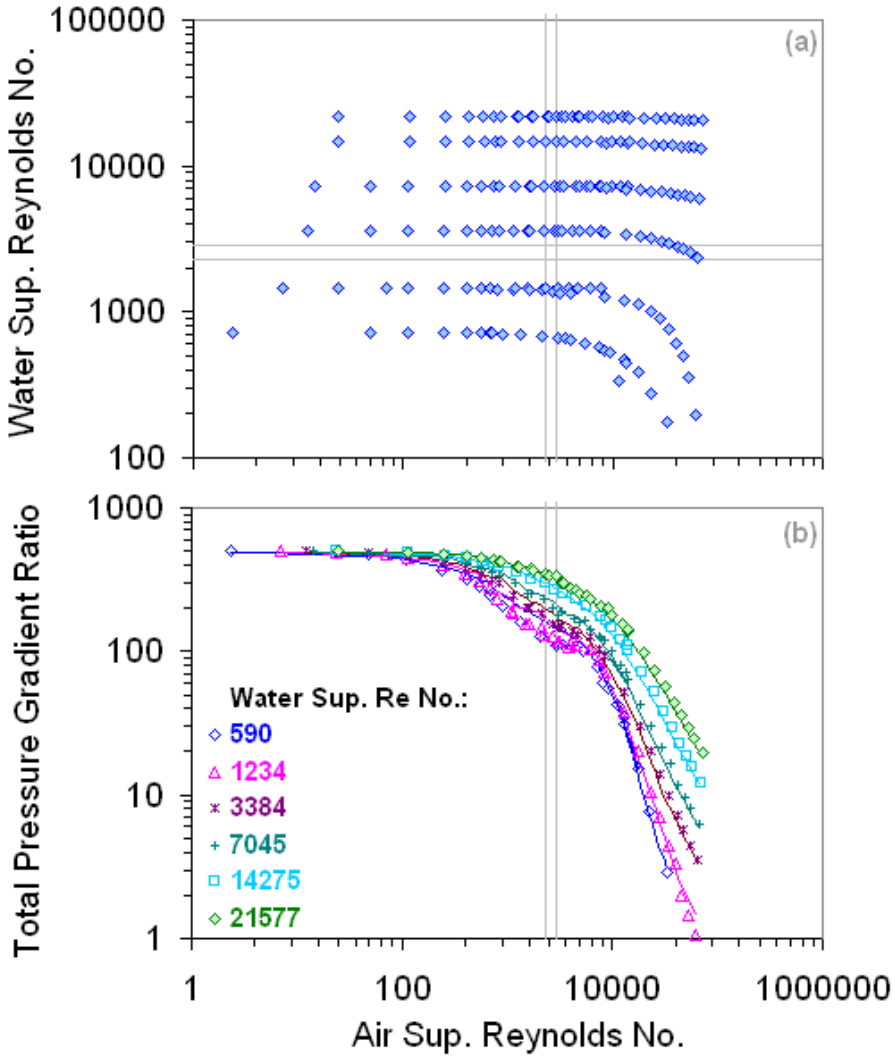

Figure 4.4.1: All of the air-water experiments of Hughmark (1959). Lines are our calculations and the points are measurements.

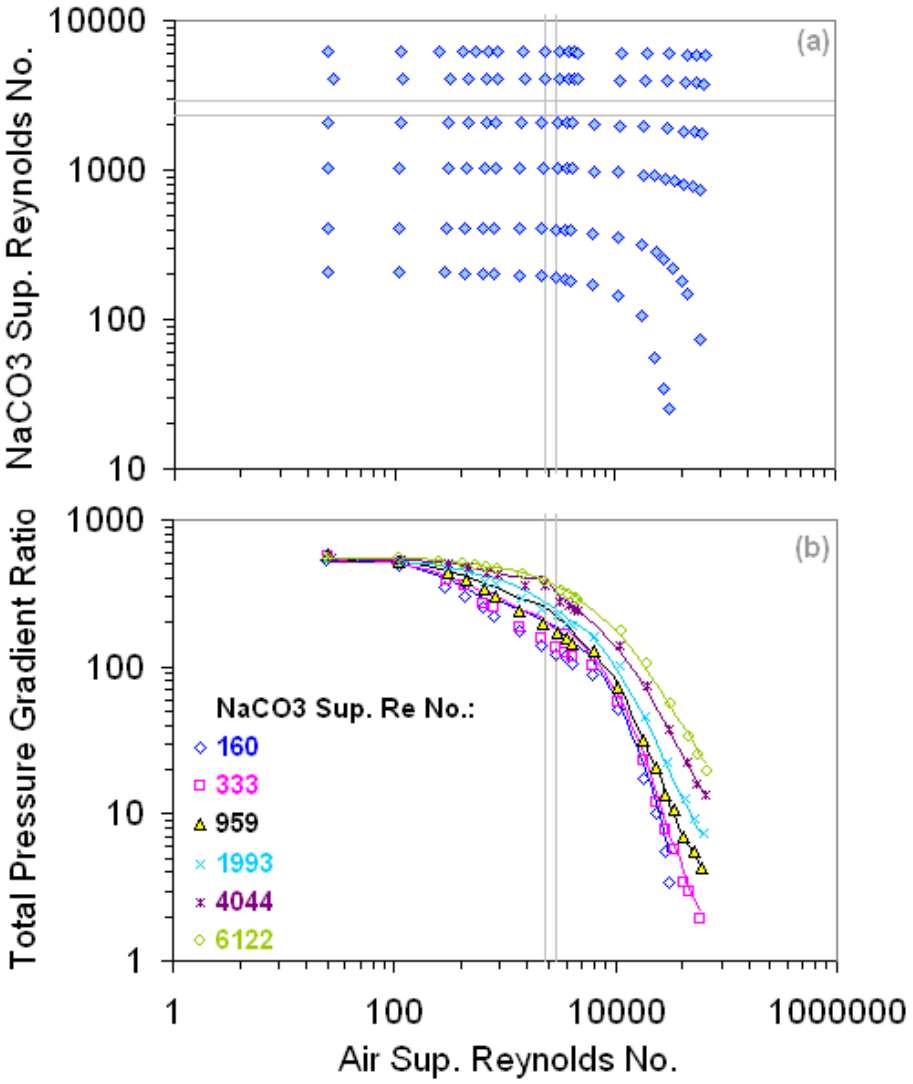

Figure 4.4.2: All of the air-sodium carbonate experiments of Hughmark (1959). Lines are our calculations and the points are measurements.

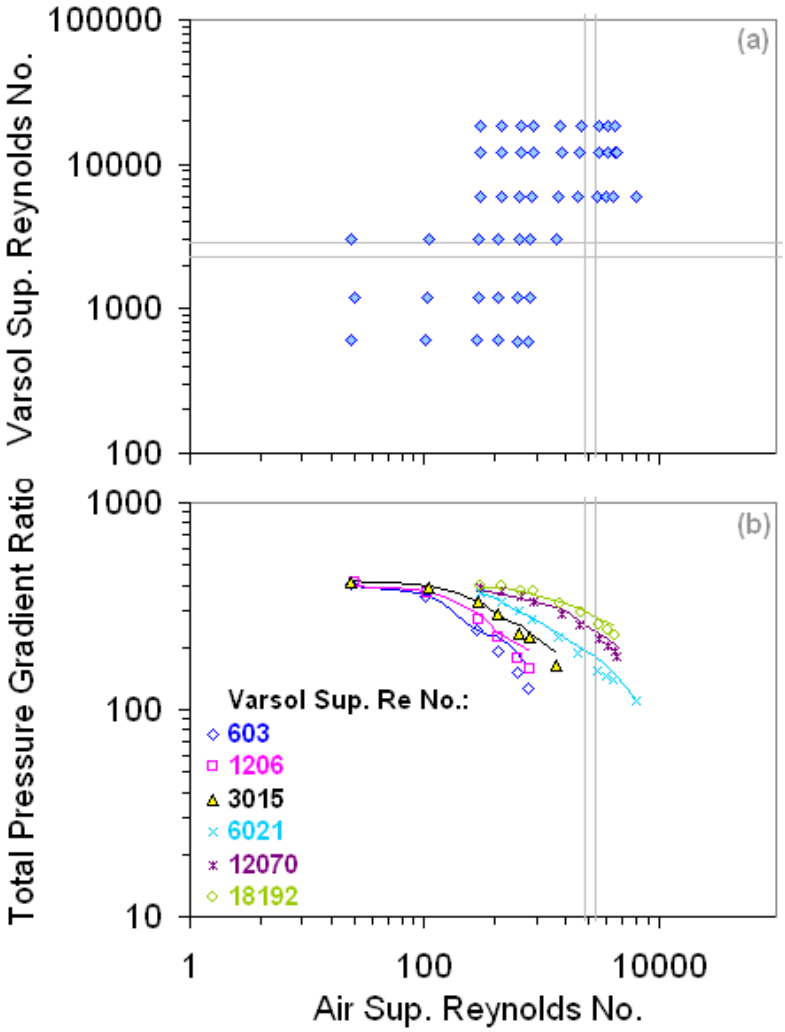

Figure 4.4.3: All of the air-varsol experiments of Hughmark (1959). Lines are our calculations and the points are measurements.

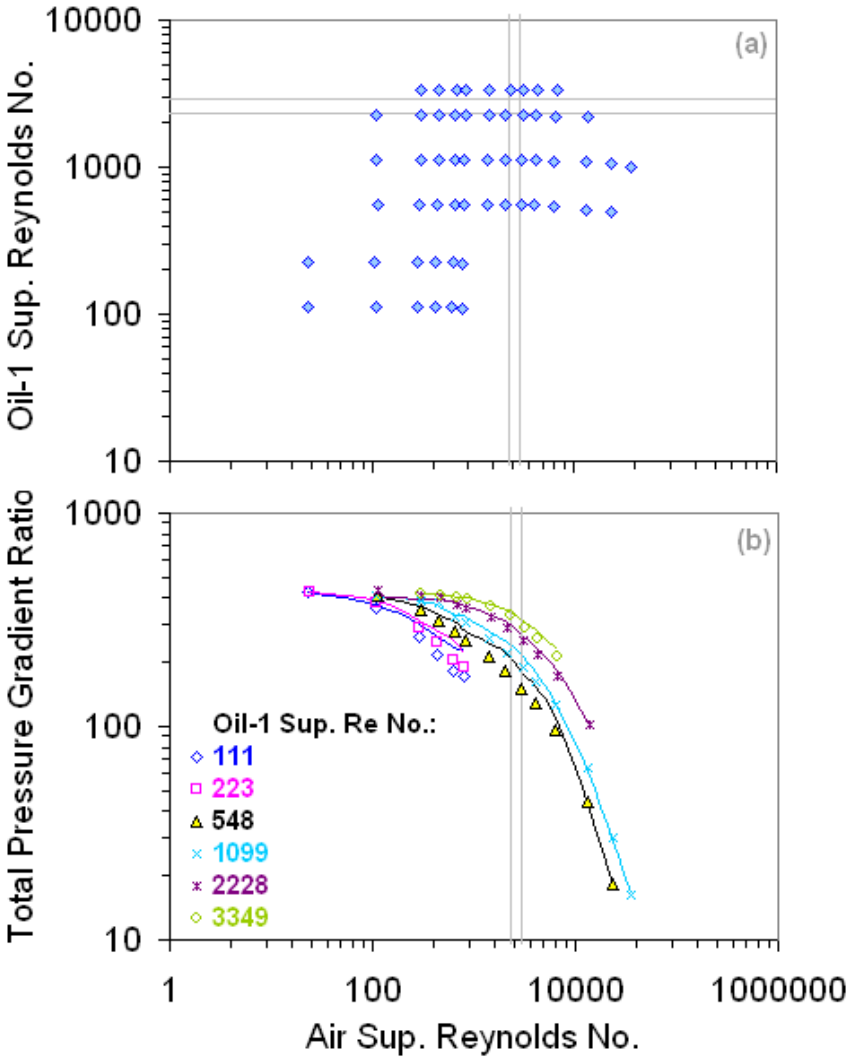

Figure 4.4.5: All of the air-oil blend 1 experiments of Hughmark (1959). Lines are our calculations and the points are measurements.

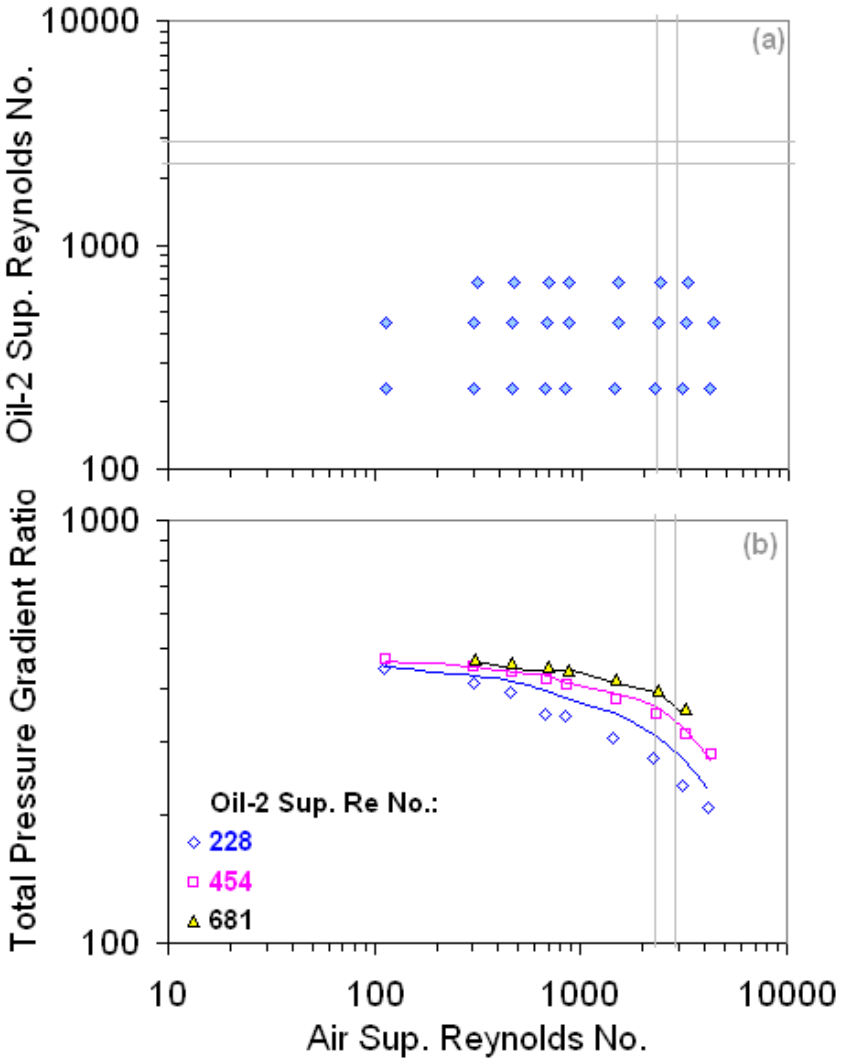

Figure 4.4.6: All of the air-oil blend 2 experiments of Hughmark (1959). Lines are our calculations and the points are measurements.

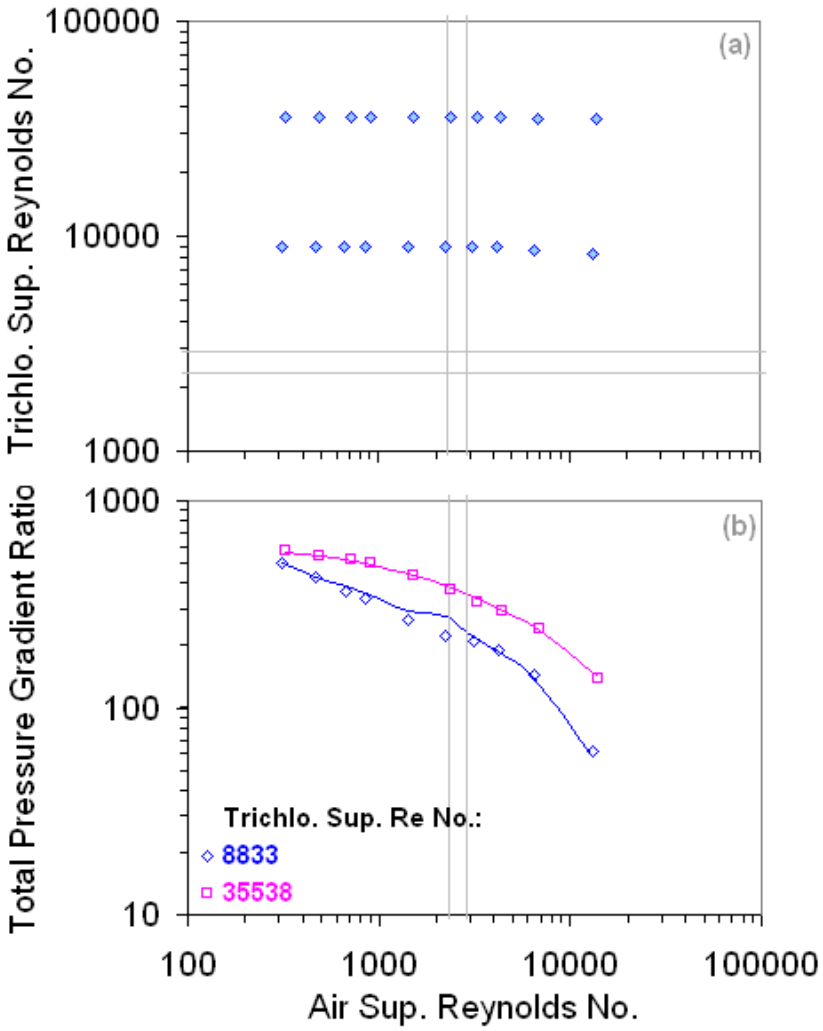

Figure 4.4.7: All of the air-trichloroethylene experiments of Hughmark (1959). Lines are our calculations and the points are measurements.

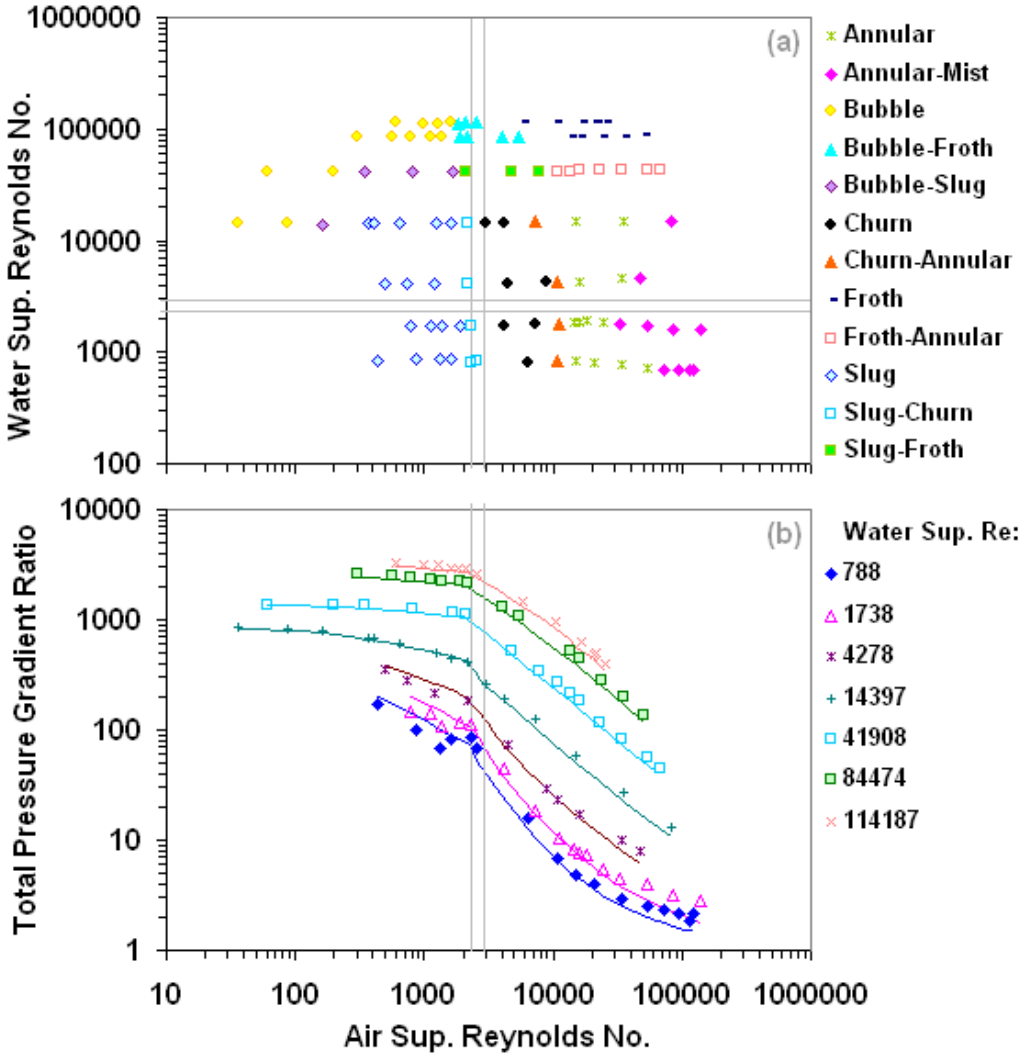

Figure 4.4.8: All of the air-water experiments of Sujumnong (1997). Lines are predictions with the ANSLIP analytical model and the points are measurements.

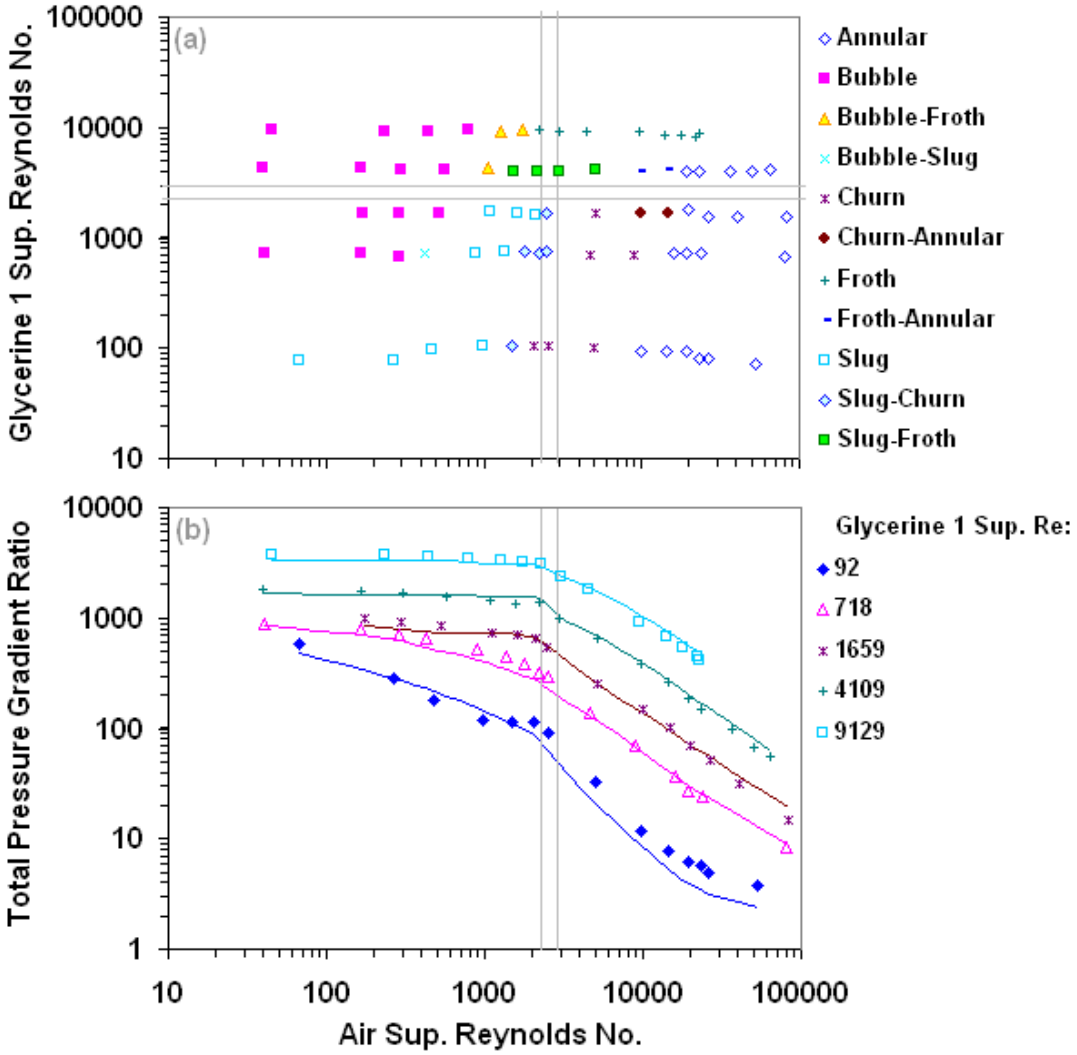

Figure 4.4.9: All of the air-glycerine blend 1 experiments of Sujumnong (1997). Lines are predictions with the ANSLIP analytical model and the points are measurements.

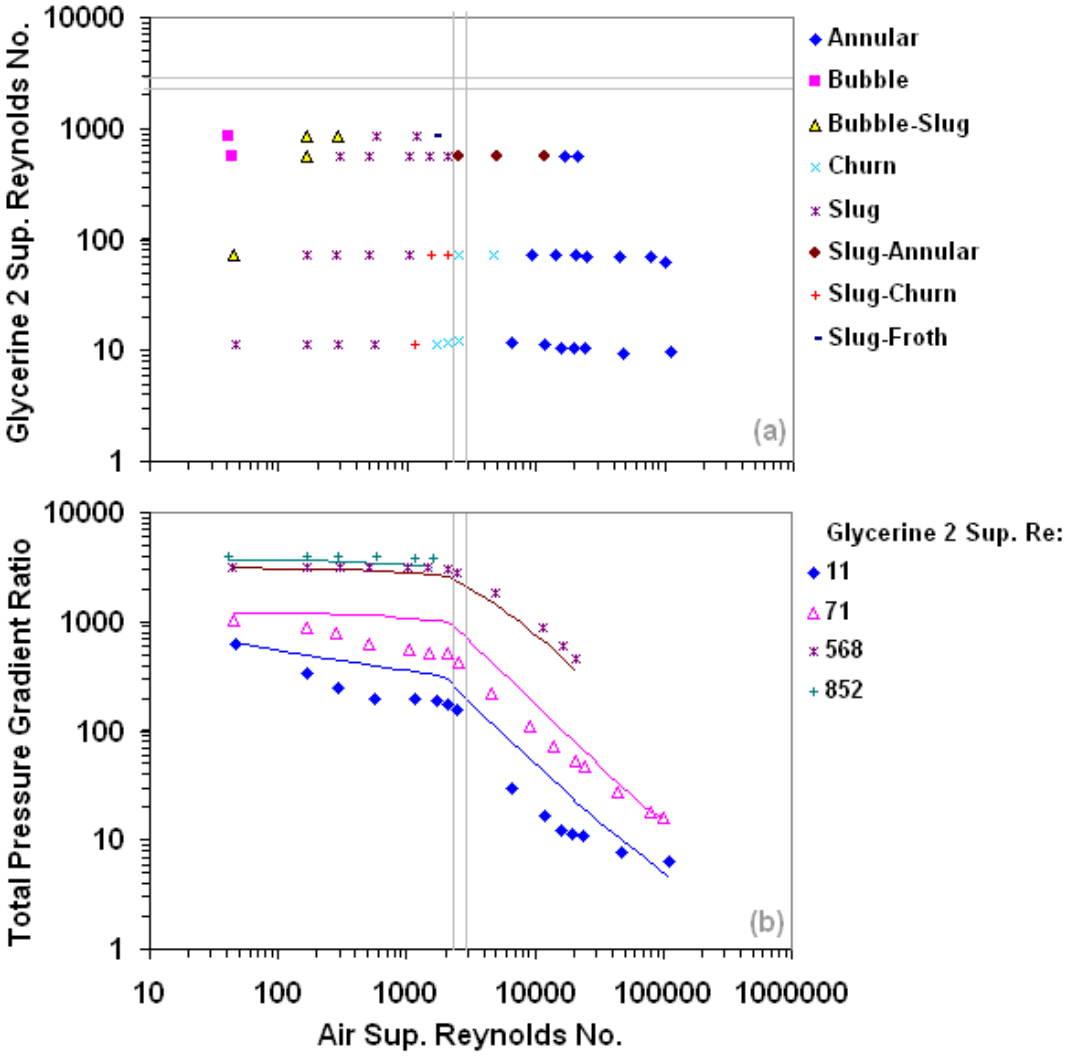

Figure 4.4.10: All of the air-glycerine blend 2 experiments of Sujumnong (1997). Lines are predictions with the ANSLIP analytical model and the points are measurements.

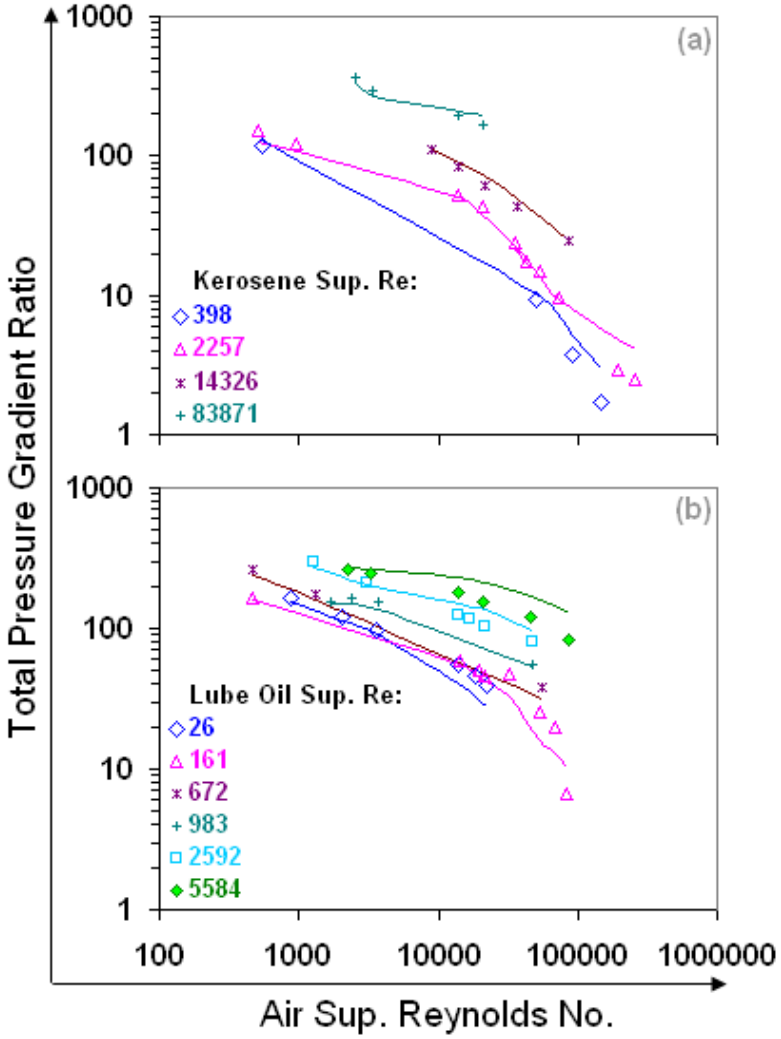

Figure 4.4.11: (a) All of the vertical upward air-kerosene experiments of Mukherjee (1979); (b) All of the vertical upward air-lube oil experiments of Mukherjee (1979). Lines are predictions with the WOLGHA model and the points are measurements.

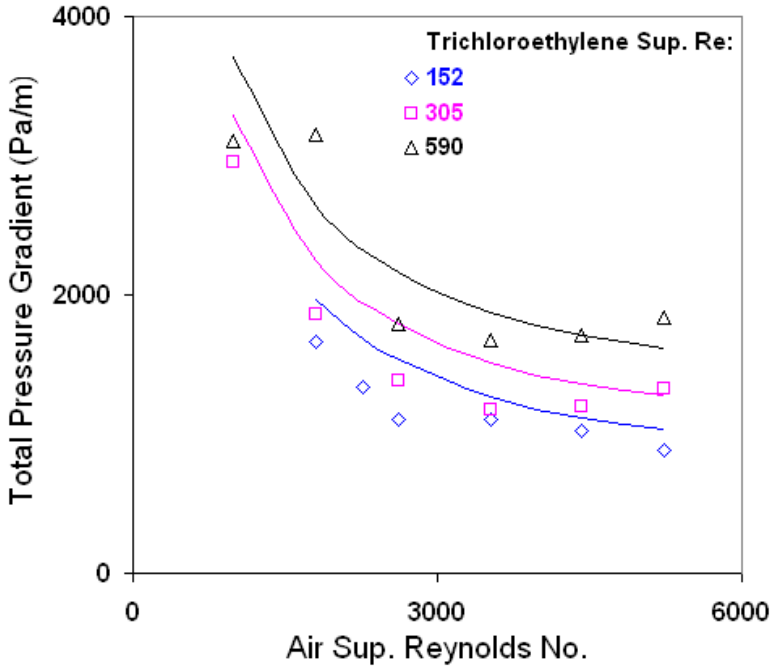

Figure 4.4.12: All of the vertical upward churn-annular experiments of Hewitt et al. (1985). Lines are predictions with the WOLGHA model and the points are measurements.

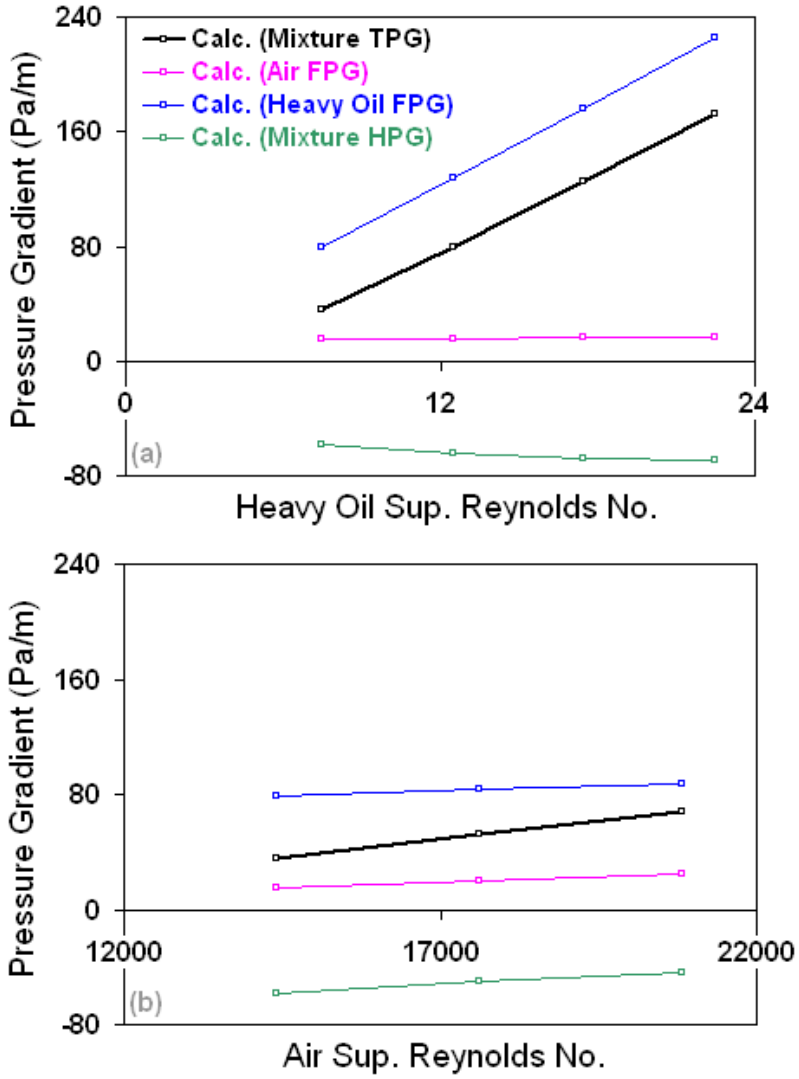

Figure 4.4.13: Predictions of the slightly down-inclined stratified-wavy high viscosity ratio air and heavy oil experiments of Brito et al. (2012).

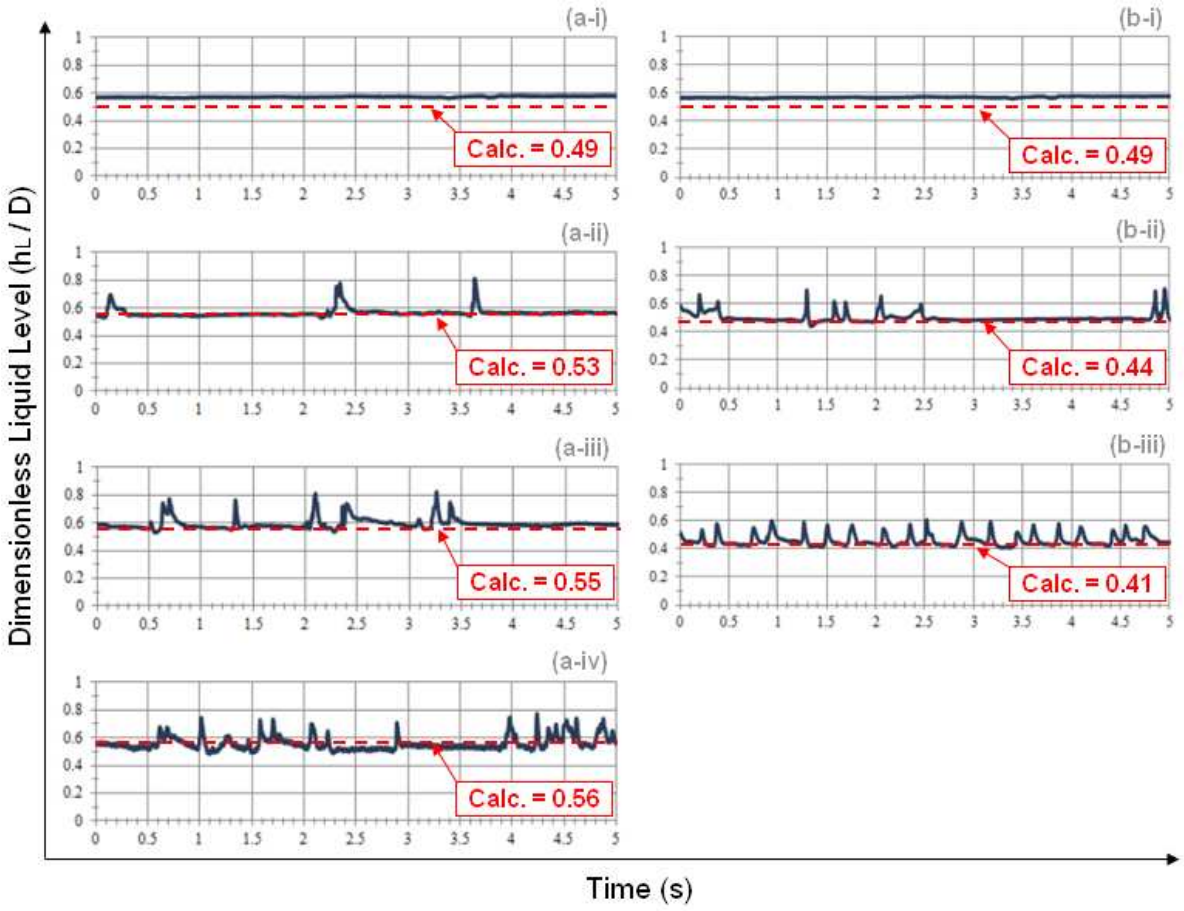

Figure 4.4.14: Comparison of our predictions of the slightly down-inclined stratified-wavy high viscosity ratio air and heavy oil experiments of Brito et al. (2012) with measured time traces of the dimensionless liquid level. The time traces in a-i to a-iv are from Fig. 8 of the reference and the time traces in b-i to b-iii are from Fig. 9 of the reference.

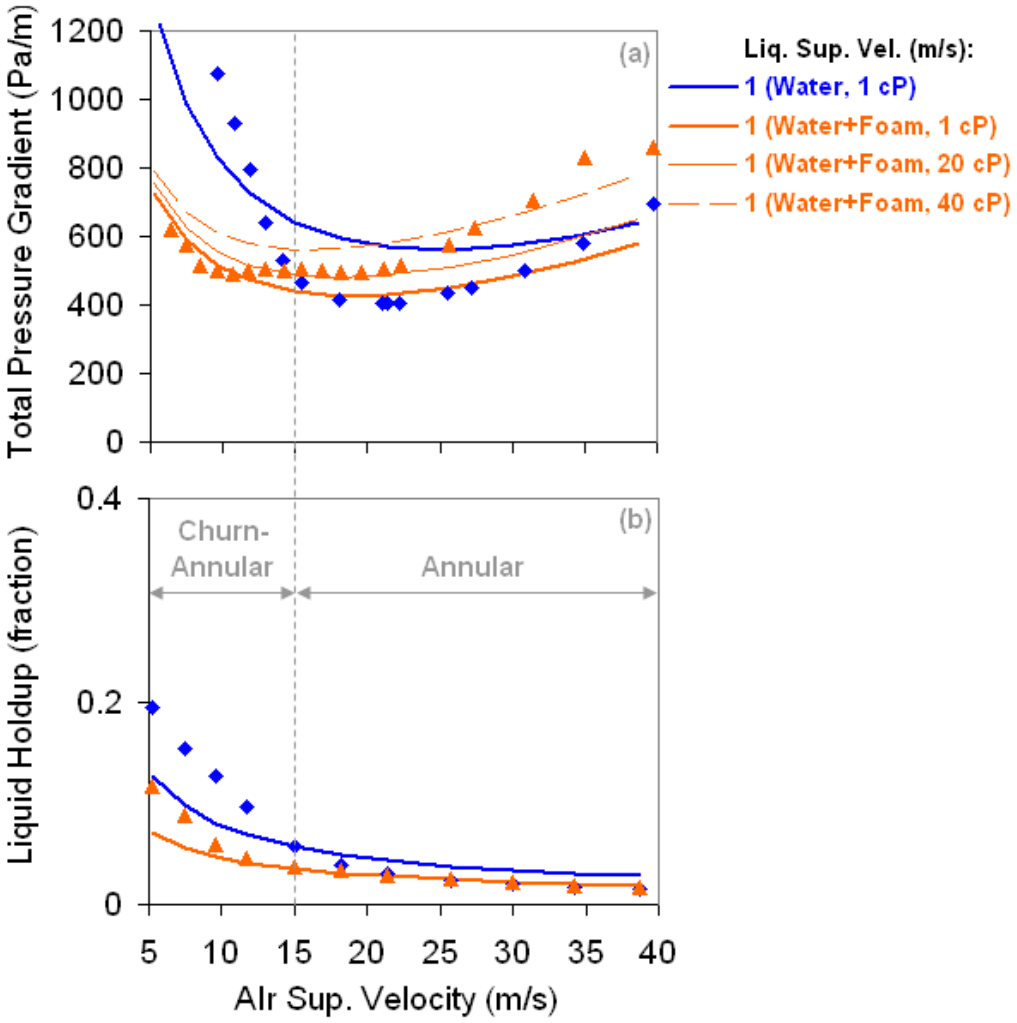

Figure 4.4.15: Predictions of the vertical upward air and water-foam experiments of van Nimwegan et al. (2012). Lines are predictions with the WOLGHA model and the points are measurements.

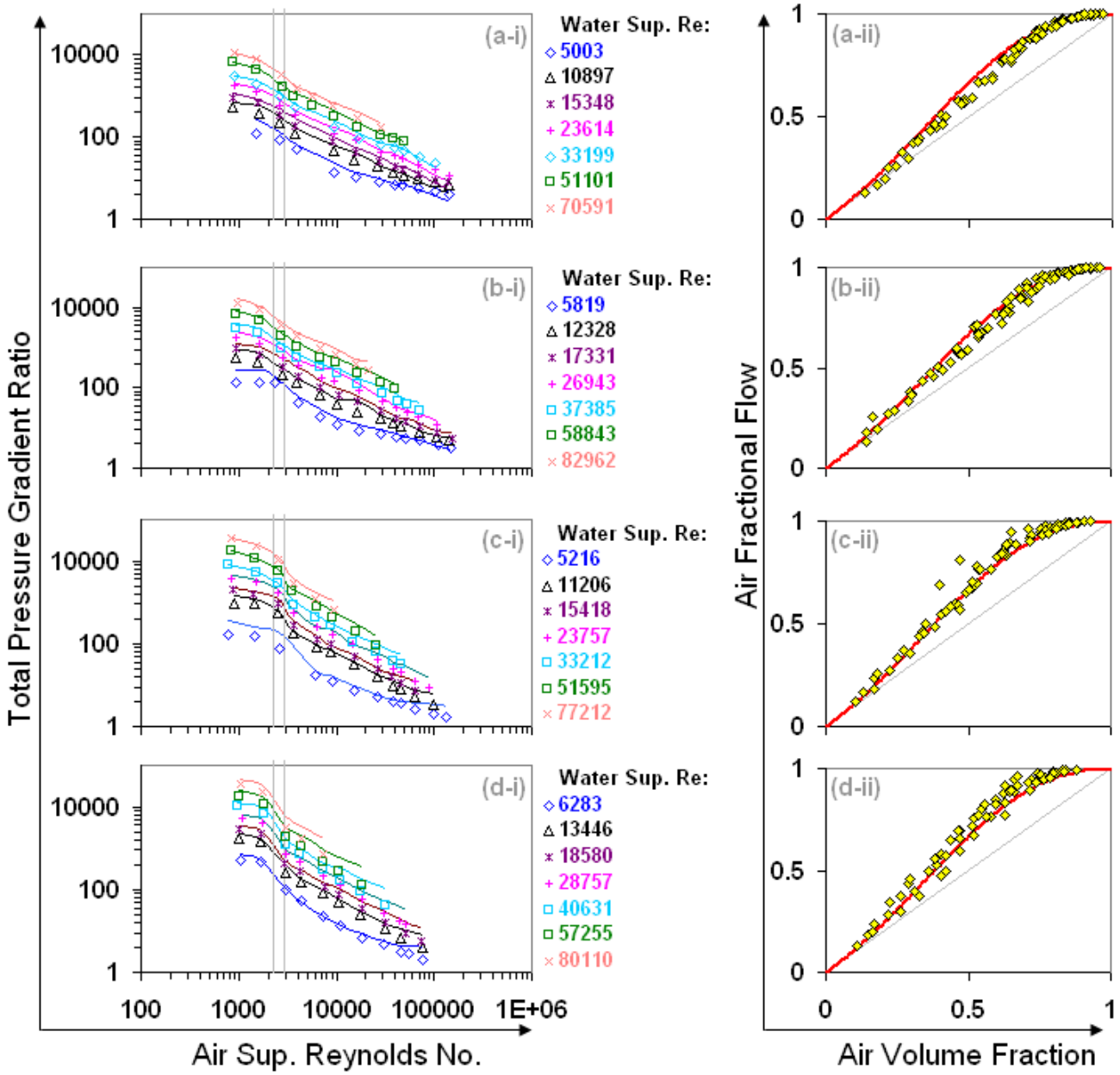

Figure 4.4.16: Validation of our analytical models with all of the horizontal wall roughness experiments of Chisolm and Laird (1958). Lines are our calculations and the points are measurements.

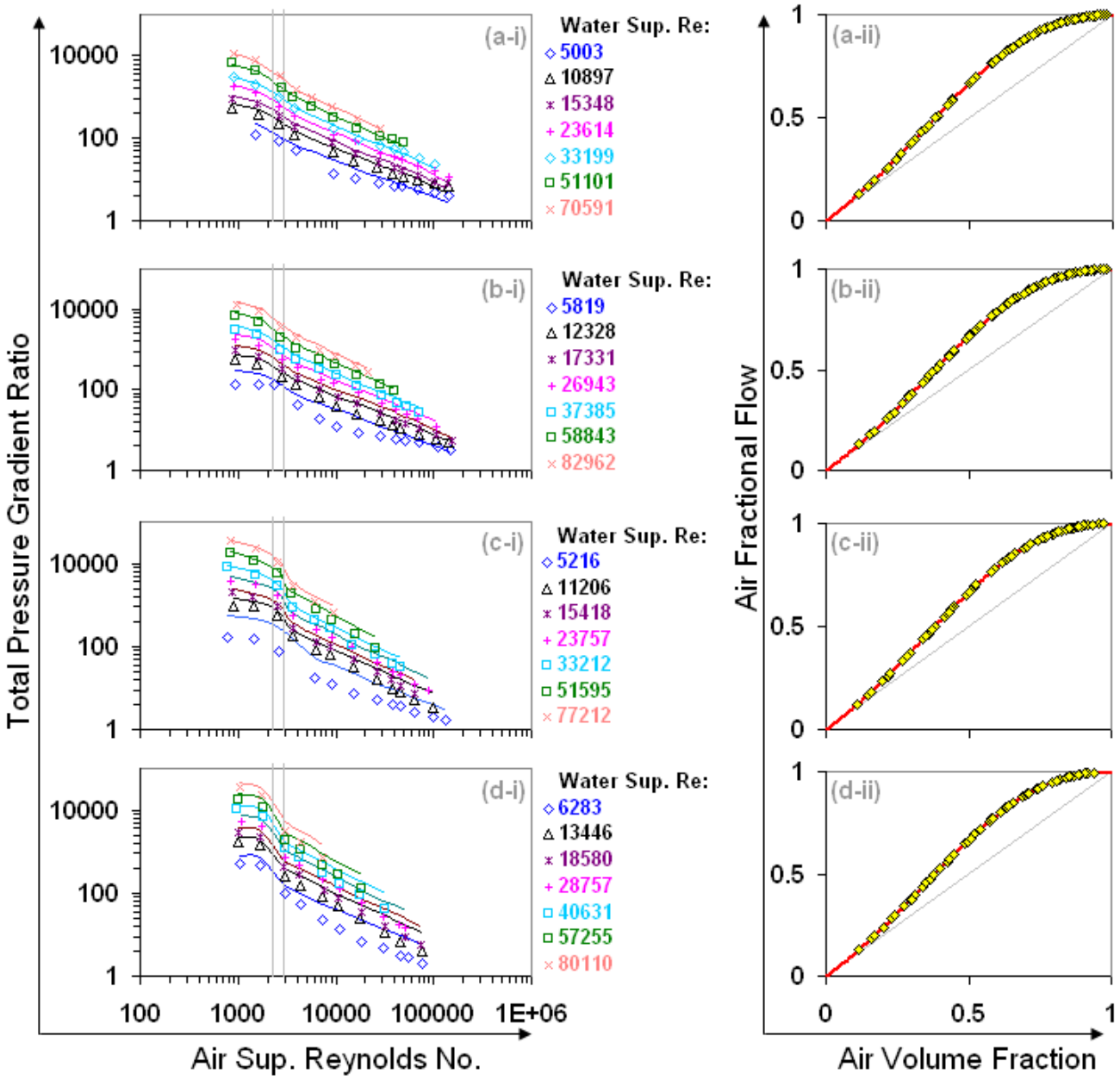

Figure 4.4.17: Prediction of all of the horizontal wall roughness experiments of Chisolm and Laird (1958). Lines are predictions with the ANSLIP analytical model and the points are measurements.

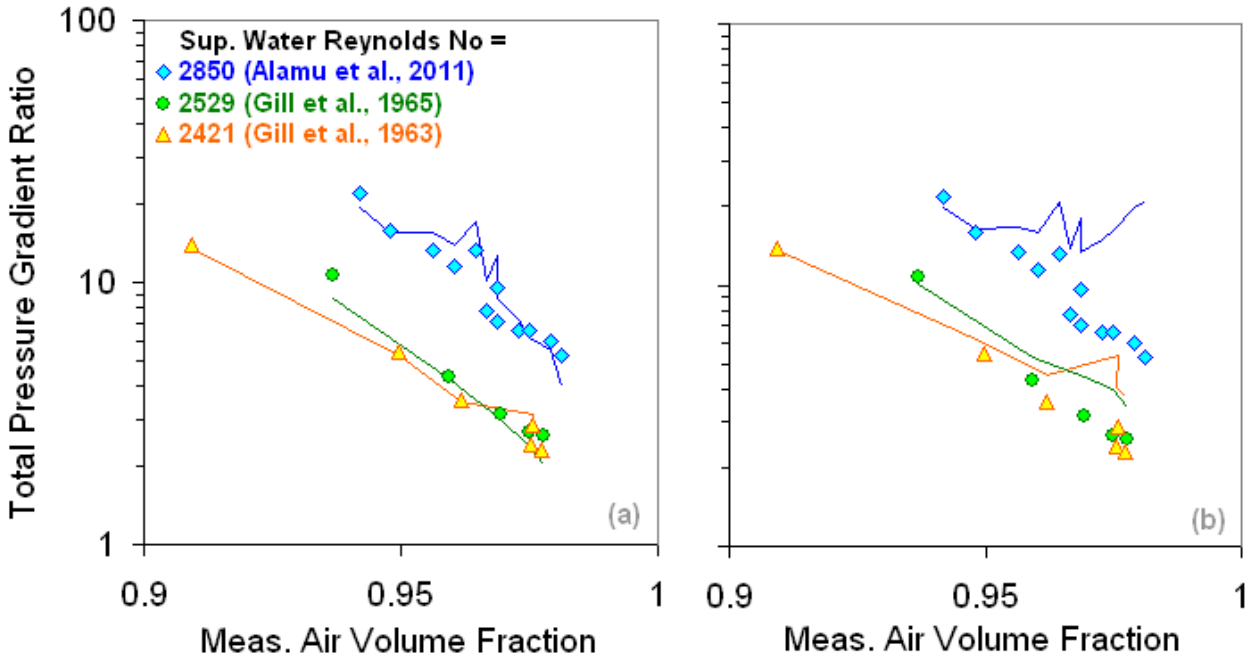

Figure 4.5.1: Demonstrating the need for accounting for entrainment with small diameter vertical upward annular flow datasets. Lines are our calculations and the points are measurements.

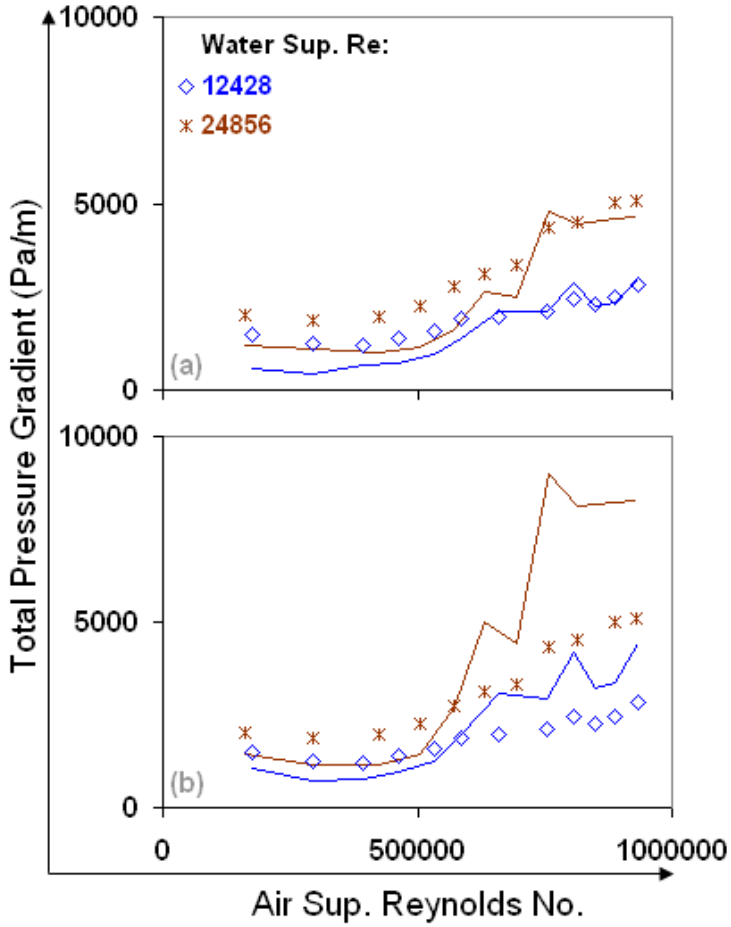

Figure 4.5.2: Demonstrating the need for accounting for entrainment with the large diameter vertical upward annular flow dataset of Hossfield and Bharathan (1982). Lines are our calculations and the points are measurements.

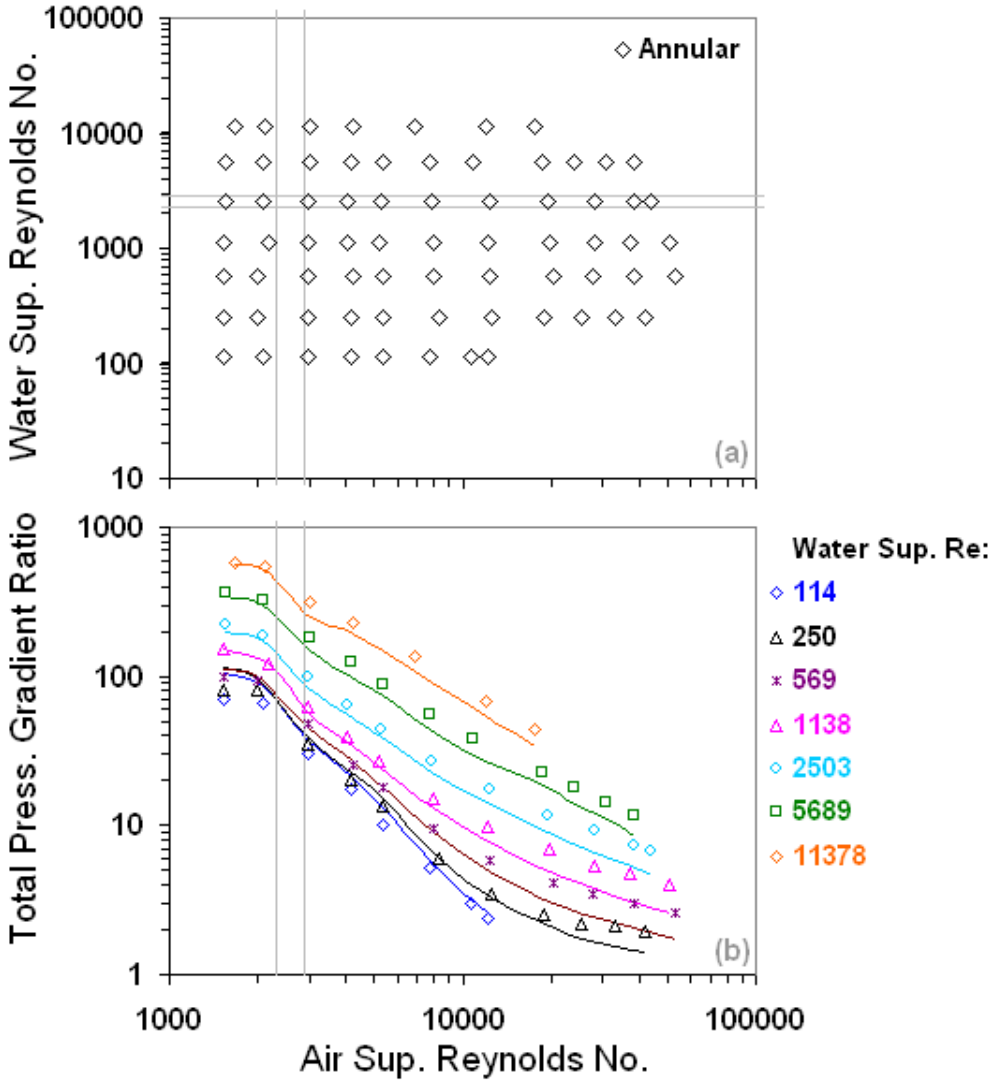

Figure 4.5.3: All of the data of the classic vertical upward annular flow dataset of Anderson and Mantzouranis (1960). Liquid entrainment fraction is predicted with the Ishii and Mishima (1982) correlation. Lines are our calculations and the points are measurements.

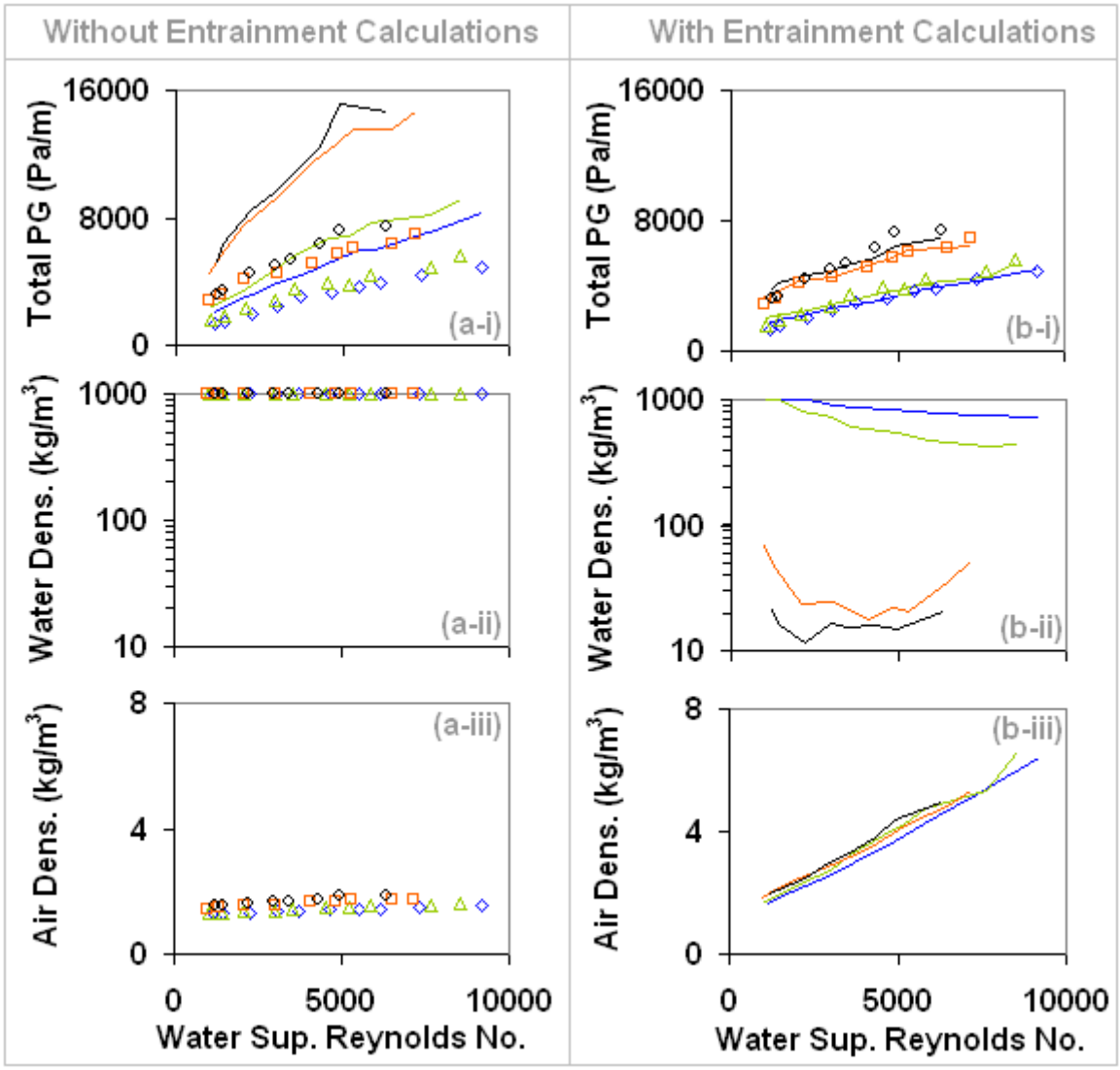

Figure 4.5.4: Demonstrating the validity of our entrainment calculations with the classic vertical upward annular flow dataset of Hewitt et al. (1961). Liquid entrainment fraction is predicted with the Ishii and Mishima (1982) correlation. Lines are our calculations and the points are measurements. The blue diamonds, green triangles, orange squares and black circles correspond to air superficial Reynolds numbers of 114661, 132175, 205703 and 224584, respectively.

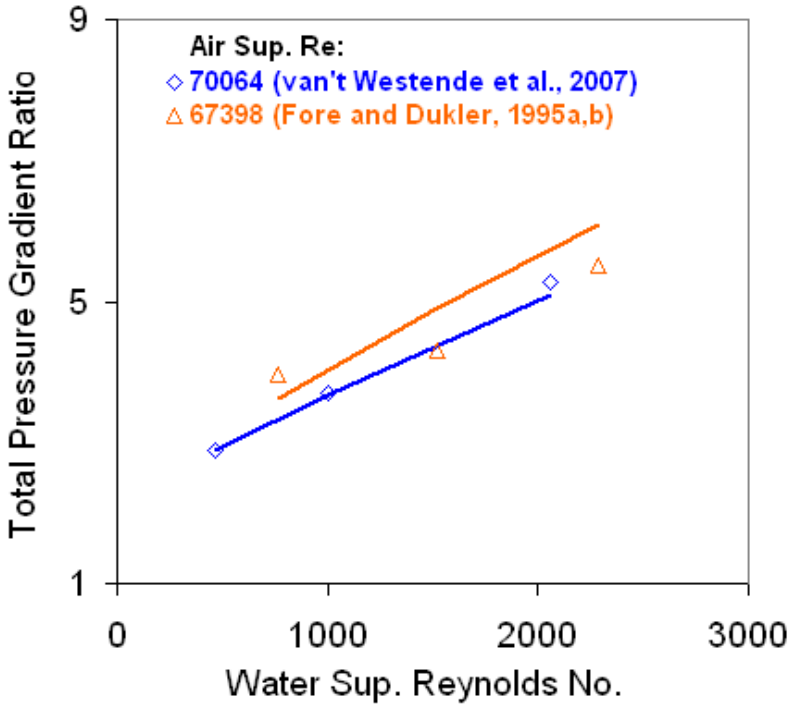

Figure 4.5.5: Demonstrating the validity of our volume fraction calculations with different vertical upward annular flow datasets. The measured liquid entrainment fraction is used in our calculations and the ANSLIP analytical model is used to predict volume fraction. Lines are our calculations and the points are measurements.

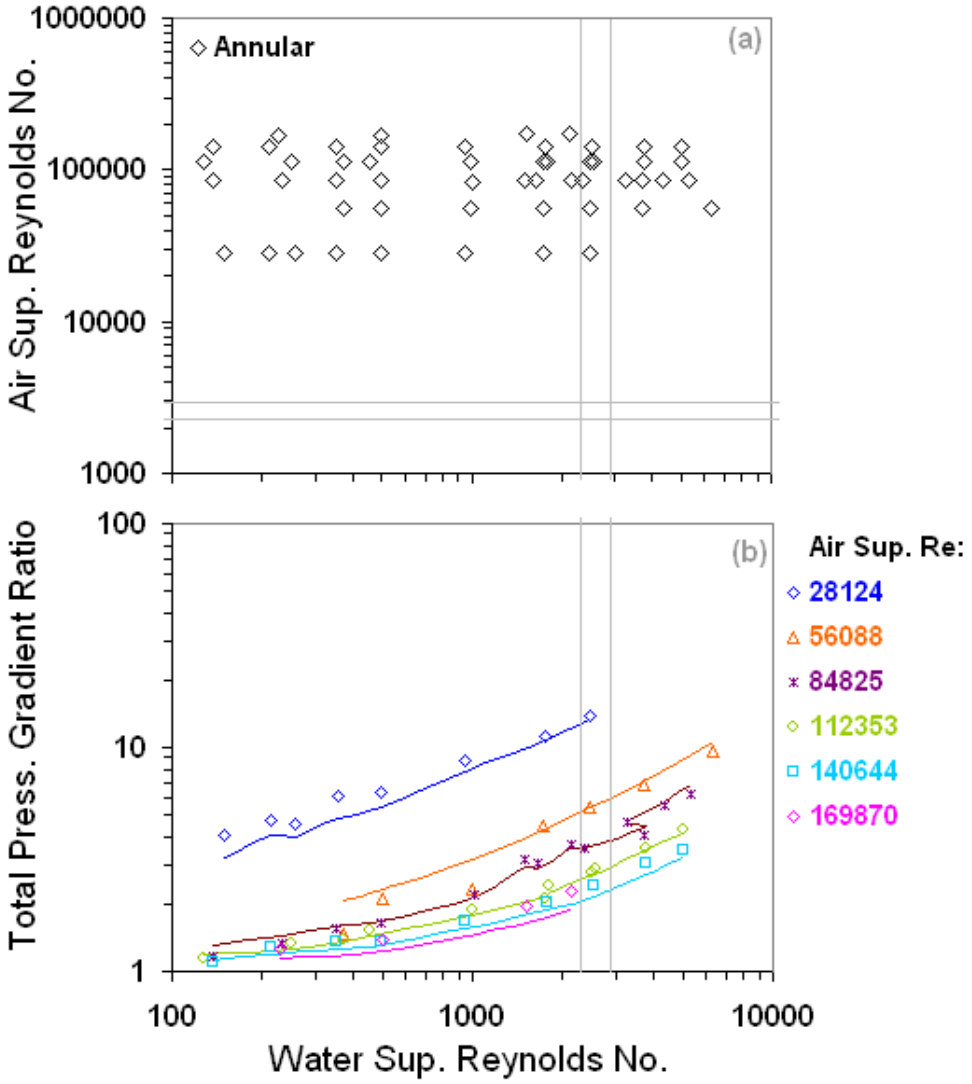

Figure 4.5.6: Demonstrating the validity of our total pressure gradient predictions with the porous sinter data of Gill et al. (1963). The volume fraction is predicted with the ANSLIP analytical model. Lines are our predictions and the points are measurements.

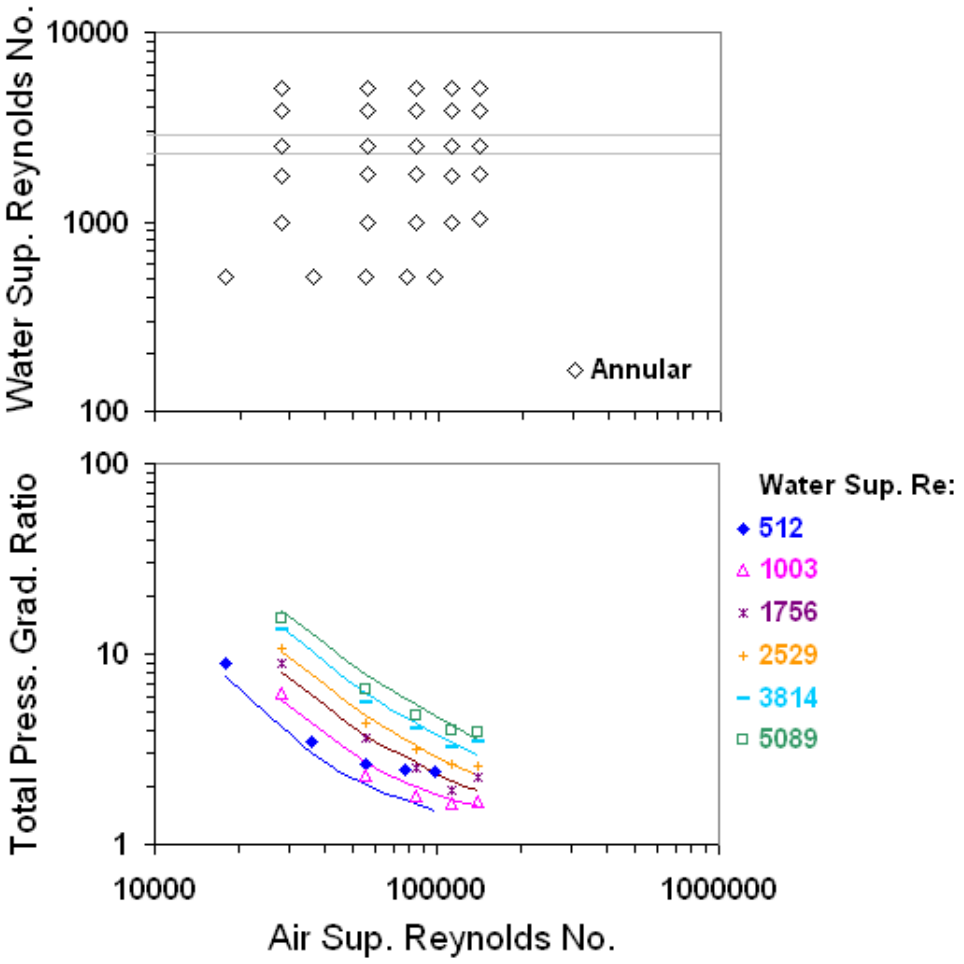

Figure 4.5.7: Demonstrating the validity of our total pressure gradient predictions with the annulus slot data of Gill et al. (1965). The volume fraction is predicted with the ANSLIP analytical model. Lines are our predictions and the points are measurements.

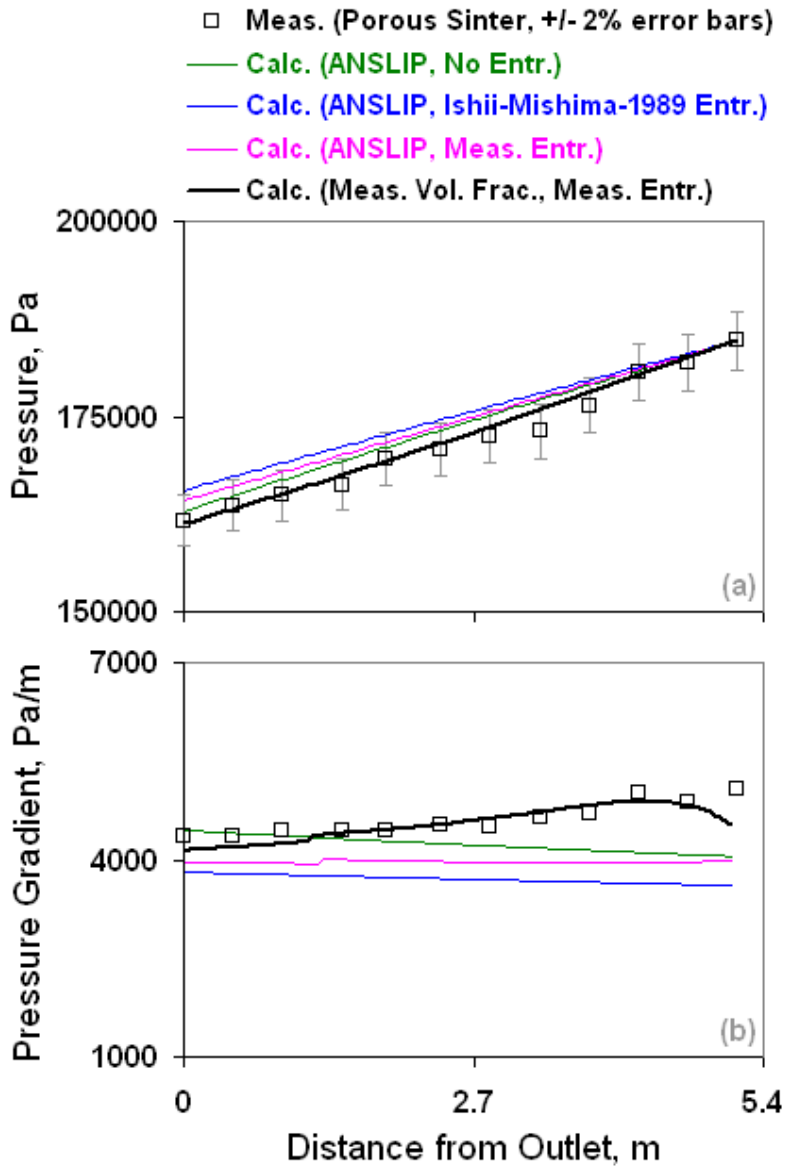

Figure 4.5.8: Demonstrating the validity of our total pressure gradient predictions with the developing-flow sampling probe studies (part 1) of Gill et al. (1962).

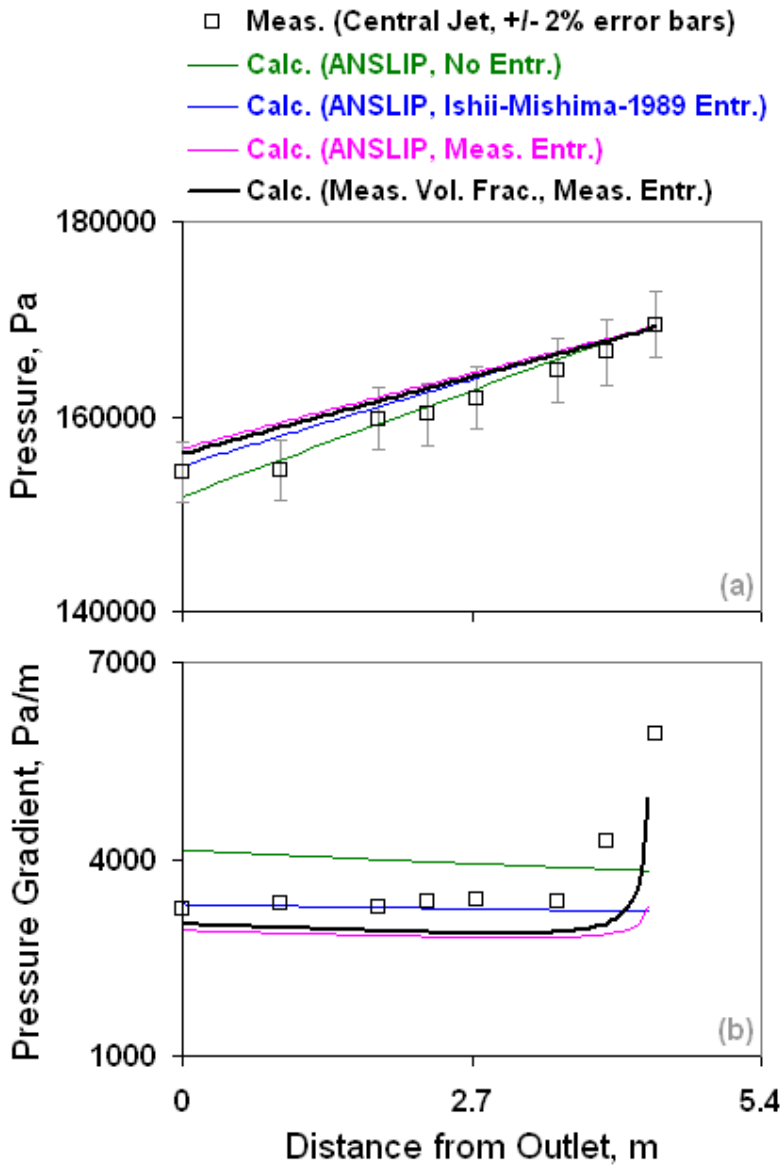

Figure 4.5.9: Demonstrating the validity of our total pressure gradient predictions with the developing-flow sampling probe studies (part 3) of Gill et al. (1967).

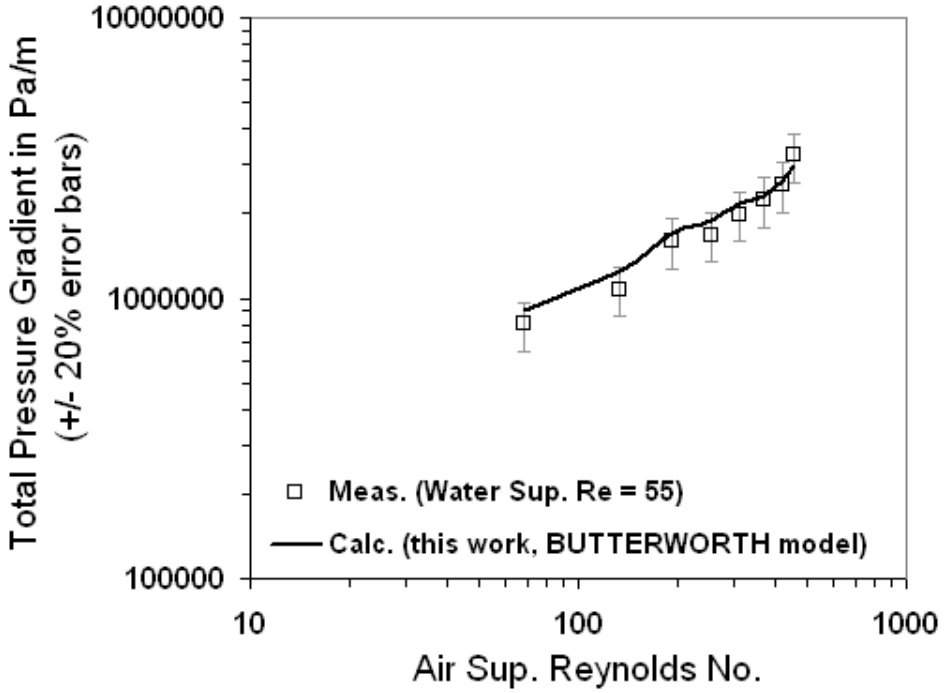

Figure 4.6.1: Prediction of laminar-flow micro-channel experiments of Saisorn and Wongwises (2009) with the BUTTERWORTH model.

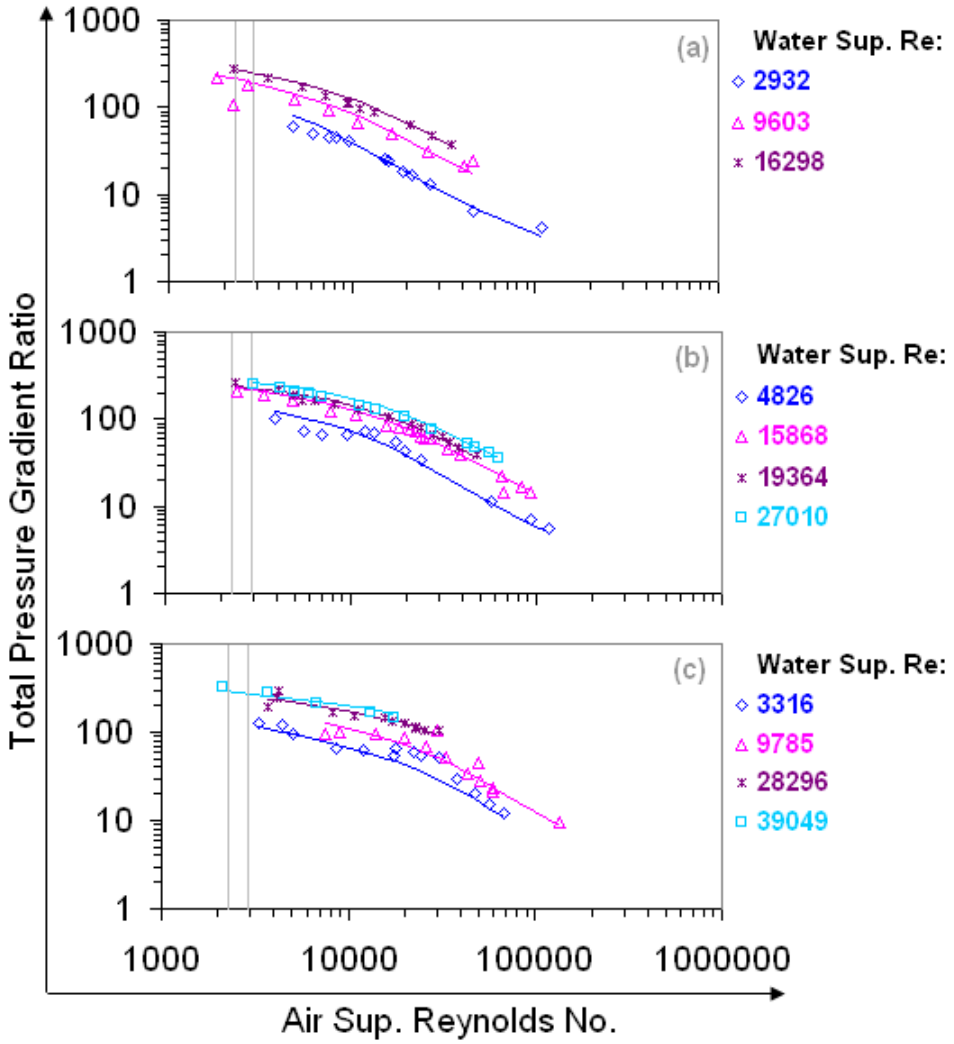

Figure 4.6.2: Prediction of the classic experiments of Short (1957) with the ANSLIP analytical model. Lines are our predictions and the points are measurements.

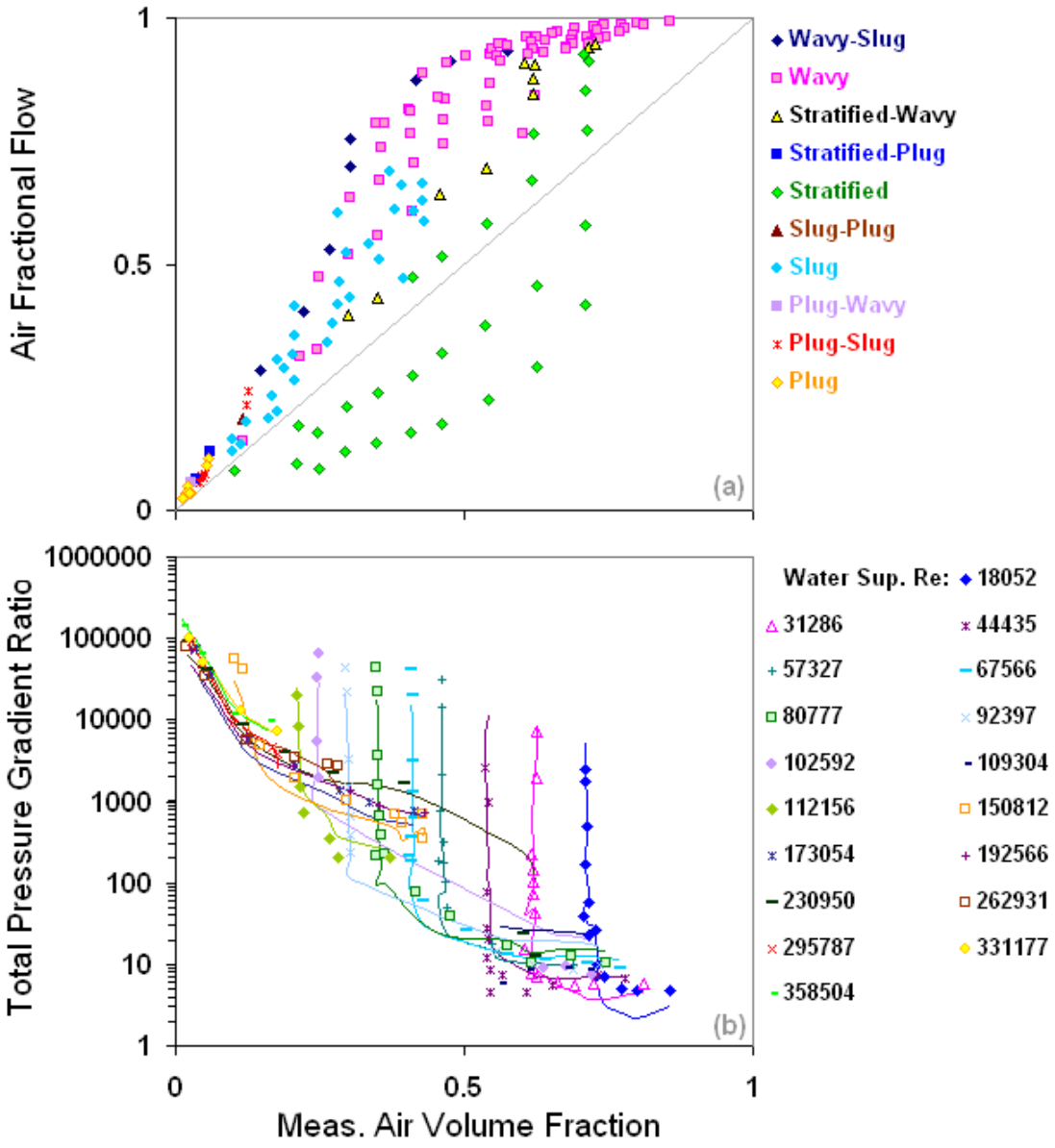

Figure 4.6.3: Demonstrating the validity of our total pressure gradient calculations with the large-diameter horizontal flow dataset of Simpson et al. (1976). Lines are our calculations and the points are measurements.

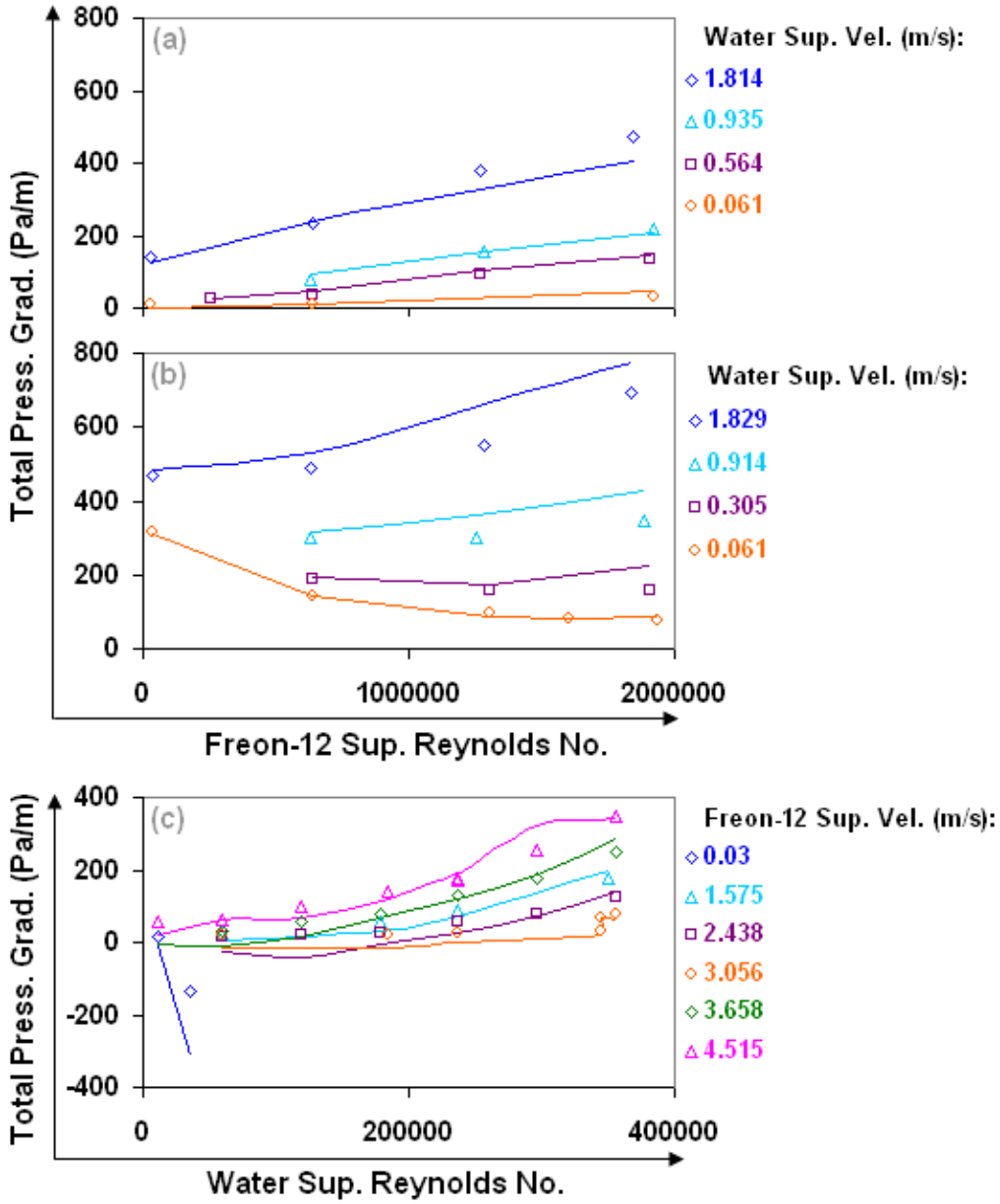

Figure 4.6.4: Demonstrating the validity of our total pressure gradient calculations with the large-diameter, high gas density, horizontal and slightly-inclined flow dataset of Crowley et al. (1986). Lines are our calculations and the points are measurements.

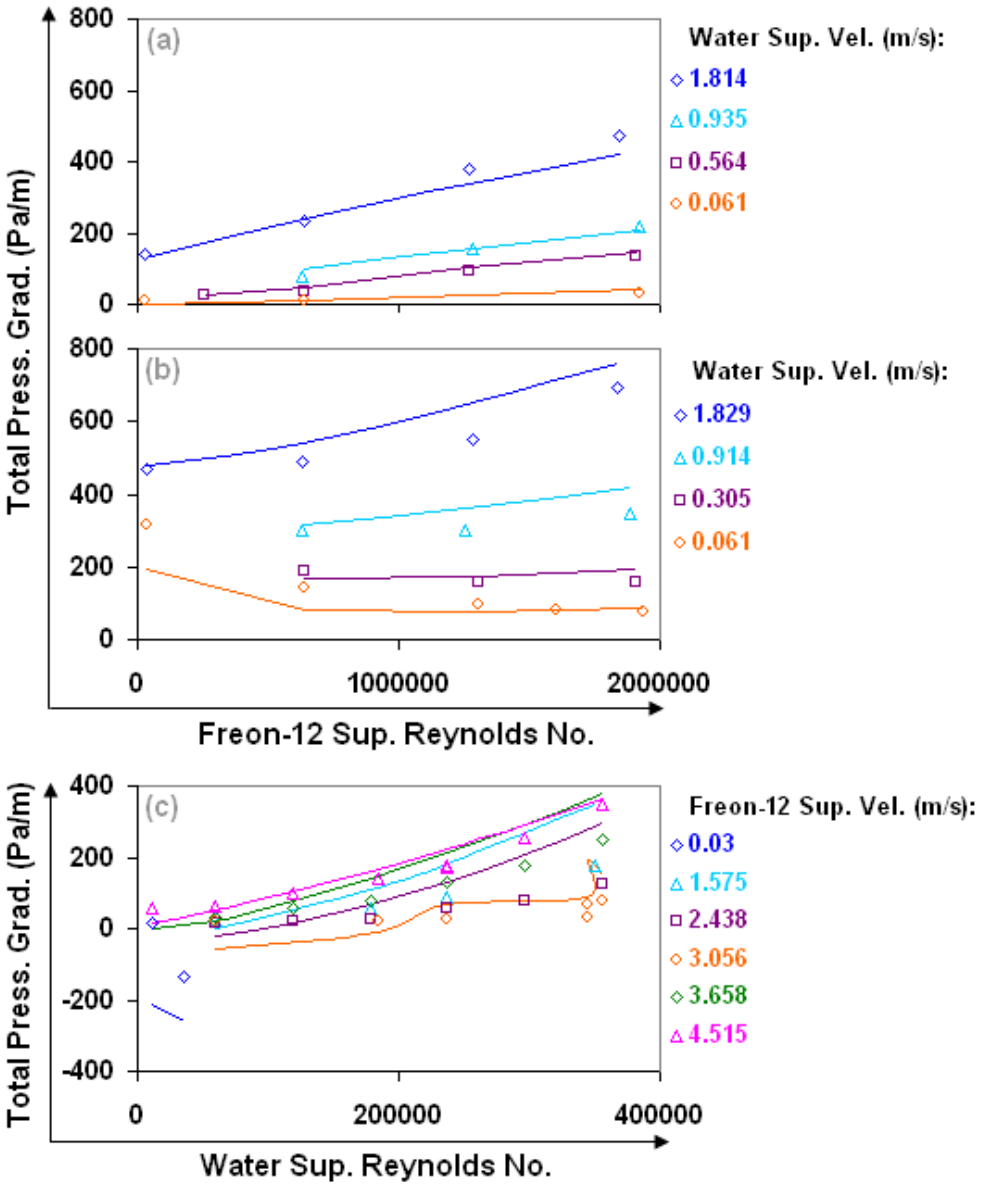

Figure 4.6.5: Prediction of the large-diameter, high gas density, horizontal and slightly-inclined flow dataset of Crowley et al. (1986) with the ANSLIP analytical model. Lines are our predictions and the points are measurements.

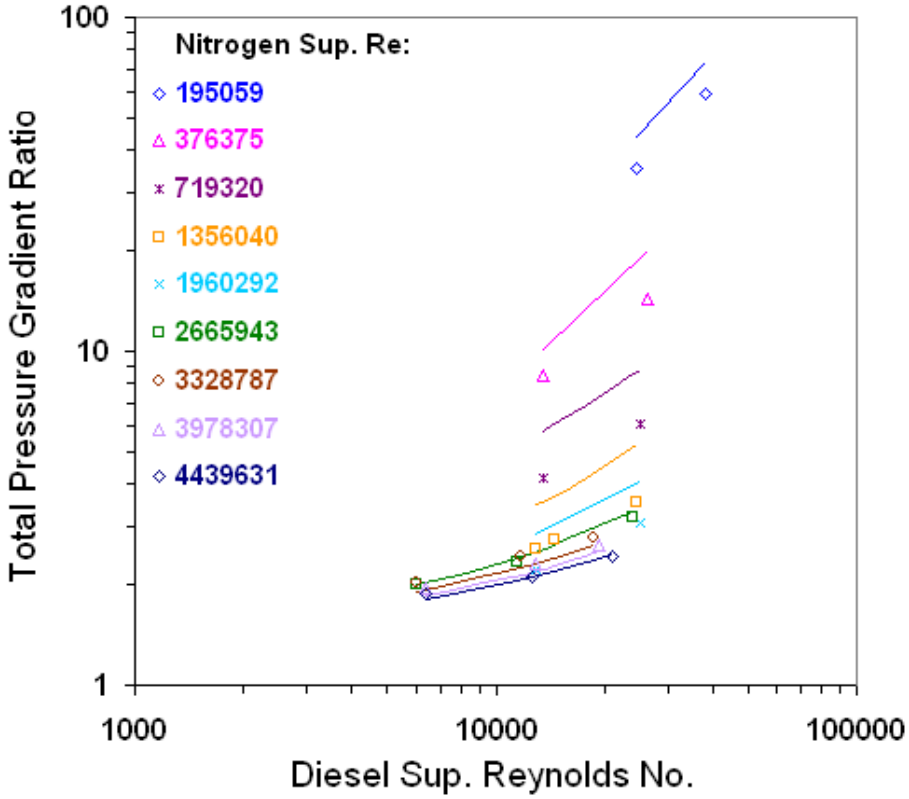

Figure 4.6.6: Prediction of the large-diameter, high gas density, horizontal flow dataset of Bendikson et al. (1987) with the ANSLIP analytical model. Lines are our predictions and the points are measurements.

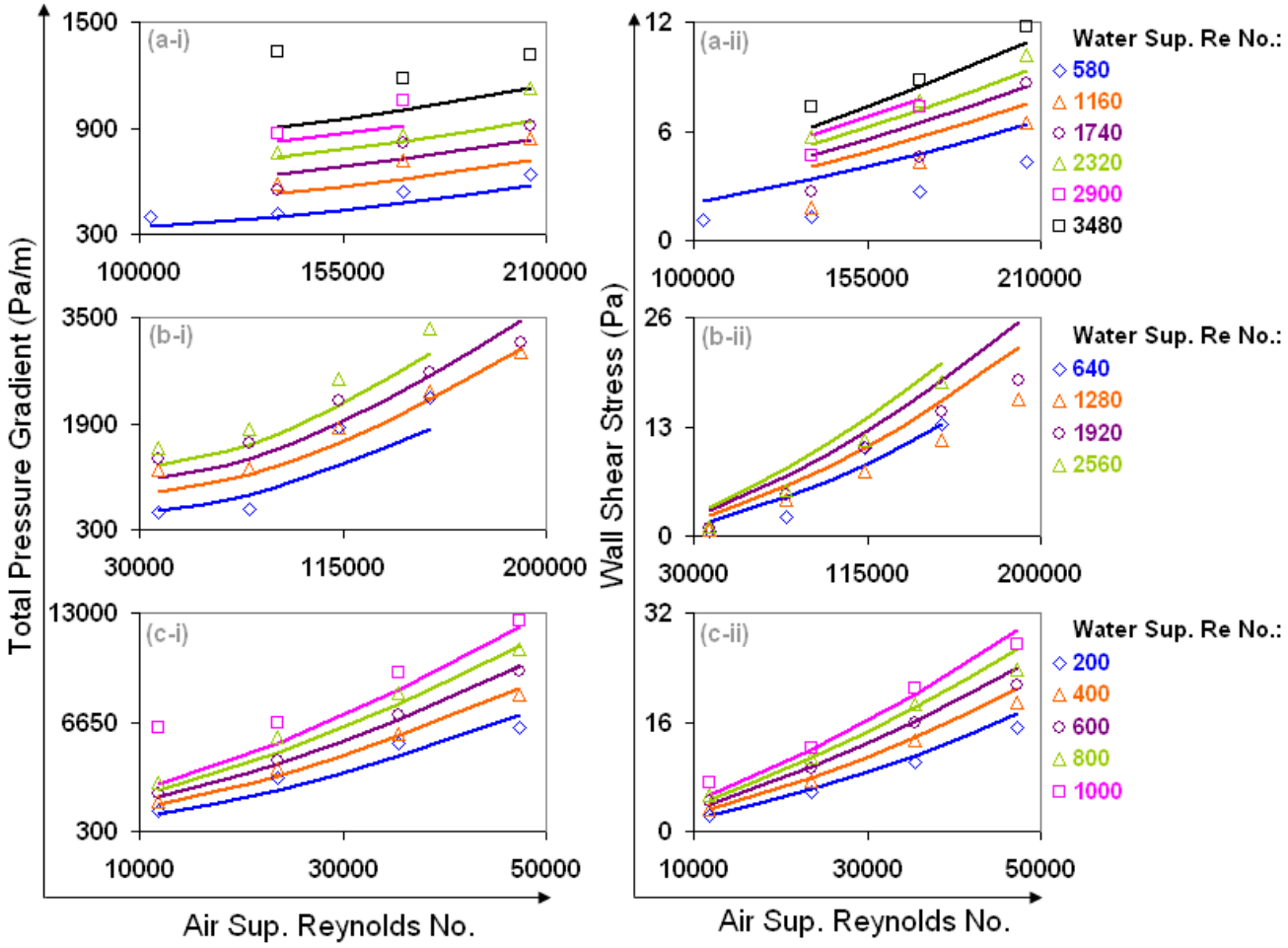

Figure 4.6.7: Prediction of the pressure gradient and wall shear stress annular flow experiments of Martin (1983) with the BUTTERWORTH model. Lines are our predictions and the points are measurements.

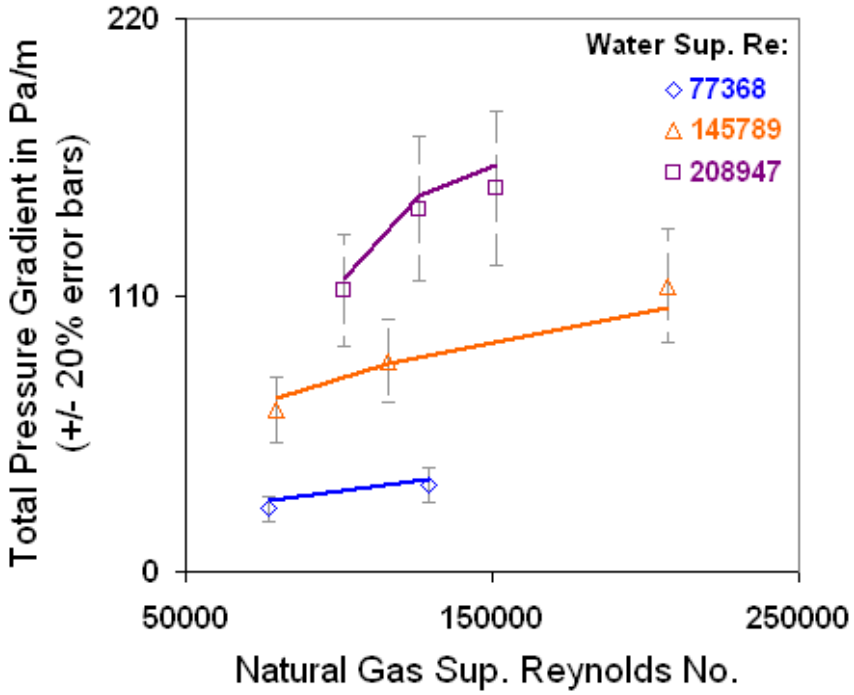

Figure 4.6.8: Prediction of the large-diameter, high gas density, horizontal slug flow dataset of Marruaz et al. (2001) with the SLIPRATIO model. Lines are our predictions and the points are measurements.

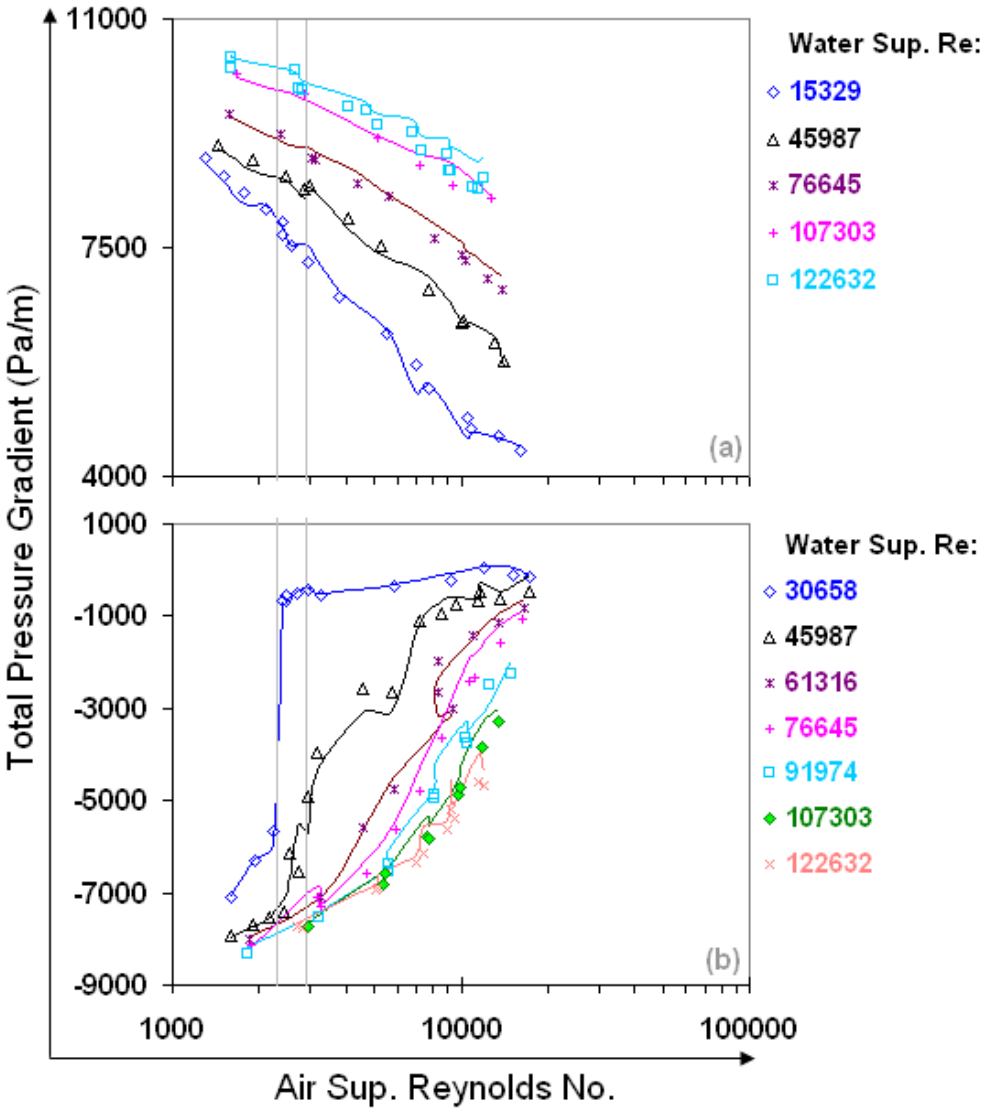

Figure 4.7.1: Demonstrating the validity of our total pressure gradient calculations with the classic (a) vertical upward and (b) vertical downward experiments of Nichols (1965). Lines are our calculations and the points are measurements.

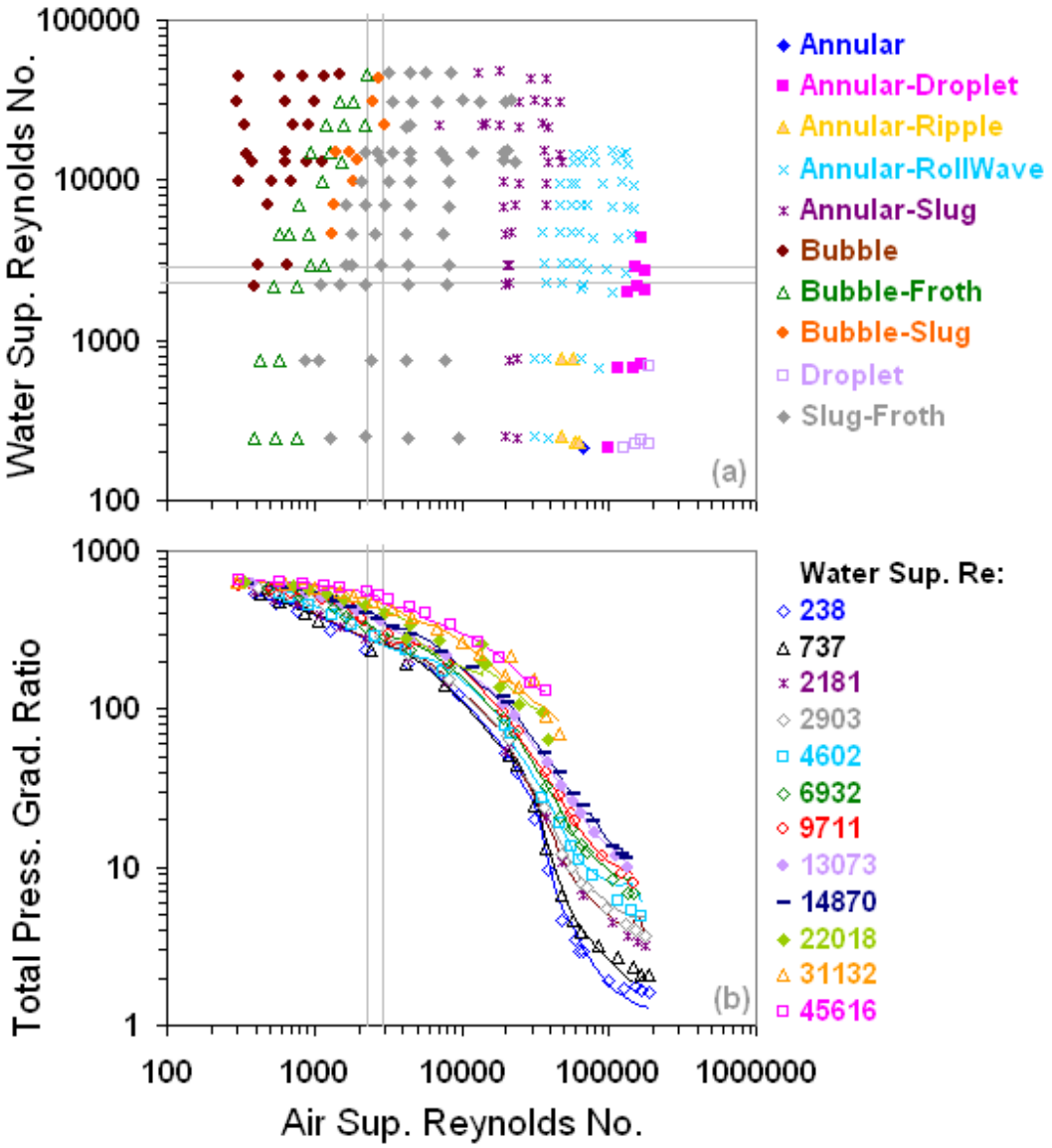

Figure 4.7.2: Demonstrating the validity of our total pressure gradient calculations with the classic vertical upward experiments of Spedding and Nguyen (1976). Lines are our calculations and the points are measurements.

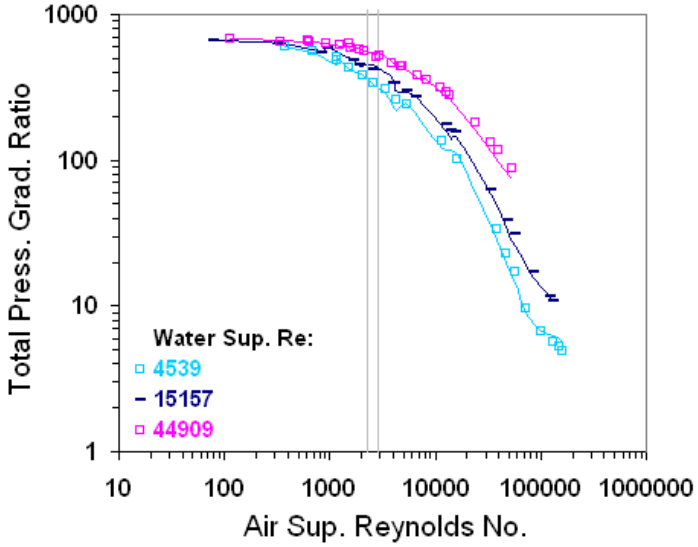

Figure 4.7.3: Validation of our total pressure gradient calculations for experiments in Spedding and Nguyen (1976) at 20 degrees from vertical. Lines are our (coupled-flow) calculations and the points are measurements.

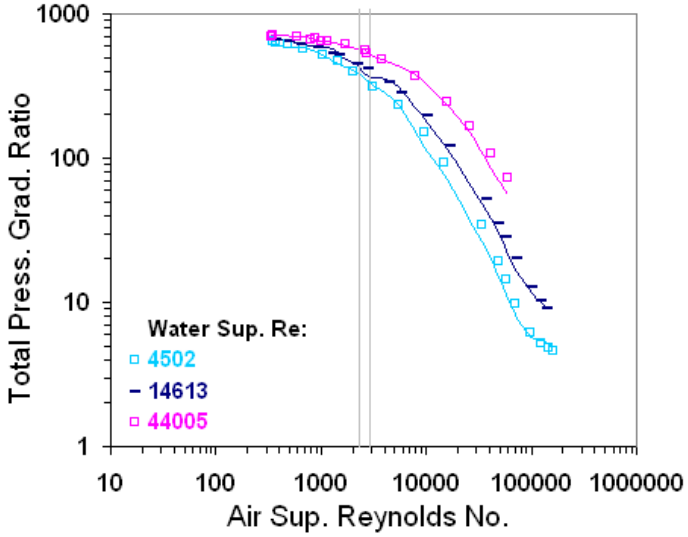

Figure 4.7.4: Validation of our total pressure gradient calculations for experiments in Spedding and Nguyen (1976) at 45 degrees from vertical. Lines are our (coupled-flow) calculations and the points are measurements.

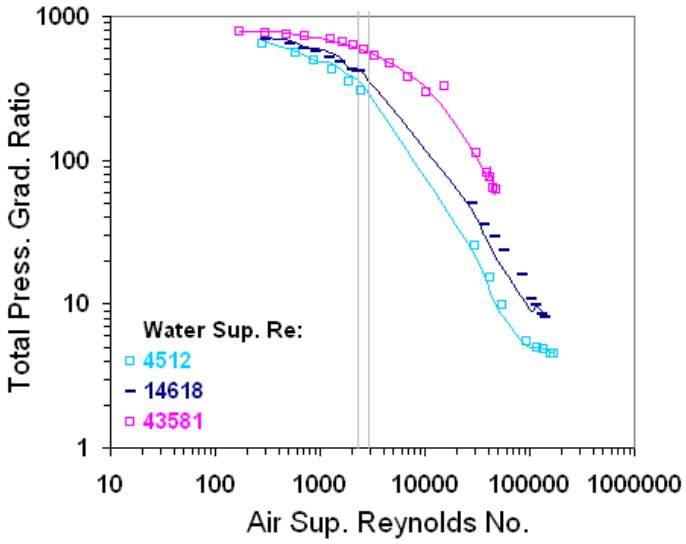

Figure 4.7.5: Validation of our total pressure gradient calculations for experiments in Spedding and Nguyen (1976) at 70 degrees from vertical. Lines are our (coupled-flow) calculations and the points are measurements.

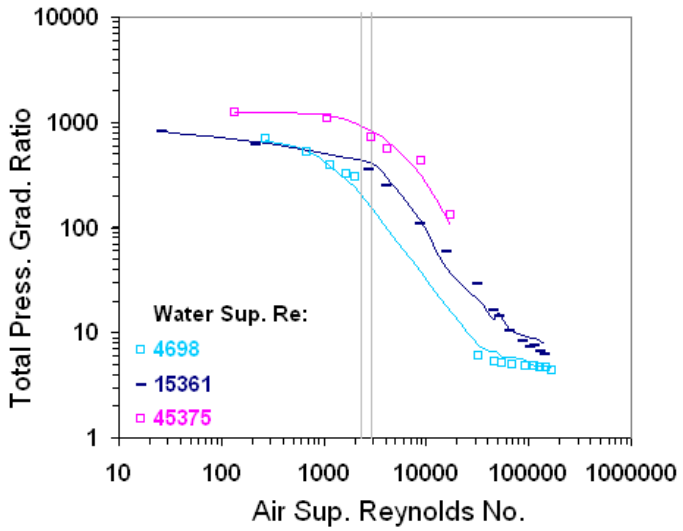

Figure 4.7.6: Validation of our total pressure gradient calculations for experiments in Spedding and Nguyen (1976) at 87 degrees from vertical. Lines are our (coupled-flow) calculations and the points are measurements.

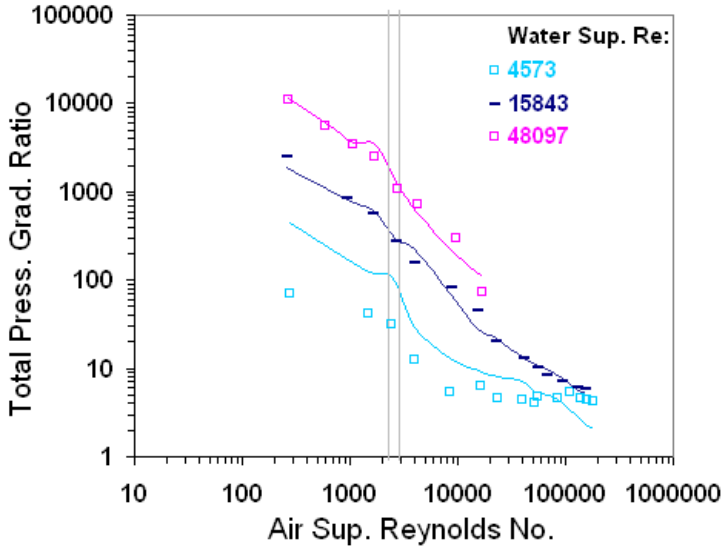

Figure 4.7.7: Validation of our total pressure gradient calculations for experiments in Spedding and Nguyen (1976) at 90 degrees from vertical. Lines are our (coupled-flow) calculations and the points are measurements.

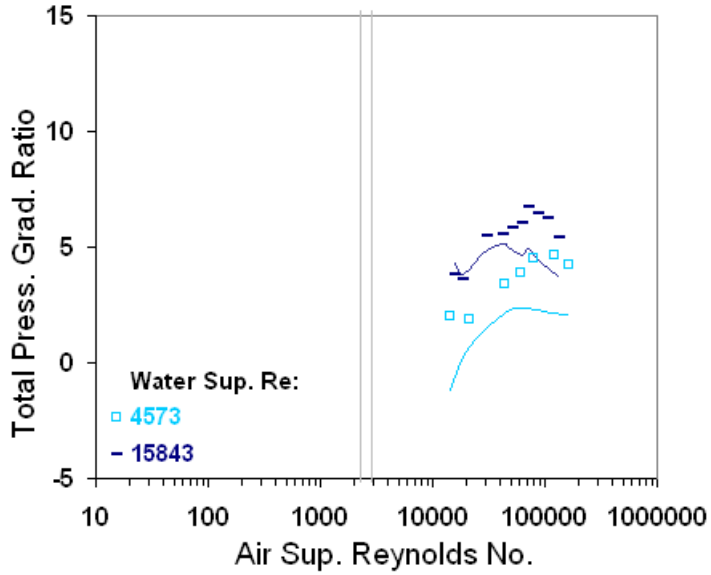

Figure 4.7.8: Validation of our total pressure gradient calculations for experiments in Spedding and Nguyen (1976) at 96 degrees from vertical. Lines are our (decoupled-flow) calculations and the points are measurements.

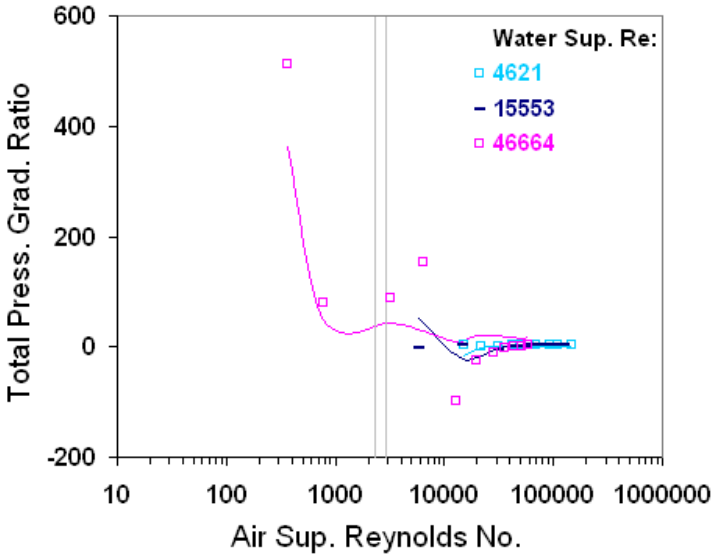

Figure 4.7.9: Validation of our total pressure gradient calculations for experiments in Spedding and Nguyen (1976) at 110 degrees from vertical. Lines are our (decoupled-flow) calculations and the points are measurements.

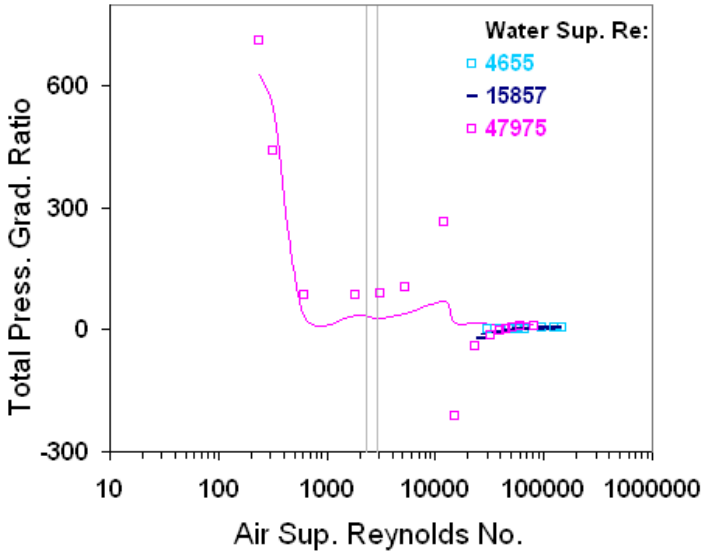

Figure 4.7.10: Validation of our total pressure gradient calculations for experiments in Spedding and Nguyen (1976) at 135 degrees from vertical. Lines are our (decoupled-flow) calculations and the points are measurements.

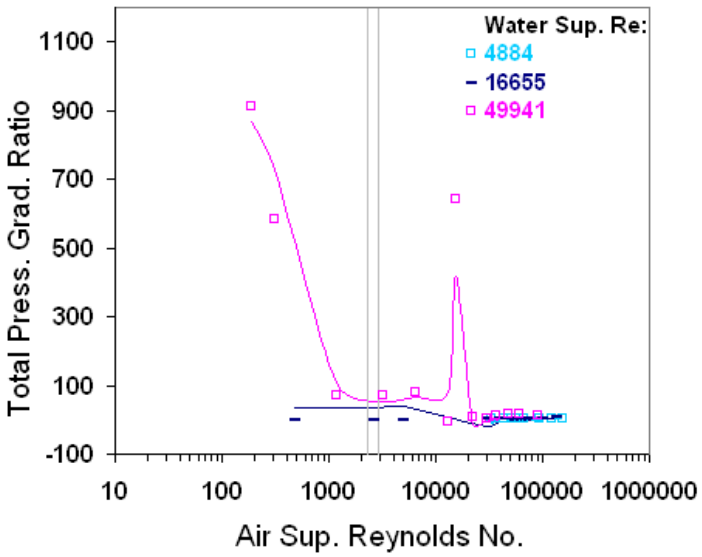

Figure 4.7.11: Validation of our total pressure gradient calculations for experiments in Spedding and Nguyen (1976) at 158 degrees from vertical. Lines are our (decoupled-flow) calculations and the points are measurements.

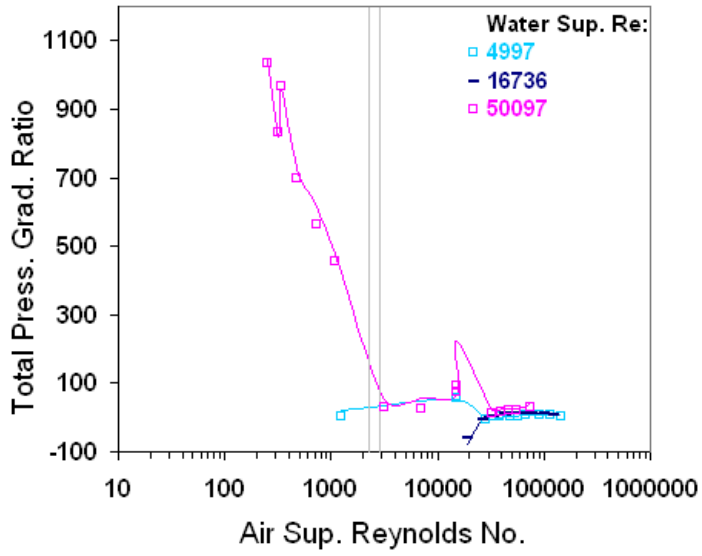

Figure 4.7.12: Validation of our total pressure gradient calculations for experiments in Spedding and Nguyen (1976) at 180 degrees from vertical. Lines are our (coupled-flow) calculations and the points are measurements.

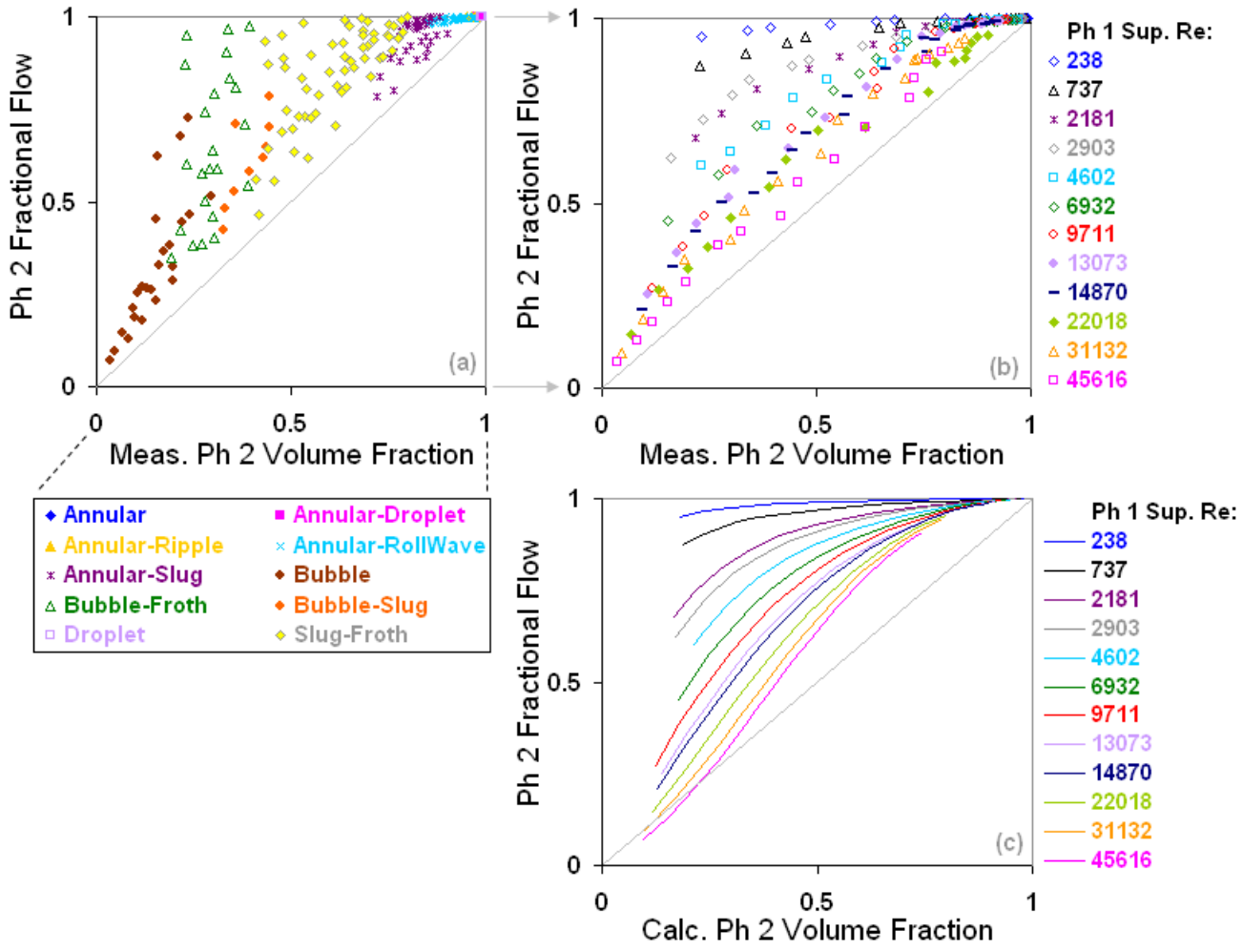

Figure 4.7.13: Prediction of the volume fraction data of the upward vertical flow dataset of Spedding and Nguyen (1976) with the WOLGHA model. Lines are our predictions and the points are measurements.

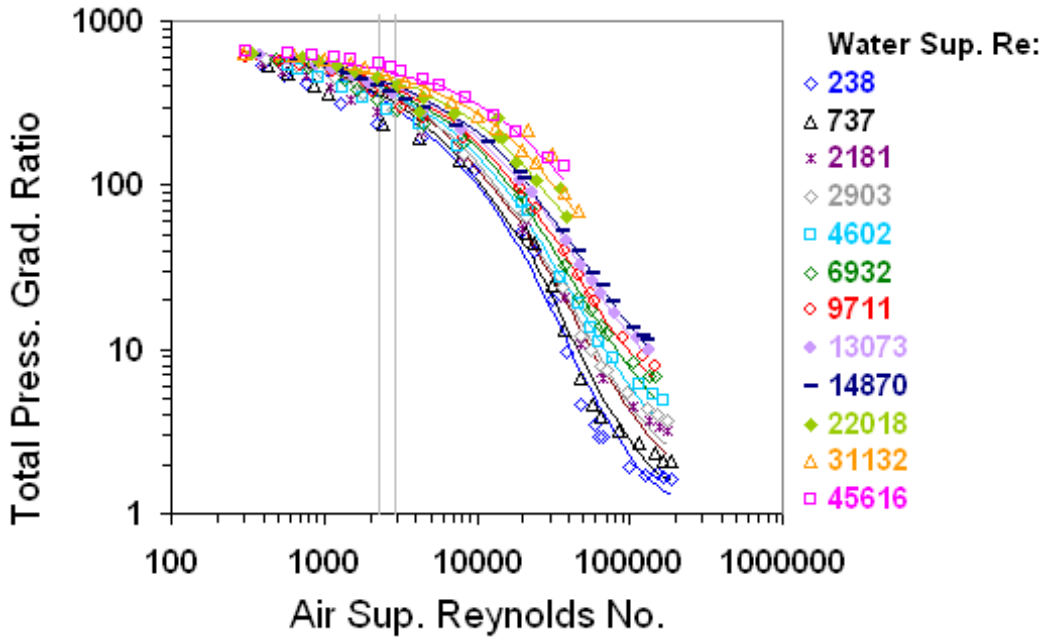

Figure 4.7.14: Prediction of the upward vertical flow dataset of Spedding and Nguyen (1976) with the WOLGHA model. Lines are our predictions and the points are measurements.

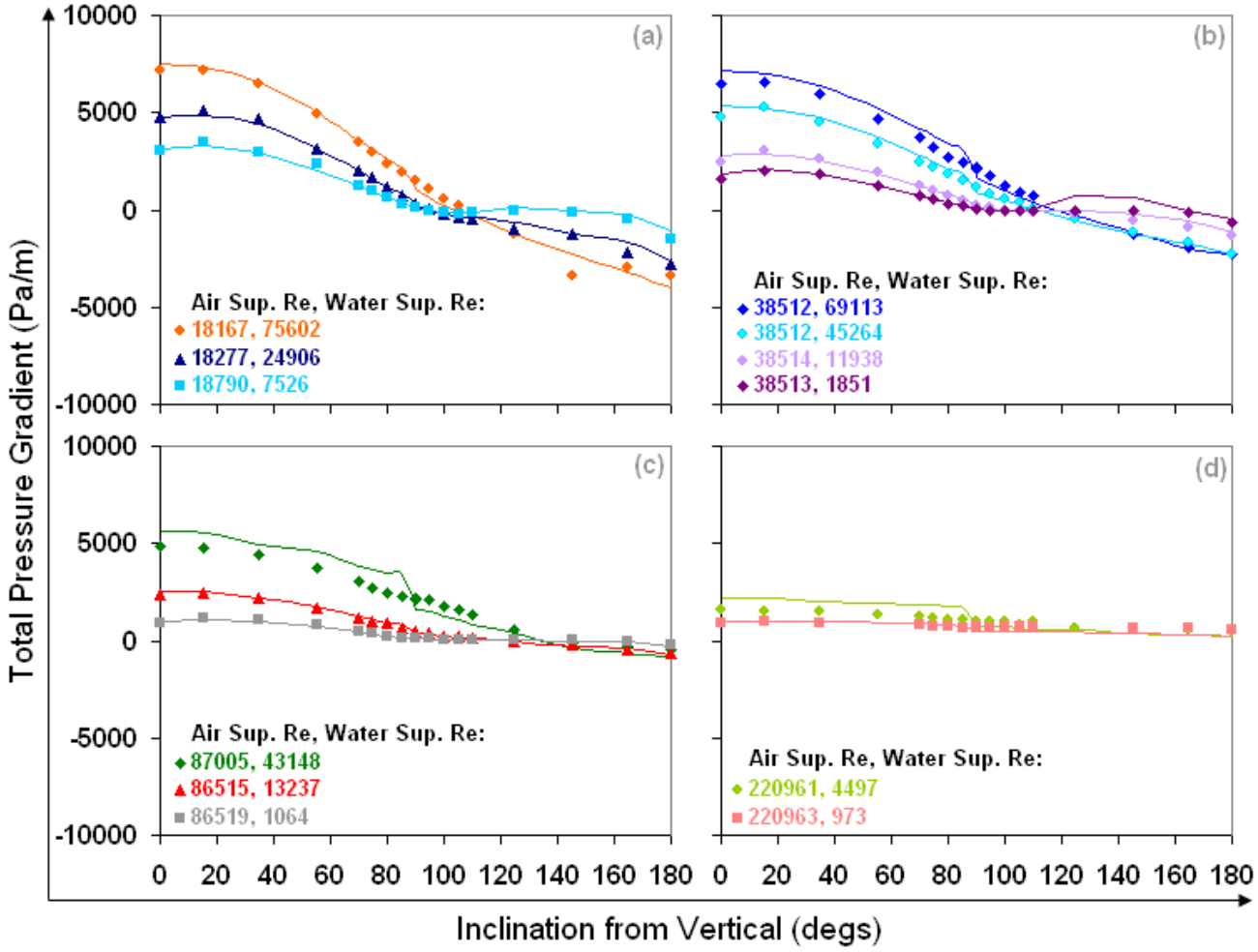

Figure 4.7.15: Demonstrating the validity of our total pressure gradient calculations with the classic 1.5-inch experiments of Beggs (1972). Lines are our calculations and the points are measurements.

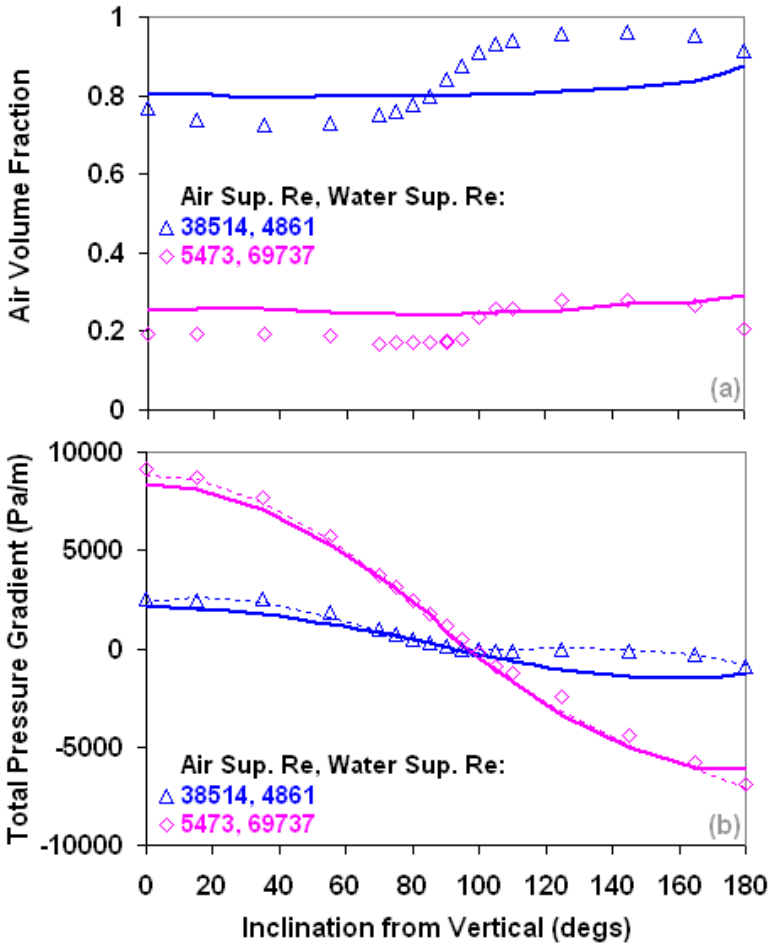

Figure 4.7.16: Validation and prediction of one high rate and low water rate dataset from the 1.5-inch experiments of Beggs (1972). Lines are our calculations and the points are measurements.

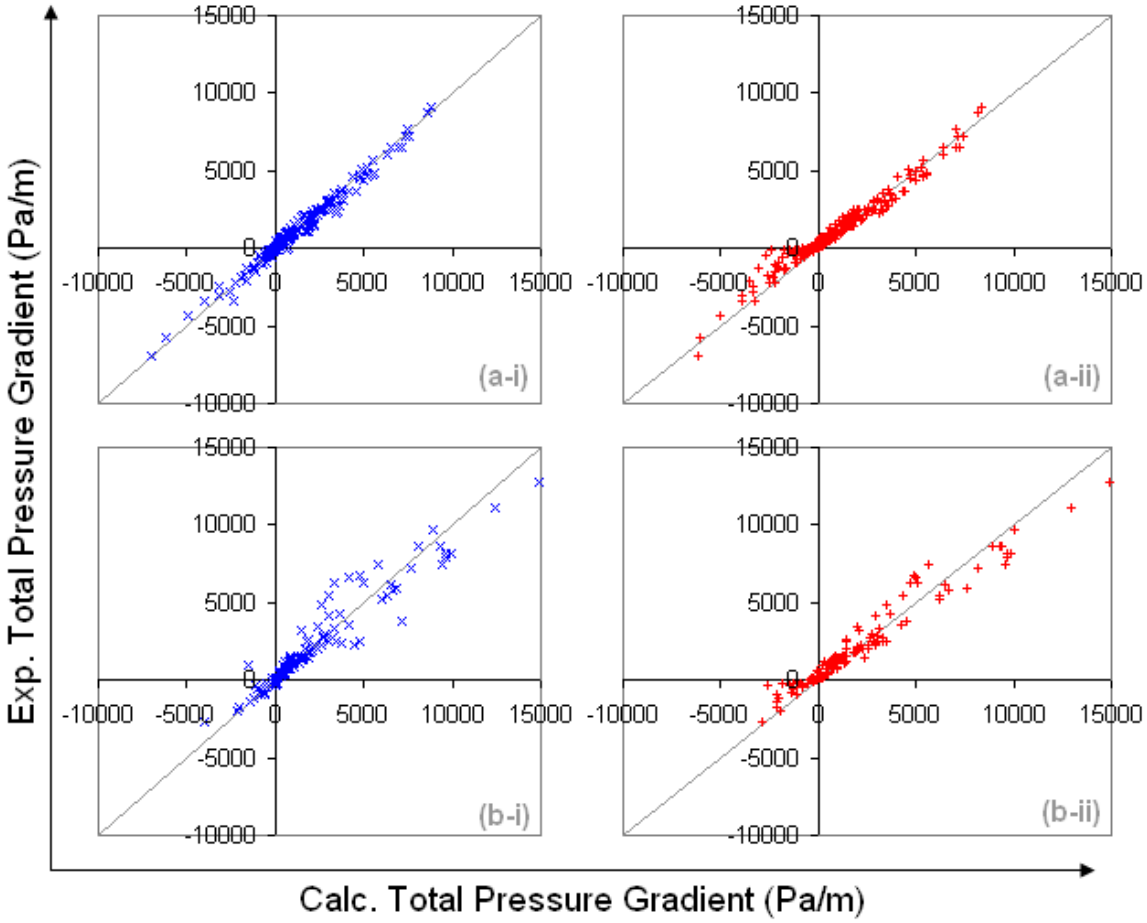

Figure 4.7.17: Validation (in blue) and prediction (in red, with the WOLGHA model) of all of the experiments of Beggs (1972).

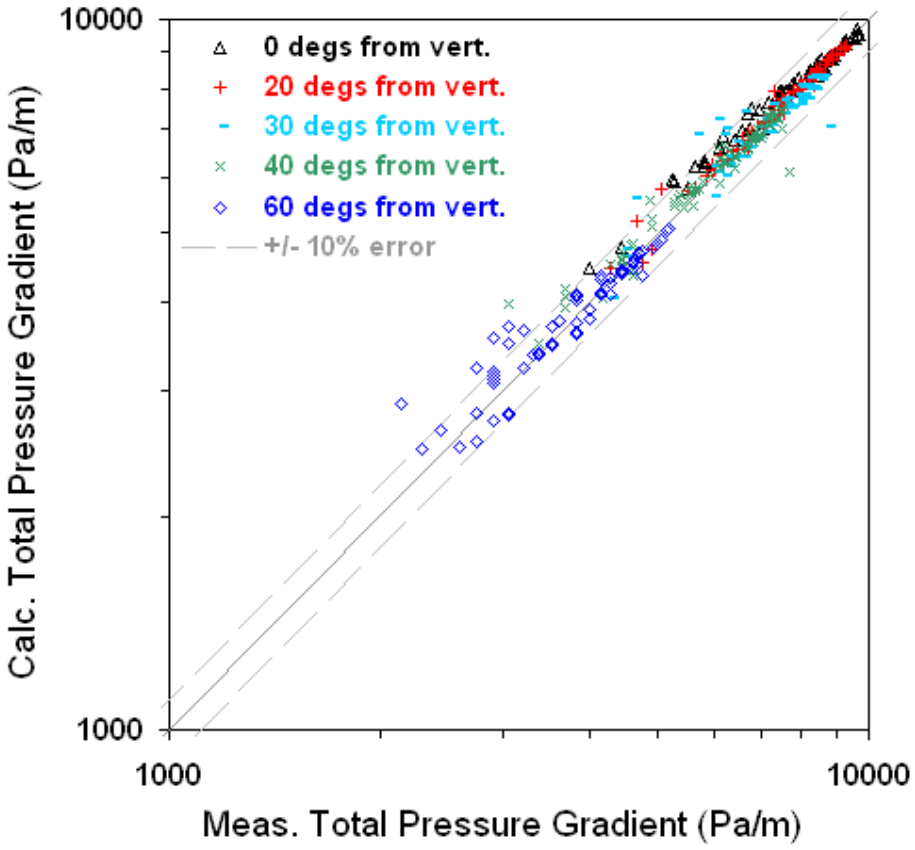

Figure 4.7.18: Prediction of all the up-inclined slug flow data of Griffith et al. (1973) with the NICKLIN model.

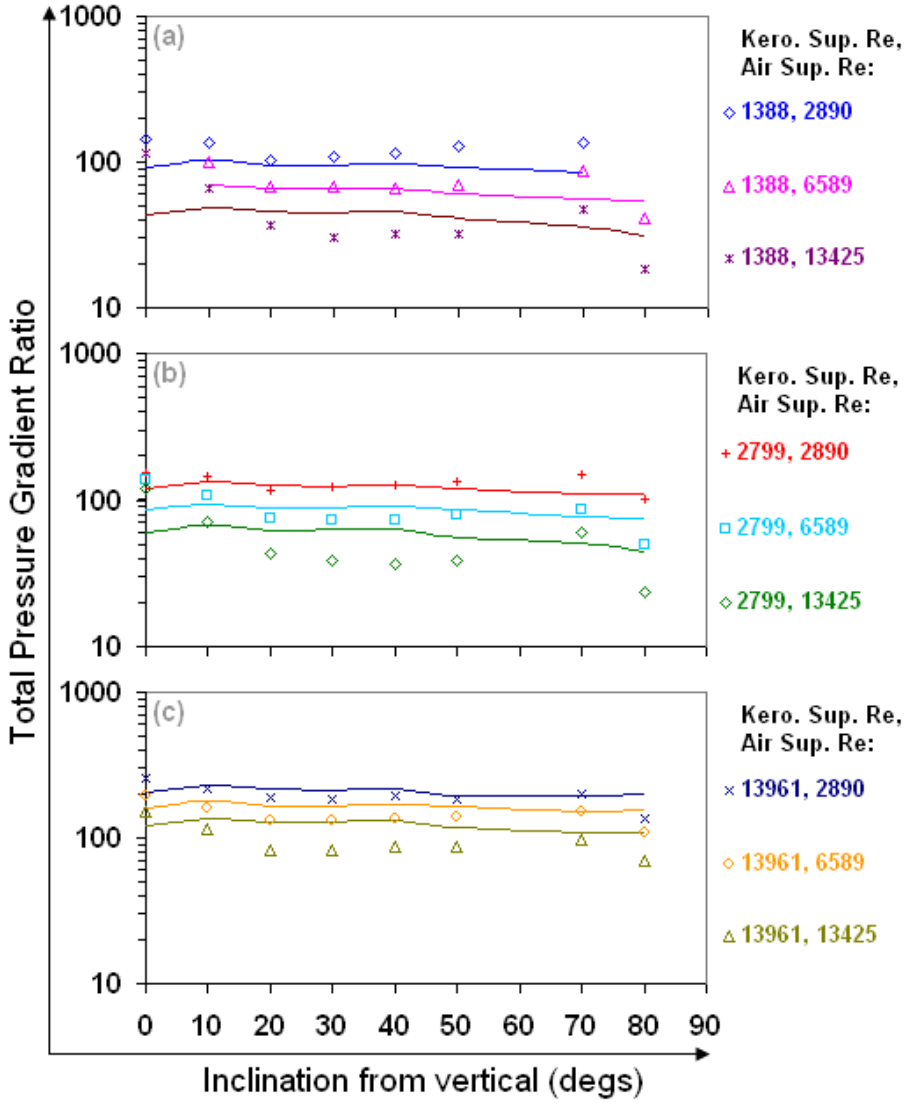

Figure 4.7.19: Prediction of the up-inclined slug flow dataset of Felizola and Shoham (1995) with the ANSLIP analytical model. Lines are our predictions and the points are measurements.

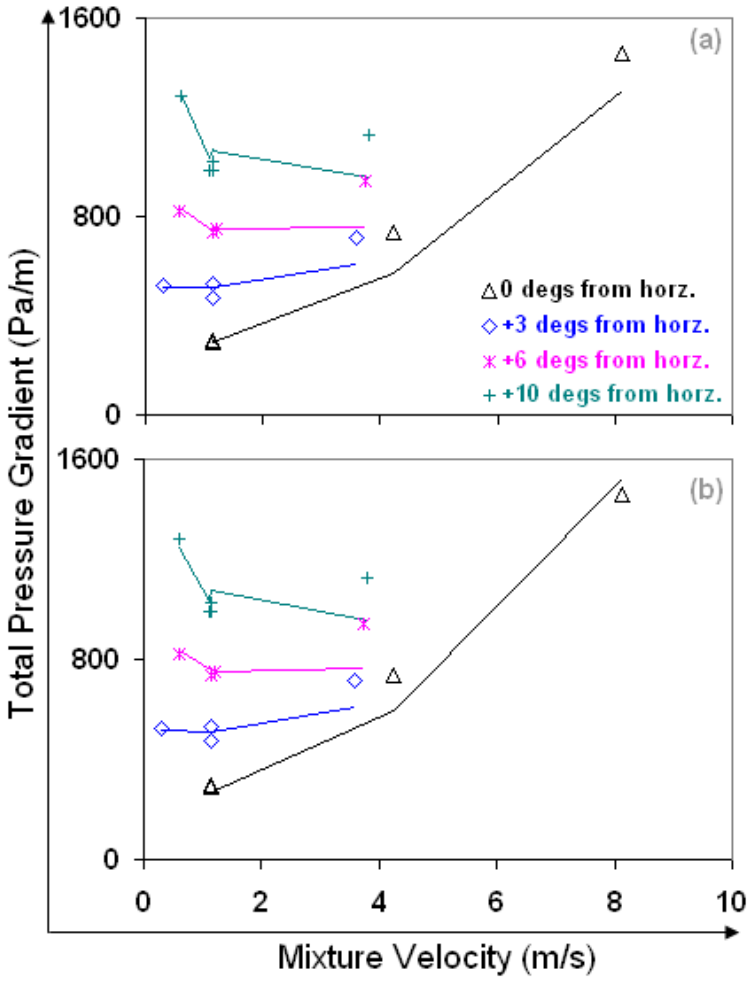

Figure 4.7.20: Validation (in a) and prediction (in b, with the BUTTERWORTH model) of the slightly up-inclined slug flow experiments of Mattar (1973). Lines are our calculations and the points are measurements.

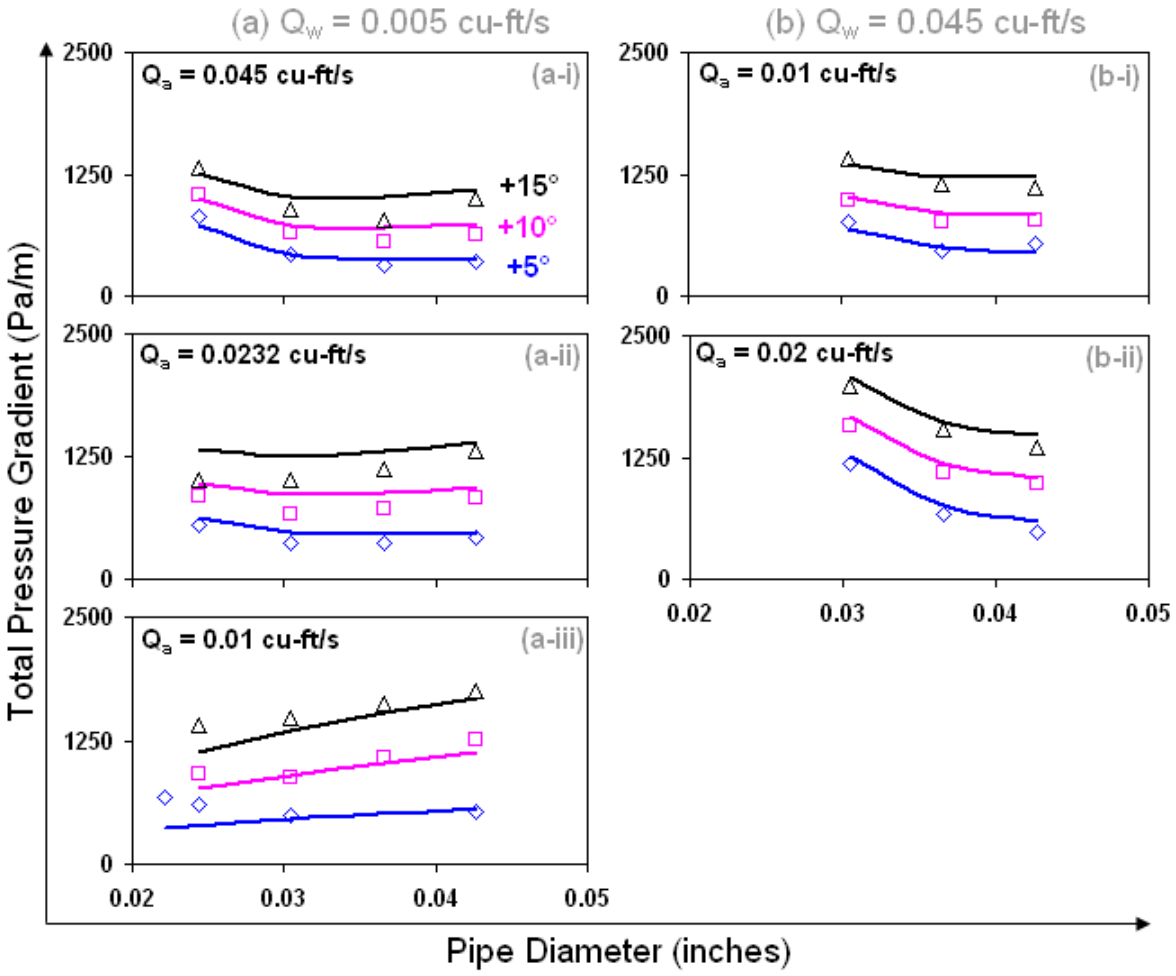

Figure 4.7.21: Prediction of the up-inclined slug flow dataset of Singh and Griffith (1970) with the NICKLIN model. Lines are our predictions and the points are measurements.

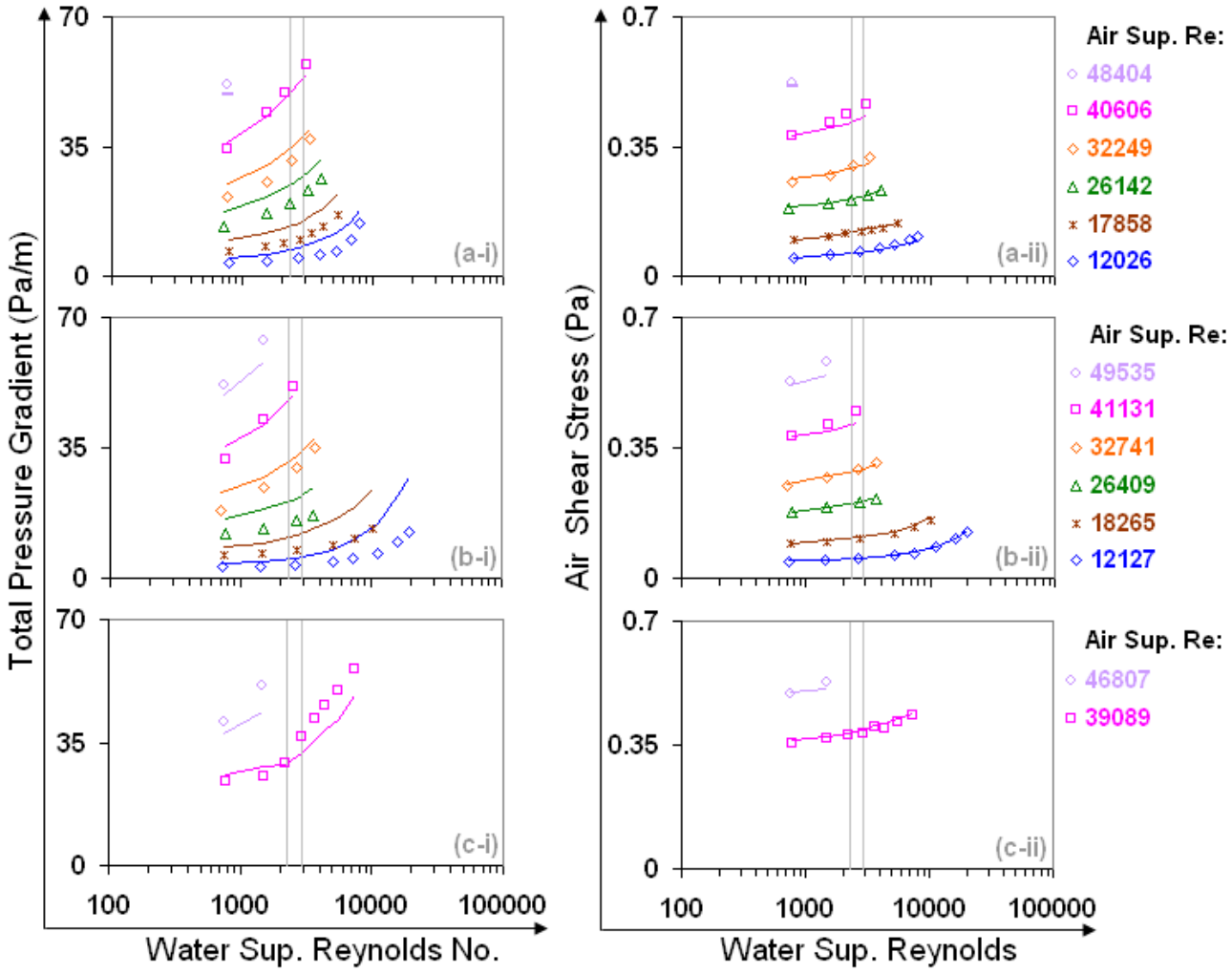

Figure 4.7.22: Demonstrating the validity of our decoupled-flow total pressure gradient and wall (total) shear stress calculations with the slightly down-inclined stratified flow experiments of Espedal (1998). Lines are our calculations and the points are measurements.

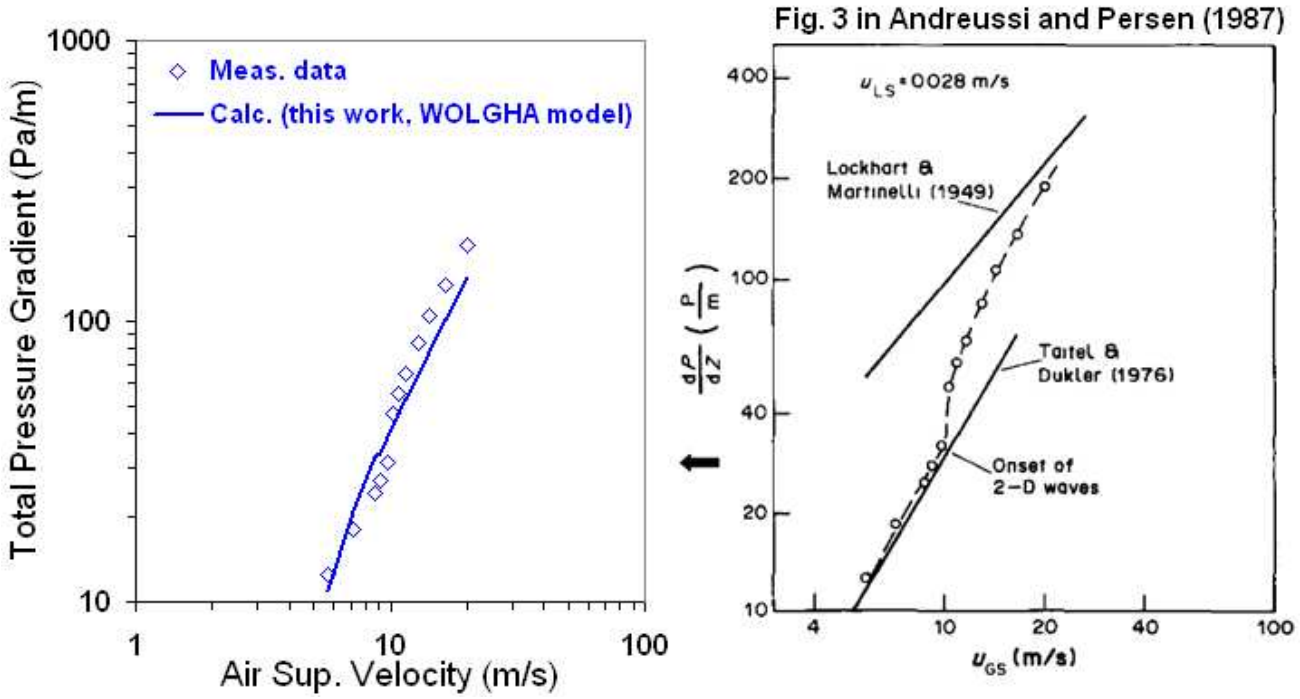

Figure 4.7.23: Prediction of the slightly down-inclined stratified flow dataset of Andreussi and Persen (1987) with the WOLGHA model. Lines are our predictions and the points are measurements.

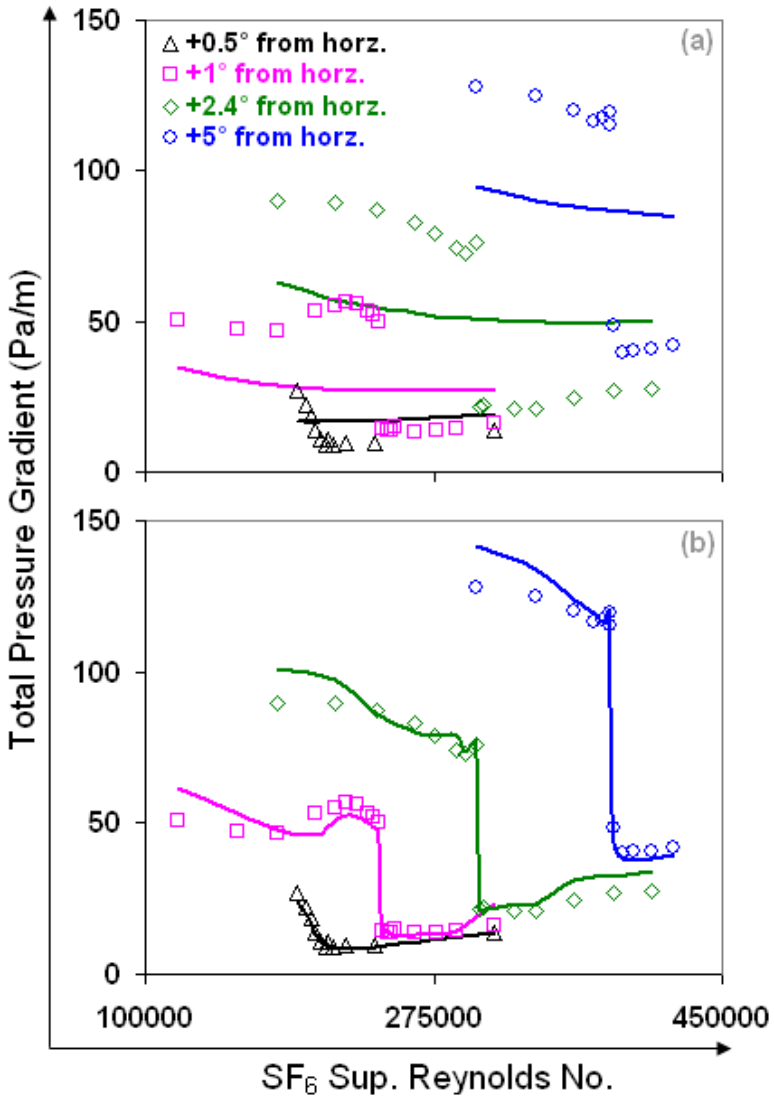

Figure 4.7.24: Demonstrating the validity of our total pressure gradient calculations with the slightly up-inclined wavy-ripply flow experiments of Langsholt and Holm (2007). In a, the lines are our calculations with the WOLGHA model and in b, the lines are our calculations with the measured gas volume fractions. The points are measurements.

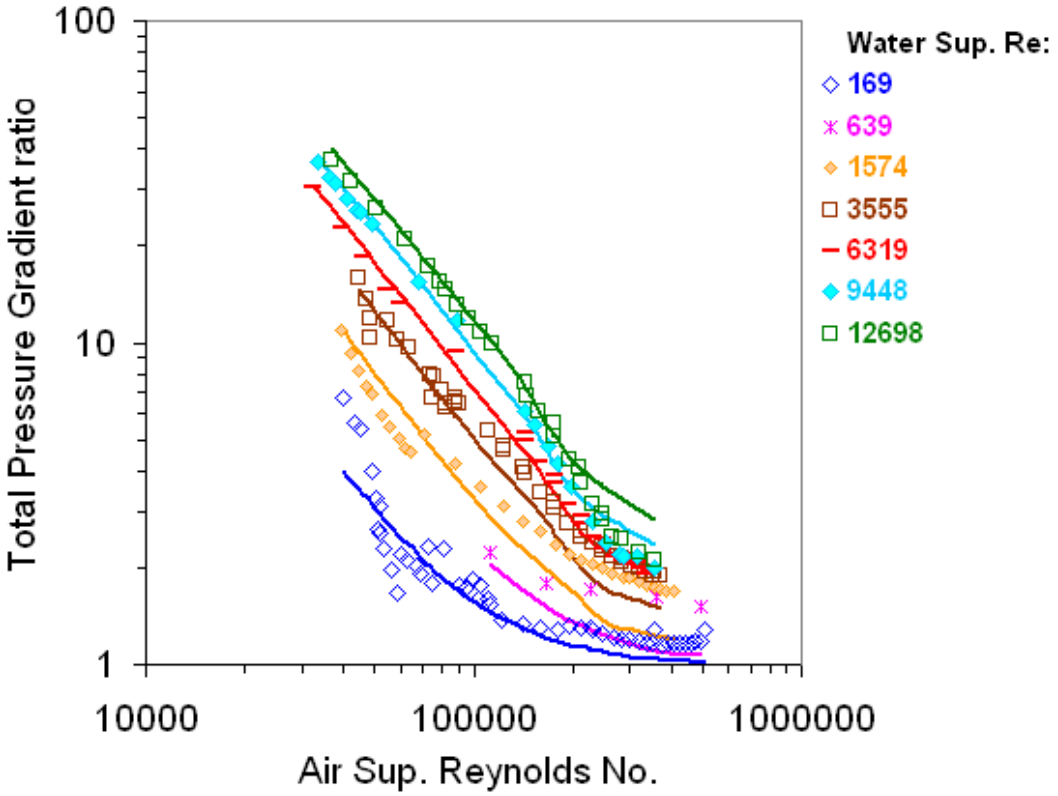

Figure 4.8.1: Prediction of the Owen (1986) dataset at 240 kPa with the ANSLIP model. Lines are our predictions and the points are measurements.

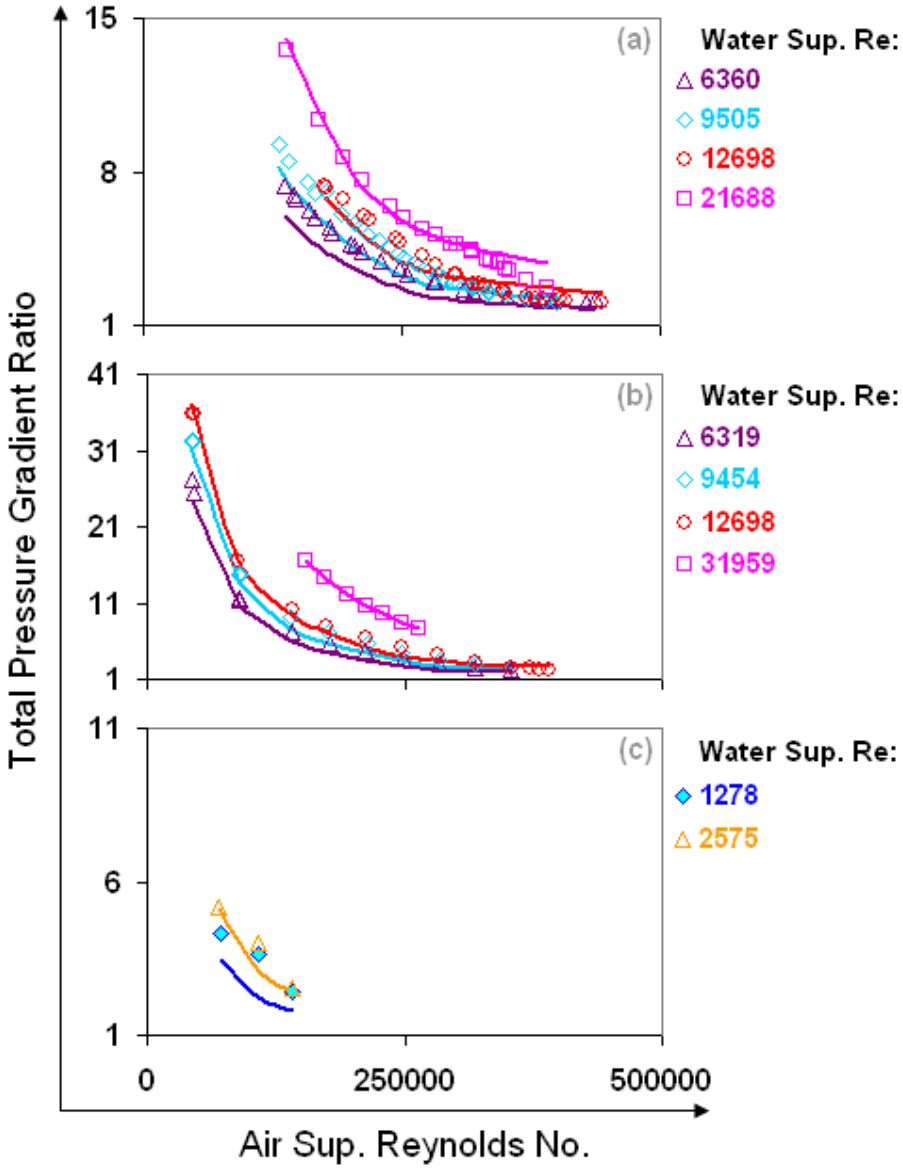

Figure 4.8.2: Prediction of Owen (1986) datasets with the ANSLIP model. Lines are our predictions and the points are measurements.

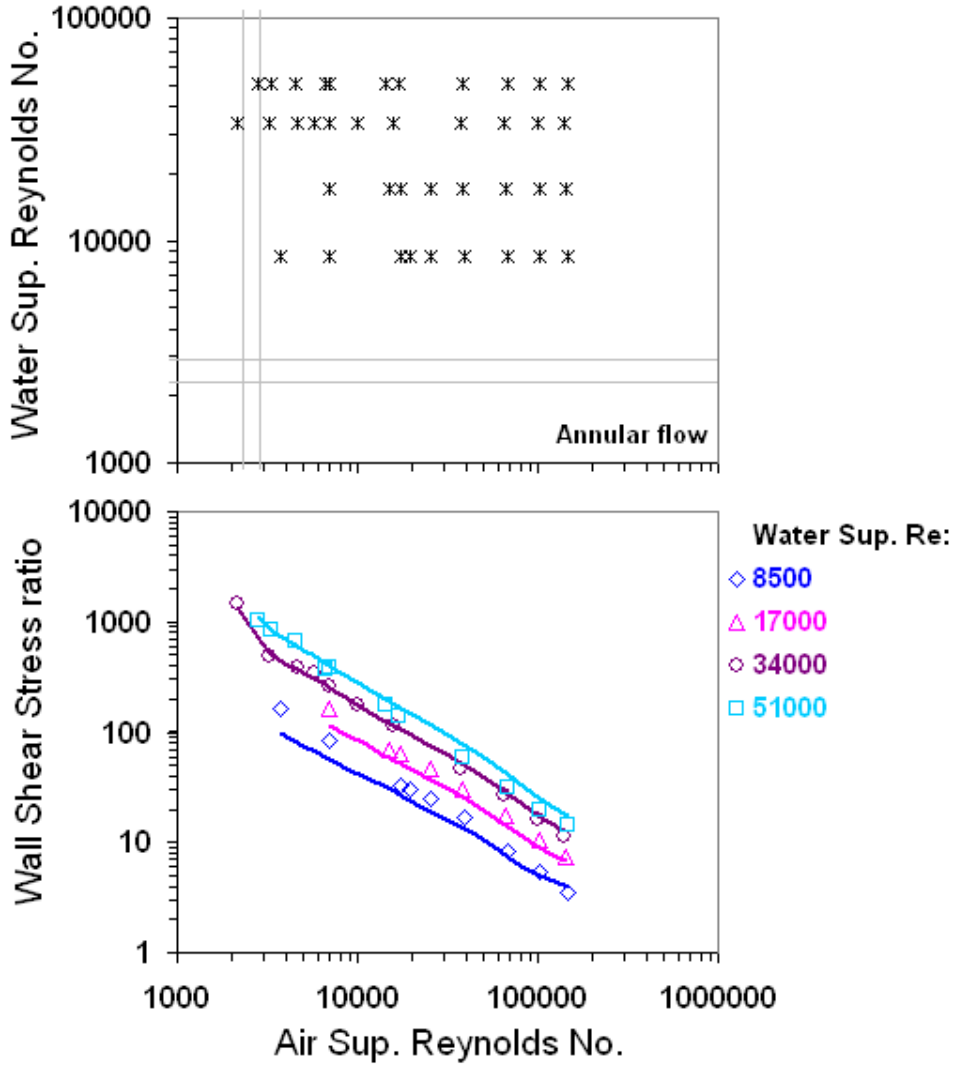

Figure 4.8.3: Prediction of the Pecherkin (1990) dataset with the ANSLIP model. Lines are our predictions and the points are measurements.

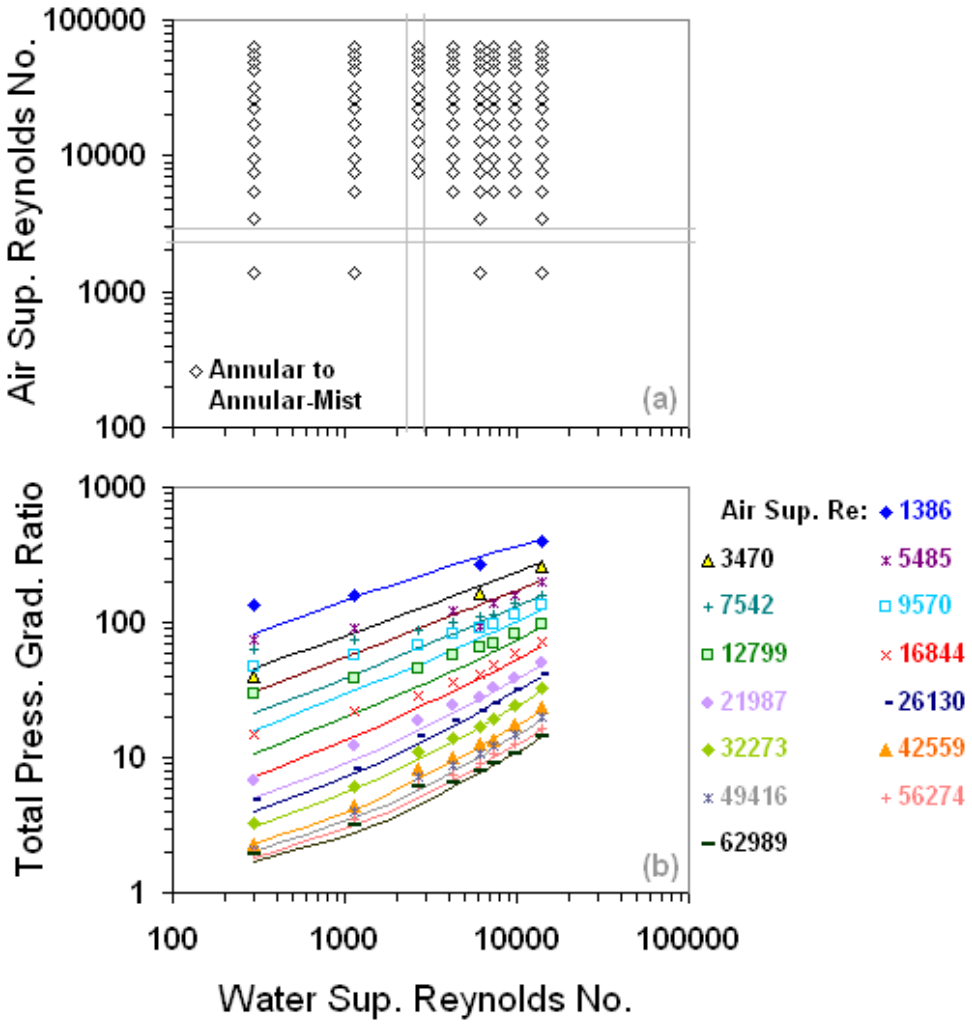

Figure 4.8.4: Prediction of the Turner (1966) 1-inch dataset with the ANSLIP model. Lines are our predictions and the points are measurements.

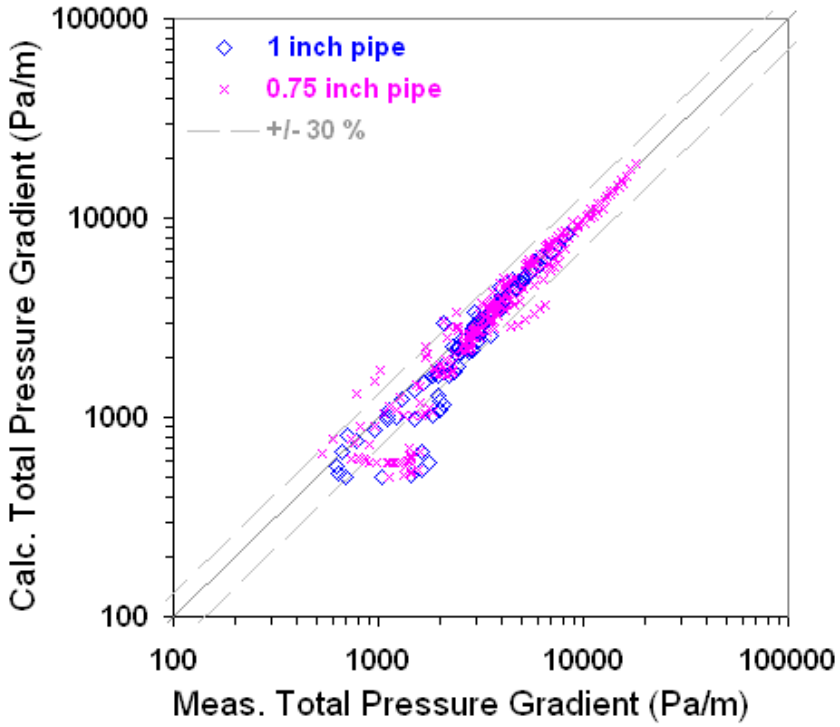

Figure 4.8.5: Prediction of the all of the Turner (1966) datasets with the ANSLIP model.

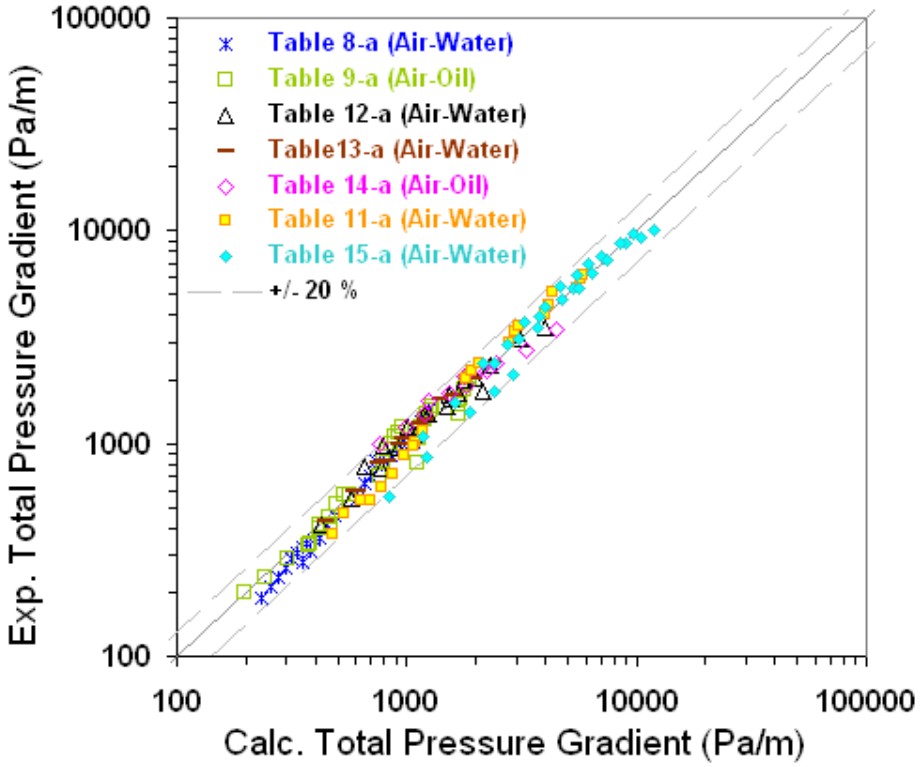

Figure 4.8.6: Prediction of the Asali (1984) datasets with the ANSLIP model for air-water flows and the CISE model for air-oil flows.

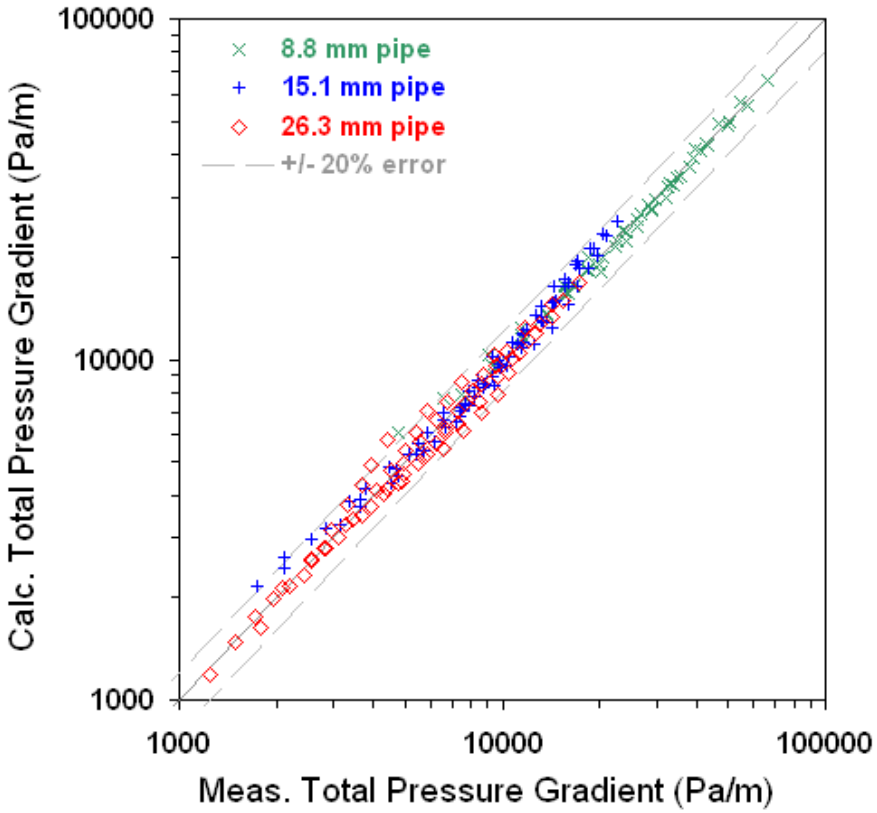

Figure 4.8.7: Prediction of the Schubring (2009) datasets with the ANSLIP model.

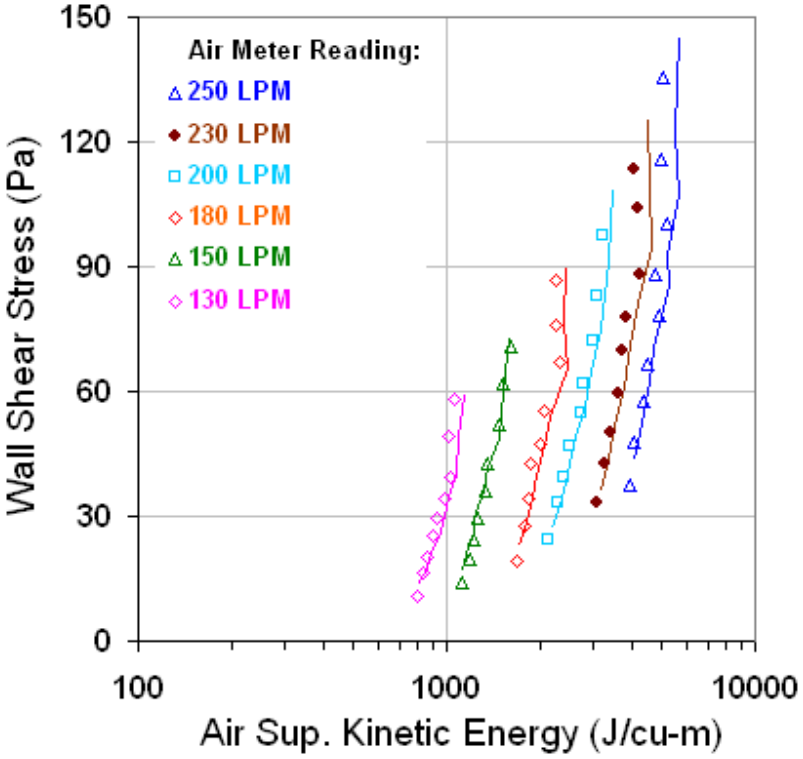

Figure 4.8.8: Prediction of the annular flow wall shear stress measurements in Fig. 4 of Schubring and Shedd with the ANSLIP model. Lines are our predictions and the points are measurements.

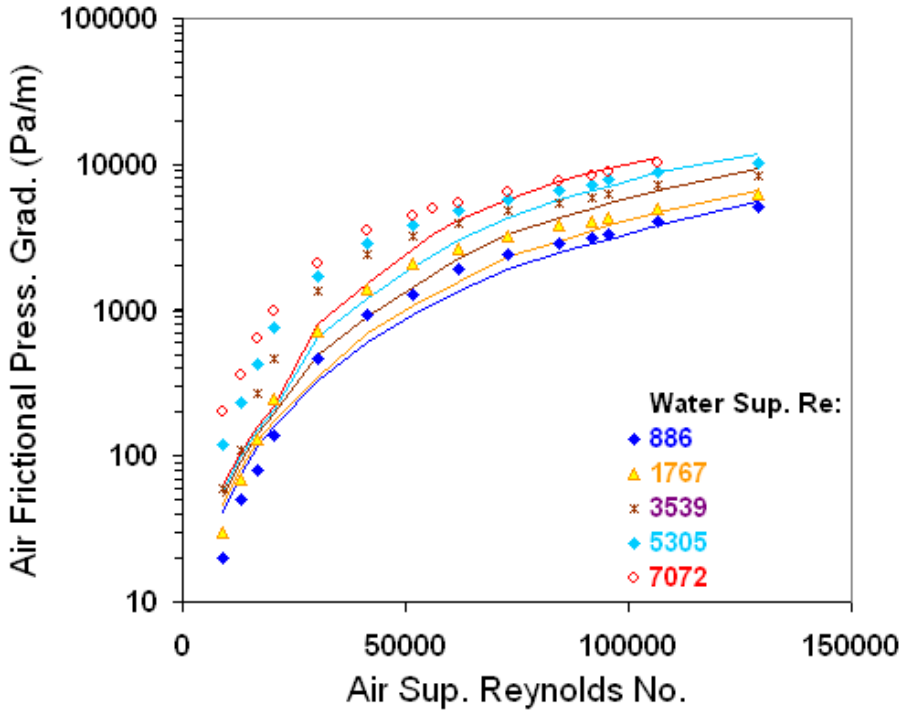

Figure 4.8.9: Prediction of the Andreussi and Zanelli (1978) dataset with the ANSLIP model. Lines are our predictions and the points are measurements.

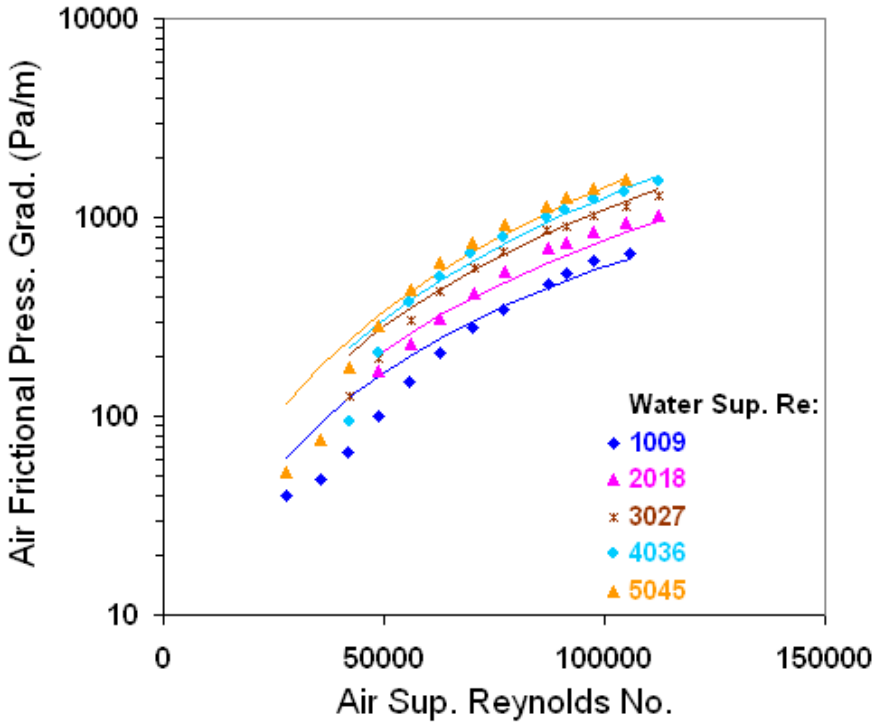

Figure 4.8.10: Prediction of the Webb (1970) dataset with the ANSLIP model. Lines are our predictions and the points are measurements.

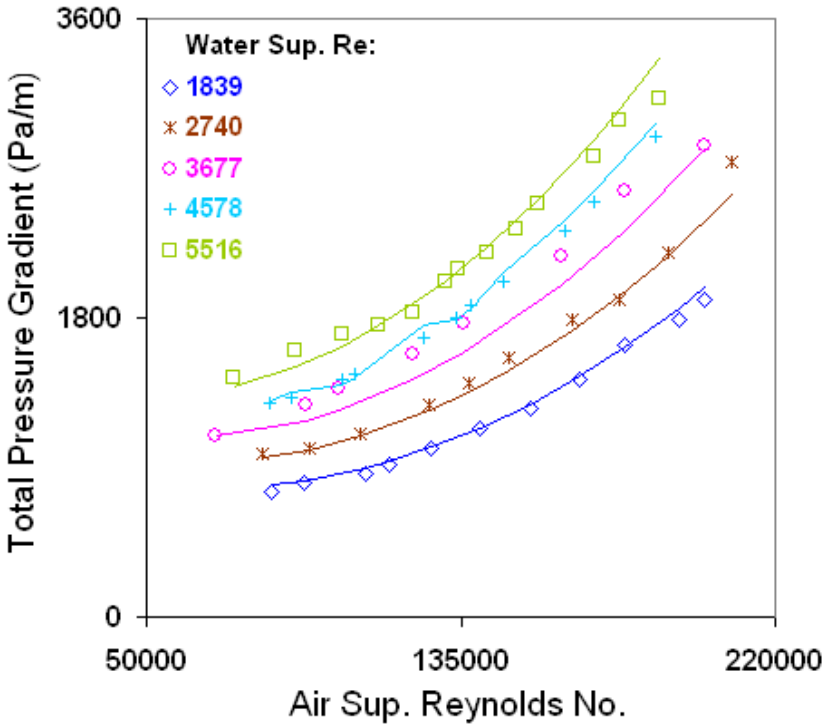

Figure 4.8.11: Prediction of the Hossfield and Bharathan (1982) annular flow dataset in a 5.1 cm pipe with the CISE model. Lines are our predictions and the points are measurements.

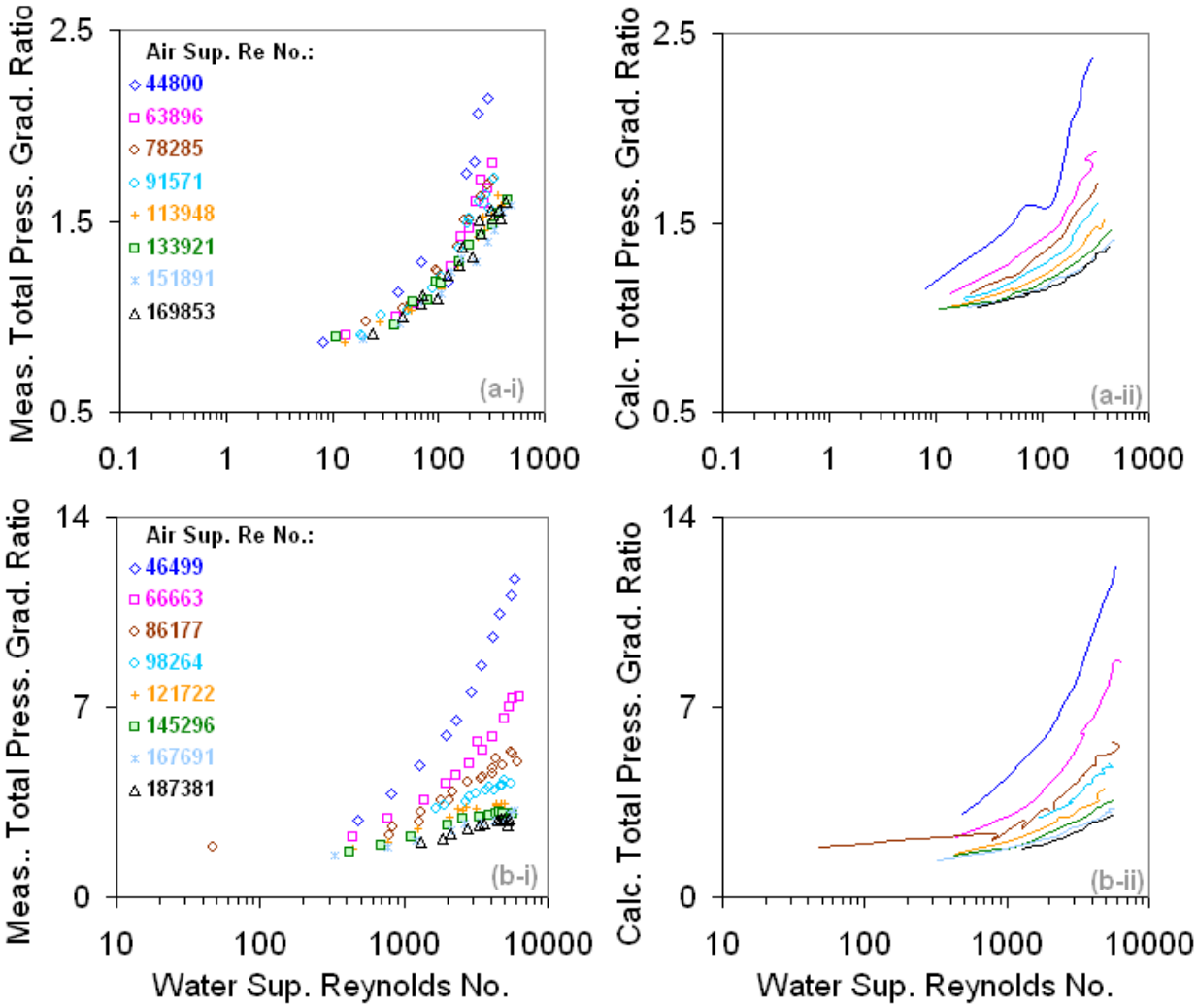

Figure 4.8.12: Prediction of the Bennet and Thornton (1978) Unit-C-PVC annular flow datasets with the BUTTERWORTH model. Lines are our predictions and the points are measurements.

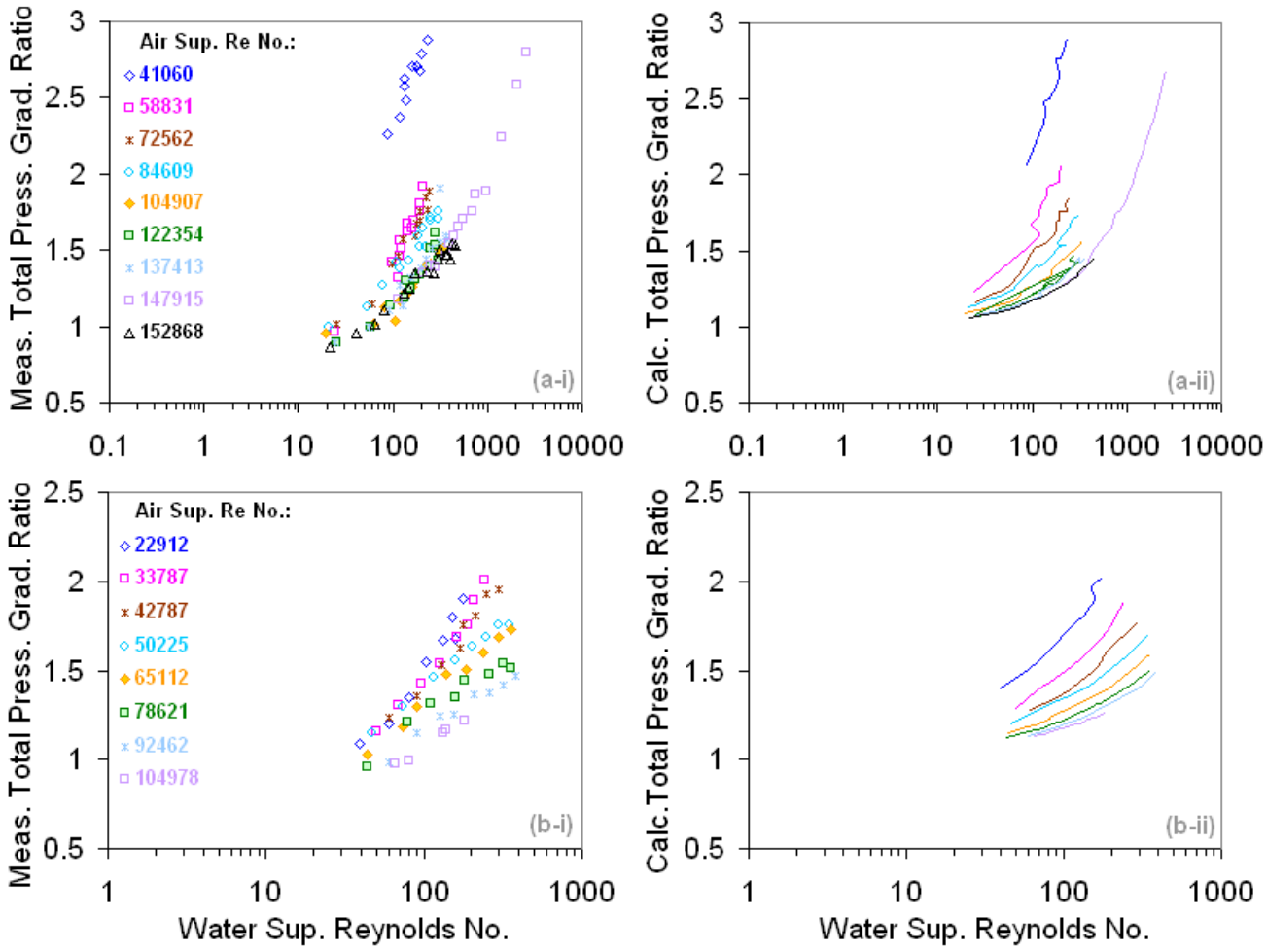

Figure 4.8.13: Prediction of the Bennet and Thornton (1978) Unit-B-Glass and Unit-A-Annulus annular flow datasets with the BUTTERWORTH model. Lines are our predictions and the points are measurements.

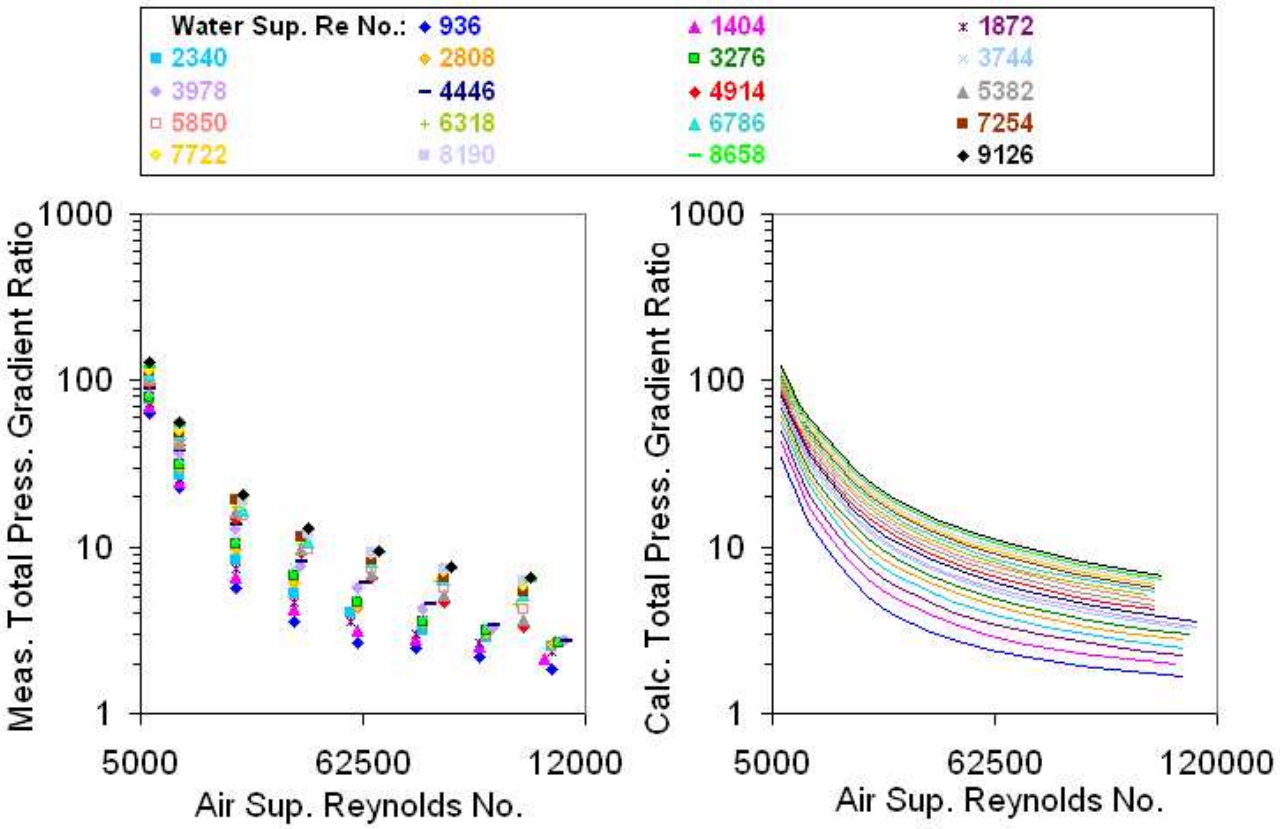

Figure 4.8.14: Prediction of the Ashwood (2010) vertical annular flow datasets with the ANSLIP model. Lines are our predictions and the points are measurements.

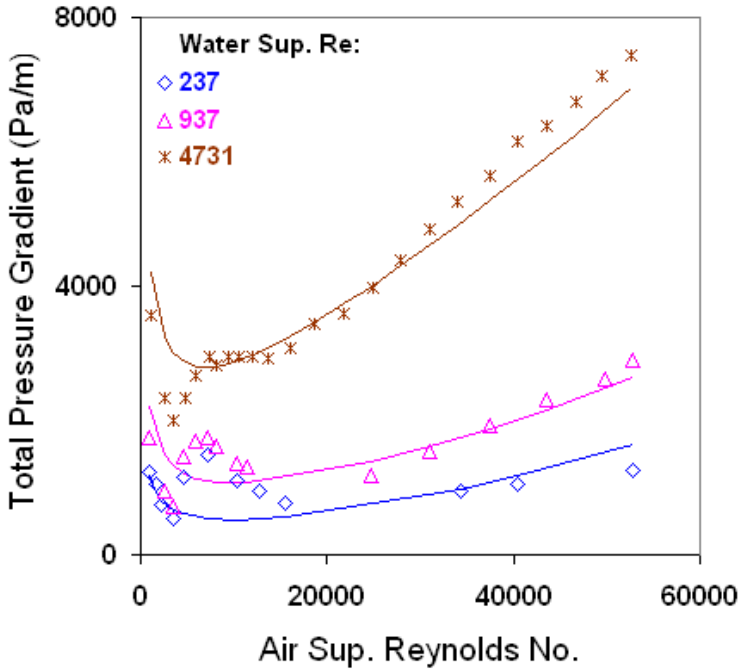

Figure 4.8.15: Prediction of the Wallis (1966) churn-annular flow datasets with the ANSLIP model. Lines are our predictions and the points are measurements.

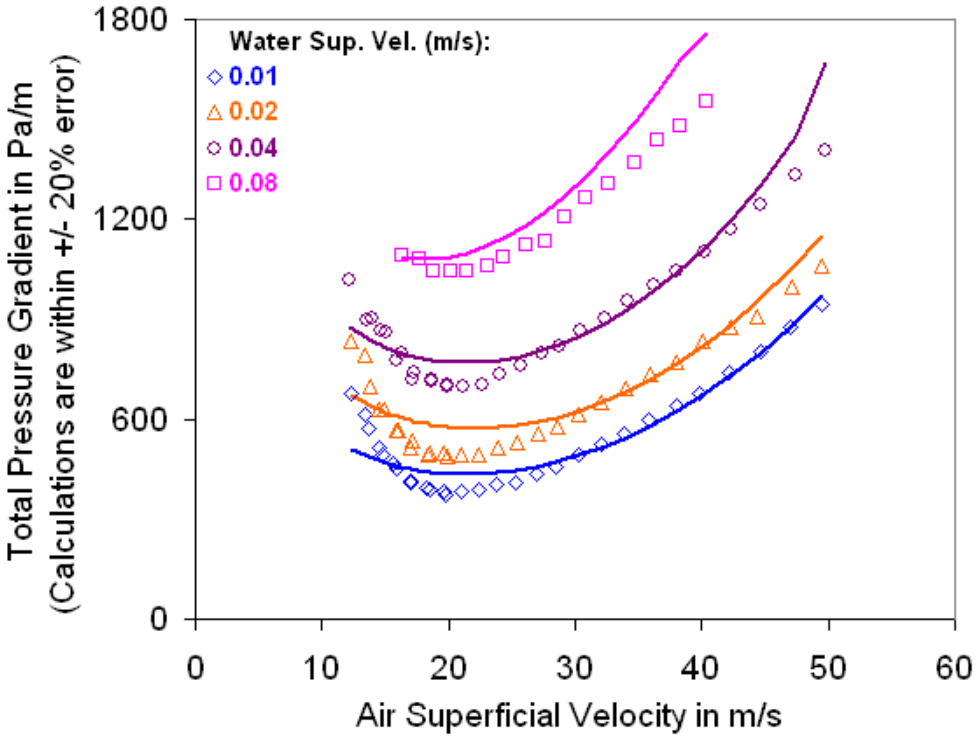

Figure 4.8.16: Prediction of the van't Westende et al. (2007) churn-annular to annular flow datasets with the CISE model. Lines are our predictions and the points are measurements.

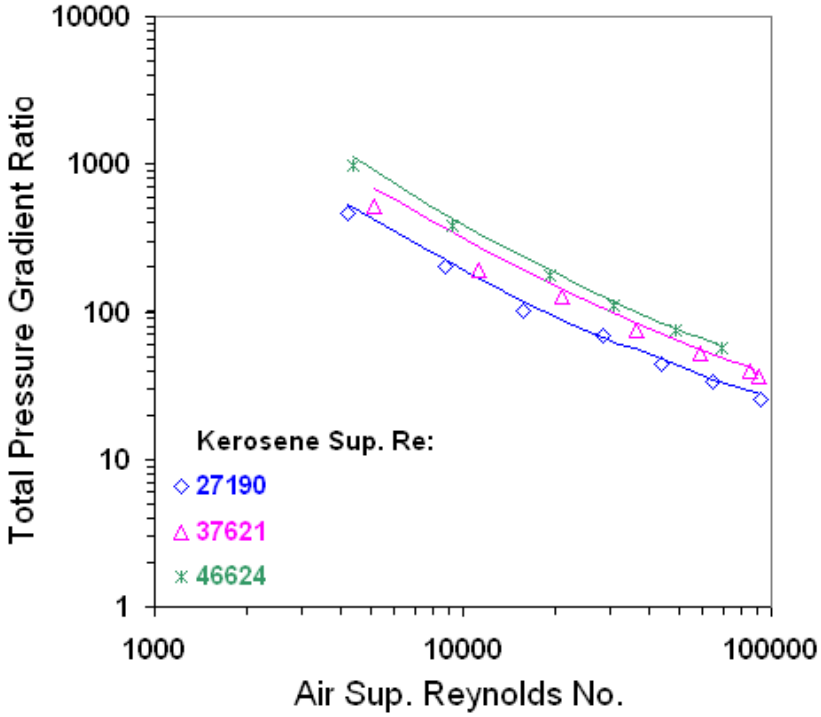

Figure 4.8.17: Prediction of the Yang (1996) horizontal slug flow datasets with the BUTTERWORTH model. Lines are our predictions and the points are measurements.

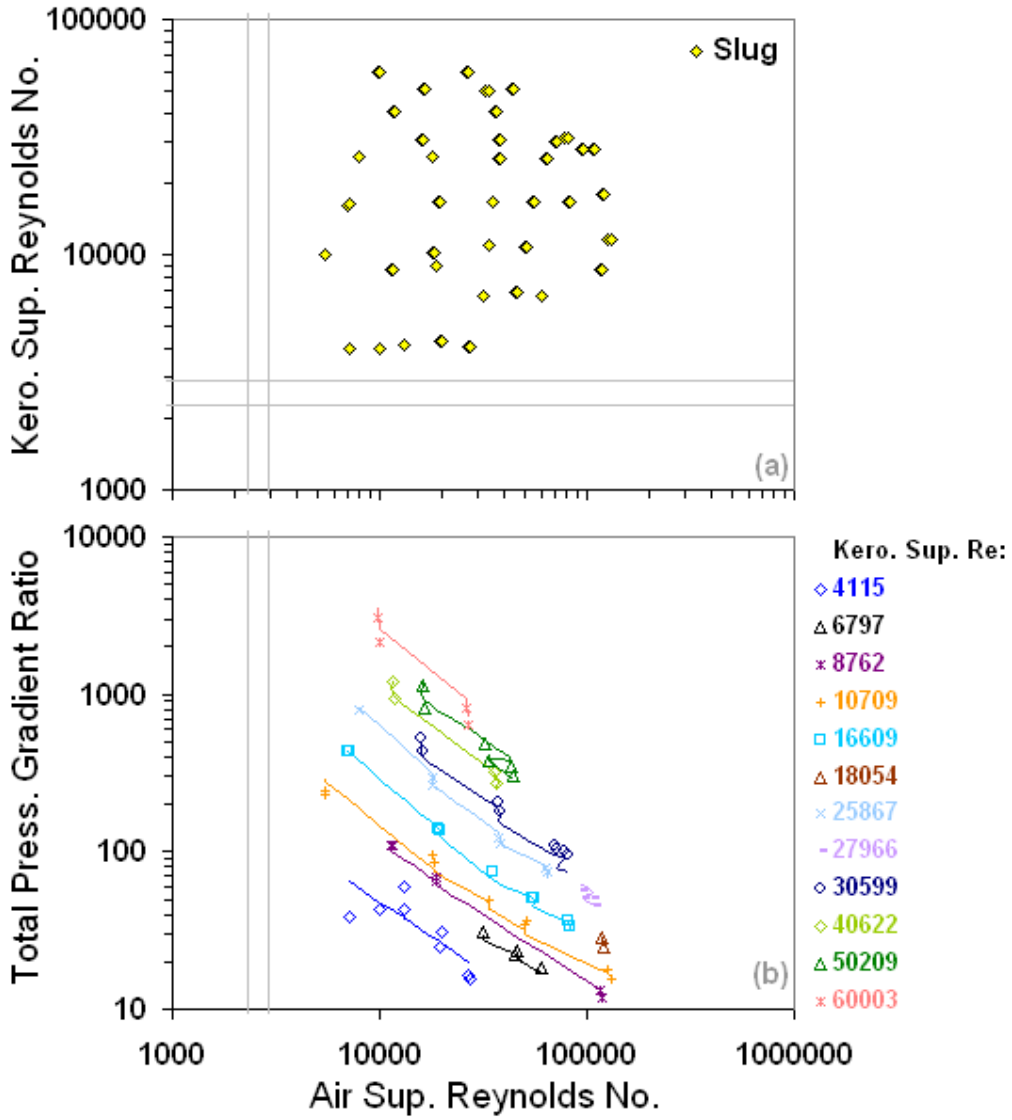

Figure 4.8.18: Prediction of the Marcano (1996) horizontal slug flow datasets with the BUTTERWORTH model. Lines are our predictions and the points are measurements.

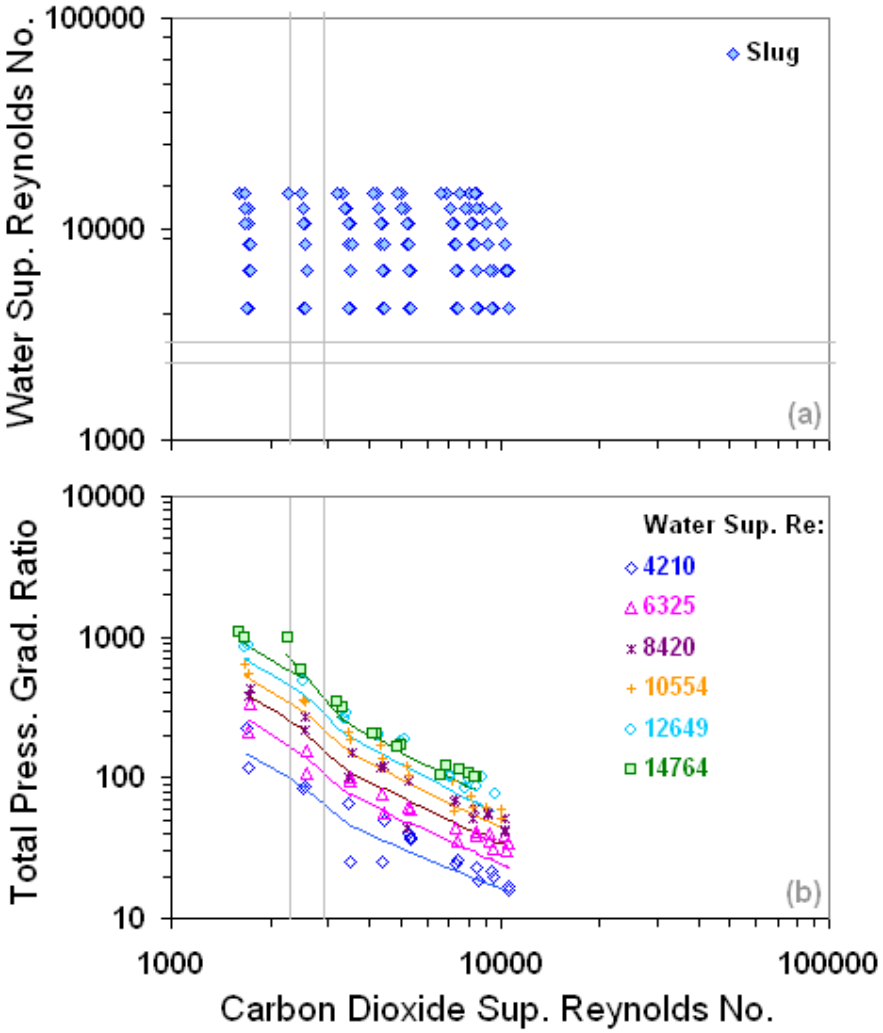

Figure 4.8.19: Prediction of the Gregory and Scott (1968) horizontal slug flow datasets with the WALLIS model. Lines are our predictions and the points are measurements.

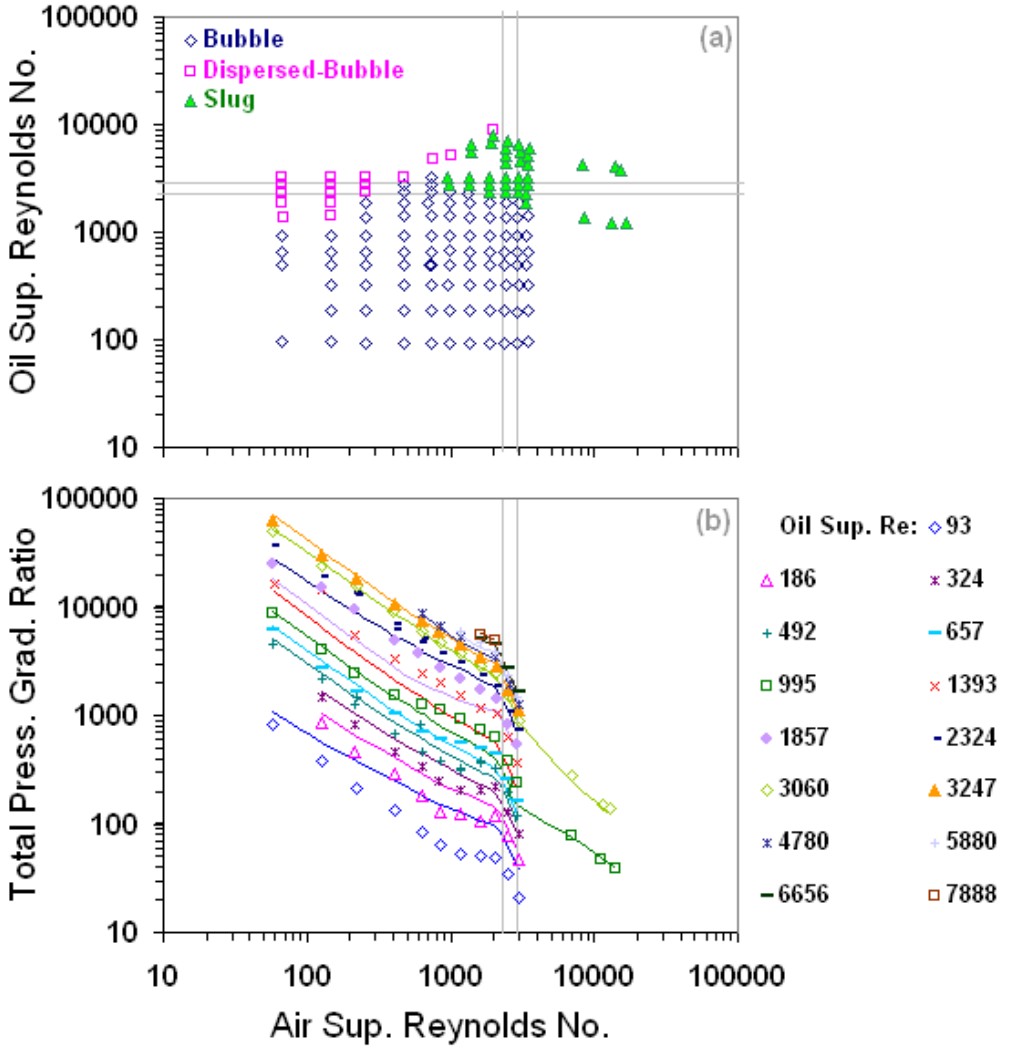

Figure 4.8.20: Prediction of the Aziz et al. (1974) horizontal bubbly flow datasets with the BUTTERWORTH model. Lines are our predictions and the points are measurements.

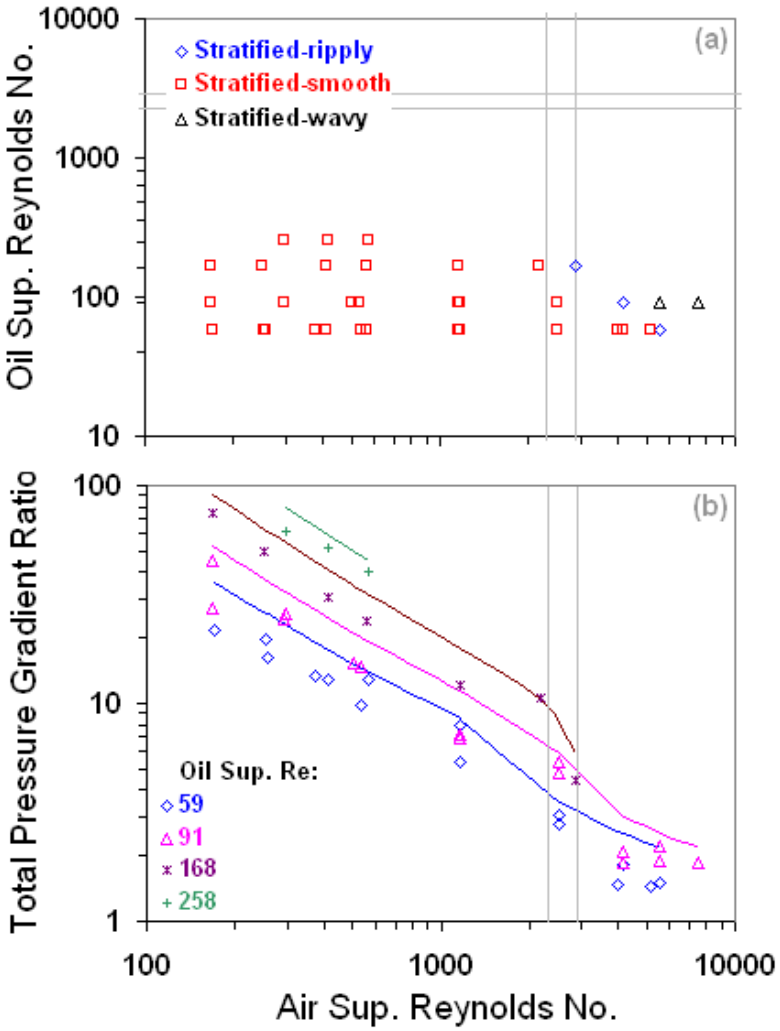

Figure 4.8.21: Prediction of the Agrawal (1971) horizontal stratified flow datasets with the BUTTERWORTH model. Lines are our predictions and the points are measurements.

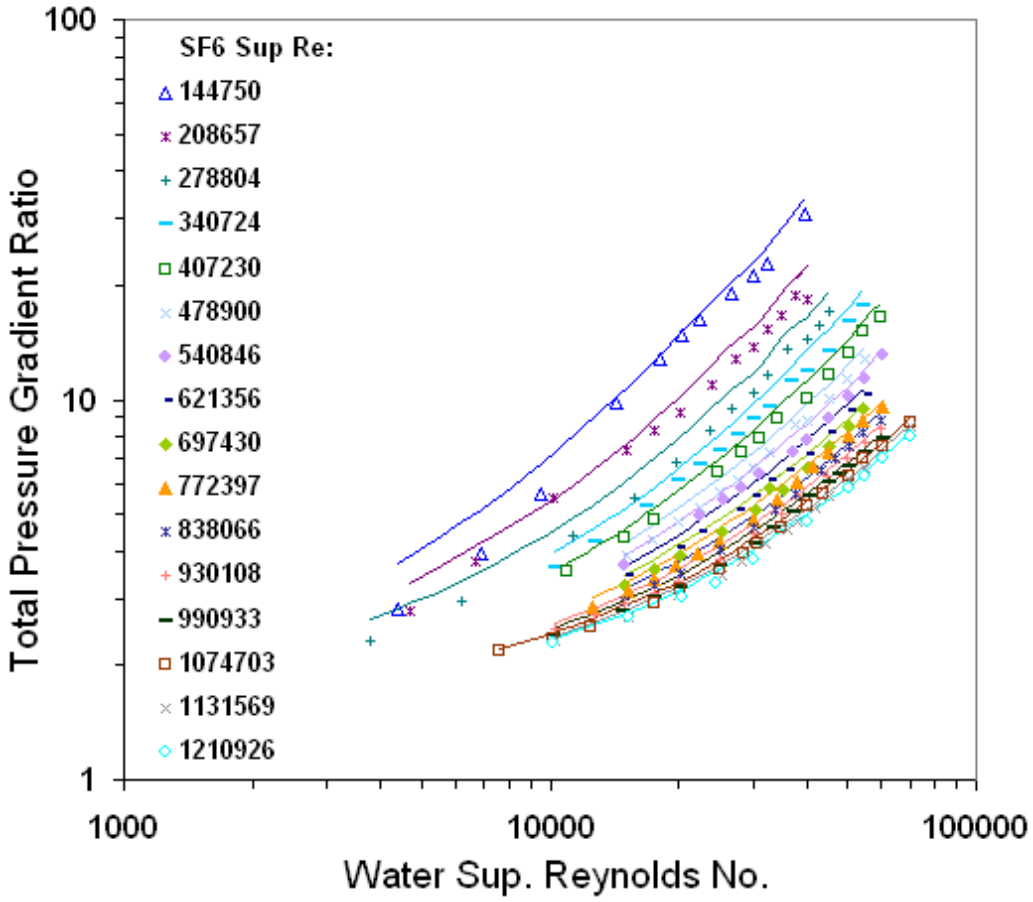

Figure 4.8.22: Prediction of the Johnson (2005) horizontal stratified roll wave flow datasets with the ANSLIP model. Lines are our predictions and the points are measurements.

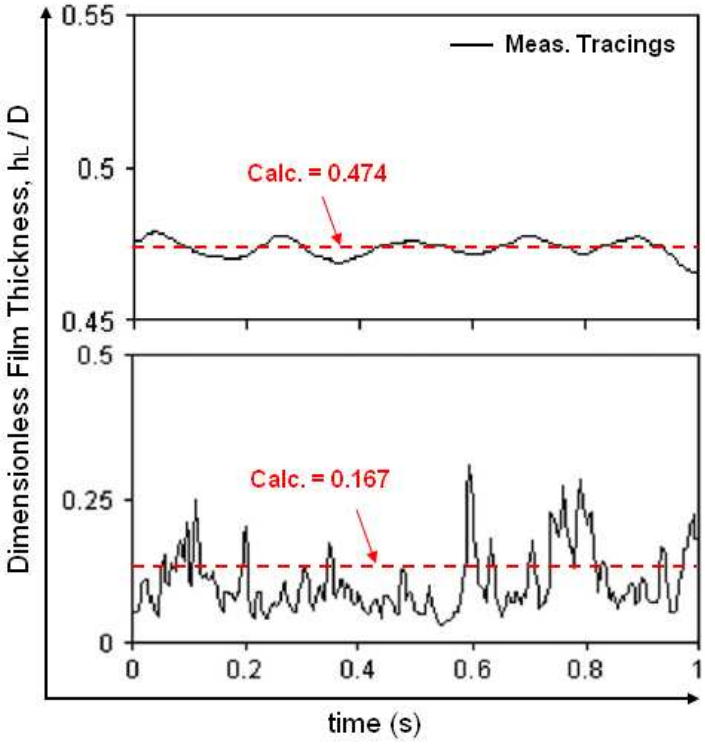

Figure 4.8.23: Prediction of the Tzotzi and Andritsos (2013) horizontal stratified flow film thickness tracings with the SLIPRATIO model.

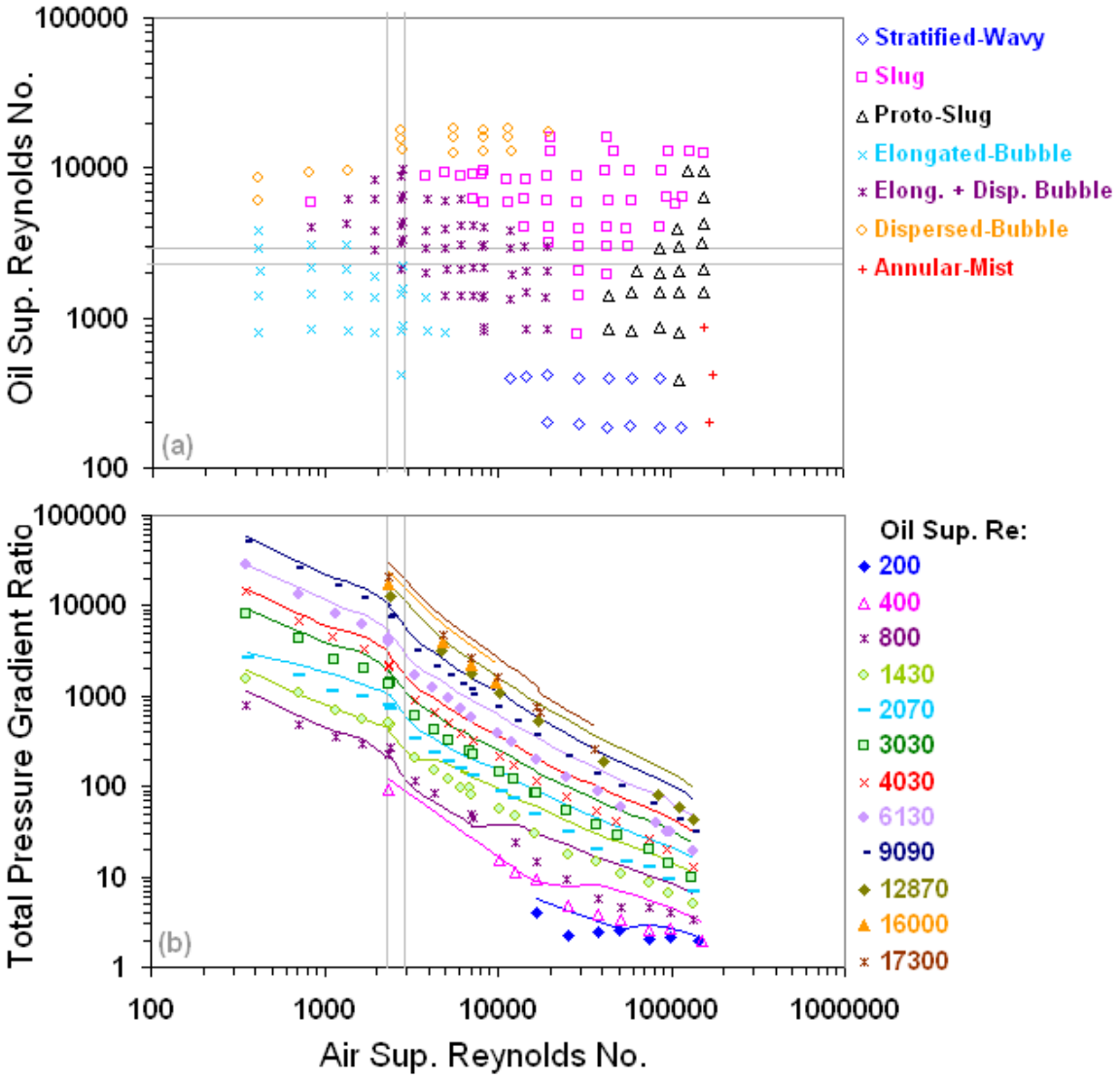

Figure 4.8.24: Prediction of the Kokal (1987) horizontal 2-inch pipe datasets with the WOLGHA model. Lines are our predictions and the points are measurements.

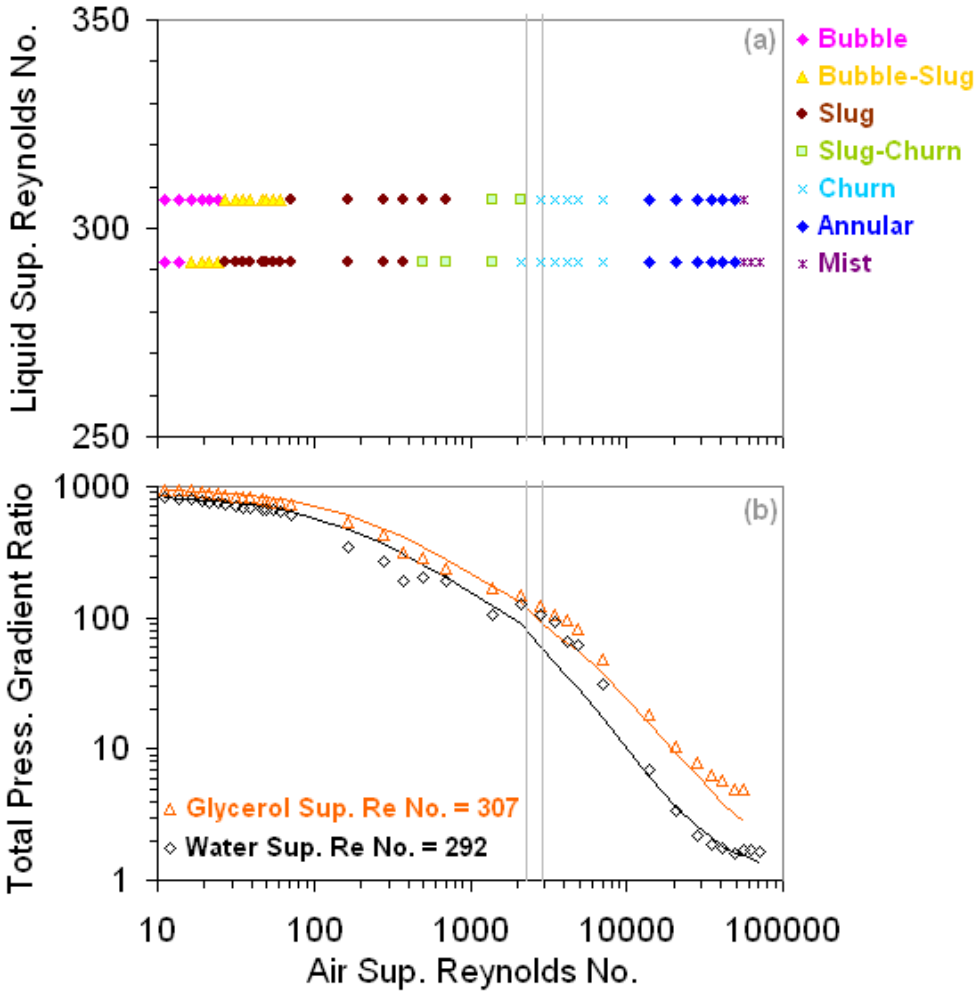

Figure 4.8.25: Prediction of the Hlaing et al. (2007) vertical flow datasets with the WOLGHA model. Lines are our predictions and the points are measurements.

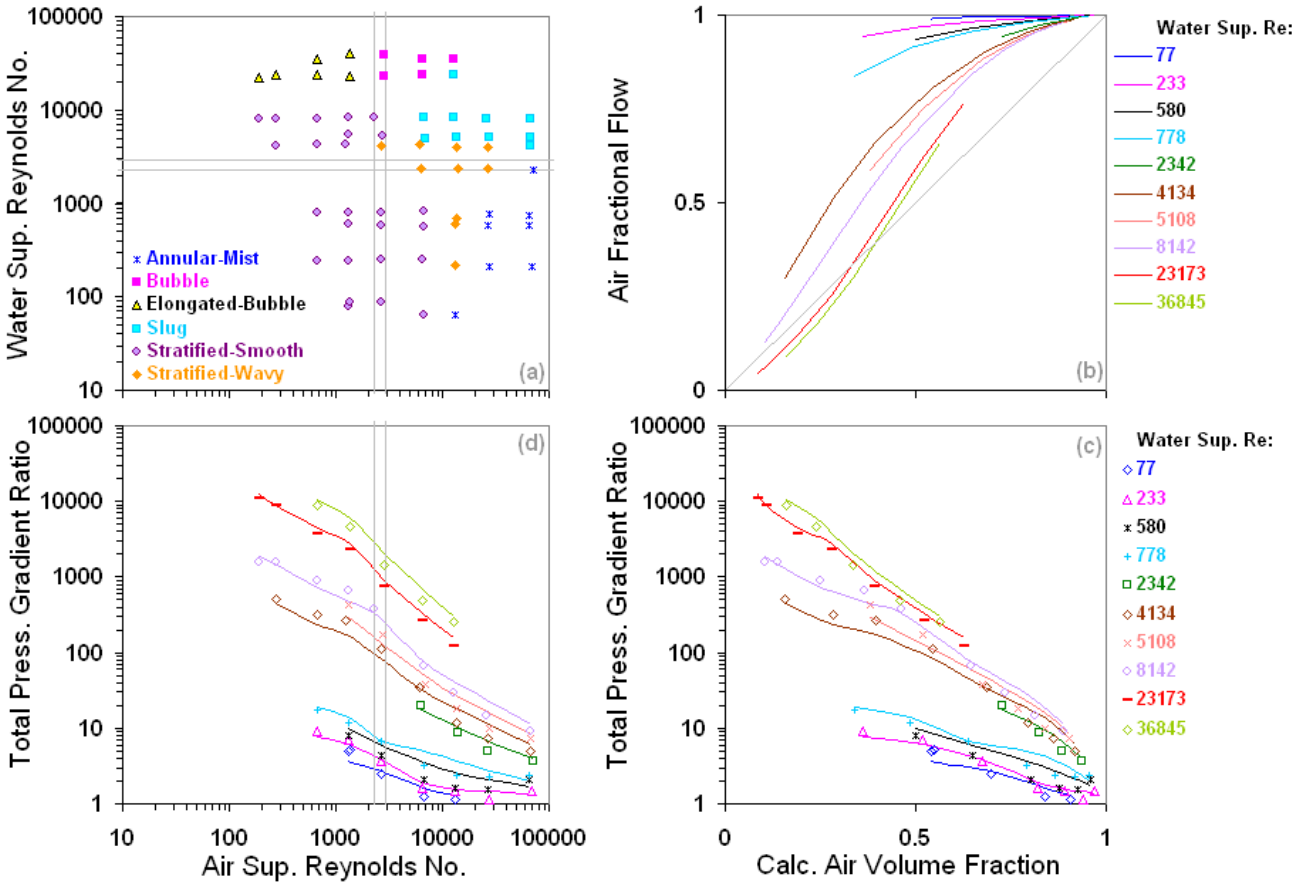

Figure 4.8.26: Prediction of the Govier and Omer (1962) horizontal flow datasets with the WOLGHA model. Lines are our predictions and the points are measurements.

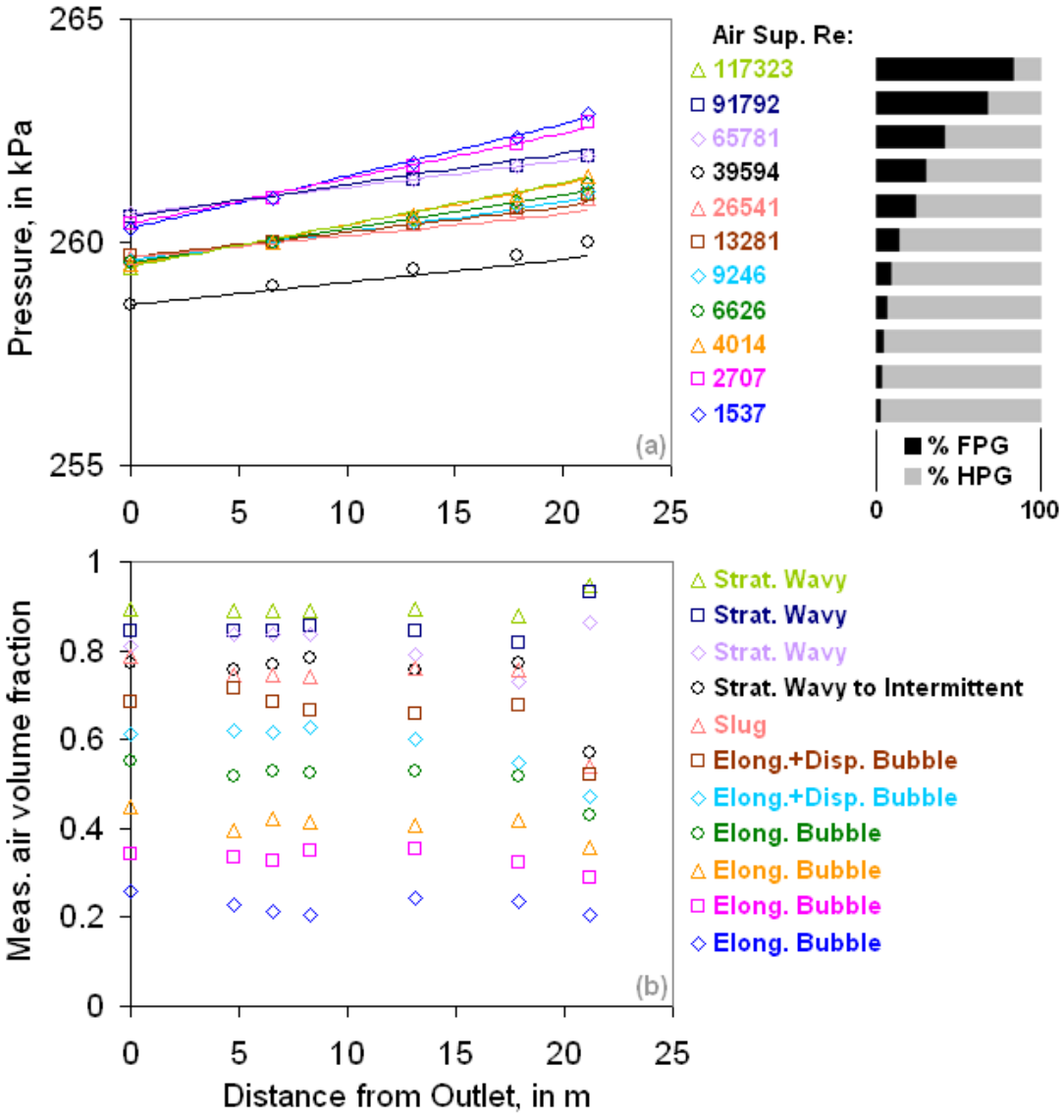

Figure 4.9.1: Model validation with the Kokal (1987) 3-inch pipe datasets at +1 degrees from horizontal. Lines are our calculations and the points are measurements.

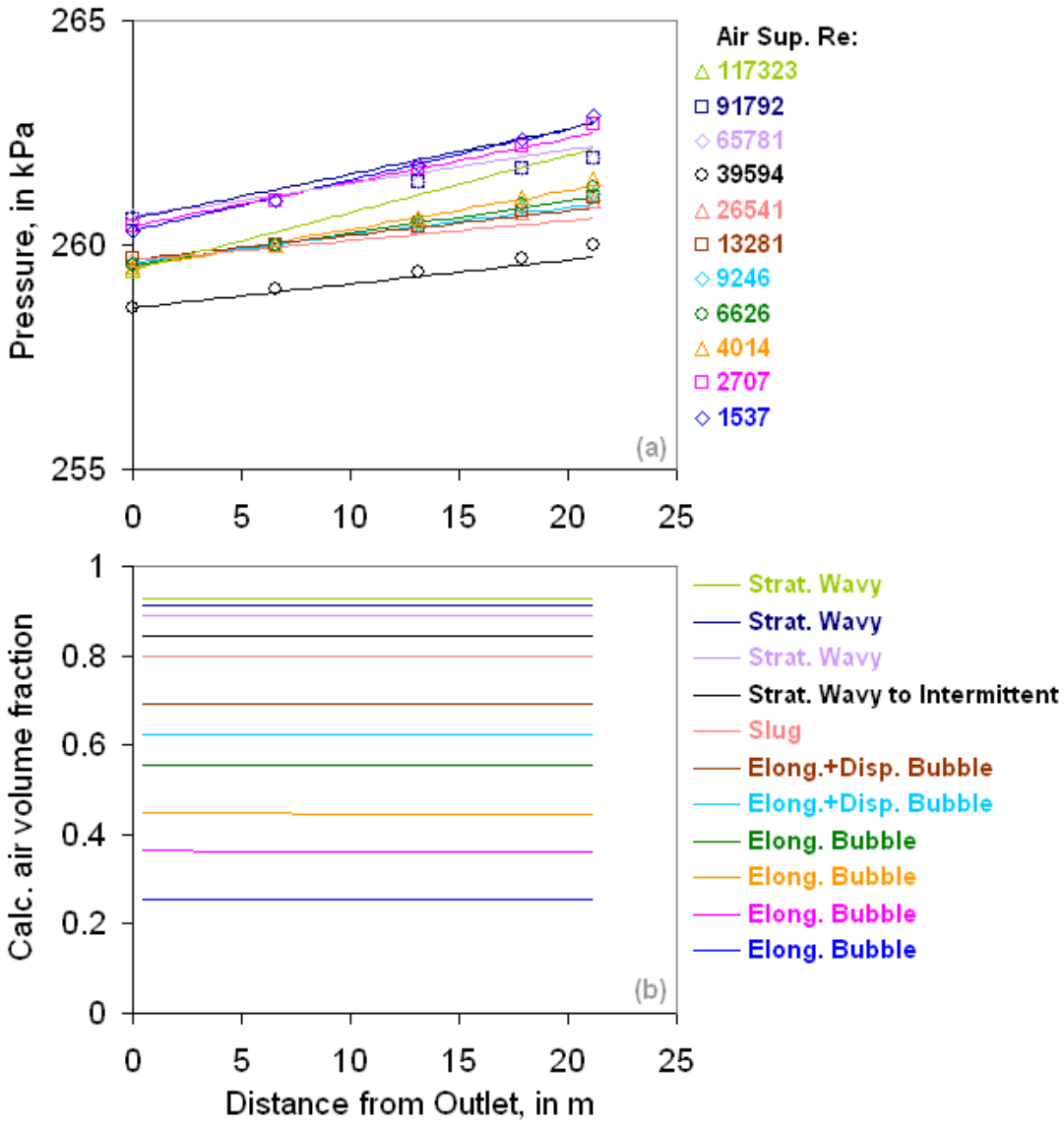

Figure 4.9.2: Prediction of the Kokal (1987) 3-inch pipe datasets at +1 degrees from horizontal with the WOLGHA model. Lines are our predictions and the points are measurements.

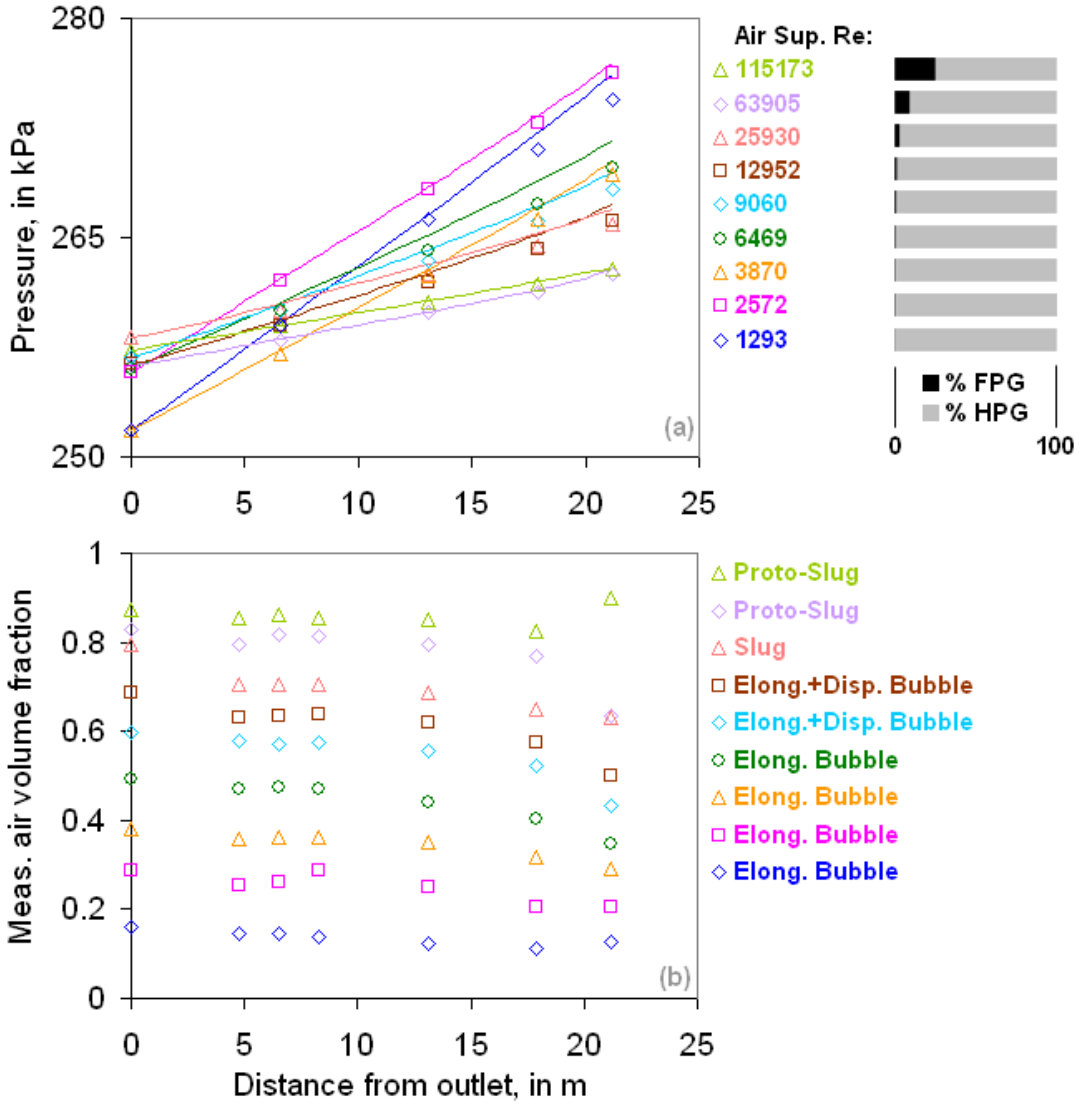

Figure 4.9.3: Model validation with the Kokal (1987) 3-inch pipe datasets at +9 degrees from horizontal. Lines are our calculations and the points are measurements.

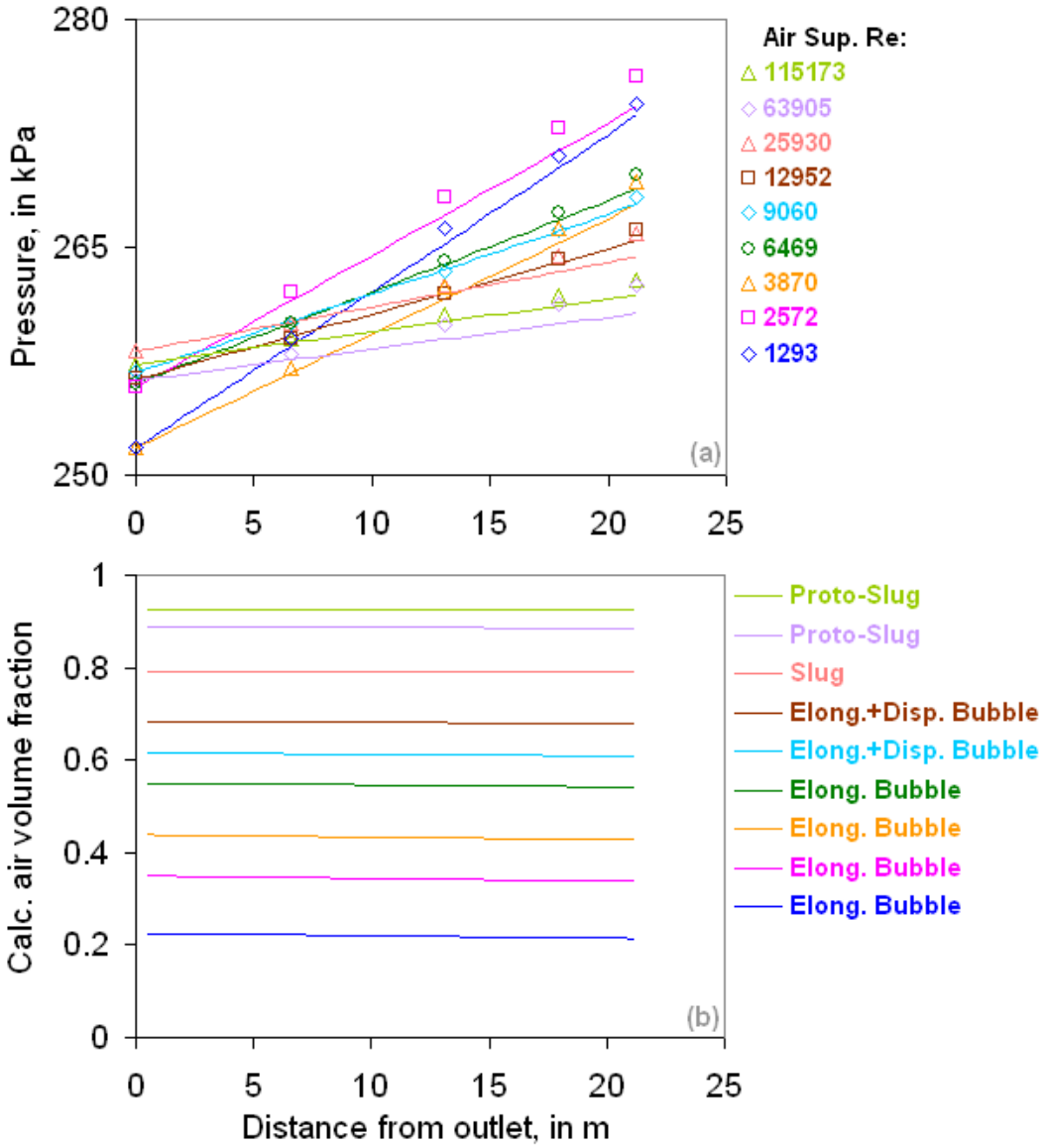

Figure 4.9.4: Prediction of the Kokal (1987) 3-inch pipe datasets at +9 degrees from horizontal with the WOLGHA model. Lines are our predictions and the points are measurements.

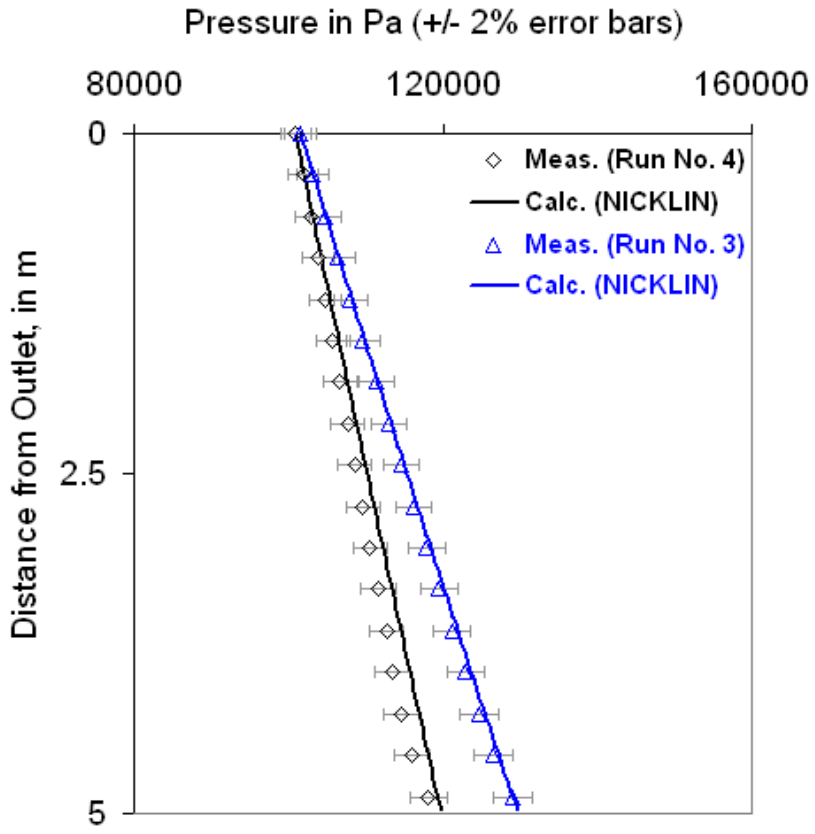

Figure 4.9.5: Prediction of two Moissis and Griffith (1960) vertical slug flow datasets with the NICKLIN model. Lines are our predictions and the points are measurements.

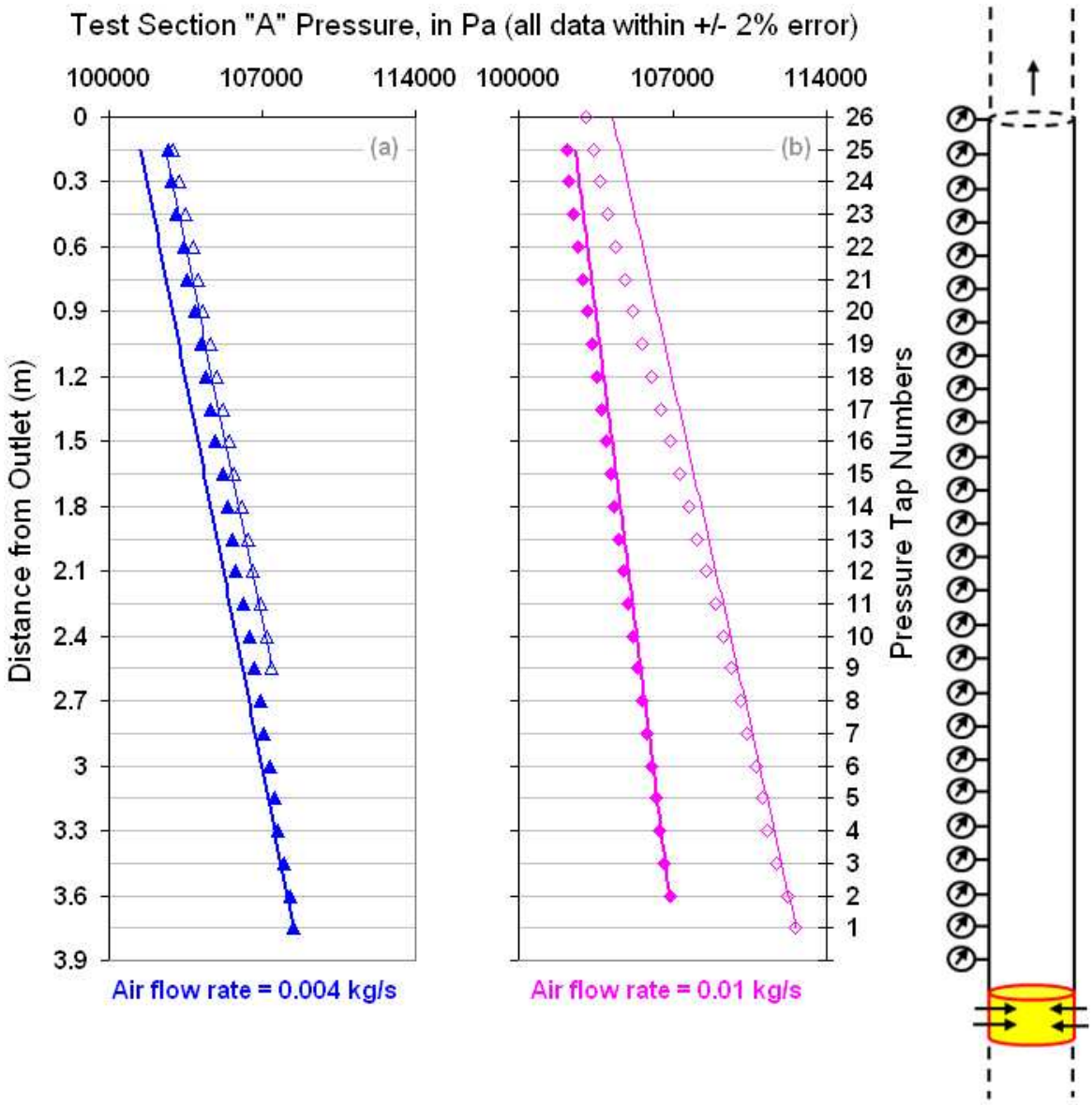

Figure 4.9.6: Prediction of representative Woods and Spedding (1996) vertical churn and annular flow datasets with the NICKLIN and ANSLIP models, respectively. Lines are our predictions and the points are measurements.

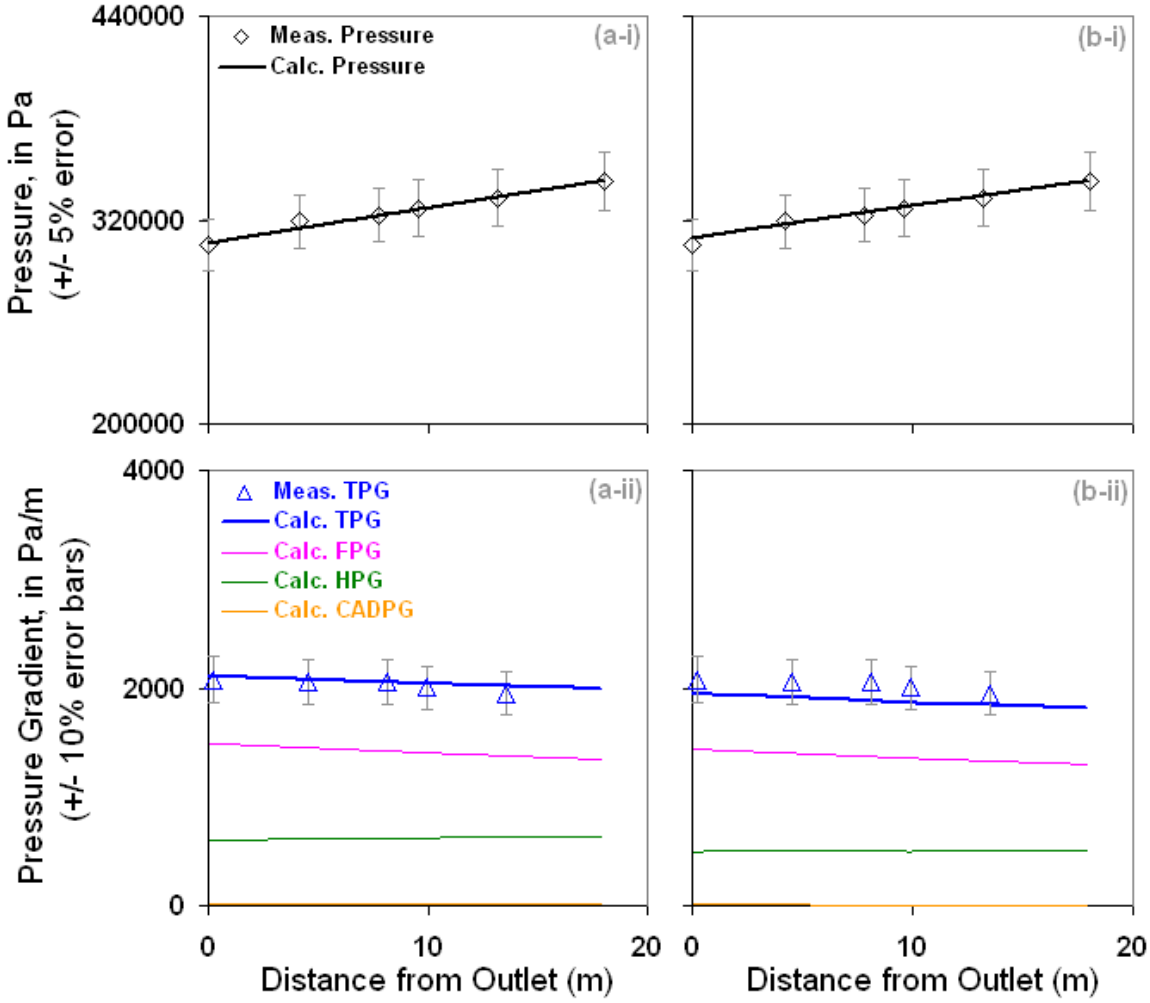

Figure 4.9.7: Prediction of run 9 (low gas rate, axial jet injector) in Brown (1978) with the ANSLIP model. Lines are our predictions and the points are measurements.

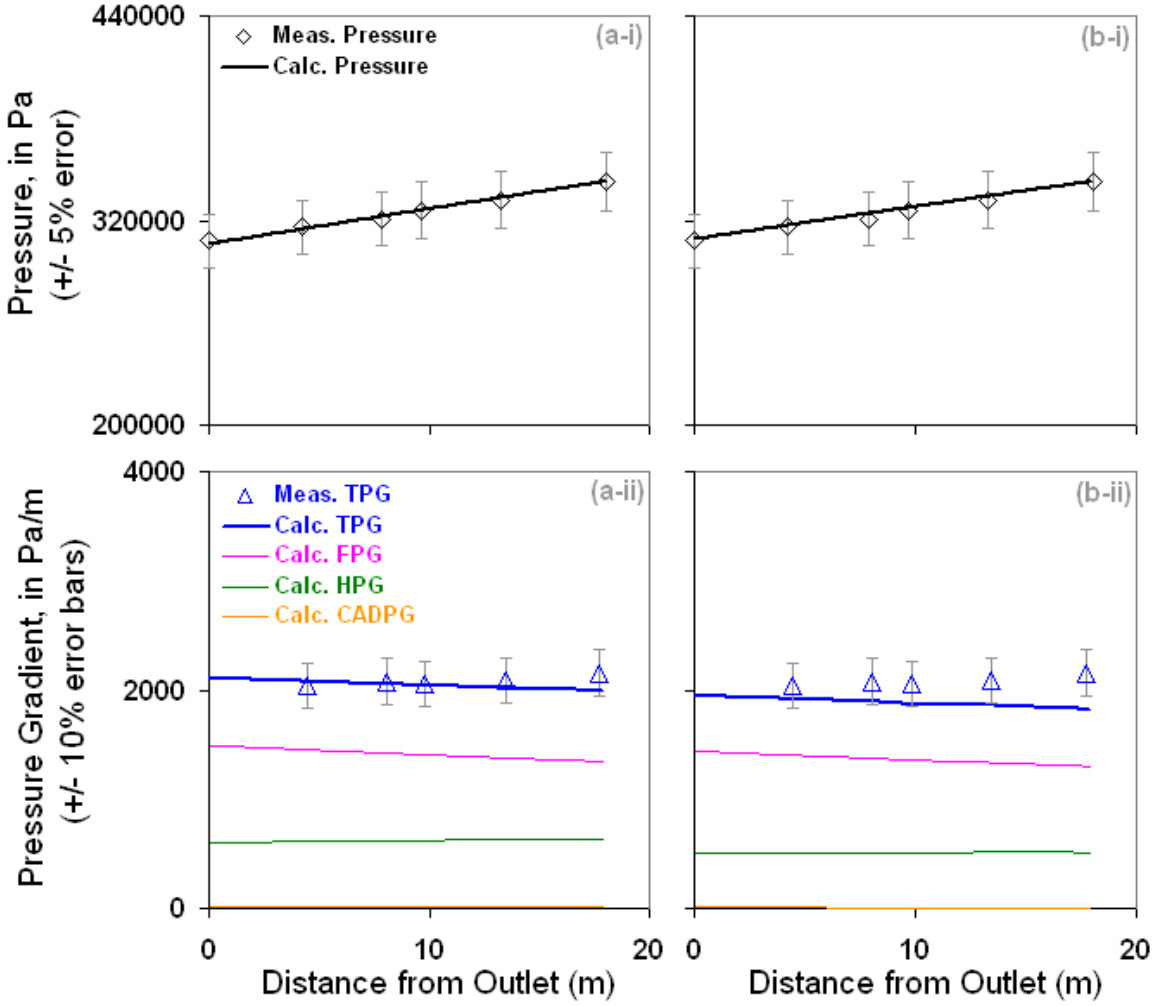

Figure 4.9.8: Prediction of run 9 (low gas rate, porous wall injector) in Brown (1978) with the ANSLIP model. Lines are our predictions and the points are measurements.

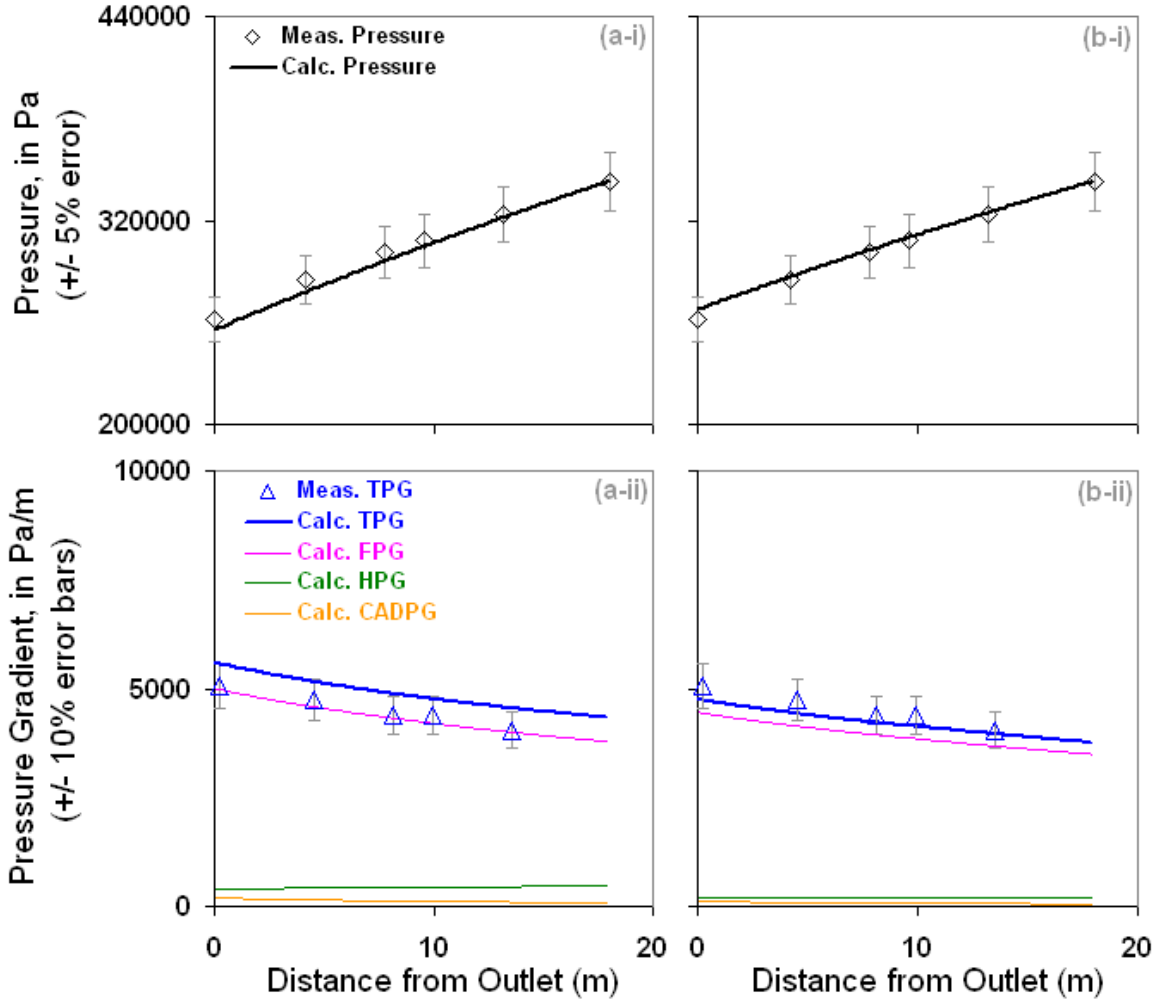

Figure 4.9.9: Prediction of run 3 (high gas rate, axial jet injector) in Brown (1978) with the ANSLIP model. Lines are our predictions and the points are measurements.

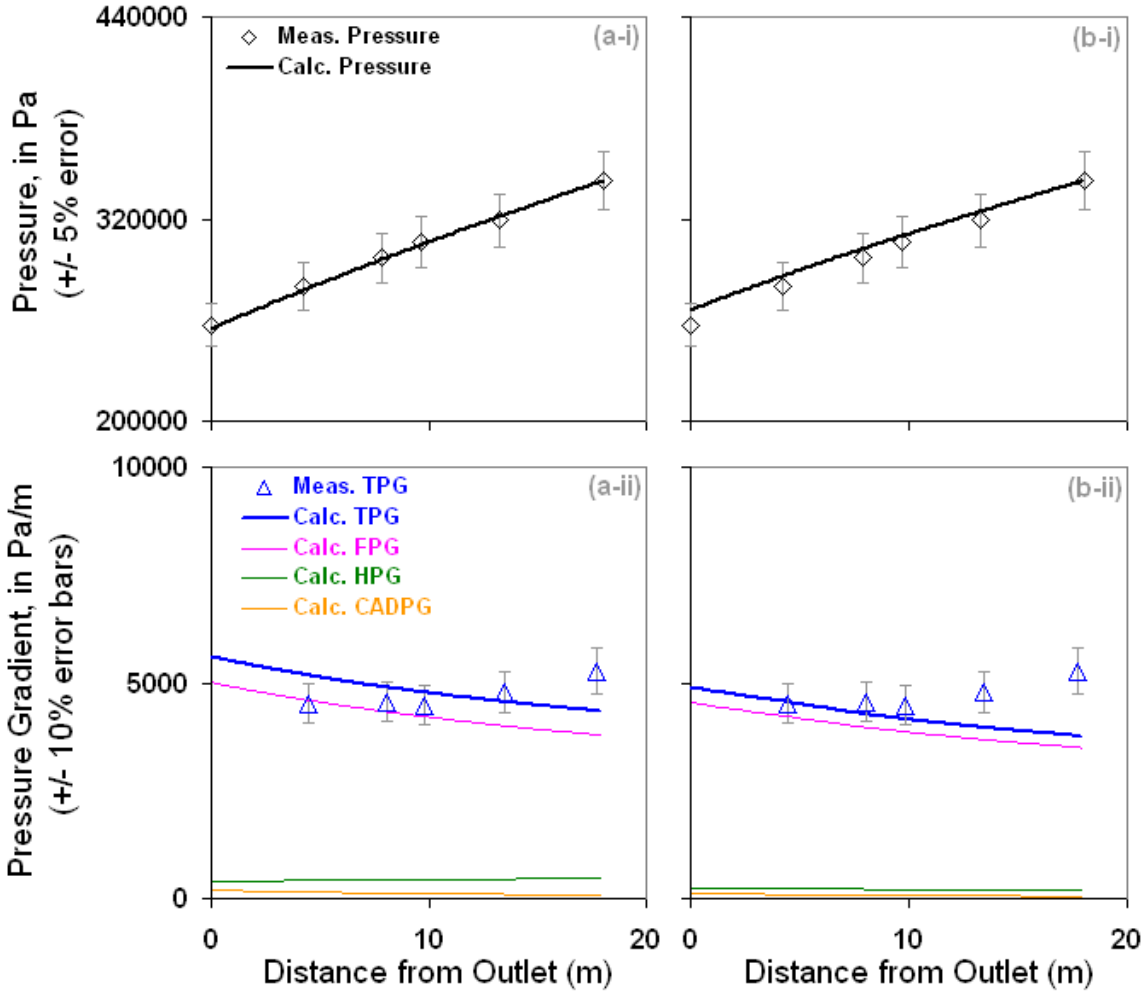

Figure 4.9.10: Prediction of run 3 (high gas rate, porous wall injector) in Brown (1978) with the ANSLIP model. Lines are our predictions and the points are measurements.

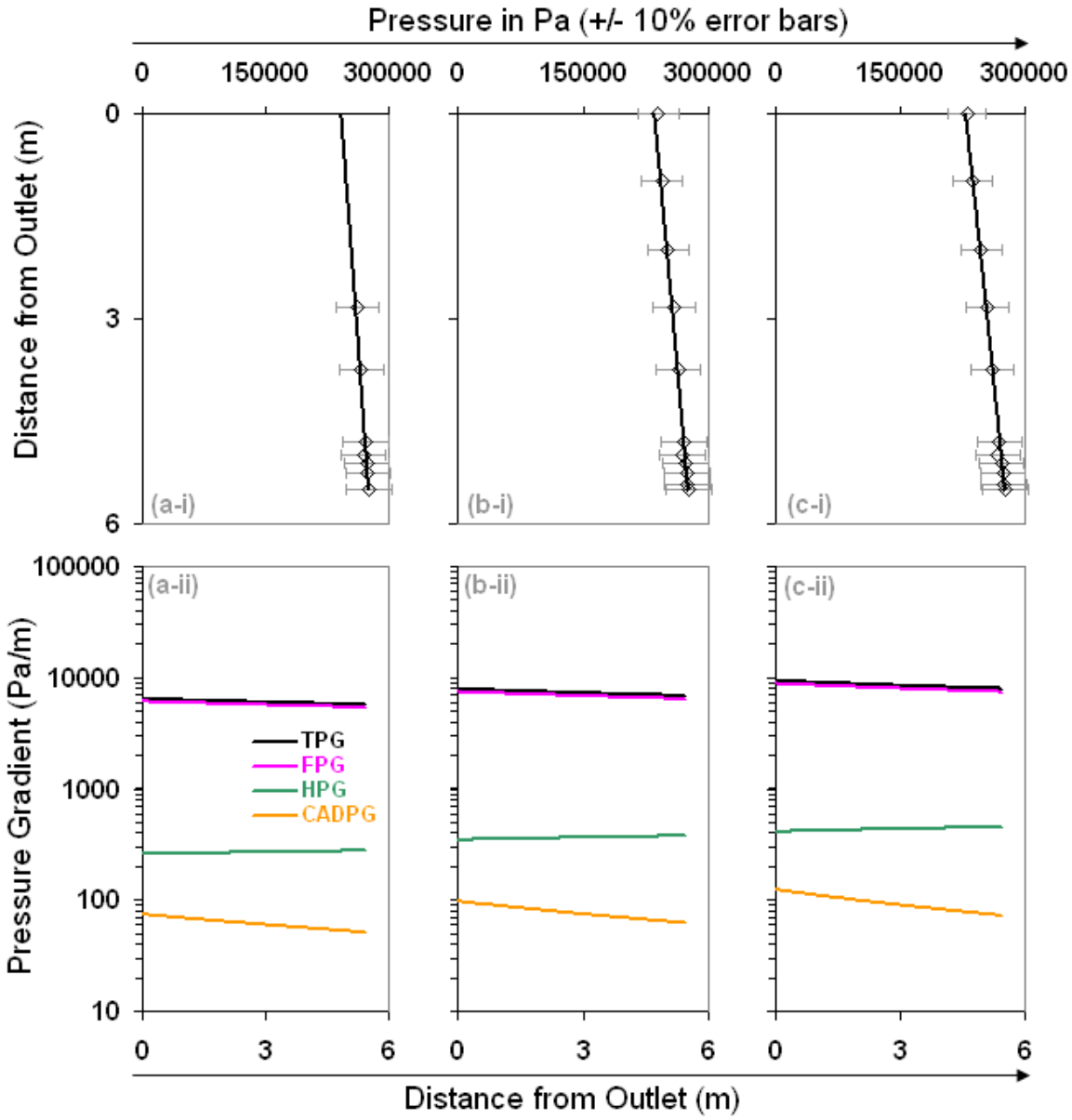

Figure 4.9.11: Prediction of run 15, 17, 19 (low water rates) in Cousins et al. (1965) with the ANSLIP model. Lines are our predictions and the points are measurements.

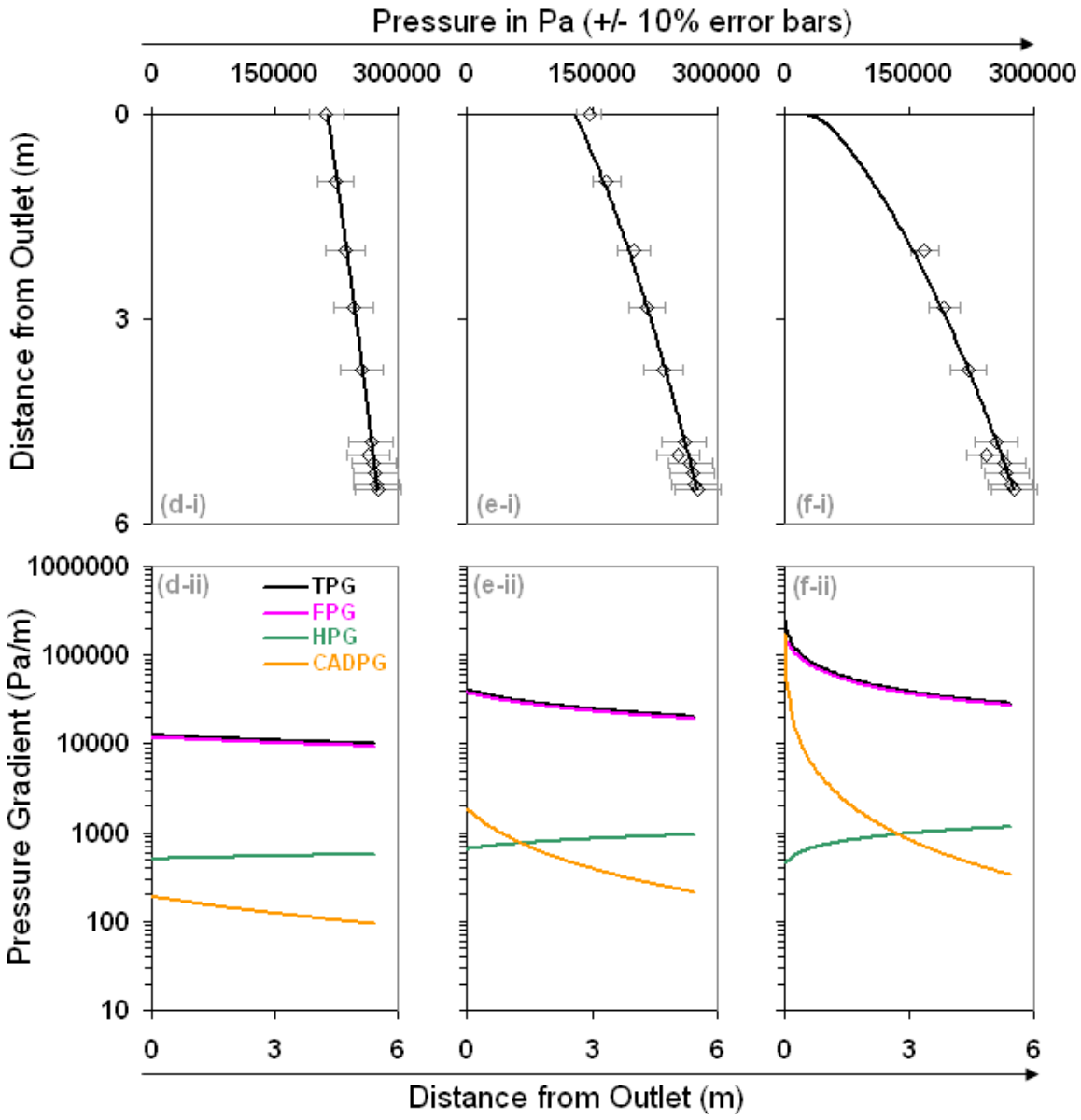

Figure 4.9.12: Prediction of run 21, 24, 26 (high water rates) in Cousins et al. (1965) with the ANSLIP model. Lines are our predictions and the points are measurements.

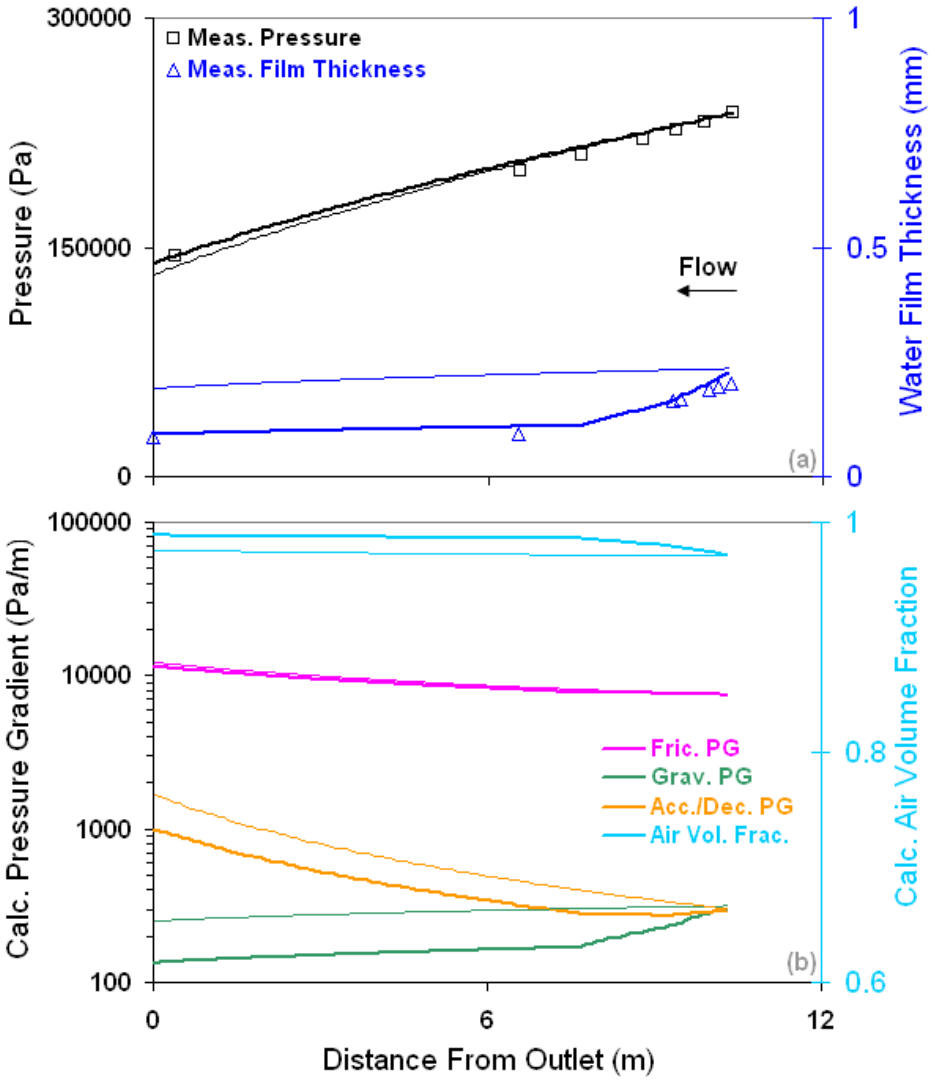

Figure 4.9.13: Example dataset calculations with the ANSLIP model for the Wolf (1995) experiments at an air mass flux of 154 kg/m^2-s and a water mass flux of 80 kg/m^2-s . Lines are our calculations and the points are measurements.

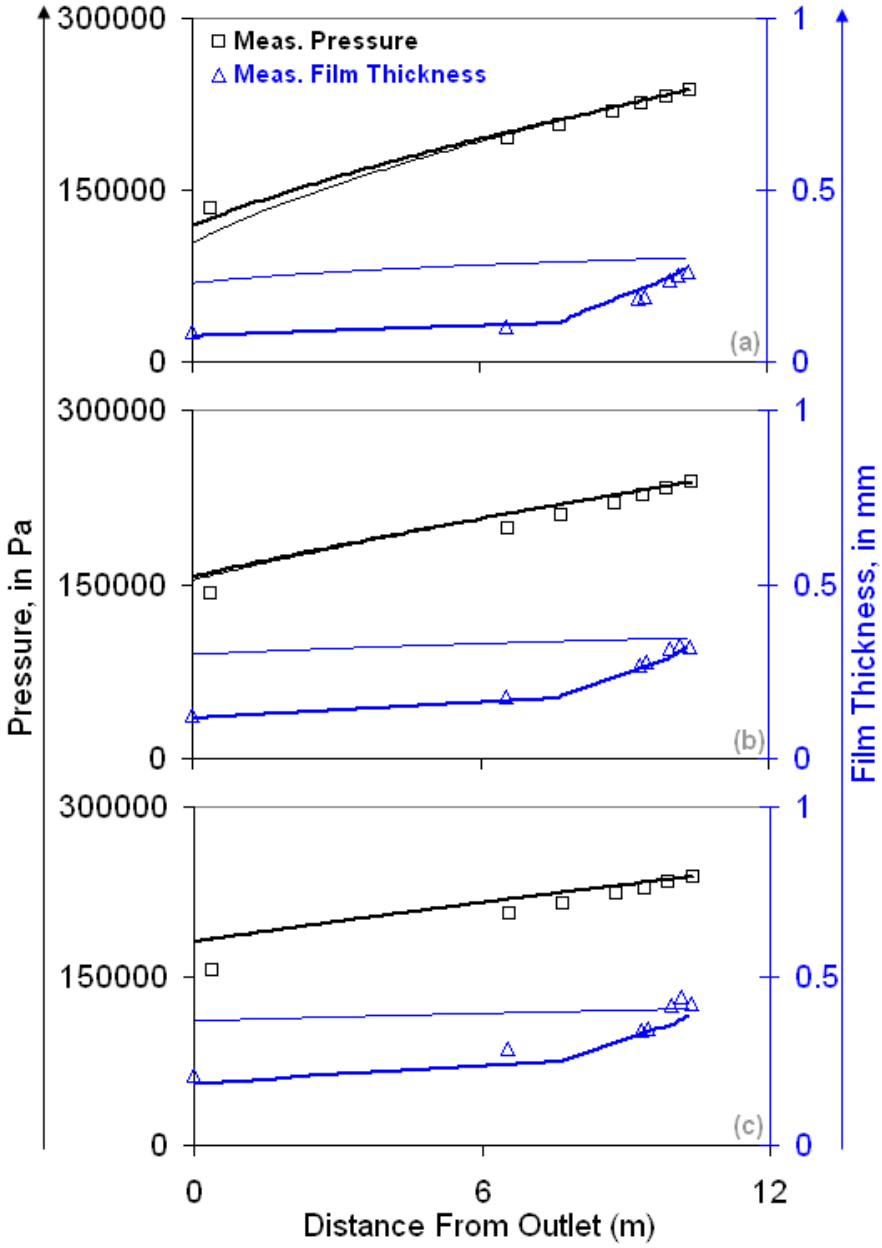

Figure 4.9.14: Example dataset calculations with the ANSLIP model for the Wolf (1995) experiments at decreasing air mass fluxes at the same water flux. Lines are our calculations and the points are measurements.

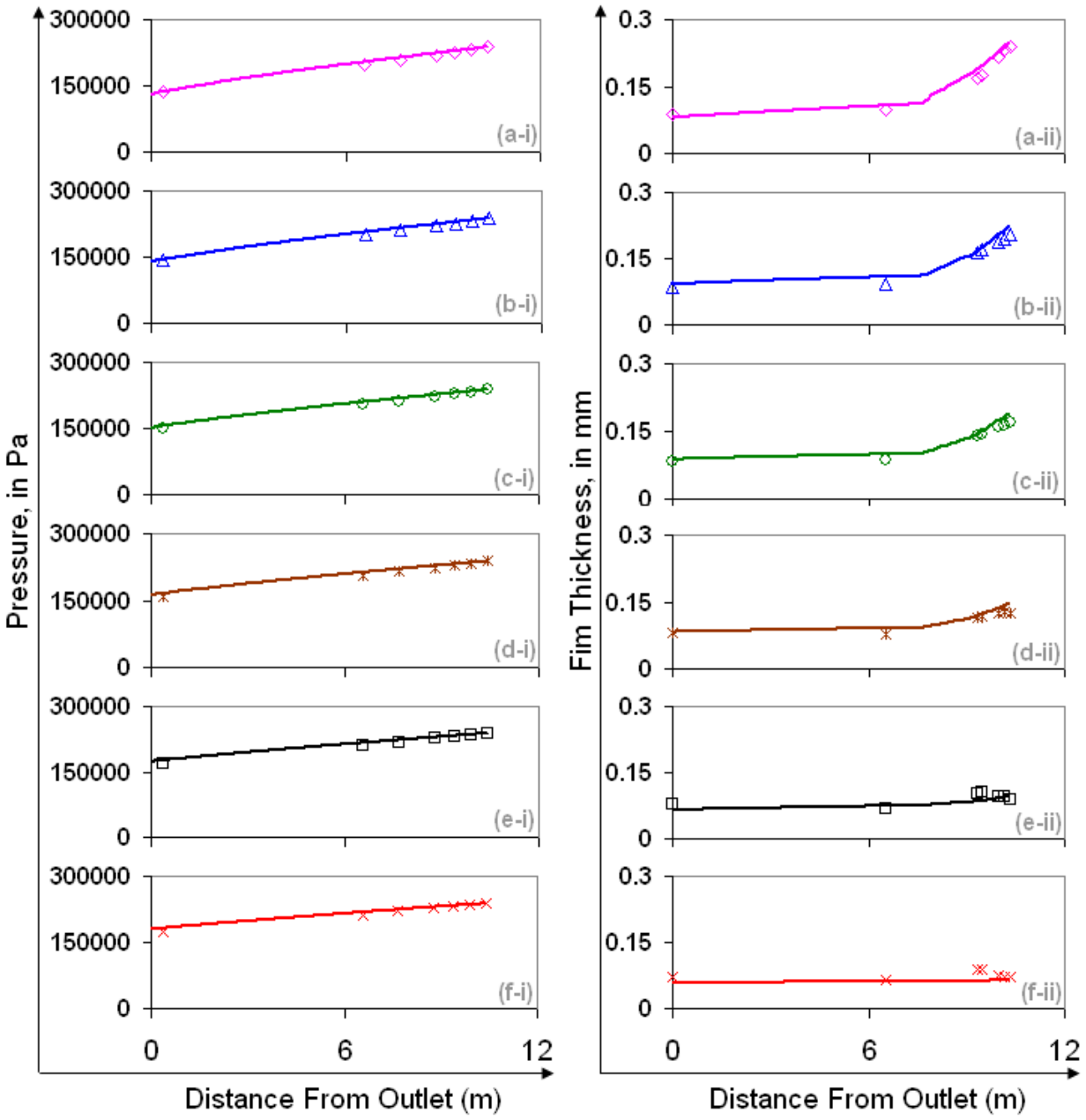

Figure 4.9.15: Example dataset calculations with the ANSLIP model for the Wolf (1995) experiments at decreasing water mass fluxes at the same air flux. Lines are our calculations and the points are measurements.

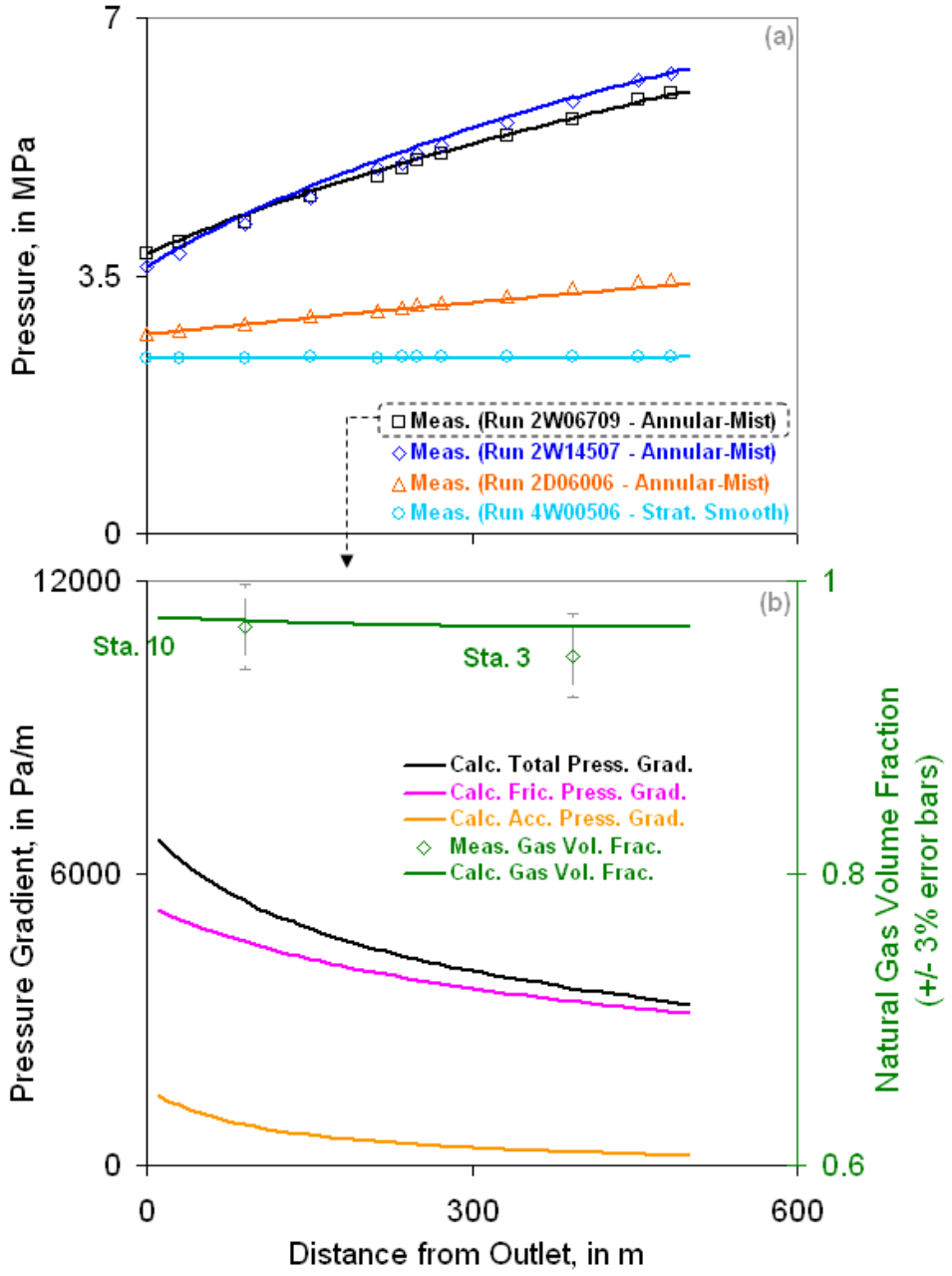

Figure 4.9.16: Prediction of representative datasets from Eaton (1966) with the WOLGHA model. Lines are our predictions and the points are measurements.

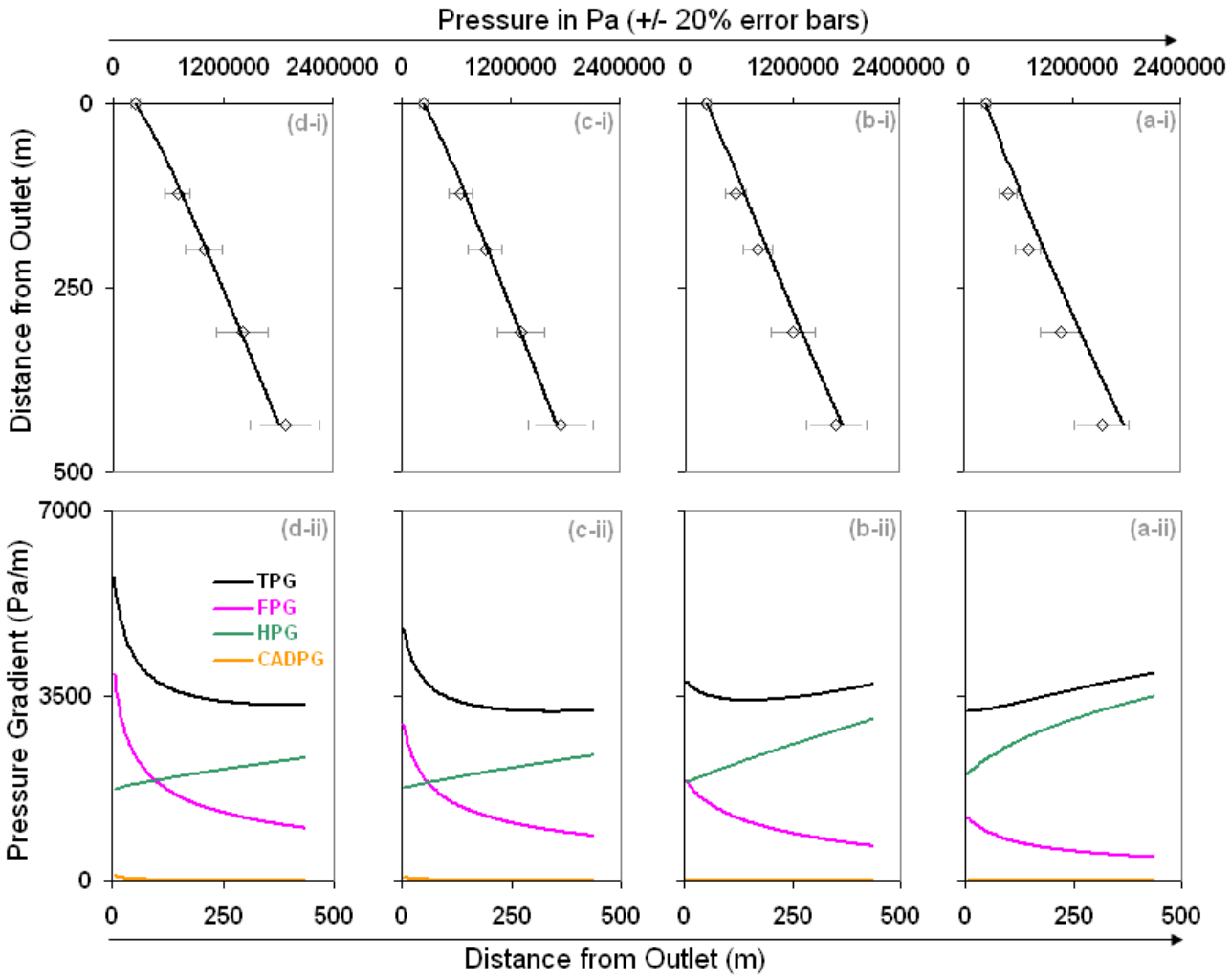

Figure 4.9.17: Predicting a change from a hydrostatic-dominated system to a friction-dominated system with the Hagedorn (1964) experiments for increasing GLR. Lines are our predictions and the points are measurements.

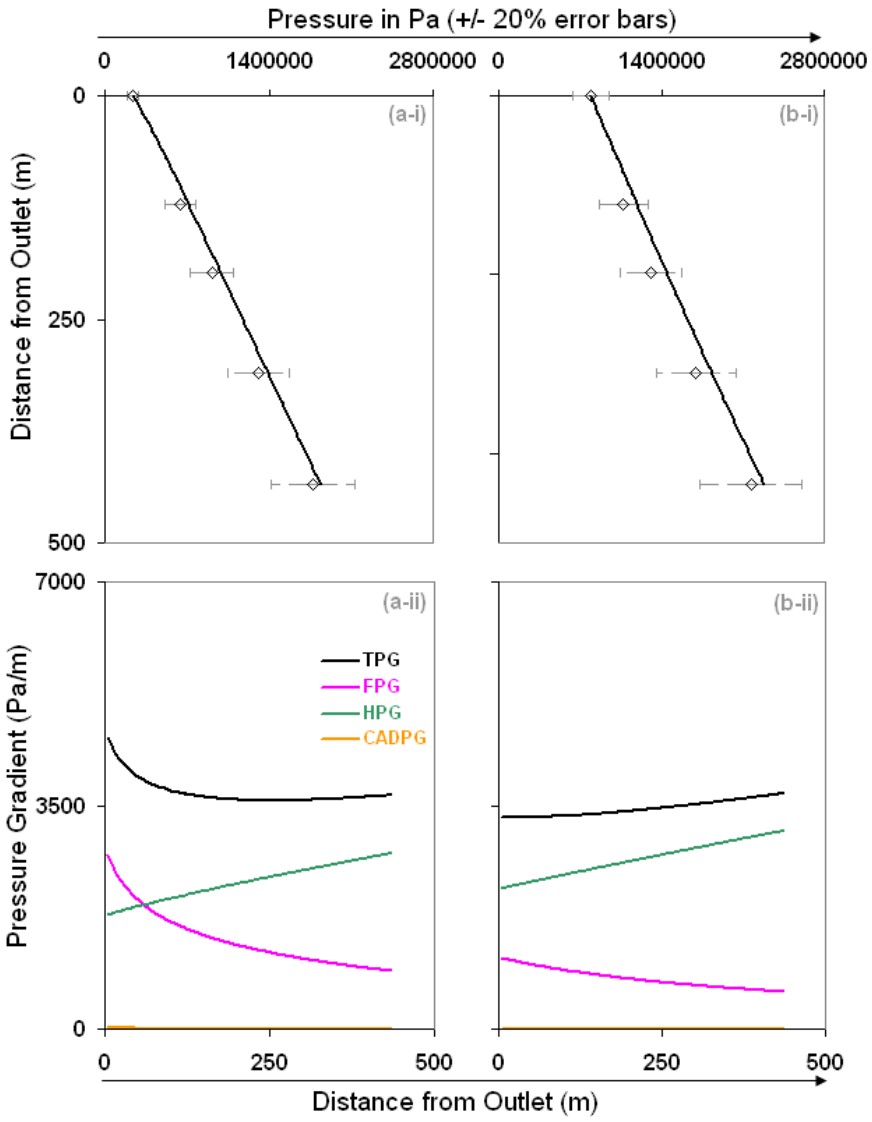

Figure 4.9.18: Predicting a change from a hydrostatic-dominated system to a friction-dominated system with the Hagedorn (1964) experiments for decreasing outlet pressure. Lines are our predictions and the points are measurements.

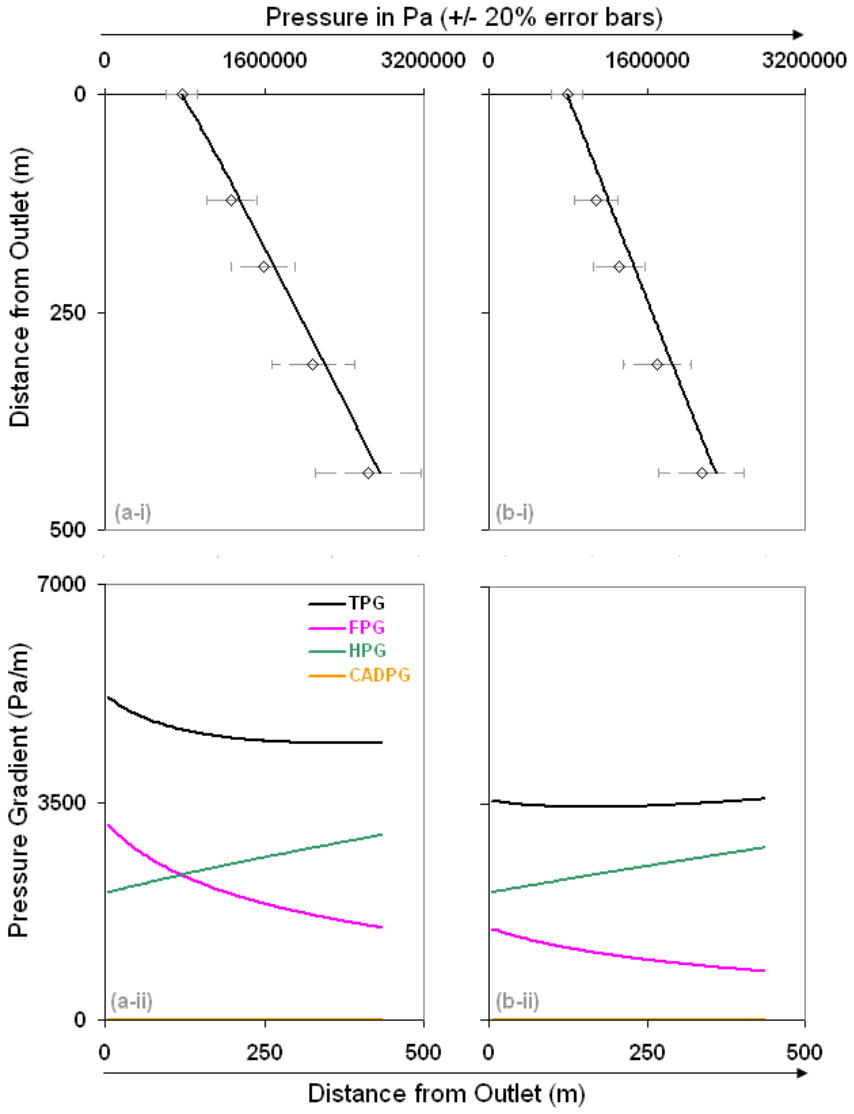

Figure 4.9.19: Predicting a change from a hydrostatic-dominated system to a friction-dominated system with the Hagedorn (1964) experiments for increasing liquid rate. Lines are our predictions and the points are measurements.

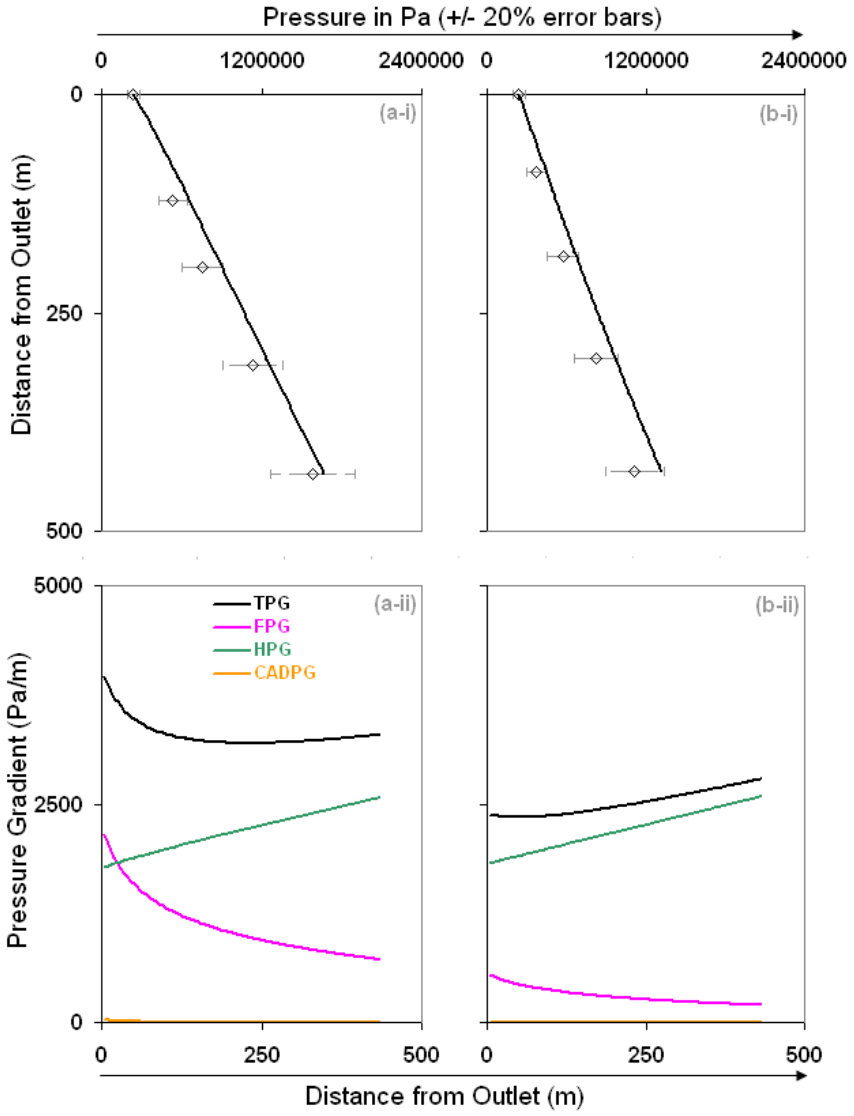

Figure 4.9.20: Predicting a change from a hydrostatic-dominated system to a friction-dominated system with the Hagedorn (1964) experiments for decreasing pipe diameter. Lines are our predictions and the points are measurements.

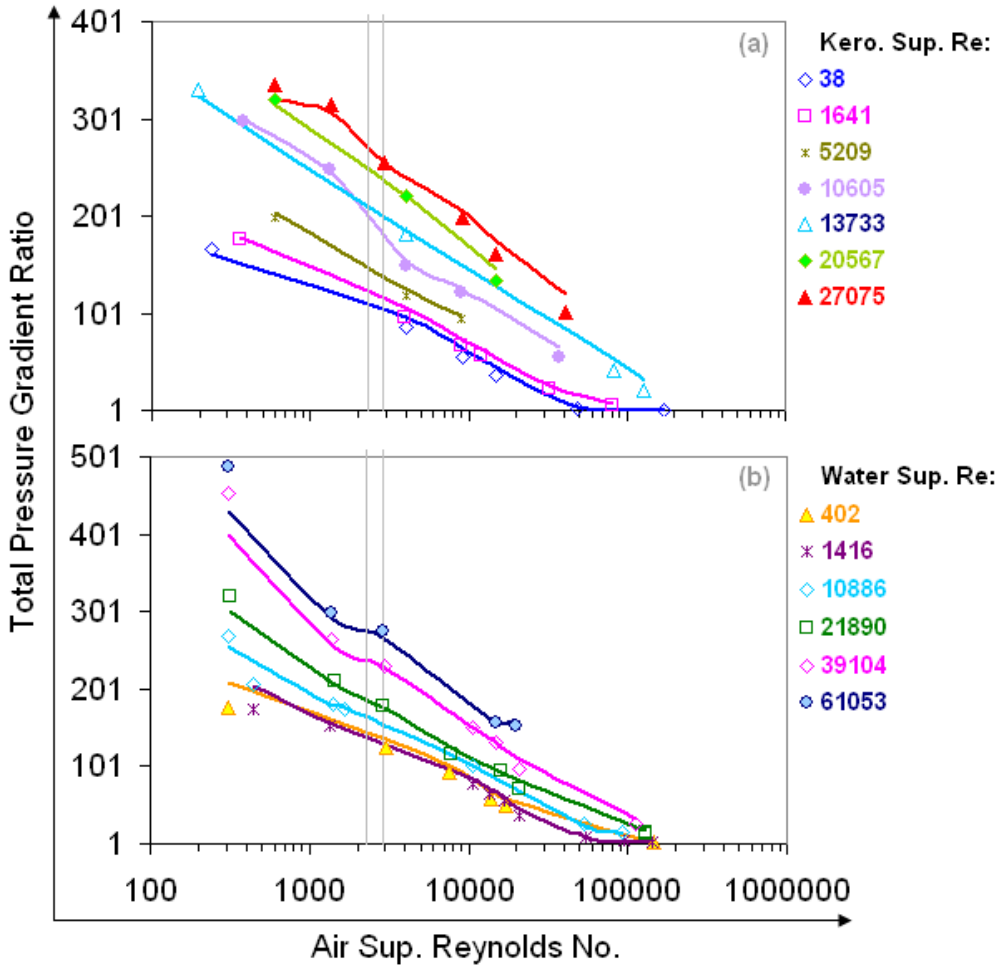

Figure 4.10.1: Model validation with the Caetano-Filho (1984) vertical annulus datasets. Lines are our calculations and the points are measurements.

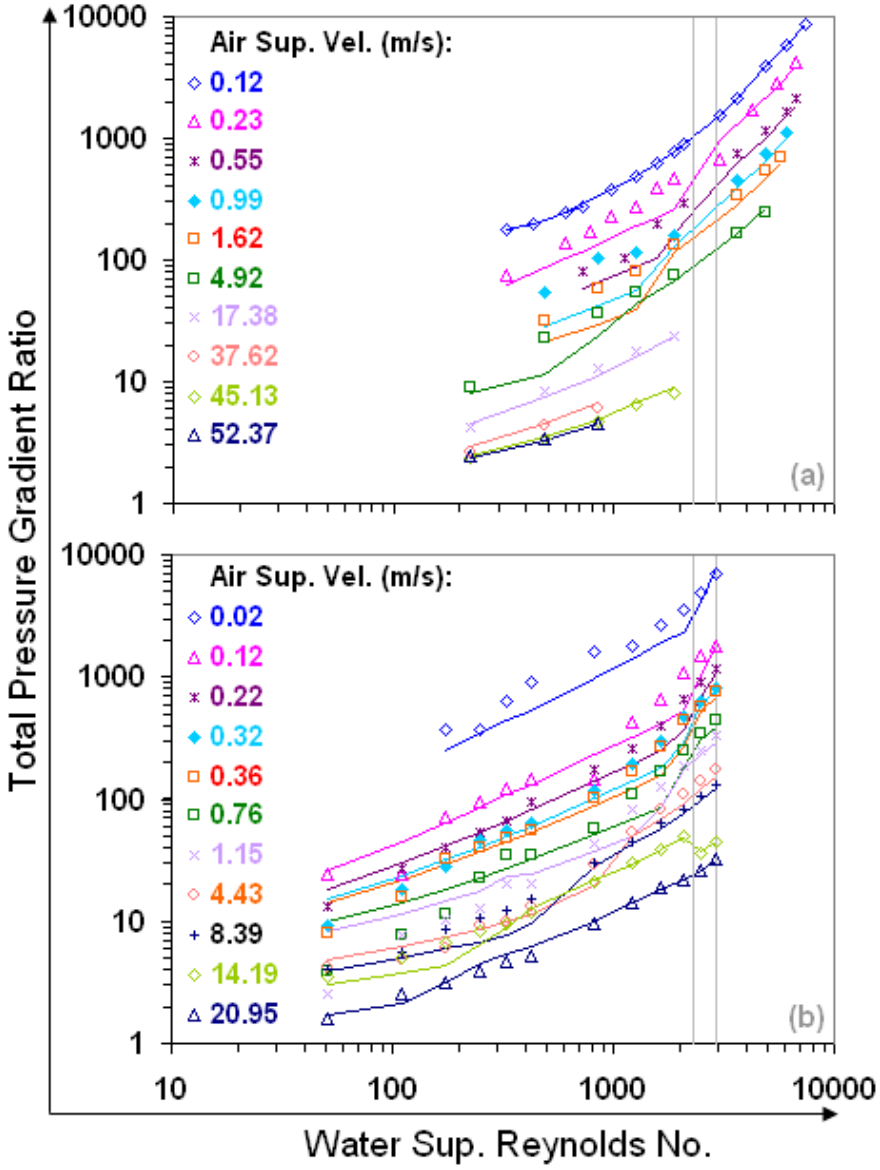

Figure 4.10.2: Model validation with the Ekberg (1998) horizontal annulus datasets. Lines are our calculations and the points are measurements.

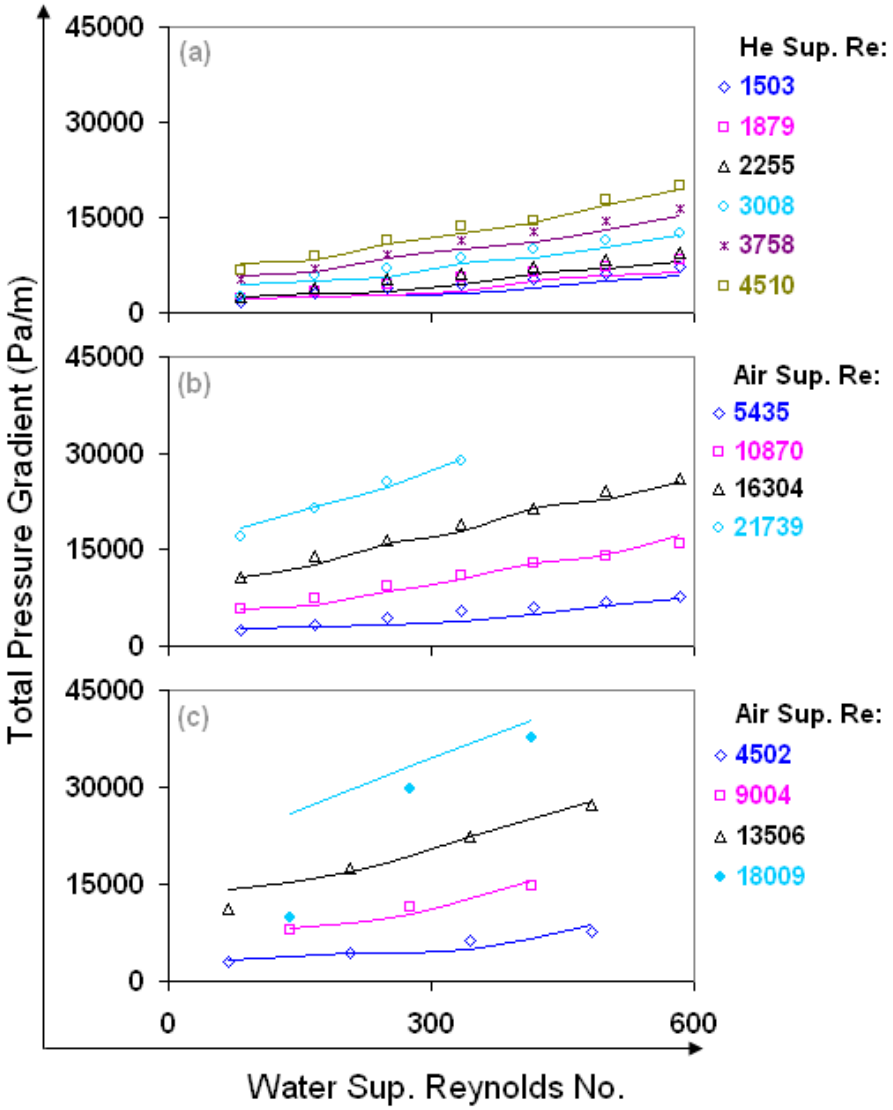

Figure 4.10.3: Model validation with the Holt (1996) mini-channel datasets. Lines are our calculations and the points are measurements.

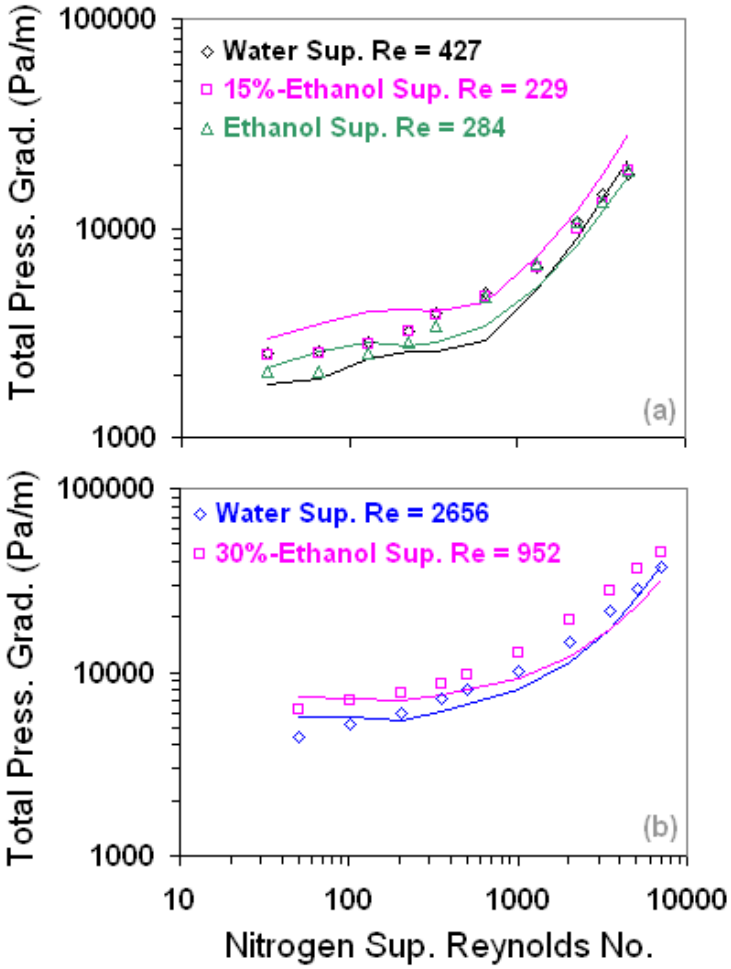

Figure 4.10.4: Model validation with the Fujita et al. (1995) mini-channel datasets. Lines are our calculations and the points are measurements.

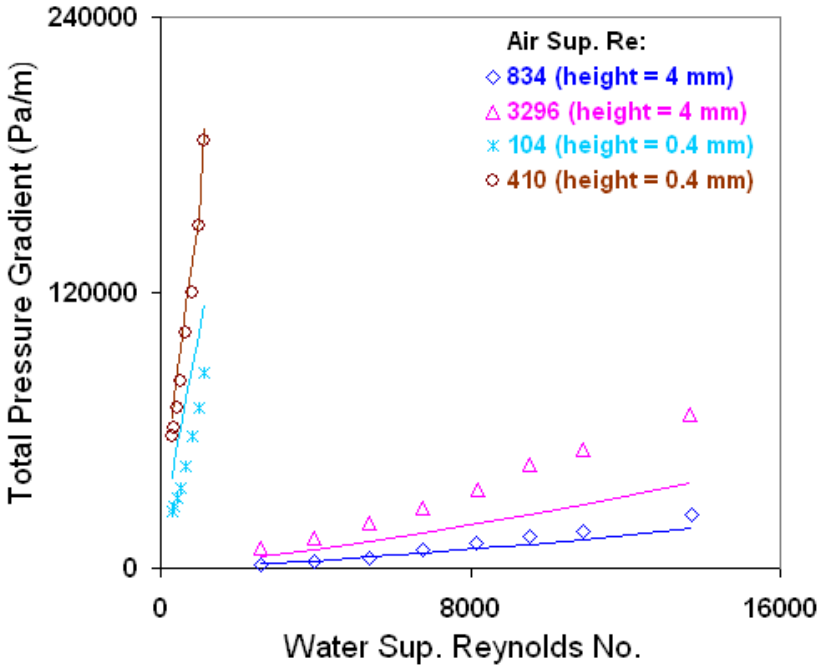

Figure 4.10.5: Prediction of the mini-channel datasets from Lee and Lee (2001) with the CISE model. Lines are our predictions and the points are measurements.

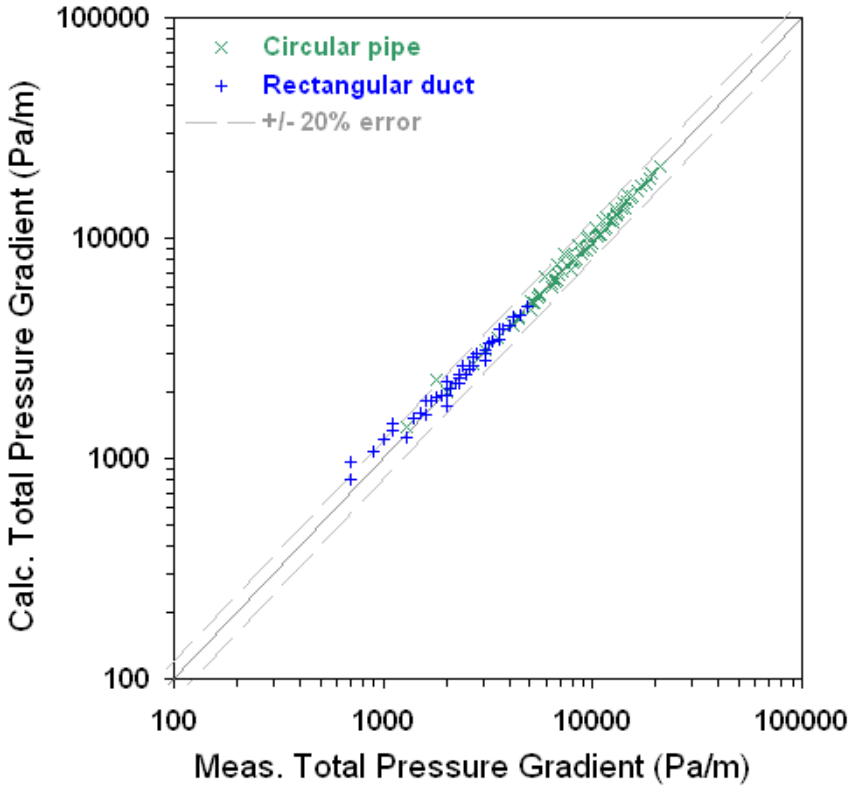

Figure 4.10.6: Prediction of the horizontal annular flow datasets from Ashwood (2010) with the ANSLIP model.

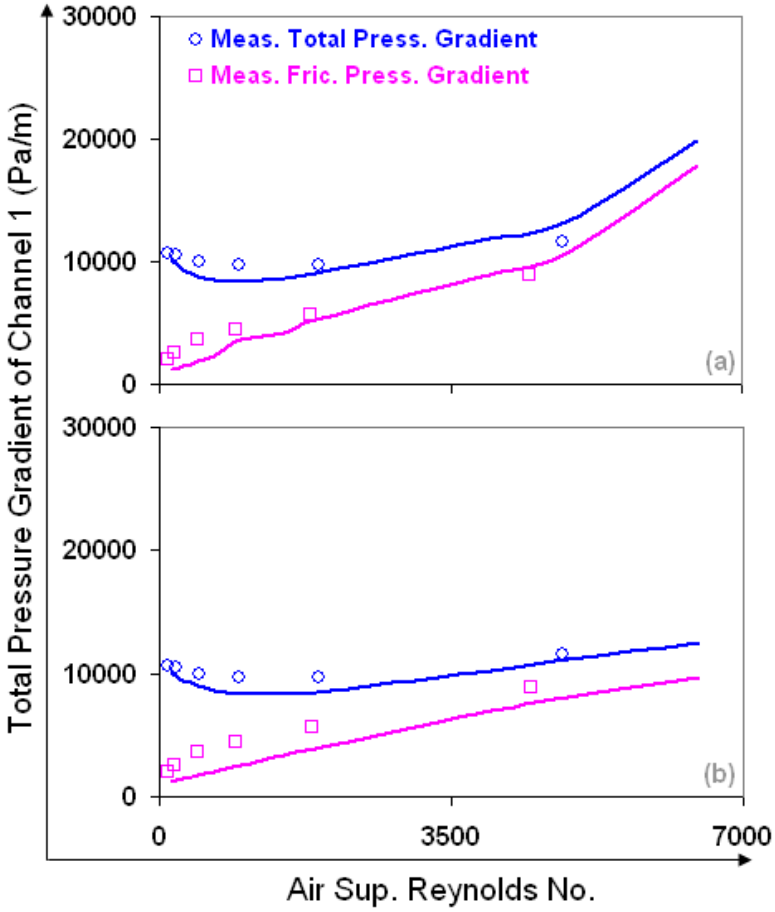

Figure 4.10.7: Representative datasets from the rod bundle experiments of Sadatomi et al. (2006). Lines are our calculations and the points are measurements.

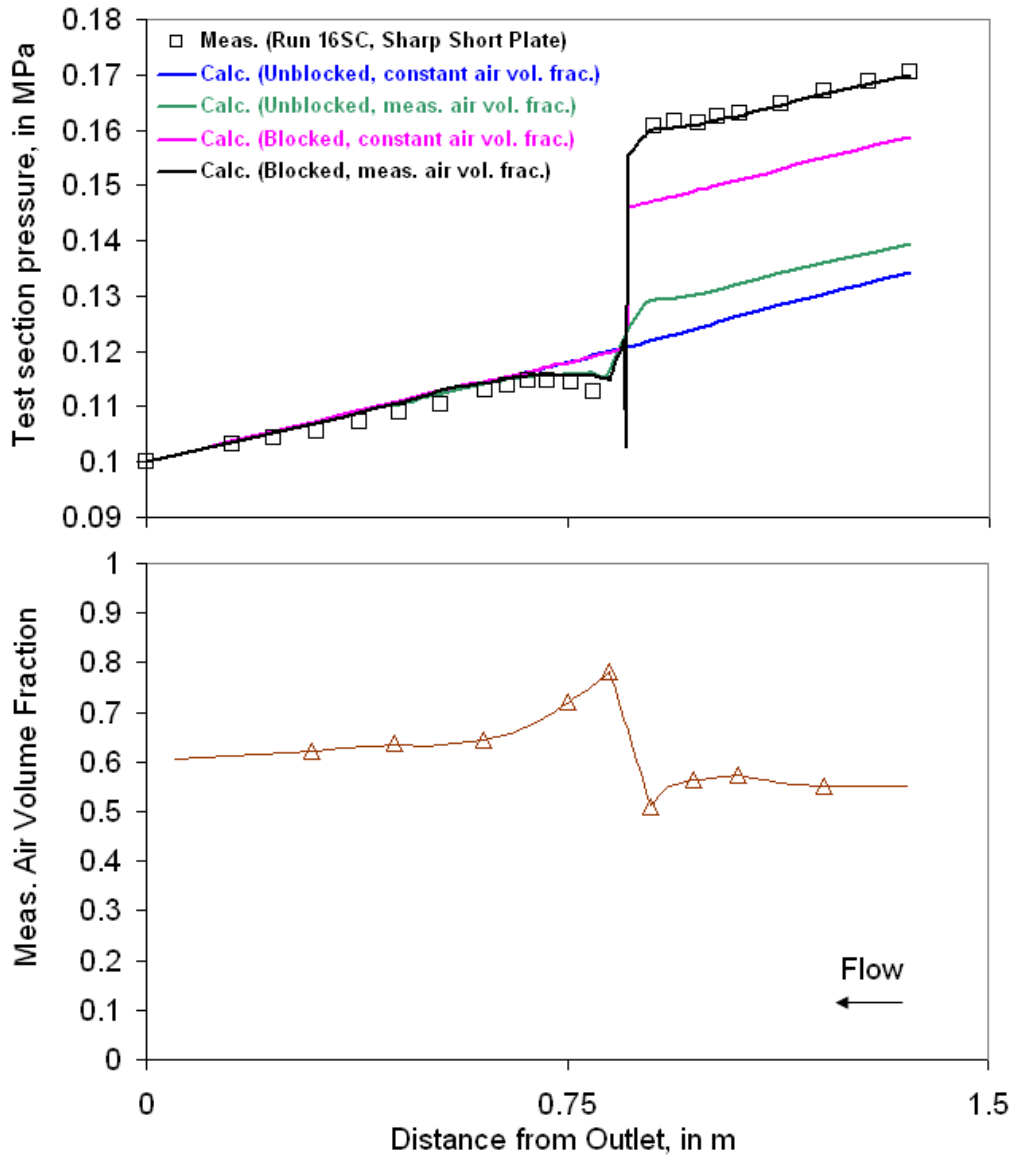

Figure 4.10.8: Careful model falsification with a representative dataset (Run 16SC) from Tapucu et al. (1988).

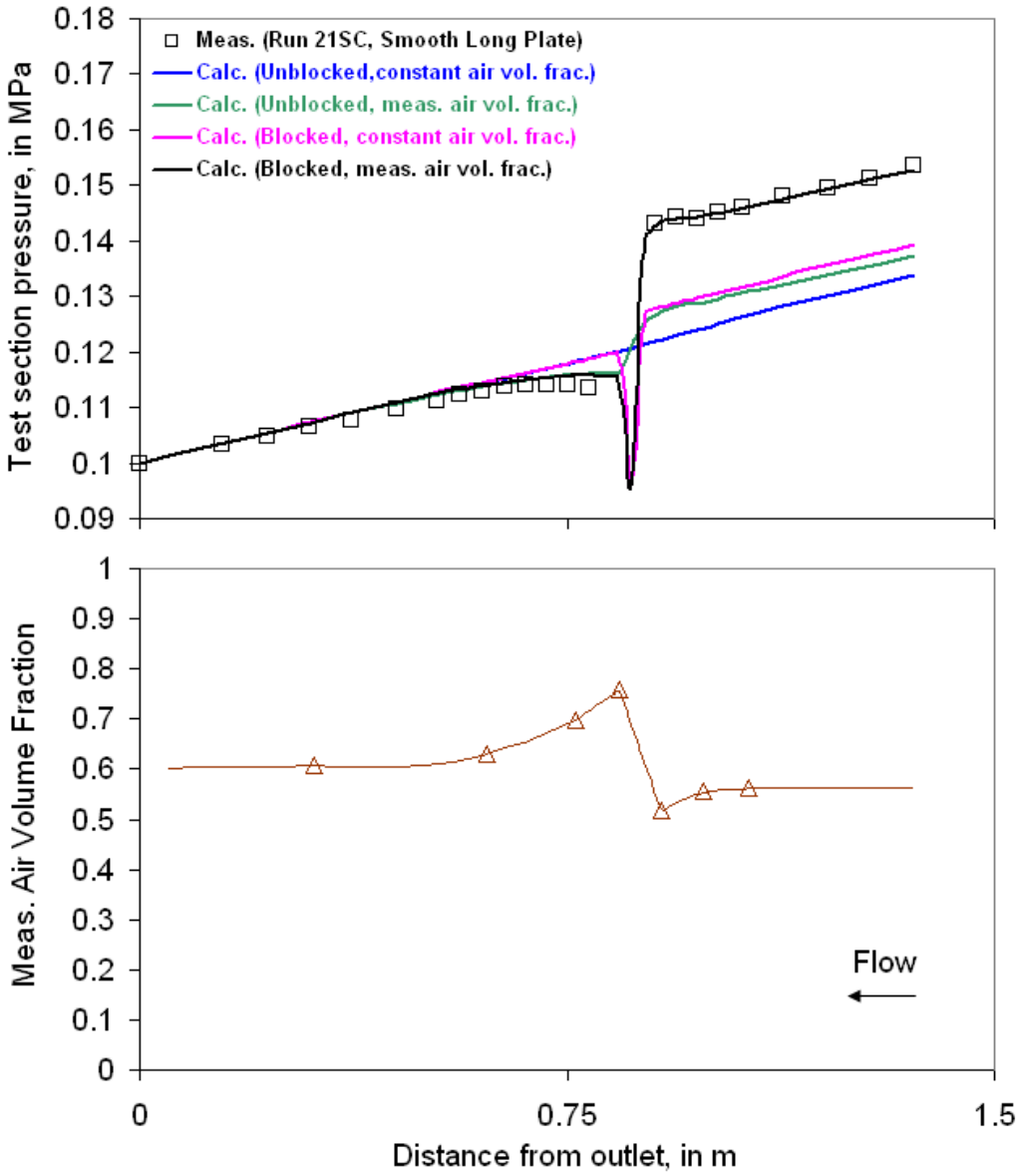

Figure 4.10.9: Careful model falsification with a representative dataset (Run 21SC) from Tapucu et al. (1988).

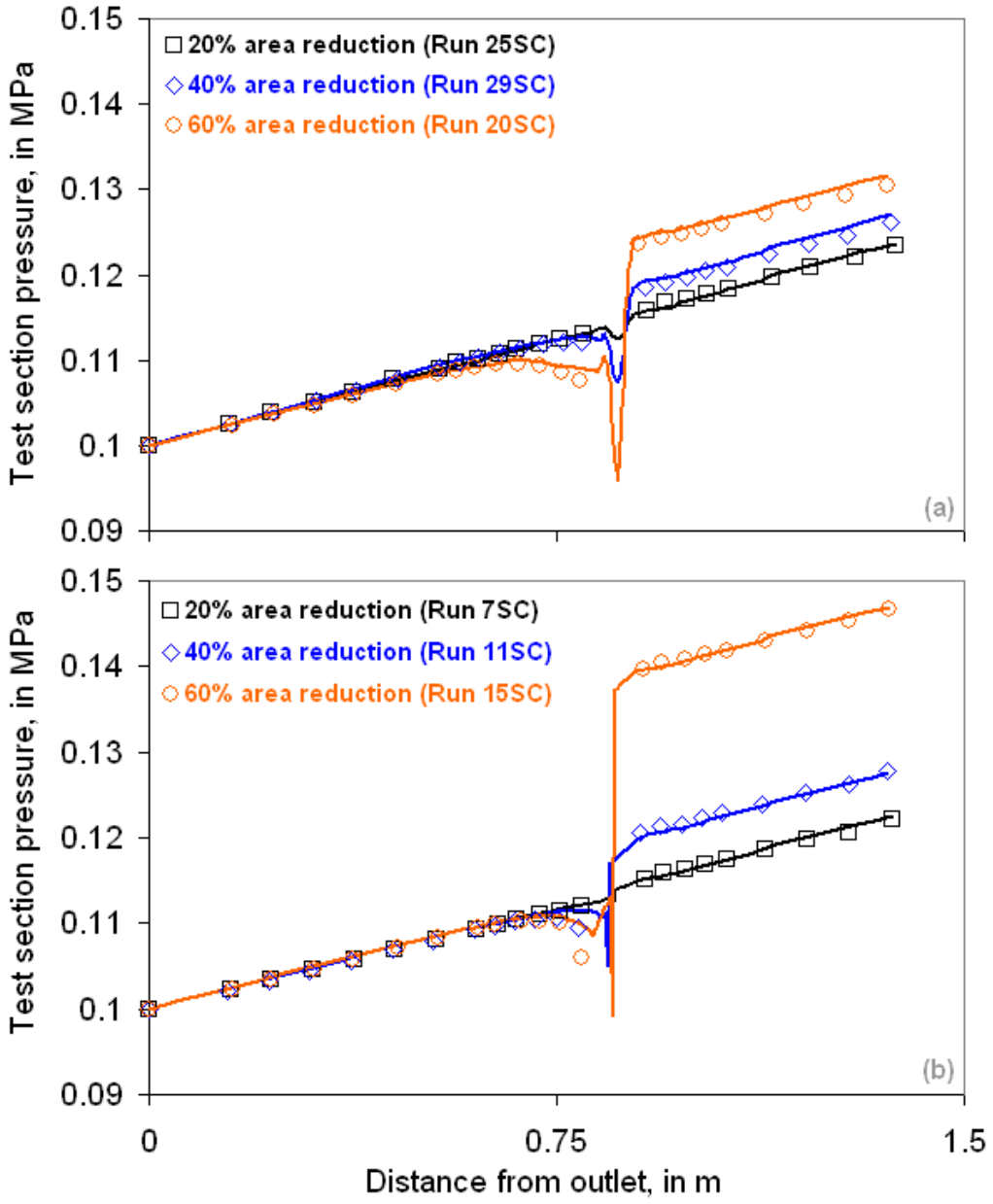

Figure 4.10.10: Model validation with representative datasets from Tapucu et al. (1988). Lines are our calculations and the points are measurements.

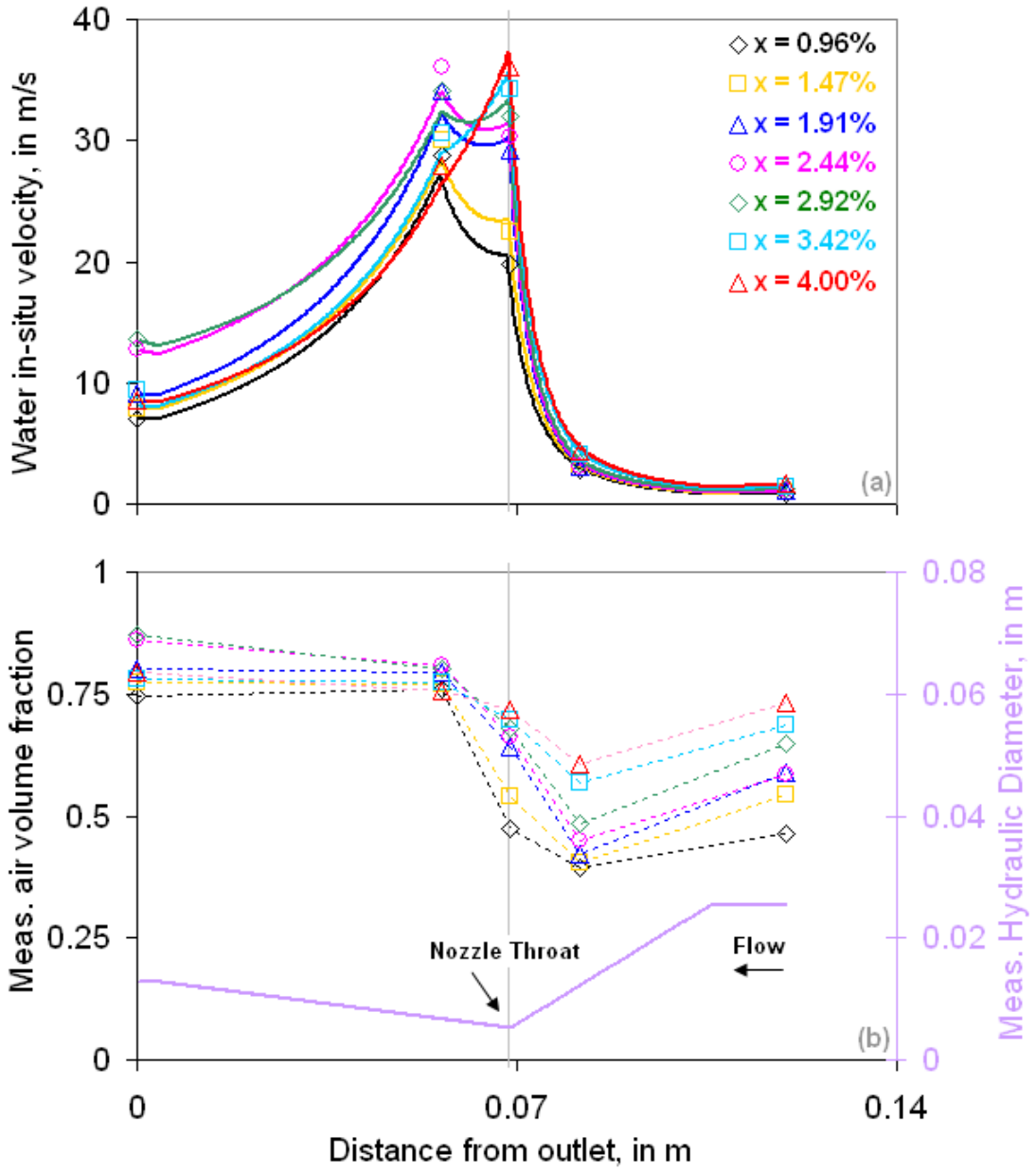

Figure 4.10.11: Model validation with representative datasets from the Vogrin (1963) multiphase nozzle flow experiments. Lines are our calculations and the points are measurements.

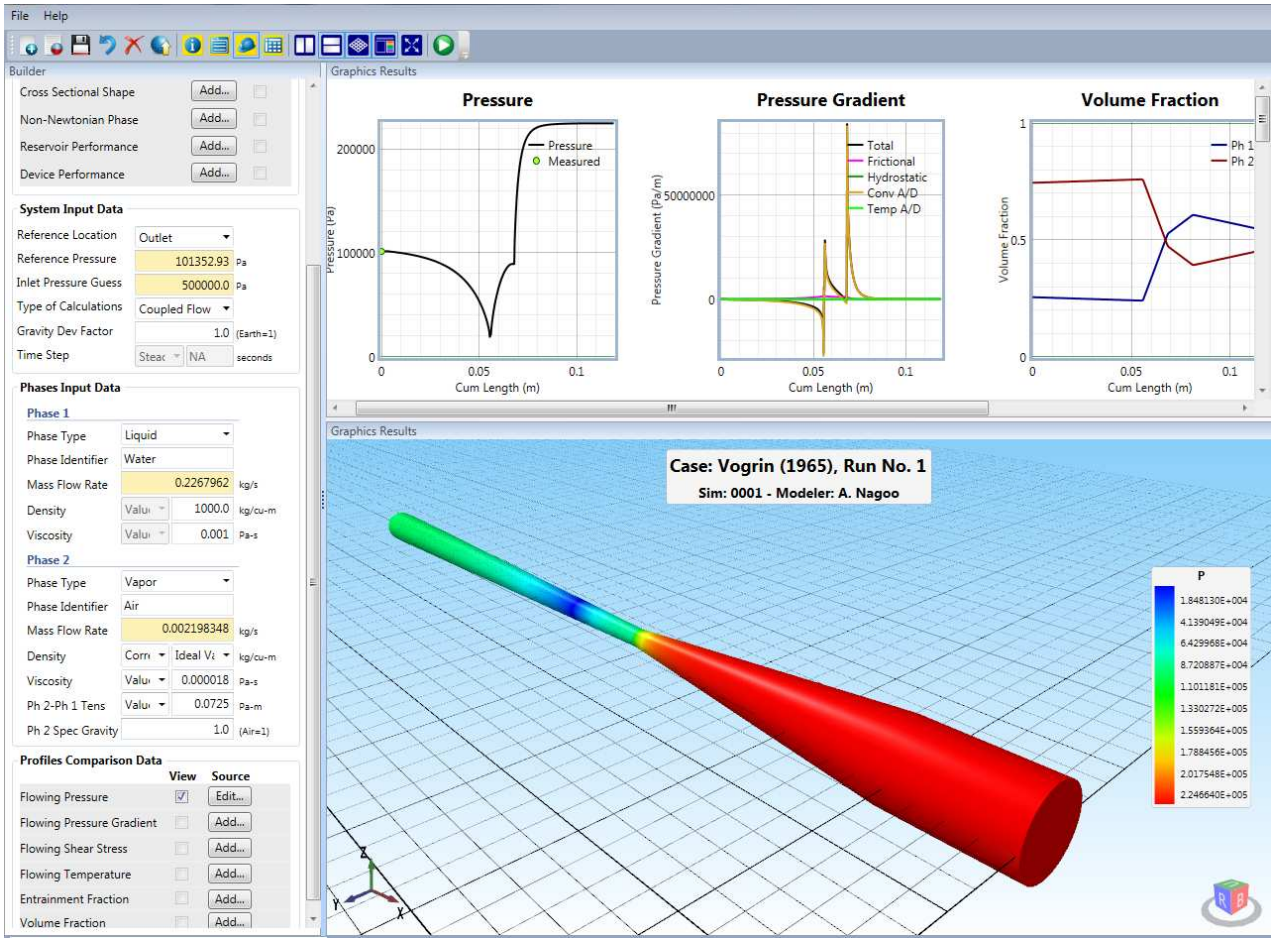

Figure 4.10.12: Example calculations for run no. 1 of Vogrin (1963) with the UTPipeFlow code.

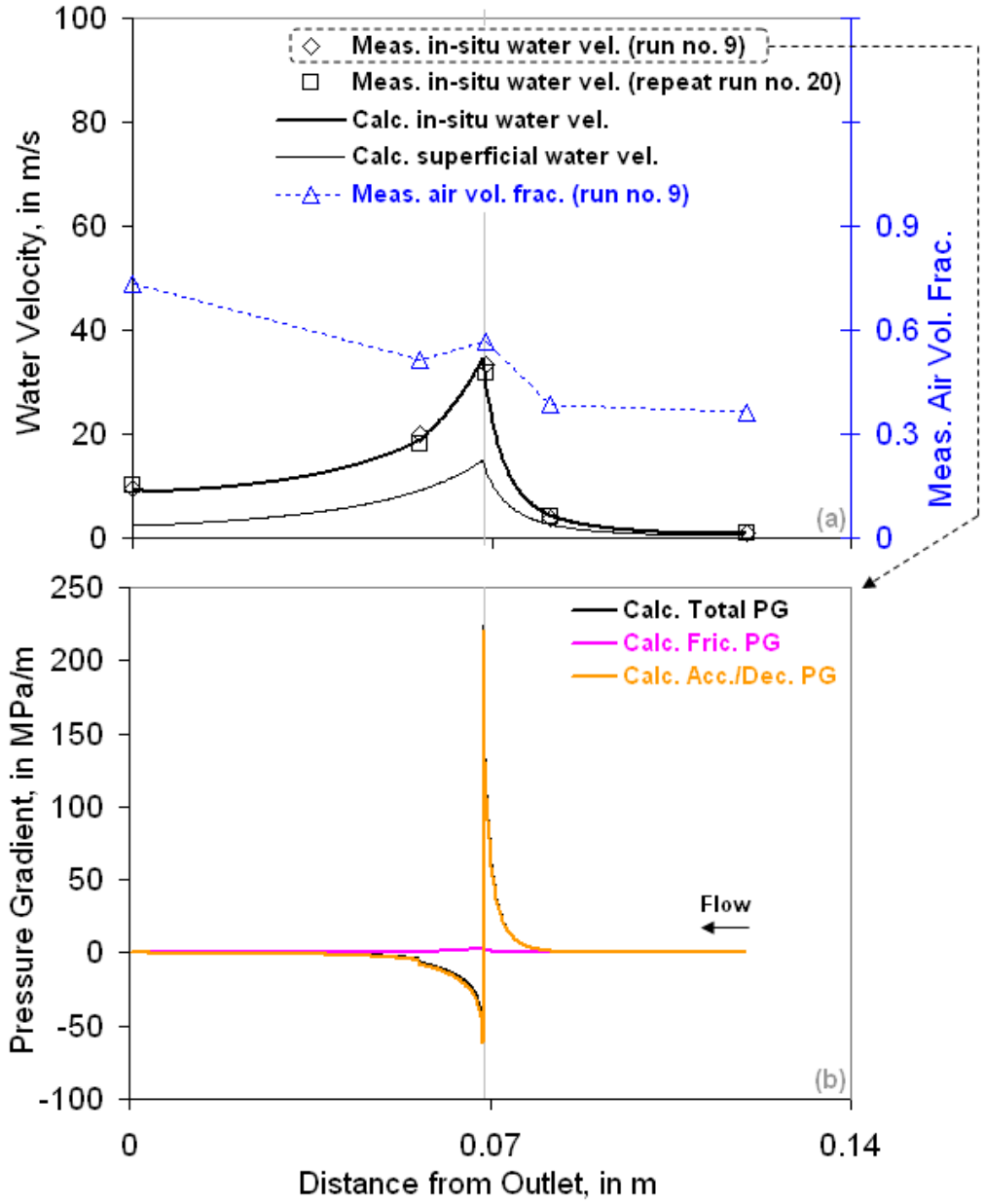

Figure 4.10.13: Example calculations for run no. 9 (low air volume fraction) of Vogrin (1963) with the UTPipeFlow code.

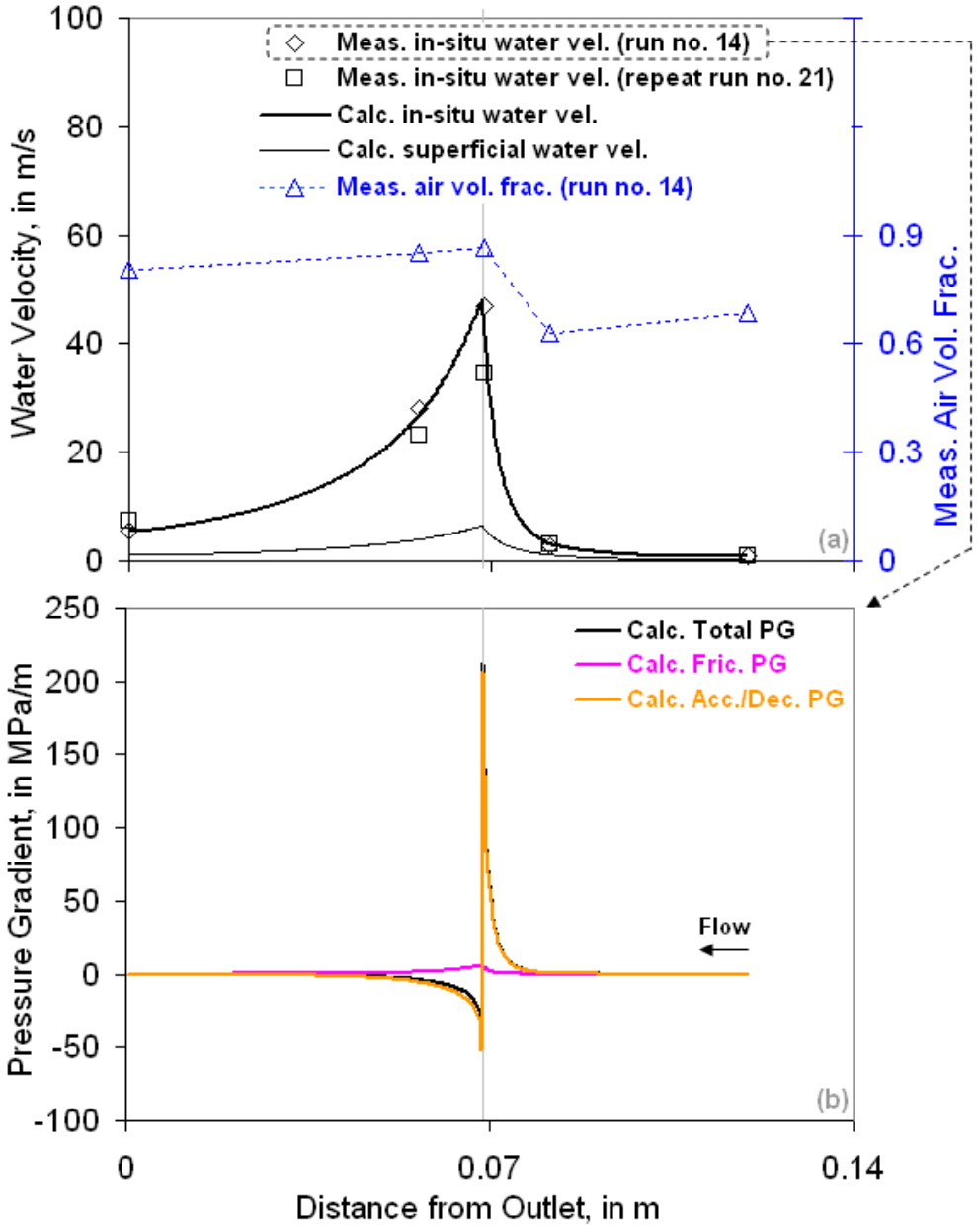

Figure 4.10.14: Example calculations for run no. 14 (high air volume fraction) of Vogrin (1963) with the UTPipeFlow code.

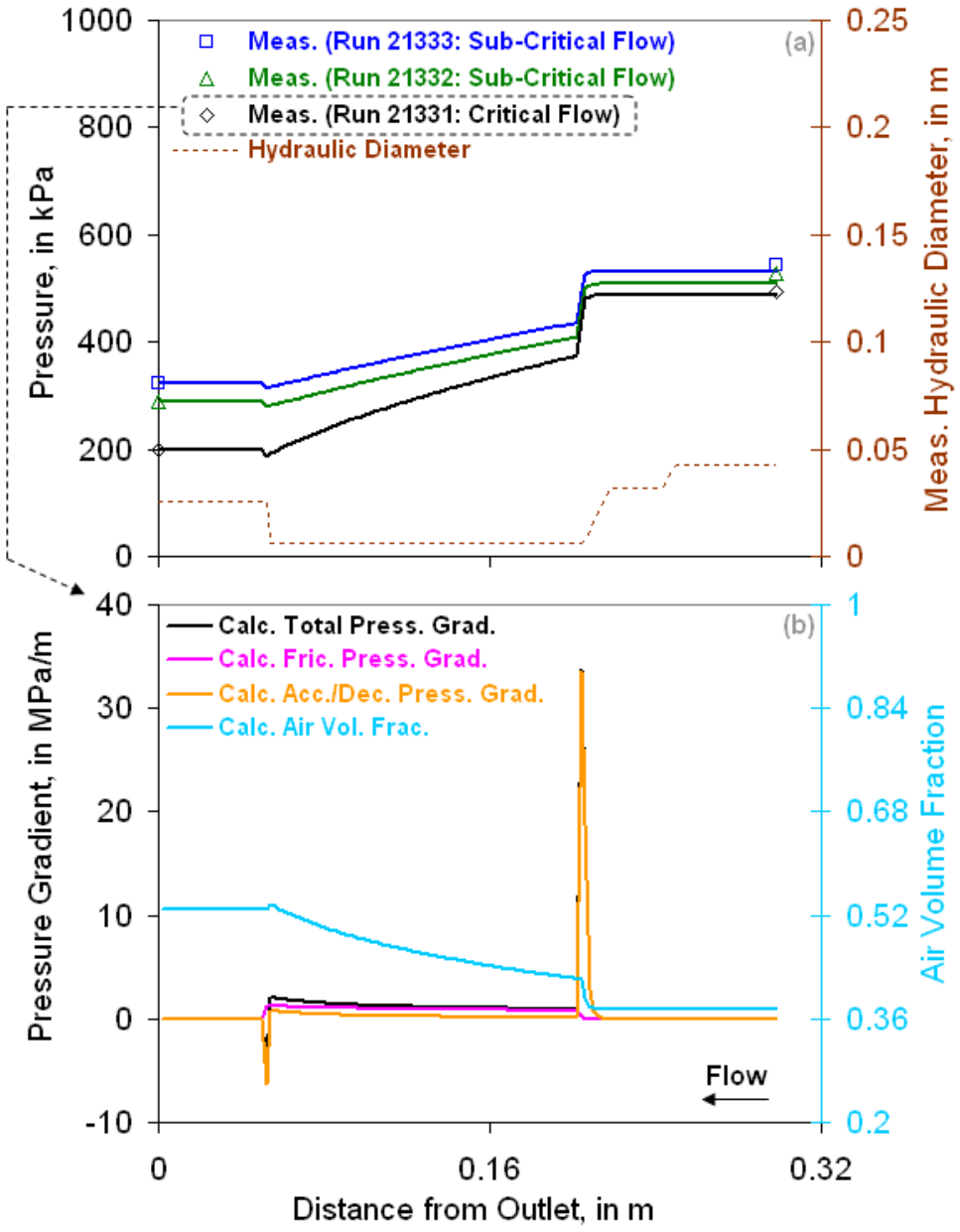

Figure 4.10.15: Prediction of representative (lower void fraction cases) sub-critical to critical multiphase choke flow datasets from Pilehvari (1980) with the ANSLIP model.

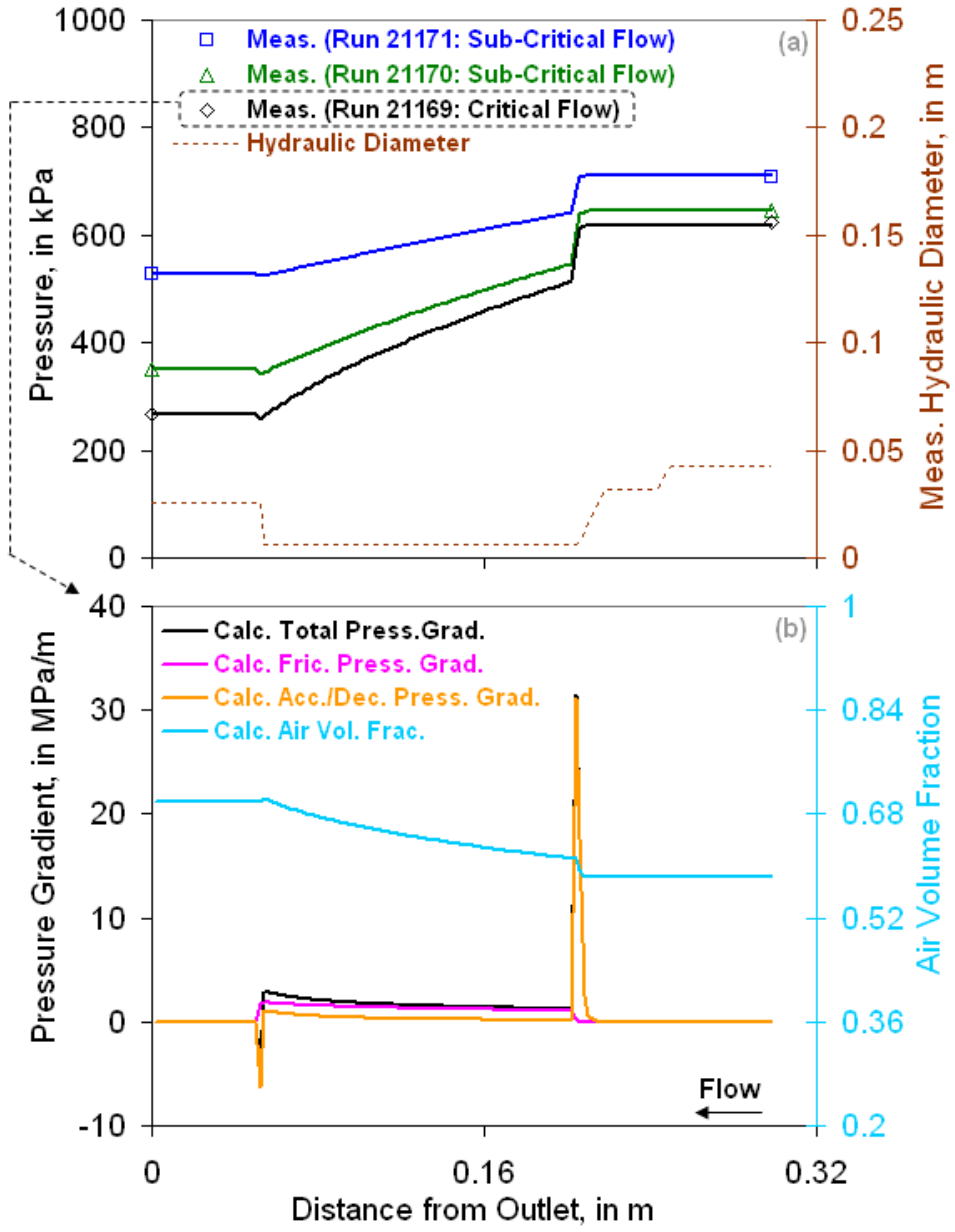

Figure 4.10.16: Prediction of representative (higher void fraction cases) sub-critical to critical multiphase choke flow datasets from Pilehvari (1980) with the ANSLIP model.

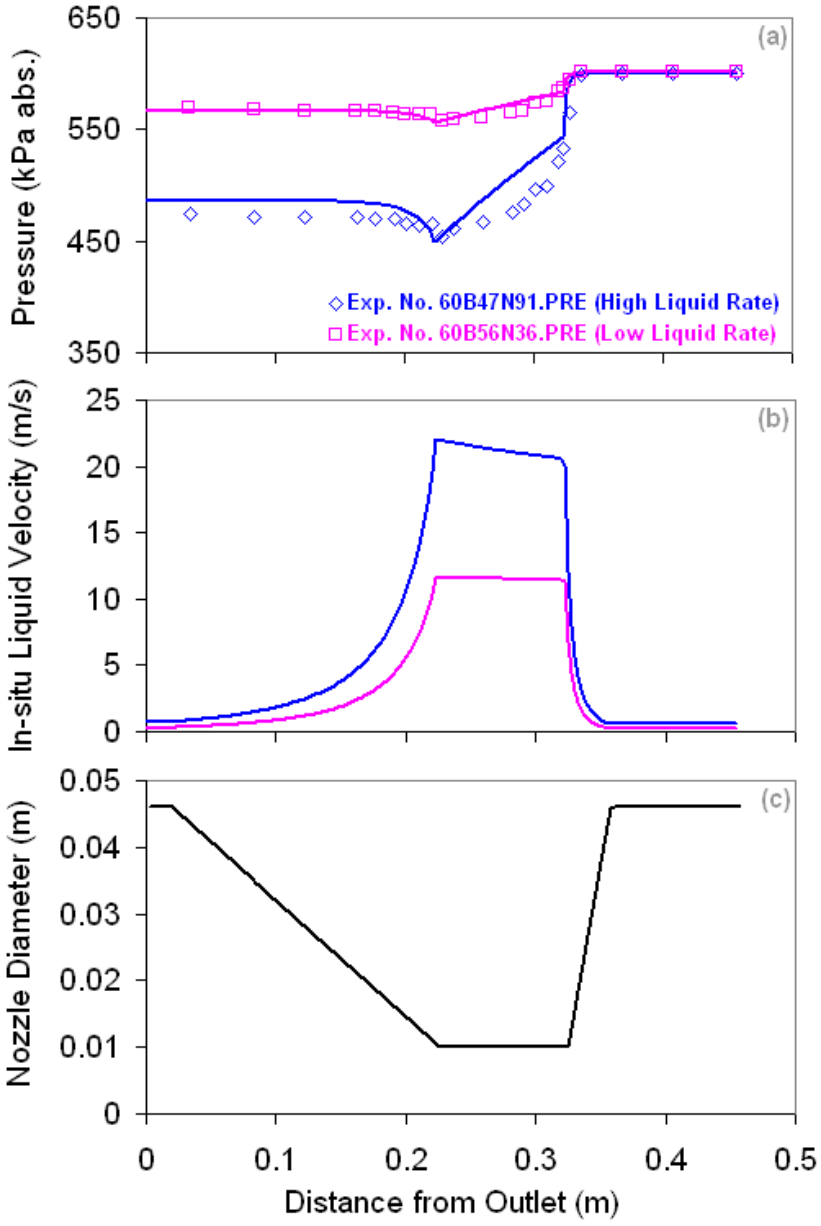

Figure 4.10.17: Prediction of representative critical multiphase nozzle flow datasets from Camelo et al. (1995) with the WOLGHA model. Lines are our predictions and the points are measurements.

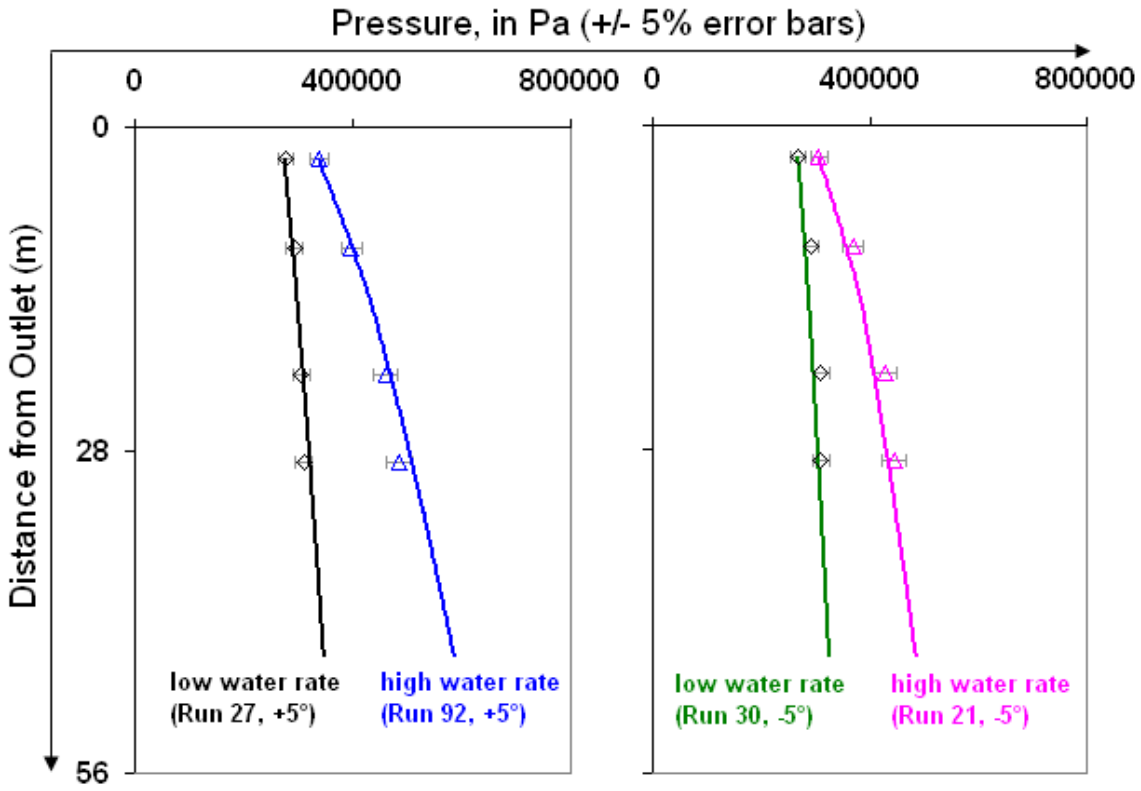

Figure 4.11.1: Prediction of representative pipeline-riser flow datasets from Juprasert (1980) with the MIST flow model. Lines are our predictions and the points are measurements.

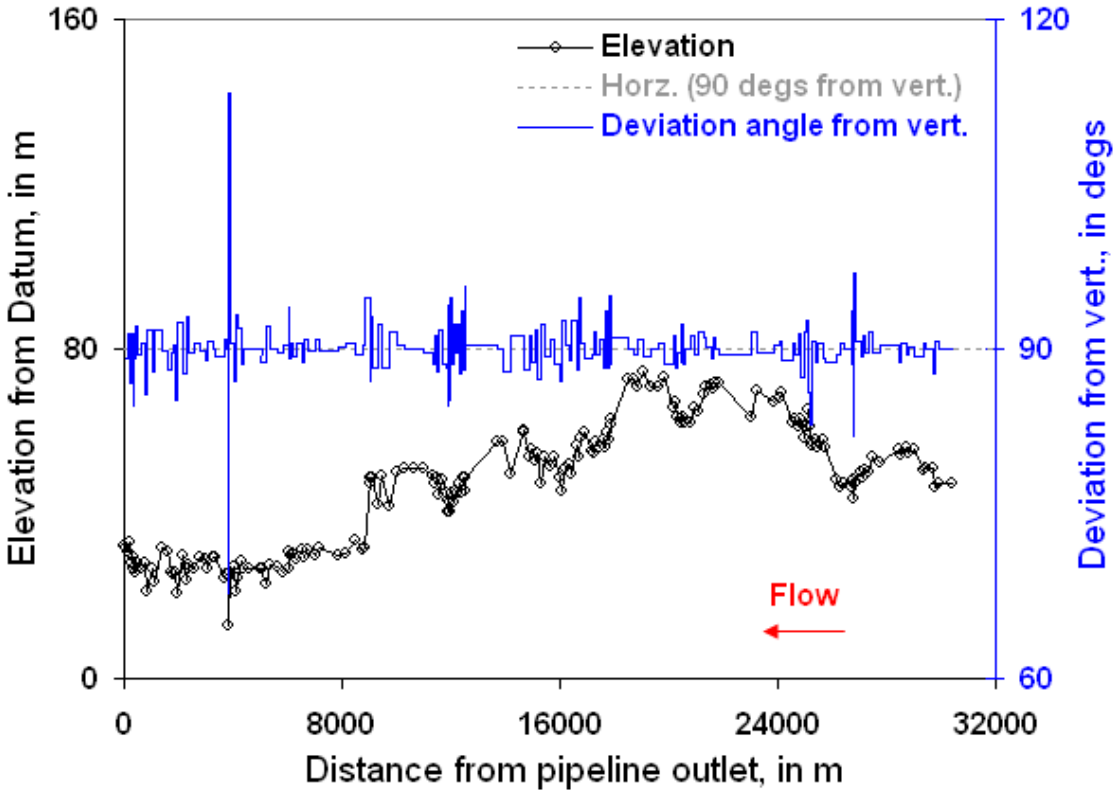

Figure 4.11.2: Elevation profile of the pipeline network in Gregory et al. (1975).

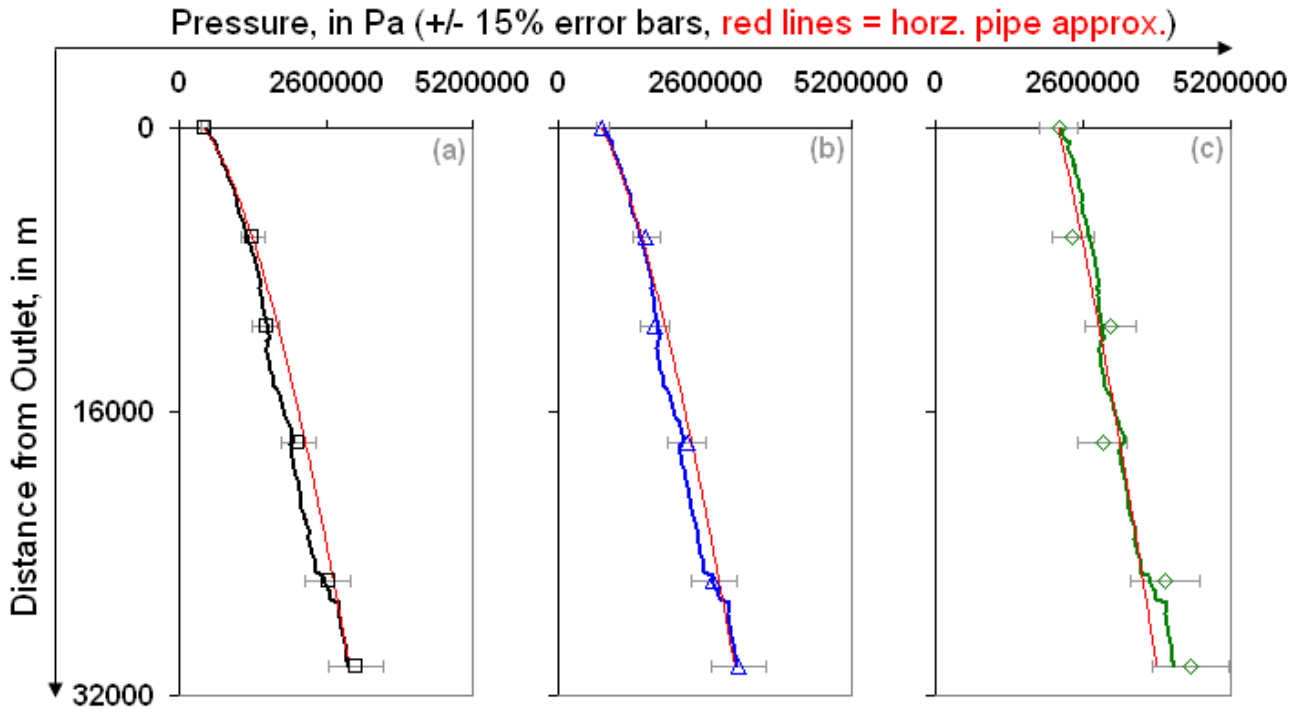

Figure 4.11.3: Prediction of representative pipeline network datasets from Gregory et al. (1975). Lines are our predictions and the points are measurements.

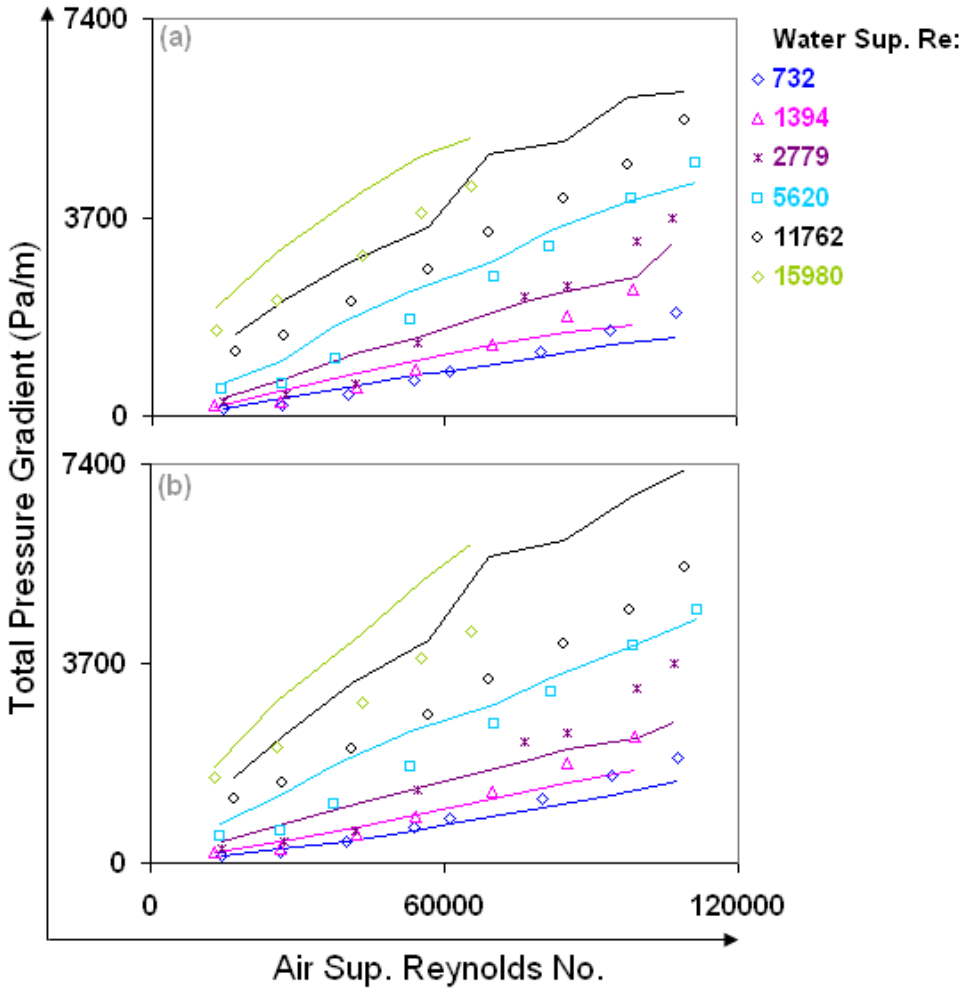

Figure 4.12.1: Representative datasets from the helical coil (coiled tubing) experiments of Boyce et al. (1968). Lines are our calculations and the points are measurements.

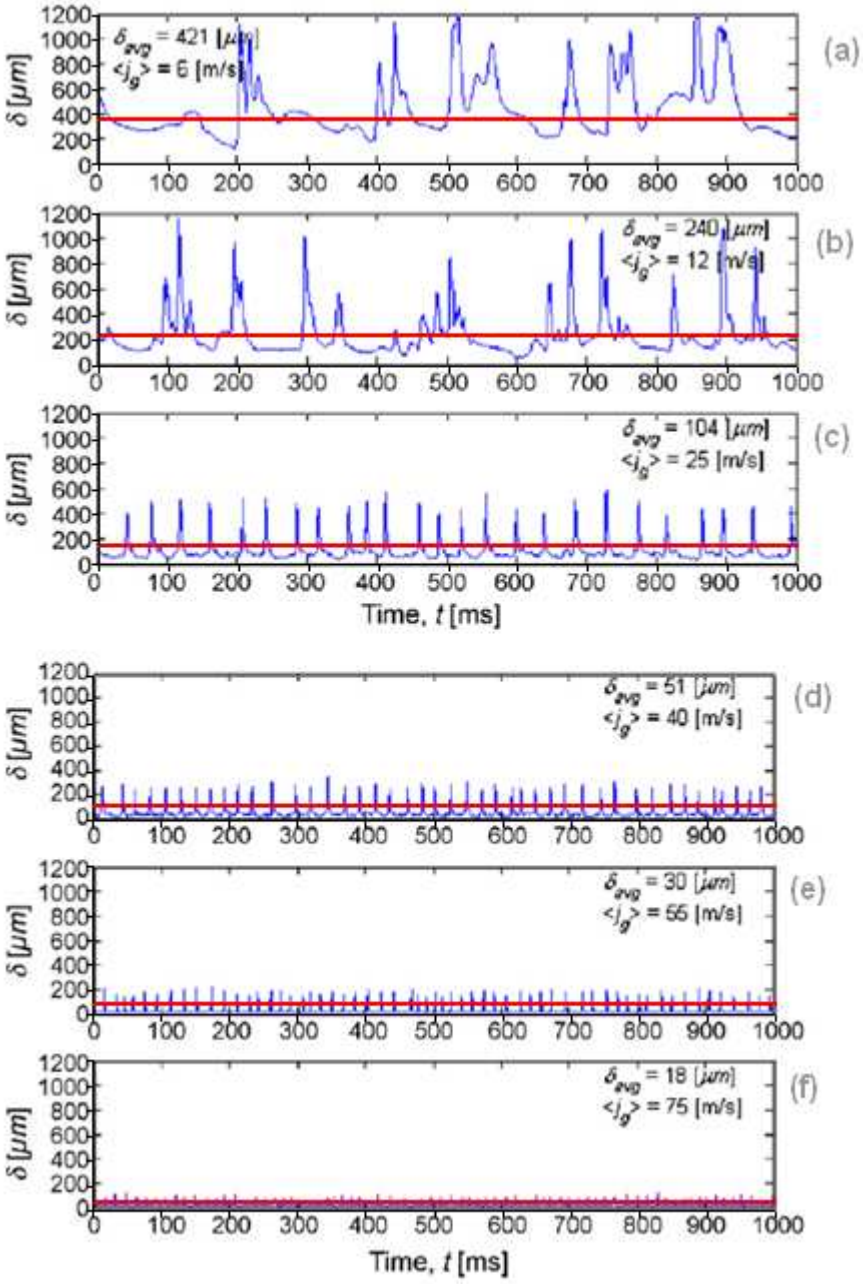

Figure 4.12.2: Prediction of the mean film thickness in Fig. 7 of Sawant et al. (2008) with the WOLGHA model.

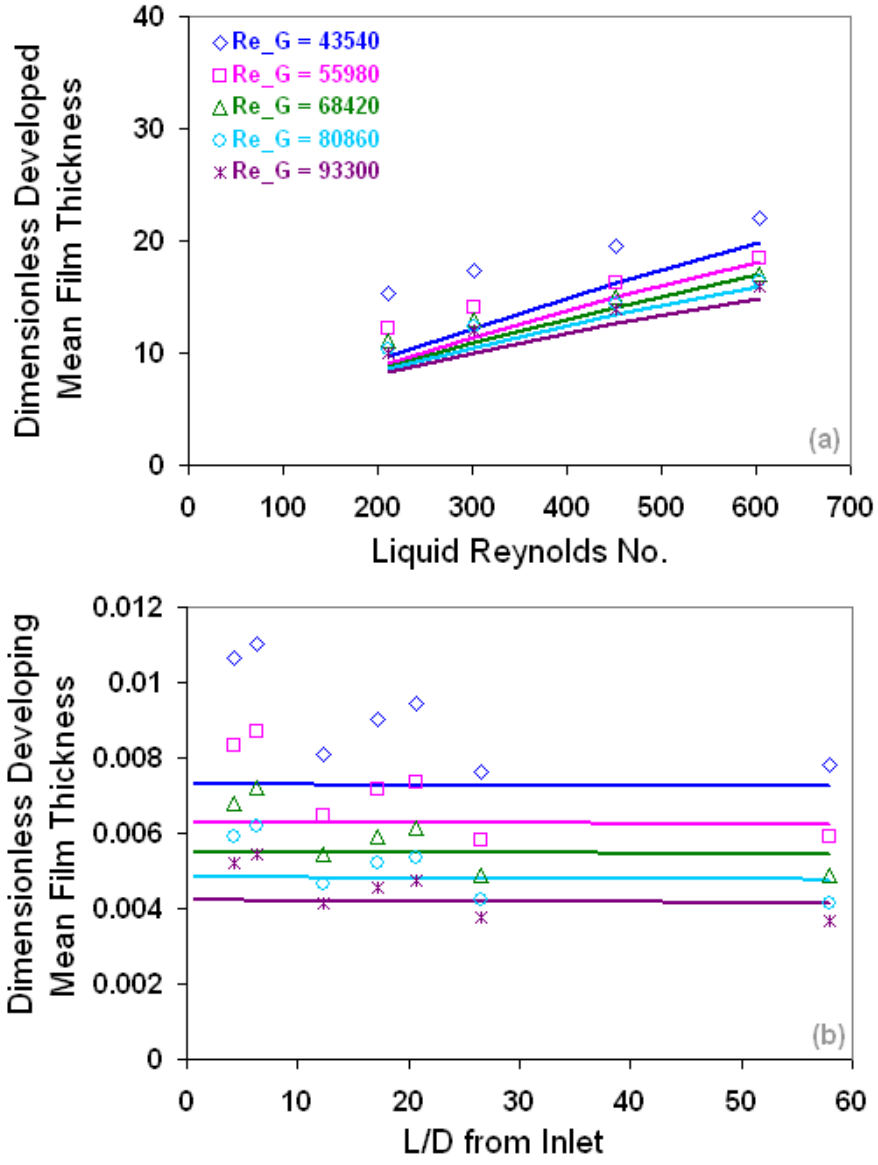

Figure 4.12.3: Prediction of the developing and developed dimensionless mean film thickness in Zhao et al. (2013) with the ANSLIP model. Lines are our predictions and the points are measurements.

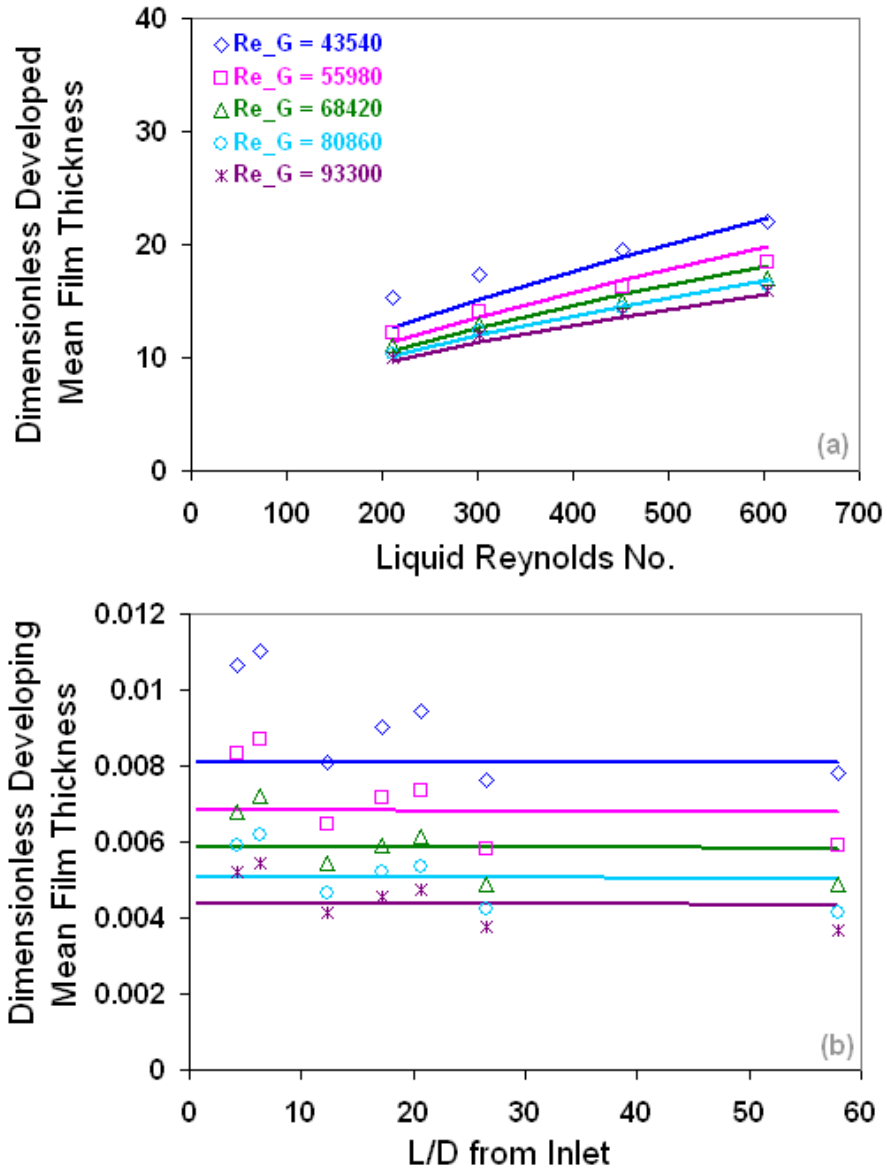

Figure 4.12.4: Prediction of the developing and developed dimensionless mean film thickness in Zhao et al. (2013) with the WOLGHA model. Lines are our predictions and the points are measurements.

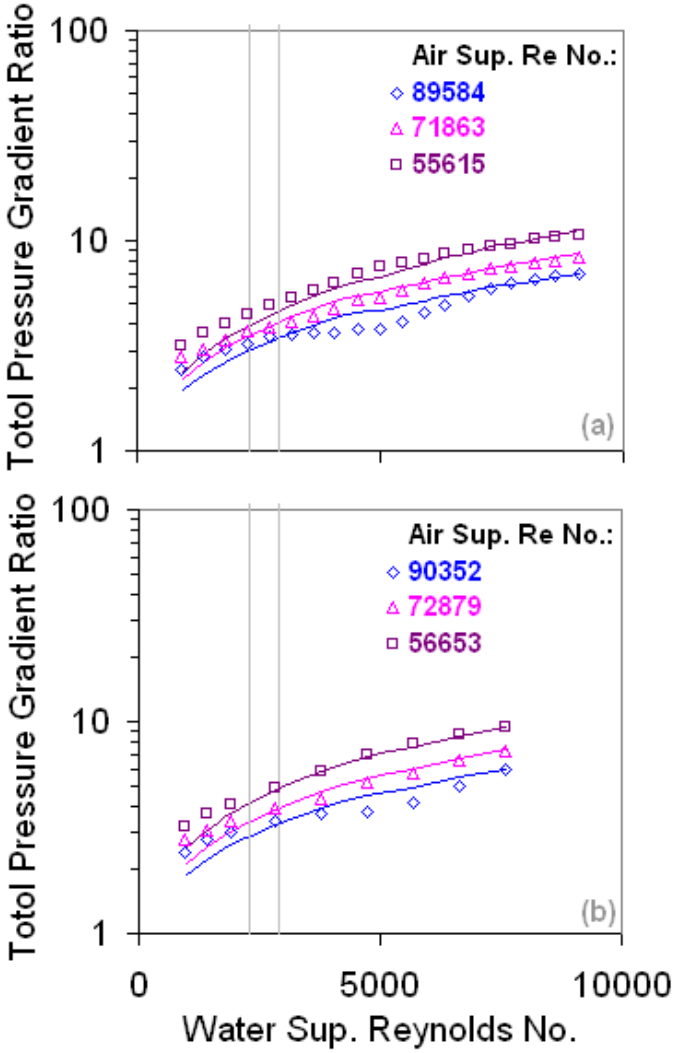

Figure 4.12.5: Prediction of the vertical annular flow datasets in Schubring (2009) for different tube materials with the ANSLIP model. Lines are our predictions and the points are measurements.

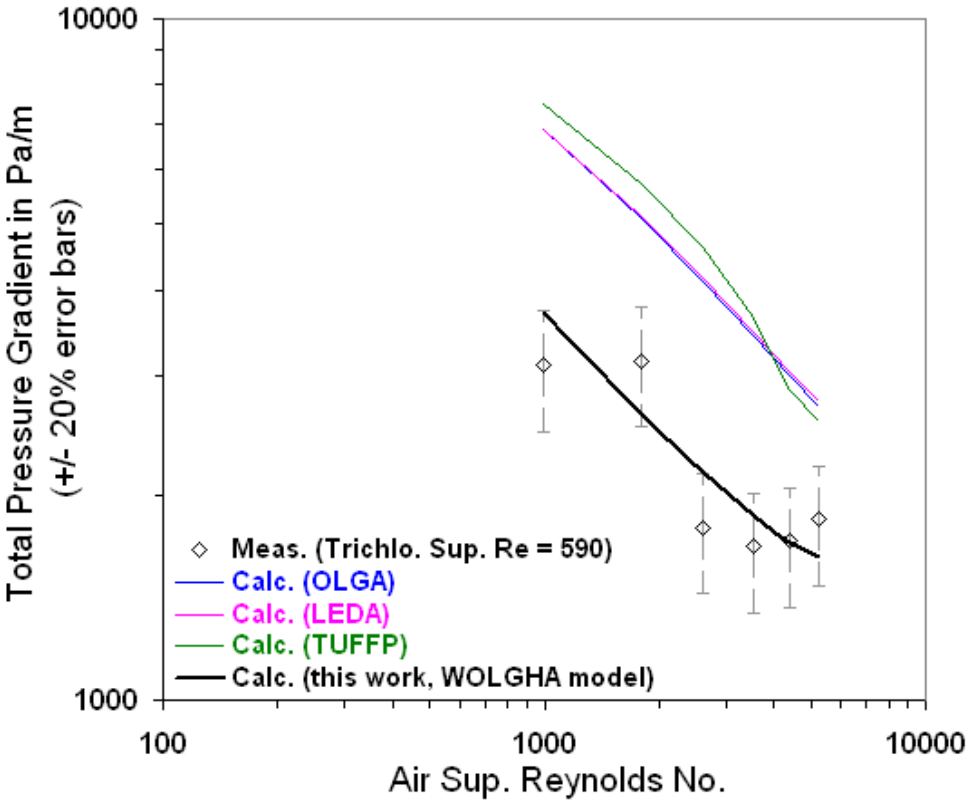

Figure 4.13.1: Comparisons of different model predictions for a dataset from Hewitt et al. (1985).

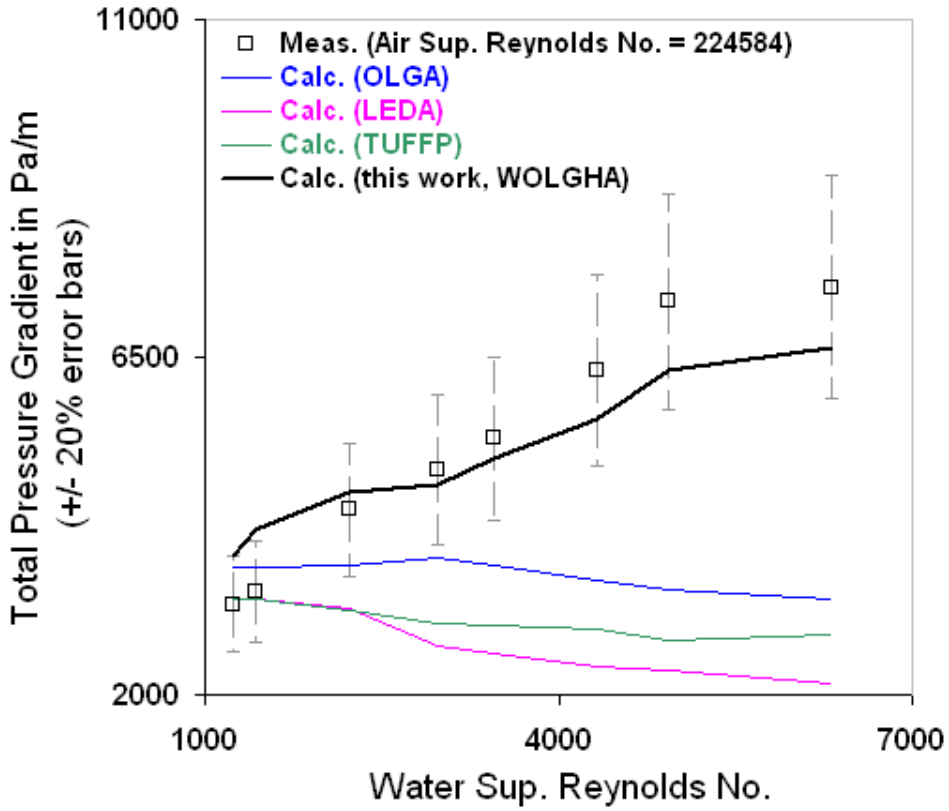

Figure 4.13.2: Comparisons of different model predictions for a dataset from Hewitt et al. (1961).

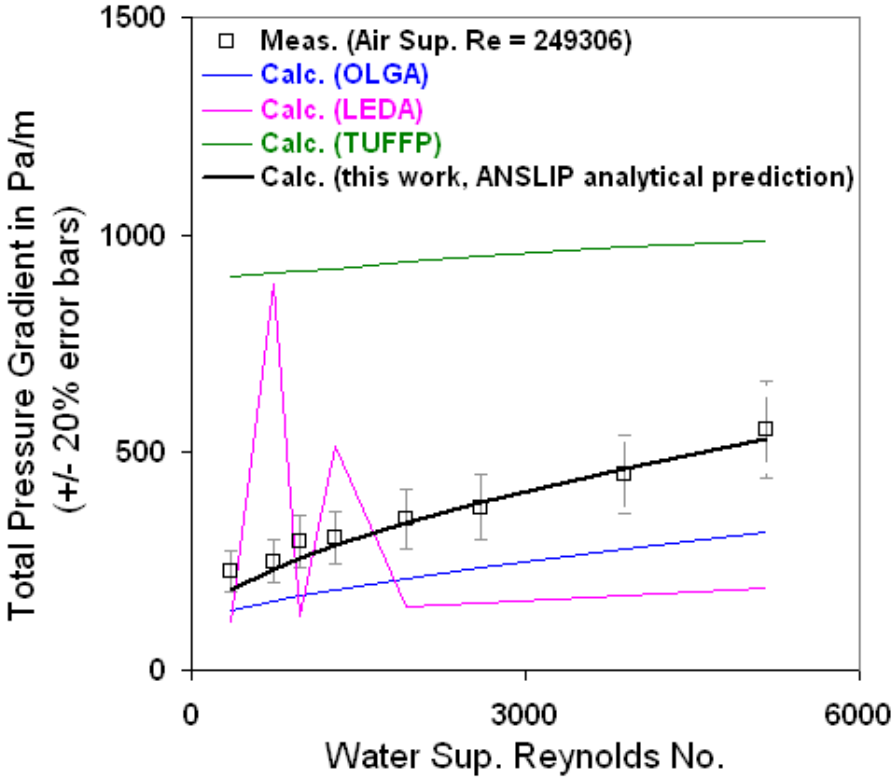

Figure 4.13.3: Comparisons of different model predictions for a dataset from Azzopardi and Gibbons (1983).

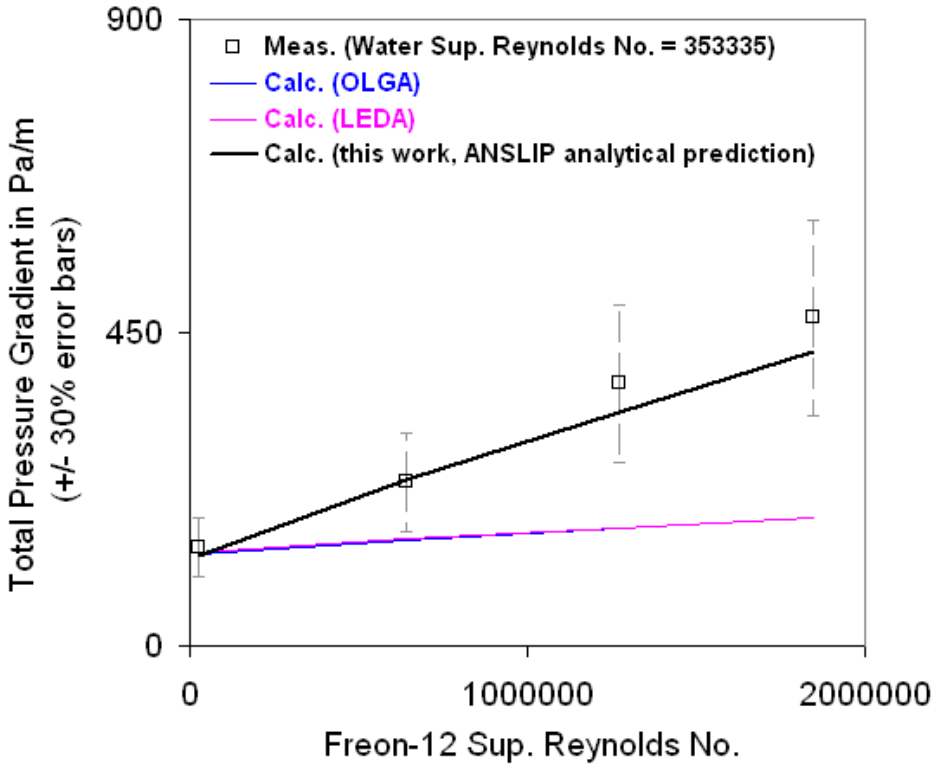

Figure 4.13.4: Comparisons of different model predictions for a dataset from Crowley et al. (1986).

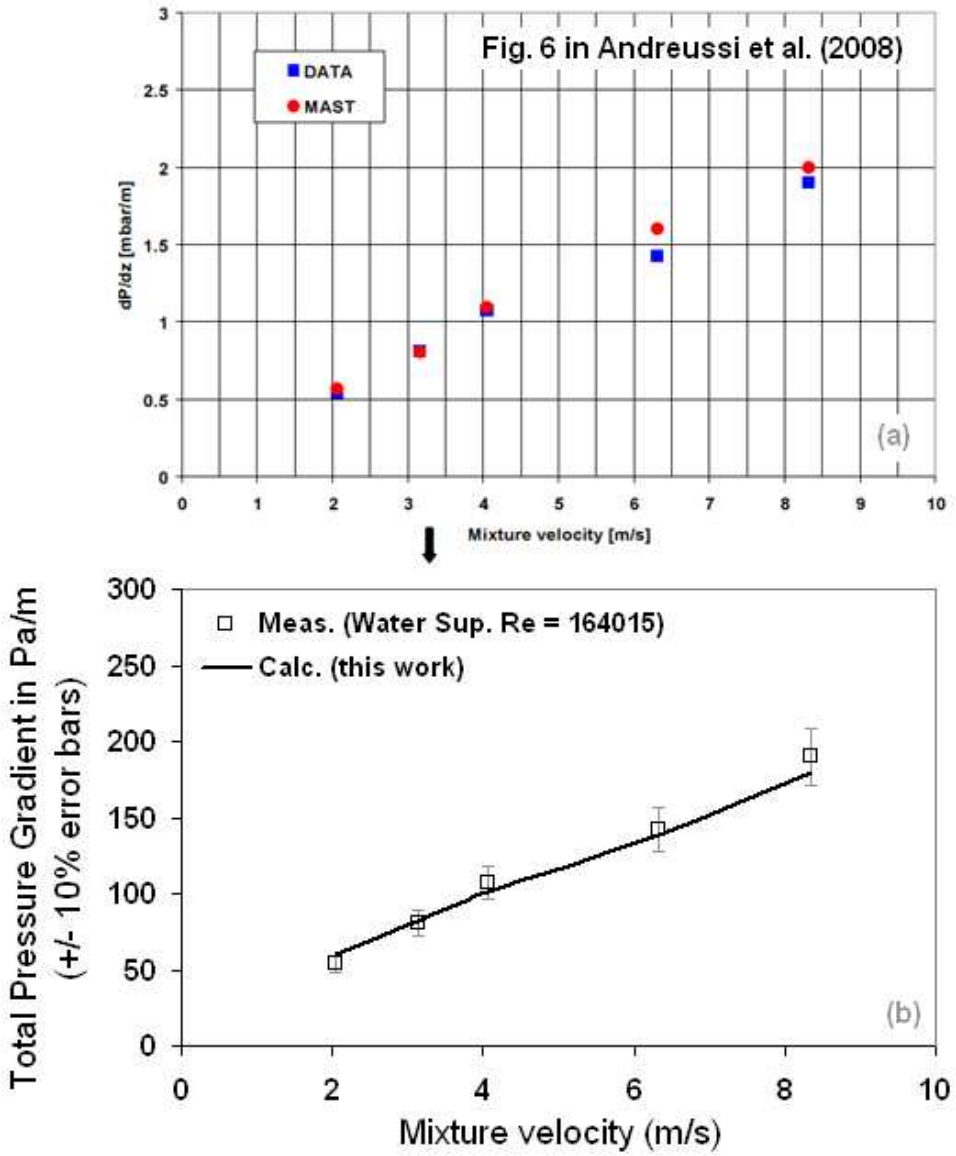

Figure 4.13.5: Comparisons of different model predictions for a dataset from Andreussi et al. (2008).

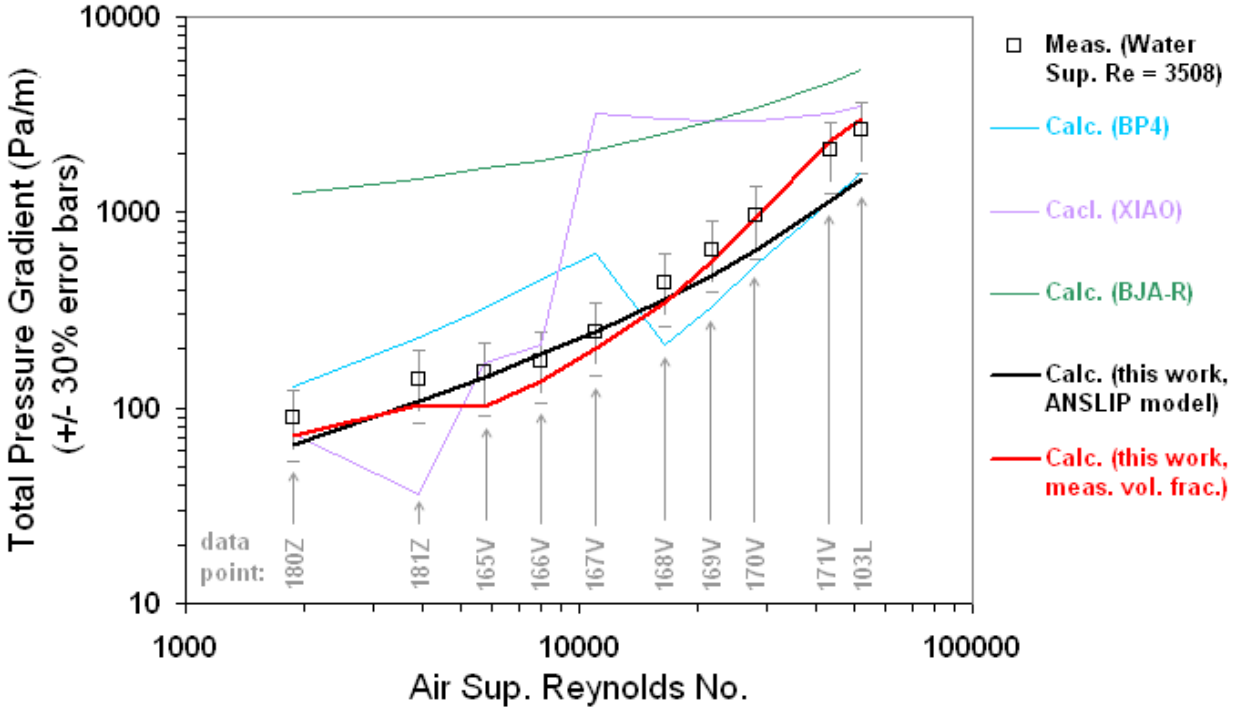

Figure 4.13.6: Comparisons of different model predictions for a dataset from Andritsos (1986).

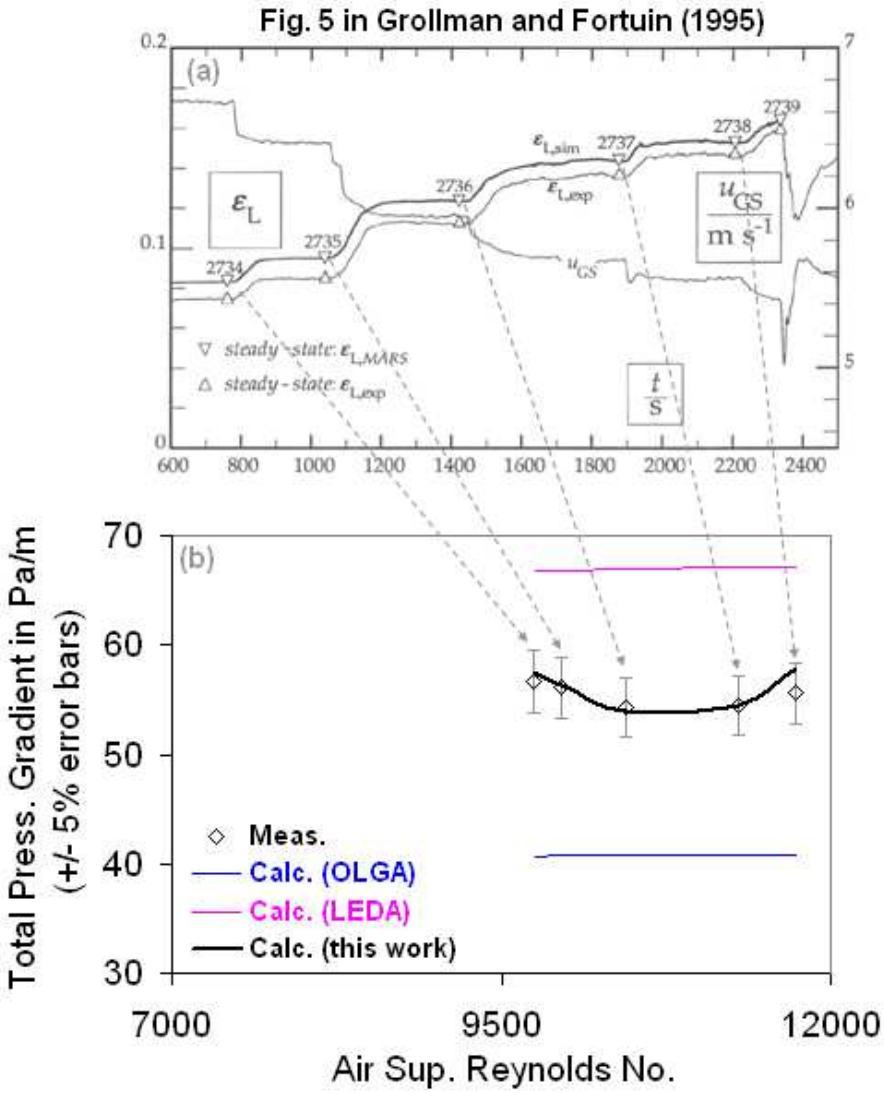

Figure 4.13.7: Model validation with representative dataset from Grollman and Fortuin (1995).

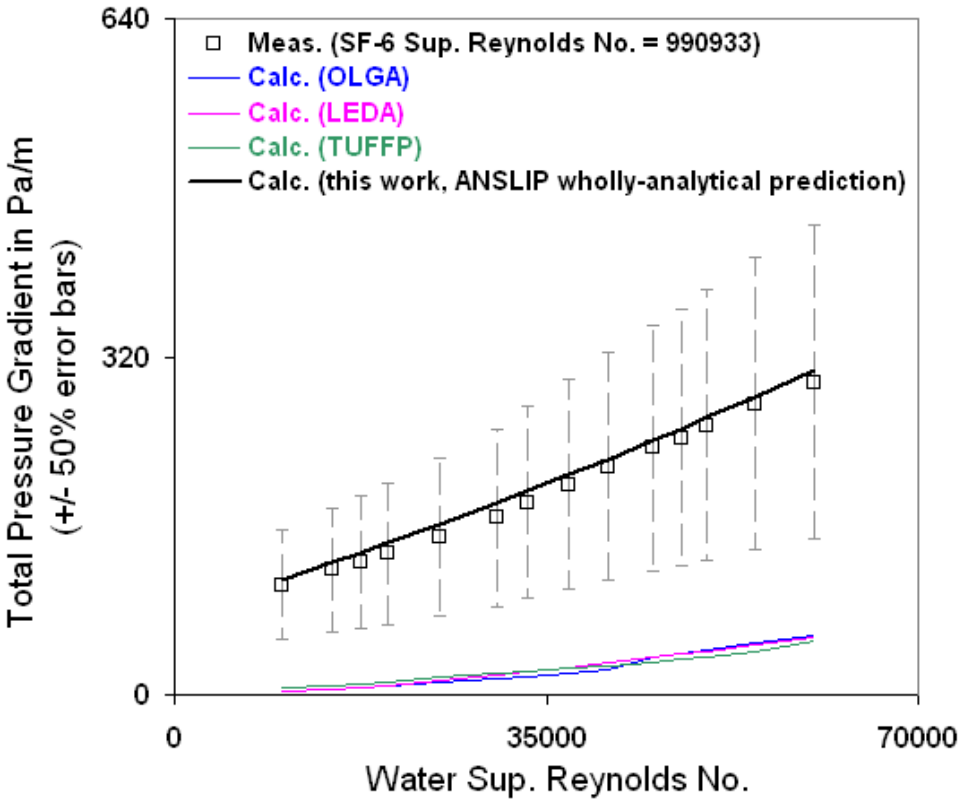

Figure 4.13.8: Comparisons of different model predictions for a dataset from Johnson (2005).

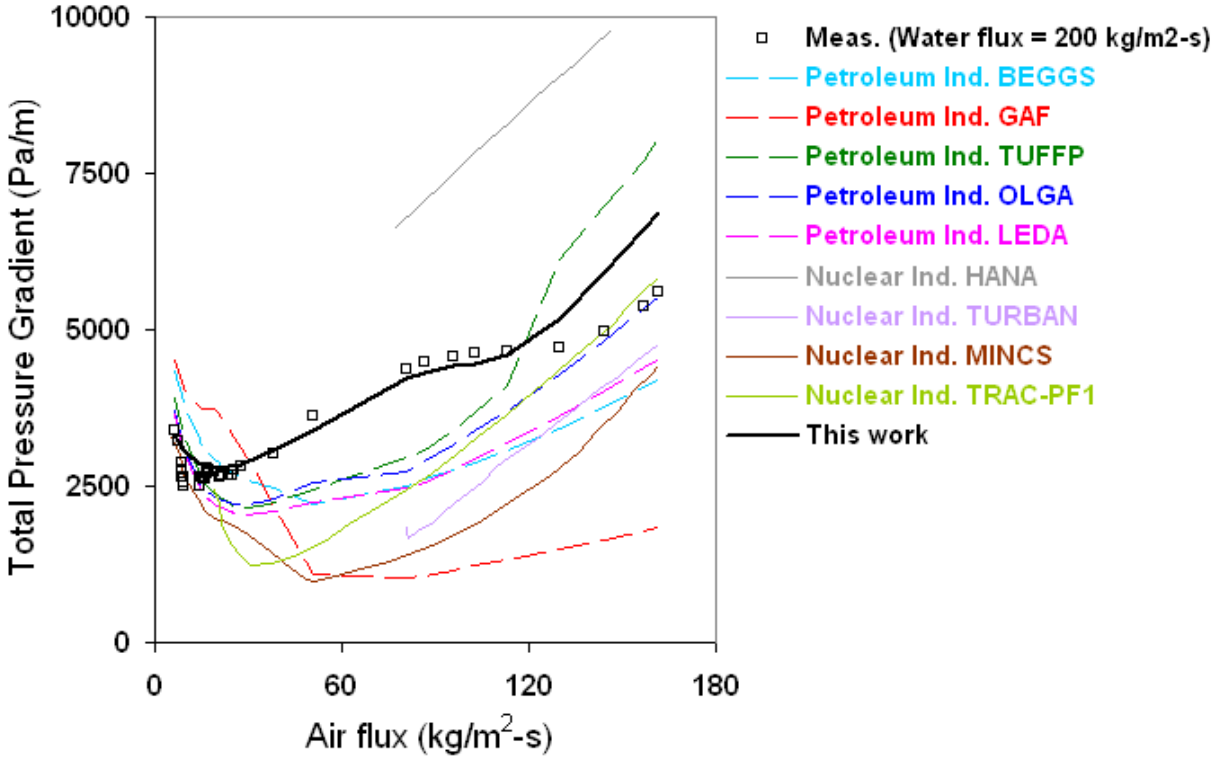

Figure 4.13.9: Comparisons of different model predictions for a dataset from Owen (1986).

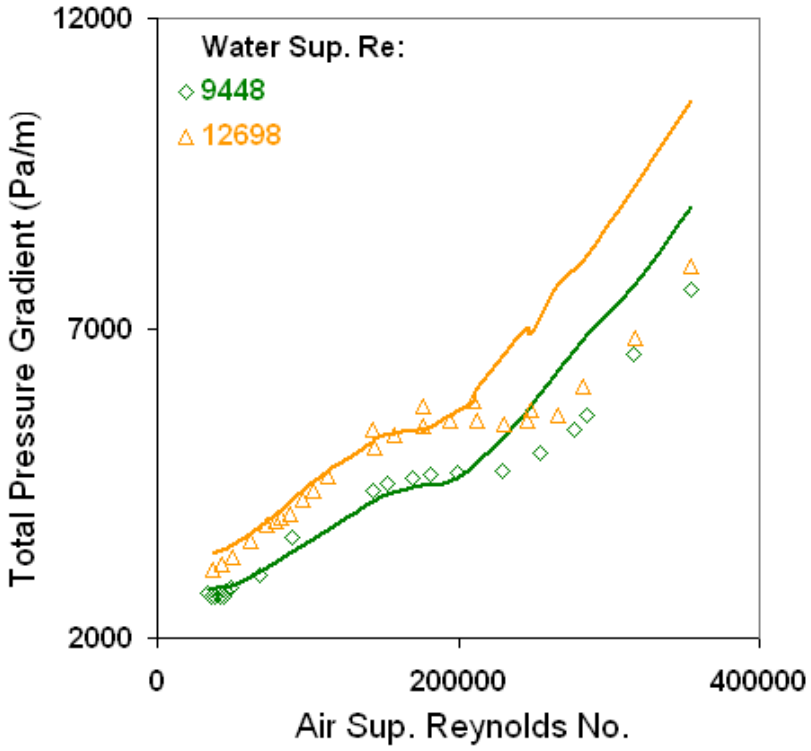

Figure 4.13.10: Prediction of two representative datasets of Owen (1986) with the ANSLIP model. Lines are our predictions and the points are measurements.

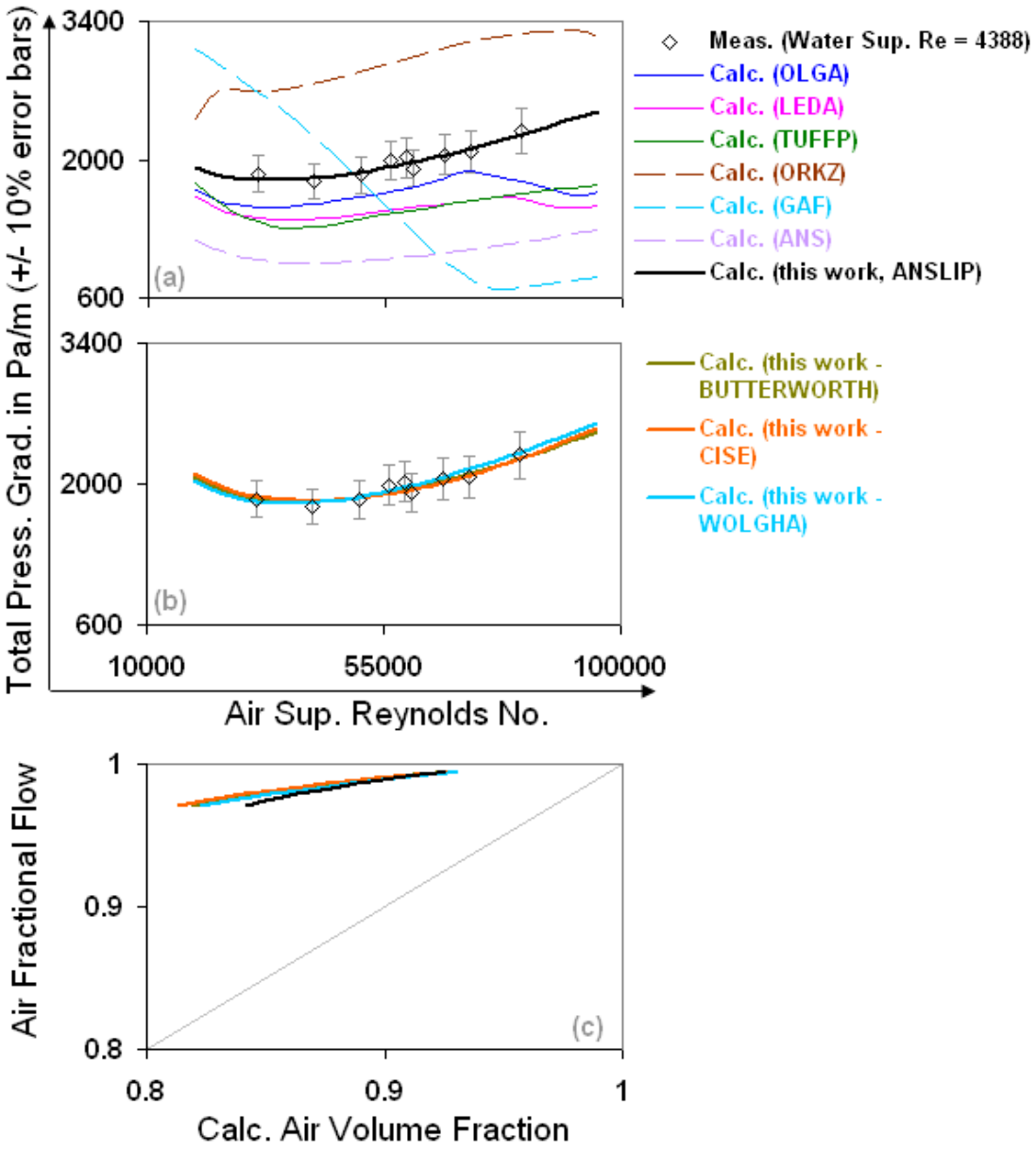

Figure 4.13.11: Comparisons of different model predictions for the churn-annular flow dataset of Barbosa Jr. et al. (2002).

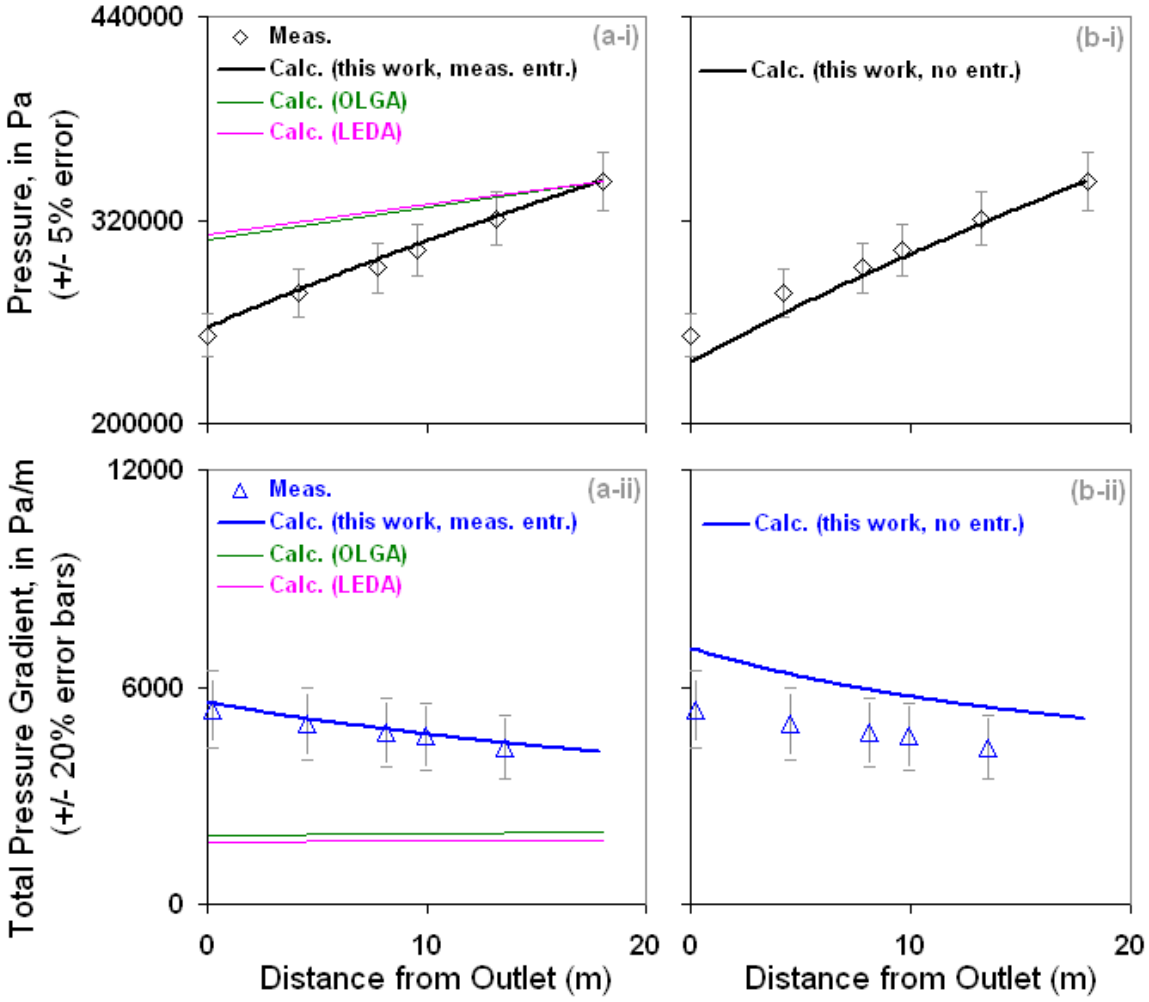

Figure 4.13.12: Comparisons of different model predictions for run 2 (high gas rate, axial jet injector) of Brown (1978).

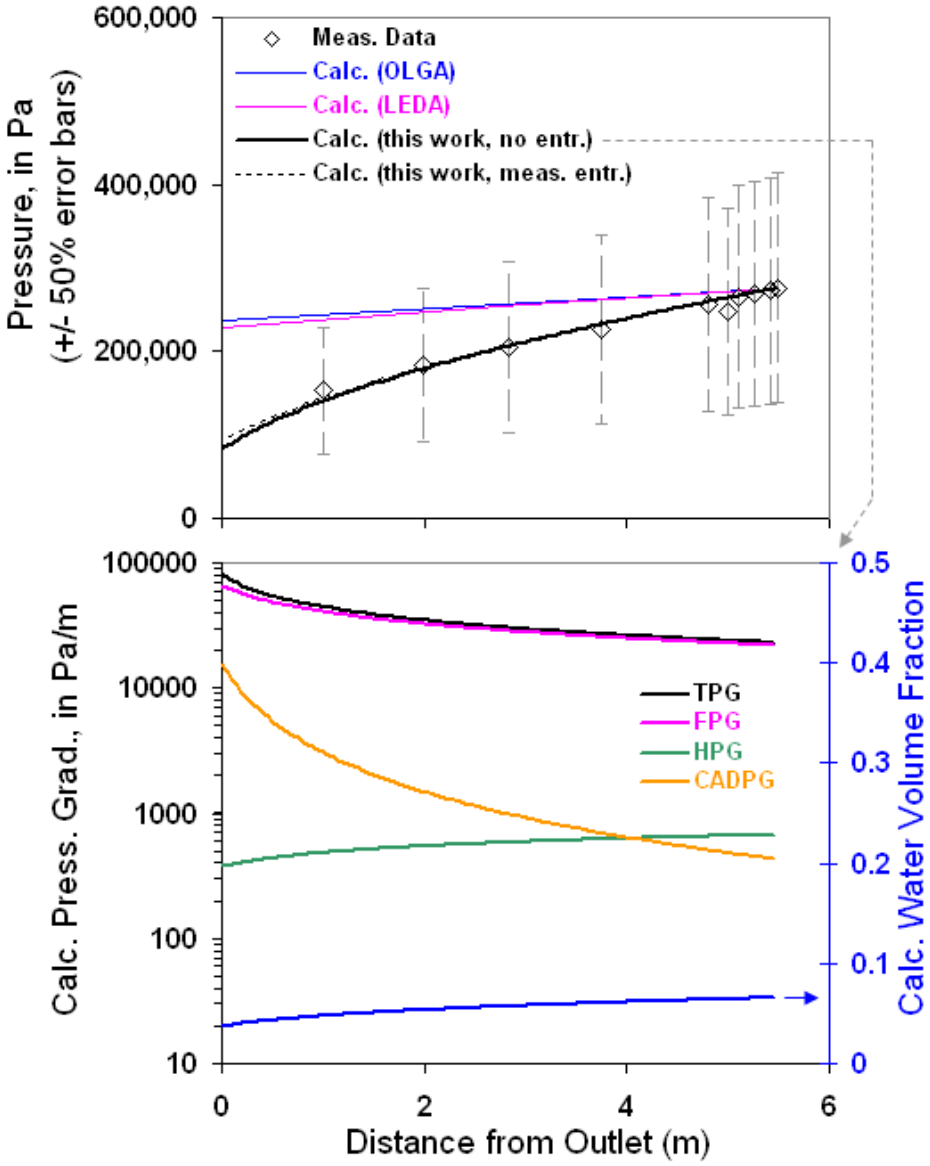

Figure 4.13.13: Comparisons of different model predictions for run 49 of Cousins et al. (1965).

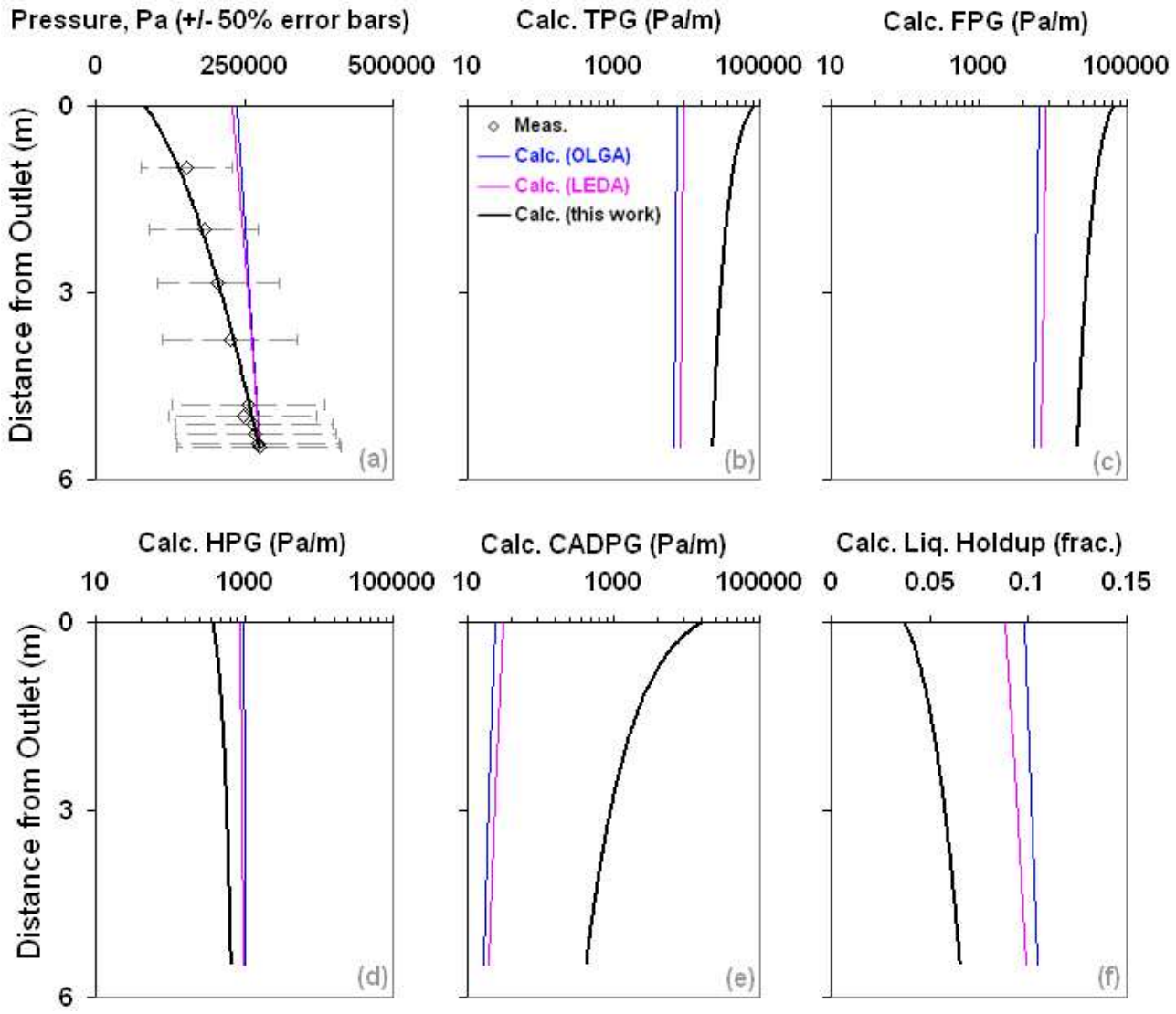

Figure 4.13.14: Comparisons of different model predictions for the pressures, pressure gradients and liquid holdup for run 49 of Cousins et al. (1965).

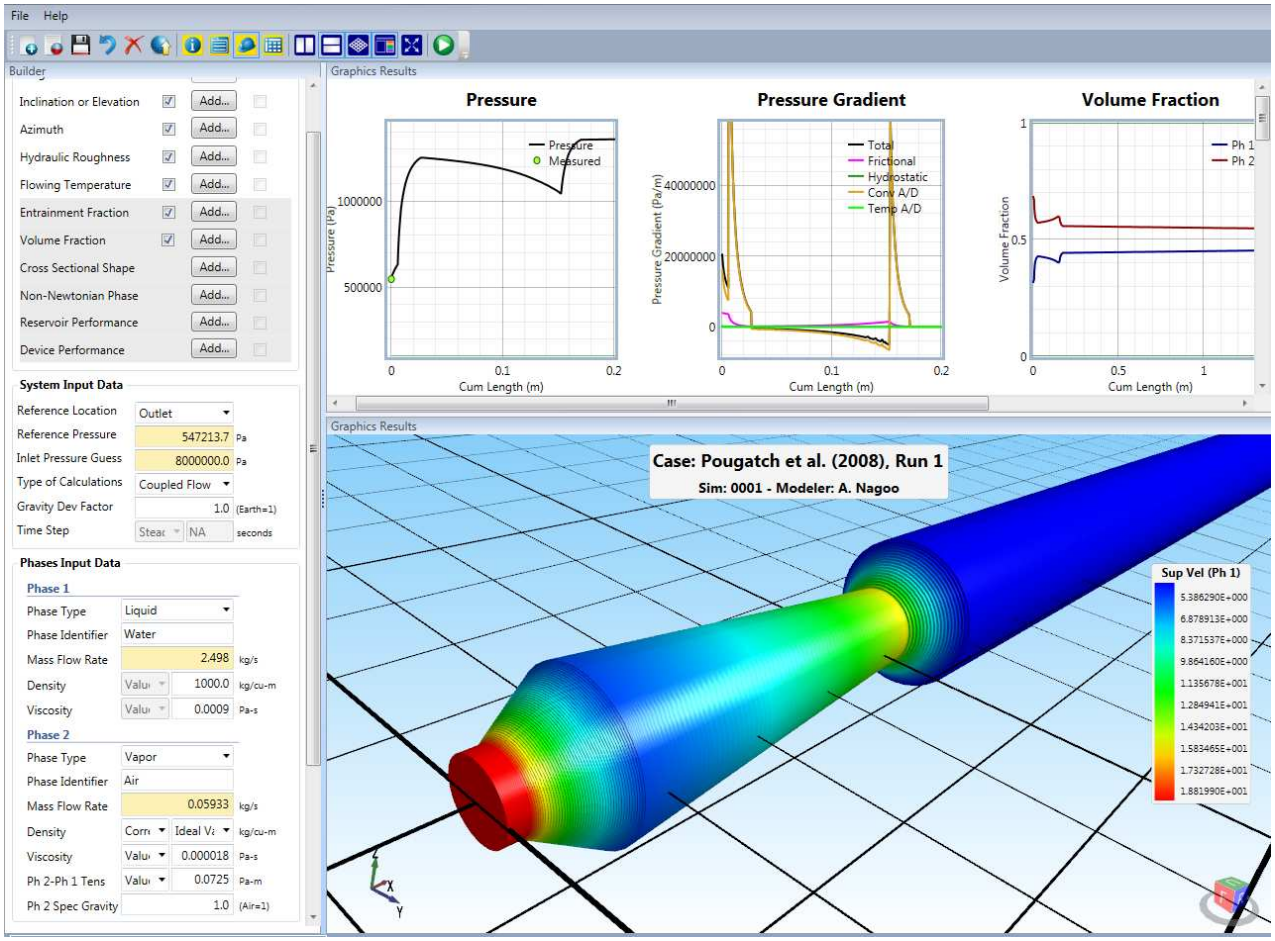

Figure 4.13.15: Example calculations for case 1 of Pougatch et al. (2008) with the UTPipeFlow code.

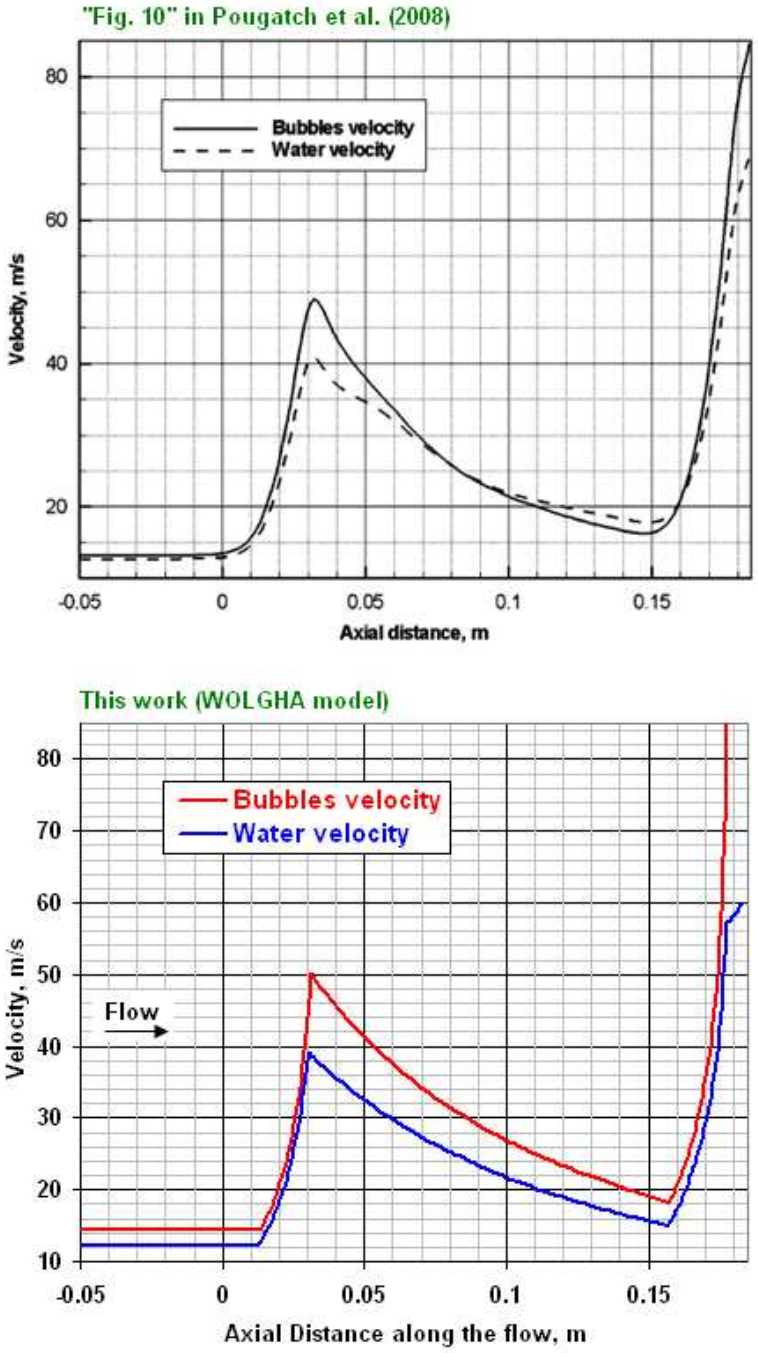

Figure 4.13.16: Comparison of the Pougatch et al. (2008) 3D/two-fluid (CMFD) model predictions with our analytical models.

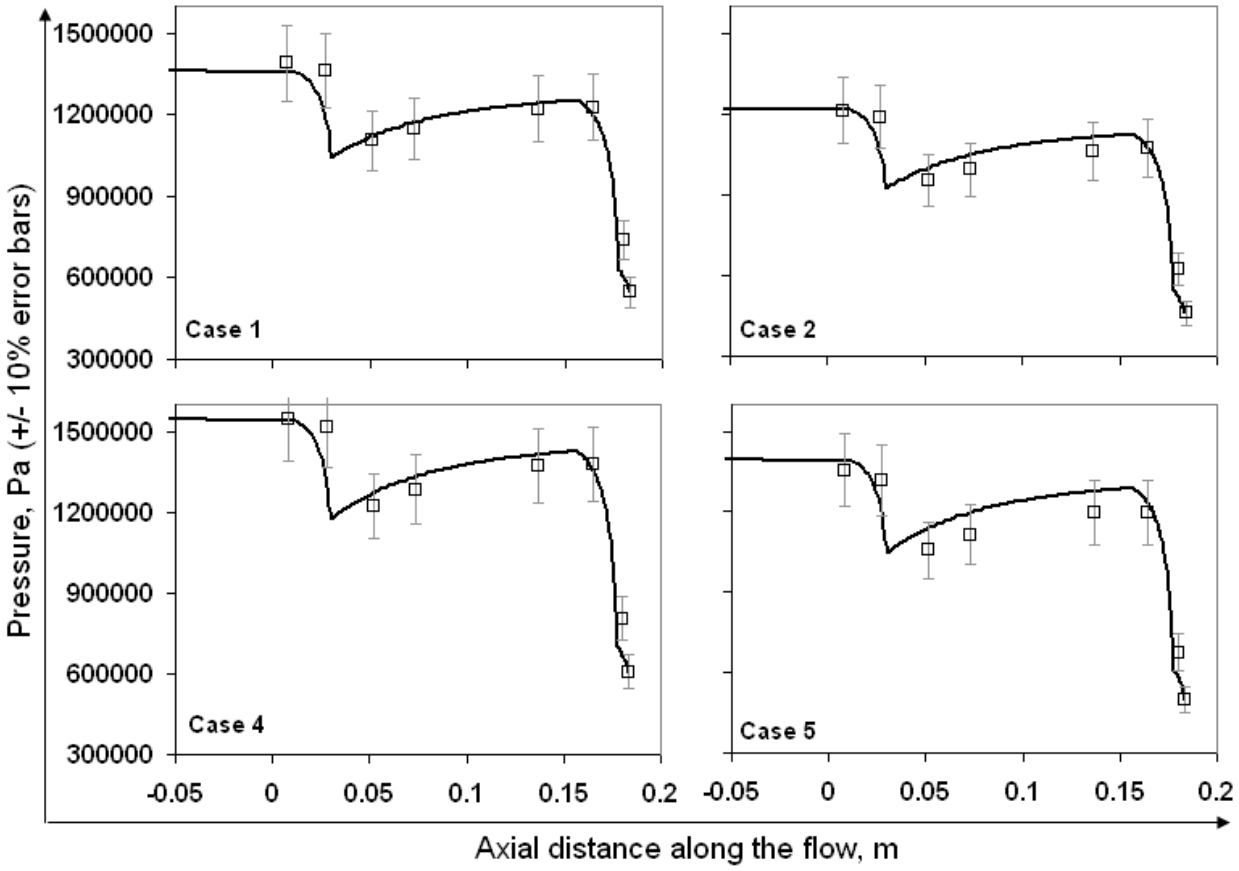

Figure 4.13.17: Predictions of the cases in Pougatch et al. (2008) with the WOLGHA model. Lines are our predictions and the points are measurements.

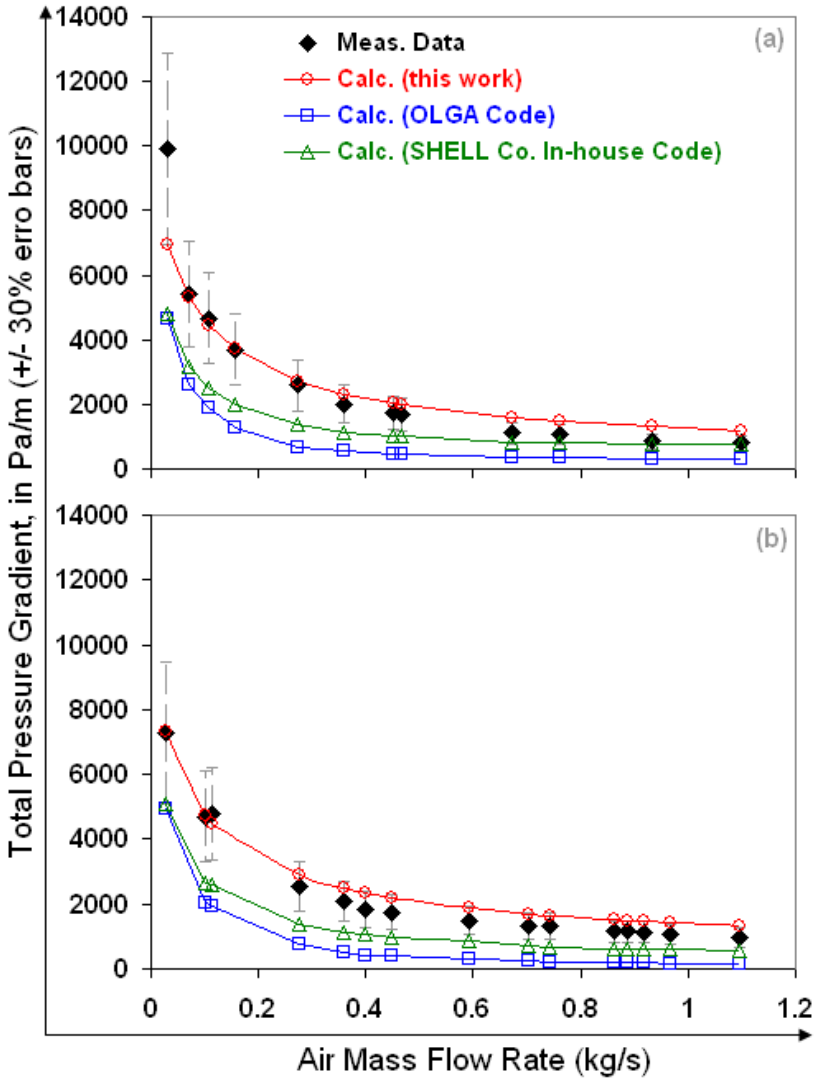

Figure 4.13.18: Predictions of representative cases in Zabaras et al. (2013) with our analytical models.

Chapter 5 – Liquid-Liquid and Fluid-Solid Flow Applications

In this chapter we perform our analytical model validations for various liquid-liquid and fluid-solid flow applications categorized under the same standardized multiphase flow problem definitions proposed in Table 1.1 in chapter 1. These two types of flow combinations are hydrodynamically similar because of the new findings of this work that:

I. The wall shear stress for liquid-liquid and fluid-solid flows is always equal to that of the dominant (or carrier) phase.

II. The influence of the passive (or dispersed) phase on the wall shear stress is only via the averaged volume fraction.

In liquid-liquid flow scenarios, there will be cases where one phase will remain the dominant phase during flow, or, will physically invert from being the dominant phase to being the passive phase, such as observed when transgressing the phase inversion point.

In fluid-solid flows, since wall shear stress-related variables such as friction factor or viscosity only has a physical significance (and experimental basis) for a fluid phase, the carrier fluid phase will always be the only phase that is responsible for shear stress (momentum flux) from the flow field to the wall – that is – the dominant phase in a fluid-solid flow is always the fluid.

Note that liquid-liquid and fluid-solid flows are always coupled flows for the same reason that single-phase flows are coupled flows – only one phase (the dominant phase) is exchanging momentum with the pipe boundary. In terms of simple hand

calculations, Eqn. 1 of Section 4.1 is the applicable version for use in steady-state, fully-developed liquid-liquid or fluid-solid flows with the only change being that:

$$\overbrace{\gamma_j}^{j\text{-dominance}} = \begin{cases} 1,0 & \forall\ j = dominant - fluid,\ passive - solid \\ 1,0 & \forall\ j = dominant - liquid,\ passive - liquid \end{cases} \quad (1)$$

5.1 Effect of Properties

We next perform validation of our analytical models against experiments with changing liquid properties. We first select the oil (phase 2) and water (phase 1) experiments from the classic horizontal flow reference of Charles et al. (1961). This choice of oil-water dataset is deliberate since the two oils used in this study were carefully prepared to have a density equal to that of the water. Thus, all of the liquids in these liquid-liquid flows had the same density (at 998 kg/m^3). Additionally, the interfacial tensions between the two oils and water were equal (at 0.045 Pa-m) and the variations in the flow rates of the phases were the same for both oil-water combinations. The only difference, then, was the viscosities of the oil – with the Wyrol-J oil having a viscosity of 0.0168 Pa-s and the Marcol-GX oil having a viscosity of 0.00629 Pa-s. This careful control of parameters allows us to determine the effect of a change in the viscosity of the oil phase in an oil-water flow on the pressure gradient.

The first predicted answer for understanding this effect is furnished by our principle of phase dominance, namely: *if* these flows are water-dominant flows, *then* there will be no change in the frictional pressure gradient provided that the volume fraction behaviors of both oil-water combinations are about the same. Conversely, the second predicted answer for understanding this effect is that: *if* these flows are oil-

dominant flows, *then* there will be a change in the frictional pressure gradient caused by a difference in the in-situ Reynolds number of the oil phases.

Fig. 5.1.1 shows our analytical model's calculations with $\gamma_1 = 1$ and $\gamma_2 = 0$ (water-dominant flows), and the measured oil volume fractions. Fig. 5.1.1a shows the calculations and measurements for the Wyrol-J oil and Fig. 5.1.1b shows the calculations and measurements for the Marcol-GX oil. The oil volume fraction measurements for both sets of experiments were not only about the same for each case, but additionally, were very close to the oil fractional flows (the no global slip values).

As is evident, our phase dominance principle accurately predicts that there would be no difference in the total (frictional) pressure gradients of these oils. Fig. 5.1.2 shows the same calculations as Fig. 5.1.1, but with the NOSLIP analytical model. Clearly, this dataset is accurately predicted by our analytical model.

Fig. 5.1.3 and 5.1.4 shows another classic horizontal oil (phase 2) and water (phase 1) experimental investigation – that of Oliemans (1986). In these core-annular, water-dominant ($\gamma_1 = 1,\ \gamma_2 = 0$), large-diameter, high viscosity ratio (heavy oil and water) experiments the water holdup measurements were correlated as a simple function of water fractional flow. Fig. 5.1.3 shows the predictions of our analytical model for the large and small pipes of these experiments at quite high oil viscosities with the water holdup correlation in this reference. Fig. 5.1.4 shows our analytical model's frictional pressure gradient calculations for various water fractional flows for one of the datasets in this reference – the data for the 2-inch pipe measurements at a heavy oil viscosity of 3.0 Pa-s and density of 975 kg/m^3. Evidently, our analytical model accurately predicts the data trends of this experimental study.

Other than classic older oil-water experiments, our analytical model can satisfactorily predict modern data as well. Fig. 5.1.5 shows data from the real heavy

crude oil (phase 2) and water (phase 1) horizontal flow experiments of Wang et al. (2011). Fig. 3 in this reference shows that there was very little averaged slip observed in these high viscosity ratio experiments, in which real heavy crudes with viscosities ranging from 0.4 to 2.0 Pa-s were obtained from "one of China's heavy crude oilfields". As demonstrated in Fig. 5.1.5, our model satisfactorily predicts these oil-dominant ($\gamma_1 = 0$, $\gamma_2 = 1$) experiments with the NOSLIP model for different water-cuts (water fractional flows).

Fig. 5.1.6 shows another recent set of horizontal, liquid-liquid flow experiments (Pouplin et al., 2011), but this time for the low viscosity ratio, homogeneous flow of n-Heptane (phase 2) and Water-Glycerine (phase 1). The n-Heptane liquid had a viscosity of 0.0004 Pa-s and a density of 684 kg/m^3. As seen in Fig. 5.1.6, our analytical model accurately predicts these water-dominant ($\gamma_1 = 1$, $\gamma_2 = 0$) experiments with the NOSLIP model for different n-Heptane fractional flows.

5.2 Effect of Rheology

We next perform validation of our analytical models against experiments with changing liquid rheology, i.e., non-Newtonian liquids. We select the two-phase non-Newtonian polymer-emulsion flows in the constricted capillary experiments of Cobos et al. (2009). The laminar-laminar flow of two non-Newtonian liquids through micro-channels is fairly common in chemical enhanced oil recovery (chemical EOR) processes (e.g., emulsified solvent flooding for heavy oil recovery). In these micro-channel experiments, five oil (phase 2) and water-polymer-surfactant (phase 1) mixtures were sheared in a homogenizer. The power law parameters describing the shear behavior of these emulsions were reported in the Table 3 of the reference. These emulsions were flowed through a converging-diverging quartz capillary tube, as shown in Fig. 5.2.1, to

represent a 200 μm x 50 μm pore-throat model of a porous medium. Their pressure-gradient flow rate response was measured with simultaneous visualization under an optical microscope.

Fig. 5.2.2 compares the predictions of our analytical theory for these water-dominant ($\gamma_1 = 1,\ \gamma_2 = 0$) experiments with the NOSLIP model for different emulsions. Note these are laminar-laminar flows, and therefore, the results shown in Fig. 5.2.2 are wholly-analytical. Our analytical theory satisfactorily predicts the measurements shown in Fig. 5.2.2 (+/- 20% error bars shown in this figure).

5.3 EFFECT OF SIZE

In this section, we perform validation of our analytical models against experiments with widely differing pipe cross-sectional areas. We first select the horizontal, laminar-laminar heavy silicone oil (phase 2) and water (phase 1) micro-channel experiments of Foroughi and Kawaji (2011). In these experiments, flow-patterns were observed and pressure gradient measurements were obtained from a 250 microns (D = 0.00025 m) fused silica circular tube. The silicone oil had a viscosity of 0.863 Pa-s, a density of 970 kg/m^3 and an interfacial tension with water of 0.043 Pa-m. Fig. 5.3.1 shows that the BUTTERWORTH model satisfactorily predicts this oil-dominant ($\gamma_1 = 0$, $\gamma_2 = 1$) dataset with our predictions within 25% of the measurements.

At the other end of scale, the large-diameter (D = 0.1063 m) tap water (phase 1) and kerosene (phase 2) experiments of Abduvayt et al. (2006) will be used to validate our analytical models. In this water-dominant ($\gamma_1 = 1,\ \gamma_2 = 0$) investigation, water holdup and total pressure gradient measurements were obtained for a wide range of phase rates at horizontal, slight upward (+0.5, +3 degrees from horizontal) and slight downward (-0.5, -3 degrees from horizontal) pipe inclinations. If we look at one dataset from this study

(i.e., increasing water rates at a fixed oil superficial velocity of 0.375 m/s) and use the measured water holdups in our analytical model calculations, we see from Fig. 5.3.2 that our model accurately reproduces the trends in the data at the various inclinations. Note that these experiments represent a combination of fairly difficult problems, namely liquid-liquid flow, up- and down-inclined flow and large-diameter flow.

Fig. 5.3.3 shows the same dataset, but this time the analytical NOSLIP model is used in our model predictions. The agreement between the experiments and our analytical models are excellent. In fact, we can use the analytical NOSLIP model to accurately predict all of the experiments in this investigation, as seen in Fig. 5.3.4.

So far in this section, we validated our analytical models for liquid-liquid flows in pipes of different sizes. We next validate our analytical models for fluid-solid flows in pipes of different sizes and for solid particles of different sizes. In these fluid (phase 2) and solid (phase 1) flows, according to our dominance principle, the fluid is always the dominant phase and thus we will always use $\gamma_1 = 0$ and $\gamma_2 = 1$ in our analytical model calculations.

Fig. 5.3.5a shows the dilute conveying, vertical, large-diameter (D = 0.192 m) flow of glass beads (phase 1) and air (phase 2) as given in Rautiainen et al. (1999). Fig. 5.3.5b shows our analytical model's calculations with the measured solids holdup used in our calculations. As seen, these results validate that our analytical model satisfactorily represents the trends in the data once the averaged volume fractions are known. This once again validates the first insight of this research – that pressure gradient is governed by relative velocity and that the flow patterns are merely the visual, spatial manifestations of relative velocity.

In the Rautiainen et al. (1999) experiments above, the averaged air volume fraction behavior when viewed as an air fractional flow graph could be accurately

represented by a SLIPRATIO model with $H_{2,1}$ = 1.8. Fig. 5.3.6 shows the predictions of our analytical model with this SLIPRATIO model. The agreement between our model's predictions and the experimental measurements is excellent.

In fact, it is a finding of this work that a constant slip ratio (the SLIPRATIO model) accurately represents a large amount of dilute conveying flows. This is consistent with the finding of the classic theoretical analysis of Standard (1961), and later, with the experiments of Singh (1982). For example, the large-diameter (D = 0.104 m), vertical flow data from the investigation of Singh (1982) is shown in Fig. 5.3.7, in which different solid particles (phase 1) and air (phase 2) could be satisfactorily modeled with our analytical model using the SLIPRATIO model of $H_{2,1}$ = 1.8. Another large-diameter (D = 0.1 m), vertical flow dataset from Reddy and Pei (1969) is shown in Fig. 5.3.8 to be accurately modeled with the SLIPRATIO model of $H_{2,1}$ = 1.8. As seen in this figure, there were four different sizes of glass beads that were flowed with air in this experimental investigation.

Another dilute conveying dataset that can be accurately predicted with the SLIPRATIO model of $H_{2,1}$ = 1.8 is the glass beads (phase 1) and air (phase 2) vertical 3-inch pipe dataset of Luo (1987). Fig. 5.3.9 shows the wide ranges of solids mass fluxes in this experimental investigation and the comparison of our analytical model's predictions with the SLIPRATIO model of $H_{2,1}$ = 1.8. As observed, the prediction is excellent.

Other SLIPRATIO analytical models can also be found to accurately predict the averaged volume fraction behaviors in dilute conveying flows. Fig. 5.3.10 shows the glass beads (phase 1) and air (phase 2) vertical flow data of Henthorn et al. (2005) to be accurately predicted with our analytical model using a SLIPRATIO model of $H_{2,1}$ = 2.4. In these 1-inch pipe experiments, two different glass bead sizes were flowed with air at

the same air rates. Also, it was shown in this reference the inability of both an existing empirical correlation and a CFD model to predict the pressure gradient behavior of this dataset. Fig. 5.3.11 shows the vertical flow experiments of Wang et al. (2000), in which a wide range of class-C 20 μm glass spheres (phase 1) and air (phase 2) flow rates can be satisfactorily predicted with our analytical model and a SLIPRATIO model of $H_{2,1}$ = 1.4.

5.4 EFFECT OF INCLINATION

We next perform validation of our analytical models against experiments with different pipe inclinations. Fig. 5.4.1 shows data from the perfect core-annular flow (PCAF) heavy oil (phase 2) and water (phase 1) experiments of Bai (1995). The heavy oil used had a viscosity of 0.601 Pa-s, a density of 905 kg/m^3 and an interfacial tension with water of 0.01227 Pa-m. For these water-dominant ($\gamma_1 = 1$, $\gamma_2 = 0$) experiments, our analytical model used the NOSLIP model to provide the vertical-upward flow predictions shown Fig. 5.4.1a as well as the vertical-downward flow predictions shown in Fig. 5.4.1b. Evidently, our analytical model accurately predicts these datasets.

Figs. 5.4.2 – 5.4.4 show the oil-dominant ($\gamma_1 = 0$, $\gamma_2 = 1$) datasets of Alkaya (2000) for slightly-inclined oil (phase 2) and water (phase 1) flows over a wide range of flow rates at inclinations of -1, +1 and +5 degrees from horizontal, respectively. In these validation figures, the lines are the calculations of our analytical model with the measured oil volume fractions. Figs. 5.4.5 – 5.4.7 show the predictions of these same datasets with the NOSLIP model. It is clear that our analytical model accurately predicts these slightly up- and down-inclined oil-water data trends.

Indeed, in many oil-water datasets, both the pressure gradient and volume fractions are measured, thus providing us an opportunity to validate and then predict these datasets. Fig. 5.4.8 shows the water-dominant ($\gamma_1 = 1$, $\gamma_2 = 0$) up-inclined oil-

water flows from the experimental investigation of Mukhopadhyaya (1977) being accurately reproduced with our analytical model using the measured oil volume fractions. Fig. 5.4.9 shows the same data as Fig. 5.4.8 being accurately predicted with our analytical model and the NOSLIP model. Clearly, the NOSLIP model is a reliable first estimate for liquid-liquid flows.

Fig. 5.4.10 shows one representative dataset from the water-dominant ($\gamma_1 = 1$, $\gamma_2 = 0$), slightly up- and down-inclined experiments of Lum et al. (2006), i.e., the dataset at a mixture velocity of 2 m/s. As this figure shows, the same tap water (phase 1) and Exxsol-D140 oil (phase 2) flow rates were maintained at different pipe inclinations, thus properly isolating the effect of pipe inclination. The lines in Fig. 5.4.10 are our analytical model predictions with the NOSLIP model. It is clear that our analytical prediction captures the global trends in the data with this simple NOSLIP model. If we now use the measured oil volume fractions with our analytical model, we get specific trends in the data being captured accurately, as seen in Fig. 5.4.11. Indeed, Fig. 5.4.12 shows all of the pressure gradient data of the Lum et al. (2006) experimental investigation being accurately reproduced by our analytical model with the measured oil volume fractions. This is proper model falsification. It is once again demonstrated that *if* the volume fraction is known, *then* our analytical models are very accurate, and the degree to which our models are in false agreement with an experiment is directly related to the degree to which the volume fraction is known. The uncertainty in our models is, in general, traceable to only the in-situ phase volume fractions of the multiphase flow.

We can repeat this kind of proper model falsification for steeply up-inclined flows such as given in the refined mineral oil (phase 2) and tap water (phase 1) experiments of Flores (1997) at pipe inclinations of 0, 15, 30 and 45 degrees from vertical. Fig. 5.4.13 shows the prediction of our analytical model using the NOSLIP model for one

representative dataset from these water dominant ($\gamma_1 = 1,\ \gamma_2 = 0$) experiments at various inclinations – the dataset at a water superficial velocity of 0.47 m/s. As in the previous example above, the NOSLIP model clearly provides a reliable prediction of the global trend in the data. In fact, Fig. 5.4.14 demonstrates that our analytical model with the NOSLIP model can accurately predict all of the hundreds of data from the Flores (1997) experimental investigation. If, however, we use the measured oil volume fractions in our analytical model, then the data can be reproduced to an even higher degree of accuracy, as seen in Fig. 5.4.15 (which is the same dataset at a water superficial velocity of 0.47 m/s but with the measured oil volume fractions) and Fig. 5.4.16.

With the reliability of the NOSLIP model demonstrated for liquid-liquid flows, we now use this model to accurate predict oil-water flows at various inclinations exhibiting different flow patterns. Fig. 5.4.17 shows our analytical model's prediction with the NOSLIP model for one representative dataset from the refined mineral oil (phase 2) and water (phase 1) slightly up- and down-inclined flow experiments of Atmaca (2007) – the dataset at an oil superficial velocity of 0.5 m/s. Clearly, the NOSLIP model furnishes quite accurate total pressure gradient predictions for this dataset. Fig. 5.4.18 shows that all of the data from the water-dominant ($\gamma_1 = 1,\ \gamma_2 = 0$) experiments of Atmaca (2007) can be accurately predicted with the NOSLIP model.

Fig. 5.4.19 shows all of the data from the slightly up- and down-inclined high viscosity ratio oil-water experiments of Grassi et al. (2008) being satisfactorily predicted with our analytical models using the NOSLIP and WOLGHA models. In these water-dominant ($\gamma_1 = 1,\ \gamma_2 = 0$) experiments, the paraffin oil (phase 2) had a viscosity of 0.799 Pa-s, a density of 866 kg/m^3 and an interfacial tension with water of 0.05 Pa-m.

5.5 EFFECT OF FLOW PATTERN

We next perform validation of our analytical models against experiments with different flow patterns. Fig. 5.5.1 shows representative data from the horizontal tap water (phase 1) and Exxsol-D140 oil (phase 2) experiments of Lovick (2004). In these water-dominant ($\gamma_1 = 1,\ \gamma_2 = 0$) experiments, the "dual-continuous" flow pattern is observed. Figs 5.5.1a, 5.5.1b and 5.5.1c show the predictions of our analytical model with the measured oil volume fractions, the NOSLIP model and the SLIPRATIO model ($H_{2,1}$ = 1.2), respectively. As can be seen, although our predictions are accurate if the volume fractions are known, the global trends in the data can still be satisfactorily captured by very simple models such as the NOSLIP or SLIPRATIO models. In fact, Fig. 5.5.2 shows that all of the data from this experimental investigation can be satisfactorily predicted with these simple models.

Fig. 5.5.3 shows all of the "oil-water dispersion" data from the horizontal water (phase 1) and SN-250 oil (phase 2) investigation of Martinez (1986) to be accurately predicted with our analytical model and a SLIPRATIO model of $H_{2,1}$ = 10. In these oil-dominant ($\gamma_1 = 0,\ \gamma_2 = 1$) experiments, there was a systematic increase in water-cut for a fairly wide range of oil and water superficial velocities.

Fig. 5.5.4 shows all the "perfect core annular flow" (PCAF) and "wavy core annular flow" (WCAF) data from the horizontal water (phase 1) and heavy fuel oil (phase 2) lubricated pipelining investigation of Arney (1994) being accurately predicted with our analytical model and the NOSLIP model. In these water-dominant ($\gamma_1 = 1,\ \gamma_2 = 0$) experiments, the "No. 6" heavy fuel oil had a viscosity of 2.0 Pa-s, a density of 992 kg/m^3 (about the same as that of the water used in these experiments) and an interfacial tension with water of 0.018 Pa-m. We emphasize that this is a wholly-analytical

prediction with the NOSLIP model accurately predicting the frictional pressure gradient behavior in the lubricated pipelining of a heavy oil and water.

Lastly, Figs. 5.5.5b-i and b-ii show all the various types of stratified flow data from the horizontal tap water (phase 1) and light refinery stream oil (phase 2) investigation of Plaxton (1995) to be accurately predicted with our analytical model and the NOSLIP model. In these water-dominant ($\gamma_1 = 1,\ \gamma_2 = 0$) experiments, both the volume fractions and total pressure gradients were measured. For comparative purposes, Figs. 5.5.5a-i and a-ii show, respectively, the measured oil volume fractions as an oil fractional flow graph and the total pressure gradient calculated from our analytical model using the measured oil volume fractions.

5.6 Effect of Flow Development

In this section, we perform validation of our analytical models against experiments with different flow development. Fig. 5.6.1 shows data from the vertical-downward water (phase 1) and ShellSolv-360 oil (phase 2) investigation of Soot (1971). The run numbers for the data shown correspond to the data that had almost identical oil and water flow rates but different injection methods for introducing the phases into the flow loop. As seen, for these water-dominant ($\gamma_1 = 1,\ \gamma_2 = 0$) experiments, if the measured oil volume fraction is used with our analytical model, an accurate prediction of the frictional pressure gradient is provided. Also shown on this figure is the case where the NOSLIP model is used with our analytical model to provide a frictional pressure gradient prediction that is still within +/- 10% error.

Fig. 5.6.2 shows the slightly up-inclined (+10 degrees from horizontal) large-diameter (D = 0.106 m) air (phase 2) and fly ash (phase 1) investigation of Carpinlioglu et al. (2002). In these fluid-solid experiments, only the entrance pressure was specified in

UTPipeFlow and the BUTTERWORTH model was used for predicting the flow development along the pipe. As seen, the agreement with the developing flow predictions from our analytical models and the experiments is excellent over the range of solids loading in the experiments from 0 to 20%.

5.7 EFFECT OF SHAPE

We next perform validation of our analytical models in a multiphase flow through a non-circular conduit. We select the horizontal particulate slurry flow of Kaushal and Tomita (2003). In these water (phase 2) and multi-size zinc tailings (phase 1) slurry flow, the same liquid and solids flow rates were maintained in a circular pipe (D_H = 0.105 m, A = 0.00865 m^2) and a rectangular pipe (D_H = 0.08 m, A = 0.01 m^2). Therefore, the only change in this investigation was the pipe shape. Fig. 5.7.1a shows the prediction of or analytical model with the ANSLIP model for the circular pipe and Fig. 5.7.1b shows our analytical model's predictions with the same ANSLIP model for the rectangular pipe. As is evident, our analytical models accurately accounts for different pipe shapes.

5.8 EFFECT OF OTHER PHENOMENA

We now perform validation of our analytical models in scenarios involving other phenomena, namely – phase inversion, pipe wall wettability, drag reducing agents and dense phase conveying.

In some liquid-liquid flow scenarios, the dominant phase can change to the passive phase under certain conditions. This is found to occur in systems that display phase inversion. In our formulation, this effect is simply captured by the change in the j-dominance of the phases. For example, for a water-dominant flow (the water being phase 1 and the oil being phase 2), the j-dominance that is specified in our model is $\gamma_1 = 1$

and $\gamma_2 = 0$. However, if this system displayed phase inversion, then the j-dominance in our models would change to $\gamma_1 = 0$ and $\gamma_2 = 1$.

Fig. 5.8.1 shows all the horizontal SN-250 oil (phase 2) and water (phase 1) homogeneous flow data of Arirachakaran (1983) to be accurately predicted by our analytical model with the NOSLIP model. Note that for oil cuts below 65%, our model used a j-dominance of $\gamma_1 = 1$ and $\gamma_2 = 0$, while for 70% oil cut and above, the j-dominance was $\gamma_1 = 0$ and $\gamma_2 = 1$. These results represent a strong validation of our dominance principle.

Fig. 5.8.2 shows total (frictional) pressure gradient data from the horizontal, refined mineral oil (phase 2) and water (phase 1) investigation of Trallero (1995) being accurately reproduced by our analytical model using the measured oil volume fractions. Note that for water rates at or below 0.6 m/s (water superficial Reynolds number = 32154) this is an oil-dominant system ($\gamma_1 = 0$ and $\gamma_2 = 1$), and for water rates at 1.0 m/s (water superficial Reynolds no. = 53589) this is a water-dominant system ($\gamma_1 = 1$ and $\gamma_2 = 0$). The thin red line in Fig. 5.8.2 (water superficial Reynolds no. = 53589) represents our analytical model's calculations as if there was no phase inversion and the thick red line represents our analytical model's calculations with phase inversion.

Other than horizontal flows that display phase inversion, there are vertical liquid-liquid flows that show this phenomenon. Fig. 5.8.3 shows the data of the Wood (1960) in which oil-dominant to water-dominant phase inversion is clearly observed and quantified. This is an important experimental investigation because two oils with about the same densities and interfacial tensions but with different viscosities were flowed with water at about the same rates. The oils were a Marcol-GX refined mineral oil with an average viscosity of 0.02 Pa-s and a Primol-D heavy mineral oil with an average viscosity of 0.15 Pa-s. Importantly, both the volume fractions and total pressure gradients were measured

for each run. Thus, the effect of the viscosity of the oil on the phase inversion point could be analyzed in this type of careful control of parameters.

To isolate the ability of our analytical models to satisfactorily model the phase inversion in these experiments, we first used the measured oil volume fractions in our analytical models. Fig. 5.8.3a-i shows all of the oil-dominant Marcol-GX data to be satisfactorily predicted with our analytical model, which correspond to water superficial velocities of 0.55 m/s and below. Fig. 5.8.3a-ii shows all of the Marcol-GX data that displayed phase inversion, which correspond to water superficial velocities of 0.978 m/s and above. The fine lines in these figures represent our analytical model's calculations without phase inversion and the thick lines represent our model's calculations with phase inversion. Figs. 5.8.3b-i shows all of the oil-dominant Primol-D data to be satisfactorily predicted with our analytical model, which correspond to water superficial velocities of 0.098 m/s and below. Fig. 5.8.3b-ii shows all of the Primol-D data that displayed phase inversion, which correspond to water superficial velocities of 0.304 m/s and above. The fine lines in these figures represent our analytical model's calculations without phase inversion and the thick lines represent our model's calculations with phase inversion. Clearly, an increase in oil-phase viscosity resulted in a lowering of the phase inversion point with respect to the water superficial velocity.

Fig. 5.8.4 represents the same predictions as given in Fig. 5.8.3 but with the NOSLIP model used with our analytical models. Evidently, the results of the wholly-analytical NOSLIP model are in very good agreement with this dataset. The NOSLIP model correctly captures the trends in the data both before and after the phase inversion point.

Another suspected external phenomenon (i.e., external to the flow hydrodynamics) that has gained recent attention is the issue of the influence of the pipe

wall wettability on the pressure gradient. Previously, in the results presented in Fig. 4.12.5 of Chapter 4 (the vertical annular vapor-liquid flow dataset of Schubring, 2009) and Fig. 4.4.16 of Chapter 4 (the horizontal vapor-liquid flow dataset of Chisolm and Laird, 1958), it was shown that the effect of changes in the tube material on the pressure gradient was via the volume fraction. Therefore, *if* there was a pipe wall wettability effect, *then* the volume fraction will change and thus the pressure gradient. Indeed, it would be an unreasonable approach to modify, say the hydraulic roughness in the frictional pressure gradient, to account for wettability since these represent fundamentally different concepts (i.e., laminar/turbulence layers in the flow field versus surface phenomena of the pipe material).

One experimental investigation that aimed to characterize the pipe wall wettability effect in horizontal liquid-liquid flow is that of Angeli and Hewitt (1998). In these oil-dominant experiments, the total pressure gradient measurements were presented for a wide range of water (phase 1) and Exxsol-D80 oil (phase 2) rates which were kept the same for two different pipes – a stainless steel pipe and a transpalite (acrylic) pipe. These results were presented in Tables 2 and 3 of the reference and stem from the dissertation of Angeli (1996).

Fig. 5.8.5 shows all the data in Tables 2 and 3 of Angeli and Hewitt (1998) being accurately predicted with our analytical models and the NOSLIP model. Fig. 5.8.5a shows the stainless steel pipe data and Fig. 5.8.5b shows the transpalite pipe data. To further investigate the possible reasons for the very minor differences between our analytical model's predictions and the experiments, we referred to the dissertation of Angeli (1996). In this work, a few of the data for the transpalite pipe also contained oil volume fraction measurements in addition to the total pressure gradient measurements. Fig. 5.8.6 shows these data. The thin, dashed lines represent our analytical model's

predictions with the NOSLIP model and the thick, solid lines represent our analytical model's predictions with the measured oil volume fractions. This result demonstrates, unambiguously, that external phenomena such as pipe wall wettability will affect the hydrodyamics of the flow via the volume fraction (i.e., via the changes in the in-situ relative velocities).

In some liquid-liquid flow cases, however, the pipe wall wettability may not only affect the volume fraction but also the phase dominance of the multiphase flow. Fig. 5.8.7 shows data from the ionic liquid (phase 1) and deionized water (phase 2) horizontal laminar-laminar, micro-channel flow investigation of Tsaoulidis et al. (2013). In this study, three different tubes displaying different wall wettabillity characteristics were used to flow deionized water and an ionic liquid (1-butyl-3-methylimidazolium) with a density of 1420 kg/m3 and a viscosity of 0.052 Pa-s. Under similar flow rates and operating conditions, the Tefzel and FEP micro-channels displayed a water-dominant behavior that could be accurately predicted with a simple drift-flux slip model of $C_0 = 2$ (Fig. 5.8.7a), while the glass micro-channel displayed an oil-dominant behavior that could be accurately predicted with the NOSLIP model (Fig. 5.8.7b). Fig. 5.8.8 shows the effect of using different volume fraction models for one of the micro-channels in the study, i.e., the ANSLIP model for the dashed line predictions and the WOLGHA model for the solid line predictions.

As previously noted, in our analytical models, external phenomena will affect the hydrodynamics of the flow via the volume fraction. Fig. 5.8.9 shows the Langsholt (2012) DRA (drag reducing agent) investigation in which tap water (phase 1) and Exxsol-D80 oil (phase 2) were flowed in a horizontal, medium diameter pipe (D = 0.1 m) with different combinations of a DRA (as seen in Fig. 7 of the reference). Fig. 5.8.9 shows three datasets at the same mixture velocity (at 1.5 m/s) but without the DRA in either

phases (Fig. 5.8.9a), with the DRA in the water phase only (Fig. 5.8.9b) and with the DRA in the oil phase only (Fig. 5.8.9c). For these water-dominant experiments, our analytical model's predictions with the NOSLIP model is shown in Fig. 5.8.9 as the thin lines and our model's predictions using the measured water holdups is shown in Fig. 5.8.9 as the thick lines. Clearly, the trends in the data are well captured by the effects of the DRA on the volume fraction.

Lastly, we look at the CFB (circulating fluidized bed) hydrodynamics experiments of O'Hern et al. (2006). These voluminous pilot-scale CFB experiments were performed at the Sandia National Laboratories to investigated the solids loading and dense phase transport at selected locations along a large-diameter (D = 0.14 m) CFB riser. Two different solid particles were flowed with air – glass beads with a density of 2500 kg/m^3 and FCC (fluid catalytic cracking) particles with a density of 1275 kg/m^3. Our purpose here is to show that if the measured solids volume fraction along the riser is enforced in UTPipeFlow, then the total pressure gradient calculations of our analytical theory are accurate, even in a dense phase transport scenario such as this one.

Fig. 5.8.10a-ii, b-ii and c-ii show the averaged solids volume fraction measurements from the differential pressure (DP) and gamma-densitometry tomography (GDT) measurements for one low gas and low solids rate case (air mass flow rate = 0.243 kg/s, glass beads mass flow rate = 1.586 kg/s), one high gas and high solids rate case (air mass flow rate = 0.341 kg/s, glass beads mass flow rate = 2.063 kg/s), and one low gas and high solids rate case (air mass flow rate = 0.246 kg/s, glass beads mass flow rate = 1.940 kg/s), respectively. Fig. 5.8.10a-i, b-i and c-i show the corresponding total pressure gradient data for the previous cases with our analytical model's calculations using the measured solids volume fraction from the DP measurements. Note that there are dozens of repeated measurements of these total pressure gradients, thus providing a strong

validation of our model's calculations. Evidently, our analytical models accurately reproduce the total pressure gradient data trends once the volume fraction is known.

Fig. 5.8.11a-ii, b-ii and c-ii show the averaged solids volume fraction measurements from the differential pressure (DP), electrical impedance tomography (EIT) and gamma-densitometry tomography (GDT) measurements for one low gas and low solids rate case (air mass flow rate = 0.230 kg/s, FCC mass flow rate = 1.053 kg/s), one high gas and high solids rate case (air mass flow rate = 0.310 kg/s, FCC mass flow rate = 1.267 kg/s), and one low gas and high solids rate case (air mass flow rate = 0.230 kg/s, FCC mass flow rate = 1.290 kg/s), respectively. Fig. 5.8.11a-i, b-i and c-i show the corresponding total pressure gradient data for the previous cases with our analytical model's calculations using the measured solids volume fraction from the DP measurements. As before, our analytical models accurately reproduce the total pressure gradient data trends once the volume fraction is known.

5.9 Effect of Modeling Method

In this section, we benchmark and compare the predictions of our universal analytical models against other liquid-liquid and fluid-solid models in the literature as well as against currently available industry codes over a wide range of scenarios.

Fig. 5.9.1 shows one of the datasets from the previously analyzed heavy oil and water experiments of Oliemans (1986) in Fig. 5.1.4. We note that once the volume fraction is correct, our analytical models will provide a very accurate prediction for pressure gradient. The right-most figure in Fig. 5.8.1 shows the various "lubricated-film model" tuning performed in the reference in an attempt to match this dataset.

Fig. 5.9.2 shows one of the datasets from another of the previously analyzed heavy oil and water datasets of Wang et al. (2011) in Fig. 5.1.5 and Fig. 1.3.16 in Chapter

1. In comparison to other models, we note the analytical NOSLIP model is very accurate for this dataset.

In fact, we can show how the NOSLIP model compares with other modeling methods and codes for quite different datasets. Fig. 5.9.3 shows one of the datasets from the previously analyzed light oil and water datasets of Pouplin et al. (2011) in Fig. 5.1.6 and Fig. 1.3.13 in Chapter 1. In comparison to other models, we note the analytical NOSLIP model is very accurate for this dataset. Fig. 5.9.4 shows one of the horizontal flow datasets from the previously analyzed heavy oil and water datasets of Grassi et al. (2008) in Fig. 5.4.19 and Fig. 1.3.10 in Chapter 1. In comparison to other models, we note the analytical NOSLIP model is, again, very accurate for this dataset. Fig. 5.9.5 shows one of the horizontal flow datasets from the previously analyzed light oil and water datasets of Plaxton (1995) in Figs. 5.5.5 and Fig. 1.3.12 in Chapter 1. In comparison to other models, we note the analytical NOSLIP model is quite accurate for this dataset.

Other than the NOSLIP model, other volume fraction models are found to satisfactorily predict the total pressure gradient behavior for different liquid-liquid and fluid-solid datasets. Fig. 5.9.6 shows one of the horizontal laminar-laminar, micro-channel flow datasets from the previously analyzed heavy oil and water datasets of Foroughi and Kawaji (2011) in Fig. 5.3.1. In comparison to other models, we note the BUTTERWORTH model is very accurate for this dataset.

Fig. 5.9.7 shows one of the air-glass beads vertical flow datasets from the previously analyzed experiments of Luo (1987) in Fig. 5.3.9. In comparison to the various two-fluid models shown in the top-most chart of Fig. 5.9.7, the analytical SLIPRATIO model provides an accurate prediction of this dataset.

Fig. 5.9.8 shows more data from the previously analyzed vertical air and fine glass spheres investigation of Wang et al. (2000), but this time re-expressed in the more traditional format of a “Zenz” plot. In comparison to the experimental results shown in the right-most chart of Fig. 5.9.8, the analytical SLIPRATIO model provides a satisfactory prediction of this dataset.

Lastly, the results shown in Fig. 5.9.9 demonstrate, in a clear and unambiguous way, that our analytical models are accurate and reproduce the trends in the data once the averaged volume fraction is known. This dataset was previously analyzed in Fig. 5.4.11 (i.e., the runs at +5 degrees from horizontal). The calculations of the different two-fluid models shown in Fig. 5.9.9 were taken from Fig. 12 of Lum et al. (2004).

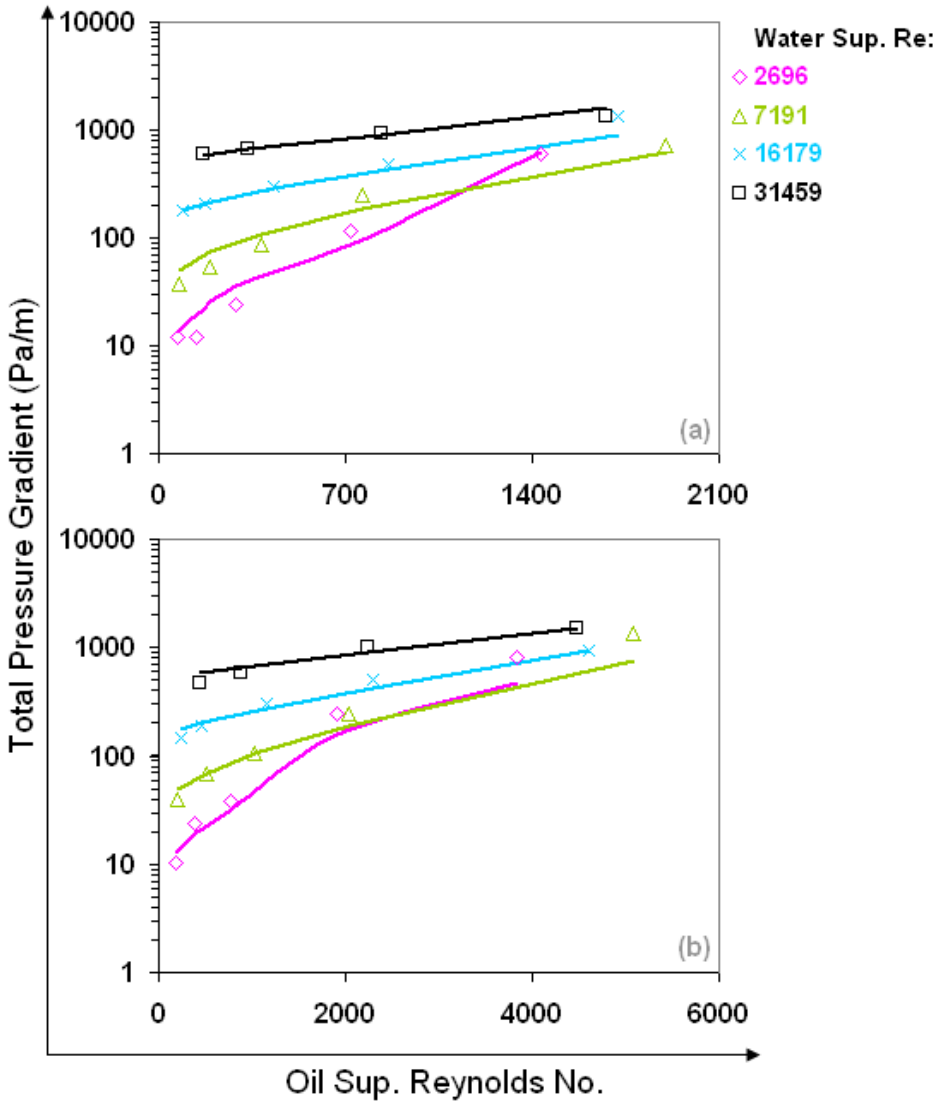

Figure 5.1.1: Validation of our analytical model against the classic horizontal liquid-liquid flow dataset of Charles et al. (1961). Lines are our calculations and the points are measurements.

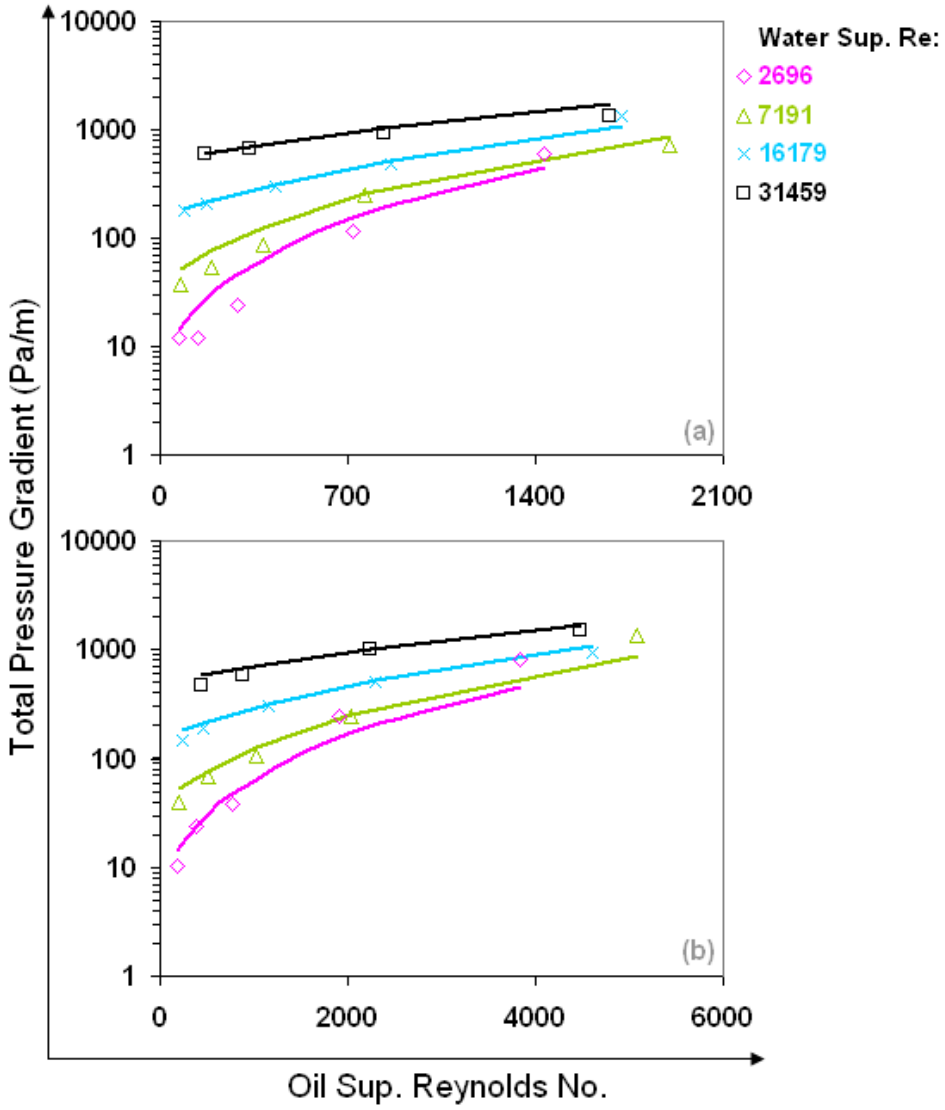

Figure 5.1.2: Prediction of the classic horizontal liquid-liquid flow dataset of Charles et al. (1961) with the NOSLIP model. Lines are our predictions and the points are measurements.

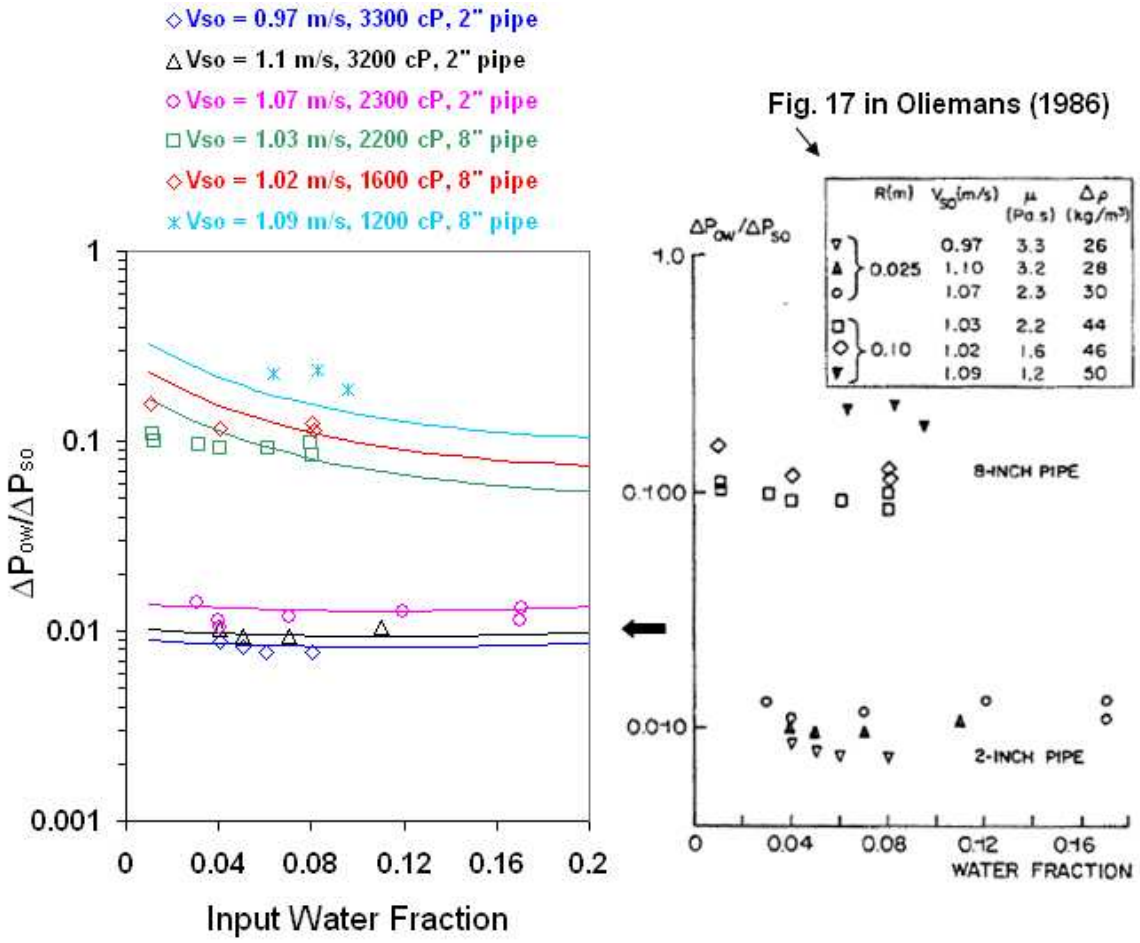

Figure 5.1.3: Prediction of the horizontal, large-diameter, heavy oil and water dataset of Oliemans (1986). Lines are our predictions and the points are measurements.

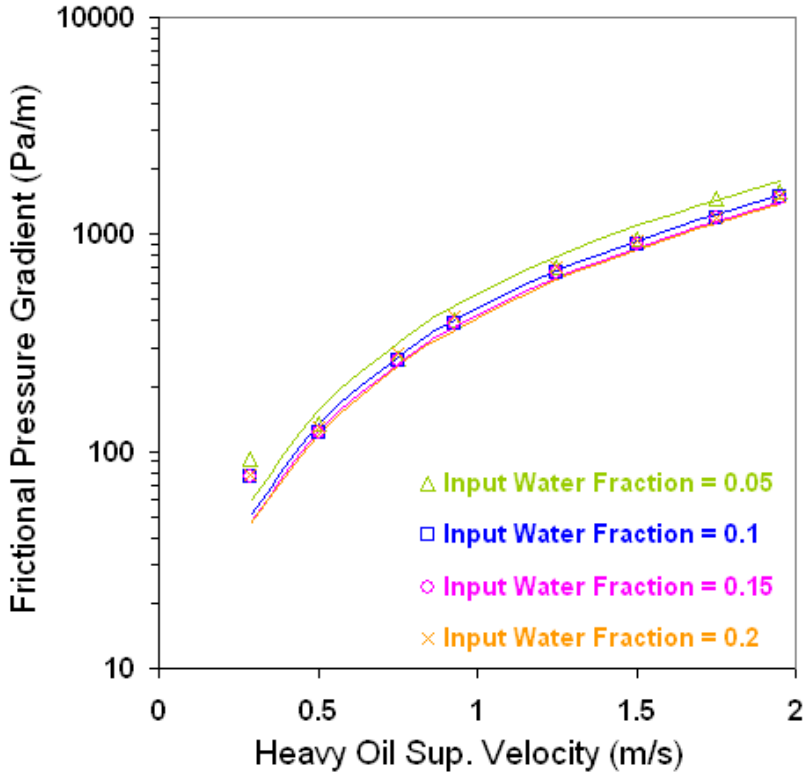

Figure 5.1.4: Prediction of the one of the datasets in the horizontal, large-diameter, heavy oil and water investigation of Oliemans (1986). Lines are our predictions and the points are measurements.

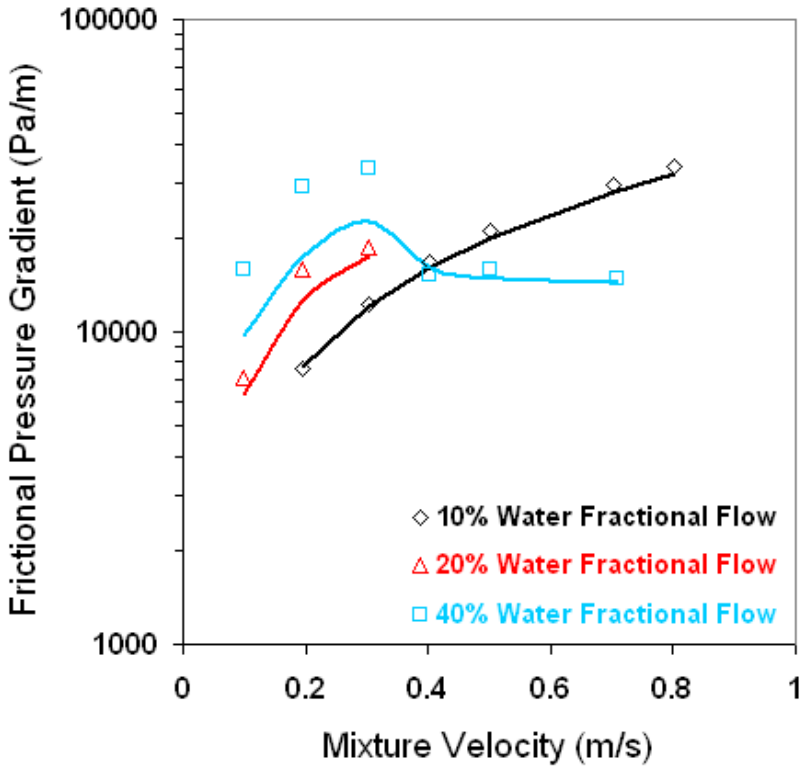

Figure 5.1.5: Prediction of the horizontal heavy oil and water flow dataset of Wang et al. (2011) with the NOSLIP model. Lines are our predictions and the points are measurements.

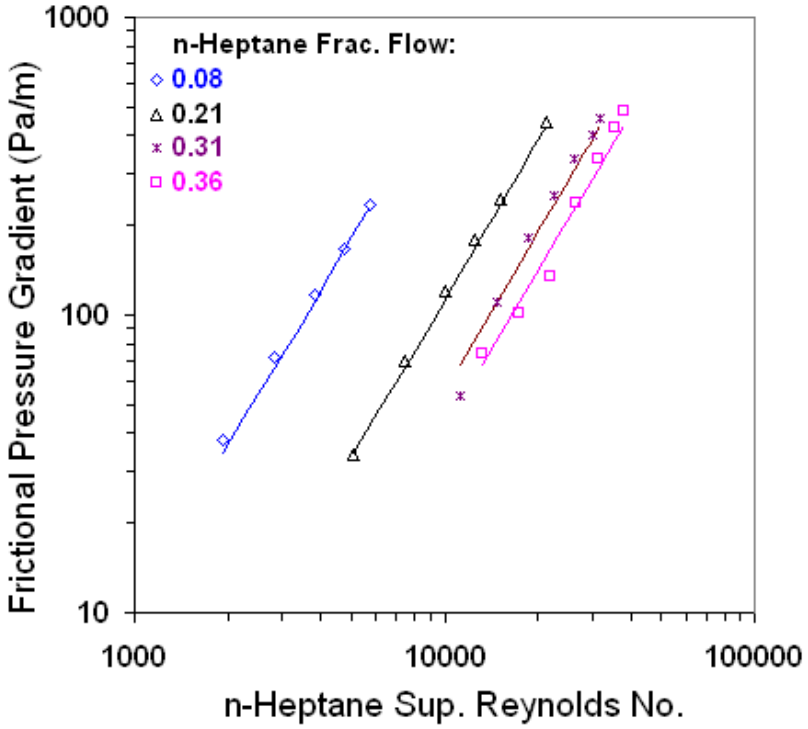

Figure 5.1.6: Prediction of the horizontal light oil and water flow dataset of Pouplin et al. (2011) with the NOSLIP model. Lines are our predictions and the points are measurements.

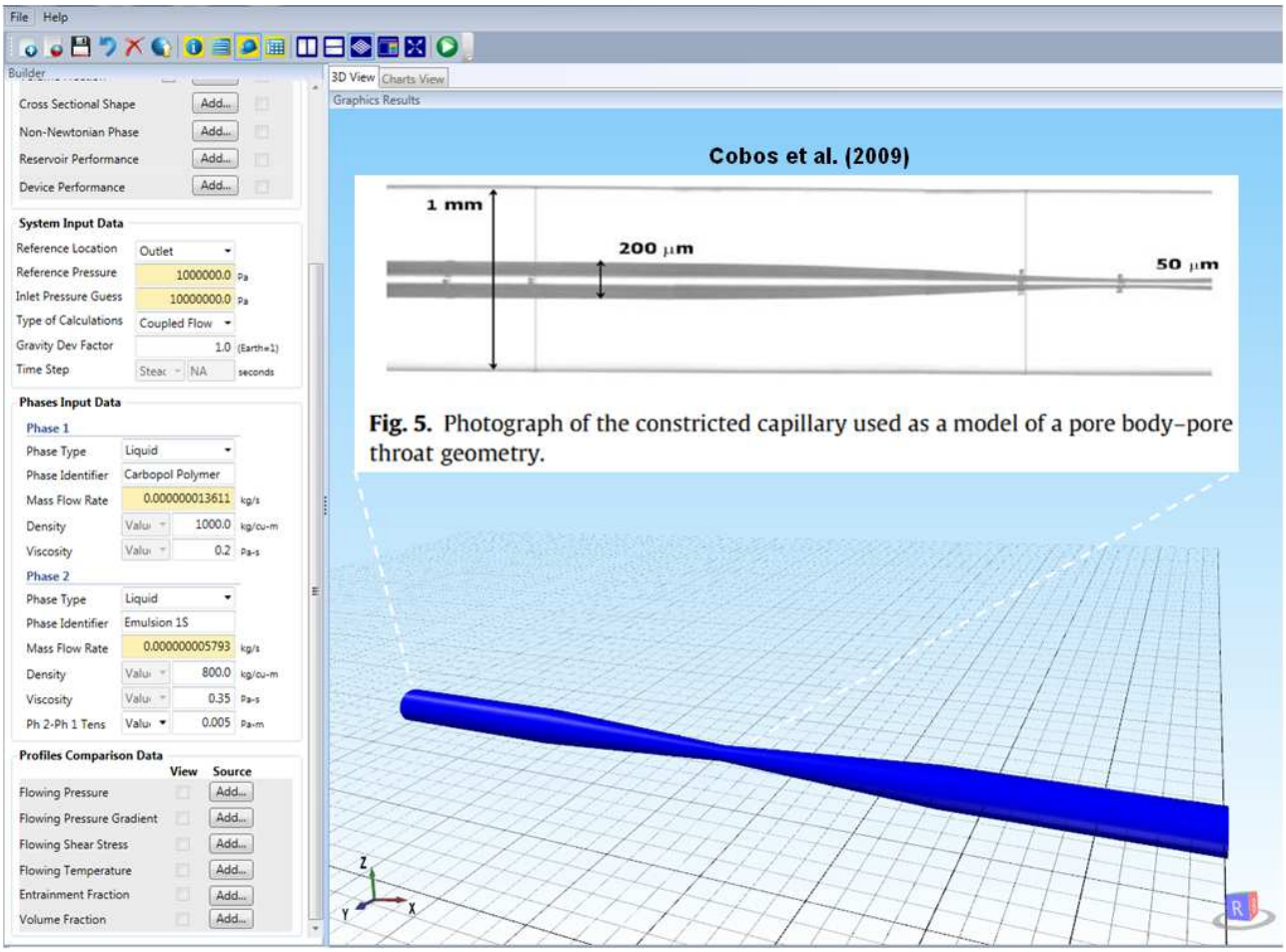

Figure 5.2.1: Example of a laminar-laminar flow of two non-Newtonian liquids through a constricted (micro-channel) capillary.

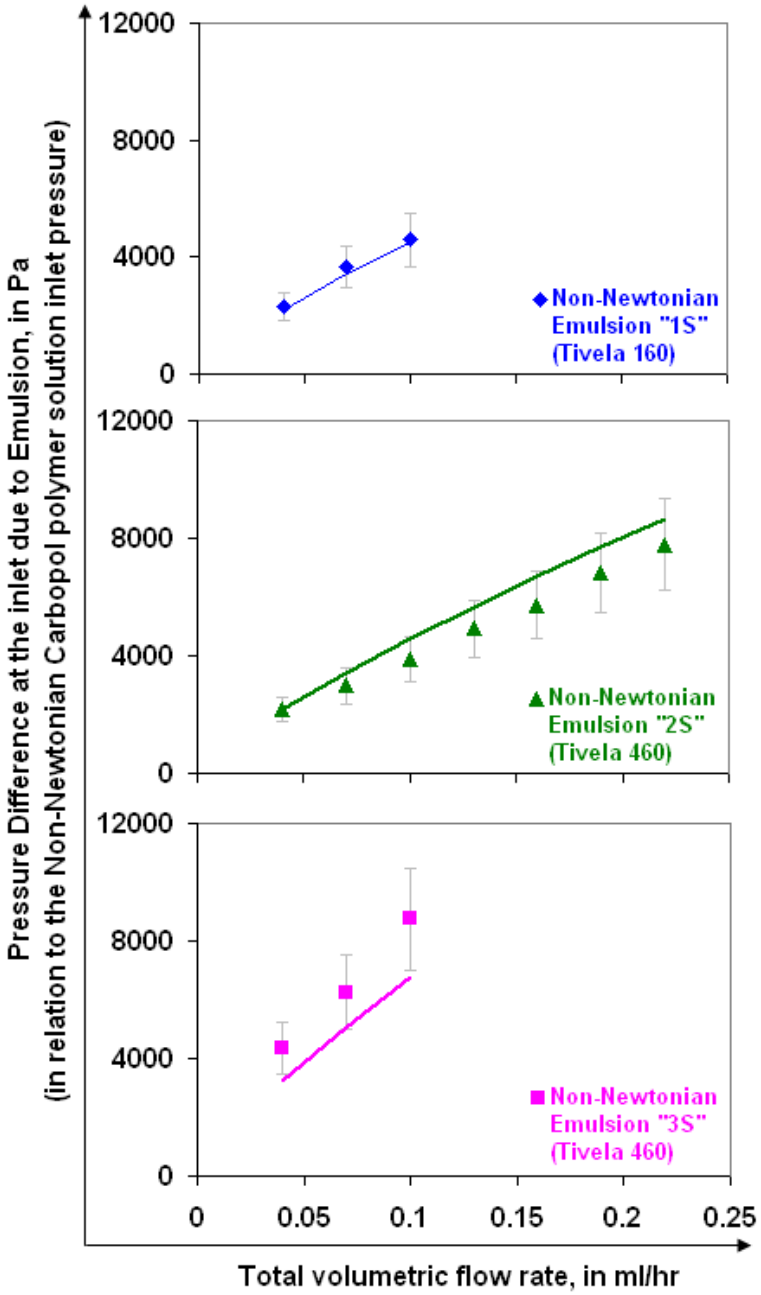

Figure 5.2.2: Prediction of the horizontal laminar-laminar, polymer-emulsion micro-channel flow dataset of Cobos et al. (2009) with the NOSLIP model. Lines are our predictions and the points are measurements.

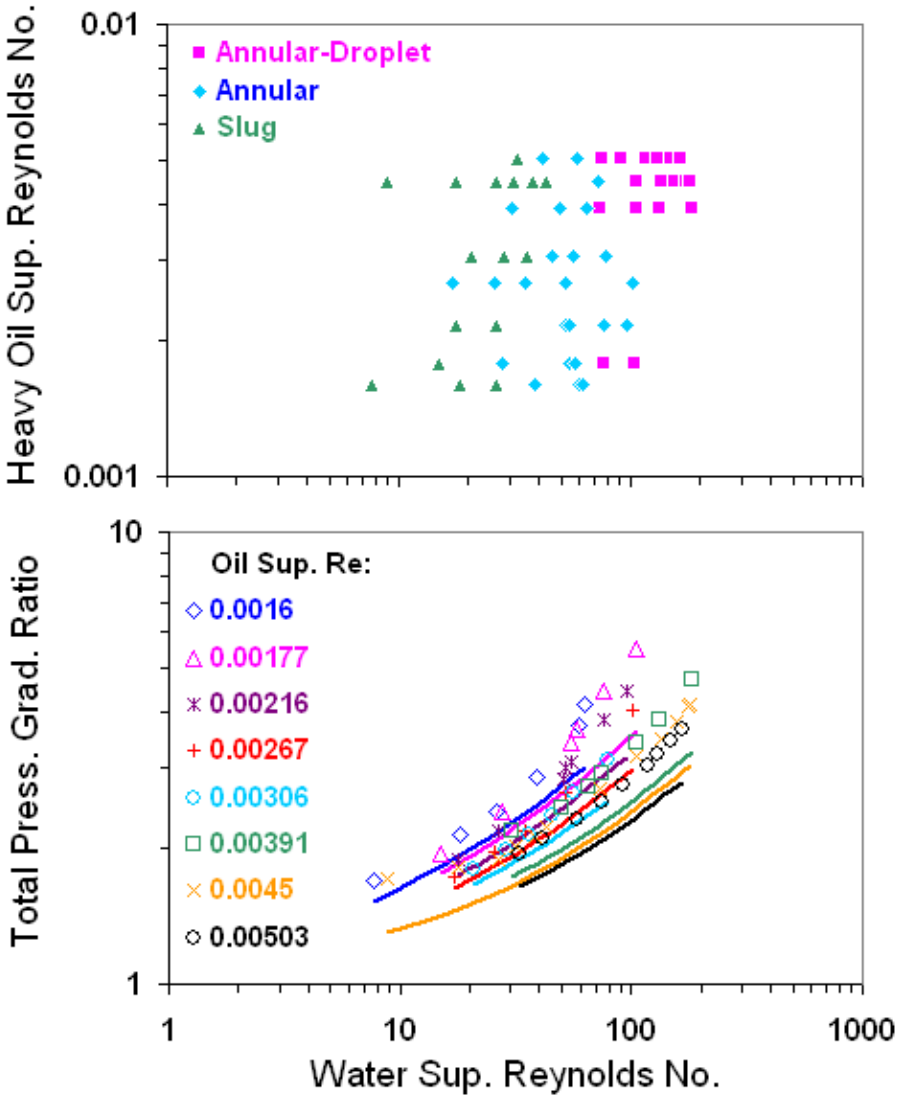

Figure 5.3.1: Prediction of the horizontal, laminar-laminar, heavy oil and water micro-channel flow dataset of Foroughi and Kawaji (2011) with the BUTTERWORTH model. Lines are our predictions and the points are measurements.

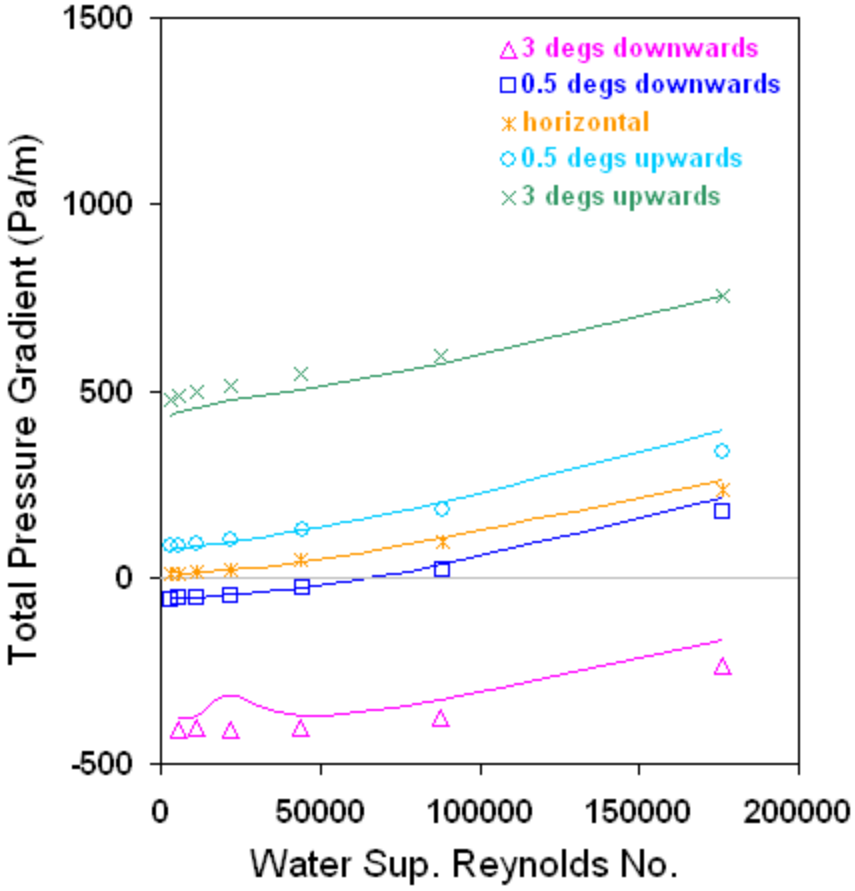

Figure 5.3.2: Validation of our analytical model against one dataset from the slightly-inclined large-diameter oil-water flow experiments of Abduvayt et al. (2006). Lines are our calculations and the points are measurements.

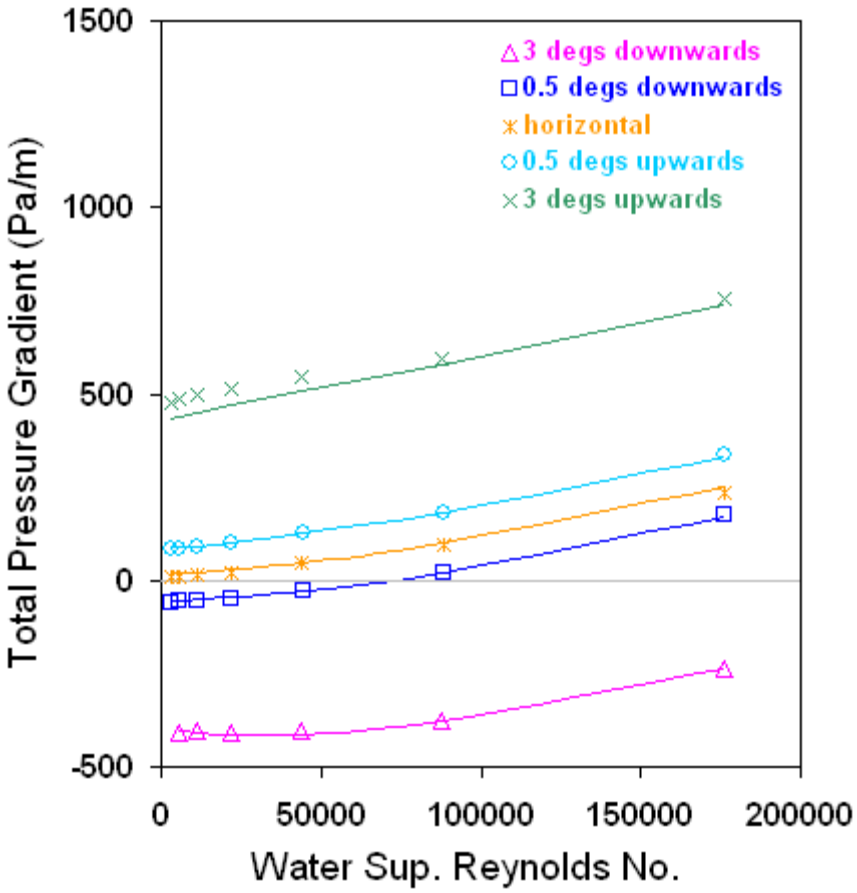

Figure 5.3.3: Prediction of one dataset from the slightly-inclined large-diameter oil-water flow experiments of Abduvayt et al. (2006) with the NOSLIP model. Lines are our predictions and the points are measurements.

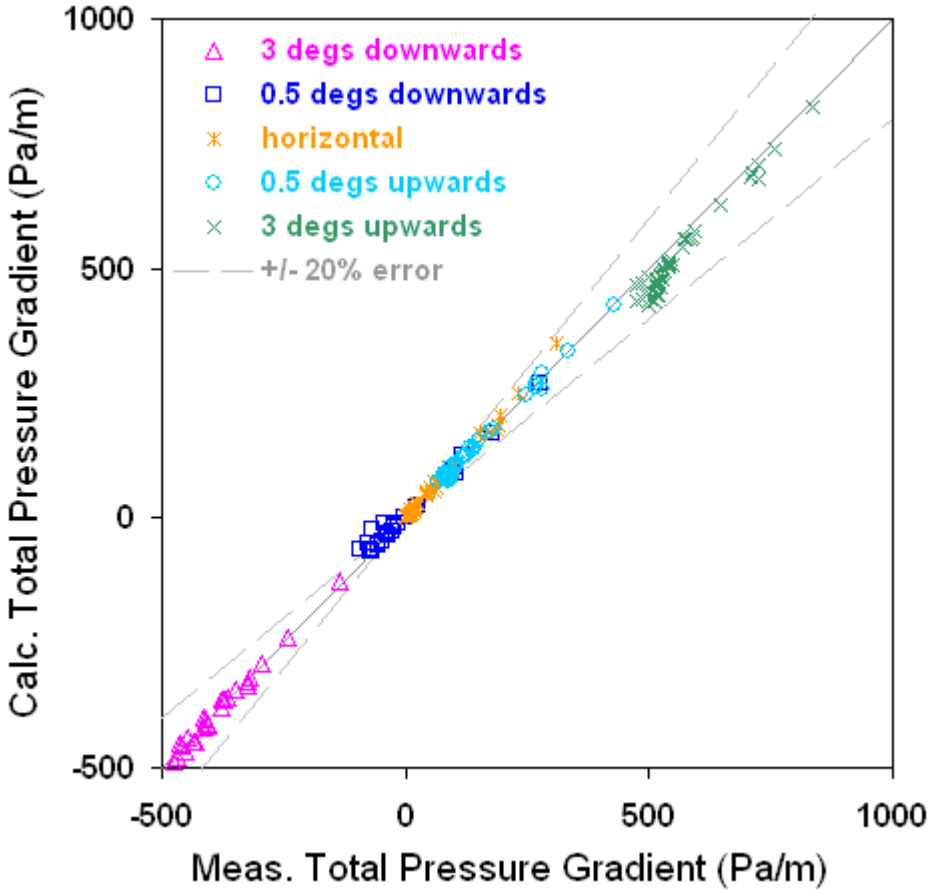

Figure 5.3.4: Prediction of all of the datasets from the slightly-inclined large-diameter oil-water flow experiments of Abduvayt et al. (2006) with the NOSLIP model.

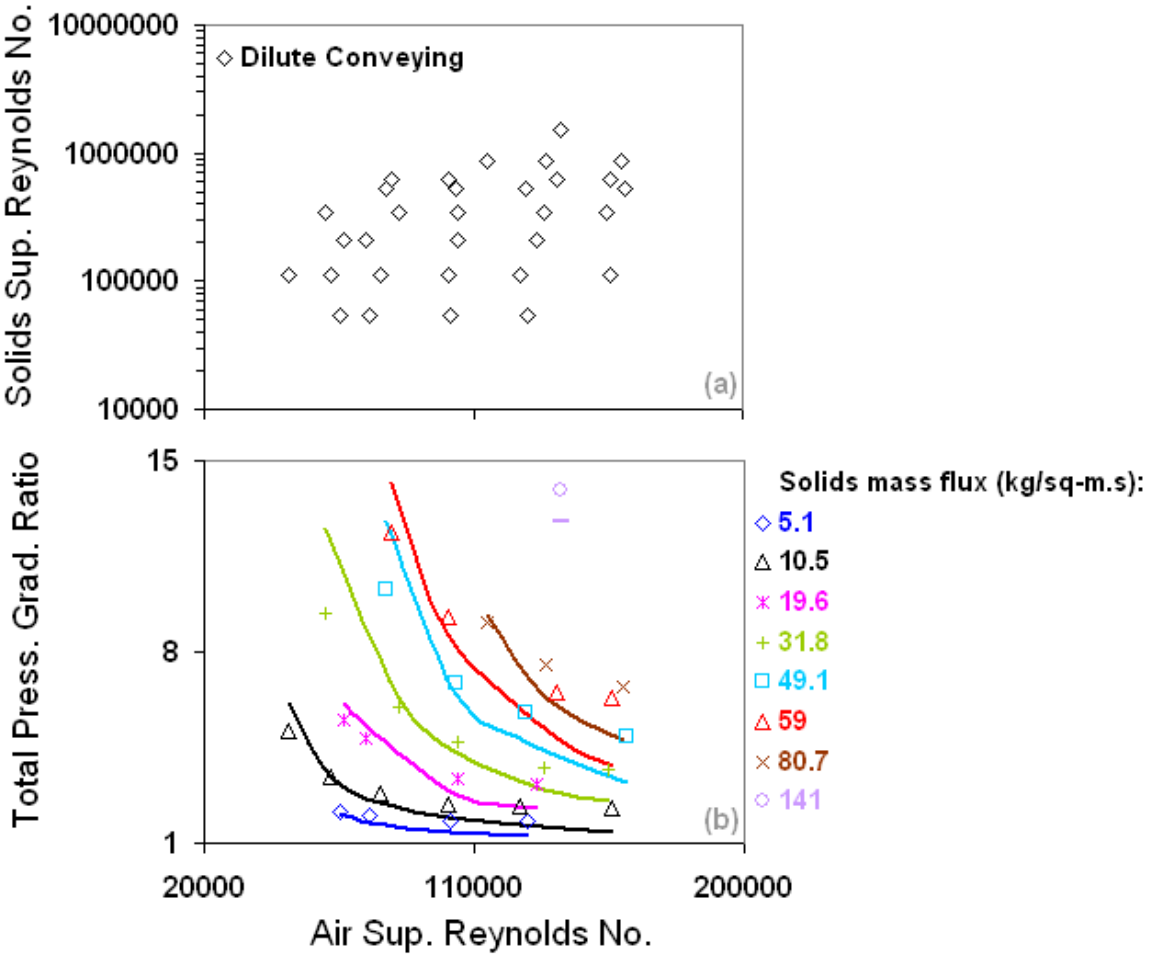

Figure 5.3.5: Validation of our analytical model against the vertical, large diameter dataset of Rautiainen et al. (1999). Lines are our calculations and the points are measurements.

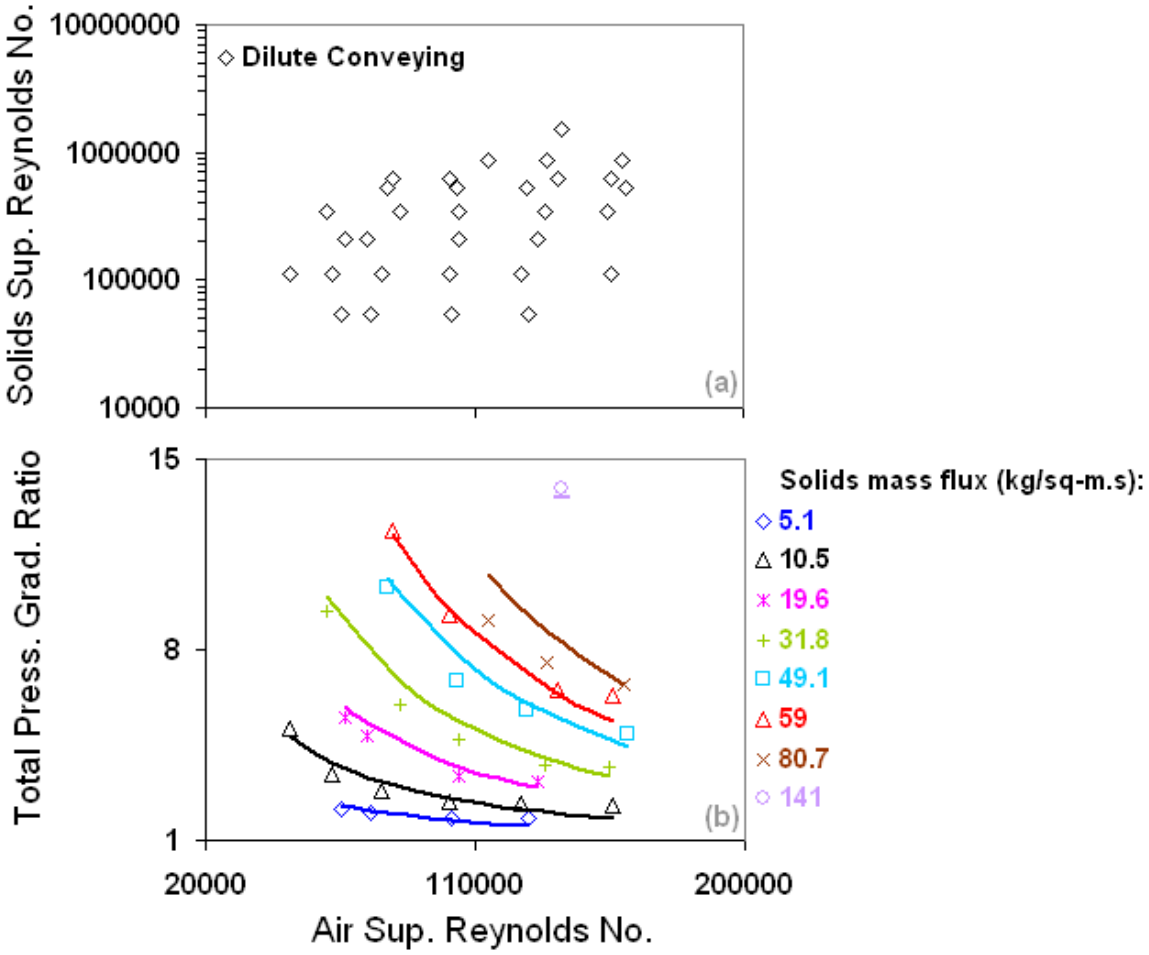

Figure 5.3.6: Prediction of the vertical, large diameter dataset of Rautiainen et al. (1999) with the SLIPRATIO model. Lines are our predictions and the points are measurements.

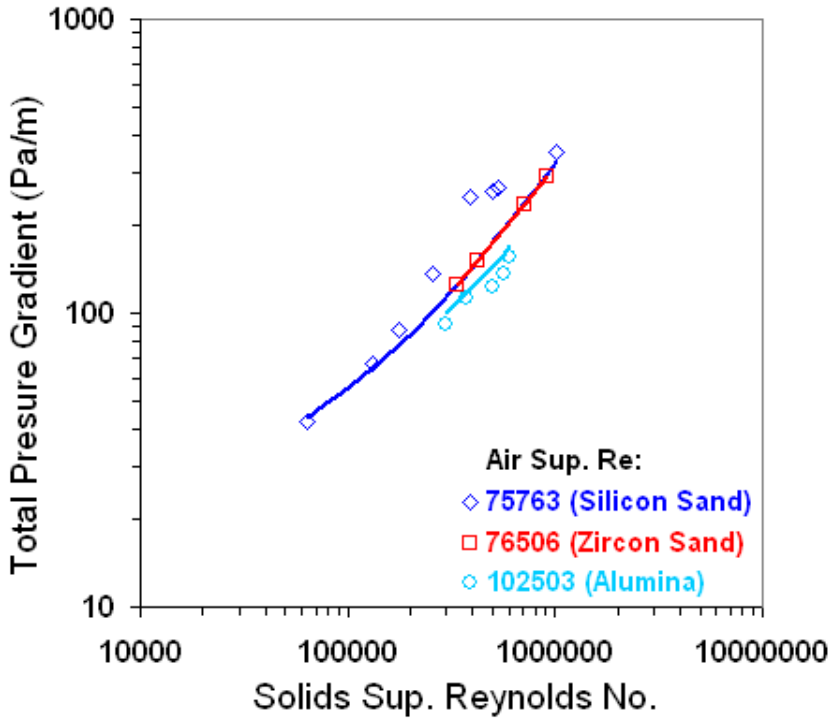

Figure 5.3.7: Prediction of the vertical, large diameter dataset of Singh (1982) with the SLIPRATIO model. Lines are our predictions and the points are measurements.

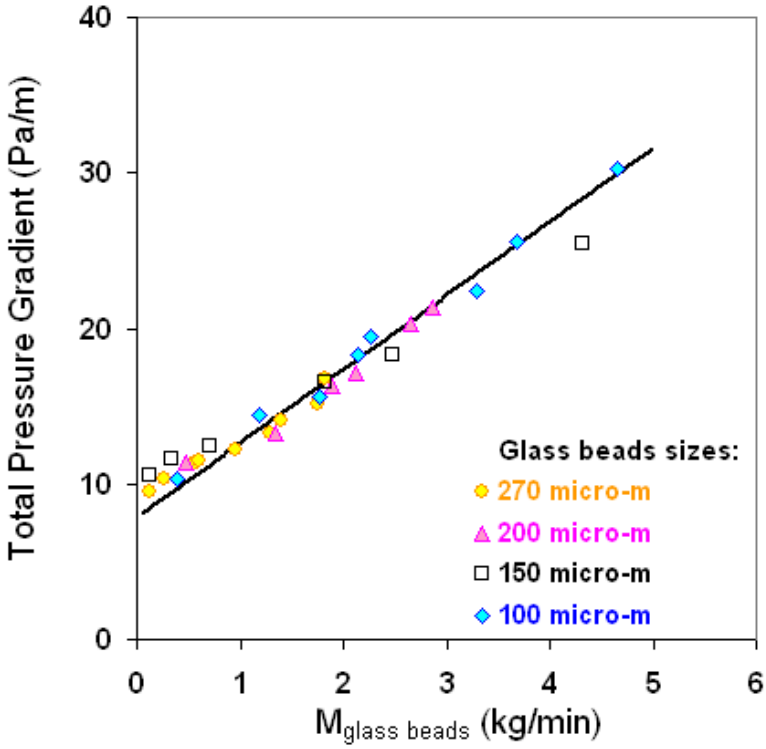

Figure 5.3.8: Prediction of the vertical, large diameter dataset of Reddy and Pei (1969) with the SLIPRATIO model. Lines are our predictions and the points are measurements.

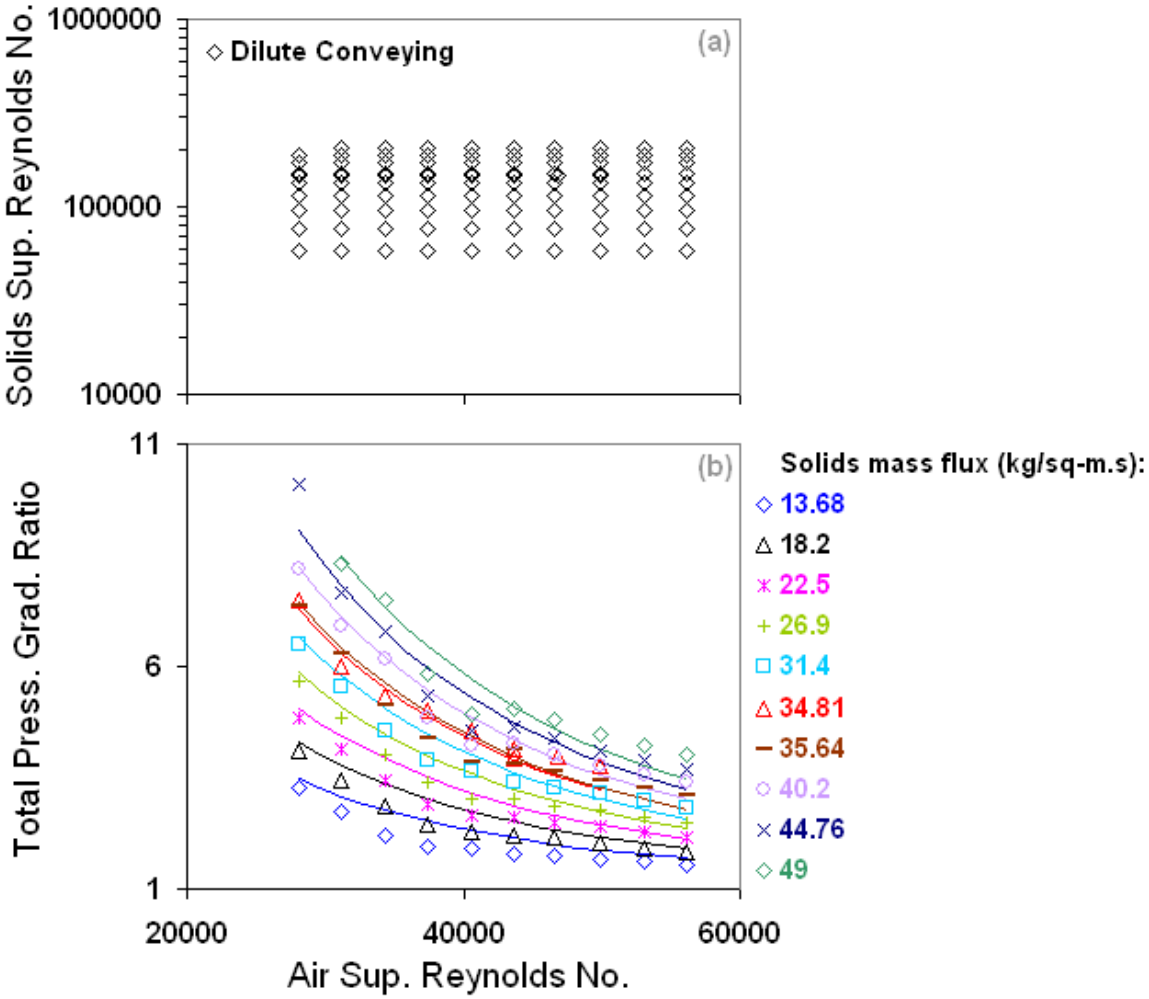

Figure 5.3.9: Prediction of the vertical air and glass beads dataset of Luo (1987) with the SLIPRATIO model. Lines are our predictions and the points are measurements.

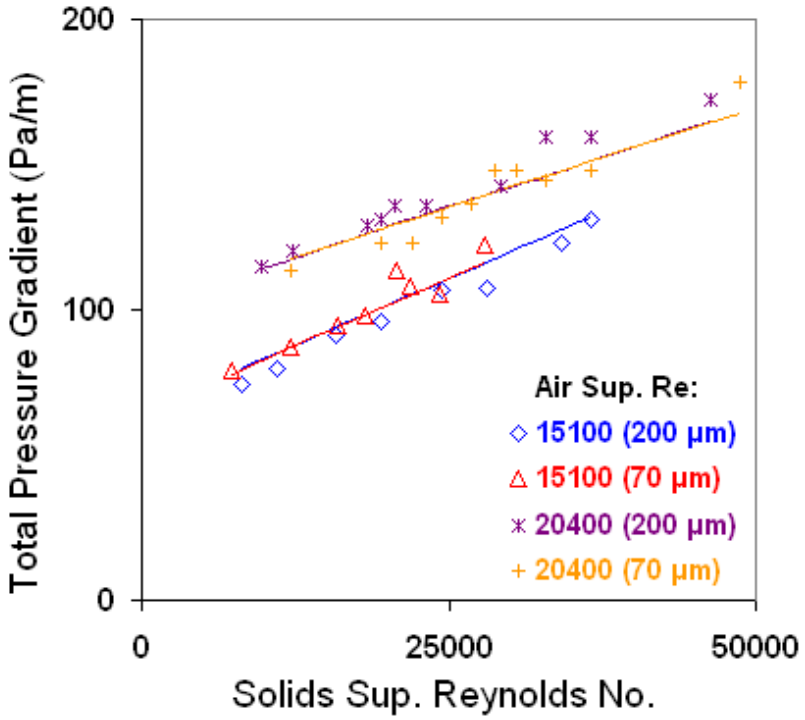

Figure 5.3.10: Prediction of the vertical air and glass beads dataset of Henthorn et al. (2005) with the SLIPRATIO model. Lines are our predictions and the points are measurements.

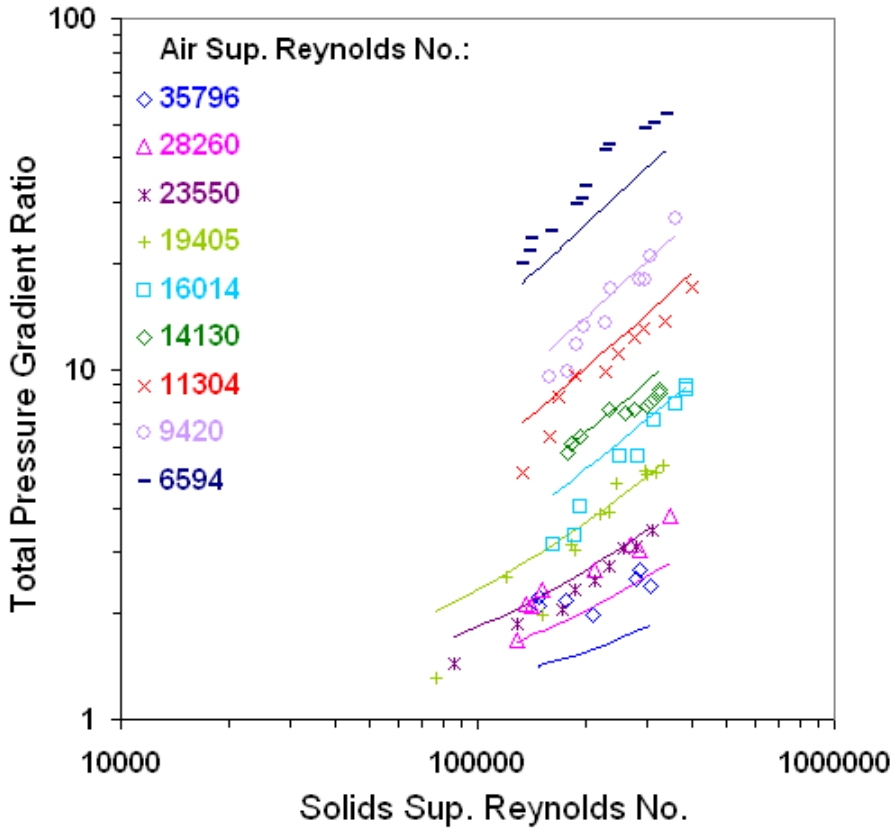

Figure 5.3.11: Prediction of the vertical air and class-C glass spheres dataset of Wang et al. (2000) with the SLIPRATIO model. Lines are our predictions and the points are measurements.

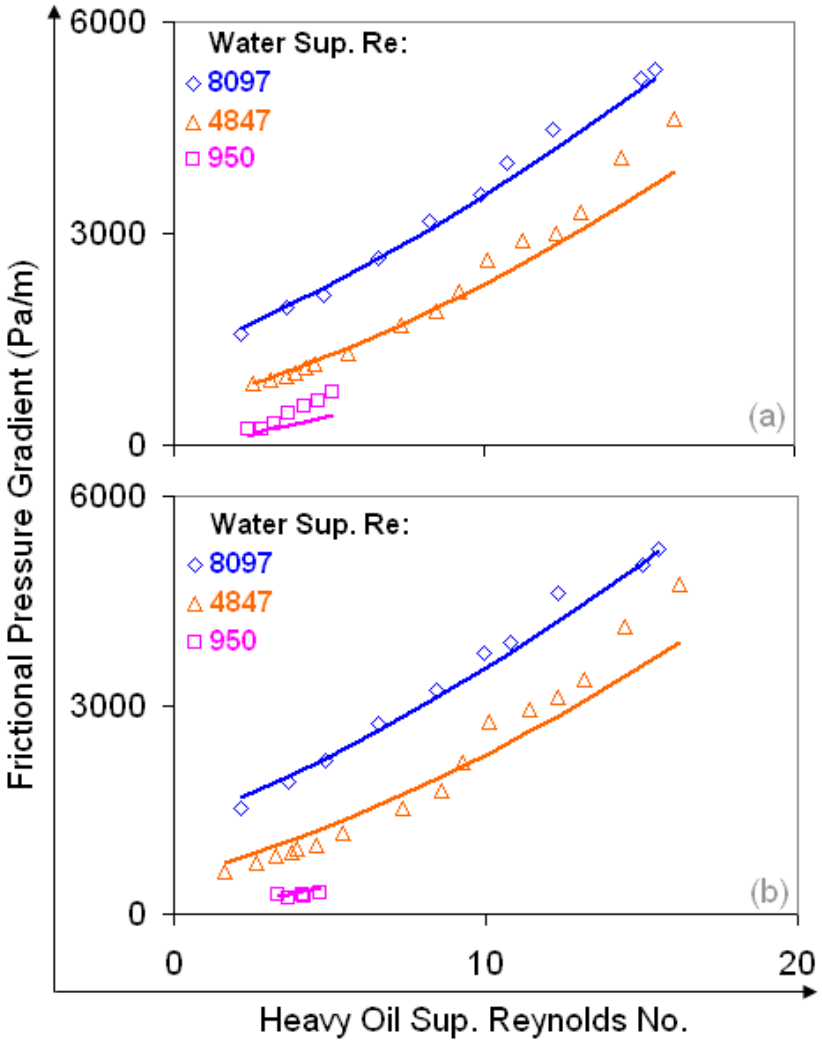

Figure 5.4.1: Prediction of the vertical-upward and vertical-downward heavy oil and water flow dataset of Bai (1995) with the NOSLIP model. Lines are our predictions and the points are measurements.

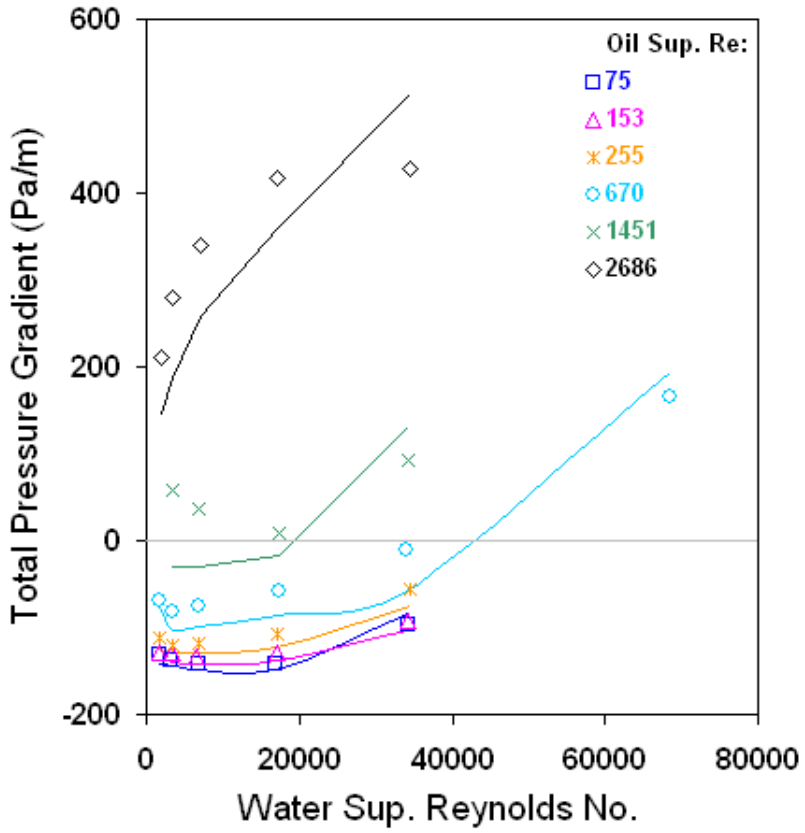

Figure 5.4.2: Validation of our analytical model against the -1 degrees from horizontal oil and water flow dataset of Alkaya (2000). Lines are our calculations and the points are measurements.

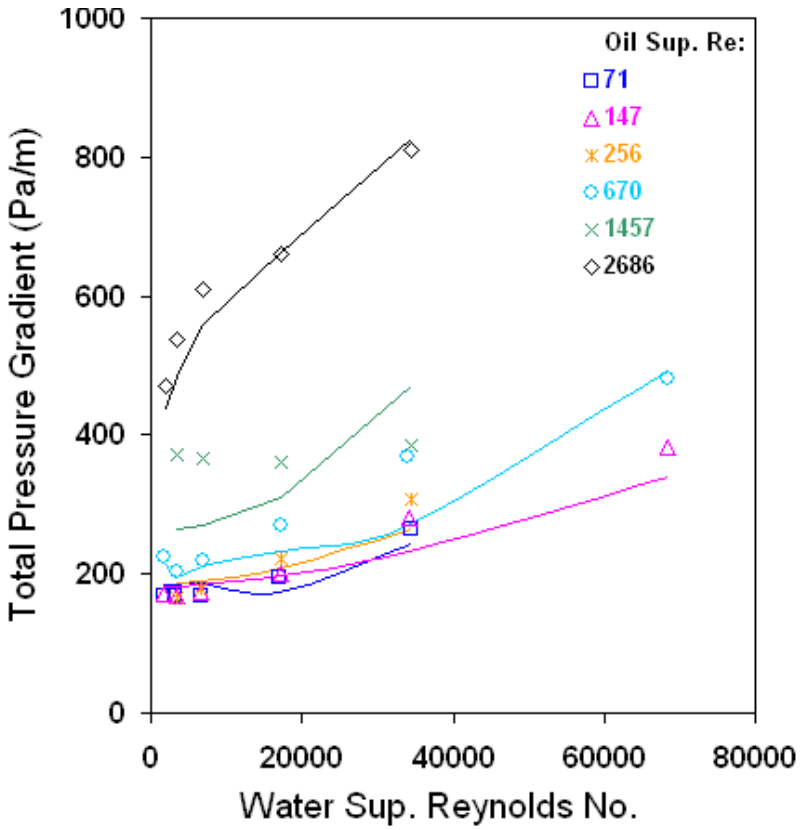

Figure 5.4.3: Validation of our analytical model against the +1 degrees from horizontal oil and water flow dataset of Alkaya (2000). Lines are our calculations and the points are measurements.

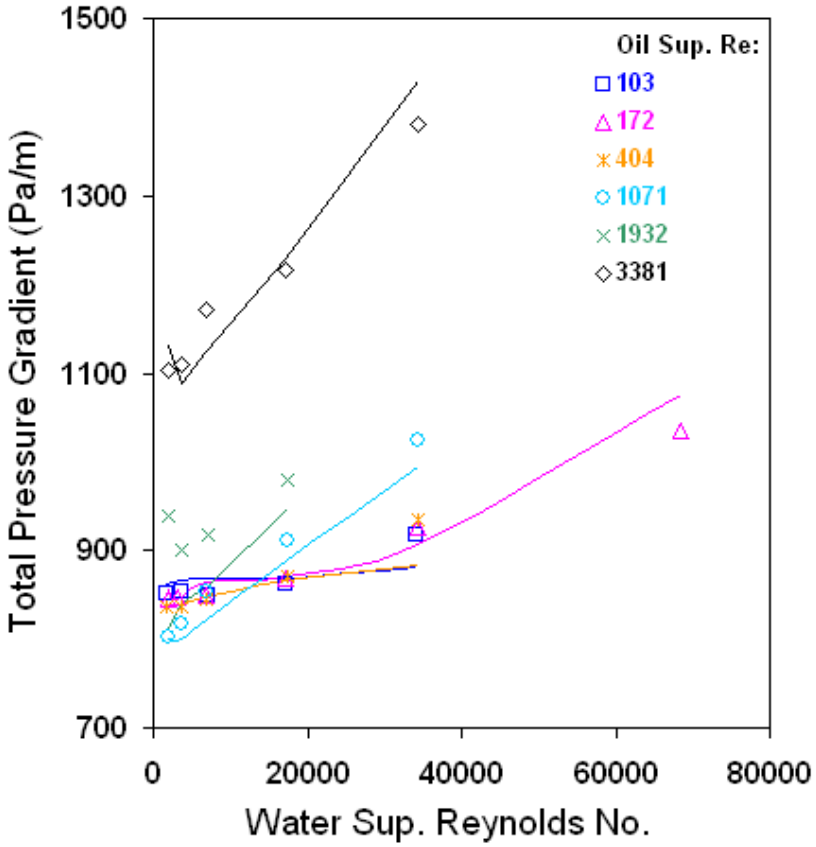

Figure 5.4.4: Validation of our analytical model against the +5 degrees from horizontal oil and water flow dataset of Alkaya (2000). Lines are our calculations and the points are measurements.

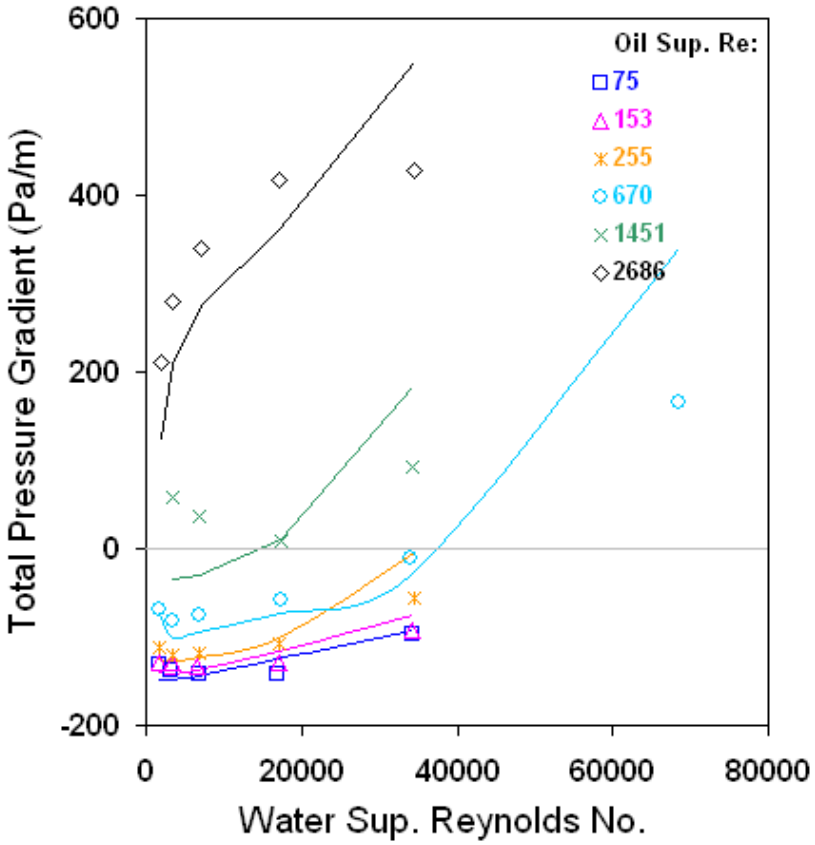

Figure 5.4.5: Prediction of the -1 degrees from horizontal oil and water flow dataset of Alkaya (2000) with the NOSLIP model. Lines are our predictions and the points are measurements.

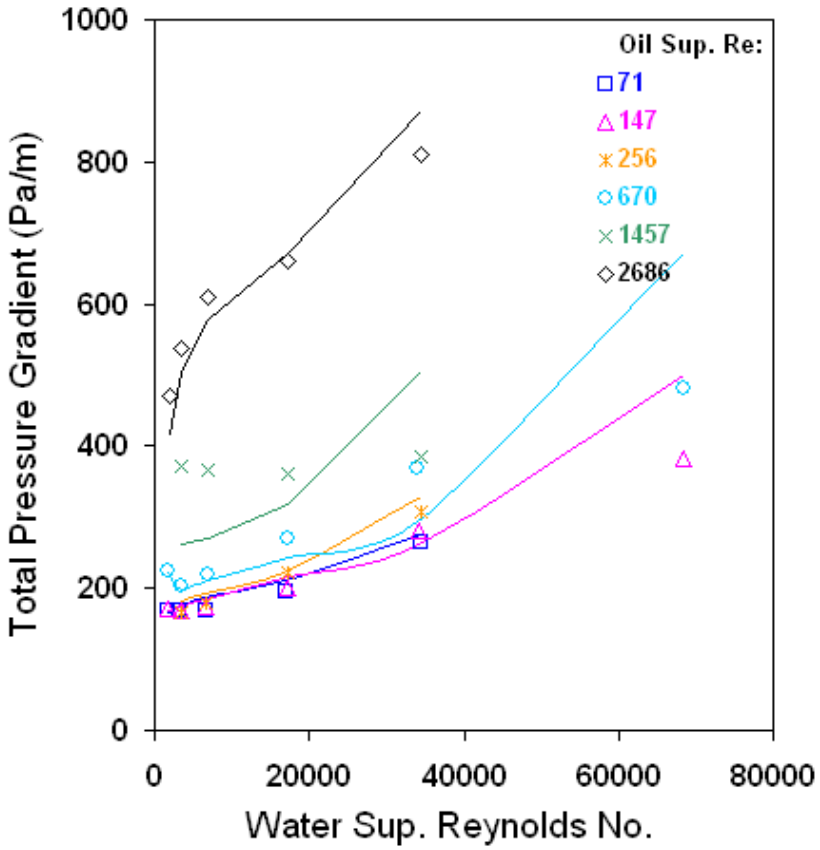

Figure 5.4.6: Prediction of the +1 degrees from horizontal oil and water flow dataset of Alkaya (2000) with the NOSLIP model. Lines are our predictions and the points are measurements.

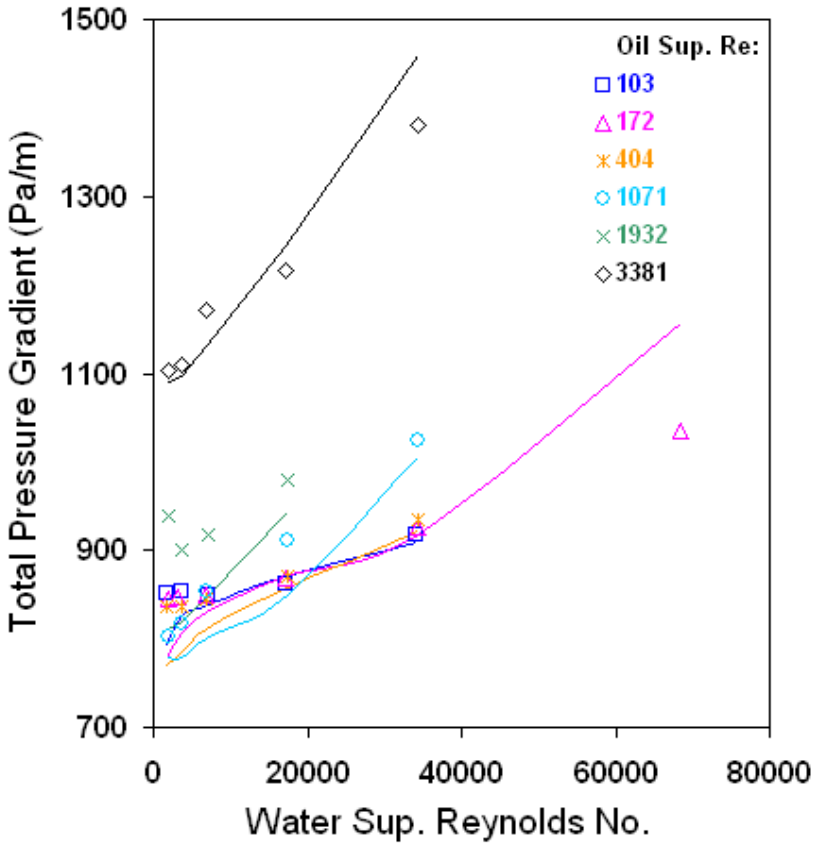

Figure 5.4.7: Prediction of the +5 degrees from horizontal oil and water flow dataset of Alkaya (2000) with the NOSLIP model. Lines are our predictions and the points are measurements.

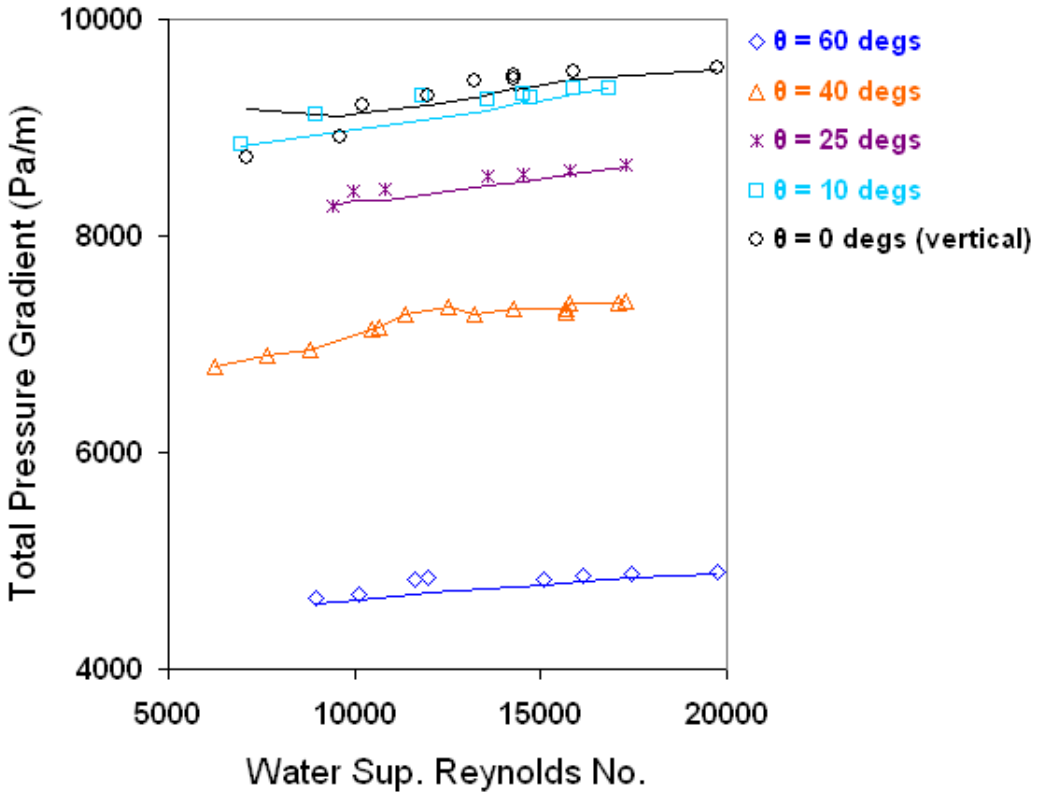

Figure 5.4.8: Validation of our analytical model against the up-inclined oil and water flow dataset of Mukhopadhyay (1997). Lines are our calculations and the points are measurements.

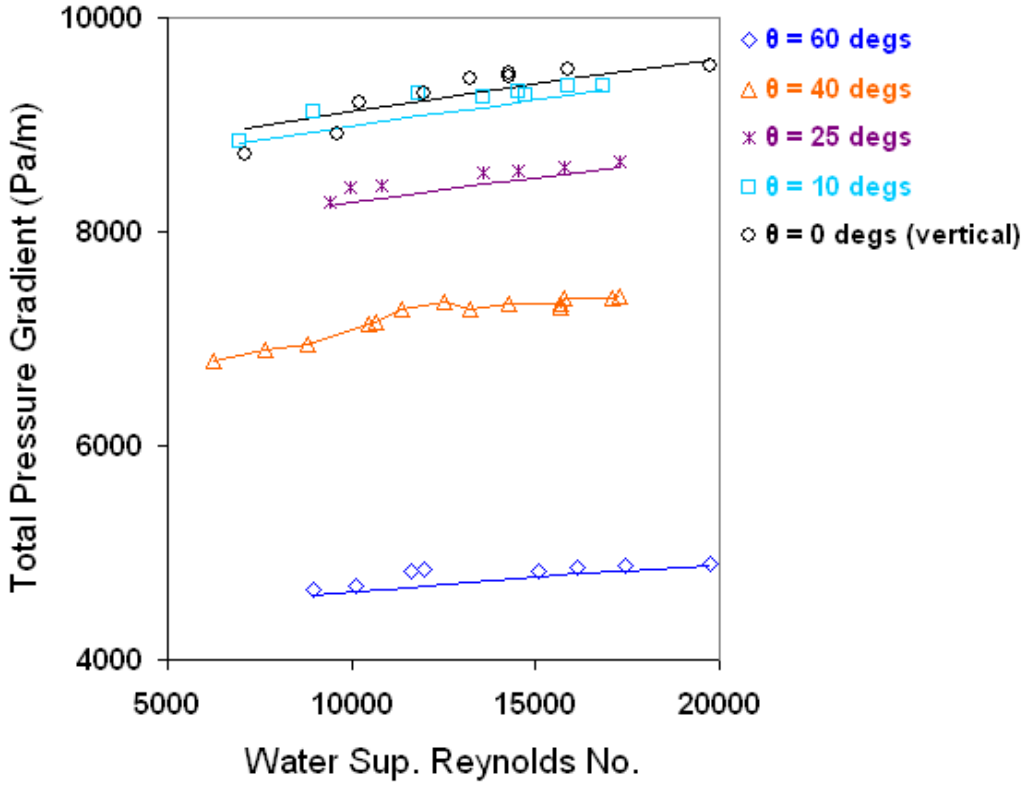

Figure 5.4.9: Prediction of the up-inclined oil and water flow dataset of Mukhopadhyay (1977) with the NOSLIP model. Lines are our predictions and the points are measurements.

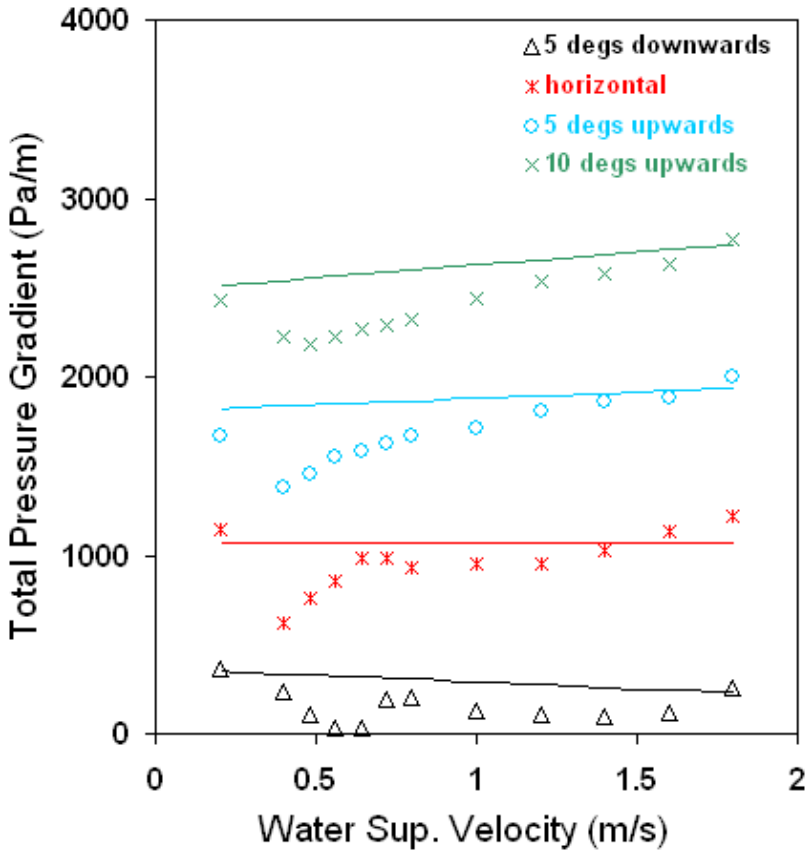

Figure 5.4.10: Prediction of a representative up- and down-inclined oil and water flow dataset of Lum et al. (2006) with the NOSLIP model. Lines are our predictions and the points are measurements.

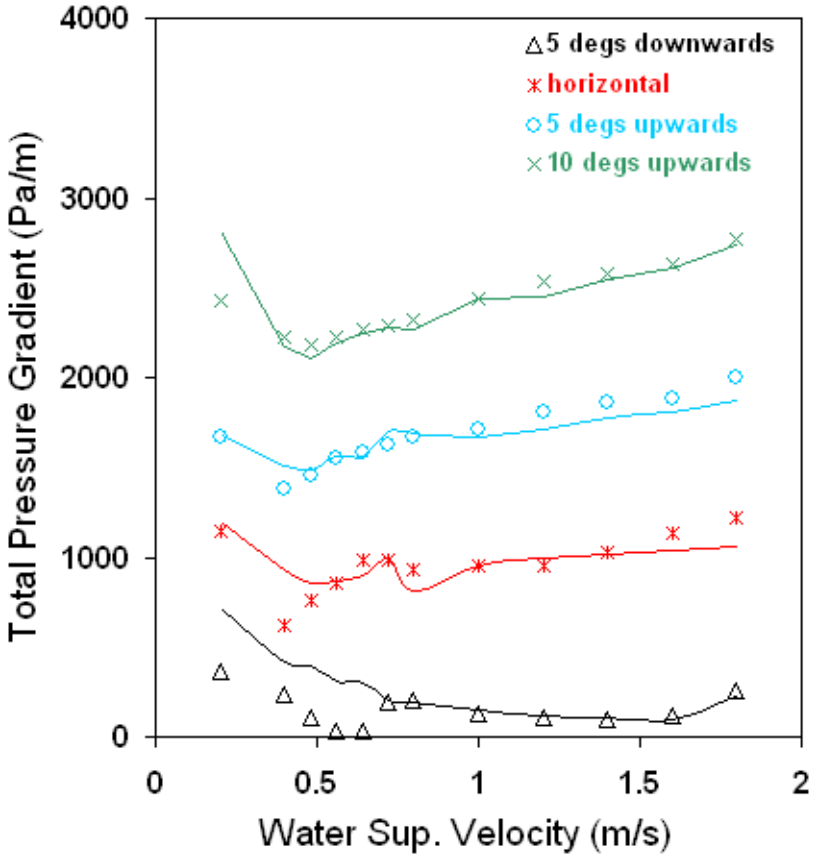

Figure 5.4.11: Validation of our analytical model against a representative up- and down-inclined oil and water flow dataset of Lum et al. (2006). Lines are our calculations and the points are measurements.

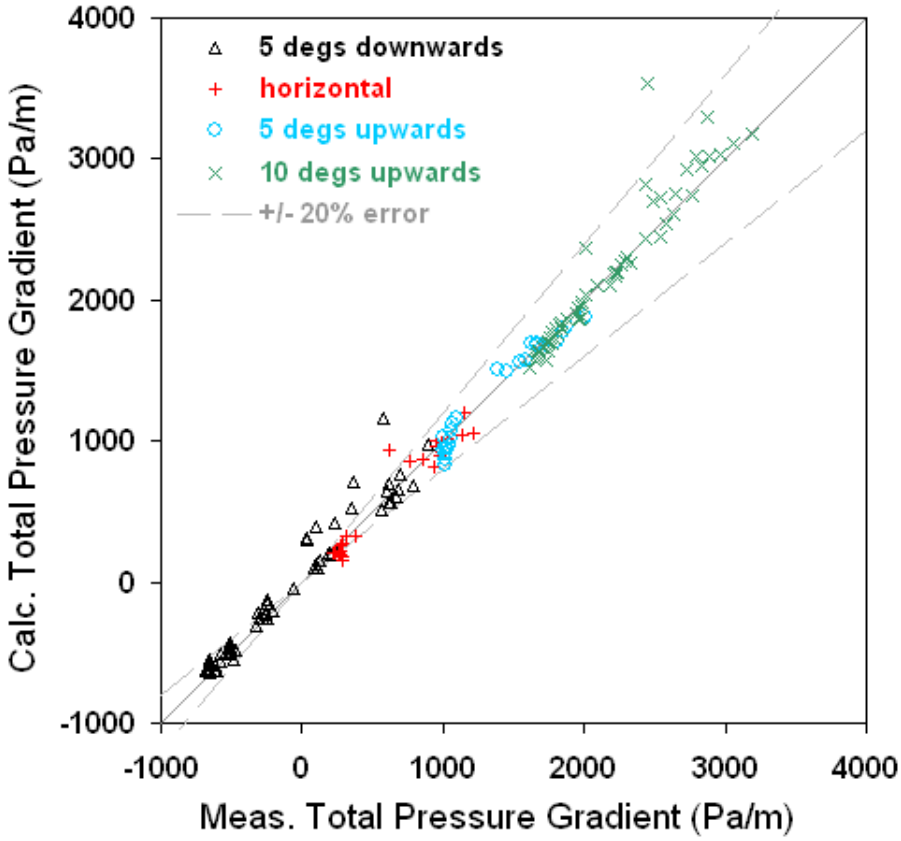

Figure 5.4.12: Validation of our analytical model against all of the up- and down-inclined oil and water flow datasets of Lum et al. (2006). Lines are our calculations and the points are measurements.

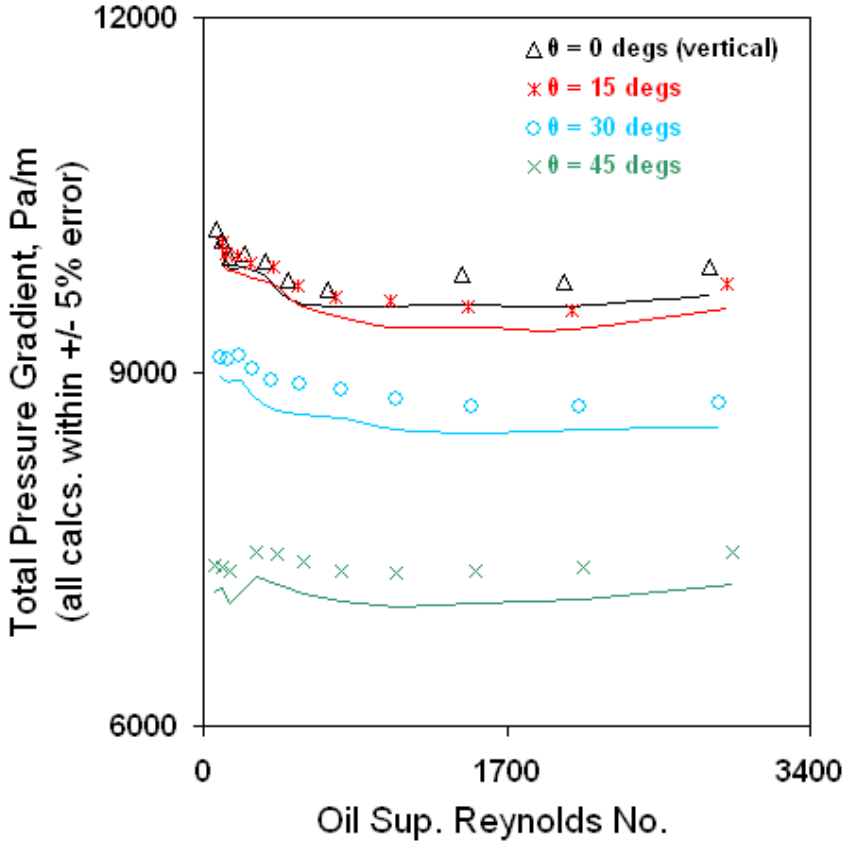

Figure 5.4.13: Prediction of a representative up-inclined oil and water flow dataset of Flores (1997) with the NOSLIP model. Lines are our predictions and the points are measurements.

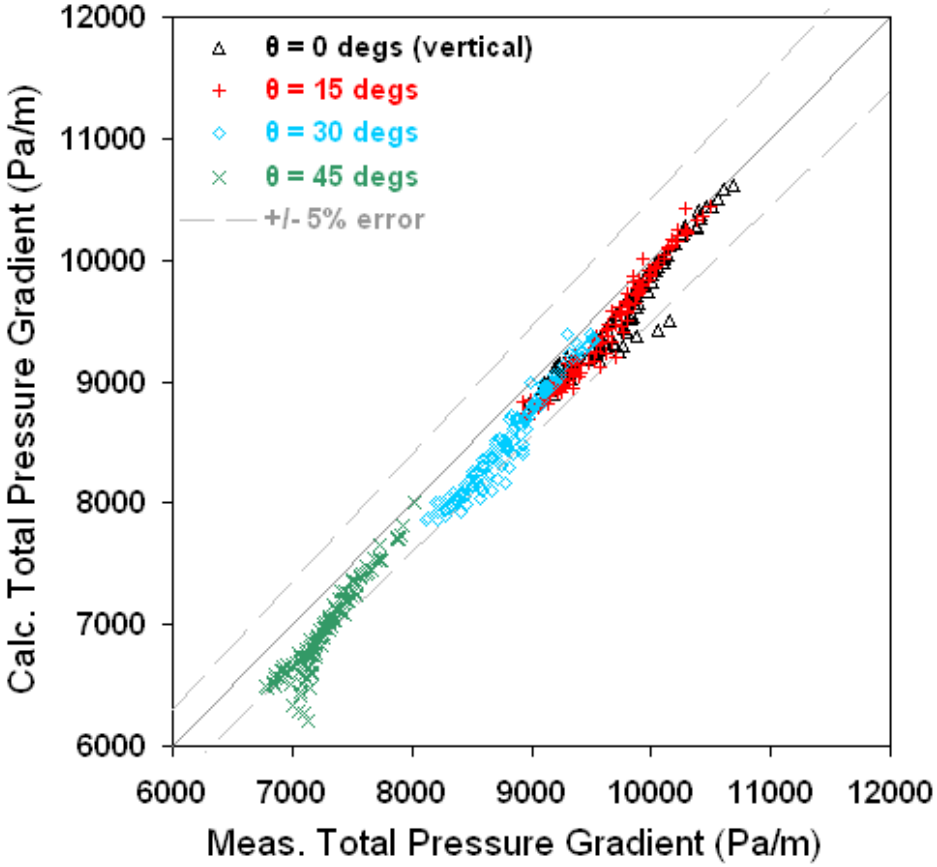

Figure 5.4.14: Prediction of all of the up-inclined oil and water flow datasets of Flores (1997) with the NOSLIP model.

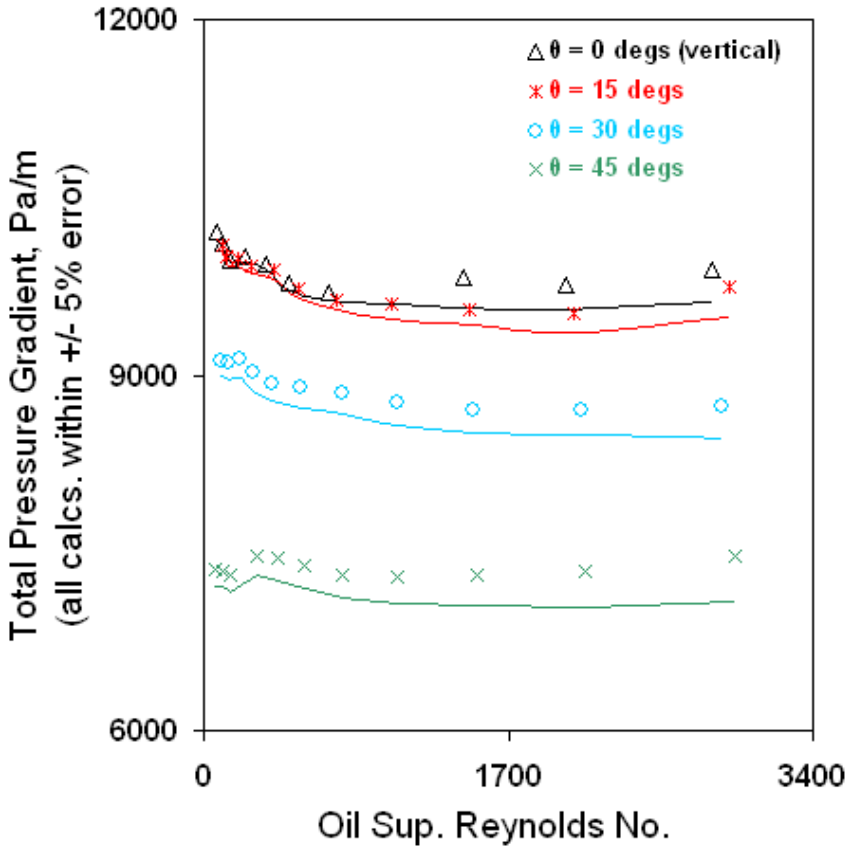

Figure 5.4.15: Validation of our analytical model against a representative up-inclined oil and water flow dataset of Flores (1997). Lines are our calculations and the points are measurements.

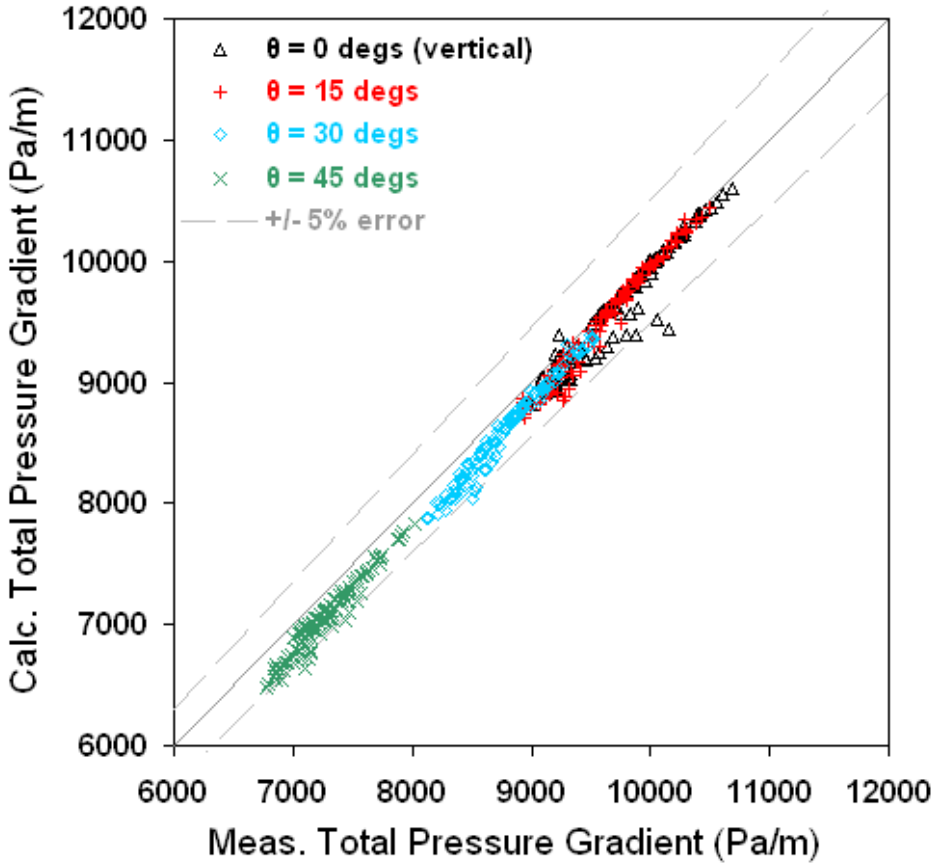

Figure 5.4.16: Validation of our analytical model against all of the up-inclined oil and water flow datasets of Flores (1997).

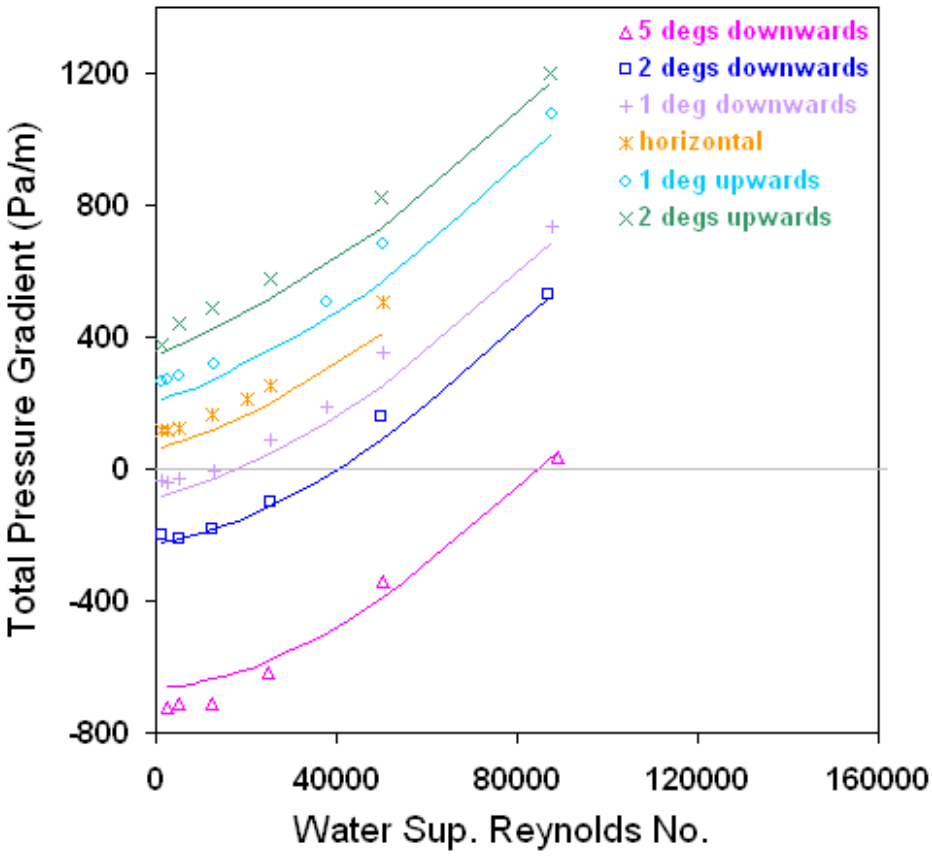

Figure 5.4.17: Prediction of a representative up- and down-inclined oil and water flow dataset of Atmaca (2007) with the NOSLIP model. Lines are our predictions and the points are measurements.

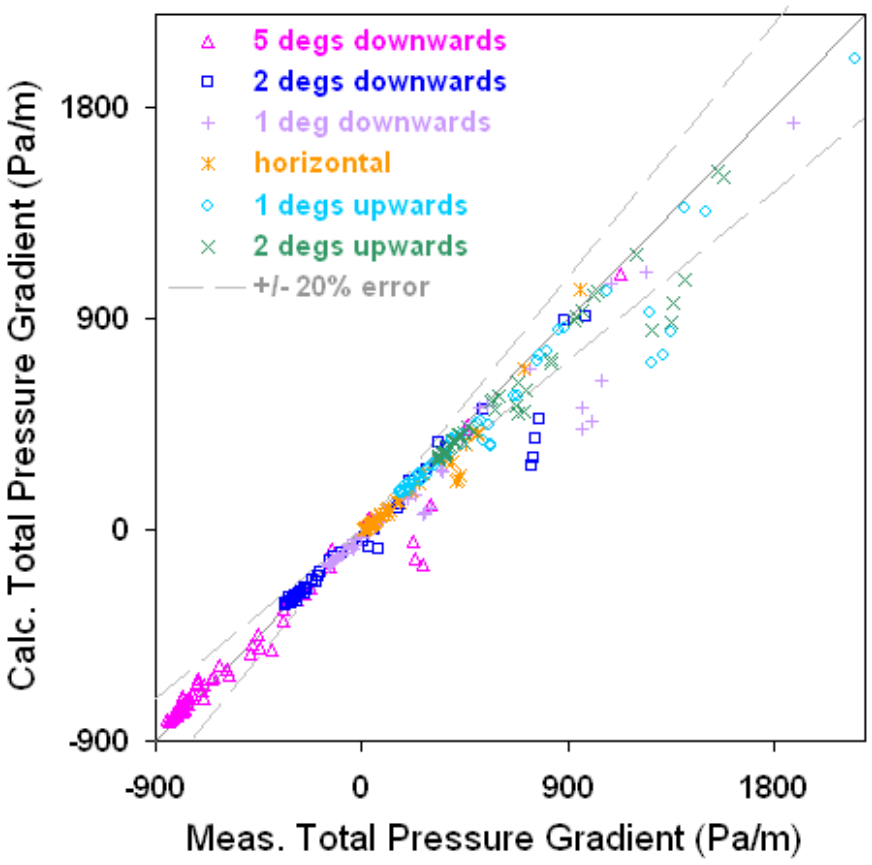

Figure 5.4.18: Prediction of all of the up- and down-inclined oil and water flow datasets of Atmaca (2007) with the NOSLIP model.

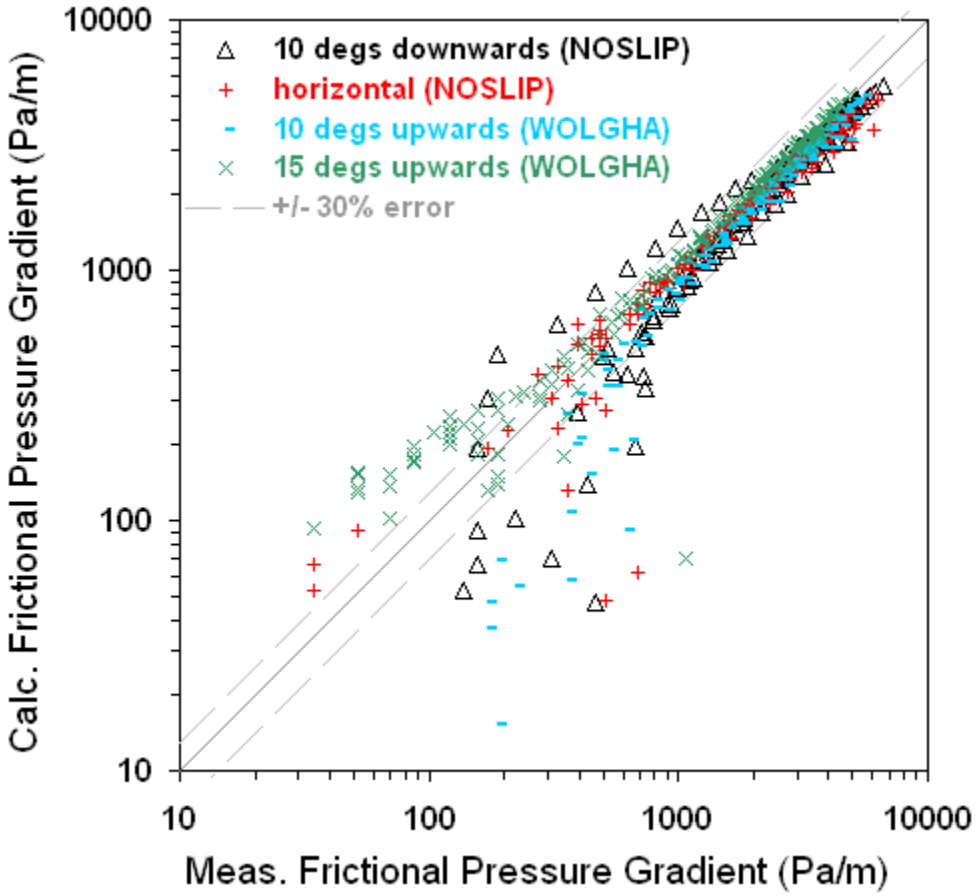

Figure 5.4.19: Prediction of all of the up- and down-inclined heavy oil and water flow datasets of Grassi et al. (2008) with the NOSLIP model.

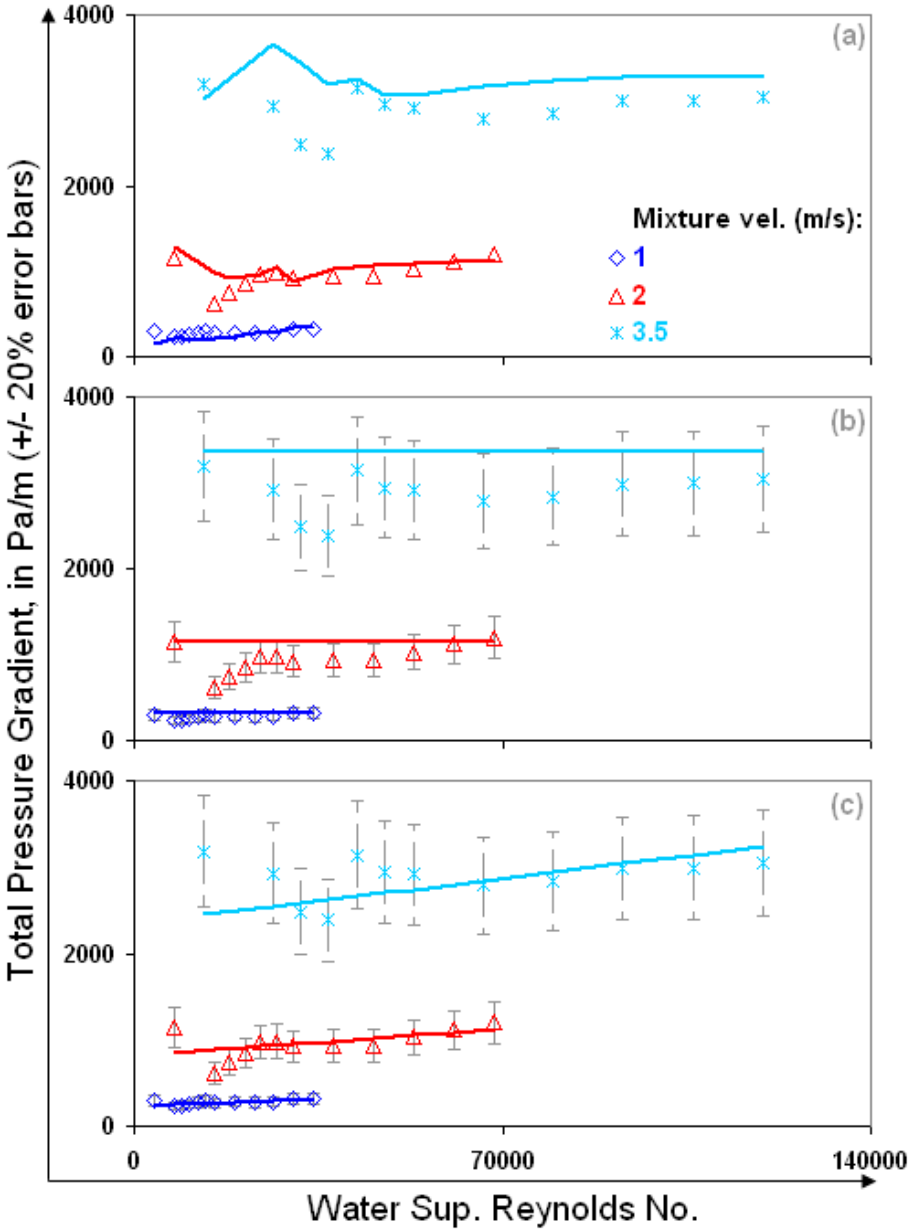

Figure 5.5.1: Prediction of representative horizontal oil and water flow datasets of Lovick (2004) with the (b) NOSLIP and (c) SLIPRATIO models. Lines are our predictions and the points are measurements.

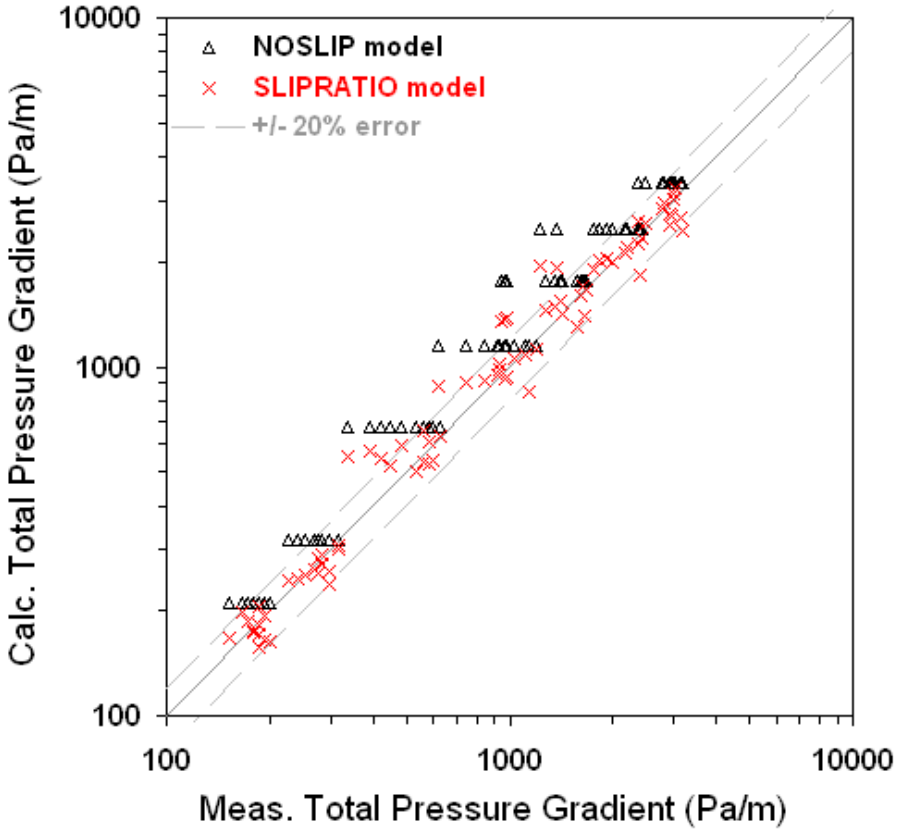

Figure 5.5.2: Prediction of all of the horizontal oil and water flow datasets of Lovick (2004) with the NOSLIP and SLIPRATIO models.

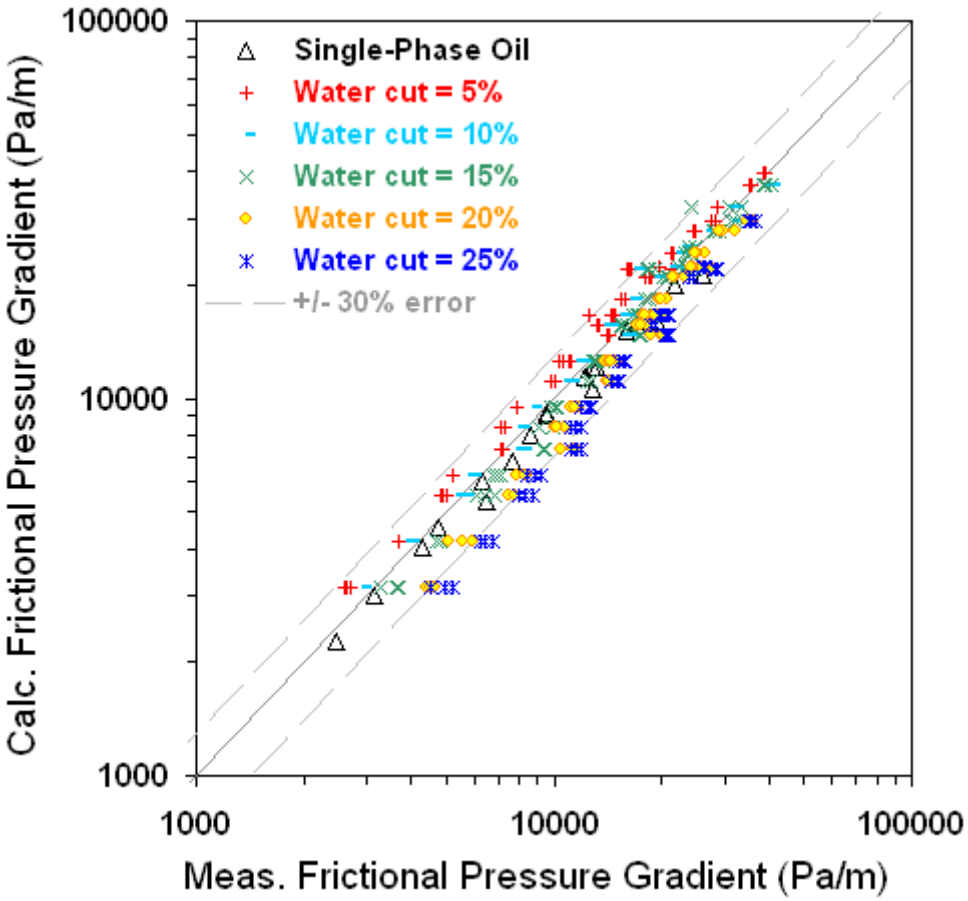

Figure 5.5.3: Prediction of all of the horizontal oil and water flow datasets of Martinez (1986) with the SLIPRATIO model.

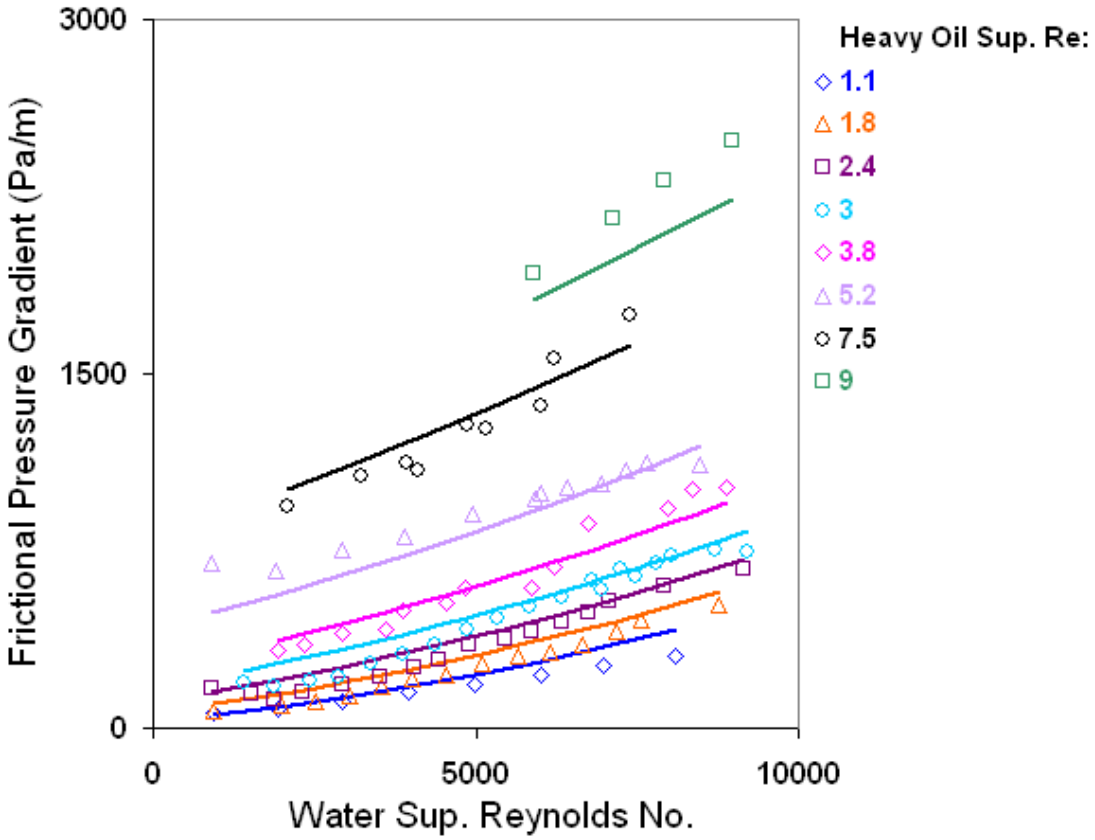

Figure 5.5.4: Prediction of the horizontal lubricated pipelining heavy oil and water flow dataset of Arney (1994) with the NOSLIP model. Lines are our predictions and the points are measurements.

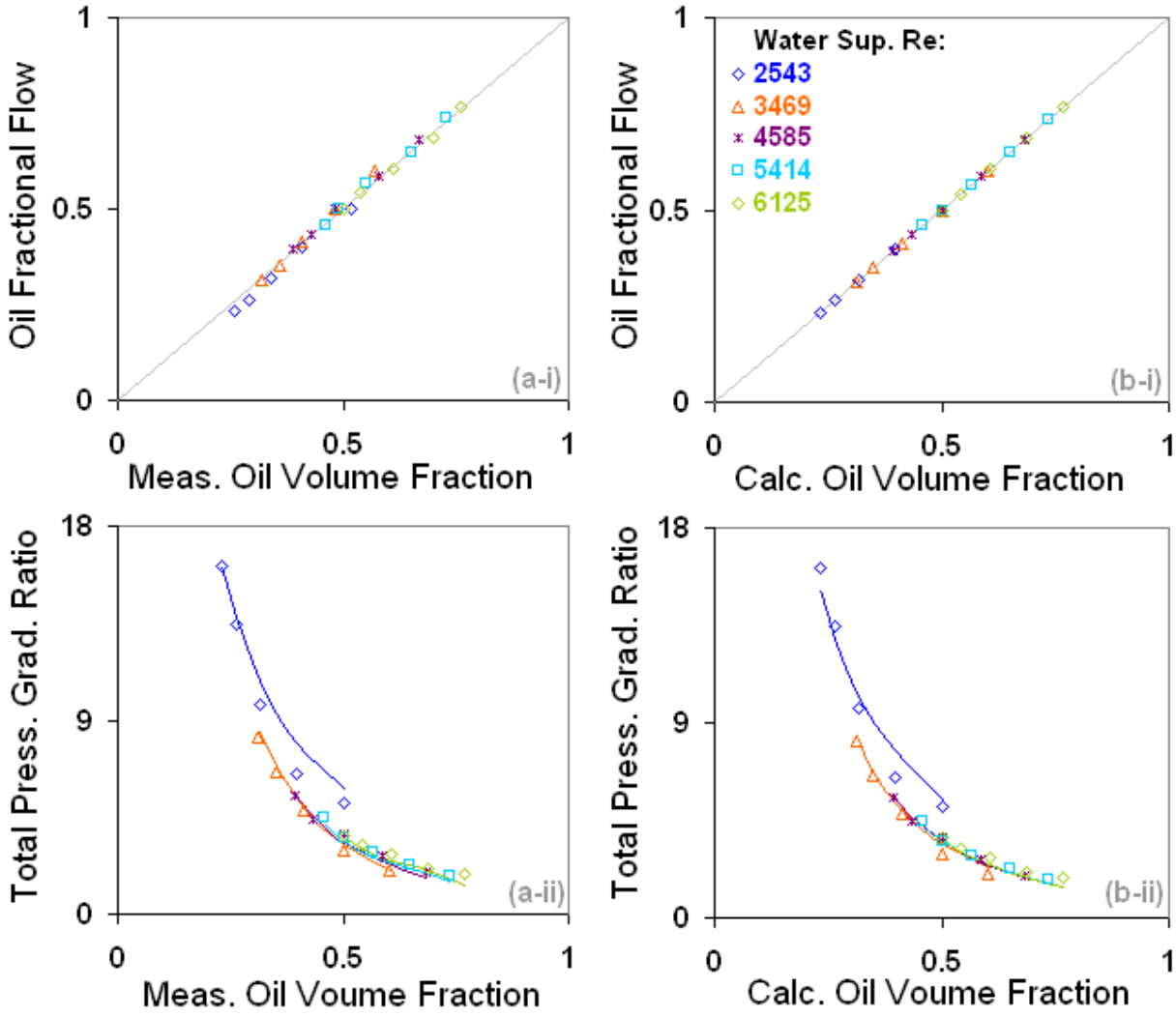

Figure 5.5.5: Prediction of the horizontal light oil and water flow dataset of Plaxton (1995) with the NOSLIP model. Lines are our predictions and the points are measurements.

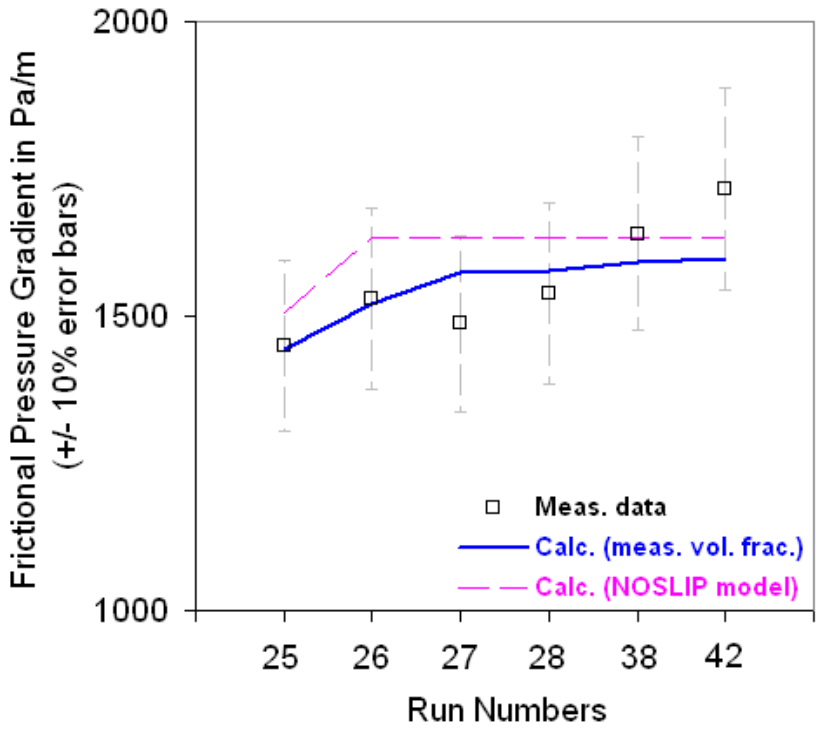

Figure 5.6.1: Validation of our analytical model against representative data from the vertical-downward oil and water flow experiments of Soot (1971).

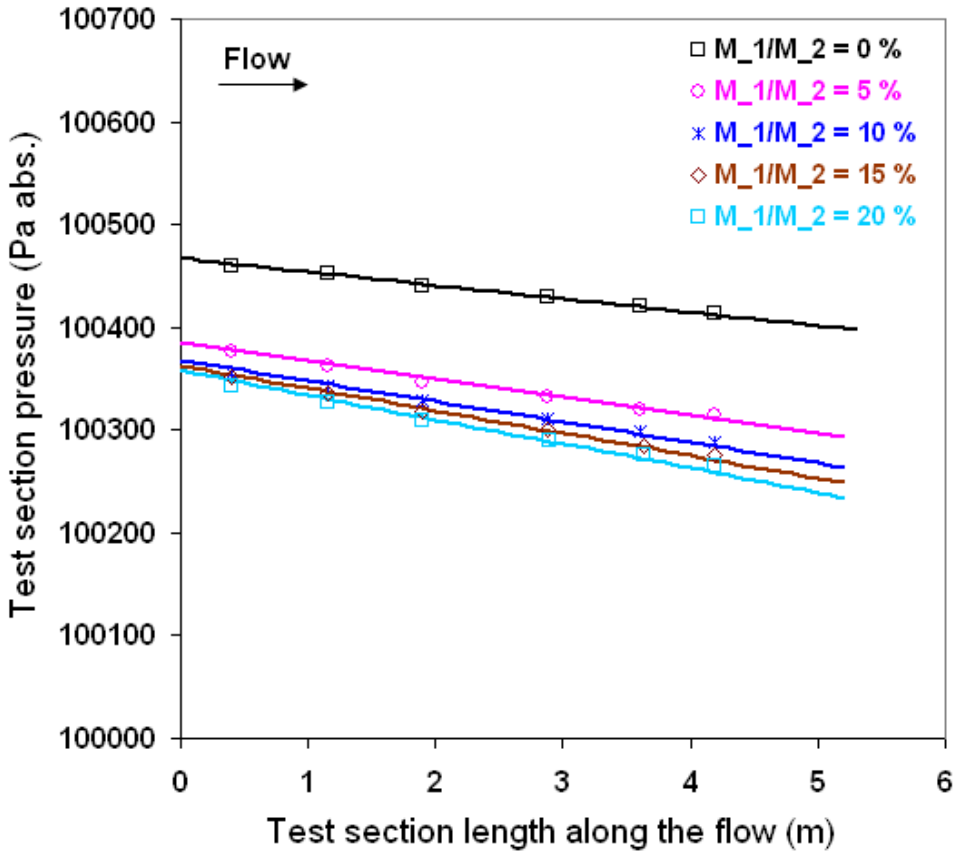

Figure 5.6.2: Prediction of the slightly up-inclined air and fly ash dataset of Carpinlioglu et al. (2002) with the BUTTERWORTH model. Lines are our predictions and the points are measurements.

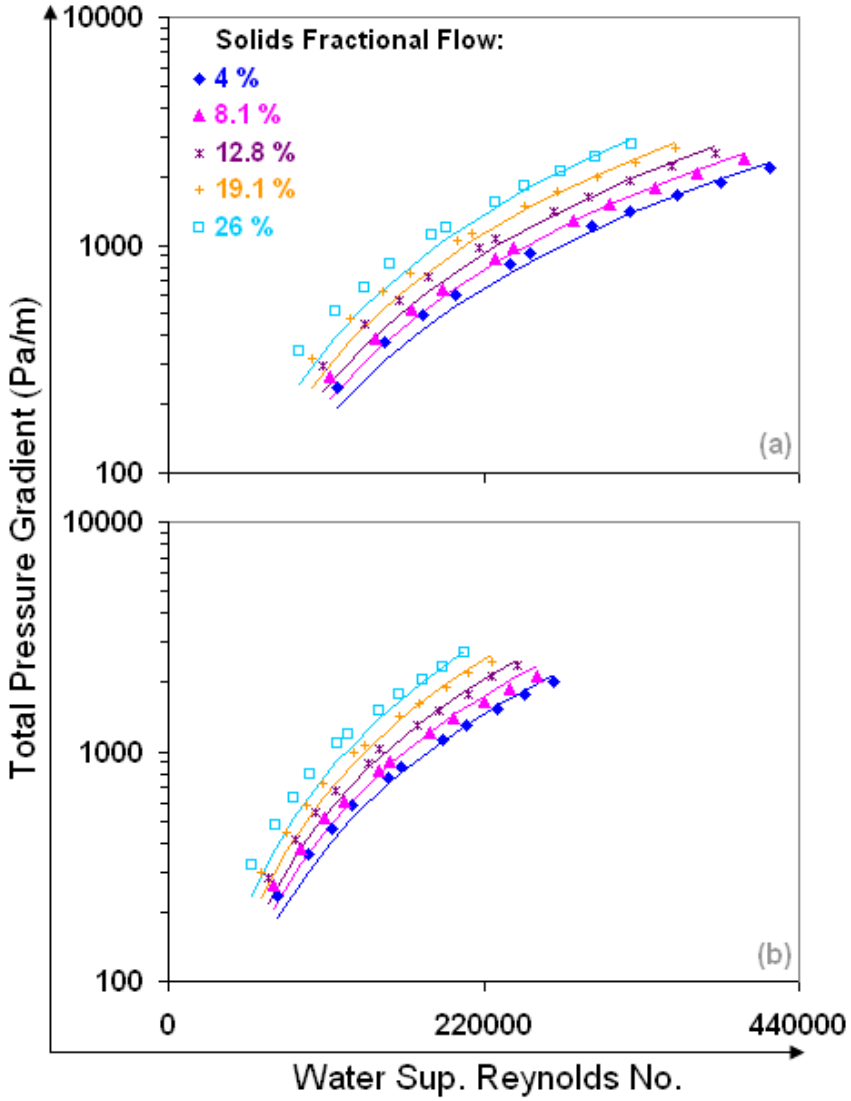

Figure 5.7.1: Prediction of the horizontal particulate slurry flow dataset of Kaushal and Tomita (2003) with the ANSLIP model. Lines are our predictions and the points are measurements.

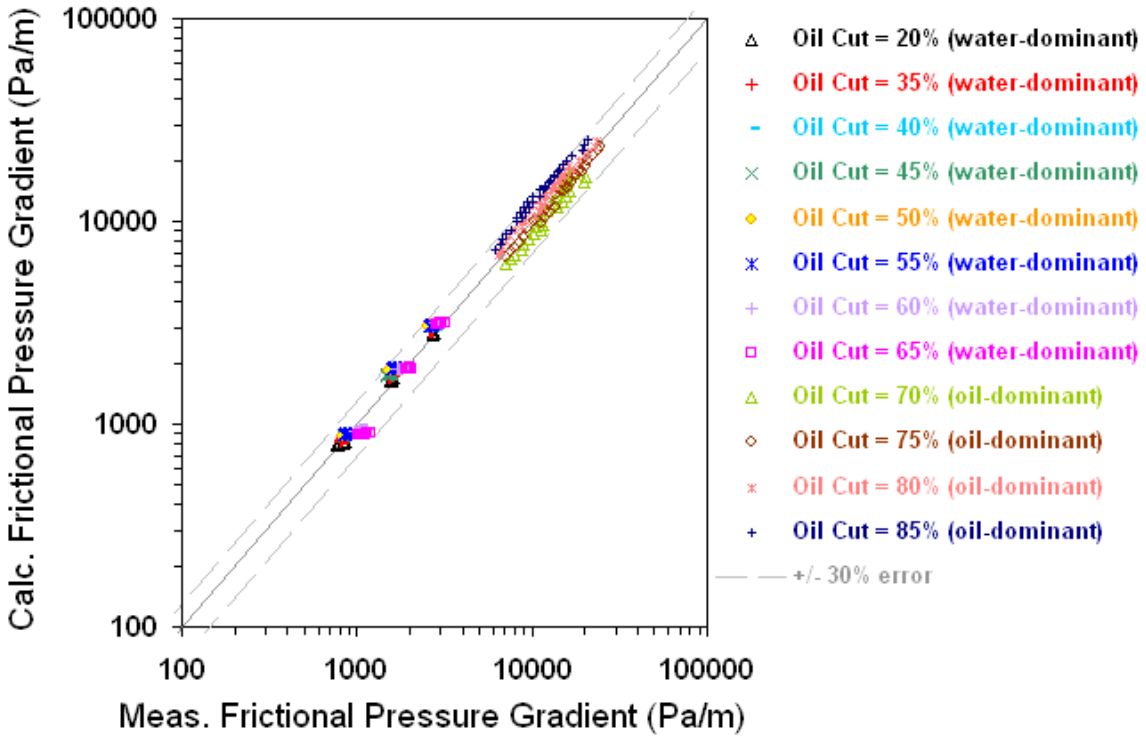

Figure 5.8.1: Prediction of all of the horizontal SN-250 oil and water flow datasets of Arirachakaran (1983) with the NOSLIP model.

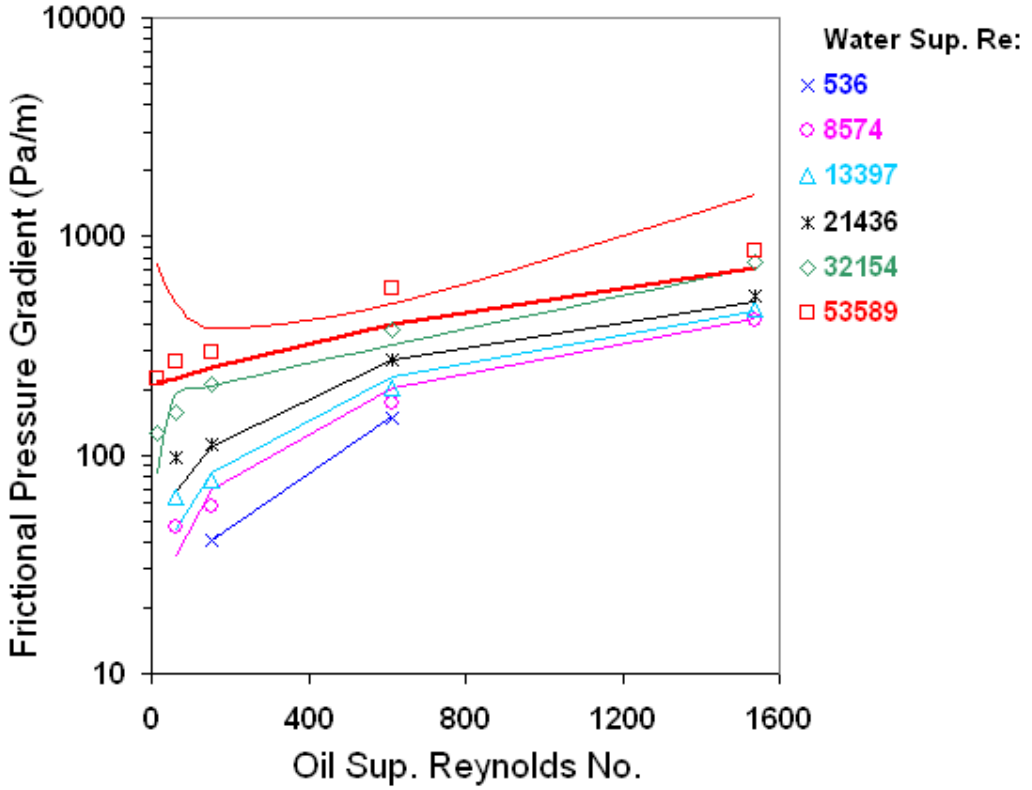

Figure 5.8.2: Validation of our analytical model against representative data from the horizontal oil and water flow experiments of Trallero (1995). Lines are our calculations and the points are measurements.

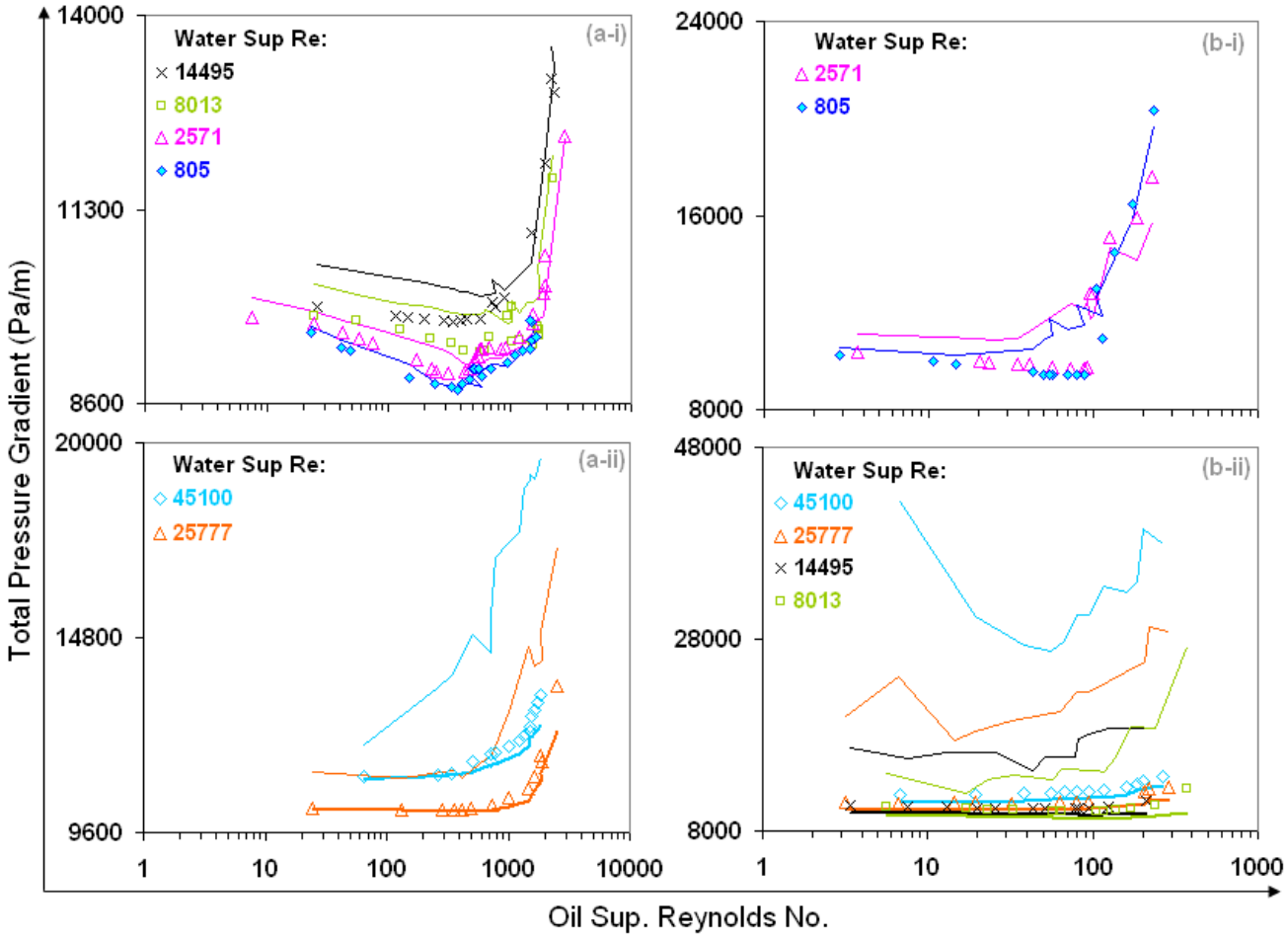

Figure 5.8.3: Validation of our analytical model against the horizontal oil and water flow experiments of Wood (1960). Lines are our calculations and the points are measurements.

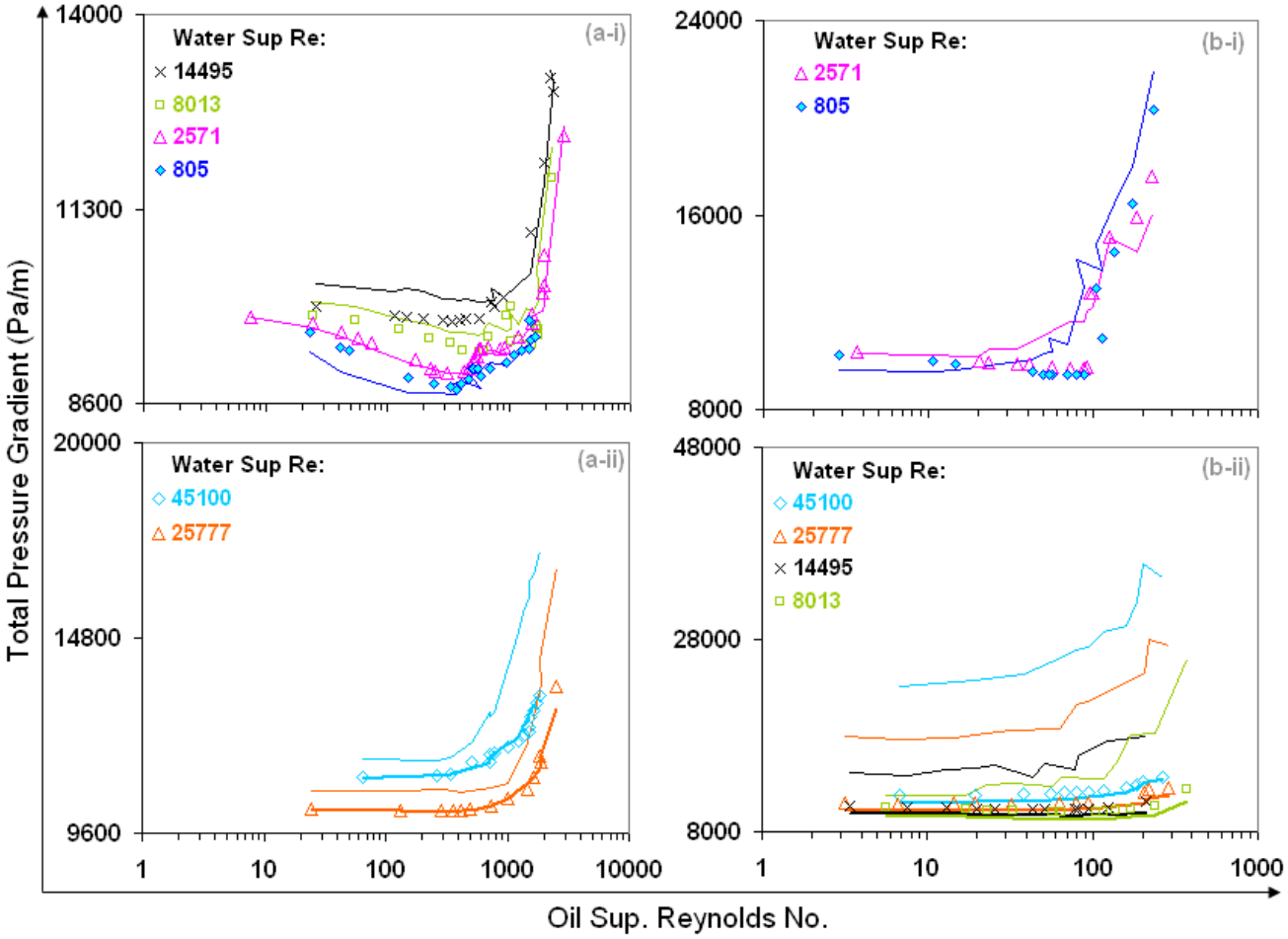

Figure 5.8.4: Prediction of the horizontal oil and water flow datasets of Wood (1960) with the NOSLIP model. Lines are our predictions and the points are measurements.

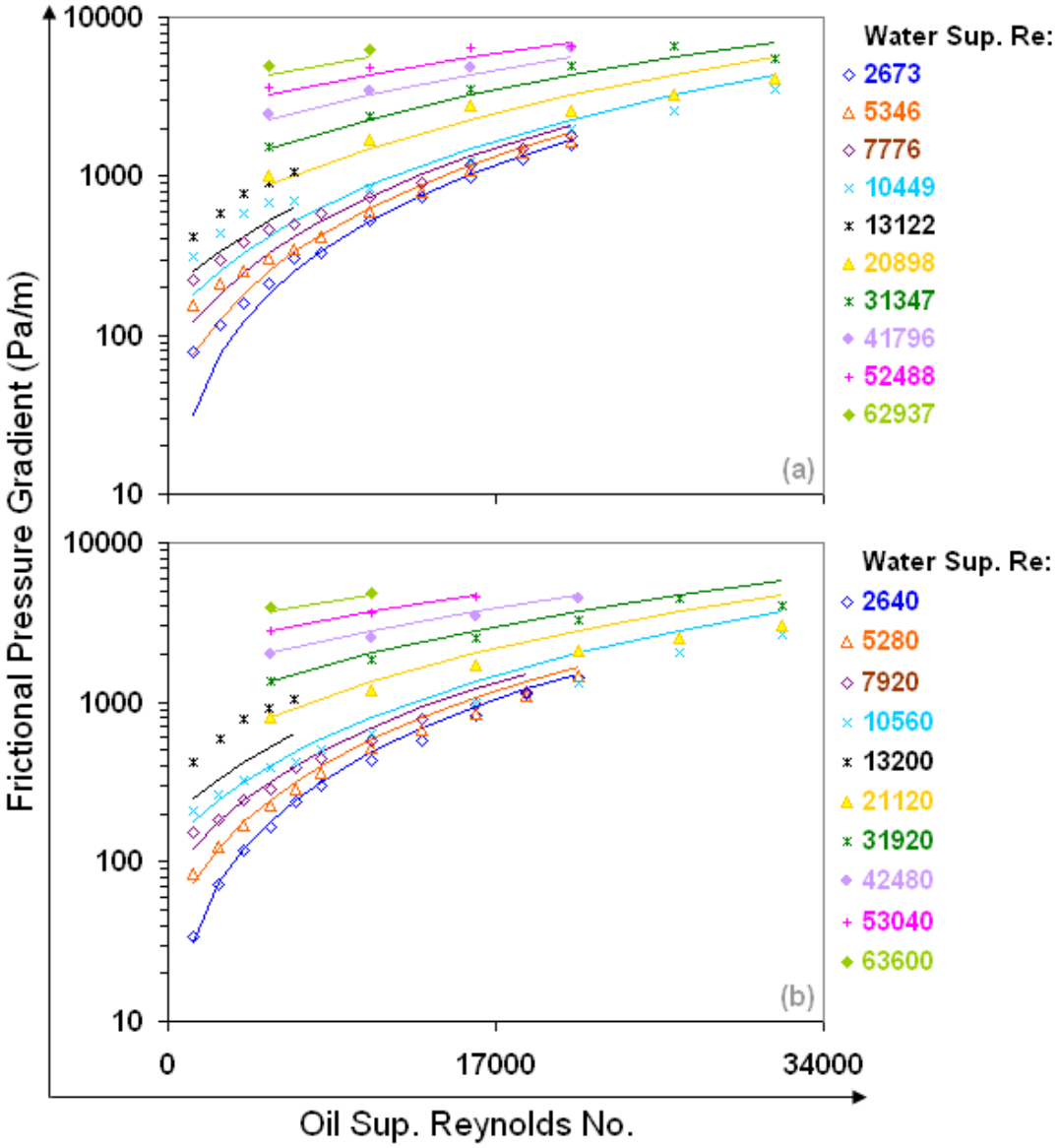

Figure 5.8.5: Prediction of the horizontal oil and water flow datasets of Angeli and Hewitt (1998) with the NOSLIP model. Lines are our predictions and the points are measurements.

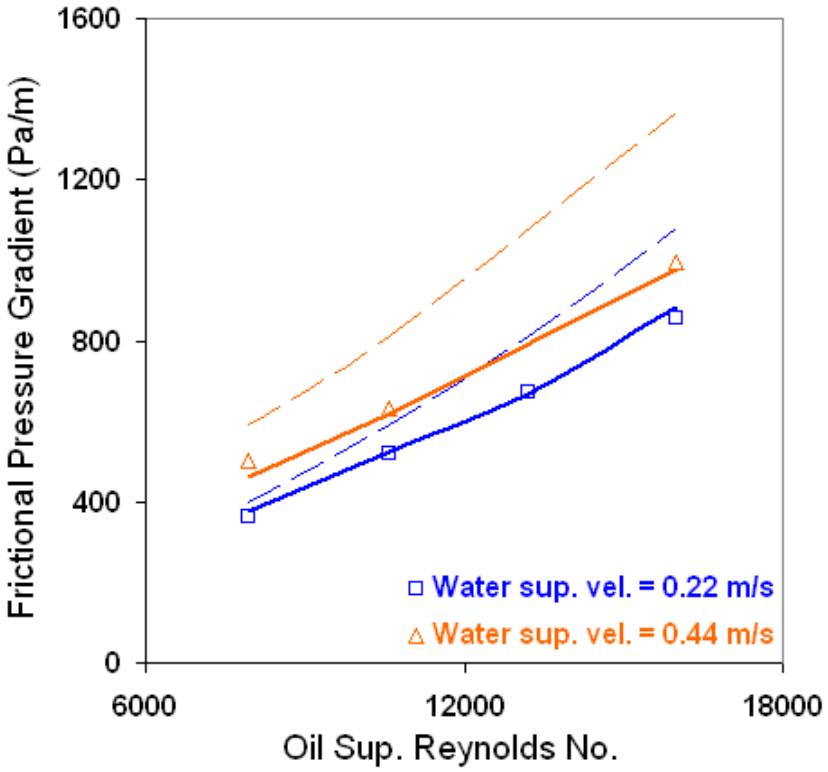

Figure 5.8.6: Validation of our analytical model against selected oil and water transpalite pipe flow experiments from Angeli (1996). Lines are our calculations and the points are measurements.

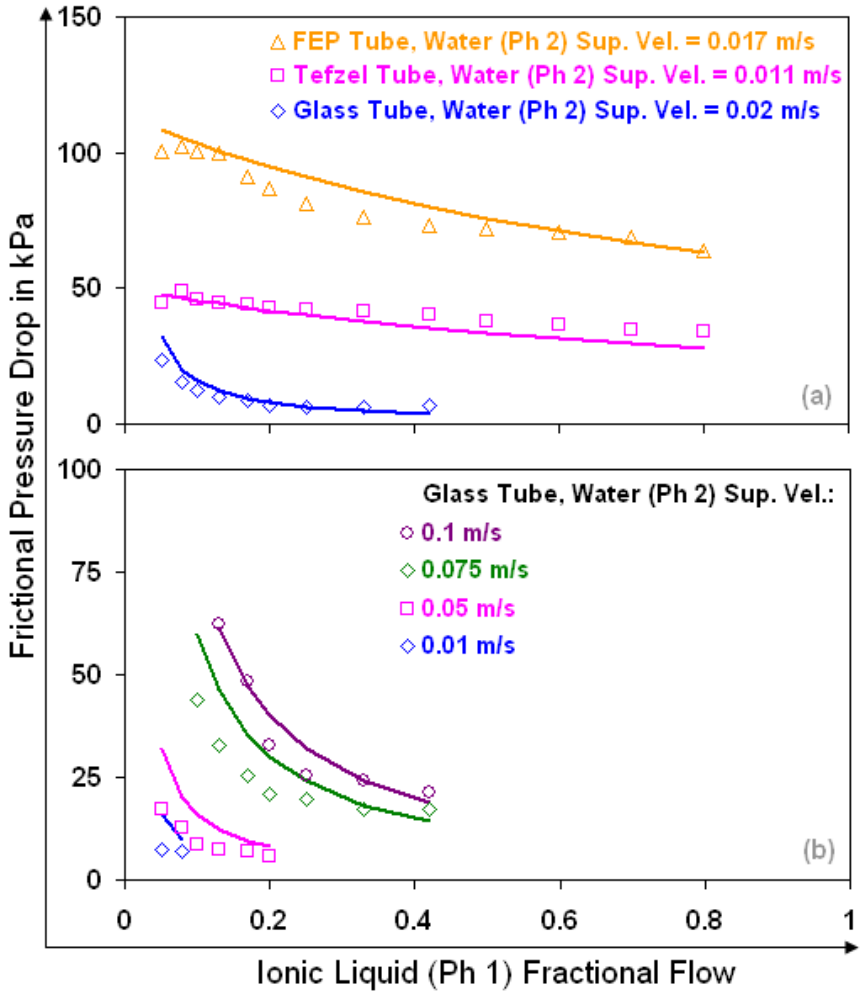

Figure 5.8.7: Prediction of the horizontal, micro-channel ionic liquid and deionized water flow datasets of Tsaoulidis et al. (2013). Lines are our predictions and the points are measurements.

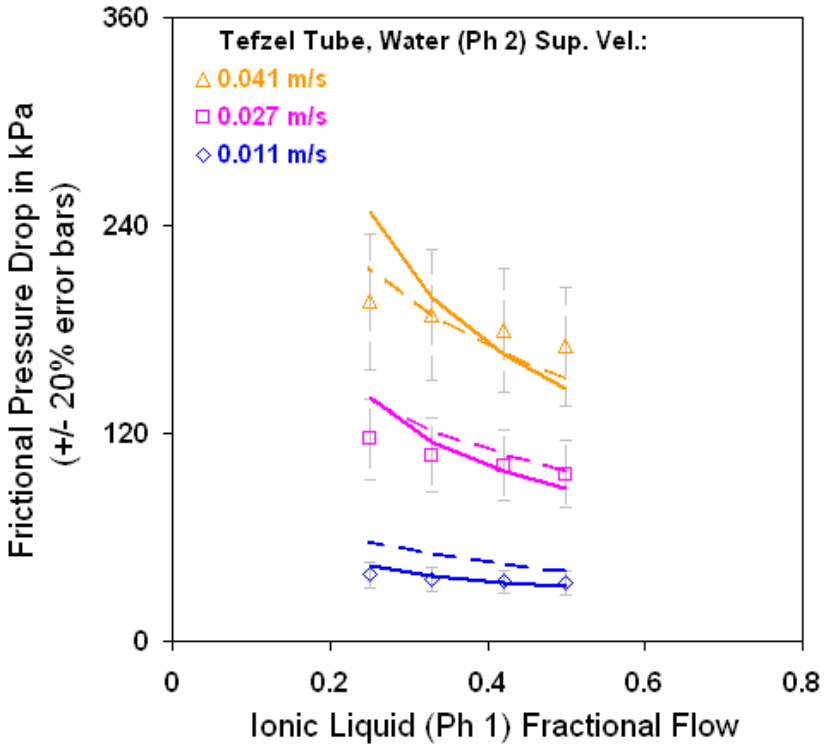

Figure 5.8.8: Comparison of two volume fraction models used for the prediction of the horizontal, micro-channel ionic liquid and deionized water flow datasets of Tsaoulidis et al. (2013). Lines are our predictions and the points are measurements.

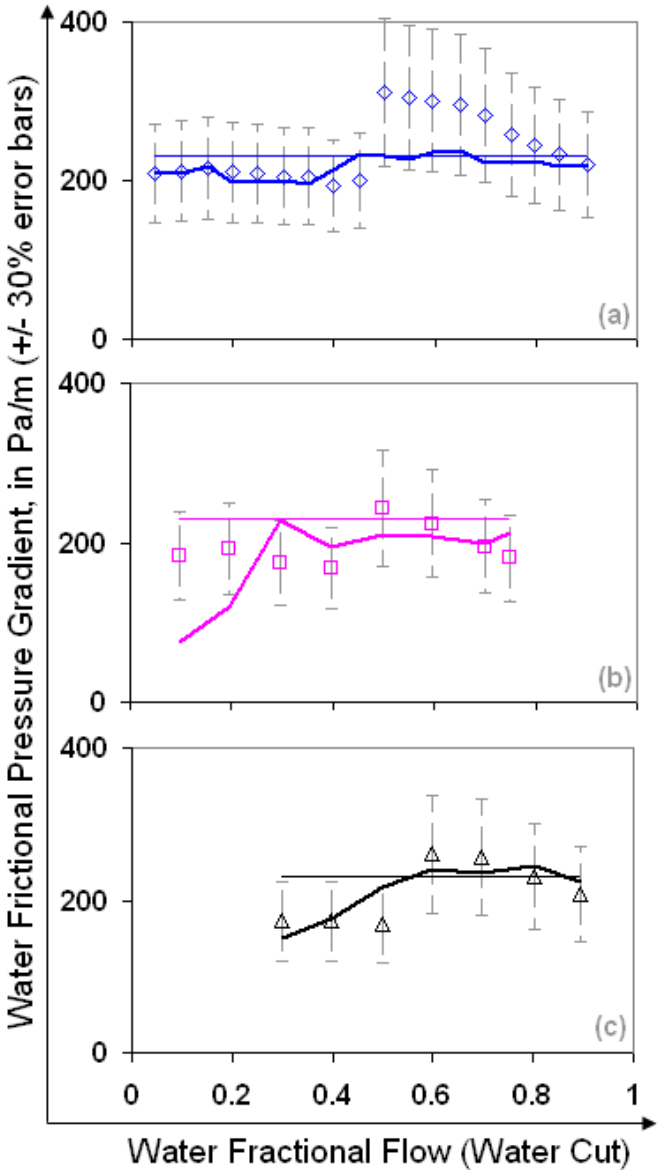

Figure 5.8.9: Validation of our analytical model against representative horizontal oil and water flow datasets from Langsholt (2012). Lines are our calculations and the points are measurements.

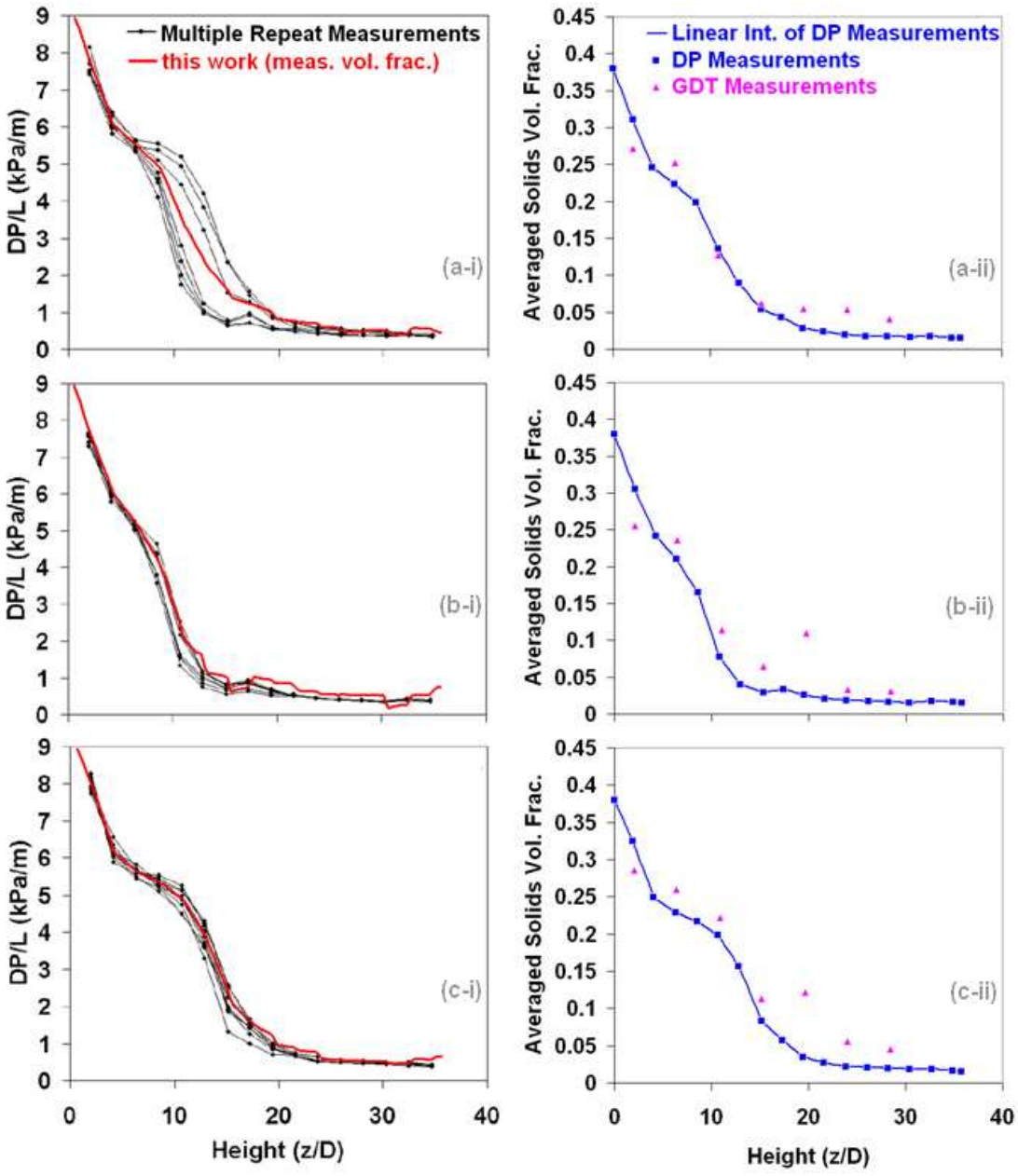

Figure 5.8.10: Validation of our analytical model against representative air and glass beads datasets from O'Hern et al. (2006). Lines are our calculations and the points are measurements.

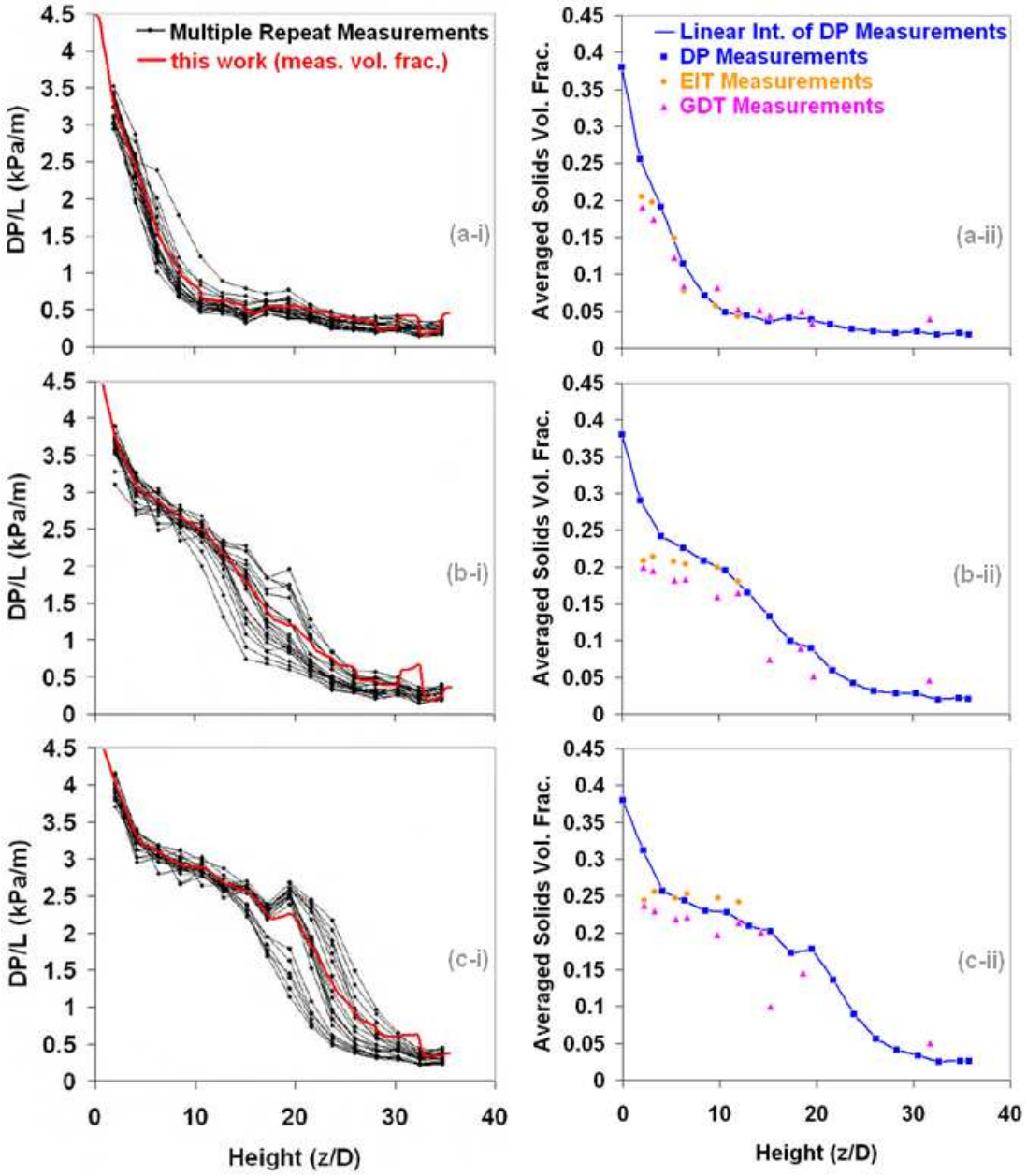

Figure 5.8.11: Validation of our analytical model against representative air and FCC particles datasets from O'Hern et al. (2006). Lines are our calculations and the points are measurements.

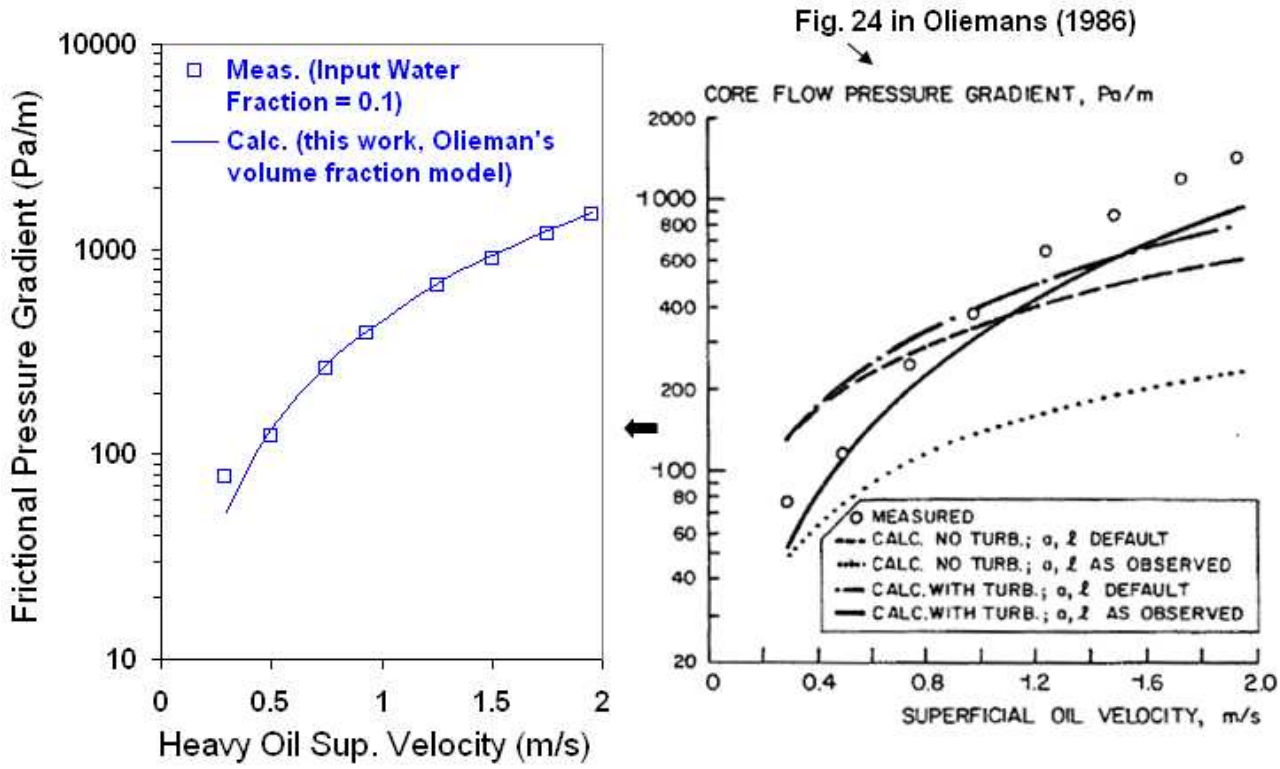

Figure 5.9.1: Comparison of the lubricating film model's predictions of Oliemans (1986) with our analytical models.

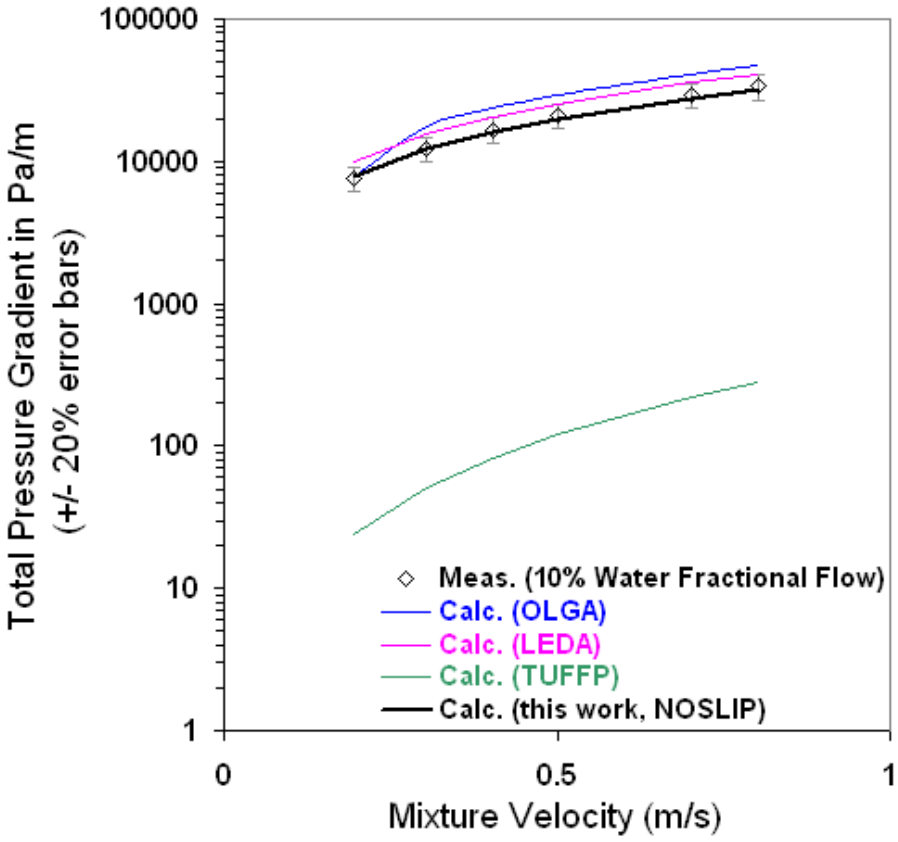

Figure 5.9.2: Comparisons of different model predictions for a representative dataset from Wang et al. (2011).

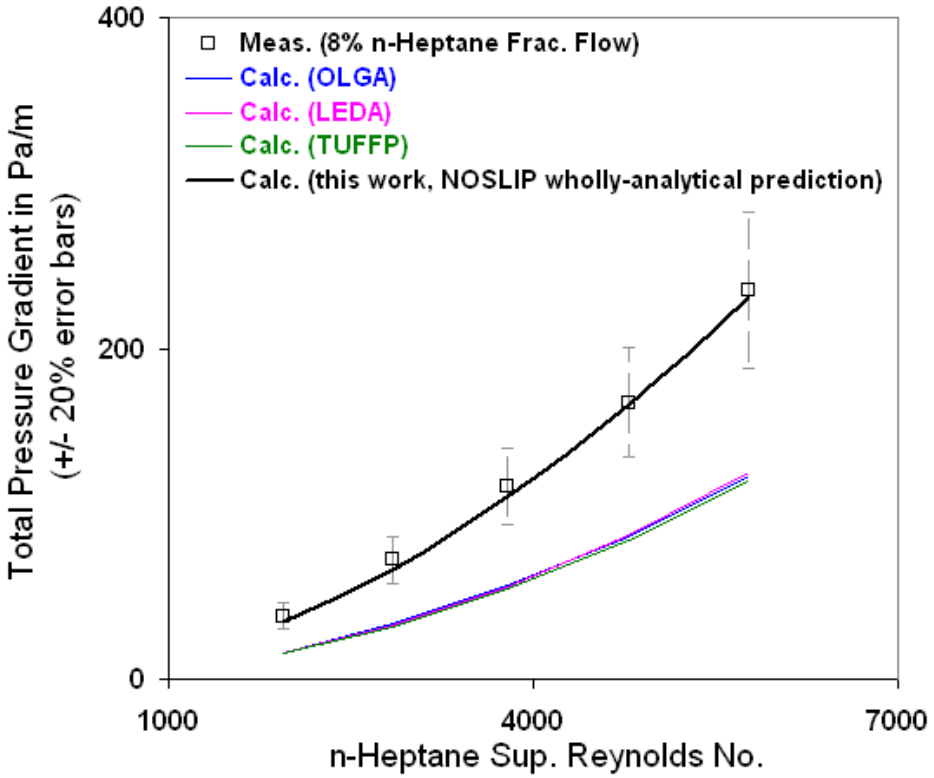

Figure 5.9.3: Comparisons of different model predictions for a representative dataset from Pouplin et al. (2011).

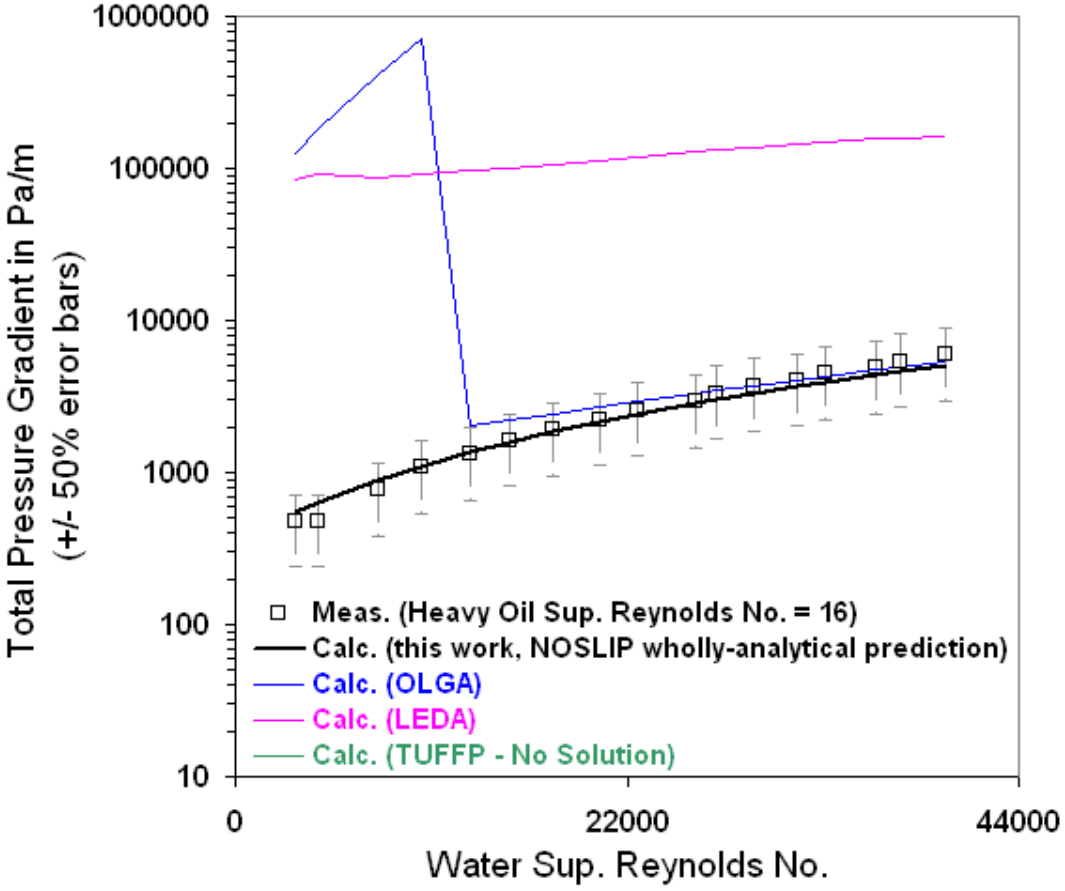

Figure 5.9.4: Comparisons of different model predictions for a representative dataset from Grassi et al. (2008).

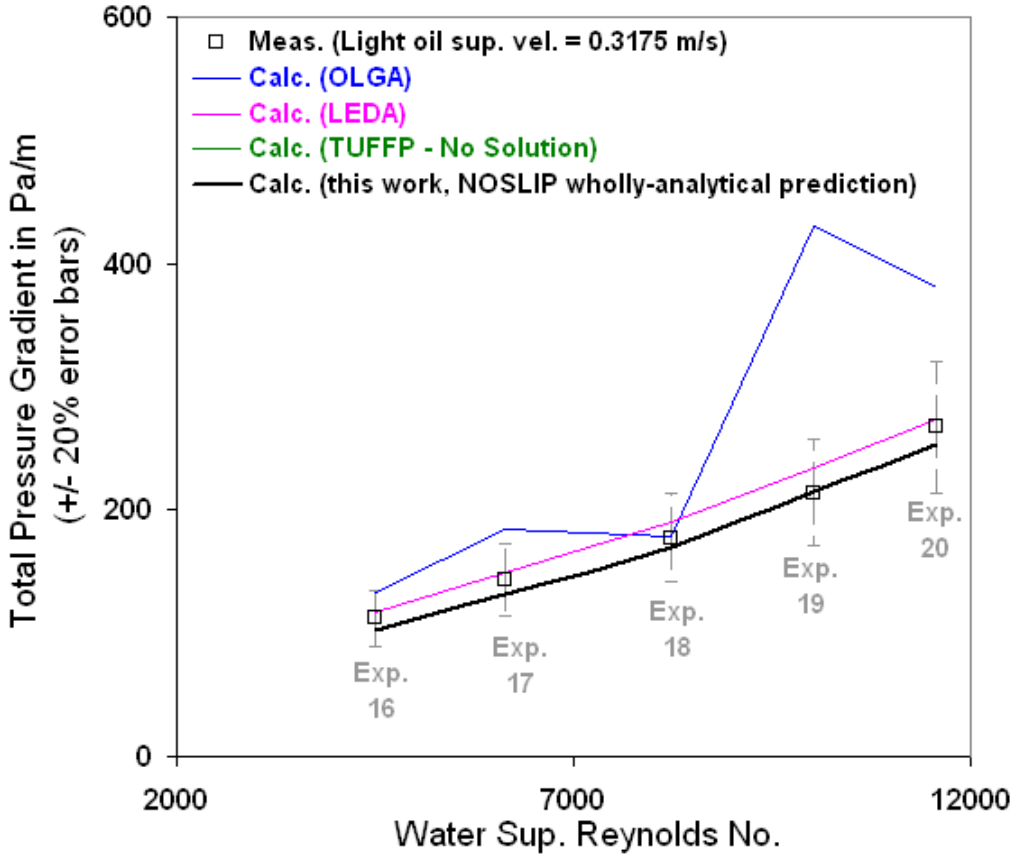

Figure 5.9.5: Comparisons of different model predictions for a representative dataset from Plaxton (1995).

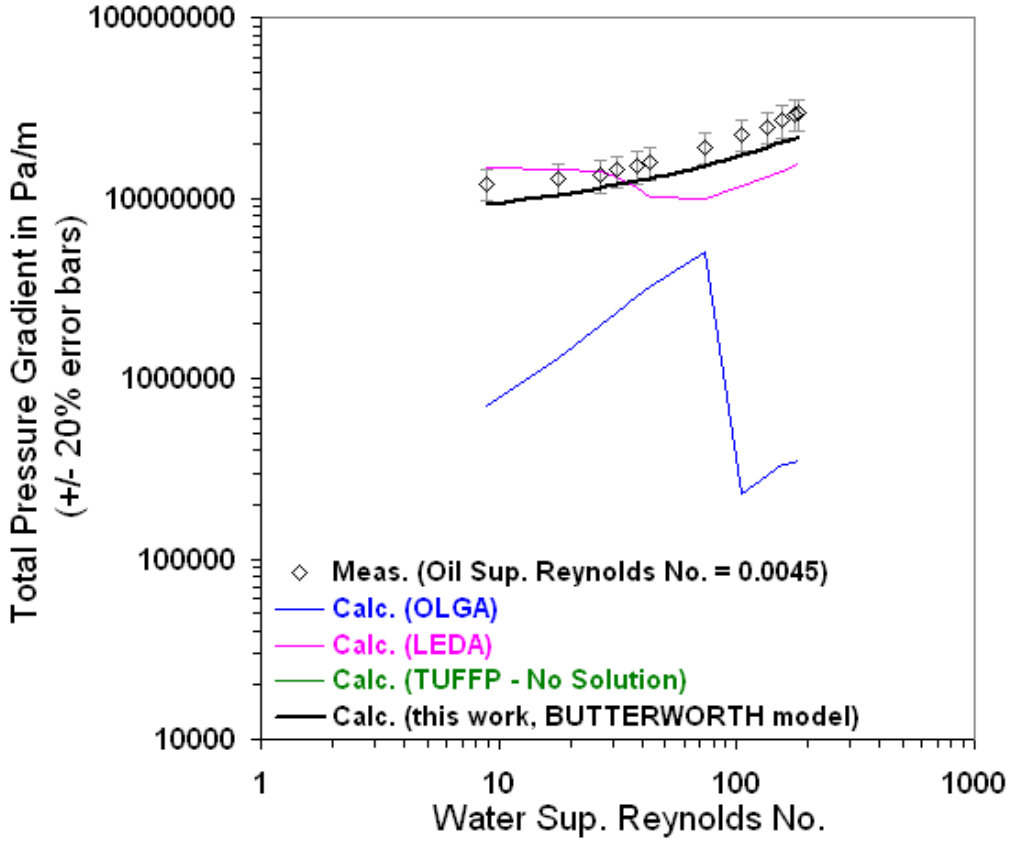

Figure 5.9.6: Comparisons of different model predictions for a representative dataset from Foroughi and Kawaji (2011).

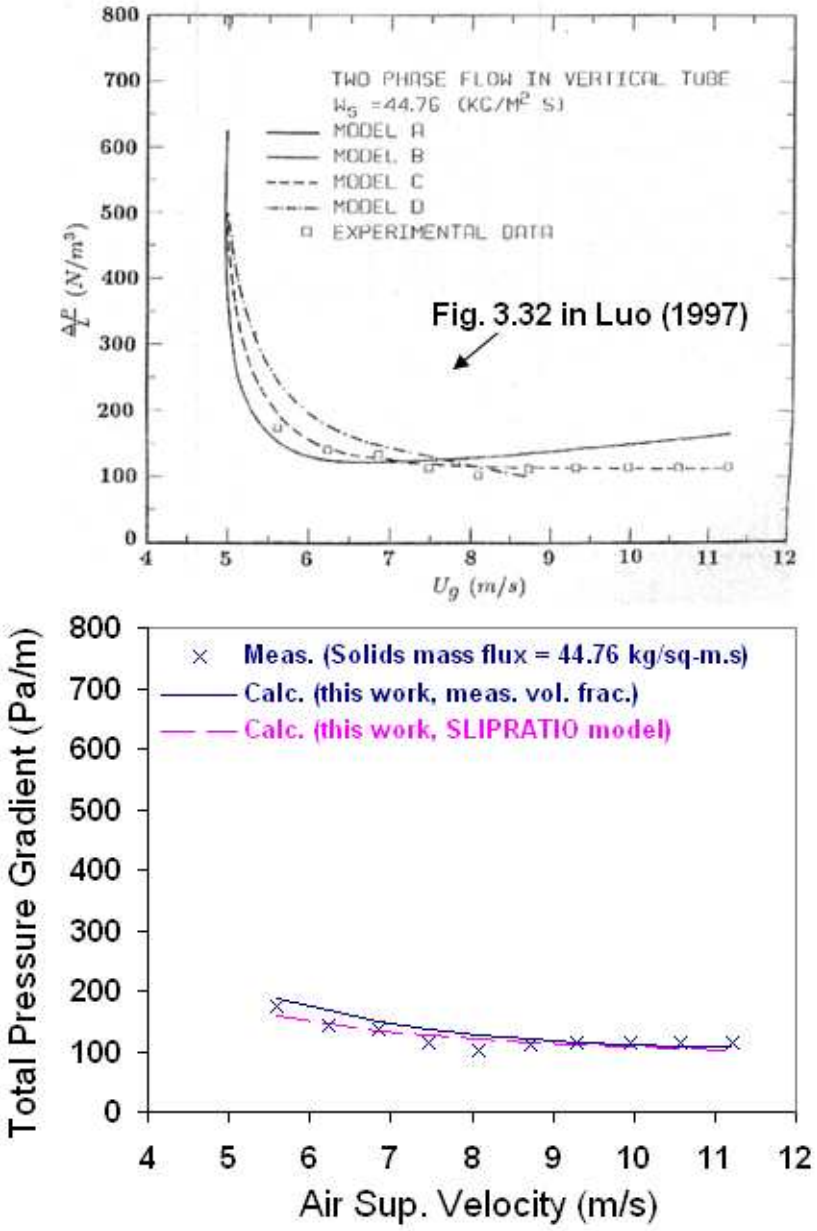

Figure 5.9.7: Comparison of the two-fluid model predictions of Luo (1987) with our analytical models.

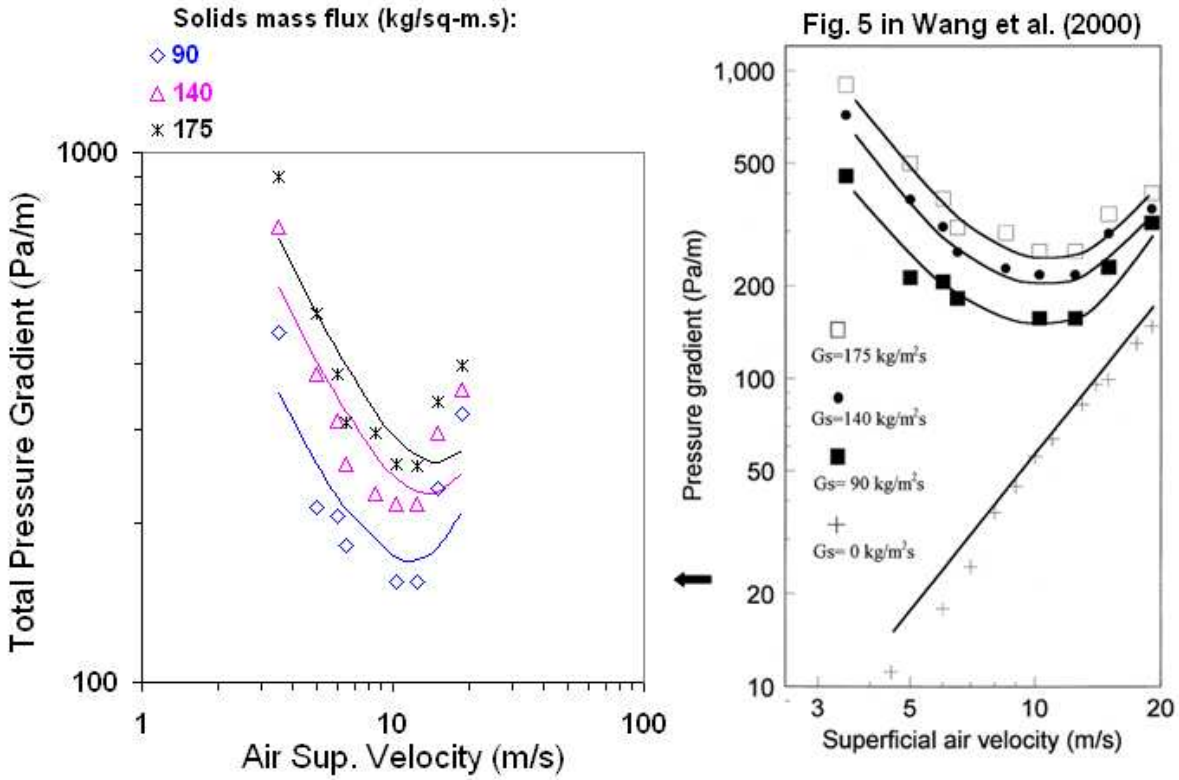

Figure 5.9.8: Comparison of our analytical model's predictions with representative data from Wang et al. (2000). Lines are our predictions and the points are measurements.

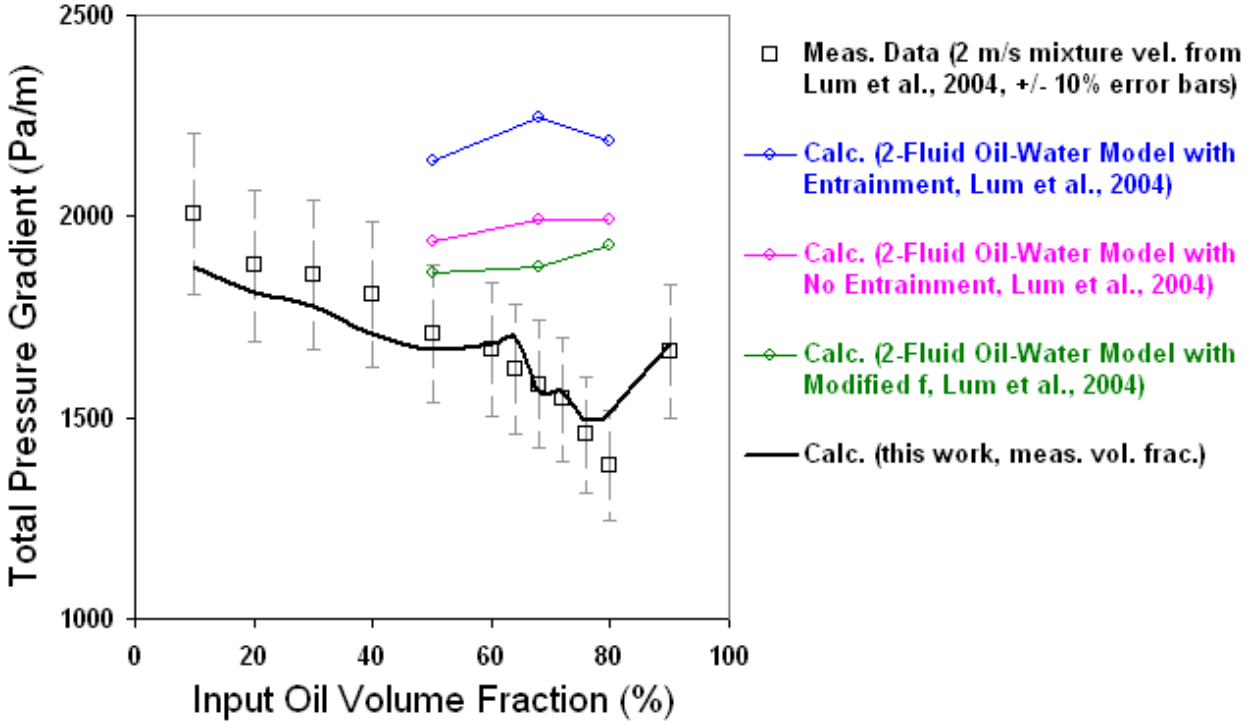

Figure 5.9.9: Comparison of the two-fluid model predictions of Lum et al. (2004) with our analytical models.

Chapter 6 – Three-Phase, Non-Newtonian and Other Complex Flows

In this chapter we continue our analytical model validations but this time for complex flow applications – these include three-phase flows, non-Newtonian flows, perforated-pipe flows and transient flows, to name a few. Since the two-phase flow validation has already been performed in chapters 4 and 5, we will focus on specific datasets in this chapter that show how we can combine the principles of chapters 2 and 3 and the applications of chapters 4 and 5 to solve the more complex flow applications of this chapter as well as the next.

6.1 Effect of Amount (Three-Phase Flows)

Fig. 6.1.1b shows the vertical air (phase 3) and Finavestan light oil A-50B (phase 2) and water (phase 1) flow data of Woods and Spedding (1996) as an air fractional flow graph. Also, Fig. 6.1.1a shows the original flow patterns observed in this wide ranging investigation as given in the reference. As seen, the air fractional flow for this three-phase flow dataset can be accurately represented by a SLIPRATIO model of $H_{3,1}$ = 22. If we combine this model with a NOSLIP model for the volume fraction of the oil (i.e., $H_{2,1}$ = 1), we can accurately predict all of the data of this water-dominant ($\gamma_1 = 1$, $\gamma_2 = 0$ and $\gamma_3 = 1$) three-phase flow investigation, as shown in Fig. 6.1.2. For comparison, Fig. 6.1.3 shows this dataset being accurately reproduced with our analytical models using the measured phase volume fractions. Thus, once again, we validate that if the volume fractions are known, our analytical models are accurate. To repeatedly demonstrate this, we will use the measured volume fractions for the remainder of the three-phase flow datasets in this section. Our purpose here is to show that the three-phase total pressure gradient calculations provided by our analytical models are very accurate once the volume fractions are known.

Fig. 6.1.4 shows the validation of our analytical model for the vertical water (phase 1), heavy dead crude oil blend (phase 2) and air (phase 3) dataset of Cazarez et al. (2010). This is a water-dominant ($\gamma_1 = 1,\ \gamma_2 = 0$ and $\gamma_3 = 1$) system. As seen, our analytical models satisfactorily reproduce this dataset.

Fig. 6.1.5 shows the validation of our analytical models for the vertical water (phase 1), Nujol mineral oil (phase 2) and air (phase 3) dataset of Shean (1976). This is a water-dominant ($\gamma_1 = 1,\ \gamma_2 = 0$ and $\gamma_3 = 1$) system in which the oil superficial Reynolds number was kept constant at about 106 for all of the runs and the water rates were systematically increased at different fixed air rates. As seen, our analytical models accurately reproduce this dataset.

Fig. 6.1.6 shows the validation of our analytical models for the slightly up-inclined water (phase 1), Exxsol-D80 oil (phase 2) and Freon/SF_6 (phase 3) datasets of Lunde et al. (1993). The three datasets shown were oil-dominant ($\gamma_1 = 0,\ \gamma_2 = 1$ and $\gamma_3 = 1$) runs at +2 degrees (Fig. 6.1.6a and "Exp. 1" in the reference), +15 degrees (Fig. 6.1.6b and "Exp. 2" in the reference) and +2 degrees (Fig. 6.1.6c and "Exp. 3" in the reference), from horizontal. As seen in Fig. 6.1.6b-i, our analytical model accurately reproduces the minimum in the total pressure gradient observed in these three-phase flow experiments. It is clear that our analytical models accurately reproduce the three-phase flow data from this experimental investigation.

Fig. 6.1.7 shows the validation of our analytical models with two representative datasets from the horizontal, low liquids loading, decoupled flow, water-dominant ($\gamma_1 = 1,\ \gamma_2 = 0$ and $\gamma_3 = 1$), three-phase air (phase 3), oil (phase 2) and water (phase 1) flow experiments of Dong (2007). It is clear that once the volume fractions are known, our analytical models are quite accurate. Note that this is a combined validation of two of our core principles – the phase dominance and decoupled flow principles.

Fig. 6.1.8 shows the validation of our analytical models with a representative decoupled flow, slightly down-inclined (-2 degrees from horizontal), oil-dominant ($\gamma_1 = 0$, $\gamma_2 = 1$ and $\gamma_3 = 1$), three-phase air (phase 3), Shell Tellus-22 oil (phase 2) and water (phase 1) flow dataset of Odozi (2000). These are runs utaow-135 to utaow-141 in the reference. As seen, our analytical models accurately reproduce this three-phase flow dataset.

In some vapor-liquid-liquid three-phase flows, there can be the additional effect of phase inversion. This is shown in the next few datasets, where it is seen that our analytical models accurately reproduce three-phase flow experiments undergoing phase inversion once the phase volume fractions are known.

Fig. 6.1.9 shows the validation of our analytical models with a representative horizontal, water-dominant ($\gamma_1 = 1$, $\gamma_2 = 0$ and $\gamma_3 = 1$), three-phase nitrogen/natural gas (phase 3), Exxsol-D60/No. 2 crude oil (phase 2) and water (phase 1) flow dataset of Valle (2000). These are the runs in Fig. 3.52 on pg. 244 of the reference. As seen, the trends in these three-phase flow data are reproduced by our analytical models. Note that this natural gas/crude oil no. 2/water dataset displayed phase inversion from a water-dominant to an oil-dominant system.

Fig. 6.1.10 shows the validation of our analytical models with a representative slightly up-inclined (+1 degrees from horizontal), high-pressure, oil-dominant ($\gamma_1 = 0$, $\gamma_2 = 1$ and $\gamma_3 = 1$), three-phase air (phase 3), oil (phase 2) and water (phase 1) flow dataset of Pan (1996). These are the runs in Fig. 6.25 on pg. 296 of the reference. As seen, the trends in these three-phase flow data are very accurately reproduced by our analytical models. Note that the dataset displayed phase inversion from an oil-dominant to a water-dominant system.

Fig. 6.1.11 shows the validation of our analytical models with two representative horizontal, water-dominant ($\gamma_1 = 1$, $\gamma_2 = 0$ and $\gamma_3 = 1$), three-phase air (phase 3), oil (phase 2) and water (phase 1) flow datasets of Hall (1992). As seen, the trends in these three-phase flow data are very accurately reproduced by our analytical models. Also, note that for the same region of low water superficial velocities, a higher oil rate (the top-most chart) can change the system from a water-dominant to an oil-dominant one, whereas a lower oil rate (the bottom-most chart) will not result in phase inversion.

6.2 EFFECT OF RHEOLOGY (NON-NEWTONIAN FLOWS)

We next perform validation of our analytical models against experiments with changing liquid rheology, i.e., non-Newtonian liquids. Fig. 6.2.1 shows the validation of our analytical models with data from the vertical experiments of Khatib and Richardson (1984). Fig. 6.2.1a shows all of the air-water data being accurately reproduced with our analytical models using the measured air volume fractions. Fig. 6.2.1b shows the flow of air (phase 2) and a shear-thinning kaolinite slurry (phase 1) at the slurry kaolin suspension concentration in water of 18.9% by volume. For this concentration, the slurry's reported values of the consistency coefficient, K_1, and its flow behavior index, n_1, were 11.2 Pa-s^n and 0.167, respectively. Clearly, our analytical models satisfactorily reproduce these datasets once the phase volume fractions are known. Fig. 6.2.2 shows the same datasets of Fig. 6.2.1 but this time with air volume fractions predicted with the ANSLIP model. As seen, the analytical ANSLIP model furnishes an accurate total pressure gradient prediction for these datasets.

Fig. 6.2.3 shows a prediction of the air (phase 2) and NLGI-Grade 2 lubricating grease (phase 1) flow experiments provided in Ruiz-Viera et al. (2006) with our analytical models using the ANSLIP model. The reported values of the grease

consistency coefficient, K_1, and its flow behavior index, n_1, were 610 Pa-s^n and 0.14, respectively. For comparison, a correlation of these data (given in the reference) is shown in the right-most chart of Fig. 6.2.3. Note that these very high grease viscosities represent an extreme case that our analytical models can satisfactorily predict.

Fig. 6.2.4 shows a prediction of the air (phase 2) and CMC-3 polymer (phase 1) horizontal and up-inclined slug flow experiments provided in Xu et al. (2007) with our analytical models using the ANSLIP model. The reported values of the polymer consistency coefficient, K_1, and its flow behavior index, n_1, were 0.972 Pa-s^n and 0.615, respectively. For comparison, a mechanistic model of these data (given in the reference) is shown in the top-most chart of Fig. 6.2.4.

Fig. 6.2.5 shows a prediction of the air (phase 2) and shear-thinning kaolinite slurry (phase 1) horizontal slug flow experiments of Farooqi and Richardson (1982b) with our analytical models using the BUTTERWORTH model. The reported values of the slurry consistency coefficient, K_1, and its flow behavior index, n_1, were 4.25 Pa-s^n and 0.175, respectively. For comparison, a 3D-CFD model of these data (given in the reference shown) is provided in the bottom-most chart of Fig. 6.2.5.

Fig. 6.2.6a shows a prediction of the air (phase 2) and viscoinelastic CMC polymer (phase 1) horizontal flow experiments of Chhabra et al. (1984) with our analytical models using the BUTTERWORTH model. The reported values of the viscoinelastic polymer consistency coefficient, K_1, and its flow behavior index, n_1, were 3.0 Pa-s^n and 0.58, respectively. For comparison, a specially-designed mechanistic model for these data (given in Fig. 15-c of Xu et al. 2009) is shown in the right-most chart of Fig. 6.2.6.

Fig. 6.2.6b shows a prediction of the air (phase 2) and viscoelastic polyacrylamide polymer (phase 1) horizontal flow experiments of Chhabra et al. (1984) with our

analytical models using the BUTTERWORTH model. The reported values of the viscoelastic (Separan AP-30) polymer consistency coefficient, K_1, and its flow behavior index, n_1, were 9.7 Pa-s^n and 0.28, respectively. Note that the importance of using the correct multiphase non-Newtonian liquid viscosity (which is a volume fraction-dependent variable) can be demonstrated using these simple experiments. For example, if we look at one of the datasets in Fig. 6.2.6b – the dataset at a liquid velocity of 0.244 m/s – then we can see the extremely wide differences in total pressure gradient calculation that can result if using a Newtonian liquid viscosity (Fig. 6.2.7). This result not only provides a strong validation of our non-Newtonian multiphase flow model provided in Section 2.2.5 of Chapter 2 (one of the core principles of this work), but also signifies an extreme risk that will be present if our properly validated non-Newtonian multiphase flow model is not used in a pipe flow modeling scenario involving multiphase flow with non-Newtonian fluids.

6.3 Effect of Flow Direction (Counter-current Flows)

In this section, we revisit the previously analyzed flooding and flow reversal datasets of Zabaras (1985) and Bharathan et al. (1979), respectively. Fig. 6.3.1a, b, c and d show the flooding datasets of Zabaras (1985) at liquid film down-flow Reynolds numbers of 310, 768, 1550 and 3100, respectively. To model these air (phase 2) and Sodium-Hydroxide-Salt-Solution (phase 1) flooding datasets with our analytical models, the only change we made to our models was that the pre-flooding data was specified as a gas-dominant system ($\gamma_1 = 0$ and $\gamma_2 = 1$) having a liquid hydrostatic pressure gradient of 0. As Fig. 6.3.1 shows, this simple change captures the trends in the data once the volume fraction is known.

Fig. 6.3.2a show the flow reversal datasets of Bharathan at al. (1979) corresponding to runs 4 and 8 of the reference. Fig. 6.3.2b shows runs 19 and 21 of this reference. In Fig. 6.3.2a, we find that no changes are required and our analytical models capture the trends in this flow reversal data once the volume fractions are known. In Fig. 6.3.2b, however, only the post-flow reversal de-flooding points require the same changes as was done for the flooding case above. Otherwise, our analytical models capture the trends in Fig. 6.3.2b once the volume fractions are known.

6.4 Effect of Flow Development (Perforated Pipe/Leak Detection)

We next perform validation of our analytical models against experiments with changing flow development. We will focus on multiphase perforated pipe flows and multiphase leak/load detection problems.

For the problem of perforated pipes, a key insight provided by this work is that these flows simply represent mass flow rate sources or sinks at various locations along a segmented pipe system. The effect of introducing a new stream of fluid, for example, is already provided for as a mass flow rate increase in our analytical models and the associated changes to the convective deceleration/acceleration pressure gradient (CADPG) at the inflow location. Indeed, it is found in this work that the CADPG dominates the other pressure gradients in a highly perforated pipe flow.

Fig. 6.4.1 shows all of the single-phase water perforated pipe flow experiments of Schulkes and Utvik (1998) being satisfactorily predicted using water sources at various segments in a segmented pipe system in UTPipeFlow. In this study, there were 56 perforations in a 14 m long test section, in which the total pressure drop over the test section was measured for a wide range of water source flow rates, Q, and water perforation flow rates, q. We note that although the comparisons of our analytical models

and the measurements in Fig. 6.4.1 are satisfactory (within 30% error), we can get an even more accurate measurement if we reduce the pipe segment diameter slightly at the perforation locations to simulate the (cross-jet) blockage of the source water entering a perforation pipe segment. This segment diameter blockage can be measured and quantified with a tracer, for example. If we now reduce the perforation segment diameter according to Eqn. 1 below and set the segment diameter blockage fraction, β, at 6 %, we can very accurately simulate this entire dataset, as shown in Fig. 6.4.2.

$$D_{\substack{perforation \\ segment}} = D_{pipe}\left(1 - \overset{\substack{blockage \\ fraction}}{\beta}\left(\frac{q}{Q+q}\right)^{\frac{1}{2}}\right) \tag{1}$$

Fig. 6.4.3 shows the perforated-pipe experimental campaign of Fayers (1995), in which a large diameter (D = 0.15 m) perforated pipe was instrumented to provide local differential pressures along the pipe for a range of single-phase oil (phase 1) and two-phase nitrogen (phase 2) and oil (phase 1) flows. These experiments can be found in the DOE contract: DE-FG22-93BC14862. As a first step (shown in Fig. 6.4.3), we ensure that the single-phase source oil flow (Q = 408 gpm, q = 0 gpm) is accurately predicted in UTPipeFlow with a hydraulic roughness of 0 (smooth pipe).

Next, in Fig. 6.4.4, we introduce perforation oil flows along the pipe to simulate oil inflow through perforations (fixed at q = 85 gpm) with a source oil flow before the perforations, Q, being variable according to Fig. 6.4.4. As can be seen, our analytical models (as implemented in UTPipeFlow) accurately simulate this perforated single-phase oil perforated pipe flow experiments.

Fig. 6.4.5 shows some of the multiphase perforated pipe flow experiments from this study, in which nitrogen inflow through perforations (fixed at q = 2300 gpm) were

flowed with a source oil flow before perforations, Q, being variable according to Fig. 6.4.5. The ANSLIP model was used in UTPipeFlow to perform these multiphase perforated pipe flow experiments. These results clearly validate that our analytical models satisfactorily predict these large-diameter multiphase perforated pipe flow experiments. Note that there are several industrial applications related to these flows, such as in an oil production wellbore with inflow through perforations, or, in an oil production horizontal wellbore gas-lifted down to the toe of the well.

We next show how our thoroughly validated analytical models can be used to predict multiphase leak or load detection. These are critical safety-related problems that demand high prediction accuracy. We revisit the previously analyzed multiphase convergent-divergent-convergent nozzle flow dataset of Pougatch et al. (2008). It was shown in Fig. 4.13.17 of chapter 4 that our analytical models accurately predict the multiphase flows though this nozzle. We now look at "case 1" in Pougatch et al. (2008) and simulate a leak event at the first nozzle throat of this device – that is – removing all of the water at this throat location. Starting at the outlet, Fig. 6.4.6a shows that our analytical models will be correctly display a leaked conduit response. The measurements for "case 1" as if there was no leak, are kept in Fig. 6.4.6a for comparison. Similarly, starting from the outlet, we can simulate the case of only gas flowing before the first nozzle throat and simulate a water load into the nozzle at this location (Fig. 6.4.6b). As seen, our analytical models provide reliably accurate simulations of these multiphase leak and load cases thus making for accurate tools for multiphase (or single-phase) leak and load detection.

6.5 EFFECT OF EXTREME CONDITION (HIGH PRESSURE)

Other than low pressure conditions typically encountered in a lab environment, there are many scenarios where an extreme condition must be predicted or analyzed. One such popular industrial example is deep offshore (or shallow on-land) well blowouts (e.g., as highlighted in Willson et al., 2013). We next select atypical, carefully-controlled lab experiments that were conducted at (relatively) high pressures.

Fig. 6.5.1 shows the large-diameter (D = 0.189 m), high pressure, vertical nitrogen (phase 2) and naphtha (phase 1) dataset of Omebere-Iyari (2006) being accurately reproduced with our analytical models. Fig. 6.5.1a and b are the datasets at 20 bars and 90 bars, respectively. The measured gas volume fractions were used in our total pressure gradient calculations. Fig. 6.5.2 shows that the data trends of this dataset could be satisfactorily predicted with the ANSLIP model.

Fig. 6.5.3 shows the large-diameter (D = 0.1064 m), high pressure, horizontal nitrogen (phase 2) and water (phase 1) dataset of Abduvayt (2003) being accurately reproduced with our analytical models. Fig. 6.5.3s and b are the datasets at 6 bars and 20 bars, respectively. The measured gas volume fractions were used in our total pressure gradient calculations. Fig. 6.5.4 shows that the data trends of this dataset could be satisfactorily predicted with the ANSLIP model.

Lastly, Fig. 6.5.5 shows the high pressure horizontal air-oil and air-water datasets of Srichai (1994) at 5 barg (Fig. 6.5.5a), 10 barg (Fig. 6.5.5b) and 15 barg (Fig. 6.5.5c). The blue squares in Fig. 6.5.5 represent the low liquid rate flows and the purple diamonds represent the high liquid rate flows. The lines in these plots are our analytical model's total pressure gradient calculations using the measured air volume fractions. It is evident that our analytical models are reliably accurate in large diameter, high pressure multiphase flows once the phase volume fractions are known.

6.6 EFFECT OF EXTERNAL FIELD (VARIABLE FORCE FIELDS)

We next perform validation of our analytical models against experiments with variable external force fields. These multiphase flows are typically encountered in the aerospace industries in which there are micro-gravity and hyper-gravity multiphase flows, as well as in magneto-hydrodynamic (MHD) multiphase flows.

Fig. 6.6.1 shows representative datasets from the transverse magnetic field vertical rectangular pipe flow experiments of Thome (1964). In these experiments, a sodium-potassium liquid metal alloy was flowed with nitrogen under various external magnetic fields. Of course, before the effect of the external magnetic force field can be quantified, the ability to represent the multiphase flow without any external force field other than gravity must first be established. We therefore select two datasets without any external force field applied and input their measured nitrogen volume fractions in our analytical models. Evidently, for these liquid metal alloy and nitrogen datasets, our analytical models satisfactorily reproduce the trends in the total pressure gradient data once the volume fractions are known.

Fig. 6.6.2 shows the horizontal micro-gravity flow of air (phase 2) and water (phase 1) from the MU-300 aircraft flight experiments of Choi et al. (2003). Fig. 6.6.2a shows the predictions of our analytical models for this dataset with the ANSLIP model and Fig. 6.6.b shows the validation of our analytical models with the measured air volume fractions used in the calculations. As seen, our analytical models accurately predict this multiphase micro-gravity flow dataset.

Fig. 6.6.3 shows a representative dataset from the horizontal micro-gravity flow of air (phase 2) and water (phase 1) from the Learjet flight experiments of Bousman and Dukler (1993). For these experiments the observed flow patterns transitioned from bubbly-slug to slug to annular flow. As seen in Fig. 6.6.3, both a validation with

measured volume fractions and a prediction with the ARMAND model accurately reproduces the trends in this dataset. This is yet another validation that pressure gradient is governed by relative velocity.

Fig 6.6.4a shows all of the micro-gravity, normal gravity and hyper-gravity (1.75g) air-water Novespace Airbus A300 flight experiments from MacGillivray (2004) being well predicted with our analytical models using the WOLGHA model. Similarly, Fig. 6.6.4b shows more micro-gravity, normal gravity and hyper-gravity data from this experimental investigation but for helium-water flows. The helium-water flows were well-predicted with the WALLIS model. It is clear from these voluminous results that our analytical models are reliably accurate for multiphase flows in variable gravity environments.

6.7 Effect of Time Change (Transient Flows)

In this section we validate our analytical models against experiments with variable time changes. In transient flows, the (mixture) temporal acceleration/deceleration pressure gradient term in our analytical models is solved with the rest of the pressure gradient terms at given time steps in the computational implementation of the analytical models of this work, UTPipeFlow. Although there are large amounts of transient multiphase flow data available in the literature (e.g., Zuber et al., 1967; Hanna, 1981; Theron, 1989; Caussade et al. 1989, DeHenau, 1992; McNulty and Sutjipto, 1992; Vigneron, 1995), we select a few representative datasets with carefully-defined (and well-reported) boundary conditions for use in the validation testing of our analytical models.

Fig. 6.7.1 shows a single-phase gas transient, denoted as “Line B” in Hannah et al. (1964). This dataset was also used for validating a transient flow program in Eilerts

(1981). In UTPipeFlow, the boundary conditions that are specified at the outlet are the gas mass flow rates and outlet pressures at given time steps and the inlet pressures are calculated. As seen in Fig. 6.7.1, a very accurate prediction is provided by UTPipeFlow.

Fig. 6.7.2 shows the same transient flow computation in UTPipeFlow as Fig. 6.7.1 but this time as a succession of steady states. There are negligible differences between Figs. 6.7.1 and 6.7.2. This signifies that before a transient flow simulation is performed it is well worth testing whether a succession of steady-states would provide a sufficiently reliable estimate. Indeed, in some industries where there are mostly slow transients (e.g., the petroleum industry), the succession of steady states should be a mandatory (simple) first approximation in transient flow studies before complex studies are justified.

Fig. 6.7.3 shows a representative air (phase 2) and water (phase 1) transient from Kohda et al. (1987). In UTPipeFlow, the boundary conditions that are specified at the outlet are the air and water mass flow rates and outlet pressures at given time steps and the inlet pressures are calculated. The ANSLIP model was used for air volume fraction prediction and the Ishii and Mishima (1982) correlation was used for entrainment prediction. As seen in Fig. 6.7.3, a satisfactory prediction is provided by UTPipeFlow.

Fig. 6.7.4 shows a representative air (phase 2) and kerosene (phase 1) dataset from Minami and Shoham (1994) – “run 3” in this reference. In this run, the outlet air rate is increased while the outlet kerosene rate remains unchanged. These rates, in combination with the outlet pressures, are the specified boundary conditions for UTPipeFlow. The pressures and kerosene volume fractions at different stations along the flow loop are calculated. The ANSLIP model was used for air volume fraction prediction and the Ishii and Mishima (1982) correlation was used for entrainment prediction. As seen in Fig. 6.7.4, a satisfactory prediction is provided by UTPipeFlow.

Fig. 6.7.5 shows another representative air (phase 2) and kerosene (phase 1) dataset from Minami and Shoham (1994) – "run 19" in this reference. In this run, the outlet kerosene rate is increased while the outlet air rate remains unchanged. These rates, in combination with the outlet pressures, are the specified boundary conditions in UTPipeFlow. The pressures and kerosene volume fractions at different stations along the flow loop are calculated. The same ANSLIP and Ishii and Mishima (1982) models are used for prediction as in Fig. 6.7.4. As seen in Fig. 6.7.45, UTPipeFlow correctly captures the trends in the data.

We next look at the recent large-diameter, riser-base gas-injection and liquids-removal transient flow experiments of Zabaras et al. (2013). The steady-state, developing flow results of this investigation were previously analyzed in Section 4.13 of Chapter 4. In these transient multiphase flow experiments, a large diameter vertical riser (D = 0.2794 m) is connected to a same-sized pipeline at a downward inclination of 11.6 degrees from horizontal. Additionally, a long radius 90-degree elbow at the same size of the riser connects the top of the riser to a gas-liquid separator. Steady-state and transient flow air-water experiments were conducted, particularly to investigate riser-base gas lift injection and riser liquids removal capability.

Fig. 6.7.6 shows some of the transient results for the low gas injection rate case in the reference (i.e., at 200 scfm). For this dataset, the BUTTERWORTH model was used for the down-inclined pipe and the NICKLIN model was used for the vertical riser. The outlet pressure boundary condition was set at 101325 Pa and the outlet gas rate in Fig. 6.7.6a provided the boundary conditions for UTPipeFlow. Fig. 6.7.6b shows the liquids removal measurements compared to a commercial transient flow code, OLGA, and our analytical models. Note that there is a gas void fraction axial drift at the beginning of the transient which is directly related to the NICKLIN gas drift velocity calculated by

UTPipeFlow. Fig. 6.7.6c shows the inlet pressure at the entrance of the pipeline compared with OLGA and our analytical models. It is evident that our analytical models satisfactorily predicts the trends in the data and provides a better accuracy than the industry code shown for this dataset.

Fig. 6.7.7 shows another set of the transient results from this study but for the high gas injection rate case (i.e., at 700 scfm). As before, the outlet pressure boundary condition was set at 101325 Pa and the outlet gas rate in Fig. 6.7.7a provided the boundary conditions for UTPipeFlow. Fig. 6.7.7b shows the liquids removal measurements compared to OLGA and our analytical models. Fig. 6.7.7c shows the inlet pressure at the entrance of the flowline compared with OLGA and our analytical models. As before, our analytical models satisfactorily predict the trends in the data.

Fig. 6.7.8 shows a ramp-up set of the transient results from this study for a gas injection rate going from 150 to 300 scfm. As before, the outlet pressure boundary condition was set at 101325 Pa and the outlet gas rate in Fig. 6.7.8a provided the boundary conditions for UTPipeFlow. Fig. 6.7.8b shows the liquids removal measurements compared to OLGA and our analytical models. Fig. 6.7.8c shows the inlet pressure at the entrance of the pipeline compared with OLGA and our analytical models. It is clear that our analytical models not only provide a consistently reliable prediction of the trends in this dataset but a higher degree of accuracy than the industry code shown.

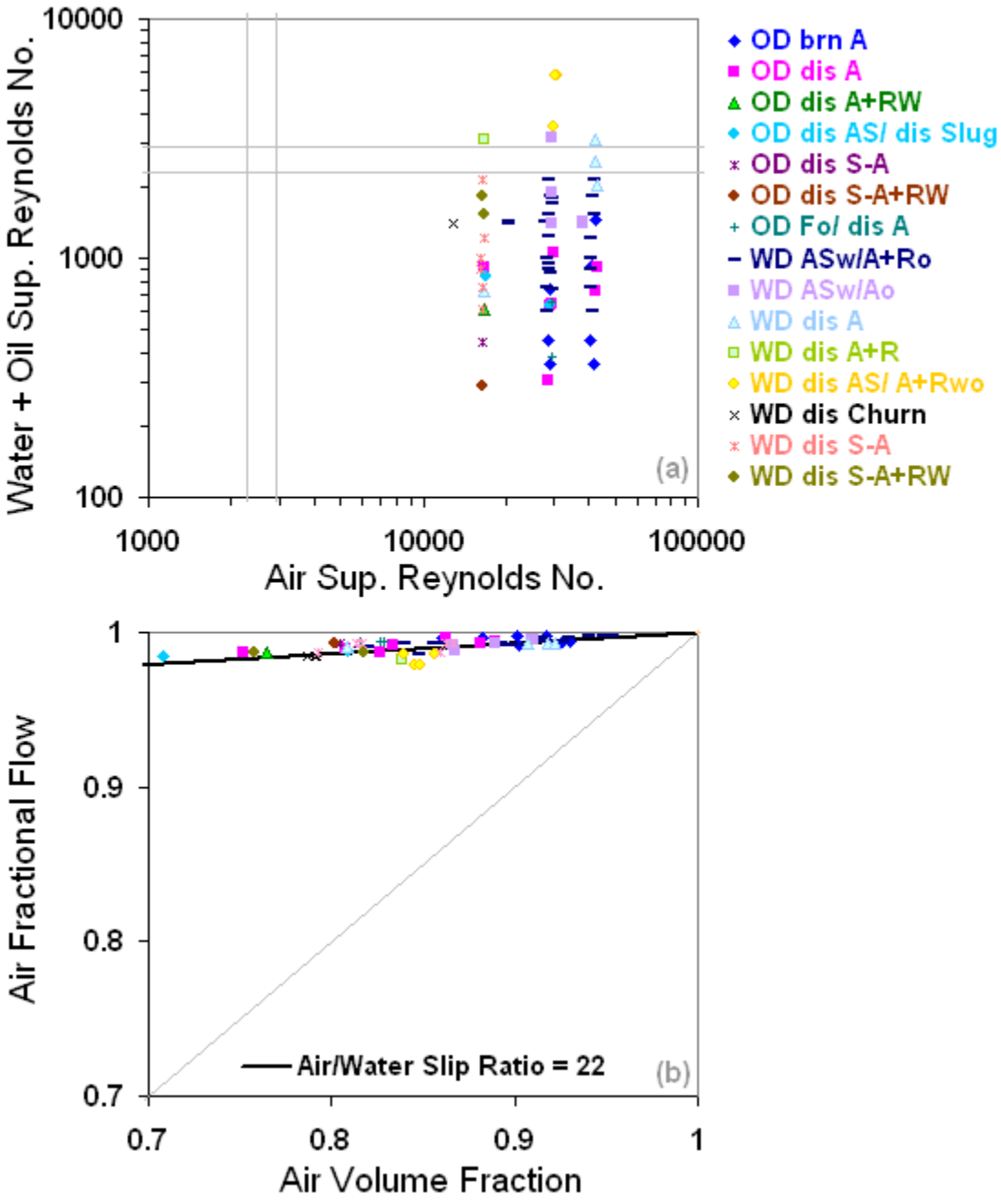

Figure 6.1.1: The vertical, three-phase flow dataset of Woods and Spedding (1996).

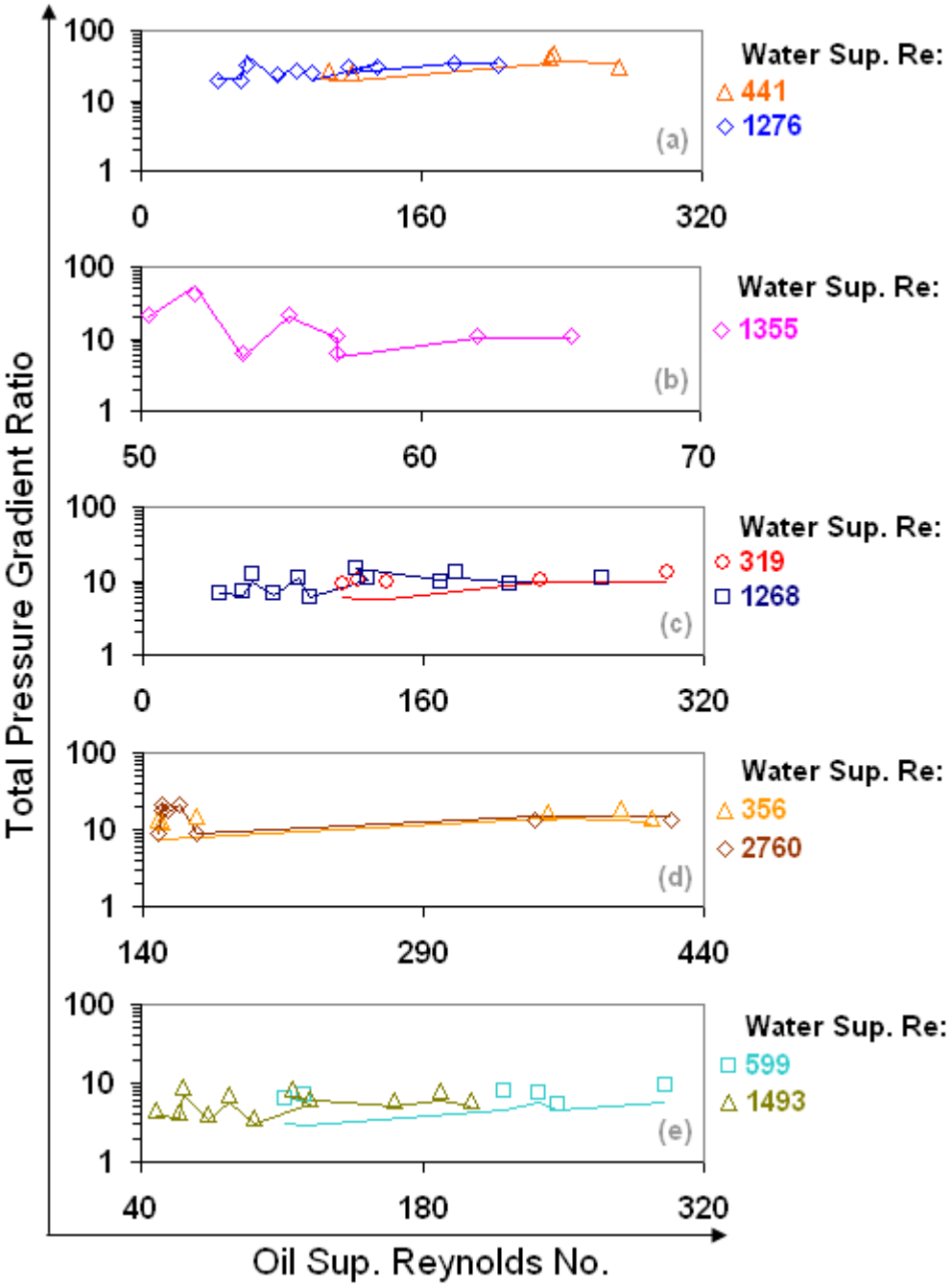

Figure 6.1.2: Prediction of the vertical, three-phase flow dataset of Woods and Spedding (1996). Lines are our predictions and the points are measurements.

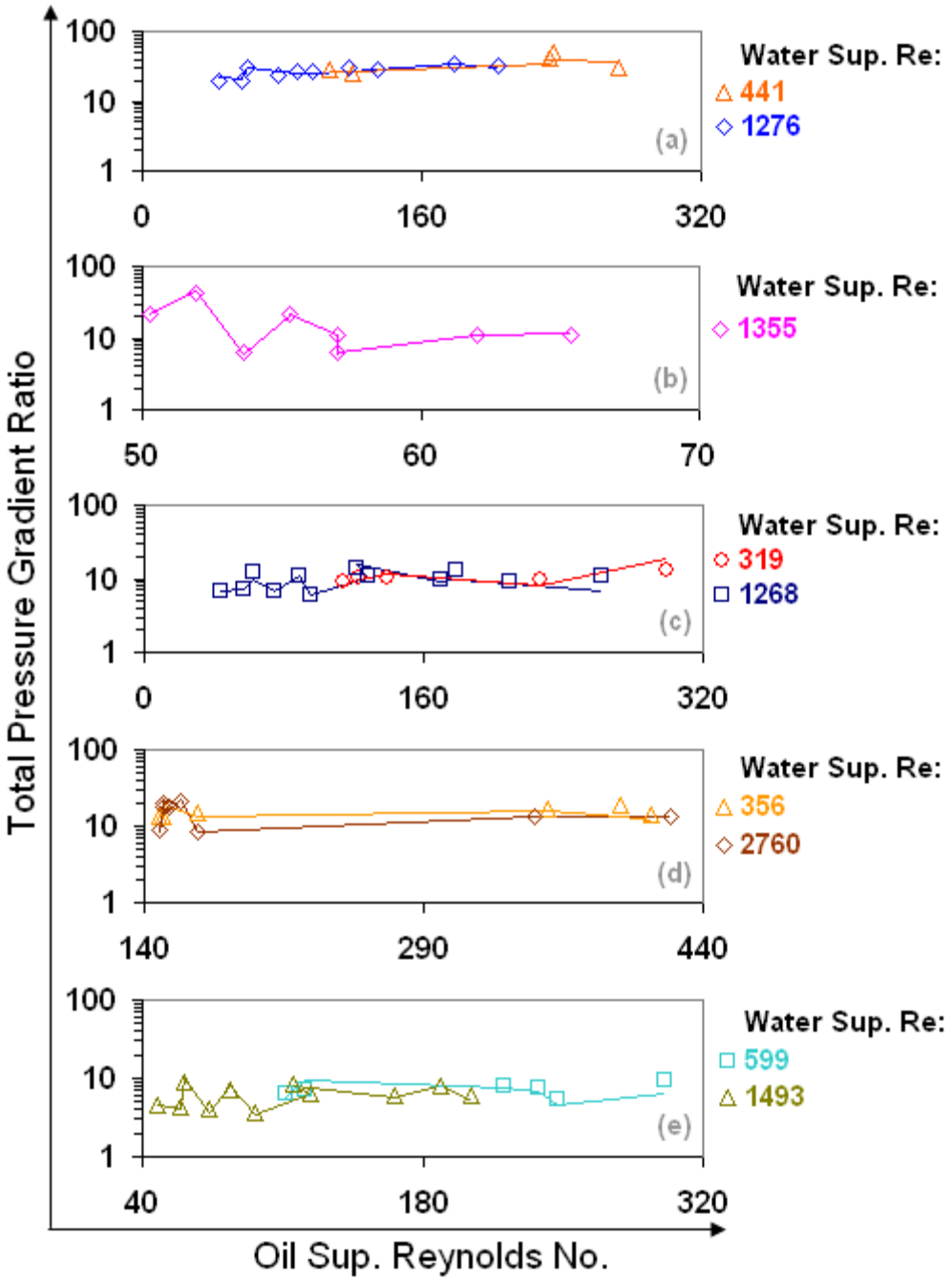

Figure 6.1.3: Model validation against the vertical, three-phase flow dataset of Woods and Spedding (1996). Lines are our calculations and the points are measurements.

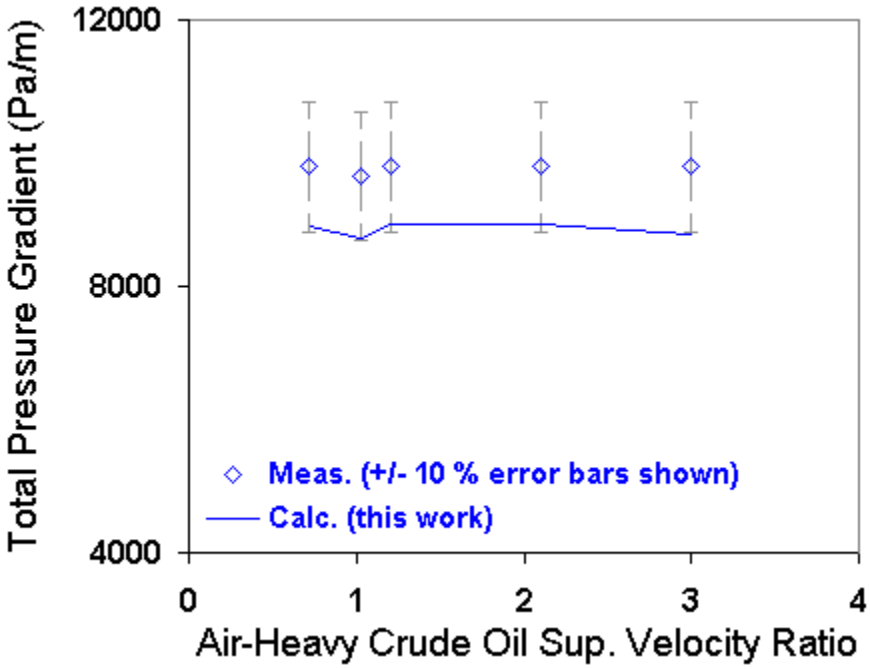

Figure 6.1.4: Model validation against the vertical heavy oil/water/gas flow dataset of Cazarez et al. (2010). Lines are our calculations and the points are measurements.

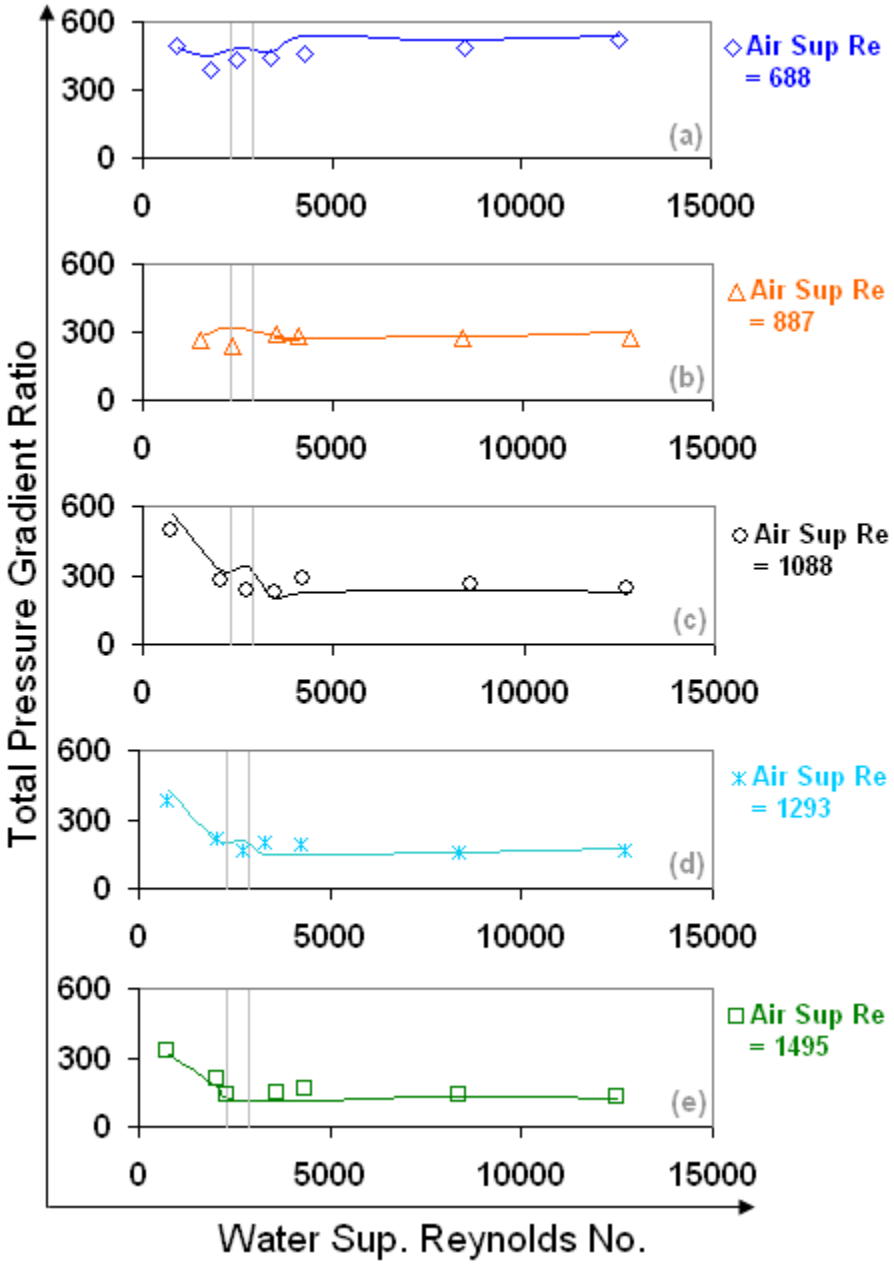

Figure 6.1.5: Model validation against the vertical oil/water/gas flow dataset of Shean (1976). Lines are our calculations and the points are measurements.

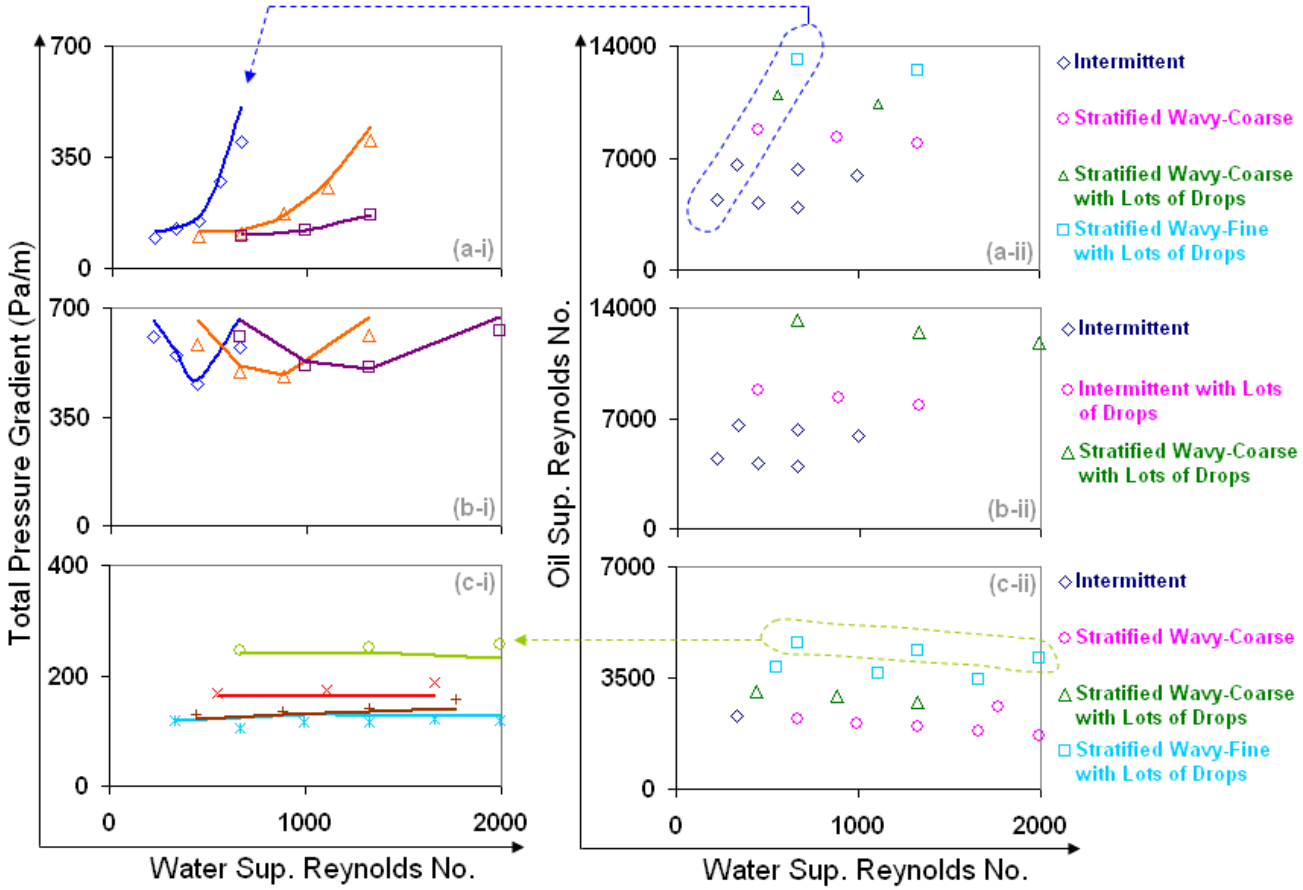

Figure 6.1.6: Model validation against slightly up-inclined three-phase flow datasets of Lunde et al. (1993). Lines are our calculations and the points are measurements.

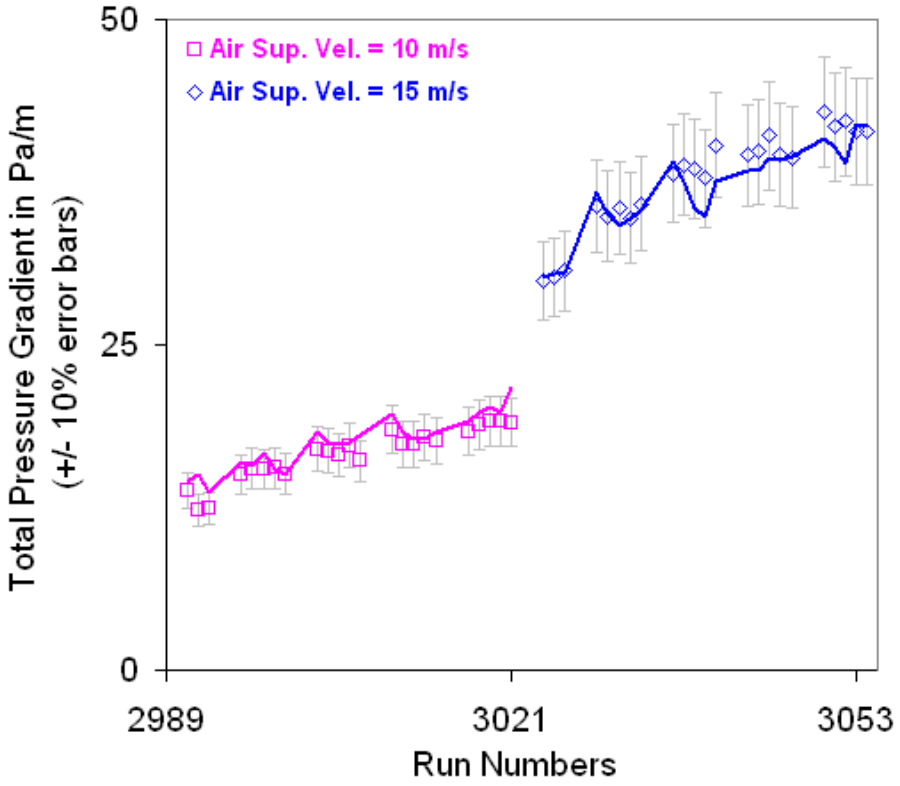

Figure 6.1.7: Model validation against horizontal, low liquids loading, three-phase flow datasets of Dong (2007). Lines are our calculations and the points are measurements.

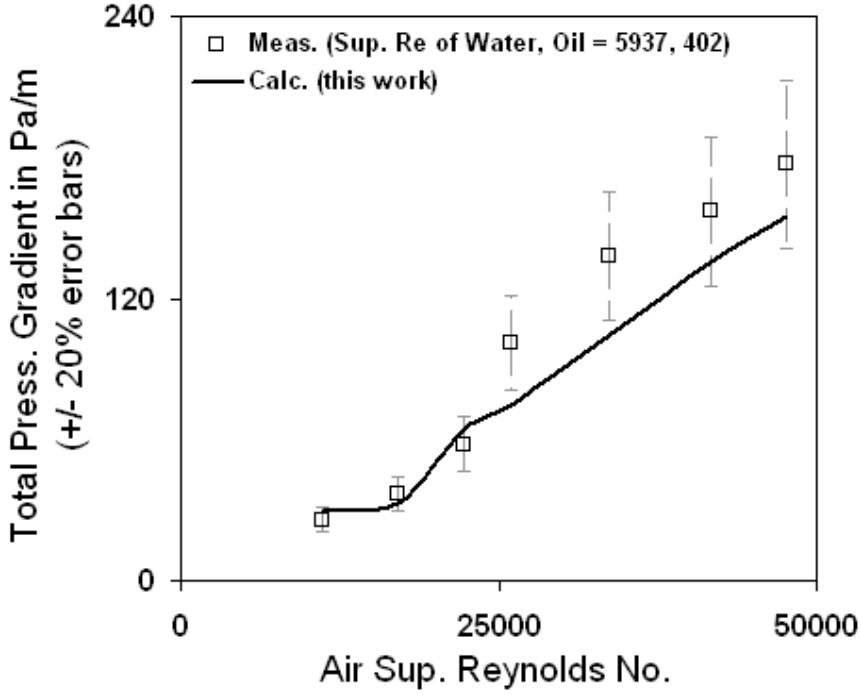

Figure 6.1.8: Model validation against a slightly down-inclined three-phase flow dataset of Odozi (2000). Lines are our calculations and the points are measurements.

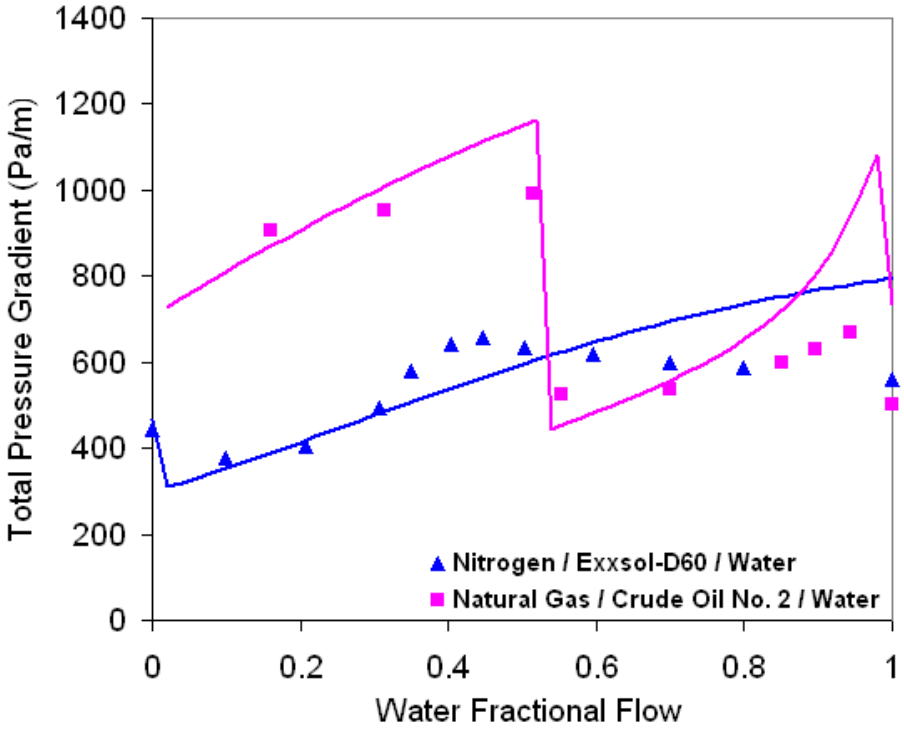

Figure 6.1.9: Model validation against horizontal three-phase flow datasets of Valle (2000). Lines are our calculations and the points are measurements.

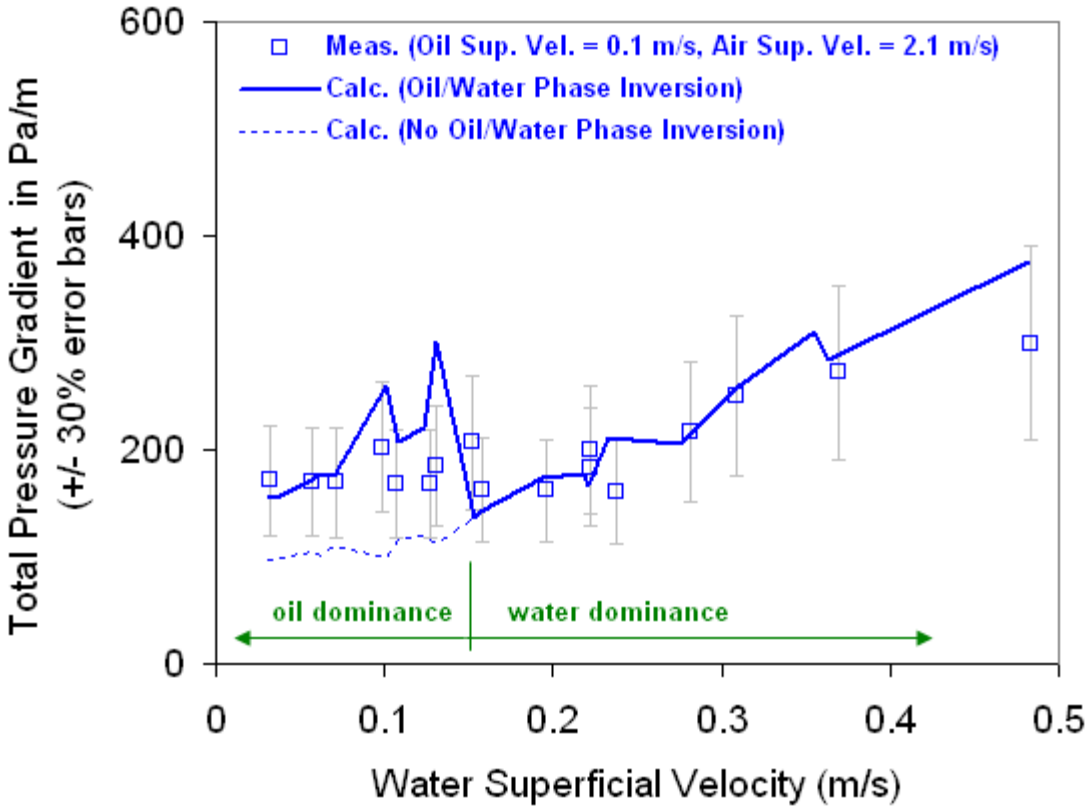

Figure 6.1.10: Model validation against a slightly up-inclined, high-pressure, three-phase flow dataset of Pan (1996). Lines are our calculations and the points are measurements.

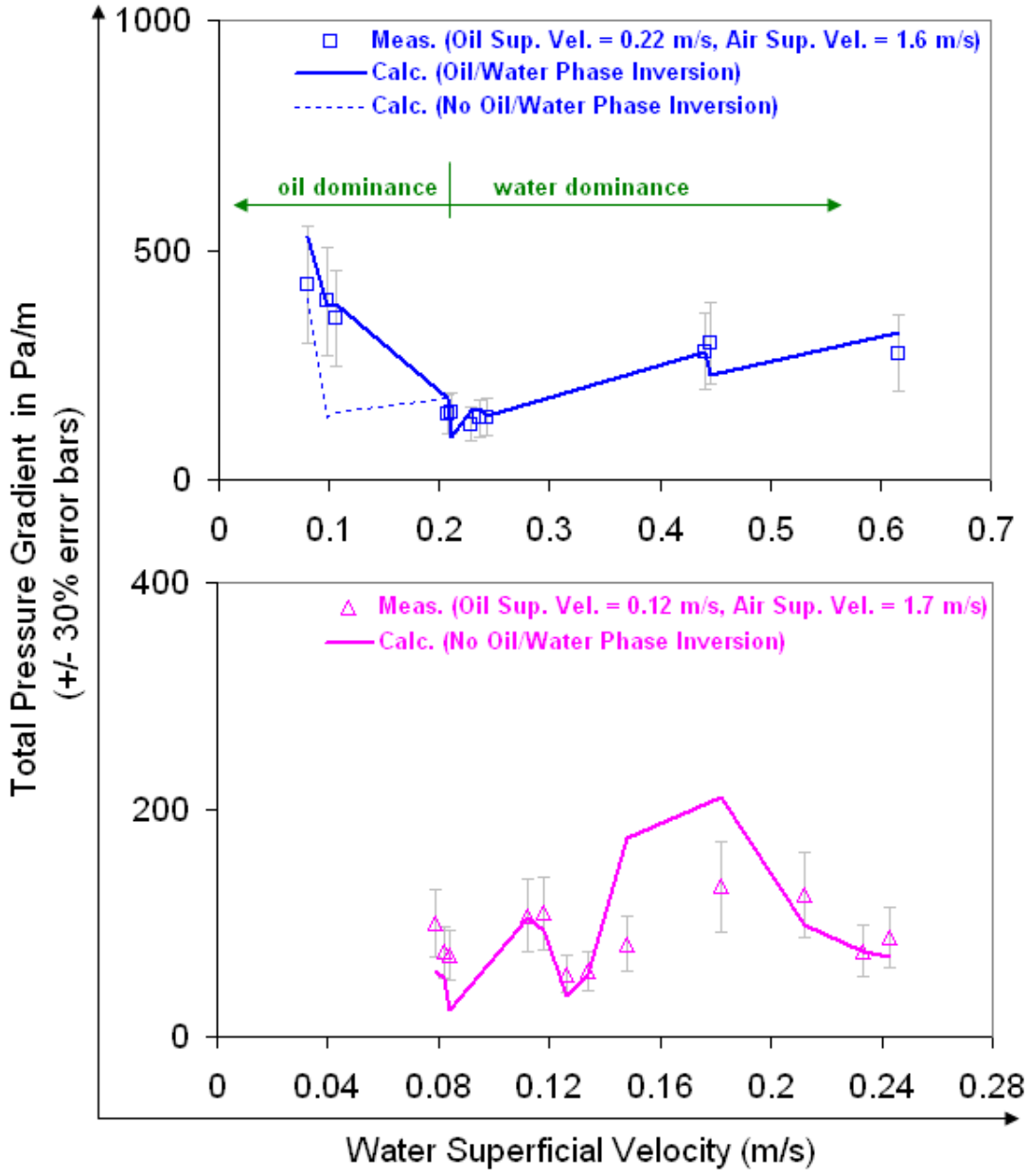

Figure 6.1.11: Model validation against horizontal, three-phase flow datasets of Hall (1992). Lines are our calculations and the points are measurements.

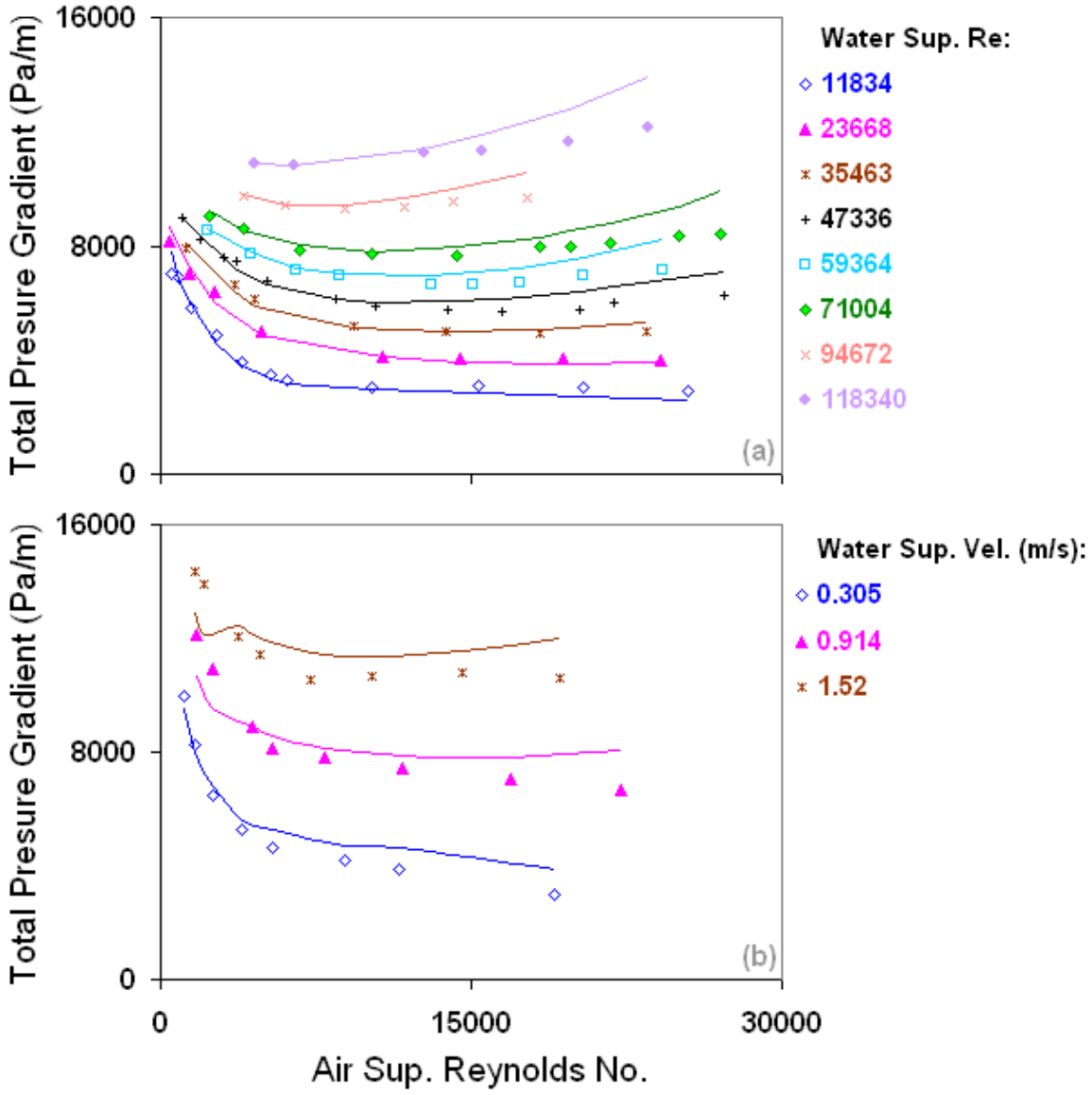

Figure 6.2.1: Model validation against vertical, non-Newtonian flow datasets of Khatib and Richardson (1984). Lines are our calculations and the points are measurements.

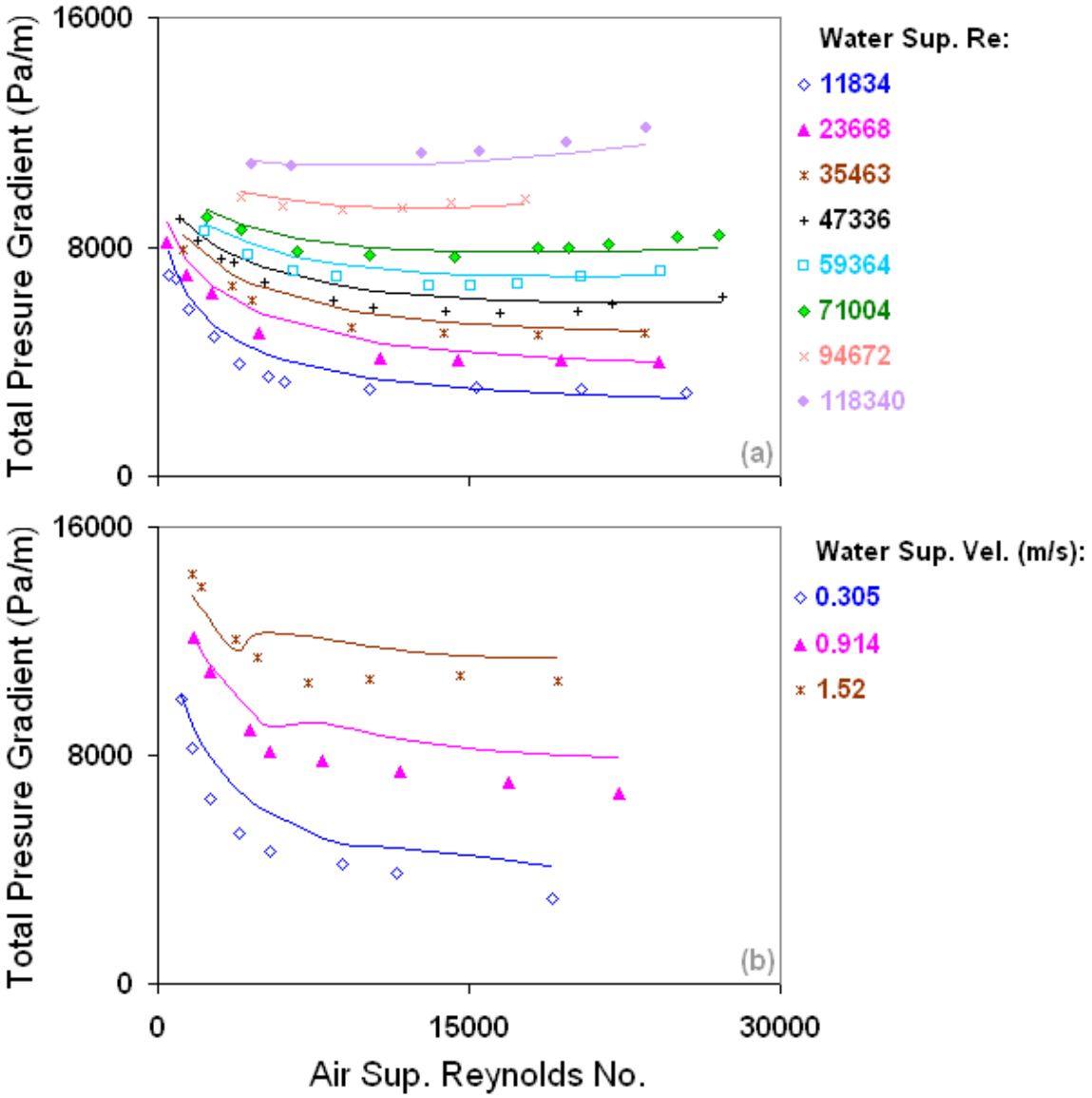

Figure 6.2.2: Prediction of vertical, non-Newtonian flow datasets of Khatib and Richardson (1984) with the ANSLIP model. Lines are our predictions and the points are measurements.

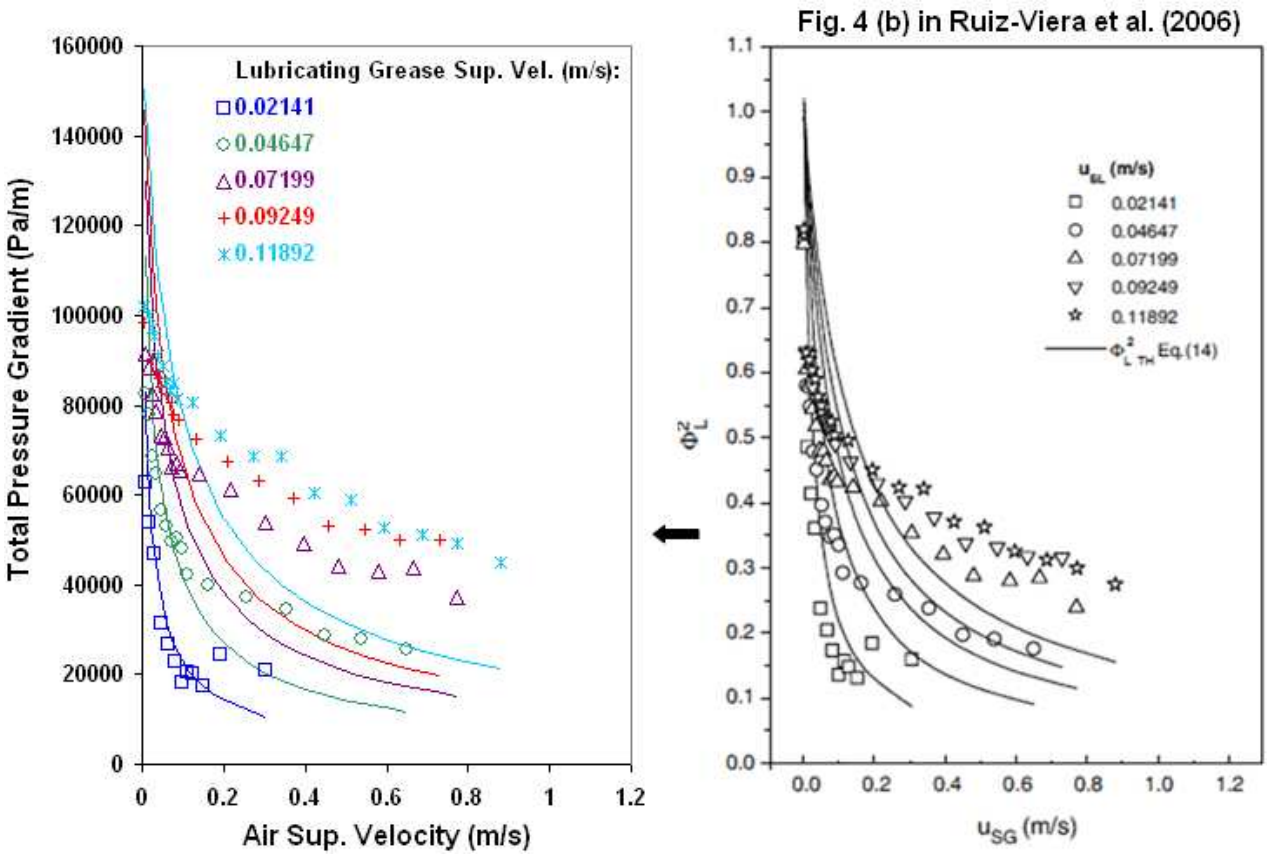

Figure 6.2.3: Prediction of horizontal, non-Newtonian lubricating grease and air flow data of Ruiz-Viera et al. (2006) with the ANSLIP model. Lines are our predictions and the points are measurements.

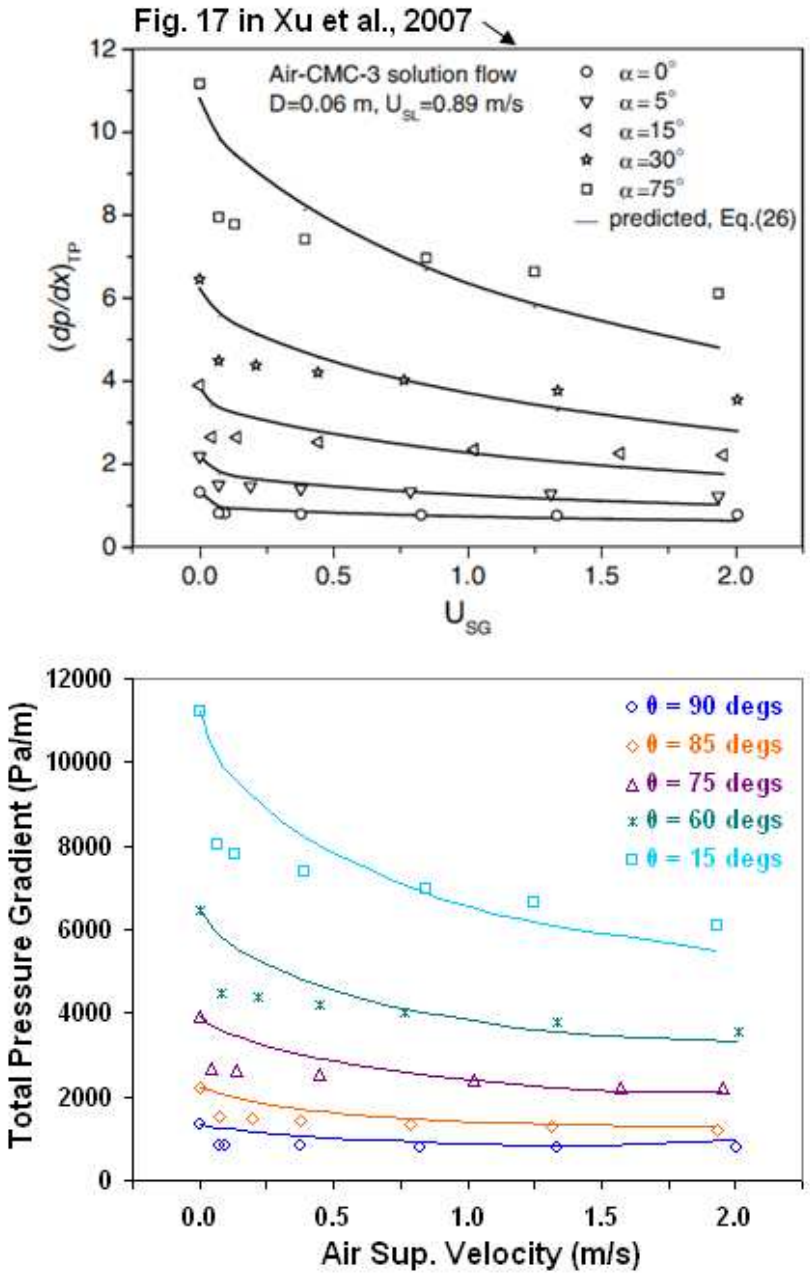

Figure 6.2.4: Prediction of up-inclined, non-Newtonian slug flow data of Xu et al. (2007) with the ANSLIP model. Lines are our predictions and the points are measurements.

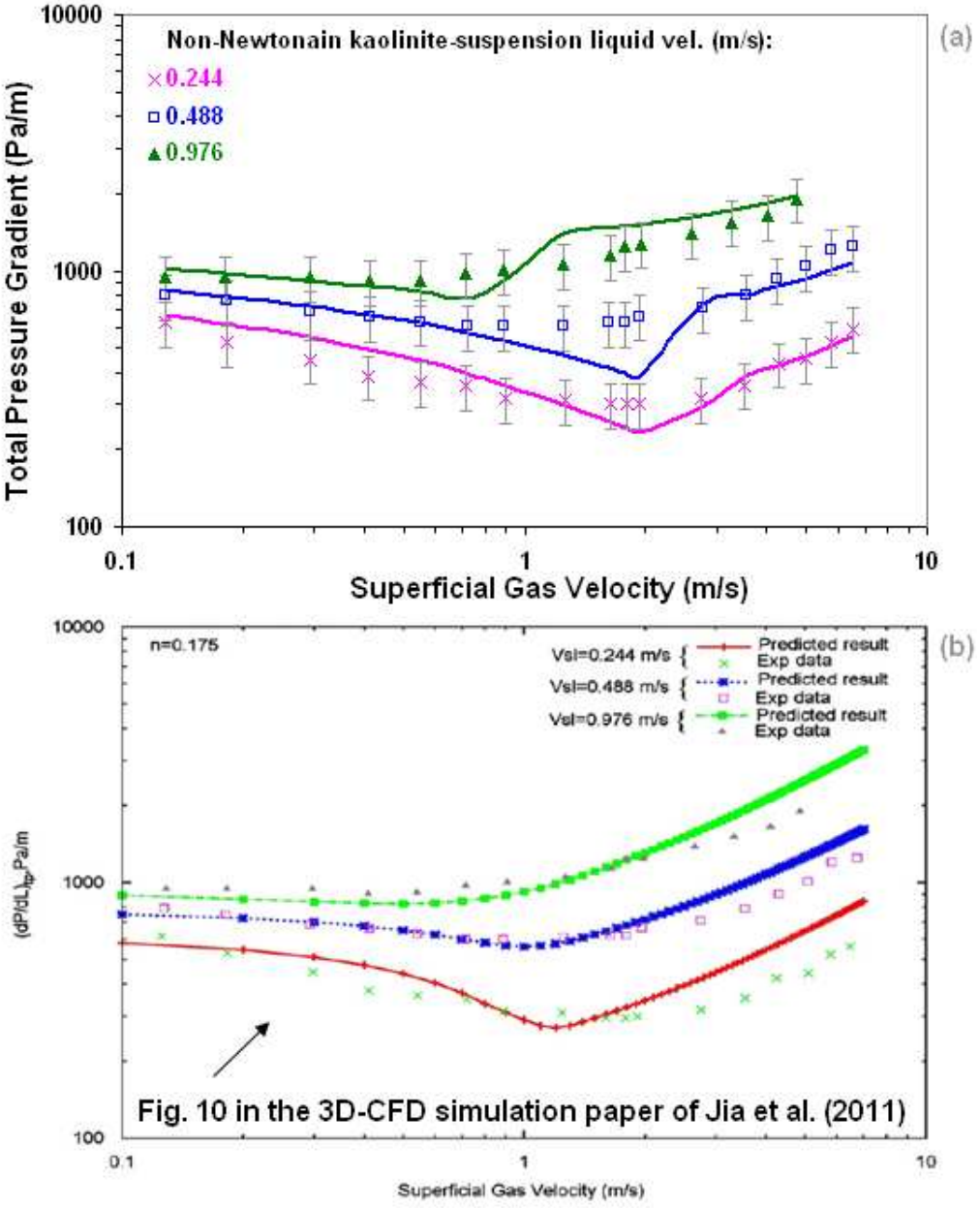

Figure 6.2.5: Prediction of horizontal, non-Newtonian slurry slug flow data of Farooqi and Richardson (1982b) with the BUTTERWORTH model. Lines are our predictions and the points are measurements.

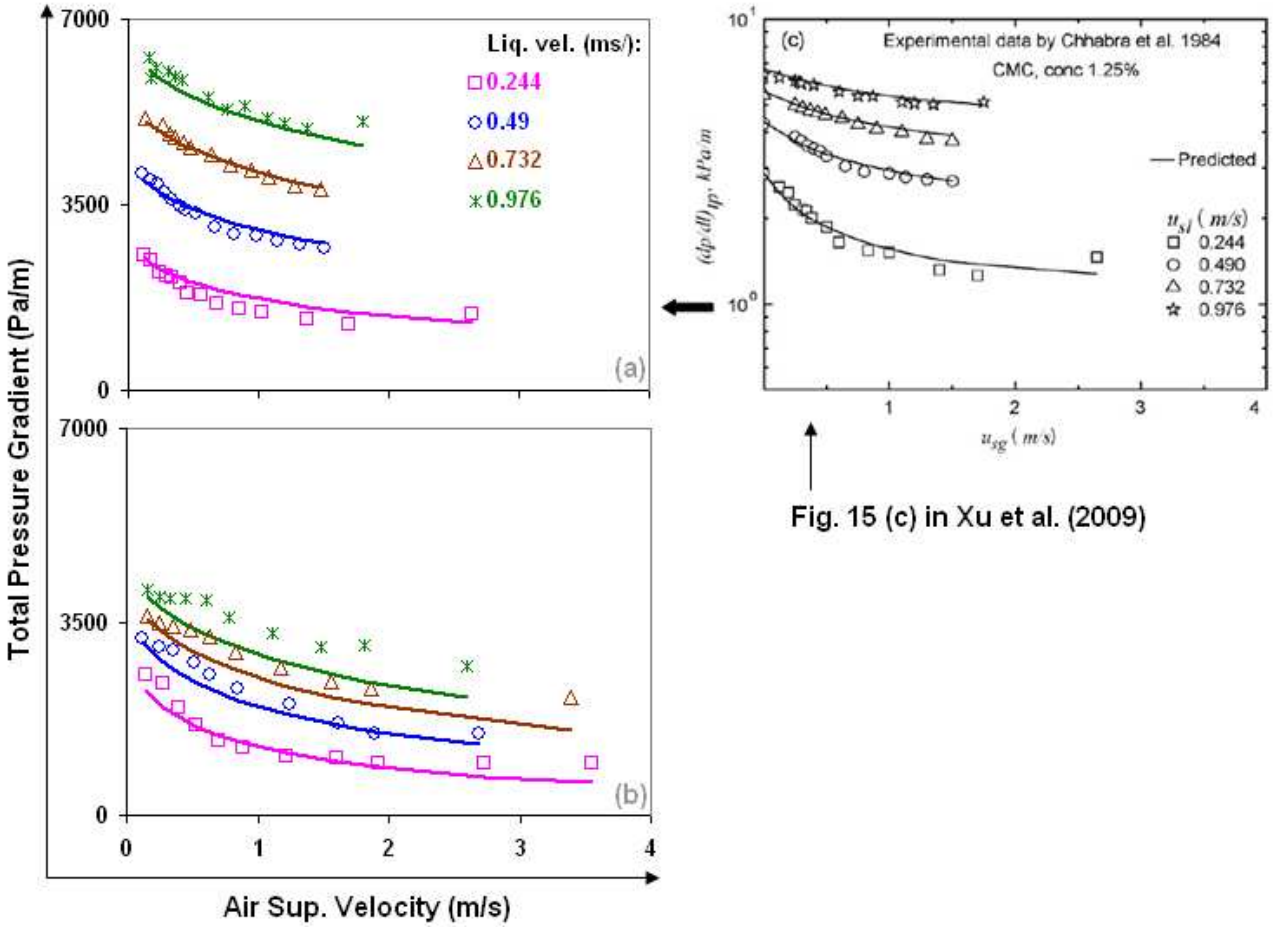

Figure 6.2.6: Prediction of horizontal, viscoinelastic (CMC) polymer flow data of Chhabra et al. (1984) with the BUTTERWORTH model. Lines are our predictions and the points are measurements.

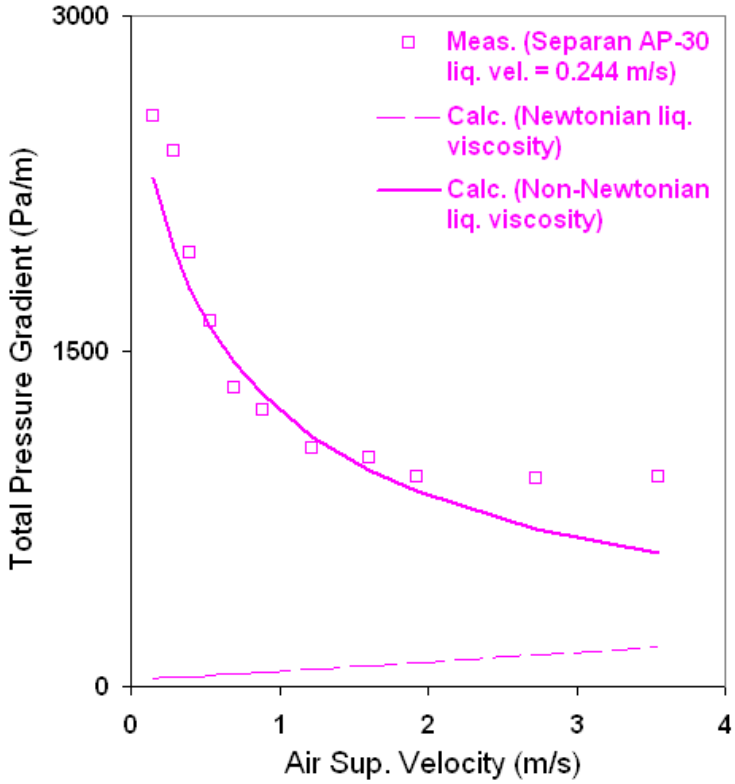

Figure 6.2.7: Showing the importance of including the correct liquid viscosity in multiphase flows with non-Newtonian fluids or fluid-mixtures.

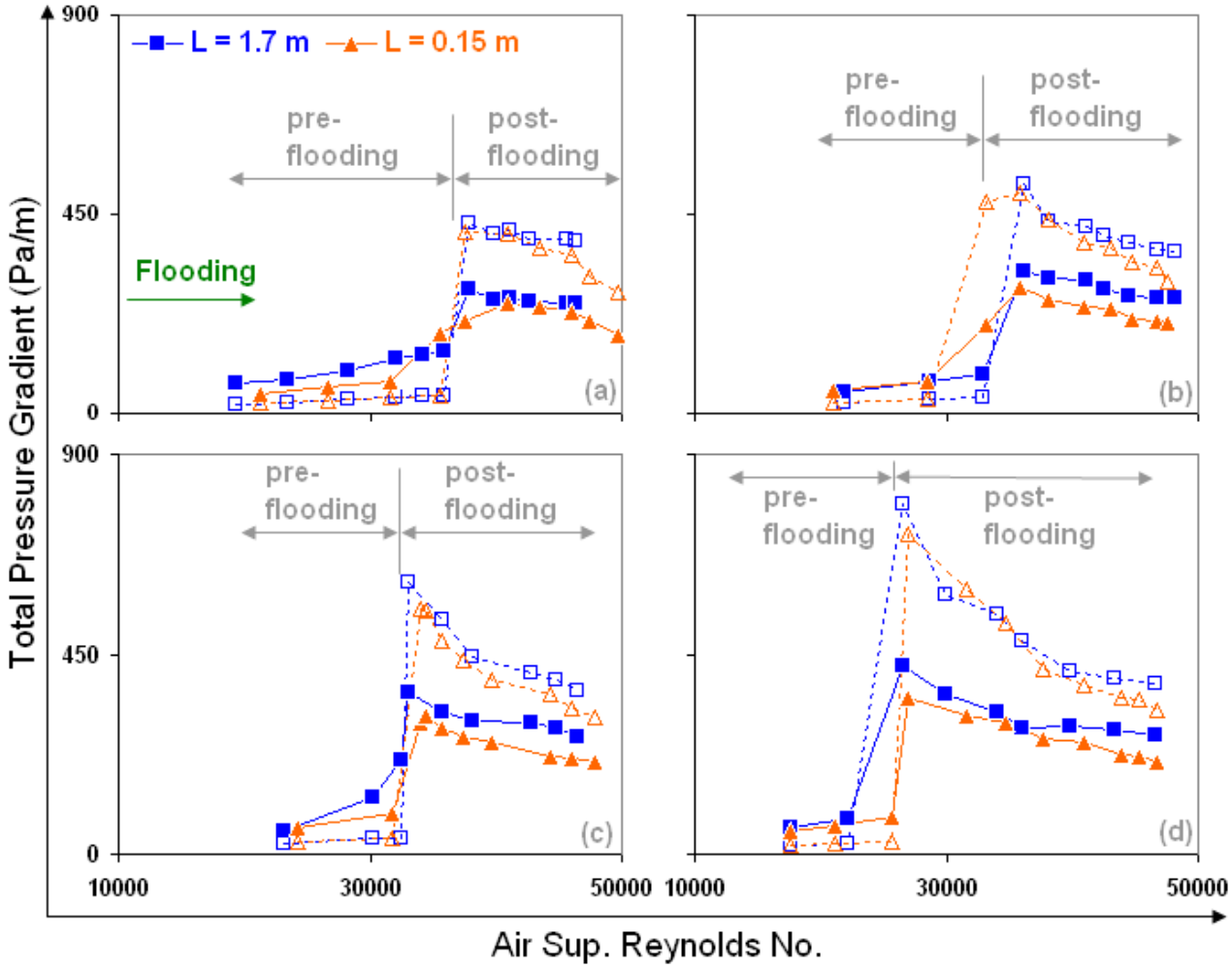

Figure 6.3.1: Model validation against vertical, flooding datasets of Zabaras (1985). Lines are our calculations and the points are measurements.

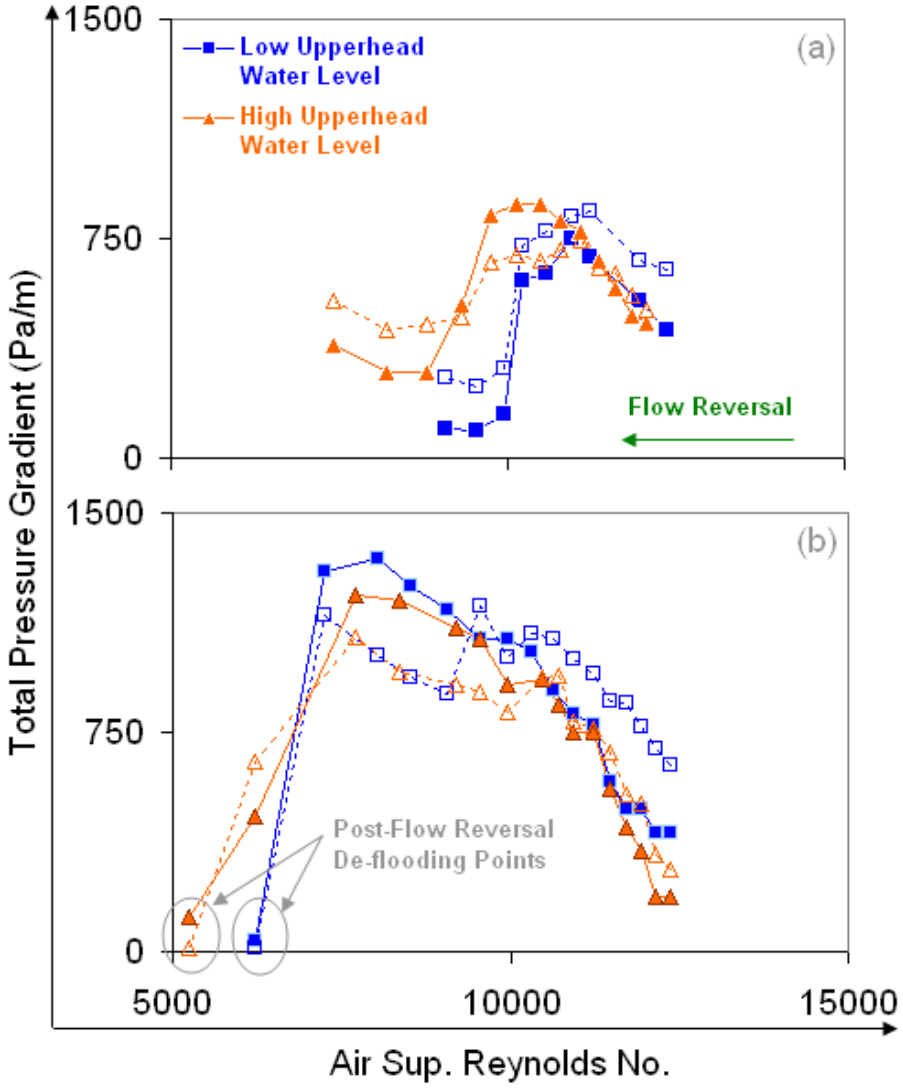

Figure 6.3.2: Model validation against vertical, flow reversal datasets of Bharathan et al. (1979). Lines are our calculations and the points are measurements.

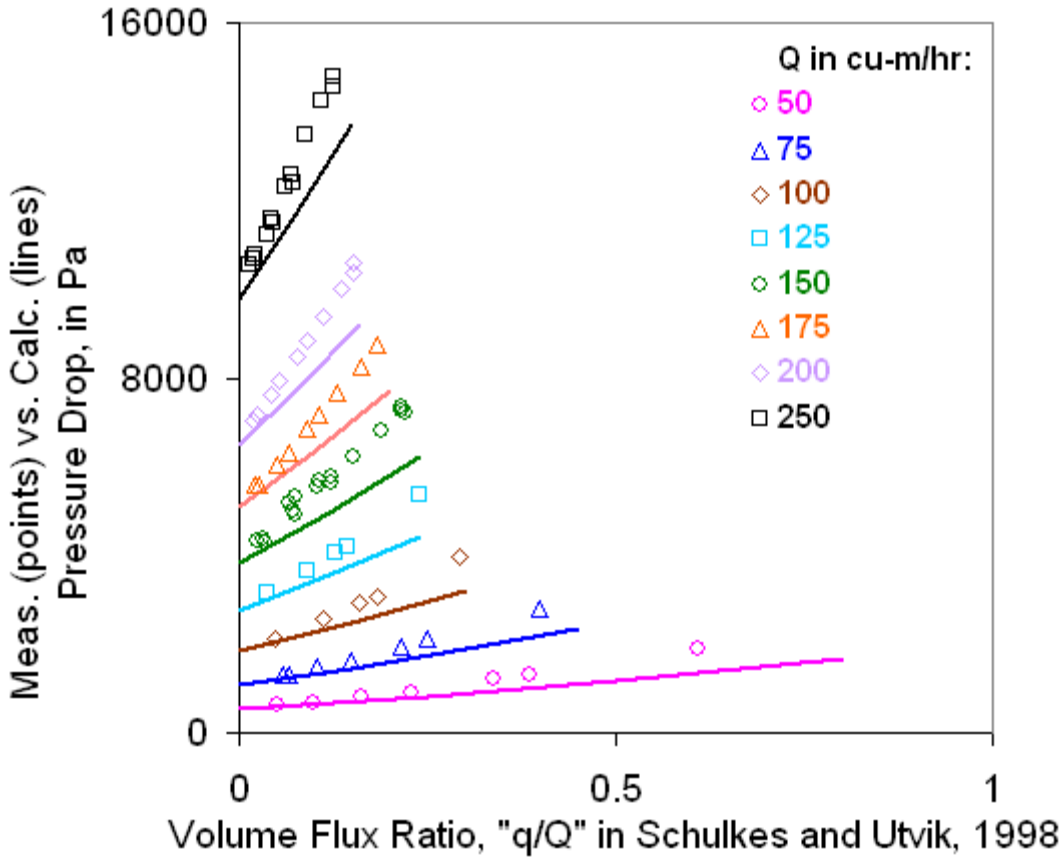

Figure 6.4.1: Prediction of the single-phase water perforated pipe experiments of Schulkes and Utvik (1998) without taking (cross-jet) blockage into account. Lines are our predictions and the points are measurements.

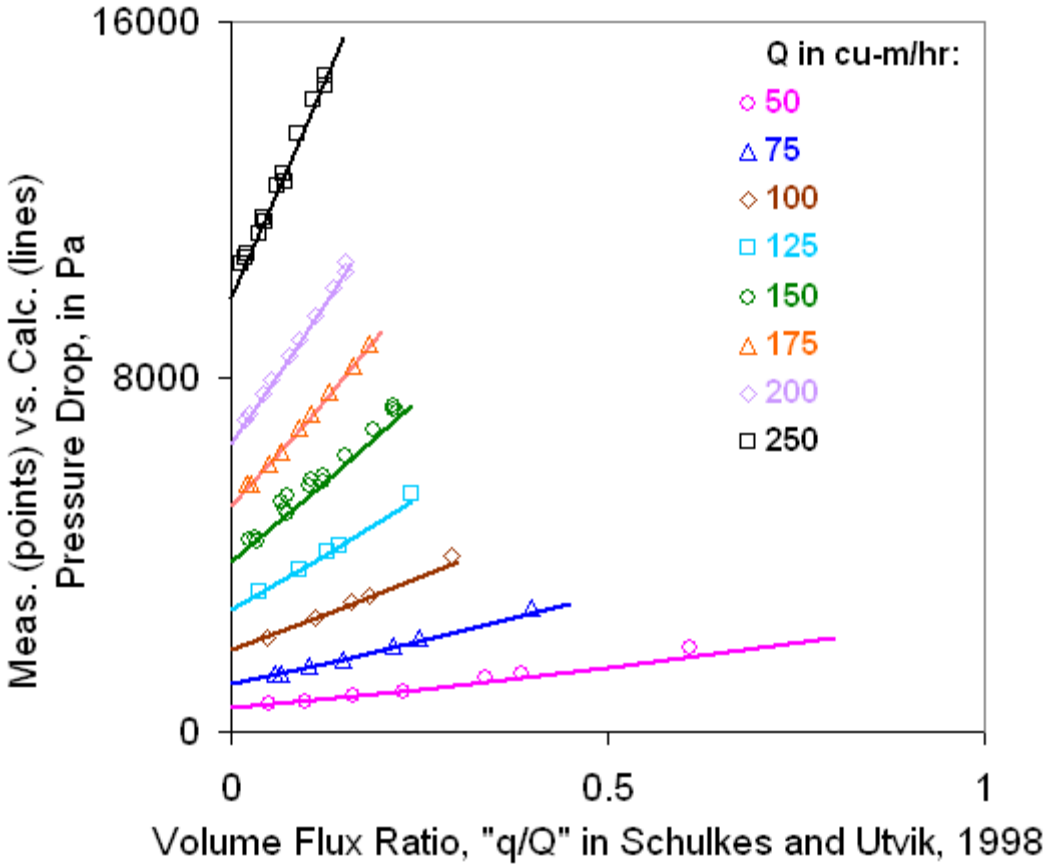

Figure 6.4.2: Prediction of the single-phase water perforated pipe experiments of Schulkes and Utvik (1998) taking (cross-jet) blockage into account. Lines are our predictions and the points are measurements.

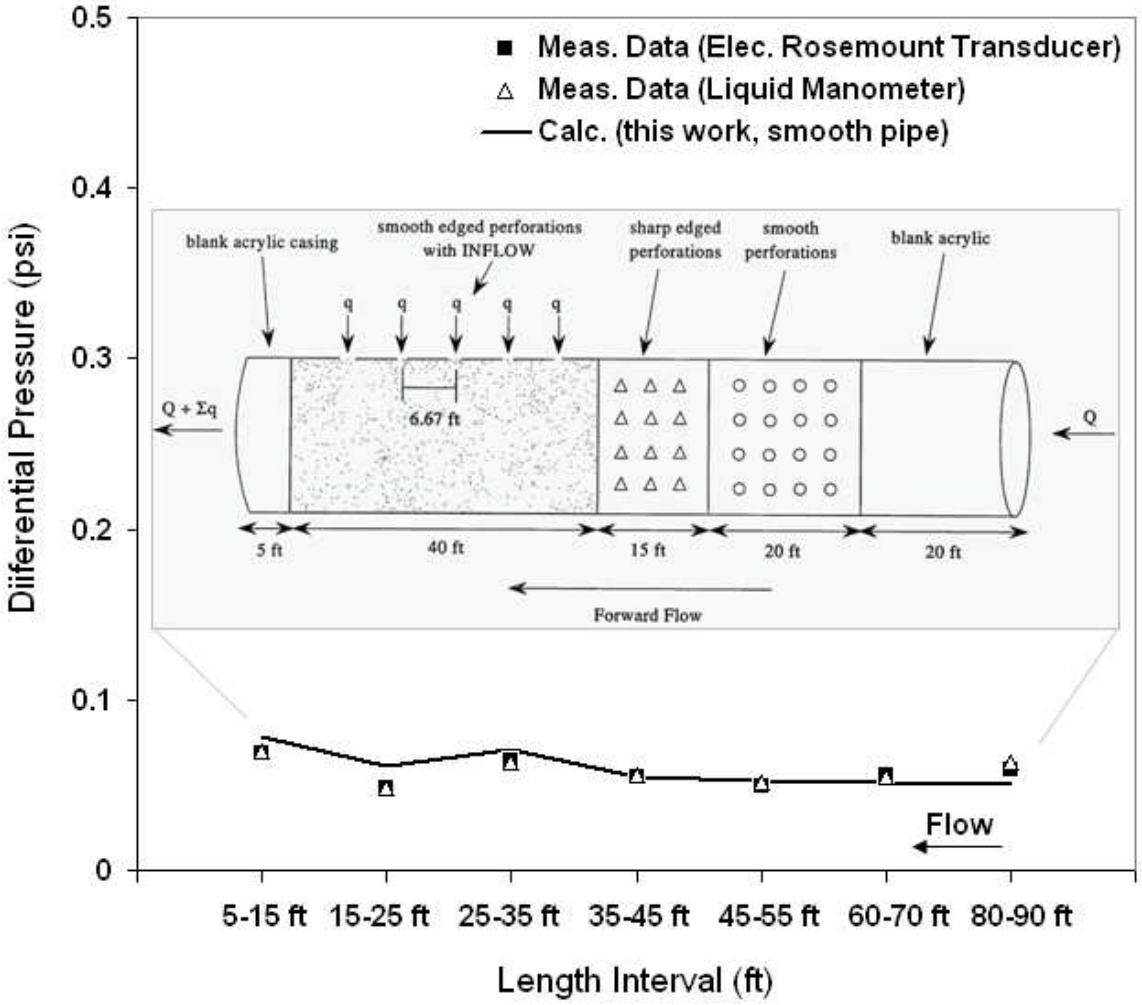

Figure 6.4.3: The Standford-Marathon large-diameter, perforated pipe flow experiments of Fayers (1995). Lines are our predictions and the points are measurements.

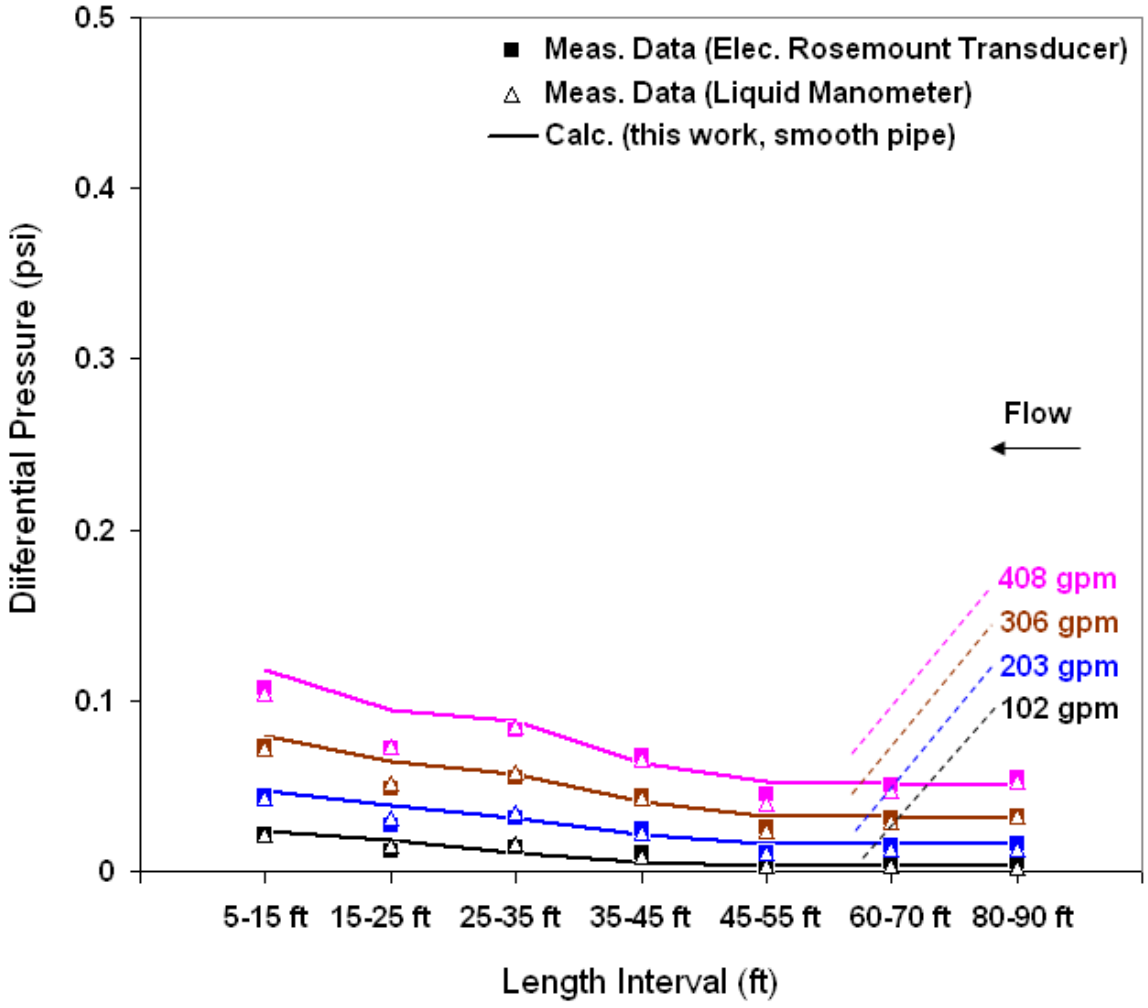

Figure 6.4.4: Prediction of the single-phase oil perforated pipe flow experiments of Fayers (1995). Lines are our predictions and the points are measurements.

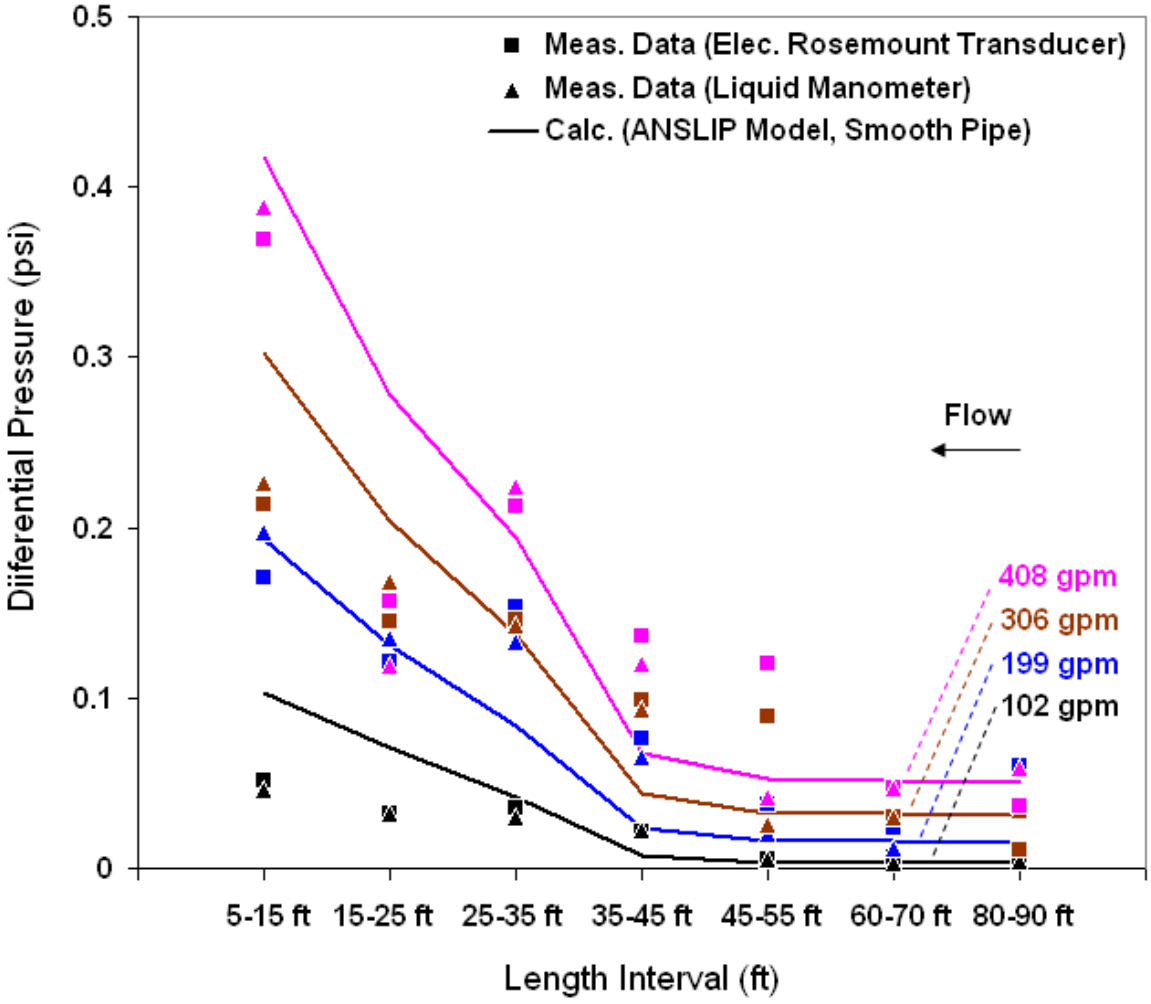

Figure 6.4.5: Prediction of the multiphase oil and nitrogen perforated pipe flow experiments of Fayers (1995) using the ANSLIP model. Lines are our predictions and the points are measurements.

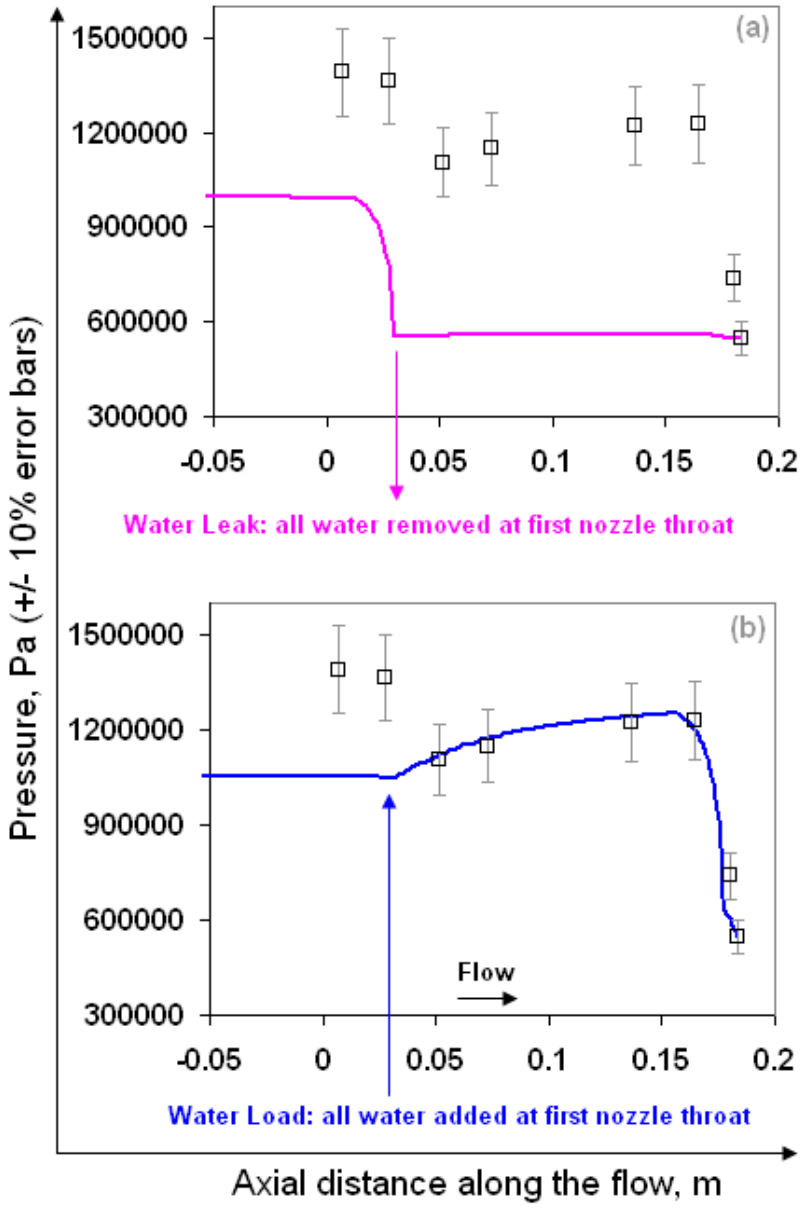

Figure 6.4.6: Simulation of multiphase leak and load detection with case no. 1 of Pougatch et al. (2008). Lines are our predictions and the points are measurements.

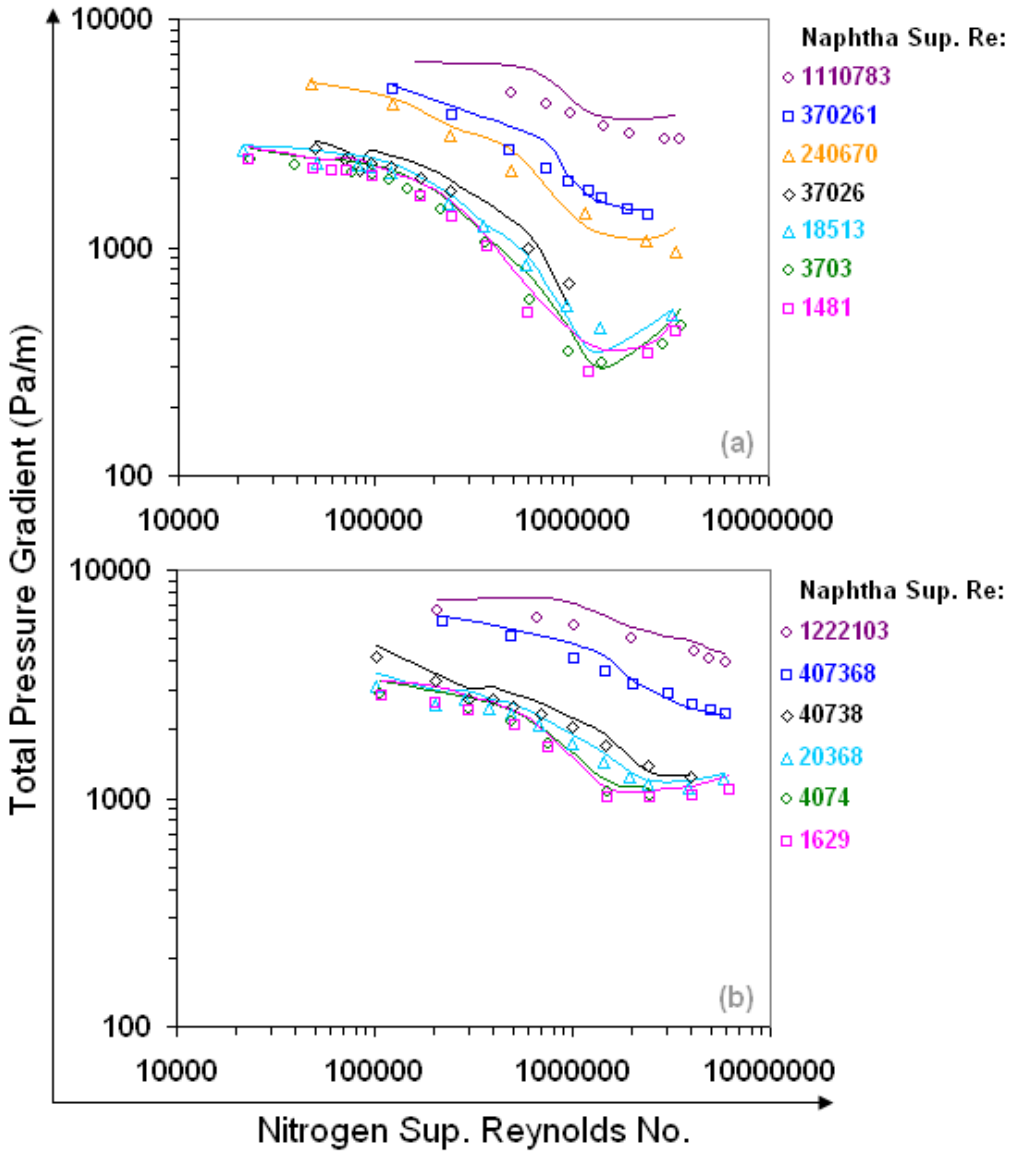

Figure 6.5.1: Model validation against the vertical, large-diameter, high-pressure datasets of Omebere-Iyari (2006). Lines are our calculations and the points are measurements.

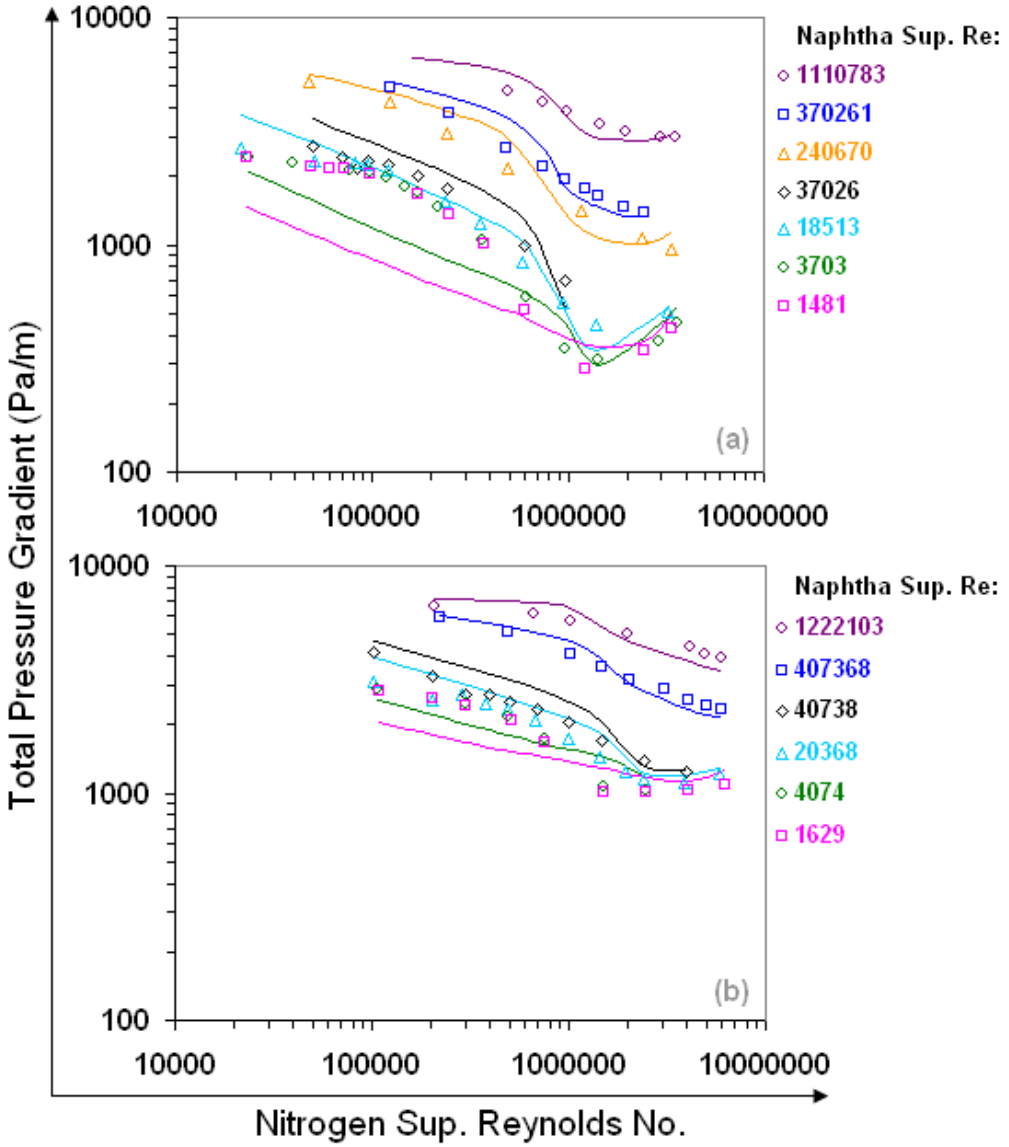

Figure 6.5.2: Prediction of the vertical, large-diameter, high-pressure datasets of Omebere-Iyari (2006) with the ANSLIP model. Lines are our predictions and the points are measurements.

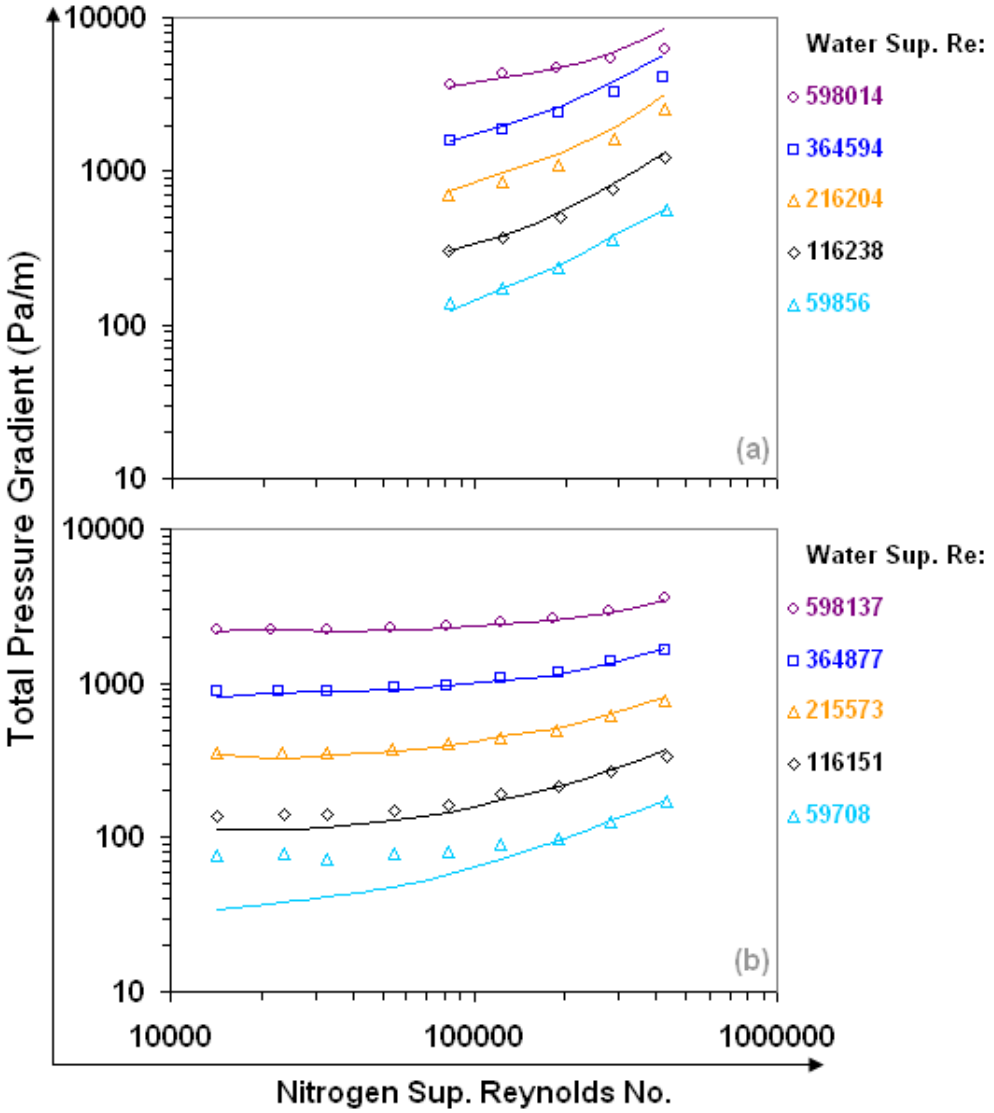

Figure 6.5.3: Model validation against the horizontal, large-diameter, high-pressure datasets of Abduvayt (2003). Lines are our calculations and the points are measurements.

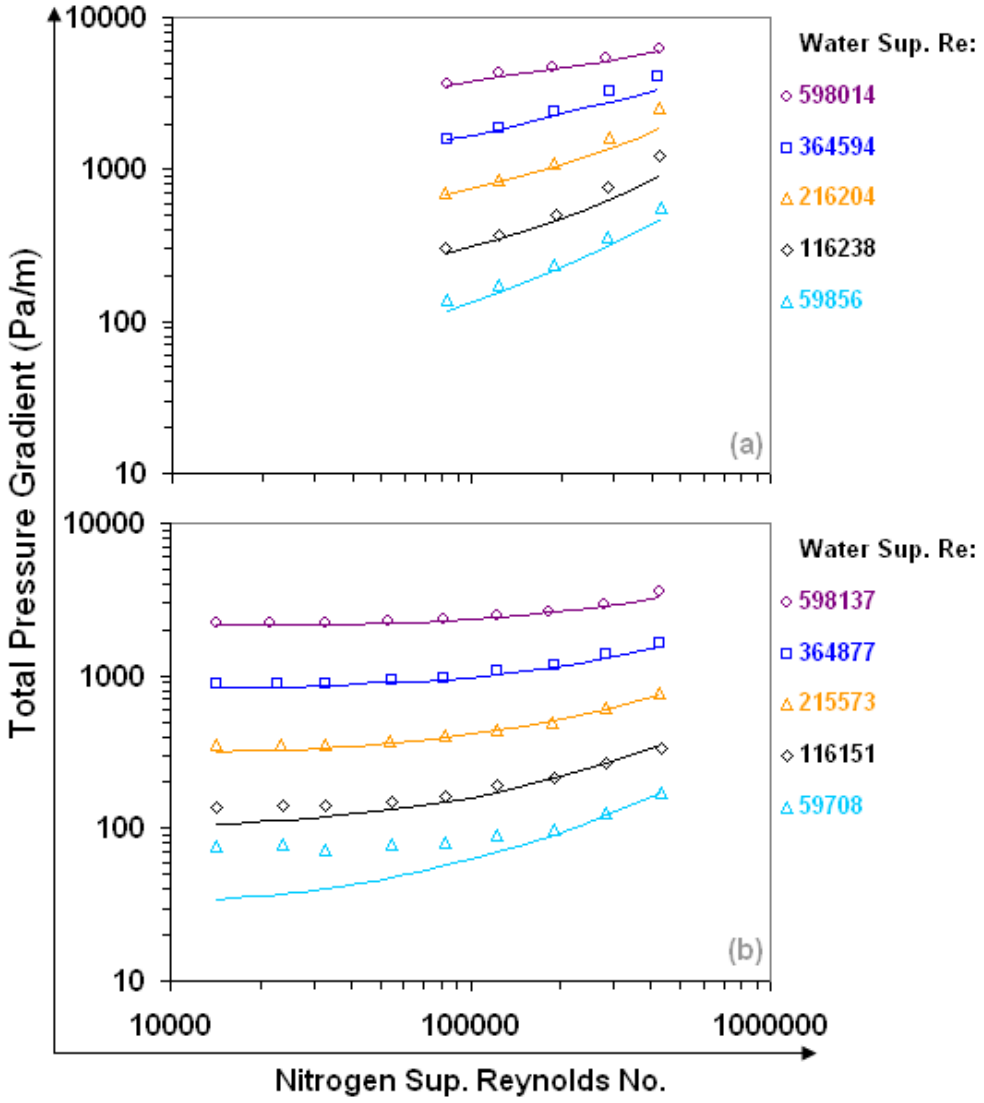

Figure 6.5.4: Prediction of the horizontal, large-diameter, high-pressure datasets of Abduvayt (2003) with the ANSLIP model. Lines are our predictions and the points are measurements.

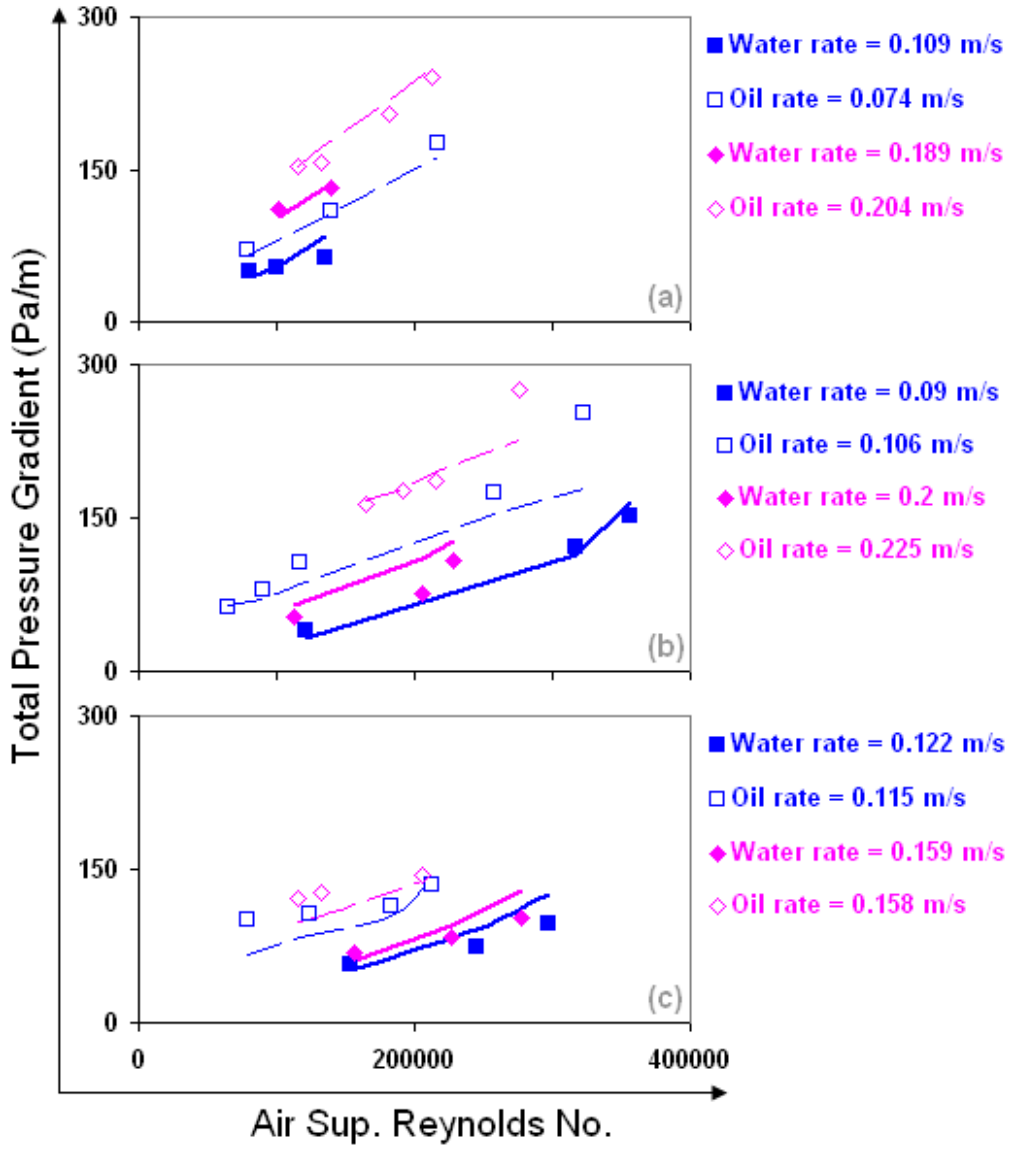

Figure 6.5.5: Model validation against the horizontal, high-pressure datasets of Srichai (2003). Lines are our calculations and the points are measurements.

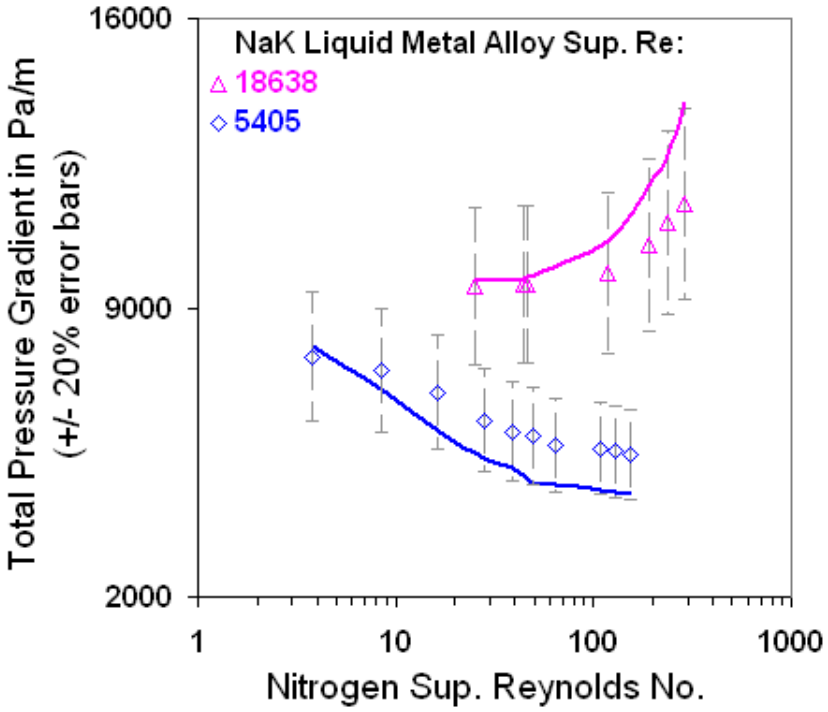

Figure 6.6.1: Model validation against vertical, rectangular pipe flow datasets of Thome (1964). Lines are our calculations and the points are measurements.

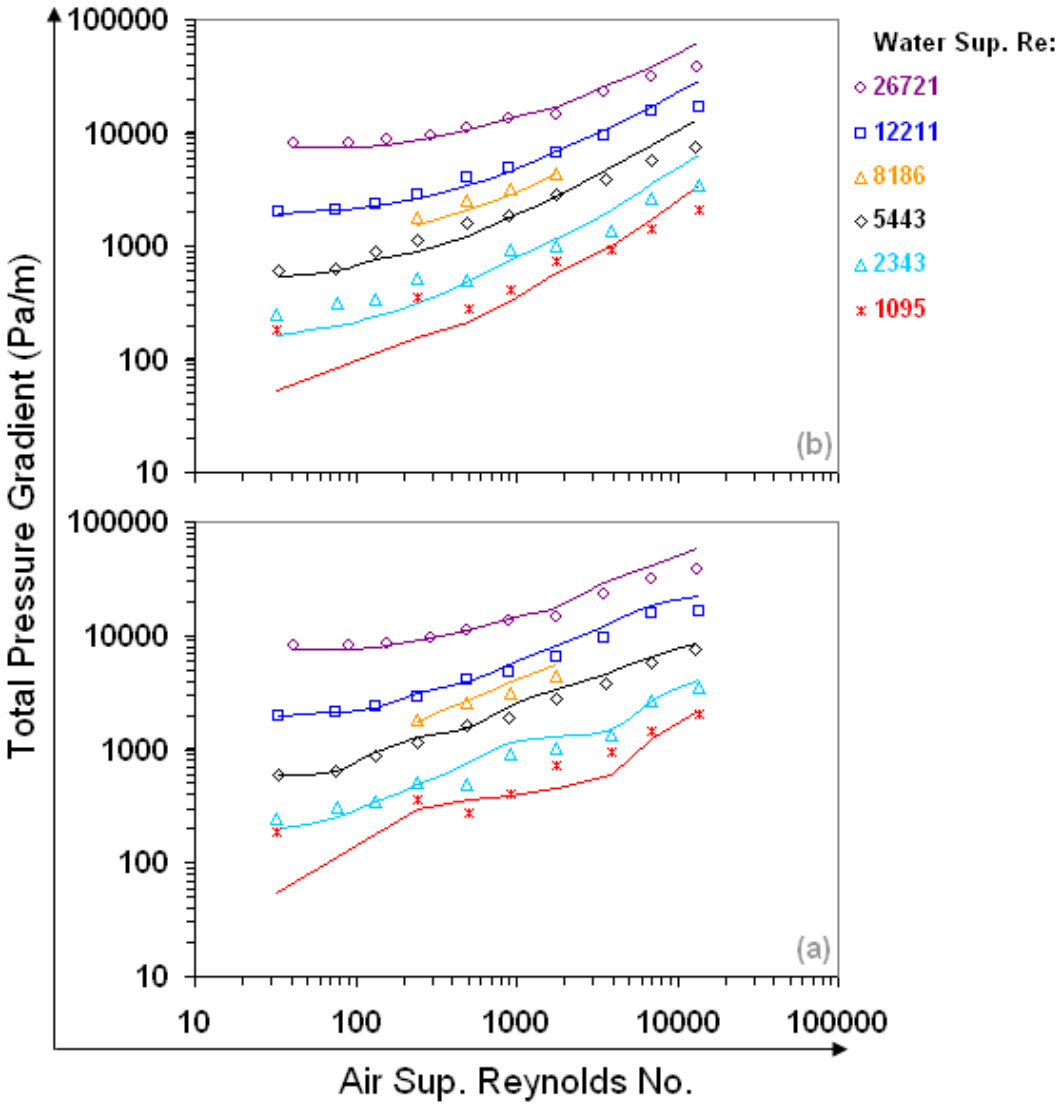

Figure 6.6.2: Prediction and validation of the horizontal, micro-gravity dataset of Choi et al. (2003). Lines are our calculations and the points are measurements.

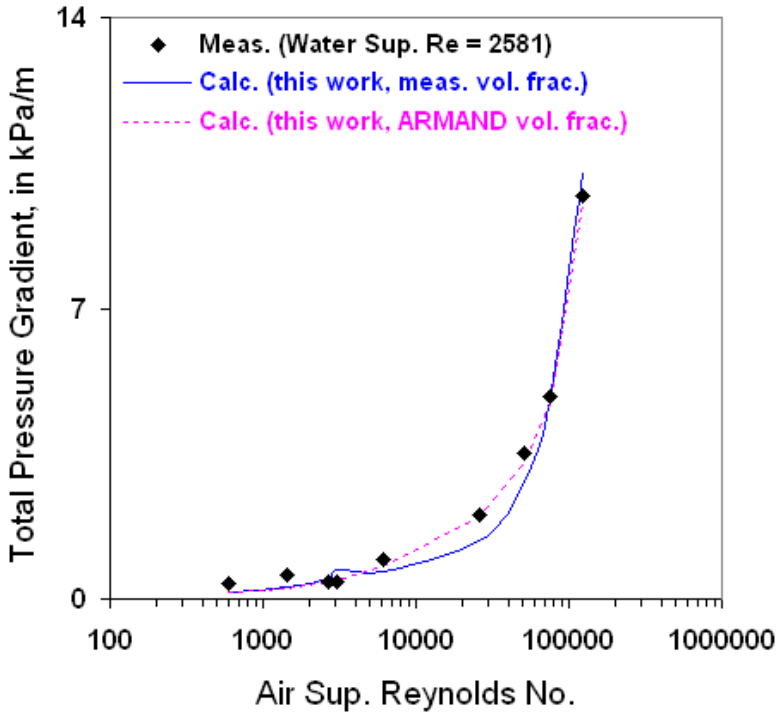

Figure 6.6.3: Prediction and validation of the horizontal, micro-gravity dataset of Bousman and Dukler (1993). Lines are our calculations and the points are measurements.

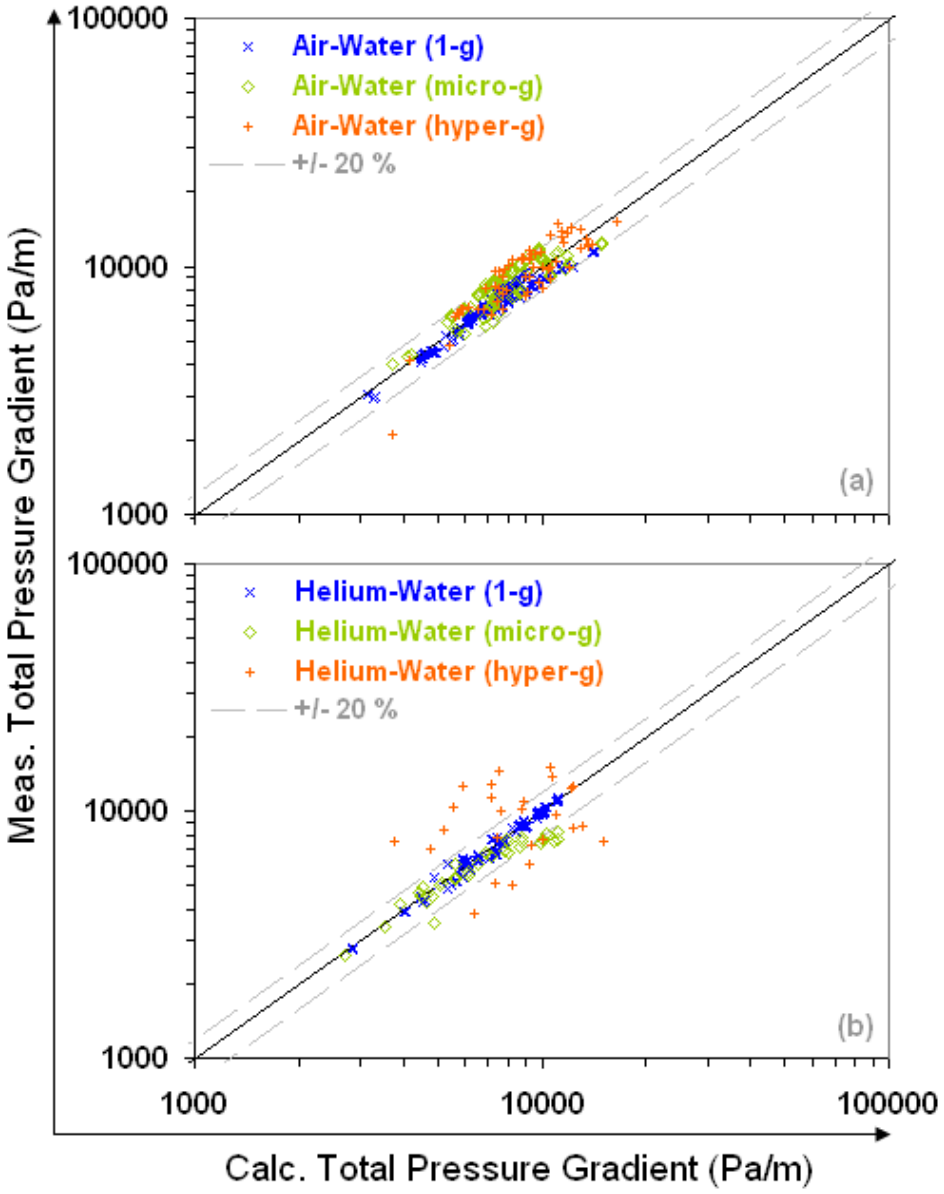

Figure 6.6.4: Prediction of the vertical, micro-gravity, normal-gravity and hyper-gravity datasets of MacGillivray (2004).

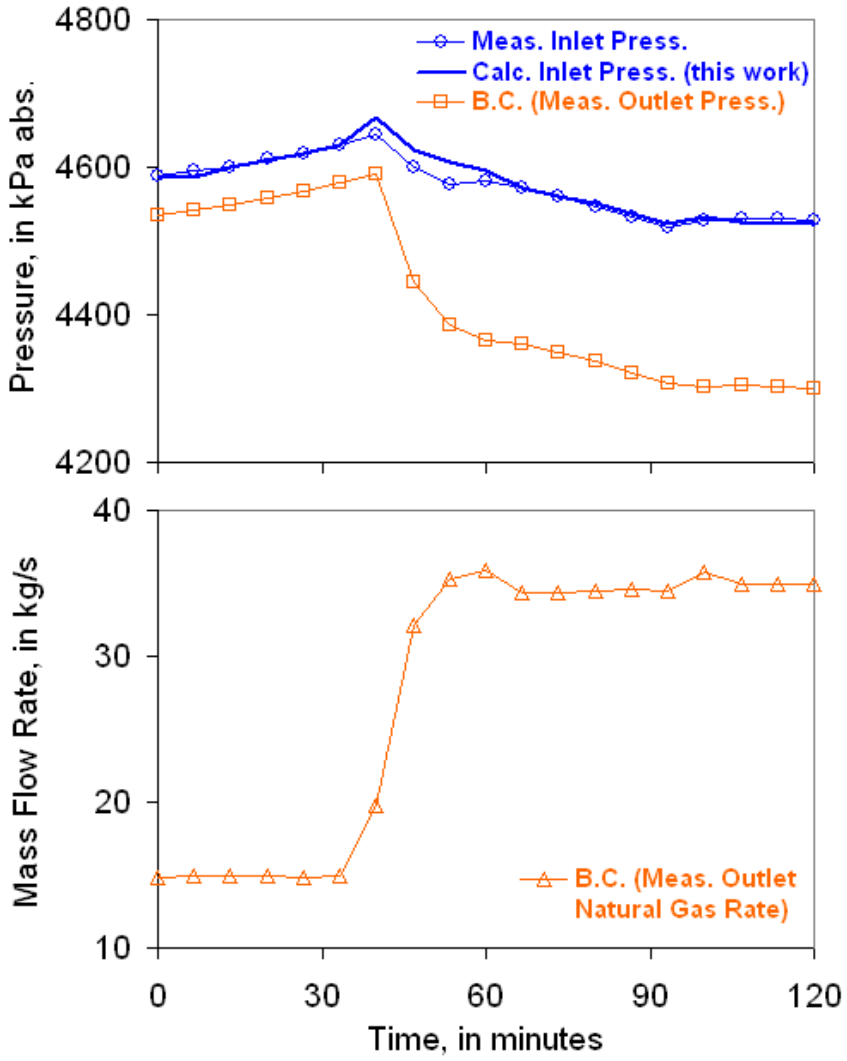

Figure 6.7.1: Prediction of the Hannah et al. (1964) Line B single-phase gas transient.

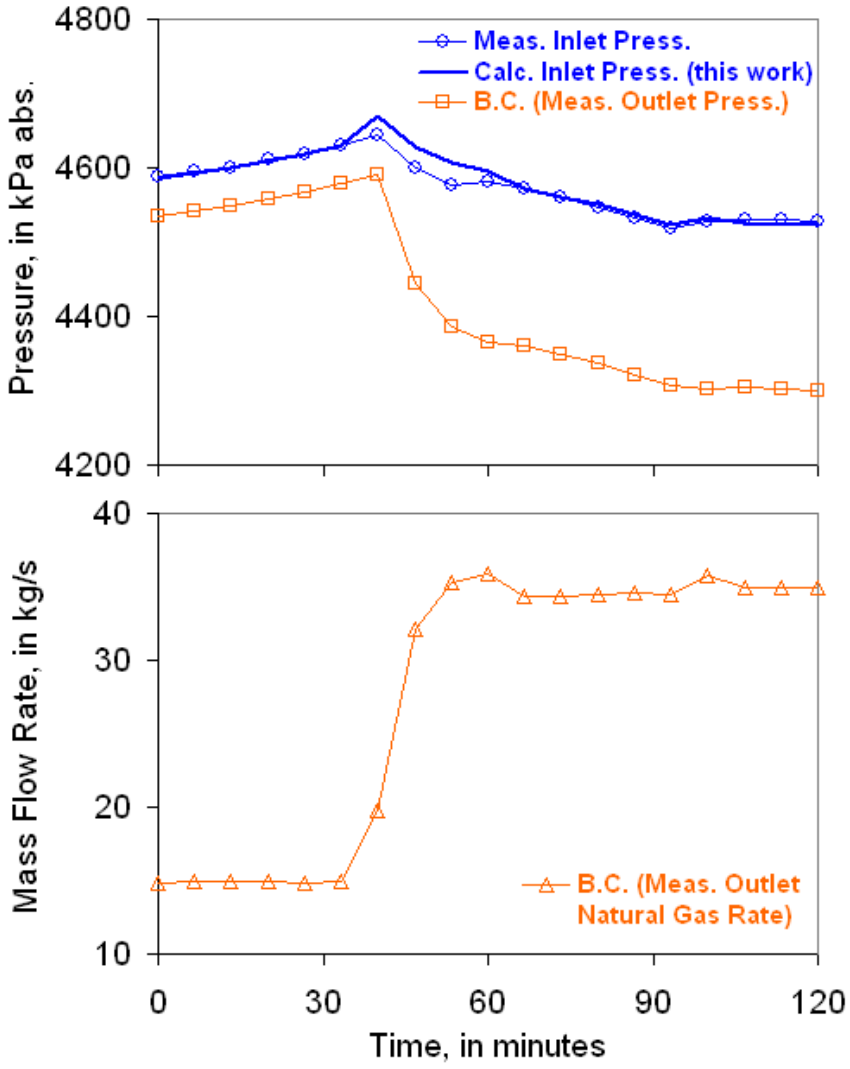

Figure 6.7.2: Prediction of the Hannah et al. (1964) Line B single-phase gas transient using a succession of steady states.

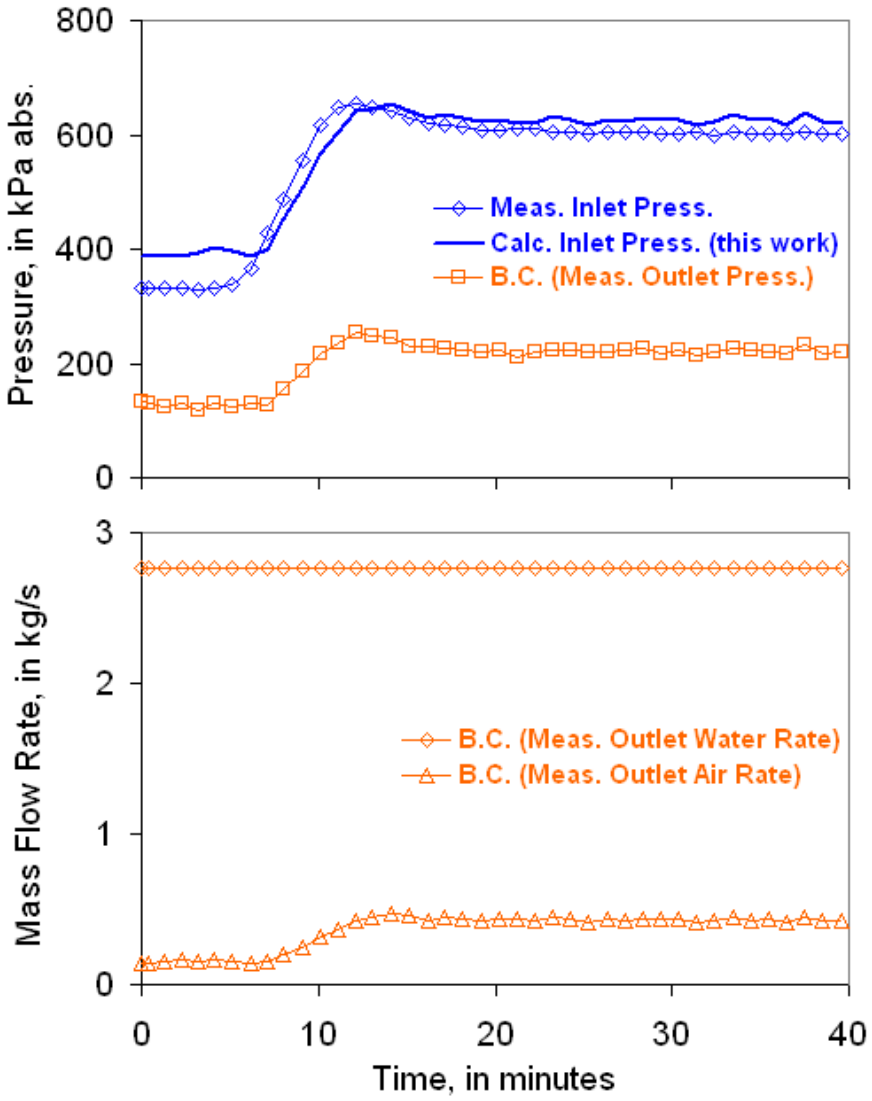

Figure 6.7.3: Prediction of a transient multiphase flow dataset from Kohda et al. (1987) using the ANSLIP model for gas volume fraction and the Ishii and Mishima (1982) model for liquid entrainment.

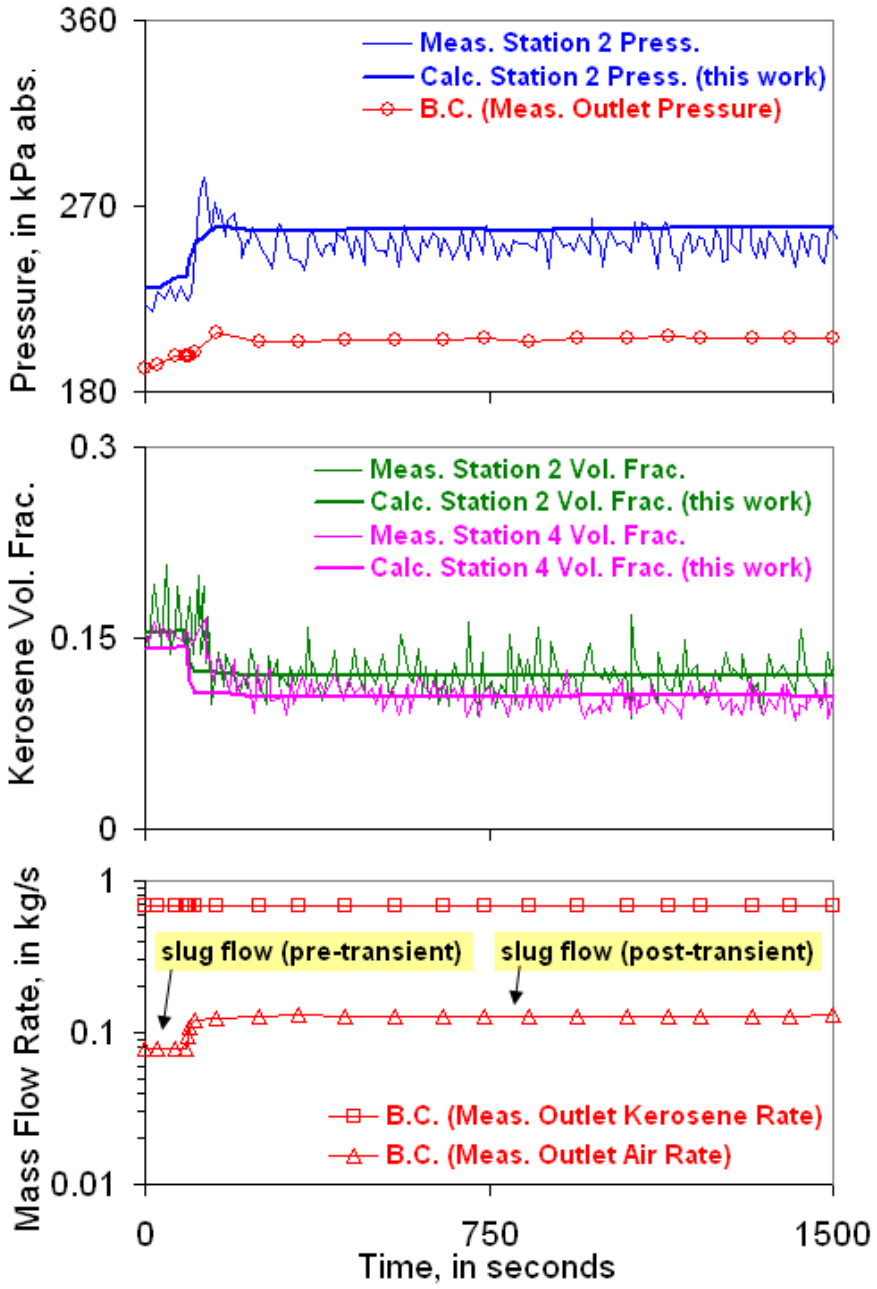

Figure 6.7.4: Prediction of a transient multiphase flow dataset from Minami and Shoham (1994) – run 3 in the reference – using the ANSLIP model for gas volume fraction and the Ishii and Mishima (1982) model for liquid entrainment.

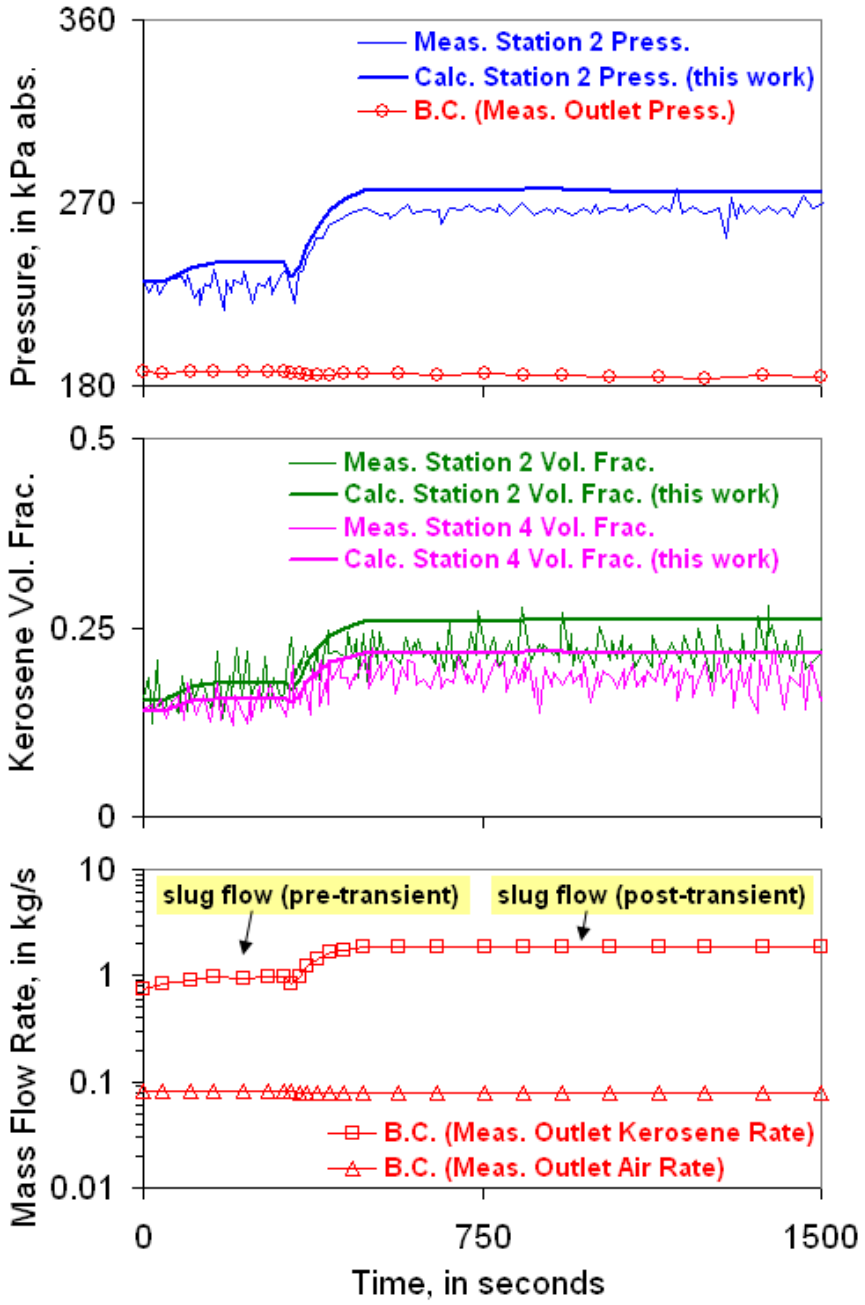

Figure 6.7.5: Prediction of a transient multiphase flow dataset from Minami and Shoham (1994) – run 19 in the reference – using the ANSLIP model for gas volume fraction and the Ishii and Mishima (1982) model for liquid entrainment.

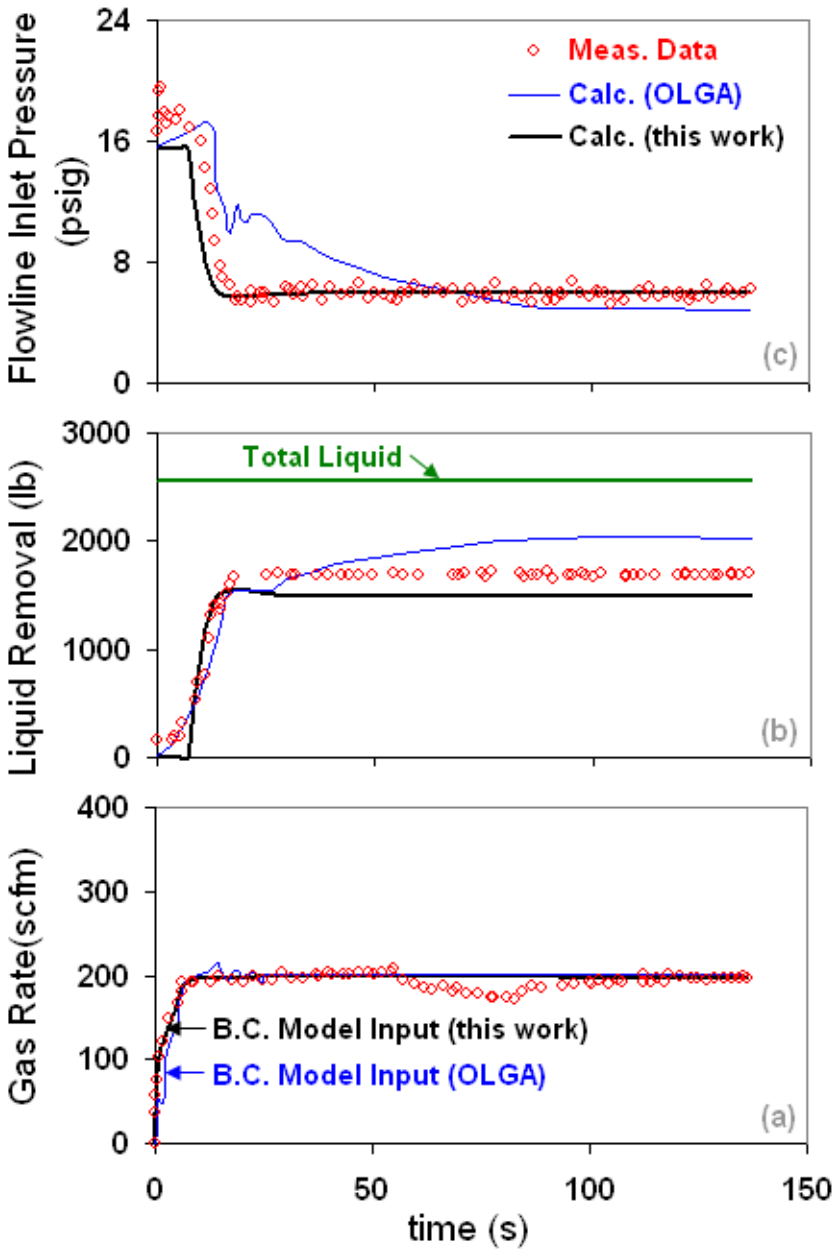

Figure 6.7.6: Prediction of a transient multiphase flow dataset from Zabaras et al. (2013) – low gas injection rate of 200 scfm.

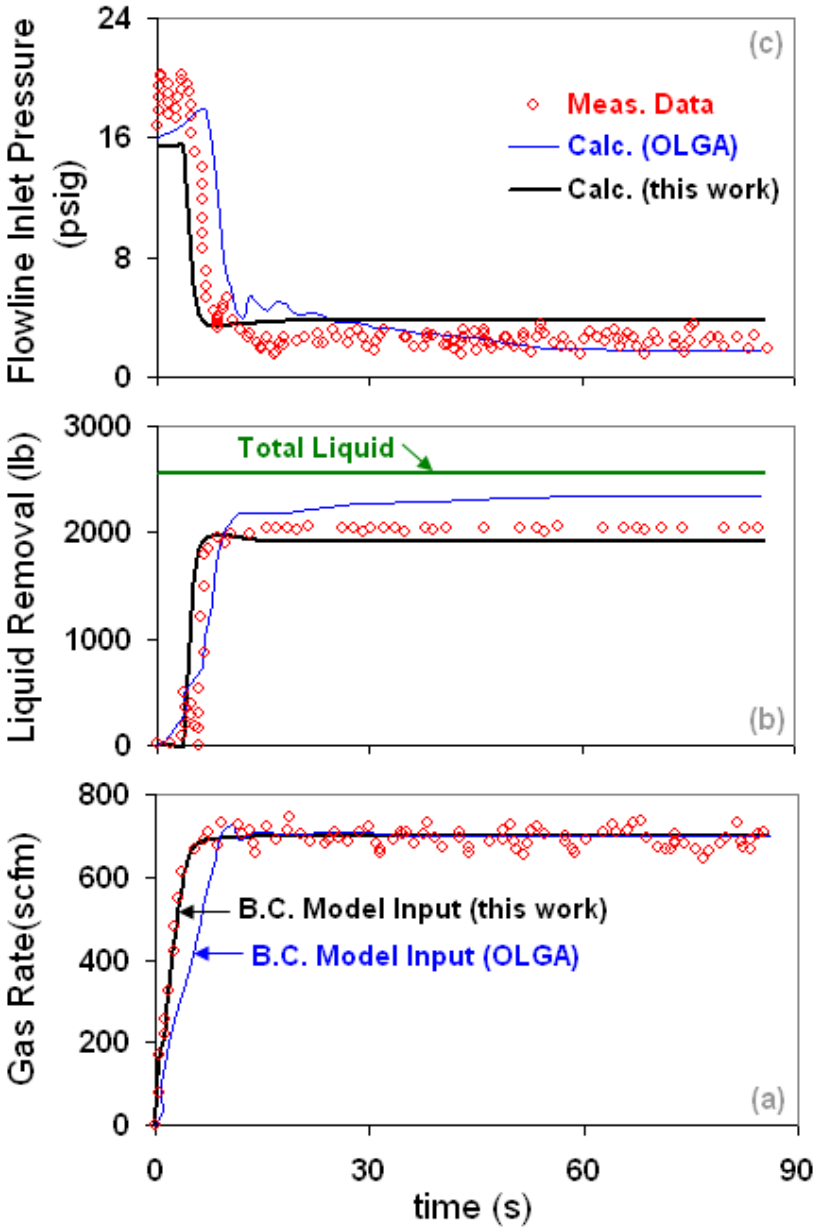

Figure 6.7.7: Prediction of a transient multiphase flow dataset from Zabaras et al. (2013) – high gas injection rate of 700 scfm.

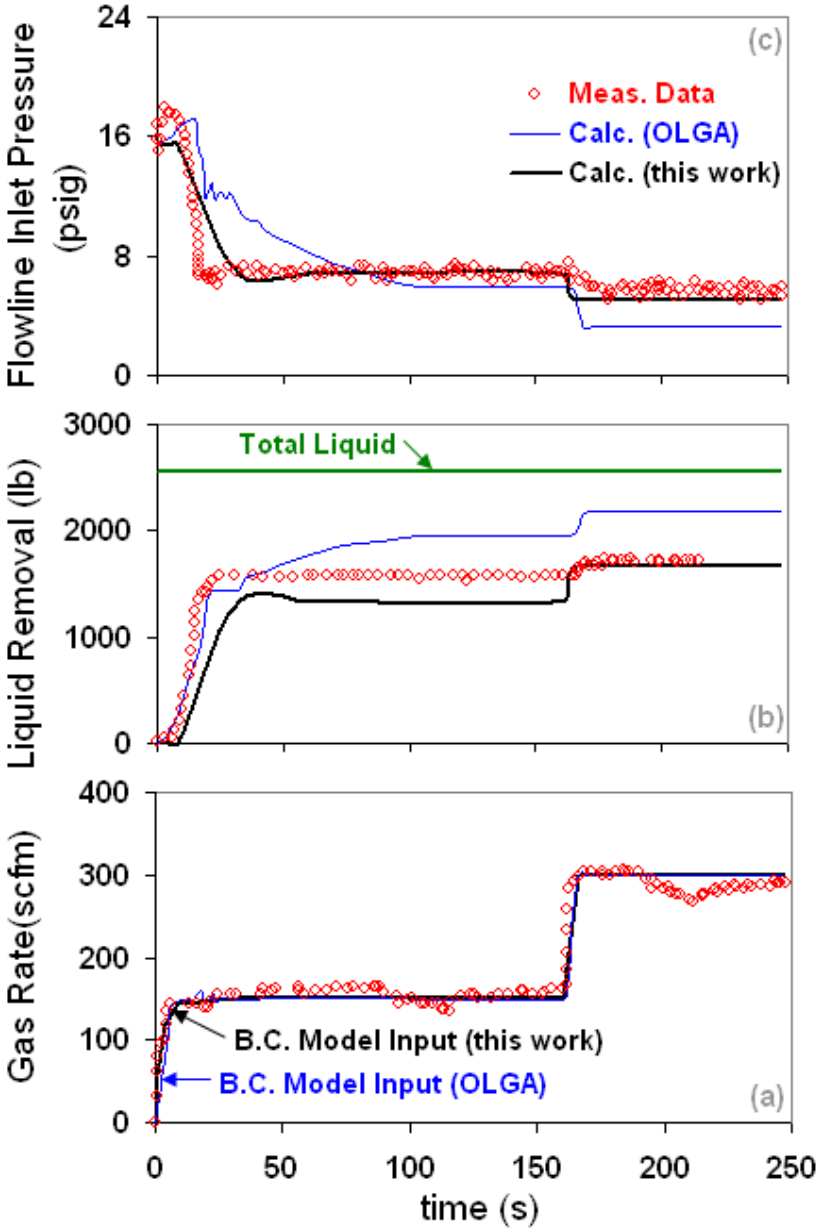

Figure 6.7.8: Prediction of a transient multiphase flow dataset from Zabaras et al. (2013) – gas injection rate ramp-up from 150 to 300 scfm.

Chapter 7 – Specialized Applications: Petroleum and Geothermal Flows

Now that our analytical models have been properly validated with wide ranging datasets and carefully interrogated/falsified with elementary tests (Chapters 3 to 6), applications of our analytical models in industrial scenarios is straightforward. In this chapter, we show the ease with which the Pipe Fractional Flow theory affords a reliably accurate prediction for multiphase pipe flow applications in the petroleum and geothermal industries. Similar to the previous chapters, we will validate our analytical models in applications categorized under the same standardized multiphase flow problem definitions in Table 1.1 in chapter 1.

7.1 Petroleum Engineering Oil-Water-Gas Relations

Before we start applying our analytical models to predict petroleum industry multiphase flows, we briefly discuss a unique feature inherent to this industry in regards to the modeling of complex petroleum fluids – that is – the need to include empirical fluid property correlations (i.e., "modified black oil" correlations or compositional PVT equations of state correlations) for the oleic, aqueous and vapor phases. Additionally, there are empirical mass exchange correlations that must be used to describe the inter-phase component mass exchange behavior between phases, usually as a function of the local pressure, local temperature and reference (surface) densities. These mass exchange correlations, such as the gas-to-oil solubility ratio, R_{so}, the gas-to-water solubility ratio, R_{sw}, or the vaporized oil-to-gas ratio, R_{vo}, will change the in-situ mass flow rates of the phases and thus greatly affect the hydrodynamics of the flow.

Figs. 7.1.1a-i, a-ii, a-iii and b shows the typical behavior of some of these mass exchange and empirical property correlations along the flow of a petroleum fluid through a wellbore from the bottom-hole to the wellhead (Figs. 7.1.1c) transitioning from single-

phase oil with dissolved gas to a two-phase gas-oil system with gas continuously coming out of solution as the pressure decreases. These charts represent the calculations of UTPipeFlow for an actual oil well – "Well 14" in Chierici et al. (1974). As seen, the trends of these correlations changes significantly across the phase transition boundary (i.e., the oil bubble point or gas dew point curves), and thus will change the mass flow rates, densities, viscosities and other properties of the phases in the multiphase flow.

For the remainder of the petroleum applications in this chapter, we state below (and keep constant) the combination of empirical property correlations used in UTPipeFlow when modeling these petroleum systems. These are:

I. The Glaso (1980) bubble point pressure (BPP) and R_{so} correlation.

II. The Ovalle et al. (2007) dew point pressure (DPP) correlation.

III. The El Banbi et al. (2006) R_{vo} correlation.

IV. The Culberson and McKetta Jr. (1951) R_{sw} correlation.

V. The McKetta Jr. and Wehe (1962) corrected-R_{sw} correlation.

VI. The Ahmed (1985) under-saturated oil compressibility correlation.

VII. The McCain et al. (1988) saturated oil compressibility correlation.

VIII. The Glaso (1980) oil formation volume factor (B_o) correlation.

IX. The Meehan (1980) water compressibility correlation.

X. The McCain (1991) water formation volume factor (B_w) correlation.

XI. The Lee et al. (1966) natural gas viscosity correlation.

XII. The Glaso (1980) dead oil viscosity correlation.

XIII. The Beggs and Robinson (1975) live oil viscosity correlation

XIV. The van Wingen (1950) water viscosity correlation.

XV. The Baker and Swerdloff (1955) gas-oil interfacial tension correlation.

XVI. The Hough et al. (1951) gas-water interfacial tension correlation.

In addition to the correlations above, we keep fixed the hydraulic wall roughness at 0.000045 m in our wellbore and pipeline computations, unless stated otherwise. Also, we enforce a linear temperature change from bottom-hole to wellhead and start all calculations from the outlet, unless stated otherwise.

7.2 GEOTHERMAL ENGINEERING STEAM-BRINE RELATIONS

Similar to the petroleum industry, there are specific empirical fluid property correlations that describe the steam-brine behavior found in geothermal wellbores and pipelines. However, a very important difference is that steam and brine flows are a subset of single-component systems, whereas petroleum fluid flows are a subset of multi-component systems. As we will see Section 7.4, we will utilize this fact to demonstrate that wellbore pressure profiles from a wide range of published steam injection and steam production geothermal wells are as a direct result of the wellbore temperature profiles via the saturated steam vapor pressure curves (i.e., the steam tables). This, of course, means that no multiphase pipe flow pressure gradient model is needed for determining the pressure drop in a geothermal well. The saturated vapor pressure curve describes the steam flow in the wellbore above the flash point and a single-phase pipe flow model describes the hot brine pressure gradient below the flash point. As surprising as this finding may first appear, this approach is in alignment with the time-honored problem-solving strategy of good engineering practice – that is – starting from the simplest explanations and testing the extent of their validity.

We also use the minimum, reliable data required to model a geothermal wellbore in UTPipeFlow, namely, the discharge total mass flow rate, the wellhead pressure, the wellhead and bottom-hole temperature and an estimation of the flash depth. In terms of

empirical property correlations, for the geothermal applications in this chapter, we state below (and keep constant) the combination of correlations used in UTPipeFlow when modeling these geothermal systems. These are:

I. The Yaws (1977) saturated steam vapor pressure correlation.

II. The Phillips et al. (1981) compressed brine density correlation.

III. The Meyer et al. (1968) compressed brine viscosity correlation.

IV. The Mercer and Faust (1975) steam density correlation.

V. The Meyer et al. (1968) steam viscosity correlation.

VI. The Wahl (1977) steam-brine interfacial tension correlation.

In addition to the correlations above, we keep fixed the hydraulic wall roughness at 0.000045 m in our geothermal wellbore and pipeline computations, unless stated otherwise. We also start all calculations from the outlet, unless stated otherwise.

7.3 Effect of Flow Rate

In this section, Figs. 7.3.1 – 7.3.3 show UTPipeFlow predictions for the high-rate annulus-produced Cornish (1976) oil wells with the NOSLIP model. Figs. 7.3.4 – 7.3.5 show UTPipeFlow predictions for the high-rate Ekofisk and Forties oil wells in Ashiem (1986) with the NOSLIP model. Figs. 7.3.6 – 7.3.8 show UTPipeFlow predictions for high oil rate Saudi Arabian wells from Al-Muraikhi (1989). Fig. 7.3.9 shows the low oil rate, annulus-produced well 26 in Chierici et al. (1974). It is evident the high accuracy displayed by our analytical models for these high and low rate wells.

7.4 Effect of Properties

With respect to wide changes in fluid properties, Figs. 7.4.1 – 7.4.7 show UTPipeFlow predictions for the heavy oil wells 1 to 8 in Chierici et al. (1974) with the

NOSLIP model. Figs. 7.4.8 – 7.4.10 show UTPipeFlow predictions for the heavy oil wells 3 to 22 in Orkiszewski (1967) with the NOSLIP model. Figs. 7.4.11 and 7.4.12 show UTPipeFlow predictions for the heavy oil wells 1 and 2 in Orkiszewski (1967), respectively, with the WOLGHA model.

7.5 Effect of Mass Change

In this section, we first highlight (in Figs. 7.5.1 – 7.5.33) a wide range of published geothermal wells exhibiting single-component steam-water mass-exchange behavior, and their modeling in UTPipeFlow in accordance with the approach outlined in Section 7.2 above. Although not discussed in this work, we note that geothermal fluids can display a steam and salts-rich brine equilibrium mass exchange behavior that differs somewhat from the saturated steam vapor pressure curves describing steam and pure water equilibrium. In this case, a deviation factor can be applied to the saturated steam vapor pressure curves to account for various steam impurities and brine salts (as discussed in Aunzo et al., 1991).

Next, UTPipeFlow predictions are shown for various two-phase and three-phase non-compositional MIST flow in oil and gas wells in Figs. 7.5.34 – 7.5.40. This is followed by UTPipeFlow predictions for two-phase and three-phase compositional MIST flow in oil and gas wells and pipelines in Figs. 7.5.41 – 7.5.49. Lastly, Fig. 7.5.50 shows UTPipeFlow predictions for the gas-condensate-water compositional flow in the annulus-produced well of Furnival and Baille (1993) with the ANSLIP model, and Figs. 7.5.51 and 7.5.52 show UTPipeFlow predictions for all of the two-phase gas-condensate compositional flow data in the Frigg-to-St. Fergus pipeline as reported in Lagiere et al. (1984) with the ANSLIP model.

7.6 EFFECT OF FLOW PATTERN

To demonstrate that our analytical models implicitly account for any flow pattern via the fractional flow models, we showcase different fractional flow models that accurately predict a wide range of well and pipeline observations.

We first start with the classic two-phase gas-condensate, large-diameter, high gas density dataset that perhaps first led multiphase flow investigators along a path of individual flow pattern model tuning – the Baker (1954) pipeline field tests. Fig. 7.6.1 shows one of those tests – experiment 1 in the reference – being quite accurately predicted with the wholly-analytical ANSLIP model. Fig. 7.6.2 shows all of the field tests in this reference being very accurately predicted with the ANSLIP model. Therefore, the first practical argument for individual flow pattern model tuning (Baker, 1954) is demonstrably countered by our analytical model's ability to very accurately predict all of the observed field data in this seminal, classic reference.

Figs. 7.6.3 – 7.6.10 show more examples of published well data being accurately predicted with the ANSLIP wholly-analytical model. Figs. 7.6.11 – 7.6.22 show UTPipeFlow predictions for various two-phase and three-phase well data with the NOSLIP model. Then, Figs. 7.6.23 – 7.6.28 show UTPipeFlow predictions for wells and pipelines exhibiting MIST flow. This is followed by UTPipeFlow predictions for two-phase and three-phase wells with the BUTTERWORTH model (Figs. 7.6.29 – 7.6.36). Figs. 7.6.37 and 7.6.52 show UTPipeFlow predictions for several published two-phase and three-phase well data with the NICKLIN model. Lastly, Figs. 7.6.53 and 7.6.54 show how combined fractional flow models can accurately explain different wellbore behavior.

7.7 EFFECT OF SIZE

With respect to changes in pipe size, Figs. 7.7.1 – 7.7.8 show UTPipeFlow predictions for the Prudhoe Bay large diameter slug and froth flow pipeline tests of Brill et al. (1981) with the ANSLIP model for upward pipe segments and the BUTTERWORTH model for downward pipe segments. Figs. 7.7.9 – 7.7.11 show UTPipeFlow predictions for the Prudhoe Bay large diameter wells from Ansari (1988) with the NOSLIP model. Figs. 7.4.11 and 7.4.12 show UTPipeFlow predictions for the heavy oil wells 1 and 2 in Orkiszewski (1967), respectively, with the WOLGHA model.

7.8 EFFECT OF INCLINATION

In this section Figs. 7.8.1 and 7.8.2 show UTPipeFlow predictions (with the ANSLIP model) for a deviated low oil rate and deviated high oil rate well of Rai et al. (1989), respectively. Then, Fig. 7.8.3 shows the pressure and gas holdup measurements from a Flow Scanner (www.slb.com/oilfield) production log of a real horizontal well from the Eagleford shale. The oil, water and gas rates are shown on the left side of Fig. 7.8.3. Also shown are the oil bubble point properties at bottom-hole conditions obtained from a PVT lab. The WOLGHA model was used in UTPipeFlow's calculations. Evidently, our analytical models simulate the results from this production log both in terms of the trends in the data as well as accuracy.

7.9 EFFECT OF FLOW DEVELOPMENT

Fig. 7.9.1 shows UTPipeFlow predictions for different datasets from the upward and downward connected-pipe experiments of Payne et al. (1979) with the ANSLIP model for upward pipe segments and the BUTTERWORTH model for downward pipe segments. Then, Figs. 7.9.2 – 7.9.4 show UTPipeFlow predictions for different gas lift runs from the classic reference of Bertuzzi et al. (1953). The fractional flow graphs in

these figures provide a new way to describe and understand the gas-lift process in terms of averaged slip. Fig. 7.9.5 shows the UTPipeFlow predictions for a deep gas lift injection well from Ansari (1988) in which gas is injected at a midway point along a flowing two-phase oil-water well.

7.10 Effect of Shape

Annulus-produced wells are common in petroleum systems and reliable field data from these kinds of flowing wells can be found in several publications. Figs. 7.10.1 – 7.10.7 show UTPipeFlow predictions for low-rate to high-rate annulus-produced oil wells from the literature with the NOSLIP and ANSLIP models.

7.11 Effect of Network

In this section, Figs. 7.11.1 and 7.11.6 show UTPipeFlow predictions for actual large, complex pipeline networks for which there are many elevation changes. Figs. 7.11.7 – 7.11.12 show UTPipeFlow predictions for pipeline networks taken from the American Gas Association (AGA) large-diameter multiphase pipeline flow databank of Greogory (1981) for which there are simplified elevation changes. These simplified networks allow for the testing and easy visualization of the pressure and holdup behavior from pipe segment to pipe segment in these networks.

7.12 Effect of Extreme Condition

As an example of a high-pressure and high-temperature (HPHT) multiphase flow scenario in the petroleum industry, Figs. 7.12.1 – 7.12.2 show UTPipeFlow predictions of all of the deepwater Gulf of Mexico HPHT gas-condensate wells of Sutton and Farshad (1983) with the NOSLIP model.

7.13 Effect of Modeling Method

In this last section, we revisit several previously analyzed datasets in Sections 7.3 to 7.12 and compare their predictions with different models, research codes and currently available industry codes. From the comparisons of UTPipeFlow's predictions benchmarked against other models with named, published (unbiased) data as identical input into them, it is evident that our analytical models are significantly more accurate than the other models selected. Furthermore, UTPipeFlow consistently captures the trends in the data.

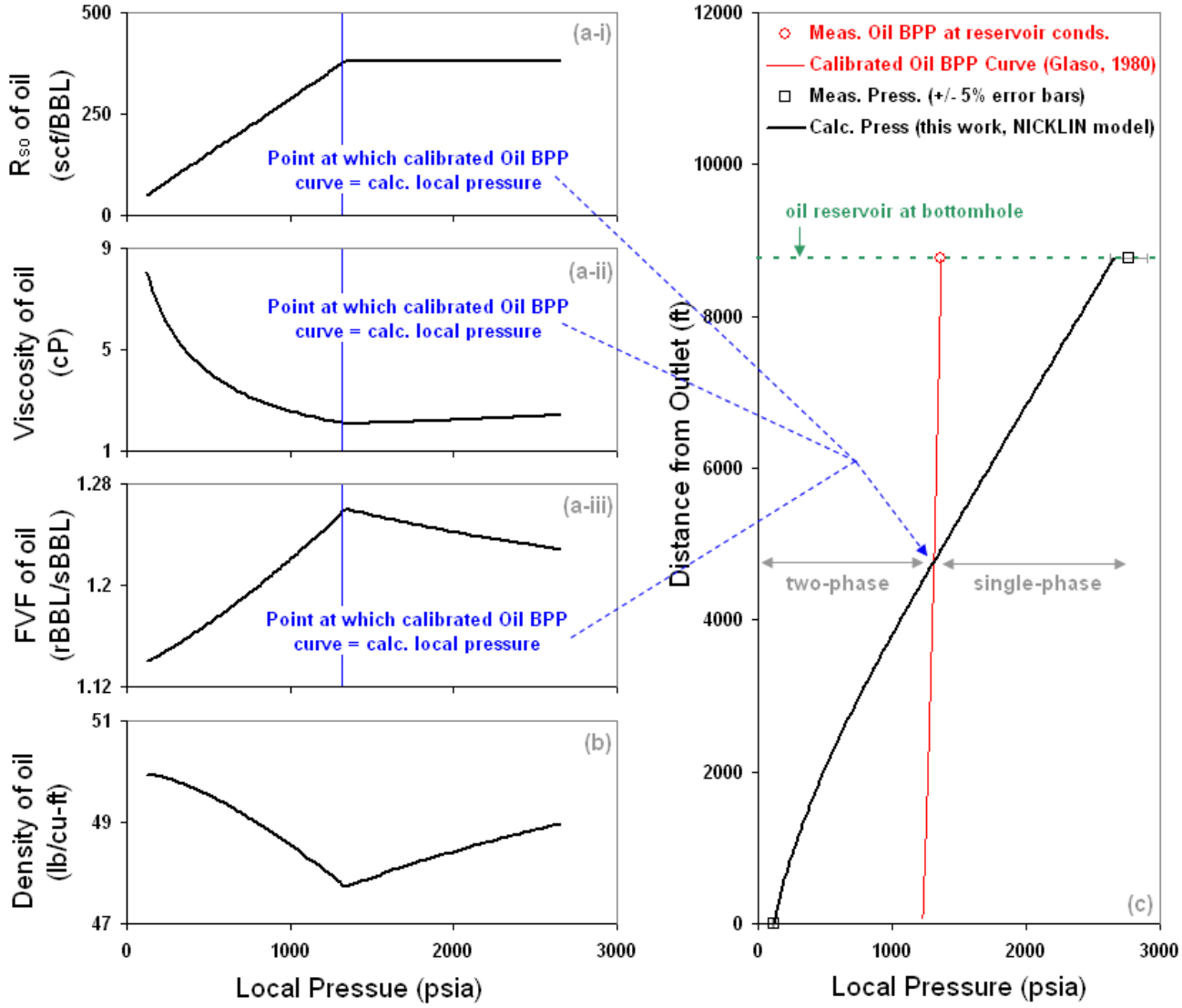

Figure 7.1.1: Demonstration of the changes in fluid properties for well 14 of Chierici et al. (1974).

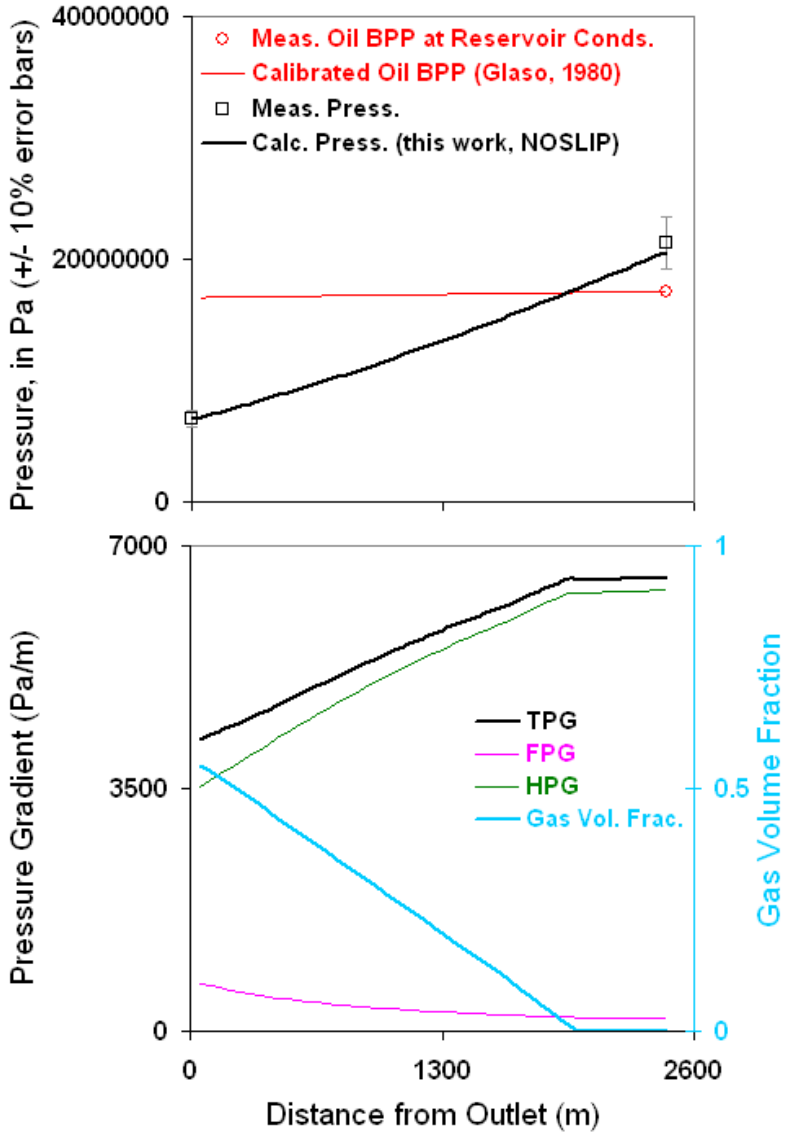

Figure 7.3.1: The high oil rate, annulus-produced well 1 in Cornish (1976).

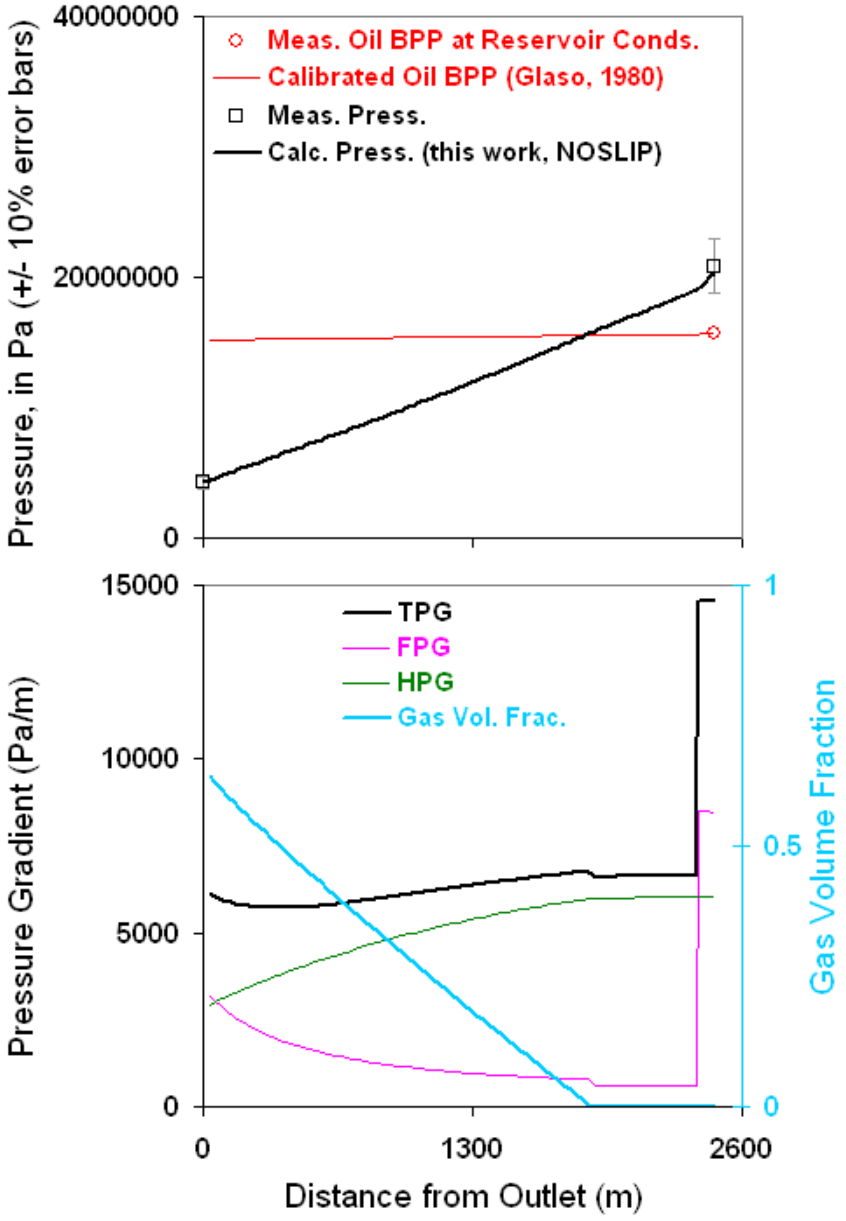

Figure 7.3.2: The high oil rate, annulus-produced well 11 in Cornish (1976).

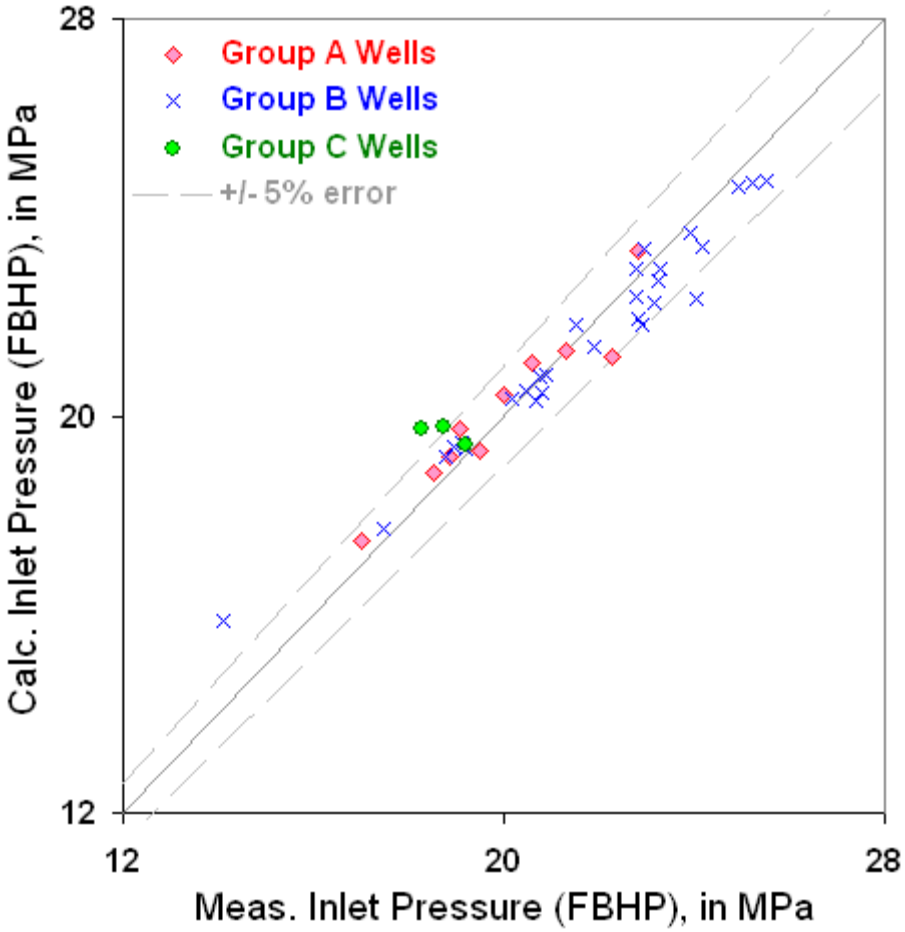

Figure 7.3.3: All of Cornish (1976) high oil rate wells accurately predicted with the wholly-analytical NOSLIP model.

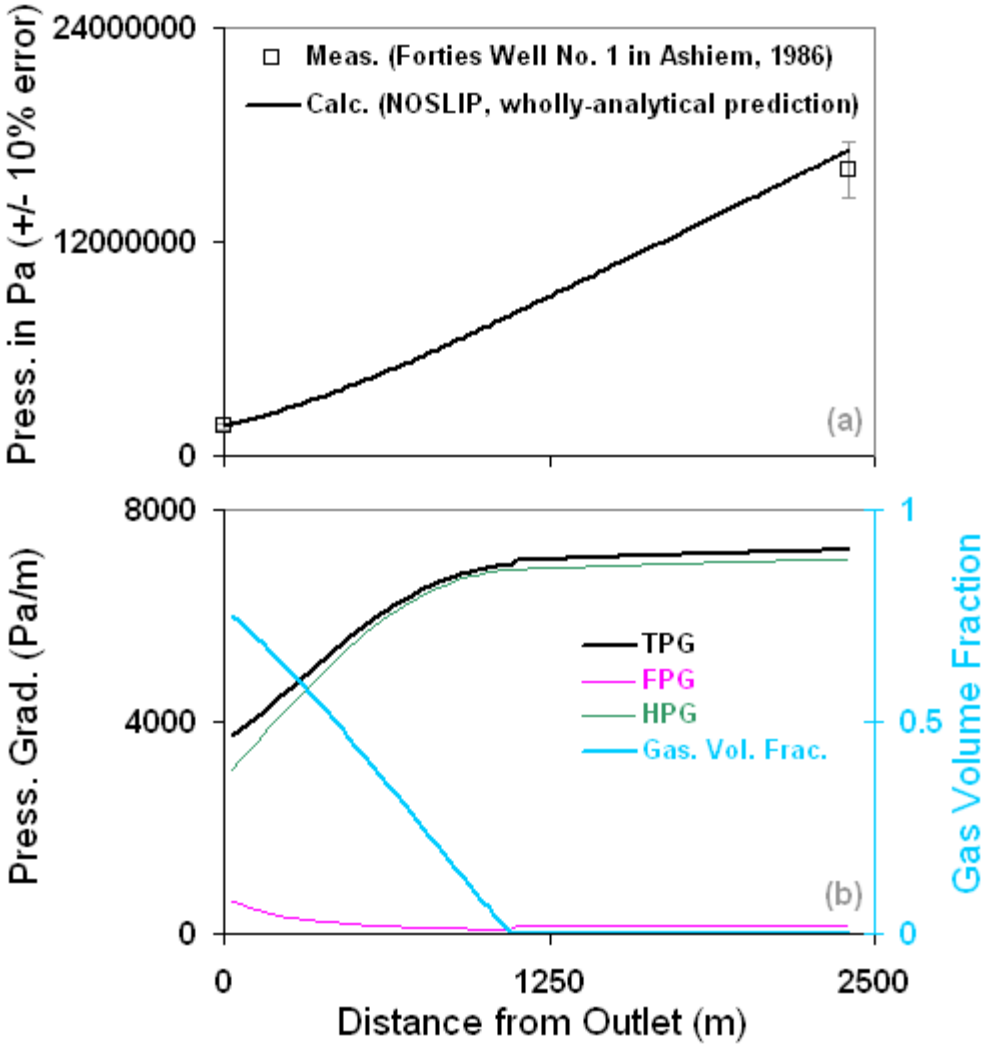

Figure 7.3.4: An example Forties high oil rate well accurately predicted with the NOSLIP wholly-analytical model.

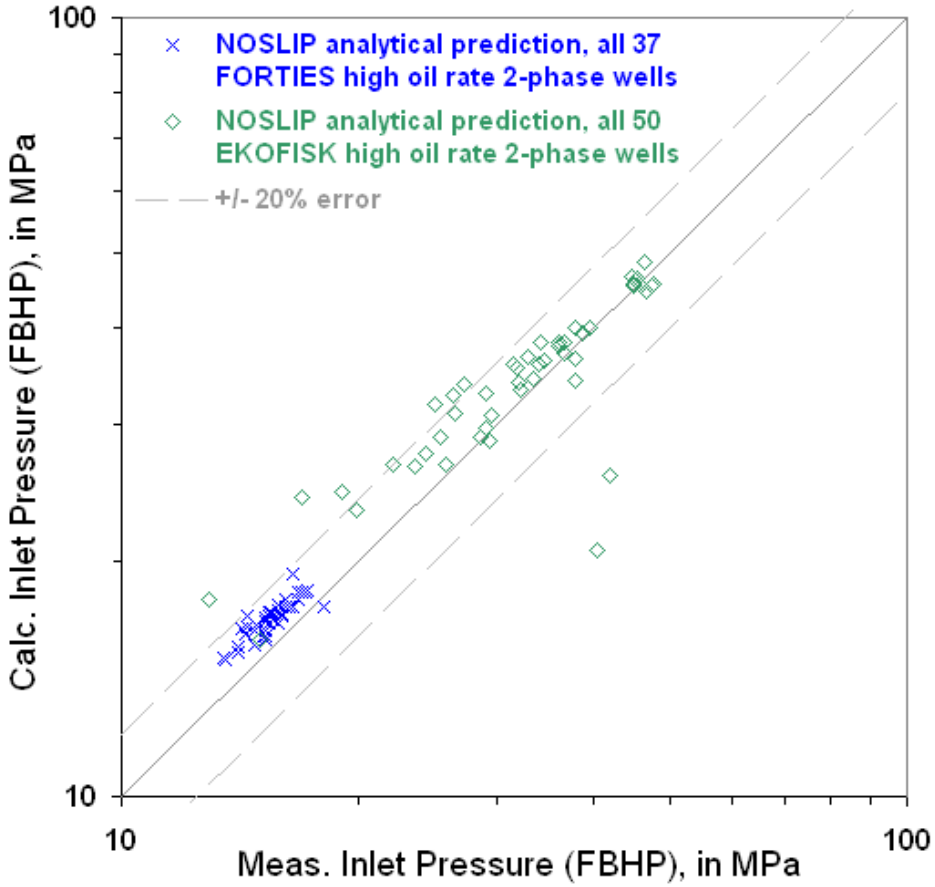

Figure 7.3.5: All of the high oil rate wells of Ashiem (1986) accurately predicted with the NOSLIP analytical model.

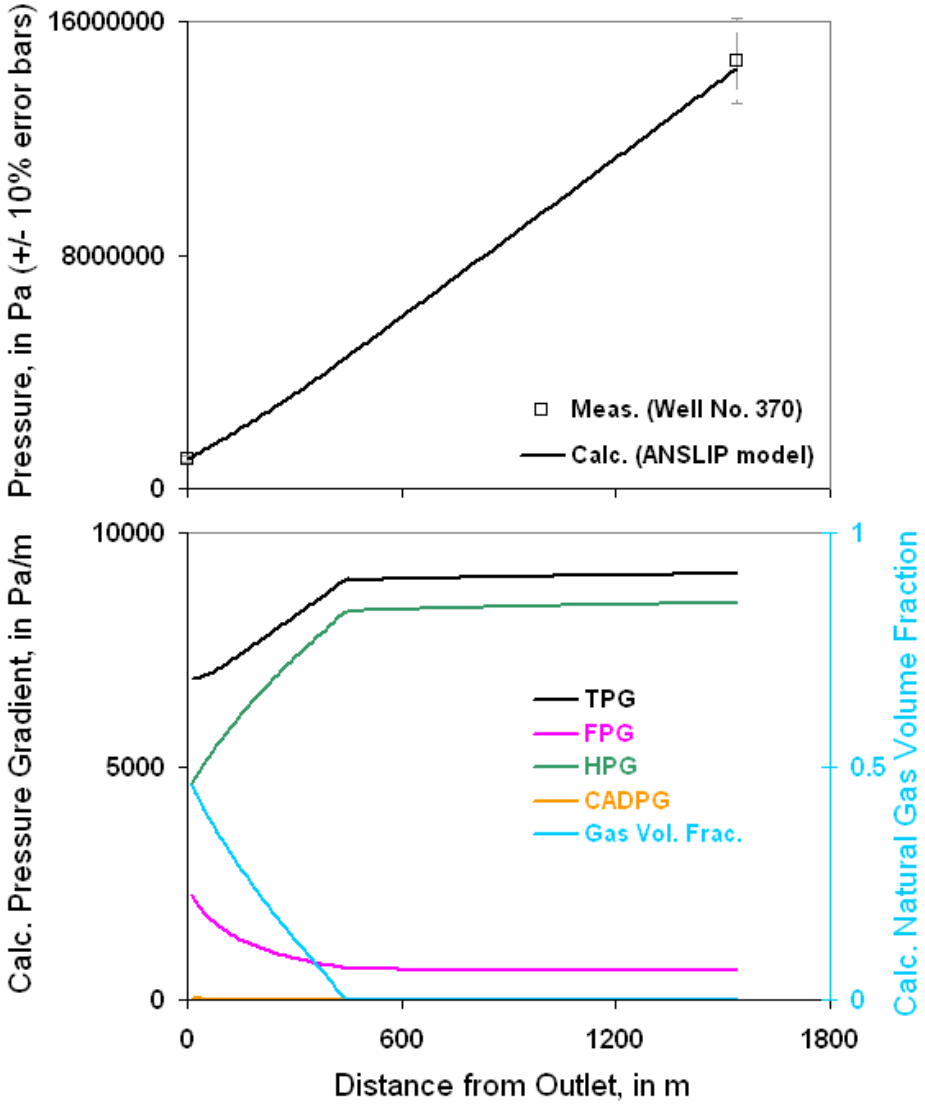

Figure 7.3.6: An example high oil rate and low GOR Saudi Arabian well from Al-Muraikhi (1989).

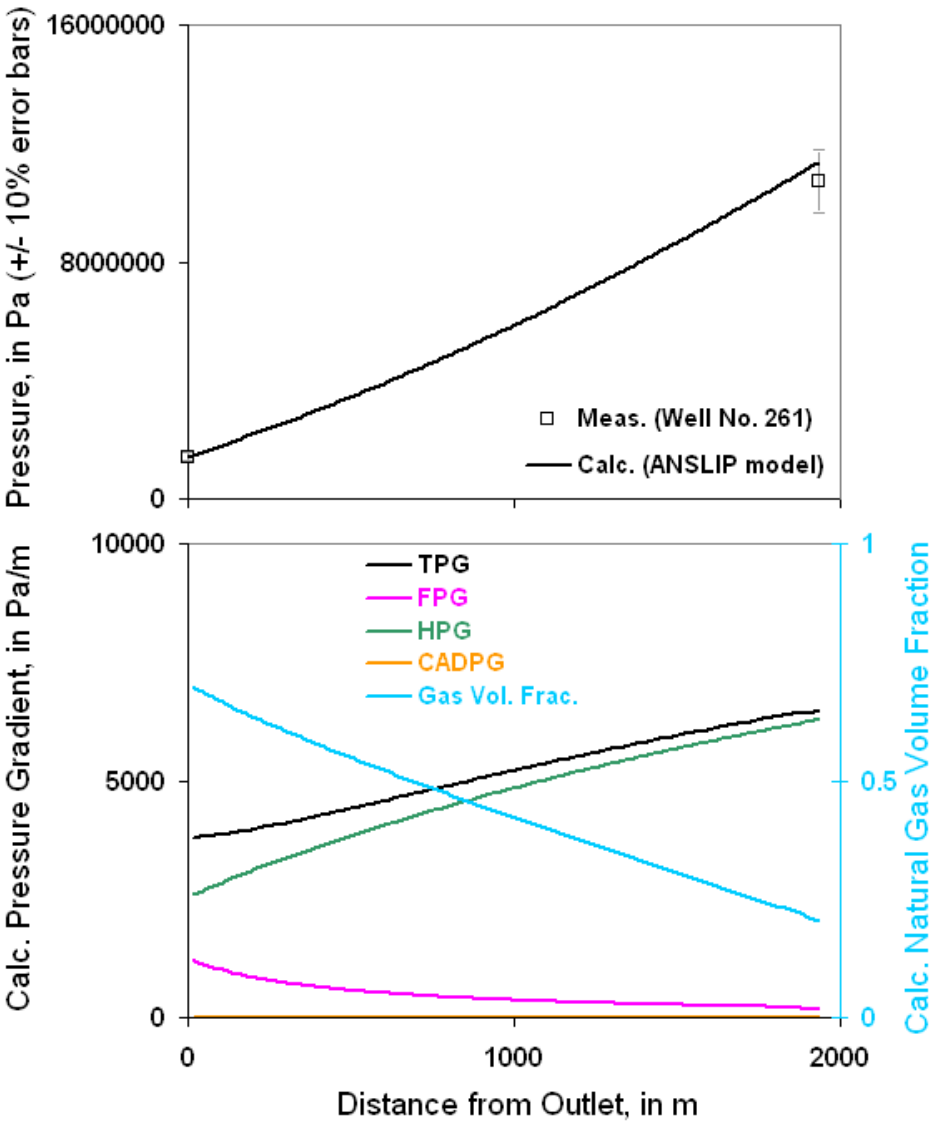

Figure 7.3.7: An example high liquids rate, low water-cut (14%), three-phase Saudi Arabian well from Al-Muraikhi (1989).

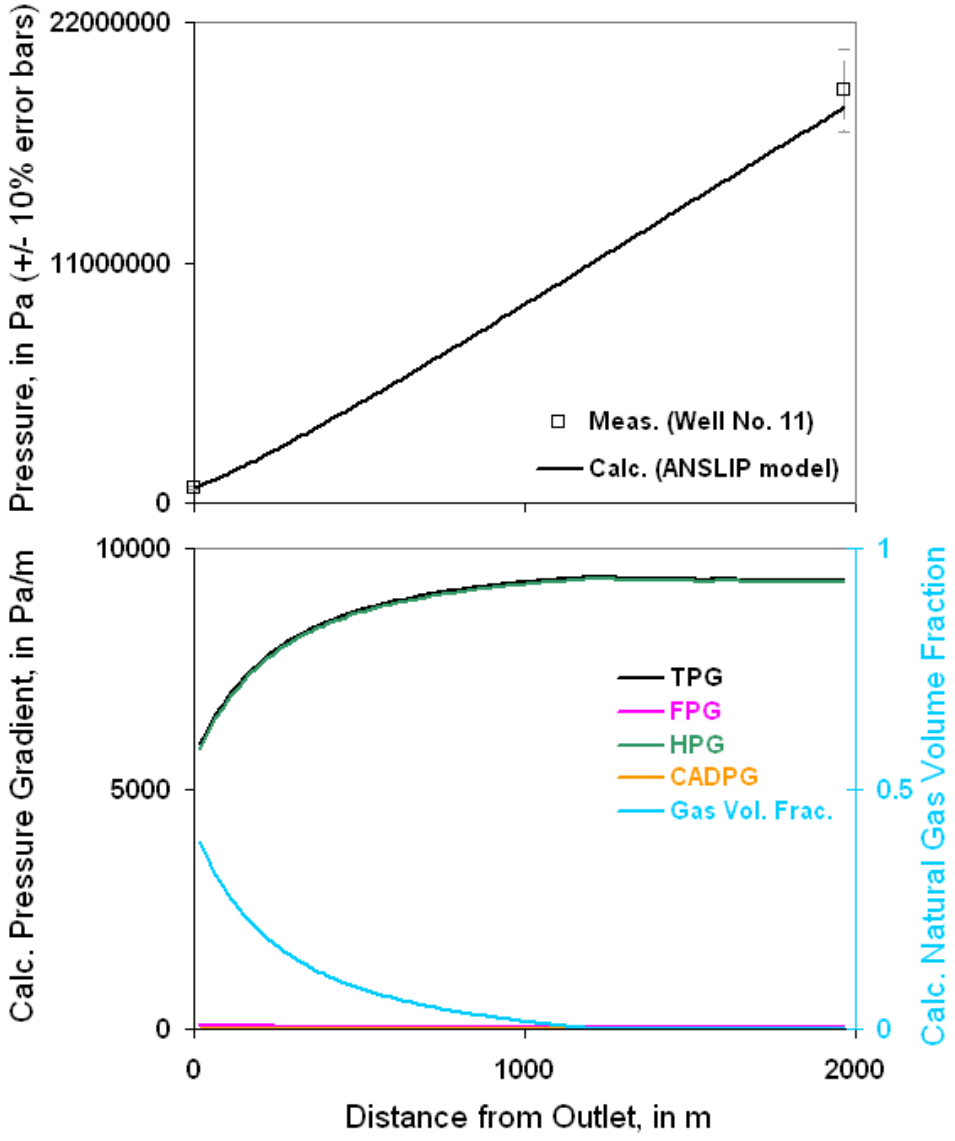

Figure 7.3.8: An example low liquids rate, high water-cut (92%), three-phase Saudi Arabian well from Al-Muraikhi (1989).

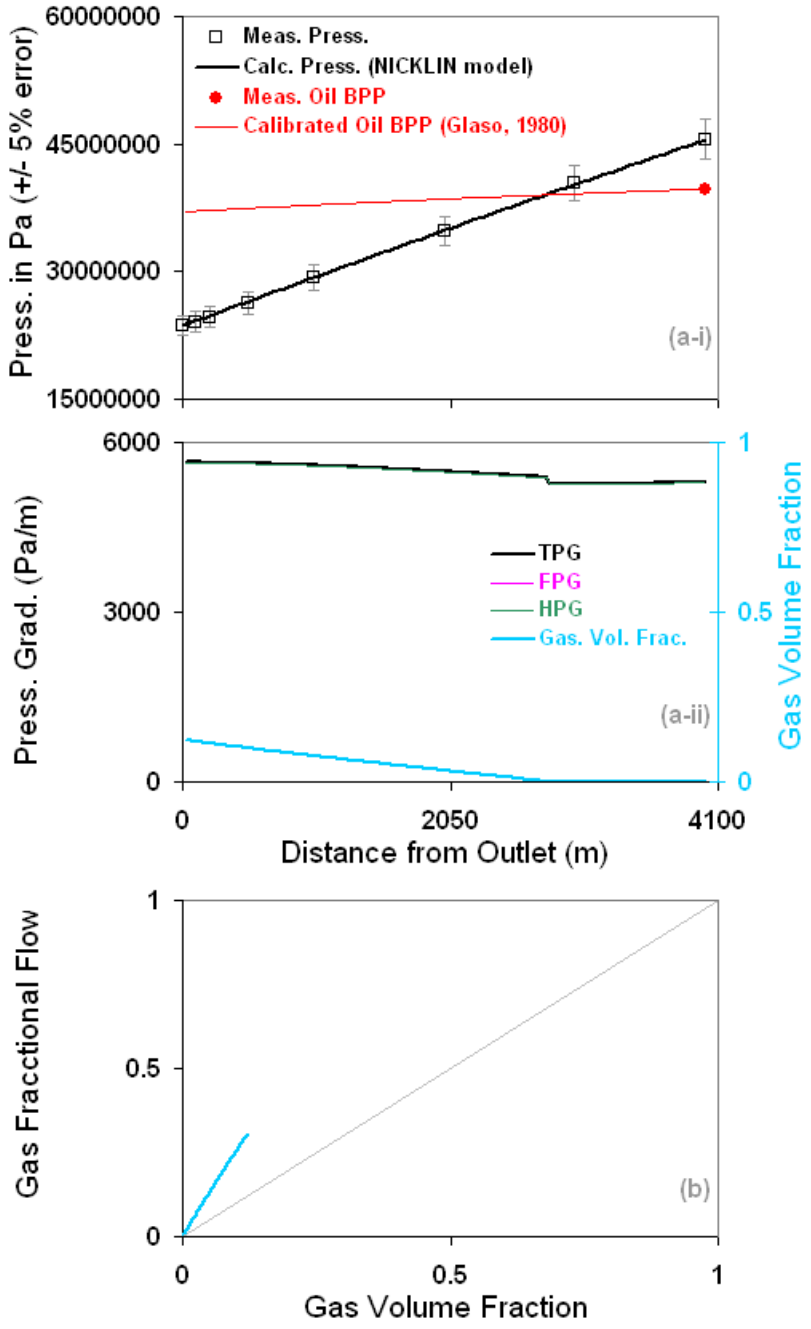

Figure 7.3.9: A low rate, annulus-produced well 26 in Chierici et al. (1974).

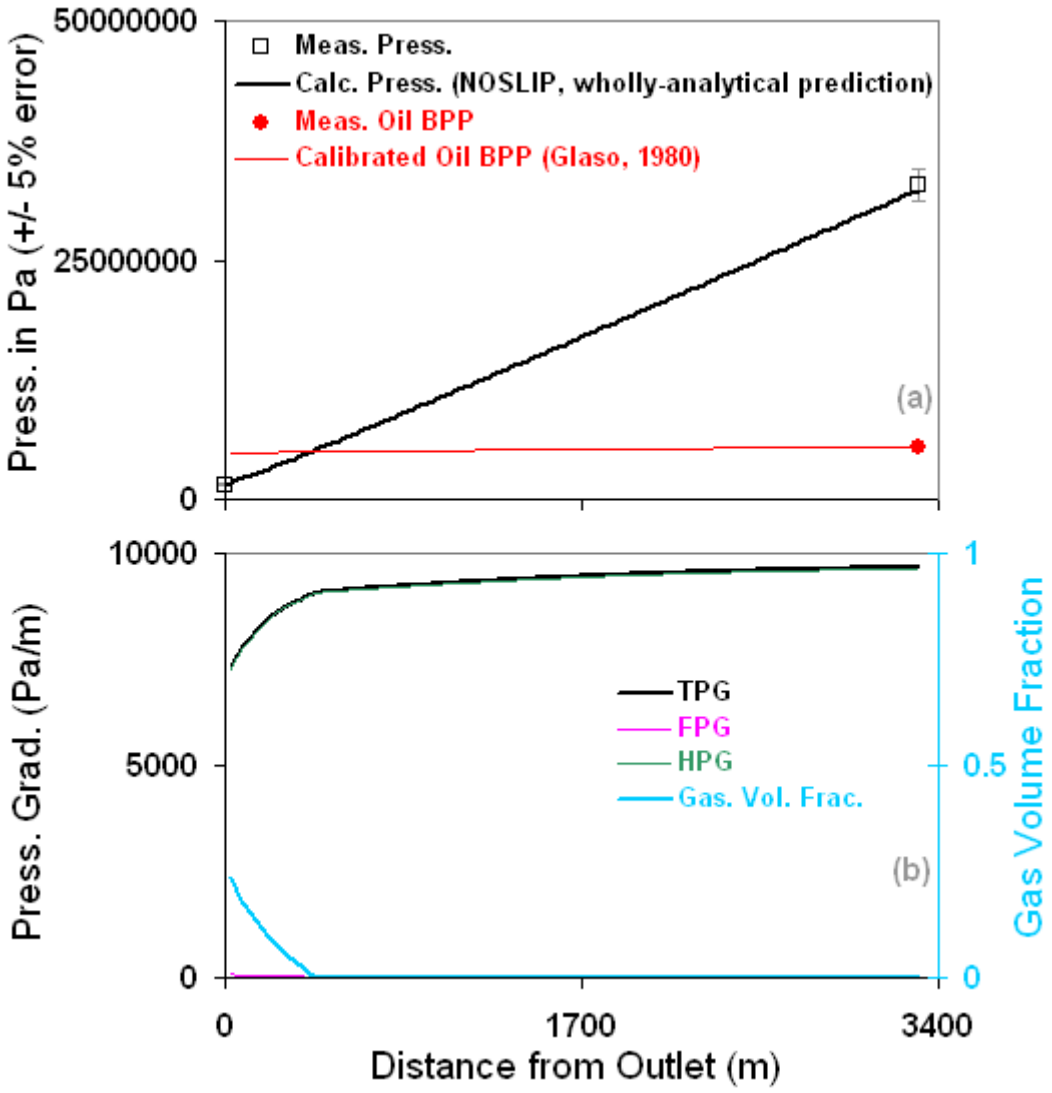

Figure 7.4.1: A heavy oil well – well 1 in Chierici et al. (1974).

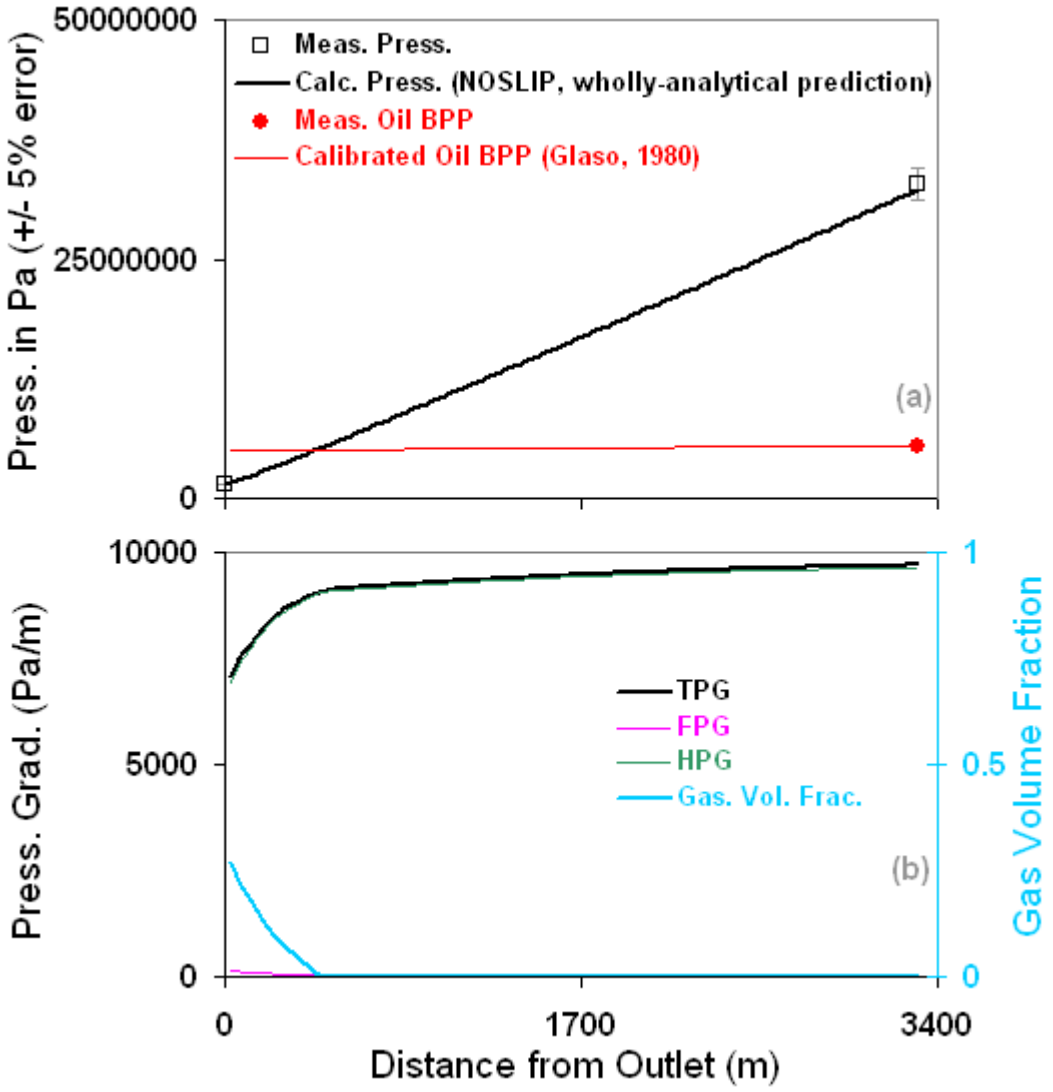

Figure 7.4.2: A heavy oil well – well 2 in Chierici et al. (1974).

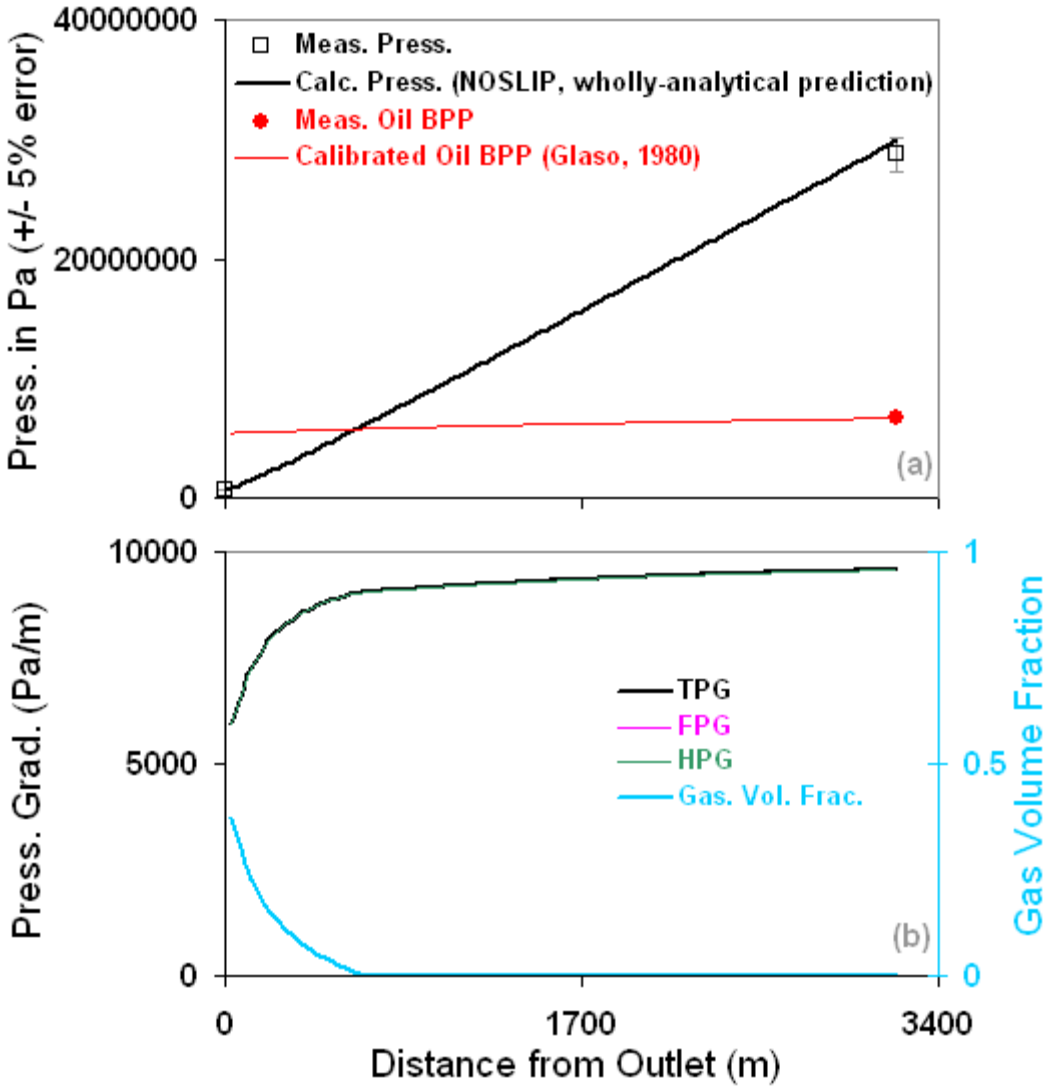

Figure 7.4.3: A heavy oil well – well 3 in Chierici et al. (1974).

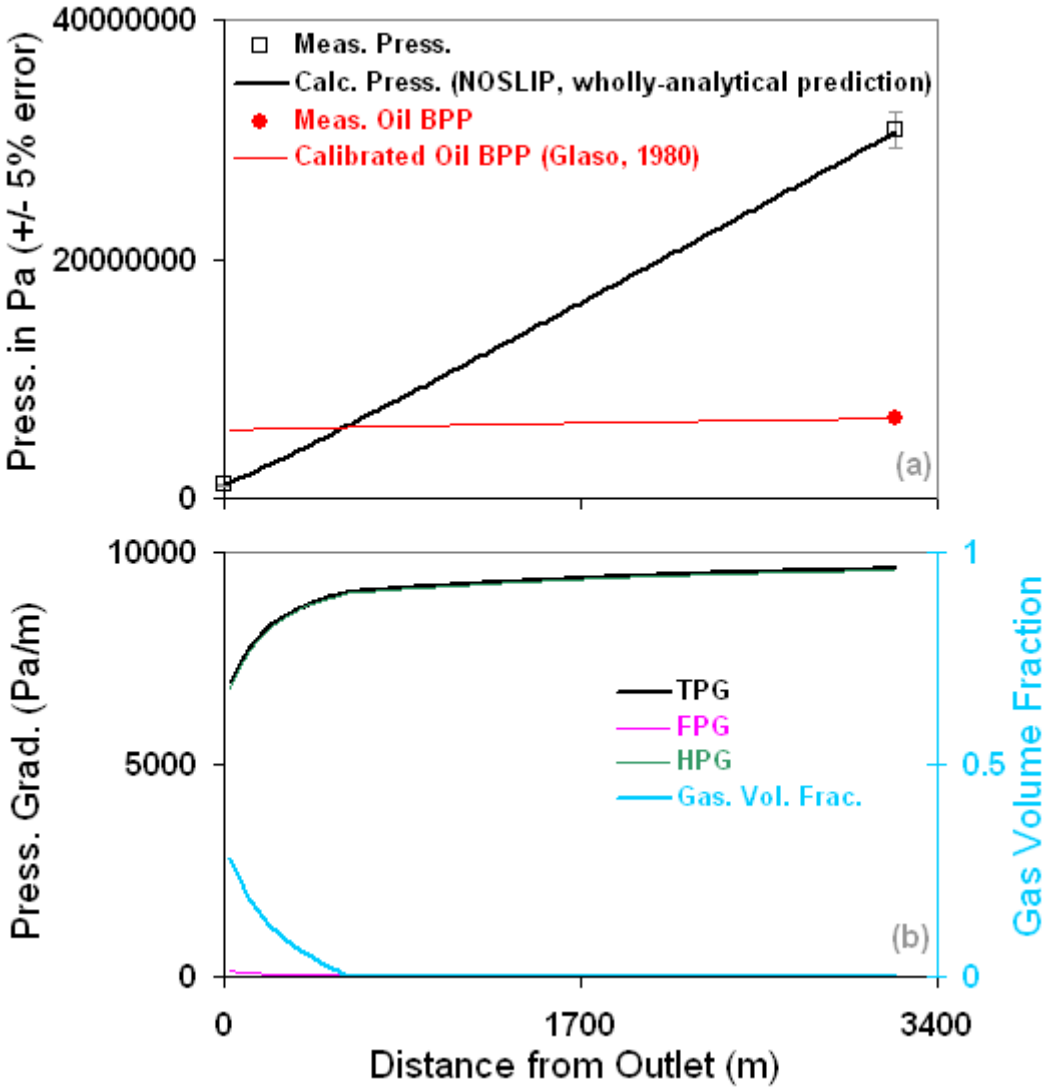

Figure 7.4.4: A heavy oil well – well 3 in Chierici et al. (1974).

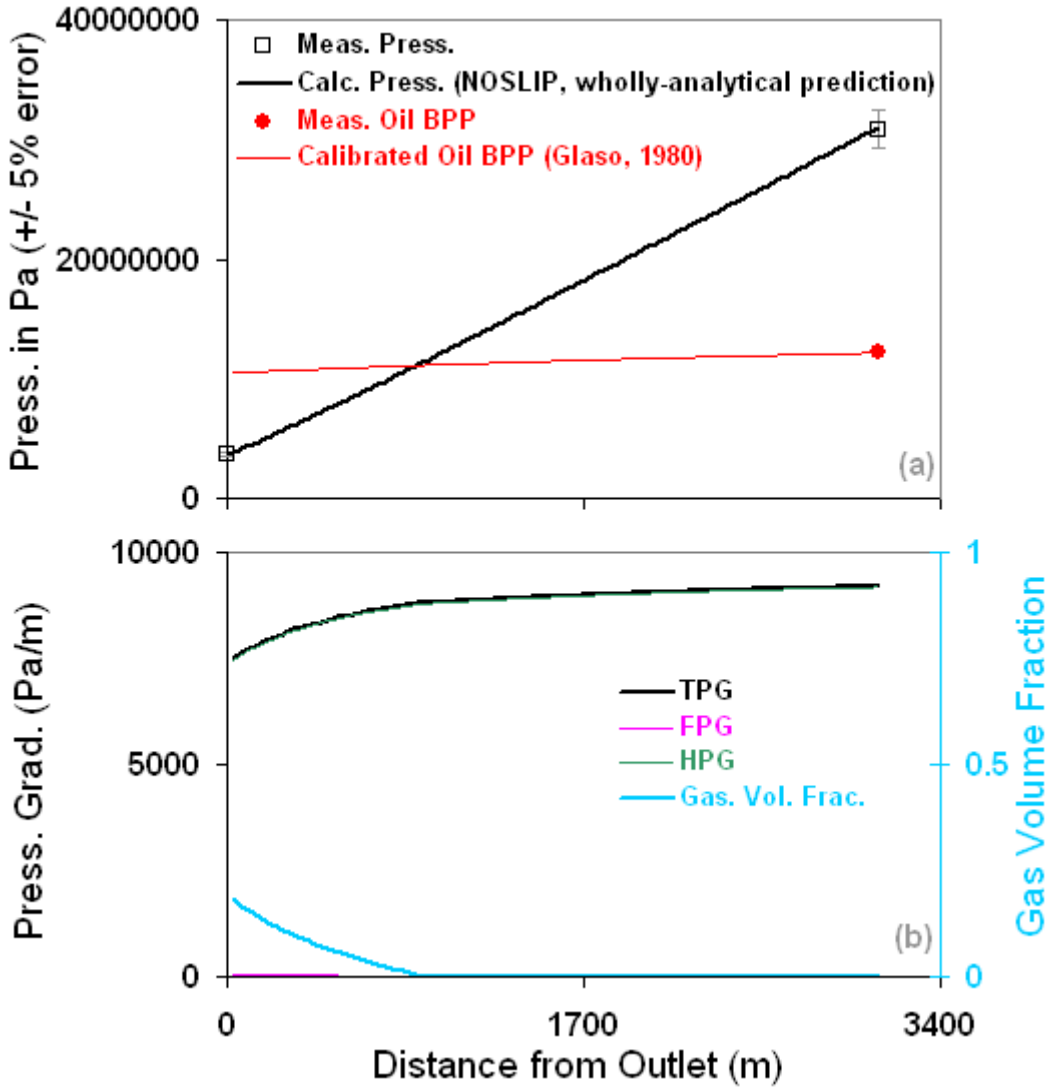

Figure 7.4.5: A heavy oil well – well 6 in Chierici et al. (1974).

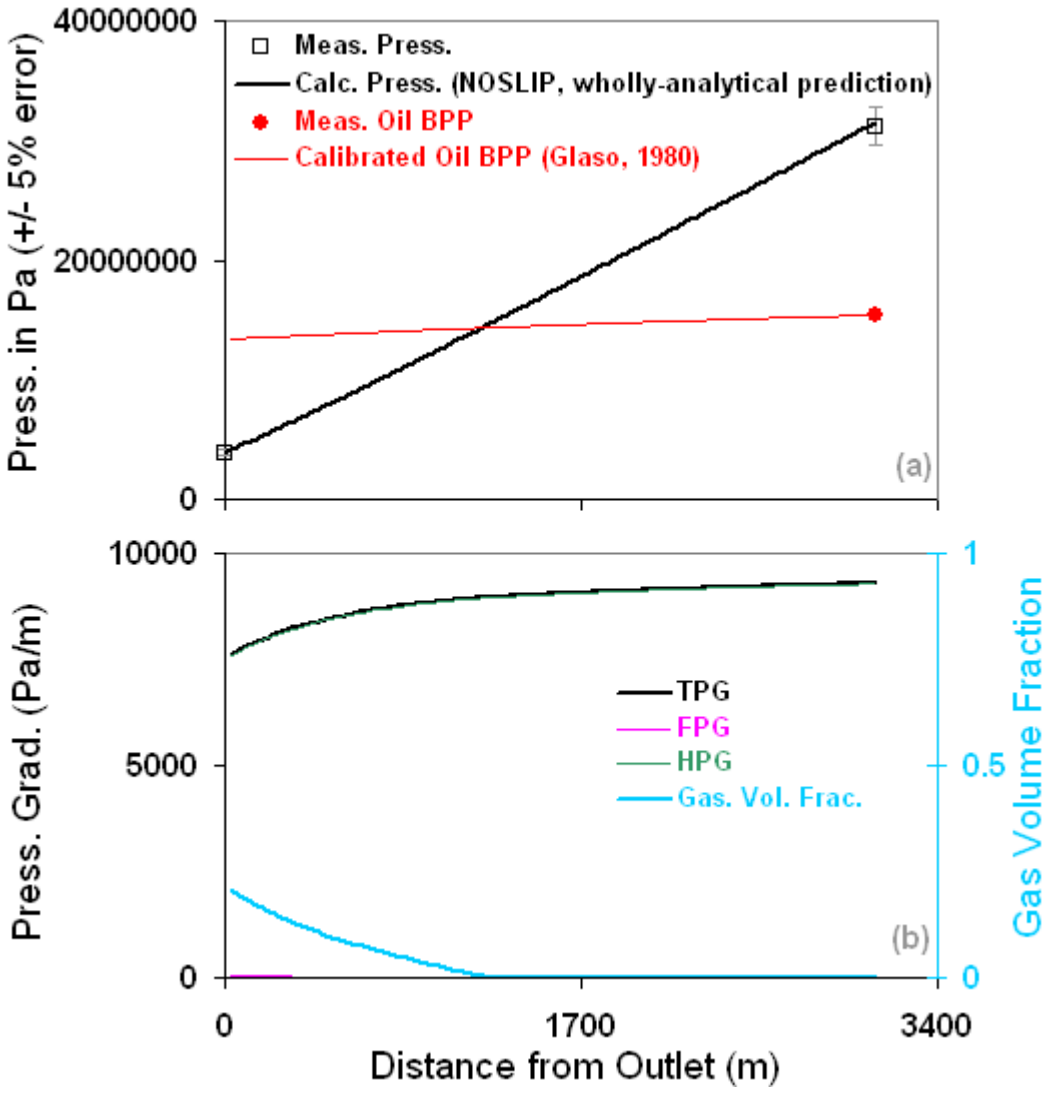

Figure 7.4.6: A heavy oil well – well 7 in Chierici et al. (1974).

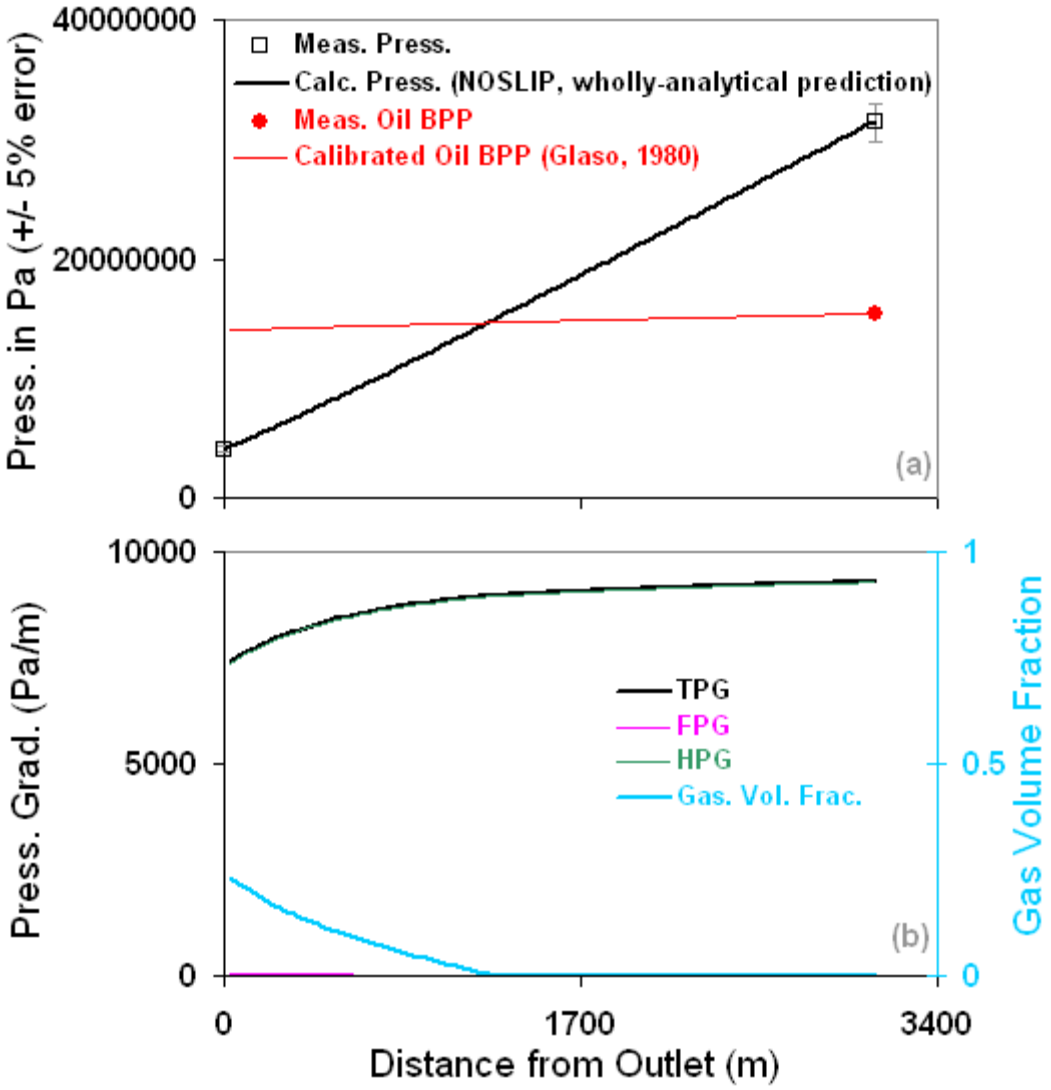

Figure 7.4.7: A heavy oil well – well 8 in Chierici et al. (1974).

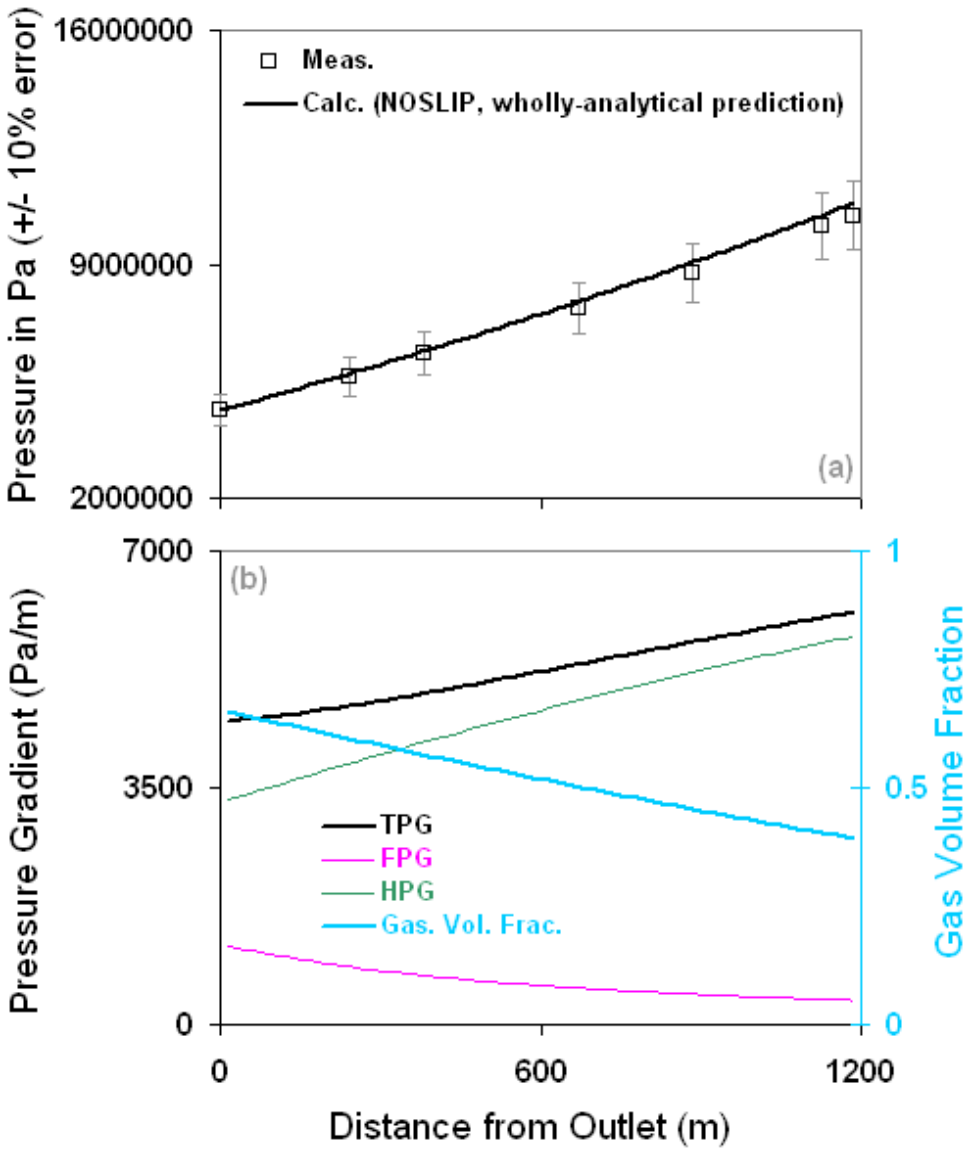

Figure 7.4.8: A heavy oil well – well 22 in Orkizsewski (1967).

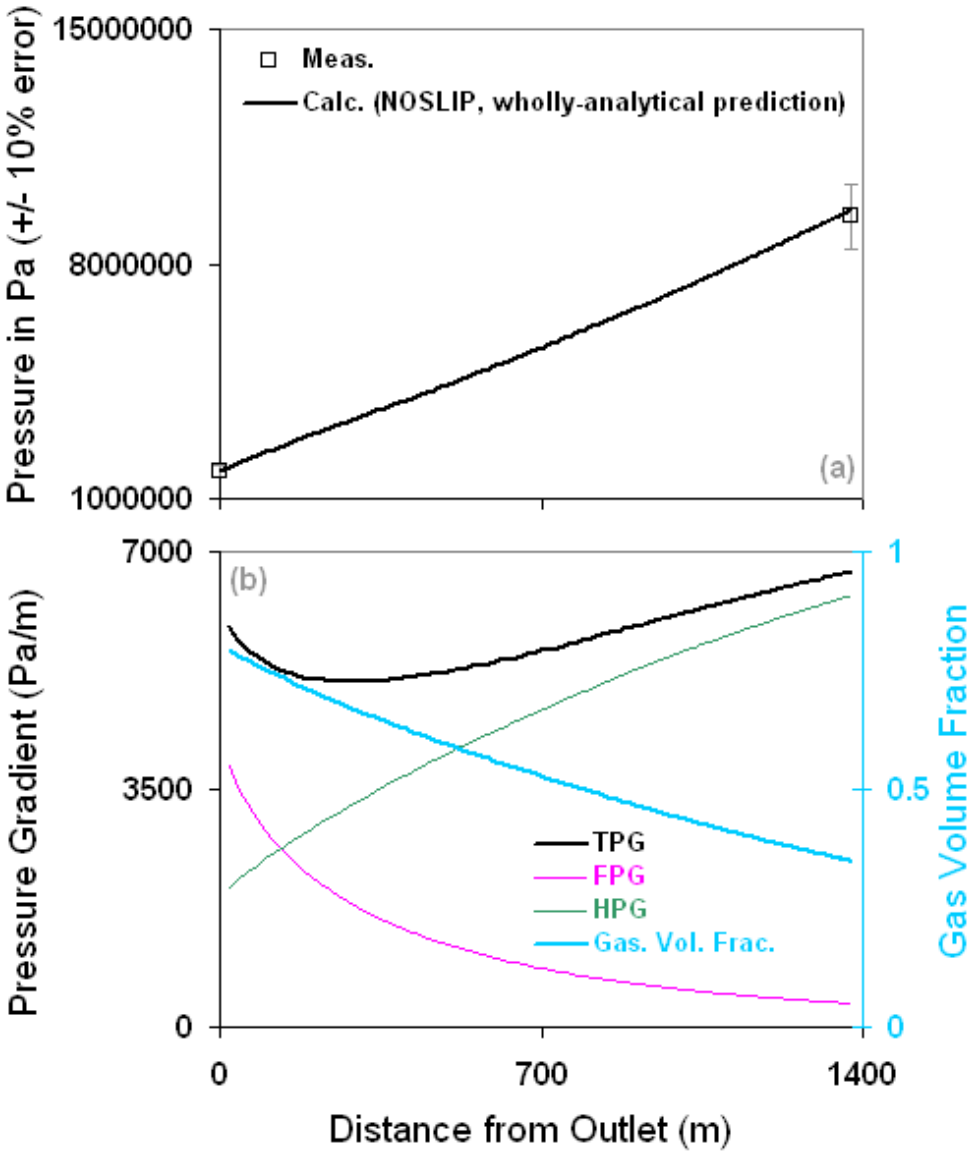

Figure 7.4.9: A heavy oil well – well 20 in Orkizsewski (1967).

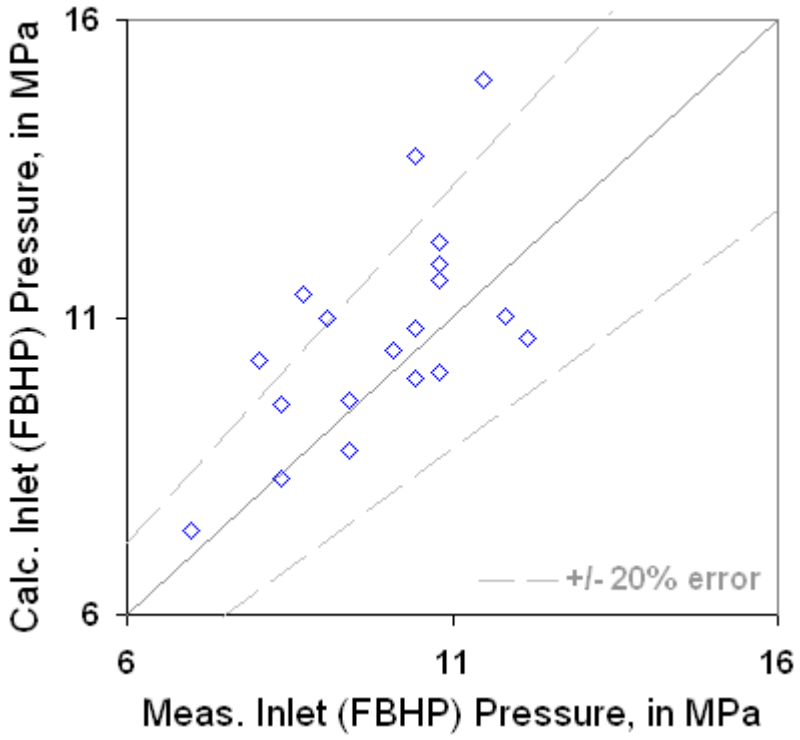

Figure 7.4.10: Prediction of Orkizsewski (1967) heavy oil wells with the wholly-analytical NOSLIP model.

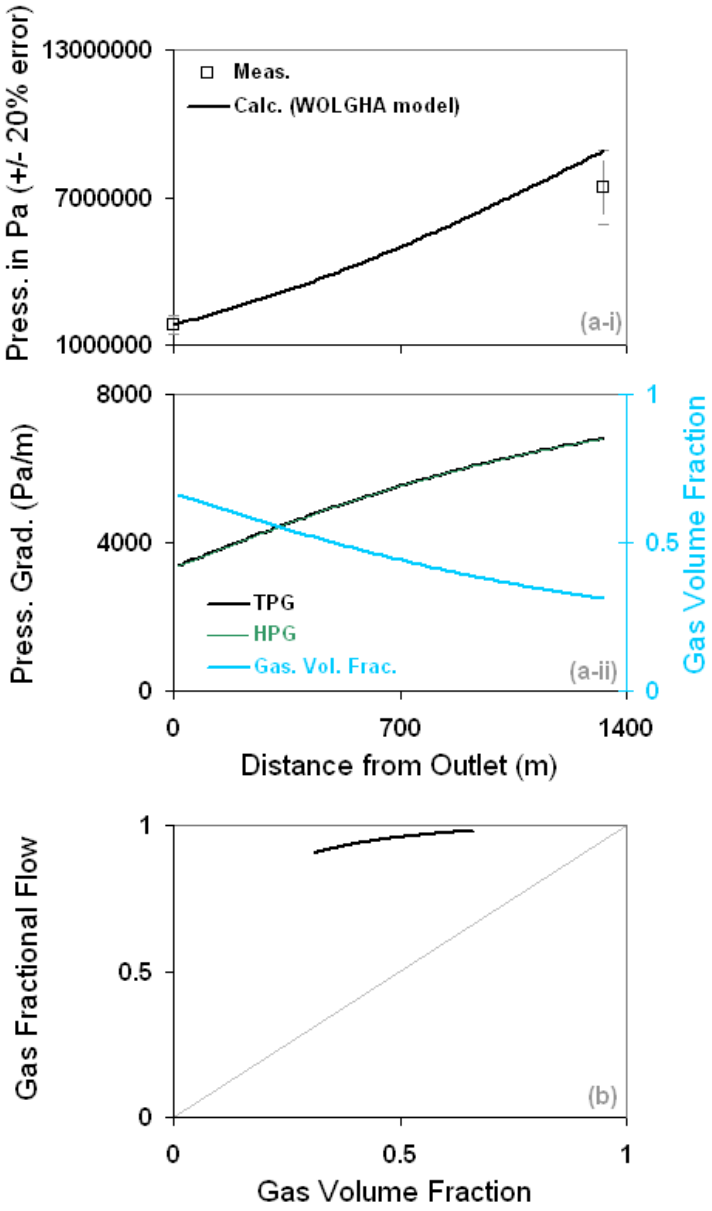

Figure 7.4.11: A heavy oil well predicted with the WOLGHA model – well 1 in Orkizsewski (1967). This is an example of one of the omitted wells in Table 2 of Ansari (1988).

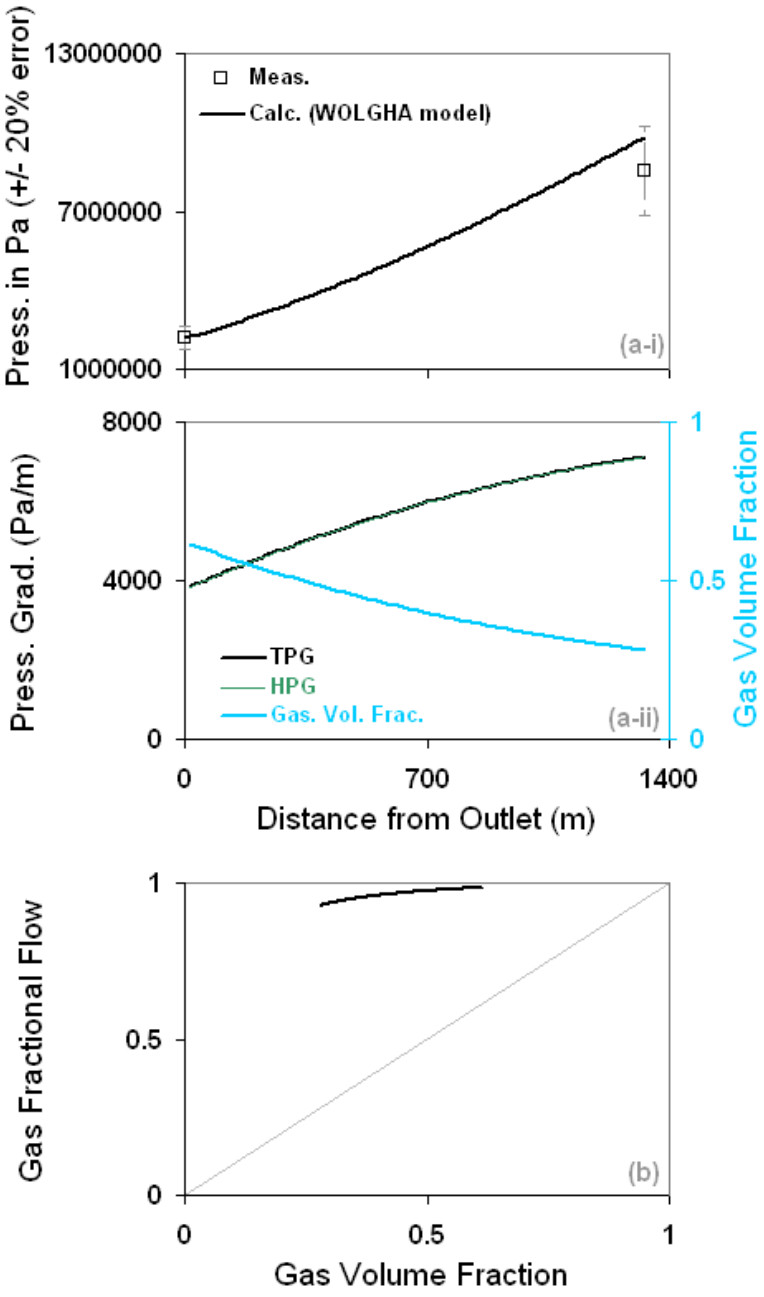

Figure 7.4.12: A heavy oil well predicted with the WOLGHA model – well 2 in Orkizsewski (1967). This is an example of another well in Table 2 of Ansari (1988).

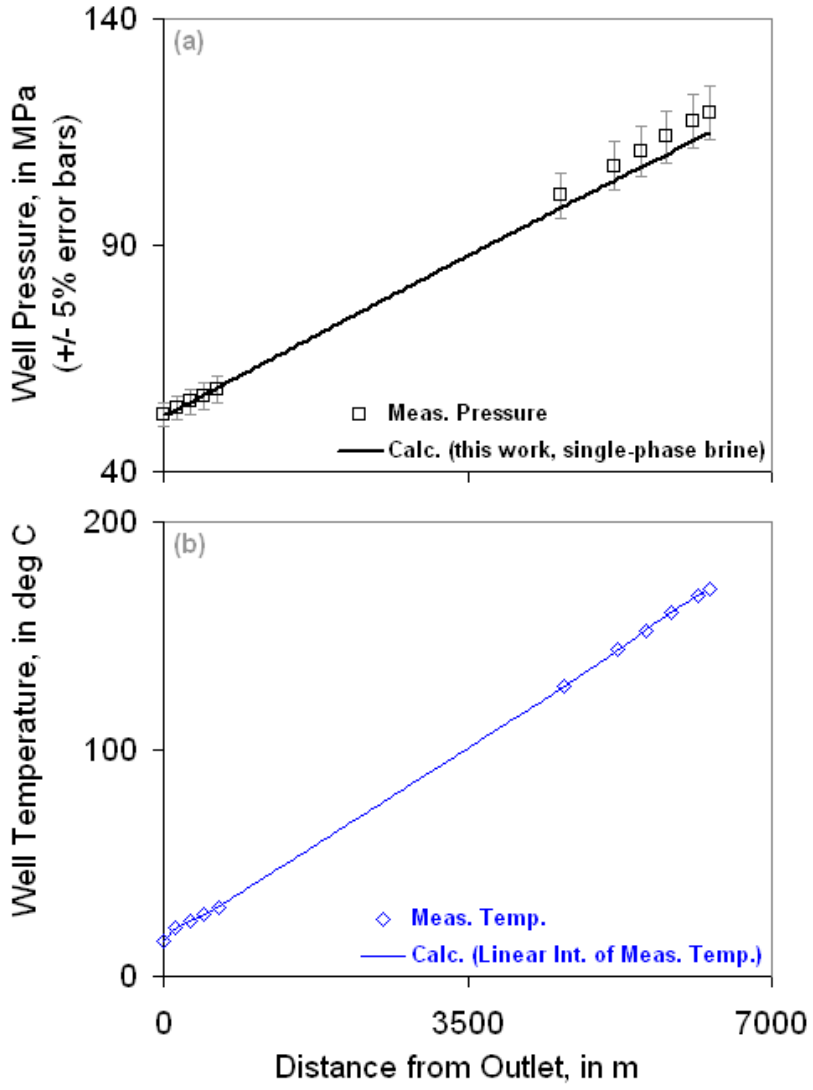

Figure 7.5.1: Single-phase brine Willi-Huton geothermal well of Riney (1991).

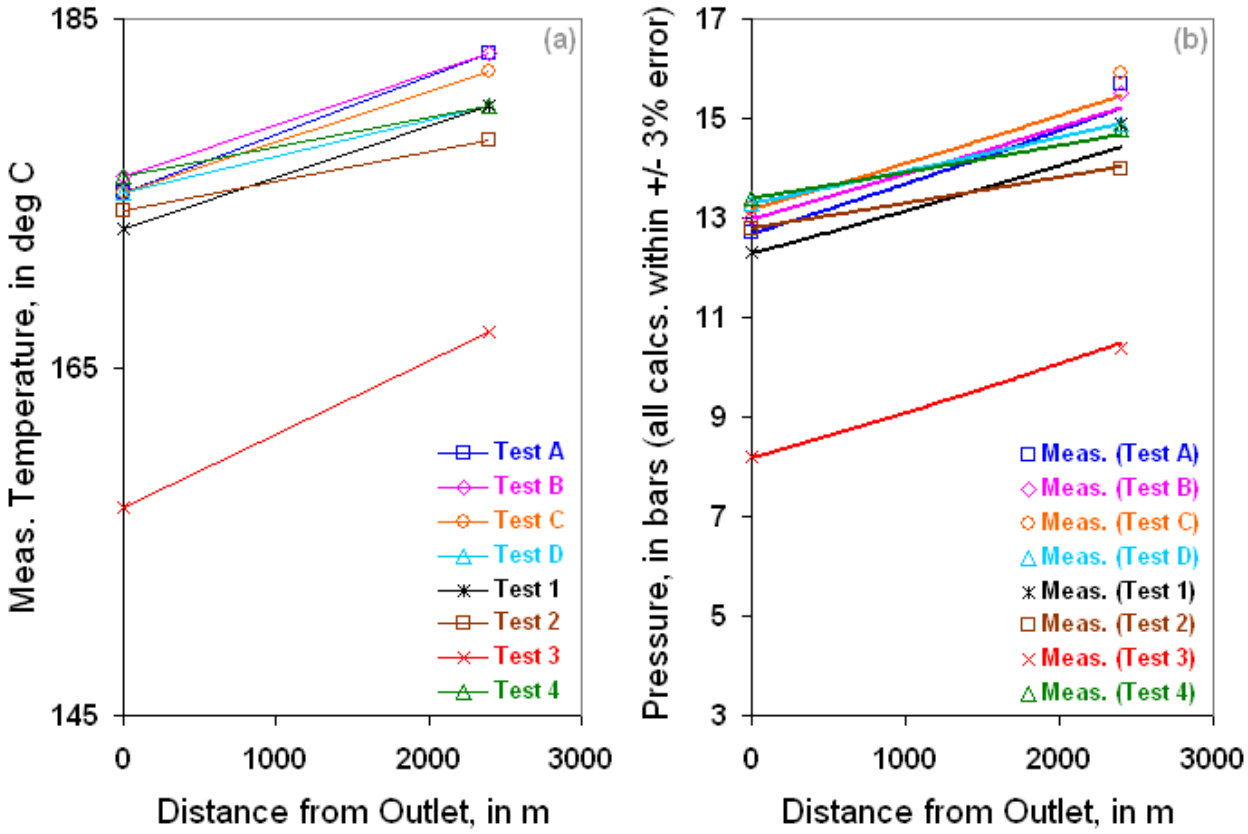

Figure 7.5.2: Steam flow for various tests of Andreussi et al. (1994). All pressures in (b) were obtained from the Yaws (1977) correlation and measured temperature in (a). The lines in (b) are our calculations.

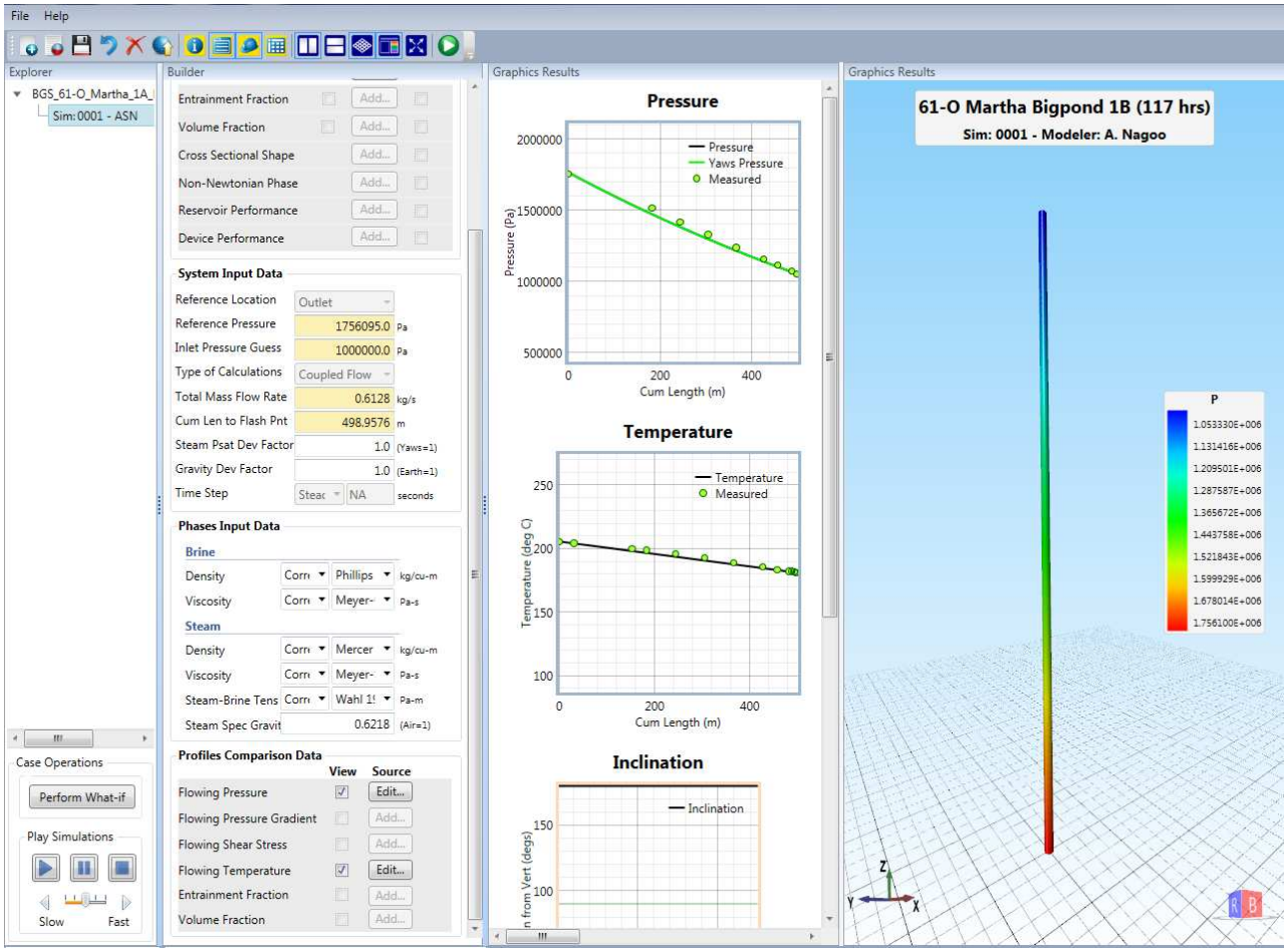

Figure 7.5.3: A steam injection well predicted with the Yaws (1977) correlation and a linear interpolation of the wellhead and bottom-hole temperature. This is the Martha Bigpond Steam Injection Test 1B from Bleakley (1964).

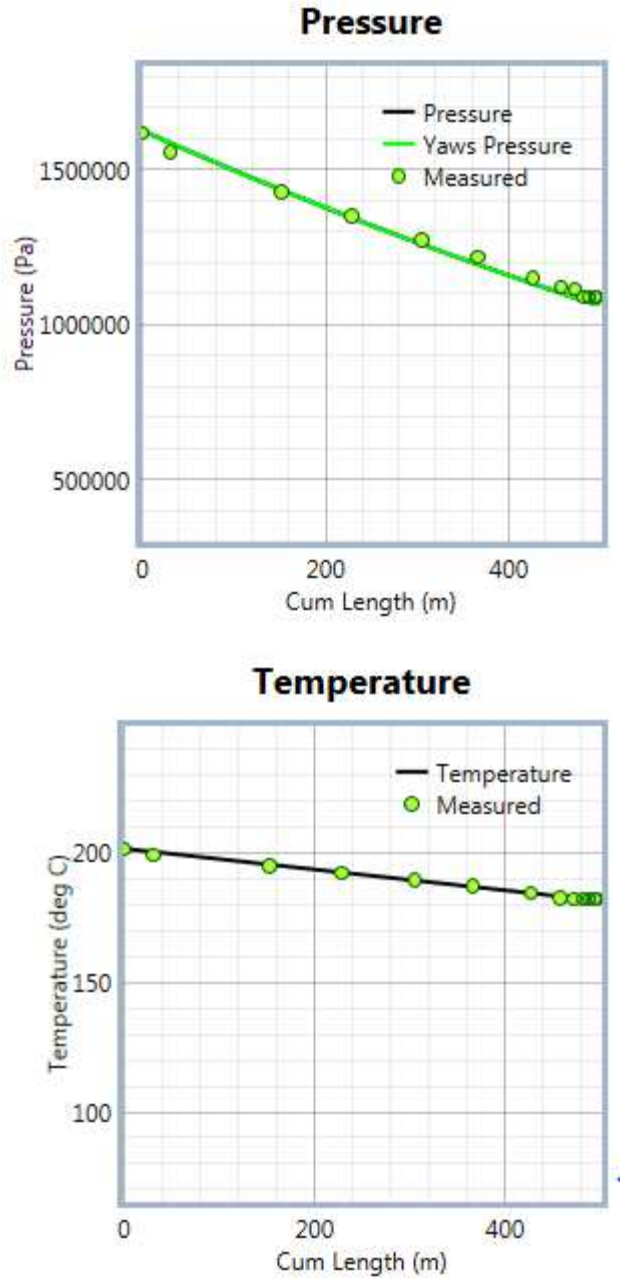

Figure 7.5.4: A steam injection well predicted with the Yaws (1977) correlation and a linear interpolation of the wellhead and bottom-hole temperature. This is the Martha Bigpond Steam Injection Test 1C from Bleakley (1964).

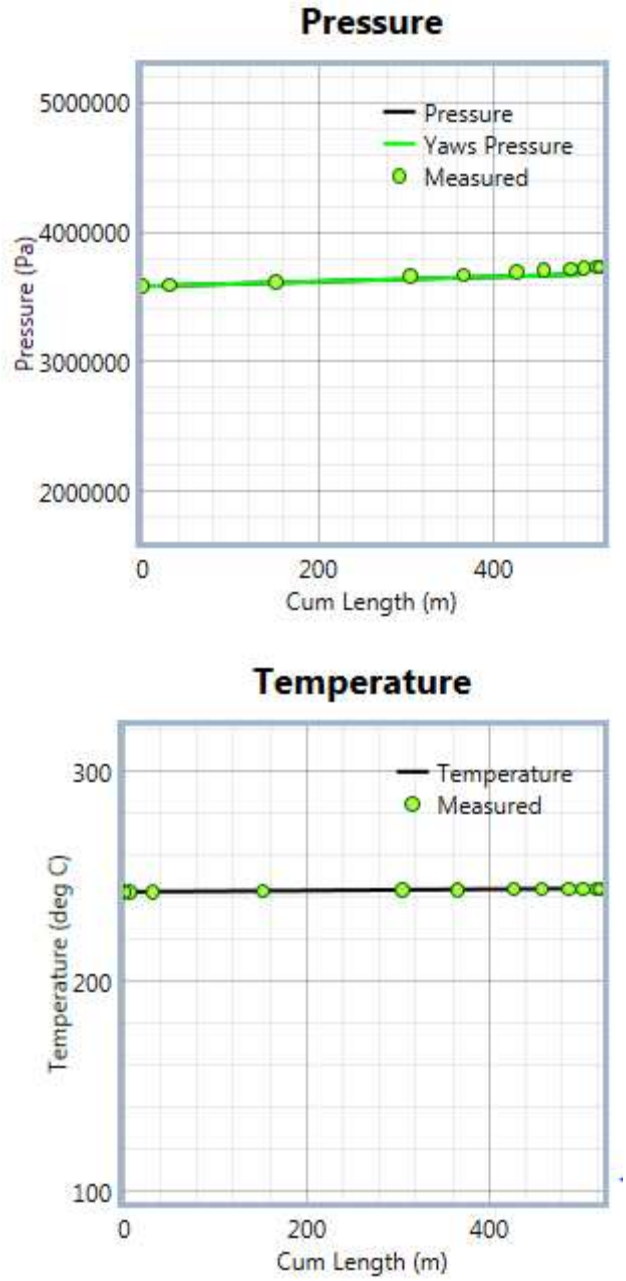

Figure 7.5.5: A steam injection well predicted with the Yaws (1977) correlation and a linear interpolation of the wellhead and bottom-hole temperature. This is the 14-W Sallie Lee Steam Injection Test 2A (308 hrs) from Bleakley (1964).

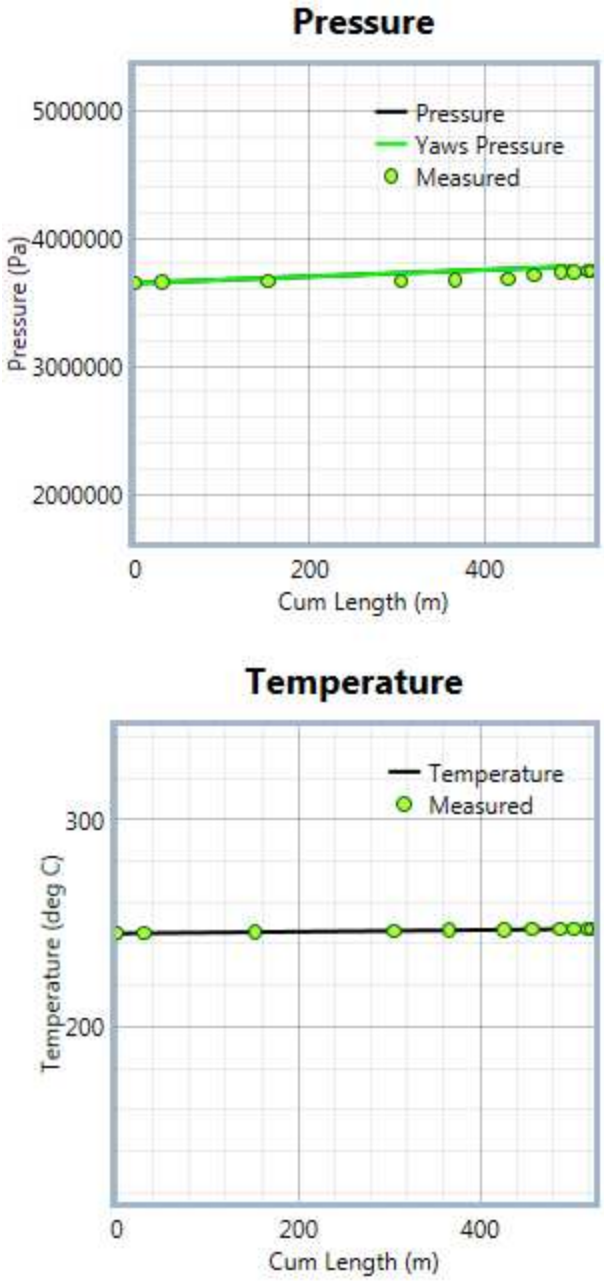

Figure 7.5.6: A steam injection well predicted with the Yaws (1977) correlation and a linear interpolation of the wellhead and bottom-hole temperature. This is the 14-W Sallie Lee Steam Injection Test 2B (177 hrs) from Bleakley (1964).

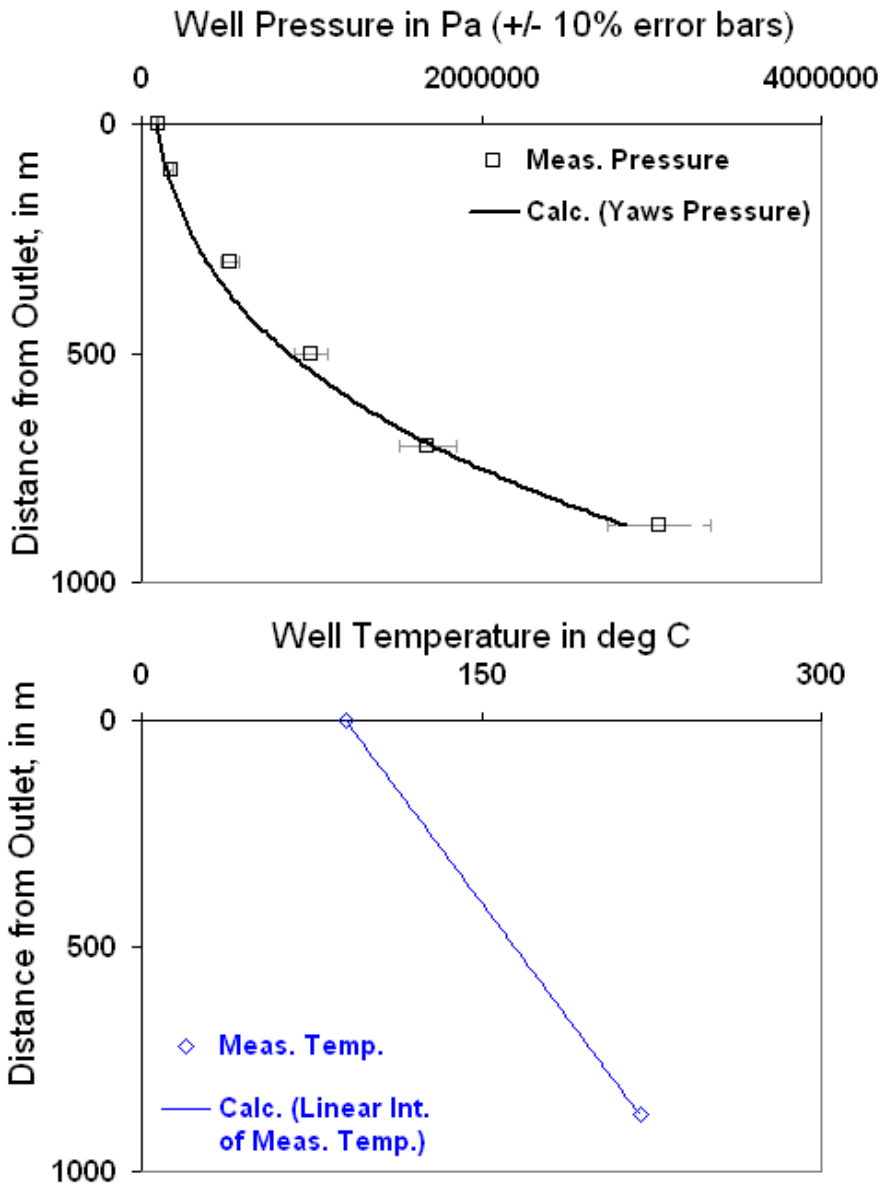

Figure 7.5.7: Geothermal well KE1-22 test 1 in Garg et al. (2004) predicted with the Yaws (1977) correlation.

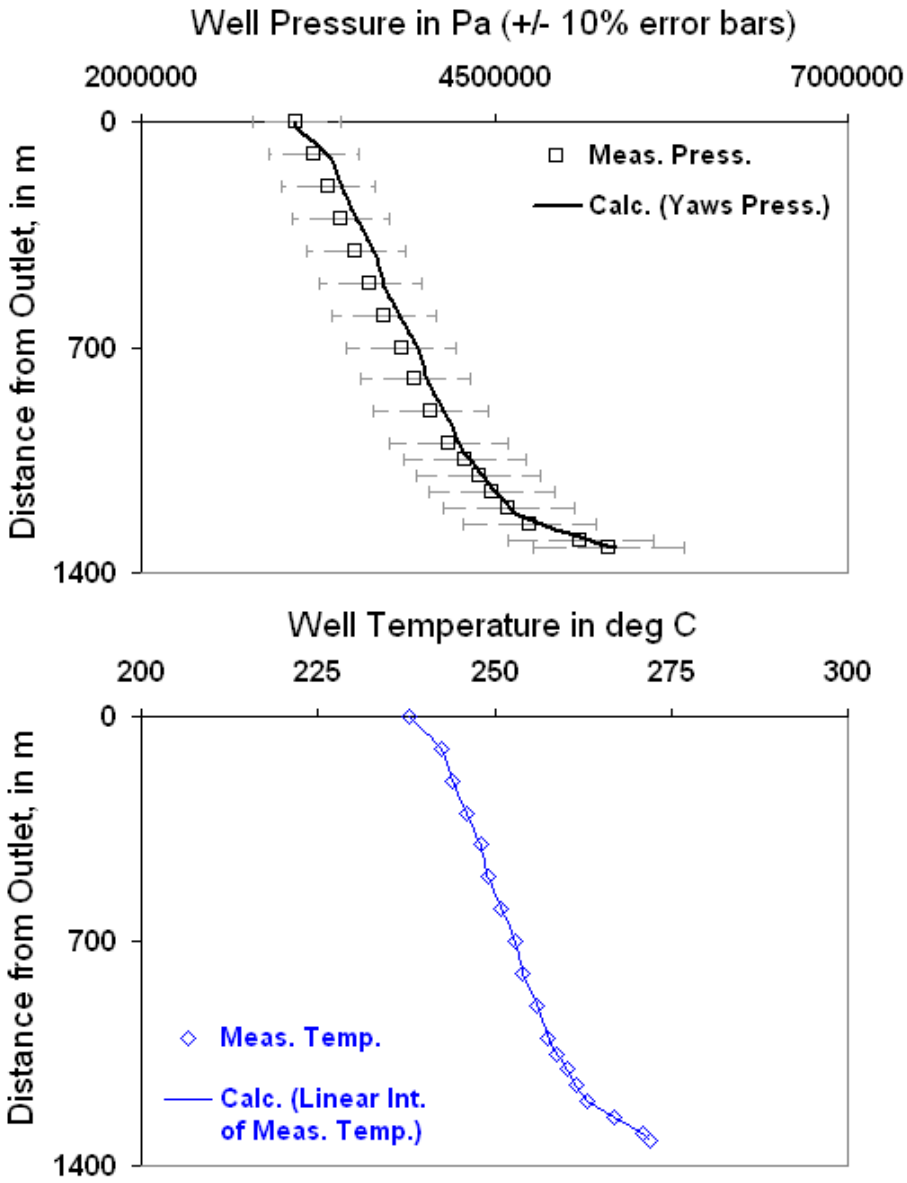

Figure 7.5.8: Geothermal well Los Azufres 18 in Ambastha and Gudmundsson (1986) predicted with the Yaws (1977) correlation.

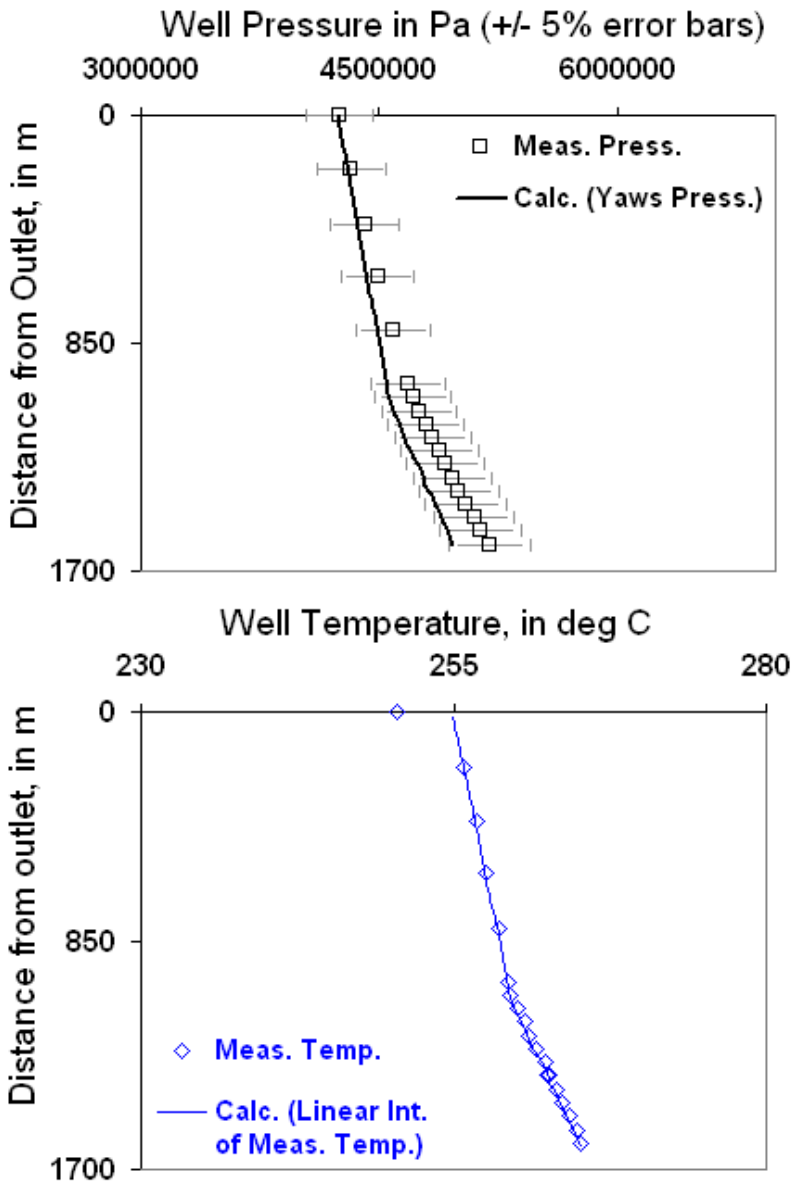

Figure 7.5.9: Geothermal well Los Azufres Az-19 in Aragon et al. (1999) predicted with the Yaws (1977) correlation.

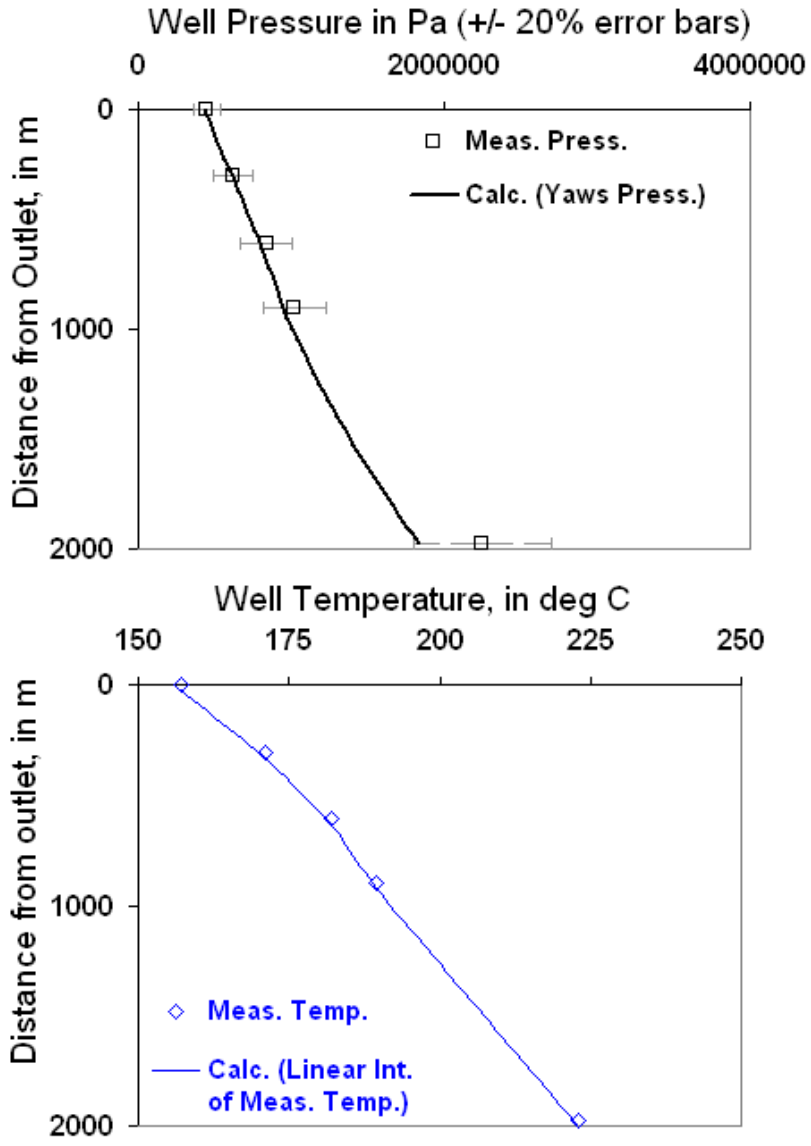

Figure 7.5.10: Geothermal well Mofete 2 in Ambastha and Gudmundsson (1986) predicted with the Yaws (1977) correlation.

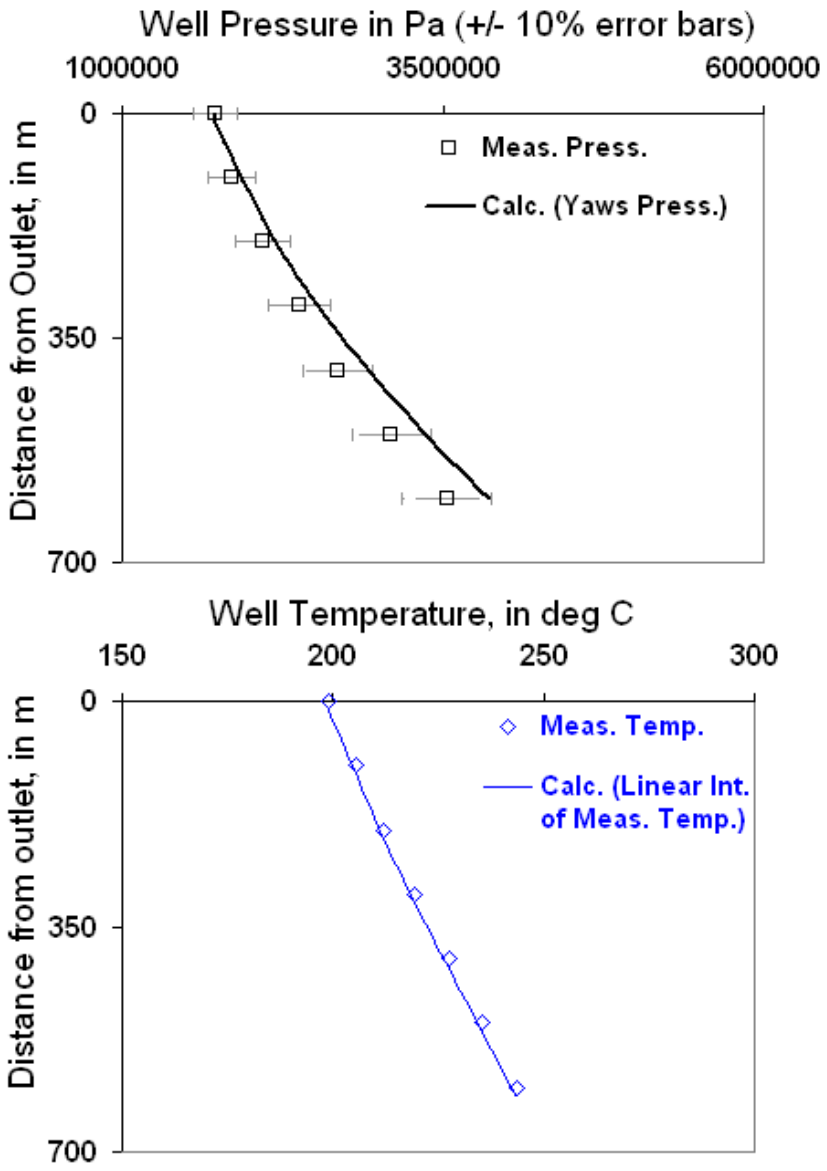

Figure 7.5.11: Geothermal well Krafla 9 in Ambastha and Gudmundsson (1986) predicted with the Yaws (1977) correlation.

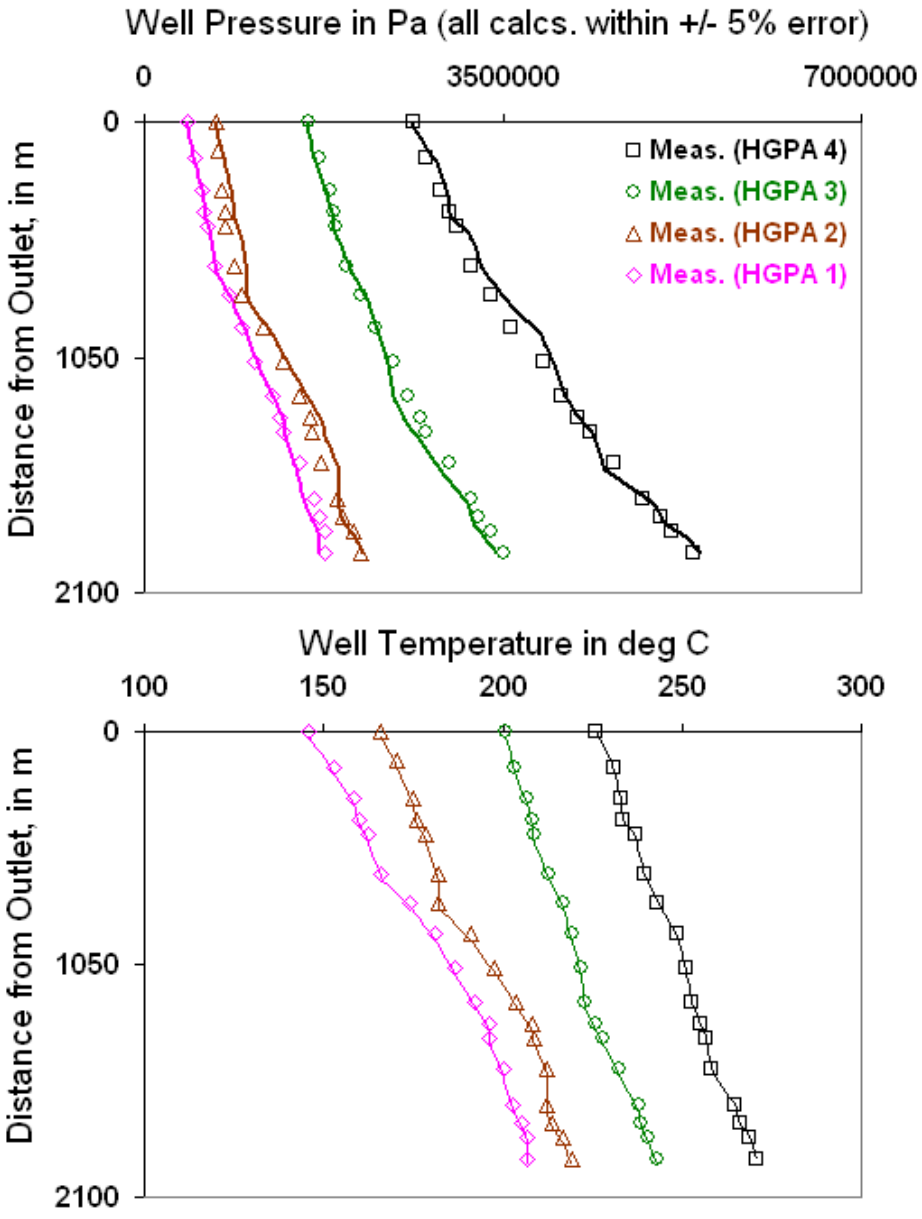

Figure 7.5.12: The multiple wellhead discharge mass flow rates of the geothermal well HGPA in Ambastha and Gudmundsson (1986) exactly follow the Yaws (1977) correlation and the measured temperature.

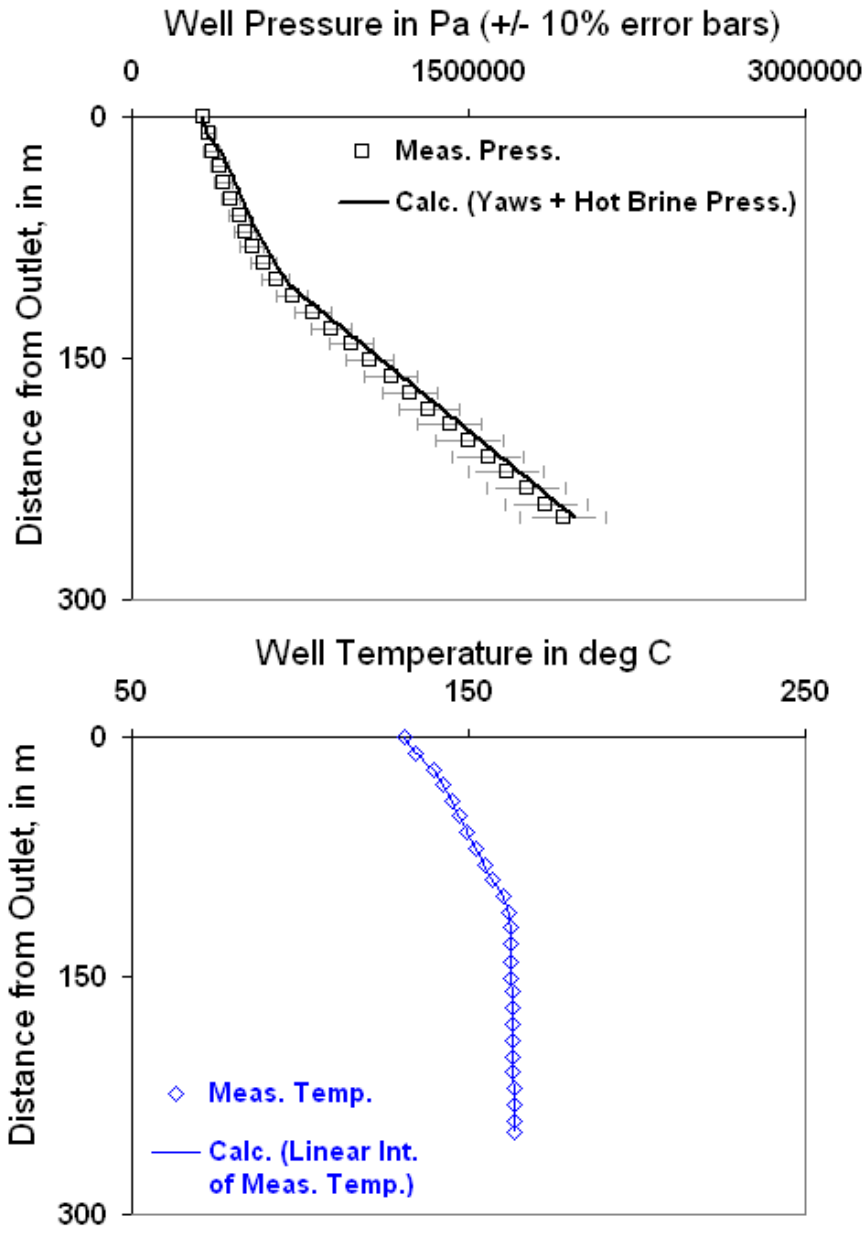

Figure 7.5.13: Geothermal well SNLG87-29 in Garg et al. (2004) predicted with the Yaws (1977) correlation above the flash point and single-phase brine flow below the flash point. The flash depth is 104 m.

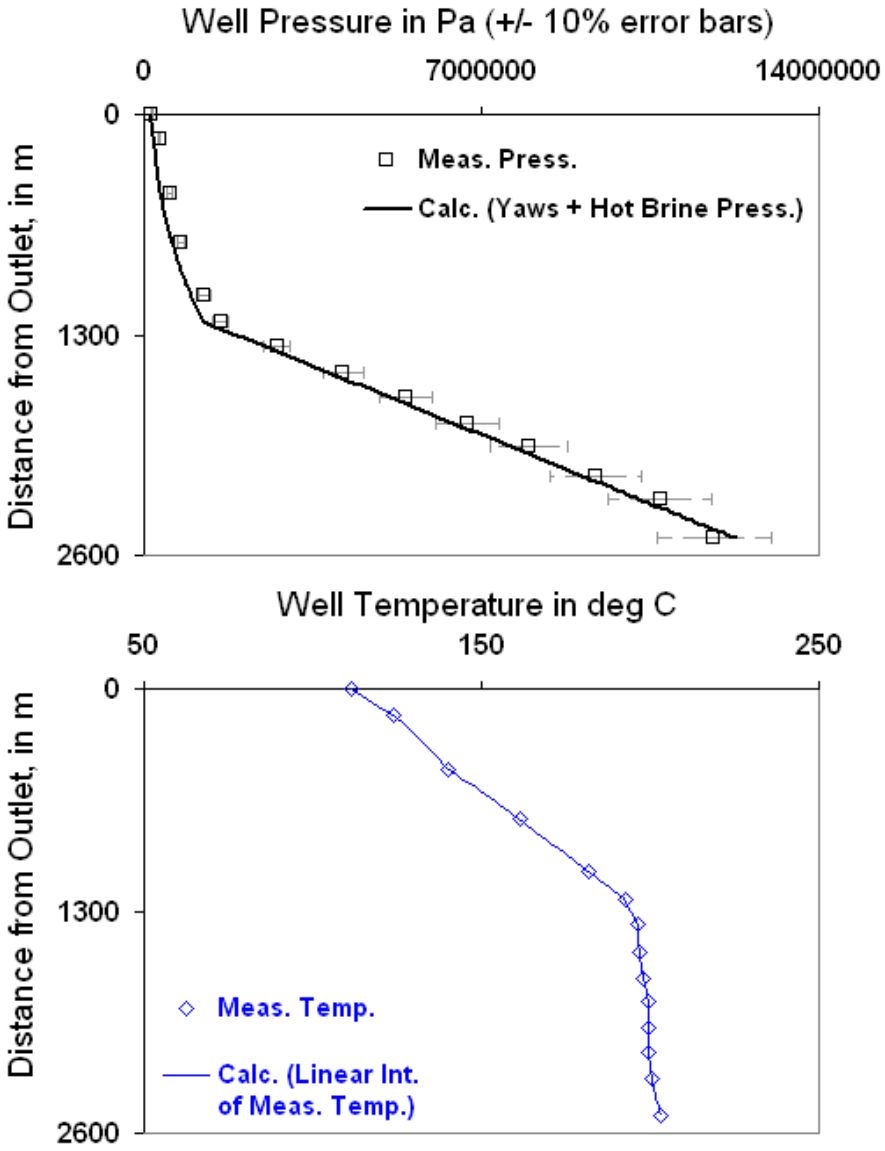

Figure 7.5.14: Geothermal well 6-1 in Bjornsson (1987) predicted with the Yaws (1977) correlation above the flash point and single-phase brine flow below the flash point. The flash depth is 1203 m.

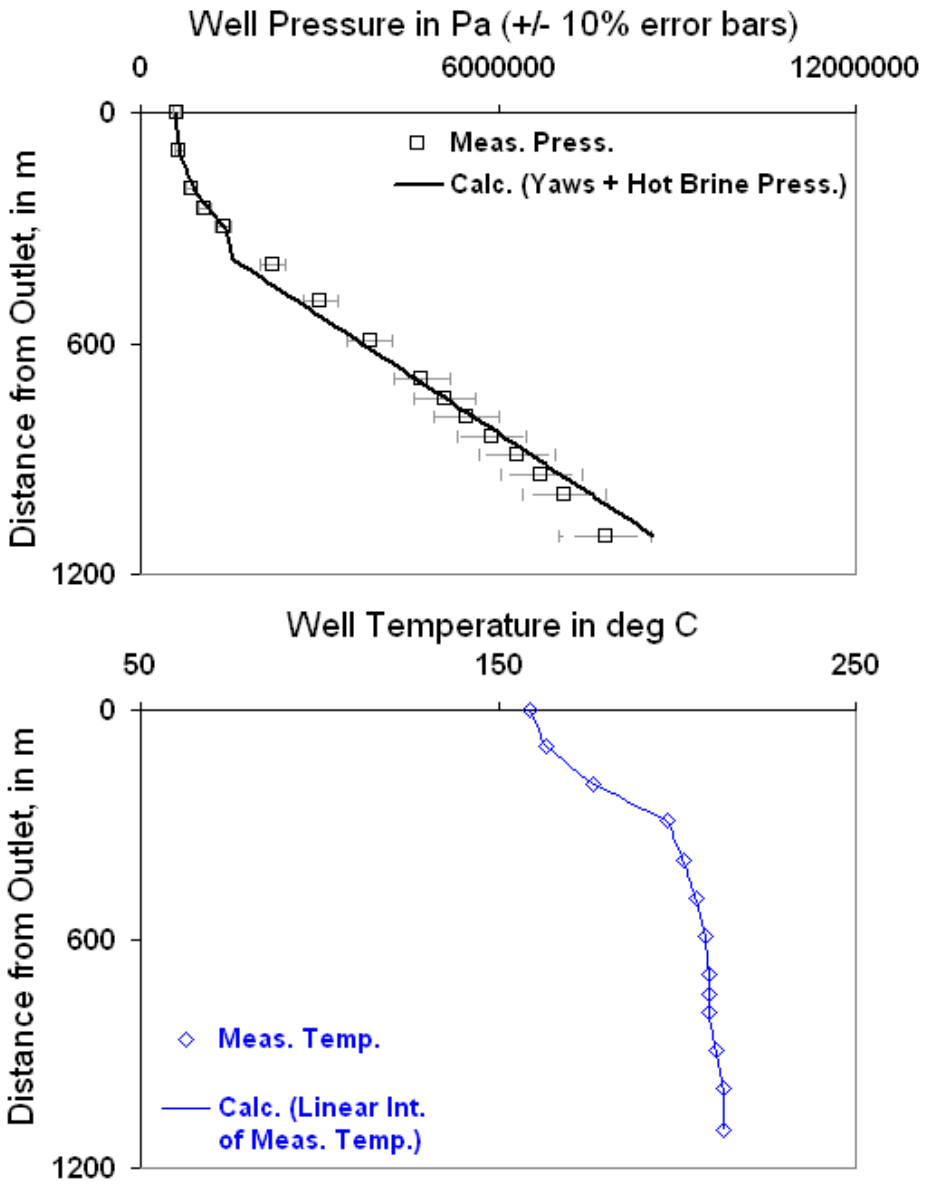

Figure 7.5.15: Geothermal well Krafla 9 in Bjornsson (1987) predicted with the Yaws (1977) correlation above the flash point and single-phase brine flow below the flash point. The flash depth is 374 m.

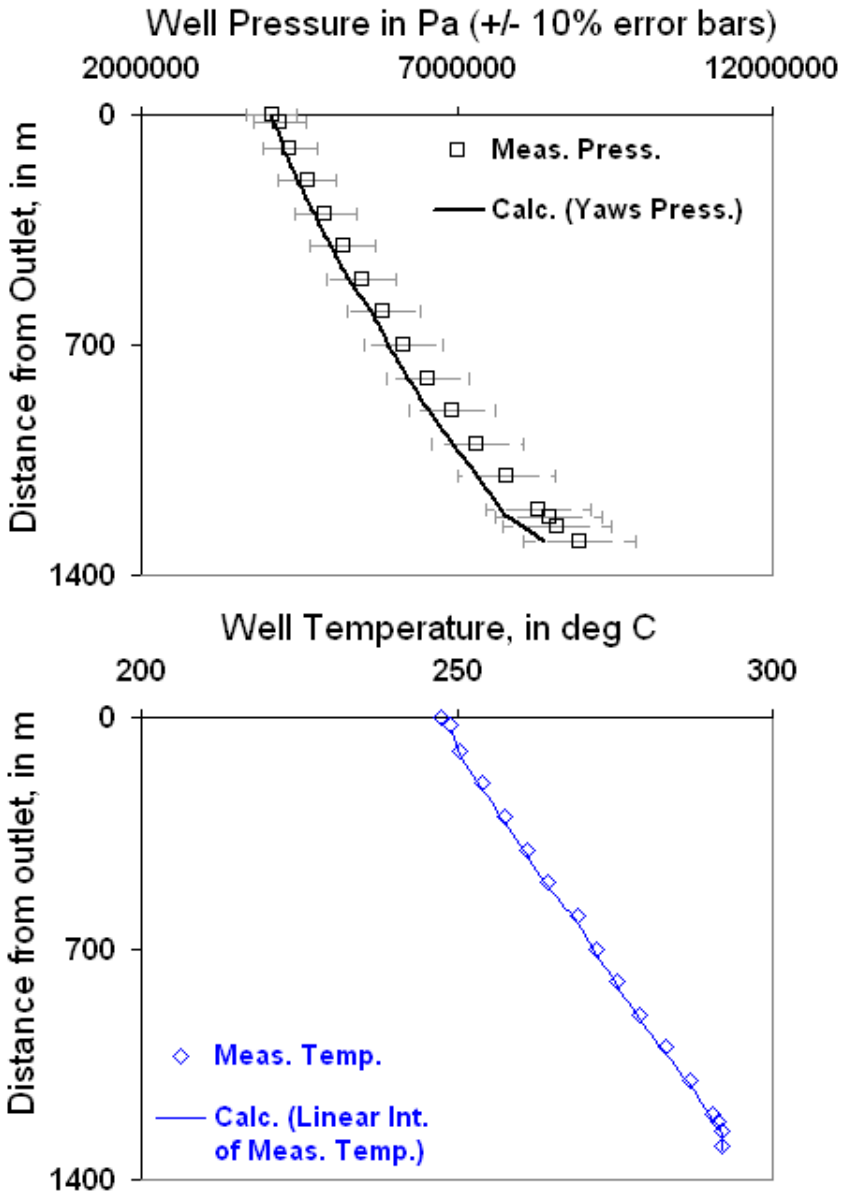

Figure 7.5.16: Geothermal well Cerro Printo 90 in Ambastha and Gudmundsson (1986) predicted with the Yaws (1977) correlation above the flash point and single-phase brine flow below the flash point. The flash depth is 1210 m.

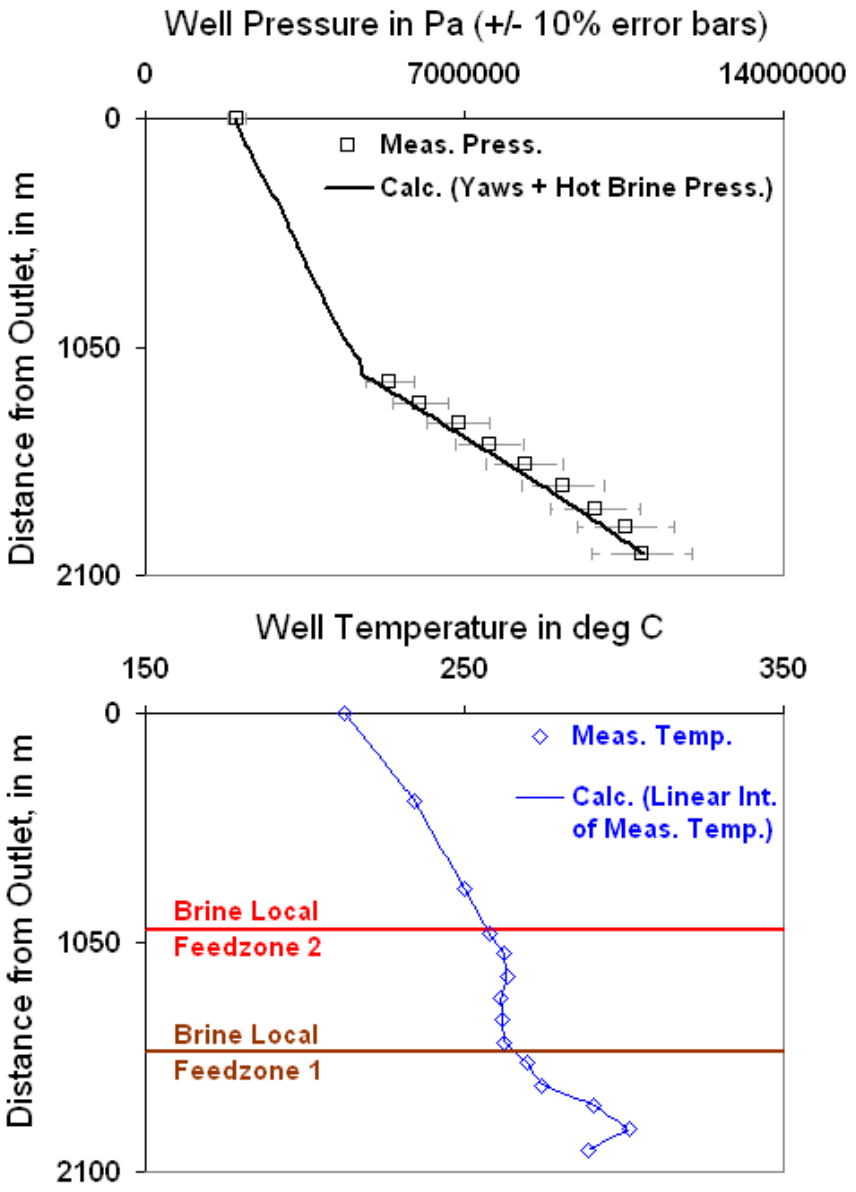

Figure 7.5.17: Geothermal well NJ-7 in Bjornsson (1987) predicted with the Yaws (1977) correlation above the flash point and single-phase brine flow below the flash point. The flash depth is 1160 m.

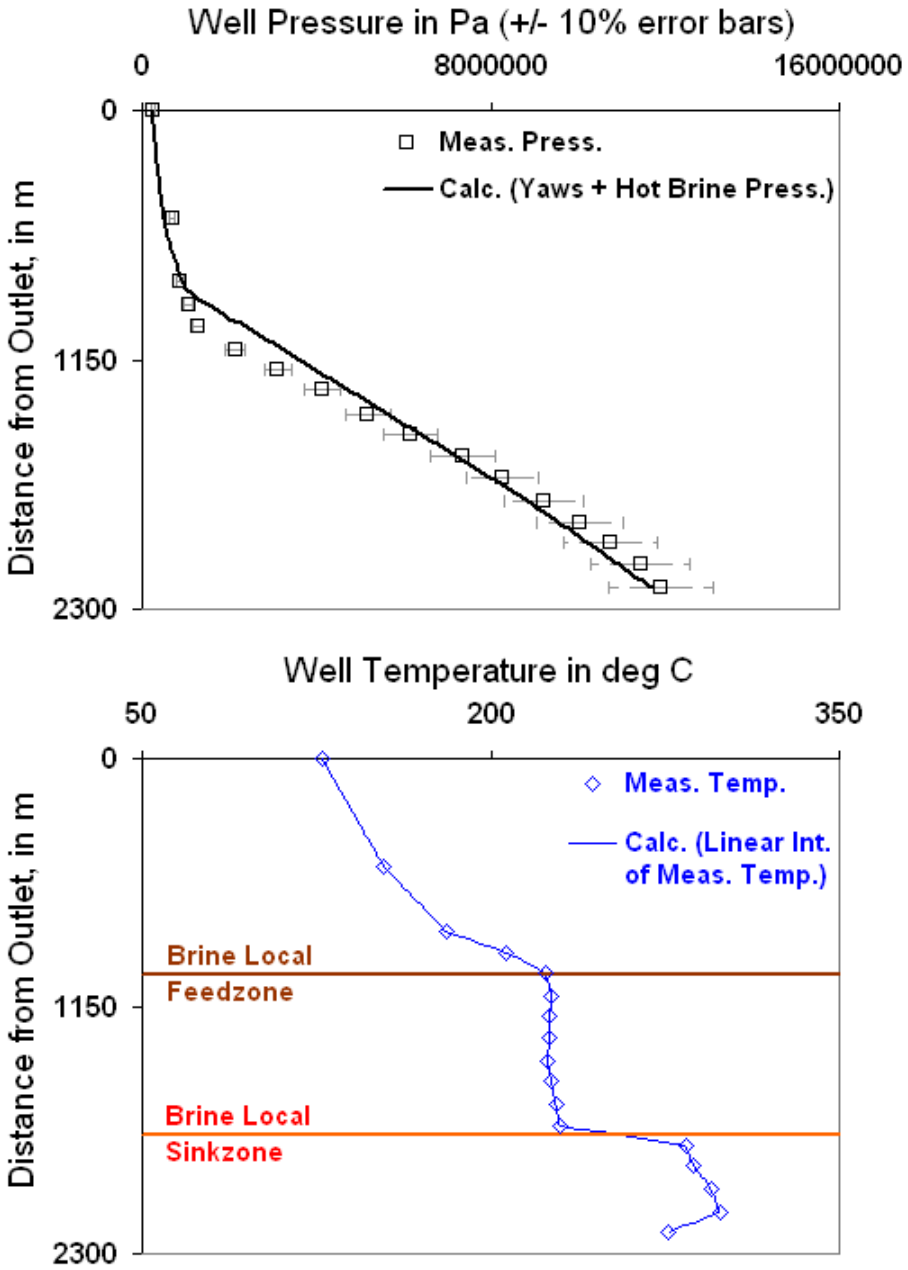

Figure 7.5.18: Geothermal well Krafla 11-1 in Bjornsson (1987) predicted with the Yaws (1977) correlation above the flash point and single-phase brine flow below the flash point. The flash depth is 958 m.

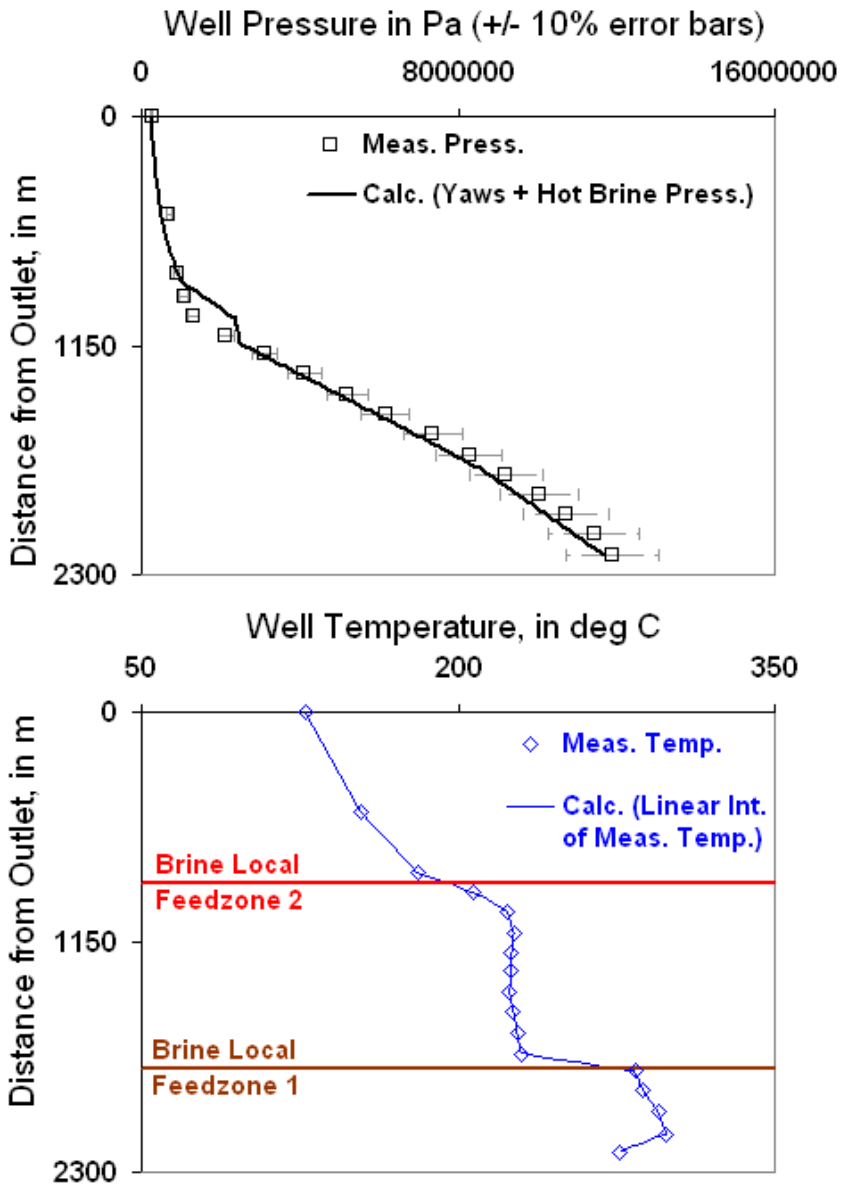

Figure 7.5.19: Geothermal well Krafla 11-2 in Bjornsson (1987) predicted with the Yaws (1977) correlation above the flash point and single-phase brine flow below the flash point. The flash depth is 1125 m.

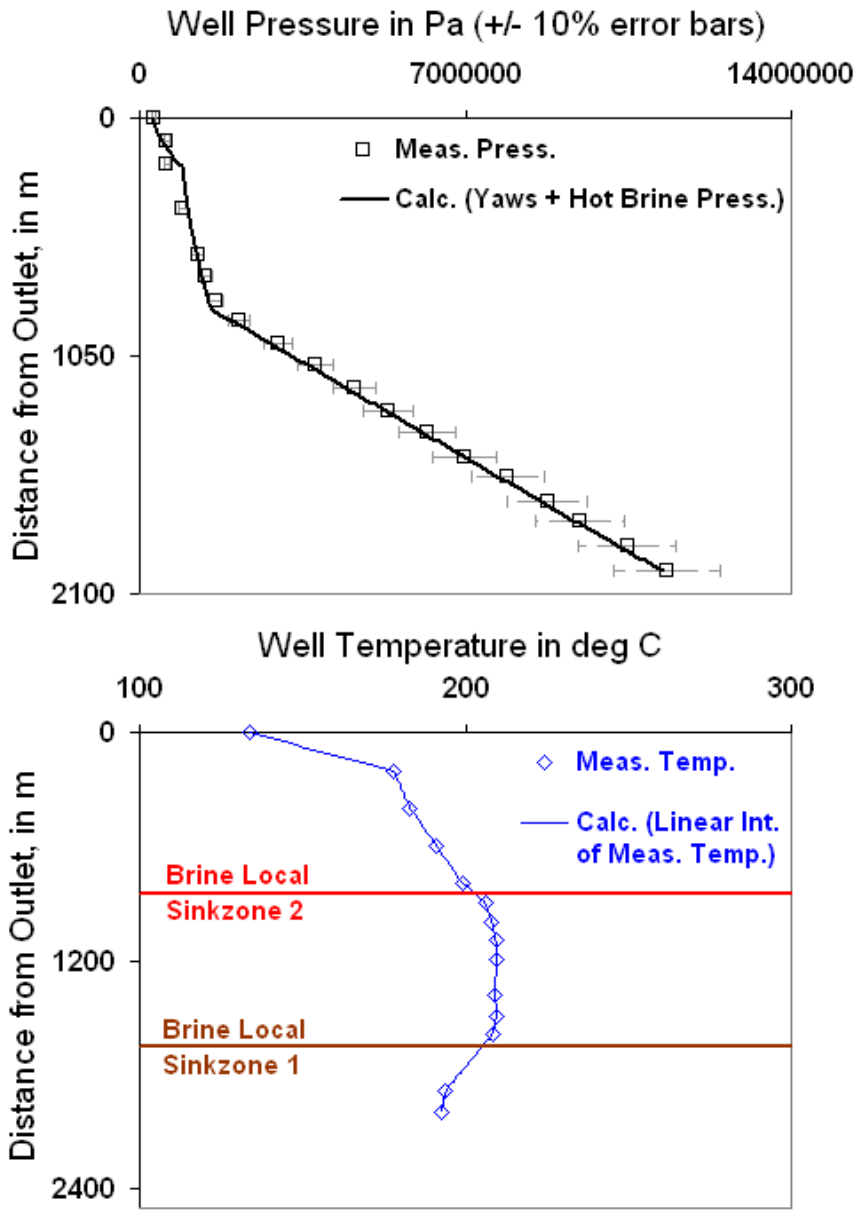

Figure 7.5.20: Geothermal well Krafla OW-201 in Bjornsson (1987) predicted with the Yaws (1977) correlation above the flash point and single-phase brine flow below the flash point. The flash depth is 840 m.

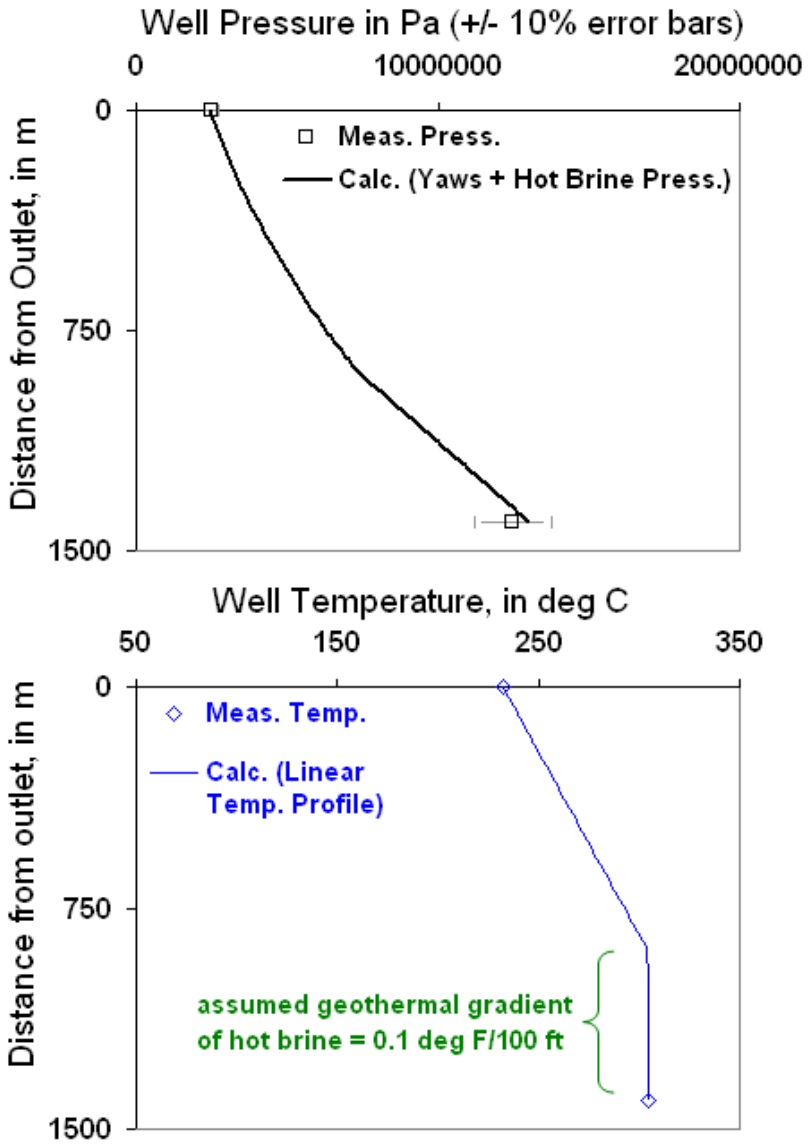

Figure 7.5.21: Geothermal well State N.1 (first rate) in Chierici et al. (1981) predicted with the Yaws (1977) correlation above the flash point, single-phase brine flow below the flash point, the known wellhead and bottom-hole temperatures, and an assumed hot brine geothermal temperature gradient. The flash depth is 890 m.

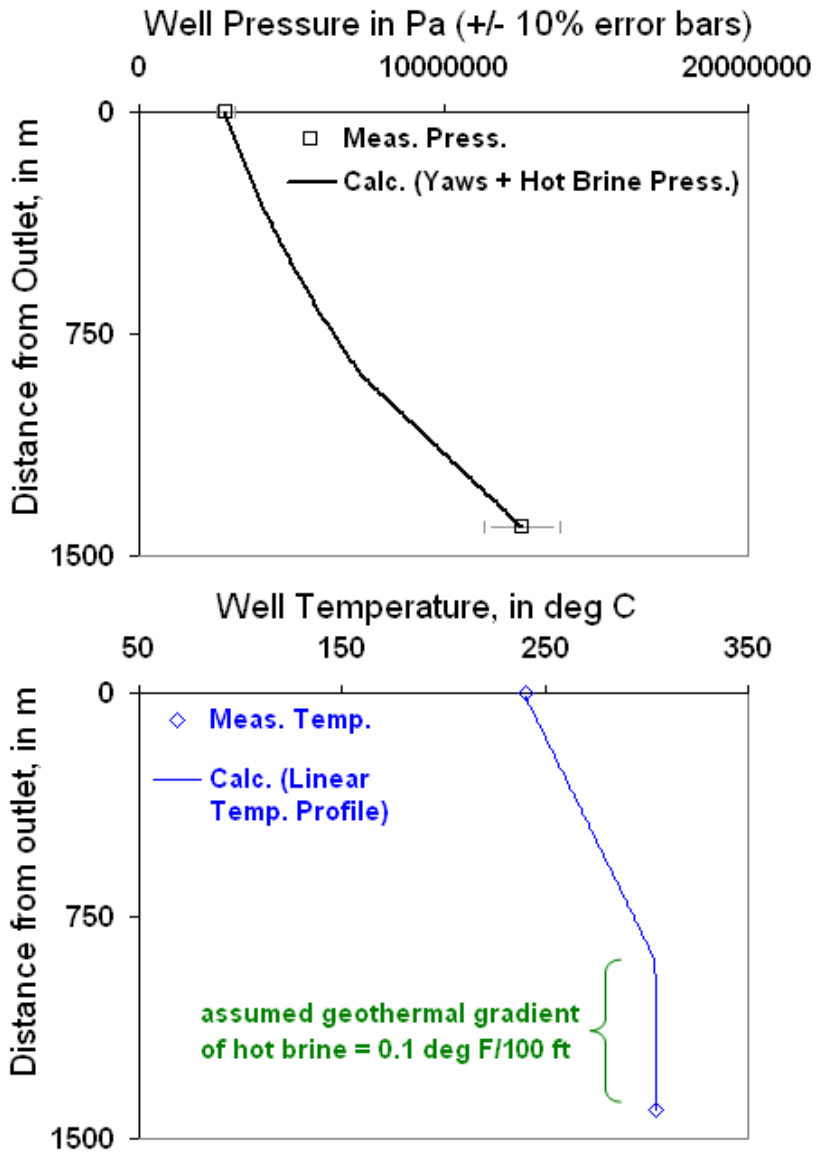

Figure 7.5.22: Geothermal well State N.1 (second rate) in Chierici et al. (1981) predicted with the Yaws (1977) correlation above the flash point, single-phase brine flow below the flash point, the known wellhead and bottom-hole temperatures, and an assumed hot brine geothermal temperature gradient. The flash depth is 887 m.

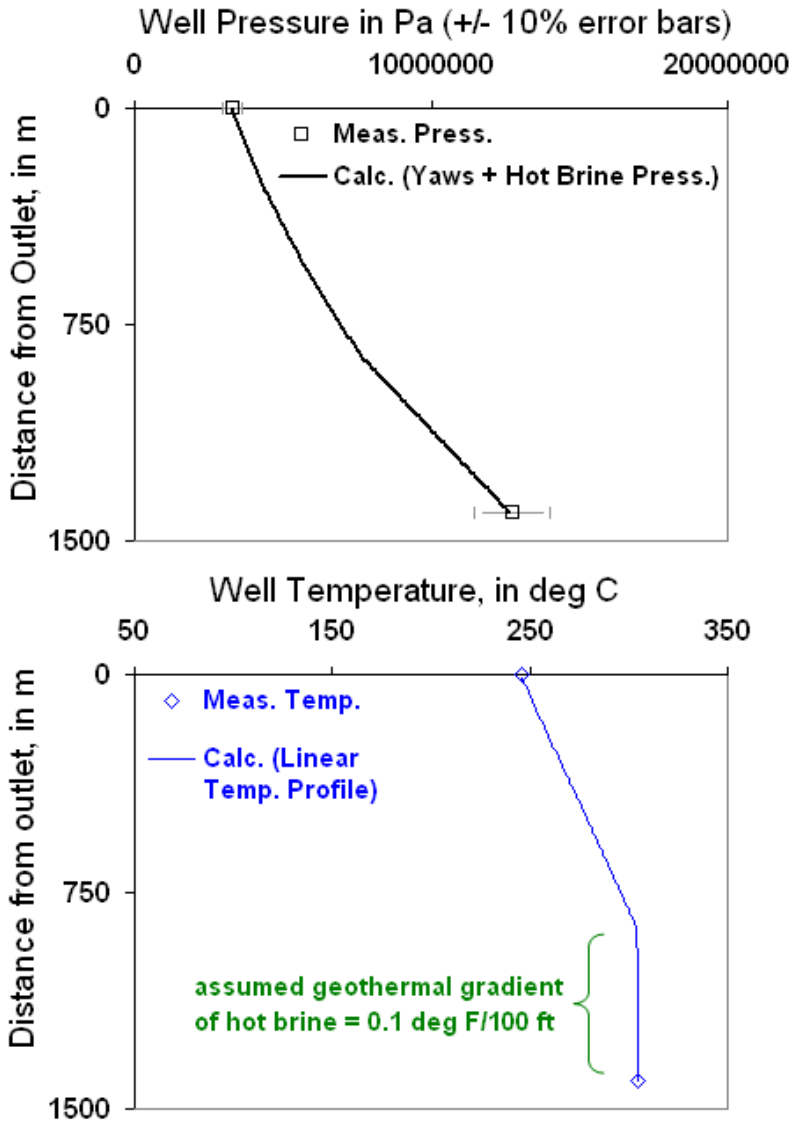

Figure 7.5.23: Geothermal well State N.1 (third rate) in Chierici et al. (1981) predicted with the Yaws (1977) correlation above the flash point, single-phase brine flow below the flash point, the known wellhead and bottom-hole temperatures, and an assumed hot brine geothermal temperature gradient. The flash depth is 861 m.

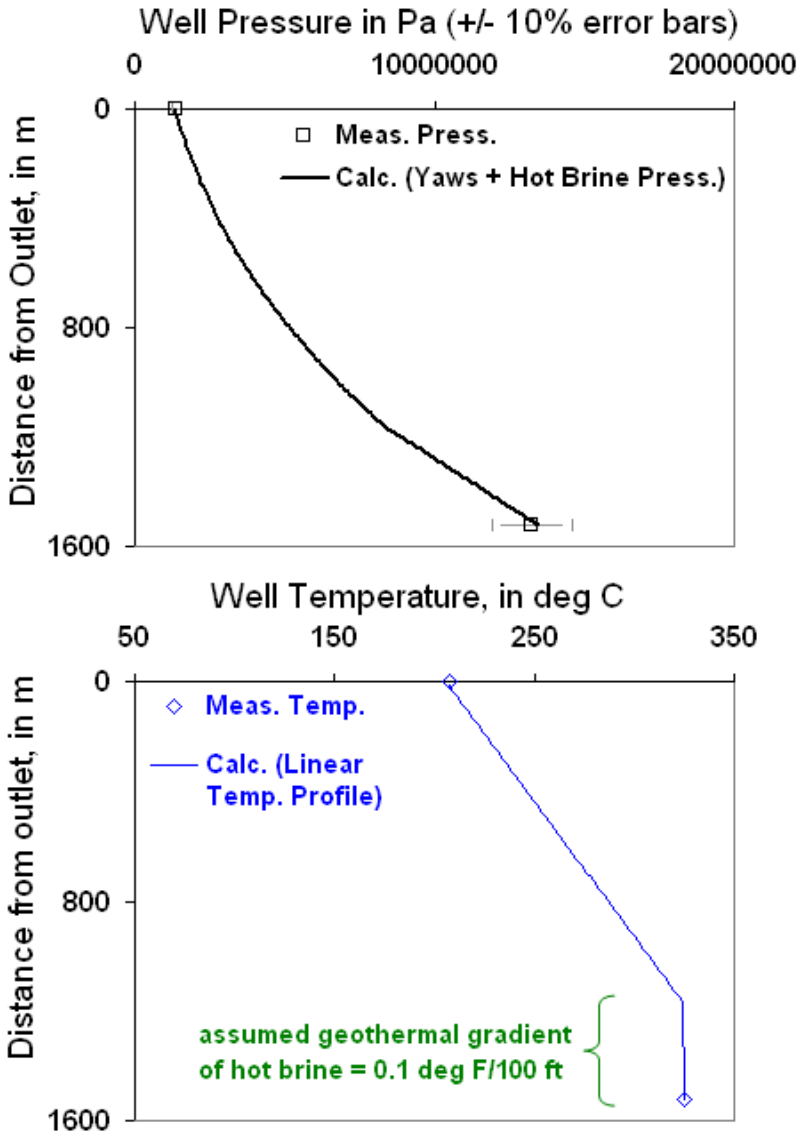

Figure 7.5.24: Geothermal well IID N.1 (first rate) in Chierici et al. (1981) predicted with the Yaws (1977) correlation above the flash point, single-phase brine flow below the flash point, the known wellhead and bottom-hole temperatures, and an assumed hot brine geothermal temperature gradient. The flash depth is 1158 m.

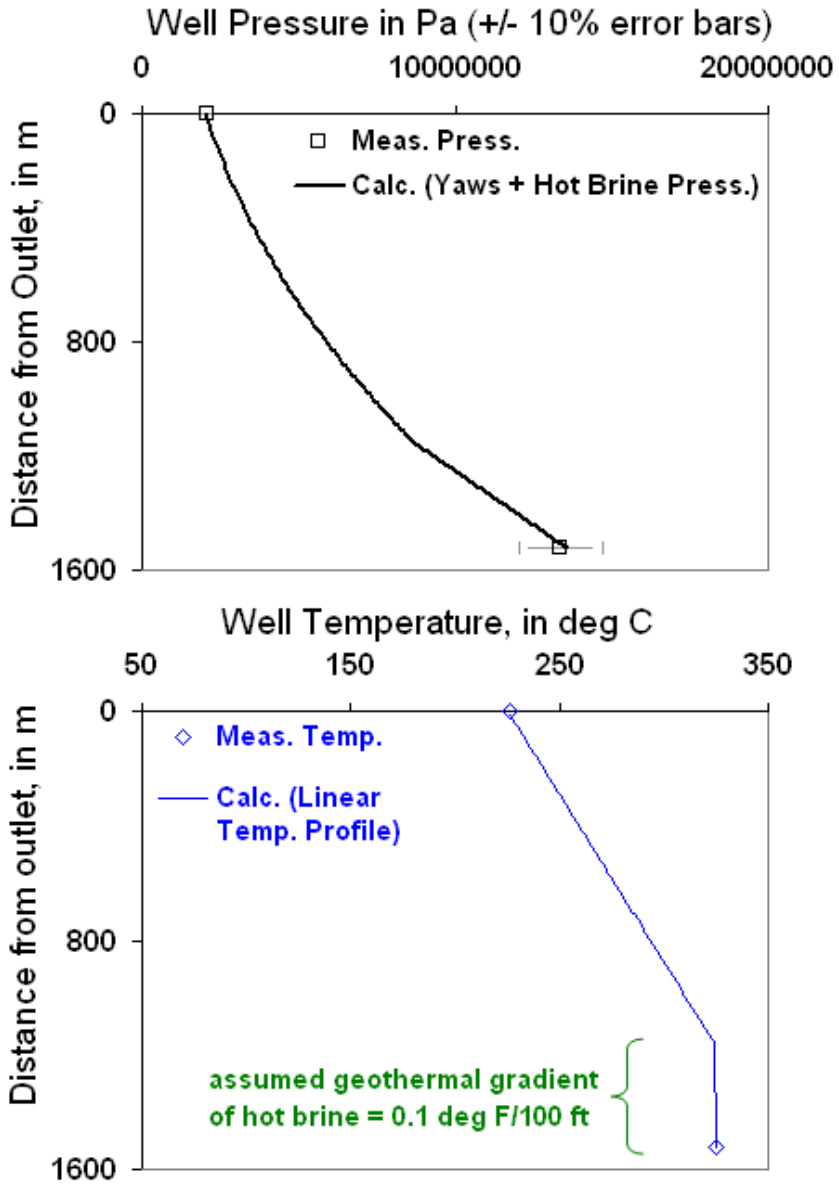

Figure 7.5.25: Geothermal well IID N.1 (second rate) in Chierici et al. (1981) predicted with the Yaws (1977) correlation above the flash point, single-phase brine flow below the flash point, the known wellhead and bottom-hole temperatures, and an assumed hot brine geothermal temperature gradient. The flash depth is 1150 m.

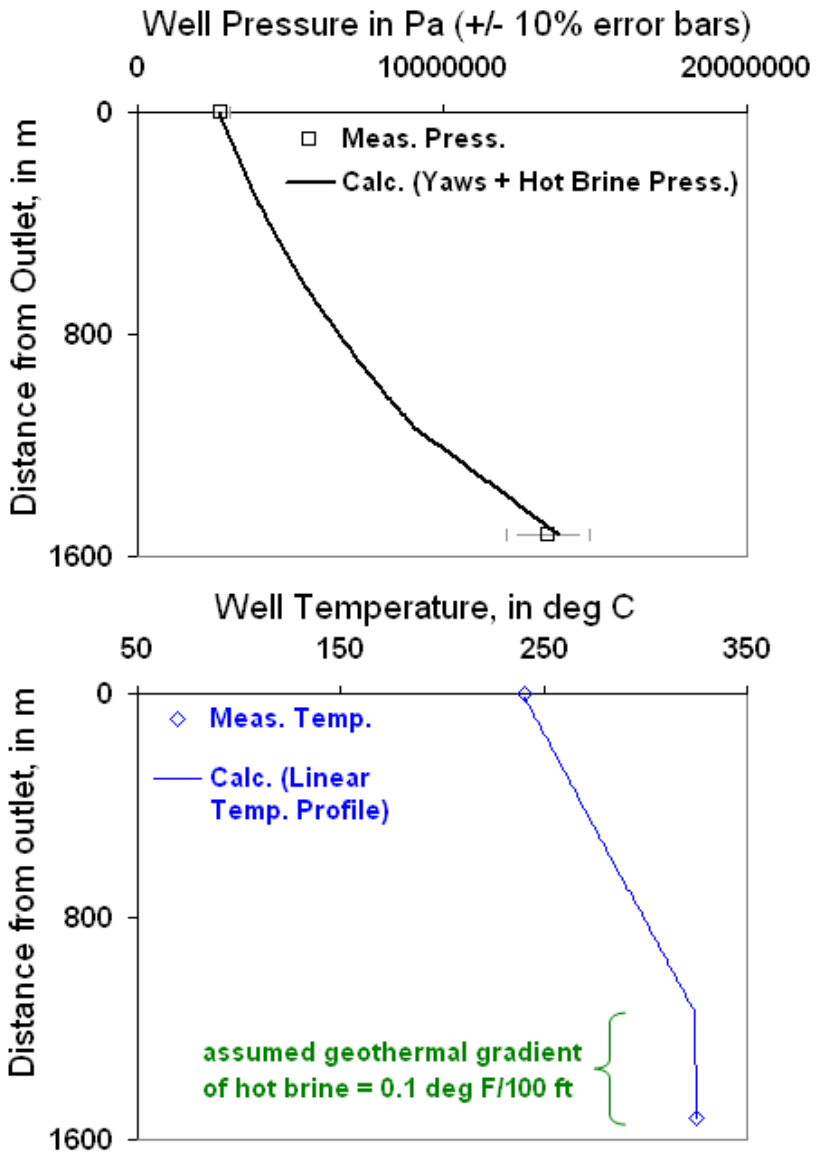

Figure 7.5.26: Geothermal well IID N.1 (third rate) in Chierici et al. (1981) predicted with the Yaws (1977) correlation above the flash point, single-phase brine flow below the flash point, the known wellhead and bottom-hole temperatures, and an assumed hot brine geothermal temperature gradient. The flash depth is 1131 m.

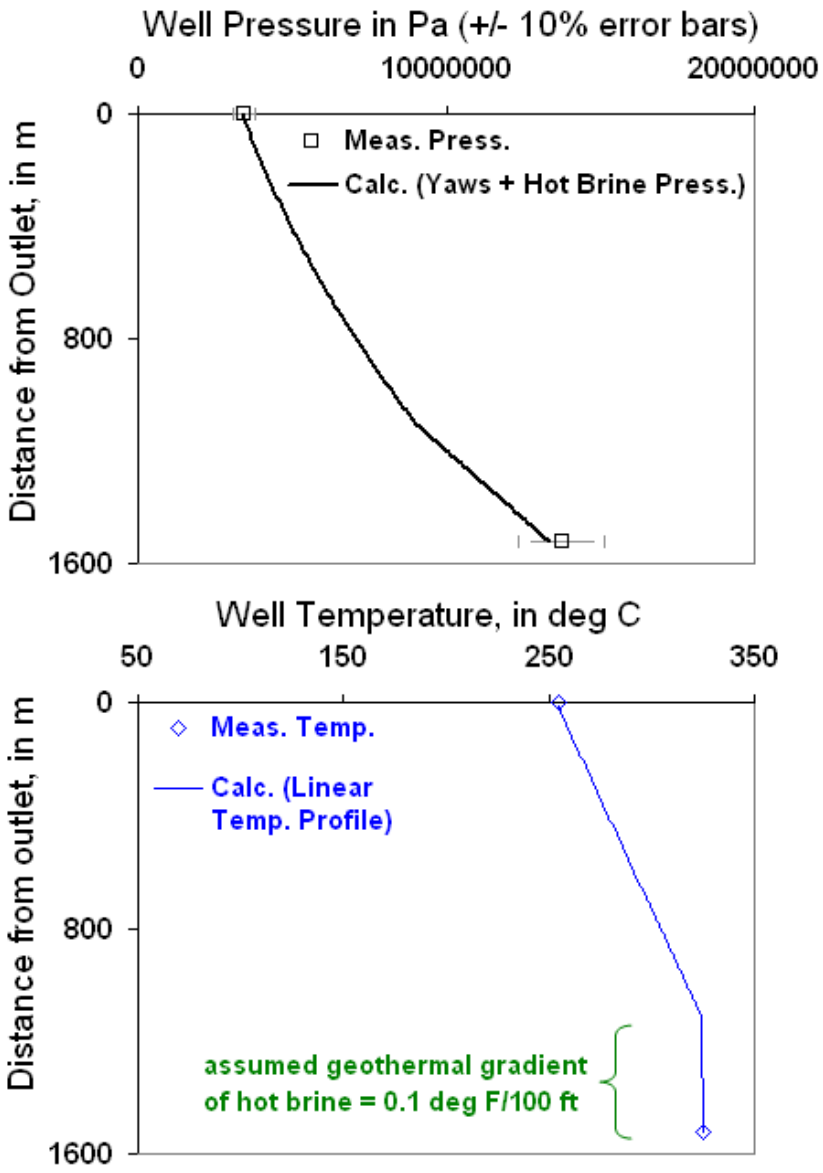

Figure 7.5.27: Geothermal well IID N.1 (fourth rate) in Chierici et al. (1981) predicted with the Yaws (1977) correlation above the flash point, single-phase brine flow below the flash point, the known wellhead and bottom-hole temperatures, and an assumed hot brine geothermal temperature gradient. The flash depth is 1103 m.

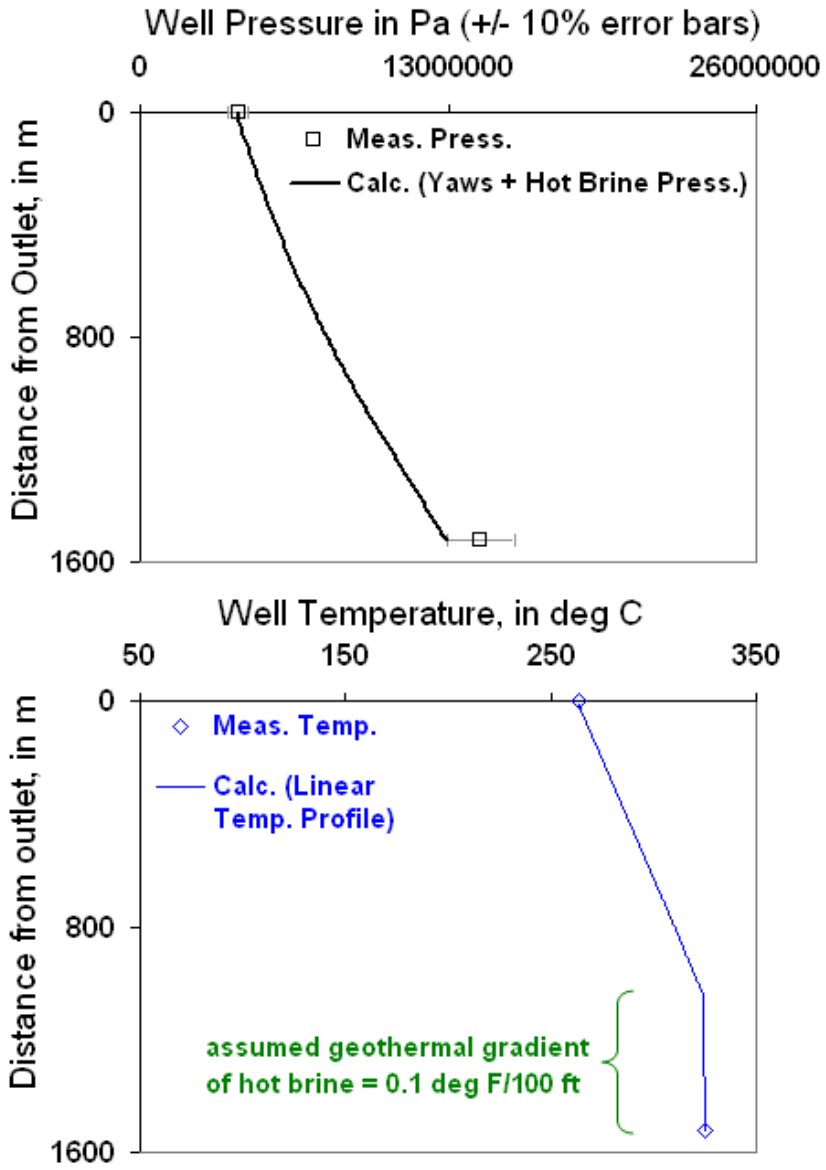

Figure 7.5.28: Geothermal well IID N.1 (fifth rate) in Chierici et al. (1981) predicted with the Yaws (1977) correlation above the flash point, single-phase brine flow below the flash point, the known wellhead and bottom-hole temperatures, and an assumed hot brine geothermal temperature gradient. The flash depth is 1028 m.

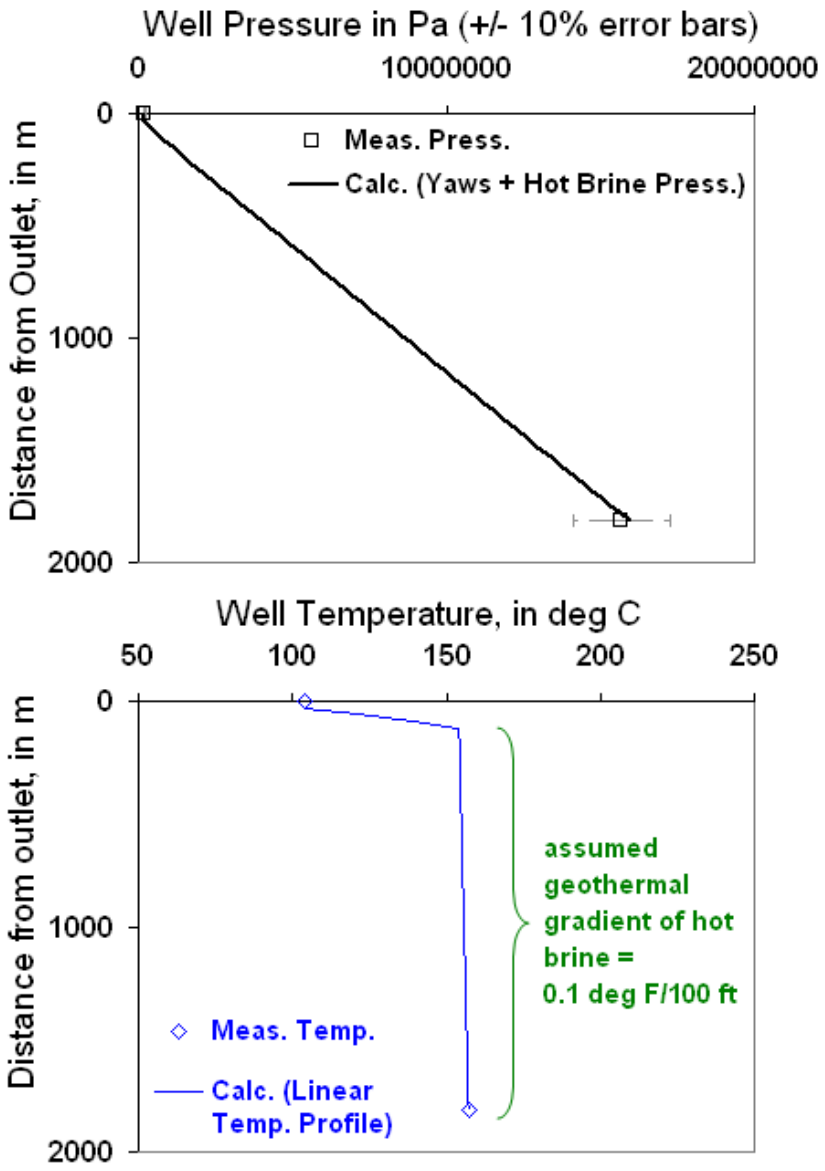

Figure 7.5.29: Geothermal well East Mesa 5-1 in Chierici et al. (1981) predicted with the Yaws (1977) correlation above the flash point, single-phase brine flow below the flash point, the known wellhead and bottom-hole temperatures, and an assumed hot brine geothermal temperature gradient. The flash depth is 86 m.

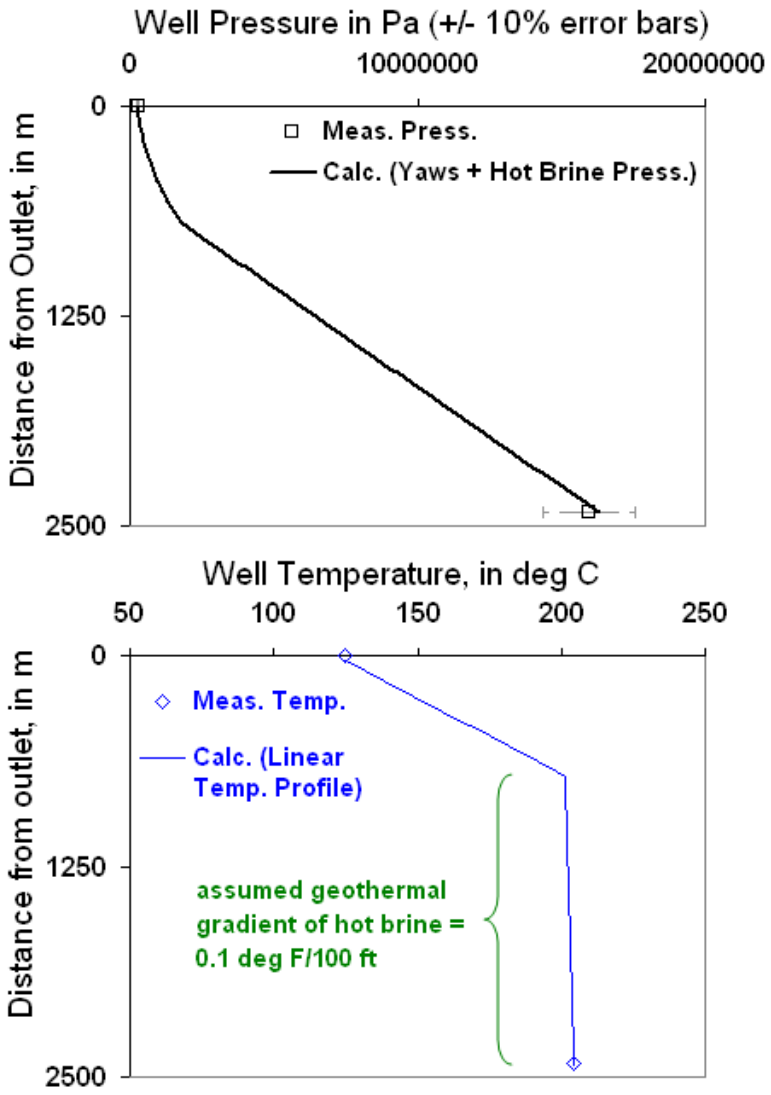

Figure 7.5.30: Geothermal well East Mesa 6-1 in Chierici et al. (1981) predicted with the Yaws (1977) correlation above the flash point, single-phase brine flow below the flash point, the known wellhead and bottom-hole temperatures, and an assumed hot brine geothermal temperature gradient. The flash depth is 687 m.

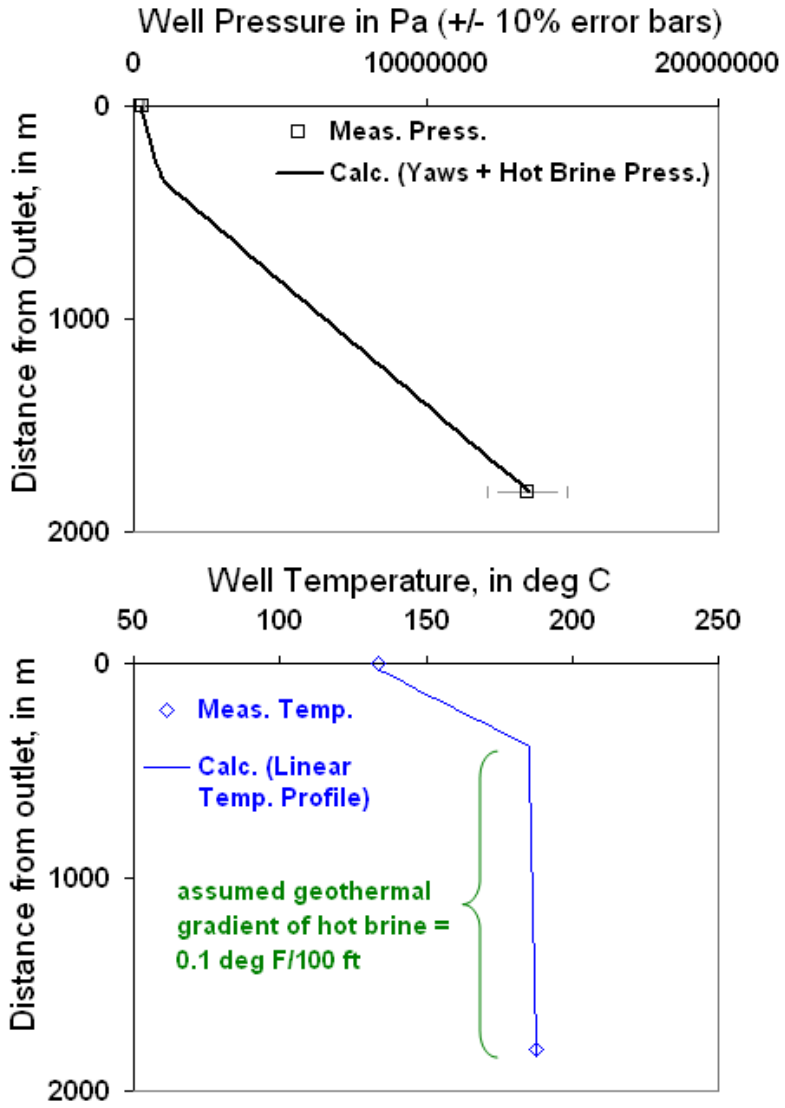

Figure 7.5.31: Geothermal well East Mesa 6-2 in Chierici et al. (1981) predicted with the Yaws (1977) correlation above the flash point, single-phase brine flow below the flash point, the known wellhead and bottom-hole temperatures, and an assumed hot brine geothermal temperature gradient. The flash depth is 358 m.

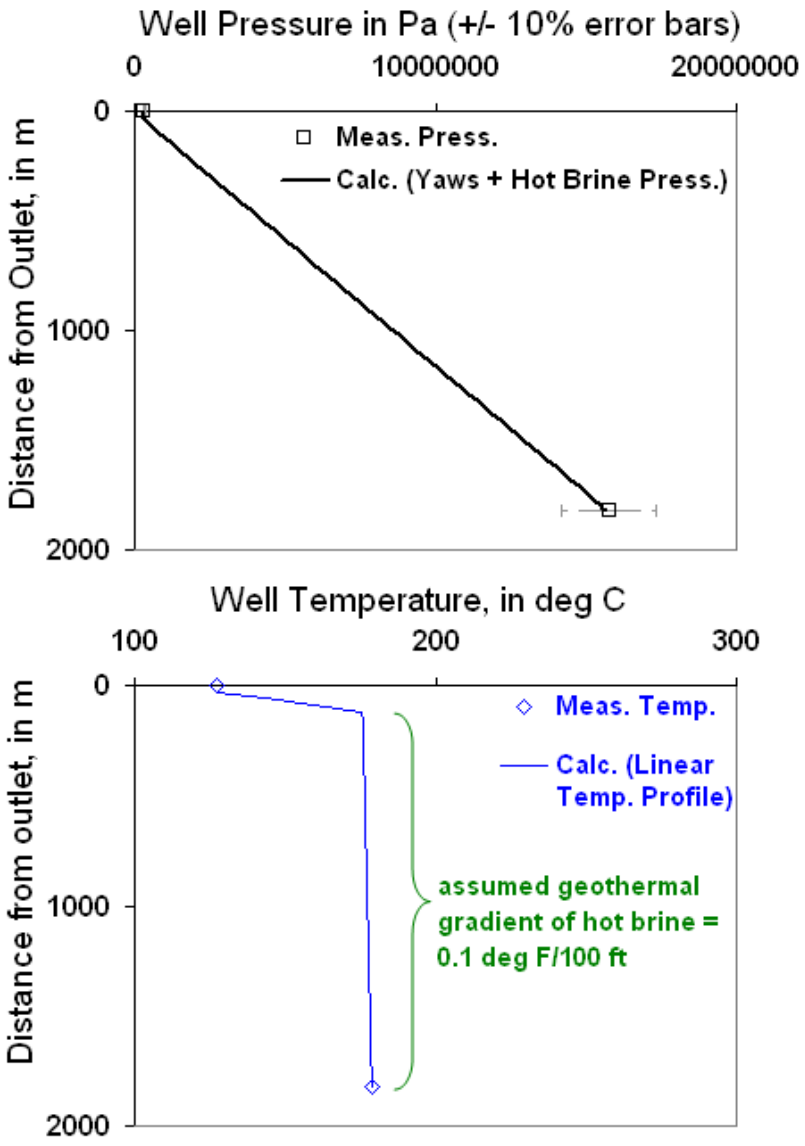

Figure 7.5.32: Geothermal well East Mesa 8-1 in Chierici et al. (1981) predicted with the Yaws (1977) correlation above the flash point, single-phase brine flow below the flash point, the known wellhead and bottom-hole temperatures, and an assumed hot brine geothermal temperature gradient. The flash depth is 86 m.

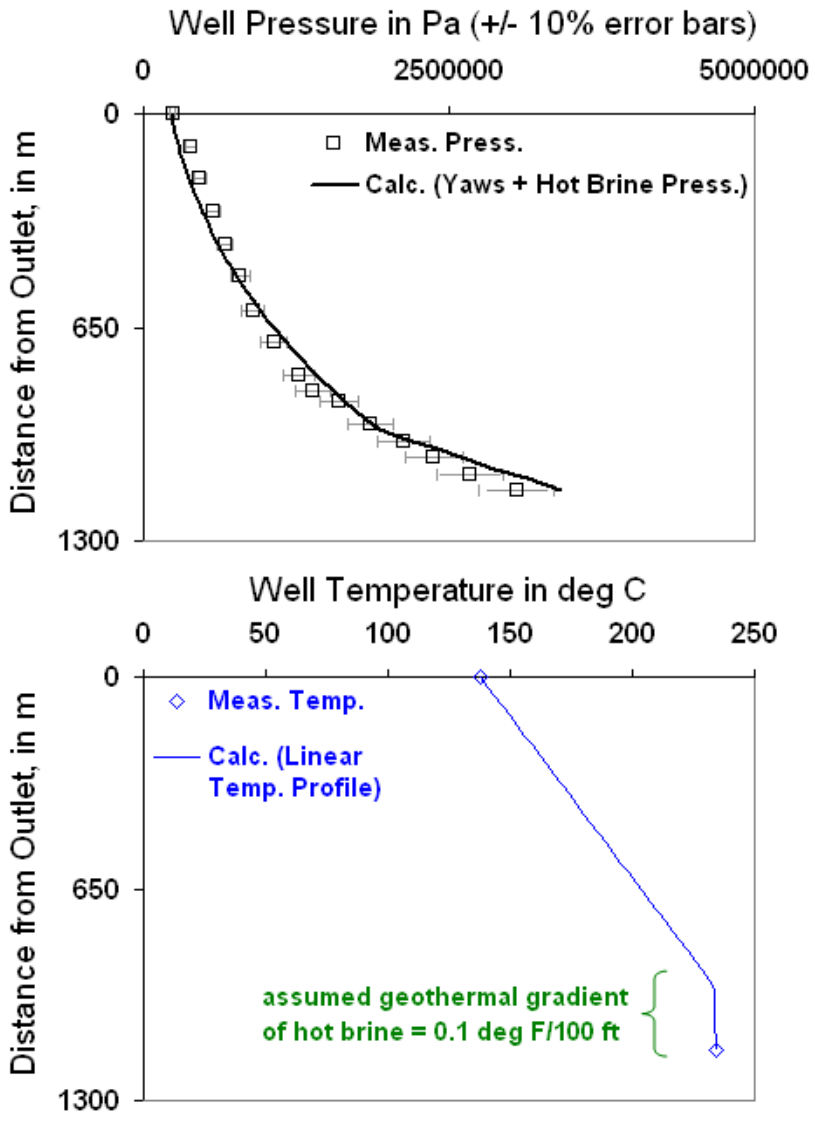

Figure 7.5.33: Geothermal well KE1-3 in Tachimori (1982) predicted with the Yaws (1977) correlation above the flash point, single-phase brine flow below the flash point, the known wellhead and bottom-hole temperatures, and an assumed hot brine geothermal temperature gradient. The flash depth is 950 m.

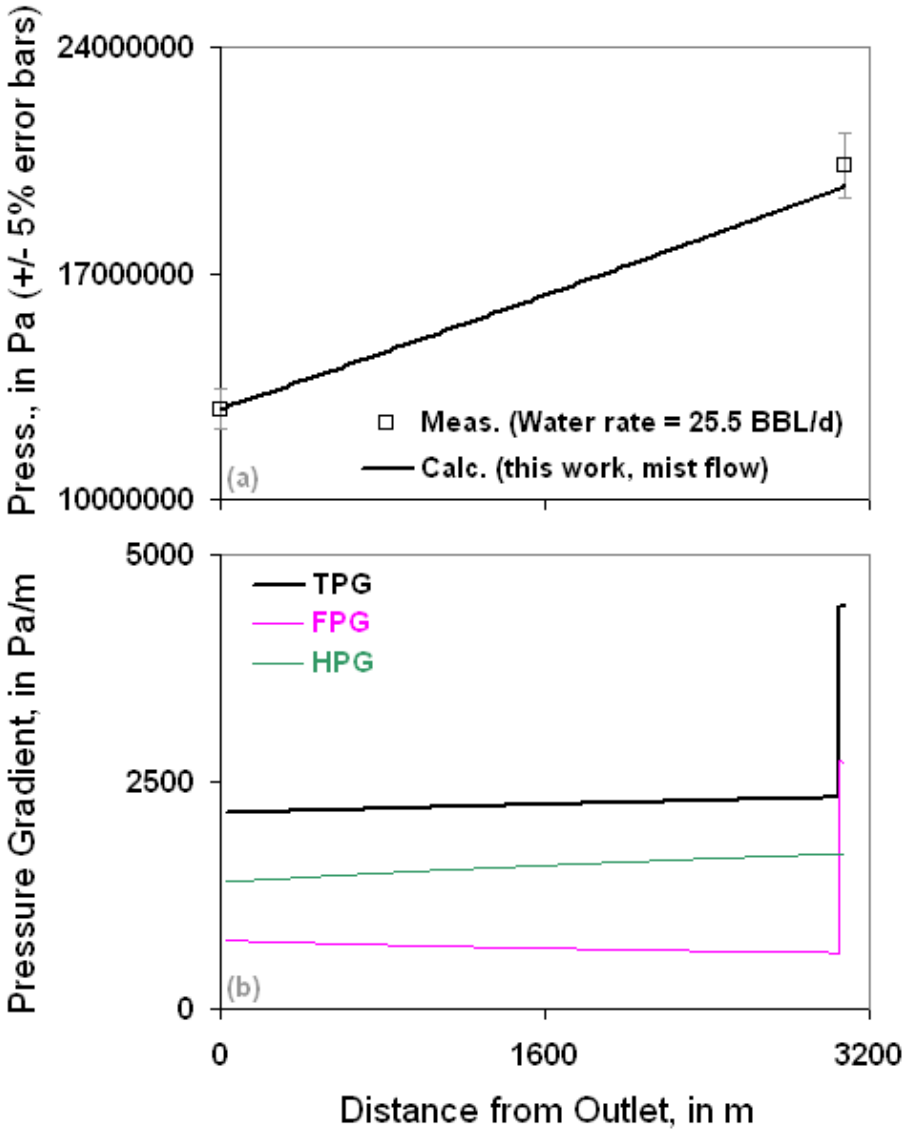

Figure 7.5.34: MIST flow in well 1 (second rate) of Reinicke et al. (1987).

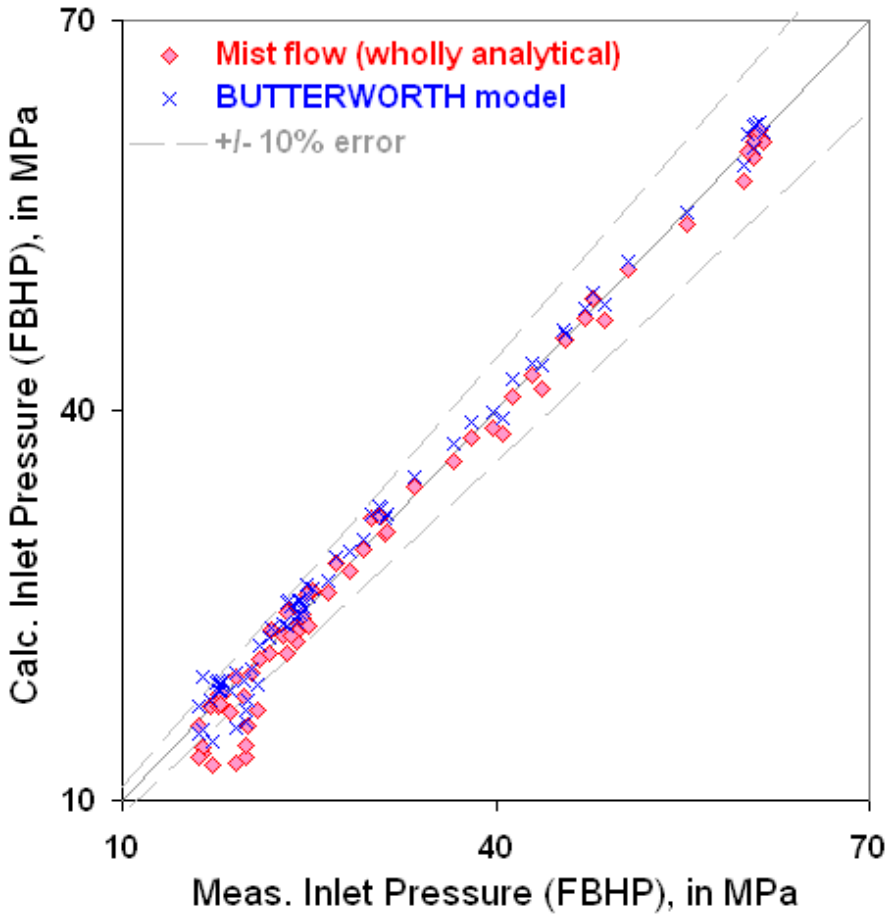

Figure 7.5.35: All of the high-water-cut rate gas-water wells in Reinicke et al. (1987) predicted wholly-analytically with MIST flow. Note that BUTTERWORTH model also furnishes an accurate prediction.

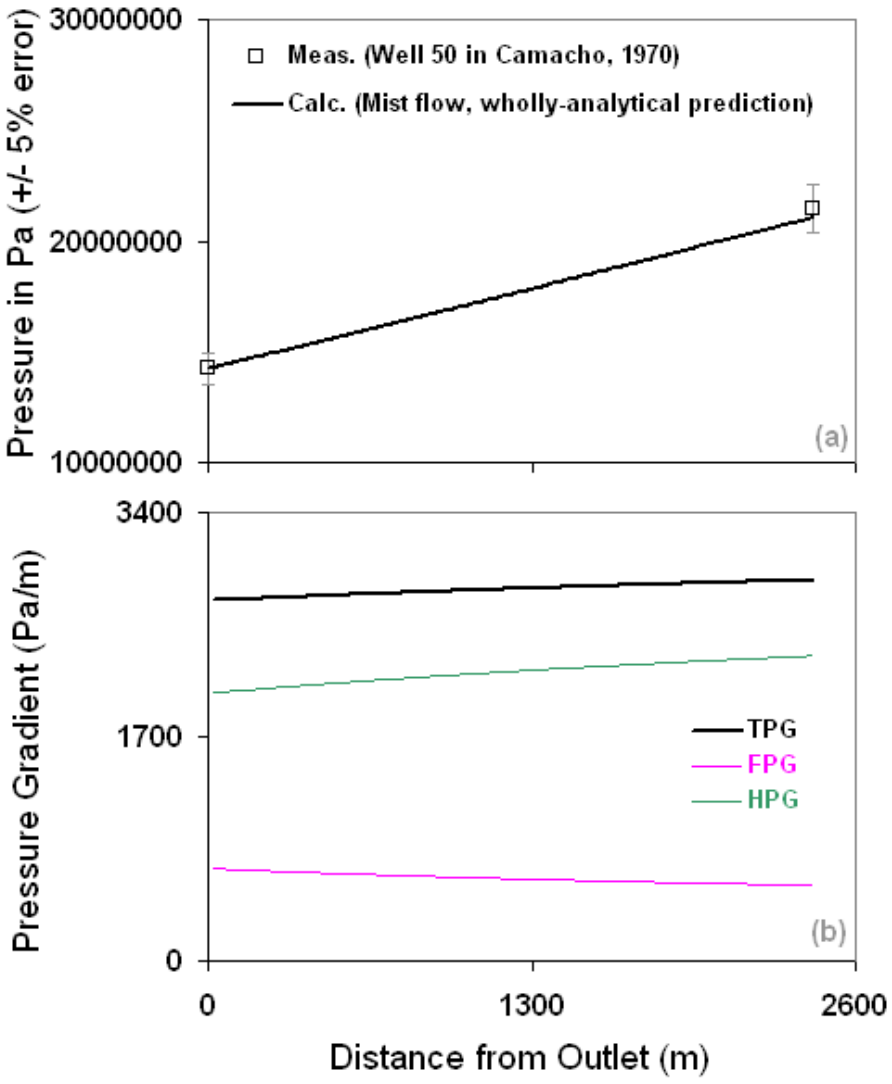

Figure 7.5.36: MIST flow in well 50 of Camacho (1970).

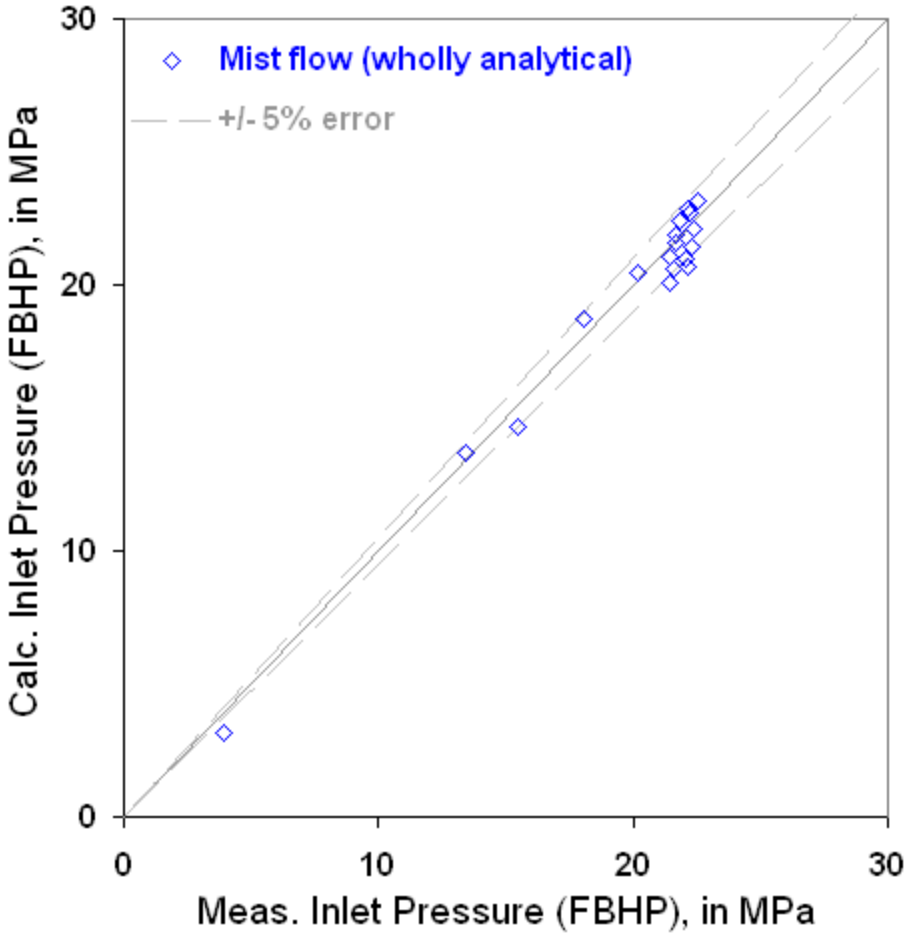

Figure 7.5.37: Representative high-GWR wells in Camacho (1970) predicted wholly-analytically with MIST flow.

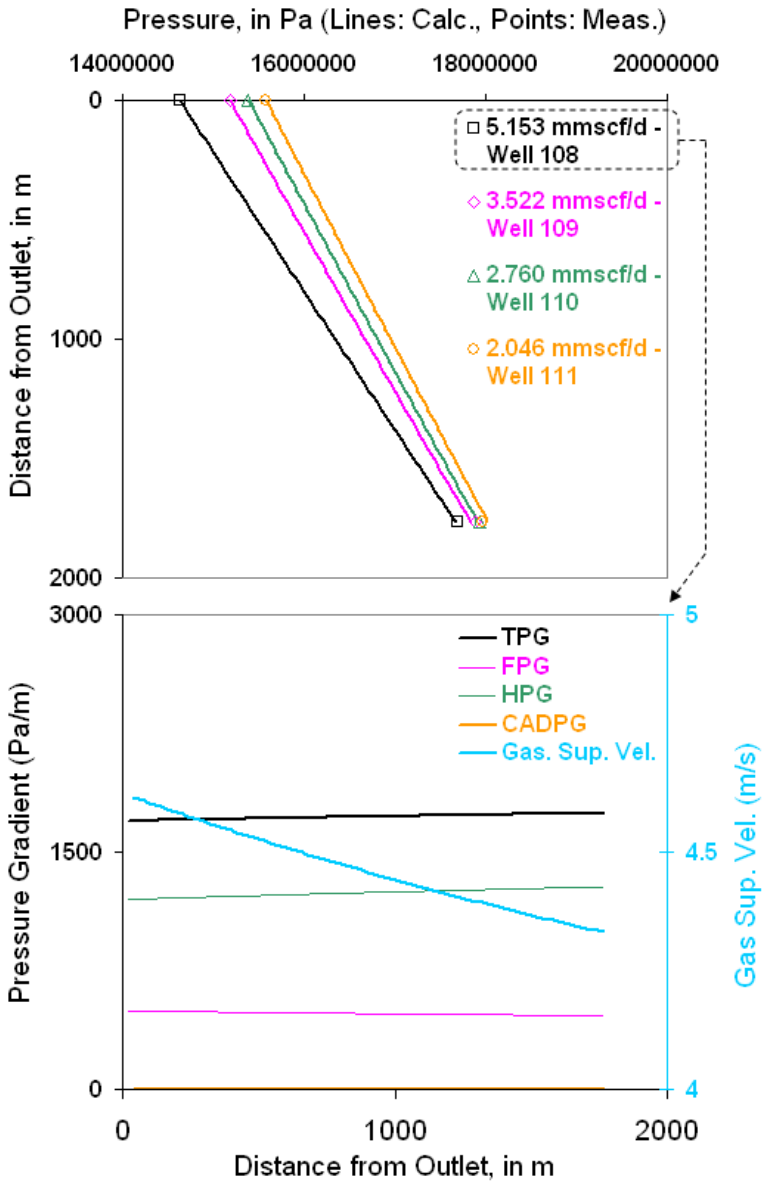

Figure 7.5.38: Validation of the single-phase high pressure natural gas predictions in UTPipeFlow from the single-phase natural gas wells in Camacho (1970).

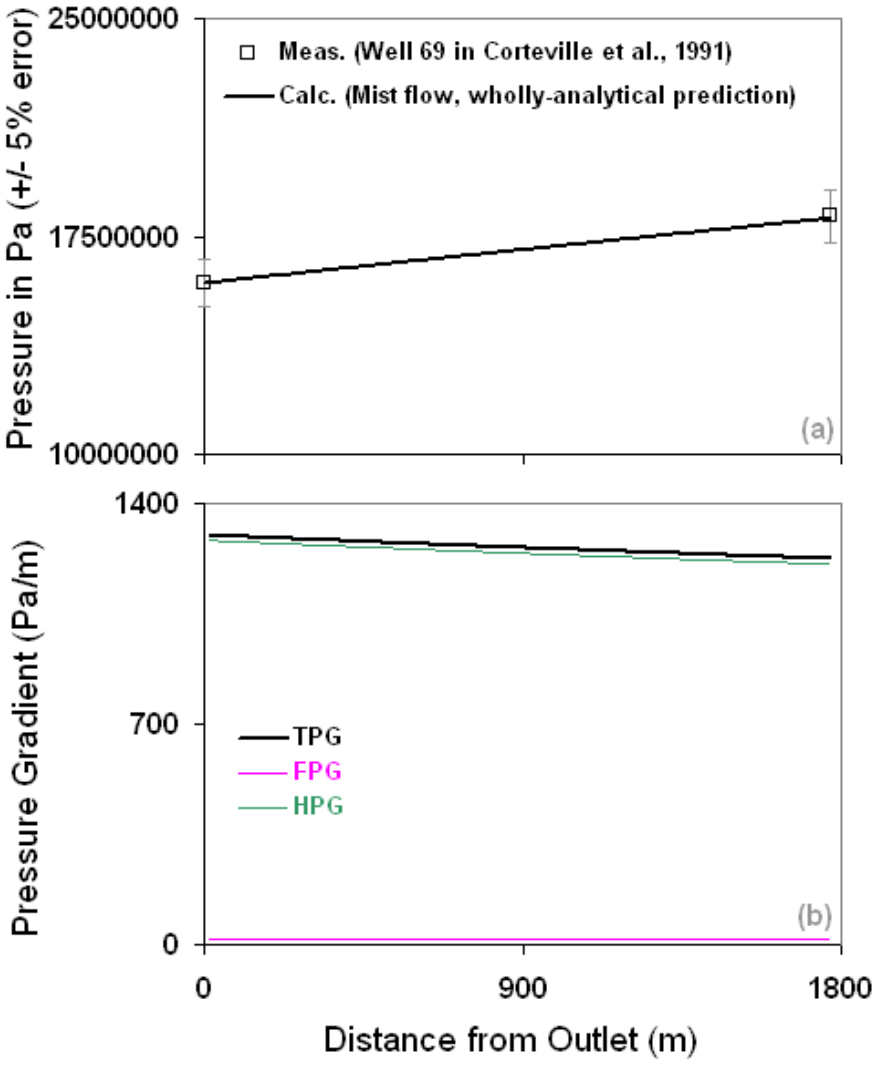

Figure 7.5.39: Two-phase MIST flow in well 69 of Corteville et al. (1991).

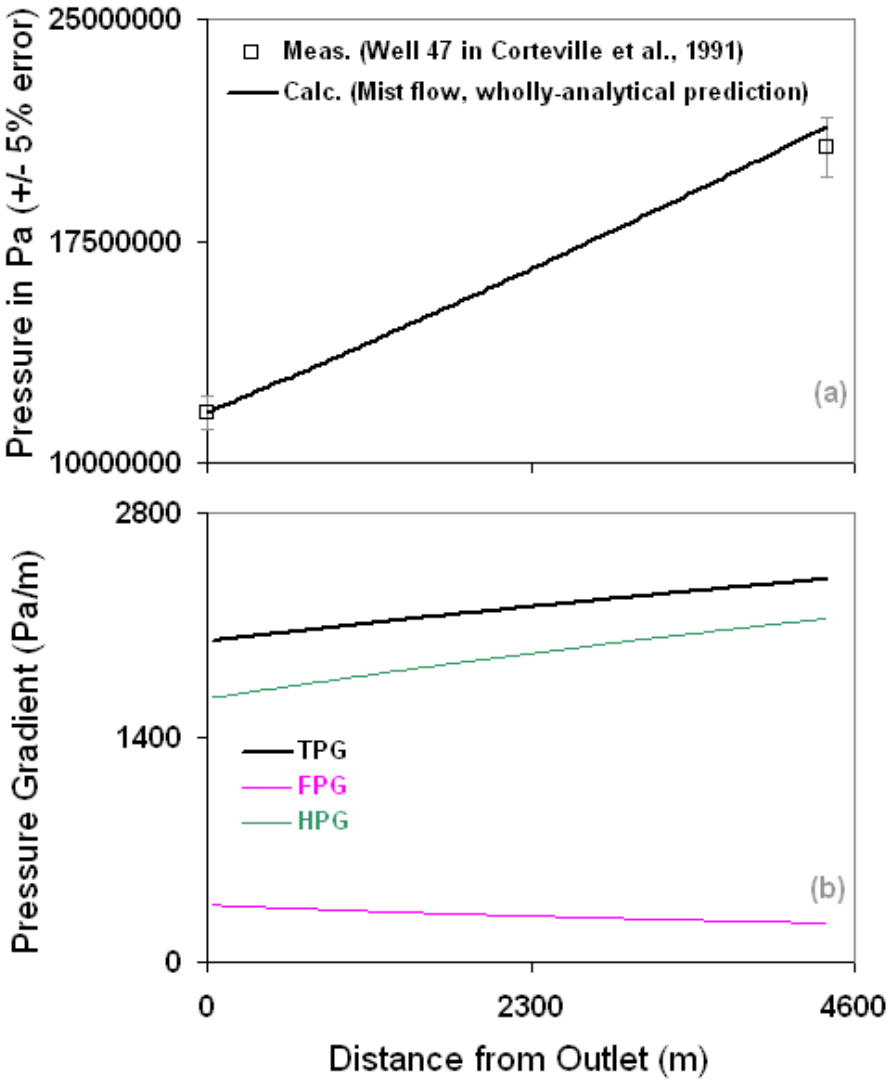

Figure 7.5.40: Three-phase MIST flow in well 47 of Corteville et al. (1991).

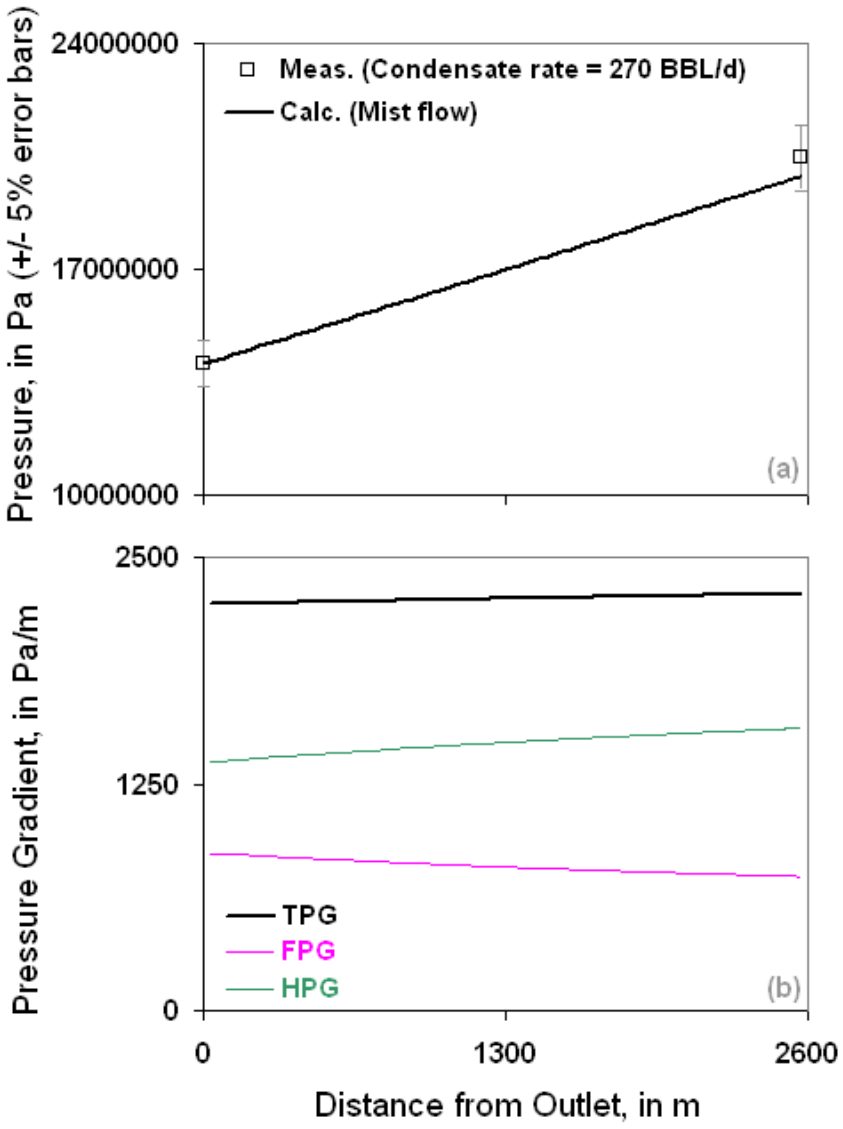

Figure 7.5.41: MIST flow in well 17 of Govier and Fogarasi (1975). The water rate is 12.2 BBL/d water and the GCR = 36259 scf/BBL.

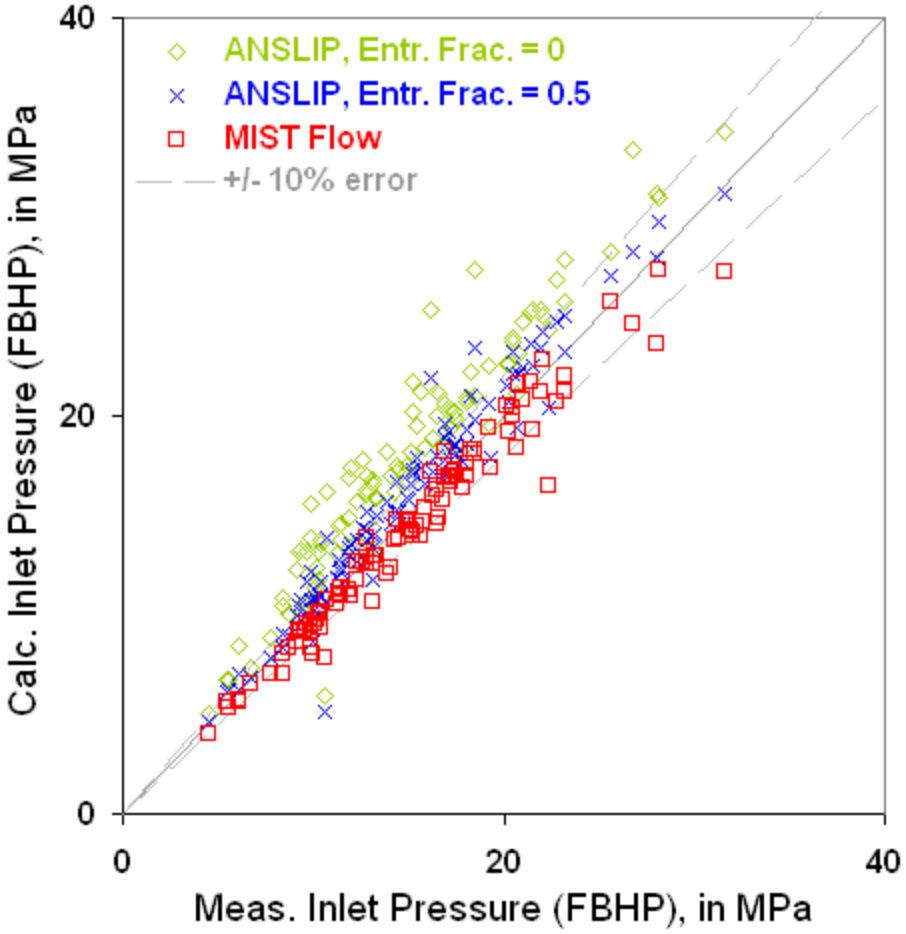

Figure 7.5.42: Validating the MIST flow predictions of all 102 low-pressure Govier and Fogarasi (1975) Canadian wells.

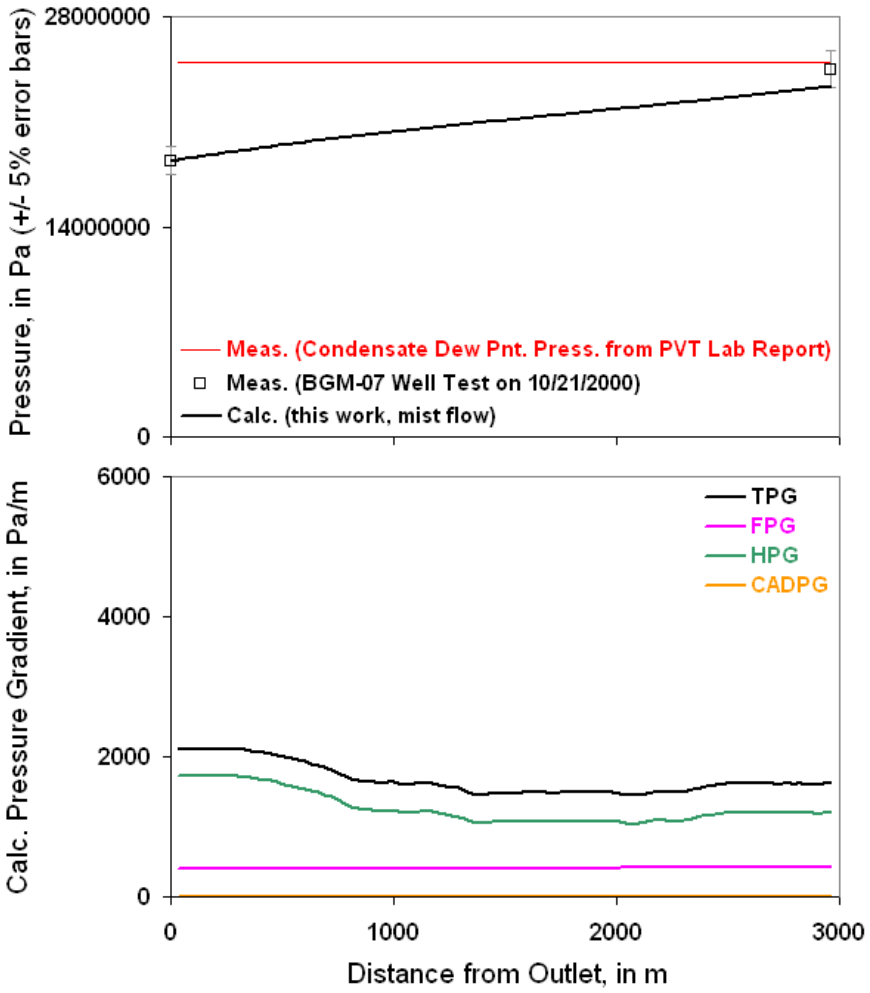

Figure 7.5.43: A deviated, compositional, high GCR well (GCR of 133,988 scf/BBL with a condensate rate of 227 BBL/d) exhibiting MIST flow. Separator conditions were 58 deg F and 956 psig, and the wellhead pressure was 2655 psig.

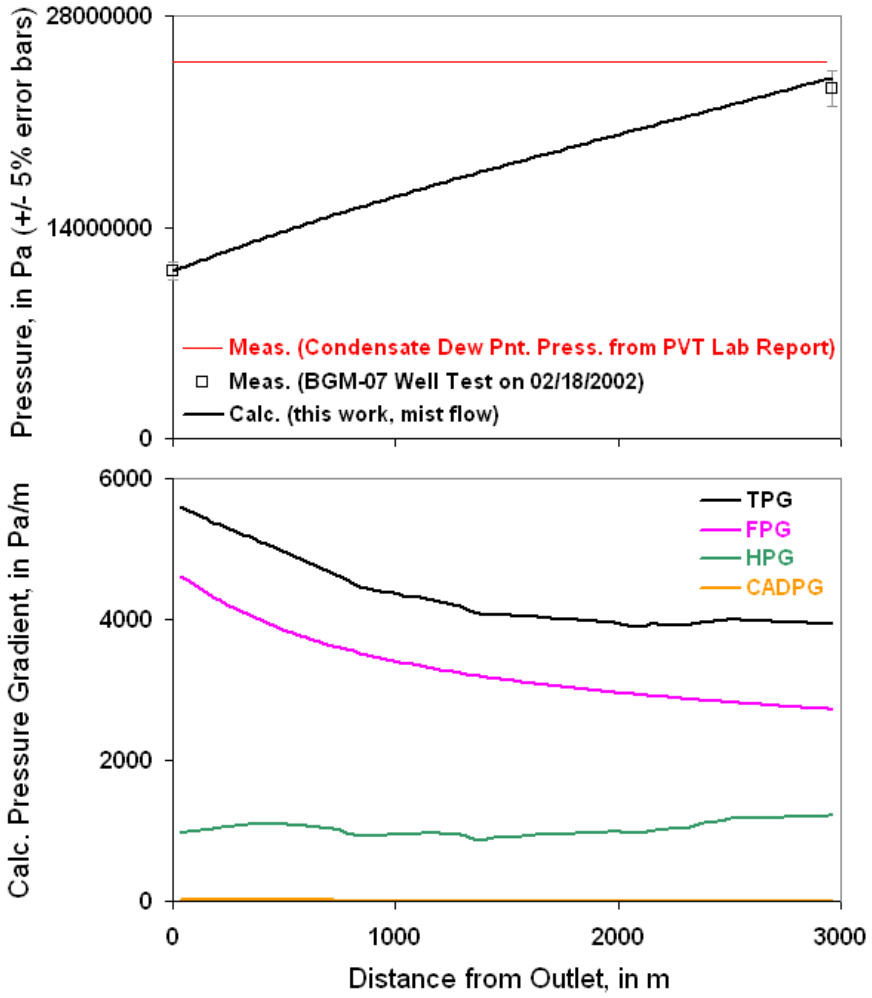

Figure 7.5.44: The same deviated, compositional, high GCR well of Fig. 7.4.43 exhibiting MIST flow but now at a later time in the life of the well (GCR of 135,441 scf/BBL with a condensate rate of 578 BBL/d). Separator conditions were 68 deg F and 1016 psig, and the wellhead pressure was 1595 psig. These facility conditions of a lower wellhead pressure and higher condensate rate in comparison to Fig. 7.4.43 results in a friction-dominant system rather that the hydrostatic-dominant system that was present earlier in this well's life.

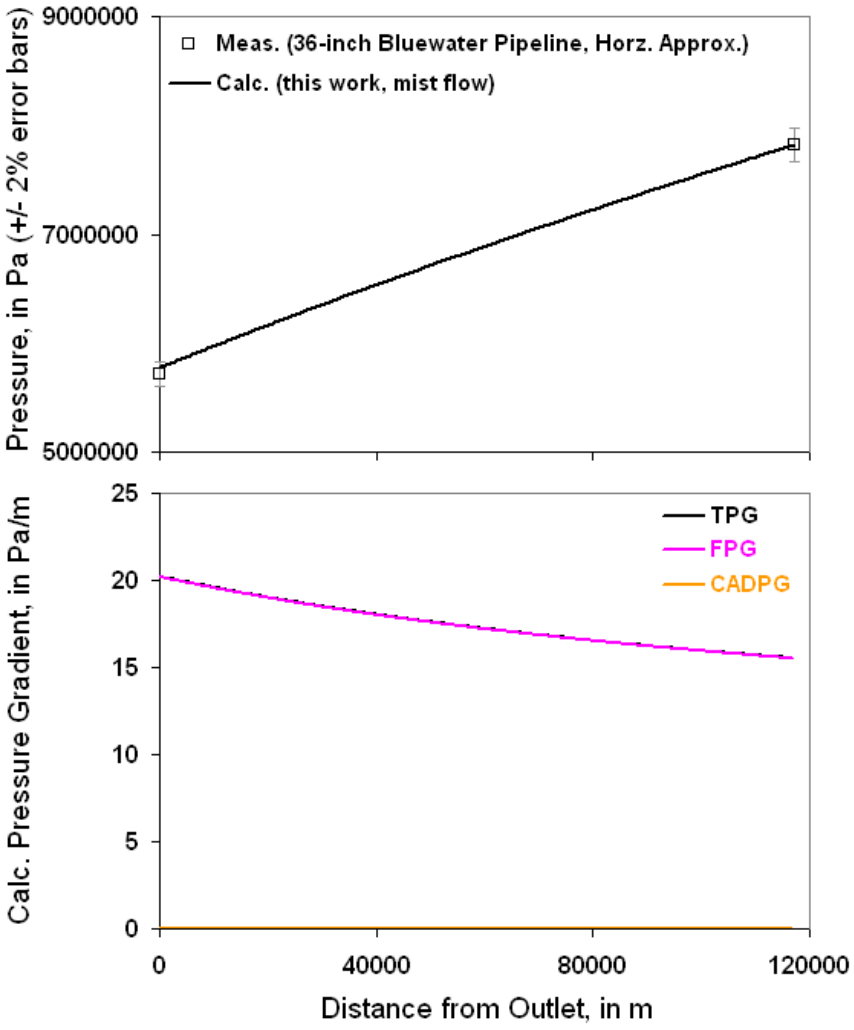

Figure 7.5.45: The 73 miles long, 36-inch diameter Bluewater gas-condensate pipeline in Crowley et al. (1986) predicted with a horizontal pipe flow approximation and the MIST flow analytical model.

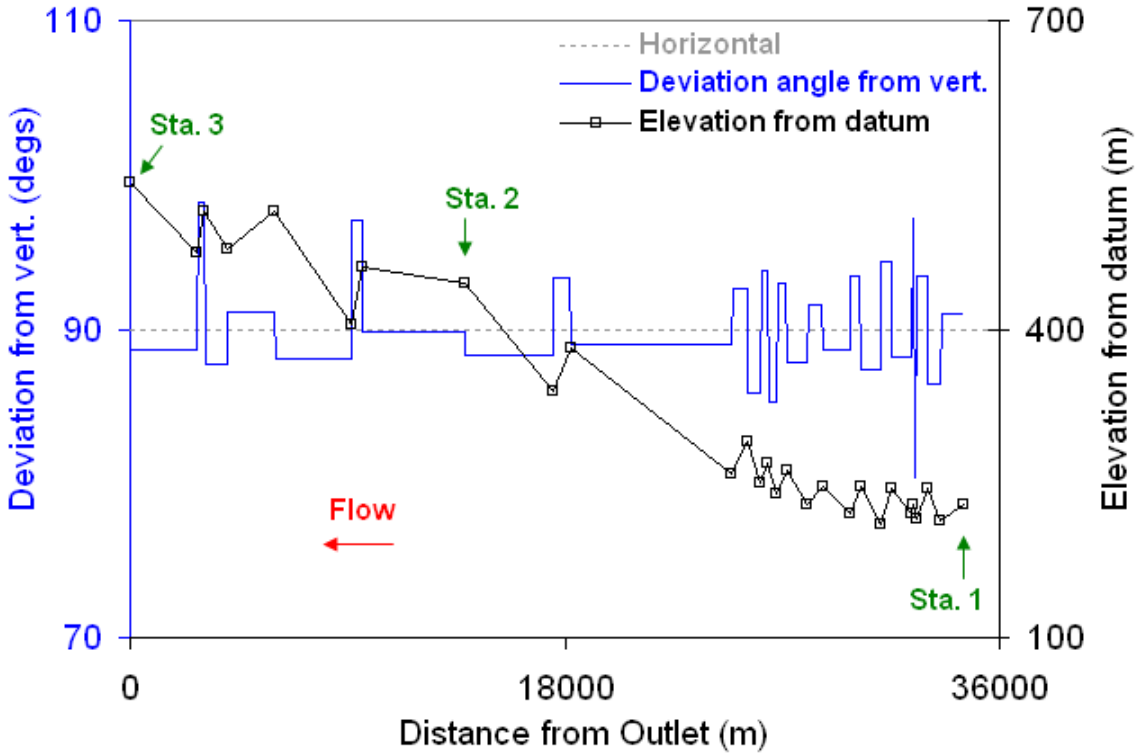

Figure 7.5.46: The elevation profile for the AGA line 72 of Gregory (1981).

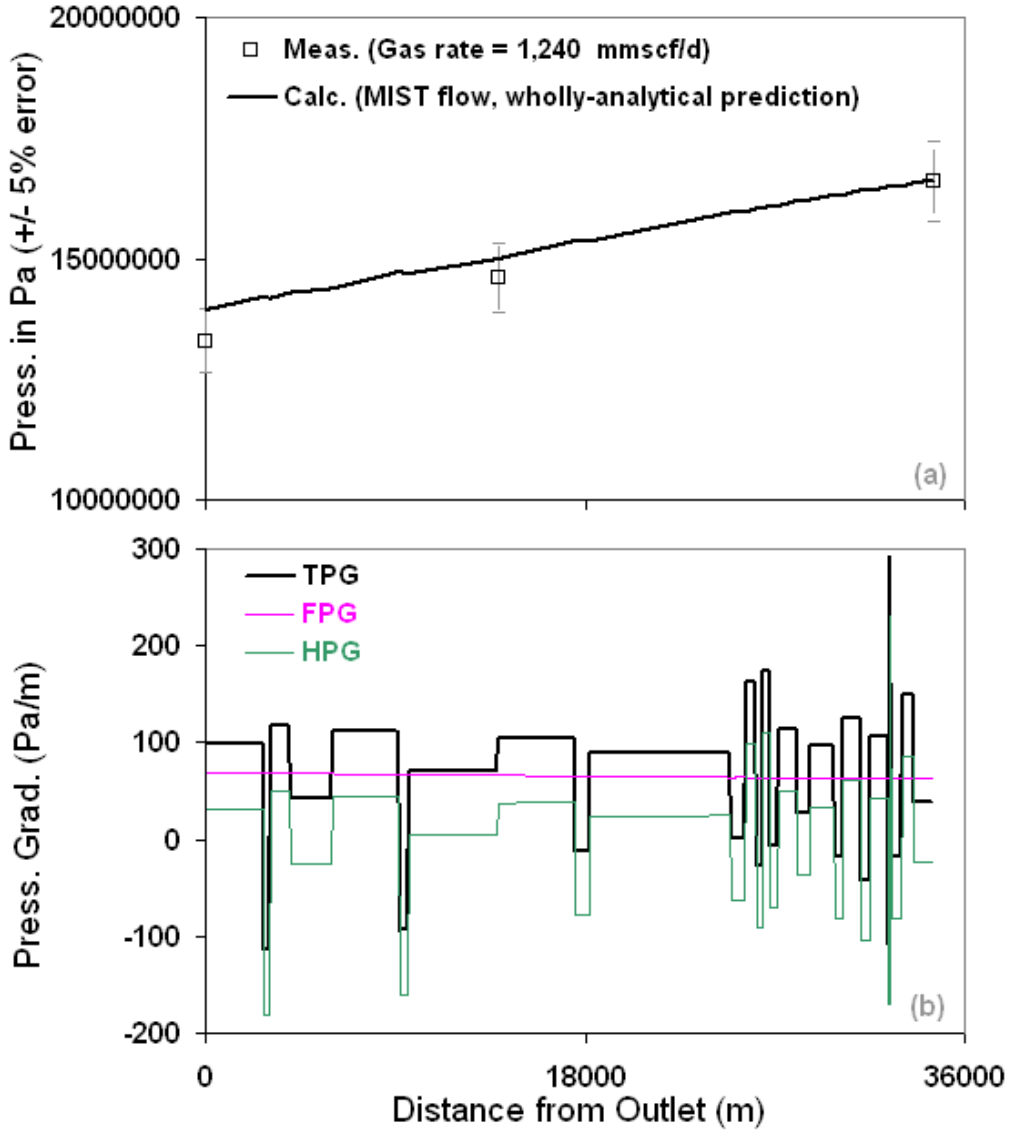

Figure 7.5.47: A representative run of the AGA line 72 of Gregory (1981).

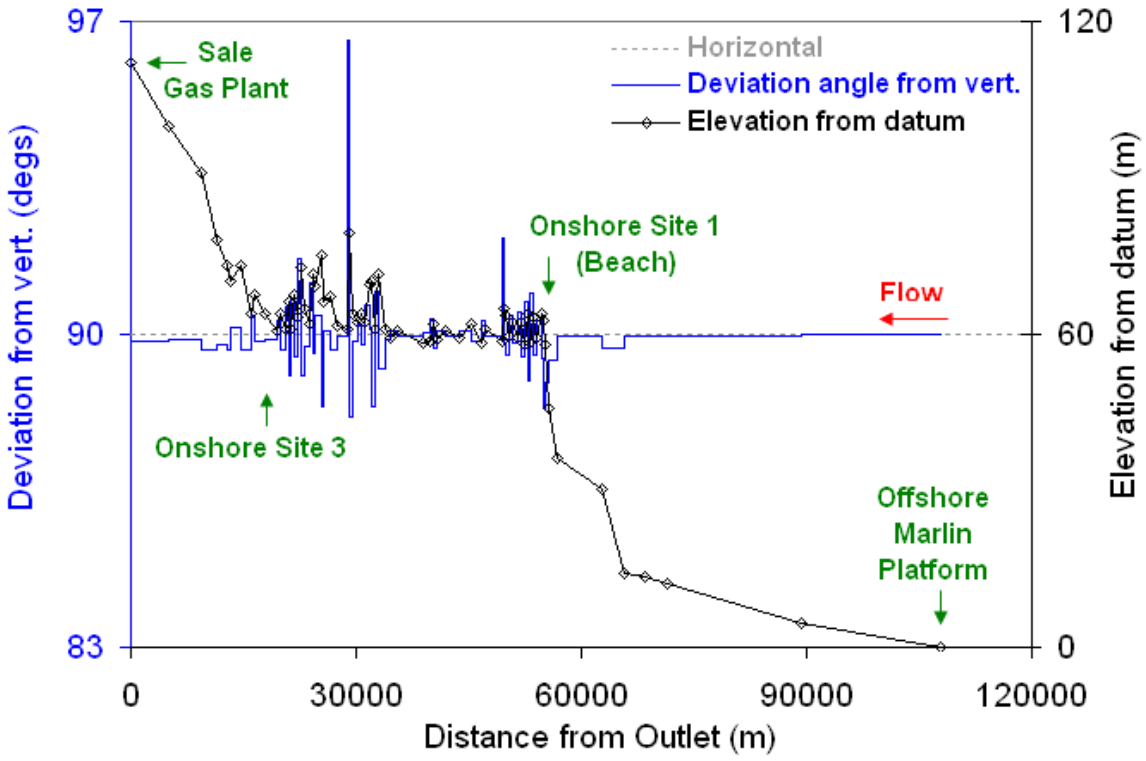

Figure 7.5.48: The elevation profile for the 20-inch AGA line 17 of Gregory (1981). This is the same pipe line as given in Cunliffe (1978).

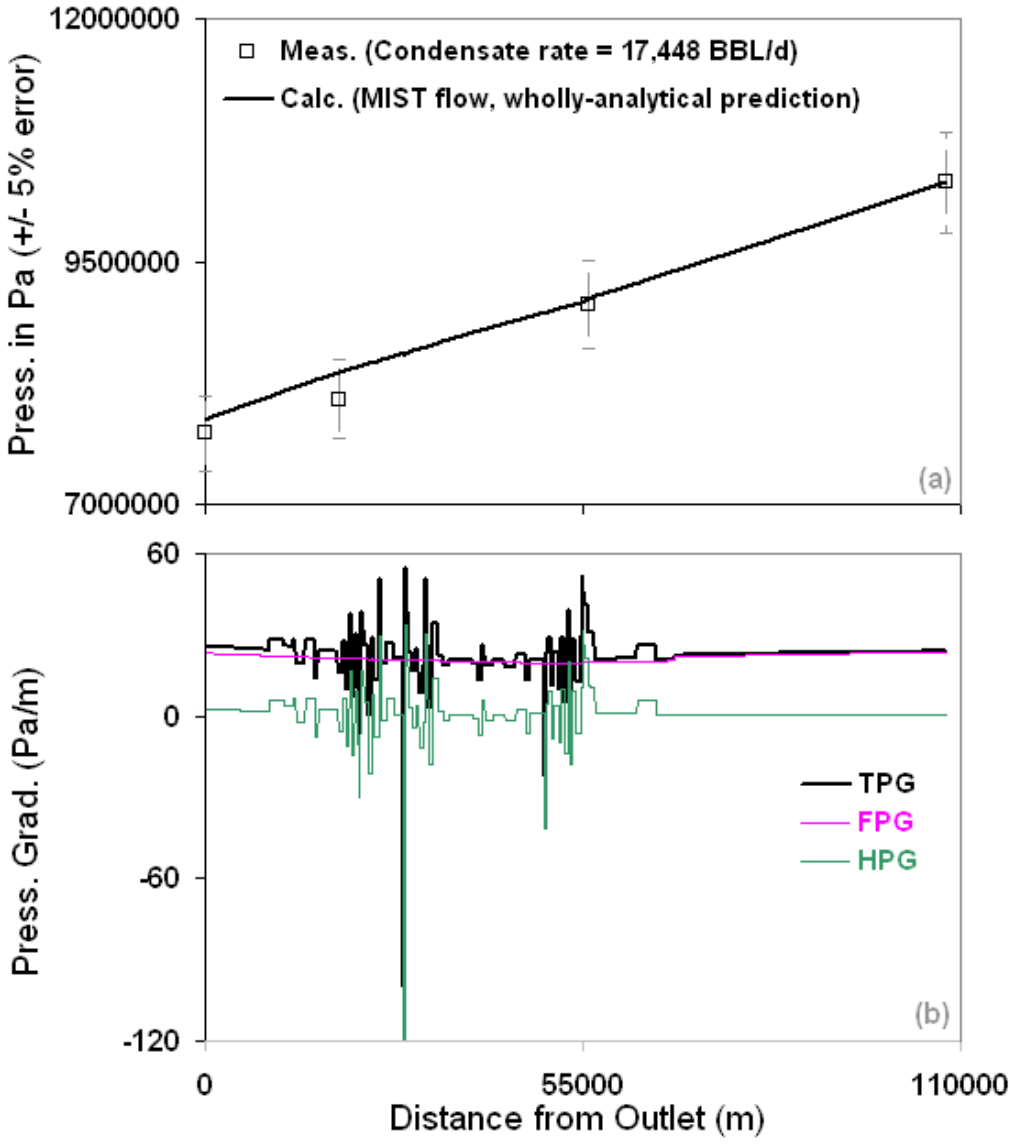

Figure 7.5.49: A representative run of the AGA line 17 of Gregory (1981).

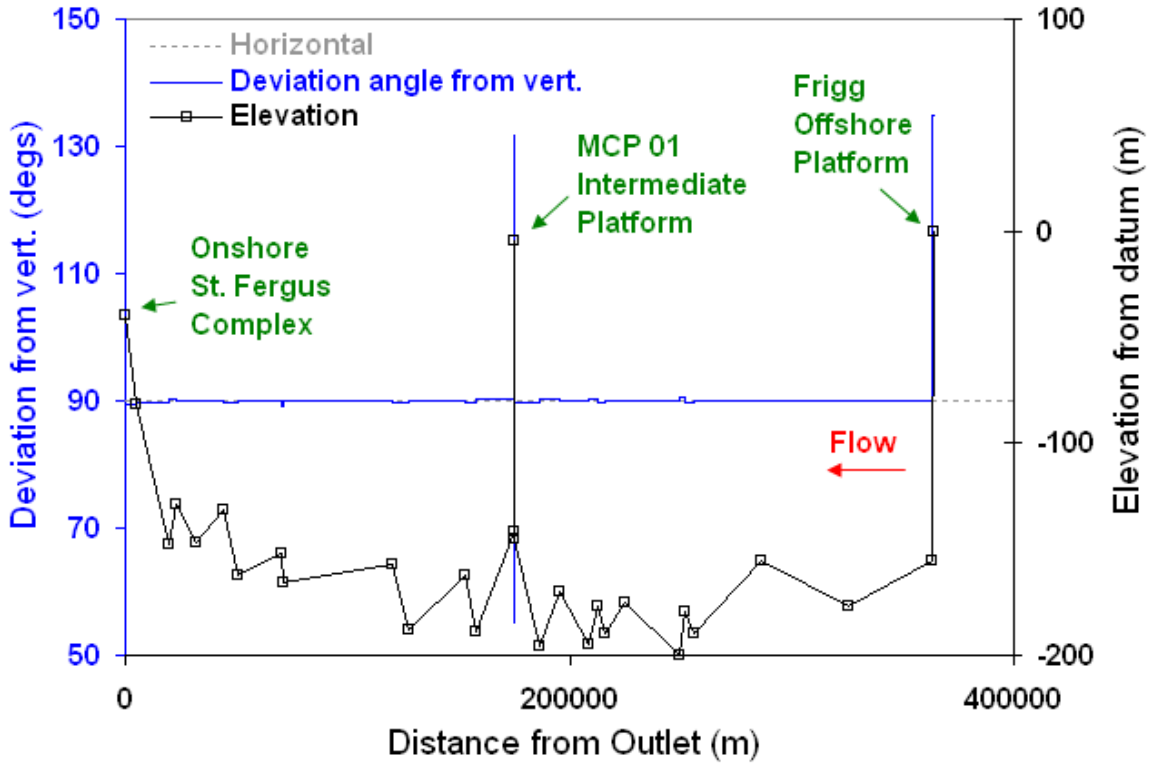

Figure 7.5.50: The elevation profile for the 226 miles long, 32-inch North Sea Frigg pipeline of Lagiere et al. (1984).

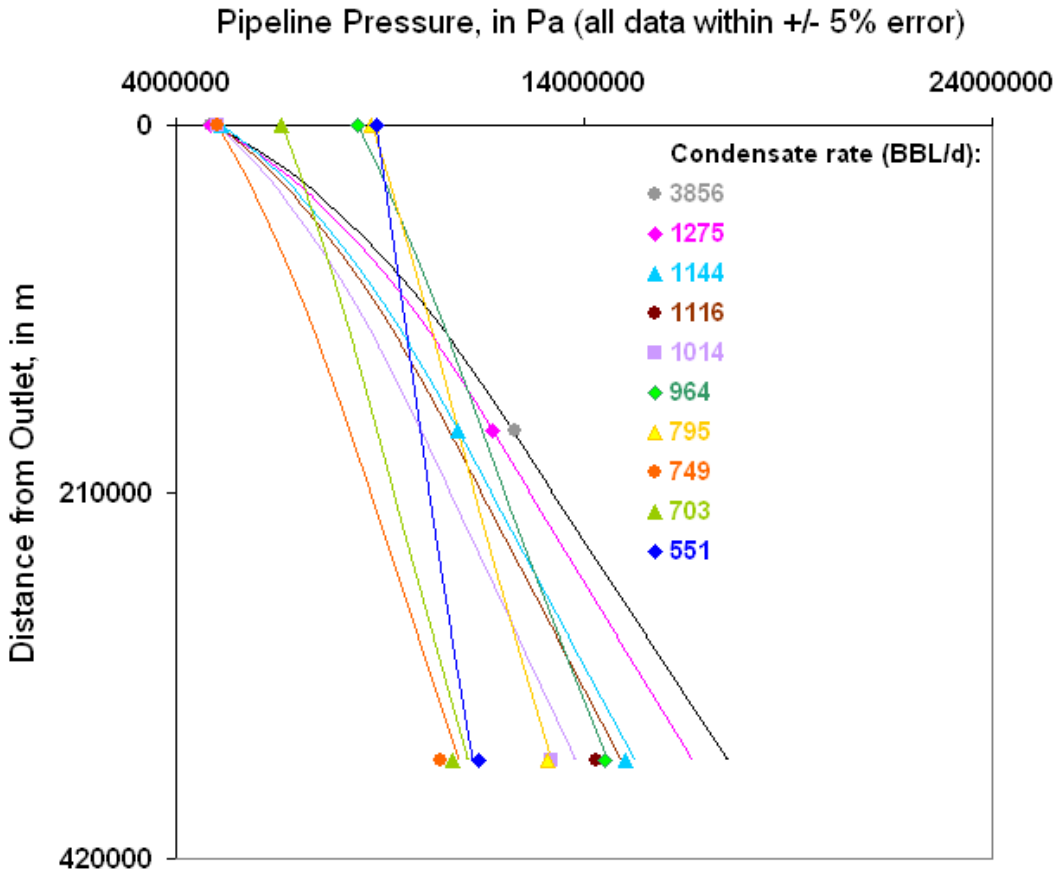

Figure 7.5.51: All of the datasets of the North Sea Frigg pipeline of Lageire et al. (1984) predicted with the wholly-analytical ANSLIP model and a horizontal pipeline approximation. Points are measurements and lines are our analytical model's predictions.

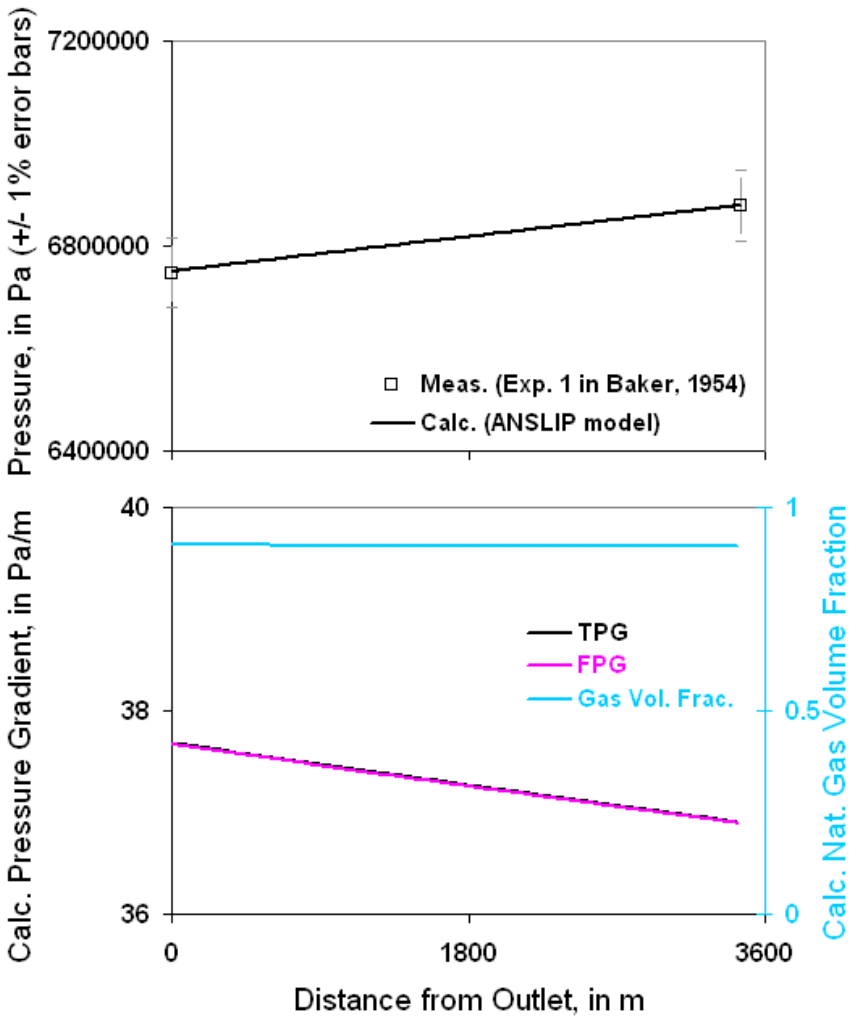

Figure 7.6.1: Experiment no. 1 in Baker (1954) predicted with the ANSLIP wholly analytical model.

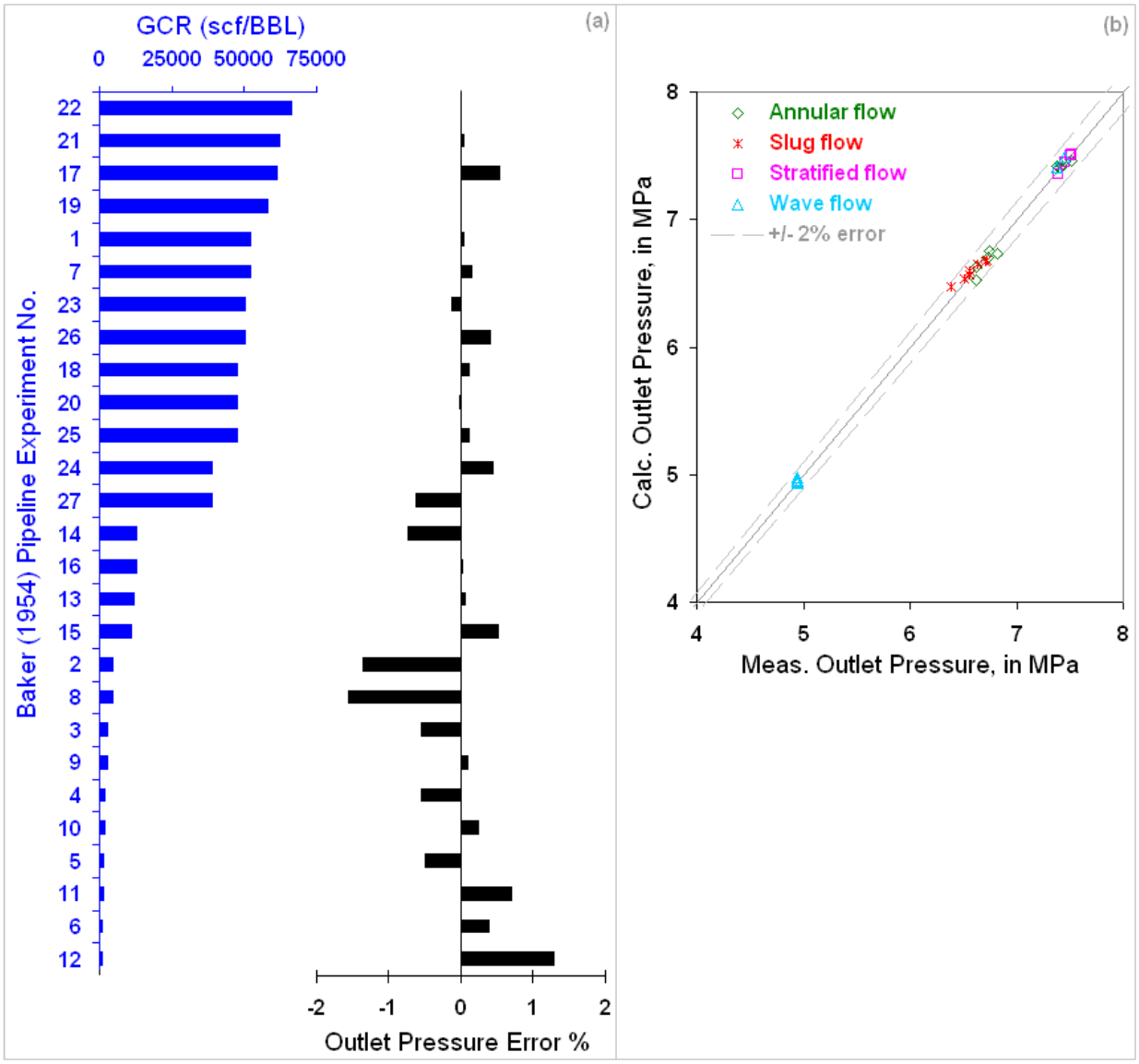

Figure 7.6.2: All of the experiments of Baker (1954) predicted with the ANSLIP wholly analytical model.

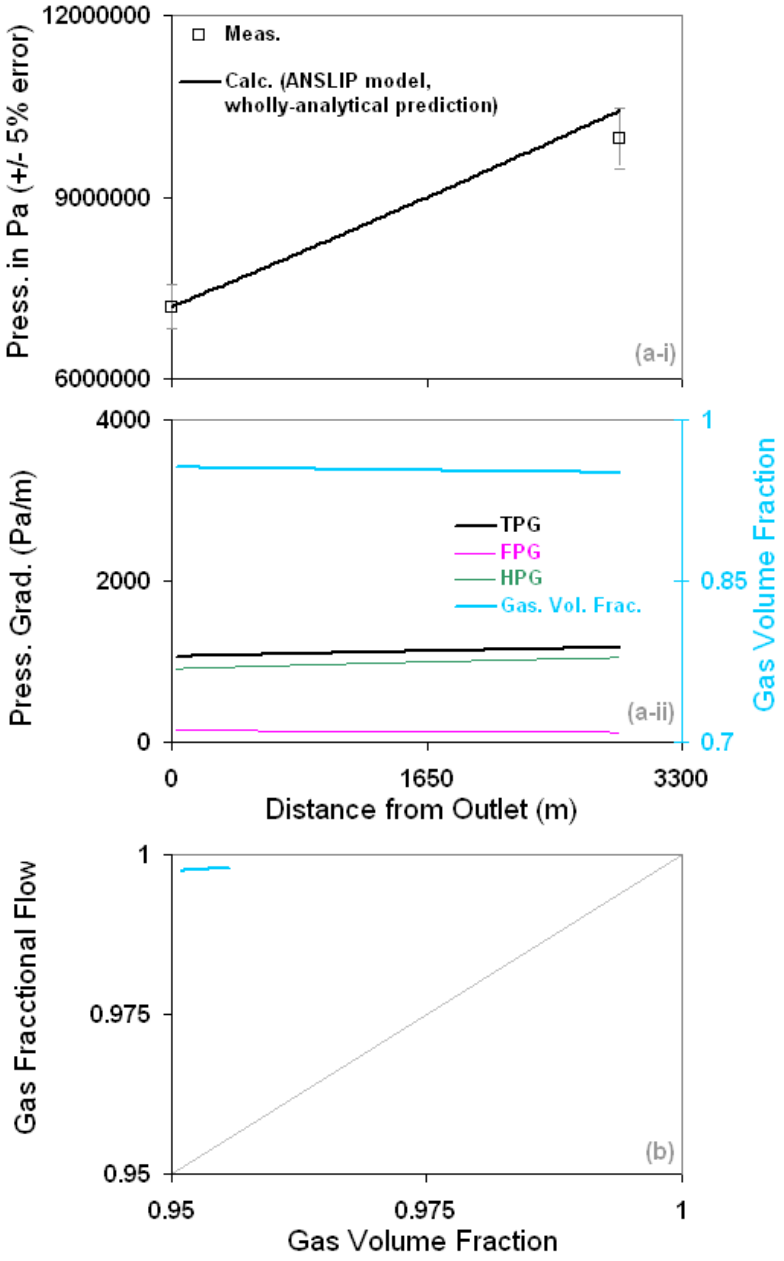

Figure 7.6.3: Prediction of the gas-water well case 4 of Chierici et al. (1974) with the ANSLIP model.

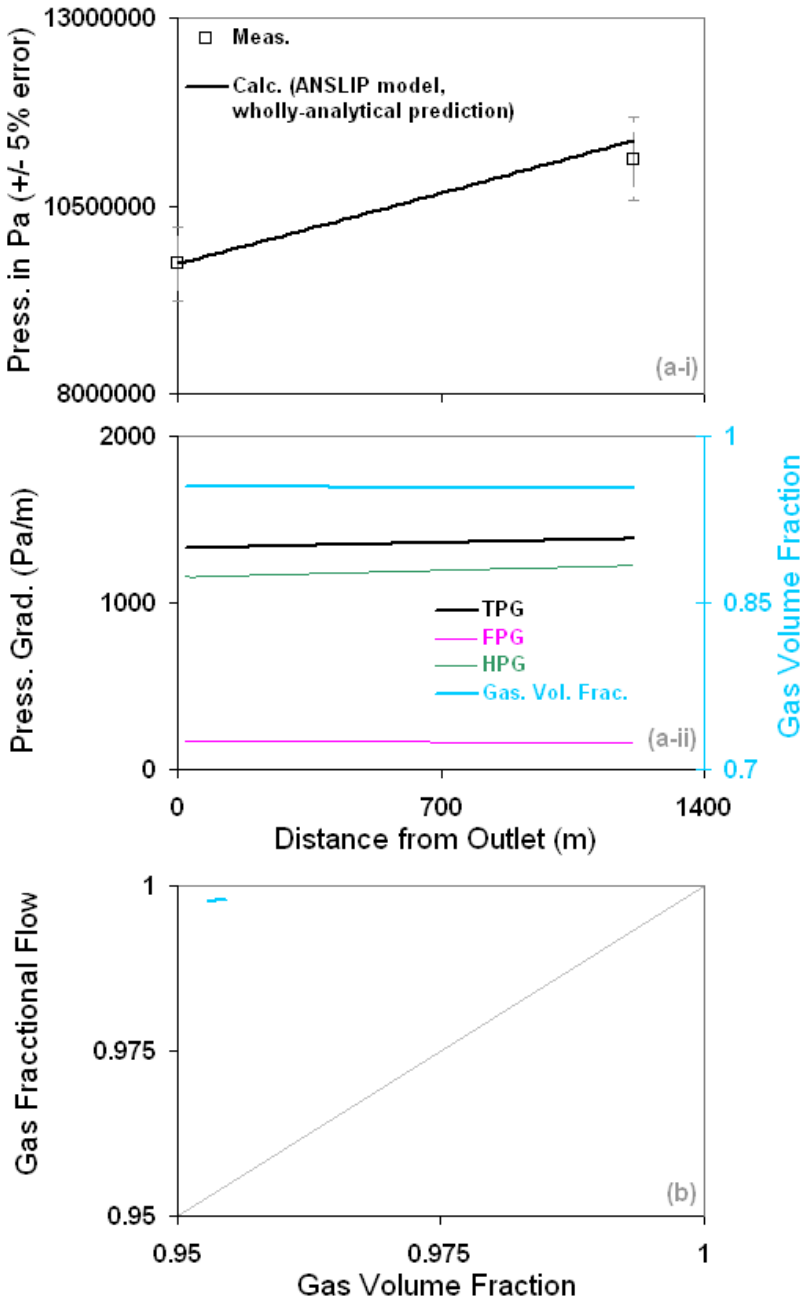

Figure 7.6.4: Prediction of the gas-water well case 5 of Chierici et al. (1974) with the ANSLIP model.

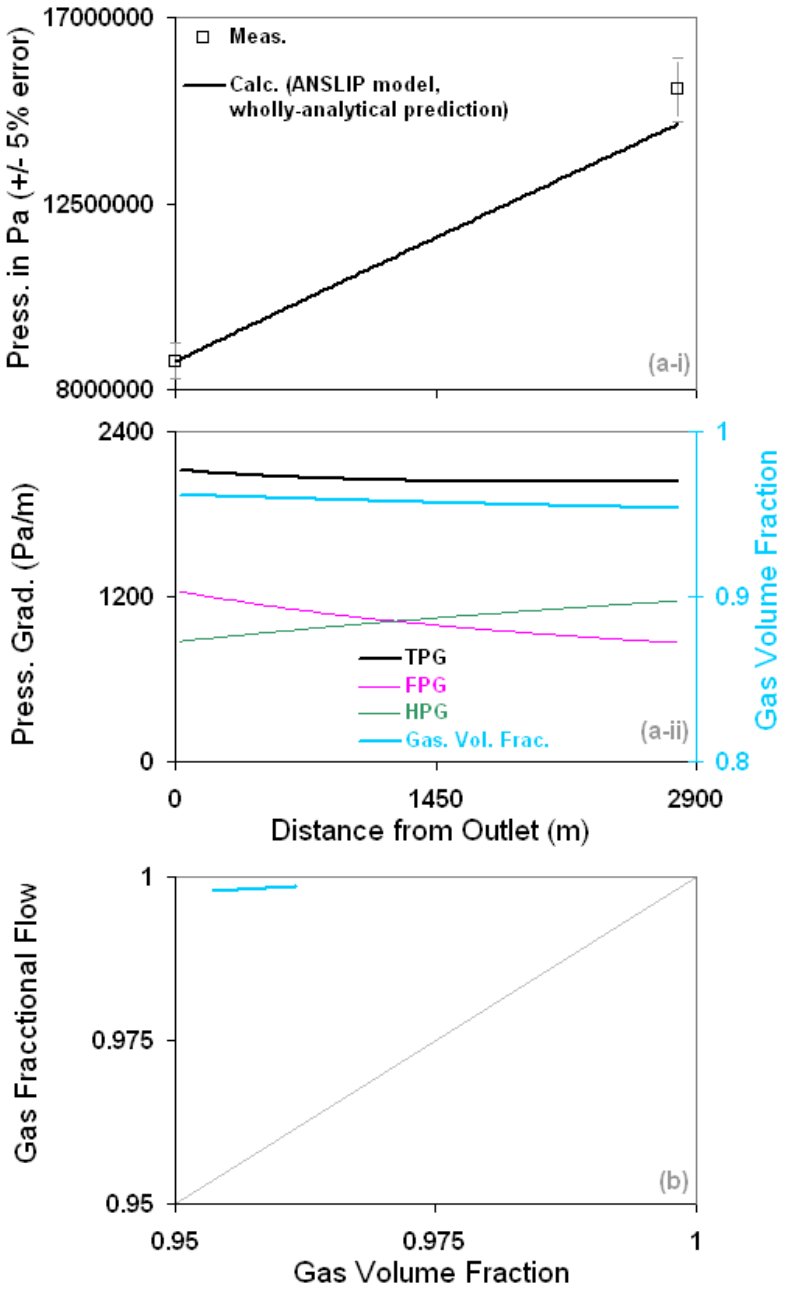

Figure 7.6.5: Prediction of the gas-water well case 6 of Chierici et al. (1974) with the ANSLIP model.

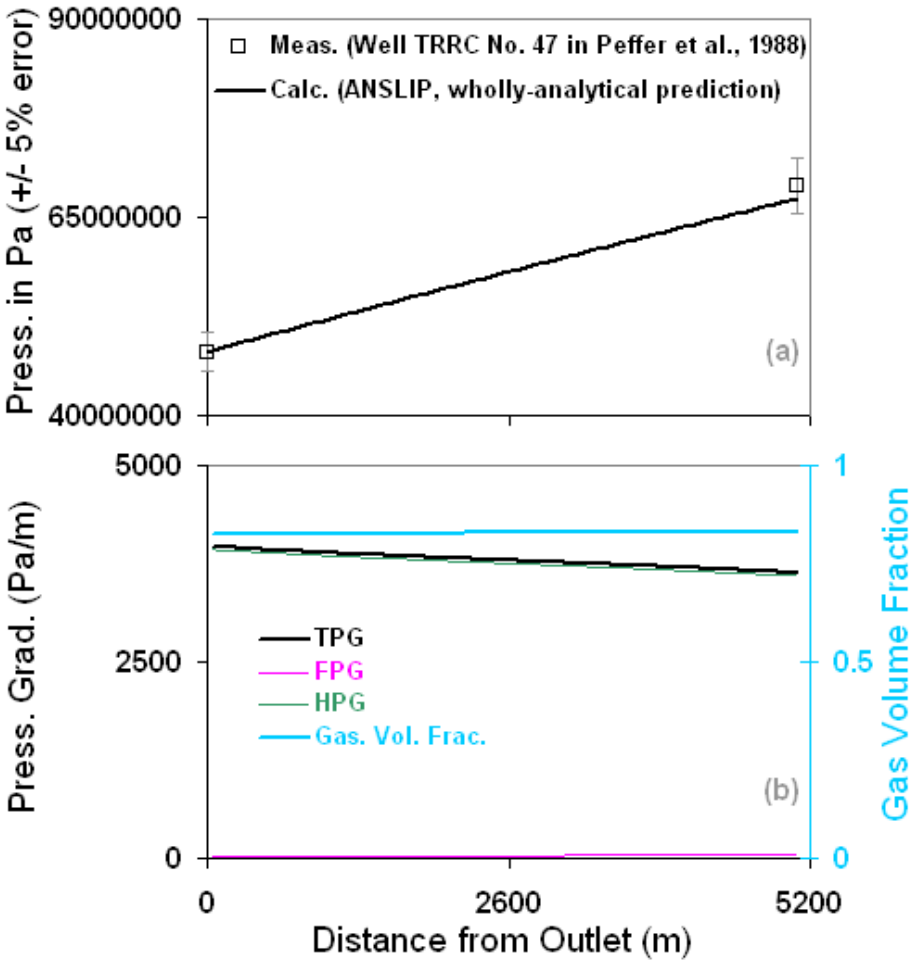

Figure 7.6.6: Prediction of the high GWR well 47 of Peffer et al. (1988) with the ANSLIP model.

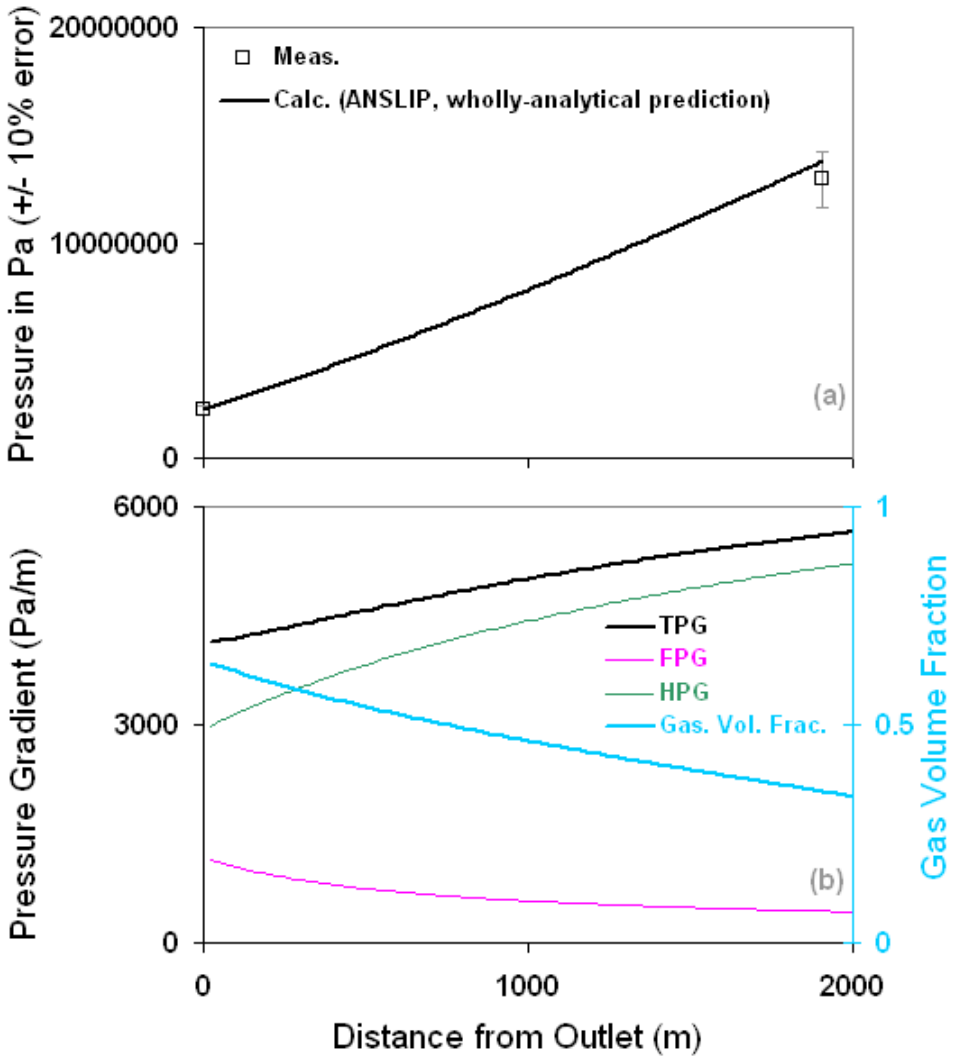

Figure 7.6.7: Prediction of the deviated three-phase well 1 of Corteville et al. (1991) with the ANSLIP model.

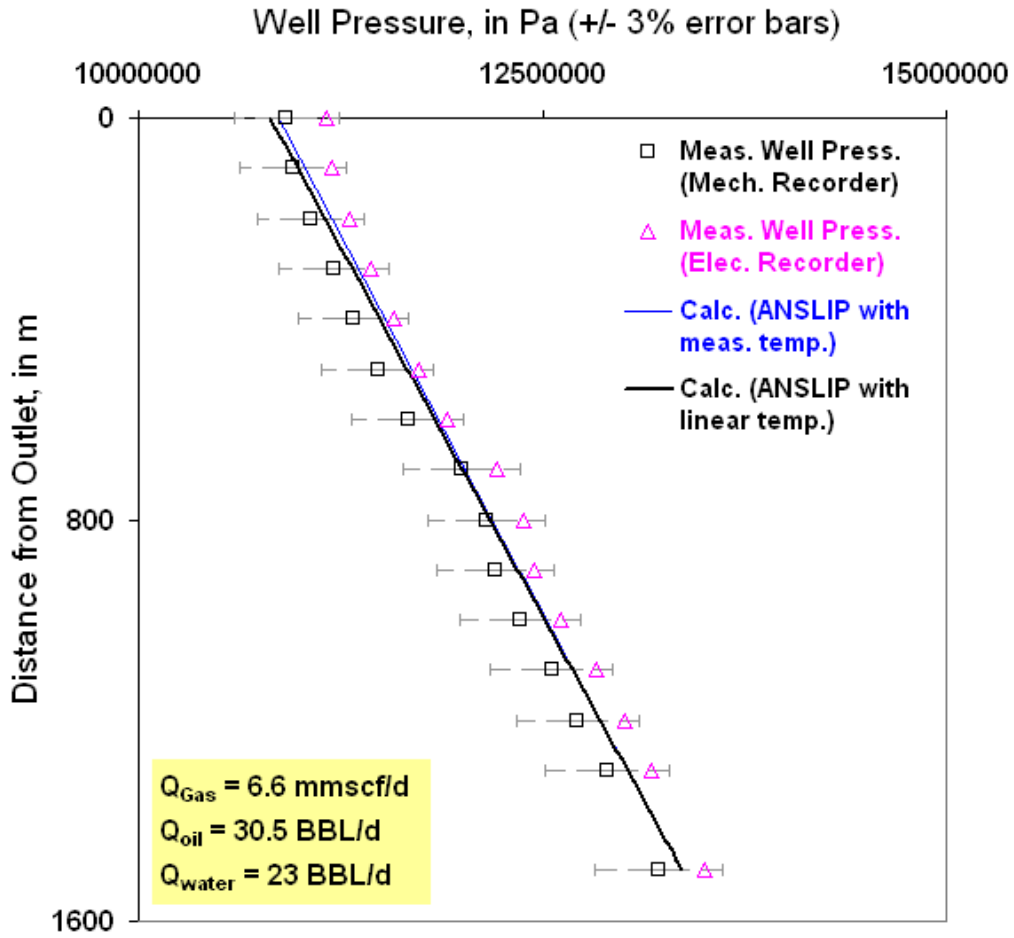

Figure 7.6.8: Prediction of the three-phase annular flow well of Alves et al. (1988) – the first rate in the reference – with the ANSLIP model.

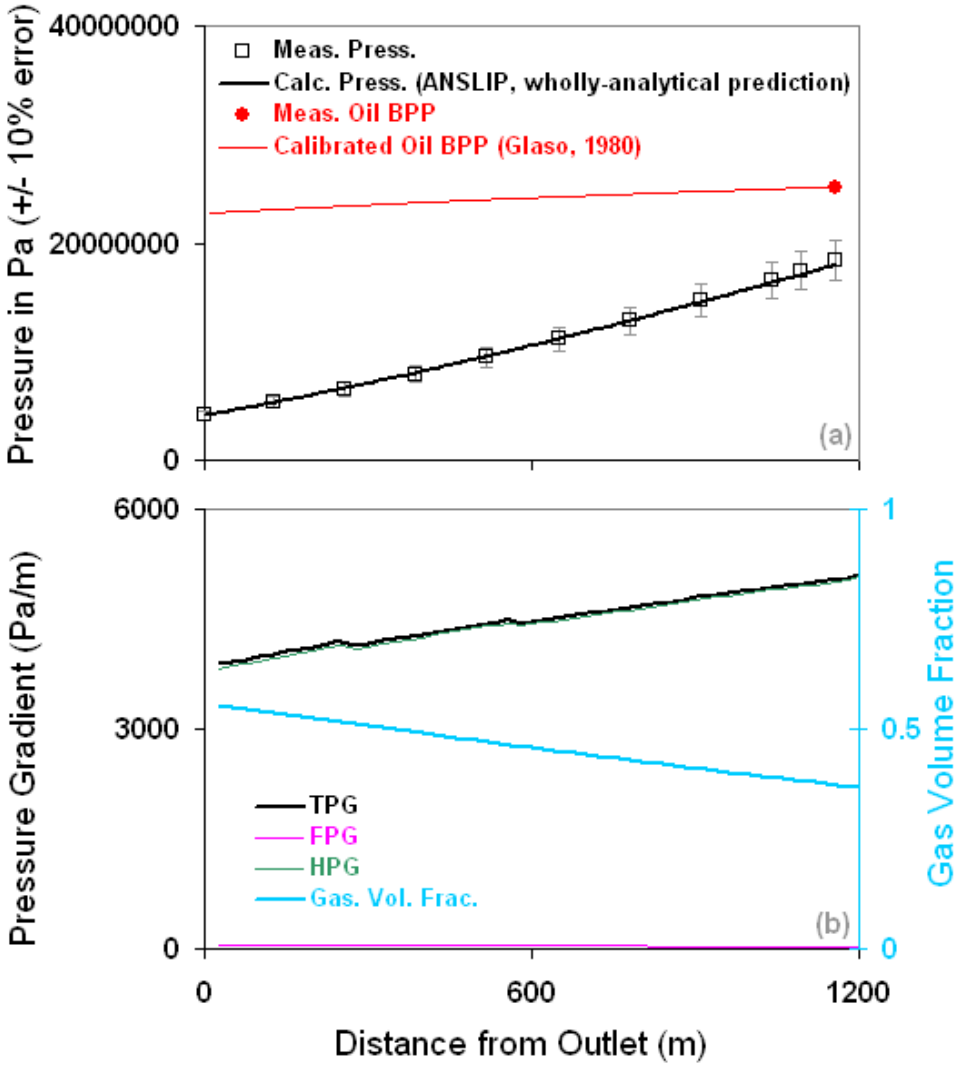

Figure 7.6.9: Prediction of the three-phase, deviated, ExxonMobil well M-3 of Griffith et al. (1973) with the ANSLIP model.

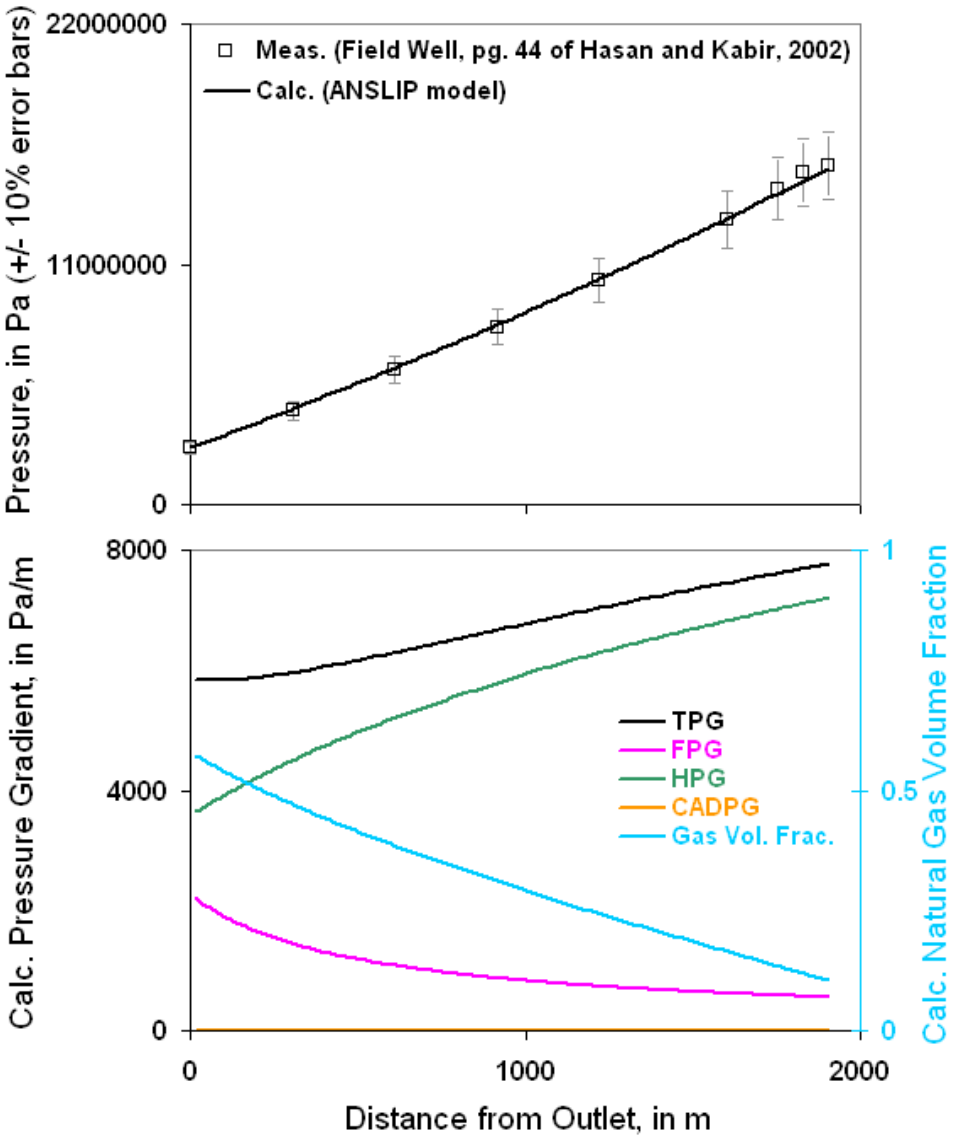

Figure 7.6.10: Prediction of the three-phase field well on pg. 44 of Hasan and Kabir (2002) with the ANSLIP wholly-analytical model.

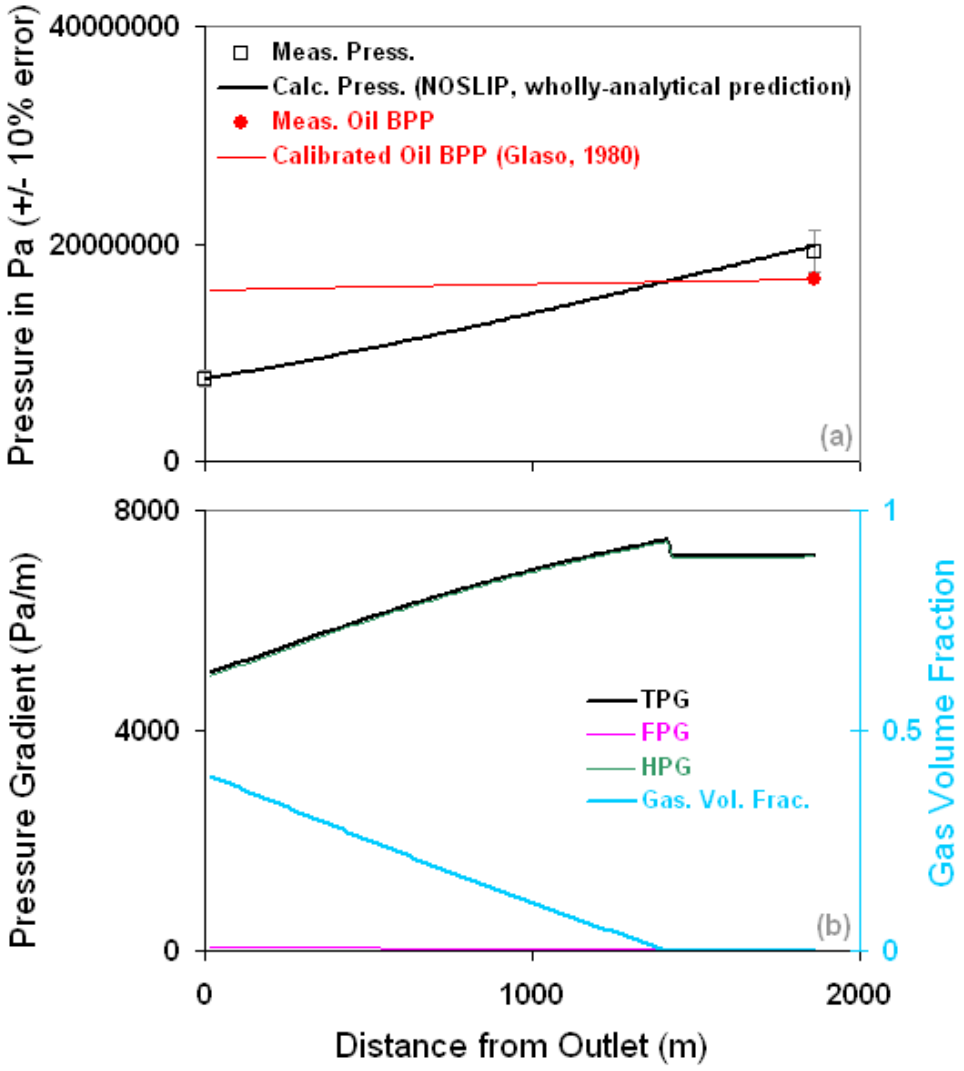

Figure 7.6.11: Prediction of the three-phase, deviated, ExxonMobil well M-6 of Griffith et al. (1973) with the NOSLIP model.

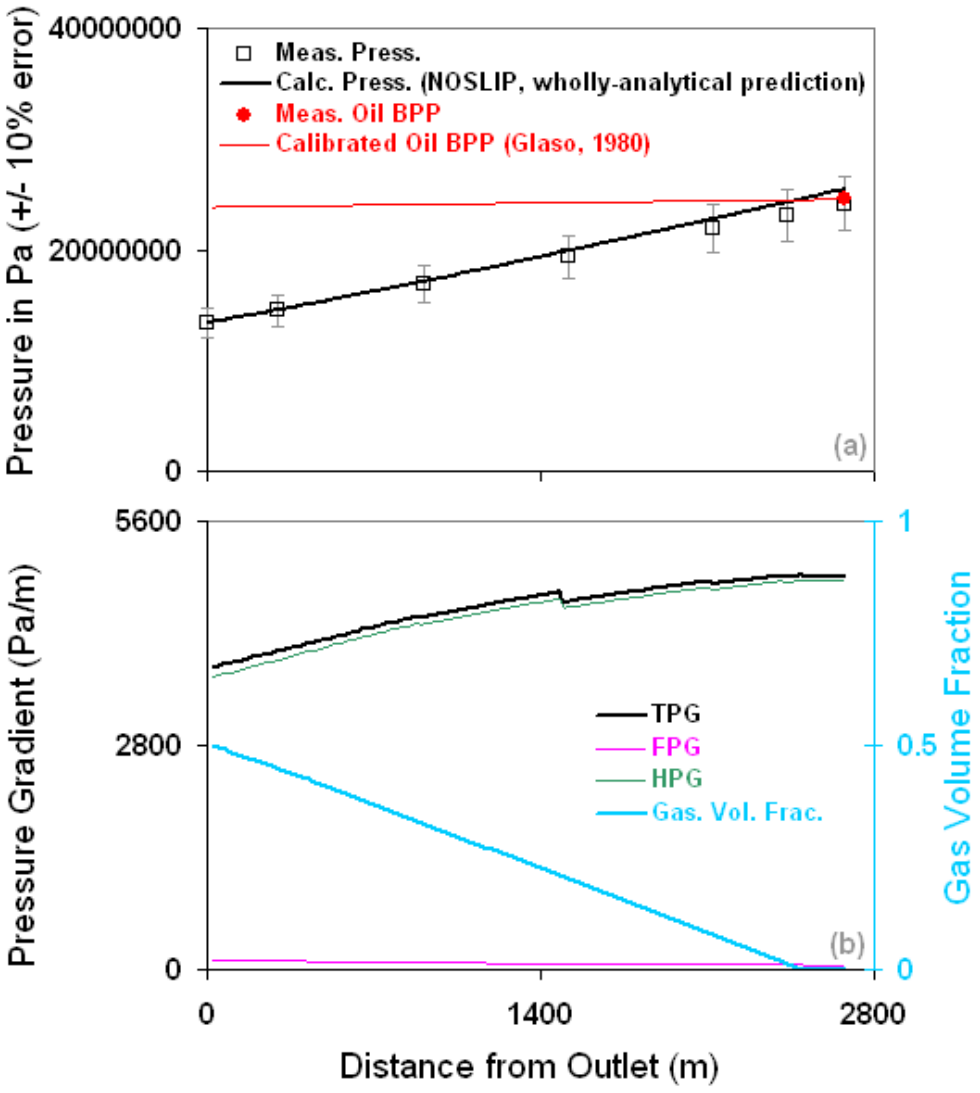

Figure 7.6.12: Prediction of the two-phase, deviated, ExxonMobil well M-10 of Griffith et al. (1973) with the NOSLIP model.

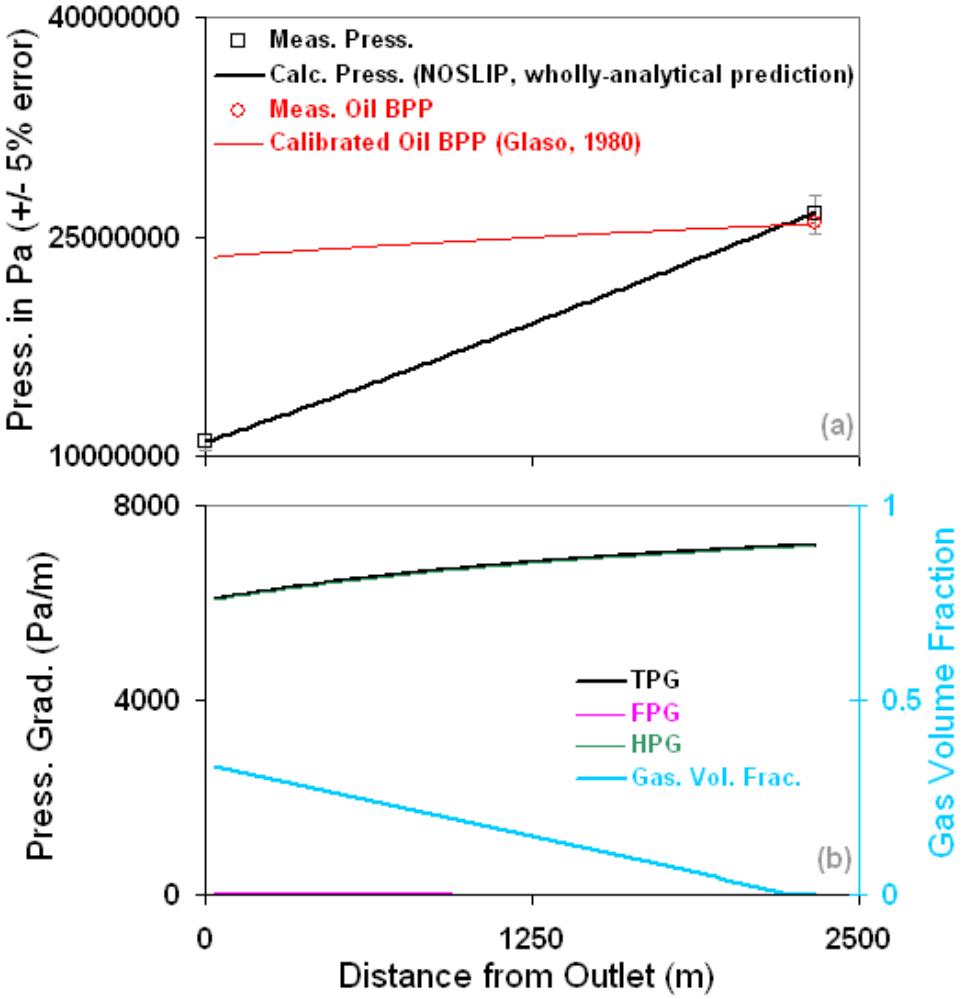

Figure 7.6.13: Prediction of well 16 of Chierici et al. (1974) with the NOSLIP model.

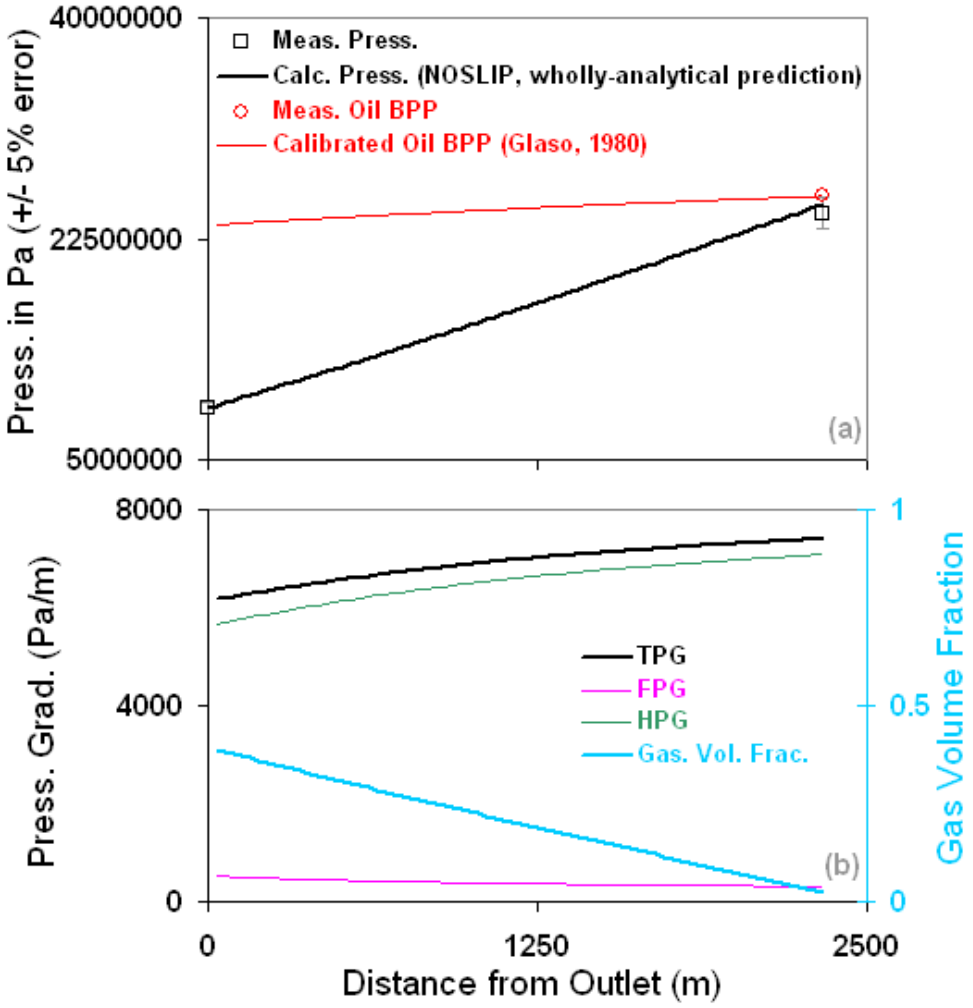

Figure 7.6.14: Prediction of well 17 of Chierici et al. (1974) with the NOSLIP model.

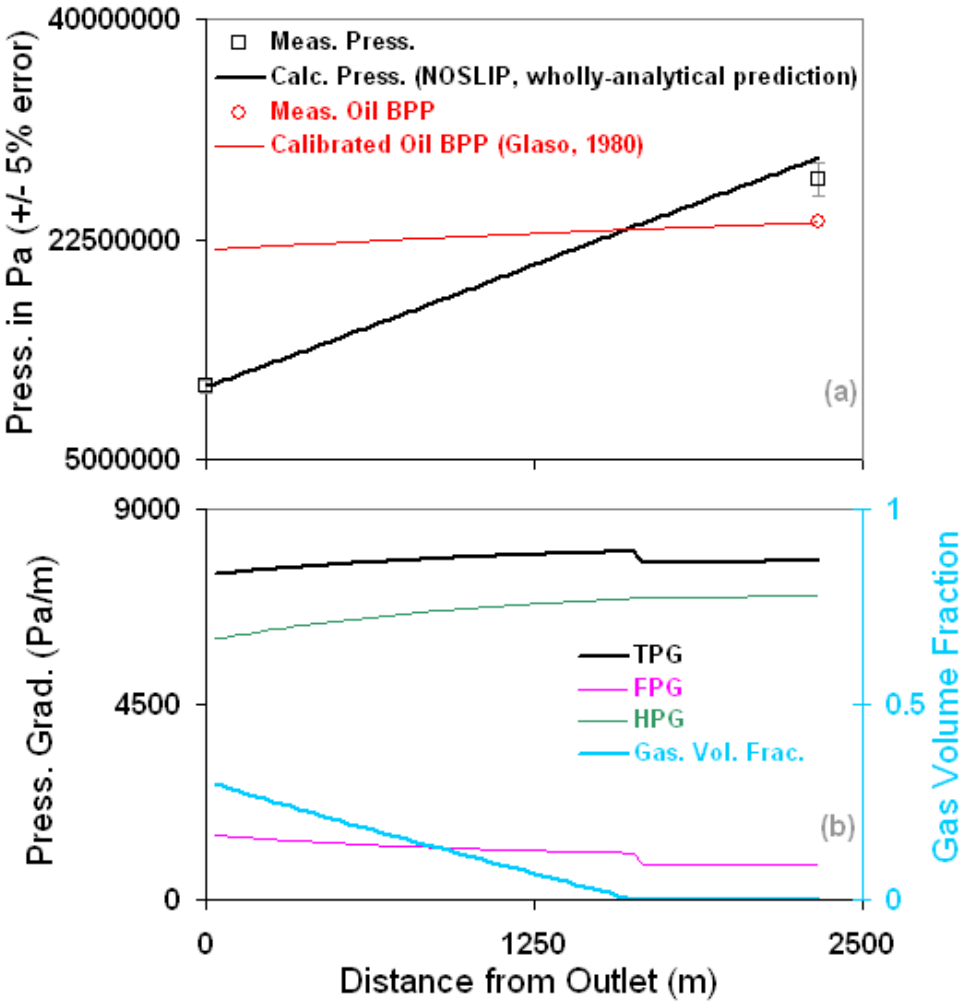

Figure 7.6.15: Prediction of well 18 of Chierici et al. (1974) with the NOSLIP model.

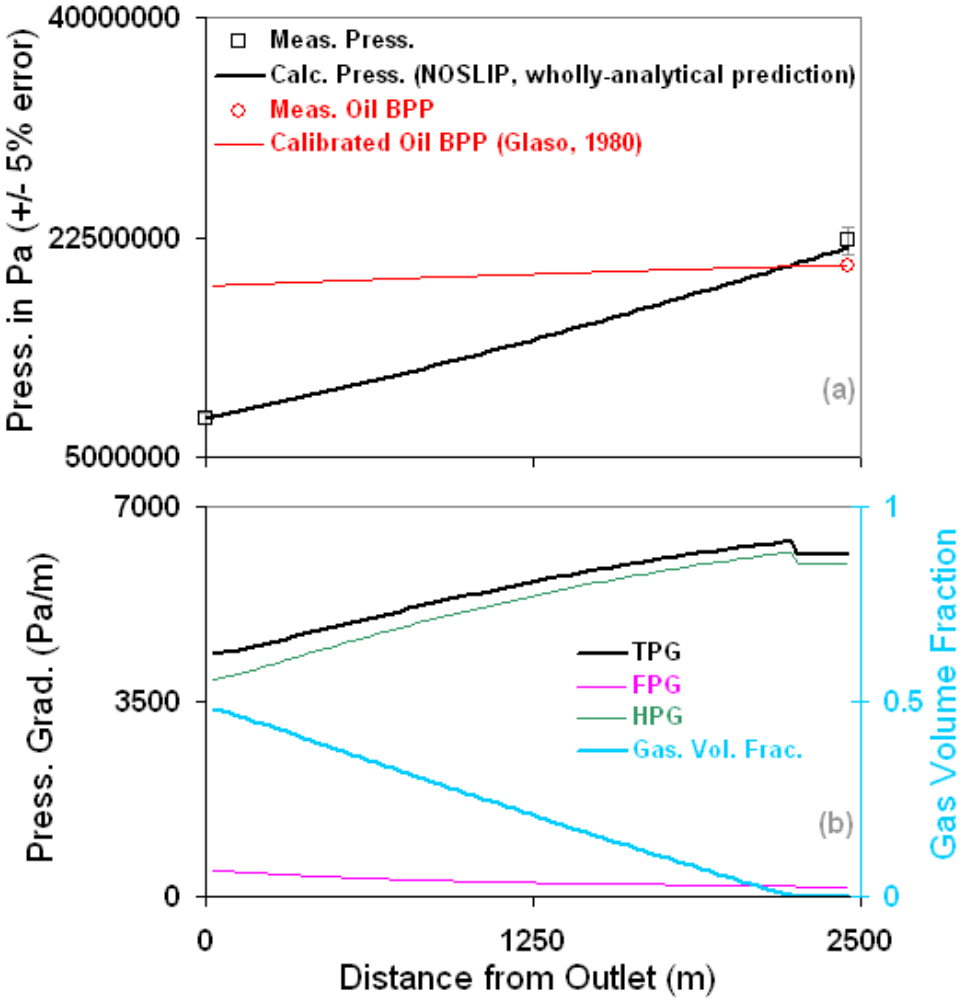

Figure 7.6.16: Prediction of well 25 of Chierici et al. (1974) with the NOSLIP model.

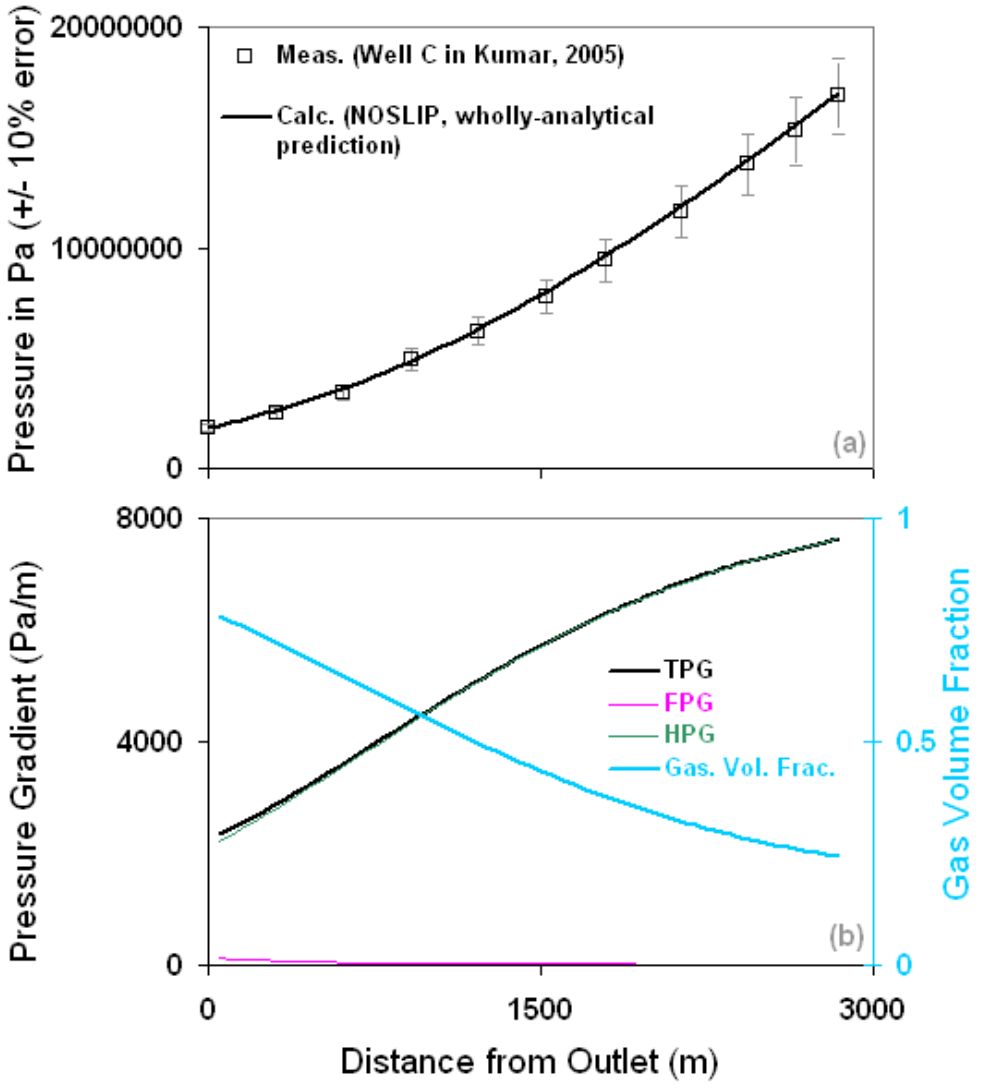

Figure 7.6.17: Prediction of the BP North America Gas (NAG) gas-water well C of Kumar (2005) with the NOSLIP model.

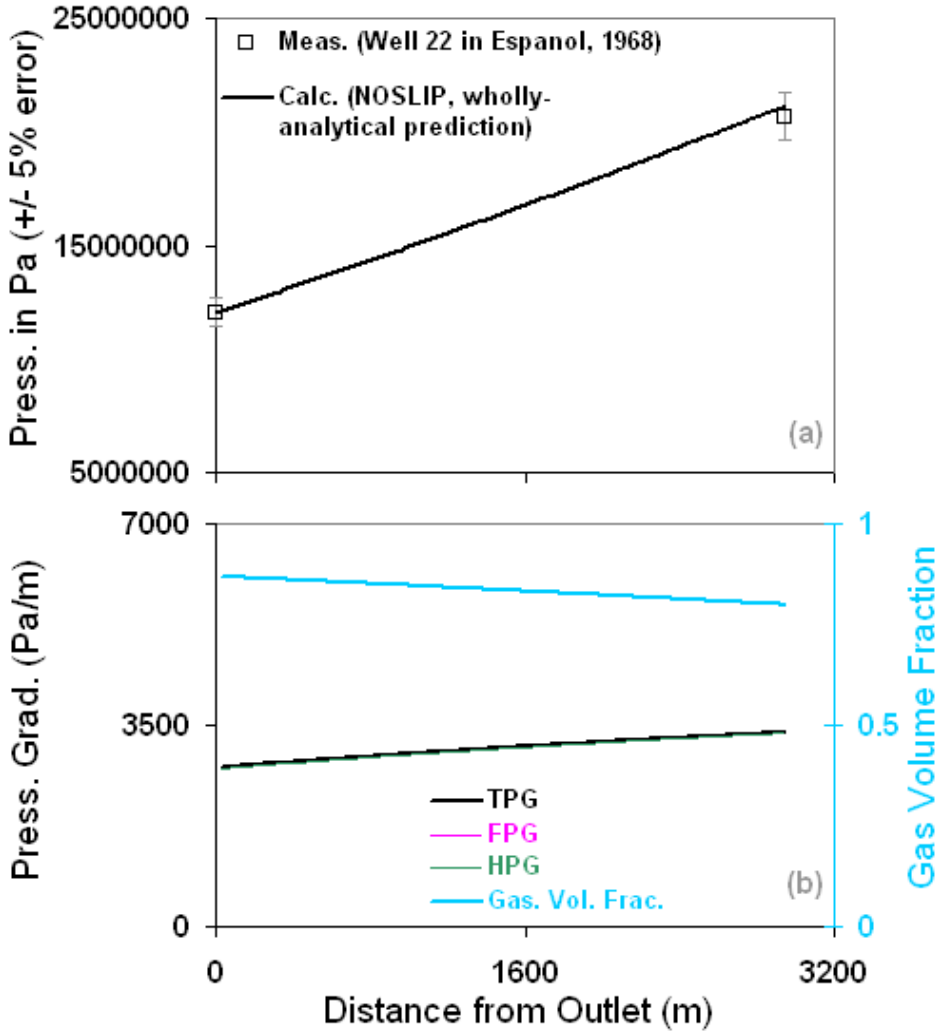

Figure 7.6.18: Prediction of well 22 of Espanol (1968) with the NOSLIP model. Note that this was considered as one the "dubious data points" that was excluded from the statistical analysis of the model validation given in Kabir and Hasan (1990).

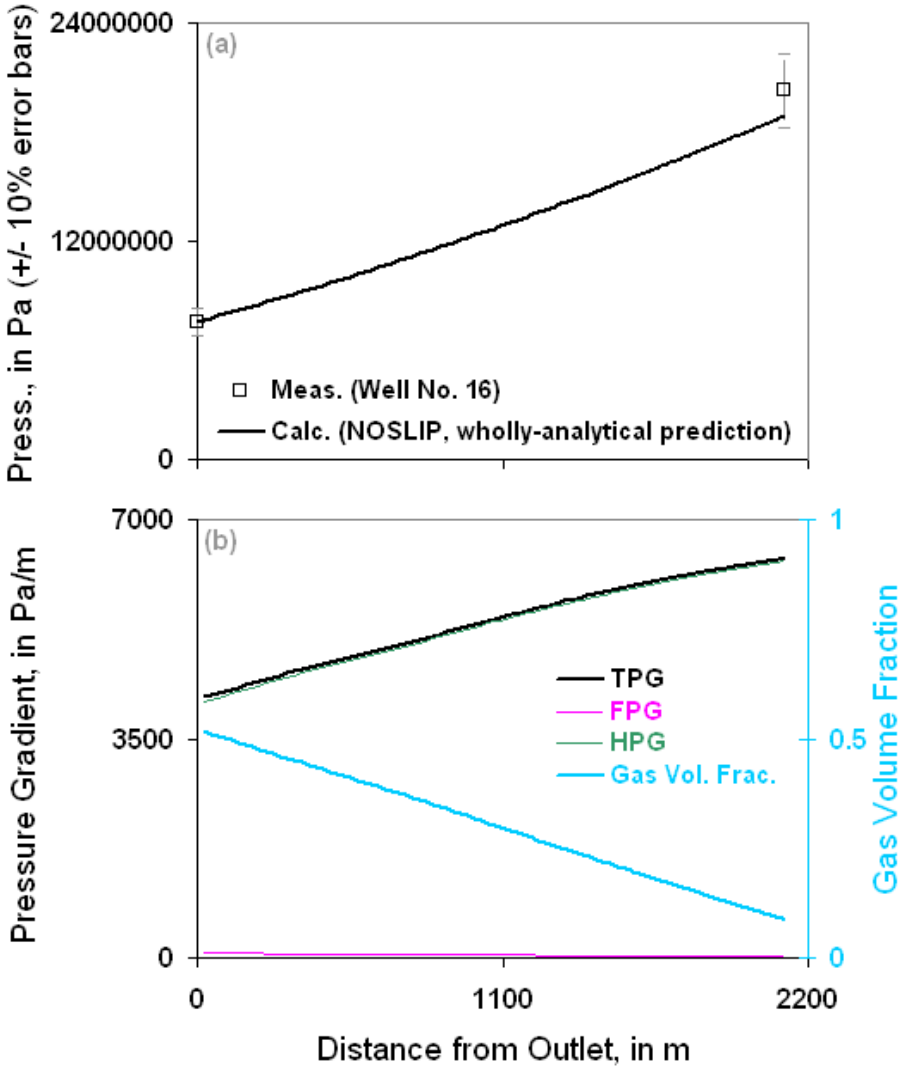

Figure 7.6.19: Prediction of well 16 of Poettmann and Carpenter (1952) with the NOSLIP model.

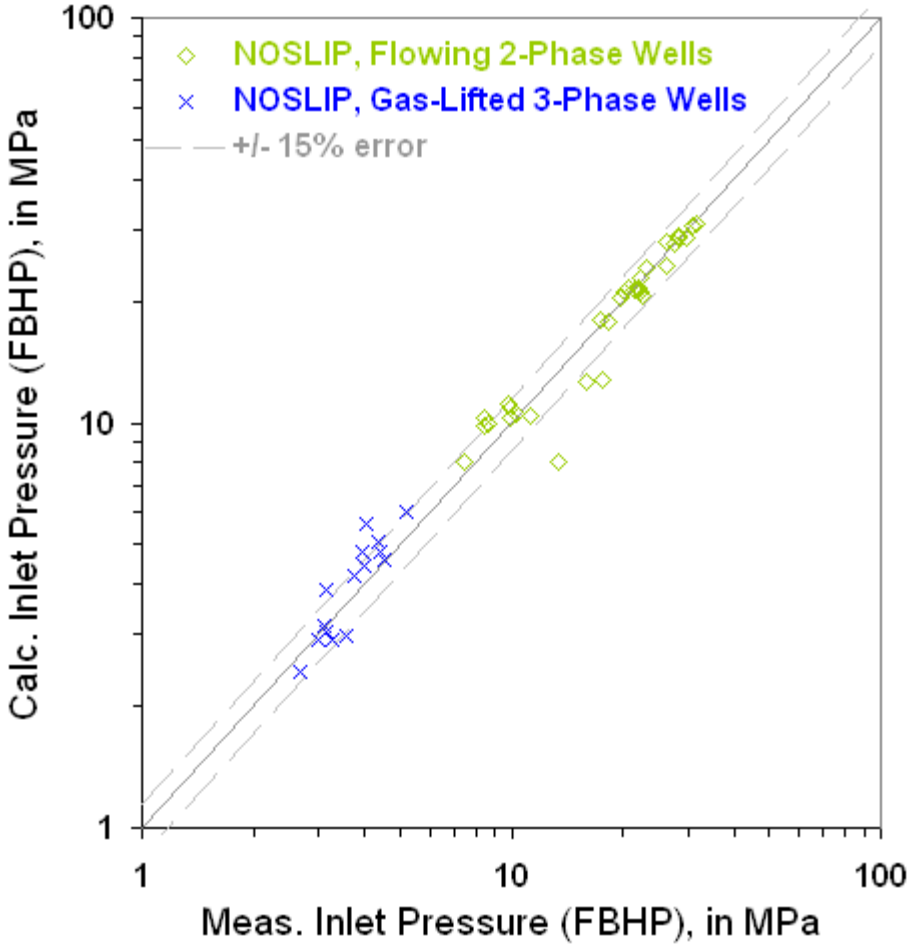

Figure 7.6.20: Prediction of all of the two-phase and gas-lifted three-phase wells of Poettmann and Carpenter (1952) with the NOSLIP model.

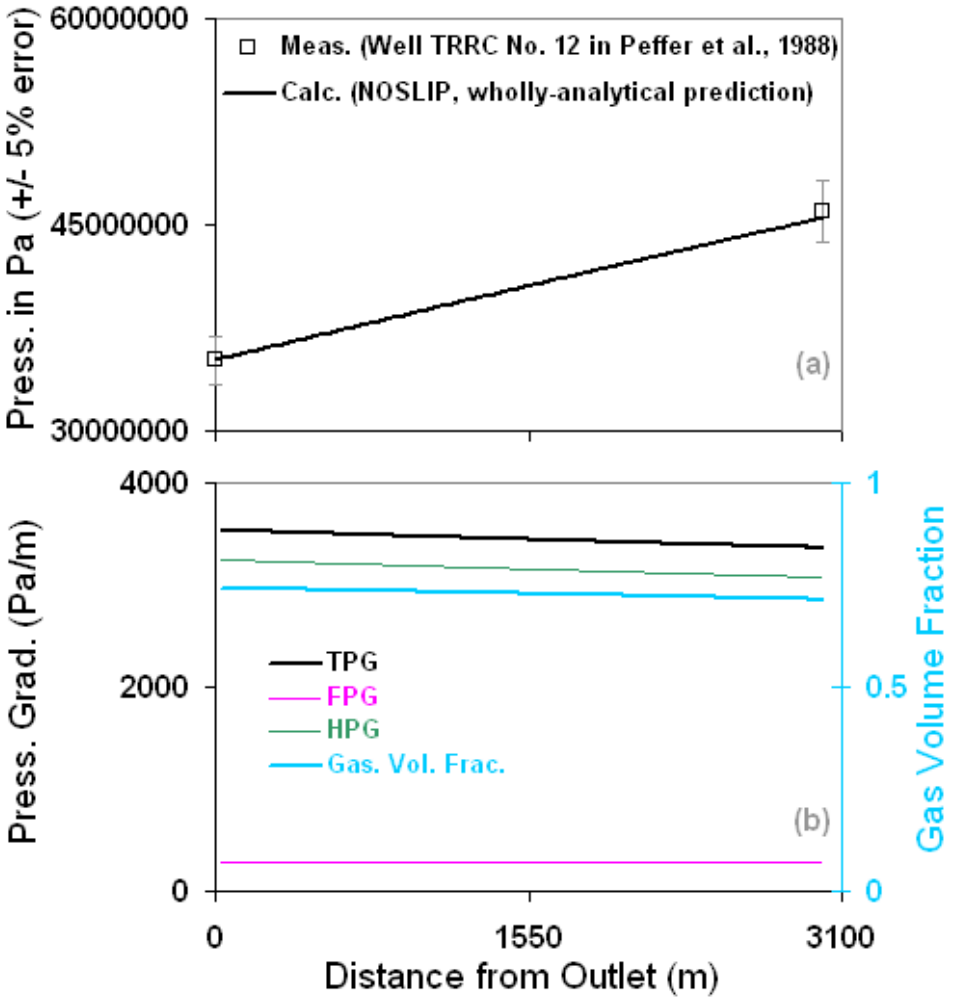

Figure 7.6.21: Prediction of well 12 of Peffer et al. (1988) with the NOSLIP model.

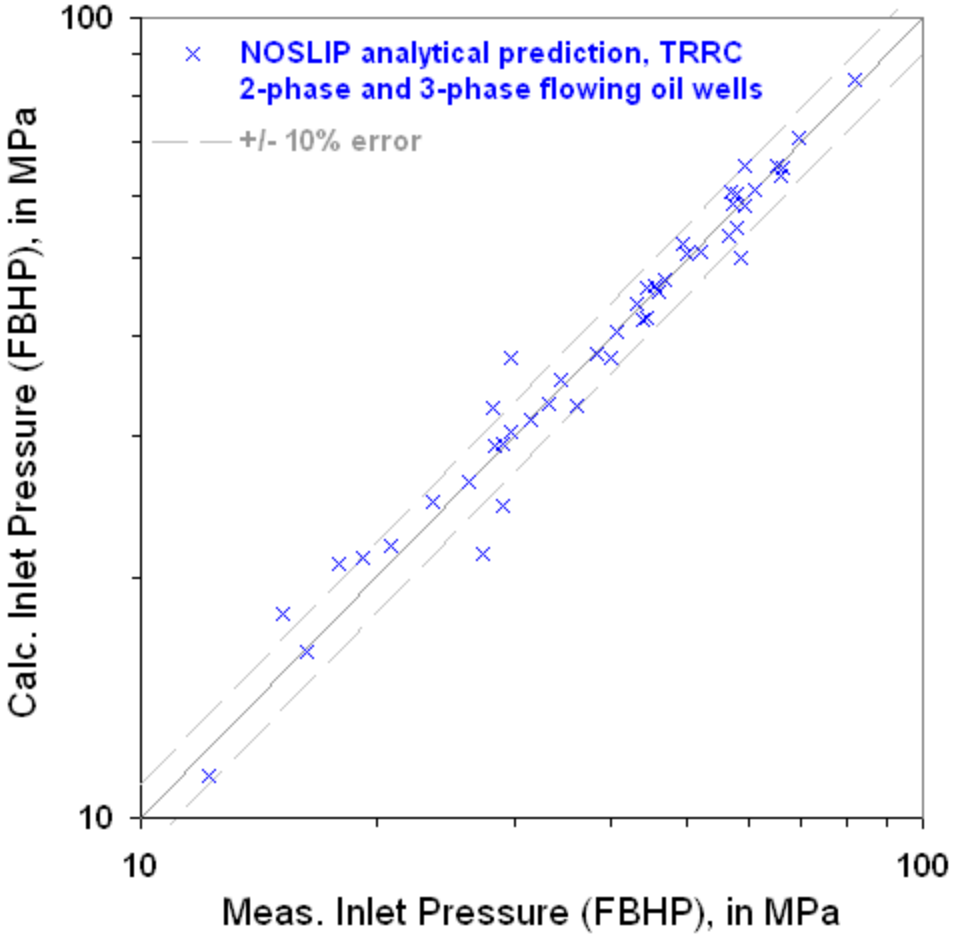

Figure 7.6.22: Prediction of all 46 two-phase and three-phase oil wells of Peffer et al. (1988) with the NOSLIP model.

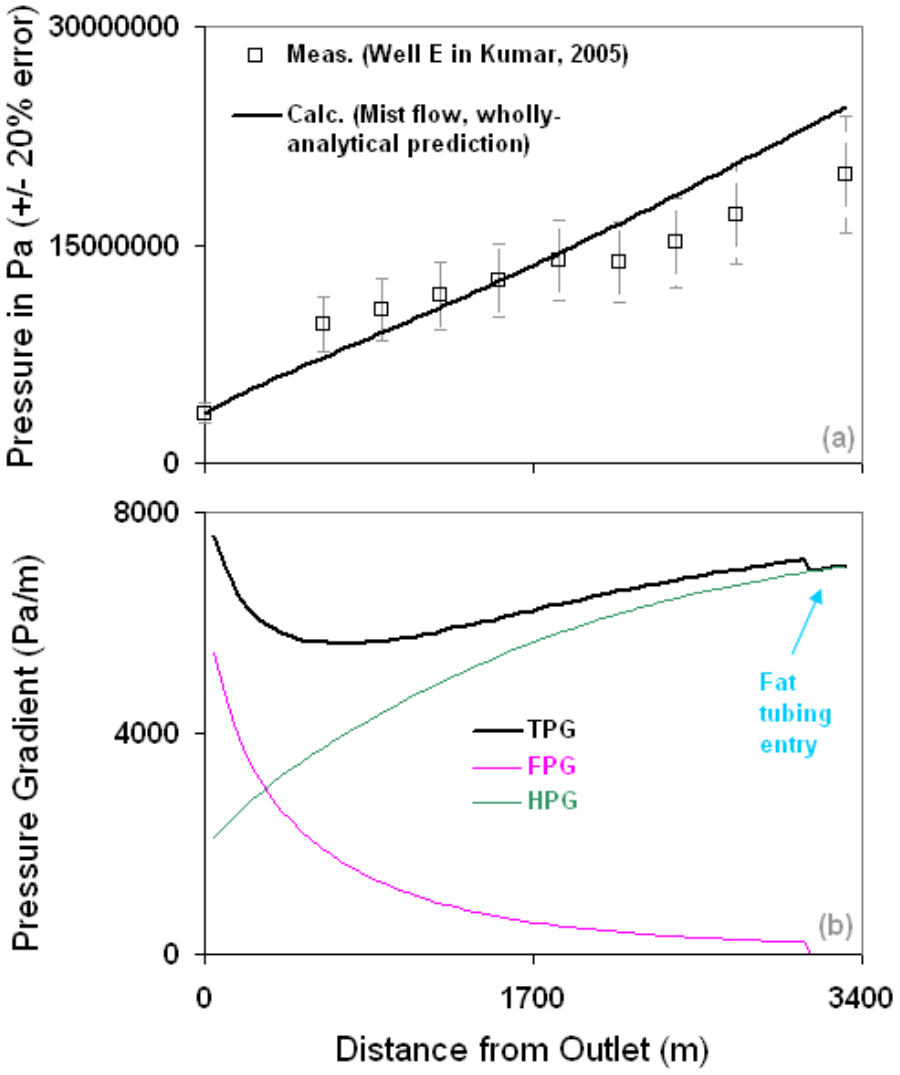

Figure 7.6.23: Prediction of the BP North America Gas (NAG) gas-water well E of Kumar (2005) with the MIST flow model.

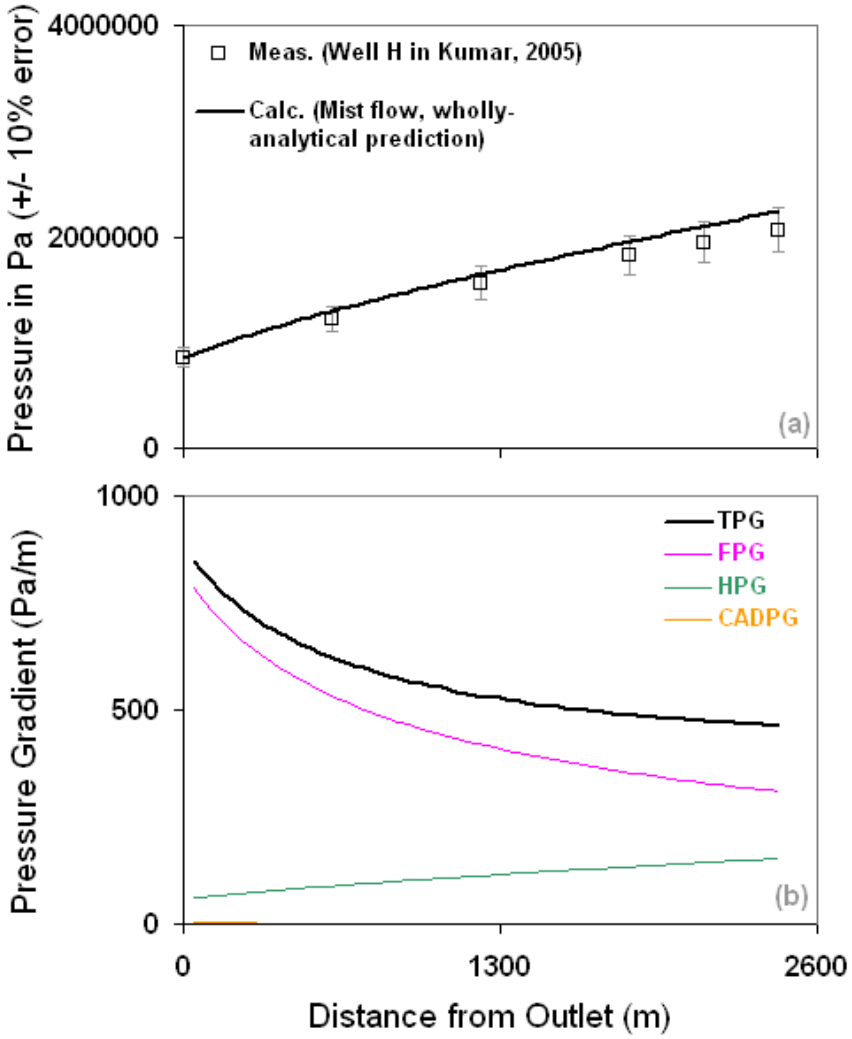

Figure 7.6.24: Prediction of the BP North America Gas (NAG) gas-water well H of Kumar (2005) with the MIST flow model.

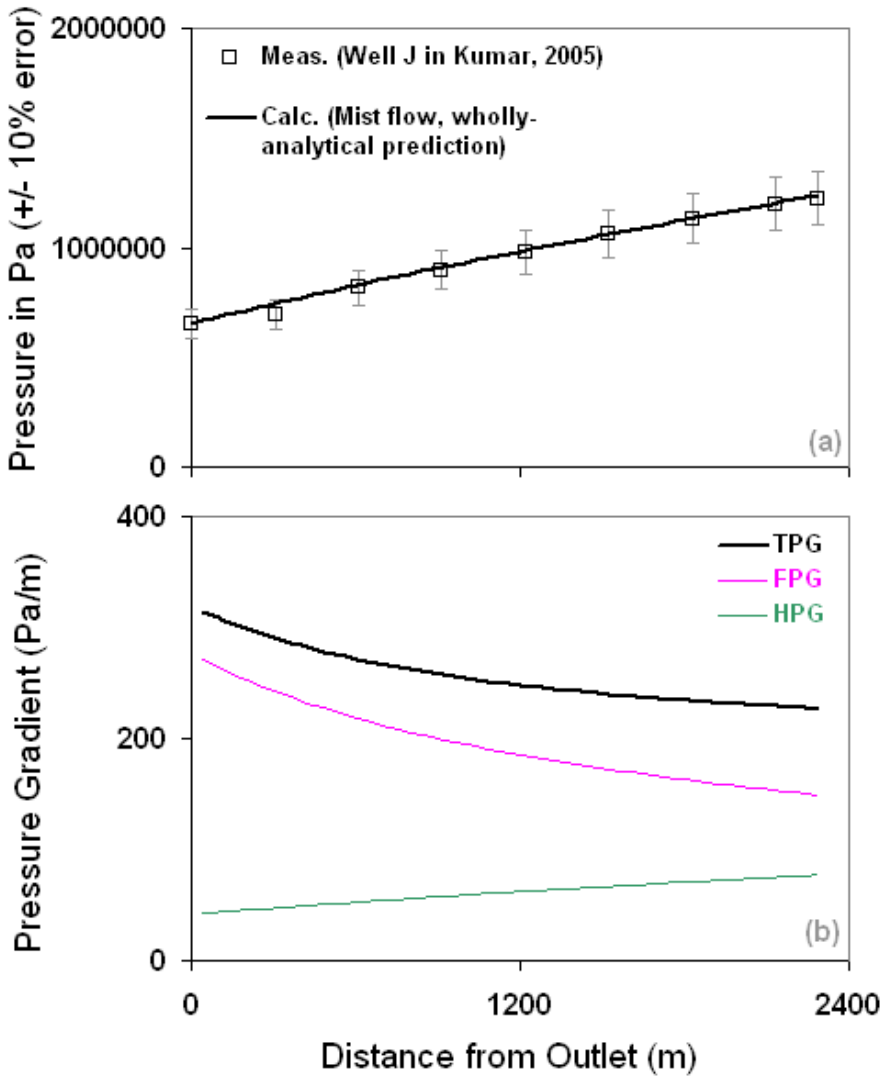

Figure 7.6.25: Prediction of the BP North America Gas (NAG) gas-water well J of Kumar (2005) with the MIST flow model.

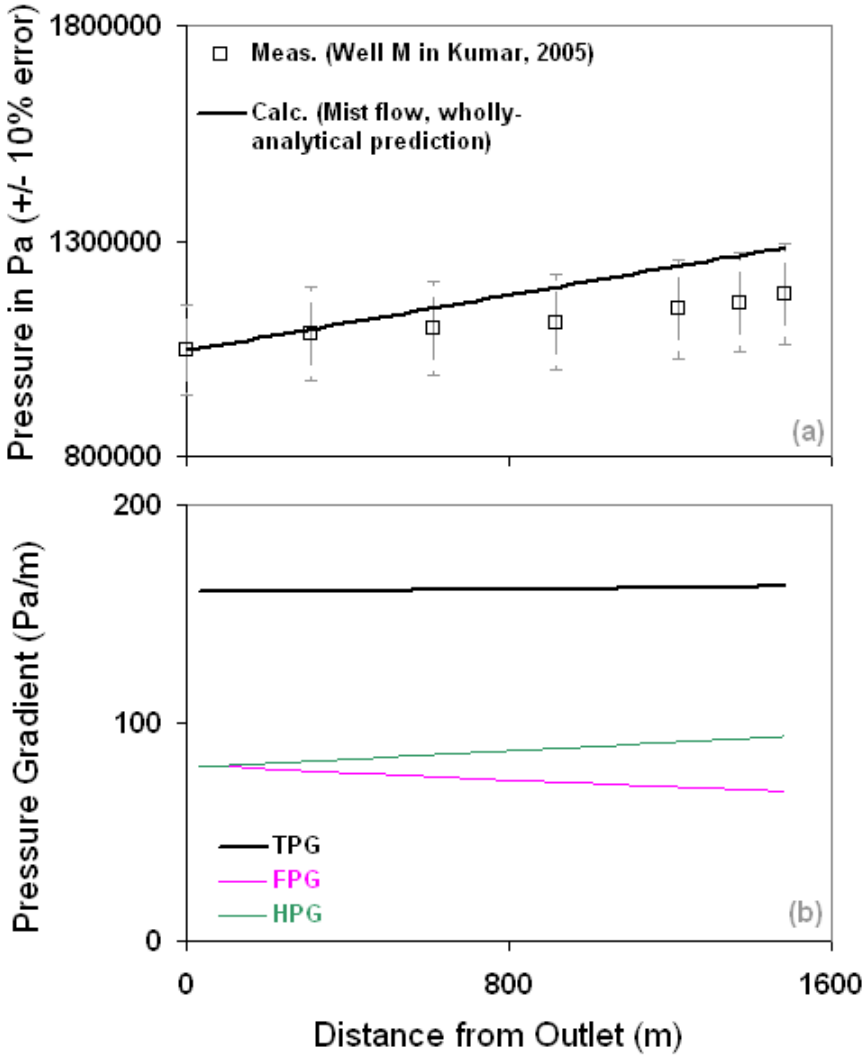

Figure 7.6.26: Prediction of the BP North America Gas (NAG) gas-water well M of Kumar (2005) with the MIST flow model.

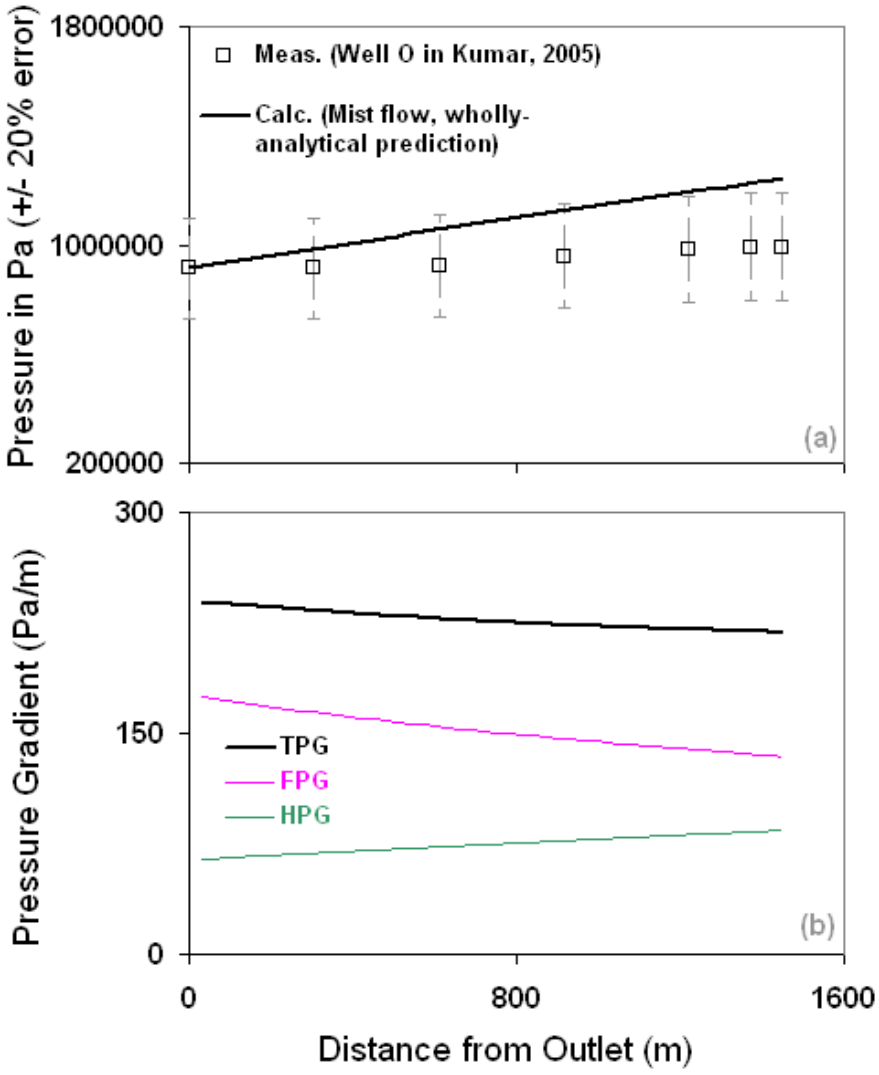

Figure 7.6.27: Prediction of the BP North America Gas (NAG) gas-water well O of Kumar (2005) with the MIST flow model.

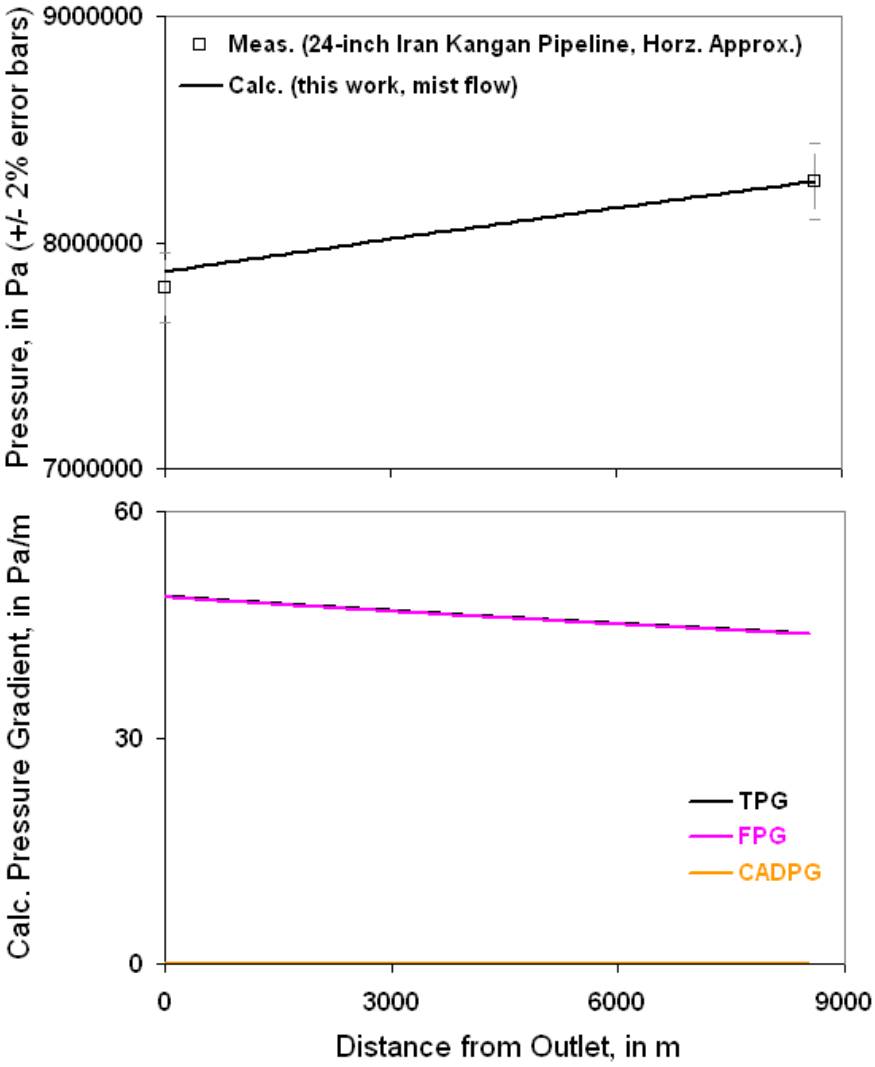

Figure 7.6.28: Prediction of the 24-inch Iranian Kangan pipeline of Mokhatab (2002) with the MIST flow model and a horizontal pipeline approximation.

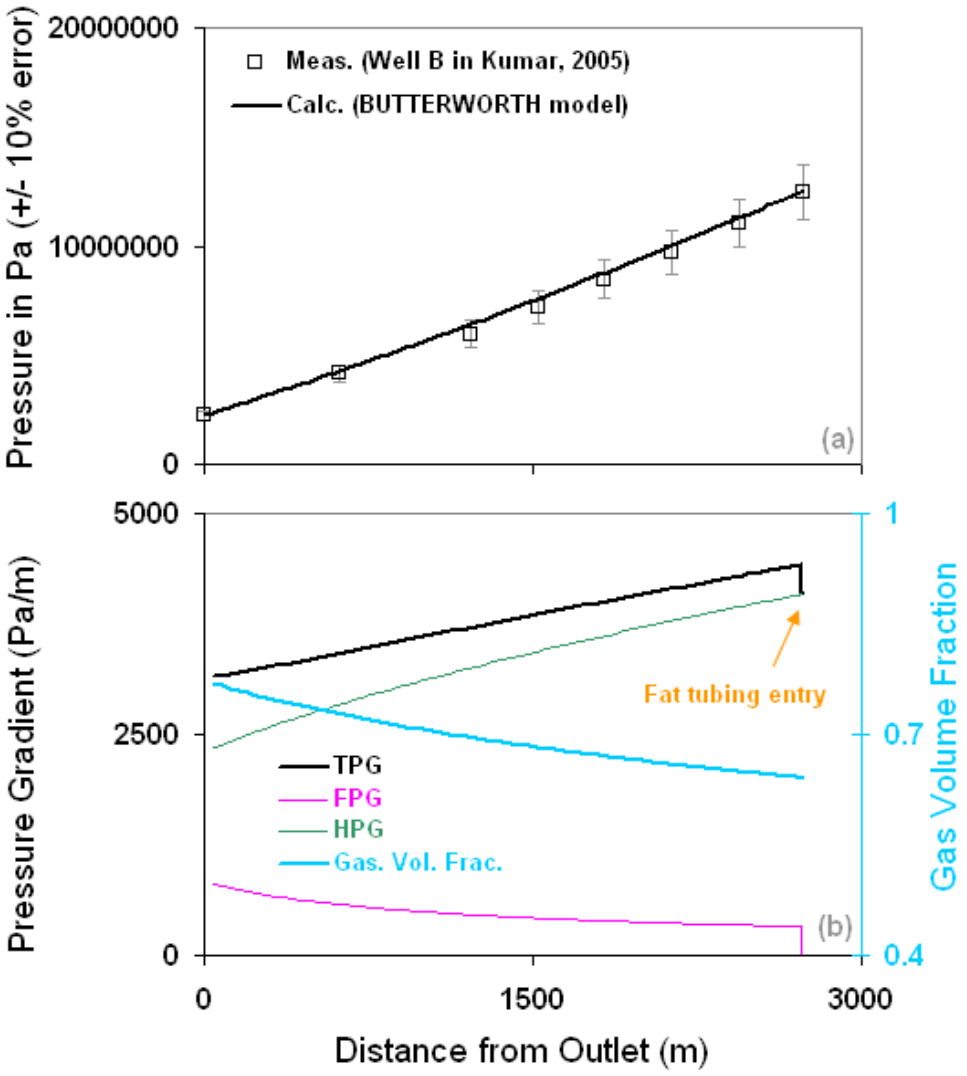

Figure 7.6.29: Prediction of the BP North America Gas (NAG) gas-water well B of Kumar (2005) with the BUTTERWORTH model.

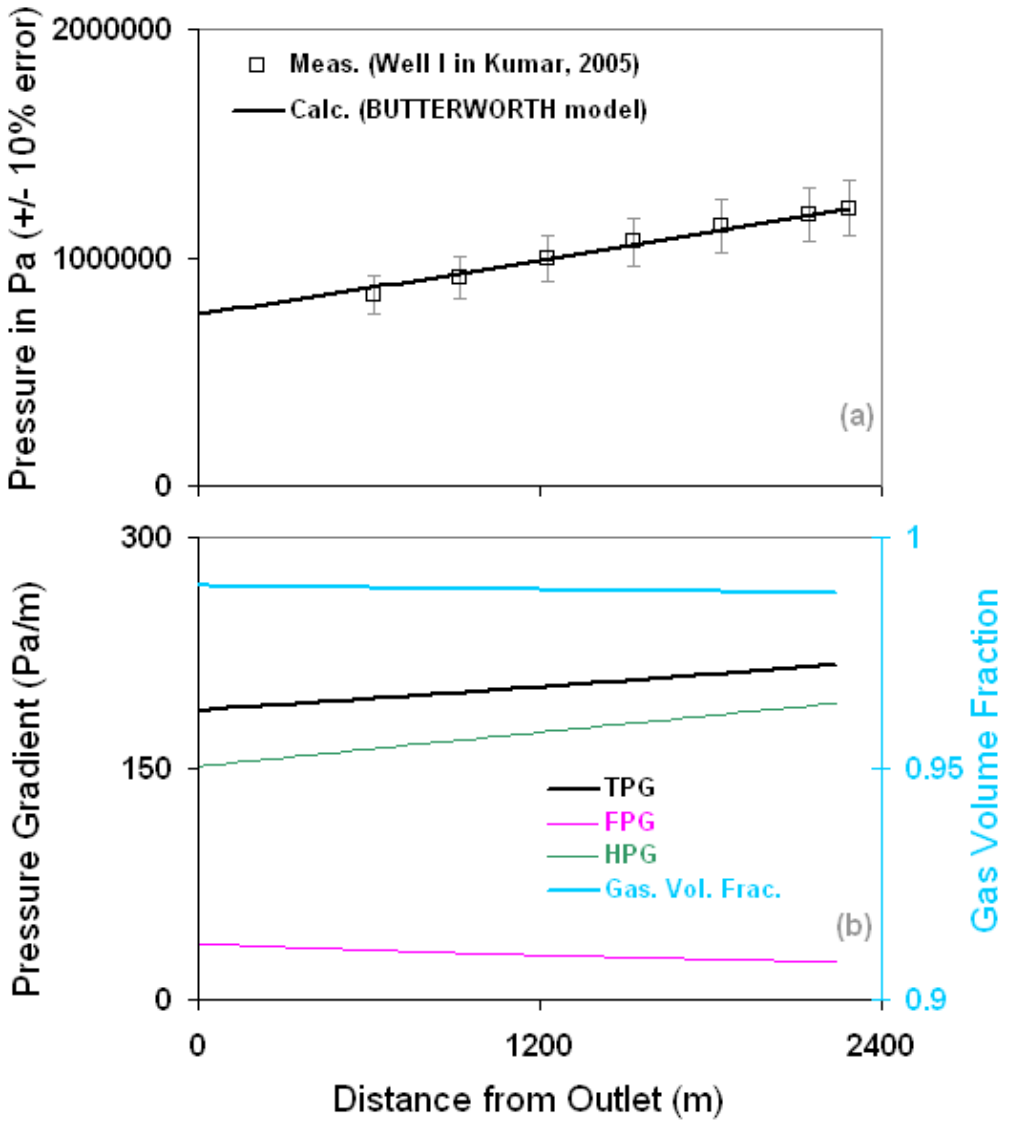

Figure 7.6.30: Prediction of the BP North America Gas (NAG) gas-water well I of Kumar (2005) with the BUTTERWORTH model.

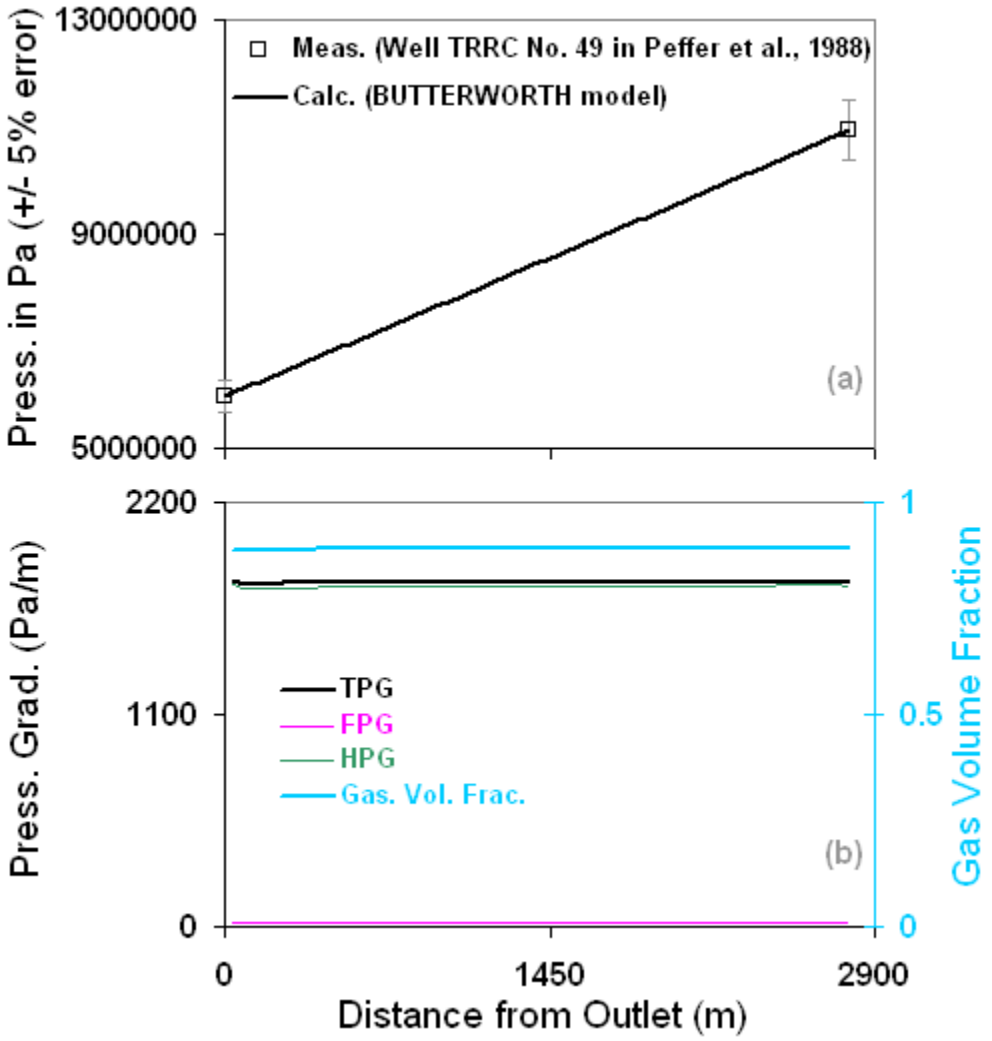

Figure 7.6.31: Prediction of the low GWR gas-water well 49 of Peffer et al. (1988) with the BUTTERWORTH model.

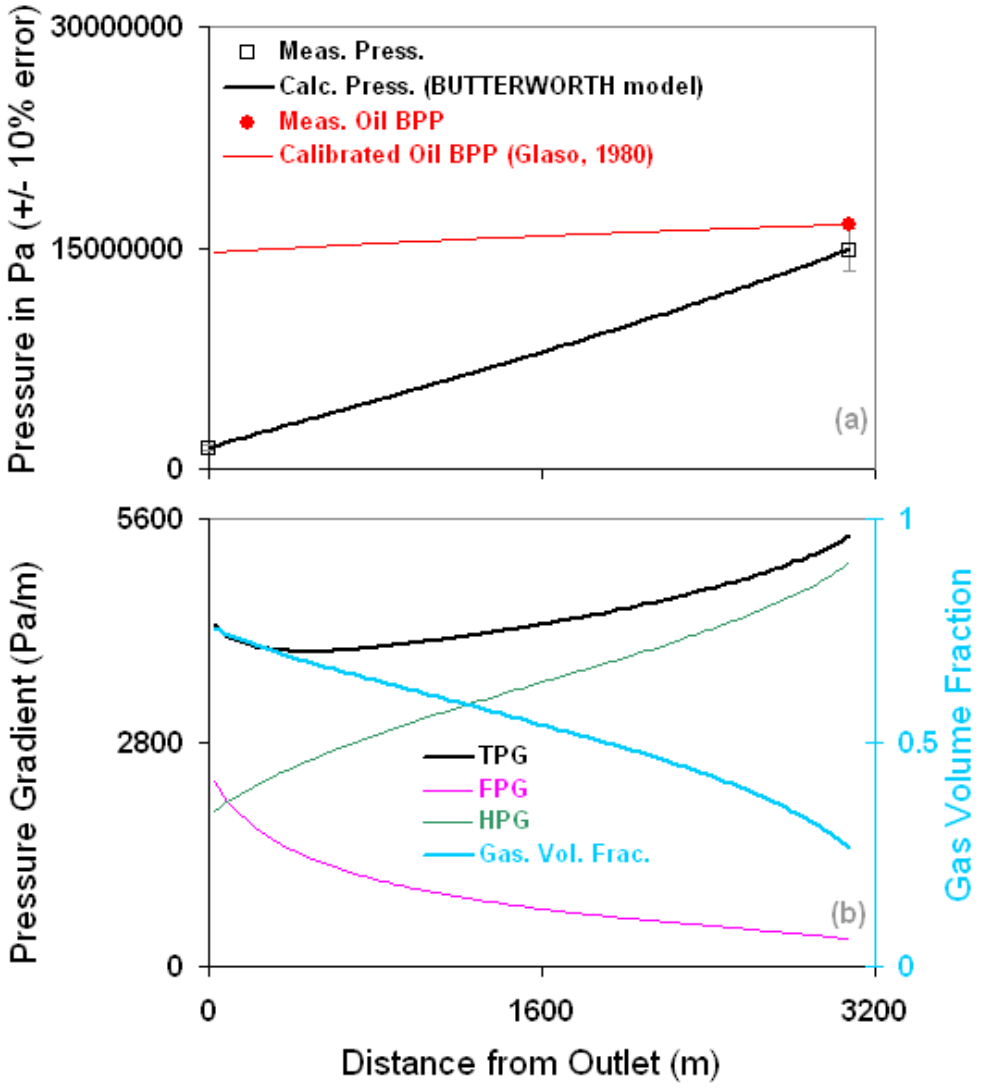

Figure 7.6.32: Prediction of the three-phase, deviated, ExxonMobil well M-5B of Griffith et al. (1973) with the BUTERWORTH model.

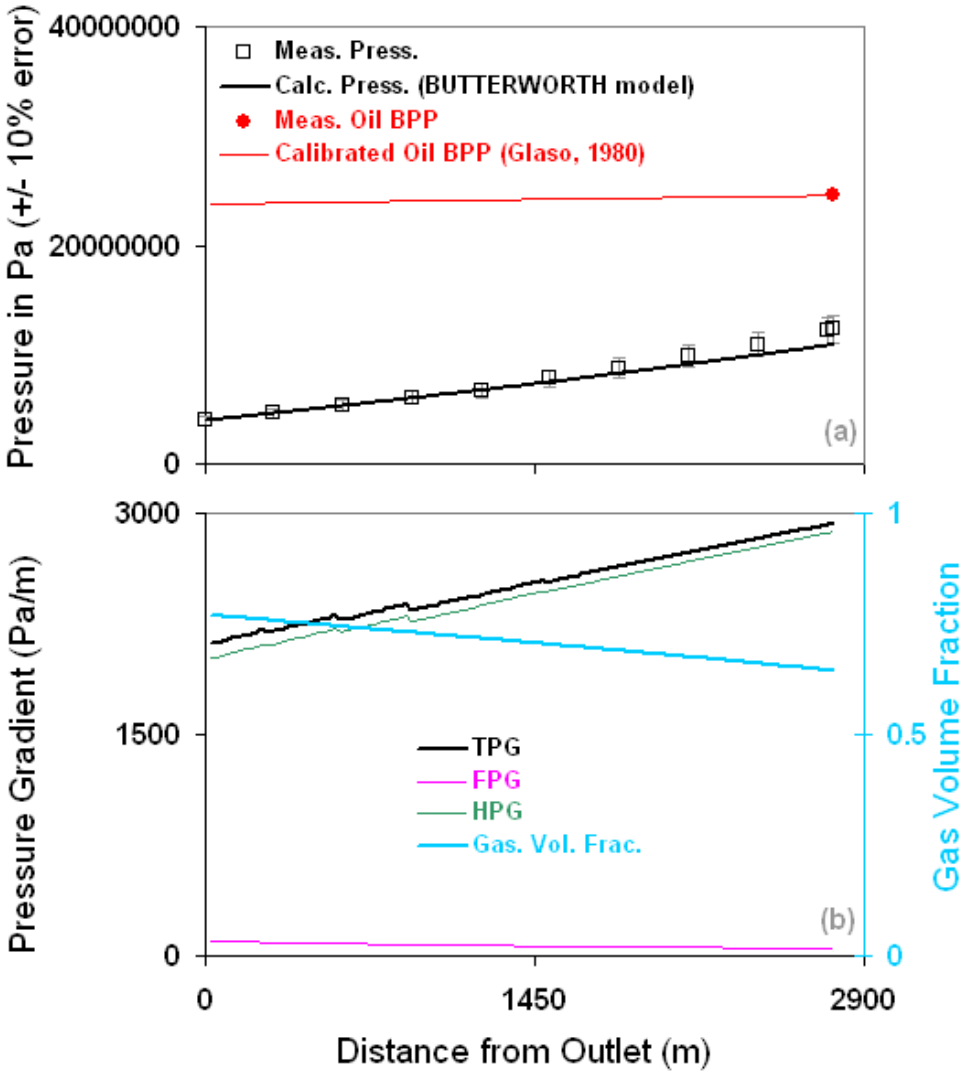

Figure 7.6.33: Prediction of the two-phase, deviated, ExxonMobil well M9 of Griffith et al. (1973) with the BUTTERWORTH model.

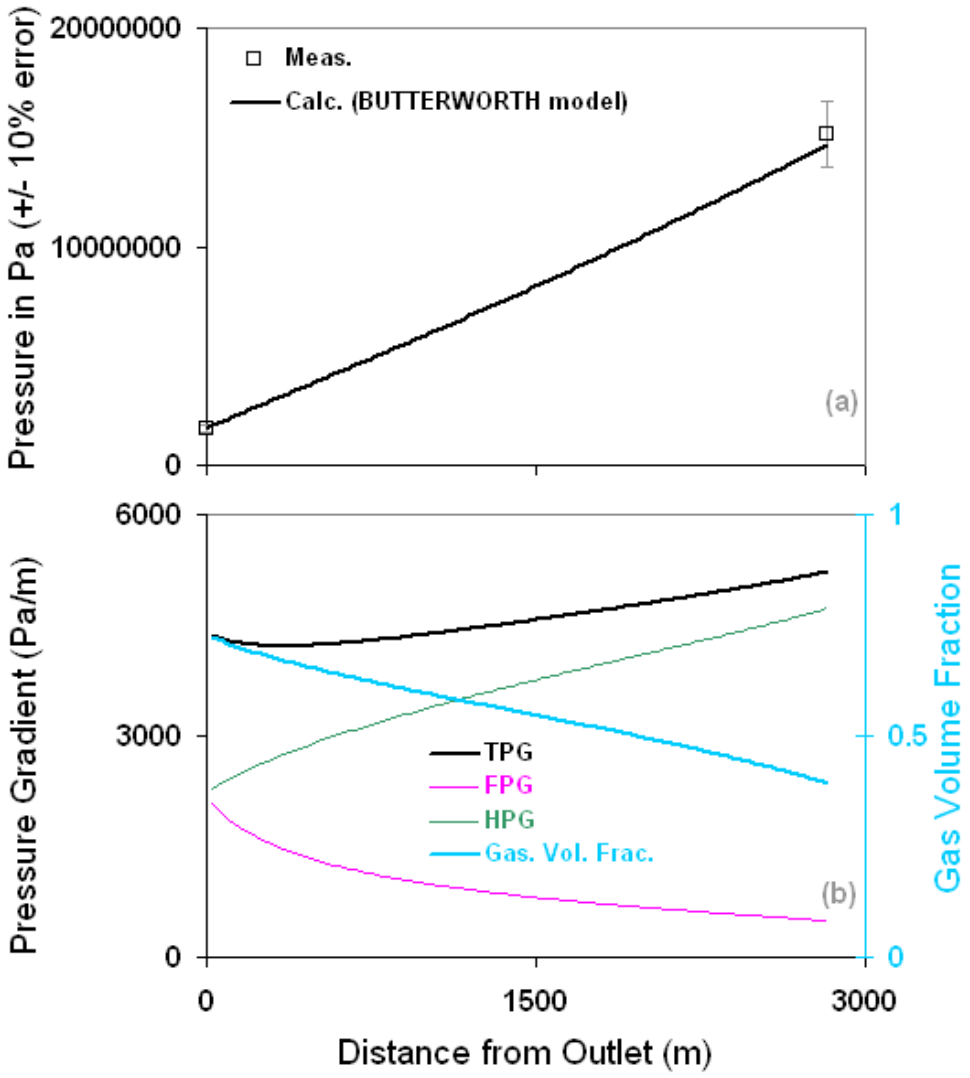

Figure 7.6.34: Prediction of the two-phase, vertical well 17 of Corteville et al. (1991) with the BUTTERWORTH model.

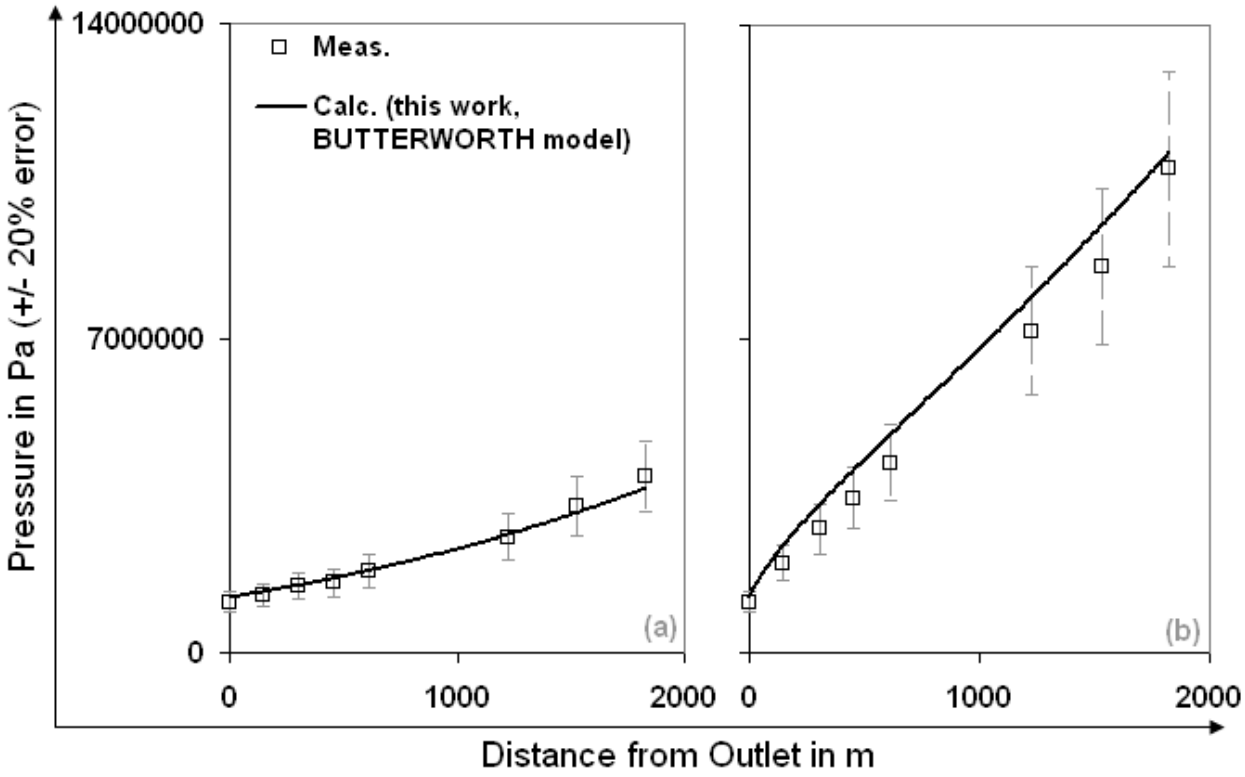

Figure 7.6.35: Prediction of test no. 14 (in a) and no. 1 (in b) of well 1 of Baxendell and Thomas (1961) with the BUTTERWORTH model.

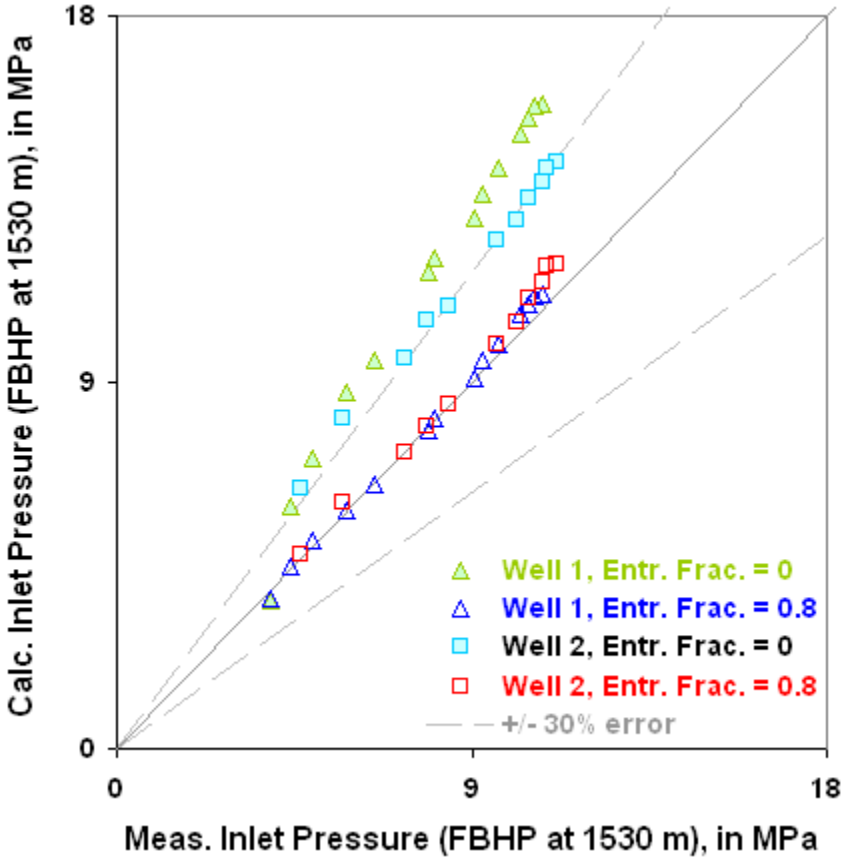

Figure 7.6.36: Prediction of the flowing bottom-hole pressures of both wells 1 and 2 of Baxendell and Thomas (1961) with the BUTTERWORTH model.

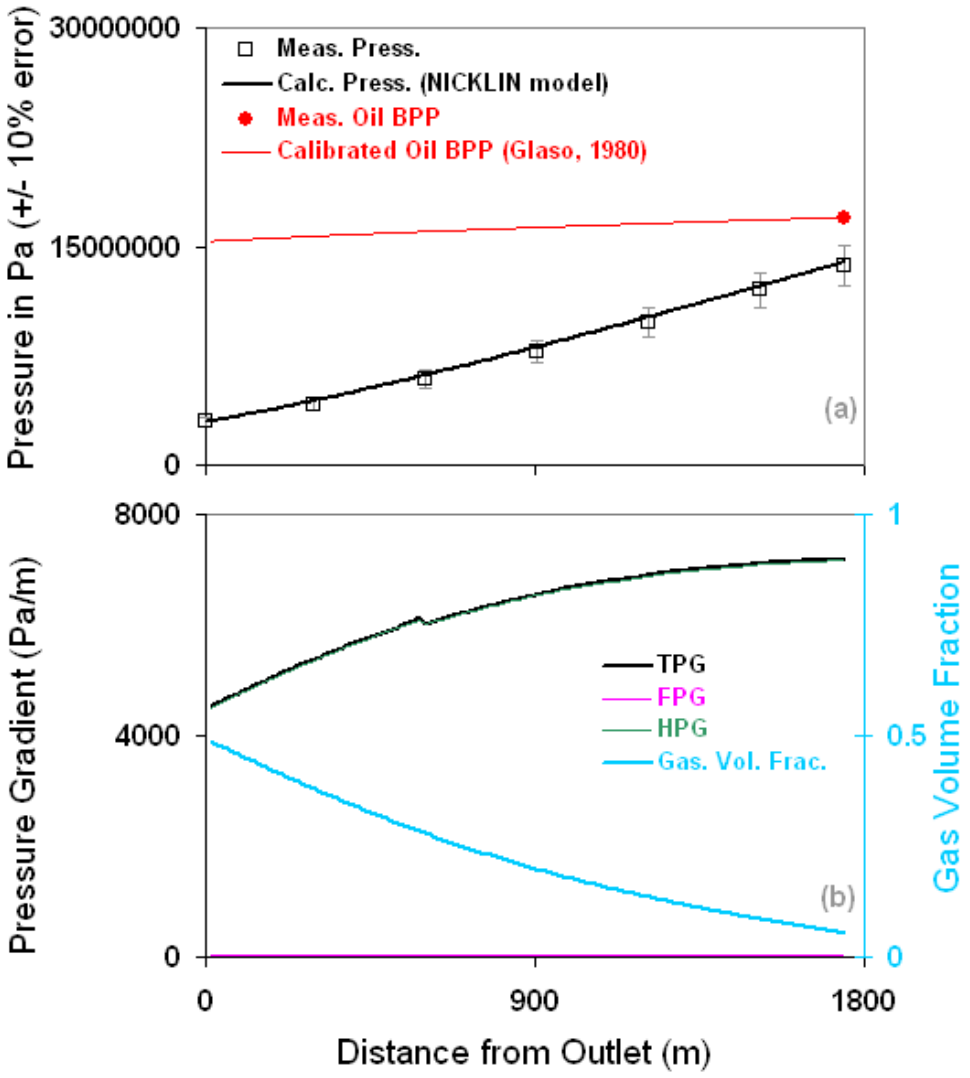

Figure 7.6.37: Prediction of the three-phase, deviated ExxonMobil well M1 of Griffith et al. (1973) with the NICKLIN model.

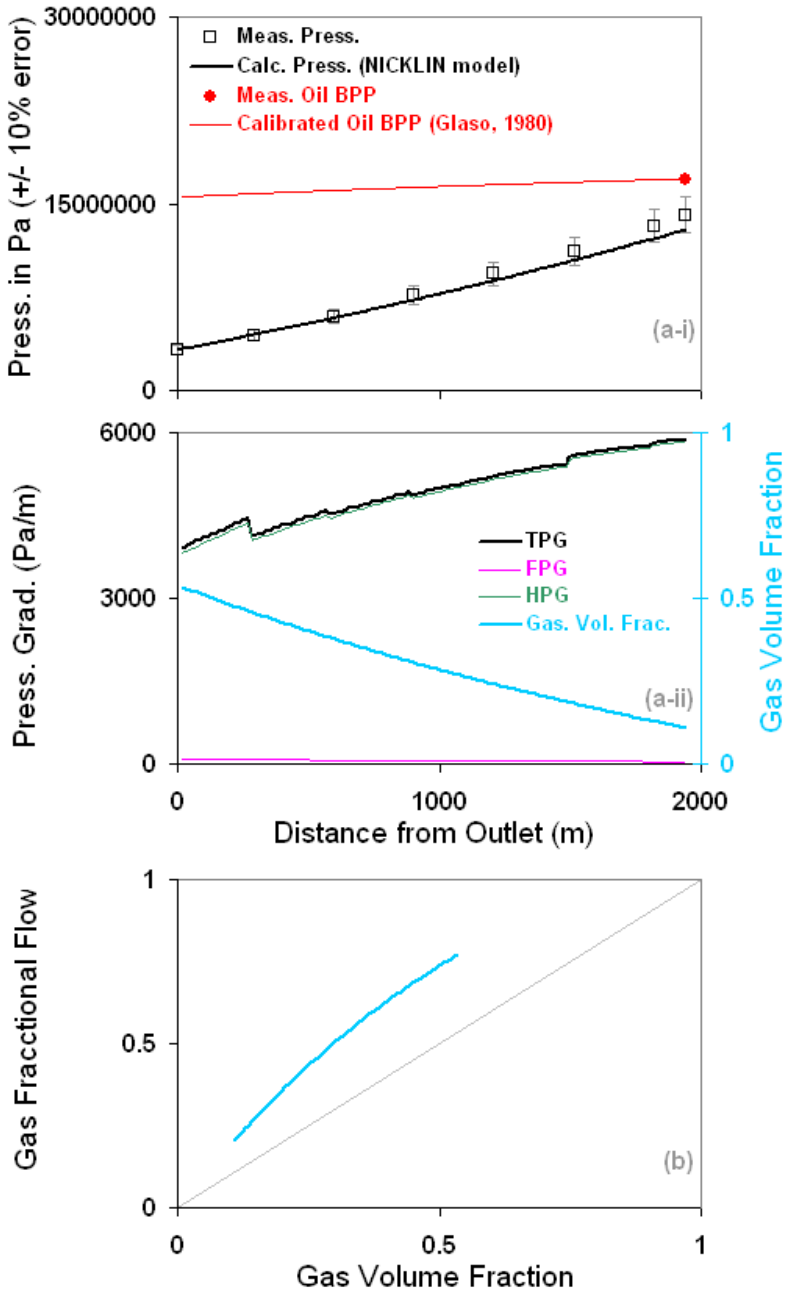

Figure 7.6.38: Prediction of the two-phase, deviated ExxonMobil well M4 of Griffith et al. (1973) with the NICKLIN model. Note the gas fractional flow graph describes the averaged slip behavior of the fluids in the well during flow.

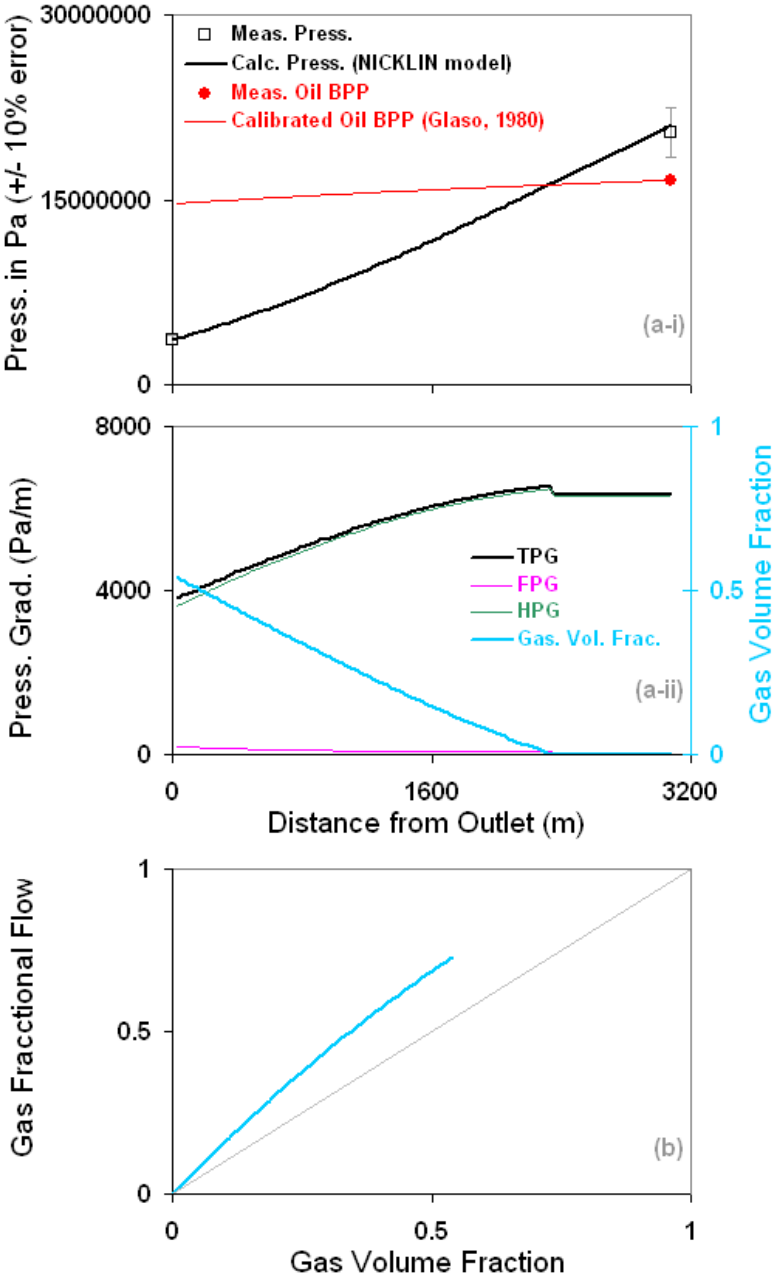

Figure 7.6.39: Prediction of the deviated ExxonMobil well M-5A of Griffith et al. (1973) with the NICKLIN model.

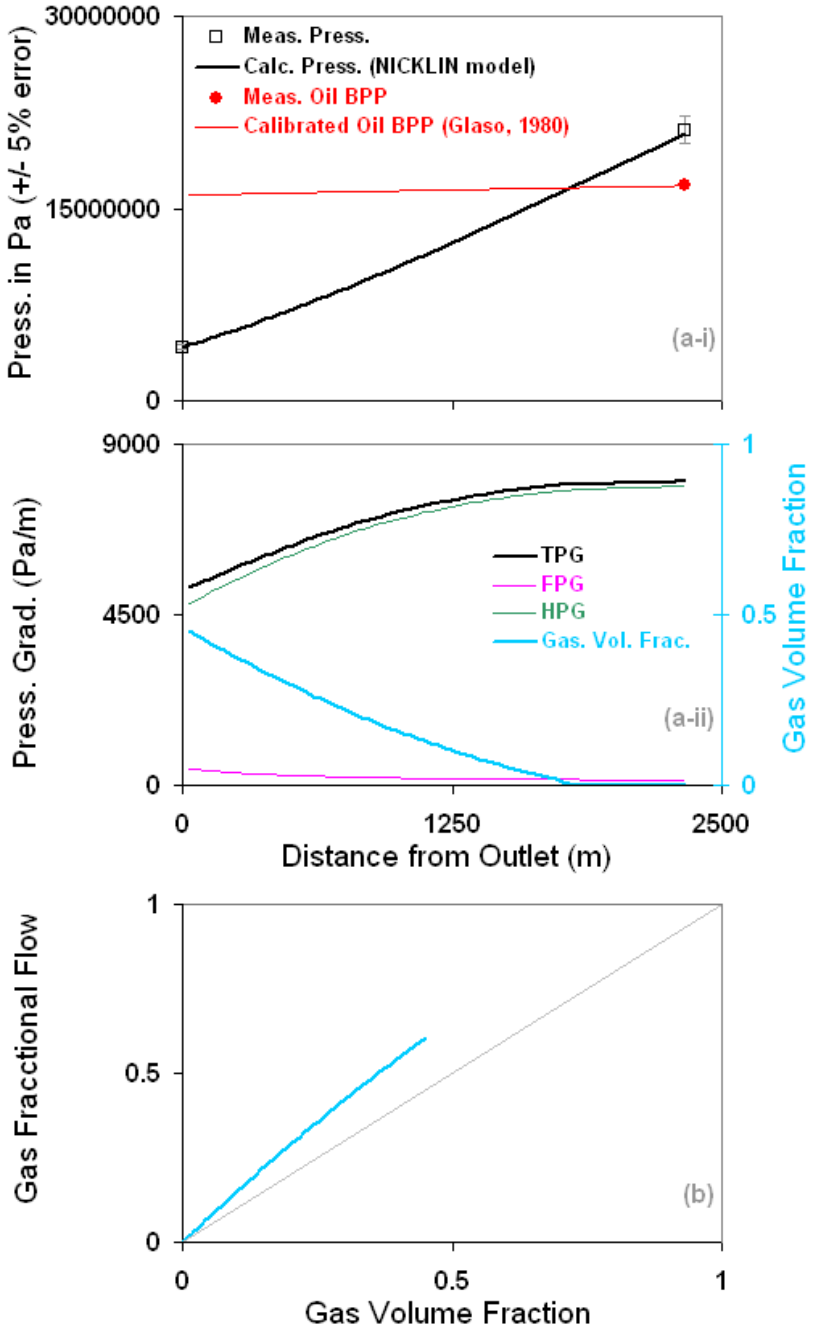

Figure 7.6.40: Prediction of well 9 of Chierici et al. (1974) with the NICKLIN model.

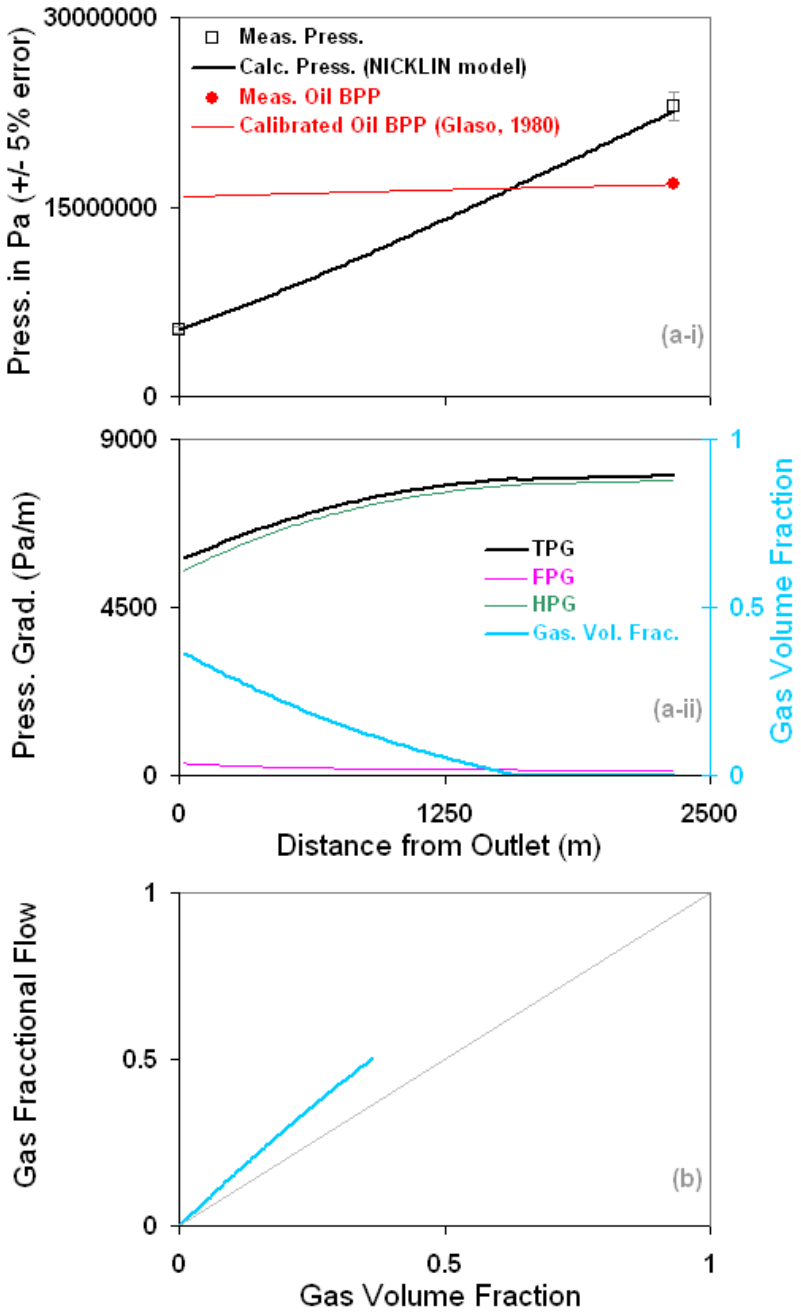

Figure 7.6.41: Prediction of well 10 of Chierici et al. (1974) with the NICKLIN model.

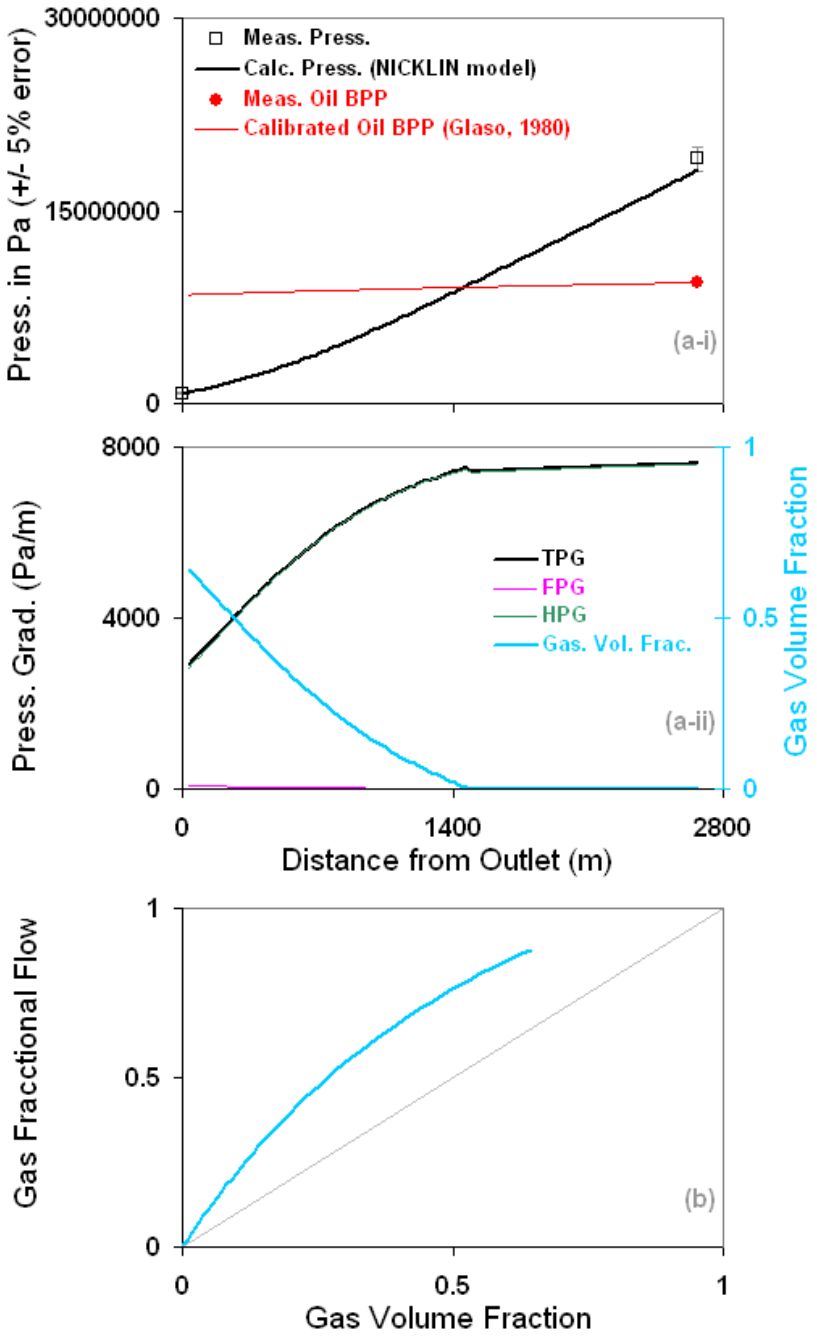

Figure 7.6.42: Prediction of well 14 of Chierici et al. (1974) with the NICKLIN model.

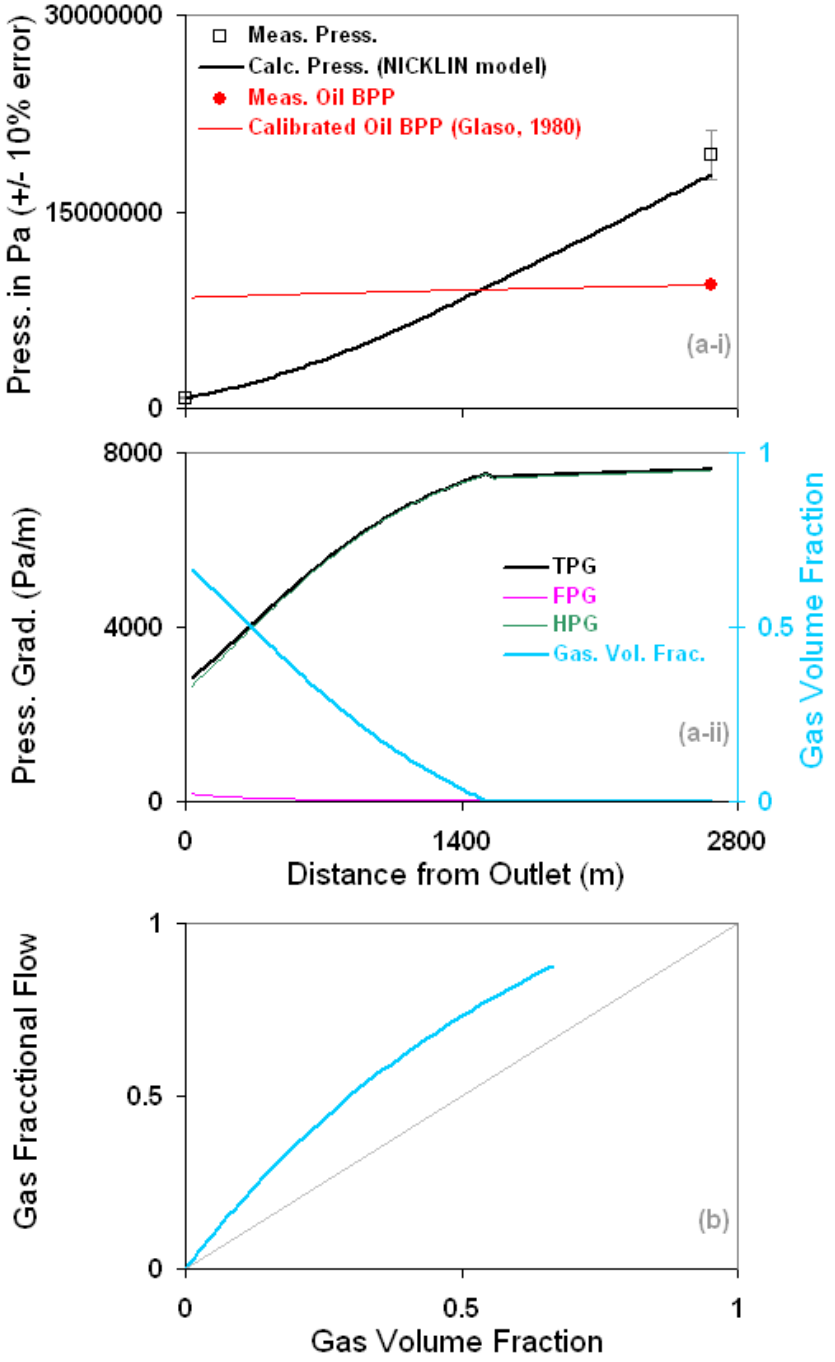

Figure 7.6.43: Prediction of well 15 of Chierici et al. (1974) with the NICKLIN model.

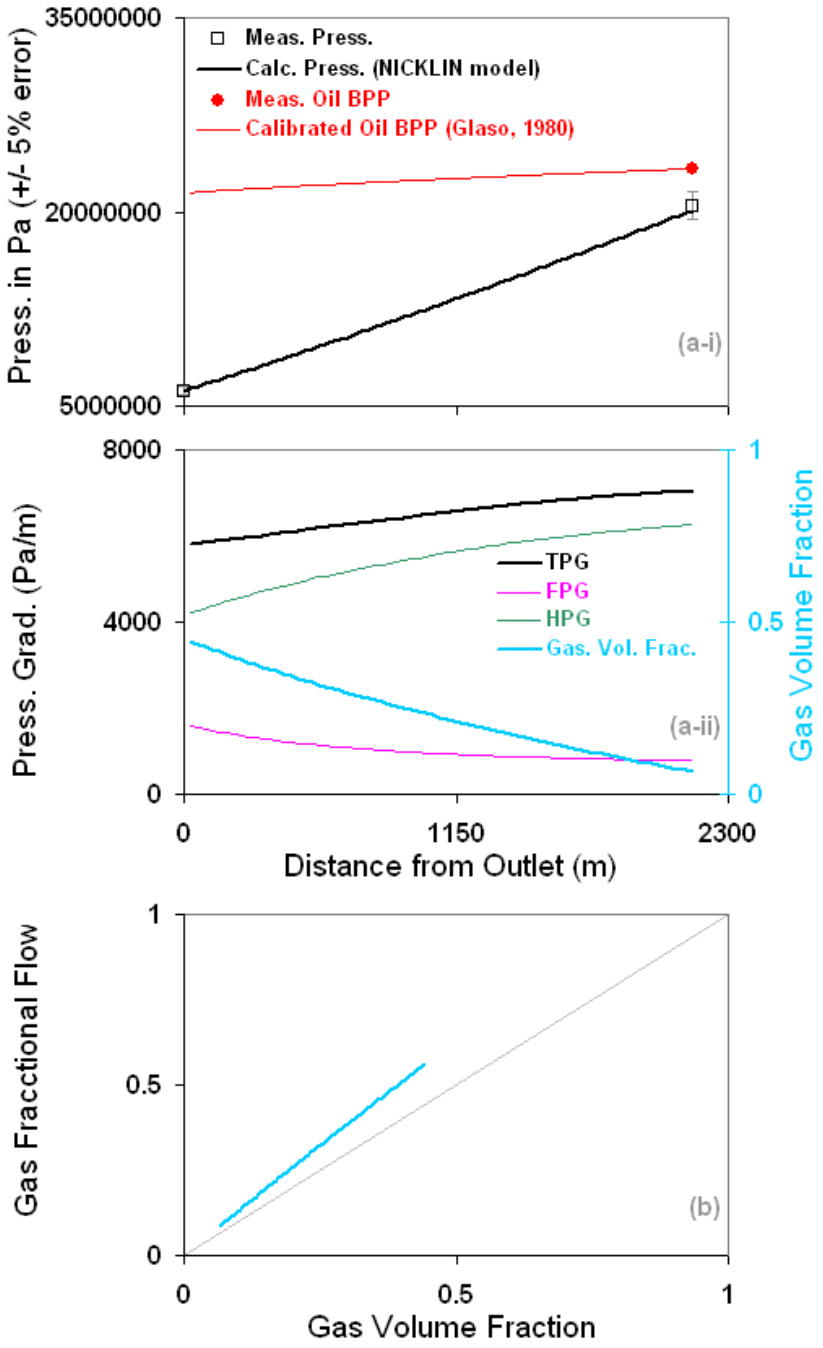

Figure 7.6.44: Prediction of well 19 of Chierici et al. (1974) with the NICKLIN model.

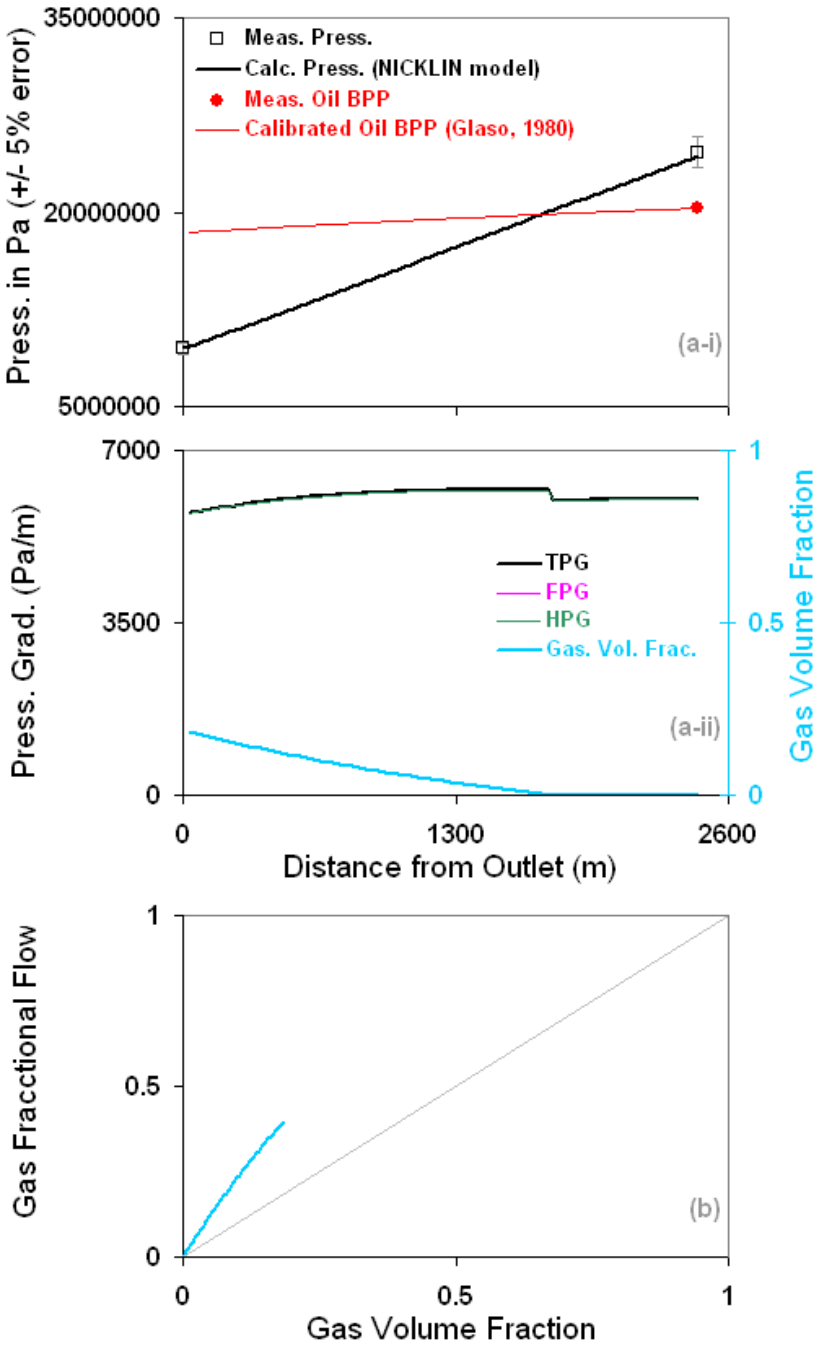

Figure 7.6.45: Prediction of well 22 of Chierici et al. (1974) with the NICKLIN model.

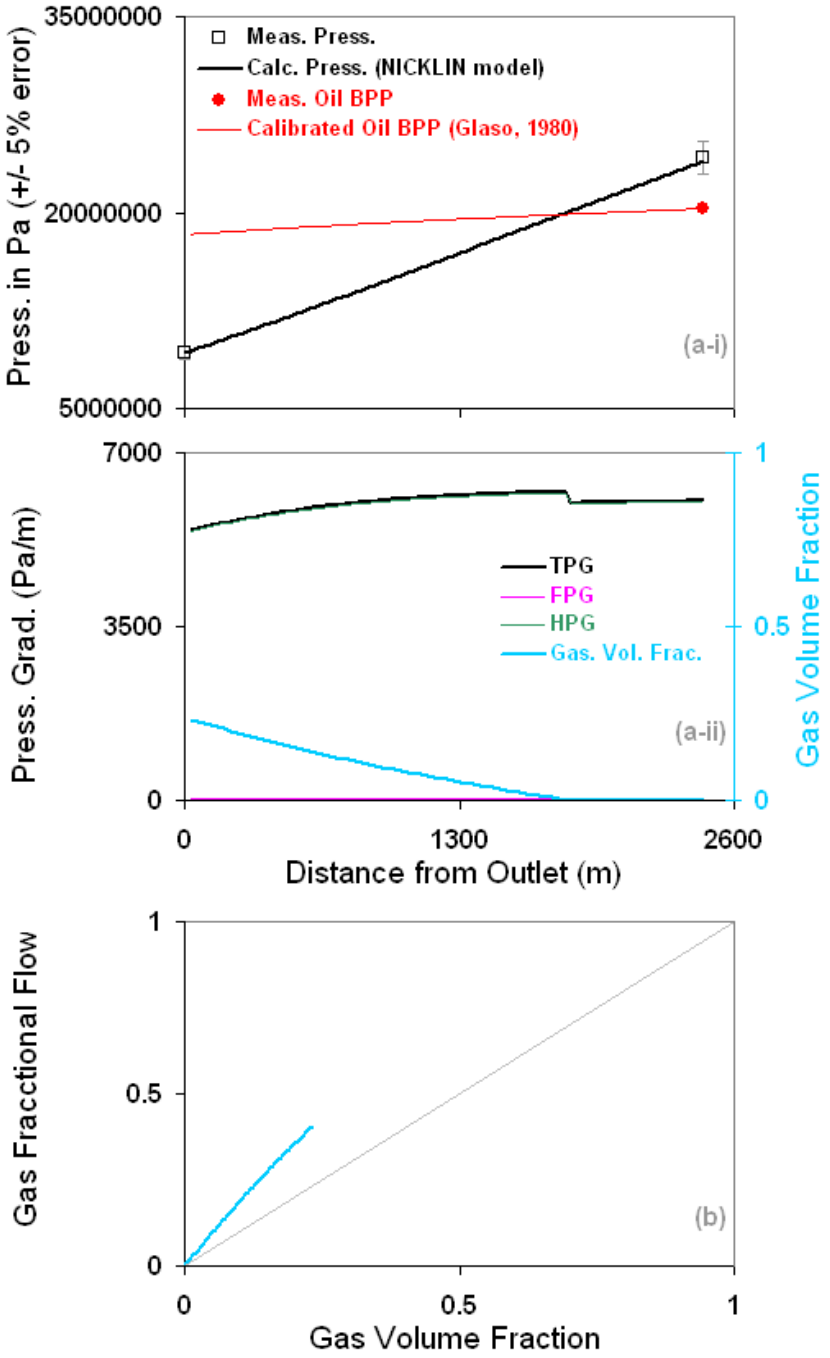

Figure 7.6.46: Prediction of well 23 of Chierici et al. (1974) with the NICKLIN model.

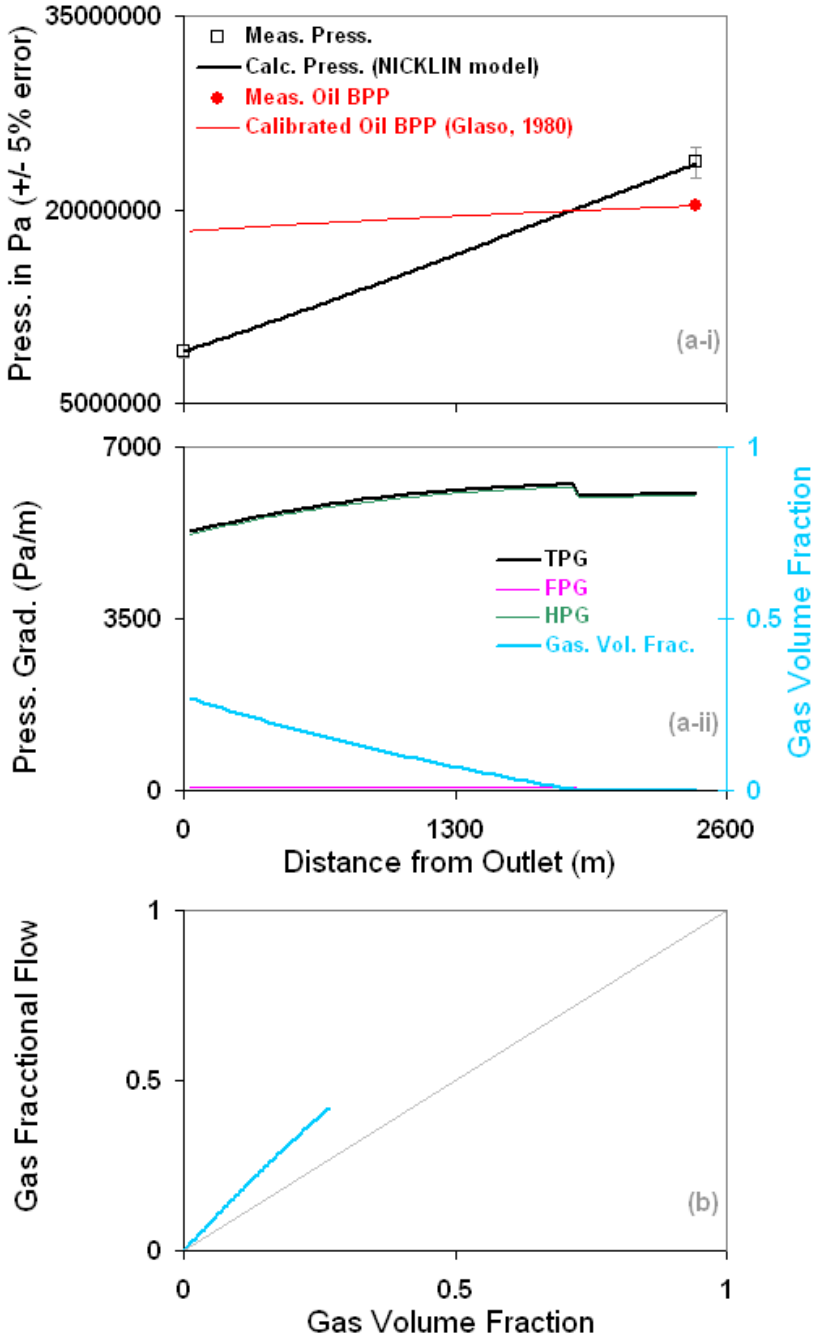

Figure 7.6.47: Prediction of well 24 of Chierici et al. (1974) with the NICKLIN model.

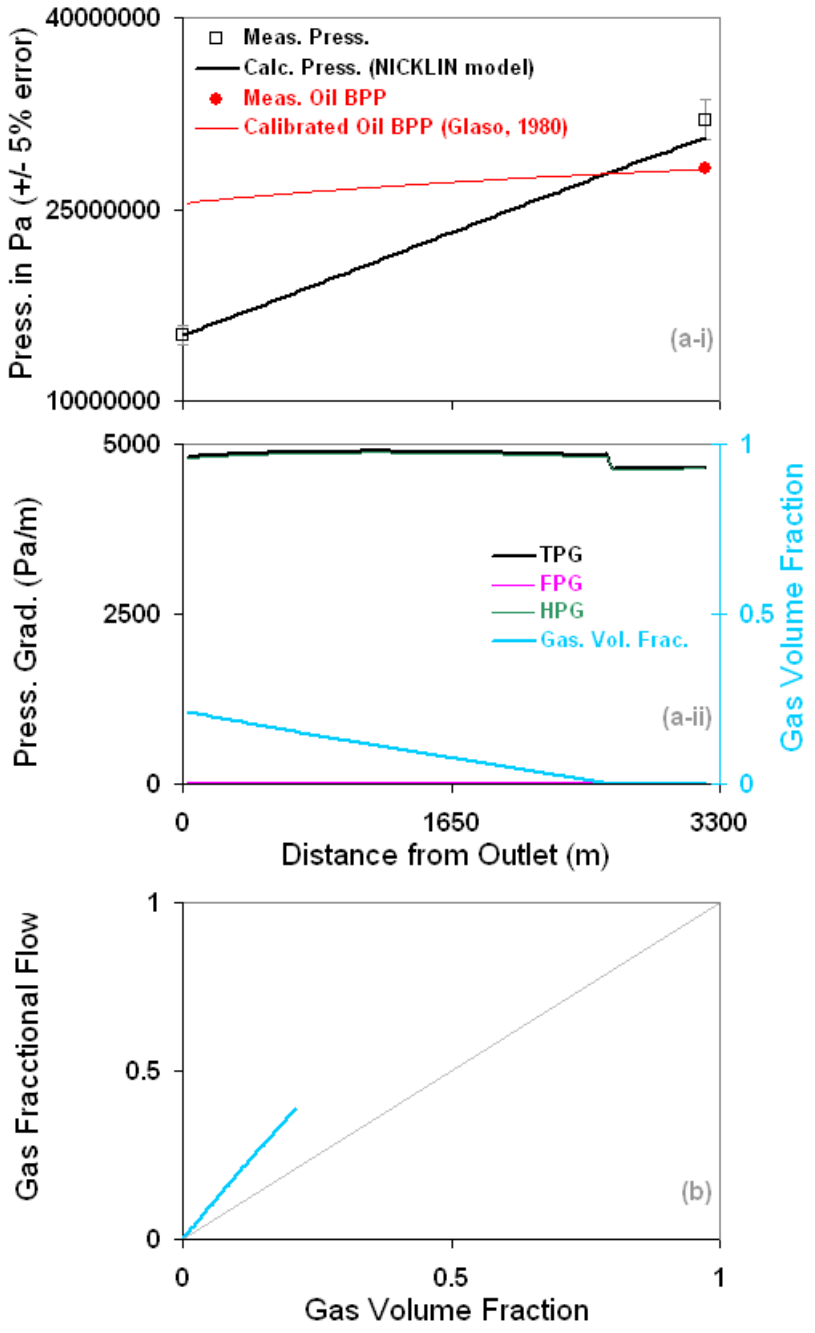

Figure 7.6.48: Prediction of well 30 of Chierici et al. (1974) with the NICKLIN model.

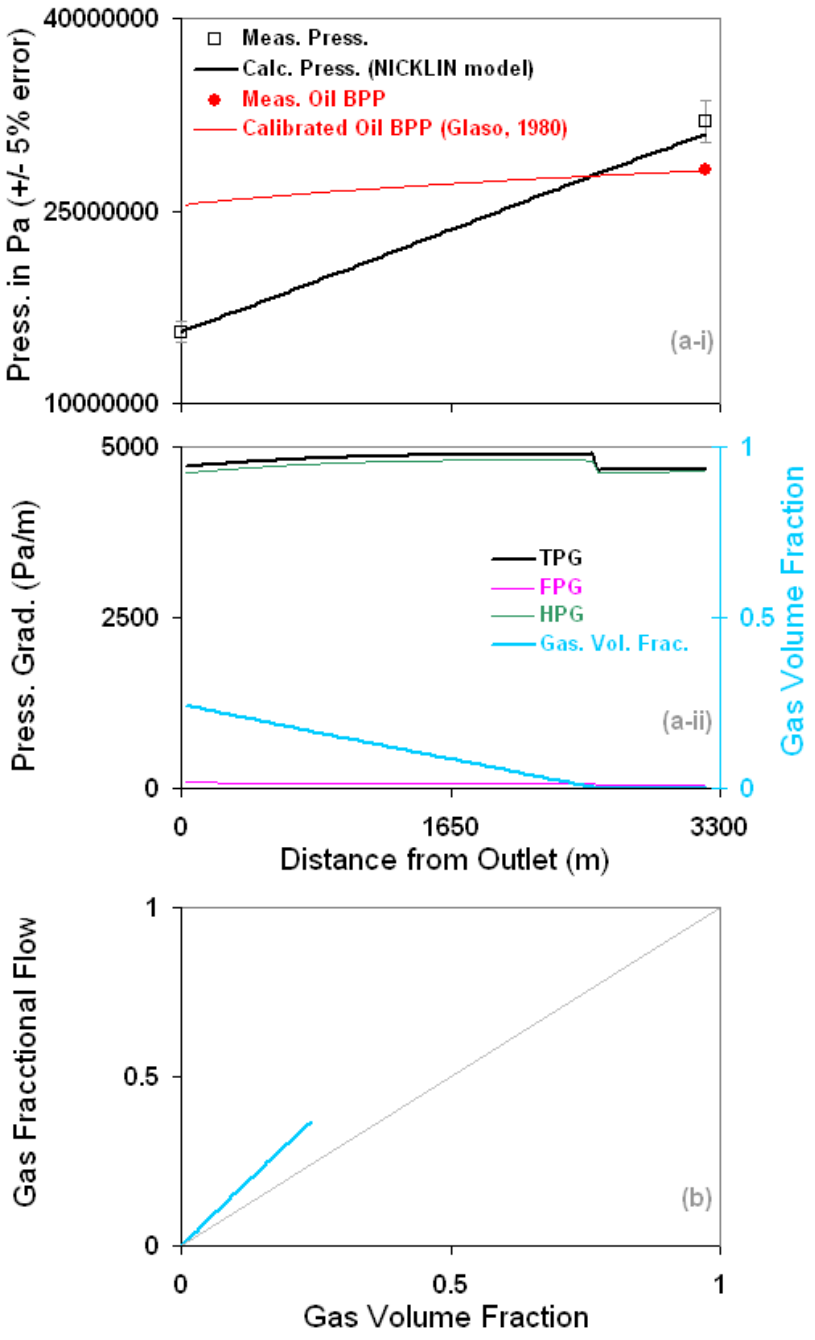

Figure 7.6.49: Prediction of well 31 of Chierici et al. (1974) with the NICKLIN model.

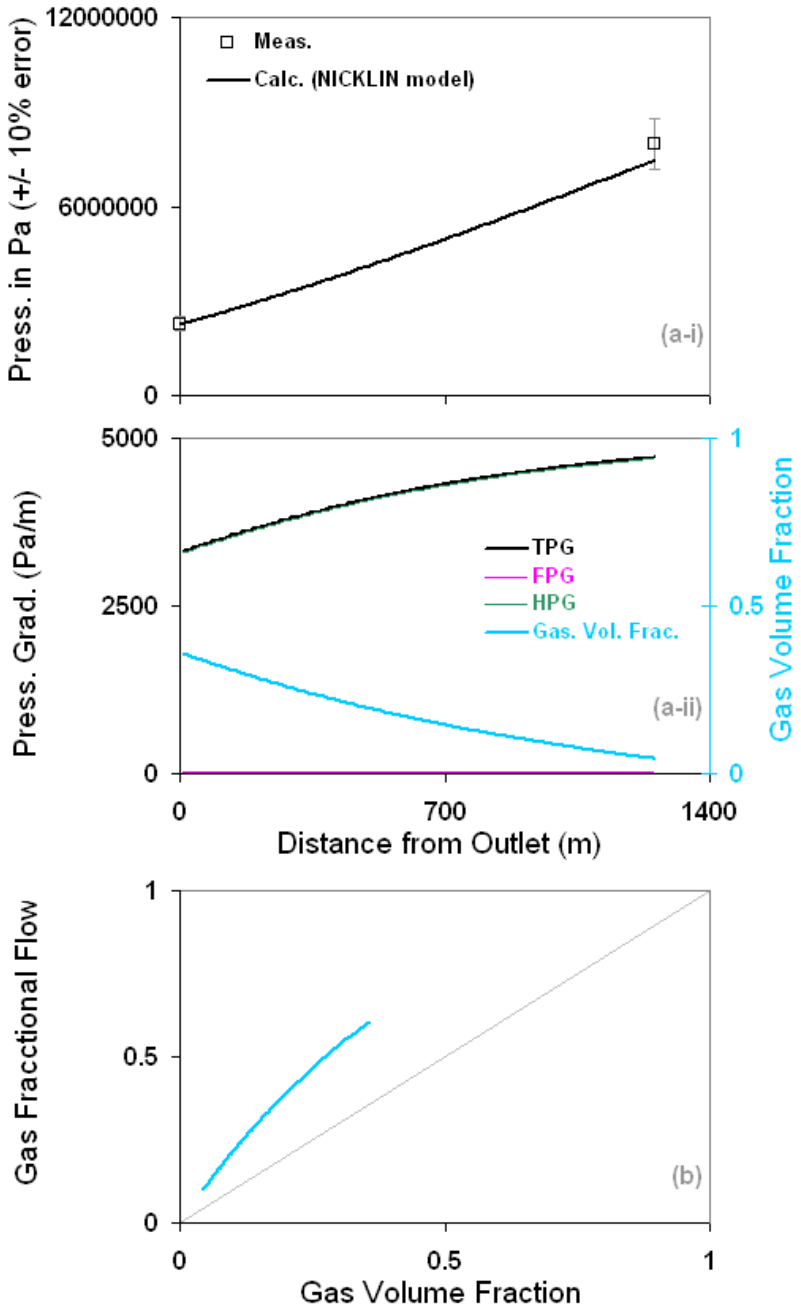

Figure 7.6.50: Prediction of the two-phase, deviated well 24 of Corteville et al. (1991) with the NICKLIN model.

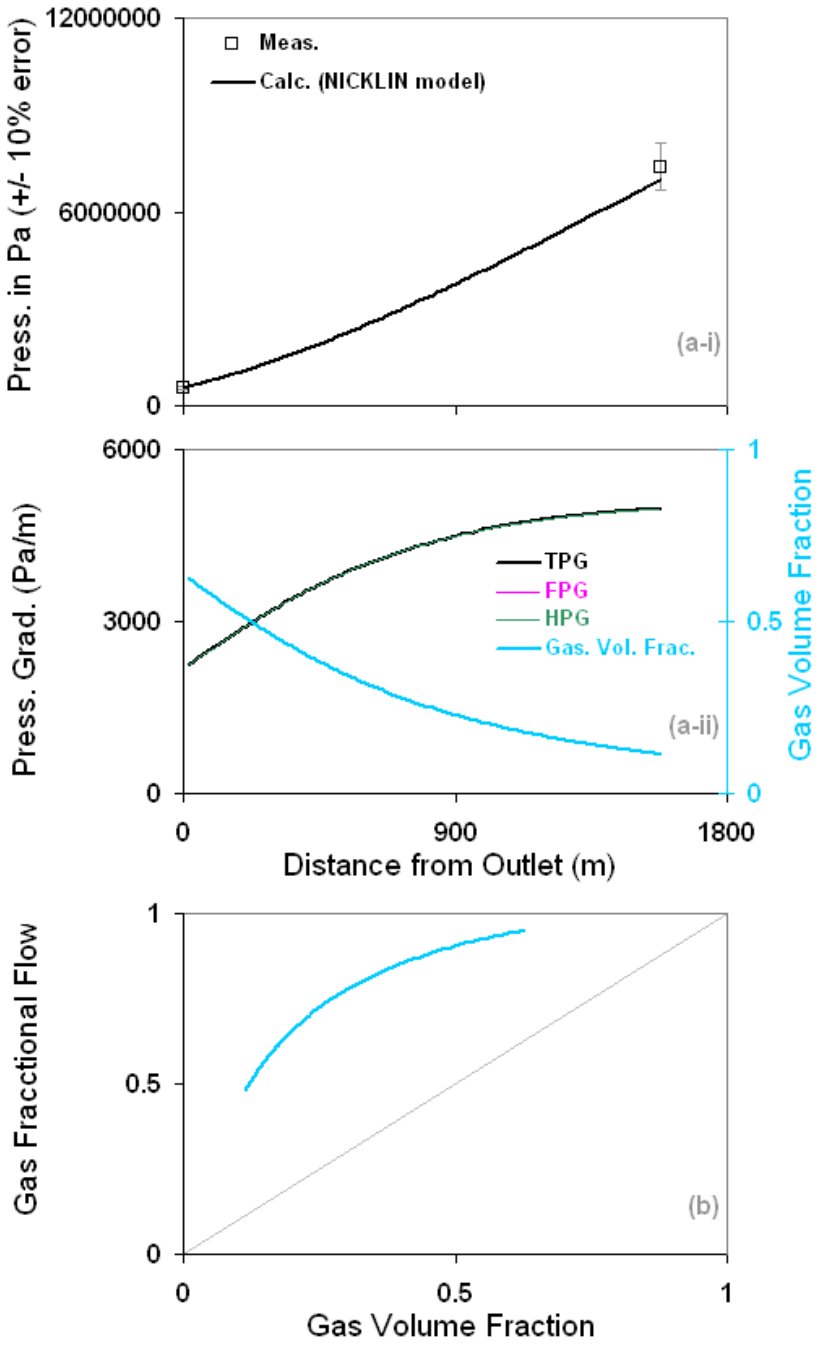

Figure 7.6.51: Prediction of the two-phase, deviated well 27 of Corteville et al. (1991) with the NICKLIN model.

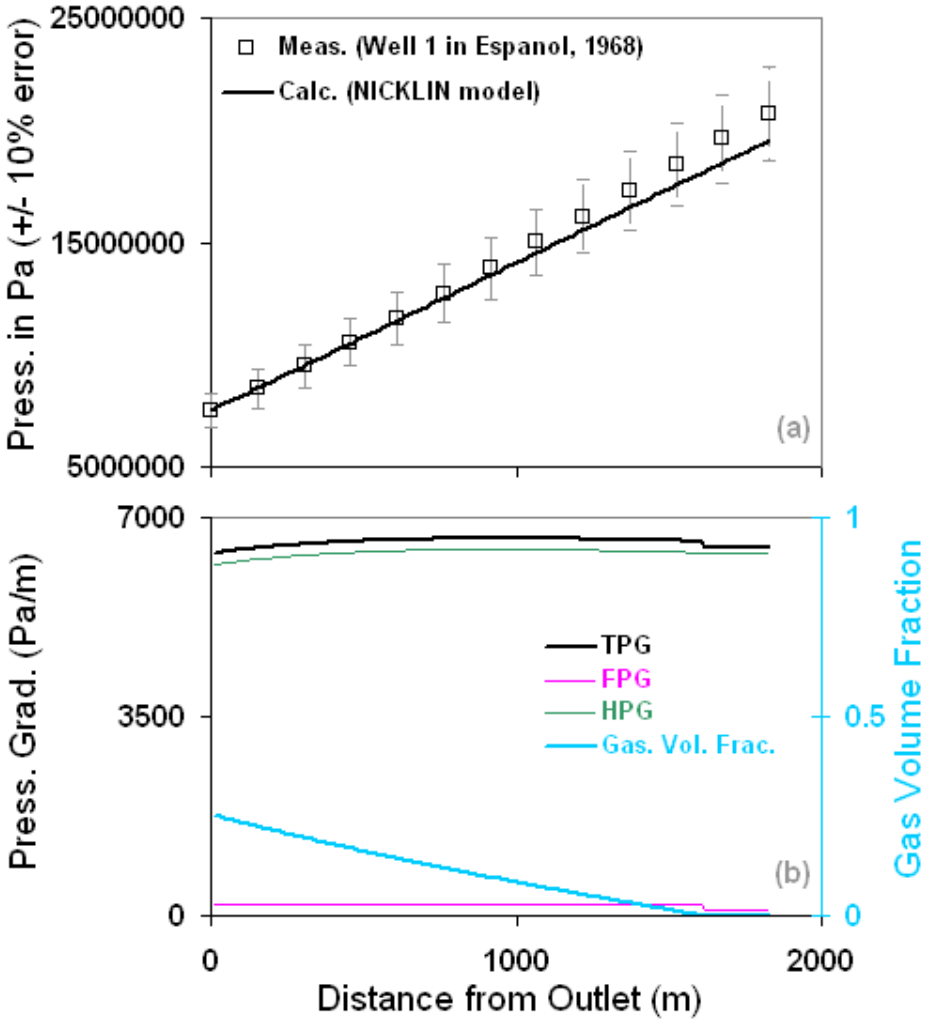

Figure 7.6.52: Prediction of well 1 of Espanol (1968) with the NICKLIN model.

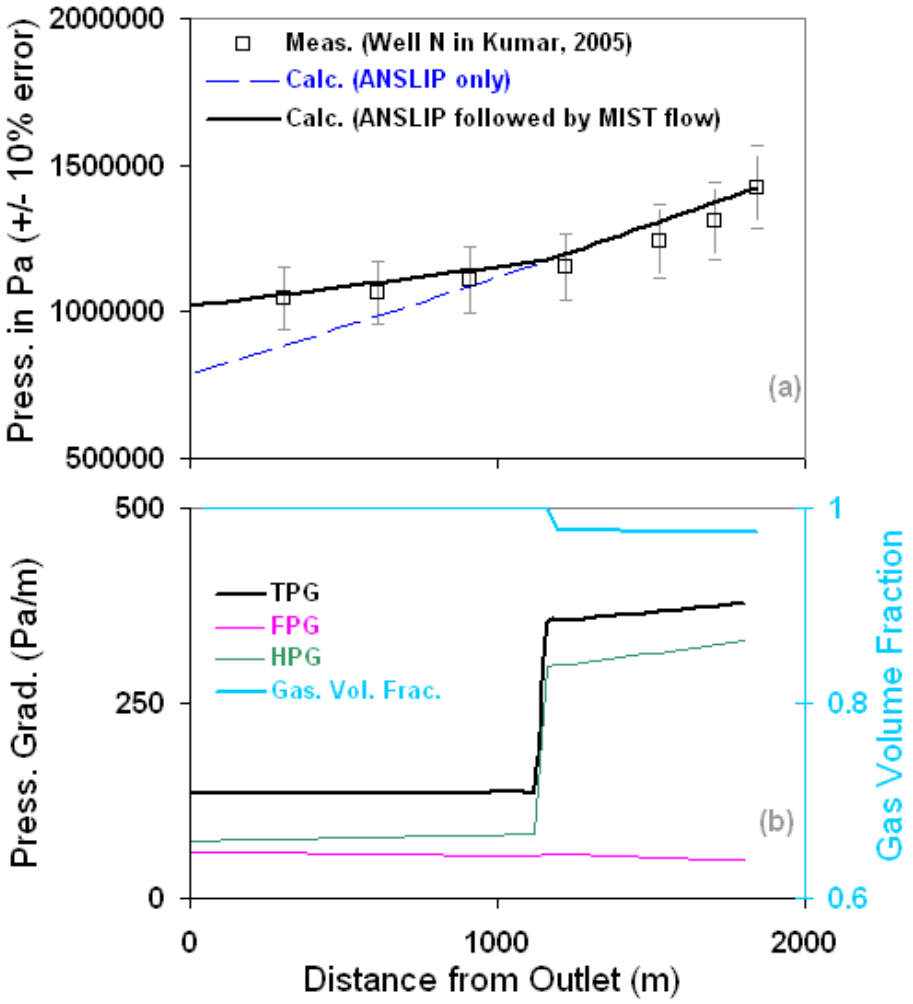

Figure 7.6.53: The use of combined fractional flow models to describe complex wellbore flows.

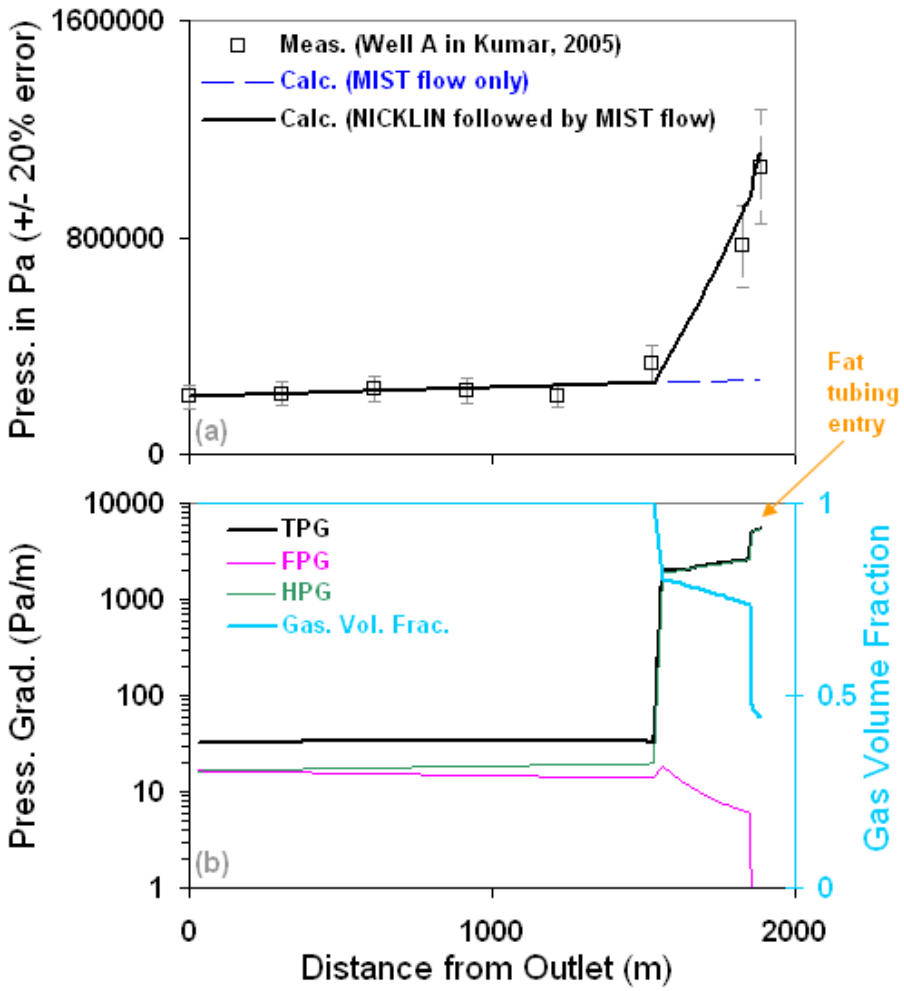

Figure 7.6.54: The use of combined fractional flow models to describe complex wellbore flows. These fractional flow models can be used to explain the averaged slip behaviors of the flowing fluids, for example in the case shown, as possibly a slug flow followed by a mist flow.

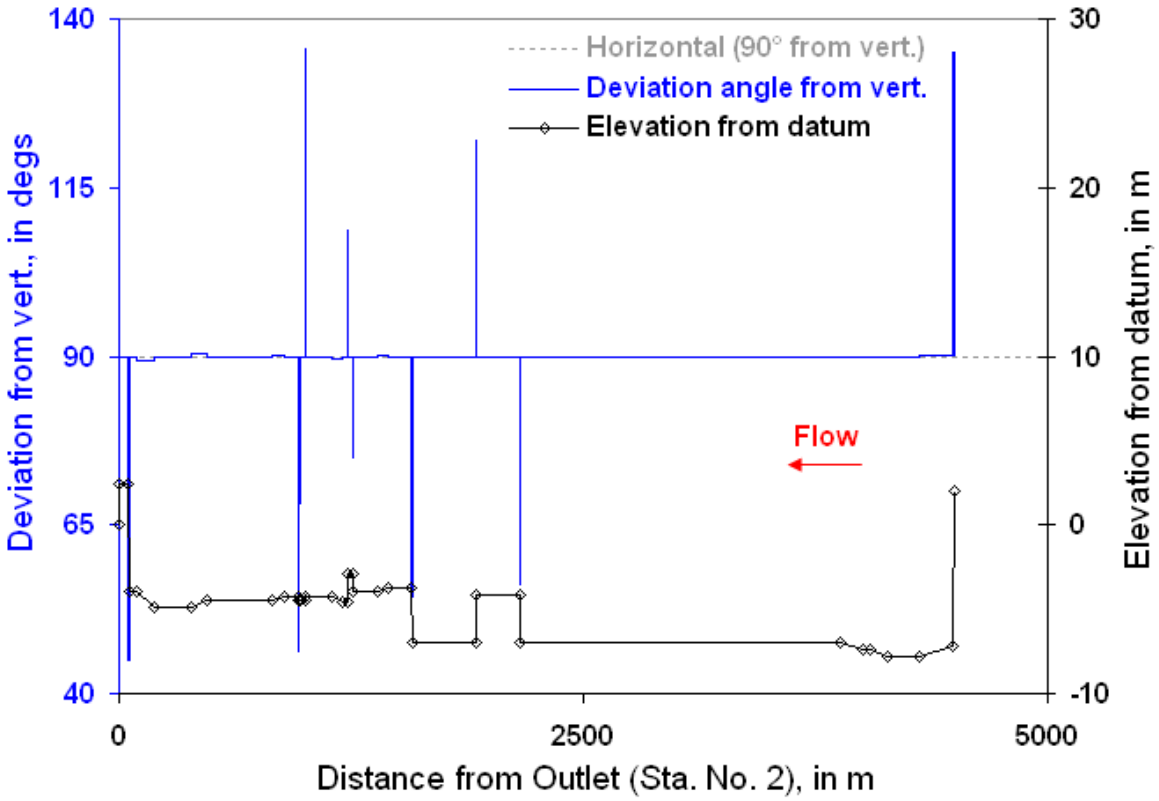

Figure 7.7.1: The elevation profile of the Prudhoe bay 12-inch and 16-inch pipelines of Brill et al. (1981).

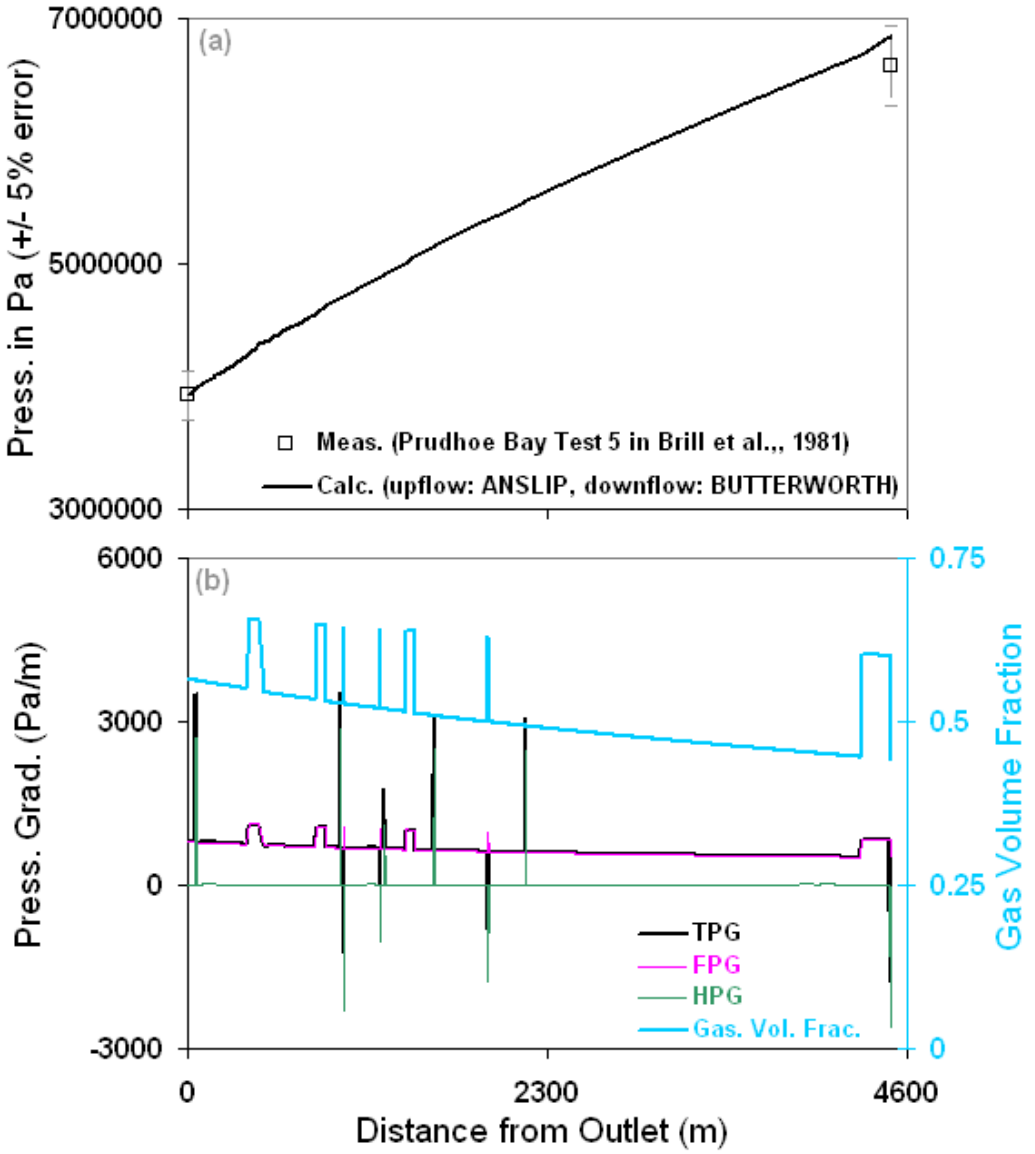

Figure 7.7.2: One example prediction from the 12-inch pipeline tests – test no. 5 of Brill et al. (1981)

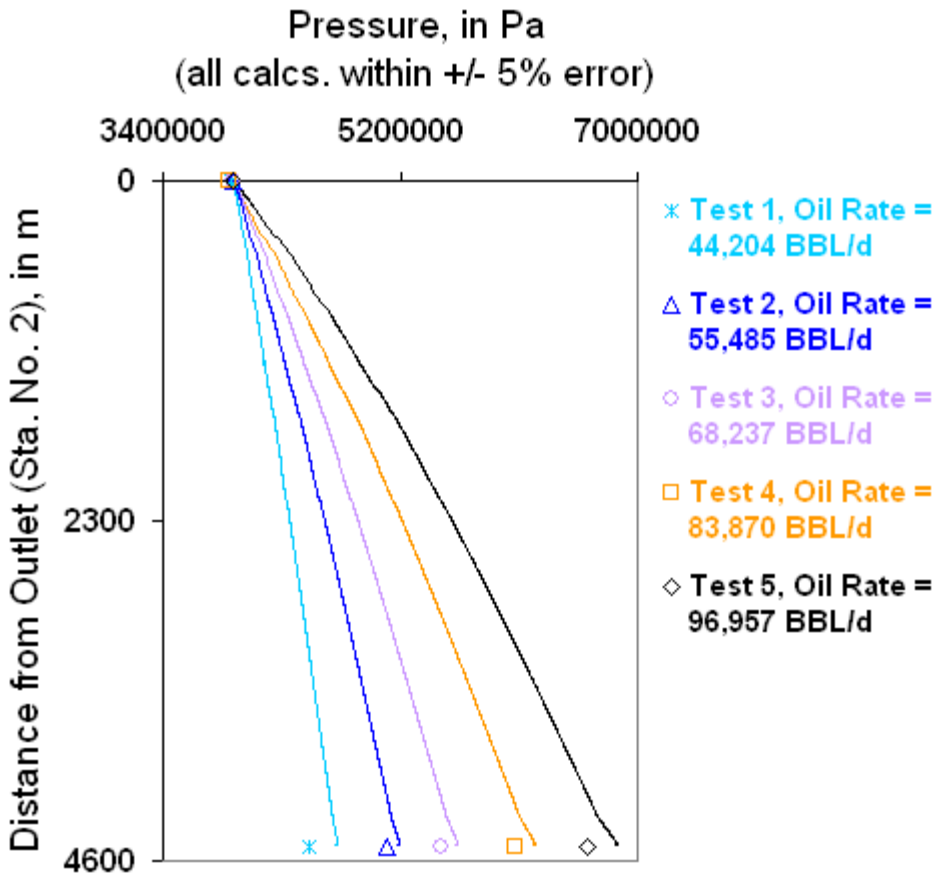

Figure 7.7.3: Prediction of the stabilized 12-inch pipeline tests of Brill et al. (1981).

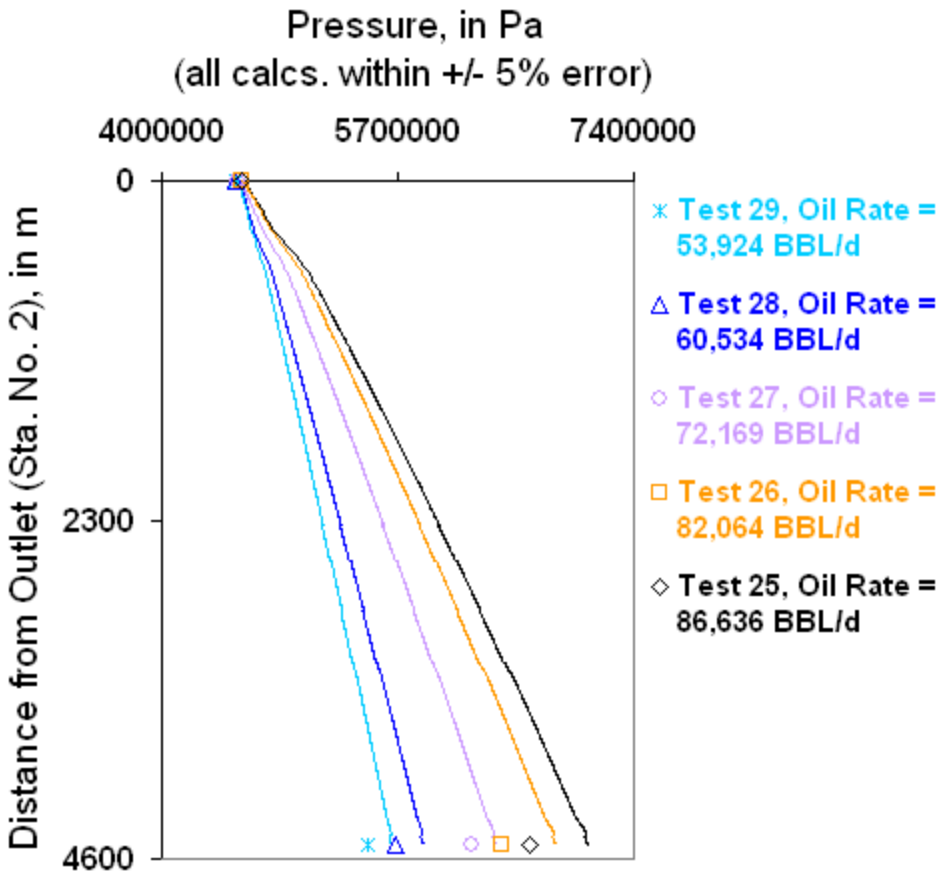

Figure 7.7.4: Prediction of the unstabilized 12-inch pipeline tests of Brill et al. (1981).

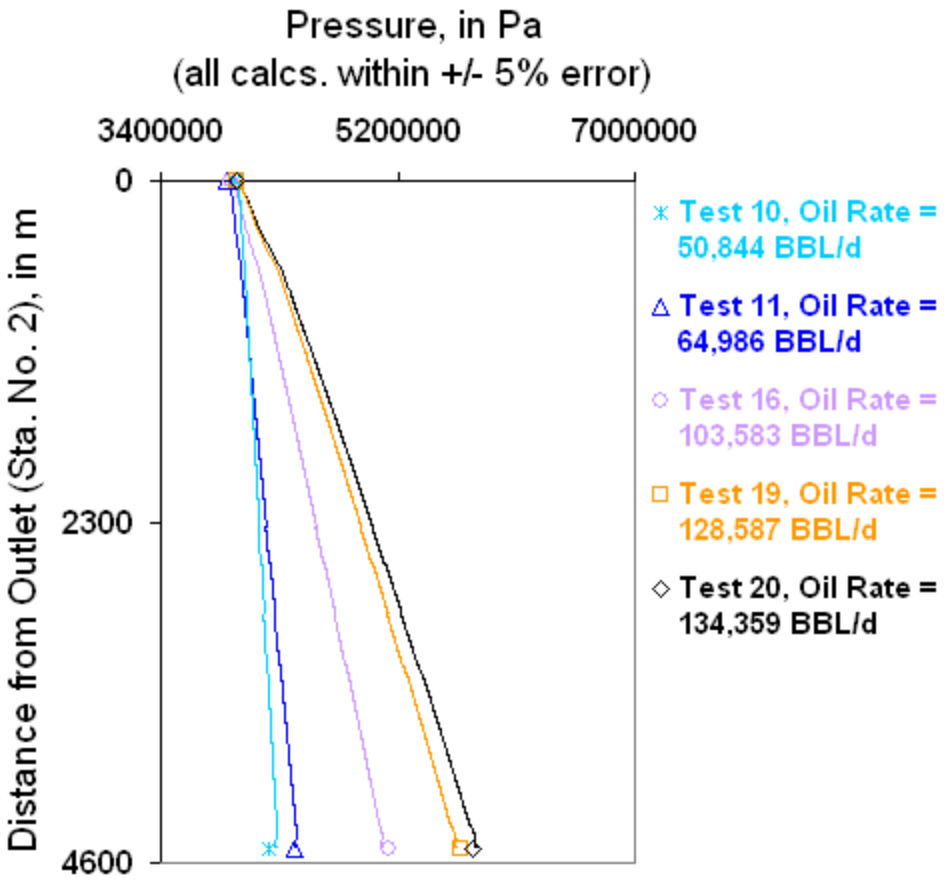

Figure 7.7.5: Prediction of the stabilized 16-inch pipeline tests of Brill et al. (1981).

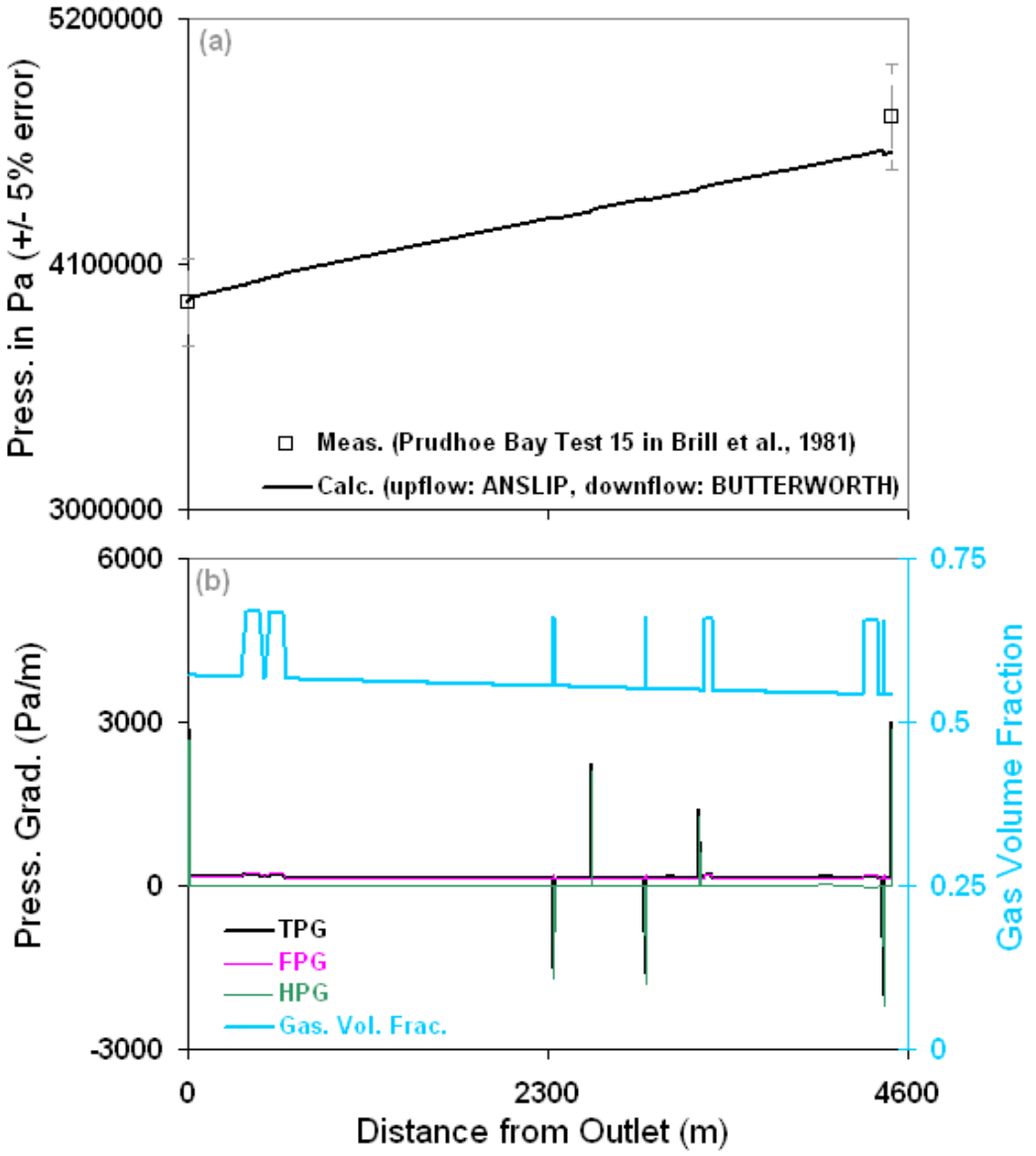

Figure 7.7.6: One example prediction from the 16-inch pipeline tests – test no. 15 of Brill et al. (1981)

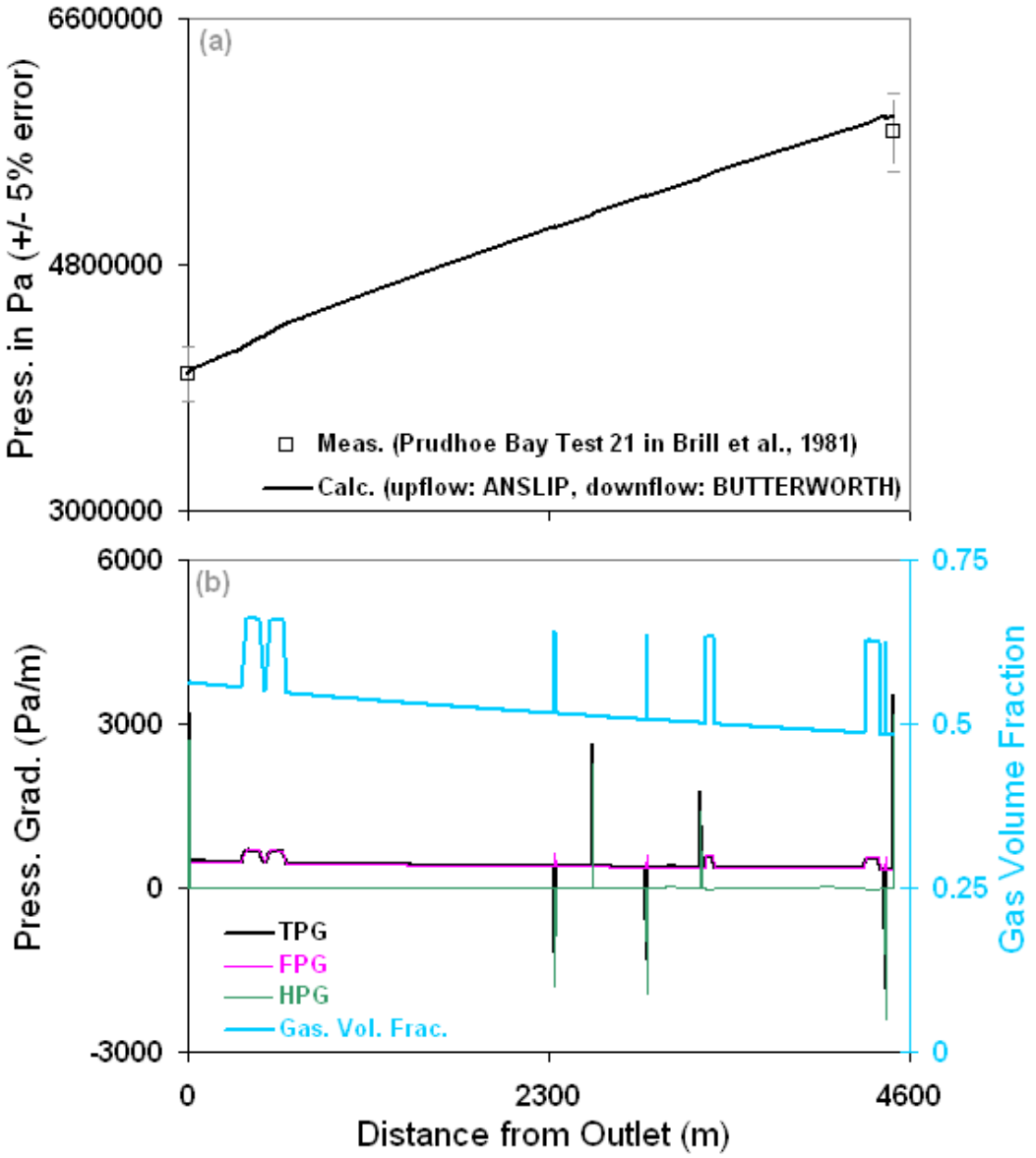

Figure 7.7.7: One example prediction from the 16-inch pipeline tests – test no. 21 of Brill et al. (1981)

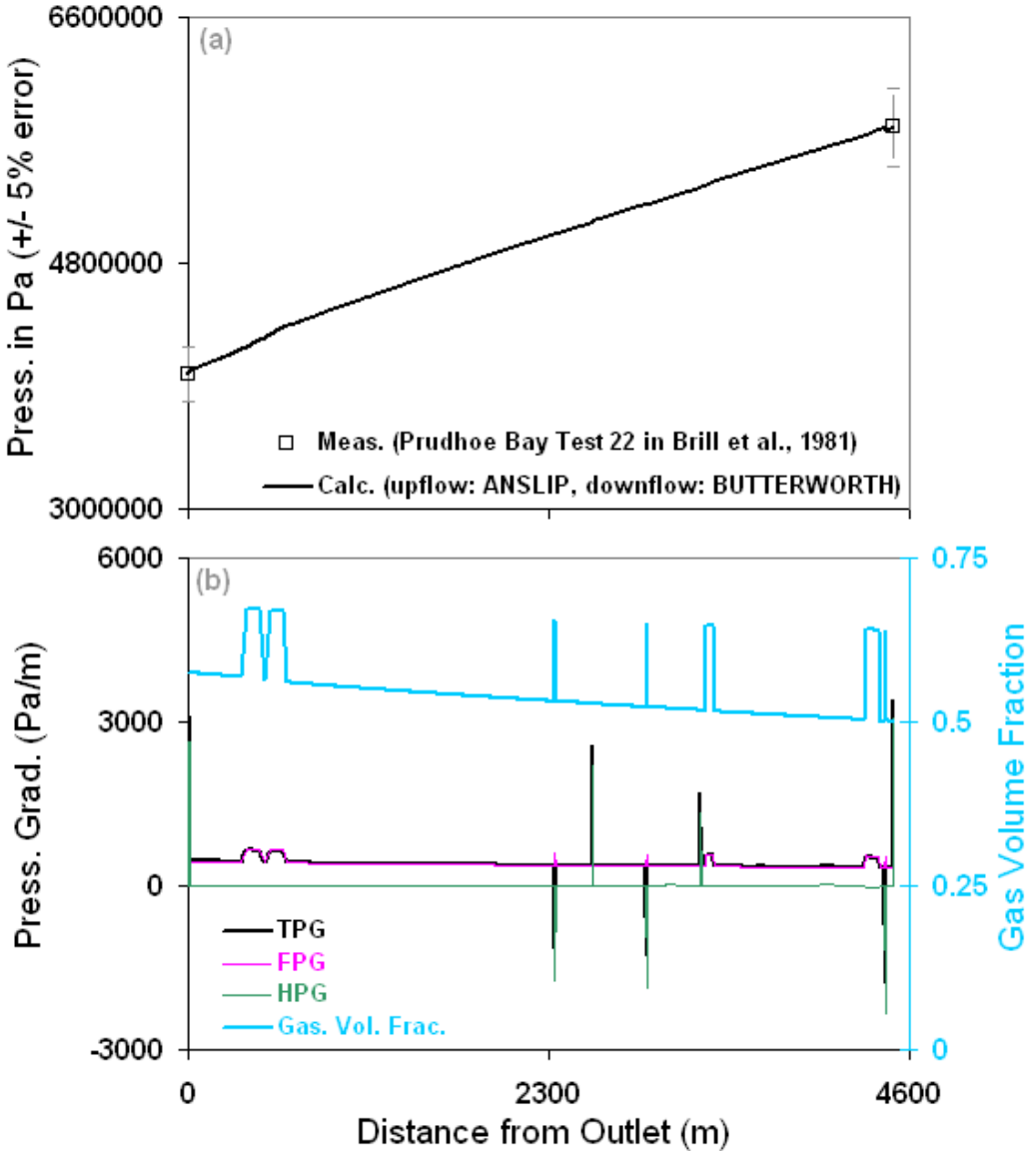

Figure 7.7.8: One example prediction from the 16-inch pipeline tests – test no. 22 of Brill et al. (1981)

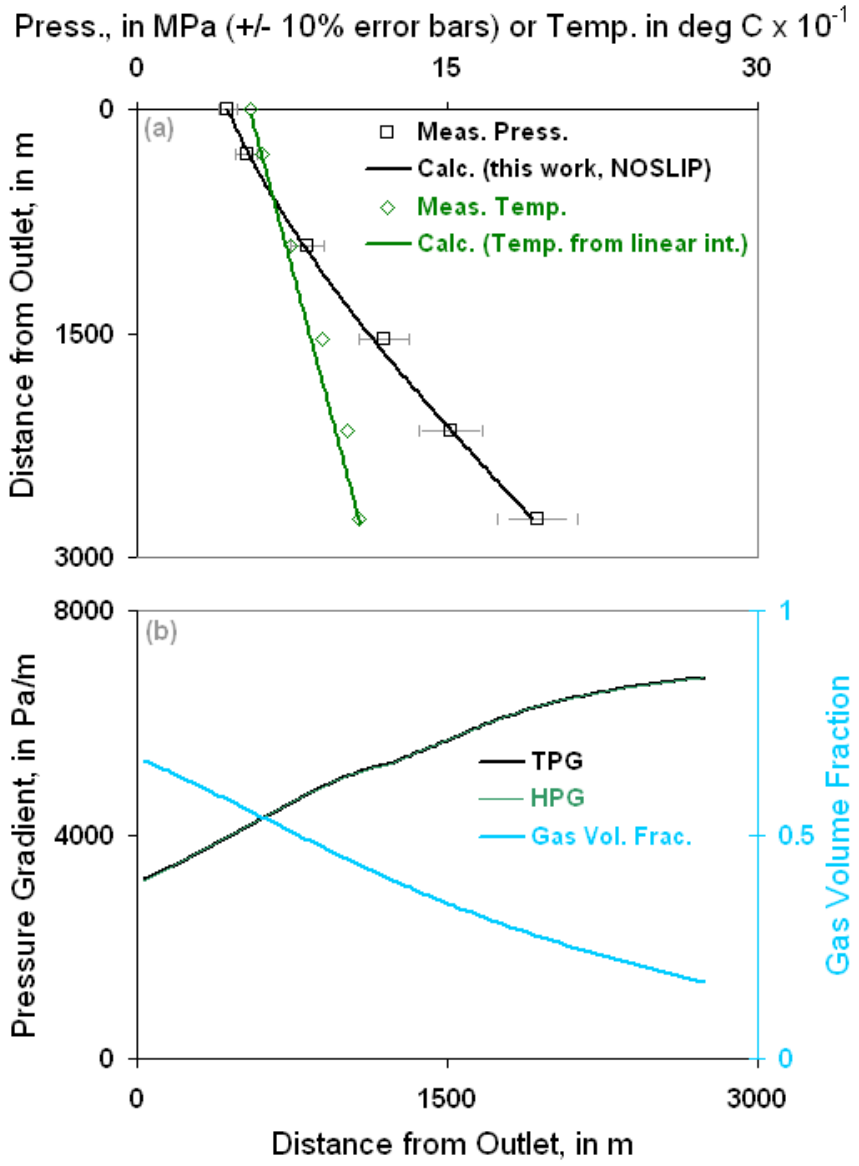

Figure 7.7.9: One example prediction of an 8-inch Prudhoe Bay well (No. 1774) from Ansari (1988) with the NOSLIP model.

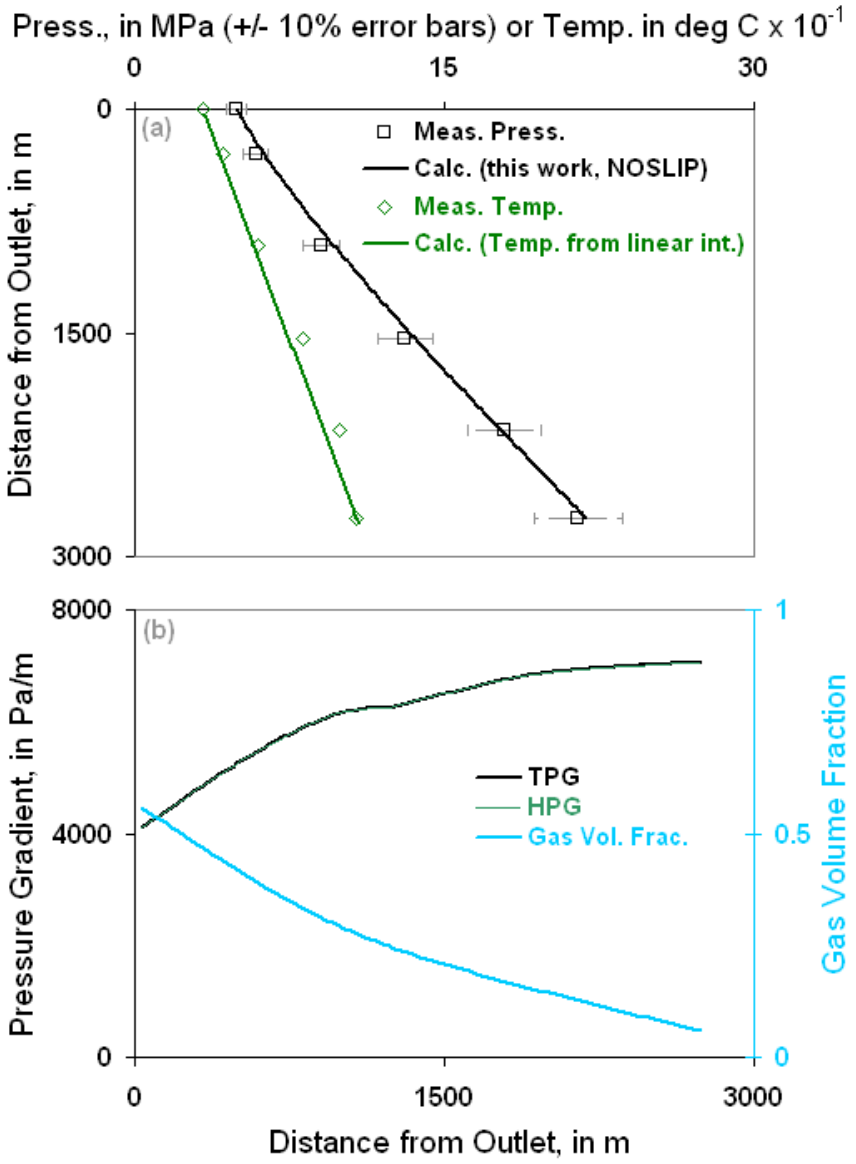

Figure 7.7.10: One example prediction of an 8-inch Prudhoe Bay well (No. 1775) from Ansari (1988) with the NOSLIP model.

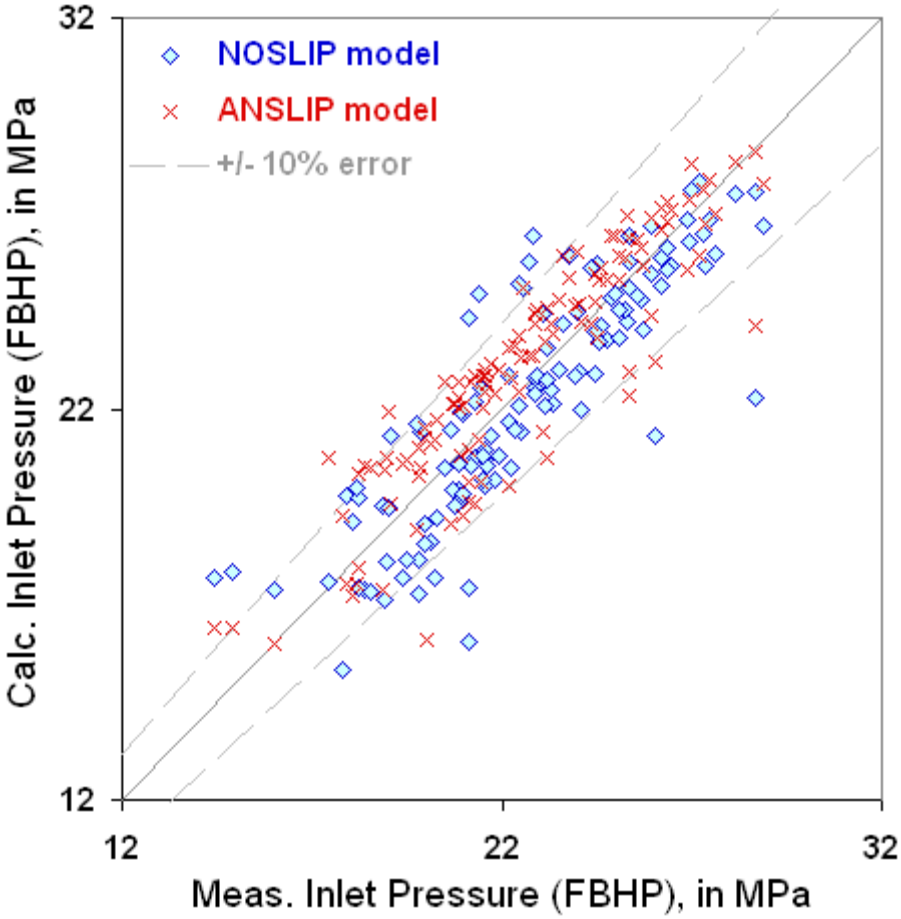

Figure 7.7.11: All of the Prudhoe Bay high-rate wells from Ansari (1988) predicted within +/- 10% error with either the NOSLIP or ANSLIP wholly-analytical models.

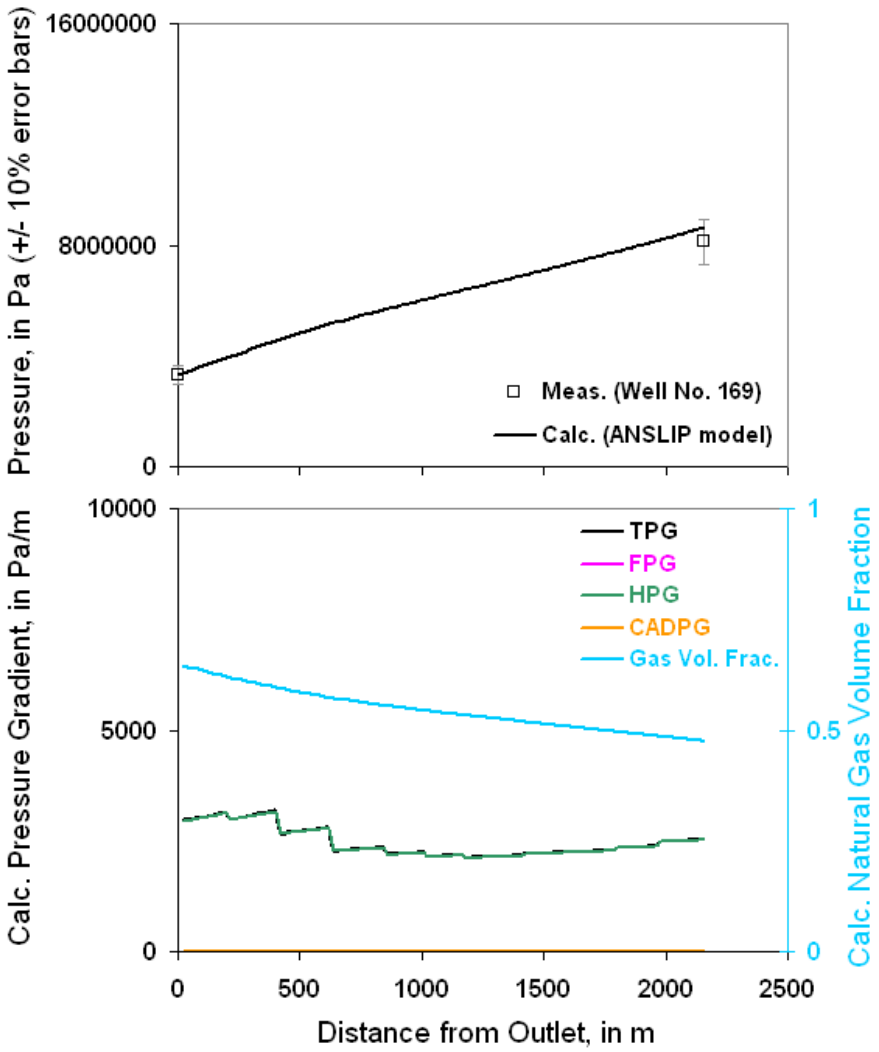

Figure 7.8.1: One example low oil rate, deviated well prediction of well 169 of Rai et al. (1989) with the ANSLIP model.

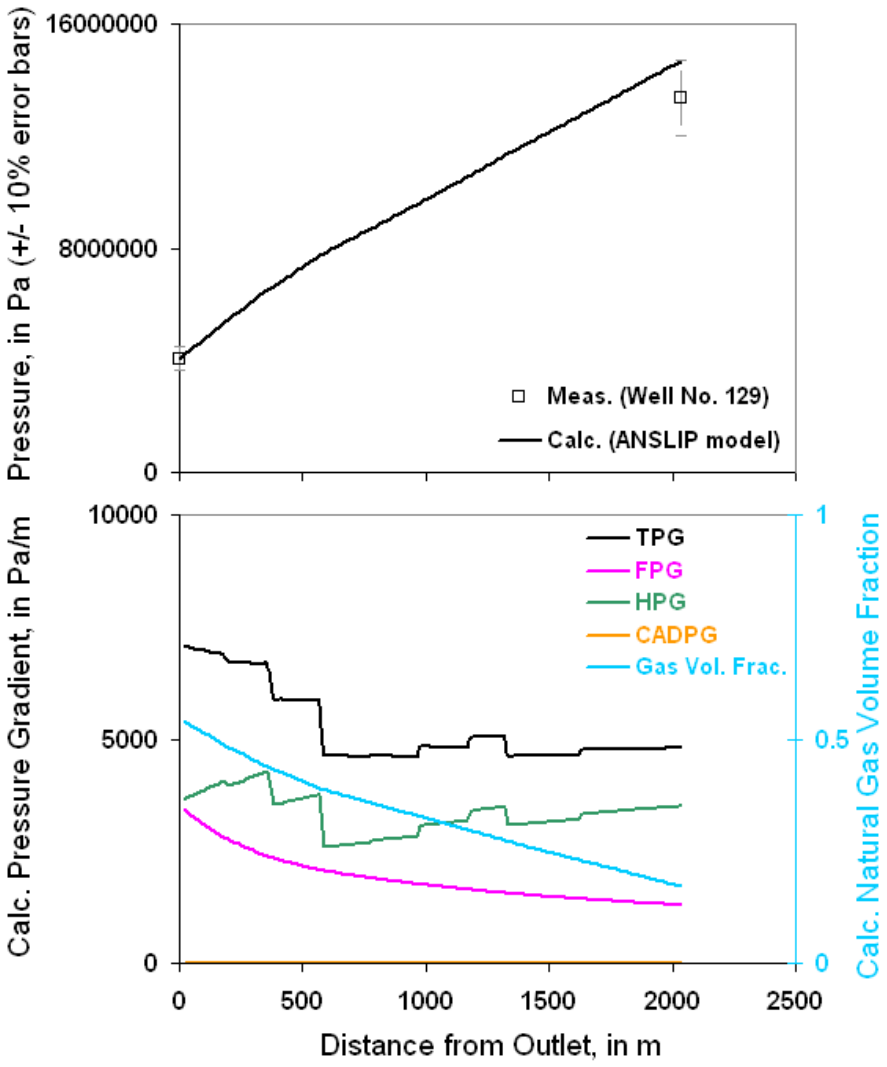

Figure 7.8.2: One example high oil rate, deviated well prediction of well 129 of Rai et al. (1989) with the ANSLIP model.

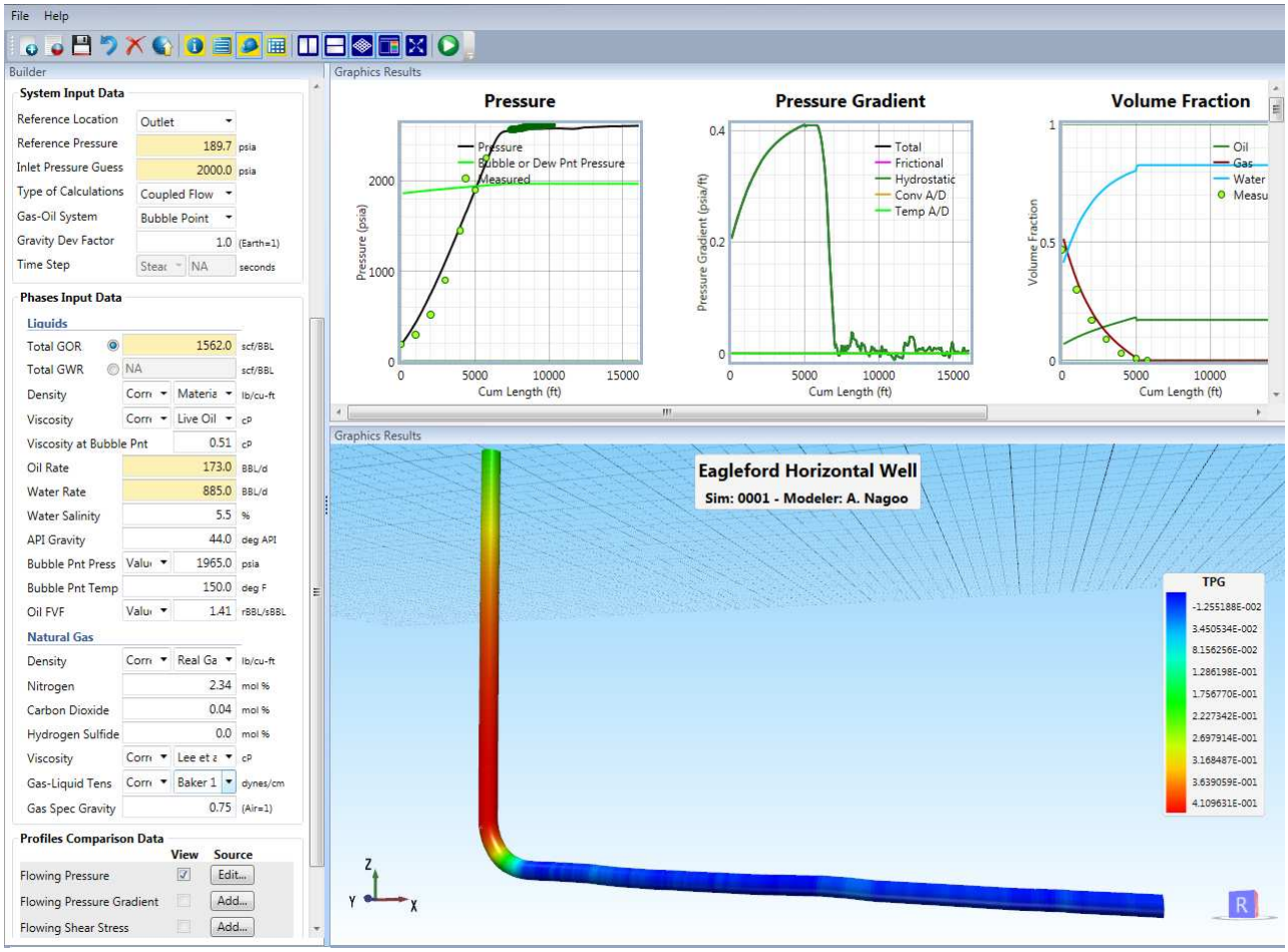

Figure 7.8.3: An actual Eagleford horizontal well predicted accurately with the WOLGHA model.

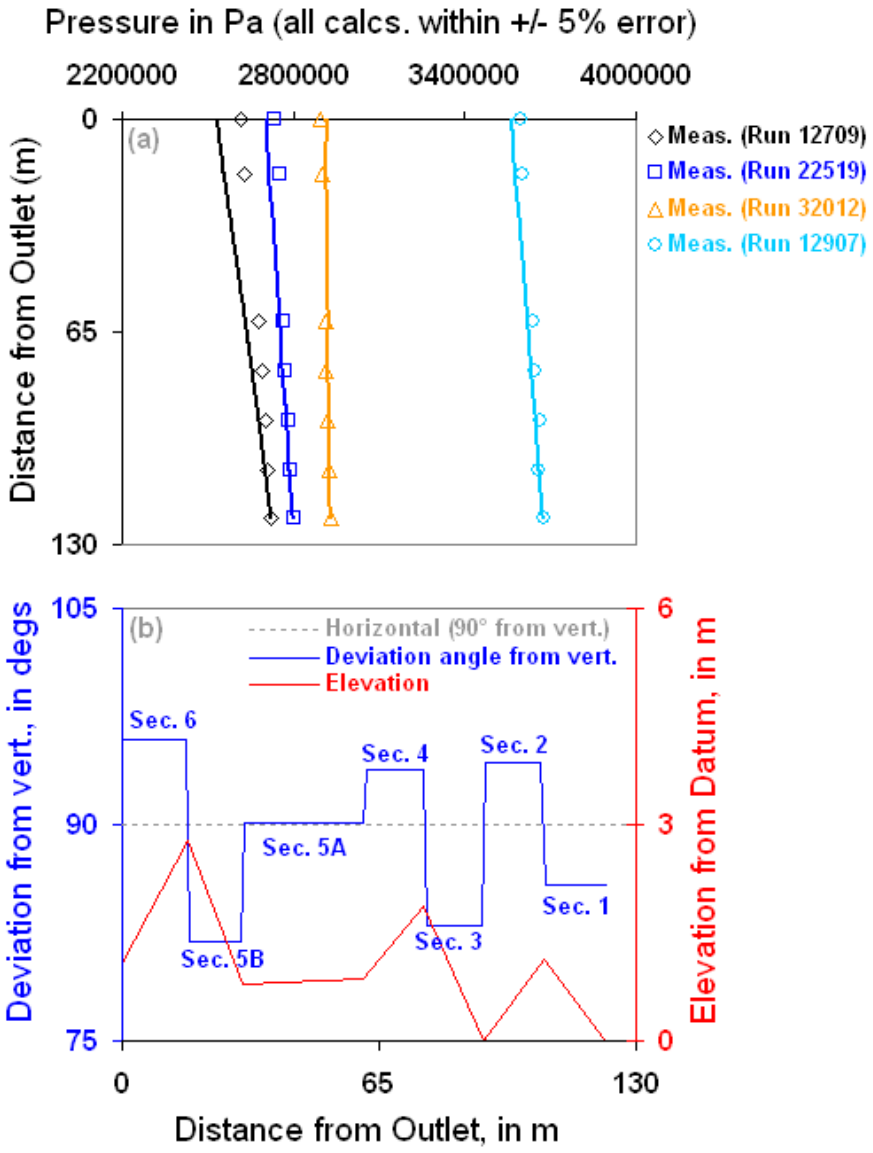

Figure 7.9.1: Example predictions of the connected-pipe network of Payne et al. (1979). Flows in upwards segments use the ANSLIP model and flows in downward segments use the BUTTERWORTH model. Lines in (a) are calculations and the points are measurements.

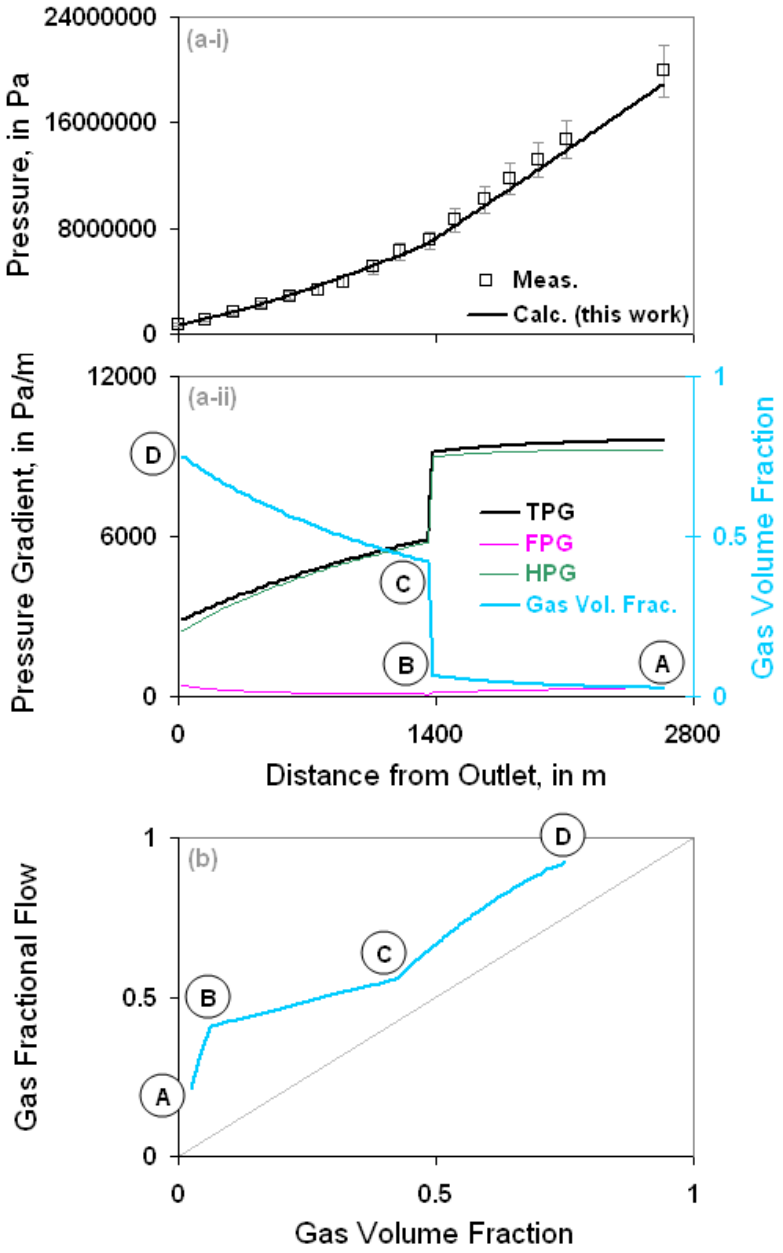

Figure 7.9.2: Prediction of gas lift in a low liquids rate well with the ANSLIP model – run 2 of Bertuzzi et al. (1953). At A, the well is flowing oil with solution gas continuously coming out. Then, at B, free gas is injected thus reducing the slip behavior significantly to that of C. From C to D the well flows with more gas coming out of solution as the pressure decreases in addition to the free gas injected.

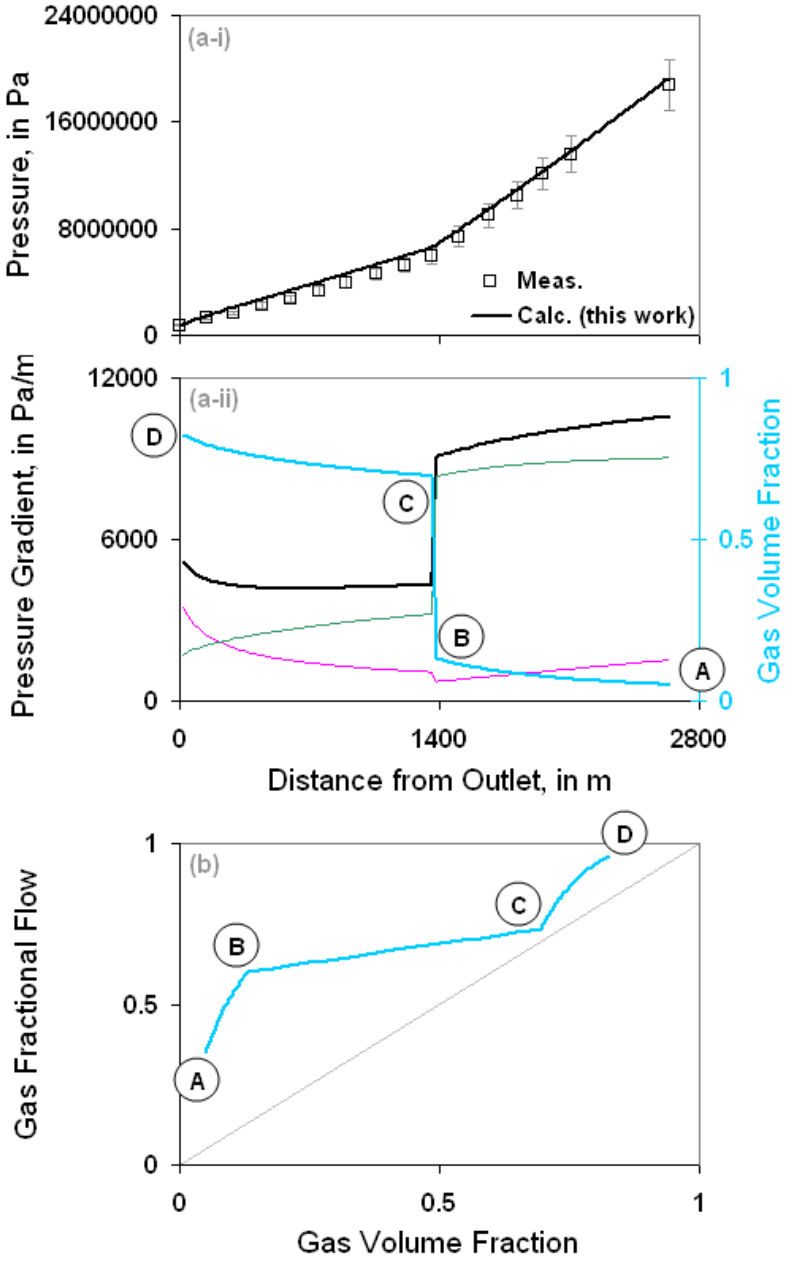

Figure 7.9.3: Prediction of gas lift in a high liquids rate well with the BUTTERWORTH model – run 1 of Bertuzzi et al. (1953).

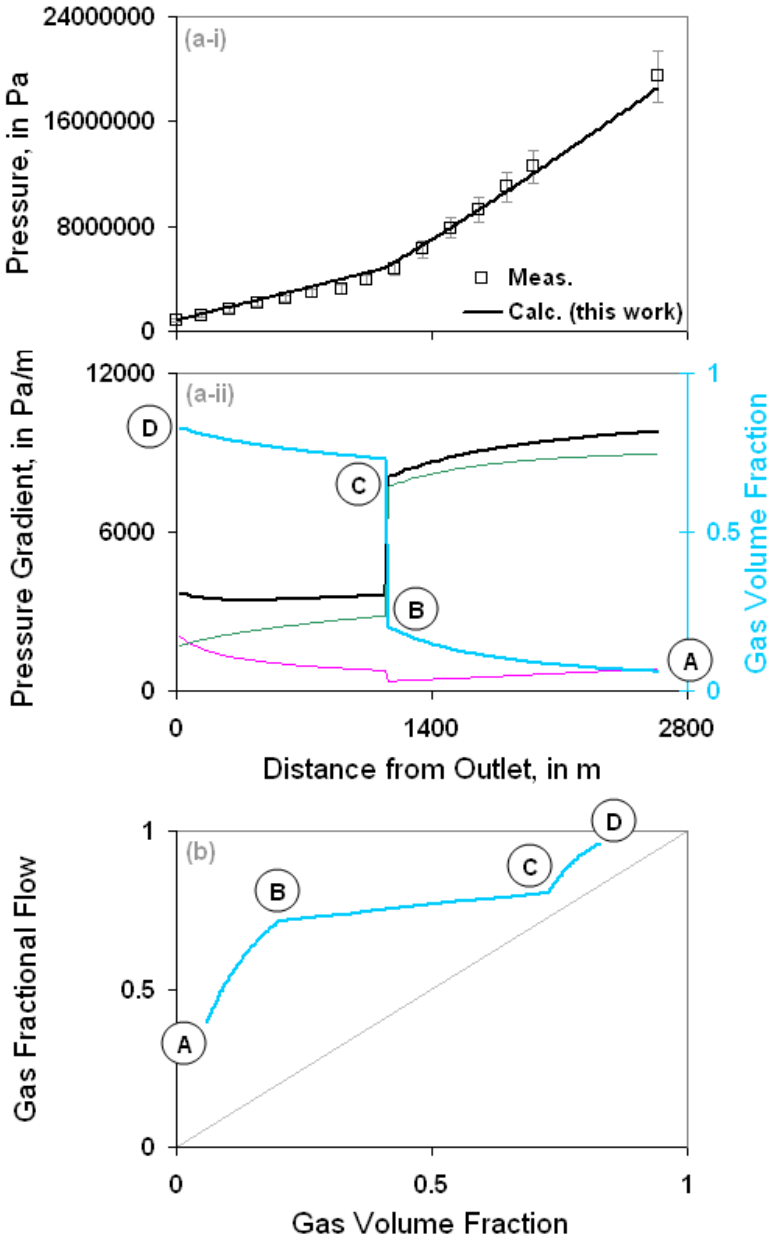

Figure 7.9.4: Prediction of gas lift in a high liquids rate well with the BUTTERWORTH model (but with shallower injection depth) – run 11 of Bertuzzi et al. (1953). As compared to Fig. 7.9.3, a shallower depth can be interpreted in the fractional flow graph as resulting in a higher slip just after gas injection (at C) and thus a poorer lift capacity resulting in a lower in-situ oil velocity than for the deeper gas injection case.

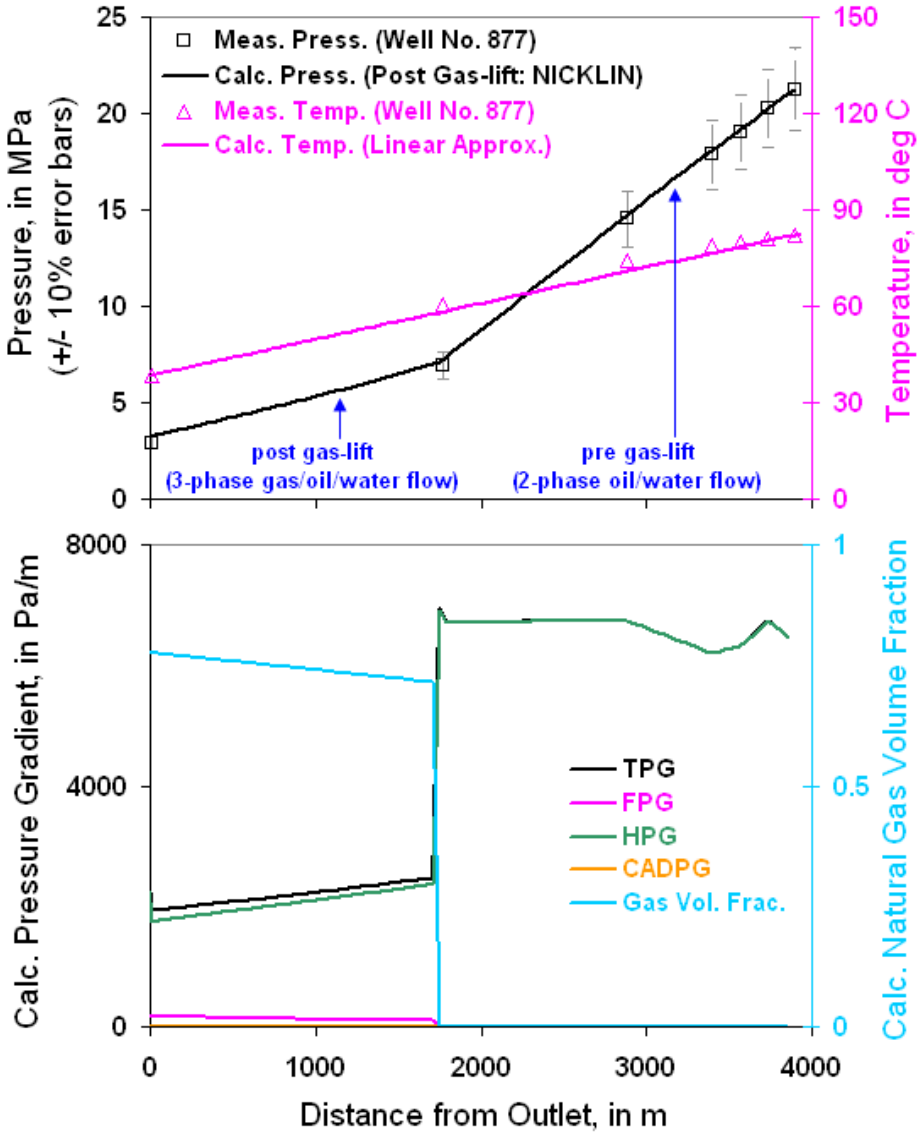

Figure 7.9.5: Prediction of deep gas lifted deviated well with the NICKLIN model from Ansari (1988).

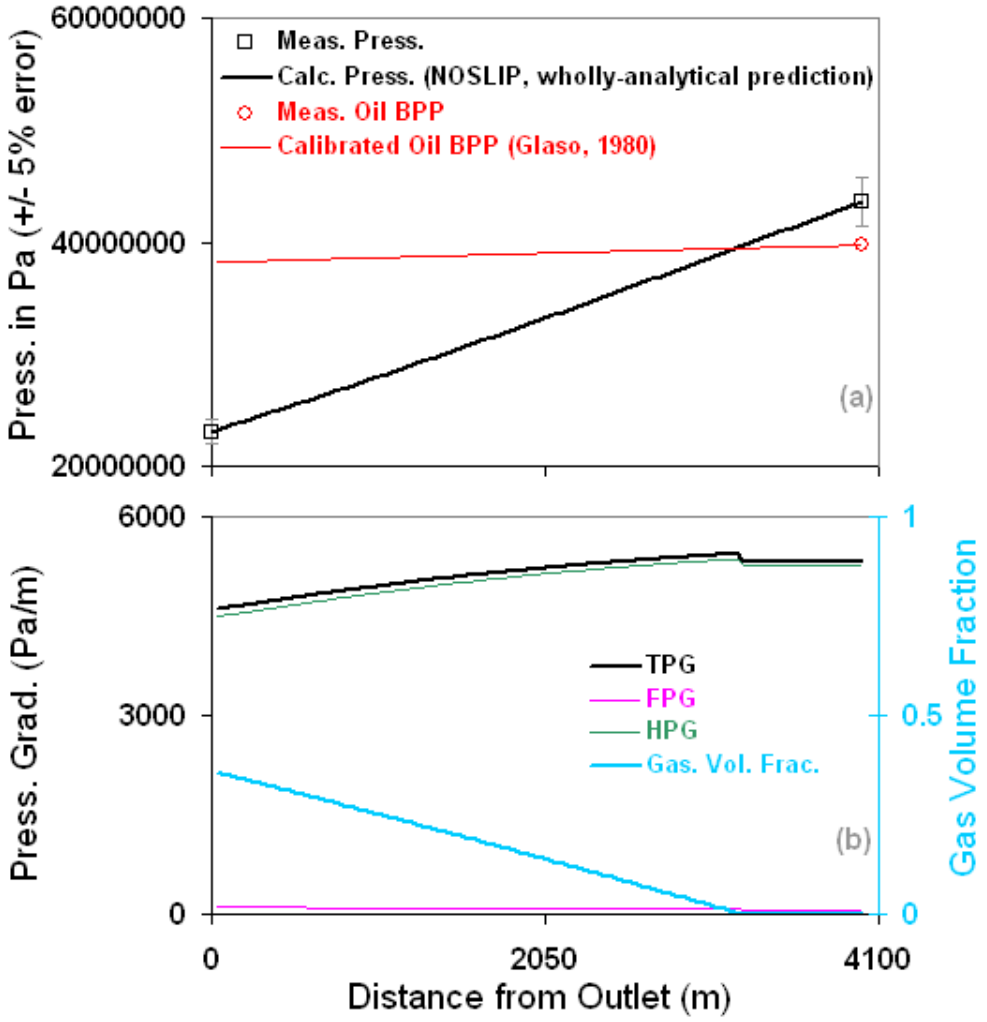

Figure 7.10.1: Prediction of well 27 of Chierici et al. (1974) with the NOSLIP model.

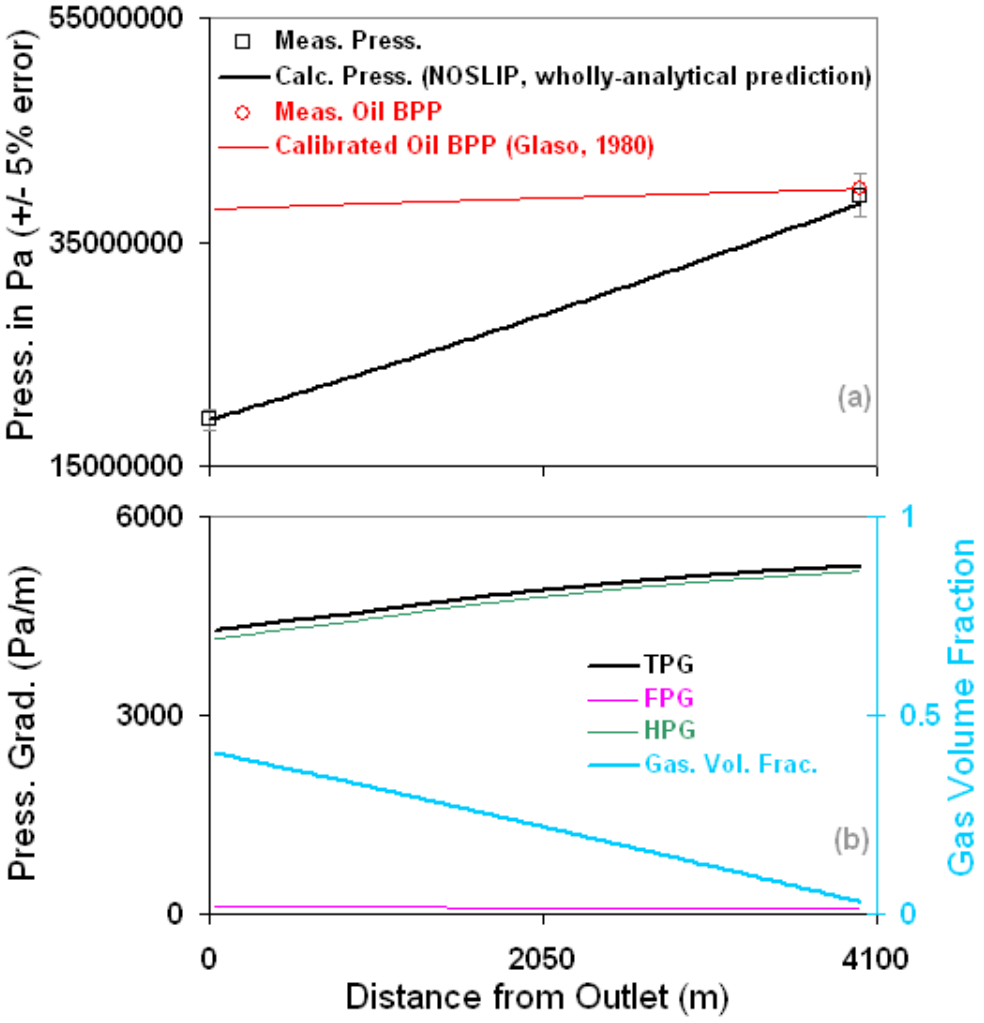

Figure 7.10.2: Prediction of well 28 of Chierici et al. (1974) with the NOSLIP model.

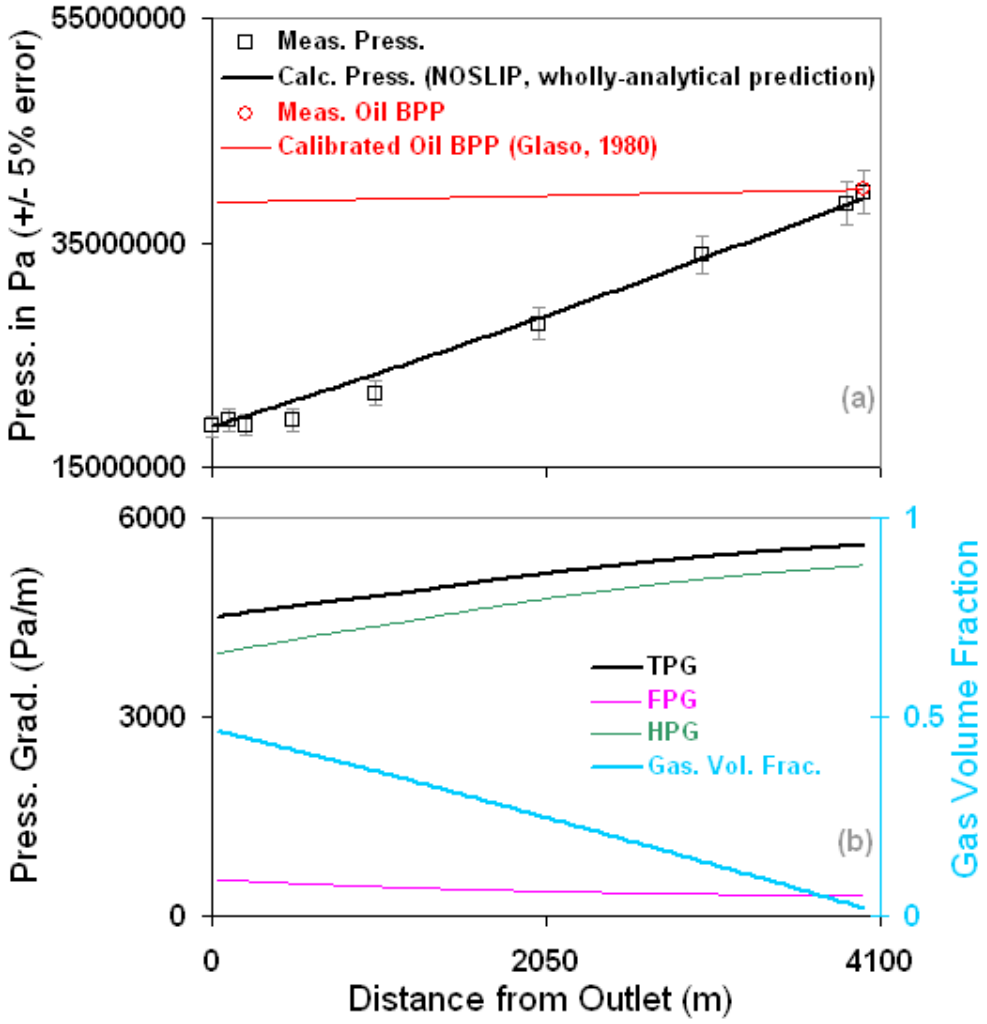

Figure 7.10.3: Prediction of well 29 of Chierici et al. (1974) with the NOSLIP model.

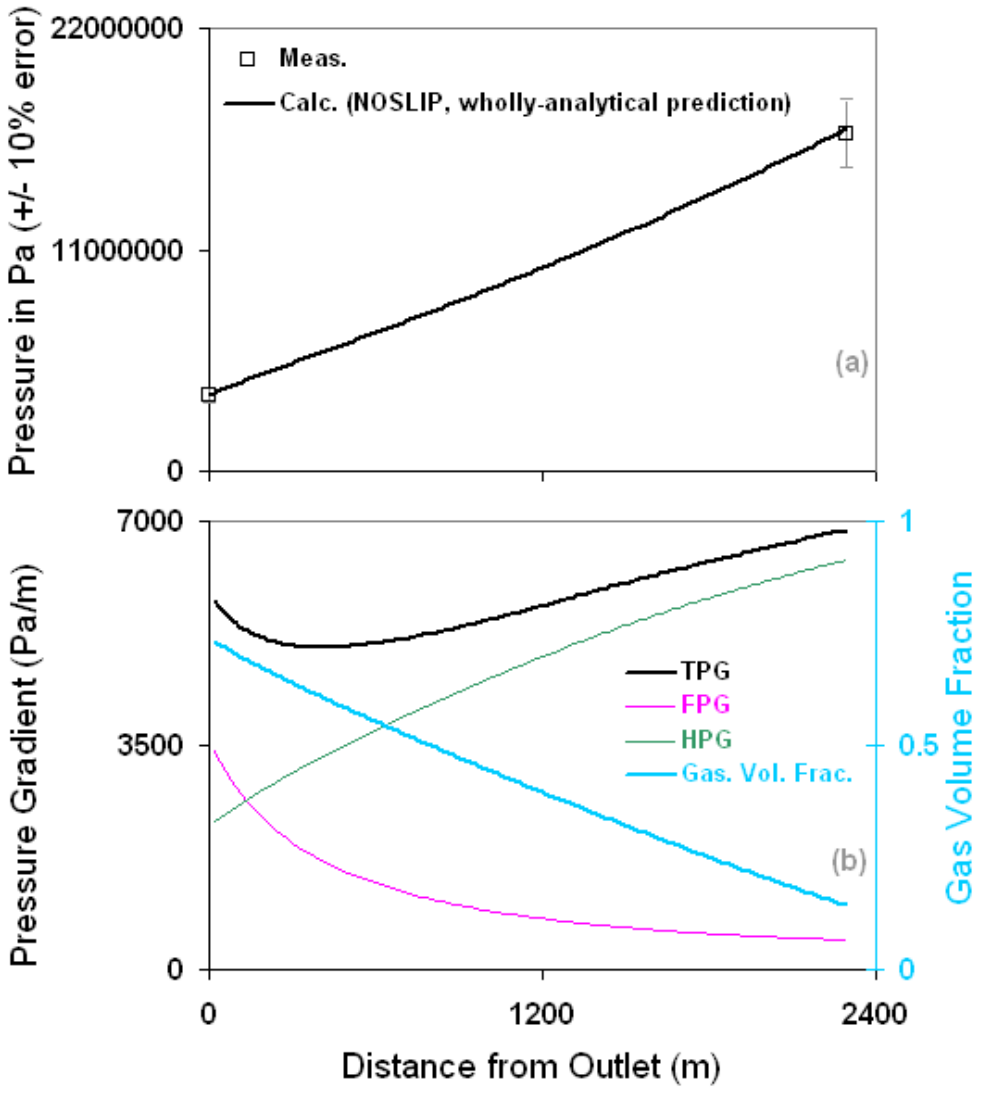

Figure 7.10.4: Prediction of well 77 of Sanchez (1972) with the NOSLIP model.

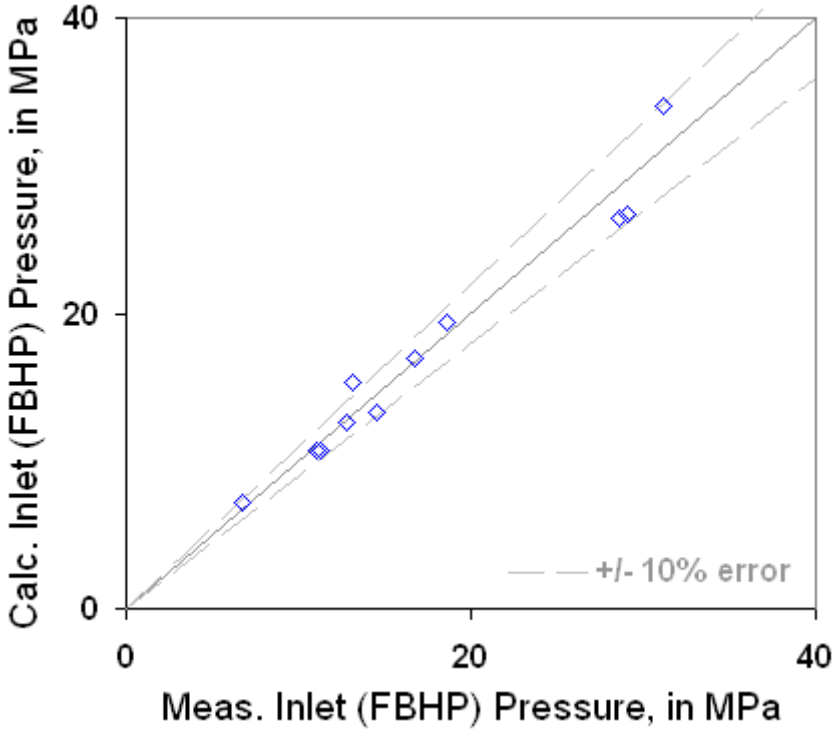

Figure 7.10.5: Prediction of representative wells of Sanchez (1972) spanning the full range of GOR's in the reference with the NOSLIP model.

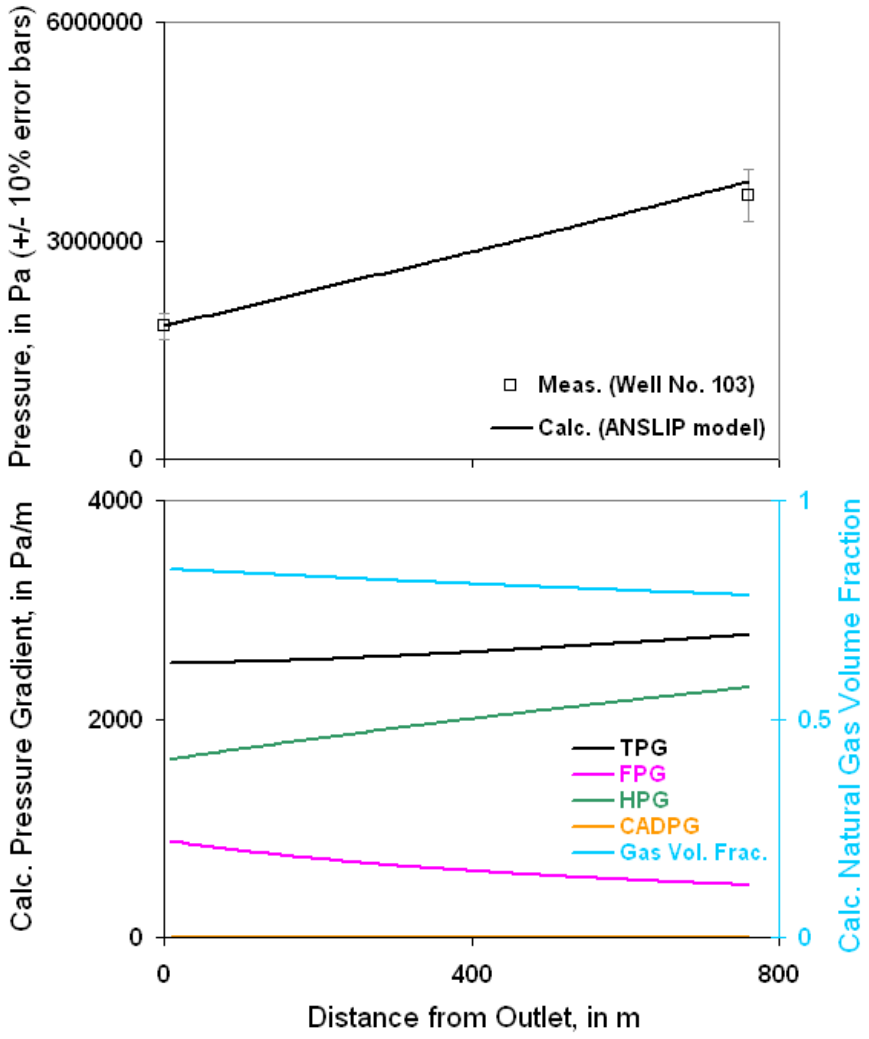

Figure 7.10.6: Prediction of a high GOR dataset of Messulam (1970) with the ANSLIP model.

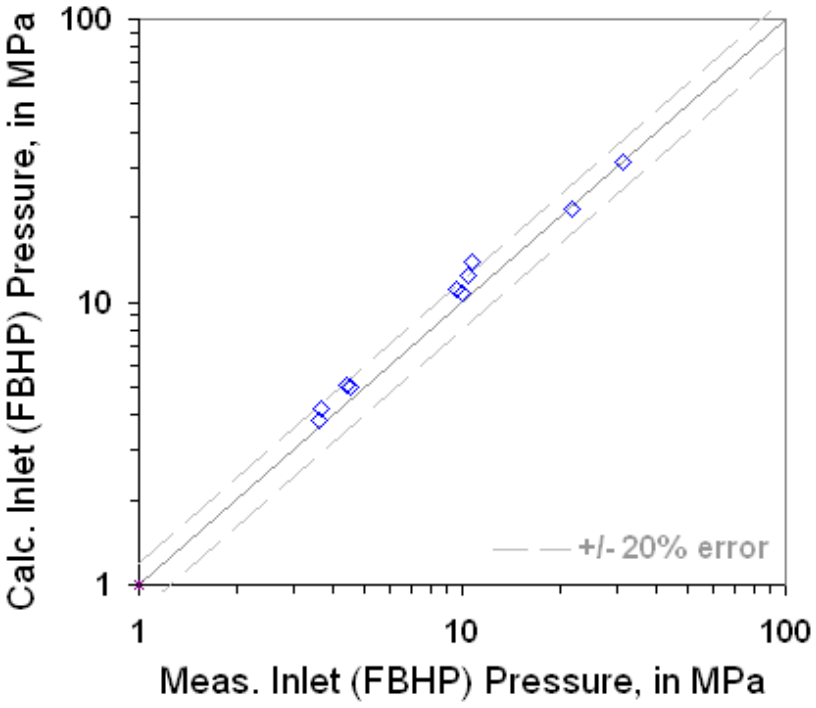

Figure 7.10.7: Prediction of representative wells of Messulam (1970) spanning the full range of GOR's in the reference with the NOSLIP model.

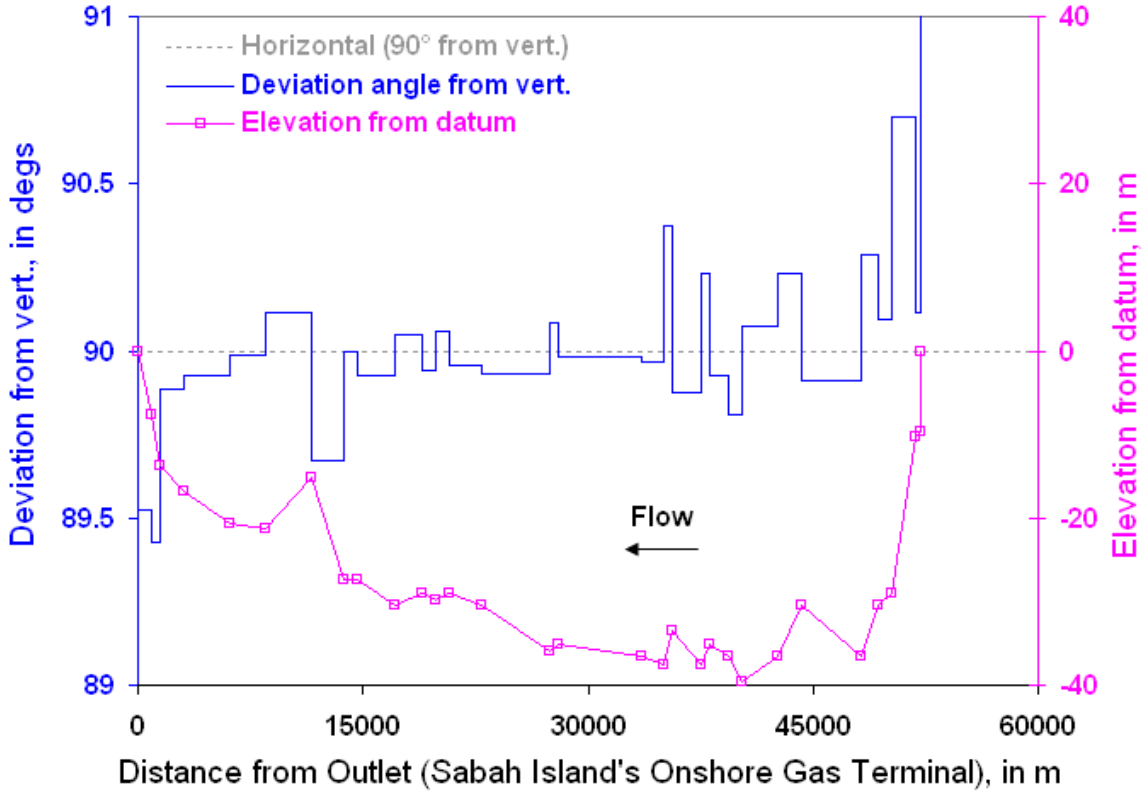

Figure 7.11.1: The elevation profile of the 32 miles long, 14-inch diameter Sabah gas-condensate pipeline from Furukawa et al. (1987).

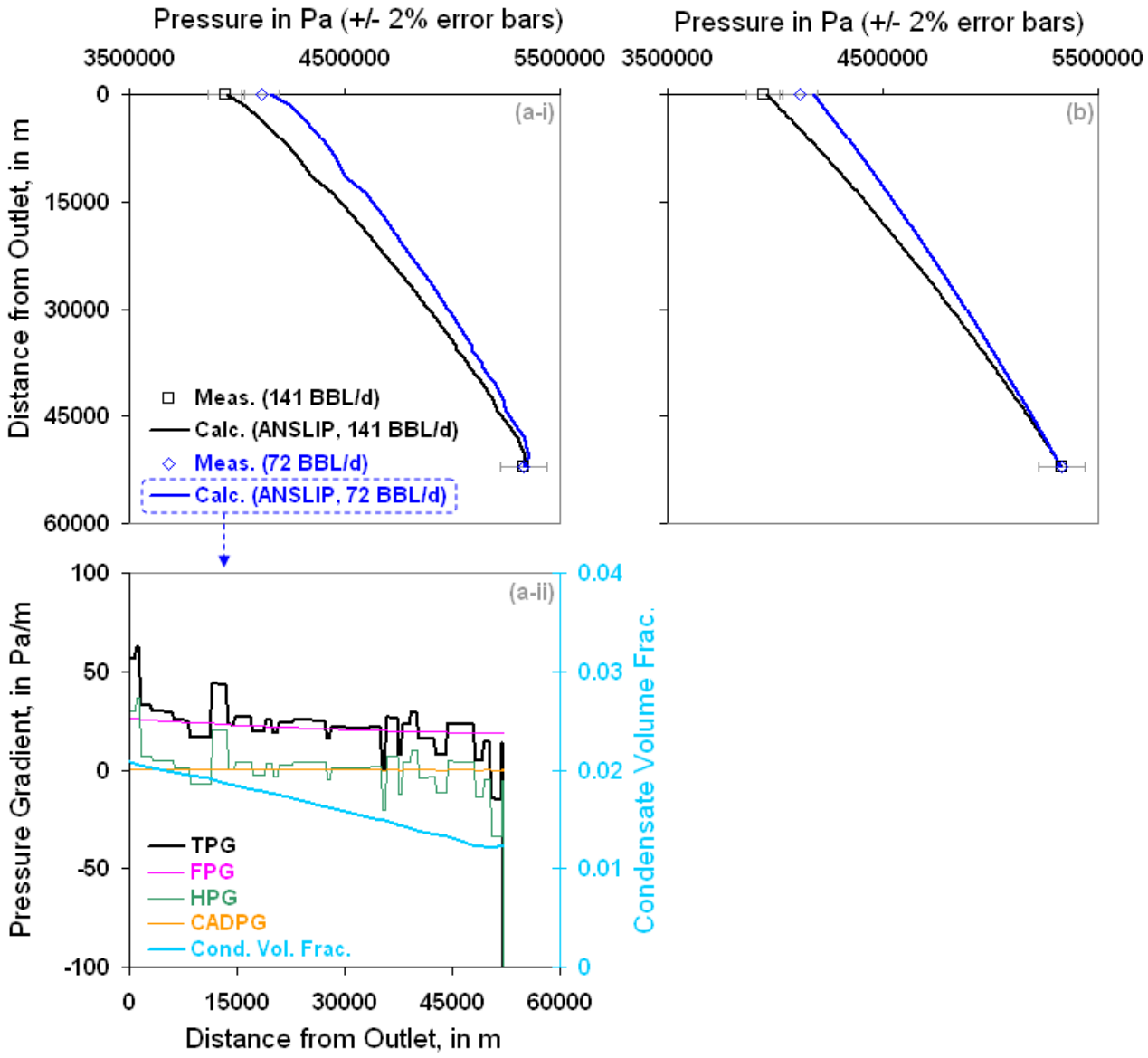

Figure 7.11.2: Prediction of the Furukawa et al. (1987) pipe network using the ANSLIP model including the elevation profile (in a) and using a horizontal pipeline approximation (in b). Note that condensate is continuously dropping out of the gas in this dew point system as the pipeline pressure decreases.

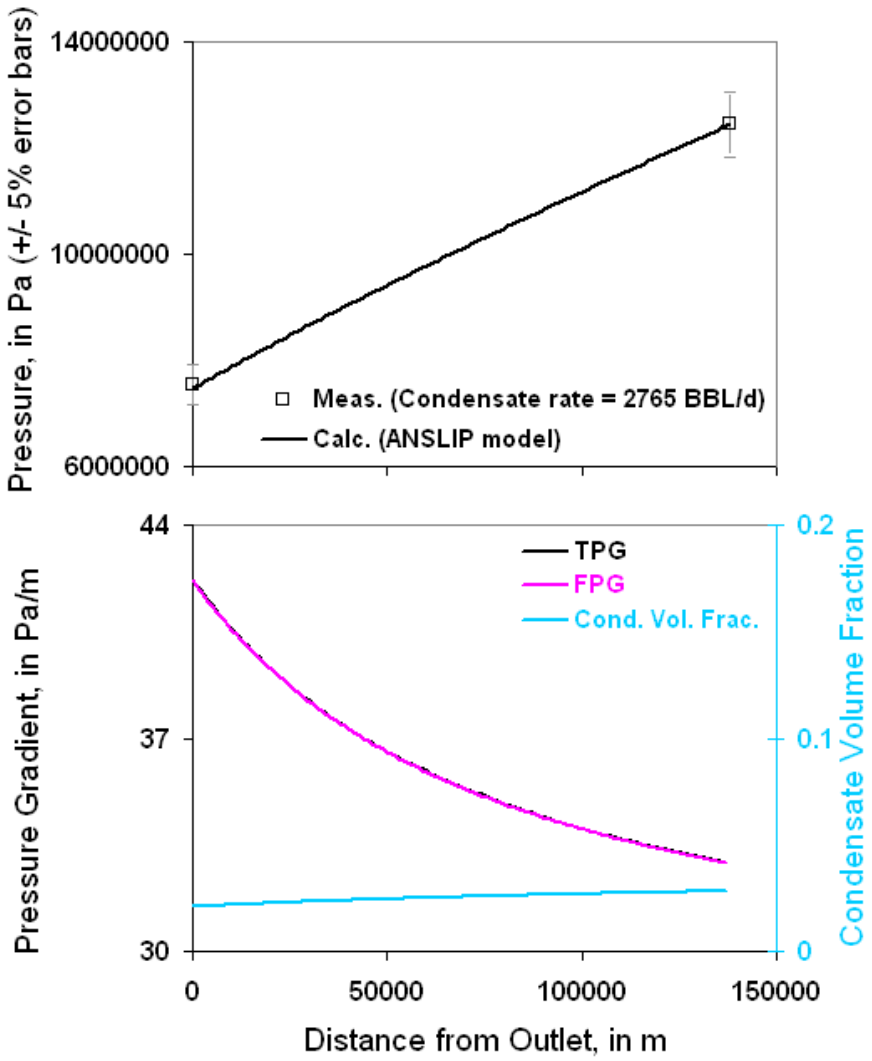

Figure 7.11.3: Prediction of the 86 miles long, three-phase, 28-inch diameter, North Sea Viking pipeline of Baker et al. (1988b) using a horizontal pipeline approximation and the ANSLIP model.

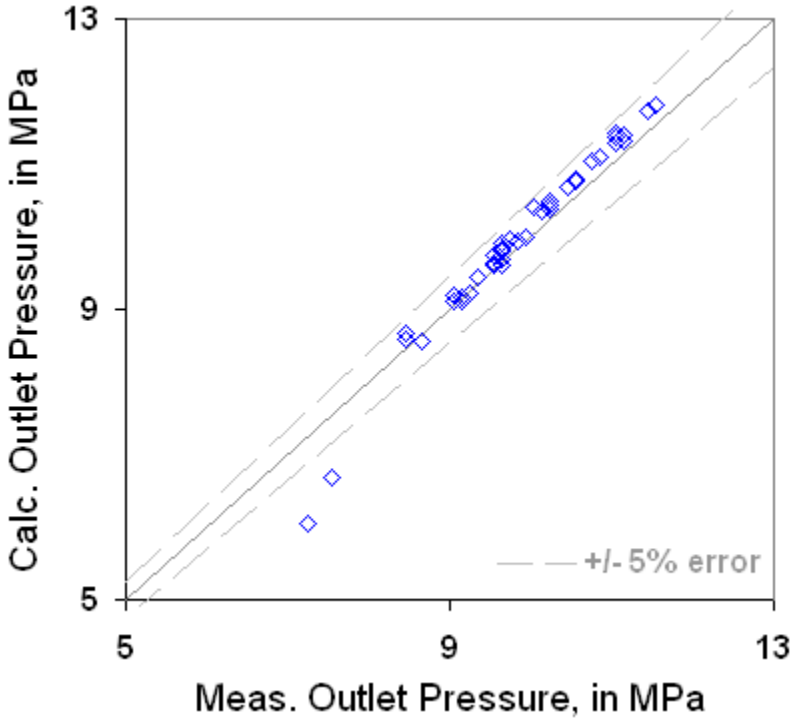

Figure 7.11.4: Prediction of all of the reported North Sea Viking pipeline datasets of Baker et al. (1988b) using a horizontal pipeline approximation and the ANSLIP model. All 48 datasets shown above are given in Table 4 of the reference. These datasets are for a GCR of 333,333 scf/BBL, increasing condensate rates of 1038 to 2860 BBL/d, and increasing water rates of 692 BBL/d to 1907 BBL/d.

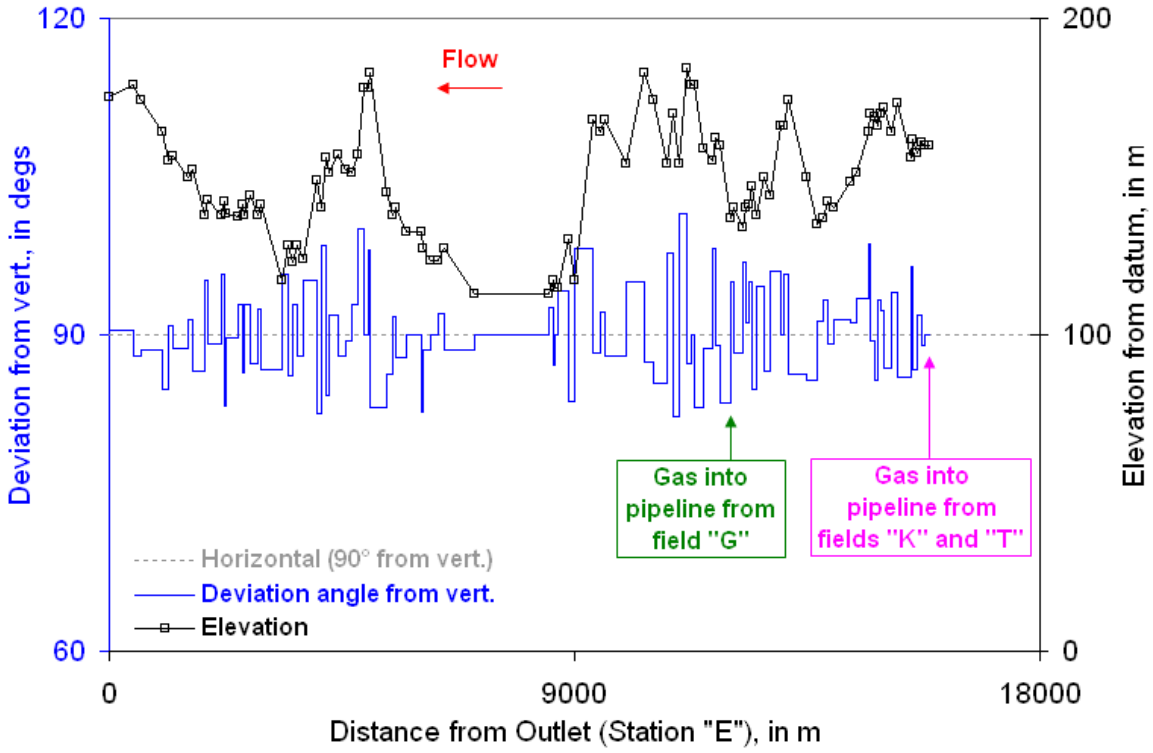

Figure 7.11.5: The elevation profile of the 10-inch diameter Tenneco pipeline network of Mucharam (1990).

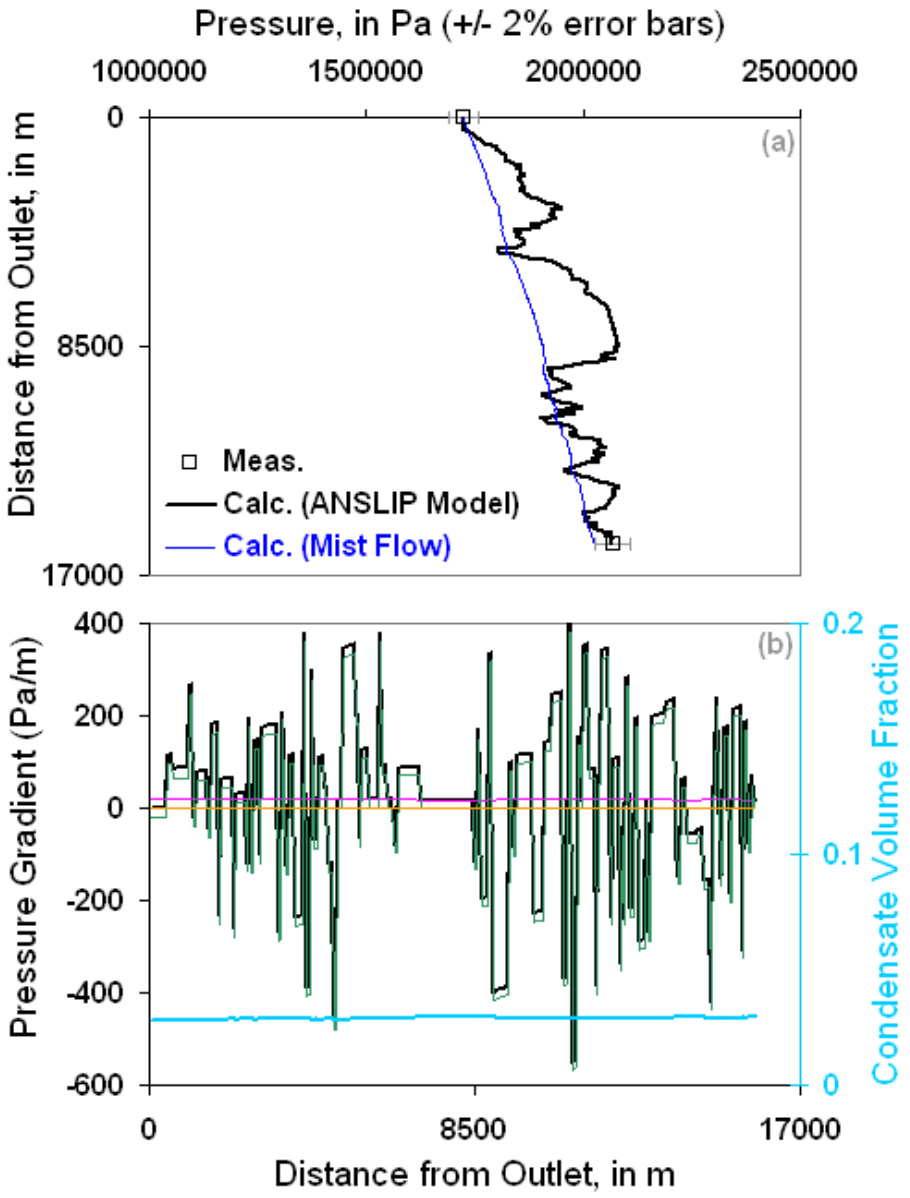

Figure 7.11.6: Prediction of the Mucharam (1990) pipeline network using the ANSLIP model or the MIST flow model.

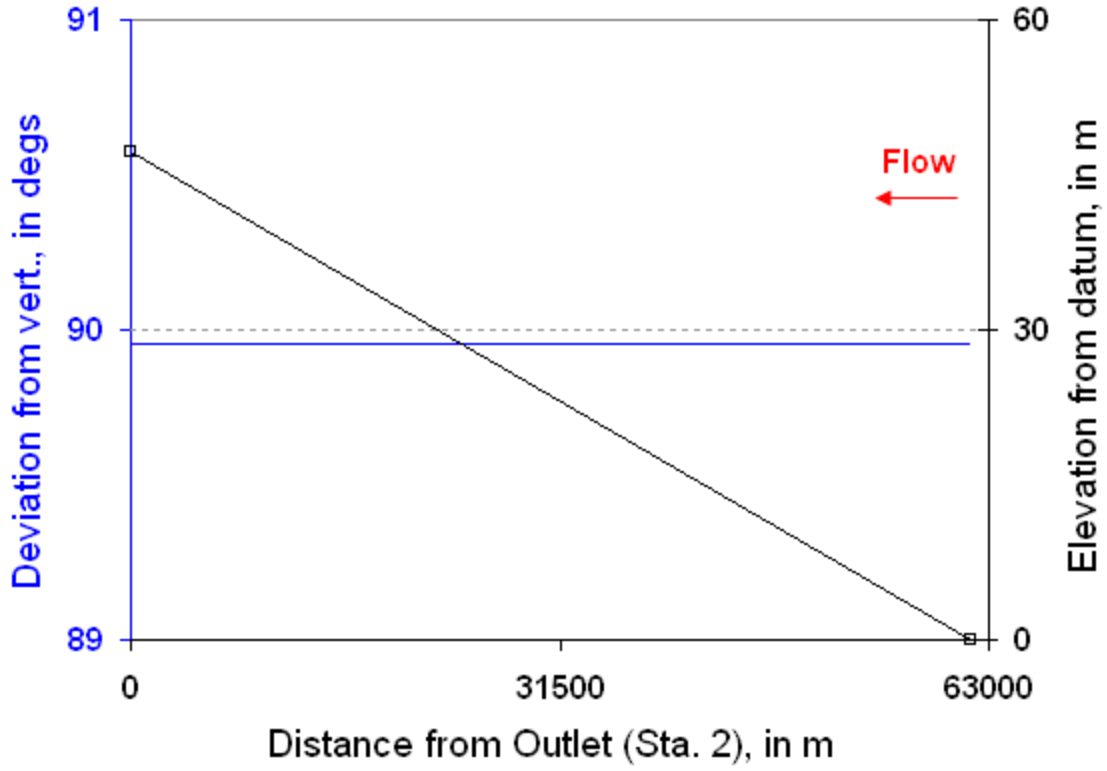

Figure 7.11.7: The simplified elevation profile of the AGA line 20 of Gregory (1981).

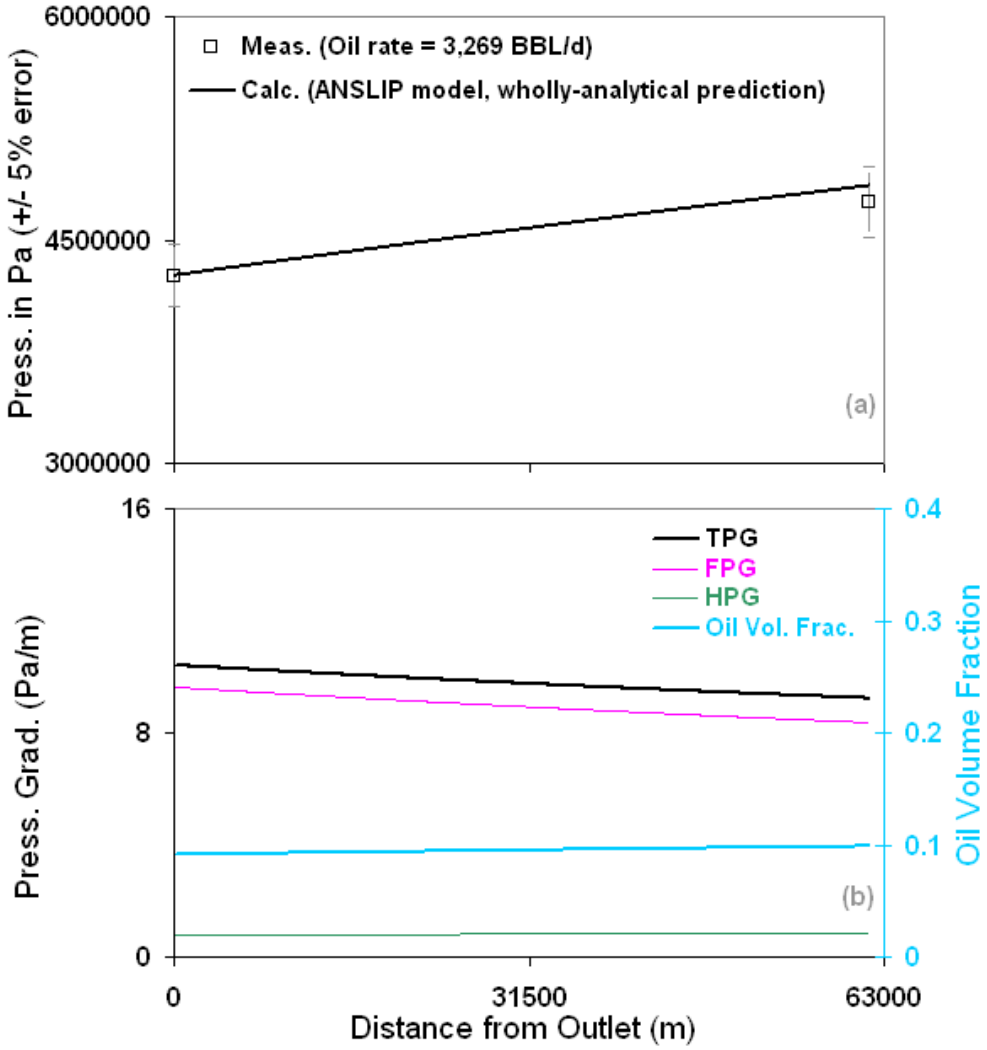

Figure 7.11.8: Prediction of run 1 of the AGA Line 20 of Gregory (1981) with the ANSLIP model.

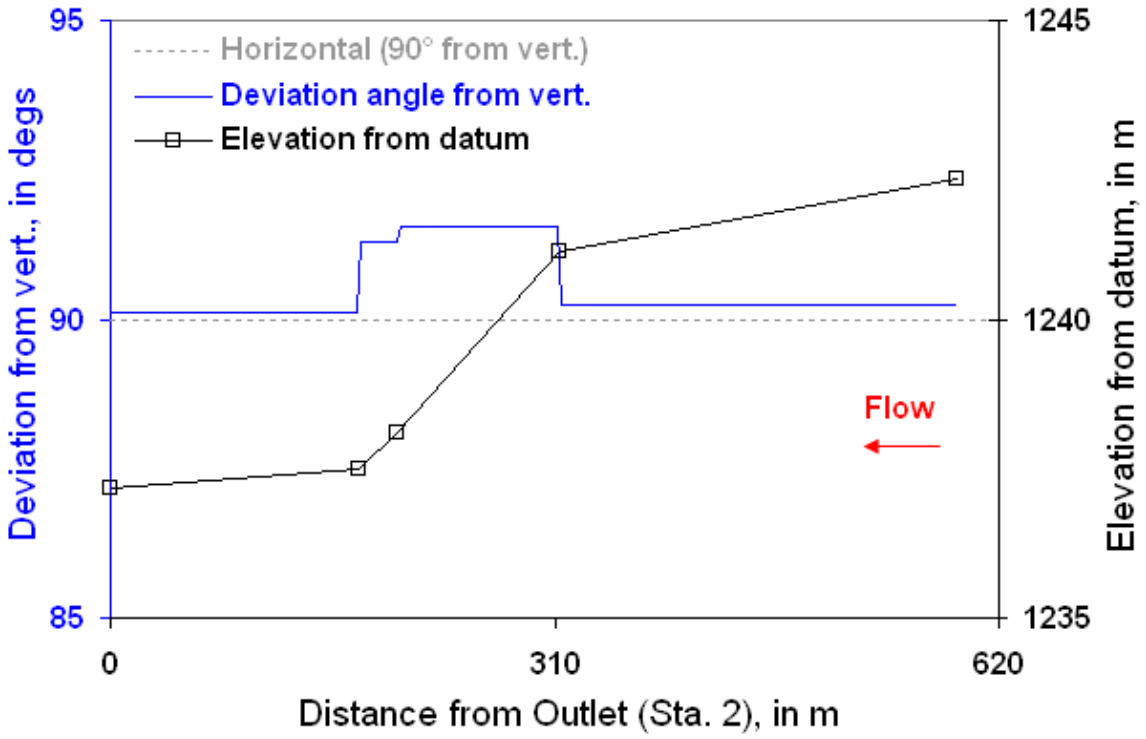

Figure 7.11.9: The simplified elevation profile of the AGA line 61 of Gregory (1981) – this is a downwards multiphase flow dataset.

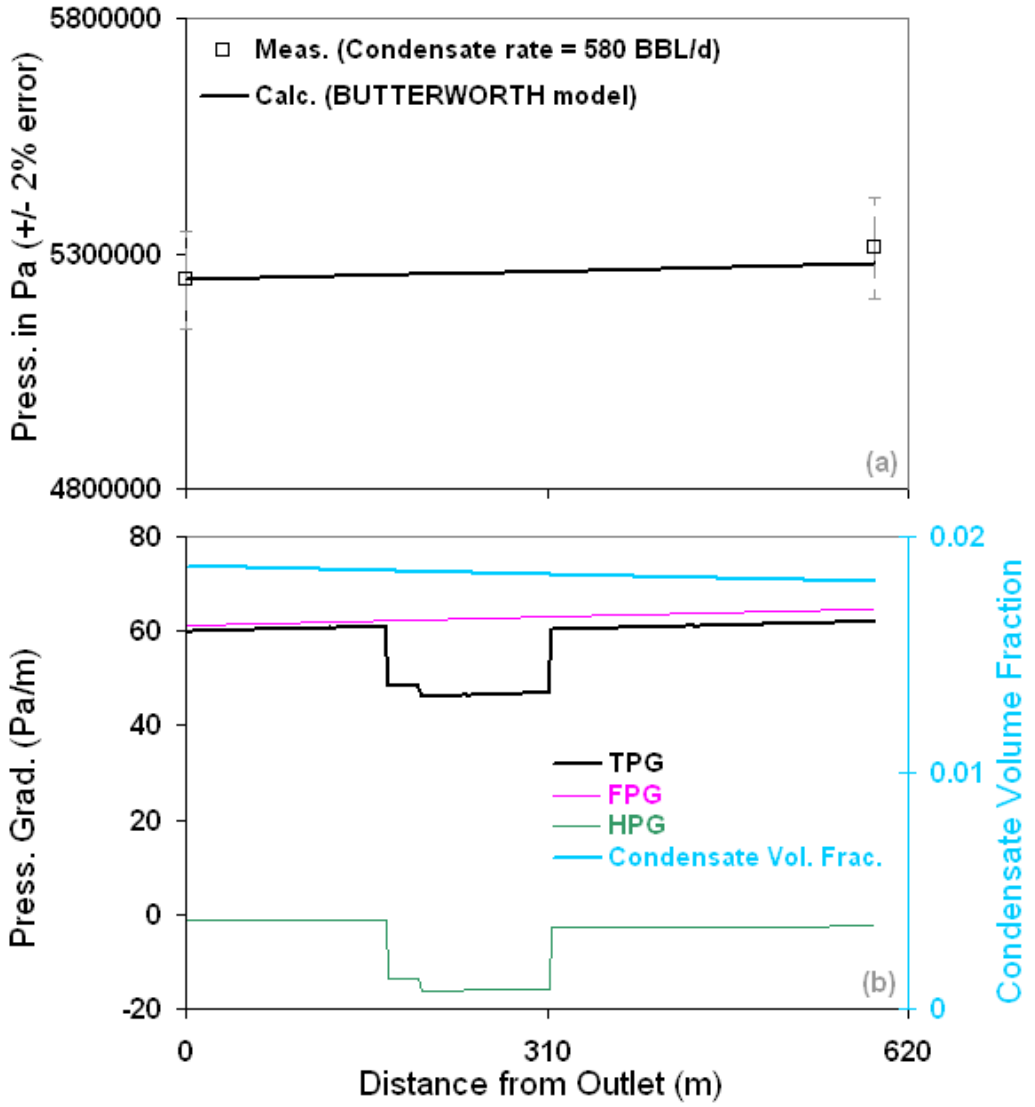

Figure 7.11.10: Prediction of the AGA line 61 pressure drop with the BUTTERWORTH model.

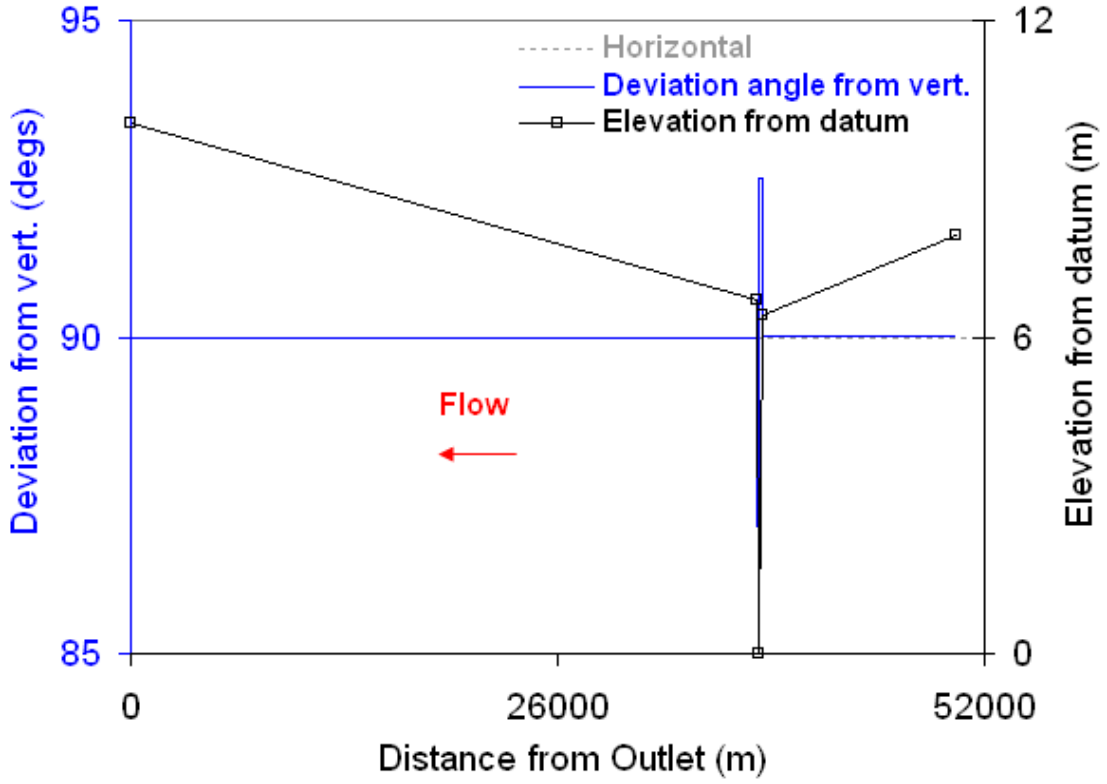

Figure 7.11.11: The simplified elevation profile of the AGA line 19 of Gregory (1981) – this is a downwards multiphase flow followed by upwards multiphase flow dataset.

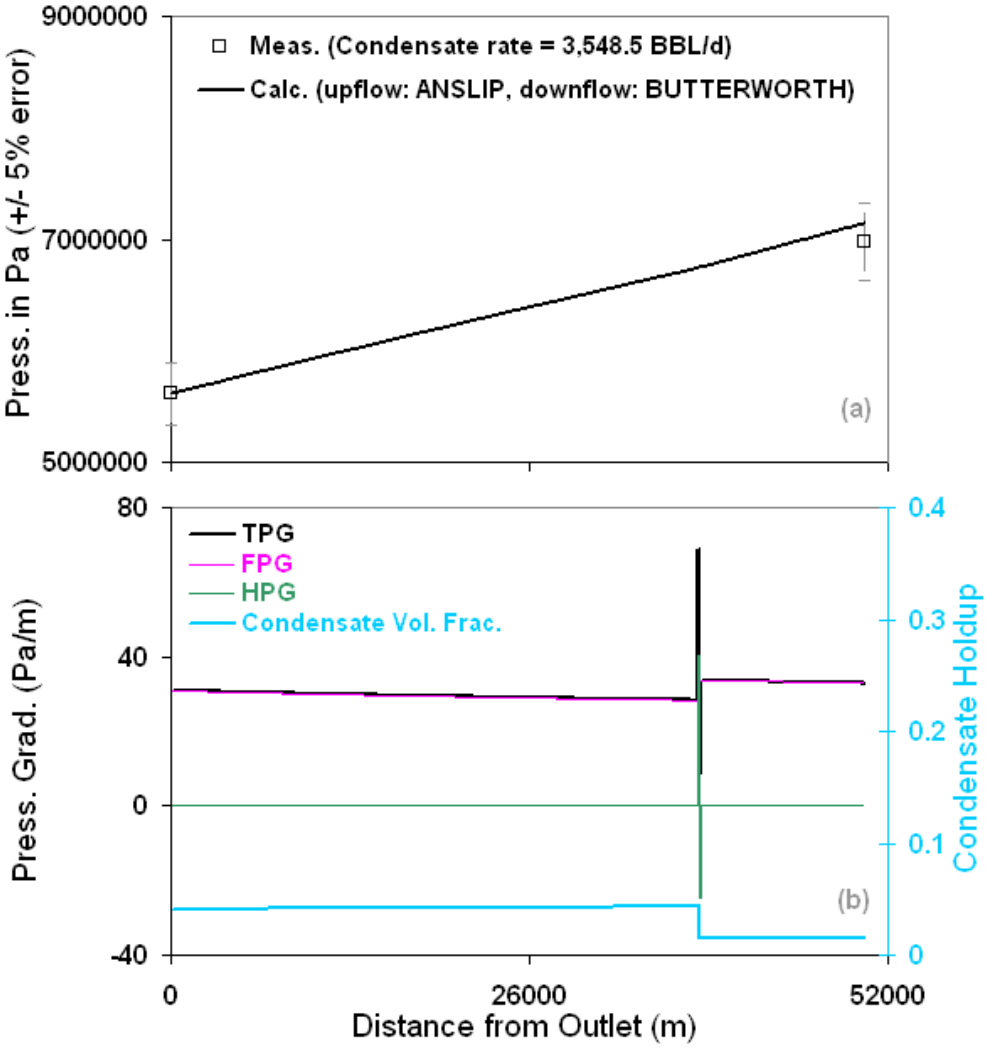

Figure 7.11.12: Prediction of the AGA line 19 (run no. 1) pressure drop.

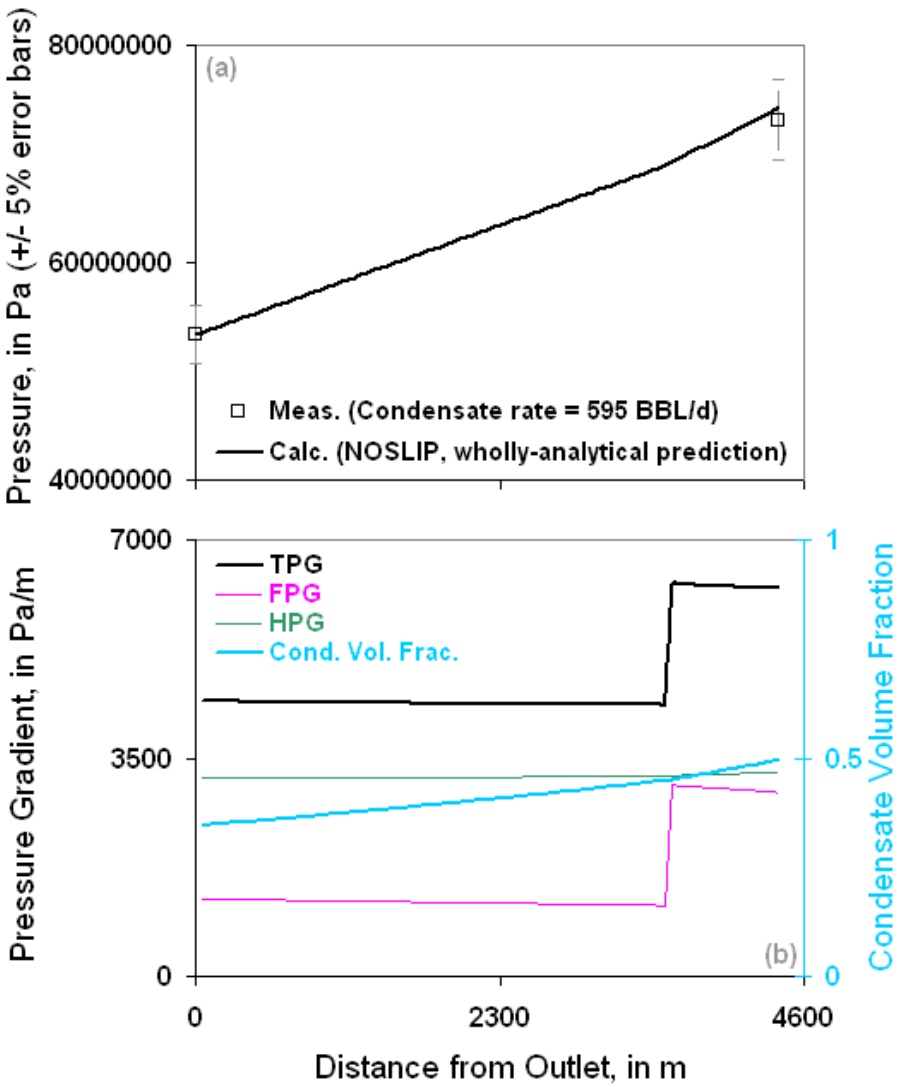

Figure 7.12.1: Example prediction of the high-pressure and high-temperature deepwater Gulf of Mexico well 23 of Sutton and Farshad (1983) with the NOSLIP model.

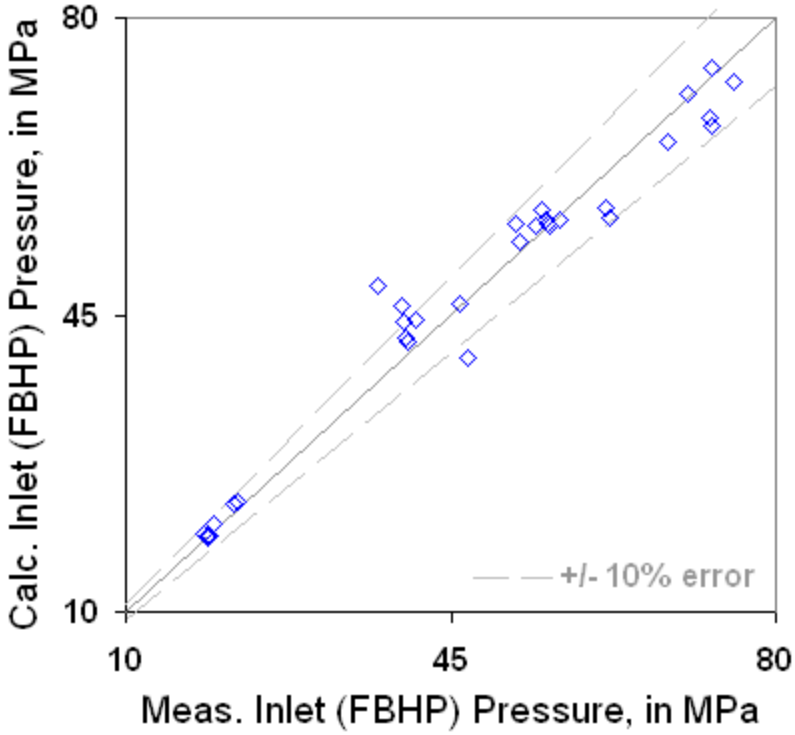

Figure 7.12.2: Prediction of all of the high-pressure and high-temperature deepwater Gulf of Mexico wells of Sutton and Farshad (1983) with the NOSLIP wholly-analytical model (starting calculations from the surface).

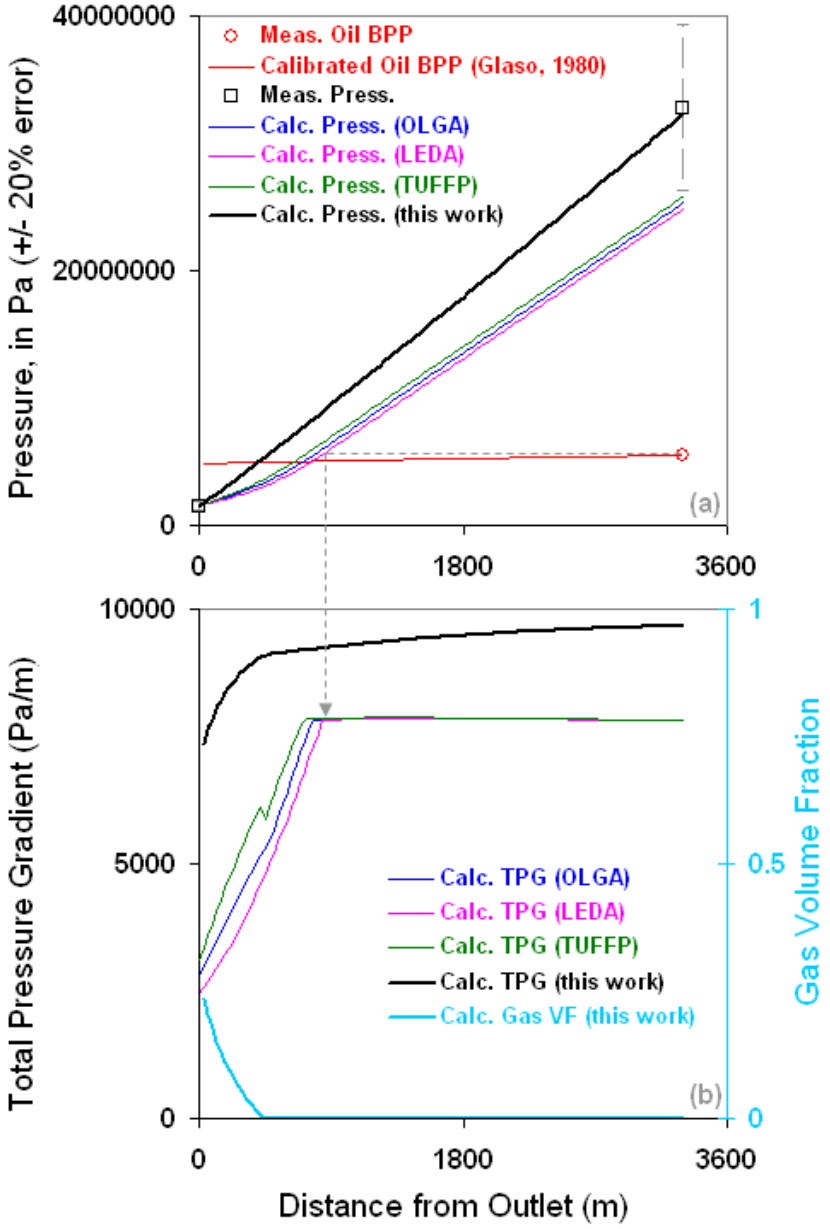

Figure 7.13.1: Comparisons of different model predictions for well 1 of Chierici et al. (1974) – this work uses the NOSLIP model.

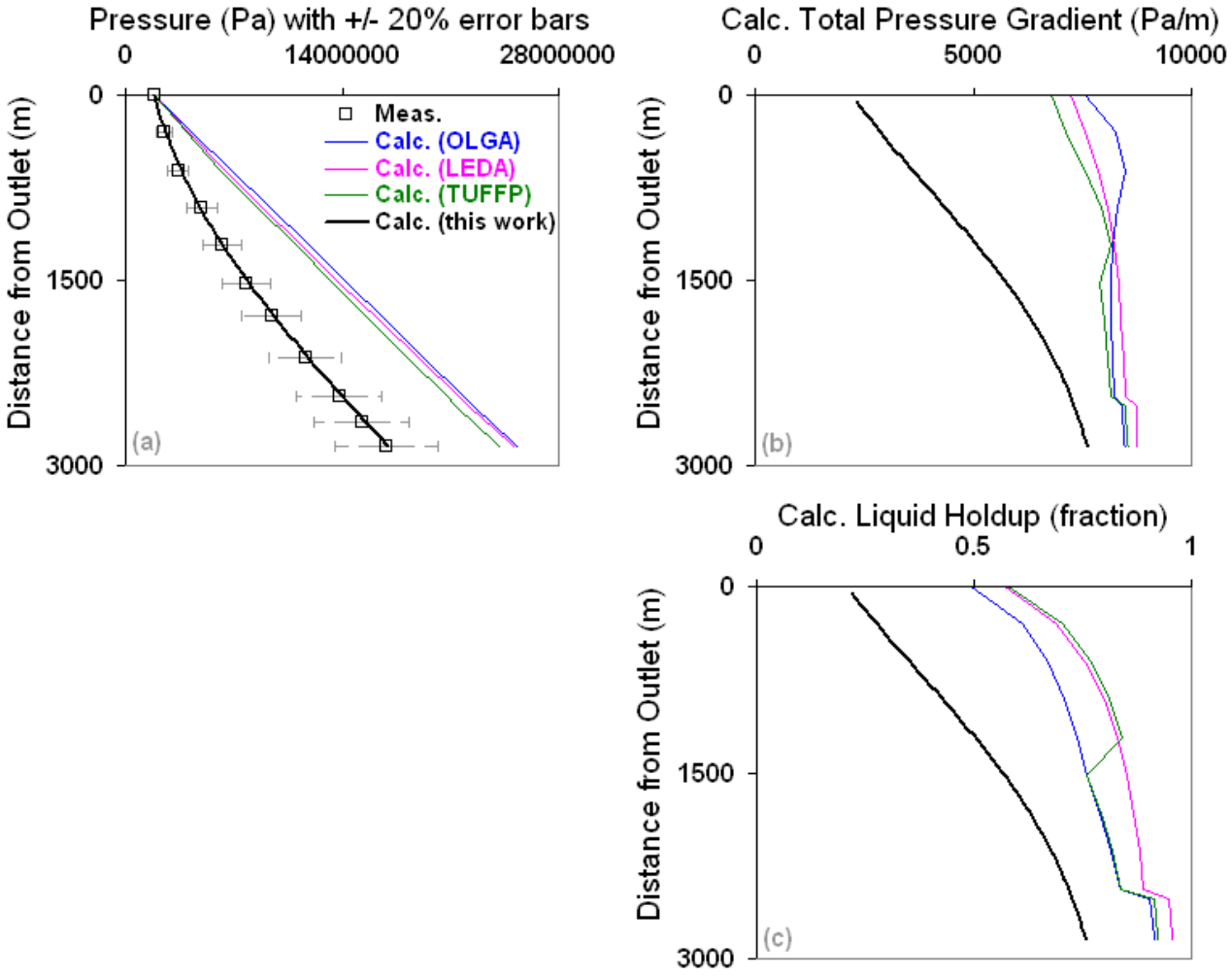

Figure 7.13.2: Comparisons of different model predictions for well C of Kumar (2005) – this work uses the NOSLIP model.

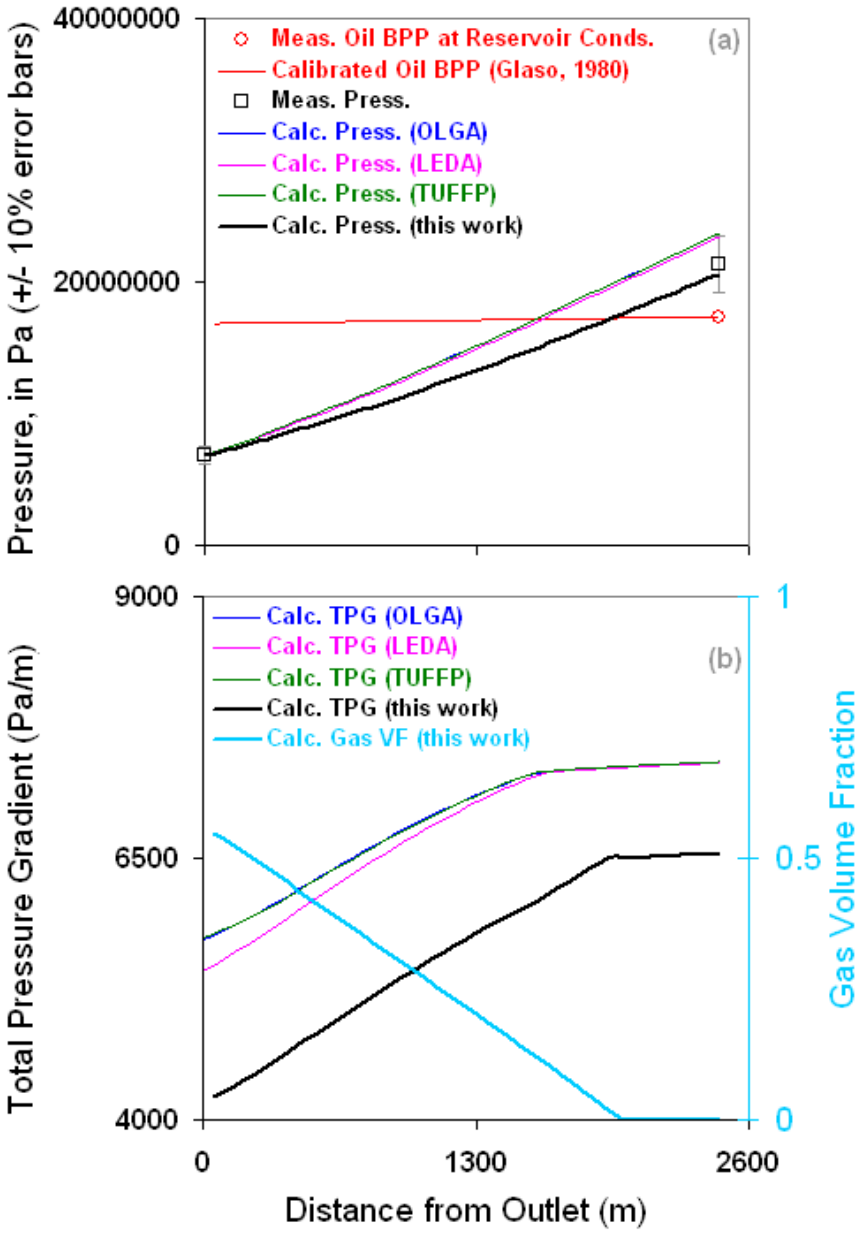

Figure 7.13.3: Comparisons of different model predictions for well 1 of Cornish (1976) – this work uses the NOSLIP model.

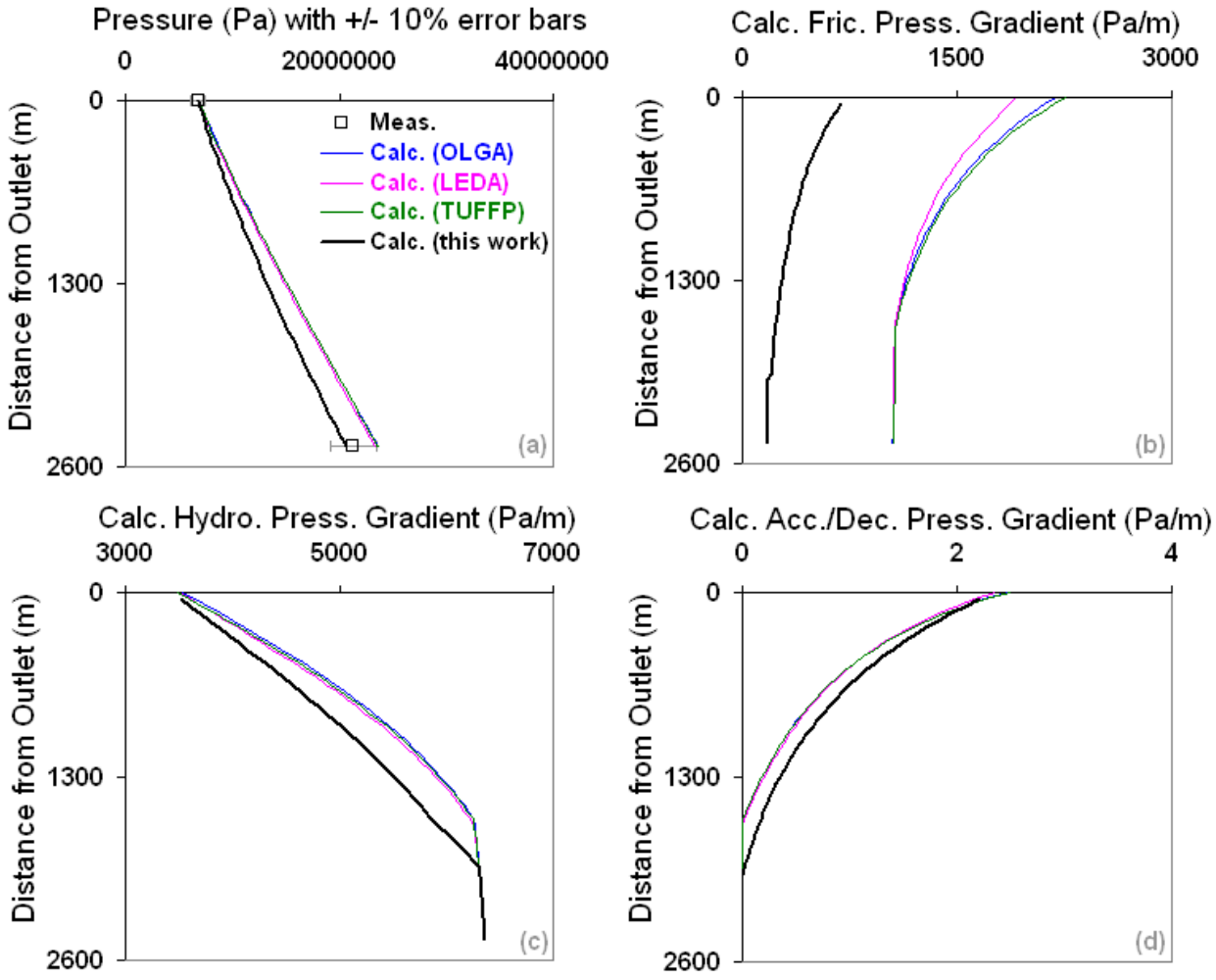

Figure 7.13.4: Interrogation of the different model predictions for well 1 of Cornish (1976).

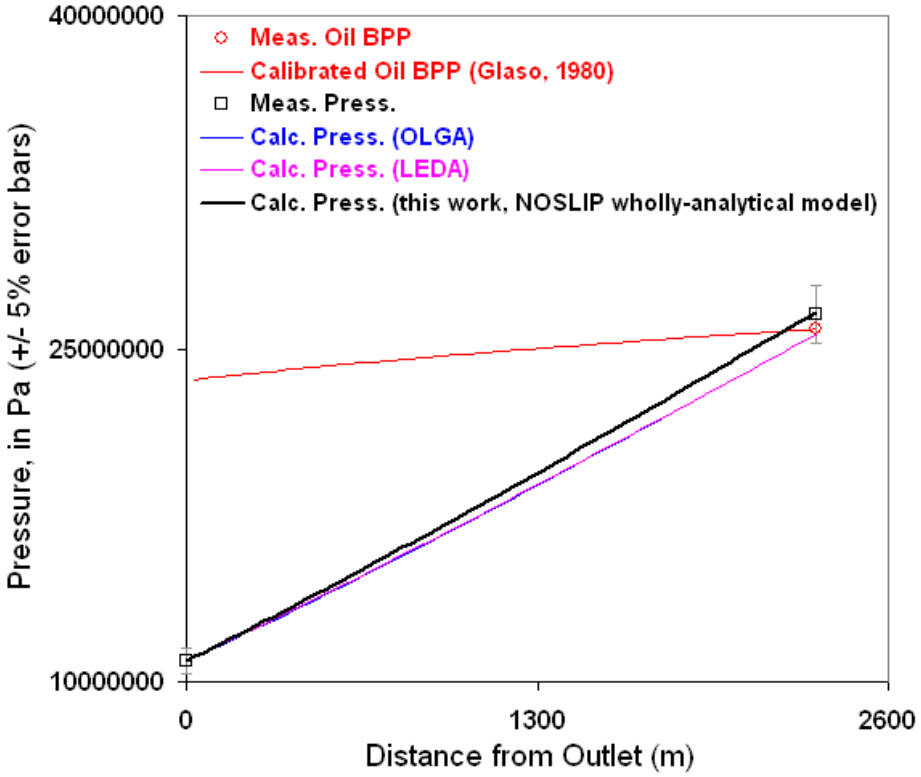

Figure 7.13.5: Comparisons of different model predictions for well 16 of Cheirici et al. (1974).

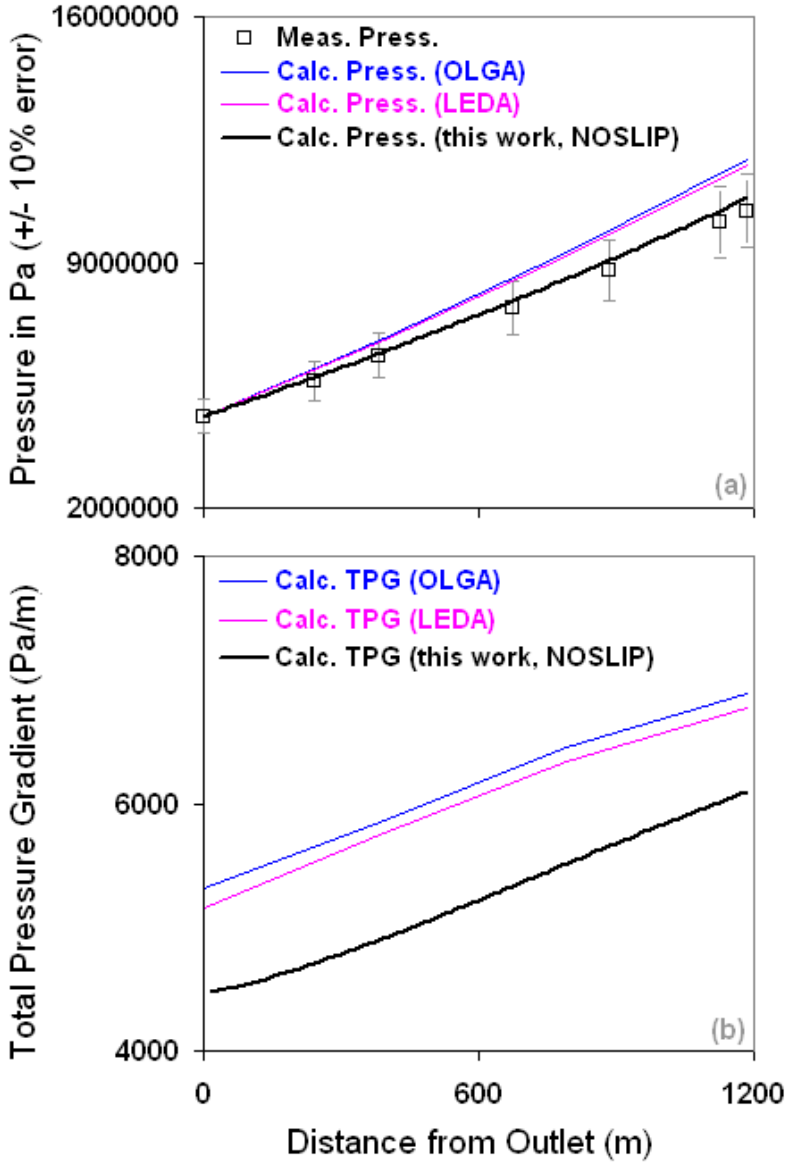

Figure 7.13.6: Comparisons of different model predictions for well 22 of Orkiszewski (1967).

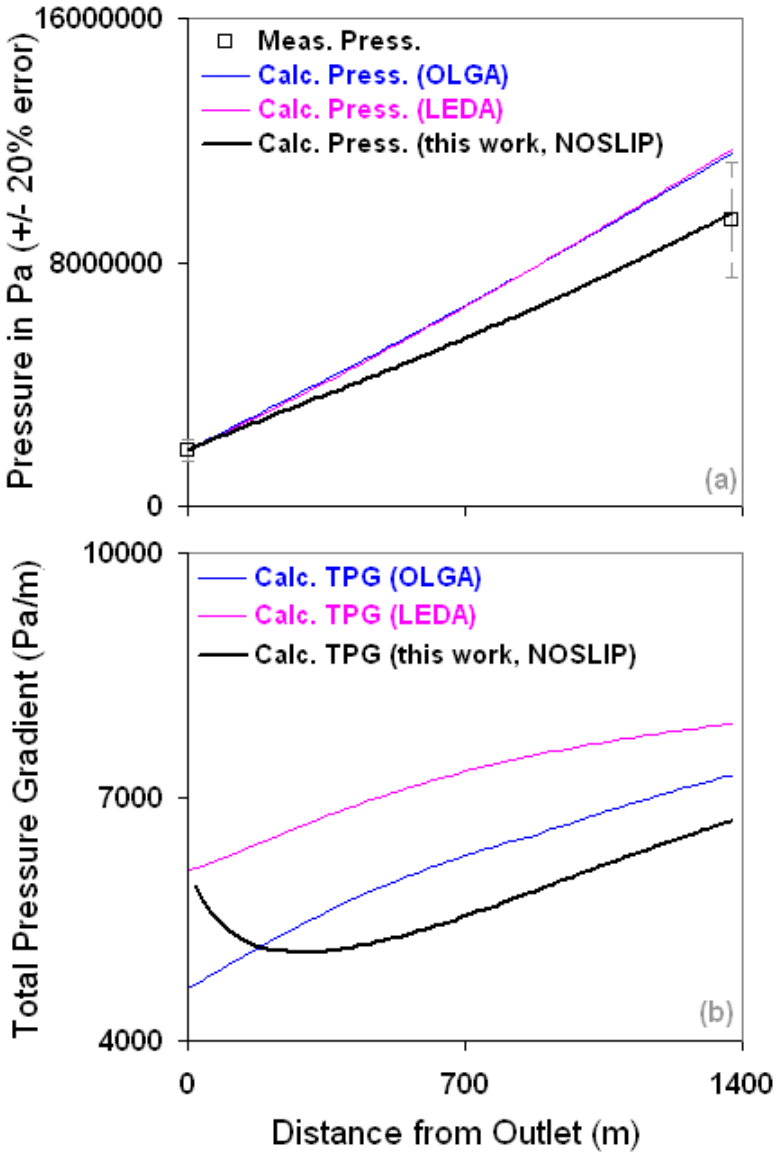

Figure 7.13.7: Comparisons of different model predictions for well 20 of Orkiszewski (1967).

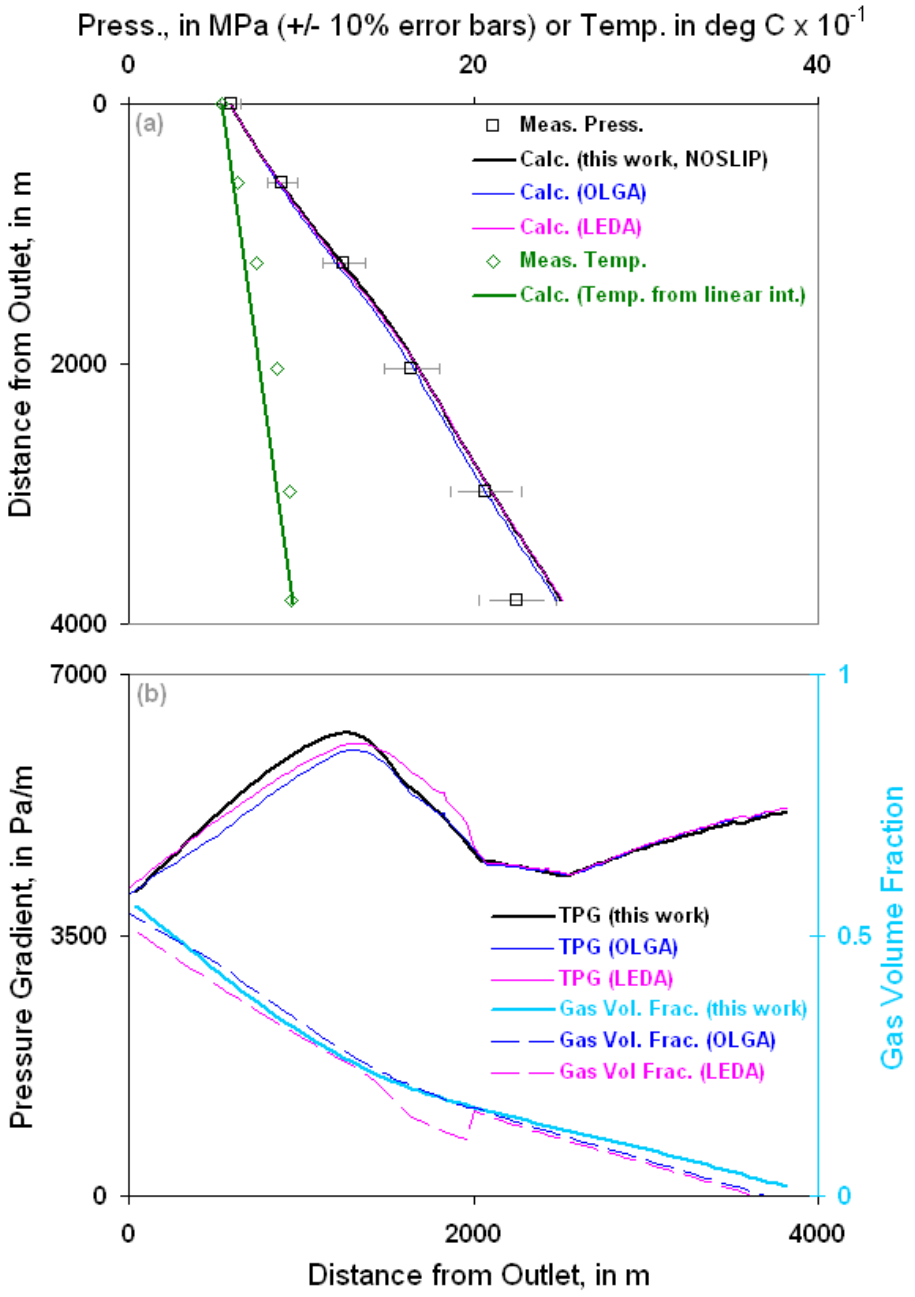

Figure 7.13.8: Comparisons of different model predictions for the 8-inch diameter well no. 1427 from Ansari (1988).

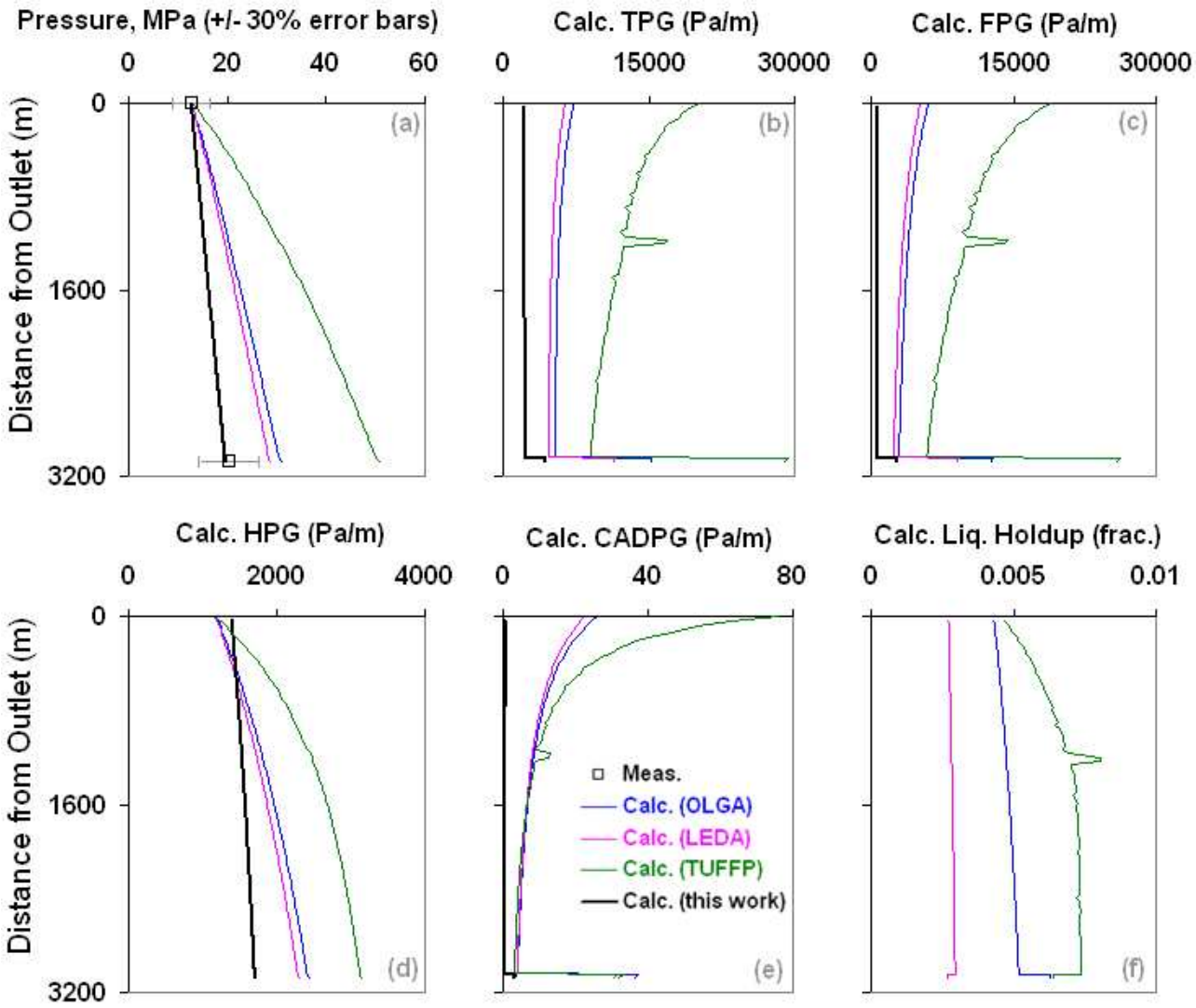

Figure 7.13.9: Comparisons of different model predictions for well 1 (second rate) of Reinicke et al. (1987) – this work uses the MIST flow model.

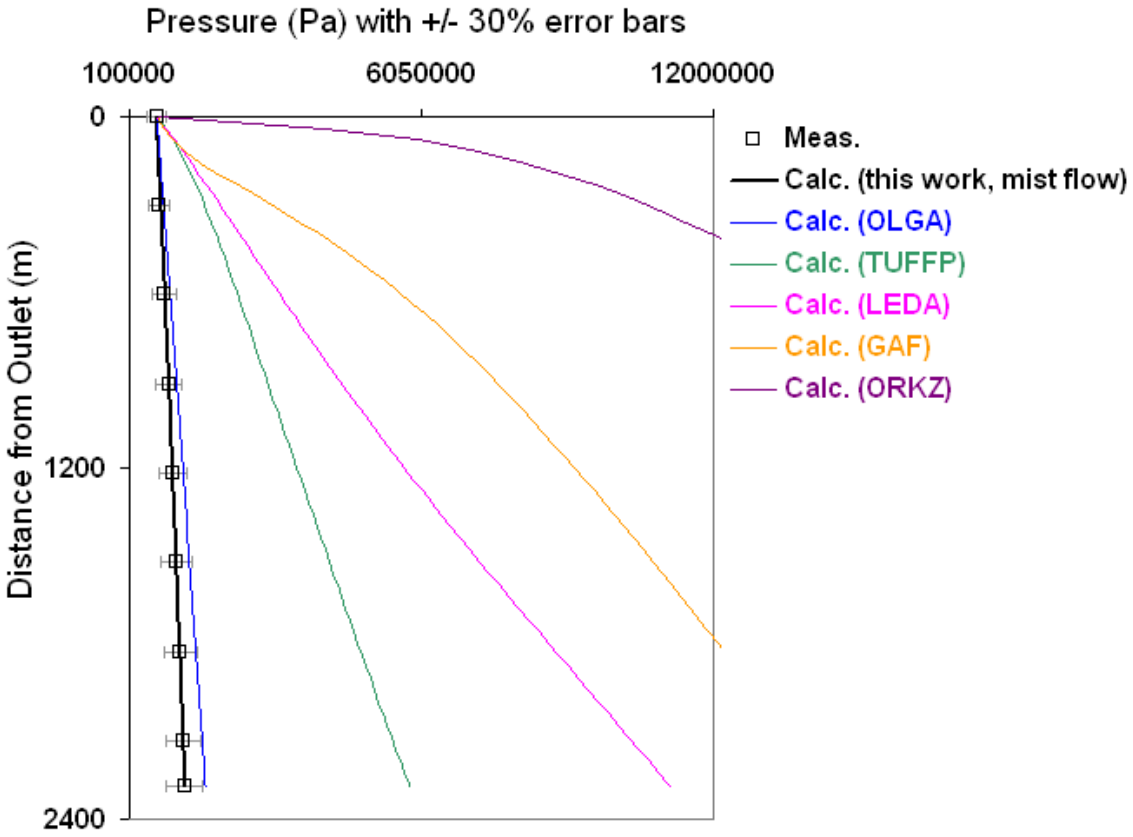

Figure 7.13.10: Comparisons of different model predictions for well J of Kumar (2005).

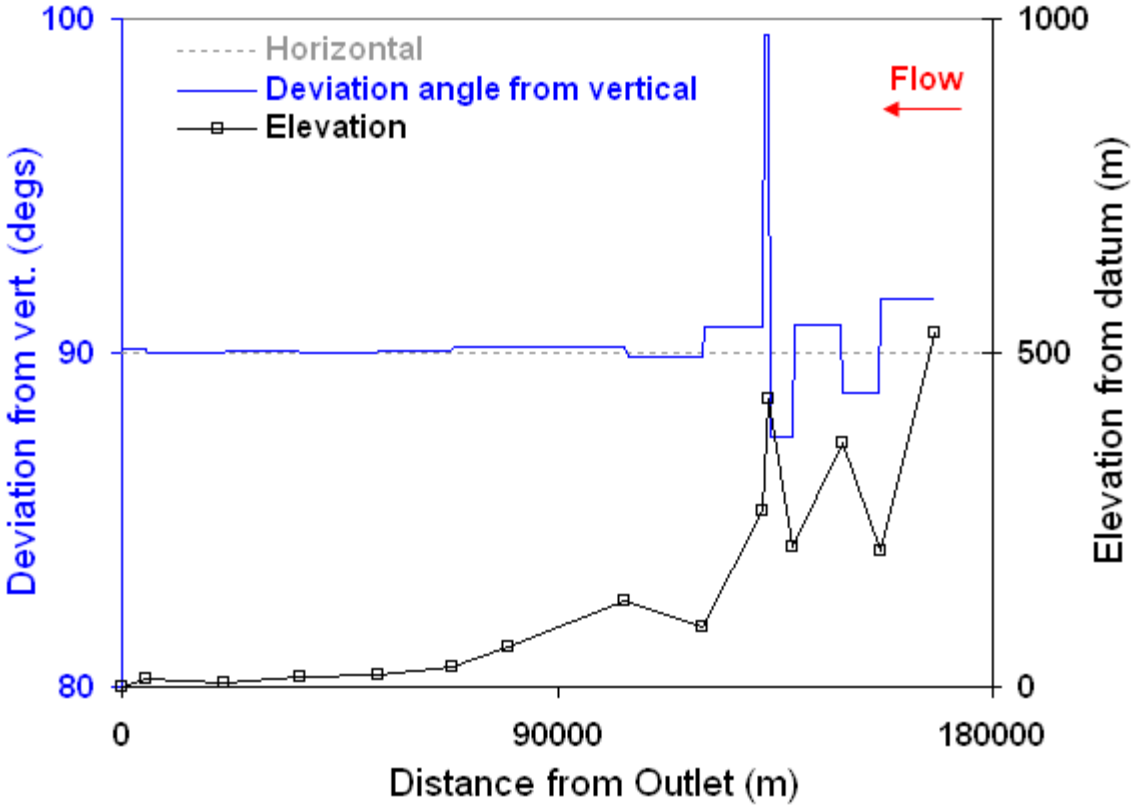

Figure 7.13.11: The elevation profile of the 104 miles long, 19-inch diameter pipeline of Moshfeghian et al. (2002).

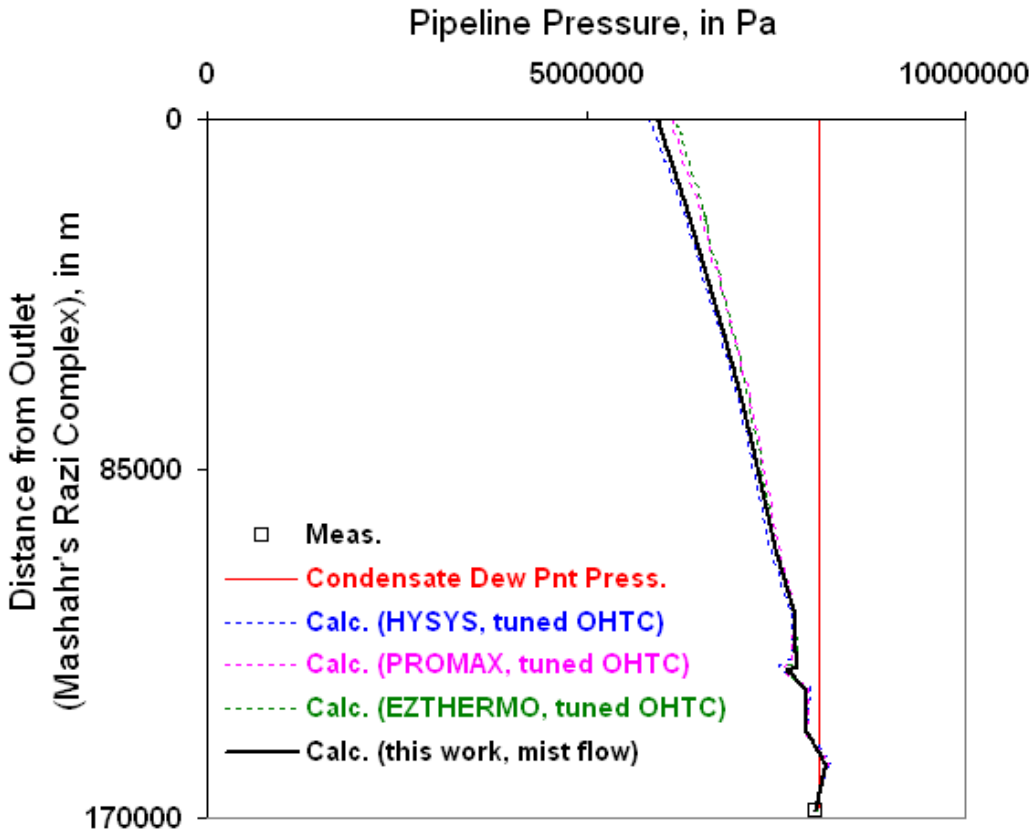

Figure 7.13.12: Comparisons of different model predictions for the pipeline of Moshfeghian et al. (2002).

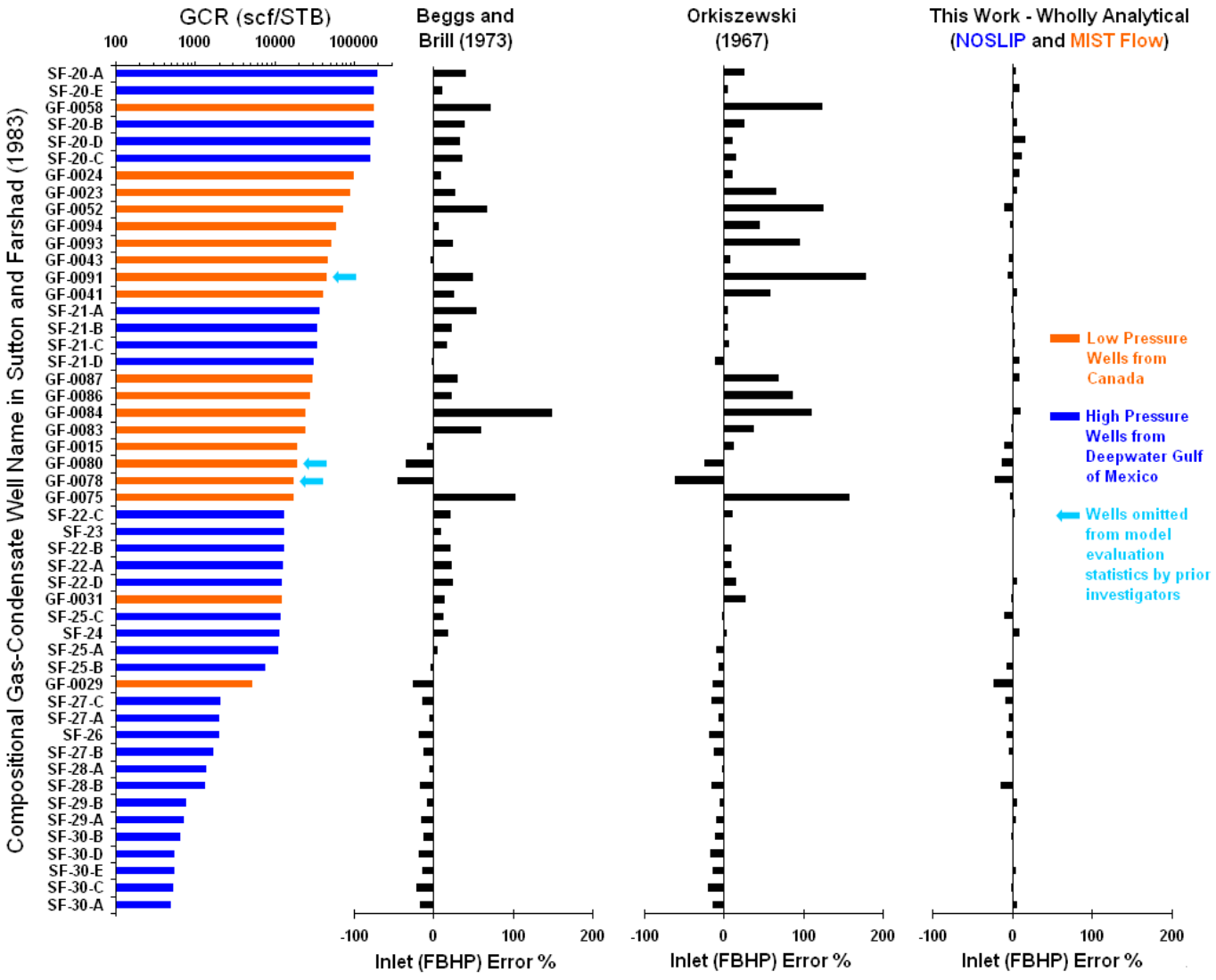

Figure 7.13.13: Comparisons of different model predictions for the datasets of Govier and Fogarasi, 1975 (GF) and Suttton and Farshad, 1983 (SF).

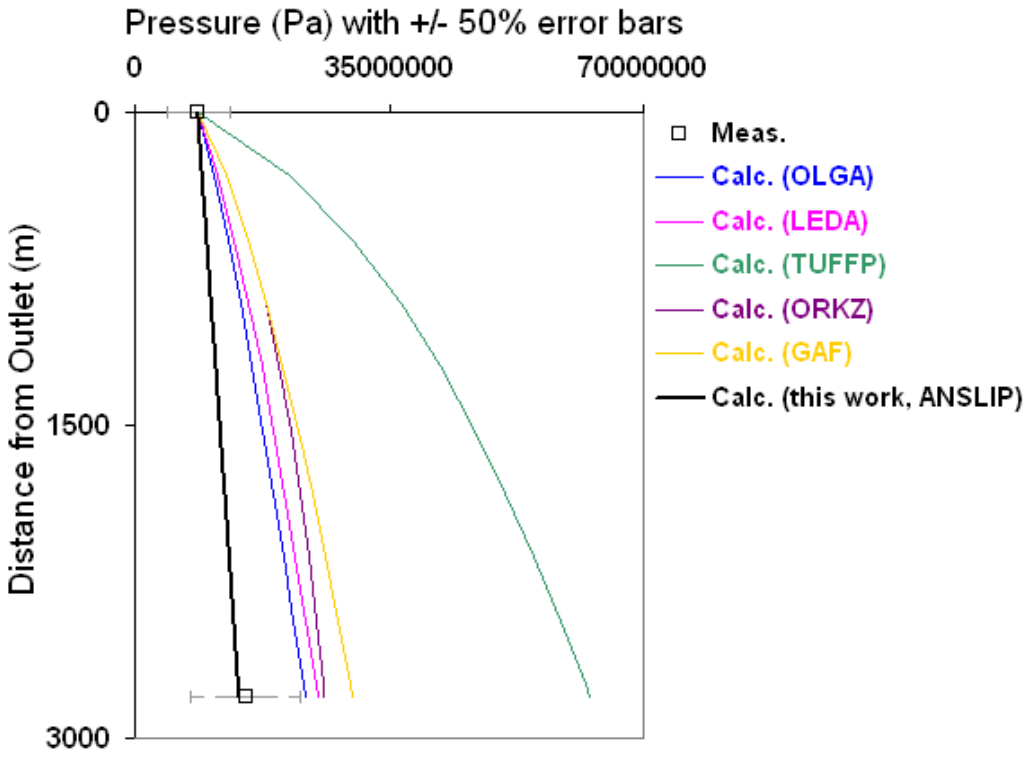

Figure 7.13.14: Comparisons of different model predictions for well case 6 of Chierici et al. (1974).

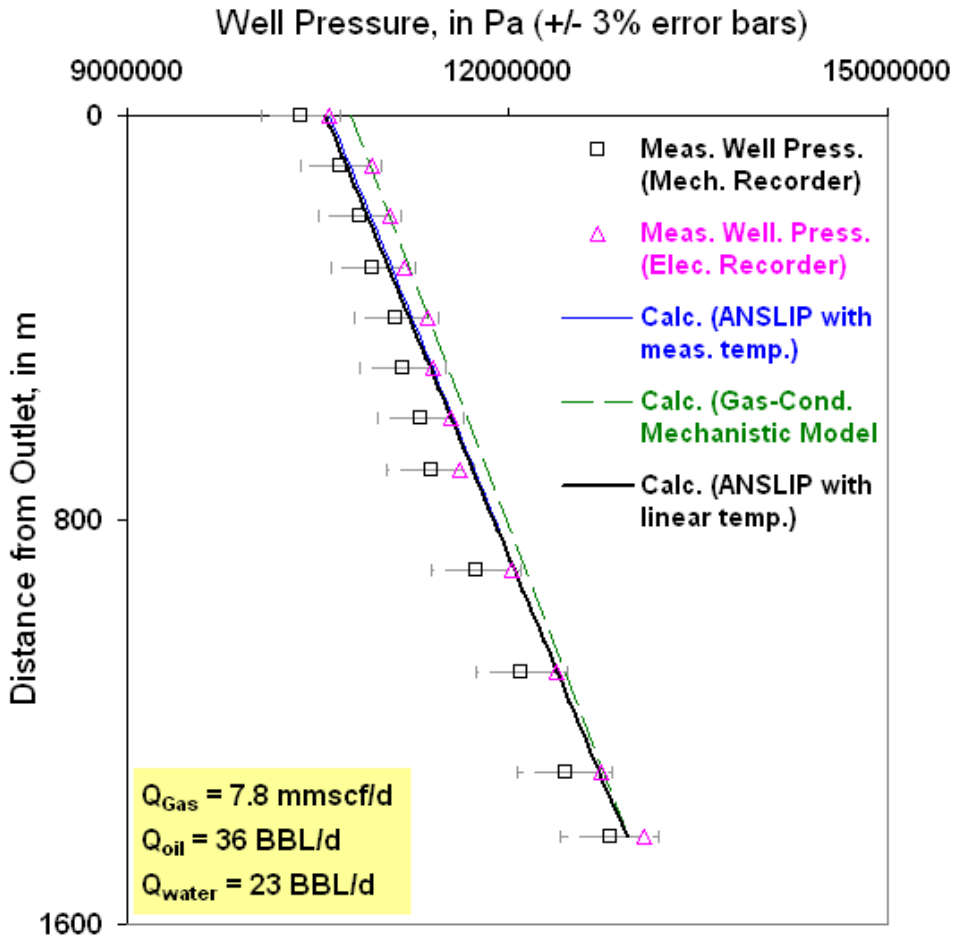

Figure 7.13.15: Comparisons of different model predictions for run 2 of Alves et al. (1988).

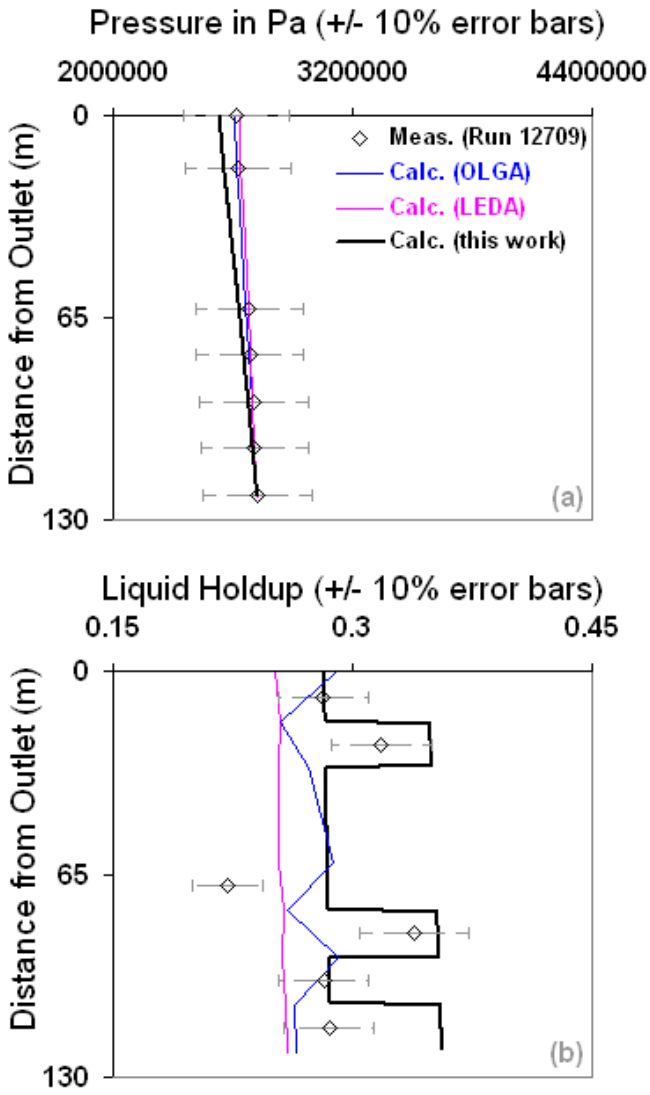

Figure 7.13.16: Comparisons of different model predictions for one run of Payne et al. (1979).

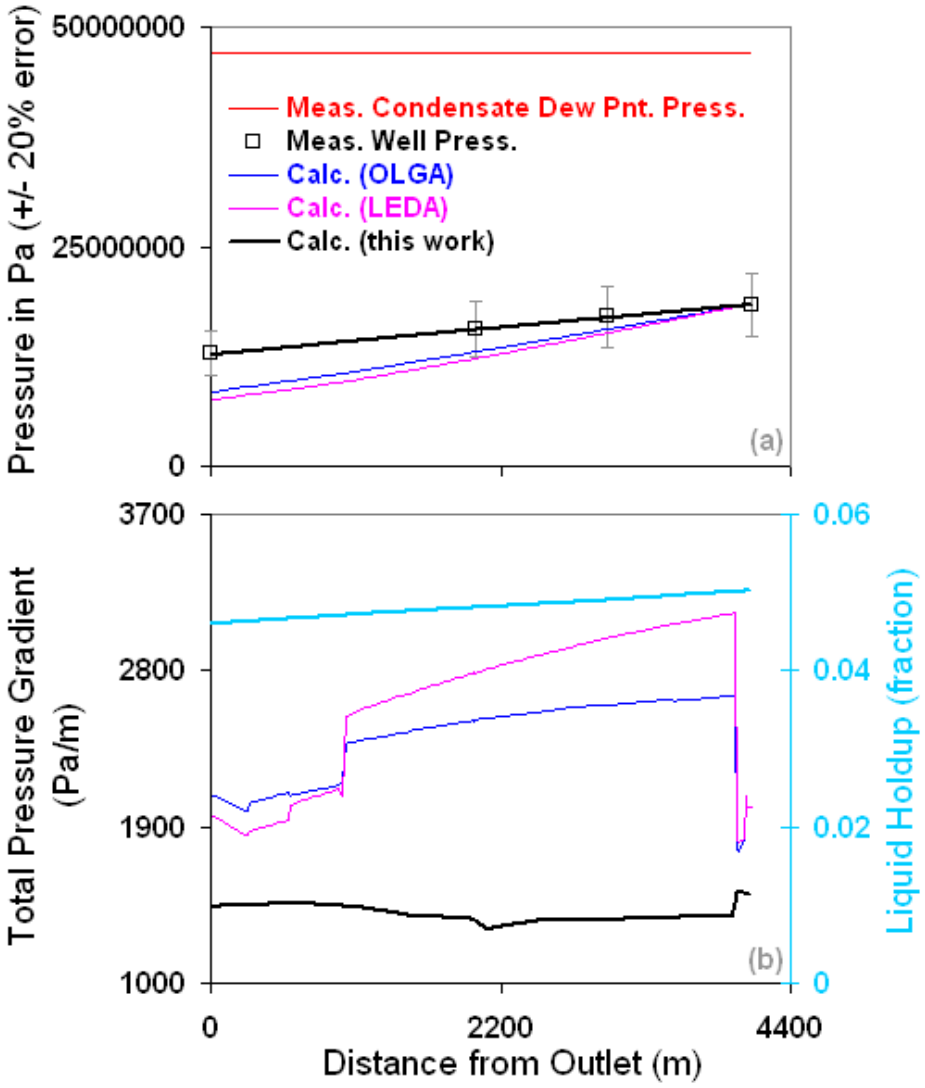

Figure 7.13.17: Comparisons of different model predictions for the annulus-produced well of Furnival and Baillie (1993) – this work uses the ANSLIP model.

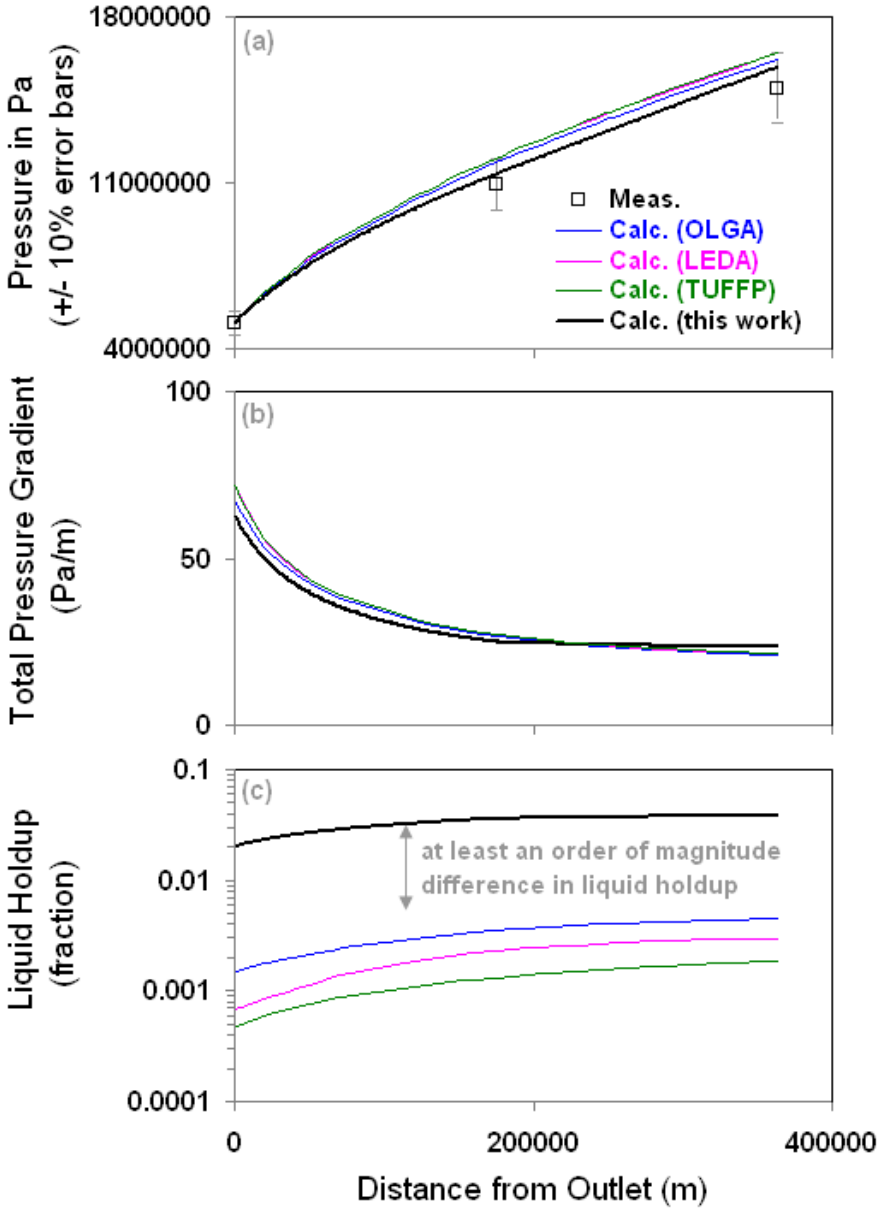

Figure 7.13.18: Comparisons of different model predictions for one run (at a condensate rate of 1144 BBL/d) of the Frigg pipeline in Lagiere et al. (1984) – this work uses the ANSLIP model.

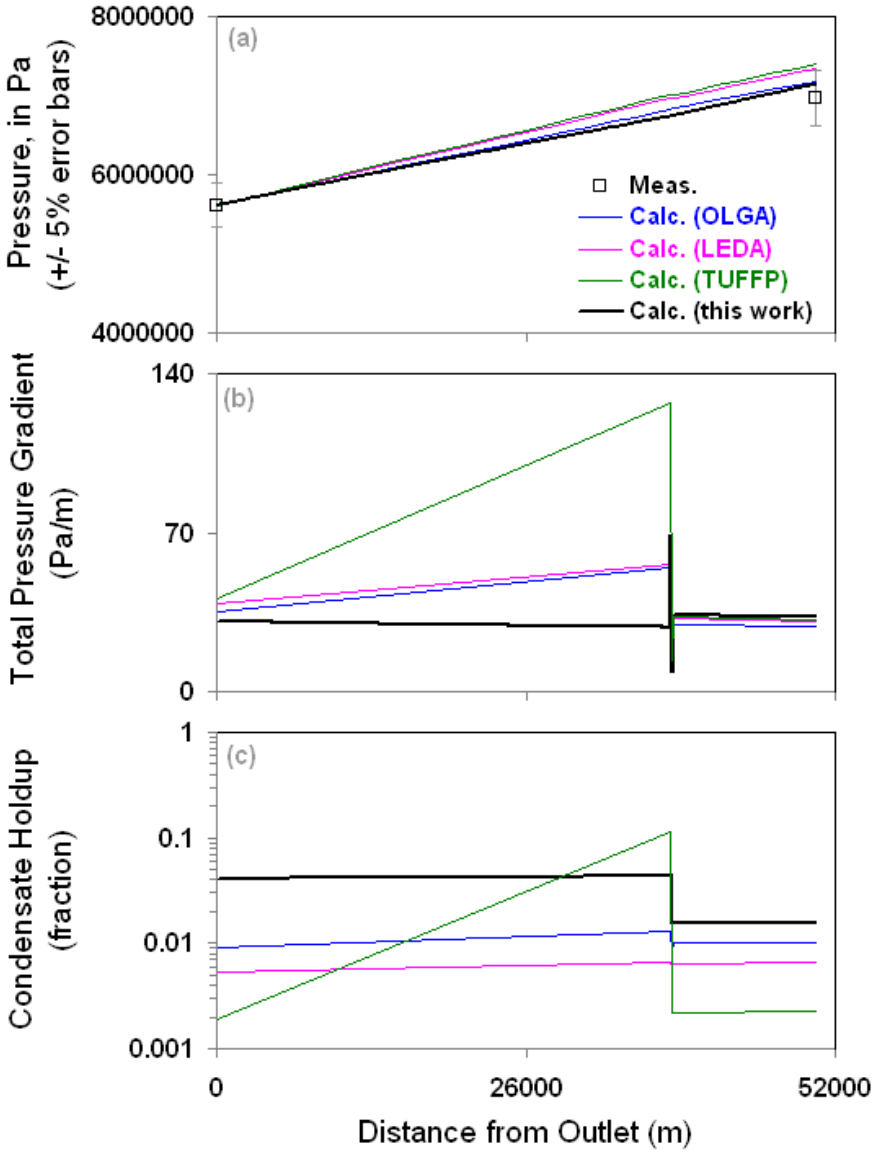

Figure 7.13.19: Comparisons of different model predictions for the AGA line 19 run, previously analyzed in Fig. 7.11.12.

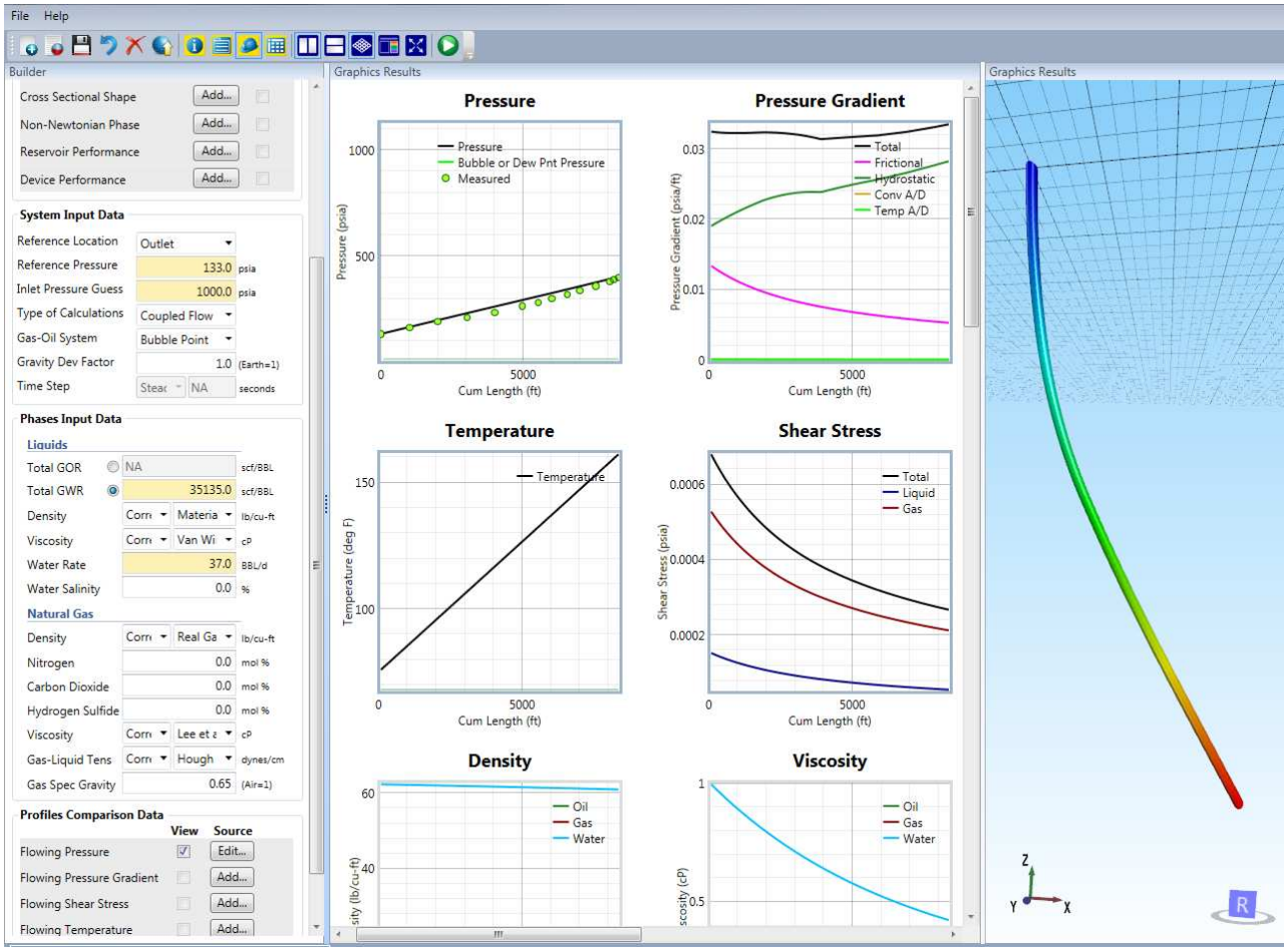

Figure 7.13.20: Our analytical model's predictions for the field gas-water well on pg. 68 of Lea et al. (2003) with the ANSLIP model.

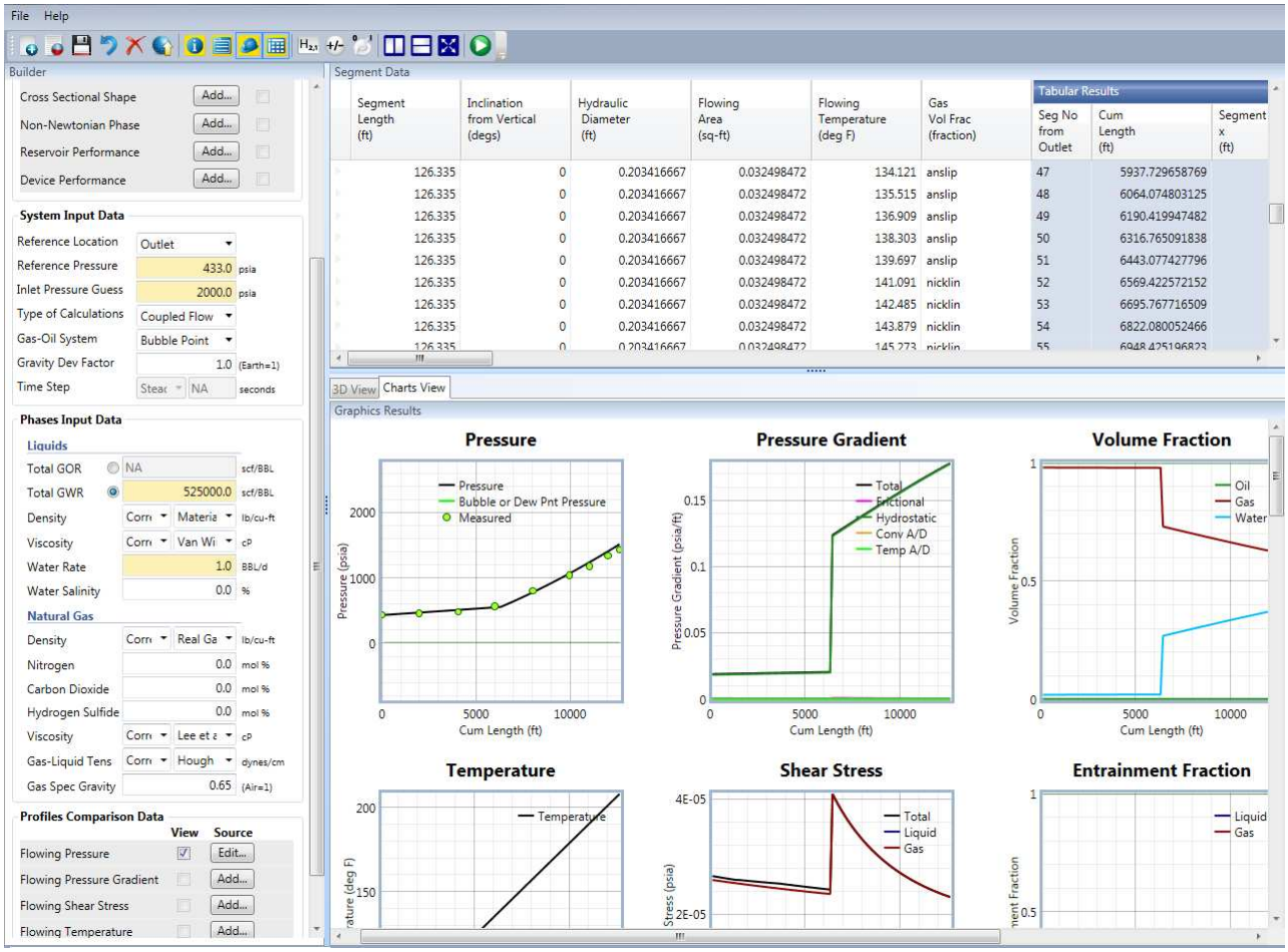

Figure 7.13.21: Our analytical model's predictions for the static-liquid-column gas well no. 11 of Sutton et al. (2003) – Fig. 8 in this reference.

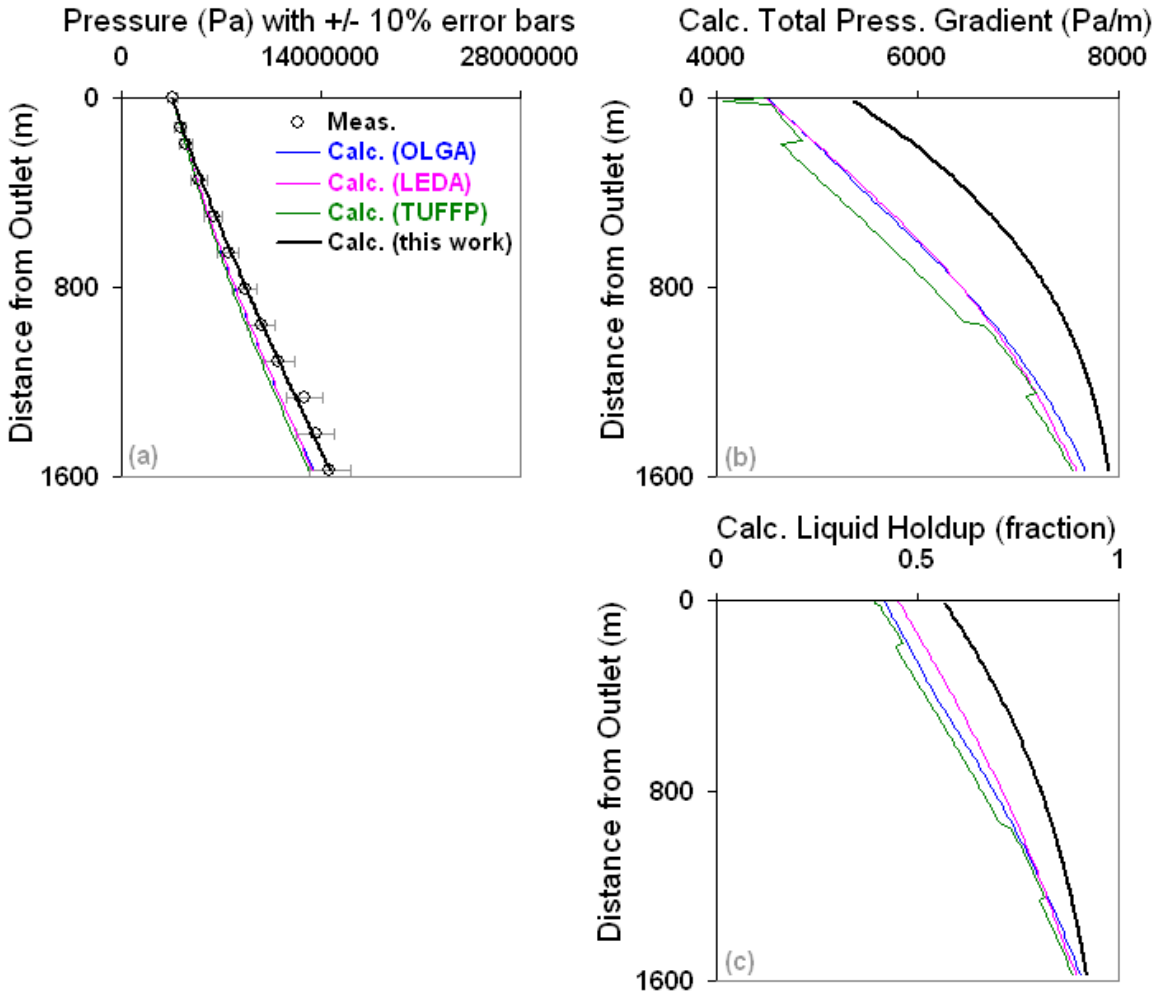

Figure 7.13.22: Comparisons of different model predictions for the first field well example in Hasan and Kabir (2002) – this work uses the NICKLIN model.

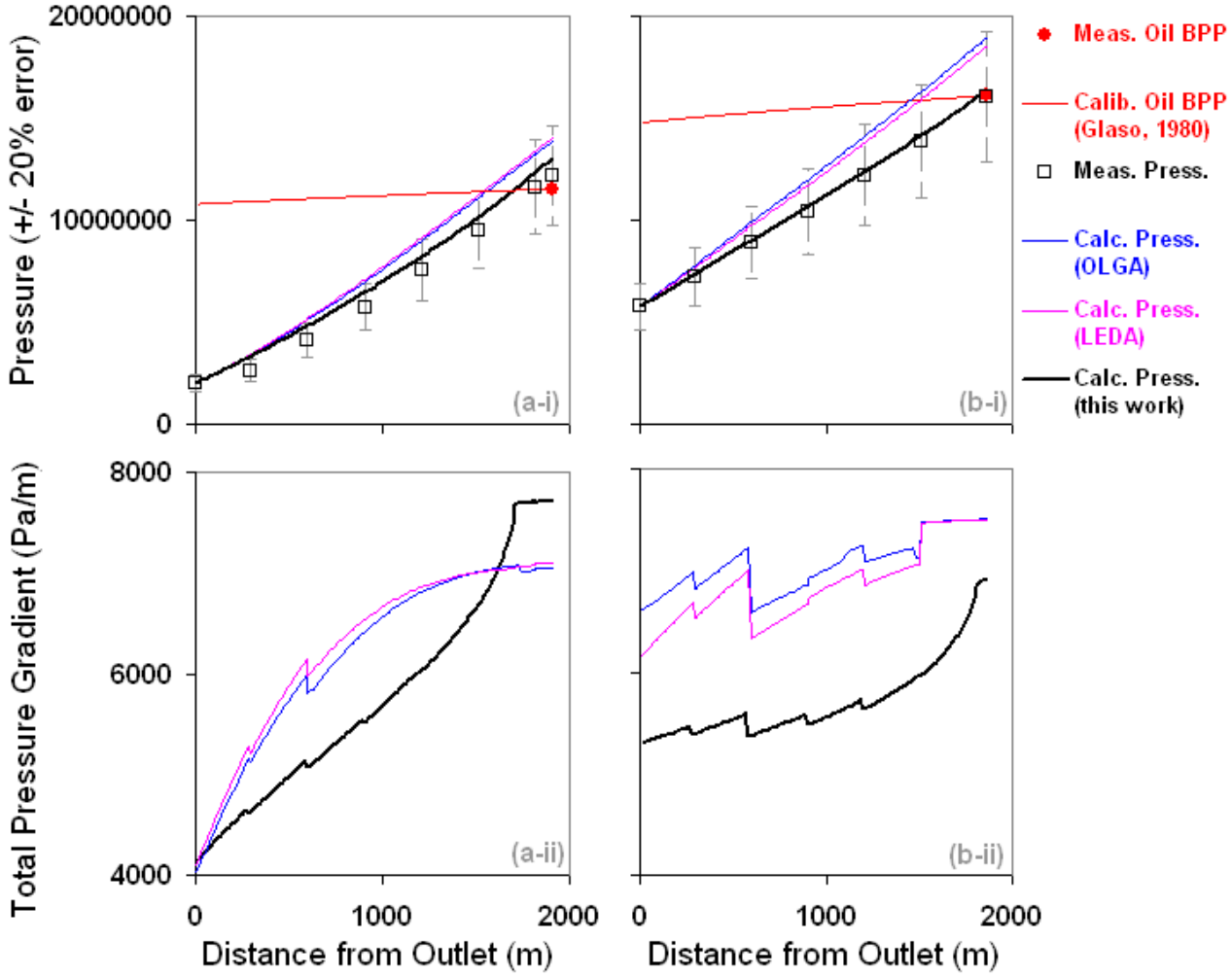

Figure 7.13.23: Comparisons of different model predictions for wells M2 (left-most charts) and M8 (right-most charts) in Griffith et al. (1973) – this work uses the BUTTERWORTH model.

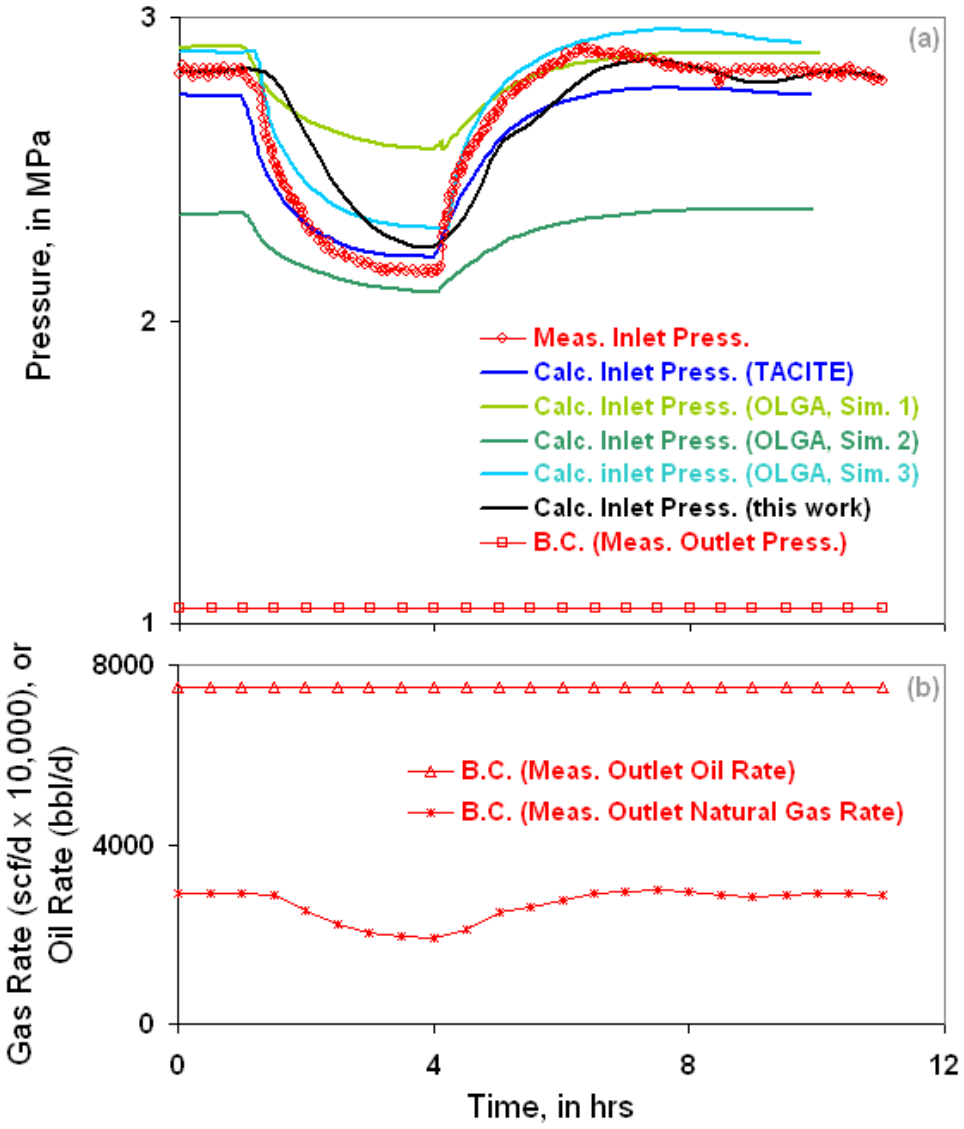

Figure 7.13.24: Comparisons of different model predictions for the 12-inch diameter Bekapai pipeline transient of Lopez et al. (1997) – this work uses the MIST flow model.

Chapter 8 – Conclusions and Future Directions

8.1 CONCLUSIONS

The contribution of this research is a simple, analytical mathematical modeling framework that connects multiphase pipe flow phenomena and satisfactorily reproduces key multiphase pipe flow experimental findings and field observations, from older classic data to modern ones. The proposed unified formulation presents, for the first time, a reliably accurate analytical solution for averaged (1D) multiphase pipe flow over a wide range of applications. This reliable accuracy is demonstrated and quantified in the wide ranging experimental datasets of Chapters 3 – 7.

The two new fundamental insights provided by this research are that:

I. Macroscopic single-phase pipe flow fluid mechanics concepts can be generalized to multiphase pipe flow.

II. Viewing and analyzing multiphase pipe flow in general terms of averaged relative flow (or *fractional flow*) can lead to a unified understanding of its resultant (global) behavior.

The first insight stems from our finding that the universal relationship that exists between pressure and velocity in single-phase flow can also be found equivalently between pressure and relative velocity in multiphase flow. This eliminates the need for a-priori flow pattern determination in calculating multiphase flow pressure gradients. Furthermore, it is proven in this work that multiphase pressure gradient is governed by relative velocity and our analytical models (Eqns. 6 and 7 of Section 2.2.4) are very accurate once the relative velocity (the volume fraction) is known. We demonstrate with large amounts of experimental evidences, that in averaged descriptions of multiphase

pipe flow, flow patterns merely represent the different possible visual manifestations (spatial configurations) of in-situ velocities and volume fractions. Flow patterns, therefore, cannot (and must not) be solved separately from pressure in multiphase flows because relative velocities and pressure cannot be separated. Clearly, it is the velocity and volume fraction cross-sectional distributions as well as their associated space- and time-averaged values (which represent the net of competing microphysical flow interactions) that play determining roles in the transport processes of the flow.

The second insight signifies that, in general, averaged multiphase flow problems can be sufficiently modeled by knowing only the averaged volume fractions. This proves that flow patterns are neatly captured in the averaged sense as different fractional flow paths in our proposed fractional flow graphs. The real power of the fractional flow graph lies in its ability to generate single-path or multiple-path traverses connecting different flow patterns thus capturing the connections between different flow phenomena. Moreover, it is found that only a few analytical fractional flow models and existing volume fraction correlations reformulated as fractional flow models can be relied upon for satisfactory prediction of averaged volume fraction (Table 3.2 of Chapter 3).

Due to their simplicity, these new insights provide for a deeper understanding of multiphase flow phenomena and a broader capability to produce quantitative answers in response to what-if questions. Demonstrations of simple, step-by-step hand calculations of the Pipe Fractional Flow Theory for a variety of example multiphase flow problems were shown in Section 4.2 of Chapter 4. Since these new insights did not draw from any precedent in the prior literature, we provided a science-oriented, comprehensive validation of our analytical models in Chapters 3 – 7. Model validation was performed against a diverse range of vapor-liquid, liquid-liquid, fluid-solid and vapor-liquid-liquid applications (over 74,000 experimental measurements from over 110 different labs and

over 6,000 field measurements). This searchable database (called ANNA and accessible via the worldwide web) represents the world's largest collection of published (cross-referable), wide-ranging averaged multiphase flow data. As shown in Section 1.3.5.2 of Chapter 1, ANNA is a unique tool now afforded via this research that can be used to objectively identify bad multiphase flow data.

A direct implication of aligning standards around the published averaged multiphase flow data is a drive towards more innovation across the disciplines where this subject is studied. The ease of downloading from or uploading to the ANNA database website creates a readily-accessible, standardized means for investigators in any part of the world to access (or freely share) various types of averaged multiphase flow data from different laboratories for use in their research studies. Moreover, the presence of large amounts of high-fidelity multiphase flow data in different categories invalidates the belief that only a certain laboratory or group of investigators are conducting special experiments relating to a niche commercial interest. Indeed, such niche interest groups must be encouraged to upload their data to the ANNA database in order that the validation data of their models become publicly-interrogable (a requisite for scientific data), thus satisfying the operational acceptance level for scientific multiphase flow models as discussed in Section 1.3.5.1 of Chapter 1. Obviously, no valid comparison can be performed between models validated with secret (or inaccessible/untraceable) data and models validated with published, peer-reviewed, cross-referable data (such as our analytical models presented in this work).

In addition to validation against published experimental data, our analytical models were benchmarked against other modeling methods and current industry codes with identical, named published data. These unbiased benchmarking comparisons represent an important aspect of this research. Not only do they highlight the

performance of available modeling methods amongst themselves, but more pointedly, they also quantify the computational performance of the Pipe Fractional Flow Theory against the available modeling methods. Therefore, these comparisons provide a long-overdue, independent assessment of practical code capabilities in different industries. The result of these comparisons is a clear and unambiguous major increase in accuracy afforded via the hypothesis-based research approach of this work.

Furthermore, by comparing the results of different modeling methods over a wide range of conditions, the central argument proffered by the proponents of the large, very complex multi-physics models (i.e., that several effects need to be explicitly accounted for with new closure relations or more conservation equations) is directly countered by the simple, self-consistent models. The provable counter-argument provided in this research is that the numerous, competing, interacting, local flow microphysics effects can be (implicitly) accounted for by just a few simple and properly validated (global) closure models that capture their collective (resultant) behavior.

The validation and benchmarking results described above affirm the central finding of this research – that simple, suitably-averaged analytical models can yield an improved understanding and significantly better accuracy than that obtained with extremely complex, tunable models. We substantiate and quantify this finding by frequently comparing our analytical model's predictions with mechanistic, multi-fluid and CMFD models which contain large amounts of conservation equations, closure relations, groups of adjustable parameters and complex numerical formulations. As seen from these comparisons throughout Chapters 4 – 7, previously held beliefs about the need for more complex modeling (e.g., the CMFD modeling approach, the "horses for courses" modeling approach) are provably countered.

8.2 FUTURE DIRECTIONS

Summarizing, it is the claim of this research that there is an underlying simplicity and connectedness in this subject if looking at the resultant macroscopic (averaged) behaviors of the flow. The observed coherencies of the macroscopic, self-organizing physical structures that define the subject are equivalently present in the macroscopic mathematical descriptions of these systems, i.e., the flow-pattern-implicit, averaged-equations mixture models that describe the net behavior of the flowing mixture.

In essence, we postulate that instead of looking at separate, component parts of a complex system (one example of a complex system being a multiphase flow in a closed conduit) and creating individual, tunable models for the perceived mechanisms that describe a small part of the system, the complex system as a whole (as a mixture of flowing phases) must honor the universal observational laws of mass, momentum and energy conservation at the averaged (global) flow scale.

The latter (mixture) approach above represents one kind of asymptotic approximation analysis, the "asymptote" being the avoidance of many details of the flow. Asymptotic approximation methods, just as scaling arguments, transport analogies, non-dimensionalization, the Reciprocal theorem and characteristic lengths are generalizing principles that have well-established roles in the analysis and understanding of transport processes and fluid mechanics. In the former (mechanistic) approach, it is a fact that it is very difficult to design properly isolated experiments to quantify the sole effect of the proposed mechanism. This is the first step. If there are no properly isolated experiments for capturing the problem, then there is little confidence in (or justification of) any model that claims to explain the mechanism(s) underlying the problem. The lack of properly isolated experiments for observing flow mechanisms is also the primary reason responsible for another fact – which is – that different mechanistic models with widely

different assumptions can be shown to predict the same flow behavior (e.g., as demonstrated in the "salutary lesson" of Hewitt, 1987).

In our view, *if* the macroscopic behavior of a complex system is known via simple, predictive, macroscopic analytical models, *then* the local behaviors of the complex system is thus bounded by the macroscopic analytical models. This signals an important future direction of research in this subject because flow characteristics of interest (e.g., slug lengths, mean film thicknesses, mean wave heights, etc.) can now be calculated *a posteriori* from reliable, deterministic predictions of global quantities (such as averaged volume fractions) from our macroscopic analytical models. This approach allows one to see flow characteristics (including uncontrollable and unpredictable quantities such as meso-scale flow field clusters and structures) in a multiphase flow in their true nature as they are – as dynamic, continuously-evolving and unknown features during flow in response to the prevailing hydrodynamic forces – and not as how they are perceived by different investigators promoting different mechanisms explaining their local behaviors.

If there is a special (rare) scenario or application where multiphase flow characteristics can be predicted by local mechanistic models in combination with local conservation equations (e.g., the Navier-Stokes equations), *then* enforcing that our macroscopic analytical models (the Nagoo-Sharma equations) are solved simultaneously with such microscopic models would present, for the first time, a reliable means of extracting local information about the multiphase flow. This is because the local mechanistic models would be bounded on one extent by the correct local behavior (the equation of motion) and on the other extent, by the correct global behavior of the multiphase flowing mixture (the analytical averaged-equations models of this work which represents the net of the competing, local flow microphysics interactions).

If our approach described above finds favor among a critical mass of investigators, *then* the goal of future scientific research in averaged multiphase pipe flow will be to start asking fundamentally different questions that will aim to discover this flow-pattern-implicit macroscopic, mixture behavior – and specifically – to be able to predict the averaged volume and entrainment fractions, which represent the most important global quantities of the flow. The task will then be, not to continue adding more modeling complexity in response to more complex flow problems, but to find the points of view from which a complex problem will appear in its greatest simplicity (i.e., to simplify rather than complicate). These points of view, if discovered, will not only permit a whole new learning of how to think about these problems in a simpler way, but also, how to generalize from a current problem to a related but presently unanticipated application. Elementary tests, designed to interrogate these points of view, must then be performed with the goal of achieving a deeper, predictive understanding.

Finally, the fact that our analytical models presented in this work reliably reproduces the key multiphase pipe flow experimental findings and field observations (from older classic data to modern ones), signifies that the use of our analytical models in existing industry codes and current averaged flow models ensures that multiphase pipe flow calculations will be consistent with the vast majority of prior published experimental observations and results. This represents a necessary, science-oriented future (change of) direction in averaged multiphase flow if existing industry codes and current averaged flow models are to become less uncertain (lower risk) and reliably predictive, with the predictability of the macroscopic (global) behavior of the flowing multiphase mixture now afforded (and governed) via the analytical models presented in this research. It remains the responsibility of all multiphase flow stakeholders to ensure that both inexperienced and experienced multiphase flow investigators use simple, properly

validated, science-based models with the least uncertainty (i.e., lowest risk) and least primary concepts (i.e., highest predictability), and to conduct simply-designed, well-instrumented, publicly-verifiable experiments.

Appendix A – Basic Multiphase Pipe Flow Terms and Definitions

In this appendix, we highlight some very often misunderstood definitions of important multiphase pipe flow variables, namely volume fractions, velocities, volume fluxes and pressures. These variables, and others related to them, appear frequently in this work.

First, a few conventions are summarized, after which volume fractions, velocities, volume fluxes and pressures are carefully defined. Next, some foundational dimensionless ratios are specified in two-phase flow forms, as examples. Then, usually overlooked fundamental descriptors such as components, phases and particles are clarified.

A.1 CONVENTIONS

Flow variables whose general units include the subscript *local* refer to variables in a micro-scale region of the flow field of a pipe at a given cross-section along the pipe axis (*local* variables). Flow variables whose general units include the subscript *pipe* refer to the macro-scale, pipe cross-sectional averaged variables at a given cross-section along the pipe axis (*global* variables). In this work, the terms *averaged*, *global* and *macro-scale* all refer to cases where pipe cross-sectional averaged flow-field variables are considered.

Flowing phase, *j*, refers to any flowing phase, which are usually gaseous, oleic, aqueous or granular phases. The convention followed here is: phases are numbered starting from unity in which higher values of j represent the less dense phases and lower values of j represent the more dense phases.

Flowing phase *in-situ velocities* are denoted by *v* and flowing phase volume fluxes (i.e. the volumetric flow rate divided by the pipe area open to flow) are denoted by *u*. *u* is alternatively referred as *superficial velocities* in the literature.

A.2 VOLUME FRACTIONS

The time-averaged local phase-j volume fraction, which is the in-situ phase-j volume concentration at some micro-scale region of the flow-field is:

$$s_j \ [=] \frac{L^3 \ of \ j}{L^3 \ of \ V_{local}} \tag{A.1}$$

Note that s_j represents the fraction of a control volume in the pipe which is occupied at any instant by phase-j, in which the control volume is much larger than the discrete fluid-phase or solid-phase particles, i.e., bubbles, droplets, globules or grains. If the sample volume is small enough, i.e., at the scale of the fluid-phase or solid-phase particles, then s_j can only be 0 or 1. Hence this variable is locally discontinuous at the fluid-phase or solid-phase particle scale. It is noteworthy to observe the analogy between this multiphase pipe flow variable at the fluid-phase or solid-phase particle scale and locally discontinuous variables in a porous media at the pore scale.

The averaged phase-j volume fraction at any cross-sectional plane, A, along a pipe is:

$$\left\langle s_j \right\rangle = \frac{1}{A}\int_A s_j dA \ [=] \frac{L^3 \ of \ j}{L^3 \ of \ V_{pipe}} \tag{A.2}$$

Note that averaged phase-j volume fraction (or saturation) as defined above refers to the cross-sectional area and time averaged in-situ phase-j volume concentration. This term is normally identified in the multiphase pipe flow literature as the *averaged void fraction* or *gas holdup* if j is gaseous, or, as the *averaged liquid holdup* or simply, *holdup*, if j is

liquid. Also, since this term is actually a time-averaged variable, it may be equivalently written as:

$$\left\langle s_j \right\rangle = \frac{\int\int s_j(A,t)\,dAdt}{\int dA \int dt} \;[=]\; \frac{L^3 \; of \; j}{L^3 \; of \; V_{pipe}} \tag{A.3}$$

A.3 VELOCITIES

The time-averaged local phase-j velocity, which is the in-situ phase-j velocity at some micro-scale region of the flow-field, in general vectorial form, is:

$$\overrightarrow{v_j} \;[=]\; \frac{L \; of \; V_{local}}{t} \tag{A.4}$$

The time-averaged local mixture velocity, which is the in-situ velocity of the mixture center-of-volume at a micro-scale region of the flow-field is:

$$\sum_{j=1}^{N_p} \left(s_j \overrightarrow{v_j} \right) = \overrightarrow{v_{mix}} \;[=]\; \frac{L \; of \; V_{local}}{t} \tag{A.5}$$

The averaged in-situ phase-j velocity at any cross-sectional plane, A, along a pipe is:

$$\left\langle\left\langle v_j \right\rangle\right\rangle = \frac{\left\langle s_j v_j \right\rangle}{\left\langle s_j \right\rangle} = \frac{\left\langle u_j \right\rangle}{\left\langle s_j \right\rangle} = \frac{\frac{q_j}{\cancel{A}}}{\frac{A_j}{\cancel{A}}} = \frac{q_j}{A_j} \;[=]\; \frac{L \; of \; V_{pipe}}{t} \tag{A.6a}$$

The term above is also known alternatively as the *weighted phase-j mean velocity* or the *actual cross-sectional area averaged phase-j velocity* in the multiphase pipe flow literature. An important aspect of the definition above is that the disappearance of phase-j is mathematically undefined. This represents the physical discontinuity that exists when a phase instantaneously disappears in the flowing mixture. This corresponds to instances when $\left\langle s_j \right\rangle$ = 0 in Eqn. A.6a above when phase-j is not present in the multiphase flow. This mathematical undefined phase-j scenario similarly appears even when a phase-j-

mass-weighted averaging definition is used for in-situ velocity describing the averaged velocity of the phase center-of-mass. In this latter definition, phase-j in-situ velocity is defined as:

$$\left\langle\left\langle v_j \right\rangle\right\rangle = \frac{\left\langle s_j \rho_j v_j \right\rangle}{\left\langle s_j \rho_j \right\rangle} \; [=] \frac{L \; of \; V_{pipe}}{t} \tag{A.6b}$$

Multiphase flow investigators usually choose an appropriate definition of in-situ velocity according to which definition appears in their formulation of the field equations. Regardless of whether Eqn. A.6a or A.6b is more appropriate for a particular scenario, it is important to realize that if these definitions of in-situ velocities are used in models, then limits must be set for $\left\langle s_j \right\rangle$ to prevent the occurrence of this special condition of phase disappearance. This is easily handled in either spreadsheet calculations or software codes by setting a limit for phase-j disappearance (e.g., $\left\langle s_j \right\rangle_{absent \; limit} = 10^{-6}$).

The averaged in-situ relative velocity between any two arbitrary phases 1 and 2, defined as the difference between the averaged in-situ phase velocities, is:

$$\left\langle\left\langle v_2 \right\rangle\right\rangle - \left\langle\left\langle v_1 \right\rangle\right\rangle = \left\langle\left\langle v_{2,1} \right\rangle\right\rangle = S_{2,1} \; [=] \frac{L \; of \; V_{pipe}}{t} \tag{A.7}$$

This term is also alternatively known as the *slip velocity* or simply, *slip*, in the multiphase pipe flow literature. Mathematically speaking, it is also known as the *integral* or *global slip*. The convention followed here for identifying and naming the subscripts of the *slip velocity*, S, is:

I. The first subscript of S is always a dispersed or passive phase in the flowing multiphase mixture, and

II. The second subscript of S is always a continuous or dominant phase that the particular dispersed-phase velocity is being compared with.

The averaged in-situ velocity ratio between any two arbitrary phases 1 and 2, defined as the ratio of the averaged in-situ phase velocities, is:

$$\frac{\langle\langle v_2 \rangle\rangle}{\langle\langle v_1 \rangle\rangle} = H_{2,1} \ [=] \ dimensionless \tag{A.8}$$

This term is alternatively known as the *slip ratio* in the multiphase pipe flow literature. The same convention used for the averaged in-situ relative velocity, as given above, is also used for the averaged in-situ velocity ratio. It is worth noting that the averaged in-situ velocity ratio becomes undefined when the continuous or dominant phase (j=1) becomes stagnant – if not properly accounted for, this can easily cause crashes in software codes.

A.4 VOLUME FLUXES

The time-averaged local phase-j volume flux, which is the phase-j volume flux at some micro-scale region of the flow-field, in general vectorial form, is:

$$\overrightarrow{u_j} = s_j \overrightarrow{v_j} \ [=] \frac{L^3 \ of \ j}{L^3 \ of \ V_{local}} \cdot \frac{L \ of \ V_{local}}{t} = \frac{L^3 \ of \ j}{L^2 \ of \ V_{local} - t} \tag{A.9}$$

The averaged phase-j volume flux at any cross-sectional plane, A, along a pipe is:

$$\langle u_j \rangle = \langle s_j v_j \rangle = \frac{q_j}{A} \ [=] \frac{L^3 \ of \ j}{L^2 \ of \ V_{pipe} - t} \tag{A.10}$$

This term is alternatively known as the *averaged phase-j superficial velocity* in the multiphase flow literature. Note that, for flowing phase-j, flowing with other phases through a pipe, the averaged in-situ phase-j velocity defined in Eqn. A.6a above is the velocity of phase-j in the presence of the other flowing phases. The averaged phase-j volume flux is the velocity of phase-j as if it were flowing in the pipe by itself. Since the averaged in-situ phase-j velocity has a smaller available flow area, it will always be greater than the averaged phase-j volume flux.

The averaged mixture volume flux in a pipe is:

$$\left\langle u_{mix} \right\rangle = \sum_{j=1}^{N_p} \left(\left\langle \left\langle v_j \right\rangle \right\rangle \left\langle s_j \right\rangle \right) = \sum_{j=1}^{N_p} \left\langle u_j \right\rangle = \frac{\sum_{j=1}^{N_p} q_j}{A} = \frac{q_{total}}{A} \ [=] \frac{L \ of \ V_{pipe}}{t} \tag{A.11}$$

This term is alternatively known as the *averaged mixture velocity* in the multiphase flow literature.

The averaged phase-j flowing fraction in a pipe is:

$$f_j = \frac{\left\langle u_j \right\rangle}{\sum_{j=1}^{N_p} \left(\left\langle u_j \right\rangle \right)} = \frac{\left\langle u_j \right\rangle}{\left\langle u_{mix} \right\rangle} = \frac{\frac{q_j}{\cancel{A}}}{\frac{q_{total}}{\cancel{A}}} = \frac{q_j}{q_{total}} \ [=] \frac{L^3 \ of \ j}{L^3 \ of \ V_{pipe}} \tag{A.12}$$

This term is alternatively known in the multiphase flow literature as the averaged volumetric flow quality or no-slip holdup (in vapor-liquid flows), or the input/delivered concentration (in liquid-liquid or liquid-solid flows, respectively). We emphasize that this term is a flow-only variable and is not a concentration (or holdup) quantity. As such, to avoid confusion, it should not be phrased in relation to concentration quantities (e.g. "no-slip holdup") because whereas concentration quantities will exist whether there is flow or not, a phase's flowing fraction will be zero if that phase does not flow.

A.5 PRESSURES

The time-averaged local phase-j pressure, which is the phase-j pressure at some micro-scale region of the flow-field, is:

$$P_j \ [=] \frac{amount \ of \ j}{L \ of \ V_{local} - t^2} \tag{A.13}$$

The time-averaged local mixture pressure, which is the mixture pressure at some micro-scale region of the flow-field, is:

$$\sum_{j=1}^{N_p} \left(s_j P_j \right) = P_{mix,local} \ [=] \frac{amount \ of \ all \ j}{L \ of \ V_{local} - t^2} \tag{A.14}$$

The averaged phase-j pressure at any cross-sectional plane, A, along a pipe is:

$$\left\langle\left\langle P_j \right\rangle\right\rangle = \frac{\left\langle s_j P_j \right\rangle}{\left\langle s_j \right\rangle} \; [=] \frac{amount\ of\ \ j}{L\ of\ V_{pipe} - t^2} \tag{A.15}$$

The term above can be alternatively called the *actual cross-sectional area averaged phase-j pressure*.

A.6 GENERALIZED DIMENSIONLESS RATIOS

The use of the generalized dimensionless ratios given in this section is an important aspect of this research. These ratios provide a deeper insight and physical explanation to correlations and seemingly random empirical equations by transforming them into meaningful relations. We provide five examples showing that simply by establishing a generalized set of dimensionless ratios, we can better understand past findings, correct them if necessary and view them from a unified context.

A.6.1 Example: Churn to Annular Flow Transition

As a first example, the transition from the churn flow pattern to the annular flow pattern has historically been observed in vertical upward air-water circular-pipe systems to be governed by different sets of criteria. In some instances, the criterion is given in the multiphase pipe flow literature as (Hetsroni, 1982):

$$\left\langle u_2 \right\rangle \left(\frac{\rho_2}{D(\Delta\rho)g} \right)^{\frac{1}{2}} > 1 \tag{A.16}$$

In other cases, the criterion is stated as (Wolf, 1995):

$$\overbrace{\left\langle u_2 \right\rangle \left(\frac{{\rho_2}^2}{\sigma_{2,1}(\Delta\rho)g} \right)^{\frac{1}{4}}}^{Kutateladze\ Number} > 3.2 \tag{A.17}$$

In Eqn. A.16 there is dependence on diameter and in Eqn. A.17 there is no dependence on diameter but a dependence on interfacial tension between phases 1 and 2. In the past, various multiphase pipe flow investigators provided different reasons for use

of one equation over the other, usually in alignment with what worked better for their own experiments. Simply by a consistent set of definitions as given below, it is seen that Eqn. A.16 is exactly equivalent to (with $\theta = 0$ degrees for vertical upward flow, and $D_H = D$ for circular pipe):

$$\overbrace{N_{Fr,s2}^{axial}}^{\substack{\text{axial Froude Number} \\ \text{phase-2}}} > 1 \qquad \text{(A.18)}$$

And similarly, Eqn. A.17 is exactly equivalent to:

$$\left(\overbrace{N_{We,s2}}^{\substack{\text{Weber Number} \\ \text{phase-2}}} \cdot \overbrace{N_{Fr,s2}^{axial}}^{\substack{\text{axial Froude Number} \\ \text{phase-2}}} \right)^{\frac{1}{2}} > 3.2 \qquad \text{(A.19)}$$

Immediately, one can see that Eqn. A.18 has a clear physical explanation in that *convective inertial* forces are beginning to dominate *buoyancy* forces in the transition between flow patterns. However, Eqn. A.19 now provides a physical basis for the avoidance of the use of Eqn. A.17 in models (and software codes) in that forces are seen to be coupled in this criterion and thus the physical meaning of this criterion is obscure.

A.6.2 Example: Slug Flow Limit

In a second example, the Taylor wavelength is defined by Kataoka and Ishii (1987) as a critical hydraulic diameter of a two-phase flow channel at which, in their opinion, slug bubbles bridging the entire diameter can no longer be sustained due to Taylor instability. It is defined by their relation as:

$$\frac{D_H}{\left(\frac{\sigma_{2,1}}{g(\Delta\rho)} \right)^{\frac{1}{2}}} \geq 40 \qquad \text{(A.20)}$$

As before, from a consistent set of definitions as given below, it is seen that Eqn. A.20 is exactly equivalent to (with $\theta = 0$ degrees for vertical upward flow):

$$\frac{N_{We,mix}}{N_{Fr,mix}^{axial}} = \left(\frac{axial\ \ buoyancy\ \ mix,1\ \ force}{interfacial\ \ tension\ \ 2,1\ \ force} \right)^{\frac{1}{2}} \geq 40 \qquad \text{(A.21)}$$

One can now see that Eqn. A.20 has a clear physical explanation in terms of the relative changes in the axial buoyancy and interfacial tension forces in the multiphase mixture.

A.6.3 Example: Stratified-Wavy Flow Froude Number

In the third example, a stratified-wavy-flow liquid Froude number definition (favored particularly by petroleum engineering investigators studying *wet-gas* or *gas-condensate* vapor-liquid systems) is given in Danielson (2003) as:

$$Fr_{wavy\ \ flow} = \frac{\left\langle\left\langle v_{liquid} \right\rangle\right\rangle}{v_{wave}} = \left(\frac{\rho_{liquid}}{\rho_{liquid} - \rho_{vapor}} \right)^{\frac{1}{2}} \frac{\left\langle\left\langle v_{liquid} \right\rangle\right\rangle}{\left(h_{liquid} g \right)^{\frac{1}{2}}} \qquad \text{(A.22)}$$

As before, from a consistent set of definitions as given below, it is seen that Eqn. A.22 is exactly equivalent to (with phase 1 = liquid, phase 2 = vapor, θ = 90 degrees for horizontal flow, liquid height = characteristic length):

$$Fr_{wavy\ \ flow} = N_{Fr,1}^{lateral} = \frac{\left\langle\left\langle v_1 \right\rangle\right\rangle}{\left(h_1 \left(\frac{\Delta\rho}{\rho_1} \right) g \overbrace{\sin\theta}^{=1} \right)^{\frac{1}{2}}} = \left(\frac{convective\ \ inertial\ \ 1\ \ force}{lateral\ \ buoyancy\ \ 2,1\ \ force} \right)^{\frac{1}{2}} \qquad \text{(A.23)}$$

One can now see that Eqn. A.23 has a clear physical explanation in terms of the ratio of the convective inertial force of phase 1 in relation to the lateral buoyancy force between phases 1 and 2. Convective inertia and buoyancy are two of the many forces (or mechanisms) that contribute to all of the terms in the momentum balance equation (i.e. the frictional, gravitational, acceleration/deceleration terms) via their effect on the volume fraction. When the stratified-wavy-flow liquid Froude number is seen in its true form in Eqn. A.23 above, then it can now be shown that the perception of this number being greater than 1 signifies that the forces governing the liquid are "frictional"

(Danielson, 2003), is incorrect. Aside from the effect of these mechanisms on the volume fraction, friction-related forces such as the molecular viscous (friction) force or the phase-to-wall or mixture-to-wall shear stresses constitute different mechanisms affecting the flow field.

A.6.4 Example: Terminal Particle Rise Velocity

For the fourth example, we consider the famous Harmathy (1960) expression for terminal rise (or slip) velocity of an isolated, smooth, rigid spherical particle (a flowing dispersed vapor phase, j) through an infinite, stationary medium (a continuous liquid phase, k). This expression is stated as:

$$v_{j,T} = 1.53\left(\frac{\sigma_{j,k}\Delta\rho g}{\rho_k^2}\right)^{\frac{1}{4}} \tag{A.24}$$

Similar forms of terminal rise velocity exist in the literature with only differences in the empirical constant of 1.53 (e.g. a constant of 2.9 instead of 1.53, in Dix, 1971). These expressions are commonplace in the Drift-flux averaged volume fraction correlations. A steady-state balance of the interfacial boundary (or total frictional drag) and buoyancy forces on the sphere can be used to derive the expression above, stated as:

$$\left(\frac{k-to-j\ \ k\ \ force}{axial\ \ buoyancy\ \ k,j\ \ force}\right)^{\frac{1}{2}} = 1 \tag{A.25a}$$

This same expression in A.25a can be restated in terms of our dimensionless ratio definitions (given at the end of this Section), as:

$$\overbrace{\left(\frac{\cancel{convective\ \ inertial}\ \ k\ \ force}{axial\ \ buoyancy\ \ k,j\ \ force}\right)^{\frac{1}{2}}}^{=N_{Fr,k}^{axial}} \overbrace{\left(\frac{k-to-j\ \ k\ \ force}{\cancel{convective\ \ inertial}\ \ k\ \ force}\right)^{\frac{1}{2}}}^{=\left(\frac{C_{D,k\to j}}{2}\right)^{\frac{1}{2}}} = 1 \tag{A.25b}$$

Note that Eqn. A.25b above, when combined with Eqn. A.38 below, is exactly equivalent to a steady-state momentum rate balance of a moving phase-k flowing around a stationary, submerged, rigid, smooth phase-j sphere. Clearly, this fact provides yet further evidence of the internal self-consistency of our carefully-chosen definitions of the dimensionless ratios below. Also, Eqn. A.25b is the same scenario (by a transformation of coordinates) describing the steady-state momentum balance of a moving (dispersed) phase-j flowing through an infinite, stationary (continuous) phase-k. Substituting Eqn. A.38 (with the characteristic velocity being the phase-k field velocity, characteristic volume being the volume of a sphere of diameter, D_p, and the characteristic area being the projected area of the sphere) into Eqn. A.25b, we get:

$$\left(\frac{\rho_k v_{k,\infty}^2 \overbrace{\left(\frac{\pi D_p^2}{4} \right)}^{\text{characteristic area}}}{\overbrace{\left(\frac{\pi D_p^3}{6} \right)}^{\text{characteristic volume}} (\Delta\rho) g \overbrace{\cos\theta}^{\substack{=1 \text{ only for} \\ \text{vertical flow}}}} \right)^{\frac{1}{2}} \left(\frac{C_{D,k\to j}}{2} \right)^{\frac{1}{2}} = 1 \qquad \text{(A.26)}$$

Rearranging Eqn. A.26 in terms of the terminal (or "T") rise velocity, we get:

$$v_{k,\infty} = v_{j,T} = \left(\frac{4}{3} \frac{D_p (\Delta\rho) g}{C_{D,k\to j} \rho_k} \right)^{\frac{1}{2}} \frac{m}{s} = \overbrace{\left(\frac{4g}{3} \right)^{\frac{1}{2}}}^{=3.62 \left(\frac{m}{s^2} \right)^{\frac{1}{2}}} \left(\frac{D_p (\Delta\rho)}{C_{D,k\to j} \rho_k} \right)^{\frac{1}{2}} \frac{m}{s} \qquad \text{(A.27)}$$

Eqn. A.27 has been derived many times in the literature and is often referred to as the particle "terminal velocity in free fall or rise" (pg. 363 in Silvestri 1964, pg. 113 in Clift et al., 1978). Note also that this equation is only valid for vertical flows and will require an adjustment, as shown in Eqn. A.26, for inclined flows. Additionally, sometimes it is found in the literature that an equivalent particle diameter, $D_{p,eq}$, is used in place of the spherical particle diameter, D_p, to account for non-spherical (ellipsoidal or distorted)

particles. As we shall next see in the fifth example below, Eqn. A.27 is also the exact equation as "Eqn. 2" in the classic Turner et al. (1969) paper with phases j and k interchanged to equivalently describe the terminal velocity of a liquid sphere globule through vapor rather than the terminal velocity of a vapor bubble sphere through liquid as above, and in which field units are used instead of SI units (as in this work). Thus, an acceleration due to gravity of 32.2 ft/s^2 is used in that paper leading to a coefficient of $6.55\ \sqrt{ft/s^2}$ in "Eqn. 2" of the paper rather than the coefficient of $3.62\ \sqrt{m/s^2}$ as shown in Eqn. A.27 above.

Next, we note that the unknowns in a typical multiphase flow experiment in Eqn. A.27 above are the total drag coefficient, $C_{D,k\to j}$, and the particle diameter, D_p. Two usual approaches for eliminating these unknowns are (Clift et al., 1978):

I. Setting $C_{D,k\to j}$ to a constant value and specifying D_p in terms of a Weber number for the particle (e.g. Turner et al. 1969).

II. Relating $C_{D,k\to j}$ directly to an Eotvos number for the particle, thus in the process, replacing D_p in terms of an interfacial tension (e.g. Harmathy, 1960).

In this example, the second method is highlighted and in the fifth example below, the first method is used. Now, the particle diameter can be related to the interfacial tension through the Eotvos number, formed from a phase's Weber number divided by its axial Froude number. Using eqns. A.36 and A.38, with appropriate characteristic definitions, the Eotvos number for phase-j in this example is:

$$N_{Eo,j} = \left(\frac{axial\ \ buoyancy\ \ j,k\ \ force}{interfacial\ \ tension\ \ j,k\ \ force} \right)^{\frac{1}{2}} = \left(\frac{\overbrace{\left(\frac{\pi D_p^3}{6} \right)}^{characteristic\ volume} (\Delta\rho) g \overbrace{\cos\theta}^{=1\ only\ for\ vertical\ flow}}{\overbrace{\pi D_p}^{characteristic\ length} \sigma_{j,k}} \right)^{\frac{1}{2}} \tag{A.28}$$

A linear relation between the total drag coefficient and the Eotvos number can then be stated as:

$$C_{D,k\to j} = \overbrace{\lambda}^{empirical\ constant} N_{Eo,j} \tag{A.29}$$

If a value of $\lambda = 4.37$ is used in eqns. A.29 and A.27, then the Harmathy et al. (1960) expression in Eqn. A.24 is recovered. In this example, we see how a consistent set of definitions allows one to easily re-interpret prior correlations in clear, physical terms inter-linking the various dimensionless force ratios under study.

A.6.5 Example: Terminal Particle Fall Velocity

In the final fifth example, we look at the directly equivalent scenario to the previous example above, i.e. the terminal fall (or slip) velocity of an isolated, smooth, rigid spherical particle (a flowing dispersed liquid phase, k) through an infinite, stationary medium (a continuous vapor phase, j). A famous model for this scenario is the unadjusted Turner et al. (1969) expression:

$$\overbrace{v_{k,T} = 1.593 \left(\frac{\overbrace{\sigma_{k,j}}^{dynes/cm} \overbrace{\Delta\rho}^{lbm/ft^3}}{\rho_j^2} \right)^{\frac{1}{4}} \frac{ft}{s}}^{Field\ Units} \ , \ or \ \overbrace{v_{k,T} = 5.465 \left(\frac{\overbrace{\sigma_{k,j}}^{Pa-m} \overbrace{\Delta\rho}^{kg/m^3}}{\rho_j^2} \right)^{\frac{1}{4}} \frac{m}{s}}^{SI\ Units} \tag{A.30}$$

We can derive Eqn. A.30 above by first noting that the equivalent expression for Eqn. A.27 in this scenario (with the identical steady-state force balance) is:

$$v_{j,\infty} = v_{k,T} = \left(\frac{4}{3} \frac{D_p (\Delta\rho) g \overbrace{\cos\theta}^{=1 \text{ only for vertical flow}}}{C_{D,j\to k}\rho_j} \right)^{\frac{1}{2}} \frac{m}{s} \tag{A.31}$$

As noted in Turner et al. (1969), a range of critical Weber numbers obtained from Hinze (1955) varied from 20 to 30. Choosing the higher value of 30, we can write:

$$\overbrace{N_{We,j}^{max}}^{\substack{Hinze\ (1955)\\ Weber\ Number\\ Limit}} = \left(\frac{convective\ inertial\ \ j\ \ force}{interfacial\ \ tension\ \ j,k\ \ force} \right)^{\frac{1}{2}} = \left(\frac{\rho_j \overbrace{\left(v_{j,\infty} \right)^2}^{\text{characterisitc velocity}} \overbrace{\left(\frac{\pi D_p^2}{4} \right)}^{\text{characterisitc area}}}{\underbrace{\pi D_p}_{\text{characterisitc length}} \ \sigma_{k,j}} \right)^{\frac{1}{2}} = \overbrace{\left(\frac{30}{4} \right)^{\frac{1}{2}}}^{=(7.5)^{\frac{1}{2}}} \tag{A.32}$$

From, Eqn. A.32 above, it now becomes clear that this criterion simply says that a liquid drop is likely to shatter once the convective inertial forces of the vapor phase-j exceeds the interfacial tension force between the vapor phase-j and liquid phase-k by about a factor of 8. This is therefore a suspected condition at which a liquid particle can retain its maximum spherical size. When Eqn. A.32 is put into Eqn. A.31 for a vertical flow scenario, we get:

$$v_{k,T} = \overbrace{\left(\frac{4g}{3} \right)^{\frac{1}{4}} \left(\frac{30}{C_{D,j\to k}} \right)^{\frac{1}{4}} \left(\frac{\sigma_{k,j}(\Delta\rho)}{\rho_j^2} \right)^{\frac{1}{4}}}^{=1.902 \left(\frac{m}{s^2} \right)^{\frac{1}{4}}} \frac{m}{s} \tag{A.33}$$

If the total drag coefficient is now assumed to be constant at 0.44, thus fitting within the "Newton's law" range for particle Reynolds number, then Eqn. A.30 will be recovered. Clift et al. (1978) discusses the validity of this value of total drag coefficient and draws attention to its proper interpretation in terms of the dominance of form drag rather than turbulence – in their words – "An alternative label for this range, the 'turbulent flow'

range, is inaccurate and misleading". Nevertheless, the interpretation of this value of total drag coefficient in terms of turbulence appears to be common in the literature (e.g. Nosseir et al. 2000, Nallaparaju, 2012).

Now, an alternative approach to that of the droplet example above can be advanced if the approach of example 4 is taken instead. This means that instead of fixing $C_{D,j\to k}$ at a constant value (e.g. 0.44 or 0.2), $C_{D,j\to k}$ can be directly related to an Eotvos number for the liquid droplet particle, thereby utilizing the vast amount of data correlated in the past that can be used to determine this relationship. As before, a linear relation between the total drag coefficient and the Eotvos number for this scenario can then be stated as:

$$C_{D,j\to k} = \overbrace{\lambda}^{\substack{empirical\\ constant}} N_{Eo,k} = \lambda \left(\frac{\overbrace{\left(\frac{\pi D_p^3}{6}\right)}^{characteristic\ volume} (\Delta\rho) g \overbrace{\cos\theta}^{\substack{=1\ only\ for\\ vertical\ flow}}}{\underbrace{\pi D_p}_{characteristic\ length} \sigma_{k,j}} \right)^{\frac{1}{2}} \qquad \text{(A.34)}$$

If a value of $\lambda = 0.34$ is used in eqns. A.33 and A.30, then the Turner et al. (1960) expression in Eqn. A.30 is recovered. Quite interestingly, Clift et al., 1978 ("Eqn. 7-13" on pg. 179 of this reference) found that for a droplet Eotvos number ≥ 5, a value of $\lambda = 0.33$ in Eqn. A.33 (with their definition for droplet Eotvos number) represented an upper limit of all of the larger-droplet terminal velocity data of Gunn and Kinzer, 1949, van der Leeden et al., 1956, Finlay, 1957 and Beard and Pruppacher, 1969, independent of the droplet size and vapor viscosity. This value was later substantiated by van Baten et al. (2003) in their CFD modeling work on airlift reactors. Thus, we see that though it may initially appear to some investigators that the Hinze (1955) Weber number limit of 30 is inconsistent with the large droplet database quoted above, these correlations must be

viewed in proper context via appropriate choices for the various definitions of dimensionless force ratios. In particular, the choices for the characteristic variables matter. In this way, a better qualitative understanding of their interrelationships and inter-consistencies (or lack thereof) can be obtained.

Before leaving this last example, we point out a few important observations related to the Turner et al. (1969) correlation in Eqn. A.30:

I. The original paper contains a correct derivation and "Eqn. 4" in the reference is exactly Eqn. A.30 (with $C_{D,j\to k}$ = 0.44) with the units of interfacial tension already in the desired field units for interfacial tension, i.e. in dynes/cm. However, the interfacial tension in "Eqn. 5" in the reference, which was the main result of the paper, was erroneously noted as being in dynes/cm. Interestingly, if the interfacial tension of "Eqn. 4" is in dynes/cm and the interfacial tension in "Eqn. 5" is in lbf/ft, then both equations are equivalent and either of them will correctly lead to the field-units coefficient of 1.593 in Eqn. A.30 above.

II. In the Turner et al. (1969) paper, as well as in several subsequent papers (e.g., Coleman, 1991, Veeken et al., 2010), uncontrolled, in-operation field data has been used in comparison with the respective theories. As noted in Turner et al. (1969), incomplete field information such liquid density or vapor gravity (to name a few) requires that estimates be provided for the missing data. Obviously, this presents the condition that any comparison with these field data can mask several compensating inadequacies in the theory. Therefore, changing or modifying the coefficient in Eqn. A.30, in any way, to fit these field data is an exercise in curve fitting and has no scientific relevance or meaning.

III. As seen in Eqn. A.30, vapor density features prominently and significantly affects calculations of the terminal droplet velocity. As vapor density is a strong function of pressure, the terminal droplet velocity is itself a function of the multiphase pipe flow total pressure gradient model used to determine the pressure profile in the wellbore. Thus, every variable or parameter that affects the flowing total pressure gradient also affects this critical velocity.

IV. Contrary to rigid particles, whether spherical or not, fluid particles have a mobile interface. Thus the tangential shear stress exerted by the continuous phase on the interfacial surface of the dispersed phase (or phases) will lead to internal circulation patterns, assuming the interfacial motions are not hindered by contaminants. In this case, interfacial movements will reduce the total drag and thus increase the dispersed phase velocity as compared to a rigid particle (Abdel-Alim and Hamielec, 1975). Thus it can be expected that a rigid particle formulation that is intended to represent a fluid particle system will lead to an under-prediction in the critical velocity required to suspend the fluid particle. This is one explanation *why* it is often found that the Turner et al. (1969) velocity predicted by Eqn. A.30 will require some kind of upward adjustment when compared against data.

In summary, with the simple examples above, we show how useful it is to have a consistent set of generalized dimensionless ratios. We provide such a set of ratios below for averaged (1D) multiphase pipe flow. Note that there can be several extensions or variations to these definitions and only one set of averaged flow definitions are provided below with the chosen characteristic velocities, areas, lengths and volumes highlighted.

As an example of an extension, in averaged (2D) multiphase flows, there can be lateral inertial forces in addition to convective (axial) inertial forces.

A.6.6 Dimensionless Momentum Rate (Force) Ratios

$$\overbrace{N_{Re,j}}^{\text{phase-j Reynolds Number}} = \left(\frac{\textit{convective inertial } j \textit{ force}}{\textit{molecular (viscous) } j \textit{ force}} \right)^{\frac{1}{2}}$$

$$= \left(\frac{\rho_j \left\langle \left\langle v_j \right\rangle \right\rangle^2 \overbrace{D_H^2}^{\textit{characteristic area}}}{\frac{\mu_j^{\,2}}{\rho_j}} \right)^{\frac{1}{2}} = \left[\left(\frac{\overbrace{\left\langle \left\langle v_j \right\rangle \right\rangle}^{\textit{characteric velocity}} \overbrace{D_H}^{\textit{characteristic length}}}{\overbrace{\left(\frac{\mu_j}{\rho_j} \right)}^{\textit{characteristic kinematic viscosity}}} \right)^2 \right]^{\frac{1}{2}} = \frac{\rho_j \left\langle \left\langle v_j \right\rangle \right\rangle D_H}{\mu_j} \tag{A.35}$$

$$\overbrace{N_{We,j}}^{\text{phase-j Weber Number}} = \left(\frac{\textit{convective inertial } j \textit{ force}}{\textit{interfacial tension } j,k \neq j \textit{ force}} \right)^{\frac{1}{2}} = \left(\frac{\rho_j \left\langle \left\langle v_j \right\rangle \right\rangle^2 D_H^2}{D_H \sigma_{j,k \neq j}} \right)^{\frac{1}{2}} = \frac{\left\langle \left\langle v_j \right\rangle \right\rangle}{\left(\frac{\sigma_{j,k \neq j}}{\rho_j \overbrace{D_H}^{\textit{characterisitc length}}} \right)^{\frac{1}{2}}} \tag{A.36}$$

$$\overbrace{N_{We,mix}}^{\text{mixture Weber Number}} = \left(\frac{\textit{convective inertial mix force}}{\textit{interfacial tension 2,1 force}} \right)^{\frac{1}{2}} = \left(\frac{\rho_1 \left\langle u_{mix} \right\rangle^2 D_H^2}{D_H \sigma_{2,1}} \right)^{\frac{1}{2}} = \frac{\left\langle u_{mix} \right\rangle}{\left(\frac{\sigma_{2,1}}{\rho_1 D_H} \right)^{\frac{1}{2}}} \tag{A.37}$$

$$\overbrace{N_{Fr,j}^{axial}}^{\text{phase-j axial Froude Number}} = \left(\frac{\textit{convective inertial } j \textit{ force}}{\textit{axial buoyancy } j,k \neq j \textit{ force}} \right)^{\frac{1}{2}} = \left(\frac{\rho_j \left\langle \left\langle v_j \right\rangle \right\rangle^2 \overbrace{D_H^2}^{\textit{characteristic area}}}{\overbrace{D_H^3}^{\textit{characteristic volume}} \left(\Delta\rho \right) g \cos\theta} \right)^{\frac{1}{2}}$$

$$= \frac{\left\langle \left\langle v_j \right\rangle \right\rangle}{\left(\overbrace{D_H}^{\textit{characterisitc length}} \left(\frac{\Delta\rho}{\rho_j} \right) g \cos\theta \right)^{\frac{1}{2}}} \tag{A.38}$$

$$\overbrace{N_{Fr,j}^{lateral}}^{\substack{\text{phase-j}\\ \text{lateral Froude Number}}} = \left(\frac{convective\ inertial\ \ j\ \ force}{lateral\ \ buoyancy\ \ j,k \neq j\ \ force} \right)^{\frac{1}{2}}$$

$$= \left(\frac{\rho_j \left\langle \left\langle v_j \right\rangle \right\rangle^2 D_H^2}{D_H^3 \left(\Delta\rho \right) g \sin\theta} \right)^{\frac{1}{2}} = \frac{\left\langle \left\langle v_j \right\rangle \right\rangle}{\left(\overbrace{D_H}^{\substack{characterisitc\ length}} \left(\frac{\Delta\rho}{\rho_j} \right) g \sin\theta \right)^{\frac{1}{2}}} \tag{A.39}$$

$$\overbrace{N_{Fr,mix}^{axial}}^{\substack{\text{mixture}\\ \text{axial Froude Number}}} = \left(\frac{convective\ inertial\ \ mixture\ \ force}{axial\ \ buoyancy\ \ mix,1\ \ force} \right)^{\frac{1}{2}}$$

$$= \left(\frac{\rho_1 \left\langle u_{mix} \right\rangle^2 D_H^2}{D_H^3 \left(\Delta\rho \right) g \cos\theta} \right)^{\frac{1}{2}} = \frac{\left\langle u_{mix} \right\rangle}{\left(D_H \left(\frac{\Delta\rho}{\rho_1} \right) g \cos\theta \right)^{\frac{1}{2}}} \tag{A.40}$$

$$\overbrace{N_{Fr,mix}^{lateral}}^{\substack{\text{mixture}\\ \text{lateral Froude Number}}} = \left(\frac{convective\ inertial\ \ mixture\ \ force}{lateral\ \ buoyancy\ \ mix,1\ \ force} \right)^{\frac{1}{2}}$$

$$= \left(\frac{\rho_1 \left\langle u_{mix} \right\rangle^2 D_H^2}{D_H^3 \left(\Delta\rho \right) g \sin\theta} \right)^{\frac{1}{2}} = \frac{\left\langle u_{mix} \right\rangle}{\left(D_H \left(\frac{\Delta\rho}{\rho_1} \right) g \sin\theta \right)^{\frac{1}{2}}} \tag{A.41}$$

A.6.7 Dimensionless Momentum Flux Ratios

$$\overbrace{N_{Re,j}}^{\substack{\text{phase-j}\\ \text{Reynolds Number}}} = \left(\frac{convective\ inertial\ \ j-momentum\ \ flux}{molecular\ \ (viscous)\ \ j-momentum\ \ flux} \right)^{\frac{1}{2}} = \left(\frac{\rho_j \left\langle \left\langle v_j \right\rangle \right\rangle^2}{\frac{\mu_j^{\ 2}}{\rho_j D_H^2}} \right)^{\frac{1}{2}} = \frac{\rho_j \left\langle \left\langle v_j \right\rangle \right\rangle D_H}{\mu_j} \tag{A.42}$$

$$\overbrace{\frac{f_{j\to wall}}{2}}^{\substack{\text{phase-j}\\ \text{Fanning friction factor}}} = \frac{j-to-wall\ \ j-momentum\ \ flux}{convective\ inertial\ \ j-momentum\ \ flux} = \frac{\tau_{j\to wall}}{\left|\left\langle\left\langle v_j\right\rangle\right\rangle\right|\left(\rho_j\left\langle\left\langle v_j\right\rangle\right\rangle - \rho_j \overbrace{v_{wall}}^{=0}\right)} \tag{A.43a}$$

$$\overbrace{\frac{C_{D,j\to k(\neq j)}}{2}}^{\substack{\text{phase-j}\\ \text{total drag coefficient}}} = \frac{j-to-k\ \ j-momentum\ \ flux}{convective\ inertial\ \ j-momentum\ \ flux} = \frac{\tau_{j\to k(\neq j)}}{\left|\left\langle\left\langle v_j\right\rangle\right\rangle\right|\left(\rho_j\left\langle\left\langle v_j\right\rangle\right\rangle - \rho_j \overbrace{v_k}^{=0}\right)} \tag{A.43b}$$

$$\begin{aligned}
\overbrace{N_{Fa\text{-}Re,j\to wall}}^{\substack{\text{phase-j}\\ \text{Fanning-Reynolds No.}}} &= \left(\frac{j-to-wall\ \ j-mom.\ \ flux}{convective\ inertial\ \ j-mom.\ \ flux}\right)\left(\frac{convective\ inertial\ \ j-mom.\ \ flux}{molecular\ (viscous)\ \ j-mom.\ \ flux}\right)^{\frac{1}{2}} \\
&= \frac{j-to-wall\ \ j-mom.\ \ flux}{\left(convective\ inertial\ \ j-mom.\ \ flux\right)^{\frac{1}{2}}\left(molecular\ (viscous)\ \ j-mom.\ \ flux\right)^{\frac{1}{2}}} \\
&= \frac{\tau_{j\to wall}}{\left(\rho_j\left\langle\left\langle v_j\right\rangle\right\rangle^2\right)^{\frac{1}{2}}\left(\frac{\mu_j^{\,2}}{\rho_j D_H^2}\right)^{\frac{1}{2}}} = \frac{\left(\frac{f_{j\to wall}}{2}\right)\rho_j\left\langle\left\langle v_j\right\rangle\right\rangle^2}{\left(\cancel{\rho_j}\left\langle\left\langle v_j\right\rangle\right\rangle^2\right)^{\frac{1}{2}}\left(\frac{\mu_j^{\,2}}{\cancel{\rho_j} D_H^2}\right)^{\frac{1}{2}}} \\
&= \left(\frac{f_{j\to wall}}{2}\right)\frac{\rho_j\left\langle\left\langle v_j\right\rangle\right\rangle D_H}{\mu_j} = \left(\frac{f_{j\to wall}}{2}\right)N_{Re,j}
\end{aligned} \tag{A.44}$$

A.6.8 Dimensionless Heat Flux Ratios

$$\overbrace{N_{Nu,wall\to j}}^{\substack{\text{phase-j}\\ \text{Nusselt Number}}} = \frac{wall-to-j\ \ j-heat\ \ flux}{molecular\ \ j-heat\ \ flux} = \frac{q_{wall\to j}}{q_{cond,j}} = \frac{+\left(\dfrac{h_{wall\to j}}{\cancel{\rho_j}\cancel{\hat{e}_{p,j}}}\right)\cancel{\Delta\left(\rho_j \hat{e}_{p,j} T_j\right)}}{+\left(\dfrac{k_j}{\cancel{\rho_j}\cancel{\hat{e}_{p,j}}}\right)\left(\dfrac{\cancel{\Delta\left(\rho_j \hat{e}_{p,j} T_j\right)}}{\overbrace{D_H}^{characteristic\ length}}\right)}$$

$$= \frac{h_{wall\to j} D_H}{k_j} = \underbrace{\left(\frac{h_{wall\to j}}{\dfrac{\cancel{\rho_j}\cancel{\hat{e}_{p,j}}}{\cancel{\langle\langle v_j \rangle\rangle}}}\right)}_{=N_{St,wall\to j}} \cdot \underbrace{\left(\frac{\dfrac{\cancel{\mu_j}}{\cancel{\rho_j}}}{\dfrac{k_j}{\cancel{\rho_j}\cancel{\hat{e}_{p,j}}}}\right)}_{=N_{Pr,j}} \cdot \underbrace{\left(\frac{\cancel{\rho_j}\cancel{\langle\langle v_j \rangle\rangle} D_H}{\cancel{\mu_j}}\right)}_{=N_{Re,j}} \tag{A.45}$$

A.7 COMPONENTS, PHASES AND PARTICLES

A.7.1 Components

In multiphase flows, *components* (or chemical species) flow as one or more phases. There can be one component/substance (e.g. methane) or several components that can exist as a particular phase. Common terms such as gas, oil or water actually refers to the gas, oil or water *pseudo-component*, i.e. they are made up of several components. In general, the gas, oil or water *pseudo-components* do not refer to the gaseous, oleic or aqueous phases, respectively. It is only in the special case where there is a different phase per *pseudo-component*, can these terms be used interchangeably. The components-mass concentration of a phase is the mass density (or simply, *density*) of that phase. The components-mole concentration of a phase is the *molar density* of that phase.

A.7.2 Phases

A.7.2.1 Thermodynamic Definition

A *phase* is a definition of the state of agglomeration of matter, which can be broadly (though not easily) defined as being solid-like or liquid-like, based on lattice-type or semi-lattice-type aggregation of component units or molecules; or gaseous-like, based on freely moving component molecules. It is the state of agglomeration of component units or molecules that we visually observe and record as a phase, and as such, the *mass of a phase* actually refers to the mass of all of the components existing as that phase.

The degree to which component units or molecules interact, which is related to their net available *free energy* (say, Gibbs free energy for pressure-temperature systems), determines the definition of the phase they will exist as. For example, if the net available Gibbs *free energy* changes, then it can be entirely possible for component units or molecules previously existing as phase-k will now exist as phase-j – this is what it meant when the *mass of a phase* changes. This is why there are different phase properties, such as component compositions, densities and viscosities, at different system pressures and temperatures.

When the net Gibbs *free energy* of all of the component units or molecules in a multiphase system is at its lowest stable value, the phases in the system is in a state of stable *phase* equilibrium. *Phase* equilibrium includes *mechanical* equilibrium (equality of pressures), *thermal* equilibrium (equality of temperatures) and *chemical potential* equilibrium (equality of fugacities), and is unrelated to *hydraulic* equilibrium or *hydrodynamic* equilibrium (Hewitt and Pulling, 1969). For example, *hydraulic* equilibrium refers to zero relative averaged in-situ phase velocities between flowing phases (or in the language of multiphase pipe flow investigators, no global slip between

the phases). *Phase* equilibrium is also separately defined in comparison to *chemical reaction* equilibrium.

A.7.2.2 Mathematical Definition

From a mathematical standpoint, a phase is defined in reference to the scale of mathematical analysis. If a phase is defined as a *locally continuous* region of matter (fictitious or not), as is normally done in microscopic analyses, then partial differential conservation and non-conservation equations may be used to represent transport relationships. If, however, a phase is defined as a *locally discontinuous* region of matter, as is evident in macro-scale analyses and equipment, then integral, flow-field-averaged balance equations may be used to represent transport relationships.

A.7.2.2 Flow Fields Definition

Other than the thermodynamic and mathematical points of view described above, some multiphase flow investigators can have their own definitions of approximations of phase-like behavior such as fields of bodies in the flow – as examples – liquid droplet in vapor field, liquid film field, vapor core field, vapor pocket in slug field, vapor bubbles in liquid field, and so on. These flow field bodies constitute the so-called "multi-field" flow models. A brief review of multi-field flow models can be found in Bonnizi et al. (2009).

In general, these fields of bodies replace the roles of actual phases in 1D, 2D or 3D multiphase flow conservation equations. This distinction is fundamental and very important. The inherent assumption is that the fields act just as components, in that there can be multiple fields simultaneously co-existing as an actual vapor, liquid or solid phase (e.g., Lahey, Jr. and Drew, 2001). This assumption naturally leads to several questions. For example, phase disappearance is well understood in both thermodynamic and transport analyses, however, if an annular liquid film is now a "phase", then in vapor-

liquid bubbly flow where there is no well-defined liquid film, does this mean that this phase disappears? And if so, how does one accommodate for the transition from the disappearance of the annular flow to the appearance of the bubbly flow? Indeed, we may reasonably ask a host of related questions:

I. What is a "gas pocket in slug" momentum conservation equation? Does the velocity of the gas in the pocket change with the size of the pocket? What principle determines the size of the pocket?

II. Do actual components exchange mass among the fields or among the phases? What, then, is a compositional model in a multi-field sense?

III. For a multi-field two-fluid case, what transition mechanisms are responsible for the rate of appearance or disappearance of the multiple fields? Are these mechanisms the same as those used for vapor-liquid or liquid-liquid inter-phase transfers in the existing literature? And if so, then what is the basis for specifying more fields than phases?

In light of these simple questions above, it would therefore seem that a much more appropriate definition of "multi-field" models is "multi-flow-pattern" models in which there are different mass, momentum and energy "conservation" equations for different flow patterns. Since (in general) the number of possible flow patterns in a multiphase flow is infinite, there is similarly no rational limit to the number of fields in a multi-field model. This fact takes concrete form in the ever increasing number of "conservation" equations of these multi-field models in some competing multiphase flow commercial codes – as examples – the 3-mass/3-momentum fields in TUFFP, 5-mass/3-momentum fields in OLGA, the 9-mass/3-momentum fields in LEDA, the 6-mass/5-momentum/1-pressure fields in MAST. Note that the "3-momentum" equations in these

models do not refer to three actual phases, but rather, in the case of OLGA, refers to the "gas and liquid droplets", "hydrocarbon film" and "water film" fields; in the case of TUFFP, refers to the "gas pocket in slug", "oil and water in film zone" and "oil and water in the slug body fields; in the case of LEDA, refers to the "gas bulk + oil and water droplets", "oil bulk + gas bubbles and water droplets" and "water bulk + gas bubbles and oil droplets" fields (Shippen and Bailey, 2012).

Similar to the flow pattern issue highlighted at the end of Section E.2 in Appendix E, multi-field modeling is a never-ending approach. It is incorrect to perceive such models as somehow advancing fundamental science-oriented understanding. Obviously, the more "conservation" equations of these ad-hoc chosen descriptions there are, the more empirical closures will be required (i.e., more flexibility for tuning models to data), which leads to unverifiable theory – the opposite of science-based prediction.

A.7.3 Particles

Specific to multiphase pipe flow, phases can be classified as being *continuous* or *dominant* if they occupy continuously connected regions of space in the pipe, or *dispersed* or *passive* if they are dispersed within a continuous phase. Dispersed phases can sometimes exist as *particles*, which can either mean solid-phase particles (e.g., sand grains) or fluid-phase particles (e.g., bubbles of a vapor-phase or droplets/globules of a liquid-phase). Clift et al. (1978) provides an apt description of how multiphase flow investigators define particles, as distinguished from the way a nuclear physicist, for example, might define them. This reference simply defines a *particle* as "a self contained body with maximum dimension between 0.5 μm and 10 cm, separated from the surrounding medium by a recognizable interface".

Dispersed phase *particles* can be of varying sizes and can coalesce, expand, collapse or disintegrate at any point and at any time during flow. Additionally, during flow, dispersed phase *particles* can exist as symmetric or asymmetric (with respect to the pipe axis) particulate-distributions within a continuous phase. These particulate-distributions can further exhibit different types of pipe cross-sectional profiles, usually described as core-peaking, uniform, intermediate and wall-peaking particulate-distributions.

Appendix B – Basic Multiphase Pipe Flow Equations

B.1 Generalized Descriptions and Foundational Equations

We present in this Section generalized forms of the field equations. These generalized forms (or descriptions) are of foundational import. Let Q be any measurable scalar or vector quantity that may or may not be conserved in a medium. If we now define a bounded region of space (i.e. a geometric volume), V, of a medium, as shown in fig. B.1 below, we can construct a mathematical description of the fluxes through that medium if we now take the position of the Eulerian observer. Recording (i.e. "accounting" for) temporal and spatial changes of the Q-transients inside and Q-fluxes across V's surface, we can say:

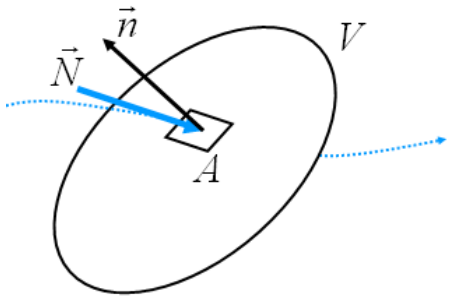

Figure B.1: An arbitrarily-shaped, open representative region V.

$$\overbrace{\frac{d}{dt}\int_V \begin{pmatrix} conc. \\ of\ Q \end{pmatrix} dV}^{\text{"Accumulation" (WITHIN BOUNDARIES OF CV)}} = \overbrace{-\int_A \vec{n} \bullet \overbrace{\begin{pmatrix} \overrightarrow{combined} \\ flux\ of\ Q \end{pmatrix}}^{=\vec{N}} dA}^{\text{"In" - "Out" (ACROSS BOUNDARIES OF CV)}} + \overbrace{\int_V \begin{pmatrix} net\ generation\ of \\ conc.\ of\ Q\ \ from \\ non-\vec{N}\ \ sources \end{pmatrix} dV}^{\text{"Source or Sink" (WITHIN BOUNDARIES OF CV)}} \qquad \text{(B.1)}$$

In fig. B.1 (and Eqn. B.1), V is a representative elemental volume (i.e. a control volume) of a medium, where Q can readily be transported across its surface (i.e. V is considered an open control volume). $\vec{N}$ is the *combined flux* of Q entering V across a surface area dA, and $\vec{n}$ is the outward pointing normal to V at this point of entry. The negative sign above exists because the outward pointing normal acts in an opposite direction to that of the combined flux of Q entering V, as depicted in fig. B.1. Note that this Eulerian approach is applicable to any type of medium.

In the presence of multiple, moving, deformable interfaces between multiple, flowing j-phases in V, V will now be divided into as many sub-regions, V_j, as there are phases, with corresponding bounding sub-region surface areas A_j.

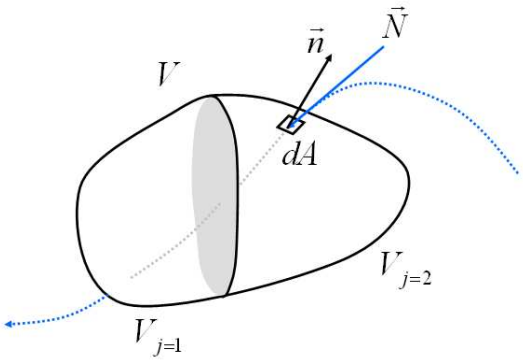

Figure B.2: An arbitrarily-shaped, open representative region V, with sub-regions, V_1 and V_2.

There will thus be j-1 phase interfaces within V. These interfaces can be considered as surfaces of discontinuity (Delhaye, 1974) between flow parameters of the phases, and thus can be treated as infinitely thin membranes, that by virtue of its essentially zero volume, is always at steady state with respect to all the transfer processes across them.

Interfacial sources of quantity-Q are thus negligible in this treatment. An example of this new multiphase scenario for the simple case of $N_p = 2$ is shown in fig. B.2 above.

For multiphase flows in a representative volume described above, we can thus generalize and write the following equation, applicable to the transport of any Q within a volume, V, of any medium, as:

$$\overbrace{\sum_{j=1}^{N_p}\left(\frac{d}{dt}\int_{V_j}\left(\begin{array}{c}conc.\\ of\ Q\end{array}\right)dV\right)}^{\text{"Accumulation" (WITHIN BOUNDARIES OF CV)}} = \overbrace{-\sum_{j=1}^{N_p}\left(\int_{A_j}\vec{n}_j\bullet\left(\overbrace{\overrightarrow{combined}}^{=\vec{N}}\begin{array}{c}\\ flux\ of\ Q\end{array}\right)dA\right)}^{\text{"In" - "Out" (ACROSS BOUNDARIES OF CV)}} \overbrace{+\sum_{j=1}^{N_p}\left(\int_{V_j}\left(\begin{array}{c}net\ generation\\ of\ conc.\ of\ Q\\ from\ non-\vec{N}\\ sources\end{array}\right)dV\right)}^{\text{"Source or Sink" (WITHIN BOUNDARIES OF CV)}} \quad \text{(B.2)}$$

The j-integrals above represent the summation of all possible paths through the respective j-volumes. Examples of "non-N sources of Q-concentration", as shown above, are the net external gravity force in the case of Q = linear momentum, or, the net internal entropy generation in the case of Q = entropy. Also, we note that the only assumption in Eqn. B.2 above is the zero-volume phase interfaces.

Now, a continuum definition of the phases within V makes it mathematically possible for the transformation of phase-j surface area integrals in Eqn. B.2, into phase-j volume integrals. The validity of the continuum definition in single-phase flow is well proven. Thus, if each sub-region V_j bounded by interfaces in multiphase flows is considered a continuum, then the validity of the local instantaneous formulation of the multiphase conservation equations is evident. This continuum hypothesis postulates that fluid phase particles (actually material points within phase-j) in the phase-j flow field are distributed continuously and thus the combined flux of Q across A_j is locally continuous. Mathematically, A_j is piecewise continuous and V_j is any simply connected region consisting of phase-j that is not changing with time. Generalizing Leibnitz rule

(Truesdell and Toupin, 1960) to multiple moving deformable interfaces and applying to the time derivative on the left side of Eqn. B.2, we can arrive at:

$$\sum_{j=1}^{N_p}\left(\frac{d}{dt}\int_{V_j}\begin{pmatrix}conc.\\of\ Q\end{pmatrix}dV\right)=\sum_{j=1}^{N_p}\left(\int_{V_j}\frac{\partial}{\partial t}\begin{pmatrix}conc.\\of\ Q\end{pmatrix}dV\right)-\int_{A_f}\left(\sum_{j=1}^{N_p}\left(\vec{n}_j\bullet\begin{pmatrix}conc.\\of\ Q\end{pmatrix}\vec{v}_f\right)\right)dA \quad \text{(B.3)}$$

In Eqn. B.3 above, $\vec{v}_f$ is the local instantaneous interface-f velocity. Similarly, applying the Gauss-Ostrogradskii Divergence theorem to the surface integral term on the right side of Eqn. B.2, we can arrive at:

$$\begin{aligned}-\sum_{j=1}^{N_p}\left(\int_{A_j}\vec{n}_j\bullet\begin{pmatrix}\overrightarrow{combined}\\flux\ of\ Q\end{pmatrix}dA\right)&=-\sum_{j=1}^{N_p}\left(\int_{V_j}\vec{\nabla}\bullet\begin{pmatrix}\overrightarrow{combined}\\flux\ of\ Q\end{pmatrix}dV\right)\\&\quad-\int_{A_f}\left(\sum_{j=1}^{N_p}\left(\vec{n}_j\bullet\begin{pmatrix}\overrightarrow{combined}\\flux\ of\ Q\end{pmatrix}\right)\right)dA\end{aligned} \quad \text{(B.4)}$$

Eqns. B.3 and B.4 are general transformations for multiple moving deformable interfaces separating multiple phases. To substantively relate these general equations to specific differential pipe flow equations in the prior literature, we simplify our focus by considering only conductive and convective fluxes passing through V in the simple arrangement shown in fig. B.2 (i.e. two sub-regions in V separated by one interface). For this case, when Eqns. B.3 and B.4 are substituted into Eqn. B.2, we get:

$$\begin{aligned}&\sum_{j=1}^{2}\left(\int_{V_j}\left(\frac{\partial}{\partial t}\begin{pmatrix}conc.\\of\ Q\end{pmatrix}+\vec{\nabla}\bullet\overbrace{\begin{pmatrix}\overrightarrow{combined}\\flux\ of\ Q\end{pmatrix}}^{=\vec{N}}-\begin{pmatrix}net\ generation\ of\\conc.\ of\ Q\ from\\external\ sources\end{pmatrix}\right)dV\right)\\&+\int_{A_{f=1}}\left(\overbrace{\sum_{j=1}^{2}\left(\vec{n}_j\bullet\begin{pmatrix}\overrightarrow{conductive}\\flux\ of\ Q\end{pmatrix}+\vec{n}_j\bullet\begin{pmatrix}conc.\\of\ Q\end{pmatrix}\left(\vec{v}_j-\vec{v}_{f=1}\right)\right)}^{net\ generation\ of\ conc.\ of\ Q\ from\ internal\ sources}\right)dA=0\end{aligned} \quad \text{(B.5)}$$

Note that the sources of Q-concentration are now split between "external" and "internal" sources. Eqn. B.5 has to be satisfied for any arbitrary volume or area and thus we can deduce the following local instantaneous field equation for the phases:

$$\frac{\partial}{\partial t}\begin{pmatrix} conc. \\ of\ Q \end{pmatrix} + \vec{\nabla}\bullet\overbrace{\begin{pmatrix} \overrightarrow{combined} \\ flux\ of\ Q \end{pmatrix}}^{=\overline{\overline{N}}} - \begin{pmatrix} net\ generation\ of \\ conc.\ of\ Q\ \ from \\ external\ sources \end{pmatrix} = 0 \qquad \text{(B.6)}$$

And the local instantaneous interface jump condition valid on interface f = 1 as:

$$\overbrace{\vec{n}_j\bullet\begin{pmatrix} \overrightarrow{conductive} \\ flux\ of\ Q \end{pmatrix} + \vec{n}_j\bullet\begin{pmatrix} conc. \\ of\ Q \end{pmatrix}\left(\vec{v}_j - \vec{v}_{f=1}\right)}^{net\ generation\ of\ conc.\ of\ Q\ from\ internal\ sources} = 0 \qquad \text{(B.7)}$$

Equating eqns. B.6 and B.7, we can arrive at <u>the general local instantaneous field equation</u> as:

$$0 = \frac{\partial}{\partial t}\begin{pmatrix} conc. \\ of\ Q \end{pmatrix} + \vec{\nabla}\bullet\overbrace{\begin{pmatrix} \overrightarrow{combined} \\ flux\ of\ Q \end{pmatrix}}^{=\overline{\overline{N}}} - \overbrace{\left(\begin{pmatrix} net\ generation\ of \\ conc.\ of\ Q\ \ from \\ external\ sources \end{pmatrix} + \begin{pmatrix} net\ generation\ of \\ conc.\ of\ Q\ \ from \\ internal\ sources \end{pmatrix}\right)}^{net\ generation\ of\ conc.\ of\ Q\ from\ non-\overline{\overline{N}}\ sources} \qquad \text{(B.8)}$$

Working forms of eqns. B.6 and B.7 for various Q can be found in Ghiaasiaan (2008), Ishii and Hibiki (2006), Boure and Delhaye (1981) among many others. For example, the microscopic single-phase "equation of motion" in BSL, is a subset of Eqn. B.8 for Q = linear momentum, with gravity as the only external force. Indeed, it now becomes clear how single-phase flow is in fact a specialized case of multiphase flow.

Note that other types of forces not previously mentioned can be taken into account in the equations above depending on the scale of analysis or if deemed necessary. For example, the two-dimensional version of the jump condition in Eqn. B.7 can include surface tension terms on the left hand side. In this case mechanical effects due to surface tension gradients such as the Marangoni effect (Sternling and Scriven, 1959; Levich and Krylov 1969) can be included. Indeed, the well-known Young-Laplace law is in fact the

momentum version of Eqn. B.7 with constant (or uniform) surface tension. Examples of the types of terms that may be included on the left side of Eqn. B.7 include:

I. Capillary pressure (Young-Laplace law).

II. Marangoni stress for situations where the interfacial temperature is not constant.

III. Disjoining pressure in applications involving thin film evaporation or condensation.

Next, it is instructive to note that the jump conditions specified in Eqn. B.7 must be supplemented by additional boundary conditions because they cannot provide sufficient matching conditions at the interface to uniquely define a problem. Indeed, as soon interfaces and their associated jump conditions are considered explicitly, new variables enter into the both the classical thermodynamic description of the system as well as the phenomenological laws and other supplementary constitutive equations. As an example, the general tensor form of Newton's law for shear stress will be modified so that the tangential shear stress tensor components will now include phase pressure and components of a deformation tensor.

In principle, the set of equations B.6 and B.7, together with appropriate closure relations (e.g. topological, constitutive or transfer equations), can be solved by *direct numerical simulation* (DNS), or by using any of several discretization methods (e.g. finite-difference, finite-element, etc.) provided that the field and interface boundary conditions are known, and more importantly, that the exact location of the phase interfacial surfaces are known at any time. The attractive feature of DNS for example, is the use of time and spatial steps small enough to capture the smallest important fluctuations over a domain large enough to capture largest important flow features – i.e.

the multi-scale problem in multiphase flows is captured. The kernel drawback, however, is that the whereabouts of the interfaces are not known a priori and in fact has to be found as part of the solution. This makes any numerical solution of the local instantaneous field equations extremely difficult and in many practical problems of interest beyond present computational capability. In order to put into context these difficulties we recall that even in single-phase turbulent flow without any interfaces, it has not been possible in the engineering sciences to obtain exact solutions expressing local instantaneous fluctuations. Single-phase flow is indeed our present ignorance-boundary, difficult though, as this may be to accept.

Summarily, the overwhelming difficulties encountered in the formulation of the local instantaneous field equations stem from (Ishii and Hibiki, 2006):

I. The existence of multiple moving deformable interfaces (i.e. a multi-boundary problem) with their motions being unknown and thus causing complicated coupling between the phase-j field equations and the interface-f jump conditions.

II. The existence of the fluctuations of dependent variables due to both turbulence and to the motions of the phase interfaces.

III. Discontinuities of properties at the phase interfaces.

Since these difficulties exist in almost all multiphase flow systems, direct application of the local instantaneous field formulation to obtain a solution, is severely limited and thus generally not feasible. Furthermore, in actual complex engineering systems such as engineering process plants or the production facilities of oil and gas systems, the microscopic (minor) details of the fluid motions and of other variables are not needed

(i.e. the microscopic details of interfaces between phases need not be defined), but rather, integrative, averaged aspects of the flow are much more important.

B.2 TIME AVERAGING

It is clear from the previous section, that simplified multiphase flow models formulated from performing some type of averaging on the local instantaneous field equations are necessary. In fact, most engineering multiphase pipe flow models, and certainly the majority (if not all) of those in the power, process, and energy engineering industries, are either implicitly or explicitly based on averaged balance equations, resulting from a combination of several averaging operators to the local instantaneous field equations. Also, we used the term "balance" to keep separate the microscopic *field equations* from the macroscopic *balance equations*, just as in BSL.

Other than the application of some form of averaging to obtain usable balance equations, averaging is also used to define mean properties (and fluid motions) that include various kinds of concentration, density, velocity and energy of each phase or of the mixture. These carefully defined mean values then can be used for various experimental purposes and for developments of empirical correlations. The choice of averaging and instrumentations are closely coupled since, in general, measured quantities represent some kinds of mean values themselves. Discussions on the various types of averaging can be found in Delhaye (1969, 1976), Boure and Delhaye (1981), Lahey, Jr. and Drew (1988), Drew and Passman (1999), Monkejord (2005), Ishii and Hibiki (2006), among others. The most common types of averaging are ensemble, time and space (area and volume) averaging. Of note is that ensemble averages are equivalent to time averages if the flow is statistically stationary (i.e., the ergodic hypothesis). In fact, the linkage between the definition of a local instantaneous variable and a typical

experimental measurement of that variable is provided by the ergodic hypothesis (Delhaye, 1968). In effect, this hypothesis states that, for a stationary flow, the average of the simultaneous observations of N experiments is equivalent to the average of N observations in time of an identical experiment (Yadigaroglu and Lahey Jr., 1976). The extensive study by Vernier and Delhaye (1968) is a good reference for further information about the equivalence of Eulerian time-averaged field equations to those obtained from Eulerian ensemble (statistical) averaging, under stationary flow condition. A good description of the specific differences between time averages and ensemble averages can be found in Section 4.1 of Carruyo (2005).

In the context of this research, by averaging, we obtain the mean values of properties and fluid motions that effectively eliminate local instantaneous fluctuations – in this sense, averaging is seen as equivalent to a low-pass filtering to eliminate high-frequency fluctuations (Prosperetti and Trygvasson, 2007). Though fluctuation details are lost (i.e., the inherent fluctuation of multiphase flow), in return we get simplified and tractable macro-scale balance equations. It is important to note however, that the statistical properties of the turbulent and interface fluctuations on the macro-scale balance equations, is accounted for by using appropriate closure relations. Drew (1983) provides an insightful analysis of the advantages and disadvantages of averaging and brings to attention the "postulation approach" that does not require a detailed consideration of averaging in order to arrive at a solution.

Following from our previously adopted Eulerian approach, we now consider Eulerian time averaging. Eulerian time averaging has been widely applied in analyzing a single-phase turbulent flow as shown in BSL, and is also used for multiphase phase flow. The use of time-averaged local instantaneous variables in multiphase flow first appeared in Frankl (1953) and was first proposed for the case of two-phase flow by Teletov (1958)

and then considered again by Vernier and Delhaye (1968). Since the most useful information in analyzing industrial flow systems is the time mean values rather than the local instant responses of the flow, its use both in experimental and analytical purposes is indispensable in turbulent flow studies. For example, mean velocity, pressure, temperature, heat transfer coefficient and friction factor are the important mean values routinely required in standard problems.

Furthermore, commonly used experimental methods and measurements are well suited for the application of the time average. It has been shown that time-averaging is particularly useful for turbulent multiphase flows (Hinze, 1959; Ishii, 1975). In these flows (which, incidentally, are the most prevalent industrial-type flows), since the transport processes are highly dependent on the local fluctuations of variables about the mean, the required constitutive equations of the conservation equations are best obtainable for a time-averaged model from experimental data. This is supported by the standard single-phase turbulent flow analysis.

In the context of turbulent flow terminology, time-averaged variables means that these variable are not affected by turbulent eddies of quantity-Q transport, which cancel themselves out in a time interval, T, where T is large enough to smooth out the local fluctuations of phase properties and turbulence yet very small compared to the macro-scale flow fluctuations, for example, changes in the flow-field pressure gradient (Delhaye and Achard, 1976).

To perform the time-averaging of the multiphase local instantaneous field equations in the previous section, we assume a fixed time-interval, T, described above and given by $[t - T/2; t + T/2]$. This assumption is identical to that made in analyzing turbulent single-phase flow. In the various flow patterns in multiphase pipe flow, phase properties suffer discontinuous changes at the phase interfaces since these interfaces are

considered as singular volume-less surfaces. Thus, if we consider a given point in the multiphase flow (i.e., a given point in V of Fig. B.2), then phase-j will pass this point intermittently. If we utilize the *phase function* definition of Drew (1983), then we can write:

$$\overbrace{X_j(\vec{x},t)}^{phase\ \ function} = \begin{cases} 1 & if\ \vec{x}\ is\ in\ \ j\ at\ time\ t \\ 0 & otherwise \end{cases} \tag{B.9a}$$

As can be seen in Eqn. B.9a, the phase-j (indicator) functions are advected by phase-j. If we now define T_j to be the cumulative residence time of phase-j passing this point in the interval T, then the local relative residence time (or local volume fraction) of phase-j at that point in V over the time interval T, is then given as:

$$s_j = \frac{T_j}{T} = \frac{1}{T}\left(\int_{|T|} X_j(\vec{x},t)\ dt \right) \tag{B.9b}$$

The mathematical (and physical) relevance of Eqn. B.9b is that the time- (or ensemble-) averaged quantity s_j will now appear with the terms in eqns. B.6 to B.8 as a result of the averaging process because phases are now competing for the same location at the same time in the flow field. Rather involved mathematical details of several postulated rules and transforms governing this procedure of time-averaging the local instantaneous field equations can be found in Drew (1983) and Drew and Wood (1985). Finally, we are now in the position to write specific time-averaged versions of Eqn. B.8 for any type of quantity, Q.

B.2.1 Total Mass Conservation Field Equations

For Q = *component-i mass in phase-j* flowing in a stationary porous solid medium (neglecting mass exchanges between flowing phases and any solid phases which may be present), we can write:

$$\frac{\partial}{\partial t}\left(\overbrace{\left(\phi s_j\right)\rho_j \underbrace{\left(\omega_{ij}\right)}_{=\frac{i-mass\ in\ j}{total\ i-mass\ in\ j}}}^{\text{conc. of i-mass in j, } \rho_{ij}}\right) = -\vec{\nabla}\bullet\left(\overbrace{-\vec{\vec{K}}_{ij}\bullet\vec{\nabla}\left(\left(\phi s_j\right)\rho_j\omega_{ij}\right)}^{\text{conductive flux of i-mass in j}} \overbrace{+\rho_j\omega_{ij}\underbrace{\left(\phi s_j\right)\vec{v}_j}_{\substack{\text{"Darcy"}\\ \text{volume}\\ \text{flux}=\vec{u}_j}}}^{\text{convective flux of i-mass in j}}\right) \tag{B.12}$$

$$\overbrace{+\left(\phi s_j\right)R_{ij}}^{\substack{\text{net generation of conc. of}\\ \text{i-mass in j from}\\ \text{external sources}}} \quad \overbrace{+R_{m,ij}}^{\substack{\text{net generation of conc. of}\\ \text{i-mass in j from}\\ \text{internal sources}}} \quad [=]\frac{i-mass\ in\ j}{L^3\ of\ V-t}$$

Also, it is evident that the total quantity-Q concentration is the sum of the individual j-phase quantity-Q concentrations (on per unit time basis), and thus for the case above, we may now write for Q = *total i-mass over all j-phases* flowing in stationary porous solid media (neglecting mass exchange between flowing fluid phases and any solid phases which may be present) as:

$$\frac{\partial}{\partial t}\left(\overbrace{\sum_{j=1}^{N_p}\left(\left(\phi s_j\right)\rho_j\omega_{ij}\right)}^{\text{conc. of total i-mass, } \rho_{i,total}}\right) = -\vec{\nabla}\bullet\left(\overbrace{\sum_{j=1}^{N_p}\left(-\vec{\vec{K}}_{ij}\bullet\vec{\nabla}\left(\left(\phi s_j\right)\rho_j\omega_{ij}\right)\right)}^{\text{conductive flux of total i-mass}} \overbrace{+\sum_{j=1}^{N_p}\left(\rho_j\omega_{ij}\left(\phi s_j\right)\vec{v}_j\right)}^{\text{convective flux of total i-mass}}\right) \tag{B.13}$$

$$\overbrace{+\sum_{j=1}^{N_p}\left(\left(\phi s_j\right)R_{ij}\right)}^{\substack{\text{net generation of conc.}\\ \text{of total i-mass from}\\ \text{external sources}}} \quad \overbrace{+\sum_{j=1}^{N_p}\left(R_{m,ij}\right)}^{\substack{\text{net generation of conc.}\\ \text{of total i-mass from}\\ \text{internal sources}}} \quad [=]\frac{total\ i-mass\ in\ all-j}{L^3\ of\ V-t}$$

Eqn. B.13 above is also referred as the *overall compositional equation* or overall component mass conservation equation in the petroleum engineering literature (Lake, 1989). Note that even though there is mass transfer occurring across flowing phase (or field) interfaces, the inability of phase interfaces to accumulate mass, i.e. the volume-less interface assumption, causes the last term in Eqn. B.13 to be zero. In other words, interface mass transfer is taken into account implicitly.

Similarly, if Q = *component-i mass in phase-j* flowing in a stationary solid pipe (neglecting mass exchanges between flowing phases and the pipe solid material), we can write:

$$\frac{\partial}{\partial t}\left(\overbrace{s_j\rho_j\omega_{ij}}^{\text{conc. of i-mass in j, } \rho_{ij}}\right) = -\vec{\nabla}\bullet\left(\overbrace{-\vec{\vec{K}}_{ij}\bullet\vec{\nabla}\left(s_j\rho_j\omega_{ij}\right)}^{\text{conductive flux of i-mass in j}} \overbrace{+\rho_j\omega_{ij}\underbrace{s_j\vec{v}_j}_{=\vec{u}_j}}^{\text{convective flux of i-mass in j}}\right) \overbrace{+s_jR_{ij}}^{\substack{\text{net generation of conc. of i-mass in j from external sources}}} \overbrace{+R_{m,ij}}^{\substack{\text{net generation of conc. of i-mass in j from internal sources}}} \quad [=]\frac{i-mass\ in\ j}{L^3\ of\ V-t} \tag{B.14}$$

As is usual for most pipe flow applications, if we neglect molecular-scale conductive mass fluxes in favor of more dominant convective mass fluxes, for Q = *total i-mass over all j-phases* flowing in a stationary solid pipe (neglecting mass exchanges between flowing phases and the pipe solid material), we can write:

$$\frac{\partial}{\partial t}\left(\overbrace{\sum_{j=1}^{N_p}\left(s_j\rho_j\omega_{ij}\right)}^{\text{conc. of total i-mass, } \rho_{i,total}}\right) = -\vec{\nabla}\bullet\left(\overbrace{\sum_{j=1}^{N_p}\left(\rho_j\omega_{ij}s_j\vec{v}_j\right)}^{\text{convective flux of total i-mass}}\right) \overbrace{+\sum_{j=1}^{N_p}\left(s_jR_{ij}\right)}^{\substack{\text{net generation of conc. of total i-mass from external sources}}} \overbrace{+\cancel{\sum_{j=1}^{N_p}\left(R_{m,ij}\right)}}^{\substack{\text{net generation of conc. of total i-mass from internal sources}}} \tag{B.15}$$

$$[=]\frac{total\ i-mass\ in\ all-j}{L^3\ of\ V-t}$$

As above, interfacial (or inter-field) mass transfer is taken into account implicitly, and thus the last term in Eqn. B.15 is zero. The details that are lost because of this implicit treatment of the interfacial transport processes can be partially restored by invoking the local equilibrium assumption that provides algebraic relations between component mass concentrations in the phases (Lake, 1989). It should be noted that the component mass conservation equations for pipe flow and for flow in a porous medium are of identical form.

One must be very cautious with respect to the "mass conservation equations" in which *phase-j mass over all components* is given as the quantity that is conserved. Only the *total component-i mass over all flowing phases* as shown in Eqn. B.15 above is conserved. In general, the mass of all components in a flowing phase is not a conserved quantity. It is only in the special cases of one component in one phase (e.g. two-component two-phase flow, three-component three-phase flow, etc.) with no interfacial mass transfer that this is allowable – in these cases the mass of a phase really means the mass of the single component (or pseudo-component) existing as that phase. Since the very nature of compositional multiphase flow models is that there are many components in each phase, then <u>any compositional multiphase pipe flow model adopting this phase-j mass conservation approach is fundamentally flawed</u>.

To determine whether a compositional multiphase flow model contains this flawed phase-j mass conservation approach, one may find empirical "interfacial mass generation" terms present in the phase-j mass equations of the model. In this case, the phase-j mass equations are arrived at by summing Eqn. B.14 over all components, yielding:

$$\frac{\partial}{\partial t}\left(\overbrace{s_j\rho_j\underbrace{\sum_{i=1}^{N_c}\left(\omega_{ij}\right)}_{=1}}^{\text{conc. of total j-mass } =\rho_{j,total}}\right)=-\vec{\nabla}\bullet\left(\overbrace{\rho_j\underbrace{s_j\vec{v}_j}_{=\vec{u}_j}\underbrace{\sum_{i=1}^{N_c}\left(\omega_{ij}\right)}_{=1}}^{\text{convective flux of total j-mass}}\right)+\overbrace{\sum_{i=1}^{N_c}\left(s_jR_{ij}\right)}^{\text{net generation of conc. of total j-mass from external sources}}+\overbrace{\sum_{i=1}^{N_c}\left(R_{m,ij}\right)}^{\text{net generation of conc. of total j-mass from internal sources}}\quad\left[=\right]\frac{total\ \ j\text{-}mass\ in\ all\text{-}i}{L^3\ of\ V-t} \tag{B.16}$$

Note that the last term in Eqn. B.16 above is <u>not zero</u> in this approach, and needs to be defined using mechanistic or empirical relations for each of the various prevailing

multiphase pipe flow patterns. This term, commonly present as evaporation or condensation in single-component flows, is usually referred to in the literature as the *interfacial mass generation rate*. In general, interfacial exchanges including this interfacial mass generation rate cannot be measured and must generally be inferred from secondary observations. Thus the various assumptions made in developing the models for this term cannot be verified independently and only a global assessment (as explained in Boure, 1987) of the models is possible, in which case such assessments can hide several compensating inadequacies. Historically, the interfacial mass generation rate has been tied to the problem of prediction of thermal non-equilibrium and interfacial areas (Yadigaroglu and Bensalem, 1987).

As an illustration of how Eqn. B.16 has been used in the past, we consider the case of a two-component, two-phase vapor-liquid flow. Eqn. B.16 can thus be written as two separate vapor and liquid mass conservation equations. As noted previously, this formulation is incorrect for compositional multiphase pipe flow (i.e. when there are more components than phases). However, with respect to this particular example, we can write the following equations:

$$\frac{\partial}{\partial t}\left(s_v \rho_v\right) = -\vec{\nabla}\bullet\left(\overbrace{\rho_v \vec{u}_v}^{=\vec{G}_v}\right) + s_v R_v + R_{m,vl} \quad [=] \frac{vapor - mass\ in\ all - i}{L^3\ of\ V - t} \tag{B.17}$$

And,

$$\frac{\partial}{\partial t}\left(s_l \rho_l\right) = -\vec{\nabla}\bullet\left(\overbrace{\rho_l \vec{u}_l}^{=\vec{G}_l}\right) + s_l R_l - R_{m,vl} \quad [=] \frac{liquid - mass\ in\ all - i}{L^3\ of\ V - t} \tag{B.18}$$

The above so-called “phase continuity” equations can be found in the majority of existing *two-fluid* (or *multi-field*) models in the literature. In some cases, investigators may

incorrectly believe that these equations must generally hold for all multiphase pipe flow scenarios (e.g., Bratland, http://drbratland.com/PipeFlow2, pg. 21, 2010).

As can be seen from the previous development, the decision whether to sum over phases or components will yield very different equations. In some scenarios, for example in compositional multiphase flows, using the incorrect formulation will lead to fundamentally flawed solutions. Lastly, one must be aware of alternative methods of accounting for changes in compositions, such as "pseudo-compositional" approaches, in which multiphase or multi-field continuity equations are solved with properties arrived at using an explicit equation of state and a flash procedure.

B.2.2 Total Momentum Conservation Field Equations

Applying Eulerian time-averaging to Eqn. B.8 for the case Q = *linear phase-j momentum* in the presence of other flowing phases (assuming j-pressure is the same in any direction), we can write:

$$\overbrace{\frac{\partial}{\partial t}\underbrace{\left(s_j\rho_j\vec{v}_j\right)}_{\substack{conc.\ of\\ j-momentum}}}^{\substack{resultant\ force\\ per\ unit\ volume\\ on\ phase-j}} = \overbrace{-\vec{\nabla}\bullet\underbrace{\left(s_j\vec{\vec{\tau}}_j + s_jP_j\right)}_{\substack{conductive\\ j-momentum\ fluxes}}}^{\substack{net\ viscous\ and\ pressure\ forces\\ per\ unit\ volume\\ on\ phase-j}} \overbrace{-\vec{\nabla}\bullet\underbrace{\left(s_j\rho_j\vec{v}_j\vec{v}_j\right)}_{\substack{convective\\ j-momentum\ flux}}}^{\substack{net\ convective\ force\\ per\ unit\ volume\\ on\ phase-j}} \overbrace{+s_j\rho_j\vec{g}}^{\substack{net\ external\ force\\ per\ unit\ volume\ on\ phase-j\\ due\ to\ gravity}}$$
$$+\sum_{f=1}^{N_f}\left(\overbrace{\vec{\Gamma}_{totf,j}}^{\substack{net\ internal\ force\\ per\ unit\ volume\ on\ phase-j\\ due\ to\ interface-f\ processes}}\right)\ [=]\ \frac{j-momentum}{L^3\ of\ V-t} \qquad \text{(B.19)}$$

The last term on the right side of Eqn. B.19 represents, in general, a combination (or total) of three effects occurring at interface-f:

I. The net force per unit volume on phase-j due to interface-f.

II. The net force per unit volume on phase-j due to mass exchange at interface-f.

III. The net force per unit volume on phase-j due to phase-j accelerating with respect to the other phases in the mixture (*virtual mass*).

Exact definitions for these different interface-f terms can be found in Levy (1999), Ghiaaisaan (2008), Ishii and Hibiki (2006) and Kleinstreuer (2003), among others. The *virtual mass* effect is usually ignored, except in cases where it can be important as in very fast transients (e.g. as in Nuclear reactor transients), where its primary purpose is to stabilize the numerical solution of the conservation equations. As such, with a few exceptions (e.g. De Henau, 1992), almost all multiphase pipe flow models in the chemical and petroleum engineering industries ignore this effect. Reviews of the effect of virtual mass on the characteristics and numerical stability in multiphase flow can be found in Lahey Jr., et al. (1980) and No and Kazimi (1981). Additionally, there can be more interface-f terms in specific applications, for example, the local wall (lubrication) and turbulent dispersion forces in vertical upward bubbly flow (Antal et al., 1991, Drew 2001, Politano et al., 2003, Guet and Ooms, 2006).

In general, interface-f terms require correlations for every different flow pattern as well as for every different combination of phases in multiphase-flow (i.e. two-phase vapor-liquid, two-phase liquid-liquid, three-phase vapor-liquid-liquid and so on). Furthermore, these correlations are for the most part based on small-diameter pipe, adiabatic, steady-state, near-atmospheric flow conditions. The inherent assumption is made when using these correlations, that they are applicable to transient, heated (diabatic), high-pressure and/or high-temperature flow conditions. Therefore, it is highly desirable to avoid the need for the last term in Eqn. B.19. Fortunately, the volume-less interface criterion makes this possible. Since the total momentum (or mixture momentum) concentration is the sum of the individual j-phase momentum

concentrations, for Q = *mixture momentum* we can write (as usual, neglecting the conductive viscous momentum flux in favor of more dominant conductive and convective momentum fluxes):

$$\overbrace{\frac{\partial}{\partial t}\underbrace{\sum_{j=1}^{N_p}\left(s_j\rho_j\vec{v}_j\right)}_{\substack{conc.\ of\\ mixture\ momentum}}}^{\substack{resultant\ force\\ per\ unit\ volume\\ on\ mixture}} = \overbrace{-\vec{\nabla}\bullet\underbrace{\sum_{j=1}^{N_p}\left(s_jP_j\right)}_{\substack{conductive\\ mixture\ momentum\\ flux\ =\ P_{mix}}}}^{\substack{net\ pressure\ force\\ per\ unit\ volume\\ on\ mixture}} \overbrace{-\vec{\nabla}\bullet\underbrace{\sum_{j=1}^{N_p}\left(s_j\rho_j\vec{v}_j\vec{v}_j\right)}_{\substack{convective\\ mixture\ momentum\\ flux}}}^{\substack{net\ convective\ force\\ per\ unit\ volume\\ on\ mixture}} \overbrace{+\vec{g}\sum_{j=1}^{N_p}\left(s_j\rho_j\right)}^{\substack{net\ external\ force\\ per\ unit\ volume\ on\ mixture\\ due\ to\ gravity}}$$

$$+\sum_{j=1}^{N_p}\left(\sum_{f=1}^{N_f}\left(\vec{\Gamma}_{totf,j}\right)\right) \quad [=]\frac{total\ momentum}{L^3\ of\ V-t} \tag{B.20}$$

Note that a mixture pressure emerges from this equation. Also, with the omission of the stress tensor, Q = *angular phase-j momentum* does not supply any new local field equation. As seen before, the last summation term is zero due to the volume-less phase interface criterion, and thus in Eqn. B.20, net interfacial momentum sources are taken into account implicitly.

B.2.3 Total Energy Conservation Field Equations

Local field equations may also be written for non-conservation quantities such as mechanical energy, thermal energy (heat) and entropy. In these field equations, irreversible mechanical-to-thermal energy conversion is present. As is shown in the next Section, sources of the net entropy generation include, as examples, the conductive (viscous) mechanical energy dissipation flux and the conductive (molecular) thermal energy flux. These micro-scale conductive fluxes are in turn partly captured in definitions of macro-scale convective wall transfer coefficients, namely friction factor coefficient (momentum transfer at the wall) and heat transfer coefficient (thermal energy transfer at the wall), respectively.

With regard to the energy field equations, normally, only two are required since the total energy conservation field equation is formed from the summation of the mechanical and thermal energy non-conservation equations. For the case Q = *phase-j mechanical energy* in the presence of other flowing phases, we can write (taking the dot product of the velocity vector and Eqn. B.19):

$$\overbrace{\frac{\partial}{\partial t}\underbrace{\left(\frac{s_j\rho_j v_j^2}{2}\right)}_{\substack{conc.\ of\\ j-mech.\ energy}}}^{\substack{resultant\ mech.\ power\\ per\ unit\ volume\ on\ phase-j}} = -\vec{\nabla}\bullet\ \underbrace{\left(s_j\vec{\vec{\tau}}_j\bullet\vec{v}_j\right)}_{\substack{conductive\ (viscous)\\ j-work\ flux}} \quad -\vec{\nabla}\bullet\underbrace{\left(\frac{s_j\rho_j v_j^2}{2}+s_jP_j\right)\vec{v}_j}_{\substack{convective\ j-mech.\\ energy\ fluxes}}$$

$$\overbrace{+s_j\rho_j\left(\vec{v}_j\bullet\vec{g}\right)}^{\substack{net\ external\ mech.\ power\\ per\ unit\ volume\\ on\ phase-j\\ due\ to\ gravity}} \quad \overbrace{-\left(-s_jP_j\left(\vec{\nabla}\bullet\vec{v}_j\right)\right)}^{\substack{net\ rate\ of\ reversible\\ mech.\ energy\ increase\\ per\ unit\ volume\ on\\ phase-j\ due\ to\ phase\\ compression(-)/expansion(+)}} \quad \overbrace{\underbrace{-\left(-s_j\vec{\vec{\tau}}_j\otimes\vec{\nabla}\vec{v}_j\right)}_{\substack{always\ positive\ for\\ Newtonian\ fluids}}}^{\substack{net\ rate\ of\ irreversible\\ mech.\ energy\ decrease\\ per\ unit\ volume\ on\\ phase-j\ due\ to\\ viscous\ dissipation}}$$

$$+\sum_{f=1}^{N_f}\left(\overbrace{\vec{v}_j\bullet\left(\vec{\Gamma}_{totf,j}\right)}^{\substack{net\ internal\ mech.\ power\\ per\ unit\ volume\ on\ phase-j\\ due\ to\ interface-f\ processes}}\right) \left[=\right]\frac{j-mech.\ energy}{L^3\ of\ V-t} \qquad \text{(B.21)}$$

Similarly, for the case Q = *phase-j thermal energy* (or j-heat) in the presence of other flowing phases, we can write:

$$\overbrace{\frac{\partial}{\partial t}\underbrace{\left(s_j\rho_j\hat{U}_j\right)}_{\substack{conc.\ of\\ j-thermal\ energy}}}^{\substack{resultant\ thermal\ power\\ per\ unit\ volume\\ on\ phase-j}} = -\vec{\nabla}\bullet\ \underbrace{\left(s_j\vec{q}_{cond,j}\right)}_{\substack{conductive\ (molecular)\\ j-heat\ flux}} \ -\vec{\nabla}\bullet\underbrace{\left(s_j\rho_j\hat{U}_j\right)\vec{v}_j}_{\substack{convective\ j-thermal\\ energy\ flux}}$$

$$\overbrace{+\left(-s_jP_j\left(\vec{\nabla}\bullet\vec{v}_j\right)\right)}^{\substack{net\ rate\ of\ reversible\\ thermal\ energy\ decrease\\ per\ unit\ volume\ on\\ phase-j\ due\ to\ phase\\ compression(+)/expansion(-)}} \ \overbrace{+\underbrace{\left(-s_j\vec{\vec{\tau}}_j\otimes\vec{\nabla}\vec{v}_j\right)}_{\substack{always\ positive\ for\\ Newtonian\ fluids}}}^{\substack{net\ rate\ of\ irreversible\\ thermal\ energy\ increase\\ per\ unit\ volume\ on\\ phase-j\ due\ to\\ viscous\ dissipation}} \qquad . \quad \text{(B.22)}$$

$$+\sum_{f=1}^{N_f}\left(\overbrace{\vec{v}_j\bullet\left(\vec{\Psi}_{totf,j}\right)}^{\substack{net\ interface-f\ thermal\ power\\ per\ unit\ volume\ on\ phase-j\\ due\ to\ interface\text{-}f\ processes}}\right)\ [=]\frac{j-thermal\ energy}{L^3\ of\ V-t}$$

Lastly, applying Eulerian time-averaging to Eqn. B.8 for the case Q = *phase-j total energy* in the presence of other flowing phases, we get from summing eqns. B.21 and B.22:

$$\overbrace{\frac{\partial}{\partial t}\underbrace{\left(\frac{1}{2}s_j\rho_jv_j^2+s_j\rho_j\hat{U}_j\right)}_{conc.\ of\ j-total\ energy}}^{\substack{resultant\ total\ power\ per\ unit\ volume\\ on\ phase-j}} = -\vec{\nabla}\bullet\ \underbrace{\left(s_j\vec{q}_{cond,j}\right)}_{\substack{conductive\ (molecular)\\ j-heat\ flux}} \ -\vec{\nabla}\bullet\ \underbrace{\left(s_j\vec{\vec{\tau}}_j\bullet\vec{v}_j\right)}_{\substack{conductive\ (viscous)\\ j-work\ flux}}$$

$$-\vec{\nabla}\bullet\underbrace{\left(\frac{1}{2}s_j\rho_jv_j^2+s_j\rho_j\hat{U}_j+s_jP_j\right)\vec{v}_j}_{\substack{convective\ j-total\ energy\ fluxes}}+\ \overbrace{s_j\rho_j\left(\vec{v}_j\bullet\vec{g}\right)}^{\substack{net\ external\ total\ power\\ per\ unit\ volume\\ on\ phase-j\ due\ to\ gravity}} \qquad \text{(B.23)}$$

$$+\sum_{f=1}^{N_f}\left(\overbrace{\vec{v}_j\bullet\left(\vec{\Gamma}_{totf,j}\right)+\vec{v}_j\bullet\left(\vec{\Psi}_{totf,j}\right)}^{\substack{net\ internal\ total\ power\\ per\ unit\ volume\ on\ phase-j\\ due\ to\ interface\text{-}f\ processes}}\right)\ [=]\frac{j-total\ energy}{L^3\ of\ V-t}$$

B.3 SPATIAL (AREA AND VOLUME) AVERAGING

We are now ready to derive one-dimensional macro-scale balance equations. In order to derive these balance equations, we first perform Eulerian area averaging of the local time-averaged phase-j properties, velocities and volume fractions over the cross-sectional area of the pipe, in order to reduce the multi-dimensional (general) time-averaged local field equations given in the previous section to simplified 1D equations. Then we perform volume averaging over the control volume. Note that we may interchange the order of these operations at any time (as explained in Boure and Delhaye, 1982; Drew, 1983). Also, the space and time averaging operators are commutative and so the order does not affect the final result (Lahey, Jr. and Drew, 1988). With regards to phase (or component) properties, the assumption of uniform properties across the flow field area is widely used and will also be adopted here.

We note that even in single-phase flow problems, the area-averaging method (which has been widely used because its simplicity) is highly desirable in many practical engineering applications. For example, the use of the wall friction factor or the wall heat transfer coefficient is closely related to the concept of the area averaging. A good review of Eulerian area averaging can be found in Ishii and Hibiki (2006), Birkhoff (1964), Delhaye (1976), among others. Lastly, the following Eulerian area averaging operator is introduced to represent the integral over a flow field area A, of a quantity X:

$$\langle X \rangle = \frac{1}{A} \int_A X \, dA \tag{B.24}$$

B.3.1 Total Mass Balance Equations

Applying the operator in Eqn. B.24 above to Eqn. B.13, we arrive at the one-dimensional (arbitrary x-direction) area-averaged field equation for Q = *total i-mass over all j-phases* in stationary porous solid media as:

$$\frac{\partial}{\partial t}\left(\overbrace{\sum_{j=1}^{N_p}\left(\left(\phi\left\langle s_j\right\rangle\right)\rho_j\omega_{ij}\right)}^{\text{conc. of total i-mass, } \rho_{i,total}}\right)=-\vec{\nabla}\bullet\left(\overbrace{\sum_{j=1}^{N_p}\left(\rho_j\omega_{ij}\underbrace{\phi\left\langle s_j v_j\right\rangle}_{\substack{\text{"Darcy"}\\ \text{volume flux}\\ =\langle u_j\rangle}}\right)}^{\text{convective flux of total i-mass}}\right) \quad \text{(B.25)}$$

$$\overbrace{+\sum_{j=1}^{N_p}\left(\phi\left\langle s_j R_{ij}\right\rangle\right)}^{\substack{\text{net generation of conc.}\\ \text{of total i-mass from}\\ \text{external sources}}} \overbrace{+\sum_{j=1}^{N_p}\left(\left\langle R_{m,ij}\right\rangle\right)}^{\substack{\text{net generation of conc.}\\ \text{of total i-mass from}\\ \text{internal sources}}} \quad [=]\frac{total\ i-mass\ in\ all-j}{L^3\ of\ V-t}$$

Applying the Gauss-Ostrogradskii Divergence Theorem to Eqn. B.25 for an averaged description of the flow, we find that the x-direction, area-averaged balance equation for Q = *total i-mass over all j-phases* in stationary porous solid media is:

$$\frac{d}{dt}\int_V\overbrace{\left(\phi\sum_{j=1}^{N_p}\left(\left\langle s_j\right\rangle\rho_j\omega_{ij}\right)\right)}^{\text{total i-mass, } M_{i,total}}dV=-\int_{A_x}\vec{n}\bullet\left(\overbrace{\sum_{j=1}^{N_p}\left(\rho_j\omega_{ij}\underbrace{\phi\left\langle s_j v_j\right\rangle}_{\substack{\text{"Darcy"}\\ \text{volume flux}\\ =\langle u_j\rangle}}\right)\vec{e}}^{\text{convective flux of total i-mass}}\right)dA \quad \text{(B.26)}$$

$$+\int_V\overbrace{\left(\phi\sum_{j=1}^{N_p}\left(\left\langle s_j R_{ij}\right\rangle\right)\right)dV}^{\substack{\text{net generation of total i-mass from}\\ \text{external sources}}} \quad [=]\frac{total\ i-mass\ in\ all-j}{t}$$

Eqn. B.26 above is the basic reservoir flow simulation equation that is solved in reservoir (porous media) simulators in the petroleum engineering discipline with appropriate modifications (e.g. extension to more or different coordinates, division by a reference density, etc.) and closure relations. One such example of those closure relations is the equation for $\langle u_j \rangle$, the averaged phase-j volume flux, which is given by the multiphase Darcy's relation. The multiphase Darcy's relation can be interpreted as another *phenomenological transport relation* or more fundamentally as a multiphase extension to a phase-j momentum balance in a porous medium. Other closure relations for Eqn. B.26 can be found in Lake (1989).

Using the same procedure as above applied to Eqn. B.15, we may write the x-direction, area-averaged balance equation for Q = *total i-mass over all j-phases* in a stationary solid pipe (neglecting mass exchanges between flowing phases and the pipe solid material, and neglecting any conductive fluxes) as:

$$\overbrace{\frac{d}{dt}\int_V \left(\sum_{j=1}^{N_p} \left(\langle s_j \rangle \rho_j \omega_{ij} \right) \right) dV}^{\text{total i-mass, } M_{i,total}} = -\int_{A_x} \vec{n} \bullet \left(\overbrace{\sum_{j=1}^{N_p} \left(\rho_j \omega_{ij} \langle s_j v_j \rangle \right) \vec{e}}^{\text{convective flux of total i-mass}} \right) dA + \overbrace{\int_V \left(\sum_{j=1}^{N_p} \left(\langle s_j R_{ij} \rangle \right) \right) dV}^{\text{net generation of total i-mass from external sources}} \quad [=] \frac{total\ i-mass\ in\ all-j}{t} \tag{B.27}$$

The only difference between eqns. B.26 and B.27 is that the phase-j volume fraction in Eqn. B.26 has the units of (L^3 of j)/(L^3 of V_{pore}) and thus the porous medium *porosity* with units of (L^3 of V_{pore})/(L^3 of V) must appear everywhere phase-j volume fraction appears, whereas in Eqn. B.27, the phase-j volume fraction directly has units of (L^3 of j)/(L^3 of V). Evidently, eqns. B.26 and B.27 are selfsame. This is to be expected since

we are conserving total component-i mass over all flowing phases, which will remain the same regardless of the medium.

Finally, we note that Eqn. B.26, in a 1-D integral finite-difference representation for a simulation cell, c, for an incompressible porous medium (e.g. a reservoir rock), can be written as:

$$\left(\frac{\bar{\phi}V_c}{\Delta t}\right)\Delta_t\left(\overbrace{\sum_{j=1}^{N_p}\left(\bar{s}_j\bar{\rho}_j\bar{\omega}_{ij}\right)}^{\text{conc. of total i-mass}}\right)+\Delta_x\left(A_x\overbrace{\sum_{j=1}^{N_p}\left(\bar{k}_{rj}\bar{\rho}_j\bar{\omega}_{ij}\bar{u}_j\right)\vec{e}}^{\text{convective flux of total i-mass}}\right)$$
$$=\overbrace{\bar{\phi}V_c\left(\sum_{j=1}^{N_p}\left(\bar{s}_j\bar{R}_{ij}\right)\right)}^{\text{net generation of total i-mass from external sources}}\ [=]\frac{total\ i\text{-}mass\ in\ all\text{-}j}{t} \tag{B.28}$$

And similarly, Eqn. B.27, in a 1-D integral finite-difference representation for a pipe medium simulation cell, c, can be written as:

$$\left(\frac{V_c}{\Delta t}\right)\Delta_t\left(\overbrace{\sum_{j=1}^{N_p}\left(\bar{s}_j\bar{\rho}_j\bar{\omega}_{ij}\right)}^{\text{conc. of total i-mass}}\right)+\Delta_x\left(A_x\overbrace{\sum_{j=1}^{N_p}\left(\bar{f}_j\bar{\rho}_j\bar{\omega}_{ij}\bar{u}_{mix}\right)\vec{e}}^{\text{convective flux of total i-mass}}\right)$$
$$=\overbrace{V_c\left(\sum_{j=1}^{N_p}\left(\bar{s}_j\bar{R}_{ij}\right)\right)}^{\text{net generation of total i-mass from external sources}}\ [=]\frac{total\ i\text{-}mass\ in\ all\text{-}j}{t} \tag{B.29}$$

Note that the form of eqns. B.28 and B.29 are identical and can be written as:

$$\left(\frac{\overline{\phi}\overline{V}_c}{\Delta t}\right)\Delta_t\left(\overbrace{\sum_{j=1}^{N_p}\left(\overline{s}_j\overline{\rho}_j\overline{\omega}_{ij}\right)}^{\text{conc. of total i-mass}}\right)+\Delta_x\left(\overbrace{A_x\sum_{j=1}^{N_p}\left(\underbrace{\overline{\gamma}_j}_{\substack{\text{multiplier}\\ \text{term}}}\ \overline{\rho}_j\overline{\omega}_{ij}\ \underbrace{\overline{u}}_{\substack{\text{velocity}\\ \text{term}}}\right)\vec{e}}^{\text{convective flux of total i-mass}}\right) \tag{B.30}$$

$$=\overbrace{\overline{\phi}\overline{V}_c\left(\sum_{j=1}^{N_p}\left(\overline{s}_j\overline{R}_{ij}\right)\right)}^{\substack{\text{net generation of}\\ \text{total i-mass from}\\ \text{external sources}}}\ [=]\frac{total\ i\text{-}mass\ in\ all\text{-}\ j}{t}$$

Now, Eqn. B.30 shows that, with minor modifications, any existing multiphase reservoir simulator can be made into a multiphase pipe simulator, utilizing a single simulation domain (same grid for both porous and pipe media), and solving the same basic total component-i mass balance equation. We simply plant the seed in his work for other investigators to recognize how easy it becomes to write such a truly integrated pipe-porous media simulator solving one equation in one domain.

In the reservoir rock (porous medium) case, the velocity term is closed by the *Darcy's relation* (a reservoir momentum balance equation) and the multiplier term (a strongly saturation-dependent term) is *relative permeability*, which can be interchangeably defined in terms of the phase fractional flow. This relative permeability term captures several multiphase porous media flow dependencies and microphysics such as wettabilty, pore structure, heterogeneity, saturation history (trapping), volume flux ratio, viscosity ratio, surface tension, etc.

For pipe flow, the velocity term is obtained from a pipe momentum balance equation (e.g., our universal mixture momentum balance, Eqn. 5 in Section 2.2.2), porosity is unity and the strongly saturation-dependent term is the phase fractional flow. Similar to the porous medium, this fractional flow term captures several multiphase pipe

flow dependencies and microphysics such as volume flux ratio, density ratio, viscosity ratio, interfacial tension, etc.

Note also that just as an examination of the number of primary dependent variables versus independent equations required to mathematically close Eqn. B.28 can be found in Lake (1989), a similar analysis can be done for the multiphase pipe flow equivalent of Eqn. B.28, that is, Eqn. B.29. A listing of the primary dependent variables for Eqn. B.29 is shown in table B.3.1 below:

Name of primary dependent variable per pipe cell, c	**No. of primary dependent variables**
Component-i in phase-j mass fractions	$N_c N_p$
Component-i in phase-j source or sink rates	$N_c N_p$
Mixture pressure	1
Mixture enthalpy	1
Mixture velocity	1
Phase-j volume fraction	N_p
Phase-j fractional flow	N_p
Phase-j density	N_p
Total:	$\mathbf{2N_cN_p + 3N_p + 3}$

Table B.3.1: Primary dependent variables in Eqn. B.29.

A listing of the independent equations required to close Eqn. B.29 is shown in table B.3.2 below:

Name of independent equation per pipe cell, c	No. of independent equations
Total component-i mass balance equations	$N_c - 1$
Total components mass balance equation	1
Component-i in phase-j source/sink rate equations	$N_p(N_c - 1)$
Total momentum balance equation	1
Total energy balance equation	1
Summation of phase-j volume fraction constraint	1
Summation of phase-j fractional flow constraint	1
Summation of component-i in phase-j constraint	N_p
Component-i in phase-j local equilibrium relations	$N_c(N_p - 1)$
Equations of State for phase-j	N_p
Phase-j fractional flow versus phase-j volume fraction relations	$N_p - 1$
Total:	$\mathbf{2N_cN_p + 3N_p + 3}$

Table B.3.2: Independent equations required to close Eqn. B.29.

From tables B.3.1 and B.3.2 above, it is now clear how the fractional flow versus volume fraction relations equations complete the mathematical closure of Eqn. B.29.

B.3.2 Total Momentum Balance Equations

The procedure of arriving at a multiphase, macro-scale, total (or mixture) momentum balance equation, which is a major result of this work, is noted in the development in Section 2.3.2.

B.3.3 Total Energy Balance Equations

Noting that the total mechanical energy concentration is the sum of the individual j-phase mechanical energy concentrations, we can apply the Gauss-Ostrogradskii Divergence Theorem to Eqn. B.21 to obtain the x-direction balance equation for Q = *total mechanical energy* in a stationary solid pipe as:

$$\overbrace{\frac{d}{dt}\int_V \left(\underbrace{\sum_{j=1}^{N_p}\left(\frac{s_j \rho_j v_j^2}{2} \right)}_{\substack{conc.\ of\ mixutre \\ mech.\ energy}} \right) dV}^{resultant\ mech.\ power\ on\ mixture} = \overbrace{-\int_{A_x} \vec{n}\bullet \underbrace{\sum_{j=1}^{N_p}\left(s_j \vec{\vec{\tau}}_j \bullet \vec{v}_j \right)}_{\substack{conductive\ (viscous) \\ mixture\ work\ flux}} dA}^{=\dot{W}_m^{(\tau)}} - \int_{A_x} \vec{n}\bullet \underbrace{\sum_{j=1}^{N_p}\left(\left(\frac{s_j \rho_j v_j^2}{2} \right) \vec{v} \right)}_{\substack{convective\ mixture \\ mech.\ (kinetic)\ energy\ flux}} dA$$

$$\overbrace{-\int_{A_x} \vec{n}\bullet \underbrace{\sum_{j=1}^{N_p}\left(s_j P_j \vec{v}_j \right)}_{\substack{convective\ mixture \\ mech.\ (pressure) \\ energy\ flux}} dA}^{net\ rate\ of\ forced-convective\ work\ on\ mixture} \quad \overbrace{+\int_V \left(\sum_{j=1}^{N_p}\left(s_j \rho_j \left(\vec{v}_j \bullet \vec{g} \right) \right) \right) dV}^{net\ external\ power\ on\ mixture\ due\ to\ gravity}$$

$$\overbrace{-\int_V \left(-\sum_{j=1}^{N_p}\left(s_j P_j \left(\vec{\nabla}\bullet \vec{v}_j \right) \right) \right) dV}^{=\dot{E}_c,\ compression\ (+ve)/expansion\ (-ve)} - \overbrace{\left(-\int_V \left(\sum_{j=1}^{N_p}\left(s_j \vec{\vec{\tau}}_j \otimes \vec{\nabla}\vec{v}_j \right) \right) dV \right)}^{=\dot{E}_{v,mix\to wall},\ always\ +ve\ for\ Newtonian\ fluids}$$

$$[=] \frac{total\ mechanical\ energy}{t} \tag{B.31}$$

Note that similar to before, the summation of the last term in Eqn. B.21 over all flowing phases is zero due to the volume-less phase interface criterion, and thus in Eqn. B.31, net interfacial mechanical energy sources are taken into account implicitly. Note also that we invoked the notation of BSL and analogously adapted it to the multiphase flow scenario above. Applying the operator in Eqn. B.24 to Eqn. B.31, we can arrive at the one-dimensional area-averaged balance equation for Q = *total mechanical energy* in a stationary solid pipe as:

$$\overbrace{\frac{d}{dt}\int_V \underbrace{\left(\sum_{j=1}^{N_p}\left(\left\langle s_j\right\rangle \rho_j\left(\frac{\left\langle\left\langle v_j\right\rangle\right\rangle^2}{2}+g_x\right)\right)\right)}_{\text{conc. of mixutre mechanical energy}} dV}^{\text{resultant mechanical power on mixture}} =$$

$$-\int_{A_x}\vec{n}\bullet\sum_{j=1}^{N_p}\left(\left\langle s_j\right\rangle \rho_j\left\langle\left\langle v_j\right\rangle\right\rangle\left(\frac{\left\langle\left\langle v_j\right\rangle\right\rangle^2}{2}+g_x+\frac{\left\langle\left\langle P_j\right\rangle\right\rangle}{\rho_j}\right)\right)\vec{e}\,dA \qquad \text{(B.32)}$$

$$\overbrace{+W_m^{(\tau)}+W_m^{(p)}}^{=\,W_m}-E_c-E_{v,mix\to wall}\ [=]\frac{total\ mechanical\ energy}{t}$$

Note that the net rate of forced-convective work on the mixture in Eqn. B.31 now forms two separate terms in Eqn. B.32. Using the same procedure for total mechanical energy above applied to Eqn. B.22, for Q = *total thermal energy* in a stationary solid pipe as, we can write:

$$\overbrace{\frac{d}{dt}\int_V \underbrace{\left(\sum_{j=1}^{N_p}\left(\left\langle s_j\right\rangle \rho_j\hat{U}_j\right)\right)}_{\substack{\text{conc. of mixutre}\\ \text{thermal energy}}} dV}^{\text{resultant thermal power on mixture}} = \overbrace{-\int_{A_x}\vec{n}\bullet\underbrace{\sum_{j=1}^{N_p}\left(\left\langle s_j\right\rangle \rho_j\hat{U}_j\left\langle\left\langle v_j\right\rangle\right\rangle\right)\vec{e}}_{\text{convective mixture thermal energy flux}}\,dA}^{\substack{\text{net boundary thermal power on mixture}\\ (+ve\ \text{for heating},\\ -ve\ \text{for cooling})}} \overbrace{+\sum_{j=1}^{N_p}\left(Q_{wall\to j}\right)}$$

$$\overbrace{-\int_{A_x}\vec{n}\bullet\underbrace{\sum_{j=1}^{N_p}\left(s_j\vec{q}_{cond,j}\right)}_{\substack{\text{conductive (molecular)}\\ \text{mixture heat flux}}}dA}^{\text{source of the net entropy generation term}}+E_c+E_{v,wall\to mix} \qquad \text{(B.33)}$$

$$[=]\frac{total\ thermal\ energy}{t}$$

Quite interestingly, Eqn. B.33 now shows the reason *why* the source of the net entropy generation term is always positive (or positive-definite) even for closed systems. This term consists of usable and unusable (dissipative) molecular energy fluxes, i.e. the viscous dissipation heating and the heat dissipation due to molecular conduction,

respectively. When these latter internal heat gradients have completely dissipated in a system (i.e. system is in state of highest disorder), the system is said to be in thermodynamic equilibrium. At that point, we are maximally ignorant of the micro-scale details of the system and the net rate of entropy generation in the system is zero. It follows then, that the macro-scale balance equation for Q = *total entropy* of the flowing mixture can be written directly from Eqn. B.33, as:

$$\overbrace{\frac{d}{dt}\int_V \left(\underbrace{\sum_{j=1}^{N_p} \left(\langle s_j \rangle \rho_j \hat{S}_j \right)}_{\text{conc. of mixutre entropy}} \right) dV}^{\text{resultant rate of total entropy in mixture (or "system")}} = \overbrace{-\int_{A_x} \vec{n} \bullet \underbrace{\sum_{j=1}^{N_p} \left(\langle s_j \rangle \rho_j \hat{S}_j \langle\langle v_j \rangle\rangle \right) \vec{e}}_{\text{convective mixture entropy flux}} dA}^{\text{net rate of total entropy into mixture (or "system") from mass fluxes}} + \overbrace{\left(\frac{\sum_{j=1}^{N_p} \left(Q_{wall \to j} \right)}{T_{wall}} \right)}^{\substack{\text{net rate of total entropy into mixture from "surroundings" (+ for heating, − for cooling)}}} \quad \text{(B.34)}$$

$$+ \overbrace{\dot{S}_{gen}}^{\text{always} \geq 0} \quad [=] \frac{\text{total entropy}}{t}$$

In Eqn. B.34 we introduced the phrasing of "system" and "surroundings" to emphasize the simple connection of this equation to more standard macroscopic descriptions of entropy balances in classical thermodynamics texts. Additionally, Eqn. B.34 can be re-stated as:

$$\overbrace{\frac{d}{dt}\int_V \left(\underbrace{\sum_{j=1}^{N_p} \left(\langle s_j \rangle \rho_j \hat{S}_j \right)}_{\text{conc. of mixutre entropy}} \right) dV + \int_{A_x} \vec{n} \bullet \underbrace{\sum_{j=1}^{N_p} \left(\langle s_j \rangle \rho_j \hat{S}_j \langle\langle v_j \rangle\rangle \right) \vec{e}}_{\text{convective mixture entropy flux}} dA}^{\text{net changes in "system" (can be +ve or −ve)}} - \overbrace{\left(\frac{\sum_{j=1}^{N_p} \left(Q_{wall \to j} \right)}{T_{wall}} \right)}^{\substack{\text{net changes in "surroundings" (can be +ve or −ve)}}} \quad \text{(B.35)}$$

$$= \dot{S}_{gen} \geq 0 \quad [=] \frac{\text{total entropy}}{t}$$

Eqn. B.35 is a statement of the second law of thermodynamics for the multiphase mixture (i.e. the system). Similarly, a statement of the first law of thermodynamics for the

multiphase mixture can be written by summing eqns. B.32 and B.33 to obtain the one-dimensional area-averaged balance equation for Q = *total energy* in a stationary solid pipe as:

$$\overbrace{\frac{d}{dt}\int_V \underbrace{\left(\sum_{j=1}^{N_p}\left(\langle s_j\rangle \rho_j\left(\frac{\langle\langle v_j\rangle\rangle^2}{2}+g_x+\hat{U}_j\right)\right)\right)}_{\text{conc. of mixutre total energy}} dV}^{\text{resultant total power on mixture}} =$$

$$-\int_{A_x}\vec{n}\bullet\underbrace{\sum_{j=1}^{N_p}\left(s_j\vec{q}_{cond,j}\right)}_{\substack{\text{conductive (molecular)}\\ \text{mixture heat flux}}} dA-\int_{A_x}\vec{n}\bullet\sum_{j=1}^{N_p}\left(\langle s_j\rangle\rho_j\langle\langle v_j\rangle\rangle\left(\frac{\langle\langle v_j\rangle\rangle^2}{2}+g_x+\frac{\overbrace{\langle\langle P_j\rangle\rangle}^{=\hat{H}_j}}{\rho_j}+\hat{U}_j\right)\right)\vec{e}\ dA \quad \text{(B.36)}$$

$$+\ W_m \qquad +\overbrace{\sum_{j=1}^{N_p}\left(Q_{wall\to j}\right)}^{\substack{\text{net boundary thermal power on mixture}\\ (+ve\ \text{for heating}, -ve\ \text{for cooling})}} \qquad [=]\frac{\text{total energy}}{t}$$

Now, invoking the notation of BSL (with the understanding that A is the cross-sectional area of the pipe in the arbitrary x-direction) and considering steady-state flow, we can re-write Eqn. B.36 (neglecting the total rate of work done on the mixture due to moving surfaces and neglecting conductive fluxes in favor of the more dominant convective fluxes) as:

$$0=-\Delta\left(\sum_{j=1}^{N_p}\left(\langle s_j\rangle\rho_j A\langle\langle v_j\rangle\rangle\left(\frac{\langle\langle v_j\rangle\rangle^2}{2}+gh+\hat{H}_j\right)\right)\right)+\sum_{j=1}^{N_p}\left(Q_{wall\to j}\right) \quad \text{(B.37)}$$

We note the mathematical convenience of introducing the enthalpy definition in Eqn. 37. Note also, by convention:

$$-\Delta(gh)=g(\Delta L)\cos\theta \quad \text{(B.38)}$$

Thus Eqn. B.37 can be restated simply as:

$$\frac{\overbrace{\Delta\left(\overbrace{\sum_{j=1}^{N_p}\left(G_j\hat{H}_j\right)}^{=\left(G\hat{H}\right)_{mix}}\right)}^{\text{thermal-dynamic}}}{\Delta L}=\overbrace{\frac{1}{A\Delta L}\underbrace{\sum_{j=1}^{N_p}\left(Q_{wall\to j}\right)}_{=Q_{wall\to mix}}}^{\text{wall heat transfer}}+\overbrace{\underbrace{\left(\sum_{j=1}^{N_p}\left(G_j\right)\right)}_{=G_{mix}}g\cos\theta}^{\text{gravitational}}$$

$$-\overbrace{\frac{1}{2}\sum_{j=1}^{N_p}\left(\frac{\Delta\left(G_j\left(\frac{G_j}{\rho_j\left\langle s_j\right\rangle}\right)^2\right)}{\Delta L}\right)}^{\substack{\text{kinetic energy increase (+ve)}\\ \text{or decrease (-ve)}}}\left[=\right]\frac{total\ energy}{L^3\ of\ V-t} \tag{B.39}$$

Eqn. B.39 above has several unique features that make it quite suitable as a general total energy flux gradient equation (e.g., for mixture temperature gradient calculation) that is valid for any multiphase flow scenario. More subtle details about this equation are discussed in reference to our general total momentum balance equation in Section 2.2.2 (Eqn. 5 in Section 2.2.2) for pressure gradient calculation in any multiphase flow scenario.

Appendix C – Examples of Intractable Model Tuning in Practice

C.1 Pressure Gradient and Volume Fraction Correction Factors

For the first example of intractable model tuning in practice, we consider the case when "correction" factors are placed in front of the phase volume fraction, hydrostatic pressure gradient or frictional pressure gradient such as is part of the standard provided features available in several multiphase pipe flow industry software (e.g. PROSPER, PIPESIM, WellFlo). For instance, it is a fact that engineers using multiphase pipe flow software in the Petroleum industry are trained to perform data-matching (alternatively referred to as "calibrating" or "VLP matching") of their wellbore flows using these tuning factors to ensure the tuned model closely fit the field data, after which, the fitted model is used for predictions. Even if these tuning factors are kept within an arbitrarily specified maximum/minimum range, say within +/- 10%, there is no scientific meaning or interpretation that can be gained by having them participate in the calculations.

The degree of tuning of multiphase flow models in some cases can be excessive and confusing, aside from the fact of being ad hoc. For instance, the PROSPER Training Course Notes (2004) describes a confusing series of matching procedures in the VLP Matching Section as: "In PROSPER, the VLP matching routine will first attempt to obtain a match by adjusting the holdup correlation. If the required adjustment is more than 5%, a multiplier will be applied to the fluid densities calculated from the PVT. If a gravity term correction of more than 10% is required, this indicates an inconsistency in the input data. The PVT and test rates should be re-checked". Evidently, apart from being ad hoc, these statements reveal the very bad basic reasoning that for any prevailing flowing conditions, adjusting various fluid property correlations related to one term of a chosen pressure gradient correlation somehow says something about the consistency of

the input data. In fact, the users of this particular software are trained to use different total pressure gradient correlations as a "quality control tool" of the input data to detect cases where "possible inconsistencies in the data could be in the PVT, equipment description (pipe I.D.) and the test measurements (rate and pressure)" – VLP Correlations Section of the PROSPER Training Course Notes (2004). Other than being fundamentally flawed reasoning, this represents the opposite of how any model (scientific or otherwise) should be tested against data.

C.2 NON-LINEAR REGRESSION TUNING

In the second example of current practice, the WellFlo Petroleum Engineering Software brochure (http://www.ep-weatherford.com/solutions/eps/WellFlo_Tuning.htm, 2013) describes features of its *tuning mode* with the statements: "In order to be certain that analysis results can be trusted to match reality, users need a way to tune their well model to measured data. … Once the measured data is entered, it can then be used to tune a variety of parameters using a powerful non-linear regression algorithm. This ensures that well models will be as accurate as possible." These statements reveal the kernel reason *why* some industrial multiphase flow tools are believed to be accurate usually by management – because the engineers who use them will almost always furnish exact matches to measured data by the use of both seen and unseen tuning factors. This feature, like the previous example, offers no scientific meaning or interpretation in regards to the ability to predict these flows. In fact, the general issue of tuning models to match data using deterministic non-linear regression (e.g., parameter estimation techniques) is an already provided feature in common workplace tools, such as Excel's *Solver*. Therefore, if ad hoc model tuning is needed in a particular multiphase flow

application and there is no requirement for a science-based understanding or result, then there is no need for a specialized multiphase flow tool.

C.3 CLOSURE RELATIONS TUNING

In the third example, we highlight the scenario where the closure relations of a model are calibrated to a particular set of data. In this case, it cannot be claimed that this tuned model is objectively "better" than any other model if the tuned model is compared against similar data conditions as that used to tune its closure relations. As obvious as this may seem, this is an existing practice in both industry and academia. For instance, some oil and gas companies will supply a preferred multiphase flow software vendor with large amounts of uncontrolled field operating data to help tune the closure relations and correlations of the model of the vendor – as a concrete example – the transfer of thirteen months of the Gulf of Mexico Gemini gas condensate field data to OLGA's Verification and Improvement Program (or OVIP) as described in Kashou et al. (2002). Indeed, in a state-of-the-art review on the OLGA code across various field applications, it was discovered that in many field cases, this particular software had only produced the desired results "after available parameters in the code were calibrated to match the results" (Ali and Yeung, 2010).

As is evident, the type of industry practice described above cannot (and must not) be relied upon for science-based predictions of multiphase flows. This is a particularly risky practice in high-pressure, high-temperature field environments where it is vital to understand and thus predict the multiphase flow behaviors in scenarios that deviate from normal operating (model-tuned) conditions.

C.4 IMMEASURABLE VARIABLES AND TUNING COEFFICIENTS

Other examples of intractable model tuning in multiphase pipe flow applications include the widespread use of immeasurable variables, such as:

I. *Apparent wall or interfacial friction factors* in the modeling of stratified flow, annular flow, perforated pipes, low liquids loading and two-fluid closure laws.

II. *Efficiency factors* or *apparent wall roughness* in natural gas transmission and distribution pipelines for accounting for the presence of liquids.

III. *Mixture viscosity or effective density* in liquid-liquid flows.

IV. *Effective solids viscosity* in fluid-solid flows.

V. *Loss or resistance coefficients* in contraction/expansion piping equipment such as valves, orifices, inflow control devices, chokes and, in general, obstructed multiphase flows.

In the second class of intractable tuning above, it should be noted that the majority of investigators in this field of natural gas pipeline networks utilize ad hoc tuning to such an extreme extent that tuning is the vehicle through which their models are validated. In one concrete example, an investigator will claim a better understanding is achieved through tuning: “The benefits SNG [Southern Natural Gas] has gained through tuning go beyond just an increase in accuracy of our flow simulation model. Through various tuning studies, planning has gained a better understanding of our system’s operations” (Fauer, 2002). Clearly, if tuning assumes such a central role in this case, then one may justifiably ask why a flow simulation model is even necessary. The quite revealing answer to this question is provided in this same reference: “The single most

important aspect of modeling is the tuning of the system. Tuning is the process of matching a model's output with real field data" (Fauer, 2002).

In the last class of intractable tuning above, there are "databases" of tuned resistance coefficients for a variety of equipment. In some instances, these databases are promoted as being tools that would increase the prediction accuracy of multiphase flow pressure gradient, e.g., the database of equipment coefficients in the *Base Solver* of the NETool code (described as being "tuned to perfection" in Johansen and Khoriakov, 2007) or the VPC (Valve Performance Clearinghouse) gas-lift database in the OLGA code. The NETool code, for example, is perceived by some industry investigators as a "best-in-art wellbore hydraulics model" (Jain et al., 2013). In other instances, tuned equipment resistance coefficients are promoted as being tools that would aid in the understanding a specific multiphase flow application, as examples, as described in the high viscosity flow loop experiments described in Miller et al. (2009), or in the tuning of choke-valve discharge coefficients (and "interfacial friction parameters") in the Hydro pipeline-riser multiphase flow loop (section 3.1.3 in Hauge, 2007).

In summary, if the tuning of multiphase flow models in complex industrial applications is necessary (as it quite often is), then tractable model tuning must be used for science-based predictions. As this work demonstrates, tractable model tuning can be enforced in the above industrial examples (and many others) and still result in very accurate solutions, i.e., all of the intractable tuning variables and parameters noted above can be avoided and therefore the serious dangers imposed by their usage in multiphase flow applications eliminated.

Appendix D – Flow Pattern: A Subjective Decision

D.1 INCONCLUSIVE DESCRIPTIONS

In this appendix, we demonstrate that flow patterns are U-variables, following from the discussion in Section 2.1.2.1. A flow pattern is a description of a set of flow field interactions (or state of agglomeration of flow field bodies) that an investigator *decides* is in its fully-developed state. There are several types and descriptions of developing (or transient) flow patterns in experiments that are not usually reported in internal lab reports or journal publications. Therefore, among the infinite possibilities of flow field descriptions that can occur during the course of the actual experiments, only the descriptions that an investigator *decides* that resemble the widely-accepted flow patterns are reported. As a concrete example, Azzopardi and Hills (2003) points out that the decision to categorize flow patterns using flash photographs in some steam-water studies at the Harwell Laboratory in the 1960's were made "by majority vote among a team of experts!". The *judgment* on how to identify flow patterns in two-phase flows is similarly present in three-phase flows (e.g., pg. 259 of Pan, 1996).

Recently, Nguyen et al. (2010) reviewed the means by which investigators make the classification decision, whether conventionally from visual, photographic or video observations (i.e. sensory perception), from pattern detection or transition indicator means, or from statistical analysis of fluctuations in structural (e.g. volume fraction) or energetic (e.g. differential pressure) signals. Unique methods for flow pattern detection have also been proposed (e.g. Cai et al., 1996, Hervieu and Seleghim, 1998). Also, surveys of studies on the statistical signal analysis methods for identifying developed flow patterns in pipe flow can be found in Hubbard (1965), Hubbard and Dukler (1966), Jones Jr. and Zuber (1975), Hewitt (1978), Vince and Lahey, Jr. (1982), Drahos and

Cermak (1989) and Costigan and Whalley (1997). More recently, attempts have been made to identify developed flow patterns based on machine learning algorithms (e.g., Ternyik et al., 1995, Osman, 2004, Trafalis et al., 2005, Tam et al., 2009), or using fractal analysis, pressure fluctuations and other methods (e.g., Vial et al., 2000).

Hewitt (1977) reminds of us of the limitations of the various methods of delineating flow patterns, and sets the overall understanding upfront: "It should be realized at the outset that the definition of flow patterns is often rather arbitrary and the classification is almost always arrived at on the basis of qualitative rather than quantitative evidence". Mao and Dukler (1993) highlight the deceptive nature of visual observations: "Visual observation of two-phase flow can be notoriously deceptive. The presence of multiple interfaces which scatter transmitted and reflected light in complex ways create visual images which may not be correct".

In reference to the modern trend of stochastic analysis methods, Whalley (1996) points out that even though various flow patterns may display idealized signal responses, the results "are rarely conclusive and so interpretation is again subjective". Proof of this latter statement can be found in the brief communications between Mao and Dukler (1993) and Hewitt and Jayanti (1993) on whether churn flow exists or not. In this case, these investigators had opposing views on the very existence of churn flow even though they both used combinations of photographic evidence, models and statistical signal analysis methods to support their arguments. Indeed, it now becomes clear that not only are flow patterns U-variables but that they will remain as U-variables because, as Persen (1986) eloquently states, "Different people look at one and the same situation and see different things".

D.2 ACCEPTED DESCRIPTIONS

Apart from the various means available to help investigators make the decision on the state of development of a prevailing flow pattern, even what is considered as an accepted developed flow pattern varies from investigator to investigator and with respect to different types of phase combinations. In some instances, one may find investigators who will make specific claims about the number of flow patterns that can be expected in a multiphase flow, e.g., "When a gas and a liquid are forced to flow together inside a pipe, there are at least 7 different geometrical configurations, or flow regimes, that are observed to occur" (McCready, 1998, http://www3.nd.edu/~mjm/flow.regimes.html). In other instances, a set of well-accepted flow patterns are grouped according to just a few basic descriptions, such as "separated", "mixed/transitional/intermittent" and "dispersed" (Ishii, 1975).

In terms of specific flow patterns, some vertical-flow, vapor-liquid investigators may promote that *cap-bubbly* should be added to the accepted set of vertical flow patterns (e.g., Schlegel et al, 2009, Qi et al., 2012). Others may advocate that *churn-annular* and *wispy-annular* should be added (e.g., Hewitt et al., 1985, Hawkes et al., 2000, Barbosa Jr. et al., 2001, Hewitt, 2012). A new investigator with an expanded vocabulary can offer yet another opinion on what constitutes an accepted set of flow patterns for a given scenario. This is a never-ending approach.

D.3 REDUCED DESCRIPTIONS

Lastly, it should be noted that not all investigators agree on whether the categorization of flow patterns into reduced, major descriptions is a useful tool for problem solving or not. As pointed examples, some researchers will promote the view that "The number of flow patterns used in any description should be limited if the

descriptions are to be of any use" (Azzopardi and Hills, 2003), or, "The trick is to make a suitable compromise with detail to obtain a minimum number of categories that provide useful starting points for the process of modeling (Dukler and Taitel, 1986), whereas others will state that development work on their flagship research code "needs to be extended to cover the whole gamut of flow regimes" (pg. 14 of the Transient Multiphase Flow Prospectus, Mattar and Hewitt, 2011).

Indeed, even if investigators were to somehow decide on reduced, major classifications of flow patterns, the ensuing detrimental impact is that it would then become a reporting necessity to change the actual flow pattern descriptions observed in experiments to that of what investigators perceive as being the closet major description of a "widely accepted" flow pattern. Unfortunately, this practice already exists in academic institutions (e.g. as shown in Table A-2 of Chen, 2001, or, in the AIChE-DIMP report of Choe and Weisman, 1974) as well as in companies that have assembled multiphase pipe flow data into interrogable databases (e.g., as is shown in section 1.3.3 of the PIPESIM User Guide, 2011). Therefore, if a model depends on the flow pattern a-priori for its solution, then this practice of changing the actual observed flow pattern data to one of the perceived, closest major descriptions could lead to a wrong classification of the model, and thus eventually, to a systematic wrong result from that model apart from the actual merits of the physical arguments or principles underlying the model.

Appendix E – Examples of Past Unreasonable Arguments and Practices

In this appendix, we furnish concrete examples of obviously bad or unreasonable arguments from the prior, published averaged multiphase pipe flow literature. These examples showcase various ways in which the reasoning upon which prior models are based may fail the first conceptual model validation criterion of Section 1.3.5.1 in Chapter 1. There are numerous examples of such arguments in the literature, such as in:

I. The omitting of test data from the model validation procedure for reason that the model could not yield a solution or failed to converge for these data (e.g., Govier and Fogarasi, 1975; Reinicke et al., 1987; Peffer et al., 1988; Barbuto and Crowley, 1991; Gomez et al., 1999; Kabir and Hasan, 2004).

II. The omitting of test data from the model validation procedure for reason that the model predicted poorly for these data and/or other selected models' predictions were equally bad (e.g., Messulam, 1970; Govier and Fogarasi, 1975, Kabir and Hasan, 1990).

III. The omitting of test data from a model validation procedure for reason that the modelers consider that the data "behave erratically" (Kabir and Hasan, 1990), i.e., the omission of five out of twenty-two wells of Orkiszewski, 1967, presumably the same five wells omitted in TUFFP's wells database, namely, Orkiszewski's well nos. 6, 14, 15, 19 and 22.

IV. The changing of measured/observed system parameters in order to obtain matches of test data to model predictions (e.g., altering the wellbore length in Aydelotte, 1980; altering the reported discharge mass flow rate in Garg et al., 1998; "complexifying" the pipeline geometry in Zakarian et al., 2009).

V. The tuning of a model to one set of small-diameter, low-pressure, air-water data and then claiming “extraordinarily good scale up properties” of the model for other fluids and “over a wide range of high pressure large-diameter data” (Biberg et al., 2009).

VI. The undertaking of an experimental multiphase flow loop campaign in search of data that supports/explains the predictions and mathematical consequences of a theory (Smith, 1999). This, of course, represents the reverse roles of an experiment and a theory.

VII. The experience-based view of a group of Petroleum investigators that a computational algorithm using the same equations and solved in the same manner with identical data in the same pipe conduit discretized in the same way, can yield significantly more model prediction errors if solving with a fixed downstream boundary condition instead of a fixed upstream one (e.g., Robinson, 1974; Ibe, 1979; Gregory et al. 1980; Rossland, 1981; Thompson, 1982; Kabir and Hasan, 1990; Barbuto and Crowley, 1991; Corteville et al., 1991; Kaya et al., 2001; Takacs, 2001; pg. 33 of Hasan and Kabir, 2002; Hasan et al., 2009, WELLFLO 7 Technical Reference Manual, Pipelines and Wells Sections, 2009).

With regard to the last issue above, which is sometimes called a “phenomenon” (Tacaks, 2001), we draw attention to readers that it is a simple matter to actually write a code of the computational algorithm in question – the “marching algorithm” – to demonstrate the equivalence of the hydrodynamic solutions (with respect to the location of the boundary conditions) arising out of this algorithm in many multiphase pipe flow scenarios. This was done by this author in contrast to acquiring the same code-copies

shared among industry consultants or passed on from academic short courses. Evidently, the algorithm itself works as intended. This finding narrows the explanation for the noted wide differences in errors among this group to the question of how the algorithm is computationally implemented in different research or commercial codes. Indeed, it would serve quite instructive to have the marching algorithm coded as part of, say an undergraduate coding assignment, to demonstrate the equivalence of the hydrodynamic solutions arising out of this algorithm.

Additionally, readers should also be aware that a historical reason for the noted wide differences in errors is that multiphase pressure gradients are considered by some members of this group to be most accurate "for a single-phase flow regime or one very close to being single-phase" (Corteville et al., 1991). Of course, the well-known observations of very poor multiphase pressure gradient predictions for annular flow and low-liquids loading directly counter such opinions. In fact, among this group, there can be found the opinion that in annular flow, "the system may be looked upon as the single-phase flow of gas through a tube of slightly reduced diameter because of the liquid film" (Hasan and Kabir, 1988a). In any event, from a purely mathematical standpoint regarding the last issue above, any equation (or equations) will give the same answer for the same data regardless of whether it is believed to be more or less accurate.

Lastly, it should be noted that in cases where test data are omitted from model validation procedures, investigators may still use the measurements of the omitted test data to summarize the range of data used in the validation. Moreover, in some cases (e.g., a careful examination of the "No. of Cases" in Table 2 of Ansari, 1988), there may be the undeclared omission of large amounts of test data in a model validation procedure.

Appendix F – Closure Relations and Applications of Decoupled Flow

F.1 Decoupled Two-Phase Flow

In this Appendix, we provide closure for the net momentum flux transfer surfaces for decoupled flow (discussed in Sections 2.2.3.1 and 2.2.3.2 of Chapter 2) in terms of simple analytical equations for two-phase, three-phase, four-phase flows, and in general, for any number of flowing phases.

If we now consider a generic two-phase flow, as shown in Fig. F.1, we see that there can be several momentum flux transfer surfaces in the flow. For phase-2 (j = 2) in a coupled two-phase flow, as shown in Fig. F.1 (a):

I. There is a unit momentum flux transfer surface from phase-2 to the wall, $Z_{2\to wall}$.

II. Because there is no preferred direction for momentum transfer to the wall, there is another unit momentum flux transfer surface from phase-2 to the wall via phase-1, $Z_{1\to wall}$.

Note that the colors of the unit momentum flux transfer surfaces (blue for phase-1 and black for phase-2, red for the difference between phases) are meant to align with the colors shown in Fig. F.1. The same line of reasoning as applied to phase-2 above also applies to phase-1. Therefore, we can define the (unit) net momentum flux transfer surfaces for phases 1 and 2 in a generic, coupled two-phase flow as:

$$\begin{aligned} Z_2^{net} &= Z_{2\to wall} + Z_{1\to wall} = Z \\ Z_1^{net} &= Z_{1\to wall} + Z_{2\to wall} = Z \end{aligned} \tag{F.1}$$

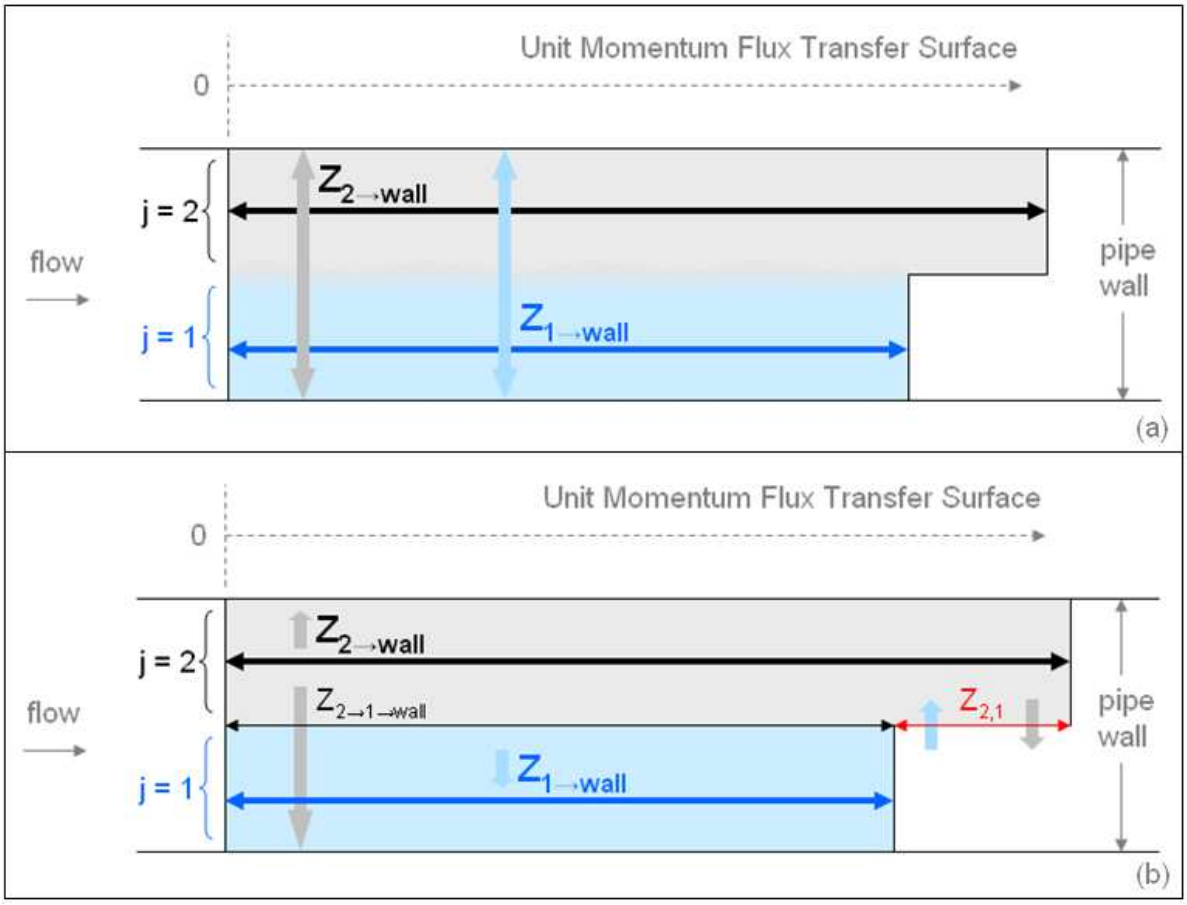

Figure F.1: Generic two-phase flow, (a) with no preferential directions for momentum transfer from the flow field to the wall – coupled flow, and (b) with preferential direction through the more efficient conductors of momentum, the more viscous (lower numbered) phases – decoupled flow.

For phase-2 in a decoupled two-phase flow, as shown in Fig. F.1 (b):

I. There is a unit momentum flux transfer surface from phase-2 to the wall, $Z_{2\rightarrow wall}$.

II. Because there is now a preferred direction for momentum transfer to the wall via phase-1 (the more viscous phase), there are two other unit momentum flux transfer surfaces $Z_{2\to1\to wall} + Z_{1\to wall} = 2Z_{1\to wall}$ from phase-2 to the wall.

III. There is a unit momentum flux transfer surface between phase-2 and its adjacent phase, phase-1, $Z_{2,1}$. This transfer surface is shared between these adjacent phases.

Therefore, we can define the (unit) net phase-2 momentum flux transfer surface in a generic, decoupled two-phase flow as:

$$Z_2^{net} = Z_{2\to wall} + 2Z_{1\to wall} + \frac{Z_{2,1}}{2} \tag{F.2a}$$

Similarly, for phase-1 in a decoupled two-phase flow, as shown in Fig. F.1 (b):

I. There is a unit momentum flux transfer surface from phase-1 to the wall, $Z_{1\to wall}$.

II. There is a unit momentum flux transfer surface between phase-1 and its adjacent phase, phase-2, $Z_{2,1}$. This transfer surface is shared between these adjacent phases.

Therefore, similar to Eqn. F.2a, we can define the (unit) net phase-1 momentum flux transfer surface in a generic, decoupled two-phase flow as:

$$Z_1^{net} = Z_{1\to wall} + \frac{Z_{2,1}}{2} \tag{F.2b}$$

F.2 DECOUPLED THREE-PHASE FLOW

We now consider a generic three-phase flow, as shown in Fig. F.2, and proceed in the same manner as before by considering the unit momentum flux transfer surfaces for each phase. For phase-3 (j = 3) in a coupled flow, as shown in Fig. F.2 (a):

I. There is a unit momentum flux transfer surface from phase-3 to the wall, $Z_{3\to wall}$.

II. Because there is no preferred direction for momentum transfer to the wall, there are two other unit momentum flux transfer surfaces from phase-3 to the wall via phases 2 and 1, $Z_{2\to wall}$ and $Z_{1\to wall}$, respectively.

As before, the colors of the unit momentum flux transfer surfaces (green for phase-1, blue for phase-2, black for phase-3, red for the differences between phases) are meant to align with the colors shown in Fig. F.2. The same line of reasoning as applied to phase-3 above also applies to phases 1 and 2. Therefore, we can define the (unit) net momentum flux transfer surfaces for phases 1, 2 and 3 in a generic, coupled three-phase flow as:

$$\begin{aligned} Z_3^{net} &= Z_{3\to wall} + Z_{2\to wall} + Z_{1\to wall} = Z \\ Z_2^{net} &= Z_{2\to wall} + Z_{3\to wall} + Z_{1\to wall} = Z \\ Z_1^{net} &= Z_{1\to wall} + Z_{2\to wall} + Z_{3\to wall} = Z \end{aligned} \tag{F.3}$$

For phase-3 in a decoupled three-phase flow, as shown in Fig. F.2 (b):

I. There is a unit momentum flux transfer surface from phase-3 to the wall, $Z_{3\to wall}$.

II. Because there is now a preferred direction for momentum transfer to the wall via phases 2 and 1 (the more viscous phases), there are four other unit momentum flux transfer surfaces $Z_{3\to 2\to wall} + Z_{2\to wall} + Z_{2\to 1\to wall} + Z_{1\to wall} = 2Z_{2\to wall} + 2Z_{1\to wall}$ from phase-3 to the wall.

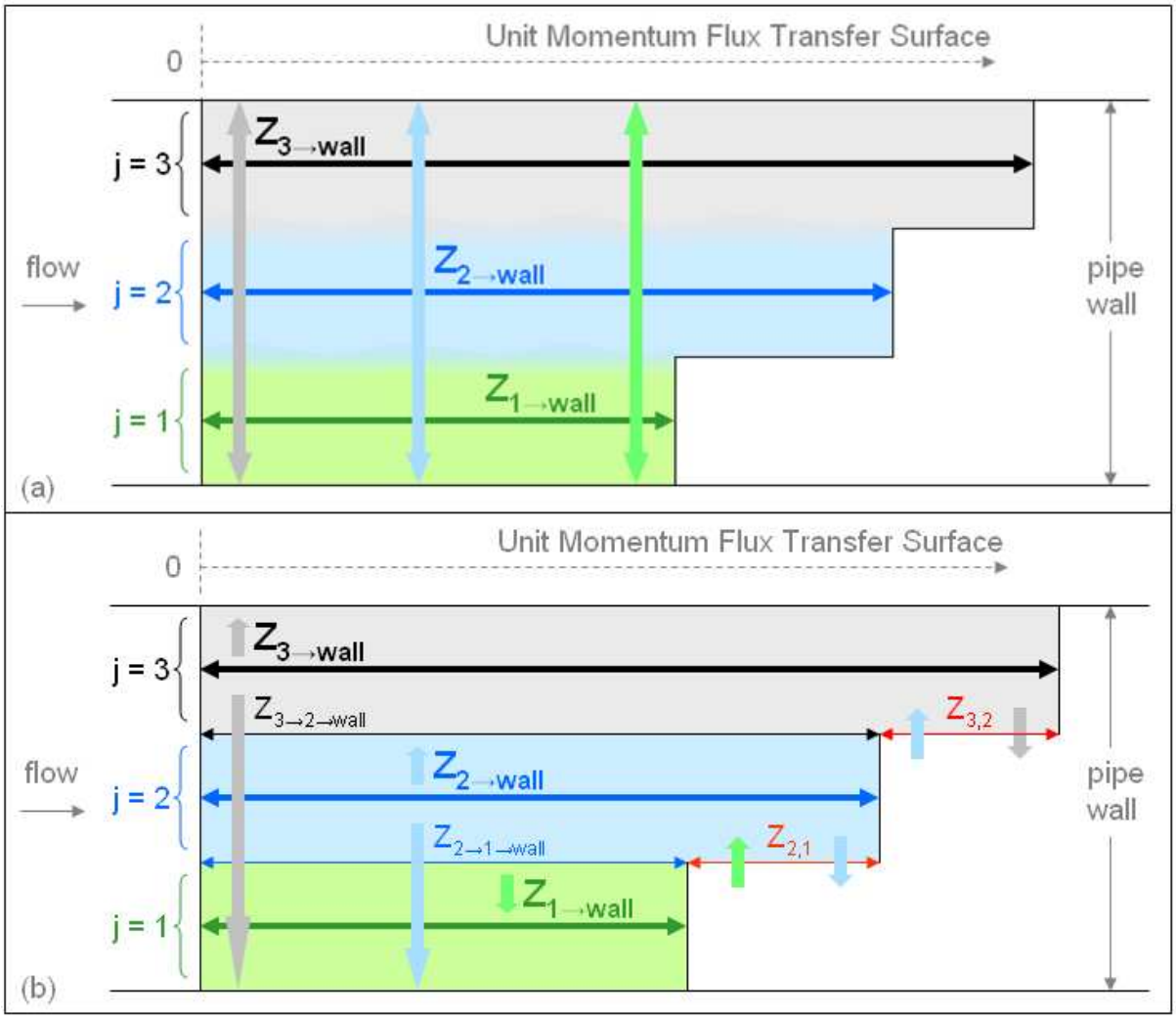

Figure F.2: Generic three-phase flow, (a) with no preferential directions for momentum transfer from the flow field to the wall – coupled flow, and (b) with a preferential direction through the more efficient conductors of momentum, the more viscous (lower numbered) phases – decoupled flow.

III. There is a unit momentum flux transfer surface between phase-3 and its adjacent phase, phase-2, $Z_{3,2}$. This transfer surface is shared between these adjacent phases.

Therefore, we can define the (unit) net phase-3 momentum flux transfer surface in a generic, decoupled three-phase flow as:

$$Z_3^{net} = Z_{3\to wall} + 2Z_{2\to wall} + 2Z_{1\to wall} + \frac{Z_{3,2}}{2} \tag{F.4a}$$

Similarly, for phase-2 in a decoupled three-phase flow, as shown in Fig. F.2 (b):

I. There is a unit momentum flux transfer surface from phase-2 to the wall, $Z_{2\to wall}$.

II. Because there is now a preferred direction for momentum transfer to the wall via phase 1 (the more viscous phase), there are two other unit momentum flux transfer surfaces $Z_{2\to 1\to wall} + Z_{1\to wall} = 2Z_{1\to wall}$ from phase-2 to the wall.

III. There is a unit momentum flux transfer surface between phase-2 and its upper adjacent phase, phase-3, $Z_{3,2}$. This transfer surface is shared between these upper adjacent phases.

IV. There is a unit momentum flux transfer surface between phase-2 and its lower adjacent phase, phase-1, $Z_{2,1}$. This transfer surface is shared between these lower adjacent phases.

Therefore, similar to Eqn. F.4a, we can define the (unit) net phase-2 momentum flux transfer surface in a generic, decoupled three-phase flow as:

$$Z_2^{net} = Z_{2\to wall} + 2Z_{1\to wall} + \frac{Z_{3,2}}{2} + \frac{Z_{2,1}}{2} \tag{F.4b}$$

Next, for phase-1 in a decoupled three-phase flow, as shown in Fig. F.2 (b):

I. There is a unit momentum flux transfer surface from phase-1 to the wall, $Z_{1\to wall}$.

II. There is a unit momentum flux transfer surface between phase-1 and its adjacent phase, phase-2, $Z_{2,1}$. This transfer surface is shared between these adjacent phases.

Therefore, we can define the (unit) net phase-1 momentum flux transfer surface in a generic, decoupled three-phase flow as:

$$Z_1^{net} = Z_{1\to wall} + \frac{Z_{2,1}}{2} \tag{F.4c}$$

F.3 Decoupled Four-Phase Flow

Following the same reasoning as the developments above, we can consider a generic four-phase flow, as shown in Fig. F.3, and proceed in the same manner as before by considering the unit momentum flux transfer surfaces for each phase. In doing this, we find (from Fig. F.3a) the (unit) net phase momentum flux transfer surfaces for phases 1, 2, 3 and 4 in a generic, coupled four-phase flow can be stated as:

$$\begin{aligned}
Z_4^{net} &= Z_{4\to wall} + Z_{3\to wall} + Z_{2\to wall} + Z_{1\to wall} = Z \\
Z_3^{net} &= Z_{3\to wall} + Z_{4\to wall} + Z_{2\to wall} + Z_{1\to wall} = Z \\
Z_2^{net} &= Z_{2\to wall} + Z_{3\to wall} + Z_{4\to wall} + Z_{1\to wall} = Z \\
Z_1^{net} &= Z_{1\to wall} + Z_{2\to wall} + Z_{3\to wall} + Z_{4\to wall} = Z
\end{aligned} \tag{F.5}$$

Similarly, we find (from Fig. F.3b) the (unit) net phase momentum flux transfer surfaces for phases 1, 2, 3 and 4 in a generic, decoupled four-phase flow can be stated as:

$$Z_4^{net} = Z_{4\to wall} + 2Z_{3\to wall} + 2Z_{2\to wall} + 2Z_{1\to wall} + \frac{Z_{4,3}}{2} \tag{F.6a}$$

$$Z_3^{net} = Z_{3\to wall} + 2Z_{2\to wall} + 2Z_{1\to wall} + \frac{Z_{4,3}}{2} + \frac{Z_{3,2}}{2} \tag{F.6b}$$

$$Z_2^{net} = Z_{2\to wall} + 2Z_{1\to wall} + \frac{Z_{3,2}}{2} + \frac{Z_{2,1}}{2} \tag{F.6c}$$

$$Z_1^{net} = Z_{1\to wall} + \frac{Z_{2,1}}{2} \tag{F.6d}$$

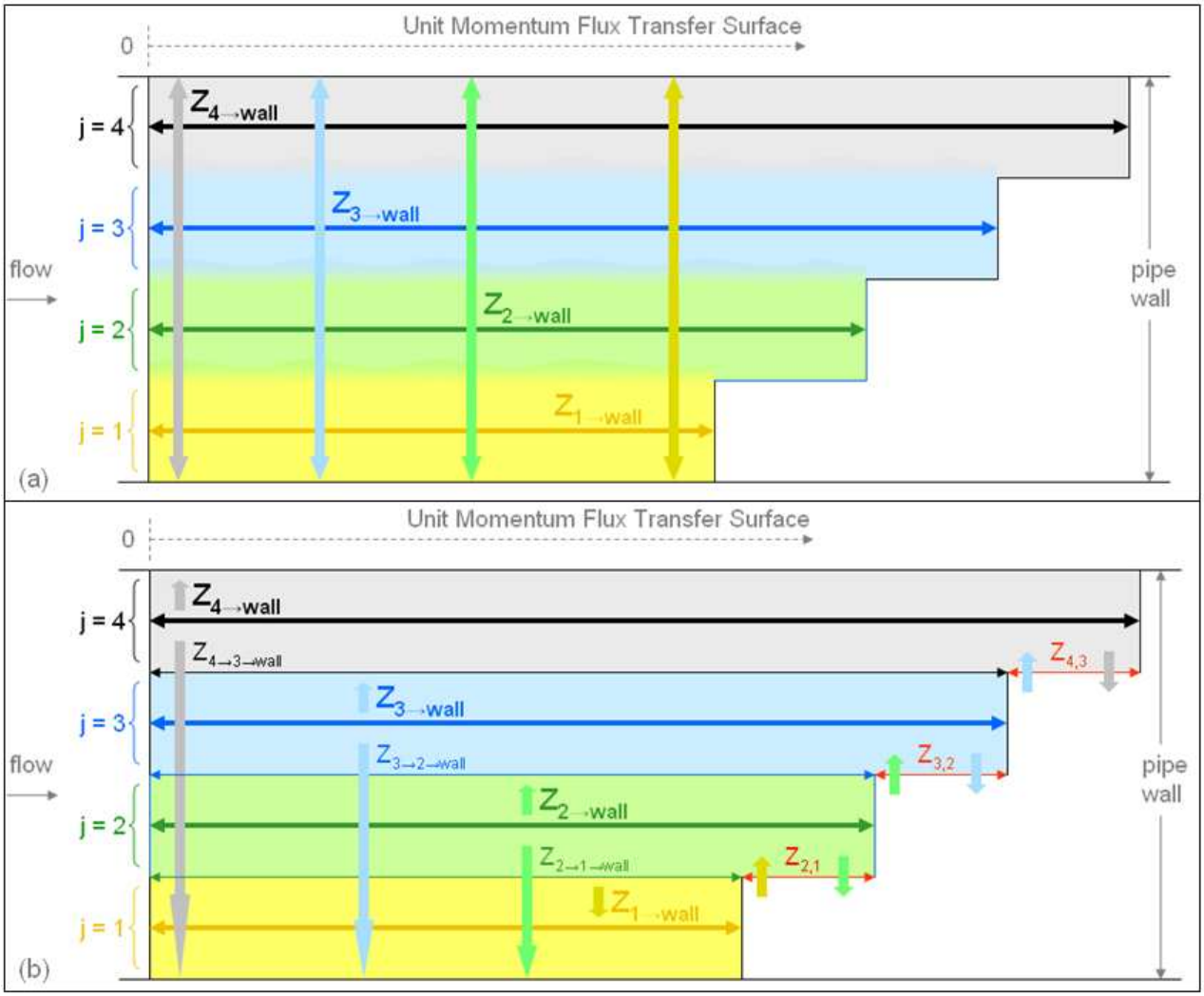

Figure F.3: Generic four-phase flow, (a) with no preferential directions for momentum transfer from the flow field to the wall – coupled flow, and (b) with a preferential direction through the more efficient conductors of momentum, the more viscous (lower numbered) phases – decoupled flow.

As before, the colors of the unit momentum flux transfer surfaces (yellowish-orange for phase-1, green for phase-2, blue for phase-3, black for phase-4 and red for the differences between phases) are meant to align with the colors shown in Fig. F.3.

F.4 DECOUPLED N-PHASE FLOW

We can now (formally) generalize the coupled and decoupled flow equations shown previously for two-phase, three-phase and four-phase flow for any number of phases. For a coupled multiphase flow of N_p phases, the general, analytical relation for Z_j^{net} is simply:

$$Z_j^{net} = \sum_{j}^{N_p} \left(Z_{j \to wall} \right) = Z \tag{F.7}$$

For a decoupled multiphase flow of N_p phases, the general, analytical relation for Z_j^{net} is:

$$Z_j^{net} = \sum_{k=1}^{N_p} \left(\overbrace{W_k(j)}^{\substack{phase-to-wall \\ path\ (wall) \\ operator}} Z_{k \to wall} + \overbrace{I_k(j)}^{\substack{phase-to-phase \\ path\ (interface) \\ operator}} \overbrace{\left(\frac{Z_{k+1,k}}{2} \right)}^{\substack{shared\ interface \\ between\ adjacent \\ phases}} \right) \tag{F.8a}$$

Where,

$$W_k(j) = \overbrace{u_k(j) + u_{k+1}(j)}^{wall\ Heaviside\ operator} \tag{F.8b}$$

And,

$$I_k(j) = \overbrace{u_k(j) u_{k+1}(N_p)\left(1 - u_{k+2}(j)\right)}^{interface\ Heaviside\ operator} \tag{F.8c}$$

And the general Heaviside function is defined as:

$$u_a(j) = \begin{cases} 0 & if\ j < a \\ 1 & if\ j \geq a \end{cases} \tag{F.8d}$$

Eqns. F.8a – F.8d describe in concise mathematical terms, the generic decoupled flow scenario of any number of phases, N_p, flowing through any arbitrary pipe cross-section.

F.5 SPECIFIC DECOUPLED FLOW APPLICATIONS

From Eqn. F.8a, the only required inputs that changes according to the pipe geometry (D_H and A) and averaged volume fraction, $\langle s_j \rangle$, are $Z_{j\to wall}$ and $Z_{j,k\neq j}$, which are the unit momentum flux transfer surfaces through which there is momentum transport from phase-j to the wall and from phase-j to phase-k, respectively. Similar to the definition of net momentum flux transfer surface, these transfer surfaces are averaged flow (mathematical) quantities that define the averaged momentum transport occurring between the flow field and the wall (and between the flowing phases themselves). Nevertheless, we can relate these quantities to an idealized physical flowing geometry of the various phases that are expected to occur in a decoupled pipe flow.

Recall, in the decoupled flow scenario, the net of the prevailing forces will ensure that the bulk movements of phases are restricted to localized regions of the flow field during flow, thereby furnishing the conditions for preferred paths for phase-to-wall momentum fluxes. Therefore, in the simplest (idealized) approximation, $Z_{j\to wall}$ and $Z_{j,k\neq j}$ can be analytically determined from the various phase interfaces formed in various pipe geometries, as if the phases flow as flat adjacent layers, as we will see in the few specific applications below.

Testing Eqns. F.8a – F.8d above, we can see that for a <u>single-phase flow</u> ($N_p = 1$):

$$Z_1^{net} = Z_{1\to wall} \tag{F.9}$$

In Eqn. F.9, $Z_{1\to wall}$ is the unit momentum flux transfer surface describing the geometry of the phase-1-to-wall interface. For single-phase flow in a circular pipe, for example, $Z_{1\to wall} = \pi D_H$.

For a <u>two-phase flow</u> ($N_p = 2$), Eqns. F.8a – F.8d yield:

$$Z_1^{net} = Z_{1\to wall} + \frac{Z_{2,1}}{2}$$
$$Z_2^{net} = Z_{2\to wall} + 2Z_{1\to wall} + \frac{Z_{2,1}}{2} \qquad \text{(F.10)}$$

In Eqn. F.10, for a rectangular pipe of width, w, and height, h, we can write:

$$Z_{1\to wall} = 2h\left(1-\langle s_2\rangle\right) + w \;,\; Z_{2\to wall} = 2h\langle s_2\rangle + w$$
$$Z_{2,1} = w \qquad \text{(F.11a)}$$

In Eqn. F.11a above, the width, w, and height, h, can be alternatively expressed in terms of the hydraulic diameter, D_H, and flowing area, A, as:

$$w = \frac{A}{D_H} + \left(A\left(\frac{A}{(D_H)^2} - 1\right)\right)^{\frac{1}{2}} \;,\; h = \frac{A}{D_H} - \left(A\left(\frac{A}{(D_H)^2} - 1\right)\right)^{\frac{1}{2}} \qquad \text{(F.11b)}$$

Similarly, in Eqn. F.10, for a circular pipe, we can write:

$$Z_{1\to wall} = D_H\left(\frac{\delta_1^{2P}}{2}\right) \;,\; Z_{2\to wall} = D_H\left(\pi - \left(\frac{\delta_1^{2P}}{2}\right)\right)$$
$$Z_{2,1} = D_H \sin\left(\frac{\delta_1^{2P}}{2}\right) \qquad \text{(F.12a)}$$

In Eqn. F.12a above, δ_1^{2P} is the circular-pipe center-angle subtending the flat phase-1 surface in a two-phase (or "2P") scenario. In this scenario, δ_1^{2P} can be geometrically (exactly) related to the phase-2 volume fraction, $\langle s_2\rangle$, as:

$$\delta_1^{2P} - \sin\delta_1^{2P} = 2\pi\left(1-\langle s_2\rangle\right) \qquad \text{(F.12b)}$$

Though δ_1^{2P} in Eqn. F.12b is not explicit in $\langle s_2\rangle$, it can be simply approximated to +/- 0.002 radians as an explicit function of $\langle s_2\rangle$ by the analytical relation (Biberg, 1999):

$$\delta_1^{2P} = 2\left(\pi\left(1-\langle s_2\rangle\right) + \left(\frac{3\pi}{2}\right)^{\frac{1}{3}}\left(1 - 2\left(1-\langle s_2\rangle\right) + \left(1-\langle s_2\rangle\right)^{\frac{1}{3}} - \langle s_2\rangle^{\frac{1}{3}}\right)\right) \qquad \text{(F.12c)}$$

The definition of δ_1^{2P} in Eqn. F.12c can then be used in the relations in Eqn. F.12a for providing simple, analytical and explicit closure of the $Z_{j\to wall}$ and $Z_{j,k\neq j}$ terms for the two-phase, circular-pipe, decoupled flow scenario described by Eqn. F.12a.

With respect to the two-phase, decoupled flow equations above, it should be kept in mind that the circular-pipe decoupled flow equations in Eqn. F.12a can be (and should be) used as a first estimate for closing Eqn. F.10 for any cross-sectional conduit shape. This may be necessary if the terms on the right hand side of Eqn. F.10 cannot easily be specified for a particular non-circular cross-section shape, e.g., in cases where $Z_{2,1}$ might change with height such as in a triangular or trapezoidal pipe.

For <u>three-phase flows</u> ($N_p = 3$), Eqns. F.8a – F.8d yield:

$$\begin{aligned} Z_1^{net} &= Z_{1\to wall} + \frac{Z_{2,1}}{2} \\ Z_2^{net} &= Z_{2\to wall} + 2Z_{1\to wall} + \frac{Z_{3,2}}{2} + \frac{Z_{2,1}}{2} \\ Z_3^{net} &= Z_{3\to wall} + 2Z_{2\to wall} + 2Z_{1\to wall} + \frac{Z_{3,2}}{2} \end{aligned} \tag{F.13}$$

In Eqn. F.13, for a circular pipe, we can write:

$$\begin{gathered} Z_{1\to wall} = D_H\left(\frac{\delta_1^{3P}}{2}\right),\ Z_{2\to wall} = D_H\left(\frac{\delta_{2\ and\ 1}^{3P}}{2}\right),\ Z_{3\to wall} = D_H\left(\pi - \left(\frac{\delta_1^{3P}}{2}\right) - \left(\frac{\delta_{2\ and\ 1}^{3P}}{2}\right)\right) \\ Z_{2,1} = D_H \sin\left(\frac{\delta_1^{3P}}{2}\right),\ Z_{3,2} = D_H \sin\left(\frac{\delta_{2\ and\ 1}^{3P}}{2}\right) \end{gathered} \tag{F.14a}$$

In Eqn. F.14a, similar to δ_1^{2P} in Eqn. F.12b, we can write for the three-phase (or "3P") case:

$$\delta_1^{3P} = 2\left(\pi\left(1-\langle s_2\rangle-\langle s_3\rangle\right)+\left(\frac{3\pi}{2}\right)^{\frac{1}{3}}\left(1-2\left(1-\langle s_2\rangle-\langle s_3\rangle\right)+\left(1-\langle s_2\rangle-\langle s_3\rangle\right)^{\frac{1}{3}}-\left(\langle s_2\rangle+\langle s_3\rangle\right)^{\frac{1}{3}}\right)\right) \tag{F.14b}$$

And,

$$\delta_{2\ and\ 1}^{3P} = 2\left(\pi\left(1-\langle s_3\rangle\right)+\left(\frac{3\pi}{2}\right)^{\frac{1}{3}}\left(1-2\left(1-\langle s_3\rangle\right)+\left(1-\langle s_3\rangle\right)^{\frac{1}{3}}-\left(\langle s_3\rangle\right)^{\frac{1}{3}}\right)\right) \tag{F.14c}$$

The definitions of δ_1^{3P} in Eqn. F.14b and $\delta_{2\ and\ 1}^{3P}$ in Eqn. F.14c can then be used in the relations in Eqn. F.14a for providing simple, analytical and explicit closure of the $Z_{j\to wall}$ and $Z_{j,k\neq j}$ terms for the three-phase, circular-pipe, decoupled flow scenario described by Eqn. F.14a.

Appendix G – Analytical Multi-Directional Entrainment

In this Appendix, we present simple, analytical closure relations describing multi-directional inter-phase entrainment in the special case of annular-dispersed vapor-liquid and vapor-liquid-liquid flows.

G.1 Bi-Directional Two-Phase Entrainment

For a phase-j flowing in a multiphase mixture of two or more phases, we can write:

$$\rho_j = \frac{G_j}{\langle u_j \rangle} = \frac{phase-j\ mass\ \ flux}{phase-j\ volume\ \ flux} \tag{G.1}$$

For phase 1 being entrained into phase 2, if we first look at j = 2, we can correct the above mass flux and volume flux for j = 2 to account for this as:

$$\rho_{2\leftarrow 1}^{corr} = \frac{G_2 \ + \ G_{1\to 2}^{entr}}{\langle u_2 \rangle \ + \ \langle u_{1\to 2}^{entr} \rangle} \tag{G.2}$$

Now, in general, entrainment is defined as:

$$E_{j\to k(\neq j)} = \frac{G_{j\to k(\neq j)}^{entr}}{G_j} \tag{G.3}$$

For phase 1 being entrained into phase 2, if we look at j = 1, we can write Eqn. G.3 as:

$$E_{1\to 2} = \frac{G_{1\to 2}^{entr}}{G_1} = \frac{\cancel{\rho_1} \langle u_{1\to 2}^{entr} \rangle}{\cancel{\rho_1} \langle u_1 \rangle} = \frac{\langle u_{1\to 2}^{entr} \rangle}{\langle u_1 \rangle} \tag{G.4}$$

Putting (G.1), (G.3) and (G.4) in (G.2), we get:

$$\rho_{2\leftarrow 1}^{corr} = \frac{\rho_2 \langle u_2 \rangle \ + \ \rho_1 \langle u_1 \rangle E_{1\to 2}}{\langle u_2 \rangle \ + \ \langle u_1 \rangle E_{1\to 2}} \tag{G.5}$$

Also, in general, by definition:

$$G_j^{corr} = G_j \ - \ G_{j\to k(\neq j)}^{entr} \tag{G.6}$$

Now, the key insight with regards to the principle of bi-directional two-phase entrainment is that during the entrainment of phase 1 into phase 2, simultaneously, the corrected phase 2 (which we will call phase 2′) will itself be entraining into the continuously diminishing phase 1 (i.e. the corrected phase 1 which we will call phase 1′). For phase 1 being entrained into phase 2, if we look at j=1, we can write:

$$G_1^{corr} = G_1 \; - \; G_{1\to 2}^{entr} \;\Rightarrow\; \cancel{\rho_{1'\leftarrow 2'}^{corr}} \left\langle u_1^{corr} \right\rangle = \cancel{\rho_{1'\leftarrow 2'}^{corr}} \left\langle u_1 \right\rangle \; - \; \cancel{\rho_{1'\leftarrow 2'}^{corr}} \left\langle u_{1\to 2}^{entr} \right\rangle \tag{G.7}$$

Putting (G.4) in (G.7), we get:

$$\left\langle u_1^{corr} \right\rangle = \left\langle u_1 \right\rangle \left(1 - E_{1\to 2}\right) \tag{G.8}$$

If we now look at j = 1′, we can now re-state Eqn. 1 as:

$$\rho_{1'\leftarrow 2'}^{corr} = \frac{G_1^{corr} \; + \; G_{2'\to 1'}^{entr}}{\left\langle u_1^{corr} \right\rangle \; + \; \left\langle u_{2'\to 1'}^{entr} \right\rangle} \tag{G.9}$$

Similar to Eqn. G.4, for phase 2′ being entrained into phase 1′, if we look at j = 2′, we can write Eqn. G.3 as:

$$E_{2'\to 1'} = \frac{G_{2'\to 1'}^{entr}}{G_{2'}} = \frac{\cancel{\rho_{2\leftarrow 1}^{corr}} \left\langle u_{2'\to 1'}^{entr} \right\rangle}{\cancel{\rho_{2\leftarrow 1}^{corr}} \left\langle u_2 \right\rangle} = \frac{\left\langle u_{2'\to 1'}^{entr} \right\rangle}{\left\langle u_2 \right\rangle} \tag{G.10}$$

Putting (G.1), (G.3), (G.7), (G.8) and (G.10) in (G.9), we can write:

$$\rho_{1'\leftarrow 2'}^{corr} = \frac{\rho_1 \left\langle u_1 \right\rangle \left(1 - E_{1\to 2}\right) \; + \; \rho_{2\leftarrow 1}^{corr} \left\langle u_2 \right\rangle E_{2'\to 1'}}{\left\langle u_1 \right\rangle \left(1 - E_{1\to 2}\right) \; + \; \left\langle u_2 \right\rangle E_{2'\to 1'}} \tag{G.11}$$

Similar to Eqn. G.7, for phase 2′ being entrained into phase 1′, if we look at j = 2′, we can write:

$$G_{2'}^{corr} = G_{2'} \; - \; G_{2'\to 1'}^{entr} \;\Rightarrow\; \cancel{\rho_{2\leftarrow 1}^{corr}} \left\langle u_{2'}^{corr} \right\rangle = \cancel{\rho_{2\leftarrow 1}^{corr}} \left\langle u_2 \right\rangle \; - \; \cancel{\rho_{2\leftarrow 1}^{corr}} \left\langle u_{2'\to 1'}^{entr} \right\rangle \tag{G.12}$$

Put (G.10) in (G.12), we get:

$$\left\langle u_{2'}^{corr} \right\rangle = \left\langle u_2 \right\rangle \left(1 - E_{2'\to 1'}\right) \tag{G.13}$$

Thus, from the simple development above, if bi-directional entrainment is occurring between any two arbitrary phases 1 and 2, then the phase densities and mass fluxes change (in order of calculation) as follows:

$$
\begin{aligned}
&\textit{Step 1 (Eqn. G.5):}\quad \rho_2 \;\rightarrow\; \rho_{2\leftarrow 1}^{corr} = \frac{\rho_2\langle u_2\rangle \;+\; \rho_1\langle u_1\rangle E_{1\rightarrow 2}}{\langle u_2\rangle \;+\; \langle u_1\rangle E_{1\rightarrow 2}} \\
&\textit{Step 2 (Eqn. G.11):}\quad \rho_1 \;\rightarrow\; \rho_{1'\leftarrow 2'}^{corr} = \frac{\rho_1\langle u_1\rangle(1-E_{1\rightarrow 2}) \;+\; \rho_{2\leftarrow 1}^{corr}\langle u_2\rangle E_{2'\rightarrow 1'}}{\langle u_1\rangle(1-E_{1\rightarrow 2}) \;+\; \langle u_2\rangle E_{2'\rightarrow 1'}} \\
&\textit{Step 3 (Eqn. G.13):}\quad G_{2'} \;\rightarrow\; G_{2'}^{corr} = \rho_{2\leftarrow 1}^{corr}\langle u_2\rangle(1-E_{2'\rightarrow 1'}) \\
&\textit{Step 4 (Eqn. G.8):}\quad G_1 \;\rightarrow\; G_1^{corr} = \rho_{1'\leftarrow 2'}^{corr}\langle u_1\rangle(1-E_{1\rightarrow 2})
\end{aligned}
\qquad \text{(G.14)}
$$

Now, a post-analysis of any of the relations above will reveal both a physically sensible and internal self-consistency. Firstly, testing the limits of Eqns. G.5 and G.8, we see that:

I. For Eqn. G.5, $\rho_{2\leftarrow 1}^{corr}\Big|_{at\ E_{1\rightarrow 2}=0} = \rho_2$

II. For Eqn. G.5, $\rho_{2\leftarrow 1}^{corr}\Big|_{at\ E_{1\rightarrow 2}=1} = \dfrac{\overbrace{\rho_2\langle u_2\rangle}^{=G_2} \;+\; \overbrace{\rho_1\langle u_1\rangle}^{=G_1}}{\langle u_2\rangle \;+\; \langle u_1\rangle} = \overbrace{\left(\dfrac{G_{mix}}{\langle u_{mix}\rangle}\right)}^{\substack{homogenous\\ mixture\ density\ (mist\ flow)}}$

III. For Eqn. G.8, $G_1^{corr}\Big|_{at\ E_{1\rightarrow 2}=0} = G_1$

IV. For Eqn. G.8, $G_1^{corr}\Big|_{at\ E_{1\rightarrow 2}=1} = \overbrace{0}^{mist\ flow}$

Now, before we can similarly begin to test the limits of Eqns. G.11 and G.13, we note that the relationship between $E_{1\rightarrow 2}$ and $E_{2'\rightarrow 1'}$ can be stated analytically. To demonstrate this, we first know that if $E_{1\rightarrow 2}=0$ (i.e. no entrainment of phase 1 into phase 2), then $\rho_{1'\leftarrow 2'}^{corr}$ in Eqn. G.11 must be $=\rho_1$. Clearly, the only value of $E_{2'\rightarrow 1'}$ that satisfies this fact is 0. Therefore, we know the functional form of $E_{2'\rightarrow 1'}$ in relation to $E_{1\rightarrow 2}$ must, at a minimum, be expressed as:

$$E_{2'\to 1'} = E_{1\to 2} \times \ ? \tag{G.15}$$

Next, from a relative volume flux standpoint, if $E_{1\to 2} = 1$ (i.e. full entrainment of phase 1 into phase 2), then $\left\langle u_{2'}^{corr} \right\rangle$ must be $= \langle u_2 \rangle - \langle u_1 \rangle$. Using Eqn. G.8, this relative volume flux can be re-arranged as:

$$\left\langle u_{2'}^{corr} \right\rangle \Big|_{\text{at } E_{1\to 2}=1} = \langle u_2 \rangle \left(1 - \frac{\langle u_1 \rangle}{\langle u_2 \rangle} \right) \tag{G.16}$$

Now, comparing Eqn. G.16 with Eqn. G.13, a general relationship for $E_{2'\to 1'}$ that will satisfy both of the limits depicted in Eqns. G.15 and G.16 is:

$$E_{2'\to 1'} = E_{1\to 2} \left(\frac{\langle u_1 \rangle}{\langle u_2 \rangle} \right)^{p-(p-1)E_{1\to 2}} = E_{1\to 2} \left(\frac{\rho_2}{\rho_1} \frac{G_1}{G_2} \right)^{p-(p-1)E_{1\to 2}} \tag{G.17}$$

In Eqn. G.17 above, the parameter, p, can be any non-negative integer number and still satisfy the limits in Eqns. G.15 and G.16 at $E_{1\to 2} = 1$. We are thus faced with a positive-infinite number of possibilities for a functional form of $E_{2'\to 1'}$, even though it is clear how this variable must behave in the limits of $E_{1\to 2} = 0$ and $E_{1\to 2} = 1$. We therefore must make a hypothesis. We postulate based on the physical argument, that $E_{2'\to 1'}$ should be related to $E_{1\to 2}$ such that the entrainment of the less dense phase, phase 2′, into the more dense phase, phase 1′, will more easily occur when there is a lower amount of phase 1′ to entrain into (i.e. at higher values of $E_{1\to 2}$). This idea is only honored for p values of 2 and greater in Eqn. G.17. With no logical reason for choosing any value of p greater than 2, we must therefore set p at its simplest valid value according to our hypothesis, i.e. at p = 2. So our revised form for Eqn. G.17 is:

$$E_{2'\to 1'} = E_{1\to 2} \left(\frac{\langle u_1 \rangle}{\langle u_2 \rangle} \right)^{2-E_{1\to 2}} = E_{1\to 2} \left(\frac{\rho_2}{\rho_1} \frac{G_1}{G_2} \right)^{2-E_{1\to 2}} \tag{G.18}$$

With an analytical relation now in hand for $E_{2'\to 1'}$, we can now go back to testing the limits of Eqns. G.11 and G.13. We see that:

V. For Eqn. G.11, $\rho_{1'\leftarrow 2'}^{corr}\Big|_{\text{at } E_{1\to 2}=0 \text{ and } \therefore E_{2'\to 1'}=0} = \rho_1$

VI. For Eqn. G.11, $\rho_{1'\leftarrow 2'}^{corr}\Big|_{\text{at } E_{1\to 2}=1} = \dfrac{\overbrace{\rho_2\langle u_2\rangle}^{=G_2} + \overbrace{\rho_1\langle u_1\rangle}^{=G_1}}{\langle u_2\rangle + \langle u_1\rangle} = \overbrace{\left(\dfrac{G_{mix}}{\langle u_{mix}\rangle}\right)}^{\substack{\text{homogenous} \\ \text{mixture density (mist flow)}}}$

VII. For Eqn. G.13, $G_{2'}^{corr}\Big|_{\text{at } E_{1\to 2}=0 \text{ and } \therefore E_{2'\to 1'}=0} = G_2$

VIII. For Eqn. G.13, $G_{2'}^{corr}\Big|_{\text{at } E_{1\to 2}=1} = \overbrace{\left(\dfrac{G_{mix}}{\langle u_{mix}\rangle}\right)}^{\substack{\text{homogenous} \\ \text{mixture density (mist flow)}}} \cdot\left(\langle u_2\rangle - \langle u_1\rangle\right)$

As before, we see that there is a clear self-consistency to all of the analytical equations developed so far.

The next question that arises is the physical maximum possible limit on the derived relation $E_{2'\to 1'}$ in Eqn. G.18 above. Aside from the fact that this postulated functional form honors all mathematical consistency checks, if unrestricted, this form of $E_{2'\to 1'}$ can yield values greater than 1. Additionally, it is a common scenario in field applications where the mass flux of phases changes according to the changing pressure and temperature flowing conditions (e.g. as with complex petroleum fluids). Hence at the point that the mass flux of phase 1 attains the same value as the mass flux of phase 2, then it is reasonable to assume that it will be unlikely that any further entrainment of phase 2 into phase 1 will occur. So from Eqn. G.18, the physical maximum value of $E_{2'\to 1'}$ is ρ_2 / ρ_1, where all of phase 1 is entrained into phase 2, and the mass flux of phase 1 is equal to that of phase 2. If we are to consider the case where phase 1 is a liquid and phase 2 is a vapor, as an example, then this would mean that at any given entrainment fraction of the liquid in the vapor, the entrainment fraction of the vapor in the liquid (either in the liquid film or in the liquid droplets or in the liquid wisps, or all of the

previous) can at most be $= E_{liq\to vap}\left(\rho_{vap}/\rho_{liq}\right)^{2-E_{liq\to vap}}$. So the final, corrected form of Eqn. G.18 is given as:

$$E_{2'\to 1'} = \min\left(E_{1\to 2}\left(\frac{\rho_2}{\rho_1}\frac{G_1}{G_2}\right)^{2-E_{1\to 2}},\ E_{1\to 2}\left(\frac{\rho_2}{\rho_1}\right)^{2-E_{1\to 2}}\right) \qquad \text{(G.19)}$$

A graphical representation of Eqn. G.19 is given in Fig. G.1 below, where the purple lines represent a relative volume flux, $\langle u_1\rangle/\langle u_2\rangle$, value of 0.001, the blue lines represent a $\langle u_1\rangle/\langle u_2\rangle$ value of 0.01 and the orange lines represent a $\langle u_1\rangle/\langle u_2\rangle$ value of 0.1. These lines show the effect of having phase 1 flow increasingly faster as it approaches the volume flux of phase 2. Figures G.1(a), (b) and (c) represent three example scenarios showing increasing density ratios between the two phases with the value in Fig. G.1(a) being typical of vapor-liquid systems at lower pressures and temperatures and the value in Fig. G.1(c) being typical of vapor-liquid systems at much higher pressures and temperatures, i.e. as found under field conditions. It is clear from this plot, that it must be expected that entrainment behavior would be quite different between systems with a high density contrast (e.g. laboratory experiments) versus systems with a lower density contrast (e.g. field systems). This is quite important by itself and is unrelated to any field scale issue. In Fig. G.1(a), a high density contrast places limits on how much of phase 2 can be entrained into phase 1, especially at higher phase 1 rates relative to phase 2. Conversely, in Fig. G.1(c), the lower density contrast permits higher phase 2 entrainment into phase 1.

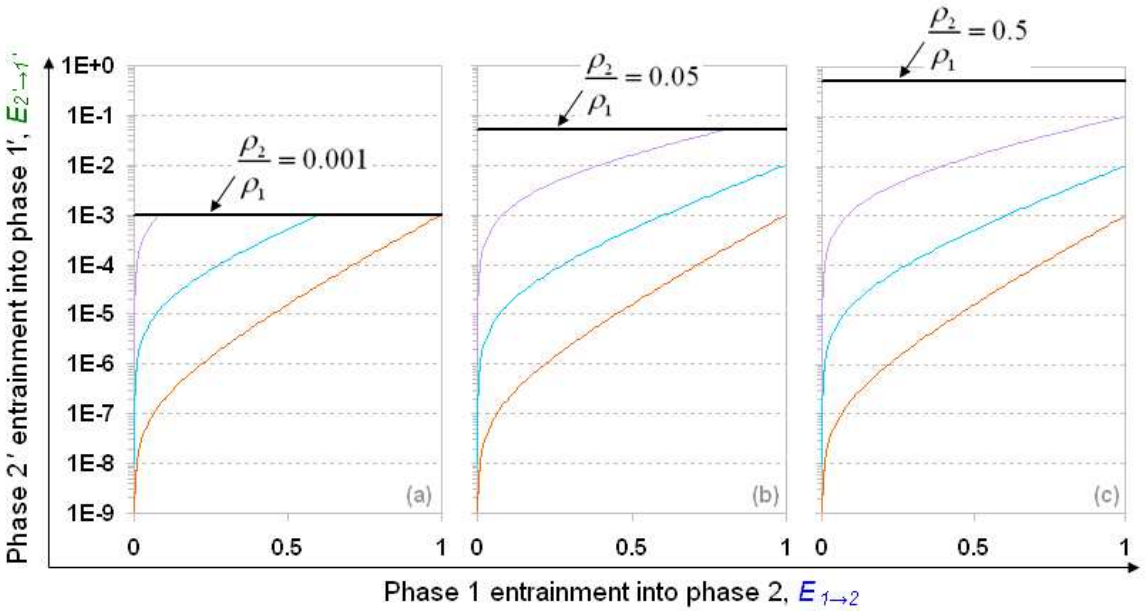

Figure G.1: Graphical representation of generalized, bi-directional two-phase entrainment (Eqn. G.19).

Lastly, it should be noted that at full entrainment of phase 1 into phase 2, the *mist flow* equations are recovered according to our development above and this results in wholly analytical relationships between phase 2 volume fraction, $\langle s_2 \rangle$ (which is = 1 at $E_{1\to 2} = 1$), $E_{1\to 2}$ and $E_{2'\to 1'}$ for a two-phase system. Additionally, we have shown that for a two-phase system with bi-directional entrainment occurring, the only additional unknown aside from $\langle s_2 \rangle$ in Eqns. 6 and 7 in Section 2.2.4, is $E_{1\to 2}$. $E_{1\to 2}$ can, of course, be either provided (measured) or predicted using a simple, explicit and reliable correlation (e.g., Ishii and Mishima, 1982). In the special scenario of *mist flow*, both $\langle s_2 \rangle$ and $E_{1\to 2}$ have values of unity and the universal mixture momentum balance equations therefore achieve their highest predictability performance possible (because they become wholly analytical) for this special scenario. We will clearly demonstrate this fact when

we compare this particular limit of our bi-directional entrainment equations developed in this section with observed two-phase mist flow applications both in the lab and the field in later chapters of this work.

G.2 QUAD-DIRECTIONAL THREE-PHASE ENTRAINMENT

Continuing the generalized, analytical development in the previous Section, we can easily extend our insights for bi-directional two-phase entrainment to a third arbitrary phase, phase 3. For phases 1 and 2 being entrained into phase 3 (and vice-versa), if we look at j = 3, we can correct the mass flux and volume flux for j = 3 to account for this as:

$$\rho_{3\,\overset{\leftarrow 1}{\leftarrow 2}}^{corr} = \frac{G_3 + G_{1\to 3}^{entr} + G_{2\to 3}^{entr}}{\langle u_3 \rangle + \langle u_{1\to 3}^{entr} \rangle + \langle u_{2\to 3}^{entr} \rangle} \tag{G.20}$$

For phase 1 being entrained into phase 3, if we look at j = 1, we can write Eqn. G.3 as:

$$E_{1\to 3} = \frac{G_{1\to 3}^{entr}}{G_1} = \frac{\cancel{\rho_1} \langle u_{1\to 3}^{entr} \rangle}{\cancel{\rho_1} \langle u_1 \rangle} = \frac{\langle u_{1\to 3}^{entr} \rangle}{\langle u_1 \rangle} \tag{G.21}$$

Similarly, for phase 2 being entrained into phase 3, if we look at j = 2, we can write Eqn. G.3 as:

$$E_{2\to 3} = \frac{G_{2\to 3}^{entr}}{G_2} = \frac{\cancel{\rho_2} \langle u_{2\to 3}^{entr} \rangle}{\cancel{\rho_2} \langle u_2 \rangle} = \frac{\langle u_{2\to 3}^{entr} \rangle}{\langle u_2 \rangle} \tag{G.22}$$

Putting (G.3), (G.21) and (G.22) in (G.20), we get:

$$\rho_{3\,\overset{\leftarrow 1}{\leftarrow 2}}^{corr} = \frac{\rho_3 \langle u_3 \rangle + \rho_1 \langle u_1 \rangle E_{1\to 3} + \rho_2 \langle u_2 \rangle E_{2\to 3}}{\langle u_3 \rangle + \langle u_1 \rangle E_{1\to 3} + \langle u_2 \rangle E_{2\to 3}} \tag{G.23}$$

Now, the key insight with regards to the principle of quad-directional three-phase entrainment is that during the entrainment of phases 1 and 2 into phase 3, simultaneously, the corrected phase 3 (which we will call phase 3′) will itself be entraining into the continuously diminishing phases 1 and 2 (i.e. the corrected phases 1 and 2 which we will

call phases 1′ and 2′, respectively). For phase 1 being entrained into phase 3, if we look at j = 1, we can write:

$$G_1^{corr} = G_1 \; - \; G_{1\to 3}^{entr} \;\Rightarrow\; \cancel{\rho_{1'\leftarrow 3'}^{corr}} \left\langle u_1^{corr} \right\rangle = \cancel{\rho_{1'\leftarrow 3'}^{corr}} \left\langle u_1 \right\rangle \; - \; \cancel{\rho_{1'\leftarrow 3'}^{corr}} \left\langle u_{1\to 3}^{entr} \right\rangle \tag{G.24}$$

Putting (G.21) in (G.24), we get:

$$\left\langle u_1^{corr} \right\rangle = \left\langle u_1 \right\rangle \left(1 - E_{1\to 3}\right) \tag{G.25}$$

Similarly, for phase 2 being entrained into phase 3, if we look at j = 2, we can write:

$$G_2^{corr} = G_2 \; - \; G_{2\to 3}^{entr} \;\Rightarrow\; \cancel{\rho_{2'\leftarrow 3'}^{corr}} \left\langle u_2^{corr} \right\rangle = \cancel{\rho_{2'\leftarrow 3'}^{corr}} \left\langle u_2 \right\rangle \; - \; \cancel{\rho_{2'\leftarrow 3'}^{corr}} \left\langle u_{2\to 3}^{entr} \right\rangle \tag{G.26}$$

Putting (G.22) in (G.26), we get:

$$\left\langle u_2^{corr} \right\rangle = \left\langle u_2 \right\rangle \left(1 - E_{2\to 3}\right) \tag{G.27}$$

If we now look at j = 1′, we can now re-state Eqn. G.1 as:

$$\rho_{1'\leftarrow 3'}^{corr} = \frac{G_1^{corr} \; + \; G_{3'\to 1'}^{entr}}{\left\langle u_1^{corr} \right\rangle \; + \; \left\langle u_{3'\to 1'}^{entr} \right\rangle} \tag{G.28}$$

Similar to Eqn. G.21, for phase 3′ being entrained into phase 1′, if we look at j = 3′, we can write Eqn. G.3 as:

$$E_{3'\to 1'} = \frac{G_{3'\to 1'}^{entr}}{G_{3'}} = \frac{\cancel{\rho_{3\overset{\leftarrow 1}{\leftarrow 2}}^{corr}} \left\langle u_{3'\to 1'}^{entr} \right\rangle}{\cancel{\rho_{3\overset{\leftarrow 1}{\leftarrow 2}}^{corr}} \left\langle u_3 \right\rangle} = \frac{\left\langle u_{3'\to 1'}^{entr} \right\rangle}{\left\langle u_3 \right\rangle} \tag{G.29}$$

Putting (G.24), (G.25) and (G.29) in (G.28), we can write:

$$\rho_{1'\leftarrow 3'}^{corr} = \frac{\rho_1 \left\langle u_1 \right\rangle \left(1 - E_{1\to 3}\right) \; + \; \rho_{3\overset{\leftarrow 1}{\leftarrow 2}}^{corr} \left\langle u_3 \right\rangle E_{3'\to 1'}}{\left\langle u_1 \right\rangle \left(1 - E_{1\to 3}\right) \; + \; \left\langle u_3 \right\rangle E_{3'\to 1'}} \tag{G.30}$$

We can repeat the analysis above for phase 2′. If we look at j = 2′, we can write:

$$\rho_{2'\leftarrow 3'}^{corr} = \frac{G_2^{corr} \; + \; G_{3'\to 2'}^{entr}}{\left\langle u_2^{corr} \right\rangle \; + \; \left\langle u_{3'\to 2'}^{entr} \right\rangle} \tag{G.31}$$

Similar to Eqn. G.22, for phase 3′ being entrained into phase 2′, if we look at j = 3′, we can write Eqn. G.3 as:

$$E_{3'\to 2'} = \frac{G^{entr}_{3'\to 2'}}{G_{3'}} = \frac{\cancel{\rho^{corr}_{3\,\overset{\leftarrow 1}{\leftarrow 2}}}\left\langle u^{entr}_{3'\to 2'}\right\rangle}{\cancel{\rho^{corr}_{3\,\overset{\leftarrow 1}{\leftarrow 2}}}\left\langle u_3\right\rangle} = \frac{\left\langle u^{entr}_{3'\to 2'}\right\rangle}{\left\langle u_3\right\rangle} \tag{G.32}$$

Putting (G.26), (G.27) and (G.32) in (G.31), we can write:

$$\rho^{corr}_{2'\leftarrow 3'} = \frac{\rho_2\left\langle u_2\right\rangle\left(1-E_{2\to 3}\right) \;+\; \rho^{corr}_{3\,\overset{\leftarrow 1}{\leftarrow 2}}\left\langle u_3\right\rangle E_{3'\to 2'}}{\left\langle u_2\right\rangle\left(1-E_{2\to 3}\right) \;+\; \left\langle u_3\right\rangle E_{3'\to 2'}} \tag{G.33}$$

Lastly, for phase 3′ being entrained into phases 1′ and 2′, if we look at j = 3′, we can write:

$$\begin{aligned} G^{corr}_{3'} &= G_{3'} \;-\; G^{entr}_{3'\to 1'} - \; G^{entr}_{3'\to 2'} \\ \textit{and},\quad \cancel{\rho^{corr}_{3\,\overset{\leftarrow 1}{\leftarrow 2}}}\left\langle u^{corr}_{3'}\right\rangle &= \cancel{\rho^{corr}_{3\,\overset{\leftarrow 1}{\leftarrow 2}}}\left\langle u_3\right\rangle - \cancel{\rho^{corr}_{3\,\overset{\leftarrow 1}{\leftarrow 2}}}\left\langle u^{entr}_{3'\to 1'}\right\rangle - \cancel{\rho^{corr}_{3\,\overset{\leftarrow 1}{\leftarrow 2}}}\left\langle u^{entr}_{3'\to 2'}\right\rangle \end{aligned} \tag{G.34}$$

Put (G.29), (G.32) in (G.34), we get:

$$\left\langle u^{corr}_{3'}\right\rangle = \left\langle u_3\right\rangle\left(1-E_{3'\to 1'}-E_{3'\to 2'}\right) \tag{G.35}$$

Thus, from the simple development above, if quad-directional entrainment is occurring among any three arbitrary phases 1, 2 and 3 (i.e. entrainment between the three phases except between phases 1 and 2), then the phase densities and mass fluxes change (in order of calculation) as follows:

$$\begin{aligned}
&\textit{Step}\ 1\ (\textit{Eqn.}\ \text{G.23}):\ \rho_3 \quad\to\quad \rho^{corr}_{3\,\overset{\leftarrow 1}{\leftarrow 2}} = \frac{\rho_3\left\langle u_3\right\rangle \;+\; \rho_1\left\langle u_1\right\rangle E_{1\to 3} \;+\; \rho_2\left\langle u_2\right\rangle E_{2\to 3}}{\left\langle u_3\right\rangle \;+\; \left\langle u_1\right\rangle E_{1\to 3} \;+\; \left\langle u_2\right\rangle E_{2\to 3}} \\
&\textit{Step}\ 2\ (\textit{Eqn.}\ \text{G.33}):\ \rho_2 \quad\to\quad \rho^{corr}_{2'\leftarrow 3'} = \frac{\rho_2\left\langle u_2\right\rangle\left(1-E_{2\to 3}\right) \;+\; \rho^{corr}_{3\,\overset{\leftarrow 1}{\leftarrow 2}}\left\langle u_3\right\rangle E_{3'\to 2'}}{\left\langle u_2\right\rangle\left(1-E_{2\to 3}\right) \;+\; \left\langle u_3\right\rangle E_{3'\to 2'}} \\
&\textit{Step}\ 3\ (\textit{Eqn.}\ \text{G.30}):\ \rho_1 \quad\to\quad \rho^{corr}_{1'\leftarrow 3'} = \frac{\rho_1\left\langle u_1\right\rangle\left(1-E_{1\to 3}\right) \;+\; \rho^{corr}_{3\,\overset{\leftarrow 1}{\leftarrow 2}}\left\langle u_3\right\rangle E_{3'\to 1'}}{\left\langle u_1\right\rangle\left(1-E_{1\to 3}\right) \;+\; \left\langle u_3\right\rangle E_{3'\to 1'}} \\
&\textit{Step}\ 4\ (\textit{Eqn.}\ \text{G.35}):\ G_3 \quad\to\quad G^{corr}_{3'} = \rho^{corr}_{3\,\overset{\leftarrow 1}{\leftarrow 2}}\left\langle u_3\right\rangle\left(1-E_{3'\to 1'}-E_{3'\to 2'}\right) \\
&\textit{Step}\ 5\ (\textit{Eqn.}\ \text{G.27}):\ G_2 \quad\to\quad G^{corr}_{2} = \rho^{corr}_{2'\leftarrow 3'}\left\langle u_2\right\rangle\left(1-E_{2\to 3}\right) \\
&\textit{Step}\ 6\ (\textit{Eqn.}\ \text{G.25}):\ G_1 \quad\to\quad G^{corr}_{1} = \rho^{corr}_{1'\leftarrow 3'}\left\langle u_1\right\rangle\left(1-E_{1\to 3}\right)
\end{aligned} \tag{G.36}$$

As in the previous Section, a post-analysis of any of the relations above will reveal both a physically sensible and internal self-consistency. Firstly, testing the limits of Eqns. G.23, G.25 and G.27, we see that:

I. For Eqn. G.23, $\rho_{3\,\overset{\leftarrow 1}{\leftarrow 2}}^{corr}\Big|_{\substack{at\ E_{1\to 2}=0 \\ and\ E_{2\to 3}=0}} = \rho_3$

II. For Eqn. G.23, $\rho_{3\,\overset{\leftarrow 1}{\leftarrow 2}}^{corr}\Big|_{\substack{at\ E_{1\to 2}=1 \\ and\ E_{2\to 3}=1}} = \dfrac{\overbrace{\rho_3\langle u_3\rangle}^{=G_3}+\overbrace{\rho_1\langle u_1\rangle}^{=G_1}+\overbrace{\rho_2\langle u_2\rangle}^{=G_2}}{\langle u_3\rangle+\langle u_1\rangle+\langle u_2\rangle} = \overbrace{\left(\dfrac{G_{mix}}{\langle u_{mix}\rangle}\right)}^{\substack{homogenous\ mixture\ density\ (mist\ flow)}}$

III. For Eqn. G.25, $G_1^{corr}\Big|_{at\ E_{1\to 3}=0} = G_1$

IV. For Eqn. G.25, $G_1^{corr}\Big|_{at\ E_{1\to 3}=1} = \overbrace{0}^{\substack{phase\ 1 \\ fully\ entrained}}$

V. For Eqn. G.27, $G_2^{corr}\Big|_{at\ E_{2\to 3}=0} = G_2$

VI. For Eqn. G.27, $G_2^{corr}\Big|_{at\ E_{2\to 3}=1} = \overbrace{0}^{\substack{phase\ 2 \\ fully\ entrained}}$

Now, we note that the relationship between $E_{1\to 3}$ and $E_{3'\to 1'}$ can be stated analytically using the same lines of reasoning as in the previous Section. In this case, an analogous relation to Eqn. G.19 can be written as:

$$E_{3'\to 1'} = \min\left(E_{1\to 3}\left(\frac{\rho_3}{\rho_1}\frac{G_1}{G_3}\right)^{2-E_{1\to 3}},\ E_{1\to 3}\left(\frac{\rho_3}{\rho_1}\right)^{2-E_{1\to 3}}\right) \tag{G.37}$$

Similarly, for phase 3′ entrainment into phase 2′, we can write the relationship between $E_{2\to 3}$ and $E_{3'\to 2'}$ as:

$$E_{3'\to 2'} = \min\left(E_{2\to 3}\left(\frac{\rho_3}{\rho_2}\frac{G_2}{G_3}\right)^{2-E_{2\to 3}},\ E_{2\to 3}\left(\frac{\rho_3}{\rho_2}\right)^{2-E_{2\to 3}}\right) \tag{G.38}$$

So, with analytical relations now in place for both $E_{3'\to 1'}$ and $E_{3'\to 2'}$, we can now go back to testing the limits of Eqns. G.30, G.33 and G.35. We see from Eqn. G.36, that:

VII. For Eqn. G.30, $\rho_{1'\leftarrow 3'}^{corr}\Big|_{\text{at } E_{1\to 3}=0 \text{ and } \therefore E_{3'\to 1'}=0} = \rho_1$

VIII. For Eqn. G.30, $\rho_{1'\leftarrow 3'}^{corr}\Big|_{\substack{\text{at } E_{1\to 3}=1 \\ \text{and } E_{2\to 3}=1}} = \dfrac{\overbrace{\rho_3\langle u_3\rangle}^{=G_3}+\overbrace{\rho_1\langle u_1\rangle}^{=G_1}+\overbrace{\rho_2\langle u_2\rangle}^{=G_2}}{\langle u_3\rangle+\langle u_1\rangle+\langle u_2\rangle} = \overbrace{\left(\dfrac{G_{mix}}{\langle u_{mix}\rangle}\right)}^{\substack{\text{homogenous} \\ \text{mixture density (mist flow)}}}$

IX. For Eqn. G.33, $\rho_{2'\leftarrow 3'}^{corr}\Big|_{\text{at } E_{2\to 3}=0 \text{ and } \therefore E_{3'\to 2'}=0} = \rho_2$

X. For Eqn. G.33, $\rho_{2'\leftarrow 3'}^{corr}\Big|_{\substack{\text{at } E_{2\to 3}=1 \\ \text{and } E_{1\to 3}=1}} = \dfrac{\overbrace{\rho_3\langle u_3\rangle}^{=G_3}+\overbrace{\rho_1\langle u_1\rangle}^{=G_1}+\overbrace{\rho_2\langle u_2\rangle}^{=G_2}}{\langle u_3\rangle+\langle u_1\rangle+\langle u_2\rangle} = \overbrace{\left(\dfrac{G_{mix}}{\langle u_{mix}\rangle}\right)}^{\substack{\text{homogenous} \\ \text{mixture density (mist flow)}}}$

XI. For Eqn. G.35, $G_{3'}^{corr}\Big|_{\substack{\text{at } E_{1\to 3}=0 \text{ and } \therefore E_{3'\to 1'}=0 \\ \text{at } E_{2\to 3}=0 \text{ and } \therefore E_{3'\to 2'}=0}} = G_3$

XII. For Eqn. G.35, $G_{3'}^{corr}\Big|_{\substack{\text{at } E_{1\to 3}=1 \\ \text{and } E_{2\to 3}=1}} = \overbrace{\left(\dfrac{G_{mix}}{\langle u_{mix}\rangle}\right)}^{\substack{\text{homogenous} \\ \text{mixture density (mist flow)}}} \cdot\left(\langle u_3\rangle-\langle u_1\rangle-\langle u_2\rangle\right)$

Summarily, we see that there is a clear self-consistency to all of the equations developed in this Section. It should be noted that at full entrainment of phases 1 and 2 into phase 3, three-phase *mist flow* equations are recovered according to our development above and this results in wholly analytical relationships between phase 3 volume fraction, $\langle s_3\rangle$ (which is = 1 at both $E_{1\to 3}=1$ and $E_{2\to 3}=1$), $E_{1\to 3}$, $E_{2\to 3}$, $E_{3'\to 1'}$ and $E_{3'\to 2'}$ for a three-phase system. Additionally, we have shown that for a three-phase system with quad-directional entrainment occurring between phase 3 and the other phases, the only additional unknowns aside from $\langle s_3\rangle$ and $\langle s_2\rangle$ in eqns. 6 and 7 in Section 2.2.4, are $E_{1\to 3}$ and $E_{2\to 3}$. Both $E_{1\to 3}$ and $E_{2\to 3}$ can be either provided (measured) or predicted using a simple, explicit and reliable correlation (e.g., Ishii and Mishima, 1982). In the special scenario of *mist flow*, $\langle s_3\rangle$, $E_{1\to 3}$ and $E_{2\to 3}$ have values of unity and the universal mixture momentum balance equations thus achieve their highest predictability performance possible (because they become wholly analytical) for this special scenario.

We will clearly demonstrate this fact when we compare this particular limit of our quad-directional entrainment equations developed in this section with observed three-phase mist flow applications both in the lab and the field in later chapters of this work.

Nomenclature

Terms already defined in the body of this document or in any of the appendices are excluded from below. The terms below are given in their order of appearance in this work:

BSL	Bird, R. B., Stewart, W. E., Lightfoot, E. N.: Transport phenomena, John Wiley & Sons, 2nd ed. (2002)
1D	One dimensional
NASA	National Aeronautics and Space Administration
ERCB	Energy Resources Conservation Board
OLGA	The OLGA software of the SPT Group, v. 6.2.7
LEDA	The LEDAFlow software of Konsberg Oil and Gas Technologies, v. 1.0.231.1
SINTEF	Stiftelsen for industriell og teknisk forskning
IFPEN	IFP (French Institute of Petroleum) Energies Nouvelles
JMBC	J. M. Burgerscentrum Research School for Fluid Mechanics
CMFD	Computational Multiphase Fluid Dynamics
TUFFP	The Tulsa University Fluid Flow Projects Joint Industry Program software, v. 2011.1
PIPESIM	Schlumberger's steady-state multiphase flow simulator, v. 11.01 http://www.software.slb.com/products/foundation/Pages/pipesim.aspx
SPE	Society of Petroleum Engineers
PSIG	Pipeline Simulation Interest Group
ATCE	Annual Technical Conference and Exhibition
CFD	Computational Fluid Dynamics
WELLFLO	Neotechnology Consultants Ltd. wellbore software, http://www.software.slb.com/pages/neotec.aspx
BBL/d	Barrels of liquid per day

scf/BBL	Standard cubic feet of gas per barrel of liquid
TRRC	Texas Rail Road Commission
Sup.	Superficial
PROSPER	Petroleum Experts Ltd. well software, http://www.petex.com/products/?ssi=3
PIPEFLO	Neotechnology Consultants Ltd. pipeline software, http://www.software.slb.com/pages/neotec.aspx
FORGAS	Neotechnology Consultants Ltd. oil and gas field modeling software, http://www.software.slb.com/pages/neotec.aspx
Re	Reynolds
L	Length of pipe [=] m
A	Conduit cross-sectional area open to flow [=] m^2
P	Pressure [=] Pa
g	Acceleration due to gravity [=] 9.81 m/s^2
G	Mass flux [=] kg/m^2-s
ρ	Density [=] kg/m^3
τ	Shear stress [=] Pa
θ	Pipe inclination from vertical [=] degrees
D_H	Hydraulic diameter [=] m
D	Circular-pipe diameter [=] m
k	Hydraulic roughness [=] m, or thermal conductivity [=] W/m-K
μ	Dynamic viscosity [=] Pa-s
σ	Interfacial tension [=] Pa-m
h	Vertical height above a datum [=] m, or heat transfer coefficient [=] W/m^2-K
LHS	Left hand side
RHS	Right hand side
LU	Lower-Upper
PSU	Penn State University

GRI	Gas Research Institute
PG	Pressure Gradient
VF	Volume Fraction
TPG	Total Pressure Gradient
FPG	Frictional Pressure Gradient
HPG	Hydrostatic Pressure Gradient
CADPG	Convective Acceleration/Deceleration Pressure Gradient
BP4	GRE mechanistic model of BP (linktype 4) in PIPESIM
XIAO	Xiao mechanistic model in PIPESIM
BJA-R	Baker-Jardine Revised mechanistic model in PIPESIM
BEGGS	Beggs and Brill Revised model in PIPESIM
GAF	Govier, Aziz and Fogarasi mechanistic model in PIPESIM
ORKZ	Orkiszewski model in PIPESIM
ANS	Ansari mechanistic model in PIPESIM
EOR	Enhanced oil recovery
DOE	Department of Energy (United States of America)
BPP	Bubble point pressure
BPT	Bubble point temperature
DPP	Dew point pressure
DPT	Dew point temperature
FVF	Formation volume factor
MAST	The Teasistemi group pipeline software, http://www.tea-group.com/mast.aspx
WellFlo	Weatherford well modeling and design software, http://www.weatherford.com/Products/Production/ProductionOptimization/Software/WellFloSoftware/index.htm
VLP	Vertical lift performance
PVT	Pressure-volume-temperature
DIMP	Design institute for multiphase processing

References

CHAPTER 1 PUBLICATIONS

1. Adames, P., Young, B.: Comparison and analysis of mechanistic models for gas-liquid flow in vertical and deviated wells, 16th Intl. Conf. on Multiphase Production Tech., Cannes, France, June 12-14 (2013)
2. Addali, A.: Monitoring gas void fraction in two-phase flow with acoustic emission, Ph.D. Thesis, School of Engineering, Cranfield University, UK (2010)
3. Ali, S. F., Yeung, H.: Experimental investigation and numerical simulation of two-phase flow in a large-diameter horizontal flow line vertical riser, J. Petroleum Science and Tech., v. 28, no. 11, pp. 1079 – 1095 (2010)
4. Al-Sarkhi, A., Sarica, C., Qureshi, B.: Modeling of droplet entrainment in co-current annular two-phase flow – a new approach, Intl. J. of Multiphase Flow, v. 39, pp. 21-28 (2012)
5. Anisimov, P. F.: International scientific-practical conference – prospects and challenges of oil and gas fields development in offshore-coastal arctic zone, Arkhangelsk, Russia (2010)
6. Ansari, A. M., Sylvester, N. D., Sarica, C., Shoham, O., Brill, J. P.: A comprehensive mechanistic model for upward flow in pipes, Soc. of Petroleum Engineers Productions and Facilities J., May, pp. 217-226 (1994)
7. Antar, B. N., Nuotio-Antar, V. S.: Fundamentals of low gravity fluid dynamics and heat transfer, CRC Press (1993)
8. Azzopardi, B. J., Taylor, S., Gibbons, D. B.: Annular two-phase flow in a large diameter tube, Intl. Conf. on the Physical Modeling of Multiphase flow, Paper F4, Coventry, England, April (1983)
9. Balasubramaniam, R., Rame, E., Kizito, J., Kassemi, M.: Two phase flow modeling: summary of flow regimes and pressure drop correlations in reduced and partial gravity: National Center for Space Exploration Research, Report NASA/CR-2006-214085 (2006)
10. Batchelor, G. K.: A brief guide to two-phase flow, Proc. of the 17th Intl. Cong. Theor. Appl. Mech., North-Holland, pp. 27-40 (1989a)
11. Batchelor, G. K.: The dynamics of a mixture of two components, 10th Australasian Fluid Mechanics Conf., December 11-15, U. of Melbourne, Australia (1989b)
12. Baxendell, P. B., Thomas, R.: The calculation of pressure gradients in high-rate flowing wells, Soc. of Petroleum Engineers J. Pet. Tech., pp. 1023-1028, October (1961)

13. Beck, I.: A challenging future for petroleum engineering software vendors, Soc. of Petroleum Engineers Computer Applications, v. 7, no. 6, pp. 132 – 134 (1995)

14. Belt, R., Djoric, B., Kalali, S., Duret, E., Larrey, D.: Comparison of commercial multiphase flow simulators with experimental and field databases, 15th Intl. Conf. on Multiphase Production, BHR Group, Cannes, France (2011)

15. Biberg, D., Holmas, H., Staff, G., Sira, T., Nossen, J., Andersson, P., Lawrence, C., Hu, B., Holmas, K.: Basic flow modeling for long distance transport of wellstream fluids, 14th Intl. Conf. on Multiphase Prod. Tech., BHR Group, Cannes, France (2009)

16. Biberg, D.: Reference letter of support – transient multiphase flow program, https://workspace.imperial.ac.uk/ceFluidMechanics/Public/Forms/AllItems.aspx (2012)

17. Bird, R. B., Stewart, W. E., Lightfoot, E. N.: Transport phenomena, 2nd ed., John Wiley and Sons (2002)

18. Brennen, C. E.: Fundamentals of multiphase flows, Cambridge University Press, Cambridge (2005)

19. Brill, J. P., Gregory, G. A.: 1st N. American conf. on multiphase technology – technology from the arctic to the tropics, BHR Group, Banff, Canada (1998)

20. Brill, J. P.: Multiphase technology – past, present and future. The world according to Brill, Opening Address, 11th Intl. Conf. on Multiphase, BHR Group, San Remo, Italy (2003)

21. Brown, D. J.: Disequilibrium in annular flow, Ph.D. Thesis, Oxford U. (1978)

22. Chereminisoff, N. P.: Encyclopedia of fluid mechanics, Volumes 1 to 10 and Supplements 1 to 3, Gulf Pub. Co. (1986)

23. Chierici, G. L., Ciucci, G. M., Sclocchi, G.: Two-phase vertical flow in oil wells – prediction of pressure drop, Soc. of Petroleum Engineers, Paper No. 4316, August (1974)

24. Choi, J., Pereyra, E., Sarica, C., Park, C., Kang, J. M.: An efficient drift-flux closure relationship to estimate liquid holdups of gas-liquid two-phase flow in pipes, Energies J., v. 5, pp. 5294-5306 (2012)

25. Cocco, R., Hyrena, C.: Collaboration for multiphase flow research – computational physics and application, Track 4 opening presentation, Proc. of the Workshop on Multiphase Flow Research, June 6-7, Morgantown, West Virginia (2006)

26. Corteville, J., Duchet-Suchaux, P., Lopez, D.: Comparison of methods for predicting pressure loss in oil and gas wells, 5th Intl. Conf. on Multiphase Production, BHR Group, Cannes, France (1991)

27. Cousins, L. B., Denton, W. H., Hewitt, G. F.: Liquid mass transfer in annular two-phase flow, UK AERE Report R4926, May (1965)

28. Crowley, C. J., Sam, R. G., Rothe, P. H.: Investigation of two-phase flow in horizontal and inclined pipes at large pipe size and high gas density, Project PR-172-507, Pipeline Research Committee, AGA, February (1986)

29. Danielson, T. J.: A simple model for hydrodynamic slug flow, 8th N. American Conf. on Multiphase Tech., BHR Group, Banff, Alberta, June 20-22 (2012a)

30. Danielson, T. J.: A simple model for hydrodynamic slug flow, Offshore Tech. Conf., Paper No. 21255 (2011)

31. Delhaye, J. M.: Thermohydraulics of two-phase systems for industrial design and nuclear engineering, Hemisphere Pub. Corp. (1981)

32. DiPippo, R.: The next steps in two-phase flow – executive summary, U.S. Dept. of Energy workshop/symposium, Brown University, Report No. GEOFLO/8 (1980)

33. Dobran, F.: A two-phase fluid model based on the linearized constitutive equations, Advances in Two-Phase Flow and Heat Transfer, NATO ASI Series, v. 63, pp. 41-59 (1983)

34. Dukler, A. E., Taitel, Y.: Flow pattern transitions in gas-liquid systems – measurements and modeling, Multiphase Sci. and Tech., v. 2 (1986)

35. Durst, F., Tsiklauri, G. V., Afgan, N. H.: Two-phase momentum, heat and mass transfer in chemical, process, and energy engineering systems, Volumes 1 and 2, Proc. of the Seminar of the Intl. Center for Heat and Mass Transfer, Dubrovnik, Yugoslavia (1978)

36. Eidsmoen, H., Roberts, I.: Issues relating to proper modeling of the profile of long gas condensate pipelines, Pipeline Simulation Interest Group, Paper No. 0501 (2005)

37. Ellul, I. R.: Dynamic multiphase simulation – the state of play, Pipeline Simulation Interest Group, Paper No. 1005 (2010)

38. Emmons, H. W.: Critique of numerical modeling of fluid mechanics phenomena, Annu. Rev. Fluid Mech., v. 2, pp. 15-36 (1970)

39. Erikson, D. D., Mai, M. C.: A transient multiphase temperature prediction program, Soc. of Petroleum Engineers, Paper No. 24790 (1992)

40. Fairhurst, P.: Reference letter of support – transient multiphase flow program, https://workspace.imperial.ac.uk/ceFluidMechanics/Public/Forms/AllItems.aspx (2010)

41. Ferguson, M. E. G., Spedding, P. L.: Measurement and prediction of pressure drop in two-phase flow, J. Chem. Tech. and Biotech., v. 63, no. 3, pp. 262-278 (1995)

42. Feuer, L. S.: The principle of simplicity, Philosophy of Science, v. 24, pp. 109-122 (1957)

43. Garg, S. K., Pritchett, J. W., Alexander, J. H.: A new liquid hold-up correlation for geothermal wells, J. Geothermics, v. 33, pp. 795-817 (2004)

44. Golan, M.: Announcement for a short course on fundamental of multiphase flow modeling, August 18-29, 2003, Intl. J. of Multiphase Flow, v. 29, pp. 1039 (2003)

45. Gomez, L. E., Shoham, O, Schmidt, Z., Chokshi, R. M., Brown, A., Northug, T.: A unified mechanistic model for steady-state two-phase flow in wellbores and pipelines, SPE Paper 56520 (1999)

46. Govier, G. W., Aziz, K.: The flow of complex mixtures in pipes, Robert E. Krieger Publishing Co. (1972)

47. Govier, G. W., Radford, B. A., Dunn, J. S. C.: The upward vertical flow of air-water mixtures – Part 1 – effect of air and water rates on flow pattern, hold-up and pressure drop, Can. J. Chem. Eng., v. 35, pp. 58-70 (1957)

48. Grassi B., Strazza, D., Poesio, P.: Experimental validation of theoretical models in two-phase high-viscosity ratio liquid-liquid flows in horizontal and slightly inclined pipes, Intl. J. of Multiphase Flow, v. 34, pp. 950-965 (2008)

49. Gregory, G. A., Aziz, K.: Design of Pipelines for Multiphase (Gas/Gas-Condensate) Flow, J. of Canadian Petroleum Technology, pp. 28-33, July (1975a)

50. Gregory, G. A., Fogarasi, M. P.: A critical evaluation of multiphase gas-liquid pipeline calculation methods, 2nd Intl. Conf. on Multiphase Flow, London, June 19-21 (1985)

51. Griffith, P., Lau, C. W., Hon, P. C., Pearson, J. F.: Two-phase pressure drop in inclined and vertical pipes, Report No. DSR 80063-81, Mobil Oil Co., Heat Transfer Laboratory, Dept. of Mech. Eng., Massachusetts Inst. Of Tech., Aug. (1973)

52. Griffith, P., Wallis, G. B.: Slug flow, technical report no. 15, Division of Sponsored Research, Massachusetts Inst. of Tech., The Office of Naval Research – DSR Project No. 7-7673 (1959)

53. Hanratty, T. J., Theofanus, T., Delhaye, J. M., Eaton, J., McLaughlin, J., Prosperetti, A., Sundaresan, S., Trygvasson, G.: Workshop findings, Proc. of the Workshop on Scientific Issues in Multiphase Flow, U. of Illinois in Champaign-Urbana, May 7-9, 2002, Intl. J. of Multiphase Flow, v. 29, pp. 1047-1059 (2003)

54. Hansen, S. B.: Introductory talk – field development and technical limitation, Proc. of the 1st Intl. Conf. on Multiphase flow, Stavanger, Norway (1987)

55. Hasan, A. R.: Void fraction in bubbly, slug and churn flow in vertical two-phase up-flow, Chem. Eng. Comm., v. 66, pp. 101-111 (1988)

56. Hernandez-Perez, V.: Gas-liquid two-phase flow in inclined pipes, Ph.D. Thesis, U. of Nottingham, UK (2007)

57. Hetsroni, G.: Handbook of multiphase systems, Hemisphere Publishing Corp. (1982)

58. Hewitt, G. F, Delhaye, J. M., Zuber, N.: Proc. of the third intl. workshop on two-phase flow fundamentals, Imperial College, London, June 15-19, 1992, Multiphase Science and Technology, v. 8 (1994)

59. Hewitt, G. F., Boure, J. A.: Some recent results and development in gas-liquid flow: a review, Intl. J. of Multiphase Flow, v. 1. pp. 139-171 (1973)

60. Hewitt, G. F., King, I., Lovegrove, P. C.: Holdup and pressure drop measurements in the two-phase annular flow of air-water mixtures, UK AERE Report R3764, June (1961)

61. Hewitt, G. F., Shires, G. L., Polezhaev, Y. V.: International encyclopedia of heat and mass transfer, CRC Press (1997)

62. Hewitt, G. F.: Going with the flow, Media bulletin outlining a selection of current research at Imperial College, http://www.imperial.ac.uk/college.asp?P=2096 (1997)

63. Hewitt, G. F.: Multiphase flow in the energy industries, J. of Engineering Thermophysics, v. 17, no. 1, pp. 12-23 (2008)

64. Hewitt, G. F.: Two-phase flow and its applications – past, present, and future, J. Heat Transfer Engineering, v. 4, no. 1, pp. 67-79 (1983)

65. Heywood, N. I., Cheng, D. C. H.: Flow in pipes, part 2 – multiphase flows, J. Phys. Technol., v. 15, pp. 291 (1984)

66. Hubbard, M. G.: An analysis of horizontal gas-liquid slug flow, Ph.D. dissertation, U. of Houston (1965)

67. Hughmark, G.: Holdup and pressure drop with gas-liquid flow in a vertical pipe, Ph.D. Dissertation, Dept. of Chem. Eng., Louisiana State U. (1959)

68. Ishii, M., Hibiki, T.: Thermo-fluid dynamics of two-phase flow, Springer (2006)

69. Issa, R. F., Tang, Z. F.: Modeling of vertical gas-liquid slug flow in a pipe, Proc. Winter Annual Meeting ASME, Dallas, Texas, pp. 65-71 (1990)

70. Jackson, D. F. B., Virues, C. J. J., Sask, D.: Investigation of liquid loading in tight gas horizontal wells with a transient multiphase flow simulator, Can. Soc. for Unconventional Gas, Soc. of Petroleum Engineers Paper No. 149477 (2011)

71. Johnson, G. W.: A study of stratified gas-liquid pipe flow, Ph.D. Dissertation, Dept. of Mathematics – Mechanics Division, U. of Oslo, Norway (2005)

72. Joseph, D. D.: Critical remarks about flow charting, Multiphase Sci. and Tech., v. 15, no. 1-4, pp. 45-51 (2003a)

73. Kabir, C. S., Hasan, A. R.: Performance of a two-phase gas/liquid flow model in vertical wells, J. Petroleum Science and Engineering, v. 4, pp. 273-289 (1990)

74. Kakac, S., Ishii, M.: Advances in two-phase flow and heat transfer – fundamentals and applications, NATO Advanced Workshop on the Advances in Two-phase Flow and Heat Transfer, Spitzingsee, Germany (1982)

75. Kakac, S., Mayinger, F.: Two phase flows and heat transfer, Volumes 1 and 2, Proc. of the NATO Advanced Study Institute, U. of Bosphorus, Istanbul, Turkey (1976)

76. Kakihana, H., Wakabahashi, J.: Proc. of second intl. topical meeting on nuclear power plant thermal hydraulics ad operations, Tokyo, Japan (1986)

77. Kashou, S., Mathews, P., Shea, D.: Transient modeling applications and lessons learned, case studies from oil and gas fields, 3rd N. American Conf. on Multiphase Tech., BHR Group, Banff, Canada (2002)

78. Kestin, J., Podowski, M. Z.: Intl. workshop on two-phase flow fundamentals, National Bureau of Standards, Gaithersburg, Maryland (1985)

79. Kestin, J.: Internal variables in the local-equilibrium approximation, Intl. Symposium on Micromechanics, Report No. DOE/ER/13687-10 (1992)

80. Kestin, J.: Local-equilibrium formalism applied to mechanics of solids, Intl. Symposium on Micromechanics, Report No. DOE/ER/13687-8 (1991)

81. Keuzenkamp, H. A., McAleer, M., Zellner, A.: The enigma of simplicity, Conf. on Simplicity and Scientific Inference, Tilburg, The Netherlands (1997)

82. Khatib, Z., Richardson, J. F.: Vertical co-current flow of air and shear shinning suspensions of kaolin, J. Chem. Eng. Res. Des., v. 62, pp. 139 (1984)

83. Khoriakov, V., Johansen, A. C., Johansen, T. E.: Transient flow modeling of advanced wells, J. Petrol. Sci. Tech., v. 86-87, pp. 99-110 (2012)

84. Kumar, N.: Improvements for flow correlations for gas wells experiencing liquid loading, Soc. of Petroleum Engineers, Paper No. 92049 (2005)

85. Lahey, Jr., R. T., Wood, R. T.: Intl. workshop of two-phase flow fundamentals, Rennselaer Polytechnic Inst., Troy, New York (1987)

86. Lahey, Jr., R. T.: Two fluid or not two fluid, Heat Transfer Engineering, v. 3, no. 2, pp. 9 (1981)

87. Lake, L. W., Bryant, S. L.: The scientific method and earth sciences, Guest Editorial, J. Energy Resources Tech., v. 128, pp. 245-246 (2006)

88. Lareo, C., Fryer, P. J., Barigou, M.: The fluid mechanics of solid-liquid two-phase flows: a review, Trans. of the Inst. of Chem. Engineers Part C, v. 75, pp. 73-105 (1997)

89. Laux, H., Meese, E., Mo, S., Unander, T. E., Johansen, S. T., Bansal, K. M., Danielson, T. J., Goldszal, A., Monden, J. I.: Multidimensional simulations of multiphase flow for improved design and management of production and processing operation, Offshore Tech. Conf., Paper OTC 19434 (2008)

90. Lea, J. F., Nickens, H. V., Wells, M. R.: Gas well deliquification, 2nd ed., Gulf Professional Pub. (2008)

91. LedaFlow Research Project: SINTEF Petroleum Research Projects, http://www.sintef.no/home/SINTEF-Petroleum-Research/Projects/2002/LedaFlow (2012)

92. Levy, S: Two-phase flow in complex systems, Wiley-Interscience Pub. Co. (1999)

93. Loth, E.: Particles, drops and bubbles – fluid dynamics and numerical methods, Draft for Cambridge University Press (2010)

94. Mao, D., Harvey III, A. D.: Transient-nonisothermal-multiphase-wellbore-model development with phase change and its application to producer wells, Soc. of Petroleum Engineers J., Paper No. 146318 (2013)

95. McCarl, B. A.: Model validation – an overview with some emphasis on risk models, Rev. Market. Agric. Econ., v. 52, pp. 153-173 (1984)

96. Moalem Maron, D., Dukler, A. E.: New concepts on the mechanisms of flooding and flow reversal phenomena, Letters in Heat and Mass Transfer, v. 8, pp. 453 – 463 (1981)

97. Nilpueng, K., Wongwises, S.: Flow pattern and pressure drop of vertical upward gas-liquid flow in sinusoidal wavy channels, Exp. Thermal and Fluid Science, v. 30, pp. 523-534 (2006)

98. Nilsen, A. S.: Simplified first principle model for severe-slugging flow in S-shaped risers, M.Sc. Thesis, Norwegian U. of Science and Technology (2012)

99. Nordsveen, M., Nossen, J.: OVIP 2007-2009 scope of work, SPT Technical Report: 34011035/TN-1 Rev. 1, August (2007)

100. Oliemans, R. V. A., Pots, B. F. M., Trompe, N.: Modelling of annular dispersed two-phase flow in vertical pipes, Intl. J. of Multiphase Flow, v. 12, no. 5, pp. 711-732 (1986)

101. Owen, D. G.: An experimental and theoretical analysis of equilibrium annular flows, Ph.D. Dissertation, Dept. of Chem. Eng., U. of Birmingham (1986)

102. Peffer, J. W., Miller, M. A., Hill, A. D.: An improved method for calculating bottomhole pressures in flowing gas wells with liquid present, Soc. of Petroleum Engineers Production Engineering, Paper No. 15655, November (1988)

103. Peng, Z., Yuan, Z., Li, T., Cai, J., Wu, X., Fan. F.: Research on multiphase flows in Thermo-Energy Engineering Institute of Southeast University, Review Paper, Intl. J. of Multiphase Flow, v. 36, pp. 119-126 (2010)

104. Pickering, P. F., Hewitt, G. F., Watson, M. J., Hale, C. P.: The prediction of flows in production risers – truth & myth?, IIR Conference, Aberdeen, http://www.feesa.net/rand.html (2001)

105. Plaxton, W. L.: Pipe flow experiments for the analysis of two-phase liquid-liquid pressure drop in horizontal wells, M.Sc. Thesis, Dept. of Petroleum Engineering, U. of Alberta, Canada (1995)

106. Podowski, M. Z.: Understanding multiphase flow and heat transfer – perception, reality, future needs, Archives of Thermodynamics, v. 26, no. 3, pp. 3-20 (2005)

107. Pouplin, A., Masbernat, O., Decarre, S., Line, A.: Wall friction and effective viscosity of a homogeneous dispersed liquid-liquid flow in a horizontal pipe, AIChE J., Fluid Mechanics and Transport Phenomena Div., v. 57, no. 5, May (2011)

108. Prosperetti, A., Trygvasson, G.: Computational methods for multiphase flow, Cambridge University Press, Cambridge (2007)

109. Prosperetti, A., Hewitt, G. F., Joseph, D. D., Matsumoto, Y., Theofanus, T. G.: Report on the panel discussion on 'modeling of multiphase flow', http://www.aem.umn.edu/people/faculty/joseph/archive/docs/allpanel.pdf, May 28th (2001)

110. Prosperetti, A..: Two-fluid modeling and averaged equations, Multiphase Sci. and Tech., v. 15, no. 1-4, pp. 181-192 (2003)

111. Rhodes, E., Scott, D. S.: Concurrent gas-liquid flow, Proc. of an Intl. Symposium on research in concurrent gas-liquid flow, U. of Waterloo, Ontario, Canada (1968)

112. Rhyne, L.: Reference letter of support – transient multiphase flow program, https://workspace.imperial.ac.uk/ceFluidMechanics/Public/Forms/AllItems.aspx (2013)

113. Rykiel, Jr.: Testing ecological models – the meaning of validation, J. Ecological modeling, v. 90, pp. 229-244 (1996)

114. Sagan, C.: The demon-haunted world – science as a candle in the dark, Ballantine Books, New York (1996)

115. Sanchez, M. J.: Comparison of correlations for predicting pressure losses in vertical multiphase annular flow, M.S. Thesis, Dept. of Petroleum Engineering, U. of Tulsa (1972)

116. Schietz, M.: Optimization of well start-up, M.Sc. Thesis, U. of Leoben, Austria (2009)

117. Schlesinger, S.: Terminology for model credibility, J. Simulation, v. 32, no. 3, pp. 103-104 (1979)

118. Serizawa, A., Fukano, T., Bataille, J.: Proc. of the second intl. conf. on multiphase flow, Kyoto, Japan (1995)

119. Shippen, M., Bailey, W. J.: Steady-state multiphase flow – past, present, and future, with a perspective on flow assurance, Energy and Fuels, v. 26, pp. 4145-4157 (2012)

120. Shirdel, M., Sepehrnoori, K.: Development of a transient mechanistic two-phase flow model for wellbores, Soc. of Petroleum Engineers J., Paper No. 142224, September (2012)

121. Shoham, O.: Mechanistic modeling of gas-liquid two-phase flow in pipes, Soc. of Petroleum Engineers (2006)

122. Shyamlal, M.: Proc. of the workshop on multiphase flow research, June 6-7, Morgantown, West Virginia (2006)

123. Sommerfeld, M., Horender, S.: Proc. of the 12th workshop on two-phase flow predictions, March 22-25, Halle, Germany (2010)

124. Spedding, P. L., Nguyen, V. T.: Data on holdup, pressure loss and flow pattern for two-phase, air-water flow in an inclined pipe. Report 122, U. of Auckland, Auckland, New Zealand (1976)

125. Stone, H. A.: Interfaces – in fluid mechanics and across disciplines, Batchelor Prize Lecture, J. Fluid Mechanics, v. 645, pp. 1-25 (2010)

126. Storkaas, E.: Stabilizing control and controllability: control solutions to avoid slug flow in pipeline-riser systems, Dr. Ing. Thesis, Dept. of Chemical Engineering, Norwegian U. of Science and Tech. (2005)

127. Stuhmiller, J. H., Ferguson, R. E.: The role of microscale processes in the modeling of two-phase flow, EPRI Report NP-1325, Palo Alto, California (1980)

128. Sundaresan, S.: Modeling the hydrodynamics of multiphase flow reactors – current status and challenges, AIChE J., v. 46, no. 6, pp. 1102-1105 (2000)

129. Takacs, G.: Considerations on the selection of an optimum vertical multiphase pressure drop prediction model for oil wells, Soc. of Petroleum Engineers, Paper No. 68361 (2001)

130. Tang. P., Yang. J., Zheng, J. Y., Lam, C. K., Wong, I., He, S., Z.: Predicting erosion-corrosion induced by the interactions between multiphase flow and structure in piping system, J. of Pressure Vessel Tech., v. 131, Dec. (2009)

131. Theofanous, T. G., Amarasooriya, W. H.: Dataset no. 1 – pressure drop and entrained fraction in fully developed flow, Multiphase Sci. and Tech., v. 6, part 1, pp. 5-13 (1992)

132. Theofanous, T. G., Dinh, T. N.: On the prediction of flow patterns as a principal scientific issue in multi-fluid flow, Multiphase Sci. and Tech., v. 15, no. 1-4, pp. 57-64 (2003)

133. Time, R. W.: Flow assurance and multiphase flow, Seminar at Aker Solutions, http://www.akersolutions.com/PageFiles/12184/Flow assurance presentation - Rune Time I.pdf, Stavanger, Norway, May 21st (2011)

134. Veeken, C. A. M., Belfroid, S. P. C.: New perspective on gas-well liquid loading and unloading, Soc. of Petroleum Engineers Production and Operations, Paper No. 134483, pp. 343 – 356 (2011a)

135. Veeken, C. A. M., Belfroid, S. P. C.: New perspective on gas-well liquid loading and unloading, Gas Well Deliquification Workshop, Denver, Colorado (2011b)

136. Veziroglu, T. N., Kakac, S.: Two-phase transport and reactor safety, Volumes 1 and 2, Proc. of the two-phase flow and heat transfer symposium workshop, Fort Lauderdale, Florida (1976)

137. Wallis G.B.: One-dimensional two-phase flow, McGraw Hill, New York (1969)

138. Wallis, G. B.: AEC Report, No. NYO-3114-14, EURAEC 1605 (1966)

139. Wallis, G. B.: Review – theoretical models of gas-liquid flows, J. Fluids Engineering, pp. 279-283 (1982)

140. Wang, H., Vedapuri, D., Cai, J. Y.: Mass transfer coefficient measurements in water/oil/gas multiphase flow, ASME J. of Energy Resources Tech., v. 123, pp. 144-149 (2001)

141. Wang, W., Gong, J., Angeli, P.: Investigation on heavy crude-water two phase flow and related flow characteristics, Intl. J. of Multiphase Flow, v. 37, pp. 1156-1164 (2011)

142. Whalley, P. B.: Book review of Handbook of Multiphase Systems, ed. by Gad Hetsroni, J. Heat Transfer Engineering, v. 4, no. 1, pp. 86-87 (1983)

143. Wilczek, F.: Simplicity, http://edge.org/response-detail/10324 (2012)

144. Woods, G. S., Spedding, P. L.: Vertical upward co-current multiphase flow, Report CE/96/WOODS, Dept. of Chem. Eng., Queen's U. of Belfast (1996)

145. Wulff, W.: Computer simulation of two-phase flow in nuclear reactors, Brookhaven National Laboratory Report No. 47783 (1992)

146. Wulff, W.: Integral methods for two-phase flow in hydraulic systems, Advances in Heat Transfer, v. 31, pp. 105-158 (1998)

147. Zheng, D. H., Che, D. F.: An investigation on near wall transport characteristics in an adiabatic upward gas-liquid two-phase slug flow, J. Heat and Mass Transfer, v. 43, pp. 1019-1036 (2007)

148. Zhou, D., Yuan, H.: New model for gas well loading prediction, Soc. of Petroleum Engineers, Paper No. 120580 (2009)

CHAPTER 2 PUBLICATIONS

1. Alves, I. N., Caetano, E. F., Minami, K., Shoham, O.: Modeling annular flow behavior for gas condensate wells, ASME FED, v. 72, pp. 87-97 (1988)

2. Andreussi, P., Minervini, A., Paglianti, A.: Mechanistic model of slug flow in near-horizontal pipes, AIChE J., v. 39, no. 8, August (1993)

3. Ansari, A. M., Sylvester, N. D., Sarica, C., Shoham, O., Brill, J. P.: A comprehensive mechanistic model for upward flow in pipes, Soc. of Petroleum Engineers Productions and Facilities J., May, pp. 217-226 (1994)

4. Arirachakaran, S.: An experimental study of two-phase oil-water flow in horizontal pipes, M.S. Thesis, U. of Tulsa (1983)

5. Arnold, G. S., Drew, D. A., Lahey, Jr., R. T.: An assessment of multiphase flow models using the second law of thermodynamics, Intl. J. of Multiphase Flow, v. 16, no. 3, pp. 481-494 (1990)

6. Ashiem, H.: MONA, An accurate two-phase well flow model based on phase slippage, Soc. of Petroleum Engineers, Prod. Eng. J., pp. 221-230, May (1986)

7. Ashwood, A. C.: Characterization of the macroscopic and microscopic mechanics in vertical and horizontal annular flow, Ph.D. Dissertation, U. of Wisconsin-Madison (2010)

8. Awad, M. M.: Two-phase flow, An Overview of Heat Transfer Phenomena, http://cdn.intechopen.com/pdfs/40637/InTech-Two_phase_flow.pdf (2012)

9. Azzopardi, B. J.: Drops in annular two-phase flow, Intl. J. Multiphase Flow, v. 23, Suppl., pp. 1-53 (1997)

10. Bai, R., Chen. K., Joseph, D. D.: Lubricated pipelining: stability of core-annular flow – Part 5 – Experiments and comparison with theory, J. Fluid Mech., v. 240, pp. 97-132, July (2006)

11. Baker, A., Nielson, K., Gabb, A.: Pressure loss, liquid holdup calculations developed – part 1 – new correlations, Oil and Gas J., pp. 55-59, March 14th (1988a)

12. Biberg, D., Holmas, H., Staff, G., Sira, T., Nossen, J., Andersson, P., Lawrence, C., Hu, B., Holmas, K.: Basic flow modeling for long distance transport of wellstream fluids, 14th Intl. Conf. on Multiphase Prod. Tech., BHR Group, Cannes, France (2009)

13. Bird, R. B.: Chem. Eng. Sci., v. 6, pp. 123-131 (1957)

14. Bobok. E.: Fluid mechanics for petroleum engineers, Dev. in Petroleum Science, Ser. 32, Elsevier (1993)

15. Boure, J. A., Delhaye, J. M.: General equations and two-phase flow modeling, Handbook of Multiphase Systems, pp. 1-36 to 1-95 (1982)

16. Brill, J. P., Beggs, H. D.: Two-phase flow in pipes, IHRDC (1975)

17. Brown, D. J.: Disequilibrium in annular flow, Ph.D. Thesis, Oxford U. (1978)

18. Chhabra, R. P., Richardson, J. F.: Non-Newtonian flow in the process industries – fundamentals and engineering applications, Butterworth Heinemann (1999)

19. Chisolm, D., Laird, A. D. K.: Trans. AIME, v. 80, pp. 276 (1958)

20. Chin, W. C.: Advanced steady-state ad transient, three-dimensional, single and multiphase, non-Newtonian simulation system for managed pressure drilling, Public Executive Summary, RPSEA Contract No. 08121-2502-01, October (2009)

21. Chin, W. C.: Managed pressure drilling – modeling, strategy and planning, Final Report, RPSEA Contract No. 08121-2502-01, June (2011)

22. Collier, J. G.: Introduction to two-phase flow and heat transfer phenomena, Proc. of NATO Advanced Study Inst., U. of Bosphorus, Istanbul, Turkey (1976)

23. Danielson, T. J., Brown, L. D., Bansal, K. M.: Flow management – steady-state and transient multiphase pipeline simulation, OTC Paper No. 11965 (2000)

24. Danielson, T. J.: Transient multiphase flow – past, present, and future with flow assurance perspective, Energy and Fuels, v. 26, pp. 4137-4144 (2012b)

25. Delhaye, J. M.: General equations for two-phase systems and their applications to air-water bubble flow and to steam-water flashing flow, ASME-69-HT-63 (1969)

26. Dinh, T. N., Nourgaliev, R. R., Theofanous, T. G.: Understanding the ill-posed two-fluid model, 10th Intl. Topical Meeting on Nuclear Reactor Thermal Hydraulics, NURETH-10, Seoul, South Korea, October 5-9 (2003)

27. DiPippo, R.: The next steps in two-phase flow – executive summary, U.S. Dept. of Energy workshop/symposium, Brown University, Report No. GEOFLO/8 (1980)

28. Drew, D. A., Wood, R. T.: Overview and taxonomy of models and methods, appendix 1, Intl. Workshop on Two-Phase Flow Fundamentals, Gaithersburg, Maryland (1985)

29. Drew, D. A.: Mathematical modeling of two-phase flow, Ann. Rev. Fluid Mech., v. 15, pp. 261-291 (1983)

30. Eidsmoen, H., Roberts, I.: Issues relating to proper modeling of the profile of long gas condensate pipelines, Pipeline Simulation Interest Group, Paper No. 0501 (2005)

31. Flanigan, O.: Effect of uphill flow on pressure drop in design of two-phase gathering systems, Oil and Gas J., March 10th (1958)

32. Gazley, C., Jr.: Interfacial shear and stability in two-phase flow, Ph.D. Dissertation, U. of Delaware (1948)

33. Gomez, L. E., Shoham, O, Schmidt, Z., Chokshi, R. M., Brown, A., Northug, T.: A unified mechanistic model for steady-state two-phase flow in wellbores and pipelines, SPE Paper 56520 (1999)

34. Govan, A. H.: Modelling of vertical annular and dispersed two-phase flows, Ph.D. Thesis, Imperial College (1990)

35. Grassi B., Strazza, D., Poesio, P.: Experimental validation of theoretical models in two-phase high-viscosity ratio liquid-liquid flows in horizontal and slightly inclined pipes, Intl. J. of Multiphase Flow, v. 34, pp. 950-965 (2008)

36. Gregory, G. A., Fogarasi, M. P.: A critical evaluation of multiphase gas-liquid pipeline calculation methods, 2nd Intl. Conf. on Multiphase Flow, London, June 19-21 (1985)

37. Gregory, G. A., Mandhane, J. M., Aziz, K.: Some design considerations for two-phase flow in pipes, J. Can. Petroleum Tech., January-March (1975b)

38. Griffith, P., Wallis, G. B.: Slug flow, technical report no. 15, Division of Sponsored Research, Massachusetts Inst. of Tech., The Office of Naval Research – DSR Project No. 7-7673 (1959)

39. Haaland, S. E.: Simple and explicit formulas for the skin friction in turbulent pipe flow, ASME J. Fluids Eng., 105, pp. 89-90 (1983)

40. Han, H.: A study of entrainment in two-phase upward cocurrent annular flow in a vertical tube, Ph.D. Thesis, Dept. of Mechanical Eng., U. of Saskatchewan (2005)

41. Hewitt, G. F., Hall-Taylor, N. S.: Annular two-phase flow, Permagon Press (1970)

42. Hewitt, G. F., Jayanti, S.: To churn or not to churn, Intl. J. of Multiphase Flow, Brief Comm., v. 19, no. 3, pp. 527-529 (1993)

43. Hewitt, G. F.: Co-current and counter-current two phase annular flow, 9th Australasian Fluid Mech. Conf., Auckland, December 8-12 (1986)

44. Hewitt, G. F.: Flow Pattern: Friend or Foe?, Intl. Symposium on Multiphase Flow and Transport Phenomena, Antalya, Turkey, Nov. (2000)

45. Hewitt, G. F.: Introduction (to benchmarking datasets), Multiphase Science and Technology, v. 3, pp. 131-144 (1987)

46. Hewitt, G. F.: Two-phase flow and its applications – past, present, and future, J. Heat Transfer Engineering, v. 4, no. 1, pp. 67-79 (1983)

47. Heywood, N. I., Cheng, D. C. H.: Flow in pipes, part 2 – multiphase flows, J. Phys. Technol., v. 15, pp. 291 (1984)

48. Hubbard, M. G.: An analysis of horizontal gas-liquid slug flow, Ph.D. dissertation, U. of Houston (1965)

49. Hung, N.: On the formulation of constitutive laws required to describe two-phase flow models, Letters in Heat and Mass Transfer, vol. 6, pp. 513-518 (1979)

50. Ishii, M., Hibiki, T.: Thermo-fluid dynamics of two-phase flow, Springer (2006)

51. Ishii, M.: Thermally induced flow instabilities in two-phase mixtures, Ph.D. Dissertation, Georgia Inst. of Tech. (1971)

52. Ishii, M.: Thermo-fluid dynamic theory of two-phase flow, Eyrolles, Paris (1975)

53. Kaya, A. S., Sarica, C., Brill, J. P.: Mechanistic modeling of two-phase flow in deviated wells, Soc. of Petroleum Engineers, Paper No. 72998 (2001)

54. Lahey, Jr., R. T., Wood, R. T.: Intl. workshop of two-phase flow fundamentals, Rennselaer Polytechnic Inst., Troy, New York (1987)

55. Lahey, Jr., R. T.: Two fluid or not two fluid, Heat Transfer Engineering, v. 3, no. 2, pp. 9 (1981)

56. Landau, L. D., Lifshitz, E. M.: Fluid mechanics, 2nd Ed., Course of Theoretical Physics, v. 6, Elsevier (1987)

57. Leal, L. G.: Advanced transport phenomena – laminar flow and convective transport processes, Cambridge University Press (2007)

58. Leung, J. C. M.: Occurrence of critical heat flux during blowdown with flow reversal, ANL Report 77-4, January (1977)

59. Levy, S: Two-phase flow in complex systems, Wiley-Interscience Pub. Co. (1999)

60. Majiros, P. G., Dukler, A. E.: Develop. Mechanics, v. 1 (1961)

61. Manadilli, G.: Replace implicit equations with sigmoidal functions, Chem. Eng. J., v. 104, no. 8, pp. 129 (1997)

62. Mao, Z. S., Dukler, A. E.: The myth of churn flow?, Intl. J. of Multiphase Flow, Brief Comm., v. 19, no. 2, pp. 377-383 (1993)

63. Martin, C. J.: Annular two-phase flow, Ph.D. Dissertation, Oxford U. (1983)

64. Massey, B. S.: Mechanics of fluids, ed. 6, Chapman & Hall (1989)

65. Metzner, A. B., Reed, J. C.: Flow of non-Newtonian fluids – correlation of the laminar, transition, and turbulent flow regimes, AIChE J., v. 1, no. 4, pp. 434-440, December (1955)

66. Milan, M., Borhani, N., Thome, J. R.: Adiabatic vertical downward air-water flow pattern map – influence of inlet device, flow development length and hysteresis effects, Intl. J. Multiphase Flow, v. 56, pp. 126-137, October (2013)

67. Mullin, T.: Experimental studies of transition to turbulence in a pipe, Ann. Rev. Fluid Mech., v. 43, pp. 1-24 (2011)

68. Nicholas, E.: Simulation of slack line flow – a tutorial, Proc. of 27th Ann. Pipeline Simulation Interest Group Conf., Paper No. 0905, Albuquerue, New Mexico, October 18-20 (1995)

69. Oddie, G., Shi., H., Durlofsky, L. J., Aziz, K., Pfeffer, B., Holmes, J. A.: Experimental study of two and three phase flows in large diameter inclined pipes, Intl. J. Multiphase Flow, v. 29, pp. 527-558 (2003)

70. Oliemans, R. V. A., Pots, B. F. M., Trompe, N.: Modelling of annular dispersed two-phase flow in vertical pipes, Intl. J. of Multiphase Flow, v. 12, no. 5, pp. 711-732 (1986)

71. Oliemans, R. V. A.: The lubricating-film model for core-annular flow, Ph.D. Dissertation, Delft University (1986)

72. Omgba-Essama, C.: Numerical modeling of transient gas-liquid flows (application to stratified and slug flow regimes), Ph.D. Thesis, Cranfield U. (2004)

73. Pan, L.: High pressure three-phase (gas/liquid/liquid) flow, Ph.D. Thesis, Imperial College (1996)

74. Persen, L. N.: The mechanics of two phase flow, Institutt For Mekanikk, U. of Tronheim (1986)

75. Prosperetti, A., Trygvasson, G.: Computational methods for multiphase flow, Cambridge University Press, Cambridge (2007)

76. Prosperetti, A..: Two-fluid modeling and averaged equations, Multiphase Sci. and Tech., v. 15, no. 1-4, pp. 181-192 (2003)

77. Reyes, Jr., J. N.: A study of non-equilibrium dispersed two-phase flow, Ph.D. Dissertation, U. of Maryland (1986)

78. Rey-Fabret, I., Deflandre, J. P., Henriot, V., Badran, F., Thiria, S.: Neural network approach for multiphase hydrodynamic simulation, 11th Intl. Conf. of Multiphase Flow, San Remo, Italy, June 11-13 (2003)

79. Sawant, P., Ishii. M., Mori, M.: Droplet entrainment correlation in vertical upward co-current annular two-phase flow, Nucl. Eng. Des., v. 238, pp. 1342-1352 (2008)

80. Schubring, D.: Behavior interrelationships in annular flow, Ph.D. Thesis, U. of Wisconsin-Madison (2009)

81. Sekoguchi, K., Sato, Y., Kariyasaki, A.: The influences of mixers, bends, and exits sections on horizontal two-phase flow, Proc. of an Intl. Sym. on Research in Cocurrent Gas-Liquid Flow, U. of Waterloo, September 18-19 (1968)

82. Shah, R. K.: Research needs in low Reynolds number flow heat exchangers, J. Heat Trans. Eng., v. 3, no. 2 (1981)

83. Shaha, J., Manolis, I. G., Hewitt, G. F.: Interfacial shear stress in transient stratified two-phase flow, 9th Intl. Conf. on Multiphase, Cannes, France, June 16-18 (1999)

84. Shippen, M., Bailey, W. J.: Steady-state multiphase flow – past, present, and future, with a perspective on flow assurance, Energy and Fuels, v. 26, pp. 4145-4157 (2012)

85. Shirdel, M.: Development of a coupled wellbore-reservoir compositional simulator for damage prediction and remediation, Ph.D. Dissertation, U. of Texas at Austin (2013)

86. Silvestri, M.: Fluid mechanics and heat transfer of two-phase annular-dispersed flow, Adv. in Heat Transfer, v. 1, pp. 355-446 (1964)

87. Slattey, J. C., Gagglioli, R. A.: Chem. Eng. Sci., v. 17, pp. 893-895 (1962)

88. Spalding, D. B.: Multiphase flow prediction in power-system equipment and components, Intl. J. of Multiphase Flow, v. 6, pp. 157-168 (1980)

89. Stewart, H. B., Wendroff, B.: Two-phase flow – models and methods, J. Comp. Physics, v. 56, pp. 363-409 (1984)

90. Stewart, H. B.: Overview of multi-fluid flow calculation methods, BNL Report 29189, Army Research Office Workshop on Multiphase Flow, Maryland, February 2-4 (1981)

91. Stone, H. A.: Interfaces – in fluid mechanics and across disciplines, Batchelor Prize Lecture, J. Fluid Mechanics, v. 645, pp. 1-25 (2010)

92. Trallero, J. L.: Oil-water flow patterns in horizontal pipes, Ph.D. Dissertation, U. of Tulsa (1995)

93. Wallis G.B.: One-dimensional two-phase flow, McGraw Hill, New York (1969)

94. Wallis G.B.: One-dimensional two-phase flow, McGraw Hill, New York (1969)

95. Whitaker, S.: Laws of continuum physics for single-phase, single-component systems, Handbook of Multiphase Systems, pp. 1-5 to 1-35 (1982)

96. Wood, R. K.: The upward vertical flow of oil-water mixtures: effect of second phase viscosity on pressure drop, flow-pattern and holdup, M.S. Thesis, Dept. of Chemical Engineering, U. of Alberta (1960)

97. Youngren, G. K., Acrivos, A.: Stokes flow past a particle of arbitrary shape – a numerical method of solution, J. Fluid Mech., v. 69, pp. 377-403 (1975)

CHAPTER 3 PUBLICATIONS

1. Abdulkadir, M., Hernandez-Perez, V., Sharaf, S., Lowndes, I. S., Azzopardi, B. J.: Experimental investigation of phase distributions of two-phase air-silicone oil flow in vertical pipe, World Acad. of Sci., Eng. and Tech., 61 (2010)
2. Andreussi, P., Zanelli, S.: Downward annular and annular-mist flow of air-water mixtures, Proc. of the Seminar of the Intl. Center for Heat and Mass Transfer, v. 2, Dubrovnik, Yugoslavia, pp. 303-314 (1978)
3. Ansari, A. M., Sylvester, N. D., Sarica, C., Shoham, O., Brill, J. P.: A comprehensive mechanistic model for upward flow in pipes, Soc. of Petroleum Engineers Productions and Facilities J., May, pp. 217-226 (1994)
4. Ansari, A. M.: A comprehensive mechanistic model for upward two-phase flow, M.S. Thesis, U. of Tulsa (1988)
5. Armand, A. A.: The resistance during the movement of a two-phase system in horizontal pipes, AERE-Trans., v. 828, no. 1, pp. 16-23 (1946)
6. Arney, M. S., Bai, R., Guevara, E., Joseph, D. D., Liu, K.: Friction factor and holdup studies for lubricated pipelining, Intl. J. of Multiphase Flow, v. 19, no. 6, pp. 1061-1076 (1993)
7. Avdeev, A. A.: Turbulent flow hydrodynamics of a bubbly two-phase mixture, J. of Eng. Physics, pp. 536-544 (1984)
8. Baldauff, J., Runge, T., Cadenhead, J., Faur, M., Marcus, R., Mas., C., North, R., Oddie, G.: Profiling and quantifying complex multiphase flow, Oilfield Review, Autumn (2004)
9. Bankoff, S. G., Lee, S. C.: A comparison of flooding models for air-water and steam-water flow, Advances in two-phase flow and heat transfer, NATO ASI Series, pp. 745-780 (1983)
10. Bankoff, S. G.: A variable density single-fluid model two-phase flow with particular reference to steam-water, J. Heat Transfer, 11 (Series B), pp. 265–272 (1960)
11. Baroczy, C. J.: Correlation of liquid fraction in two-phase flow with application to liquid metals, Report NAA-SR-8171 (1963)
12. Becker, K. M., Letzter, A.: Flooding and deflooding measurement for countercurrent flow of air and water in vertical channels, Report KTH-NEL-25 (1978)

13. Beggs, J. P., Brill, H. D.: A Study of Two-Phase Flow in Inclined Pipelines, Journal of Petroleum Technology, pp. 607-617, May (1973)

14. Bensler, H. P.: Determination de l'aire interfaciale du taux de vide et du diametre moyen de Sauter dans un ecoulement a bulles a partir d'un faisceau d'ultrasons, Ph.D. Thesis, Institut National Polytechnique de Grenoble, France (1990)

15. Bhagwat, S. M., Ghajar, A. J. : A flow pattern independent drift flux model based void fraction correlation for a wide range of gas-liquid two phase flow, Intl. J. Multiphase Flow, v. 59, pp. 186-205 (2014)

16. Bharathan, D., Wallis, G. B., Richter, H. J.: Air-Water countercurrent annular flow, Topical Report, EPRI Research Project 443-2, NP-1165, September (1979)

17. Blasius, P. R. H.: Das Aehnlichkeitsgesetz bei Reibungsvorgangen in Flüssigk eiten. Forschungsheft, v. 131, pp. 1-41 (1913)

18. Brill. J. P.: Transportation of liquids in multiphase pipelines under low liquid loading conditions, Final Report, GRI Project (1996)

19. Buckley, S. E., Leverett, M. C.: Mechanism of fluid displacement in sands, Trans. AIME, v. 146, pp. 107-116 (1942)

20. Bunner, B., Tryggvason, G.: Dynamics of homogeneous bubbly flows: Part 1. Rise velocity and microstructure of the bubbles, J. Fluid Mech., v. 466, pp. 17–52 (2002)

21. Bunner, B., Tryggvason, G.: Effect of bubble deformation on the stability and properties of bubbly flows, J. Fluid Mech., v. 495, pp. 77–118 (2003)

22. Butterworth, D.: A comparison of some void-fraction relationships for co-current gas-liquid flow, Brief Comm., Intl. J. of Multiphase Flow, v. 1, pp. 845-850 (1975)

23. Cabello, R., Cardenas, C., Lombano, G., Ortega, P., Brito, A., Trallero, J., Colmenares, J.: Pruebas experimentales con kerosen/aire para el estudio de flujo tapon con sensores capacitivos en una tuberia horizontal, INT-8898,2001. PDVSA INTEVEP, pp. 50 (2001)

24. Celata, G. P., Cumo, M., Farello, G. E., Setaro, T.: Hysteresis effect in flooding, Brief Comm., Intl. J. Multiphase Flow, v. 17, no. 2, pp. 283-289 (1991)

25. Chen, J. J., Spedding, P. L.: An analysis of holdup in horizontal two-phase gas liquid flow, Int. J. Multiphase Flow, v. 2, pp. 147–159 (1983)

26. Chexal, B., Lellouche, G.: Void fraction correlation for generalized applications, Prog. Nucl. Energy, v. 27, no. 4, pp. 255-295 (1992)

27. Chiba, N., Takahashi, Y.: Generation of micro air bubbles of uniform size in water, Presented at 3rd Intl. Symp. Cavitation, Grenoble, France (1998)

28. Chiva, S., Julia, J. E., Hernandez, L., Mendez, S., Munoz-Cobo, J. L., Romero, A.: Experimental study on two-phase flow characteristics using conductivity probes and laser doppler anemometry in a vertical pipe, Chem. Eng. Commun., v. 197, pp. 180–191 (2010)

29. Cioncolini, A., Thome, J. R.: Void fraction prediction in annular two-phase flow, Intl. J. Multiphase Flow, v. 43, pp. 72-84 (2012)

30. Clark, N. N., Flemmer, R. L.: Predicting the holdup in two-phase bubble upflow and downflow using the Zuber and Findlay Drift-Flux model, AIChE J., v. 31, no. 3, pp. 500-503, March (1985)

31. Clark, N. N., Rezkallah, K. S.: A study of drift velocity in bubbly two-phase flow under microgravty conditions, Intl. J. Multiphase Flow, v. 27, pp. 1533-1554 (2001)

32. Clift, R., Pritchard, C. L., Nedderman, R. M.: The effect of viscosity on the flooding conditions in wetted wall columns, Chem. Eng. Sci., v. 21, pp. 87-95 (1966)

33. Coddington, P., Macian, R.: A study of the performance of void fraction correlations used in the context of drift-flux two-phase flow models, Nucl. Eng. Des., v. 215, pp. 199-216 (2002)

34. Collier, J. G., Wallis, G. B.: Two-phase flow and heat transfer, notes for a summer course, v. 2, Dartmouth College, July (1966)

35. Corteville, J., Duchet-Suchaux, P., Lopez, D.: Comparison of methods for predicting pressure loss in oil and gas wells, 5th Intl. Conf. on Multiphase Production, BHR Group, Cannes, France (1991)

36. Czop, V., Barbier, D., Dong, S.: Pressure drop, void fraction and shear stress measurements in adiabatic two-phase flow in coiled tube, Nucl. Eng. Des., v. 149, pp. 323–333 (1994)

37. Danielson, T. J., Brown, L. D., Bansal, K. M.: Flow management – steady-state and transient multiphase pipeline simulation, OTC Paper No. 11965 (2000)

38. Das, A. K., Das, P. K: Peak structure in downward gas-liquid bubbly flow and its transition to slug flow – a numerical investigation, Intl. J. Multiphase Flow, v. 40, pp. 136-143 (2012)

39. Davis, M. R.: The determination of wall friction for vertical and horizontal two-phase bubbly flows, J. Fluids Eng., pp. 173-179 (1974)

40. Delhaye, J. M.: Some issues related to the modelling of interfacial areas in gas-liquid flows, Part II: modelling the source terms for dispersed flows, C. R. Acad. Sci., Paris, Sér. Ilb t. 329, pp. 473–486 (2001)

41. Dhulesia, H., Lopez, D.: Critical evaluation of mechanistic two-phase flow pipeline and well simulation models, Soc. of Petroleum Engineers, Paper No. 36611 (1996)

42. Diener, R., Friedel, L.: Reproductive accuracy of selected void fraction correlations for horizontal flow and vertical upflow, Proc. of the German-Japanese Sym. on Multiphase Flow, Karlsruhe, Germany, pp. 17-32, August 23-25 (1994)

43. Drew, D. A., Lahey, Jr., R. T.: The virtual mass and lift force on a sphere in rotating and straining flow, Intl. J. Multiphase Flow, v. 13, no. 1, pp. 113-121 (1987)

44. Dukler, A. E., Smith, L.: Two phase interactions in countercurrent flow studies of the flooding mechanism, Summary Report No. 2, NUREG/CR-0617, US Nuclear Regulatory Commission FIN No. B5684 (1977)

45. Eriksen, S., Midttveit, O.: PLT - Overcoming changing multiphase flow behavior along horizontal sections, http://bergen.spe.no/publish_files/ODS2007_SPE_Eriksen_Hydro.pdf (2010)

46. Ervin, E. A., Tryggvason, G.: The rise of bubbles in a vertical shear flow, ASME J. Fluid Eng., v. 119, pp. 443–449 (1997)

47. Fauske, H.: Critical two-phase, steam–water flows, Proc. of the 1961 Heat Transfer and Fluid Mechanics Institute, Stanford University Press (1961)

48. Flanigan, O.: Effect of uphill flow on pressure drop in design of two-phase gathering systems, Oil and Gas J., March 10th (1958)

49. Franca, F., Laehy, Jr., R. T.: The use of drift-flux techniques for the analysis of horizontal two-phase flows, Intl. J. Multiphase Flow, v. 18, no. 6, pp. 787-801 (1992)

50. Fujikawa, S., Zhang, R., Hayama, S., Peng, G.: The control of micro-air-bubble generation by a rotational porous plate, Intl. J. Multiphase Flow, v. 29, pp. 1221–1236 (2003)

51. Fujita, H., Ohara, T., Hirota, M., Furuta, H.: Gas-liquid flow in flat channels with small channel clearance, Advances in Multiphase Flow, pp. 441 (1995)

52. Garcia, F., Garcia, R., Joseph, D. D.: Composite power law holdup correlations in horizontal pipes, Intl. J. Multiphase Flow, v. 31, pp. 1276-1303 (2005)

53. Garnier, C., Lance, M., Marie, J. L.: Measurement of local flow characteristics in buoyancy-driven bubbly flow at high void fraction, Exp. Therm. Fluid Sci., v. 26, pp. 811-815 (2002)

54. Ghajar, A. J., Tang, C. C.: Void fraction and flow patterns of two-phase gas-liquid flow in various pipe inclinations, 7th Intl. Conf. on Heat Transfer, Fluid Mech. And Thermodynamics, HEFAT2010, July 19-21 (2010)

55. Godbole, P. V.: Study of flow patterns and void fraction in vertical upward two-phase flow, M.S. Thesis, Oklahoma State U. (2009)

56. Gomez, L. E., Shoham, O, Schmidt, Z., Chokshi, R. M., Brown, A., Northug, T.: A unified mechanistic model for steady-state two-phase flow in wellbores and pipelines, SPE Paper 56520 (1999)

57. Gould, T., Ramsey, E.: Design of Offshore Gas Pipelines Accounting For Two-Phase Flow, Gas Technology, SPE Reprint Series, No. 13 Volume II, (1977)

58. Greskovich, E. J., Cooper, W. T.: Correlation and prediction of gas liquid holdups in inclined upflows, AIChE J., v. 21, pp. 1189–1192 (1975)

59. Griffith, P., Snyder, G. A.: The Bubbly-Slug Transition in a High Velocity Two-Phase Flow, MIT Report 5003-29, TID-20947, July (1964)

60. Griffith, P., Wallis G. B: Two-phase slug flow, J. Heat Transfer, v. 83, pp. 307-318 (1961)

61. Griffith, P.: Characteristics of bubbly flow, Multiphase Science and Technology J., v. 3, pp. 155-162 (1987)

62. Guet, S., Ooms, G., Oliemans, R. V. A., Mudde, R. F.: Bubble injector effect on the gaslift efficiency, AIChE J., v. 49, no. 9, pp. 2242-2252 (2003)

63. Guet, S., Ooms, G., Oliemans, R. V. A., Mudde, R. F.: Bubble size effect on low liquid input drift-flux parameters, Chem. Eng. Sci., v. 59, pp. 3315-3329 (2004)

64. Guet, S., Ooms, G.: Fluid mechanical aspects of the gas-lift technique, Ann. Rev. Fluid Mech., v. 38, pp. 255-249 (2006)

65. Guzhov, A. L., Mamayev, V. A., Odishariya, G. E.: A study of transportation in gas liquid systems, 10th Intl. Gas Union Conf., Hamburg, Germany, June 6–10 (1967)

66. Hagedorn, A. R., Brown, K. E.: Experimental Study of Pressure Gradients Occurring During Continuous Two-phase Flow in Small Diameter Vertical Conduits, J. Petroleum Technology, pp. 475-484 (1965)

67. Hagedorn, A. R.: Experimental study of pressure gradients occurring during continuous two-phase flow in small diameter vertical conduits, Experimental Gas Lift project, Ph.D. Dissertation, U. of Texas at Austin (1964)

68. Haoues, L., Olekhnovitch, A. N., Teyssedou, A.: Numerical study of the influence of the internal structure of a horizontal bubbly flow on the average void fraction, Nucl. Eng. Des., v. 239, pp. 147-157 (2009)

69. Hasan, A. R., Kabir, C. S., Rahman, R.: Predicting liquid gradient in a pumping-well annulus, SPEPE, pp. 113-120, February (1988)

70. Hasan, A. R., Kabir, C. S.: A study of multiphase flow behavior in vertical wells, Soc. of Petroleum Engineers Prod. Eng., Paper No. 15138, pp. 263-272, May (1988a)

71. Hasan, A. R., Kabir, C. S.: Fluid flow and heat transfer in wellbores, Soc. of Petroleum Engineers (2002)

72. Hasan, A. R., Kabir, C. S.: Predicting multiphase flow behavior in a deviated well, Soc. of Petroleum Engineers Production Engineering, Paper No. 15449, November (1988b)

73. Hasan, A. R.: Void fraction in bubbly, slug and churn flow in vertical two-phase up-flow, Chem. Eng. Comm., v. 66, pp. 101-111 (1988)

74. Herringe, R. A., Davis, M. R.: Flow structure and distribution effects in gas-liquid mixture flows, Intl. J. Multiphase Flow, v. 4, pp. 461-486. (1978)

75. Hetsroni, G.: Handbook of multiphase systems, Hemisphere Publishing Corp. (1982)

76. Hewitt, G. F, Delhaye, J. M., Zuber, N.: Multiphase Science and Technology J., v. 3 (1987)

77. Hewitt, G. F., Wallis, G. B.: Flooding and associated phenomena in falling film flow in a tube, UK AERE Report R4022 (1963)

78. Hewitt, G. F.: Co-current and counter-current two phase annular flow, 9th Australasian Fluid Mech. Conf., Auckland, December 8-12 (1986)

79. Hibiki, T., Goda, H., Kim, S., Ishii, M., Uhle, J.: Structure of vertical downward bubbly flow, Intl. J. Heat Mass Transfer, v. 47, pp. 1847-1862 (2004)

80. Hibiki, T., Ishii, M., Xiao, Z.: Local flow measurements of vertical upward air-water flow in round tube, Intl. J. Heat Mass Transfer, v. 44, pp. 1869–1888 (2001)

81. Hibiki, T., Ishii, M.: Distribution parameter and drift velocity of drift-flux model in bubbly flow, Intl. J. Heat and Mass Transfer, v. 45, pp. 707-721 (2002)

82. Hoogendoorn, C. J.: Gas–liquid flow in horizontal pipes, Chem. Eng. Sci., v. 9, pp. 205–217 (1959)

83. IAEA: Thermal-hydraulic relationships for advanced water cooled reactors, Report IAES-TECDOC-1203, Intl. Atomic Energy Agency (2001)

84. Ilic, V., Senyolcu, M.: Effect of flow obstructions on void fraction profile in vertical air/water flow, 10th Australasian Fluid Mech. Conf., U. of Melbourne, December 11-15 (1989)

85. Ishii, M., Hibiki, T.: Thermo-fluid dynamics of two-phase flow, Springer (2006)

86. Ishii, M., Mishima, K.: Liquid transfer and entrainment correlation for droplet-annular flow, 7th Intl. Heat Transfer Conf., Muchen (1982)

87. Ishii, M.: Thermo-fluid dynamic theory of two-phase flow, Eyrolles, Paris (1975)

88. Jakobsen, H. A., Sannaes, B. H., Grevskott, S., Svendsen, H. F.: Modeling of vertical bubble-driven flows, Review, Ind. Eng. Chem. Res., v. 36, pp. 4052-4074 (1997)

89. Joseph, D. D., Ocando, D.: Slip velocity and lift, J. Fluid Mech., pp. 1-24 (2002)

90. Joseph, D. D.: Opportunities for extracting correlations from numerical and real experiments using digital technology, Multiphase Science and Tech., v. 15, Issues 1-4, pp. 173-176 (2003b)

91. Joseph, D. D.: Power law correlations for lift from direct numerical simulation of solid liquid flow, 4th Intl. Conf. Multiphase Flow, New Orleans, http://www.aem.umn.edu/people/faculty/joseph/archive/docs/4thConf-MultiphFlow.pdf (2001)

92. Kamp, A., Colin, C., Fabre, J.: Bubbly flow in a pipe – influence of gravity upon void and velocity distributions, 3rd World Conf. on Exp. Heat Transfer, Fluid Mech. And Thermodynamics, Honolulu (1993)

93. Karimi, G.: An experimental study of falling films in counter-current annular flow in a vertical tube, Ph.D. Dissertation, Dept. of Chem. Eng. and Applied Chemistry, U. of Toronto (1998)

94. Kariyosaki, A.: Behavior of a gas bubble in a liquid flow with a linear velocity profile, Proc. 7th Two-phase Flow Sympos. Of Japan (1985)

95. Kashinsky, O. N., Randin, V. V.: Downward bubbly gas-liquid flow in a vertical pipe, Intl. J. Multiphase Flow, v. 25, pp. 109-138 (1999)

96. Kawamura, T., Sakamoto, J., Motoyama, H., Kato, H., Miyanaga, M.: Experimental study on the effect of bubble size on the microbubble drag reduction, Proc. Intl. Conf. Multiph. Flow, ICMF5, Yokohama, Japan (2004)

97. Kaya, A. S., Sarica, C., Brill, J. P.: Mechanistic modeling of two-phase flow in deviated wells, Soc. of Petroleum Engineers, Paper No. 72998 (2001)

98. Koide, K., Kato, S., Tanaka, Y., Kubota, H.: Bubble generated from porous plate, J. Chem. Eng. Jpn., v. 5, pp. 51–56 (1968)

99. Koval, E. J.: A method for predicting the performance of unstable miscible displacement in heterogeneous media, Soc. of Petroleum Engineers, Paper No. 450, June (1963)

100. Krepper, E., Lucas, D., Prasser, H.-M.: On the modelling of bubbly flow in vertical pipes, Nucl. Eng and Des., v. 235, pp. 597-611 (2005)

101. Lahey, Jr., R. T., Moody, F. J.: The thermal-hydraulics of a boiling water nuclear reactor, 2nd ed., American Nuclear Society (1993)

102. Lahey, Jr., R. T.: The analysis of phase separation and phase distribution phenomena using two-fluid model, Nucl. Eng. Des., v. 122, pp. 17-40 (1990)

103. Langsholt, M., Holm, H.: Liquid accumulation in gas-condensate pipelines – an experimental study, 13th Intl. Conf. Multiphase Prod. Tech., Edinburgh (2007)

104. Lareo, C. A., Fryer, P. J.: Vertical flows of solid-liquid food mixtures, J. Food Eng., v. 36, pp. 417-443 (1998)

105. Lareo, C., Fryer, P. J., Barigou, M.: The fluid mechanics of solid-liquid two-phase flows: a review, Trans. of the Inst. of Chem. Engineers Part C, v. 75, pp. 73-105 (1997)

106. Liu, T. J., Bankoff, S. G.: Structure of air-water bubbly flow in a vertical pipe - I - liquid mean velocity and turbulence measurements, Advances in gas-liquid flows, ASME FED, v. 99, pp. 9-17 (1990a)

107. Liu, T. J., Bankoff, S. G.: Structure of air-water bubbly flow in a vertical pipe -II - void fraction, bubble velocity and bubble size distribution, Advances in gas-liquid flows, ASME FED, v. 99, pp. 19-26 (1990b)

108. Liu, T. J.: Investigation of the wall shear stress in vertical bubbly flow under different bubble size conditions, Intl. J. Multiphase Flow, v. 23, no. 6, pp. 1085-1109 (1997)

109. Lockhart R. W., Martinelli, R. C.: Proposed correlation of data for isothermal two-phase, two- component flow in pipes, J. Chem. Eng. Process, v. 45, no. 1, pp. 39–48 (1949)

110. Luo, K. M.: Experimental gas-solid vertical transport, Ph.D. Dissertation, Illinois Institute of Tech. (1987)

111. Malnes, D.: Slip ratios and friction factors in the bubble flow regime in vertical tubes, Report KR-110, Institutt for Atomenergi. Kjelles, Norway (1966)

112. Manera, A., Prasser, H.-M., Van Der Hagen, T. H. J. J.: Suitability of drift-flux models, void fraction evolution, and 3-D flow pattern visualization during stationary and transient flashing flow in a vertical pipe, Nucl. Tech. J., v. 152, October (2005)

113. Mao, D., Harvey III, A. D.: Transient-nonisothermal-multiphase-wellbore-model development with phase change and its application to producer wells, Soc. of Petroleum Engineers J., Paper No. 146318 (2013)

114. Mathure, N.: Study of flow patterns and void fraction in horizontal two-phase flow, M.S. Thesis, Oklahoma State U. (2010)

115. Mendez-Diaz, S., Zenit, R., Chiva, S., Munoz-Cobo, J. L., Martinez-Martinez, S.: A criterion for the transition from wall to core peak gas volume fraction distributions in bubbly flows, Brief Comm., Intl. J. Multiphase Flow, v. 43, pp. 56-61 (2012)

116. Mendez-Diaz, S.: Medida experimental de la concentracion de area interfacial en flujos bifasicos finamente dispersos y en transicion, Ph.D. Dissertation, Universidad Politecnica de Valencia (2008)

117. Mishima, K., Ishii, M.: Flow Regime Transition Criteria for Upward Two-Phase Flow in Vertical Tubes, Intl. J. Heat Mass Transfer, v. 27, pp. 773 (1984)

118. Morel, C., Ruyer, P., Seiler, N., Lavieville, J. M.: Comparison of several models for multi-size bubbly flows on an adiabatic experiment, Intl. J. Multiphase Flow, v. 36, pp. 25-39 (2010)

119. Mudde R. F., Saito, T.: Hydrodynamical similarities between bubble column and bubbly pipe flow, J. Fluid Mech, v. 437, pp. 203–228 (2001)

120. Mudde, R. F.: Gravity-driven bubbly flows, Ann. Rev. Fluid Mech., v. 37, pp. 393-423 (2005)

121. Mullin, T.: Experimental studies of transition to turbulence in a pipe, Ann. Rev. Fluid Mech., v. 43, pp. 1-24 (2011)

122. Nakoryakov, V. K., Kashinsky, O. N., Burdukov, A. P. and Odnoral, V. P.: Local characteristics of upward gas-liquid flows, Intl. J. Multiphase Flow, v. 7, pp. 63-81 (1981)

123. Nguyen, V. T., Song, C.-H., Bae, B.-U., Euh, D.-J.: Modeling of bubble coalescence and break-up considering turbulent suppression phenomena in bubbly two-phase flow, Intl. J. Multiphase Flow, v. 54, pp. 31-42 (2013)

124. Nicklin, D. J., Wilkes, J. O., Davidson, J. F.: Two-phase flow in vertical tubes, Trans. Inst. Chem. Engrs., v. 40, pp. 61 (1962)

125. Nishino, H., Yamazaki, Y.: A new method of evaluating steam volume fractions in boiling systems, J. Soc. Atomic Energy Japan, v. 5, pp. 39-59 (1963)

126. Nusselt, W.: Z. Ver. Dtsch. Ing., v. 60, pp. 541 (1916)

127. Olekhnovich, A. N., Pokhvalov, Y. E.: An equation for calculating true volumetric void fraction, Therm. Eng., v. 36, no. 11, pp. 636–639 (1989)

128. Ortega, P., Trallero, J., Colmenares, J., Brito, A., Cabello, R., Gonzalez, P.: Experimentos y validacion de modelo para prediccion del gradiente de presion de flujo tapon en tuberias horizontales para un sistema bifasico altamente viscoso aceite (1200 cP)/aire, INT-8879,2001. PDVSA INTEVEP, pp. 37 (2001)

129. Ortega, P., Trallero, J., Colmenares, J., Cabello, R., Gonzalez, P.: Modelo para la prediccion de la caida de presion en flujo tapon para una tuberia horizontal, INT-8123,2000. PDVSA INTEVEP, pp. 19 (2000)

130. Oshinowo, T., Charles, M. E.: Vertical two-phase flow – part II – holdup and pressure drop, Can. J. Chem. Eng., v. 52, pp. 438-448 (1974)

131. Owen, D. G.: An experimental and theoretical analysis of equilibrium annular flows, Ph.D. Dissertation, Dept. of Chem. Eng., U. of Birmingham (1986)

132. Papathanassiou, G., Meader, P. F., DiPippo, R., Dickinson, D. A.: Void fraction correlations in two-phase horizontal flow, Los Alamos National Laboratory Report No. GEOFLO/17, LAUR-83-1902, May (1983)

133. Plaxton, W. L.: Pipe flow experiments for the analysis of two-phase liquid-liquid pressure drop in horizontal wells, M.Sc. Thesis, Dept. of Petroleum Engineering, U. of Alberta, Canada (1995)

134. Politano, M. S., Carrica, P. M., Converti, J.: A model for turbulent polydisperse two-phase flow in vertical channels, Intl. J. Multiphase Flow, v. 29, pp. 1153-1182 (2003)

135. Premoli, A., Francesco, D., Prima, A.: An empirical correlation for evaluating two-phase mixture density under adiabatic conditions, European Two-Phase Flow Group Meeting, Milan, Italy (1970)

136. Prosperetti, A., Trygvasson, G.: Computational methods for multiphase flow, Cambridge University Press, Cambridge (2007)

137. Pushkina, O. L., Sorokin, Y. L.: Breakdown of liquid film motion in vertical tubes, Heat Transfer Soviet Res., v. 1, pp. 56-64 (1969)

138. Qi, F. S., Yeoh, G. H., Cheumg, S. C. P., Yu, J. Y., Krepper, E., Lucas, D.: Classification of bubbles in vertical gas-liquid flow – Part 1 – an analysis of experimental data, Intl. J. Multiphase Flow, v. 39, pp. 121-134 (2012)

139. Radovcich, N. A., Moissis, R.: The Transition from Two-Phase Bubble Flow to Slug Flow, MIT Report 7-7673-22, June (1962)

140. Ragland, W. A., Ganic, E. N.: Flooding in countercurrent two-phase flow, Advances in two-phase flow and heat transfer, NATO ASI Series, pp. 505-538 (1983)

141. Robinson, J. R.: Development of a two-phase flow well data bank and an evaluation study of pressure loss methods applied to directional oil wells, M.S. Thesis, U. of Tulsa (1974)

142. Rose, S. C., Jr.: Some hydrodynamic characteristics of bubbly mixtures flowing vertically upward in tubes, Ph.D. Dissertation, Massachusetts Inst. Of Tech. (1964)

143. Rossland, L.: Investigation of the performance of pressure loss correlations for high capacity wells, M.S. Thesis, U. of Tulsa (1981)

144. Rouhani, Z.: Effect of wall friction and vortex generation on radial void distribution – the wall-vortex effect, Aktiebolaget Atomenergi Report AE-497 (1974)

145. Serizawa A., Kataoka, I., Michiyoshi, I.: Turbulence structure of air-water bubbly flow - II - Local properties, Intl. J. Multiphase. Flow, v. 2, pp. 235-246 (1975)

146. Serizawa, A., Kataoka, I., Zun, I, Michiyoshi, I.: Bubble size effect on phase distribution, Proc. Japan-US Sem. On Two-phase Flow Dynamics, Ohtsu, Japan, pp. 15-20 (1988)

147. Serizawa, A., Kataoka, I.: Phase distribution in two-phase flow, Proc. ICHMT Conf. Transport., pp. 179 (1987)

148. Shawkat, M. E., Ching, C., Shoukri, M.: Bubble and liquid turbulence characteristics of bubble flow in a large diameter vertical pipe, Intl. J. Multiphase Flow, v. 34, pp. 765-785 (2008)

149. Shi, H., Holmes, J., Aziz, K.: Drift-Flux modeling of multiphase flow in wellbores, Soc. of Petroleum Engineers, Paper No. 84228 (2003)

150. Shiralkar, B. S.: Local void fraction measurements in Freon-114 with a hot-wire anemometer, General Electric Report NEDE-13158 (1970)

151. Shirdel, M.: Development of a coupled wellbore-reservoir compositional simulator for damage prediction and remediation, Ph.D. Dissertation, U. of Texas at Austin (2013)

152. Shoukri, M., Hassan, I., Gerges, I.: Two-phase bubbly flow structure in large diameter vertical pipes, Can. J. Chem. Eng., v. 81, pp. 205-211, April (2003)

153. Simpson, H. C., Rooney, D. H., Grattan, E., Al-Samarrae, F.: Flow pattern and pressure drop studies, Reports 1, 2 and 3, Research Contract RD/1065/014, Dept. of Mechanical Engineering, U. of Strathclyde (1976)

154. Singhal, M.: The effect of dispersed phase buoyancy on phase distribution, Ph.D. Dissertation, Rensselaer Polytechnic Inst. (2004)

155. Soliman, M., Schuster, J. R., Berenson, P. J.: A general heat transfer correlation for annular flow condensation, Trans. ASME, J. Heat Transfer, v. 90, pp. 267-276 (1968)

156. Song, C. H., No, H. C., Chung, M. K.: Investigation of bubble flow developments and its transition based on the instability of void fraction waves, Intl. J. Multiphase Flow, v. 21, pp. 381-404 (1995)

157. Spalding, D. B.: Multiphase flow prediction in power-system equipment and components, Intl. J. of Multiphase Flow, v. 6, pp. 157-168 (1980)

158. Spedding, P. L., Nguyen, V. T.: Data on holdup, pressure loss and flow pattern for two-phase, air-water flow in an inclined pipe. Report 122, U. of Auckland, Auckland, New Zealand (1976)

159. Spedding, P. L., Spence, D. R.: Prediction of holdup in two-phase flow, Intl. J. Eng. Fluid Mech., v. 2, no. 1, pp. 109-118 (1989)

160. Staub, F. W., Walmet, G. E.: Heat transfer and hydraulics – the effects of subcooled voids, Report EURAEC-2120, NYO-3679-8, May (1969)

161. Staub, F. W., Zuber, N.: A program of two-phase flow investigation, 5th Quarterly Report, GEA-4631 (1964)

162. Stosic, Z. V., Stevanovic, V. D.: A comparative analysis of bubbly flow void fraction based on different approaches for interfacial drag force, Exp. Heat Trans. Fluid Mech. Therm., Celata, Di Marco, Goulas, Mariani (eds.), Edizioni ETS, Pisa, pp. 1393-1400 (2001)

163. Strand, O.: An experimental investigation of stratified two-phase flow in horizontal pipes, Ph.D. Thesis, U. of Oslo, Norway (1993)

164. Sujumnong, M.: Heat transfer, pressure drop and void fraction in two-phase, two-component flow in a vertical tube, Ph.D. Dissertation, U. of Manitoba (1997)

165. Taitel, Y., Barnea, D., Dukler, A. E.: A film model for the prediction of flooding and flow reversal for gas-liquid flow in vertical tubes, Intl. J. Multiphase Flow, v. 8, no. 1, pp. 1-10 (1982)

166. Taitel, Y., Bornea, D., Dukler, A. E.: Modeling flow pattern transitions for steady upward gas-liquid flow in vertical tubes, AIChE J., vol. 26, pp. 345-354 (1980)

167. Takamasa, T., Goto, T., Hibiki, T., Ishii. M.: Experimental study of interfacial area trnasport of bubbly flow in small diameter tube, intl. J. Multiphase Flow, v. 29, pp. 395-409 (2003)

168. Theofanous, T. G., Amarasooriya, W. H.: Dataset no. 1 – pressure drop and entrained fraction in fully developed flow, Multiphase Sci. and Tech., v. 6, part 1, pp. 5-13 (1992)

169. Thom, J. R., S.: Prediction of pressure drop during forced circulation boiling water, Int. J. Heat and Mass Transfer, v. 7, pp. 709-724 (1964)

170. Thompson, L. G.: Determination of optimum combination of pressure loss and PVT property correlations for predicting pressure gradients in upward two-phase flow, M.S. Thesis, U. of Tulsa (1982)

171. Tomiyama, A.: Struggle with computational bubble dynamics, 3rd Intl. Conf. on Multiphase Flow, ICMF'98, Lyon, France, June 8-12 (1998)

172. Trygvasson, G., Esmaeeli, A., Lu, J., Biswas, S.: Direct numerical simulation of gas/liquid multiphase flows, Fluid Dynamics Research, v. 38, pp. 660-681 (2006)

173. Turner, J. M., Wallis, G. B.: The separate cylinders models of two-phase flow, Paper No. NYO-3114-6, Dartmouth College (1965)

174. Vijayan, P. K., Patil, A. P., Pikhwal, D. S., Saha, D., Raj, V. V.: An assessment of pressure drop and void fraction correlations with data from two-phase natural circulation loops, Heat and Mass Transfer, v. 36, pp. 541-548 (2000)

175. Wallis G.B.: One-dimensional two-phase flow, McGraw Hill, New York (1969)

176. Wallis, G. B., Makkenchery, S.: The hanging film phenomenon in vertical annular two-phase flow, Technical Brief, ASME J. Fluids Eng., v. 96, pp. 297-298 (1974)

177. Wang, S. K., Lee, S. L., Jones, O. C., Lahey, Jr., R. T.: Local void fraction measuring techniques in two-phase using hot-wire anemometry, Intl. J. Multiphase Flow, v. 23, pp. 327–343 (1987)

178. Watterson, J. K., Cooper, R. K., Spedding, P. L.: Prediction of pressure loss and holdup in two-phase horizontal stratified roll-wave pipe flow, Research Notes, Ind. Eng. Chem. Res., v. 41, pp. 6621-6622 (2002)

179. Woldesmayat, M. A., Ghajar, A. J.: Comparison of void fraction correlations for different flow patterns in horizontal and upward inclined pipes, Intl. J. of Multiphase Flow, v. 33, pp. 347-370 (2007)

180. Zabaras, G. J.: Studies of vertical annular gas-liquid flows, Ph.D. Dissertation, Dept. of Chemical Engineering, U. of Houston (1985)

181. Zapke, A., Kroger, D. G.: Countercurrent gas-liquid flow in inclined and vertical ducts – I – flow patterns, pressure drop characteristics and flooding, Intl. J. Multiphase Flow, v. 26, pp. 1439-1455 (2000)

182. Zenit R, Koch D. L., Sangani A.: Measurements of the average properties of a suspension of bubbles rising in a vertical channel, J. Fluid Mech., v. 429, pp. 307–41 (2001)

183. Zhao, H. D, Lee, K. C., Freeston, D. H.: Geothermal two-phase flow in horizontal pipes, Proc. World Geothermal Congress 2000, Kyushu-Tokyo, Japan, May 28–June 10, pp. 3349–3353 (2000)

184. Zheng, D., Che, D.: Experimental study on hydrodynamic characteristics of upward gas-liquid slug flow, Intl. J. Multiphase Flow, v. 32, pp. 1191-1218 (2006)

185. Zivi, S. M.: Estimation of steady state steam void fraction by means of the principle of minimum entropy production, Trans. ASME, J. Heat Transfer, v. 86, pp. 247–252 (1964)

186. Zuber, N., Findlay, J. A.: Average volumetric concentration in two-phase flow systems, J. of Heat Transfer, Transactions ASME, 87, 453-468 (1965)

187. Zuber, N.: One the variable density single-fluid model for two-phase flow with particular reference to steam-water flow, J. Heat Transfer, Trans. ASME, Ser. C., v. 82, pp. 265-272 (1960)

188. Zun, I., Malahovsky, A.: The terminal properties of single gas bubbles, Proc. 3rd Chem. Eng. Congress, Graz, pp. 112-119 (1982)

189. Zun, I.: The transverse migration of bubbles influenced by walls in vertical bubbly flow, Intl. J. Multiphase Flow, v. 6, pp. 583 (1980)

190. Zun, I.: Transition from wall void peaking to core void peaking in turbulent bubbly flow, Trans. Phenom. Multiphase Flow, pp. 205 (1988)

CHAPTER 4 PUBLICATIONS

1. Agrawal, S. S.: Slug flow in horizontal pipes, M.S. Thesis, U. of Calgary (1971)
2. Alamu, M. B., Azzopardi, B. J.: Simultaneous investigation of entrained liquid fraction, liquid film thickness and pressure drop in vertical annular flow, J. Energy Resour. Tech., v. 133, June (2011)
3. Anderson, G. H., Mantzouranis: Two-phase (gas-liquid) flow phenomena – I – pressure drop and hold-up for two-phase flow in vertical tubes, Chem. Eng. Sci., v. 12., pp. 109-126 (1960)
4. Andreussi, P., Bonizzi, M., Di Lullo, A., Margarone, M., Scotti, A., Taddei, S.: Advanced simulation of gas-liquid pipelines, 6th N. American Conf. on Multiphase Tech., BHR Group, Banff, Alberta, June 4-6 (2008)
5. Andreussi, P., Persen, L. N.: Stratified gas-liquid flow in downwardly inclined pipes, Intl. J. Multiphase Flow, v. 13, no. 4, pp. 565-575 (1987)
6. Andreussi, P., Zanelli, S.: Downward annular and annular-mist flow of air-water mixtures, Proc. of the Seminar of the Intl. Center for Heat and Mass Transfer, v. 2, Dubrovnik, Yugoslavia, pp. 303-314 (1978)
7. Andritsos, N.: Effect of pipe diameter and liquid viscosity on horizontal stratified flow, Ph.D. Dissertation, U. of Illinois at Urbana-Champaign (1986)
8. Asali, J. C.: Entrainment in vertical gas-liquid annular flows, Ph.D. Dissertation, U. of Illinois at Urbana-Champaign (1984)
9. Ashwood, A. C.: Characterization of the macroscopic and microscopic mechanics in vertical and horizontal annular flow, Ph.D. Dissertation, U. of Wisconsin-Madison (2010)
10. Aziz, K., Gregory, G. A., Nicholson, M.: Some observations on the motion of elongated bubbles in horizontal pipes, Can. J. Chem. Eng., v. 52, pp. 695-702 (1974)
11. Azzopardi, B. J., Taylor, S., Gibbons, D. B.: Annular two-phase flow in a large diameter tube, Intl. Conf. on the Physical Modeling of Multiphase flow, Paper F4, Coventry, England, April (1983)
12. Badie, S.: Horizontal stratifying/annular gas-liquid flow, Ph.D. Thesis, Imperial College (2000)
13. Barbosa, Jr., J. R., Hewitt, G. F., Konig, G., Richardson, S. M.: Liquid entrainment, droplet concentration and pressure gradient at the onset of annular flow in a vertical pipe, Intl. J. Multiphase Flow, v. 28, pp. 943-961 (2002)

14. Beggs, H. D.: An experimental study of two-phase flow in inclined pipes, Ph.D. Dissertation, U. of Tulsa (1972)

15. Bendiksen, K., Brandt, I., Jacobsen, K. A., Pauchon, C: Dynamic simulation of multiphase transportation systems, Multiphase Technology and Consequences for Field development Forum, Stavanger, Norway (1987)

16. Bennet, J. A. R., Thornton, J. D.: Data on the vertical flow of air-water mixtures in the annular and dispersed flow regions – part I – preliminary study, Trans. Inst. Chem. Engrs., v. 39, pp. 101-112 (1961)

17. Boyce, B. E., Collier, j. G., Levy, J.: Hold-up and pressure drop measurements in the two-phase flow of air-water mixtures in helical coils, Proc. of an Intl. Sym. on Research in Co-current Gas-liquid flow, U. of Waterloo, pp. 203-231, Sept. (1968)

18. Brill. J. P.: Transportation of liquids in multiphase pipelines under low liquid loading conditions, Final Report, GRI Project (1996)

19. Brito, R., Pereyra, E., Sarica, C.: Stratified flow for downward highly viscous two-phase flow, 8th N. American Conf. Multiphase Tech., June 20-22, Banff, Alberta, Canada (2012)

20. Brown, D. J.: Disequilibrium in annular flow, Ph.D. Thesis, Oxford U. (1978)

21. Caetano-Filho E. F.: Two-phase flow in a vertical annulus, M.S. Thesis, U. of Tulsa (1984)

22. Camelo, E., Lemonnier, H., Ochterbeck, J., Selmer-Olsen, S.: Characterization of non-equilibrium effects on high quality critical flows, Proc. of the 7th Intl. Meeting on Nuclear Reactor Thermal-Hydraulics, NURETH-7, pp. 111-130, Saratoga Springs, September 10-15 (1995)

23. Chisolm, D., Laird, A. D. K.: Trans. AIME, v. 80, pp. 276 (1958)

24. Cousins, L. B., Denton, W. H., Hewitt, G. F.: Liquid mass transfer in annular two-phase flow, UK AERE Report R4926, May (1965)

25. Crowley, C. J., Sam, R. G., Rothe, P. H.: Investigation of two-phase flow in horizontal and inclined pipes at large pipe size and high gas density, Project PR-172-507, Pipeline Research Committee, AGA, February (1986)

26. Eaton, B. A.: The prediction of flow patterns, liquid holdup and pressure losses occurring during continuous two-phase flow in horizontal pipelines, Ph.D. Dissertation, U. of Texas at Austin (1966)

27. Ekberg, N. P.: Two-phase flow in horizontal thin annuli, M.S. Thesis, Georgia Inst. of Tech. (1998)

28. Espedal, M.: An experimental investigation of stratified two-phase pipe flow at small inclinations, Dr. Ing. Thesis, Norwegian U. of Sci. and Tech. (1998)

29. Fan, Y.: An investigation of low-liquid loading gas-liquid stratified flow in near-horizontal pipes, Ph.D. Dissertation, U. of Tulsa (2005)

30. Felizola, H., Shoham, O.: A unified model for slug flow in upward inclined pipes, J. Energy Resour. Tech., v. 117, pp. 7-12, March (1995)

31. Fore, L. B., Dukler, A. E.: Droplet deposition and momentum transfer in annular flow, AIChE J., v. 41, pp. 2040-2047 (1995a)

32. Fore, L. B., Dukler, A. E.: The distribution of drop size and velocity in gas-liquid annular flow, Intl. J. Multiphase Flow, v. 21, pp. 137-149 (1995b)

33. Fujita, H., Ohara, T., Hirota, M., Furuta, H.: Gas-liquid flow in flat channels with small channel clearance, Advances in Multiphase Flow, pp. 441 (1995)

34. Gill, L. E., Hewitt, G. W., Hitchon, J. W.: Sampling probe studies of the gas core in annular two-phase flow: part 1 – the effect of length on phase and velocity distribution, UKAEA Report No. 3954 (1962)

35. Gill, L. E., Hewitt, G. W., Lacey, P. M.: Data on the upwards annular flow of air-water mixtures, Chem. Eng. Sci., v. 20, pp. 71-88 (1965)

36. Gill, L. E., Hewitt, G. W., Lacey, P. M.: Sampling probe studies of the gas core in annular two-phase flow: part 2 – studies of the effect of phase flow rates on phase and velocity distribution, UKAEA Report No. 3955 (1963)

37. Gill, L. E., Hewitt, G. W.: Sampling probe studies of the gas core in annular two-phase flow: part 3 – distribution of velocity and droplet flowrate after injection through an axial jet, UKAEA AERE Report No. M1202 (1967)

38. Govier, G. W., Omer, M. M.: Horizontal pipe flow of air water mixtures, Can. J. Chem. Eng., 40, pp. 93-104 (1962)

39. Gregory, G. A., Mandhane, J. M., Aziz, K.: Some design considerations for two-phase flow in pipes, J. Can. Petroleum Tech., January-March (1975b)

40. Gregory, G. A., Scott, D. S.: Physical and chemical mass transfer in horizontal cocurrent gas-liquid slug flow: Proc. of an Intl. Symposium on research in concurrent gas-liquid flow, U. of Waterloo, Ontario, Canada, pp. 633-666 (1968)

41. Griffith, P., Lau, C. W., Hon, P. C., Pearson, J. F.: Two-phase pressure drop in inclined and vertical pipes, Report No. DSR 80063-81, Mobil Oil Co, Heat Transfer Laboratory, Dept. of Mech. Eng., Massachusetts Inst. Of Tech., Aug. (1973)

42. Grollman, E., Fortuin, J. M. H.: Transient gas-liquid flow in upward sloping pipes, approaching the wavy-to-slug flow transition, Trans. ASME, FED-v. 225, Gas Liquid Flows, pp. 23-30 (1995)

43. Haaland, S. E.: Simple and explicit formulas for the skin friction in turbulent pipe flow, ASME J. Fluids Eng., 105, pp. 89-90 (1983)

44. Hagedorn, A. R.: Experimental study of pressure gradients occurring during continuous two-phase flow in small diameter vertical conduits, Experimental Gas Lift project, Ph.D. Dissertation, U. of Texas at Austin (1964)

45. Hewitt, G. F, Delhaye, J. M., Zuber, N.: Multiphase Science and Technology J., v. 3 (1987)

46. Hewitt, G. F., King, I., Lovegrove, P. C.: Holdup and pressure drop measurements in the two-phase annular flow of air-water mixtures, UK AERE Report R3764, June (1961)

47. Hewitt, G. F., King, I., Lovegrove, P. C.: Holdup and pressure drop measurements in the two-phase annular flow of air-water mixtures, UK AERE Report R3764, June (1961)

48. Hewitt, G. F., Martin, C. J., Wilkes, N. S.: Experimental and modeling studies of annular flow in the region between flow reversal and the pressure drop minimum, PCH, v. 6, no. 1/2, pp. 69-86 (1985)

49. Hlaing, N. D., Sirivat, A., Siemanond, K., Wilkes, J. O.: Vertical two-phase flow regimes and pressure gradients – effect of viscosity, Exp. Therm. Fluid Sci., v. 31, pp. 567-577 (2007)

50. Holt, A. J.: Two-phase pressure drop and void fraction in narrow channels, Ph.D. Thesis, U. of Nottingham (1996)

51. Hossfield, L. M., Bharathan, D.: Interfacial friction in cocurrent upward annular flow, Final Report, EPRI Research Project 443-2, NP-2326, March (1982)

52. Hughmark, G.: Holdup and pressure drop with gas-liquid flow in a vertical pipe, Ph.D. Dissertation, Dept. of Chem. Eng., Louisiana State U. (1959)

53. Ishii, M., Mishima, K.: Liquid transfer and entrainment correlation for droplet-annular flow, 7th Intl. Heat Transfer Conf., Muchen (1982)

54. Ito, H.: Friction factors for turbulent flow in curved pipes, J. Eng., v. 81, pp. 123-134 (1959)

55. Johnson, G. W.: A study of stratified gas-liquid pipe flow, Ph.D. Dissertation, Dept. of Mathematics – Mechanics Division, U. of Oslo, Norway (2005)

56. Juprasert, S.: Two-phase flow in an inclined pipeline-riser system, M.S. Thesis, U. of Tulsa (1978)

57. Khatib, Z., Richardson, J. F.: Vertical co-current flow of air and shear shinning suspensions of kaolin, J. Chem. Eng. Res. Des., v. 62, pp. 139 (1984)

58. Kokal, S. L.: An experimental study of two-phase flow in inclined pipes, Ph.D. Dissertation, U. of Calgary (1987)

59. Langsholt, M., Holm, H.: Liquid accumulation in gas-condensate pipelines – an experimental study, 13th Intl. Conf. Multiphase Prod. Tech., Edinburgh (2007)

60. Lee, J. L., Lee, S. Y.: Pressure drop correlations for two-phase flow within horizontal rectangular channels with small heights, Intl J. Multiphase Flow, v. 27, pp. 783-796 (2001)

61. Marcano, R.: Slug characteristics for two-phase horizontal flow, M.S. Thesis, U. of Tulsa (1996)

62. Marruaz, K. S., Goncalves, M. A. L., Gaspari, E., Ribeiro, G. S., Franca, F. A., Rosa, E. S.: Horizontal slug flow in a large-size pipeline – experimentation and modeling, J. Braz. Soc. Mech. Sci., v. 23, no. 4 (2001)

63. Martin, C. J.: Annular two-phase flow, Ph.D. Dissertation, Oxford U. (1983)

64. Mattar, L.: Air-oil slug flow in an upward inclined pipe, M.S. Thesis, U. of Calgary (1973)

65. Moissis, R., Griffith, P.: Entrance effects in a developing slug flow, Technical Report No. 18, The Office of Naval Research, DSR Project No. 7-7673, June (1960)

66. Mukherjee, H.: An experimental study of inclined two-phase flow, Ph.D. Dissertation, U. of Tulsa (1979)

67. Nichols, C. R.: A study of the vertical flow of air-water mixtures, Ph.D. Dissertation, U. of Maryland (1965)

68. Oliemans, R. V. A., Pots, B. F. M., Trompe, N.: Modelling of annular dispersed two-phase flow in vertical pipes, Intl. J. of Multiphase Flow, v. 12, no. 5, pp. 711-732 (1986)

69. Owen, D. G.: An experimental and theoretical analysis of equilibrium annular flows, Ph.D. Dissertation, Dept. of Chem. Eng., U. of Birmingham (1986)

70. Pecherkin, N. I.: Effect on concurrent gas flow on structure of liquid film and wall shear stress, Phase-Interface Phenomena in Multiphase Flow, Hewitt, Mayinger, Riznic (eds.), Hemisphere Pub. Co., pp. 105-120 (1990)

71. Pilehvari, A. A.: Experimental study of subcritical two-phase flow through wellhead chokes, Research Report, Tuls U. Fluid Flow Projects, September (1980)

72. Pougatch, K., Salcudean, M., Chan, E., Knapper, B.: Modelling of compressible gas-liquid flow in a convergent-divergent nozzle, Chem. Eng. Sci., v. 63, pp. 4176-4188 (2008)

73. Sadatomi, M., Kano, K., Kawahara, A., Mori, N.: Void fraction and pressure drop in two-phase equilibrium flows in a vertical 2x3 rod bundle channel – assessment of correlations against the present subchannel data, JSME Intl. J., Series B, v. 49, no. 2, pp. 279-286 (2006)

74. Saisorn, S., Wongwises, S.: An experimental investigation of two-phase air-water flow through a horizontal circular micro-channel, Exp. Therm. Fluid Sci., v. 33, pp. 306-315 (2009)

98. Sawant, P., Ishii. M., Mori, M.: Droplet entrainment correlation in vertical upward co-current annular two-phase flow, Nucl. Eng. Des., v. 238, pp. 1342-1352 (2008)

75. Schubring, D., Shedd, T. A.: Prediction of wall shear for horizontal annular air-water flow, Intl. J. Heat and Mass Transfer, v. 52, pp. 200-209 (2009)

76. Schubring, D.: Behavior interrelationships in annular flow, Ph.D. Thesis, U. of Wisconsin-Madison (2009)

77. Short, W. L.: The upwards vertical flow of air-water mixtures – effect of diameter on flow pattern, holdup and pressure drop, M.Sc. Thesis, Dept. of Chem. Eng., U. of Alberta, Canada (1957)

78. Simpson, H. C., Rooney, D. H., Grattan, E., Al-Samarrae, F.: Flow pattern and pressure drop studies, Reports 1, 2 and 3, Research Contract RD/1065/014, Dept. of Mechanical Engineering, U. of Strathclyde (1976)

79. Singh, G., Griffith, P.: Determination of the pressure drop optimum pipe size for a two-phase slug flow in an inclined pipe, J. Engineering for Industry, Trans. ASME, pp. 717-726, November (1970)

80. Spedding, P. L., Nguyen, V. T.: Data on holdup, pressure loss and flow pattern for two-phase, air-water flow in an inclined pipe. Report 122, U. of Auckland, Auckland, New Zealand (1976)

81. Sujumnong, M.: Heat transfer, pressure drop and void fraction in two-phase, two-component flow in a vertical tube, Ph.D. Dissertation, U. of Manitoba (1997)

82. Tapucu, A., Teyssedou, A., Geckinli, M., Troche, N.: Experimental study of diversion cross-flow caused by subchannel blockages, volume 2 – two-phase flow, Final Report, EPRI NP-3459, volume 2, Research Project 1378-1, February (1988)

83. Turner, J. M.: Annular two-phase flow, Ph.D. Dissertation, Dartmouth College (1966)

84. Tzotzi, C., Andritsos, N.: Interfacial shear stress in wavy stratified gas-liquid flow in horizontal pipes, Intl. J. Multiphase Flow, v. 54, pp. 43-54 (2013)

85. van Nimwegen, A. T., Portela, L. M., Henkes, R. A. W. M.: A first look at the hydrodynamics o fair-water-foam flow for gas well deliquification, 8th N. American Conf. Multiphase Tech., June 20-22, Banff, Alberta, Canada (2012)

86. van't Westende, J. M. C., Kemp, H. K., Belt, R. J., Portela, L. M., Mudde, R. F., Oleimans, R. V. A.: On the role of droplets in cocurrent annular and churn-annular pipe flow, Intl. J. Multiphase Flow, v. 33, pp. 595-615 (2007)

87. Vogrin, J. A.: An experimental investigation of two-phase, two-component flow in a horizontal, converging-diverging nozzle, ANL-6754, AEC Research and Development Report, July (1963)

88. Wallis G.B.: One-dimensional two-phase flow, McGraw Hill, New York (1969)

89. Wallis, G. B.: AEC Report, No. NYO-3114-14, EURAEC 1605 (1966)

90. Webb, D. R.: Two phase flow phenomena, Ph.D. Thesis, U. of Cambridge, Trinity Hall (1970)

91. Wolf, A.: Film structure of vertical annular flow, Ph.D. Dissertation, Dept. of Chem. Eng., Imperial College of Science, Technology and Medicine (1995)

92. Woods, G. S., Spedding, P. L.: Vertical upward co-current multiphase flow, Report CE/96/WOODS, Dept. of Chem. Eng., Queen's U. of Belfast (1996)

93. Yang, J.: Investigation of downward intermittent flow in inclined pipes, Ph.D. Dissertation, U. of Tulsa (1996)

94. Zabaras, G., Menon, R., Schoppa, W., Wicks III, M.: Large diameter riser laboratory gas-lift tests, Offshore Tech. Conf., Paper No. 23968 (2013)

95. Zhao, Y., Markides, C. N., Matar, O. K., Hewitt, G. F.: Intl J. Multiphase Flow, v. 55, pp. 111-129 (2013)

CHAPTER 5 PUBLICATIONS

1. Abduvayt, P., Manabe, R., Watanabe, T., Arihara, N.: Analysis of oil-water flow tests in horizontal, hilly terrain, and vertical pipes, Soc. of Petroleum Engineers, Paper No. 90096, (2006)

2. Alkaya, B.: Oil-water flow patterns and pressure gradients in slightly inclined pipes, M.S. Thesis, U. of Tulsa (2000)

3. Angeli, P., Hewitt, G. F.: Pressure gradient in horizontal liquid-liquid flows, Intl. J. Multiphase Flow, v. 24, pp. 1183-1203 (1998)

4. Angeli, P.: Liquid-liquid dispersed flows in horizontal pipes, Ph.D. Thesis, Imperial College (1996)

5. Arirachakaran, S.: An experimental study of two-phase oil-water flow in horizontal pipes, M.S. Thesis, U. of Tulsa (1983)

6. Arney, M. S.: Selected topics in the fluid mechanics of immiscible liquids, Ph.D. Dissertation, U. of Minnesota (1994)

7. Atmaca, S.: Characterization of oil-water flows in inclined pipes, M.S. Thesis, U. of Tulsa (2007)

8. Bai, R.: Traveling waves in a high viscosity ratio and axisymmetric core annular flow, Ph.D. Dissertation, U. of Minnesota (1995)

9. Carpinlioglu, M. O., Ozbelge, T. A., Oruc, V.: Flow frictional resistance in pneumatic conveying of solid particles through inclined lines, J. Powder Tech., v. 125, pp. 292-297 (2002)

10. Charles, M. E., Govier, G. W., Hodgson, G.W.: The horizontal pipeline flow of equal density oil-water mixtures, Can. J. Chem. Eng., pp. 27-36, February (1961)

11. Chisolm, D., Laird, A. D. K.: Trans. AIME, v. 80, pp. 276 (1958)

12. Cobos, S., Carvalho, M. S., Alvarado, V.: Flow of oil-water emulsions through a constricted capillary, Intl. J. Multiphase Flow, v. 35, pp. 507-515 (2009)

13. Flores, J. G.: Oil-water flow in vertical and deviated wells, Ph.D. Dissertation, U. of Tulsa (1997)

14. Foroughi, H., Kawaji, M.: Viscous oil-water flows in a microchannel initially saturated with oil – flow patterns and pressure drop characteristics, Intl. J. Multiphase Flow, v. 37, pp. 1147-1155 (2011)

15. Grassi B., Strazza, D., Poesio, P.: Experimental validation of theoretical models in two-phase high-viscosity ratio liquid-liquid flows in horizontal and slightly inclined pipes, Intl. J. of Multiphase Flow, v. 34, pp. 950-965 (2008)

16. Henthorn, K. H., Park, K., Curtis, J. S.: Measurement and prediction of pressure drop in pneumatic conveying – effect of particle characteristics, mass loading, and Reynolds number, Ind. Eng. Chem. Res., v. 44, pp. 5090-5098 (2005)

17. Kaushal, D. R., Tomita, Y.: Comparative study of pressure drop in multisized particulate slurry flow through pipe and rectangular duct, Intl. J. Multiphase Flow, v. 29, pp. 1473-1487 (2003)

18. Langsholt, M.: An experimental study on polymeric type DRA used in single- and multiphase flow with emphasis on degradation, diameter scaling and the effects in three-phase oil-water-gas flow, 8th N. American Conf. on Multiphase Tech., BHR Group, Banff, Alberta, June 20-22 (2012)

19. Lovick, J.: Horizontal, oil-water flows in the dual continuous flow regime, Ph.D. Dissertation, Imperial College (2004)

20. Lum, J. Y. L., Al-Wahaibi, T., Angeli, P.: Upward and downward inclination oil-water flows, Intl. J. Multiphase Flow, v. 32, pp. 413-435 (2006)

21. Lum, J. Y. L., Lovick, J., Angeli, P.: Low inclination oil-water flows, Can. J. Chem. Eng., v. 82, pp. 303-315, April (2004)

22. Luo, K. M.: Experimental gas-solid vertical transport, Ph.D. Dissertation, Illinois Institute of Tech. (1987)

23. Martinez, A. E.: The flow of oil-water mixtures in horizontal pipes, M.S. Thesis, U. of Tulsa (1986)

24. Mukhopadhyay, H.: An experimental study of oil-water flow in inclined pipes, M.S. Thesis, U. of Tulsa (1977)

25. O'Hern, T. J., Trujillo, S. M., Torczynski, J. R., Tortora, P. R., Oelfke, J. B., Bhusarapu, S.: Circulating fluidized bed hydrodynamics experiments for the multiphase fluid dynamics research consortium (MFDRC), Sandia Report, No. SAND2006-4914 Unlimited Release, August (2006)

26. Oliemans, R. V. A.: The lubricating-film model for core-annular flow, Ph.D. Dissertation, Delft University (1986)

27. Plaxton, W. L.: Pipe flow experiments for the analysis of two-phase liquid-liquid pressure drop in horizontal wells, M.Sc. Thesis, Dept. of Petroleum Engineering, U. of Alberta, Canada (1995)

28. Pouplin, A., Masbernat, O., Decarre, S., Line, A.: Wall friction and effective viscosity of a homogeneous dispersed liquid-liquid flow in a horizontal pipe, AIChE J., Fluid Mechanics and Transport Phenomena Div., v. 57, no. 5, May (2011)

29. Rautiainen, A., Stewart, G., Poikolainen, V., Sarkomaa, P. : An experimental study of vertical pneumatic conveying, J. Powder Tech., v. 104, pp. 139-150 (1999)

30. Reddy, K. V. S., Pei, D. C. T. : Particle dynamics in solid-gas flow in a vertical pipe, Ind. Eng. Chem. Funds., v. 8, no. 3, pp. 490-497 (1969)

31. Schubring, D.: Behavior interrelationships in annular flow, Ph.D. Thesis, U. of Wisconsin-Madison (2009)

32. Singh, B.: Analysis of pressure drop in vertical pneumatic conveying – generalized approach for gas-particle and liquid-particle systems, J. Powder Tech., v. 32, pp. 179 – 191 (1982)

33. Soot, P. M.: A study of two-phase liquid-liquid flow in pipes, Ph.D. Dissertation, Oregon State U. (1971)

34. Standard, B.: A theoretical analysis of pneumatic conveying, Trans. Inst. Chem. Engrs., v. 39, pp. 321-327 (1961)

35. Trallero, J. L.: Oil-water flow patterns in horizontal pipes, Ph.D. Dissertation, U. of Tulsa (1995)

36. Tsaoulidis, D., Dore, V., Angeli, P., Plechkova, N. V., Seddon, K. R.: Flow patterns and pressure drop of ionic liquid-water two-phase flows in microchannels, Intl. J. Multiphase Flow, v. 54, pp. 1-10 (2013)

37. Wang, F. J., Xhu, J. x., Beeckmans, J. M.: Pressure gradient and particle adhesion in the pneumatic transport of cohesive fine powders, Intl. J. Multiphase Flow, v. 26, pp. 245-265 (2000)

38. Wang, W., Gong, J., Angeli, P.: Investigation on heavy crude-water two phase flow and related flow characteristics, Intl. J. of Multiphase Flow, v. 37, pp. 1156-1164 (2011)

39. Wood, R. K.: The upward vertical flow of oil-water mixtures: effect of second phase viscosity on pressure drop, flow-pattern and holdup, M.S. Thesis, Dept. of Chemical Engineering, U. of Alberta (1960)

CHAPTER 6 PUBLICATIONS

1. Abduvayt, P.: Experimental and modeling studies for gas-liquid two-phase flow in slightly-inclined pipes at low- and high-pressure conditions, Ph.D. Dissertation, Waseda U., Japan (2003)

2. Bharathan, D., Wallis, G. B., Richter, H. J.: Air-Water countercurrent annular flow, Topical Report, EPRI Research Project 443-2, NP-1165, September (1979)

3. Bousman, W. S., Dukler, A. E.: Studies of gas-liquid flow in microgravity – void fraction, pressure drop and flow patterns, Trans. ASME FED-v. 175, Fluid Mechanics Phenomena in Microgravity, pp. 23-36 (1993)

4. Caussade, B., Fabre, J., Jean, C., Ozon, P., Theron, B. : Unsteady phenomena in horizontal gas-liquid slug flow, Multiphase Flow Proc. of the 4th Intl. Conf., pp. 469-484 (1989)

5. Cazarez, O., Montoya, D., Vital, A. G., Bannwart, A. C.: Modeling of three-phase heavy oil-water-gas bubbly flow in upward vertical pipes, Intl. J. Multiphase Flow, v. 36, no. 6, pp. 439-448 (2010)

6. Chhabra, R. P., Farooqi, S. I., Richardson, J. F.: Isothermal two-phase flow of air and aqueous polymer solutions in a smooth horizontal pipe, Chem. Eng. Res. Des., v. 62, pp. 22 (1984)

7. Choi, B., Fujii, T., Asano, H., Sugimoto, K.: A study of the flow characteristics in air-water two-phase flow under microgravity (Results of Flight Experiments), JSME Intl. Journal, Series B, v. 46, No. 2, pp. 262 (2003)

8. De Henau, V.: A study of terrain induced slugging in two-phase flow pipelines, Ph.D. Thesis, U. of Waterloo (1992)

9. Dong, H.: An experimental study of low liquids loading gas-oil-water flow in horizontal pipes, M.S. Thesis, U. of Tulsa (2007)

10. Eilerts, C. K.: Program MPTF for computing multiple pipe transient flow of gas, Suppl. 4-81, Verification of Computing Procedure by Comparison of Results with Data of Flow Tests, Pipeline Simulation Interest Group, Paper No. 8105 (1981)

11. Farooqi, S. I., Richardson, J. F.: Horizontal flow of air and liquid (Newtonian and non-Newtonian) in a smooth pipe, part I – a correlation for average liquid holdup, Trans. IChemE, v. 60, pp. 292-322 (1982a)

12. Farooqi, S. I., Richardson, J. F.: Horizontal flow of air and liquid (Newtonian and non-Newtonian) in a smooth pipe, part II – average pressure drop, Trans. IChemE, v. 60, pp. 323-333 (1982b)

13. Fayers, F. J.: Productivity and injectivity of horizontal wells, Annual Report for March 10, 1994 to March 9, 1995, DOE contract no. DE-FG22-93BC14862, July (1995)

14. Hall, A. R. W.: Multiphase flow of oil, water and gas in horizontal pipes, Ph.D. Thesis, Imperial College (1992)

15. Hanna, B. N.: The formulation and numerical solution of a transient, one-dimensional, unequal velocity, two-phase flow model, Ph.D. Thesis, U. of Waterloo (1981)

16. Hannah, K. W., Batey, E. H., Wilkinson, J. F.: Transient flow of gas, A Special Report on The Pipeline Research Project NX-37, American Gas Association (1964)

17. Ishii, M., Mishima, K.: Liquid transfer and entrainment correlation for droplet-annular flow, 7th Intl. Heat Transfer Conf., Muchen (1982)

18. Jia, N., Gourma, M., Thompson, C. P.: Non-Newtoniaan multiphase flows – on drag reduction, pressure drop and liquid wall friction factor, Chem. Eng. Sci., v. 66, pp. 4742-4756 (2011)

19. Khatib, Z., Richardson, J. F.: Vertical co-current flow of air and shear shinning suspensions of kaolin, J. Chem. Eng. Res. Des., v. 62, pp. 139 (1984)

20. Kohda, K., Suzukawa, Y., Furukawa, H.: Analysis of transient gas-liquid two-phase flow in pipelines, ASME Pipeline Engineering Symposium-ETCE, Dallas, Texas (1987)

21. Lunde, K., Nuland, S., Lingelem, M.: Aspects of three-phase flows in gas condensate pipelines, 6th Intl. Conf. on Multiphase Production, BHR Group, Cannes, France, June 16-18(1993)

22. MacGillivray, R. M.: Gravity and gas density effects on annular flow average film thickness and frictional pressure drop, M.S. Thesis, U. of Saskatchewan (2004)

23. McNulty, J. G., Sutjipto, J. W.: An investigation of transient two-phase flow patterns in a horizontal pipe, Offshore Tech. Conf., Paper No. 7040 (1992)

24. Minami, K., Shoham, O.: Transient Two-phase Flow Behavior in Pipelines – Experiments and Modeling, Intl. J. Multiphase Flow, vol. 20, No. 4, pp. 739-752 (1994)

25. Odozi, U. A.: Three-phase gas/liquid/liquid slug flow, Ph.D. Thesis, Imperial College (2000)

26. Omebere-Iyari, N. K.: The effect of pipe diameter and pressure in vertical two-phase flow, Ph.D. Thesis, U. of Nottingham (2006)

27. Pan, L.: High pressure three-phase (gas/liquid/liquid) flow, Ph.D. Thesis, Imperial College (1996)

28. Pougatch, K., Salcudean, M., Chan, E., Knapper, B.: Modelling of compressible gas-liquid flow in a convergent-divergent nozzle, Chem. Eng. Sci., v. 63, pp. 4176-4188 (2008)

29. Ruiz-Viera, M. J., Delgado, M. A., Franco, J. M., Sanchez, M. C., Gallegos, C.: On the drag reduction for the two-phase horizontal pipe flow of highly viscous non-Newtonian liquid/air mixtures – case of lubricating grease, Intl. J. Multiphase Flow, v. 32, pp. 232-247 (2006)

30. Schulkes, R. M. S. M., Utvik, O. H.: Pressure drop in a perforated pipe with radial inflow – single-phase flow, Soc. of Petroleum Engineers J., Paper No. 38448, March (1998)

31. Shean, A. R.: Pressure drop and phase fraction in oil-water-air vertical pipe flow, M.S. Thesis, Massachusetts Inst. of Tech. (1976)

32. Srichai, S.: High pressure separated two-phase flow, Ph.D. Dissertation, Dept. of Chem. Eng., Imperial College of Science, Technology and Medicine (1994)

33. Theron, N.: Ecoulements diphasiques instationaires en conduite horizontale, Dr. Ing. Thesis, Inst. Nat. Polytechnique de Toulouse (1989)

34. Thome, R. J.: Effect of a transverse magnetic field on vertical two-phase flow through a rectangular channel, Argonne National Laboratory, AEC Research and Development Report ANL-6854, March (1964)

35. Valle, A.: Three phase gas-oil-water pipe flow, Ph.D. Thesis, Imperial College (2000)

36. Vigneron, F.: Analysis of imposed two-phase flow transients in horizontal pipes, part 1 – experimental results, Research Report, U. of Tulsa Fluid Flow Projects (1995)

37. Willson, S. M., Nagoo, A. S., Sharma, M. M.: Analysis of potential bridging scenarios during blowout events, SPE/IADC Drilling Conf. Exhib., Paper No. 163438, March 5-7 (2013)

38. Woods, G. S., Spedding, P. L.: Vertical upward co-current multiphase flow, Report CE/96/WOODS, Dept. of Chem. Eng., Queen's U. of Belfast (1996)

39. Xu, J., Wu, Y., Li, H., Guo, J., Chang, Y.: Study of drag reduction by gas injection for power-law fluid flow in horizontal stratified and slug flow regimes, Chem. Eng. J., v. 147, pp. 235-244 (2009)

40. Xu, J., Wu, Y., Shi, Z., Lao, L., Li, D.: Studies on two-phase co-current air/non-Newtonian shear-thinning fluid flows in inclined smooth pipes, Intl. J. Multiphase Flow, v. 33, pp. 948-969 (2007)

41. Zabaras, G. J.: Studies of vertical annular gas-liquid flows, Ph.D. Dissertation, Dept. of Chemical Engineering, U. of Houston (1985)

42. Zabaras, G., Menon, R., Schoppa, W., Wicks III, M.: Large diameter riser laboratory gas-lift tests, Offshore Tech. Conf., Paper No. 23968 (2013)

43. Zuber, N., Staub, F. W., Bijwaard, G., Kroeger, P. G.: Steady state and transient void fraction in two-phase flow systems – final report for the program of two-phase flow investigation, Volumes 1 and 2, Report GEAP-5417, US AEC contract no. AT(04-3)-189, January (1967)

CHAPTER 7 PUBLICATIONS

1. Ahmed, T.: Compositional modeling of Tyler and Mission Canyon formation oils with CO2 and lean gases, Final Report submitted to Montanans on a New Track for Science (1985)

2. Al-Muraikhi, A. J.: Evaluation of vertical multiphase flow correlations for Saudi Arabian field conditions, M.S. Thesis, King Fahd U. of Petr. and Min. (1989)

3. Alves, I. N., Caetano, E. F., Minami, K., Shoham, O.: Modeling annular flow behavior for gas condensate wells, ASME FED, v. 72, pp. 87-97 (1988)

4. Ambastha, A. K., Gudmundsson, J. S.: Pressure profiles in two-phase geothermal wells – comparison of field data and model calculations, Proc. 11th Workshop on Geothermal Res. Eng., Stanford U., January 21-23 (1986)

5. Andreussi, P., Minervini, A., Paglianti, A., Sabatelli, F.: Two-phase flow of brine in long pipelines – analysis of field experiments, Geothermics J., v. 23, no. 1, pp. 33-41 (1994)

6. Ansari, A. M.: A comprehensive mechanistic model for upward two-phase flow, M.S. Thesis, U. of Tulsa (1988)

7. Aragon, A., Garcia, A., Baca, A., Gonzalez, E.: Comparison of measured and simulated pressure and temperature profiles in geothermal wells, Geofisica Intl., v. 38, no. 1, pp. 35-42 (1999)

8. Ashiem, H.: MONA, An accurate two-phase well flow model based on phase slippage, Soc. of Petroleum Engineers, Prod. Eng. J., pp. 221-230, May (1986)

9. Aunzo, Z. P., Bjornsson, G., Bodvarsson, G. S.: Wellbore models GWELL, GWNACL, and HOLA user's guide, Lawrence Berkeley Nat. Laboratory, Earth Sci. Div., Report No. LBL-31428, http://escholarship.org/uc/item/6wt2d5b7, October (1991)

10. Baker, A., Nielson, K., Gabb, A.: Field data test new holdup, pressure-loss calculations for gas, condensate pipelines – Part 2, Oil and Gas J., pp. 78-86, March 21st (1988b)

11. Baker, O., Swerdloff, W.: Calculations of surface tension, part 3 – calculations of surface tension Parachor values, Oil and Gas J., v. 43, pp. 141 (1955)

12. Baker, O: Design of pipe lines for simultaneous flow of oil and gas, Oil and Gas J., 53, pp. 185–190 (1954)

13. Baxendell, P. B., Thomas, R.: The calculation of pressure gradients in high-rate flowing wells, Soc. of Petroleum Engineers J. Pet. Tech., pp. 1023-1028, October (1961)

14. Beggs. H. D., Robinson, J. R.: Estimating the viscosity of crude oil systems, J. Petroleum Tech., pp. 1140-1141, September (1975)

15. Bertuzzi, A. F., Welchon, J. K., Poettmann, F. H.: Description and analysis of an efficient continuous-flow gas-lift installation, Petr. Trans. AIME, v. 198, pp. 217-278 (1953)

16. Bjornsson, G.: A multi-feedzone geothermal wellbore simulator, M.S. Thesis, Lawrence Berkeley Laboratory Report LBL-23546, May (1987)

17. Bleakley, W. B.: Here are case histories of two thermal projects, Oil and Gas J., pp. 123-130, October 26th (1964)

18. Brill, J. P., Schmidt, Z., Coberly, W. A., Herring, J. D., Moore, D. W.: Analysis of two-phase tests in large-diameter flow lines in Prudhoe Bay field, Soc. of Petroleum Engineers of AIME, Paper No. 8305, June (1981)

19. Camacho, C. A.: Comparison of correlations for predicting pressure losses in high gas-liquid ratio vertical wells, M.S. Thesis, U. of Tulsa (1970)

20. Chierici, G. L., Ciucci, G. M., Sclocchi, G.: Two-phase vertical flow in oil wells – prediction of pressure drop, Soc. of Petroleum Engineers, Paper No. 4316, August (1974)

21. Chierici, G. L., Giannone, G., Schlocchi, G., Terzi, L.: A wellbore model for two-phase flow in geothermal reservoirs, Soc. of Petroleum Engineers, Paper No. 10315 (1981)

22. Cornish, R. E.: The vertical multiphase flow of oil and gas at high rates, Soc. of Petroleum Engineers, Paper No. 5791 (1976)

23. Corteville, J., Duchet-Suchaux, P., Lopez, D.: Comparison of methods for predicting pressure loss in oil and gas wells, 5th Intl. Conf. on Multiphase Production, BHR Group, Cannes, France (1991)

24. Crowley, C. J., Sam, R. G., Rothe, P. H.: Investigation of two-phase flow in horizontal and inclined pipes at large pipe size and high gas density, Project PR-172-507, Pipeline Research Committee, AGA, February (1986)

25. Culberson, O. L., McKetta Jr., J. J.: Phase equilibria in hydrocarbon-water systems III – the solubility of methane in water at pressures to 10,000 psia, J. Petroleum Tech., v. 3, no. 8, pp. 223-226 (1951)

26. Cunliffe, R. S.: Prediction of condensate flow rate in large diameter high pressure wet-gas pipelines, Australian Petroleum Exploration Assoc. J., vol. 18, pp. 171-177 (1978)

27. El-Banbi, A. H., Fattah, K. A., Sayyouh, M. H.: New modified black-oil correlations for gas condensate and volatile oil fluids, Soc. of Petroleum Engineers, Paper No. 102240 (2006)

28. Espanol, H. J. H.: Comparison of three methods for calculating a pressure traverse in vertical multiphase flow, M.S. Thesis, U. of Tulsa (1968)

29. Furnival, S. R., Baillie, J. M. : Successful prediction of condensate wellbore behavior using an EOS generated from black oil data, Soc. of Petroleum Engineers, Offshore Eur. Conf., Paper No. 26683 (1993)

30. Furukawa, H., Kohda, K., Suzukawa, Y.: Evaluation of compositional two-phase liquid holdup and pressure-loss correlation, ASME Pipeline Engineering Symposium, Dallas (1987)

31. Garg, S. K., Pritchett, J. W., Alexander, J. H.: A new liquid hold-up correlation for geothermal wells, Geothermics J., v. 33, pp. 795-817 (2004)

32. Glaso, O.: Generalized pressure-volume-temperature correlations, J. Petroleum Tech., pp. 785-795, May (1980)

33. Govier, G. W., Fogarasi, M.: Pressure drop in wells producing gas and condensate, J. Can. Pet. Tech. pp. 28-41, Oct.-Dec. (1975)

34. Gregory, G. A.: Gas-liquid flow in large diameter pipelines, Final Report, American Gas Association Project PR-148-110 (1981)

35. Griffith, P., Lau, C. W., Hon, P. C., Pearson, J. F.: Two-phase pressure drop in inclined and vertical pipes, Report No. DSR 80063-81, Mobil Oil Co., Heat Transfer Laboratory, Dept. of Mech. Eng., Massachusetts Inst. Of Tech., Aug. (1973)

36. Hasan, A. R., Kabir, C. S.: Fluid flow and heat transfer in wellbores, Soc. of Petroleum Engineers (2002)

37. Hough, E. W., Rzasa, M. J., Wood, B. B.: Interfacial tensions at reservoir pressures and temperatures – apparatus and the water-methane system, Petrol. Trans. AIME, no. 192, pp. 57-60 (1951)

38. Kabir, C. S., Hasan, A. R.: Performance of a two-phase gas/liquid flow model in vertical wells, J. Petroleum Science and Engineering, v. 4, pp. 273-289 (1990)

39. Kumar, N.: Improvements for flow correlations for gas wells experiencing liquid loading, Soc. of Petroleum Engineers, Paper No. 92049 (2005)

40. Lagiere, M., Miniscloux, C., Roux, A.: Computer two-phase flow model predicts pipeline pressure and temperature profiles, Oil and Gas J., pp. 82-92, April 9th (1984)

41. Lea, J. F., Nickens, H. V., Wells, M. R.: Gas well deliquification, 2nd ed., Gulf Professional Pub. (2008)

42. Lee, A. L., Gonzalez, M. H., Eakin, B. E.: The viscosity of natural gases, J. Petroleum Tech., pp. 997-1000, August (1966)

43. Lopez, D., Dhulesia, H., Leporcher, E., Duchet-Suchaux, P.: Performances of transient two-phase flow models, Soc. of Petroleum Engineers, Paper No. 38813 (1997)

44. McCain Jr., W. D., Rollins, J. B., Villena, A. J.: The coefficient of isothermal compressibility of black oils at pressures below the bubble point, SPE Form. Eval. J., no. 3, pp. 659-662, September (1988)

45. McCain Jr., W. D.: Reservoir fluid property correlations – state of art, SPE Res. Eng. J., pp. 266-272 (1991)

46. McKetta Jr., J. J., Wehe, A. H.: Petroleum Refining J., no. 8, p. 153 (1958)

47. Meehan, D. N.: A correlation for water compressibility, Petr. Eng. J., pp. 125-126 (1980)

48. Mercer, J. W., Faust, C. R. : Simulation of water- and vapor-dominated hydrothermal reservoirs, Soc. of Petroleum Engineers, Paper No. 5520 (1975)

49. Messulam, S. A. G.: Comparison of correlations for predicting multiphase flow pressure losses in vertical pipes, M.S. Thesis, U. of Tulsa (1970)

50. Meyer, C. A., McClintock, R. B., Silvestri, G. J., Spencer, R. C.: 1967 ASME Steam Tables, ASME, 2nd ed., New York (1968)

51. Mokhatab, S.: Correlation predicts pressure drop in gas-condensate pipelines, Oil and Gas J., pp. 66-68, January 28th (2002)

52. Moshfeghian, M., Johannes, A. H., Maddox, R. N.: Thermodynamic properties are important in predicting pipeline operations accurately, Oil and Gas J., February 4th (2002)

53. Mucharam, L.: One-dimensional compositional modeling of gas and condensate flow in pipelines, Ph.D. Dissertation, Penn State U. (1990)

54. Orkiszewski, J.: Predicting Two-Phase Pressure Drops in Vertical Pipes, SPE J. Pet. Tech., pp. 829-838, June (1967)

55. Ovalle, A. P., Lenn, C. P., McCain Jr., W. D. : Tools to manage gas/condensate reservoirs – novel fluid property correlations on the basis of commonly available field data, Soc. of Petroleum Engineers Reservoir Evaluation and Engineering, Paper No. 112977 (2007)

56. Payne, G. A., Palmer, C. M., Brill, J. P., Beggs, H. D.: Evaluation of inclined-pipe, two-phase liquid holdup and pressure-loss correlations using experimental data, J. Petroleum Tech., Paper No. 6874, pp. 1198-1208 (1979)

57. Peffer, J. W., Miller, M. A., Hill, A. D.: An improved method for calculating bottomhole pressures in flowing gas wells with liquid present, Soc. of Petroleum Engineers Prod. Eng., Paper No. 15655, November (1988)

58. Phillips, S. L., Igbene, A., Fair, J. A., Ozbek, H., Tavana, M.: A technical databook for geothermal energy utilization, Lawrence Berkeley Laboratory, U. of California, Berkeley (1981)

59. Poettmann, F. H., Carpenter, P. G.: The multiphase flow of gas, oil and water through vertical flow string with application to the design of lift installation, API Drilling and Production Practices, 257 (1952)

60. Rai, R., Singh, I., Srinivasan, S.: Comparison of multiphase flow correlations with measured field data of vertical and deviated oil wells in India, Soc. of Petroleum Engineers Prod. Eng., Paper no. 16880, August (1989)

61. Reinicke, K. M., Remer, R. J., Hueni, G.: Comparison of measured and predicted pressure drops in tubing for high-water-cut gas wells, SPE Prod. Eng. J., pp. 165-177, Aug. (1987)

62. Riney, T. D.: Analysis of preliminary testing of Willis Hulin well no. 1, Technical Report, Lawrence Berkeley Laboratory DOE/LBL Contract No. DE-AC03-76SF00098, September (1991)

63. Sanchez, M. J.: Comparison of correlations for predicting pressure losses in vertical multiphase annular flow, M.S. Thesis, Dept. of Petroleum Engineering, U. of Tulsa (1972)

64. Sutton, R. P., Cox, S. A., Williams Jr., G., Stolz, R. P., Gilbert, J. V.: Gas well performance at subcritical rates, Soc. of Petroleum Engineers, Paper No. 80887 (2003)

65. Sutton, R. P., Farshad, F. F.: Utilization of the Peng-Robinson equation of state in multiphase flow pressure-gradient calculations in oil and gas wells, Soc. of Petroleum Engineers of AIME, Paper No. 11884 (1983)

66. Tachimori, M.: A numerical simulation model for vertical flow in geothermal wells, Proc. 8th Workshop Geothermal Res. Eng., Stanford U., December (1982)

67. van Wingen, N.: Recovery of oil in the United States, American Petr. Inst., no. 127 (1950)

68. Wahl, E. F.: Geothermal energy utilization, Wiley, New York (1977)

69. Yaws, C. L.: Physical properties, McGraw-Hill Pub. Co., New York (1977)

CHAPTER 8 PUBLICATIONS

1. Hewitt, G. F.: Introduction (to benchmarking datasets), Multiphase Science and Technology, v. 3, pp. 131-144 (1987)

APPENDIX A PUBLICATIONS

1. Abdel-Alim, A. N., Hamielec, A. E.: A theoretical and experimental investigation of the effect of internal circulation on the drag of spherical droplets falling at terminal velocity in liquid media, I. and E. C. Funds., v. 14, pp. 308-312 (1975)

2. Beard, K. V., Pruppacher, H. R.: J. Atmos. Sci., v. 26, pp. 1066-1072 (1969)

3. Bonnizi, M., Andreussi, P., Banerjee, S.: Flow regime independent, high resolution multi-field modeling of near-horizontal gas-liquid flows in pipelines, Intl. J. Multiphase Flow, v. 35, pp. 34-46 (2009)

4. Clift, R., Grace, J. R., Weber, M. E.: Bubbles, drops and particles, Dover Pubs. (1978)

5. Coleman, S. B., Hartley, B. C., McCurdy, D. G., Norris III, L. H.: A new look at predicting gas-well load-up, J. Petrol. Tech., v. 43, no. 3, pp. 329-333 (1991)

6. Danielson, T. J.: Influence of fluid properties on multiphase flow prediction, 11th Intl. Conf. Multiphase Prod., San Remo, June 11-13 (2003)

7. Dix, G. E.: Vapor void fractions for forced convection with subcooled boiling at low flow rates, General Electric Report NEDO-10491, Ph.D. Dissertation, U. of California Berkeley (1971)

8. Findlay, B. A.: Ph.D. Thesis, U. of Birmingham (1957)

9. Gunn, R., Kinzer, G.: The terminal velocity of fall for water droplets in stagnant air, J. Meteorology, v. 6, pp. 243-248 (1949)

10. Harmathy, T. Z.: Velocity of large drops and bubbles in media of infinite or restricted extent, AICheE J., v. 6, pp. 281 (1960)

11. Hetsroni, G.: Handbook of multiphase systems, Hemisphere Publishing Corp. (1982)

12. Hewitt, G. F., Pulling, D. J.: Liquid entrainment in adiabatic steam-water flow, Tech. Report AERE-R5374, UKAEA Research Group (1969)

13. Hinze, J. O.: Fundamentals of the hydrodynamic mechanism of splitting in dispersion processes, AIChE J., v. 1, no. 3, pp. 289 (1955)

14. Kataoka, I., Ishii, M.: Drift flux model for large diameter pipe and new correlation for pool void fraction, Intl. J. Heat Mass Transfer, v. 30, no. 9, pp. 1927-1939 (1987)

15. Lahey Jr., R. T., Drew, D. A.: The analysis of two-phase flow and heat transfer using a multidimensional, four-field, two-fluid model, Nucl. Eng. Des. J., v. 204, no. 1-3, pp. 29-44 (2001)

16. Nallaparaju, Y. D.: Prediction of liquid loading in gas wells, Soc of Petroleum Engineers, Paper No. 155356 (2012)

17. Nossier, M. A., Darwich, T. A., Sayyouh, M. H., El Sallaly: A new approach for accurate prediction of loading in gas wells under different flowing conditions, Soc of Petroleum Engineers, Paper No. 66540 (2000)

18. Shippen, M., Bailey, W. J.: Steady-state multiphase flow – past, present, and future, with a perspective on flow assurance, Energy and Fuels, v. 26, pp. 4145-4157 (2012)

19. Silvestri, M.: Fluid mechanics and heat transfer of two-phase annular-dispersed flow, Adv. in Heat Transfer, v. 1, pp. 355-446 (1964)

20. Turner, R. G., Hubbard, M. G., Dukler, A. E.: Analysis and prediction of minimum flow rate for the continuous removal of liquids from gas wells, Soc. of Petroleum Engineers Gas Tech. Symp., Paper No. 2198 (1969)

21. van Baten, J. M., Ellenberger, J., Krishna, R.: Using CFD to describe the hydrodynamics of internal air-lift reactors, Can. J. Chem. Eng., v. 81, issue 3-4, pp. 660-668 (2003)

22. van der Leeden, P., Nio, L. D., Suratman, P. C.: Appl. Sci. Res., Sect. A, v. 5, pp. 338-348 (1956)

23. Veeken, K., Hu, B., Schiferli, W.: Gas-well liquid-loading-field-data analysis and multiphase-flow modeling, Soc. of Petroleum Engineers Eur. Oil and Gas Conf. and Exhib., Paper No. 123657 (2010)

24. Wolf, A.: Film structure of vertical annular flow, Ph.D. Dissertation, Dept. of Chem. Eng., Imperial College of Science, Technology and Medicine (1995)

APPENDIX B PUBLICATIONS

1. Antal, S. P., Lahey Jr., R. T., Flaherty, J. E.: Analysis of phase distribution in fully developed laminar bubbly two-phase flow, Intl. J. Multiphase Flow, v. 17, pp. 635-652 (1991)
2. Birkhoff, G.: Averaged conservation laws in pipes, J. of Math. Anal. And Applic., vol. 8, pp. 66-77 (1964)
3. Boure, J. A., Delhaye, J. M.: General equations and two-phase flow modeling, Handbook of Multiphase Systems, pp. 1-36 to 1-95 (1982)
4. Boure, J. A., Delhaye, J. M.: Thermohydraulics of two-phase systems for industrial design and nuclear engineering, Hemisphere, chap. 12, pp. 353-403 (1981)
5. Boure, J. A.: Two-phase flow models – the closure issue, Multiphase Sci. and Tech., v. 3, Hemisphere (1987)
6. Carruyo, M. A. M.: Evolution of bubble size distribution for turbulent air-water flow in pipelines, M.S. Thesis, U. of Calgary (2005)
7. De Henau, V.: A study of terrain induced slugging in two-phase flow pipelines, Ph.D. Thesis, U. of Waterloo (1992)
8. Delhaye, J. M., Achard, J. L.: On the averaging operators introduced in two-phase flow modeling, OECD/NEA Specialists' Meeting on Transient Two-phase Flow, Toronto, August (1976)
9. Delhaye, J. M.: Equations Fondamentales des Ecoulements Diphasiques, Centre d'Etudes Nucleaires de Grenoble, Reports CEA-R-3429 1 and 2 (1968)
10. Delhaye, J. M.: General equations for two-phase systems and their applications to air-water bubble flow and to steam-water flashing flow, ASME-69-HT-63 (1969)
11. Delhaye, J. M.: Jump conditions and entropy sources in two-phase systems: Local instant formulation, Intl. J. of Multiphase Flow, vol. 1, pp. 395-409 (1974)
12. Drew, D. A., Passman, S. L.: Theory of multicomponent fluids, Springer Verlag (1999)
13. Drew, D. A., Wood, R. T.: Overview and taxonomy of models and methods, appendix 1, Intl. Workshop on Two-Phase Flow Fundamentals, Gaithersburg, Maryland (1985)
14. Drew, D. A.: A turbulent dispersion model for particles and bubbles, J. Eng. Math., v. 41, pp. 259-274 (2001)
15. Drew, D. A.: Mathematical modeling of two-phase flow, Ann. Rev. Fluid Mech., v. 15, pp. 261-291 (1983)

16. Frankl, F. I.: On the theory of motion of sediment suspensions, Soviet Physics Doklady, Academii Nauk SSSR, v. 92, pp. 247-250 (1953)

17. Ghiaasiaan, S. M.: Two-phase flow, boiling and condensation, Cambridge Univ. Press (2008)

18. Guet, S., Ooms, G.: Fluid mechanical aspects of the gas-lift technique, Ann. Rev. Fluid Mech., v. 38, pp. 255-249 (2006)

19. Hinze, J. W.: Turbulence, McGraw-Hill, New York (1959)

20. Ishii, M., Hibiki, T.: Thermo-fluid dynamics of two-phase flow, Springer (2006)

21. Ishii, M.: Thermo-fluid dynamic theory of two-phase flow, Eyrolles, Paris (1975)

22. Kleinstreuer, C: Two-phase flow – theory and applications, Taylor and Francis Co. (2003)

23. Lahey Jr., R. T., Cheng, L. Y., Drew, D. A., Flaherty, J. E.: The effect of virtual mass on the numerical stability of accelerating two-phase flows, Intl. J. Multiphase Flow, v. 6 (1980)

24. Lahey Jr., T. R., Drew, D. A.: The three-dimensional time and volume averaged conservation equations of two-phase flow, Advs. In Nuclear Science and Tech., Plenum Press, vol. 20, pp. 1-69 (1988)

25. Lake, L. W.: Enhanced oil recovery, Prentice-Hall (1989)

26. Levich, V. G., Krylov, V. S.: Surface-tension-driven phenomena, Ann. Rev. Fluid Mech., 1, pp. 293-316 (1969)

27. Levy, S: Two-phase flow in complex systems, Wiley-Interscience Pub. Co. (1999)

28. Munkejord, S. T.: Analysis of the two-fluid model and the drift-flux model for numerical calculation of two-phase flow, Ph.D. Thesis, Nor. U. of Sci. and Tech. (2005)

29. No, H. C., Kazimi, M. S.: The effect of virtual mass on the characteristics and the numerical stability in two-phase flows, MIT Energy Laboratory Report No. MIT-EL-81-023, DOE contract no. DE-AC02-78ET37218, April (1981)

30. Politano, M. S., Carrica, P. M., Converti, J.: A model for turbulent polydisperse two-phase flow in vertical channels, Intl. J. Multiphase Flow, v. 29, pp. 1153-1182 (2003)

31. Prosperetti, A., Trygvasson, G.: Computational methods for multiphase flow, Cambridge University Press, Cambridge (2007)

32. Sternling, C. V., Scriven, L. E.: Interfacial turbulence – hydrodynamic instability and the Marangoni effect , AIChE J., 5, pp. 514-523 (1959)

33. Teletov, S. G.: Two-phase flow hydrodynamics – 1 – hydrodynamics and energy equations, Bulletin of Moscow University, v. 2 (1958)

34. Truesdell, C. A., Toupin, R. A.: The classical field theories, Encyclopedia of Physics, vol. 3, Springer Verlag (1960)

35. Vernier, P., Delhaye, J. M.: General two-phase flow equations applied to the thermohydrodynamics of boiling water nuclear reactors, Energie Primaire, vol. 4, no. 1-2 (1968)

36. Yadigaroglu, G., Bensalem, A.: Interfacial mass generation rate modeling in non-equilibrium two-phase flow, Multiphase Sci. and Tech., v. 3, pp. 85-127 (1987)

37. Yadigaroglu, G., Lahey Jr., R. T.: On the various forms of the conservation equations in two-phase flow, Intl. J. Multiphase Flow, v. 2, pp. 477-494 (1976)

APPENDIX C PUBLICATIONS

1. Ali, S. F., Yeung, H.: Experimental investigation and numerical simulation of two-phase flow in a large-diameter horizontal flow line vertical riser, J. Petroleum Science and Tech., v. 28, no. 11, pp. 1079 – 1095 (2010)

2. Fauer, D.: The making of a useful pipeline simulation model, Pipeline Simulation Interest Group, Paper No. 02W2 (2002)

3. Hauge, E.: Modeling and simulation of anti-slug control in Hydro experimental multiphase flow loop, M.Sc. Thesis, Nor. U. of Sci. and Tech. (2007)

4. Jain, R., Syal, S., Long, T., Wattenbarger, C., Kosik, I.: An integrated approach to design completions for horizontal wells for unconventional reservoirs, Soc. of Petroleum Engineers J., Paper No. 147120 (2013)

5. Johansen, T. E., Khoriakov, V.: Iterative techniques in modeling of multiphase flow in advanced wells and the near well region, J. Petrol Sci. Eng., v. 58, pp. 49-67 (2007)

6. Kashou, S., Mathews, P., Shea, D.: Transient modeling applications and lessons learned, case studies from oil and gas fields, 3rd N. American Conf. on Multiphase Tech., BHR Group, Banff, Canada (2002)

7. Miller, G. J., Pinguet, B. G., Theuveny, B., Mosknes, P. O.: The influence of liquid viscosity on multiphase flow meters, http://www.vannforeningen.no/ikbViewer/ Content/778329/14_Miller, TUV NEL Ltd. (2009)

APPENDIX D PUBLICATIONS

1. Azzopardi, B. J., Hills, J.: Flow patterns, transitions and models for specific flow patterns, Modeling and Experimentation in Two-Phase Flow, ed. V. Bertola, Springer Wein, New York (2003)

2. Barbosa, Jr., J. R., Govan, A. H., Hewitt, G. F: Visualization studies of churn flow in a vertical pipe, Intl. J. Multiphase Flow, v. 27, pp. 2105-2127 (2001)

3. Cai, Y., Wambsganss, M. W., Jendrzejczyk, J. A.: Application of chaos theory in identification of two-phase flow patterns and transitions in small, horizontal, rectangular channel, ASME J. Fluid Engineering, v. 118, pp. 383-390 (1996)

4. Chen, Y.: Modeling gas-liquid flow in pipes: flow pattern transitions and drift-flux modeling, M.S. Report, Stanford University (2001)

5. Choe, W. G., Weisman, J.: Flow patterns and pressure drop in co-current vapor-liquid flow – a state of the art report, Report for NSF Grant GK-40490, U. of Cincinnati (1974)

6. Costigan, G., Whalley, P. B.: Slug flow regime identification from dynamic void fraction measurements in vertical air-water flows, Intl. J. Multiphase Flow, v. 23, pp. 263-282 (1997)

7. Drahos, J., Cermak, J.: Diagnosis of gas-liquid flow patterns in chemical engineering systems, Chem. Eng. Process., v. 26, pp. 147-164 (1989)

8. Dukler, A. E., Taitel, Y.: Flow pattern transitions in gas-liquid systems – measurements and modeling, Multiphase Sci. and Tech., v. 2 (1986)

9. Hawkes, N. J., Lawrence, C. J., Hewitt, G. F.: Studies of wispy-annular flow using transient pressure gradient and optical measurements, Intl. J. Multiphase Flow, v. 26, pp. 1565-1582 (2000)

10. Hervieu, E., Seleshim Jr., P.: An objective indicator for two-phase flow pattern transition, Nucl. Eng. Des., v. 184, pp. 421-435 (1998)

11. Hewitt, G. F., Jayanti, S.: To churn or not to churn, Intl. J. of Multiphase Flow, Brief Comm., v. 19, no. 3, pp. 527-529 (1993)

12. Hewitt, G. F., Martin, C. J., Wilkes, N. S.: Experimental and modeling studies of annular flow in the region between flow reversal and the pressure drop minimum, PCH, v. 6, no. 1/2, pp. 69-86 (1985)

13. Hewitt, G. F.: Churn and wispy annular flow regimes in vertical gas-liquid flows, Energy and Fuels, v. 26, pp. 4067-4077 (2012)

14. Hewitt, G. F.: Measurement of two phase flow parameters, Academic Press, London (1978)

15. Hewitt, G. F.: Two-phase flow patterns and their relationship to two-phase heat transfer, Two-phase Flows and Heat Transfer, Kakac and Mayinger (eds.), Hemisphere, v. 1, pp. 11-35 (1977)

16. Hubbard, M. G., Dukler, A. E.: The characterization of flow regimes for horizontal two-phase flow, Proc. Heat Transfer and Fluid Mechanics Inst., Stanford U. Press, pp. 100-121 (1966)

17. Hubbard, M. G.: An analysis of horizontal gas-liquid slug flow, Ph.D. dissertation, U. of Houston (1965)

18. Ishii, M.: Thermo-fluid dynamic theory of two-phase flow, Eyrolles, Paris (1975)

19. Jones Jr., O. C., Zuber, N.: The interrelation between void fraction fluctuations and flow patterns in two-phase flow, Intl. J. Multiphase Flow, v. 2, pp. 273-306 (1975)

20. Mao, Z. S., Dukler, A. E.: The myth of churn flow?, Intl. J. of Multiphase Flow, Brief Comm., v. 19, no. 2, pp. 377-383 (1993)

21. Matar, O. K., Hewitt, G. F.: TMF prospectus, Joint Programme on Transient and Complex Multiphase Flows and Flow Assurance, http://multiphase.tech.cranfield.ac.uk/docs/TMF_Prospectus.pdf (2011)

22. Nguyen, V. T., Euh, D. J., Song, C. H. : An application of the wavelet analysis technique for the objective discrimination of two-phase flow patterns, Intl. J. Multiphase Flow, v. 36, pp. 755-768 (2010)

23. Osman, E. A.: Artificial neural networks models for identifying flow regimes and predicting liquid holdup in horizontal multiphase flow, Soc. of Petroleum Engineers, Paper No. 86910 (2004)

24. Pan, L.: High pressure three-phase (gas/liquid/liquid) flow, Ph.D. Thesis, Imperial College (1996)

25. Persen, L. N.: The mechanics of two phase flow, Institutt For Mekanikk, U. of Tronheim (1986)

26. Qi, F. S., Yeoh, G. H., Cheumg, S. C. P., Yu, J. Y., Krepper, E., Lucas, D.: Classification of bubbles in vertical gas-liquid flow – Part 1 – an analysis of experimental data, Intl. J. Multiphase Flow, v. 39, pp. 121-134 (2012)

27. Schlegel, J. P., Sawant, P., Paranjape, S., Ozar, B., Hibiki, T., Ishii, M.: Void fraction ad flow regime in adiabatic upward teo-phase flow in large diameter vertical pipes, Nucl. Eng. Des., v.239, pp. 2864-2874 (2009)

28. Tam, H. K., Tam, L. M., Ghajar, A. J., Cheong, C. W.: Development of a unified flow regime map for a horizontal pipe with the support vector machines, Proc. 2nd Intl. Symp. Computational Mechanics (ISCM II), Hong Kong, November 30th – December 3rd (2009)

29. Ternyik, J., Bilgesu, J. I., Mohaghegh, S., Rose, D. M.: Virtual measurement in pipes, part 1 – flowing bottomhole pressure under multiphase flow and inclined wellbore conditions, Soc. of Petroleum Engineers, Paper No. 30975 (1995)

30. Trafalis, T. B., Oladunni, O., Papavassiliou, D. V.: Two-phase flow regime identification with a multiclassification support vector machine (SVM) model, Ind. Eng. Chem. Res., v. 44, pp. 4414-4426 (2005)

31. Vial, C., Camarasa, E., Poncin, S., Wild, G., Midoux, N., Bouillard, J.: Study of hydrodynamic behavior in bubble columns and external-loop airlift reactors through analysis of pressure fluctuations, Chem. Eng. Sci., v. 55, pp. 2957-2973 (2000)

32. Vince, M. A., Lahey Jr., R. T.: On the development of an objective flow regime indicator, Intl. J. Multiphase Flow, v. 8, pp. 93-124 (1982)

33. Whalley, P. B.: Two-phase flow and heat transfer, Oxford Chemistry Primers, v. 42, Oxford U. Press (1996)

APPENDIX E PUBLICATIONS

1. Ansari, A. M.: A comprehensive mechanistic model for upward two-phase flow, M.S. Thesis, U. of Tulsa (1988)

2. Aydelotte, S. R.: Transient well testing in two-phase geothermal reservoirs, Lawrence Berkeley Laboratory Report LBL-10562, March (1980)

3. Barbuto, F. A. de A., Crowley, C. J.: On the comparison between two mechanistic models to predict pressure gradients in vertical two-phase flows, 5th Intl. Conf. on Multiphase Production, pp. 307-313, June 19-21, Cannes (1991)

4. Biberg, D., Holmas, H., Staff, G., Sira, T., Nossen, J., Andersson, P., Lawrence, C., Hu, B., Holmas, K.: Basic flow modeling for long distance transport of wellstream fluids, 14th Intl. Conf. on Multiphase Prod. Tech., BHR Group, Cannes, France (2009)

5. Corteville, J., Duchet-Suchaux, P., Lopez, D.: Comparison of methods for predicting pressure loss in oil and gas wells, 5th Intl. Conf. on Multiphase Production, BHR Group, Cannes, France (1991)

6. Garg, S. K., Combs, J., Kodama, M., Gokou, K.: Analysis of production/injection data from slim holes and large diameter wells at the Kirishima geothermal field, Japan, Proc. 23rd Workshop on Geothermal Reservoir Engineering, Stanford U., January 26-28 (1998)

7. Gomez, L. E., Shoham, O, Schmidt, Z., Chokshi, R. M., Brown, A., Northug, T.: A unified mechanistic model for steady-state two-phase flow in wellbores and pipelines, SPE Paper 56520 (1999)

8. Govier, G. W., Fogarasi, M.: Pressure drop in wells producing gas and condensate, J. Can. Pet. Tech. pp. 28-41, Oct.-Dec. (1975)

9. Gregory, G. A., Fogarasi, M., Aziz, K.: Analysis of vertical two-phase flow calculations – crude oil-gas flow in well tubing, J. Can. Petrol. Tech., v. January-March (1980)

10. Hasan, A. R., Kabir, C. S., Wang, X.: A robust steady-state model for flowing-fluid temperature in complex wells, Soc. of Petroleum Engineers, Paper No. 109765 (2009)

11. Hasan, A. R., Kabir, C. S.: A study of multiphase flow behavior in vertical wells, Soc. of Petroleum Engineers Prod. Eng., Paper No. 15138, pp. 263-272, May (1988a)

12. Hasan, A. R., Kabir, C. S.: Fluid flow and heat transfer in wellbores, Soc. of Petroleum Engineers (2002)

13. Ibe, M. C.: Determination of the best combination of pressure loss and PVT property correlations for use in upward two-phase flow, M.S. Thesis, U. of Tulsa (1979)

14. Kabir, C. S., Hasan, A. R.: Performance of a two-phase gas/liquid flow model in vertical wells, J. Petroleum Science and Engineering, v. 4, pp. 273-289 (1990)

15. Kabir, C. S., Hasan, A. R.: Simplified wellbore flow modeling in gas-condensate Systems, Soc. of Petroleum Engineers, Paper No. 89754 (2004)

16. Kaya, A. S., Sarica, C., Brill, J. P.: Mechanistic modeling of two-phase flow in deviated wells, Soc. of Petroleum Engineers, Paper No. 72998 (2001)

17. Messulam, S. A. G.: Comparison of correlations for predicting multiphase flow pressure losses in vertical pipes, M.S. Thesis, U. of Tulsa (1970)

18. Orkiszewski, J.: Predicting Two-Phase Pressure Drops in Vertical Pipes, SPE J. Pet. Tech., pp. 829-838, June (1967)

19. Peffer, J. W., Miller, M. A., Hill, A. D.: An improved method for calculating bottomhole pressures in flowing gas wells with liquid present, Soc. of Petroleum Engineers Production Engineering, Paper No. 15655, November (1988)

20. Reinicke, K. M., Remer, R. J., Hueni, G.: Comparison of measured and predicted pressure drops in tubing for high-water-cut gas wells, SPE Prod. Eng. J., pp. 165-177, Aug. (1987)

21. Robinson, J. R.: Development of a two-phase flow well data bank and an evaluation study of pressure loss methods applied to directional oil wells, M.S. Thesis, U. of Tulsa (1974)

22. Rossland, L.: Investigation of the performance of pressure loss correlations for high capacity wells, M.S. Thesis, U. of Tulsa (1981)

23. Smith, S. P.: Experimental investigation of multiple solutions for liquid holdup in upward inclined stratified flow, M.Sc. Thesis, U. of Calgary (1999)

24. Takacs, G.: Considerations on the selection of an optimum vertical multiphase pressure drop prediction model for oil wells, Soc. of Petroleum Engineers, Paper No. 68361 (2001)

25. Thompson, L. G.: Determination of optimum combination of pressure loss and PVT property correlations for predicting pressure gradients in upward two-phase flow, M.S. Thesis, U. of Tulsa (1982)

26. Zakarian, E., Holm, H., Larrey, D.: Discretization methods for multiphase flow simulation of ultra-long gas-condensate pipelines, 14th Intl. Conf. Multiphase Prod. Tech., BHR Group, Cannes, June 17-19 (2009)

APPENDIX F PUBLICATIONS

1. Biberg, D.: An explicit approximation for the wetted angle in two-phase stratified pipe flow, Can. J. Chem. Eng., v. 77, pp. 1221-1224 (1999)

APPENDIX G PUBLICATIONS

1. Ishii, M., Mishima, K.: Liquid transfer and entrainment correlation for droplet-annular flow, 7th Intl. Heat Transfer Conf., Muchen (1982)